

AD-A274 352



Internatio....  
Journal of



# quantum chemistry

QUANTUM CHEMISTRY

SYMPOSIUM NO 27, 1993

Proceedings of the  
International Symposium on  
Atomic, Molecular, and  
Condensed Matter  
Theory and  
Computational  
Methods

Held at the Ponce de Leon Conference Center  
St Augustine, Florida, March 13-20, 1993

Editor in Chief: Per-Olov Löwdin

Special Editors: N. Yngve Öhrn  
John R. Sabin  
Michael C. Zerner

An Interscience\* Publication  
published by JOHN WILEY & SONS

New York • Chichester • Brisbane • Toronto •  
Singapore

JQSAP  
ISSN 0360 8832

DTIC  
ELECTE  
DEC 21 1993  
S E D

Approved for public release  
Distribution

93-30462



92 13 4 3073

*International Journal of* QUANTUM CHEMISTRY

Quantum Chemistry Symposium No. 27

*Proceedings of the  
International Symposium on  
Atomic, Molecular, and Condensed Matter  
Theory and Computational Methods*

DTIC QUALITY INSPECTED 3

Held at St. Augustine, Florida, March 13-20, 1993

**Editor-in-Chief:** Per-Olov Löwdin

**Special Editors:** N. Yngve Öhrn, John R. Sabin, and  
Michael C. Zerner

an Interscience® Publication  
published by JOHN WILEY & SONS

John Wiley & Sons Inc.  
605 Third Avenue  
New York, NY 10158  
\$95.00 NWW 20 Dec 93

Accession For	
NTIS	CRA&I <input checked="" type="checkbox"/>
DTIC	TAB <input type="checkbox"/>
Unannounced <input type="checkbox"/>	
Justification <b>\$95.00</b>	
By .....	
Distribution /	
Availability Codes	
Dist	Availability or Special
<b>A-1</b>	



# *International Journal of* QUANTUM CHEMISTRY

## Quantum Chemistry Symposia

### Honorary Editorial Board:

Gerhard Herzberg      Kenichi Fukui

Editor-in-Chief: Per-Olov Lowdin

Editors: Jean-Louis Calais      N. Yngve Öhrn

Associate Editors: Erkki Brändas      Osvaldo Goscinski      John R. Sabin      Michael Zerner

### Editorial Board:

Tang Au-Chin	Laurens Jansen	Kimio Ohno	Alberte Pullman
Enrico Clementi	Norman H. March	Robert G. Parr	Bernard Pullman
Raymond Daudel	Roy McWeeny	Ruben Pauncz	Harrison Shull
Ernest Davidson	Saburo Nagakura	John A. Pople	Rudolf Zahradnik
George G. Hall			

### Advisory Editorial Board:

M. V. Basilevsky	G. Corongiu	M. S. Jhon	P. A. Kollman	M. A. Ratner
M. Bénard	G. Del Re	P. Jorgensen	C. Leforestier	W. G. Richards
F. Bernardi	P. Fulde	J. Jortner	S. Lunell	D. Salahub
J. Bertran	M. García-Sucre	U. Kaldor	Z. B. Maksic	N. F. Stepanov
G. Biczó	J. Gerratt	M. Karelson	J. P. Malneü	A. J. Thakkar
D. Bishop	N. C. Handy	J. Katriel	P. Mezey	O. Tapia
R. Carbó	A. E. Hansen	D. Klein	H. Monkhorst	S. B. Trickey
P. Carsky	J. T. Hynes	M. Klessinger	J. Oddershede	F. Weinhold
L. Cederbaum	B. Jezierski		P. Pulay	H. Weinstein

This volume constitutes a part of the annual subscription to the *International Journal of Quantum Chemistry*; vols 45–48, and as such is supplied without additional charge to subscribers. Single copies can be purchased from the Subscription Department, John Wiley & Sons, Inc.

The *International Journal of Quantum Chemistry* (ISSN 0020-7608) is published semi-monthly with two extra issues in November, by John Wiley & Sons, Inc. Copyright © 1993 John Wiley & Sons, Inc. All rights reserved. No part of this publication may be reproduced in any form or by any means, except as permitted under section 107 or 108 of the 1976 United States Copyright Act, without either the prior written permission of the publisher, or authorization through the Copyright Clearance Center, 27 Congress Street, Salem, MA 01970, (508) 744-3350, fax (508) 745-9379. Second-class postage paid at New York, NY, and at additional mailing offices.

The code and the copyright notice appearing at the bottom of the first page of an article in this journal indicate the copyright owner's consent that copies of the article may be made for personal or internal use, or for the personal or internal use of specific clients, on the condition that the copier pay for copying beyond that permitted by Sections 107 or 108 of the U.S. Copyright Law. This consent does not extend to other kinds of copying, such as copying for general distribution, for advertising or promotional purposes, for creating new collective works, or for resale. Such permission requests and other permission inquiries should be addressed to the Permissions Dept. Subscription price (1993), \$2,465.00 in the US, \$2,725.00 in Canada and Mexico, \$2,822.50 outside North America. All subscriptions outside US will be sent by air. Personal rate (available only if there is an institutional subscription), \$125.00 in North America, \$255.00 outside North America. Subscriptions at the personal rate are available only to individuals. Payment must be made in US dollars drawn on a US bank. Claims for undelivered copies will be accepted only after the following issue has been received. Please enclose a copy of the mailing label. Missing copies will be supplied when losses have been sustained in transit and where reserve stock permits. Please allow four weeks for processing a change of address. For subscription inquiries, please call (212) 850-6645.

Postmaster: Send address changes to Subscription Department, John Wiley & Sons, Inc., 605 Third Avenue, New York, New York 10158.

Printed in the United States of America

This journal is printed on acid-free paper.

# Contents

Introduction	
<i>N. Y. Öhrn, J. R. Sabin, and M. C. Zerner</i>	ix
List of Participants	xi
My Life as a Physicist: Memories and Perspectives	
<i>C. C. J. Roothaan</i>	1
New Algorithms for Calculating $3n-j$ Symbols	
<i>C. C. J. Roothaan</i>	13
The Diatomic Molecule Project at LMSS 1956–1966: Broken Bottlenecks	
<i>B. J. Ransil</i>	25
Statistical Electron Correlation Coefficients for 29 States of the Heliumlike Ions	
<i>N. M. Cann, R. J. Boyd, and A. J. Thakkar</i>	33
Investigation of the Correlation Energy Component of the Intermolecular Interaction Energy	
<i>E. Kapuy, F. Bogár, C. Kozmutza, and E. Tfirst</i>	43
Triple Excitations in Coupled-Cluster Theory: Energies and Analytical Derivatives	
<i>J. D. Watts and R. J. Bartlett</i>	51
Electron Propagator Theory with the Ground State Correlated by the Coupled-Cluster Method	
<i>L. Meissner and R. J. Bartlett</i>	67
On the Removal of the Exchange Singularity in Extended Systems	
<i>G. Aissling and H. J. Monkhorst</i>	81
In Memoriam: Michael Andreas Schlüter, 1945–1992	
<i>L. Fritsche, H. Monkhorst, and S. Trickey</i>	91
Local Density and Gradient-Corrected Functionals for Short-Range Correlation: Antiparallel-Spin and Non-RPA Contributions	
<i>J. P. Perdew</i>	93
Asymptotic Structure of the Kohn–Sham Effective Potential at Metal Surfaces	
<i>M. K. Harbola and V. Sahni</i>	101
Correlation Corrected Band Structures of Quasi 1D and 2D Periodic Systems and Level Distributions of Disordered Chains: New Method with Correlation for Dynamic Nonlinear Optical Properties of Periodic Polymers	
<i>J. Ladik and P. Otto</i>	111

Third-Order Møller-Plesset Perturbation Theory of Electron Correlation in Infinite Systems: A Comparison of Carbon- and Silicon-Based Polymers <i>S. Suhai</i> .....	131
Spin-Polarized LCGTO-FF Band Structure Technique: Application to 3d Transition Metal Monolayers <i>J. C. Boettger</i> .....	147
Density-Functional Theory in Glass Chemistry <i>M. P. Teter</i> .....	155
<i>Ab Initio</i> Investigation of Void Stabilization: Oxygen in Nickel <i>R. C. Boehm and A. Banerjee</i> .....	163
V <sup>4+</sup> Doping into SiO <sub>2</sub> , ZrO <sub>2</sub> and ZrSiO <sub>4</sub> Structures. An <i>Ab Initio</i> Perturbed Ion Study <i>J. Andrés, A. Beutrán, J. Carda, and G. Monrós</i> .....	175
Towards an Understanding of the Electronic Structure of Mott-Insulating Transition Metal Oxides <i>C. Mei and V. H. Smith, Jr.</i> .....	187
Electronic and Geometric Characteristics of Precrystalline Structures in Highly Dispersed Rh Catalysts <i>G. L. Estiu and M. C. Zerner</i> .....	195
Electronic States Induced by a Ga Vacancy in the GaAs <sub>1-x</sub> P <sub>x</sub> Alloy <i>L. M. R. Scolfaro, R. Pintanel, A. Fazzio, and J. R. Leite</i> .....	213
Electronic Stopping Power for Protons in an LiF Monolayer <i>J. Z. Wu, S. B. Trickey, and J. R. Sabin</i> .....	219
Some Density-Functional LMTO Studies of Electronic Properties of Quasi-One-Dimensional Systems <i>M. Springborg</i> .....	227
Rules for Intrinsically (Super) Conducting Polymers <i>G. Aissing, H. J. Monkhorst, and C. Hu</i> .....	245
Energetics of Small Clusters of Stabilized Jellium: Continuum and Shell-Structure Effects <i>M. Brajczewska, C. Fiolhais, and J. P. Perdew</i> .....	249
Density-Functional and <i>Ab Initio</i> Computational Studies of Palladium Clusters <i>J. M. Seminario, M. C. Concha, and P. Politzer</i> .....	263
Multiconfigurational Spin-Adapted Single-Reference Coupled Cluster Formalism <i>X. Li and J. Paldus</i> .....	269

Computation and Analysis of the Full Configuration Interaction Wave Function of Some Simple Systems <i>G. L. Bendazzoli and S. Evangelisti</i> . . . . .	287
A Note on the Calculation of Some Transformation Coefficients <i>Z. Wen</i> . . . . .	303
Rigorous Interpretation of Electronic Wavefunctions. IV. Origins of the Unusual Stability of the 1,3-Dimethylimidazol-2-Ylidene Carbene <i>J. Cioslowski</i> . . . . .	309
Molecular SCF Calculations Using a Basis of Numerical Orbitals <i>J. D. Talman</i> . . . . .	321
Basis Set Dependence of <i>Ab-Initio</i> Calculated Vibration Frequencies <i>M. Flock and M. Ramek</i> . . . . .	331
Double and Quadruple Zeta Contracted Gaussian Basis Sets for Hydrogen through Neon <i>A. J. Thakkar, T. Koga, M. Saito, and R. E. Hoffmeyer</i> . . . . .	343
Kinetic Energy Component in the Divide-and-Conquer Method <i>Z. Zhou</i> . . . . .	355
Statistical Microdynamics of Extended Systems in Natural Function Spaces <i>R. G. Brown and M. Cifan</i> . . . . .	363
Determinantal Inequalities among $\langle r^n \rangle$ <i>P. Csavinsky</i> . . . . .	377
Relativistic Quantum Defect Orbital Calculations of Singlet-Singlet Transitions in the Zinc and Cadmium Isoelectronic Sequences <i>C. Lavín, P. Martin, I. Martin, and J. Karwowski</i> . . . . .	385
Properties of the Two-Electron Ionization Ladder and Related Good Quantum Numbers <i>Y. Komninos, S. Themelis, M. Chrysos, and C. A. Nicolaidis</i> . . . . .	399
A Comparison of Ground-State Averages in Electron Propagator Theory <i>J. V. Ortiz</i> . . . . .	407
Comparison of Ground and Triplet State Geometries of Malonaldehyde <i>K. Luth and S. Scheiner</i> . . . . .	419
Electric Multipole Moment Integrals Evaluated over Slater-Type Orbitals <i>X. Zheng and M. C. Zerner</i> . . . . .	431
Success and Pitfalls of the Dielectric Continuum Model in Quantum Chemical Calculations <i>A. H. de Vries, P. Th. van Duijnen, and A. H. Juffer</i> . . . . .	451

Quantum Field Theoretical Methods in Chemically Bonded Systems. V. Potential Energy Curves for $N_2$ ( $X^1 \Sigma_g^+ \rightarrow 2N(^4S)^*$ ) <i>T. E. Sorensen, W. B. England, and D. M. Silver</i> . . . . .	467
<i>Ab initio</i> SCF Investigation of the Potential Energy Surface of 4-Aminobutanol <i>A.-M. Kelterer and M. Ramek</i> . . . . .	479
Solvent Effect on the Potential Surface of the Proton Transfer in $[H_3N-H-NH_3]^+$ <i>J. Gao</i> . . . . .	491
Instability in Chemical Bonds. II. Theoretical Studies of Exchange-Coupled Open-Shell Systems <i>K. Yamaguchi, M. Okumura, K. Takada, and S. Yamanaka</i> . . . . .	501
Quantum Wavepacket Dynamics for the $^1\Sigma^+$ States of Boron Hydride <i>J. Broeckhove, B. Feyen, P. Van Leuven, R. Cimraglia, and M. Persico</i> . . . . .	517
An Improved Eikonal Treatment of Rotationally Inelastic He—H <sub>2</sub> Scattering <i>J. M. Cohen and G. R. Famini</i> . . . . .	527
Assessment of Molecular Shape Fluctuations Along Dynamic Trajectories <i>G. A. Arteca</i> . . . . .	547
Quantum Functional Sensitivity Analysis for the 3-D ( $J = 0$ ) H + H <sub>2</sub> Reaction <i>J. Chang and N. J. Brown</i> . . . . .	567
Theoretical Study of the Reaction of Cd ( $^1S$ , $^3P$ , $^1P$ ) with the Methane Molecule <i>S. Castillo, A. Ramírez-Solís, and E. Poulain</i> . . . . .	587
Use of Energy Partitioning for Predicting Primary Mass Spectrometric Frag- mentation Steps: A Preliminary Account <i>I. Mayer and Á. Gömöry</i> . . . . .	599
Light Particles Interacting with Organic Molecules <i>N. H. March</i> . . . . .	607
Partial Widths of Feshbach Funnel Resonances in the Na(3p) · H <sub>2</sub> Exciplex <i>S. L. Mielke, G. J. Tawa, D. G. Truhlar, and D. W. Schwenke</i> . . . . .	621
Critical Test of PM3-Calculated Proton Affinities <i>P. Burk, K. Herodes, I. Koppel, and I. Koppel</i> . . . . .	633
ZnO Clusters Models: An AM1 and MNDO Study <i>J. B. L. Martins, E. Longo, and J. André</i> . . . . .	643
Correlation and Pairing in $C_{60}^{2n-}$ Ions. Superconductivity of Alkali and Alkaline Earth Compounds of C <sub>60</sub> <i>S. Larsson and L. Rodriguez-Monge</i> . . . . .	655
<i>Ab Initio</i> Coupled and Uncoupled Hartree-Fock Calculations of the Polar- izabilities of Finite and Infinite Polyacetylene Chains <i>B. Champagne, D. H. Mosley, and J.-M. André</i> . . . . .	667

A Green's Function Calculation of the Zero-Voltage STM Resistance of a One-Dimensional Chain Coupled to Two Jellium Surfaces <i>V. Mujica and G. Doyen</i> . . . . .	687
Intramolecular Coupling Effect in the Refractive Index for a Simple Three-Level Model of Molecules Diluted in Water <i>M. Garcia-Sucre, J. L. Paz, E. Squitieri, and V. Mujica</i> . . . . .	699
Theoretical Study of the C- vs. O-Acylation of Metal Enolates. Frontier Molecular Orbital Analysis Including Solvent Effects <i>V. G. Saragoni, R. R. Contreras, A. J. Aizman</i> . . . . .	713
Quantum Defect Orbital Study of Electron Transitions in Rydberg Molecules. I. Triatomic Hydrogen <i>I. Martin, J. Karwowski, G. H. F. Diercksen, and C. Lavin</i> . . . . .	723
<i>Ab Initio</i> Study of the Ground and Excited States of LiNe <i>J. Sadlej and W. D. Edwards</i> . . . . .	731
Theoretical Study of the Geometric Structures and Energetic Properties of Anionic Clusters. $\text{Ag}_n^-$ ( $n = 2$ to 6) <i>I. G. Kaplan, R. Santamaria, and O. Novaro</i> . . . . .	743
Accurate LCAO Ground State Calculations of $\text{HeH}^{2+}$ Using Slater-Type Orbitals <i>B. Etemadi and H. W. Jones</i> . . . . .	755
Low-Lying States of $\text{SF}_6$ and $\text{SF}_6^-$ : Electron Affinity of $\text{SF}_6$ and Electron Detachment of $\text{SF}_6^-$ <i>K. W. Richman and A. Banerjee</i> . . . . .	759
High Performance Computing in Chemistry and Massively Parallel Computers: A Simple Transition? <i>R. A. Kendall</i> . . . . .	769
Atomistic Simulations on Parallel Architectures <i>R. K. Kalia, W. Jin, S. W. de Leeuw, A. Nakano, and P. Vashishta</i> . . . . .	781
Efficient Computation of Electron-Repulsion Integrals in <i>Ab Initio</i> Studies of Polymeric Systems <i>D. H. Mosley, J. G. Fripiat, B. Champagne, and J.-M. André</i> . . . . .	793
Experiments Pursuant to Determining the Barrier Traversal Time for Quantum Tunneling <i>M. J. Hagmann and L. Zhao</i> . . . . .	807
Theoretical Studies of the Oxidation of N- and S-Containing Compounds by Cytochrome P450 <i>G. H. Loew and Y.-T. Chang</i> . . . . .	815
Author Index . . . . .	827

## Introduction

The 33rd annual Sanibel Symposium, organized by the faculty and staff of the Quantum Theory Project of the University of Florida, was held March 13 to 20, 1993, at the Ponce de Leon Conference Center located at the north gate of the city of St. Augustine, Florida. In spite of extreme weather conditions with high winds, rain, and cold temperatures that crippled air traffic along the entire eastern seaboard, over 320 participants gathered for 8 days of lectures and informal discussions. Tornadoes touched down at the conference site and the schedule had to be worked around power outages and telephone interruptions, but the adverse conditions did not in the least affect the high quality of the daily schedule packed with plenary sessions in the morning and late afternoon, and with poster presentations in the evening, often lasting until midnight.

The program contained a special tribute to the work of Professor Clemens Root-haan and a retrospective on the Chicago School of Theoretical Chemistry, with some of the key members of that school representing several generations of scientists giving plenary lectures.

The format of the symposium adopted for the past few years was followed again this year with a compact 8-day schedule with an integrated program of quantum biology, quantum chemistry, and condensed matter physics. The topics of the sessions covered by these proceedings include Advanced Scientific Computing, Interaction of Photons and Matter, Quantum Molecular Dynamics, Electronic Structure Methods, Polymeric Systems, and Quantum Chemical Methods for Extended Systems.

Special sessions were held in memory of Thomas D. Bouman and Michael Schlüter, who both were regular participants in these symposia.

The articles have been subjected to the ordinary refereeing procedures of *The International Journal of Quantum Chemistry*. The articles presented in the sessions on quantum biology and associated poster sessions are published in a separate volume of the *The International Journal of Quantum Chemistry*.

The organizers acknowledge the following sponsors for their support of the 1993 Sanibel Symposium:

- U.S. Army Research Office (Physics) CRDEC through Grant DAAH04-93-G-0072 "The views, opinions, and/or findings contained in this reports are those of the author(s) and should not be construed as an official Department of the Army position, policy, or decision, unless so designated by other documentation."
- U.S. Environmental Protection Agency through Grant N00014-93-1-0343
- The Office of Naval Research (Physics and Chemistry), through Grant N00014-93-1-0343

"This work relates to Department of Navy Grant N00014-93-1-0343 issued by the Office of Naval Research. The United States Government has a royalty-free license throughout the world in all copyrightable material contained in the publication."

- U.S. Department of Energy through Grant DE-FG05-93ER615
- Digital Equipment Corporation
- IBM
- Kendall Square
- The University of Florida

Very special thanks go to the staff of the Quantum Theory Project of the University of Florida for handling the numerous administrative, clerical, and practical details. The organizers are proud to recognize the contributions of Mrs. Judy Parker, Ms. Robin Bastanzi, Mrs. Sue Linsley, Ms. Arline Succow, Mr. Sullivan Beck, Dr. Agustin Diz, Dr. Erik Deumens, Dr. Hugh Taylor. All the graduate students of the Quantum Theory Project, who served as "gofers" are gratefully recognized for their contributions to the 1993 Sanibel Symposium.

N. Y. ÖHRN  
J. R. SABIN  
M. C. ZERNER



# 1993 Sanibel Symposia List of Participants

**WILLIAM ADAMS**  
Rutgers University  
Department of Chemistry  
P.O. Box 939  
Piscataway, NJ 08855-0939

**REINHART AHLRICHS**  
Universitat Karlsruhe  
Inst. f. Phys. Chemie  
Kaiserstr. 12  
Karlsruhe D-7500 Germany

**GERRARD AISSING**  
University of Florida  
Quantum Theory Project  
362 Williamson Hall  
Gainesville, FL 32611-2085

**ARIE AIZMAN**  
Universidad Tecnica Federico Santa Maria  
Department of Chemistry  
Casilla 110-V, Valparaiso  
Chile

**STEVE ALEXANDER**  
University of Florida  
Department of Physics  
Gainesville, FL 32611-2085

**JAN ANDZELM**  
BIOSYM Technologies, Inc.  
9685 Scranton Road  
San Diego, CA 92121-2777

**GUSTAVO ARTECA**  
Laurentian University  
Chemistry & Biochemistry Dept.  
Ramsey Lake Road  
Sudbury, ON P3E 2C6  
Canada

**VIKTORYA AVIYENTE**  
Bogazici University  
Chemistry Department  
Bebek, Istanbul 80815  
Turkey

**NAOUM BACALIS**  
National Hellenic Research Foundation  
Vassileos Constantinous 48  
Athens GR-11635  
Greece

**PAUL BAGUS**  
IBM Research Division  
K32/802, 650 Harry Road  
San Jose, CA 95120-6099

**ANNA BALKOVA**  
University of Florida  
Quantum Theory Project  
370 Williamson Hall  
Gainesville, FL 32611-2085

**LAURENZ BALTZER**  
J. C. Baltzer AG Science Publishers  
Asterweg 1A  
Amsterdam, HL 1031  
The Netherlands

**AJIT BANERJEE**  
INEL  
P.O. Box 1625  
Idaho Falls, ID 83415-2208

**VICTOR BARANOVSKI**  
University of Georgia  
CCQC  
Athens, GA 30602

**SULLIVAN BECK**  
University of Florida  
Quantum Theory Project  
348 Williamson Hall  
Gainesville, FL 32611-2085

**DARIO BEKSIC**  
University of Florida  
Quantum Theory Project  
215 Williamson Hall  
Gainesville, FL 32611-2085

**ARMANDO BELTRÁN**  
Universitat Jaume I  
Dept. of Experimental Sciences  
Apartat 242, Castello  
Spain

RAJIV BENDALE  
University of Florida  
Quantum Theory Project  
378 Williamson Hall  
Gainesville, FL 32611-2085

GIAN BENDAZZOLI  
University of Bologna  
Chimica Fisica ed Inorganica  
Viale Risorgimento  
Bologna I-40136  
Italy

CHARLIE BENDER  
Ohio Supercomputer Center  
1224 Kinnear Road  
Columbus, OH 43212

DAVID BERATAN  
University of Pittsburgh  
Department of Chemistry  
Pittsburgh, PA 15260

GORAN BERGSON  
Uppsala University  
Department of Chemistry  
P.O. Box 531  
Uppsala S-75121  
Sweden

SIGALIT BERKOVIC  
Tel-Aviv University  
Department of Chemistry  
15/6 Spinoza St.  
Rehovot 76452  
Israel

MANUEL BERRONDO  
Brigham Young University  
Department of Physics  
296 ESC  
Provo, UT 84602-1022

R. BERRY  
University of Chicago  
Chemistry Department  
5735 So. Ellis Avenue  
Chicago, IL 60637-1403

DAVID BISHOP  
University of Ottawa  
Department of Chemistry  
Ottawa, ON K1M 073  
Canada

FRANK BLANEY  
Smithkline Beecham Medicinal Research Center  
Computational Chemistry  
Coldharbour Road  
Harlow Essex CM19 4AD  
England

JONATHAN BOETTGER  
Los Alamos National Laboratory  
Group-T, MS B221  
Los Alamos, NM 87545

VLASTA BONACIC-KOUTECKY  
Freie Universitat Berlin  
Inst. f. Phys. und Theo. Chem.  
Takustr. 3  
Berlin, 33 1000  
Germany

RICHARD BONE  
McMaster University  
Chemistry Department  
1280 Main Street, W.  
Hamilton, ON L8S 4M1  
Canada

SLOBADAN BOSANAC  
R. Boskovic Institute  
Bijenicka C. 54  
Zagreb 41004  
Croatia

EDWARD BOUDREAUX  
University of New Orleans  
Department of Chemistry  
New Orleans, LA 70148-2810

MARCUS BREWSTER  
Pharmos Corporation University of Florida  
P.O. Box 730  
Alachua, FL 32615

NILS BRINCK  
University of New Orleans  
Department of Chemistry  
New Orleans, LA 70148-2820

JAN BROECKHOVE  
RUCA  
Dept. Informatica  
Groenenborgerlaan 171  
Antwerp B2020  
Belgium

**RIA BROER**

University of Groningen  
Dept. of Chemical Physics  
Nijenborgh 4  
Groningen, AG 9747  
The Netherlands

**ANDERS BROO**

University of Florida  
Quantum Theory Project  
362 Williamson Hall  
Gainesville, FL 32611-2085

**FRANK BROWN**

Glaxo Inc. Research Institute  
Structural & Biophysical Group  
5 Moore Drive, 3.4034  
Res. Triangle Park, NC 27709

**PAUL CADE**

University of Massachusetts  
Chemistry Department  
Amherst, MA 01003

**NATALIE CANN**

Dalhousie University  
Department of Chemistry  
Halifax, Nova Scotia B3H 4J3  
Canada

**CHRISTIAN CARDENAS**

University of Florida  
Quantum Theory Project  
362 Williamson Hall  
Gainesville, FL 32611-2085

**SIDONIO CASTILLO-ANIMAS**

Universidad Autonoma Metropolitana-  
Azcapotzalco  
Depto. de Fisica  
Av. San Pablo No 180  
Azcapotzalco, DF 02200  
Mexico

**EDUARDO CASTRO**

Universidad Nacional de La Plata  
Departamento de Quimica  
47 y 115 C.C. 962  
La Plata, Bs. As. 1900  
Argentina

**SUBHAS CHAKRAVORTY**

Indiana University  
Department of Chemistry  
Bloomington, IN, IN 47405

**MATT CHALLCOME**

Florida State University  
SCRI  
Tallahassee, FL 32306

**BENOÎT CHAMPAGNE**

University of Florida  
Quantum Theory Project  
372 Williamson Hall  
Gainesville, FL 32611-2085

**JOHNNY CHANG**

Lawrence Berkeley Laboratory  
M/S B29C-100  
Cyclotron Road  
Berkeley, CA 94720-0001

**YAN-TYNG CHANG**

Molecular Research Institute  
845 Page Mill Road  
Palo Alto, CA 94304-1011

**HANSONG CHENG**

Air Products & Chemical, Inc.  
MIS/RES  
7201 Hamilton Boulevard  
Allentown, PA 18195-1501

**PAUL CHUN**

University of Florida  
Department of Molecular Bio.  
Box 100245  
J.H.M.H.C.  
Gainesville, FL 32610-0245

**MIKAEL CIFTAN**

Duke University  
Department of Physics  
2606 Tryon Road  
Durham, NC 27705

**JERZY CIOSLOWSKI**

Florida State University  
Department of Chemistry  
Tallahassee, FL 32306-3006

ENRICO CLEMENTI

CRS4

P.O. Box 488

Cagliari I-09100

Italy

JOEL COHEN

U.S. Army Chemical Research Development  
& Engineering Ctr.

SMCCR-RSP-C

Aberdeen Proy. Gr., MD 21010-5423

DON COMEAU

University of Florida

Quantum Theory Project

372 Williamson Hall

Gainesville, FL 32611-2085

CHIARA COMETTA-MORINI

Technische Universitat Munchen

Theoretische Physik, T38

Boltzmannstrass

Garching D08046

Germany

RENATO CONTRERAS

Universidad de Chile

Departamento de Quimica

Casilla 653, Santiago

Chile

MICHAEL COOLIDGE

Frank J. Seiler Research Laboratory

2345 Vanderbilt Drive

Suite 2A35

USAF Academy, CO 80840-6272

HERBERT da COSTA

University of Florida

Quantum Theory Project

372 Williamson Hall

Gainesville, FL 32611-2085

PETER CSAVINSZKY

University of Maine

Department of Physics

Bennett Hall

Orono, ME 04469-0108

ROBIN DAVIES

University of Wales

College of Cardiff

Welsh School of Pharmacy

King Edward VII Avenue

Cardiff, Wales CF1 3XF

United Kingdom

EDGAR DAZA

Universidad Nacional de Colombia

Departamento de Quimica

Calle 53, No. 28016, Apto. 501

Santafe de Bogota

Colombia

JANET DEL BENE

Youngstown State University

Department of Chemistry

Youngstown, OH 44555

JOHN DELOS

Harvard University Center of Astrophysics

60 Garden Street

Mail Stop 14

Cambridge, MA 02138

ALEXANDER DEMCHENKO

Florida State University

Inst. of Molecular Biophysics

B-165, MBB 452

Tallahassee, FL 32306-3015

JOHN DETRICH

IBM

E39S MS4305

11400 Burnet Road

Austin, TX 78758

ERIK DEUMENS

University of Florida

Quantum Theory Project

362 Williamson Hall

Gainesville, FL 32611-2085

AGUSTIN DIZ

University of Florida

Quantum Theory Project

376 Williamson Hall

Gainesville, FL 32611-2085

MARIA DONNAMARIA  
IFLYSIB-(UNLP) 59 N0789  
CC565 (1900) La Plata  
La Plata  
Argentina

XIOFENG DUAN  
Southern Illinois University  
Chemistry Department  
Carbondale, IL 62901-4409

PIET VAN DUIJEN  
University of Groningen  
Chemistry Department  
Nijenborgh 4  
Groningen, AG 9747  
The Netherlands

W. EDWARDS  
University of Idaho  
Department of Chemistry  
Moscow, ID 83844-2343

MOSHE EISENBERG  
SUNY School of Medicine  
Pharmacological Sciences  
Stony Brook, NY 11794-8651

IAN ELLERY  
Digital Equipment Corp.  
5000 N.W. 34th St. Suite 18  
Gainesville, FL 32605-8666

WALTER ENGLAND  
University of Wisconsin  
Chemistry Department  
3210 North Cramer Street  
Milwaukee, WI 53211

LEIF ERIKSSON  
Dalhousie University  
Department of Chemistry  
Halifax, Nova Scotia B3H 4J3  
Canada

GUILLERMINA ESTIU  
Universidad Nacional de La Plata  
Departamento de Química  
Calle 47 y 115, CC 962  
La Plata 1900  
Argentina

BABAK ETEMADI  
Florida A&M University  
Department of Physics  
Tallahassee, FL 32307

WALTER FABIAN  
Karl-Franzens-Universität Graz  
Organische Chemie  
Heintichstr 28  
Graz A-8010  
Austria

DAVID FAGERBURG  
Eastman Chemical Co.  
Research Labs  
P.O. Box 1972  
Kingsport, TN 37662

KIM FERRIS  
Pacific Northwest Laboratories  
P.O. Box 999, K2-44  
Richland, WA 99352

KALUS FIEDLER  
Kai e.v. WIP 005822/C  
Rudower Chaussee 5  
Berlin, D-0-1199  
Germany

CARLOS FIOLHAIS  
University of Coimbra  
Department of Physics  
Coimbra P-3000  
Portugal

GEORGE FITZGERALD  
Cray Research  
655 E. Lone Oak Drive  
Eagan, MN 55044

MICHAELA FLOCK  
Technical University of Graz  
Institut für Physikalische und Theoretische Chemie  
Graz A-8010  
Austria

ROBERT FLURRY  
University of New Orleans  
625 Dauphine Street  
New Orleans, LA 70112

PAUL FRIEDMAN  
Pratt Institute  
Math & Science Department  
200 Willoughby Avenue  
Brooklyn, NY 11205

ERHARD GEY  
WIP KAIEV  
Zinsgutstrasse 9  
Berlin D-1199  
Germany

LOTHAR FRITSCHÉ  
TU Clausthal  
Institut für Theoretische  
Physik, Leibnizstrasse 10  
Clausthal, Zellerfeld 3392  
Germany

ERIC GLENDENING  
Battelle Pacific Northwest Lab  
MS K1-90, Battelle Blvd.  
Richland, WA 99352

PATRICIO FUENTEALBA  
Universidad de Chile  
Depto. de Física  
Las Palmeras 3425, Cas. 653, Santiago  
Chile

LIONEL GOODMAN  
Rutgers University  
Chemistry Department  
Wright & Rieman Laboratories  
New Brunswick, NJ 08903

JIALI GAO  
State University of New York at Buffalo  
Department of Chemistry  
3425 Main Street  
Buffalo, NY 14214

OSVALDO GOSCINSKI  
Uppsala University  
Quantum Theory Project  
Box 518  
Uppsala S-751-20  
Sweden

MAXIMO GARCIA-SUCRE  
IVIC  
Centro de Física  
Apatado 21827  
Caracas 2020A  
Venezuela

ANTE GRAOVAC  
The R. Boskovic Institute  
POB 1016  
Bijenicka C. 54  
Zagreb HR-41001  
Croatia

JORGE GARZA  
Universidad Autónoma Metropolitana-Iztapalapa  
Department of Chemistry  
Av. Michoacán y Purísima  
Mexico, DF 09340  
Mexico

STEVEN GWALTNEY  
University of Florida  
Quantum Theory Project  
345 Williamson Hall  
Gainesville, FL 32611-2085

JURGEN GAUSS  
Universität Karlsruhe  
Institut für Physikalische Chemie  
Karlsruhe D7500  
Germany

DARUIH HABIBOLLAHZADEH  
University of New Orleans  
Department of Chemistry  
New Orleans, LA 70148-2820

JOSEPH GERRATT  
University of Bristol  
School of Chemistry  
Cantock's Close  
Bristol BS8 1PS  
United Kingdom

MARK HAGMANN  
Florida International University  
Electrical and Computer Eng.  
University Park Campus  
Miami, FL 33199

# LIST OF PARTICIPANTS

xvii

AAGE HANSEN  
University of Copenhagen  
Department of Chemistry  
Copenhagen DK-2100  
Denmark

FRANK HARRIS  
University of Utah  
Chemistry Department  
Salt Lake City, UT 84112-3692

LEO HERBETTE  
University of Connecticut Health Center  
Radiology Department  
263 Farmington Avenue  
Farmington, CT 06030-2017

JORGE HERNANDEZ-COBOS  
Universidad Nacional Autonoma de Mexico  
Lab. de Cuernavaca  
Apdo. Postal 139-B  
Cuernavaca, Morelos 62190  
Mexico

JESUS HERNANDEZ-TRUJILLO  
Universidad Nacional Autonoma de Mexico  
Departamento de Fisica y Quimica Teorica  
Mexico, DF 04510  
Mexico

RICHARD HILDERBRANDT  
The National Science Foundation  
Chemistry Division  
1800 6th Street, N.W.  
Washington, DC 20550

JURGEN HINZE  
Universitat Bielefeld  
Fakultat fur Chemie  
Bielefeld D 4800  
Germany

HIROAKI HIROSE  
University of Florida  
Quantum Theory Project  
379 Williamson Hall  
Gainesville, FL 32611-2085

THOMAS HOCKSWENDER  
PPG Industries  
P.O. Box 9  
Allison Park, PA 15101

MILAN HODOSCEK  
NIH  
Bldg 12A, RM 2057  
Bethesda, MD 20814

GEORG HOHLNEICHER  
University of Cologne  
Physikal Chemie  
Luxembargarstr. 116, Koln 5000  
Germany

MING-JU HUANG  
University of Florida  
Center for Drug Discovery  
P.O. Box 100497  
Gainesville, FL 32610-0497

ERIC JAKOBSSON  
University of Illinois NCSA  
4039 Beckman Institute  
405 North Mathews Avenue  
Urbana, IL 61801-2300

HERBERT JONES  
Florida A&M University  
Department of Physics  
Tallahassee, FL 32307

KENNETH JORDAN  
University of Pittsburgh  
Department of Chemistry  
Chevron Science Center  
Pittsburgh, PA 15260

KARL JUG  
Universitat Hannover  
Theoretische Chemie  
Am Kleinen Felde 30  
Hannover 1 3000  
Germany

RAJIV KALIA  
Louisiana State University  
Physics & Astronomy Dept.  
225 B Nicholson Hall  
Baton Rouge, LA 70803-4001

ILYA KAPLAN  
UNAM  
Instituto de Fisica  
Apartado Postal 20-364  
Mexico, DF 01000  
Mexico

## EDE KAPUY

Jozsef Attila University  
Theoretical Physics Department  
Aradi vertanuk tere 1  
Szeged H-6720  
Hungary

## RICK KENDALL

Pacific Northwest Laboratory  
Molecular Science Research Ctr  
P.O. Box 999, MSIN K1-90  
Richland, WA 99352

## JAMES KING

U.S. Army Edgewood RD&E Center  
SCBRD-RTS  
Aberdeen Prov. Gr., MD 21010-5423

## ROBERT KIRBY

Allelix Biopharmaceuticals, Inc.  
6850 Goreway Drive  
Mississauga, ON L4V 1P1  
Canada

## BERNARD KIRTMAN

University of California  
Department of Chemistry  
Santa Barbara, CA 93106-9510

## LEO KLASINC

Louisiana State University  
Department of Chemistry  
Baton Rouge, LA 70803-1804

## HENRIK KOCH

UNI-C  
Olof Palmes Alle 38  
Aarhus N 8200  
Denmark

## PETER KOLLMAN

University of California  
Pharmaceutical Chemistry Dept.  
School of Pharmacy  
San Francisco, CA 94143-0446

## YANNIS KOMNINOS

National Hellenic Research Foundation  
Theoretical Chemistry Dept.  
Vs. Constantinou Ave. 48  
Athens 11635  
Greece

## ANDREW KOMORNICKI

Polyatomics Research Institute  
1101 San Antonio Road  
Suite 420  
Mountain View, CA 94043

## ANTONIOS KOURES

Allied Signal  
50 E. Algonquin Road  
Des Plaines, IL 60017

## PAWEL KOZLOWSKI

Indiana University  
Department of Chemistry  
Bloomington, IN 47405-4001

## CORNELIE KOZMUTZA

Technical University of Budapest  
Physics Institute  
Budafok ut 8  
Budapest 1111  
Hungary

## CARLOS KUBLI-GARFIAS

University of Mexico Biologia de Des  
Mexico City, DF 04511  
Mexico

## JAMES KUNETZ

University of Florida  
Maternal Science Dept  
AMRC, One Progress Blvd.  
Alachua, FL 32615

## JANOS LADIK

Universitat Erlangen Nurnberg  
Inst. for Theor. Chemistry  
Egerlandstr. 3  
Erlangen 8520  
Germany

## BILL LAIDIG

Proctor & Gamble Co.  
Miami Valley Labs.  
P.O. Box 398707  
Cincinnati, OH 45239-8707

## EVERETT LARSON

Brigham Young University  
Physics & Astronomy Depts.  
296 Eyring Science Center  
Provo, UT 84602



## SVEN LARSSON

Chalmers Tekniska Hogskola  
Physical Chemistry Department  
Goteborg S-41296  
Sweden

## LUCAS LATHOUWERS

University Antwerp  
Mathematics Department  
Groenenborgerlaan 171  
Antwerp 2020  
Belgium

## WALTER LAUDERDALE

Frank J. Seiler Research Laboratory  
2354 Vandenberg Drive  
Suite 2A35  
USAF Academy, CO 80840-6272

## DON LAUFFER

Phillips Petroleum Co  
205 CPL PRC  
Bartlesville, OK 74004

## RICHARD LAVERY

Institut de Biologie Physico-Chimique  
Lab de Biochimie Theorique  
13, Rue Pierre et Marie Curie  
Paris 75005  
France

## CARMEN LAVÍN

Universidad de Valladolid  
Depto. de Química Física  
Valladolid 47005  
Spain

## PIERRE LEBRETON

The University of Illinois at Chicago  
Chemistry Department (M/C 111)  
801 W. Taylor St., Room 4500  
Chicago, IL 60607-7061

## JOSE LEITE

University of Sao Paulo  
Instituto de Física  
CP 20516  
Sao Paulo, SP 01498-970  
Brazil

## DANUTA LESZCZYNSKA

Jackson State University  
Chemistry Department  
1400 Lynch Street  
Jackson, MS 39217

## JERZY LESZCZYNSKI

Jackson State University  
Chemistry Department  
1400 Lynch Street  
Jackson, MS 39217

## LAN LEWIS-BEVAN

U.S. Environmental Protection Agency  
Health Effect Research Lab.  
Research Tri. Pk., NC 27711

## JIN LI

Proteus Molecular Design Ltd.  
48 Stockport Road  
Maple, Cheshire SK6 6AB  
United Kingdom

## ANTONIO LINO

Universidade Federal de Uberlandia  
Depto. de Ciencias Fisicas  
Campus Santa Monica  
Uberlandia, MG 38400-902  
Brazil

## GILDA LOEW

Molecular Research Institute  
845 Page Mill Road  
Palo Alto, CA 94304

## LAWRENCE LOHR

National Science Foundation  
Chemistry Division, Room 340  
1800 G Street, N.W.  
Washington, DC 20550

## RICARDO LONGO

University of Florida  
Quantum Theory Project  
348 Williamson Hall  
Gainesville, FL 32611-2085

## PER-OLOV LOWDIN

University of Florida  
Quantum Theory Project  
312 Williamson Hall  
Gainesville, FL 32611-2085

## KARL LUTH

Southern Illinois University  
Department of Chemistry  
Carbondale, IL 62901-4409

NORMAN MARCH  
Oxford University  
Theoretical Chemistry Dept.  
5 South Parks Road  
Oxford OX1 3UB  
England

CRAIG MARSH  
University of Georgia  
Center for Computational Chem.  
4th Floor, Chemistry Bldg.  
Athens, GA 30602

INMACULADA MARTIN  
Universidad de Valladolid  
Depto. de Quimica Fisica  
Valladolid 47005  
Spain

MARTIN MARTINOV  
Florida State University  
IMB  
Tallahassee, FL 32306

J. B. MARTINS  
Universitat Juame I  
Department de Ciencies Exp.  
Apartat 224  
Castello 12080  
Spain

ISTVAN MAYER  
The Hungarian Academy of Sciences  
Institute for Chemistry  
P.O. Box 17  
Budapest H-1525  
Hungary

EARL MCDOW  
Digital Equipment Corp.  
5000 N.W. 34th St. Suite 18  
Gainesville, FL 32605-8666

SEAN McGLYNN  
Louisiana State University Chemistry Department  
Baton Rouge, LA 70803

A. McLEAN  
IBM Corporation  
K35/802  
650 Harry Road  
San Jose, CA 95120-6099

LESZEK MEISSNER  
University of Florida  
Quantum Theory Project  
386 Williamson Hall  
Gainesville, FL 32611-2085

FRANCISCO MENDEZ  
Universidad Autonoma Metropolitana-Iztapalapa  
Depto. de Quimica  
Av. Michocan y Purisima  
Mexico, DF  
Mexico

THEODOROS MERCOURIS  
National Research Foundation  
Theoretical Chemistry Dept.  
Vas. Constantinou Ave. 48  
Athens 11635  
Greece

SARA MEZA-HOJER  
Mexican University  
Facultad de Quimica  
Div. de Estudios de Posgrado  
Ciudad Universitaria, DF 04510  
Mexico

DAVID MICHA  
University of Florida  
Quantum Theory Project  
366 Williamson Hall  
Gainesville, FL 32611-2085

SAITO MINORU  
Protein Engineering Research Institu..  
6-2-3, Furuedai  
Suita, Osaka 565  
Japan

JOHN MINTMIRE  
Naval Research Laboratory  
Code 6179  
Washington, DC 20375-5342

BENNY MOGENSEN  
University of Florida  
Quantum Theory Project  
372 Williamson Hall  
Gainesville, FL 32611-2085

VICENTE MOLINER  
Universitat Jaume I  
Dept. of Experimental Sciences  
242 Apartat  
Castellon 12080  
Spain

LUIS MONTERO  
CSIC  
Instituto de Estructura de la Materia  
Madrid 28006  
Spain

MARK MONTOYA  
University of Florida  
Dept. of Chemical Engineering  
Gainesville, FL 32611

JORGE MORALES  
University of Florida  
Quantum Theory Project  
340 CRB  
Gainesville, FL 32611-2085

MIGUEL MORALES-CORTES  
Universidad Autonoma Metropolitana-Iztapalapa  
Dept. de Quimica  
Av. Michoacan y Purisima  
Mexico, DF 09340  
Mexico

JULES MOSKOWITZ  
New York University  
Chemistry Department  
31 Washington Place  
New York, NY 10003

DAVID MOSLEY  
Universitaires Notre-Dame de la Paix  
Departement de Chimie  
Rue de Bruxelles 61  
Namur B-5000  
Belgium

GLORIA MOYANO  
Universidad Nacional de Colombia  
Departamento de Quimica  
Santa Fe de Bogota, DC  
Colombia

VLADIMIRO MUJICA  
Northwestern University  
Chemistry Department  
2145 Sheridan  
Evanston, IL 60208

FLORIAN MULLER-PLATHE  
Swiss Federal Institute of Technology  
Lab. for Physical Chemistry  
ETH Zentrum  
Zurich CH-8092  
Switzerland

DJAMALADDIN MUSAIEV  
Institute for Molecular Science  
Myodaiji, Okasaki 444  
Japan

BENGT NAGEL  
Royal Institute of Technology  
Dept. of Theoretical Physics  
Stockholm S-100 44  
Sweden

ASIRI NANAYAKKARA  
Florida State University  
SCRI  
Tallahassee, FL 32306

HUGO NAZARENO  
Universidade de Brasilia  
Departamento de Fisica  
Brasilia, DF 70910-900  
Brazil

JEFF NICHOLS  
IBM University of Utah  
Department of Chemistry  
4528 HEB  
Salt Lake City, UT 84112

WILLEM NIEUWPOORT  
University of Groningen  
Lab. of Chemical Physics  
Nijenborgh 4  
Groningen, AG 9747  
The Netherlands

MARCEL NOOIJEN  
University of Florida  
Quantum Theory Project  
371 Williamson Hall  
Gainesville, FL 32611-2085

JENS ODDERSHEDE  
Odense University  
Department of Chemistry  
Campusvej 55  
Odense M DK-5230  
Denmark

N OHRN  
University of Florida  
Quantum Theory Project  
363 Williamson Hall  
Gainesville, FL 32611-2085

NEVIN OLIPHANT  
University of Florida  
Quantum Theory Project  
377 Williamson Hall  
Gainesville, FL 32611-2085

VICENT ORTIZ  
University of New Mexico  
Chemistry Department  
Albuquerque, NM 87131

ROMAN OSMAN  
Mount Sinai School of Medicine  
Physiology & Biophysics Dept  
One Gustave L. Levy Place  
New York, NY 10029

GEORGE PACK  
University of Illinois College of Medicine  
Biomedical Sciences  
1601 Parkview Avenue  
Rockford, IL 61107

JOSEF PALDUS  
University of Waterloo  
Applied Mathematics Dept  
University Avenue  
Waterloo, Ontario N2L 3G1  
Canada

PAOLO PALMIERI  
University of Bologna  
Chimica Fisica ed Inorganica  
Fiale del Risorgimento 4  
Bologna 40136  
Italy

CHANI PANGALI  
170 Tracer Lane  
Waltham, MA 02154-1379

WILLIAM PARKINSON  
Southeastern Louisiana University  
Chemistry & Physics Department  
Hammond, LA 70402

JOHN PERDEW  
Tulane University  
Department of Physics  
New Orleans, LA 70118-5555

AJITH PERERA  
University of Florida  
Quantum Theory Project  
345 Williamson Hall  
Gainesville, FL 32611-2085

JUAN PEREZ  
Molecular Research Institute  
845 Page Mill Road  
Palo Alto, CA 94304-1011

WILLIS PERSON  
University of Florida  
Department of Chemistry  
Gainesville, FL 32611

KIRK PETERSON  
Battelle Pacific Northwest Lab  
Molecular Science Research Center, K1-95, P.O.  
Box 999  
Richland, WA 99352

PETER POLITZER  
University of New Orleans  
Department of Chemistry  
New Orleans, LA 70148-2820

EMILE POP  
Pharmos Corporation  
P.O. Box 730  
Alachua, FL 32615

VLADIMIR POPONIN  
Russian Academy of Sciences  
Lebedev Physics Institute  
Leninsky Prospect 53  
Moscow 117994  
Russia

ENRIQUE POULAIN  
Instituto Mexicano del Petroleo  
Apdo 14-805  
Mexico, DF 07730  
Mexico

MICHAEL PROBST  
Innsbruck University  
Department of Chemistry  
Innsbruck A-6020  
Austria

PETER PULAY  
University of Arkansas  
Department of Chemistry and Biochemistry  
Fayetteville, AR 72701-1201

ALBERTE PULLMAN  
Institut de Biologie Physico-Chimique  
13, rue Pierre et Marie Curie  
Paris 75005  
France

BERNARD PULLMAN  
Institut de Biologie Physico-Chimique  
13, rue Pierre et Marie Curie  
Paris 75005  
France

JAMES RABINOWITZ  
U.S. Environmental Protection Agency  
Health Effects Research Laboratory  
Research Triangle Park, NC 27711

MICHAEL RAMEK  
Technical University of Graz  
Institut für Physikalische und Theoretische Chemie  
Graz A-8010  
Austria

JOSE RECAMIER  
Universidad Nacional Autónoma de México  
Laboratorio de Cuernavaca  
Apartado Postal 139-B  
Cuernavaca, Morelos 62191  
México

WILLIAM RHODES  
Florida State University  
Department of Chemistry  
Tallahassee, FL 32306

NIGEL RICHARDS  
University of Florida  
Department of Chemistry  
Gainesville, FL 32611

LUIS RINCON  
Instituto Venezolano de Investigaciones Científicas  
Department of Chemistry  
Apartado 21827  
Caracas 1020-A  
Venezuela

C. C. J. ROOTHAAN  
University of Chicago  
Department of Physics  
5735 S. Ellis Avenue  
Chicago, IL 60637

JOHN ROSENBERG  
University of Pittsburgh  
Biological Sciences Dept  
A-234 Langley Hall  
Pittsburgh, PA 15260

KLAUS RUEDENBERG  
Iowa State University  
Department of Chemistry  
Ames, IA 50010

KEITH RUNGE  
University of Florida  
Quantum Theory Project  
345 Williamson Hall  
Gainesville, FL 32611-2085

JACK SABIN  
University of Florida  
355 Williamson Hall  
Gainesville, FL 32611

VIRAHT SAHNI  
Brooklyn College of CUNY  
Department of Physics  
2900 Bedford Avenue  
Brooklyn, NY 11210-2889

LYNN SALEMI  
University of Florida  
Quantum Theory Project  
345 Williamson Hall  
Gainesville, FL 32611-2085

NESSIMA SALHI  
Uppsala University  
Dept. of Quantum Chemistry  
P.O. Box 518  
Uppsala S-75120  
Sweden

**HENRY SCHAEFER III**

University of Georgia  
CCQC  
Chemistry Building  
Athens, GA 30602

**CHRISTINA SCHARNAGL**

Technische Universität München  
Theoretische Physik  
Boltzmannstrasse  
Garching D-8046  
Germany

**GEORGE SCHATZ**

Northwestern University  
Department of Chemistry  
Evanston, IL 60208-3113

**STEVE SCHEINER**

Southern Illinois University  
Department of Chemistry  
Carbondale, IL 62091

**HAROLD SCHERAGA**

Cornell University  
Baker Lab of Chemistry  
Department of Chemistry  
Ithaca, NY 14853-1301

**PETER SCHMIDT**

Office of Naval Research  
Chemistry Division  
800 N. Quincy Street  
Arlington, VA 22217-5000

**LUISA SCOLFARO**

Universidade de São Paulo  
Instituto de Física  
Caixa Postal 20518  
São Paulo 07498  
Brazil

**GOTTHARD SEIFERT**

Technische Universität Dresden  
Inst. f. Theoret. Physik  
Mommstr. 13  
Dresden D-0-8027  
Germany

**HIDEO SEKINO**

University of Florida  
Quantum Theory Project  
370 Williamson Hall  
Gainesville, FL 32611-2085

**JORGE SEMINARIO**

University of New Orleans  
Department of Chemistry  
New Orleans, LA 70148-2820

**RON SHEPARD**

Argonne National Laboratory  
Chemistry Division  
Argonne, IL 60439

**JOHN SIMONS**

The University of Utah  
Department of Chemistry  
Salt Lake City, Utah 84112

**YVES SMEYERS**

Consejo Superior de Investigaciones Científicas  
Inst. de Estructura Materia  
Calle Serrano no. 123  
Madrid E-28006  
Spain

**JACK SMITH**

Union Carbide  
Catalyst Skills Center  
P O. Box 8361  
So. Charleston, WV 25303

**VEDENE SMITH**

Queen's University  
Department of Chemistry  
Kingston, ON K7L 3N6 Canada

**HUMBERTO SOSUN**

UMIST  
Department of Chemistry  
Manchester M60 1QD  
United Kingdom

**MICHAEL SPRINGBORG**

Universität Konstanz  
Fakultät für Chemie  
Postfach 5560  
Konstanz S-W-7750  
Germany

**RICHARD SQUIRE**

Marshall University  
Department of Chemistry  
901 W. DuPont Avenue  
Belle, WV 25015

**JOHN STANTON**

University of Florida  
Quantum Theory Project  
367 Williamson Hall  
Gainesville, FL 32611-2085

**RICK STEVENS**

Argonne National Laboratory  
Mathematics & Computer Science  
9700 South Cass Avenue  
Argonne, IL 60439

**GERNOT STOLLHOFF**

Max-Planck-Institut für Festkörperforschung  
Heisenbergstr. 1  
Stuttgart, 80 D-7000  
Germany

**SANDOR SUHAI**

German Cancer Research Centre  
Molecular Biophysics Group  
INF 280  
Heidelberg W-6900  
Germany

**BRIAN SUTCLIFFE**

University of York  
Department of Chemistry  
Heslington, York YO15DD  
England

**ALEXANDER SYTNIK**

Florida State University  
Inst. of Molecular Biophysics  
MBB 452, B-165  
Tallahassee, FL 32306-3015

**KRYSTYNA SZCZEPANIAK**

University of Florida  
Department of Chemistry  
CLB 309  
Gainesville, FL 32611

**JAMES TALMAN**

University of Western Ontario  
Applied Mathematics Department  
London, Ontario N6A 5B7  
Canada

**MICHAEL TETER**

Corning Incorporated FR5—Sullivan Park  
Applied Process Research  
Corning, NY 14831

**AJIT THAKKAR**

University of New Brunswick  
Chemistry Department  
Bag Service #45222  
Fredericton, NB E3B 6E2  
Canada

**MARK THOMPSON**

Pacific Northwest Laboratories  
P.O. Box 999, MS K1-90  
Richland, WA 99352

**COLIN THOMSON**

University of St. Andrews  
Department of Chemistry  
North Haugh  
St. Andrews, Fife KY169ST  
Scotland

**IGOR TOPOL**

Program Resources Inc.  
NCI-FCRDC  
P.O. Box B  
Frederick, MD 21702

**SAMUEL TRICKEY**

University of Florida  
Quantum Theory Project  
362 Williamson Hall  
Gainesville, FL 32611

**DONALD TRUHLAR**

University of Minnesota  
Department of Chemistry  
207 Pleasant Street, S.E.  
Minneapolis, MN 55455-0431

**NOZOMU UCHIDA**

University of Florida  
One Progress Blvd., #14  
Alachua, FL 32615

**TEREZA VARNALI**

Bogazici University  
Chemistry Department  
FEF Kimya  
Bebek, Istanbul 80815  
Turkey

**DAN VASILESCU**

Universite de Nice  
Laboratoire de biophysique  
Sophia Antipolis, Parc Valrose  
Nice, Cexex 2 06108  
France

**ALBERTO VELA**

Universidad Autonoma Metropolitana-Iztapalapa  
Department of Chemistry  
Av. Michoacan y Purisima  
Mexico, DF 09340  
Mexico

**ROBERT VERGENZ**

University of North Florida  
Natural Science  
Jacksonville, FL 32216

**DRAZEN VIKIC-TOPIC**

National Institute of Health  
NIDDK/LAC  
9000 Rockville Pike  
Bethesda, MD 20892-0008

**JOSE VILLAVECES**

Grupo de Quimica Teorica  
U. Nacional de Columbia  
Transv. 9a No 133-28  
Bogota, DC  
Colombia

**LUUK VISSCHER**

University of Groningen  
Department of Chemical Physics  
Nijenborgh 4  
Groningen, AG 9747  
The Netherlands

**WARREN WARREN**

Princeton University  
Department of Chemistry  
Frick Chemical Labs  
Princeton, NJ 08544

**JOHN WATTS**

University of Florida  
Quantum Theory Project  
377 Williamson Hall  
Gainesville, FL 32611-2085

**JOHN WEARE**

University of California  
Chemistry 0340  
9500 Gilman Drive  
La Jolla, CA 92093-0304

**BRIAN WEINER**

Penn State University  
Physics Department  
College Place  
DuBois, PA 15801

**ZHENYI WEN**

Indiana University  
Department of Chemistry  
Bloomington, IN 47405

**WILLIAM WORLEY, JR.**

Hewlett-Packard Laboratories  
MS 3U-2  
Page Mill Road  
Palo Alto, CA 94303

**PAUL WORMER**

University of Nijmegen  
Inst. of Theor. Chemistry  
Toernooiveld  
Nijmegen, ED 6525  
The Netherlands

**JOSEPH WORTH**

AT&T Bell Labs  
MS4C528  
101 Crawfords Corner Road  
Holmdel, NJ 07733-3030

**JIN ZHONG WU**

University of Florida  
Quantum Theory Project  
368 Williamson Hall  
Gainesville, FL 32611-2085

**ROBERT WYATT**

University of Texas  
Department of Chemistry  
Austin, TX 78712

**SHEN-XIU XIAO**

Sichuan University  
Department of Chemistry  
P.O. Box 75  
Chengdu, Sichuan 610064  
China

**KIZASHI YAMAGUCHI**

Osaka University  
Department of Chemistry  
Toyonaka, Osaka 560  
Japan



## LIST OF PARTICIPANTS

xxvii

DARRIN YORK  
National Institute of Environmental Health  
Sciences  
Lab. of Mol. Toxicology  
P.O. Box 12233, Mail Drop B302  
Research Triangle Park, NC 27709

MICHAEL ZERNER  
University of Florida  
Quantum Theory Project  
362 Williamson Hall  
Gainesville, FL 32611-2085

LIYANG ZHAO  
Florida International University  
Electrical and Computer Eng.  
University Park Campus  
Miami, FL 33199

XUEHE ZHENG  
University of Florida  
Quantum Theory Project  
440 CRB  
Gainesville, FL 32611-2085

ZHONGXIANG ZHOU  
University of North Carolina  
Department of Chemistry  
CB# 3290  
Chapel Hill, NC 27599-3290

RENATE ZWAANS  
University of Utrecht  
Theoretical Chemistry Group  
Padualaan 14  
Utrecht, CH 3584  
The Netherlands



Professor C. C. J. Roothaan. Craig Burleigh Photography © 1991

# My Life as a Physicist: Memories and Perspectives

CLEMENS C. J. ROTHHAAN

*Departments of Physics and Chemistry, University of Chicago, Chicago, Illinois 60637 and Pipeline Computers, Inc., 5235 S. University Ave. Chicago, Illinois 60615*

This paper constitutes a brief personal history from my beginnings as a physicist through the period of my discovery and consolidation of what has since become the self-consistent field theory of molecular structure. My career as a molecular theorist began only a few short years after the most traumatic experiences of my life took place during World War II. My growth as a scientist did not stop during those difficult years, but proceeded as if driven by forces independent of the surrounding events.

It is only during the last decade or so that I have spoken somewhat more freely about the painful experiences described below. However, those events were always vividly present in my mind. I hope that sharing those memories with my friends and colleagues will help them to understand me better, and perhaps also the human condition. And since my training in the fundamentals of physics occurred during those years, my account may also offer some insight into how learning can, and does, occur under improbable circumstances.

But first I like to turn back to my childhood, when I experienced the earliest stirrings of scientific curiosity. I am certain that my interest in science began when I was three years old. I did not understand how toasters, lamps and irons depended on a wire coming out of the wall. In those days, wall outlets were surface mounted and covered by porcelain caps. One day I found an outlet whose cap had crumbled. I began to put my finger systematically on the various exposed parts, intent on getting some response from this mysterious gadget. I finally did, in the form of an electric shock that made me withdraw my finger abruptly, and imbued me with great respect for the mysterious force I had just experienced.

This was one experiment that I reported to no one; I was brought up in a proper home and had sense enough to know that, whatever I had done, it was wrong. The experience increased my prudence but in no way diminished my curiosity. By the age of seven, I was conducting less dangerous experiments with batteries, lights, switches and electric bells. Radio broadcasting was just beginning around that time. At the age of ten, I built my first crystal receiver and, throughout my teens, I continued experimenting with radio reception to the extent that my meager budget allowed.

During my last two years at the gymnasium (high school), I elected the mathematical-scientific curriculum. After graduation, I enrolled at the Technical University of Delft in the Department of Electrical Engineering.

Class attendance at Delft was optional; to satisfy requirements, one only had to pass yearly examinations. During my first two years there, I spent my afternoons in the shops and laboratories, but rarely attended lectures; I preferred to study textbooks and the required literature on my own. The extensive language training mandated in Dutch gymnasia made this self-study possible, since by the time we graduated, we were able to read the scientific literature in French, German and English.

During my third year—it was now 1938–1939—I became dissatisfied with my academic program. The electrical engineering curriculum in Delft was a two-track program, one with emphasis on electric power (transformers, transmission lines, electric motors), the other emphasizing electronics and acoustics. I had a strong interest in the latter, but could not avoid a number of mandatory courses in the former, which interested me very little. I had heard that in the German technical institutes, it was possible to take a program in which one could concentrate fully on electronics and acoustics. To explore this option, I spent the spring of 1939 auditing classes at the Technical University of Karlsruhe.

During the summer of 1939, which I spent at my parental home in Nijmegen, all hope for peace in Europe evaporated. Events moved swiftly. In July, the Hitler–Stalin pact was signed. By mid-August, it was clear that Poland would not yield, that Germany would attack and that France and England would be brought into the war. On August 29, 1939, the Netherlands government declared a general mobilization in order to defend its neutrality as it had successfully done during World War I.

During peacetime, Dutch university students were always permitted, and indeed encouraged, to complete their academic studies before fulfilling their military obligation. These deferrals were now revoked and, on my 21st birthday, which coincided with the date of the mobilization, I was inducted into the Royal Engineers Regiment of the Netherlands Army.

The officer corps of that regiment consisted almost exclusively of graduates of the University of Delft. The army now faced a dilemma: the students from Delft who had been inducted should be given officers training, but a prerequisite for the latter was prior graduation from the university.

After about six weeks, during which we were billeted in Rotterdam basically doing nothing, the army resolved its dilemma by sending the entire student contingent of the Royal Engineers back to school in uniform. We were billeted in one of the university buildings requisitioned for the purpose. After an hour of drill in the morning, we attended classes and laboratories as normal students for the rest of the day.

Having concluded earlier that year that I did not want to continue with the electrical engineering program at Delft, half of which did not turn me on, I decided to become a physicist. So, while the world situation around us became more ominous all the time, I eagerly devoured all the physics I could absorb.

The Physics Department at Delft had recently acquired R. Kronig as its resident theoretician. Kronig's lectures, together with lectures by H. A. Kramers, who came

in once a week from neighboring Leiden for that purpose, opened up the world of physics for me. I also learned differential geometry and its relation to relativity and quantum mechanics from J. A. Schouten, who had pioneered a very original approach to those subjects.

Our lives were rudely interrupted in the early morning hours of May 10, 1940, when the German attack on the Netherlands and Belgium was launched—as was Nazi custom, with no declaration of war. The only declaration of war by Germany in World War II was against the United States after Pearl Harbor, direct invasion not being an option.

Our group of student soldiers, who had had no more training than morning drills for about six months, and who had never fired a gun, was now deployed around Delft to cope with German paratroopers and glider convoys descending on an airfield a few kilometers out of town close to The Hague, the seat of the government. I was assigned to guard one of the canal bridges on the outskirts of Delft. Quaking in my boots one night, I fired my only shot of the war, missing a moving shadow that later turned out to be a goat grazing in a nearby meadow. The paratroopers were contained by more experienced forces, thereby permitting the Dutch government to escape to England.

After four days, The Netherlands was crushed by the overwhelming military might of Germany. It was utterly depressing. Nevertheless, despite our defeat, we believed in an ultimate allied victory, and continued to believe so even after the narrow escape of the British Expeditionary Forces from Dunkirk and the subsequent fall of France.

Initially, the German occupation of the Netherlands was relatively benign. Upon demobilization, the Dutch army was allowed to return to civilian life rather than being interned in POW camps. Thus, in the fall of 1940, I returned to Delft as a civilian graduate student in physics.

The Physics Department had recently begun to use teaching assistants, and I had the good fortune to be selected to assist in an advanced laboratory where several classical experiments were set up for student training. Among these were the determination of  $e/m$  by subjecting an electron beam to balancing electrostatic and magnetic deflections, and the famous Milliken oil drop experiment for the determination of  $e$ . The laboratory was directed by a distinguished lady, Dr. H. van Leeuwen, who had been a student and research assistant with H. A. Lorentz. In today's academic environment, Miss van Leeuwen would undoubtedly occupy a prestigious chair.

Gradually the German occupiers tightened the noose and began to interfere in virtually every aspect of life. The food stores that had been stockpiled by the Dutch government to be prepared for a blockade were now carted off to Germany. The first measures against Jews were instituted, beginning with registration, followed by restriction of movement and exclusion from gainful employment. In the spring of 1941, university students were required to sign a loyalty oath stating that they would not undertake any acts of resistance or sabotage against the occupier.

We students considered it dishonorable to sign such a declaration and—perhaps

naively—decided to register a protest by boycotting classes. In retaliation, the German authorities closed down the universities of Leiden and Delft. Leiden remained closed during the entire war, but Delft was allowed to reopen a few months later.

Once again, after a relatively brief interruption, I was able to resume my studies and to continue as a student and teaching assistant in physics for about two more years. Fortunately, the physics faculty remained intact and library resources were more than adequate despite the absence of new acquisitions.

By late 1942, the allies were gaining strength and we were heartened by news of major German defeats in North Africa and Stalingrad. However, the occupation itself was becoming increasingly oppressive. Dutch resistance gradually stiffened, culminating in a series of strikes during the month of April, 1943.

The Germans responded by declaring martial law. Young men were now grabbed off the streets, routinely and at random, to be carted off as slave labor in German factories. Since university communities would be prime targets for this practice, I decided to clear out of Delft for a while and lie low at my family's home in Nijmegen. For the same reason, my youngest brother John returned from Groningen where he was a medical student; Victor, our middle brother, was still living in Nijmegen where he was studying sociology.

When the three of us were together, Victor informed us that he was engaged with a group of friends in underground activities. Shortly thereafter, on April 30, 1943, he received a phone call alerting him that several members of his group had been arrested by the security police (Sicherheitsdienst or SD).

Victor promptly took off on his bicycle. John and I reasoned that the SD did not have anything on us; foolishly, we decided to stay put. A few hours later, the SD, reinforced by collaborationist Dutch Police, showed up. Unimpressed by our declarations of non-involvement, they immediately placed us under arrest. They never found Victor, who managed to remain in hiding throughout the war.

John and I spent the night in the police lockup in Nijmegen. At dawn we were put on an army truck to take us to a military court in Hengelo, about 90 km away. On the truck we met four of Victor's co-conspirators—one laborer, Marinus, and three university students. Later that afternoon, the three students were sentenced to the firing squad (they were shot the next morning), and Marinus was given a long term in concentration camp, while John and I were relegated to the police lockup in Hengelo.

We stayed in that police lockup for three and a half months. We managed to get books sent to us from our respective university libraries, and tried to keep our minds focused on our studies. I remember struggling through Hermann Weyl's "Raum, Zeit und Materie".

We became relatively permanent fixtures in the lockup; most "guests", comprising common criminals, black marketeers, political dissenters, and Jews who had been flushed out of hiding, stayed only a few days. I remember seven Jews who came in during that period. Three managed to commit suicide in their cells: John and I carried out their bodies.

On August 13, 1943, John and I were suddenly removed from the lockup and transferred to the concentration camp at Vught (between 'sHertogenbosch and Eindhoven). We were never convicted of anything—this was simply "Schutzhaft" (protective custody). We were to stay there until September 5, 1944.

In Vught, we found new opportunities to keep our academic interests alive. John, as a medical student, managed to capture the much-coveted position of hospital orderly. Miraculously, I got back into physics.

Vught is not far from Eindhoven, which was then, as it is now, the company town of the electronics giant N. V. Philips. The top management, including the son-in-law of the company founder, had been evacuated by the Dutch army to England, where they could continue to direct Philips' worldwide operations for the benefit of the allied cause. However, other managers—including the founder's son—had been left behind in Eindhoven. Now they were forced by the Germans to produce electronic components and devices for the German war effort. At the same time, the ranks of Philips employees were repeatedly subjected to arbitrary drafts of personnel to serve as slave labor in German factories.

The executives of Philips then suggested to their German overlords that they be permitted to tap the pool of labor in the nearby camp of Vught. This proposal was received favorably, and thus Philips was encouraged to set up manufacturing facilities inside the camp. Working in the "Philips Commando" was considered a great privilege.

Although the Philips Commando employed only a small fraction of the camp population, its mere presence improved the ambiance of the camp significantly. Each morning a group of Philips managers came into the camp to direct the manufacturing operations, namely of electric razors and short-wave radios. The radios also had to be tested at the end of the assembly line, providing us with an excellent source of "forbidden" news on a daily basis.

For the academically inclined, the Philips management created the "Computation Chamber" in which about two dozen professors, students, and scientists from industry got various research assignments. I was invited to join that group.

My first assignment, as a member of the Chamber, was to carry out a Kronig-Penney calculation of the Schroedinger equation for a one-dimensional finite crystal. This constituted in a sense my first experience as a practising quantum theoretician. When that was finished, complete with beautifully drawn graphs of wavefunctions and charge densities, I was given a much more ambitious project, consisting of a calculation of elastic constants in a classical crystal, where the interaction between lattice sites consisted of central as well as non-central forces.

This problem had been formulated by Dr. Druivesteyn of Philips, who had consulted with my professors in Delft to give me a project that would further my academic program. To learn the field, I struggled through Max Born's monograph "Dynamik der Kristallgitter". My assignment was completed, and a final report transmitted to the Philips Management in Eindhoven, a few days before the camp was evacuated on September 5, 1944. After the war, this work was accepted in Delft as my master's thesis.

The evacuation of camp Vught conformed to standard Nazi practice that no concentration camp inmates should ever be liberated. The allied armies were poised for a push northward just a few dozen kilometers to the south of us. Unfortunately for us, that push occurred 12 days later.

On the day of the evacuation, about 500 prisoners who had been in solitary confinement were executed. The remaining few thousand "less dangerous" inmates were crammed into railroad cattle cars, and began a three-day journey which ended on September 8, 1944 at the camp "Sachsenhausen", also called "Oranienburg" after the nearby Berlin suburb of that name.

The world of concentration camps reminds me of Dante's description of the seven levels of Hell. At the deepest level were the extermination camps with gas chambers, and also some camps nicknamed "Nacht und Nebel" (Night and Fog) from which virtually no-one came out alive. Sachsenhausen—like Dachau and Buchenwald—was somewhere in the middle; I estimate the survival rate at 15–20%. Vught had been comparatively benign, due in no small part to the presence of the Philips civilians.

In Sachsenhausen I had to suspend my pursuit of physics and focus every ounce of energy on survival. Bruno Bettelheim attributed his own survival to his will to live and to his understanding of the sociology of the camp structure. I concur that these were necessary prerequisites, but they were by no means sufficient; in order to survive one also needed a good deal of luck.

I judged that being a university student would be of little value in landing a good job. Thus, at intake registration I declared that I was an electrician. My brother John professed to be a medical orderly. After a short while, I landed a good job with a "Baukommando" (construction commando), where I started as a draftsman and later served as an electrician. Unfortunately, John ended up in menial work.

The winter of 1944–1945 was harsh. Every morning at 4:00 a.m., we had to brave the elements standing at attention for about one and a half hours at "Appell" (roll call), wearing no more than flimsy indoor clothing. After roll call, the prisoners regrouped to march off to arrive at 6:00 a.m. at their regular work assignments.

By the end of January 1945 the Russian army was on German soil, less than 60 km from Berlin and our camp. The German army dug in for a tenacious defense of their capital and, on February 1, 1945, camp officials began a gradual evacuation of Sachsenhausen, moving inmates to the north and west in order to prevent liberation of the prisoners by the advancing Russians. My brother John went with one of these transports to the infamous camp Bergen-Belsen, where he perished from deprivation and typhoid in late March.

I stayed in Sachsenhausen until the final evacuation on April 20 when, guarded by SS troops, with the Russian army at our heels, we began a forced march which lasted 12 days and covered 160 km. The SS had made no provision for feeding or billeting the tens of thousands of undernourished miserable victims whom they were now driving like a herd of cattle to nowhere, either to die along the road or, probably, be drowned in the Baltic Sea. Anyone whose strength gave out and sat down was promptly shot. I have made a rough guess that at least one-third of us perished. My own life was saved in large measure by a fellow prisoner who, as a



long-time inmate of Sachsenhausen, had been better connected than I and had thus been able to acquire a stockpile of food which he generously shared with me.

After about one week of this life-and-death struggle, small rays of hope began to break through. Swiss staffers from an International Red Cross depot in the Baltic port of Lübeck courageously took matters in their own hands. They loaded their trucks with food parcels which had been destined for POW camps, and supplied any prisoners they could find on the roads with their precious life-saving gifts.

The Red Cross representatives also convinced our SS guards—who had by now been abandoned by their officers, and were quite demoralized—to let collapsing prisoners be taken on the Red Cross trucks. Fearful of retribution by the prisoners, who at this point outnumbered the guards about fifty to one, our remaining guards gradually disappeared from sight. Many were Eastern Europeans who had been forced into service and who were eager to return to their homelands. As we now continued on our own, we were joined by a new group: German soldiers desperately rushing to the West to avoid capture by the Russians. Our march ended about halfway between Berlin and Denmark in Schwerin, the regional capital of Mecklenburg, where we met American troops. It was May 2, 1945.

I was repatriated to the Netherlands in late May—I do not remember the exact date. After resting up for a few weeks, I returned to Germany to see if I could find some trace of my brother John. After arrival in the Bergen-Belsen area, it became obvious to me that he could not possibly have survived. Later investigation turned up testimony from a few survivors that he had indeed succumbed about five weeks before war's end.

I returned to Delft about September 1, 1945, and was officially granted my diploma of "Ingenieur", roughly equivalent to a Master's degree, on October 15. I had by then applied for, and obtained, a postgraduate fellowship at the University of Chicago. I arrived in Chicago on January 6, 1946.

Chicago was then the most exciting place to be for a young physicist. It boasted the famous site of the first self-sustaining nuclear chain reaction; among the physics faculty were Enrico Fermi, Edward Teller, Maria Goeppert-Mayer, and Robert Mulliken. Nuclear research was of course *de rigueur*. However, since nuclear research was then still cloaked in heavy secrecy, I concluded that as an alien I would be better off in a program that was not encumbered by government-imposed restrictions. I applied to and was accepted by Robert Mulliken as a research student to pursue the study of molecular structure and spectra.

My studies at Delft had given me an excellent foundation in mechanics, electricity and magnetism, thermodynamics and statistical mechanics, and of course advanced calculus and other subjects in mathematics. However, I had not learned much about nuclear physics, quantum mechanics and, in modern mathematics, linear algebra and group theory. I spent the period between January 1946 and June 1947 filling in some of these gaps, as well as carrying out semiempirical molecular orbital calculations on several simple organic molecules with "alphas and betas".

I passed the Ph.D. candidacy examination in physics in June 1947. Shortly thereafter Professor Mulliken suggested semiempirical MO calculations on substituted

benzenes as my thesis subject. Through the good offices of Maria Mayer, I also received at that time an offer from Professor Karl Herzfeld of the Catholic University of America in Washington, DC, to join the physics faculty as an instructor. I accepted that offer and spent the next two years teaching in Washington while working on my thesis, making frequent trips to Chicago to confer with Mulliken.

I began with summarizing the theoretical foundations of the calculations I was to perform. Mulliken expressed his approval and praise for the first account he received. However, I was not satisfied with the current state of the art. All MO calculations started with a "one-electron Hamiltonian", but I could not find a definition of the latter anywhere in the literature.

I realized that a similar problem had been faced for atoms by Hartree and Fock [1]. At least for closed-shell atoms, there was a clear definition of the one-electron Hartree-Fock Hamiltonian: it emerged in the process of applying the  $N$ -electron variation principle to a Slater determinant of orbitals which had to be optimized. Furthermore, F. Seitz and others had extended the model to deal with solids, albeit again limited to a closed-shell system [2]. Clearly, the model was also applicable to molecules, most of which are, conveniently, closed-shell systems. The difficulty with standard MO theory was that a mystical one-electron Hamiltonian was adopted before anything at all could be written down.

The solution to the puzzle came to me in June 1948. I had returned from Washington to Chicago for the summer to work intensively on my thesis. I went with a group of friends, including my future wife, to a concert by the Chicago Symphony Orchestra at its open-air summer home in Ravinia Park, north of Chicago. Lying in the grass, listening to the music and looking at the stars, it suddenly flashed through my head that standard MO theory did not start with the right question. Just like Hartree, Fock and Seitz had applied the variation principle to an  $N$ -electron Slater determinant of yet to be determined orbitals, one should start the same way with molecules, with the additional constraint that the MOs are constructed as linear combinations of atomic orbitals (LCAO). Nowadays we prefer to say that the MOs are constructed from a predetermined basis set.

The LCAO approximation for the MOs was of course not new; it had been used for years by Mulliken, Lennard-Jones and others in semi-empirical calculations. However, entering this approximation formally into the  $N$ -electron variation principle provided a new and much better mathematical point of departure for electronic structure calculations on molecules.

When I communicated my insight to Mulliken, he fully understood its significance. It is a testimony to his stature as a scientist and human being that he wholeheartedly supported that I would now dedicate myself primarily to working out the details of what I then called the LCAO-SCF theory, rather than the thesis topic originally assigned.

Having returned to Washington in the fall of 1948, I continued working out the details of the LCAO-SCF theory during the following Academic year. The first three chapters were completed in late 1948, consisting, respectively, of an introduction, a derivation of the closed-shell molecular Hartree-Fock-SCF equations,

and the analogous derivation of the LCAO-SCF equations [3]. Publication in a journal had to be postponed until after the Ph.D. degree was granted and the Ph.D. committee had approved the final version of my dissertation.

In June 1949 I returned to Chicago, this time as a research associate, for a full year. That period in Chicago proved even more stimulating and exciting than my earlier stays in Mulliken's laboratory. I had the privilege of interacting with many young physicists and theoretical chemists who came to quench their thirst at this watering hole. I recall many stimulating discussions with Jake Bigeleisen, Mike Kasha, Christopher Longuet-Higgins, Al Matsen, Harden McConnell, Bob Parr, and Bill Price. I thank them for the many good conversations we had.

During that year, the remaining four chapters of my thesis were completed [4]. These four chapters covered, respectively, ionization and excitation processes, the use of symmetry in the Hartree-Fock-SCF model, the use of symmetry in the LCAO-SCF model, and an LCAO-SCF calculation of the benzene molecule. The thesis was accepted and approved by the committee in June 1950.

The last chapter of my thesis, the LCAO-SCF calculation of benzene, constituted only a crude and approximate application of the new theoretical framework. This was, however, all that could be done within a reasonable time frame, due to the unavailability of adequate computational tools in those days. The inclusion of this last chapter also put to rest the reservations as expressed by one of the committee members, "never mind all those beautiful formalities—what can you really calculate?" In the published version of my thesis [5] I decided to omit this last chapter, since I was convinced that much better and more interesting and convincing calculations would be carried out within a few years.

While our work in Chicago was available prior to official publication to our colleagues worldwide through our Technical Reports [5a], we were not always informed about developments in other laboratories as they were occurring. Thus, while I was working out the LCAO-SCF theory, I was not aware of the parallel development in Cambridge, England, by Lennard-Jones and Hall [6-9]. A comparison between these two separate developments seems in order.

The two developments show a great deal of similarity, both in subject matter and in methodology. This is evidenced in particular by the adoption of a single Slater determinant to describe the ground state of a closed-shell molecule; the transformability of the one-electron functions; the application of the  $N$ -electron variation principle to derive the molecular Hartree-Fock-SCF equations as well as the LCAO-SCF equations; the exploitation of symmetry; and the treatment of ionization and excitation processes.

The most significant difference between the two developments is in the interpretation and exploitation of the LCAO-SCF equations. Hall observed that these equations simplify considerably if  $M$ , the number of atomic orbitals, equals  $N$ , the number of occupied molecular orbitals [9]. Restricting himself to that special case,  $M = N$ , he then derived useful relations between ionization potentials of related chemical compounds. On the other hand, dealing with the general case where  $M > N$ , I noted that these equations exhibit a striking resemblance to the Hartree-Fock equations. I proposed that these equations be adopted to calculate wavefunc-

tions for molecules in actual practice, using an iterative procedure, henceforth to be called the "LCAO-SCF method" [3].

After obtaining my degree, I was invited to join the faculty of the Physics Department of the University of Chicago, and I accepted. With strong support from Robert Mulliken and his junior colleague John R. Platt, I now embarked on a broad-based program, using my thesis as a blueprint, to develop the tools necessary for calculating all-electron wavefunctions of atoms and molecules routinely and accurately. Henceforth, the work of Mulliken, Platt and myself would be conducted under the auspices of the "Laboratory for Molecular Structure and Spectra" (LMSS).

My first major task was to systematize the calculation of one- and two-electron integrals over the basis functions from which the MOs are constructed. This work got a significant boost when I was joined by Klaus Rüdénberg, who had come to Chicago from Zürich with his mentor, Professor Gregor Wentzel, who had joined our physics faculty in 1948.

A comprehensive integrals project which would cover polyatomic molecules made up of any atoms in the periodic table was clearly too ambitious. Thus we settled for diatomic molecules consisting of atoms in the first two rows of the periodic table. We furthermore adopted the Slater-type basis functions as the most suitable building blocks for the construction of MOs. Klaus tackled the mathematically most demanding class of these integrals, namely the two-center two-electron exchange integrals; I dedicated myself to the remaining types.

A second major task was to prepare ourselves to use digital computers, first for calculating the integrals we were working on, and later for developing programs implementing other mathematical procedures which crop up in calculations on atoms and molecules. This was no small undertaking, since the first computers available to us had no floating point hardware, while the systems software consisted of binary input and output routines only; compilers, and even assemblers, were still in the future.

Many of the tools needed by LMSS in this broad-based program were contributed by energetic dedicated research associates and graduate students. Prominent among the former were Reinhart Ahlrichs, Paul Cade, Enrico Clementi, Serafin Fraga, Juergen Hinze, Sigeru Huzinaga, Włodzimierz Kolos, Sigrid Peyerimhoff, Bernie Ransil, Robert Sack and Lutek Wolniewicz; and among the latter, Paul Bagus, Howard Cohen, John Detrich, Winnifred Huo, Yong-ki Kim, Gulzari Malli, Doug McLean, Charles Scherr, Chris Wahl, Andy Weiss, Bill Worley and Megumu Yoshimine.

While the first LCAO-SCF model could deal satisfactorily with closed-shell systems, an analogous satisfactory treatment of open-shell systems remained elusive for quite a while. In fact, this problem was endemic in virtually all SCF formulations, and had been side-stepped by Hartree for atoms by introducing somewhat artificial approximations in implementing the  $N$ -electron variation principle [1].

The solution to this puzzle, which I discovered in 1958, was another instance where one had to ask the right question: the variation principle had to be modified so that all degenerate  $N$ -electron wavefunctions, which jointly represent the open

shell, participate equally in the variational process [10]. While this extension of LCAO-SCF theory did not lead to a simple scheme for all conceivable cases, nevertheless a large class of open-shell problems now became easily accessible.

In 1962 I became director of the University of Chicago Computation Center; I held that position until 1968. Since then I have spent considerable time and effort on the design and development of computer hardware and software for large-scale scientific calculations. However, I never lost interest in physics and quantum chemistry. During the mid-1970s I worked intensively, in collaboration with my former student John Detrich, on relativistic effects in atoms and molecules [11,12], and from about 1980, again with John Detrich, on the MCSCF (multi-configuration self-consistent field) model of electronic structure [13,14]. I expect to continue alternating between physics, quantum chemistry, and computer development for the foreseeable future.

In conclusion, I want to thank Professor Orville-Thomas for his kindness and patience, and for inviting me to write this account. I also thank all my friends and colleagues who have contributed to this issue of "Theochem".

### Bibliography

- [1] D. R. Hartree, *The Calculation of Atomic Structures* (Wiley, New York, 1957).
- [2] F. Seitz, *The Modern Theory of Solids* (McGraw-Hill, New York, 1940, Chapters VI and VII).
- [3] C. C. J. Roothaan, Technical Report, Physics Department, University of Chicago, 9/1/48-5/31/49, Paper no. 12.
- [4] C. C. J. Roothaan, Technical Report, Physics Department, University of Chicago, 8/1/49-3/31/50, Paper no. 14.
- [5] C. C. J. Roothaan, *Rev. Mod. Phys.*, **23**, 69 (1951).
- [5a] Professor Lennard-Jones was on the distribution list, and thus received the LCAO-SCF formulation by mid-1949.
- [6] Sir John Lennard-Jones, *Proc. R. Soc. London, Ser. A*, **198**, 1 (1949).
- [7] Sir John Lennard-Jones, *Proc. R. Soc. London, Ser. A*, **198**, 14 (1949).
- [8] G. G. Hall and Sir John Lennard-Jones, *Proc. R. Soc. London, Ser. A*, **202**, 155 (1950).
- [9] G. G. Hall, *Proc. R. Soc. London, Ser. A*, **205**, 541 (1951).
- [10] C. C. J. Roothaan, *Rev. Mod. Phys.*, **32**, 179 (1960).
- [11] J. H. Detrich and C. C. J. Roothaan, in *The Uncertainty Principle and Foundations of Quantum Mechanics*, W. C. Price and S. S. Chissick, Eds. (Wiley-Interscience, London, 1977, pp. 395-437).
- [12] J. H. Detrich and C. C. J. Roothaan, in *Relativistic Effects in Atoms, Molecules, and Solids*, G. L. Malli, Ed. (Plenum, New York and London, 1981, pp. 169-182).
- [13] C. C. J. Roothaan and J. H. Detrich, *Phys. Rev. A*, **27**, 29 (1983).
- [14] C. C. J. Roothaan, *Aust. J. Phys.*, **43**, 439 (1990).

# New Algorithms for Calculating $3n-j$ Symbols

CLEMENS C. J. ROTHAAAN\*

*Departments of Physics and Chemistry, University of Chicago, Chicago, Illinois 60637,  
and Hewlett-Packard Laboratories, 1501 Page Mill Road, Palo Alto, California 94304*

## Abstract

Compact expressions are presented for the  $3n-j$  symbols, where  $1 \leq n \leq 4$ , which feature sums over products of binomial coefficients, and certain integer triangular coefficients. The triangular coefficients in turn can be expressed as products of binomial coefficients. Thus in the formulas presented for the  $3n-j$  symbols, the dependence on numerous factorials, formally as well as computationally, has been completely eliminated. While formulas which incorporate summations over products of binomial coefficients have been known for the  $3-j$  and  $6-j$  symbols, the introduction of the triangular coefficients, and the application of the binomial/triangular scheme to  $3n-j$  symbols with  $n > 2$ , provide important new results. The new formulas are simpler, and they permit more efficient computations of the  $3n-j$  symbols, both in exact and in floating point format, than most schemes which are currently in use. © 1993 John Wiley & Sons, Inc.

## Introduction

The algebra of angular momenta occupies a central position in the quantum mechanical description of numerous physical systems and/or phenomena. The structure of atoms and nuclei, the rotational spectra of molecules, and many scattering processes provide typical examples. In practical calculations one always encounters the so-called  $3n-j$  symbols, where  $n = 1, 2, \dots$ ; they arise from the coupling and recoupling of angular momenta, and from the evaluation of matrix elements of irreducible tensors. For the details of the definitions and applications we refer to the standard literature [1–15].

## Racah's Formulas for $3-j$ and $6-j$ Symbols

In explicit calculations of the  $3-j$  and  $6-j$  symbols the most commonly used formulas are slight modifications of the famous formulas of Racah [3]. We adhere to prevailing practice, while introducing slight changes in notation to suit our purposes; specifically we define the  $3-j$  and  $6-j$  symbols by

---

\* Research carried out in part during the author's stay as a visiting professor at the University of Delaware, Newark, DE, 1987–88.

$$\begin{aligned}
\begin{pmatrix} a & b & c \\ \alpha & \beta & \gamma \end{pmatrix} &= \delta_{\alpha+\beta+\gamma, 0} (-1)^{a-b-\gamma} \Delta_{abc} \\
&\times \sqrt{(a-\alpha)!(b-\beta)!(c-\gamma)!(a+\alpha)!(b+\beta)!(c+\gamma)!} \\
&\times \sum_z \frac{(-1)^z}{(b+\beta-z)!(a-\alpha-z)!(a+b-c-z)!} \\
&\quad \times (c-a-\beta+z)!(c-b+\alpha+z)!z!
\end{aligned} \quad (1)$$

$$\begin{aligned}
\begin{Bmatrix} a & b & c \\ d & e & f \end{Bmatrix} &= \Delta_{abc} \Delta_{aef} \Delta_{dhf} \Delta_{dec} \\
&\times \sum_z \frac{(-1)^z}{(b+c+e+f-z)!(c+a+f+d-z)!} \\
&\quad \times (a+b+d+e-z)! \\
&\times \frac{(z+1)!}{(z-a-b-c)!(z-c-f-a)!} \\
&\quad \times (z-f-d-b)!(z-d-e-c)!
\end{aligned} \quad (2)$$

where

$$\Delta_{abc} = \sqrt{\frac{(b+c-a)!(c+a-b)!(a+b-c)!}{(a+b+c+1)!}} \quad (3)$$

The sums in Eqs. (1, 2) are limited by the requirement that the arguments of the factorials must be nonnegative. It should be noted that the essence of Eq. (1) was first given by van der Waerden [1], a fact which has often been overlooked.

Note that  $a, b, c, d, e, f$  are  $j$ -quantum numbers: they must be nonnegative integer or half integer. The  $j$ -triples  $(a, b, c), (a, e, f), (d, b, f), (d, e, c)$  must satisfy the *triangular condition*, e.g.,  $(a, b, c)$  must be capable of forming a *vector coupling triangle* of integer circumference. Due to these conditions, the four quantities  $a + b + c, b + c - a, c + a - b, a + b - c$  are all nonnegative integers.

In a similar vein  $\alpha, \beta, \gamma$  are  $m$ -quantum numbers; the  $m$ -triple  $(\alpha, \beta, \gamma)$  is constrained by  $\alpha + \beta + \gamma = 0$ , as evident from Eq. (1). Also the  $jm$ -pairs  $(a, \alpha), (b, \beta), (c, \gamma)$  must satisfy the *line-segment condition*, e.g.,  $-a \leq \alpha \leq a$ , integer steps being implied; hence  $a \pm \alpha, b \pm \beta, c \pm \gamma$  are all nonnegative integers.

From Eqs. (1-3) it is clear that a 3- $j$  or 6- $j$  symbol is in general the positive or negative square root of a positive rational fraction, or zero. Such numbers have been called *root-rational fractions*, or RRFs, by Stone and Wood [16]; we suggest that they be called *semi-rational numbers*, a term we shall adhere to in this article.

### Binomial and Triangular Coefficients

The binomial coefficients are the expansion coefficients of  $(x + y)^a$ ; for non-negative integer values of  $a$ , which covers our present needs, they are given by

$$\begin{pmatrix} a \\ b \end{pmatrix} = \frac{a!}{b!(a-b)!}, \quad 0 \leq b \leq a \quad (4)$$

Obviously  $b$  is also a nonnegative integer, and the binomial coefficients are positive integers.

In his investigations of internal symmetries of the  $3-j$  symbol, Regge [10] discovered the importance of the square form

$$\begin{array}{|c|c|c|} \hline b+c-a & c+a-b & a+b-c \\ \hline a-\alpha & b-\beta & c-\gamma \\ \hline a+\alpha & b+\beta & c+\gamma \\ \hline \end{array} \quad (5)$$

which we shall call the *Regge square*. The sum of the elements of each row or column of that square is equal to the circumference of the triangle,  $a+b+c$ .

Following in Regge's footsteps, we define six positive integer quantities, to be called *triangular coefficients*, or shortly *T-coefficients*, with respect to the *rows* and the *columns* of the Regge square (5), namely

$$\left. \begin{aligned} T_{abc} &= \frac{(a+b+c+1)!}{(b+c-a)!(c+a-b)!(a+b-c)!} \\ T_{abc, \alpha\beta\gamma}^- &= \frac{(a+b+c+1)!}{(a-\alpha)!(b-\beta)!(c-\gamma)!} \\ T_{abc, \alpha\beta\gamma}^+ &= \frac{(a+b+c+1)!}{(a+\alpha)!(b+\beta)!(c+\gamma)!} \\ T_{abc, \alpha}^1 &= \frac{(a+b+c+1)!}{(b+c-a)!(a-\alpha)!(a+\alpha)!} \\ T_{abc, \beta}^2 &= \frac{(a+b+c+1)!}{(c+a-b)!(b-\beta)!(b+\beta)!} \\ T_{abc, \gamma}^3 &= \frac{(a+b+c+1)!}{(a+b-c)!(c-\gamma)!(c+\gamma)!} \end{aligned} \right\} \quad (6)$$

To highlight the relation between the  $T$ -coefficients and the Regge square we introduce the *T-coefficient array*

	$T_{abc, \alpha}^1$	$T_{abc, \beta}^2$	$T_{abc, \gamma}^3$
$T_{abc}$	$(b+c-a)!$	$(c+a-b)!$	$(a+b-c)!$
$T_{abc, \alpha\beta\gamma}^-$	$(a-\alpha)!$	$(b-\beta)!$	$(c-\gamma)!$
$T_{abc, \alpha\beta\gamma}^+$	$(a+\alpha)!$	$(b+\beta)!$	$(c+\gamma)!$

(7)

The triangular coefficient  $T_{abc}$  is the only one which depends exclusively on the  $j$ -quantum numbers  $a, b, c$ , and will be called the *principal triangular coefficient*, the other five will be called *associated triangular coefficients*. It will become clear in the following that the associated  $T$ -coefficients play a role only in the  $3-j$  coefficients, while principal  $T$ -coefficients play a role in all  $3n-j$  coefficients.

Comparison of Eq. (3) with the first Eq. (6) yields

$$\Delta_{abc} = \frac{1}{\sqrt{T_{abc}}} \quad (8)$$



Note also that the triple product of the  $T$ -coefficients from the *rows* of the Regge square (5) is equal to the corresponding product from the *columns*, as expressed by

$$T_{abc} T_{abc, \alpha\beta\gamma}^- T_{abc, \alpha\beta\gamma}^+ = T_{abc, \alpha}^1 T_{abc, \beta}^2 T_{abc, \gamma}^3 \quad (9)$$

The triangular coefficients can easily be expressed in terms of binomial coefficients. Using Eqs. (4, 6) we find

$$\left. \begin{aligned} T_{abc} &= \binom{a+b+c+1}{b+c-a} \binom{2a+1}{c+a-b} (a+b-c+1) \\ T_{abc, \alpha\beta\gamma}^- &= \binom{a+b+c+1}{a-\alpha} \binom{b+c+\alpha+1}{b-\beta} (c-\gamma+1) \\ T_{abc, \alpha\beta\gamma}^+ &= \binom{a+b+c+1}{a+\alpha} \binom{b+c-\alpha+1}{b+\beta} (c+\gamma+1) \\ T_{abc, \alpha}^1 &= \binom{a+b+c+1}{b+c-a} \binom{2a+1}{a-\alpha} (a+\alpha+1) \\ T_{abc, \beta}^2 &= \binom{a+b+c+1}{c+a-b} \binom{2b+1}{b-\beta} (b+\beta+1) \\ T_{abc, \gamma}^3 &= \binom{a+b+c+1}{a+b-c} \binom{2c+1}{c-\gamma} (c+\gamma+1) \end{aligned} \right\} \quad (10)$$

It will be shown in the following sections that in general a  $3n-j$  symbol can be factorized into a product  $QR$ , where  $R$  is an integer, which can be positive, negative, or zero, while the *normalization factor*  $Q$  is the *reciprocal square root of a product of triangular coefficients*.

For the  $3-j$  and  $6-j$  symbols, the integer  $R$  can be factorized into a product  $ST$ , where  $T$  is a *triangular coefficient*, and  $S$  is a *sum over products of binomial coefficients*.

For the  $9-j$  and  $12-j$  symbols, the integer  $R$  is a *sum over products of  $S$ -sums from  $6-j$  symbols, multiplied by  $2z+1$* , where  $z$  is the summation variable.

We shall speak accordingly of  $QST$  factorization for the  $3-j$  and  $6-j$  symbols, and  $QR$  factorization for the  $9-j$  and  $12-j$  symbols. Pending proofs of these claims of factorization, it is clear that a precomputed table of binomial coefficients is all we need to calculate  $3n-j$  symbols without any explicit reference to factorials.

### ***QST* Factorization of the $3-j$ Symbol**

In view of Eqs. (1, 6, 8, 9) we can write the  $3-j$  symbol in the form

$$\begin{pmatrix} a & b & c \\ \alpha & \beta & \gamma \end{pmatrix} = Q_{abc, \alpha\beta\gamma} R_{abc, \alpha\beta\gamma} \quad (11)$$

where

$$Q_{abc, \alpha\beta\gamma} = \frac{1}{\sqrt{T_{abc} T_{abc, \alpha\beta\gamma}^- T_{abc, \alpha\beta\gamma}^+}} = \frac{1}{\sqrt{T_{abc, \alpha}^1 T_{abc, \beta}^2 T_{abc, \gamma}^3}} \quad (12)$$

and

$$R_{abc, \alpha\beta\gamma} = \delta_{\alpha+\beta+\gamma, 0} (-1)^{a-h-\gamma} (a+b+c+1)! \\ \times \sum_z \frac{(-1)^z}{(b+\beta-z)!(a-\alpha-z)!(a+b-c-z)!} \\ \times (c-a-\beta+z)!(c-b+\alpha+z)!z! \quad (13)$$

We now show that  $R_{abc, \alpha\beta\gamma}$  is an integer which can be factorized in six different ways, namely as the product of any one of the triangular coefficients (10) and a corresponding sum over triple products of binomial coefficients, to be called a 3- $j$  S-sum.

In Eq. (13) we convert the factorial outside the sum,  $(a+b+c+1)!$ , into any one of the triangular coefficients by inserting the appropriate denominators, while inserting compensating numerators under the summation sign. Each of these three numerators can then be combined with a pair of factors in the denominator to yield a binomial coefficient. We thus obtain six different factorizations of  $R_{abc, \alpha\beta\gamma}$  into  $S, T$  companions, namely

$$R_{abc, \alpha\beta\gamma} = S_{abc, \alpha\beta\gamma} T_{abc} = \tilde{S}_{abc, \alpha\beta\gamma} T_{abc, \alpha\beta\gamma} = S_{abc, \alpha\beta\gamma}^+ T_{abc, \alpha\beta\gamma}^+ \\ = S_{abc, \alpha\beta\gamma}^1 T_{abc, \alpha} = S_{abc, \alpha\beta\gamma}^2 T_{abc, \beta} = S_{abc, \alpha\beta\gamma}^3 T_{abc, \gamma} \quad (14)$$

where

$$\left. \begin{aligned} S_{abc, \alpha\beta\gamma} &= \delta_{\alpha+\beta+\gamma, 0} (-1)^{a-h-\gamma} \\ &\times \sum_z (-1)^z \binom{b+c-a}{b+\beta-z} \binom{c+a-h}{a-\alpha-z} \binom{a+b-c}{a+b-c-z} \\ S_{abc, \alpha\beta\gamma}^- &= \delta_{\alpha+\beta+\gamma, 0} (-1)^{a-h-\gamma} \\ &\times \sum_z (-1)^z \binom{a-\alpha}{a-\alpha-z} \binom{b-\beta}{a+b-c-z} \binom{c-\gamma}{b+\beta-z} \\ S_{abc, \alpha\beta\gamma}^+ &= \delta_{\alpha+\beta+\gamma, 0} (-1)^{a-h-\gamma} \\ &\times \sum_z (-1)^z \binom{a+\alpha}{a+b-c-z} \binom{b+\beta}{b+\beta-z} \binom{c+\gamma}{a-\alpha-z} \\ S_{abc, \alpha\beta\gamma}^1 &= \delta_{\alpha+\beta+\gamma, 0} (-1)^{a-h-\gamma} \\ &\times \sum_z (-1)^z \binom{b+c-a}{b+\beta-z} \binom{a-\alpha}{a-\alpha-z} \binom{a+\alpha}{a+b-c-z} \\ S_{abc, \alpha\beta\gamma}^2 &= \delta_{\alpha+\beta+\gamma, 0} (-1)^{a-h-\gamma} \\ &\times \sum_z (-1)^z \binom{c+a-b}{a-\alpha-z} \binom{b-\beta}{a+b-c-z} \binom{b+\beta}{b+\beta-z} \\ S_{abc, \alpha\beta\gamma}^3 &= \delta_{\alpha+\beta+\gamma, 0} (-1)^{a-h-\gamma} \\ &\times \sum_z (-1)^z \binom{a+b-c}{a+b-c-z} \binom{c-\gamma}{b+\beta-z} \binom{c+\gamma}{a-\alpha-z} \end{aligned} \right\} \quad (15)$$

Analogous to the  $T$ -coefficient array (7) we introduce the 3- $j$   $S$ -sum array

	$S_{abc, \alpha\beta\gamma}^1$	$S_{abc, \alpha\beta\gamma}^2$	$S_{abc, \alpha\beta\gamma}^3$	
$S_{abc, \alpha\beta\gamma}$	$\begin{pmatrix} b+c-a \\ b+\beta-z \end{pmatrix}$	$\begin{pmatrix} c+a-b \\ a-\alpha-z \end{pmatrix}$	$\begin{pmatrix} a+b-c \\ a+b-c-z \end{pmatrix}$	(16)
$S_{abc, \alpha\beta\gamma}^-$	$\begin{pmatrix} a-\alpha \\ a-\alpha-z \end{pmatrix}$	$\begin{pmatrix} b-\beta \\ a+b-c-z \end{pmatrix}$	$\begin{pmatrix} c-\gamma \\ b+\beta-z \end{pmatrix}$	
$S_{abc, \alpha\beta\gamma}^+$	$\begin{pmatrix} a+\alpha \\ a+b-c-z \end{pmatrix}$	$\begin{pmatrix} b+\beta \\ b+\beta-z \end{pmatrix}$	$\begin{pmatrix} c+\gamma \\ a-\alpha-z \end{pmatrix}$	

Note that any  $S$ ,  $T$  companions of Eqs. (14) appear in the exact same position in the corresponding arrays (16) and (7), respectively.

Combining Eqs. (11) and (14) we obtain as our final result for the 3- $j$  symbol the six equivalent  $QST$  factorizations

$$\left. \begin{aligned} \begin{pmatrix} a & b & c \\ \alpha & \beta & \gamma \end{pmatrix} &= Q_{abc, \alpha\beta\gamma} S_{abc, \alpha\beta\gamma} T_{abc} \\ \begin{pmatrix} a & b & c \\ \alpha & \beta & \gamma \end{pmatrix} &= Q_{abc, \alpha\beta\gamma} S_{abc, \alpha\beta\gamma}^- T_{abc, \alpha\beta\gamma}^- \\ \begin{pmatrix} a & b & c \\ \alpha & \beta & \gamma \end{pmatrix} &= Q_{abc, \alpha\beta\gamma} S_{abc, \alpha\beta\gamma}^+ T_{abc, \alpha\beta\gamma}^+ \\ \begin{pmatrix} a & b & c \\ \alpha & \beta & \gamma \end{pmatrix} &= Q_{abc, \alpha\beta\gamma} S_{abc, \alpha\beta\gamma}^1 T_{abc, \alpha}^1 \\ \begin{pmatrix} a & b & c \\ \alpha & \beta & \gamma \end{pmatrix} &= Q_{abc, \alpha\beta\gamma} S_{abc, \alpha\beta\gamma}^2 T_{abc, \beta}^2 \\ \begin{pmatrix} a & b & c \\ \alpha & \beta & \gamma \end{pmatrix} &= Q_{abc, \alpha\beta\gamma} S_{abc, \alpha\beta\gamma}^3 T_{abc, \gamma}^3 \end{aligned} \right\} \quad (17)$$

where the  $Q$ ,  $S$ ,  $T$  factors are given by Eqs. (12, 15, 10), respectively.

In Eqs. (17) all six  $T$ -coefficients, the associated ones as well as the principal one, occur on an equal footing. It is worth noting that any one of the six Eqs. (17) can be derived from any other one by exploiting symmetry properties of the 3- $j$  symbol given by Wigner [2], Racah [3], and especially Regge [10].

The sum  $S_{abc, \alpha\beta\gamma}$  given by the first Eq. (17) was proposed some time ago by Nachamkin [18] and by Varshalovich et al. [15], and has recently been incorporated into a 3- $j$  computer program by Lai and Chiu [20]. However in all these instances the complete formulas for the 3- $j$  symbol, which still contain numerous factorials, are in practice much more onerous than any one of our Eqs. (17). Also, Nachamkin's [18] formula for the 3- $j$  symbol contains an error, having two factors in the numerator which belong in the denominator.

### QST Factorization of the 6- $j$ Symbol

The 6- $j$  symbol as defined by Eq. (2) refers to and is determined by four vector coupling triangles, namely  $(a, b, c)$ ,  $(a, e, f)$ ,  $(d, b, f)$ ,  $(d, e, c)$ . We shall call the triangle  $(a, b, c)$  the *primary triangle* of the 6- $j$  symbol, due to the appearance of  $a, b, c$  as the upper indices of the 6- $j$  symbol; each of the other three *secondary triangles* arises from two lower indices, and the upper index above the third lower index.

In actual fact the four triangles are equivalent, and the selection of one triangle as the primary one is arbitrary. Mathematically this is expressed by the statement that the 6- $j$  symbol is invariant under exchange of any pair of upper indices with the corresponding pair of lower indices:

$$\begin{Bmatrix} a & b & c \\ d & e & f \end{Bmatrix} = \begin{Bmatrix} a & e & f \\ d & b & c \end{Bmatrix} = \begin{Bmatrix} d & b & f \\ a & e & c \end{Bmatrix} = \begin{Bmatrix} d & e & c \\ a & b & f \end{Bmatrix} \quad (18)$$

Another important symmetry relation states that the 6- $j$  symbol is invariant under any permutation of the three columns:

$$\begin{aligned} \begin{Bmatrix} a & b & c \\ d & e & f \end{Bmatrix} &= \begin{Bmatrix} b & c & a \\ e & f & d \end{Bmatrix} = \begin{Bmatrix} c & a & b \\ f & d & e \end{Bmatrix} \\ &= \begin{Bmatrix} a & c & b \\ d & f & e \end{Bmatrix} = \begin{Bmatrix} b & a & c \\ e & d & f \end{Bmatrix} = \begin{Bmatrix} c & b & a \\ f & e & d \end{Bmatrix} \end{aligned} \quad (19)$$

The symmetry relations (18, 19) were given by Wigner [2]; they can easily be verified directly from Eq. (2).

The QST factorization of the 6- $j$  symbol is considerably simpler than the corresponding process for the 3- $j$  symbol. In view of Eqs. (2, 8) we can write the 6- $j$  symbol in the form

$$\begin{Bmatrix} a & b & c \\ d & e & f \end{Bmatrix} = Q_{def}^{abc} R_{def}^{abc} \quad (20)$$

where

$$Q_{def}^{abc} = \frac{1}{\sqrt{T_{abc} T_{acf} T_{dbf} T_{dec}}} \quad (21)$$

and

$$\begin{aligned} R_{def}^{abc} &= \sum_z \frac{(-1)^z}{(b+c+e+f-z)!(c+a+f+d-z)!(a+b+d+e-z)!} \\ &\quad \times \frac{(z+1)!}{(z-a-b-c)!(z-e-f-a)!(z-f-d-b)!(z-d-e-c)!} \end{aligned} \quad (22)$$

We now show that  $R_{def}^{abc}$  is an integer, which can be written as the product of any one of the four triangular coefficients  $T_{abc}$ ,  $T_{def}$ ,  $T_{dbf}$ ,  $T_{dec}$ , and a sum over quadruple products of binomial coefficients, to be called a 6- $j$   $S$ -sum.

In view of the equivalence of the four vector coupling triangles, it is sufficient to show this factorization for just one choice of the four  $T$ -coefficients. Accordingly, in Eq. (22) we introduce  $T_{abc}$ , the  $T$ -coefficient associated with the primary triangle, as the factor outside the sum, and the reciprocal of  $T_{abc}$  under the summation sign, yielding

$$R_{def}^{abc} = S_{def}^{abc} T_{abc} \quad (23)$$

where

$$S_{def}^{abc} = \sum_z (-1)^z \begin{pmatrix} z+1 \\ z-a-b-c \end{pmatrix} \begin{pmatrix} b+c-a \\ z-e-f-a \end{pmatrix} \times \begin{pmatrix} c+a-b \\ z-f-d-b \end{pmatrix} \begin{pmatrix} a+b-c \\ z-d-e-c \end{pmatrix} \quad (24)$$

Combining Eqs. (20) and (23) we obtain as our final result for the 6- $j$  symbol

$$\left\{ \begin{matrix} a & b & c \\ d & e & f \end{matrix} \right\} = Q_{def}^{abc} S_{def}^{abc} T_{abc} \quad (25)$$

where the  $Q$ ,  $S$ ,  $T$  factors are given by Eqs. (21, 24, 10), respectively.

Lai and Chiu [20] also used a sum over quadruple products of binomial coefficients which resembles our sum  $S_{def}^{abc}$ , Eq. (24). However in order to convert the summation term from quotients of factorials to products of binomial coefficients, they inserted what turns out to be fragments from two different triangular coefficients as numerators under the summation sign. Consequently, the compensating fragments outside the sum cannot be combined into a triangular coefficient, and their complete result for the 6- $j$  symbol cannot easily be recast into a formula free of explicit factorials.

### QR Factorization of the 9- $j$ Symbol

The 9- $j$  symbol was defined by Wigner [2] and by Arima et al. [6] in connection with the coupling of four angular momenta. Nowadays it is customary to adopt as the starting point for further analysis or computation a formula in terms of 6- $j$  symbols, namely [16,19,21]

$$\left\{ \begin{matrix} a & b & c \\ d & e & f \\ g & h & i \end{matrix} \right\} = \sum_z (-1)^{2z} (2z+1) \left\{ \begin{matrix} a & d & g \\ h & i & z \end{matrix} \right\} \left\{ \begin{matrix} b & e & h \\ d & z & f \end{matrix} \right\} \left\{ \begin{matrix} c & f & i \\ z & a & b \end{matrix} \right\} \quad (26)$$

The derivation of Eq. (26) is generally attributed to Wigner [2]. It is also claimed to have been discovered by Jahn [5]; another independent derivation, in slightly different form, was given by Arima et al. [6].

Each row and each column of the 9- $j$  symbol must form a vector coupling triangle; one consequence of this is that in Eq. (26) the values of the summation index  $z$

are either all integer or all half integer. Hence the factor  $(-1)^{2z}$  under the summation sign is a constant, namely  $+1$  or  $-1$ , for  $z$  integer or half integer, respectively.

The symmetry properties of the  $9-j$  symbol have been analyzed in detail by Jahn and Hope [5]. Simply put, the  $9-j$  symbol is invariant when subjected to a reflection at either diagonal, or to an even (cyclic) permutation of the rows or columns; and the  $9-j$  symbol is multiplied by  $(-1)^o$  when subjected to an odd (anticyclic) permutation of the rows or columns, where

$$\sigma = a + b + c + d + e + f + g + h + i \quad (27)$$

For example

$$\begin{Bmatrix} a & b & c \\ d & e & f \\ g & h & i \end{Bmatrix} = \begin{Bmatrix} i & f & c \\ h & e & b \\ g & d & a \end{Bmatrix} = \begin{Bmatrix} b & c & a \\ e & f & d \\ h & i & g \end{Bmatrix} = (-1)^o \begin{Bmatrix} c & b & a \\ f & e & d \\ i & h & g \end{Bmatrix} \quad (28)$$

We now proceed to derive from Eq. (26) a formula which is more suitable for our purposes. We apply Eq. (26) to the last member of Eqs. (28), and use some of the symmetry relations (18, 19) so that the summation variable  $z$  appears as the upper left index in each  $6-j$  symbol. As indicated above, the phase factor  $(-1)^{\sigma+2z}$  is independent of the summation variable  $z$ , and can be converted, using the fact that all relevant triangles have integer circumferences, into  $(-1)^r$ , where

$$\tau = \sigma - 2a - 2e - 2i = -a + b + c + d - e + f + g + h - i \quad (29)$$

Our new formula for the  $9-j$  symbol in terms of  $6-j$  symbols then becomes

$$\begin{Bmatrix} a & b & c \\ d & e & f \\ g & h & i \end{Bmatrix} = (-1)^r \sum_z (2z + 1) \begin{Bmatrix} z & b & d \\ a & g & c \end{Bmatrix} \begin{Bmatrix} z & f & h \\ e & b & d \end{Bmatrix} \begin{Bmatrix} z & g & c \\ i & f & h \end{Bmatrix} \quad (30)$$

Using Eqs. (30, 25, 21) we obtain as our final result for the  $9-j$  symbol

$$\begin{Bmatrix} a & b & c \\ d & e & f \\ g & h & i \end{Bmatrix} = Q_{abc, def, ghi} R_{abc, def, ghi} \quad (31)$$

where

$$Q_{abc, def, ghi} = \frac{1}{\sqrt{T_{abc} T_{def} T_{ghi} T_{adg} T_{beh} T_{cfi}}} \quad (32)$$

and

$$R_{abc, def, ghi} = (-1)^r \sum_z (2z + 1) S_{aeg}^{zbd} S_{ebd}^{zfh} S_{ifh}^{zgc} \quad (33)$$

The difference between Eq. (30) and Eqs. (31-33) is not trivial. In the first case the sum is over products of semi-rational numbers, while in the second case the sum is over products of integers. The occurrence of the summation index  $z$  as the upper left element in each  $6-j$  symbol, together with the fact that each of the three  $z$ -dependent primary triangles occurs once more as a secondary triangle, causes the

$Q$ -factors from the three 6- $j$  symbols to combine into a  $z$ -independent  $Q$ -factor for the 9- $j$  symbol.

We note that Eq. (33) contains four formal summations, namely those required for each of the three  $S$ -factors, and the explicit summation over  $z$ . Extensive efforts to reformulate the 9- $j$  symbol so that one or more of the summations can be carried out analytically were undertaken by Jucys and Bandzaitis [13], and by Ališauskas and Jucys [17]; they succeeded in deriving a formula containing one less summation. Starting from that formula, Lai and Chiu [21] attempted to recast the general term under the triple sum as a product of binomial coefficients. Introducing some needed constant factorials, they managed to convert the summation term into a product of eight binomial coefficients and three factorials. Our own attempt, making some different choices, resulted in eight binomial coefficients and two factorials. Needless to say, for both conversions the constant factors outside the sum contain many factorials which cannot be combined into triangular coefficients. Both these conversions at least achieve that the required summation is over products of integers, which is a necessary prerequisite for obtaining exact results.

### QR Factorization of Two 12- $j$ Symbols

Two 12- $j$  symbols have been defined: one by Jahn and Hope [5] in connection with the coupling of five angular momenta, and another one by Elliott and Flowers [8] as the matrix element of a particular irreducible tensor. Following Judd [12] we shall refer to them as 12- $j$  symbols of the first and the second kind, respectively. The original notation adopted by Jahn and Hope [5] for the first kind has been replaced by a more sensible one proposed by Ord-Smith [7].

The two 12- $j$  symbols are defined by very similar formulas, namely

$$\left. \begin{aligned} \left\{ \begin{matrix} l & a & b & d & e & g & h & j \\ k & & c & & f & & i & \end{matrix} \right\}^{(1)} &= \sum_z (-1)^{\sigma+z} (2z+1) \\ &\times \left\{ \begin{matrix} z & b & c \\ a & k & l \end{matrix} \right\} \left\{ \begin{matrix} z & f & e \\ d & b & c \end{matrix} \right\} \\ &\times \left\{ \begin{matrix} z & h & i \\ g & f & e \end{matrix} \right\} \left\{ \begin{matrix} z & l & k \\ j & h & i \end{matrix} \right\} \\ \left\{ \begin{matrix} k & a & b & d & e & g & h & j \\ l & & c & & f & & i & \end{matrix} \right\}^{(2)} &= \sum_z (2z+1) \\ &\times \left\{ \begin{matrix} z & b & c \\ a & l & k \end{matrix} \right\} \left\{ \begin{matrix} z & f & e \\ d & b & c \end{matrix} \right\} \\ &\times \left\{ \begin{matrix} z & h & i \\ g & f & e \end{matrix} \right\} \left\{ \begin{matrix} z & l & k \\ j & h & i \end{matrix} \right\} \end{aligned} \right\} \quad (34)$$

where

$$\sigma = a + b + c + d + e + f + g + h + i + j + k + l \quad (35)$$

The difference between the two  $12-j$  symbols is in the topology of the index structure. In Eqs. (34) the upper right index pair of each  $6-j$  symbol appears again as the lower right index pair of its right neighbor; the last upper index pair,  $lk$ , appears as the first lower index pair in the  $12-j$  symbol of the second kind, but reversed as  $kl$  in the  $12-j$  symbol of the first kind. The latter "twisted" index structure was illustrated by Ord-Smith [7] in a diagram using a Möbius strip.

Comparing Eqs. (34) for the  $12-j$  symbols with Eq. (30) for the  $9-j$  symbol, the analogy is striking. Using Eqs. (34, 25, 21) we obtain as our final results for the  $12-j$  symbols

$$\left. \begin{aligned} \left\{ \begin{matrix} l & a & b & d & e & g & h & j \\ k & & c & & f & & i & \end{matrix} \right\}^{(1)} &= Q_{lbeh, adgj, kcfi}^{(1)} R_{lbeh, adgj, kcfi}^{(1)} \\ \left\{ \begin{matrix} k & a & b & d & e & g & h & j \\ l & & c & & f & & i & \end{matrix} \right\}^{(2)} &= Q_{kbeh, adgj, lcfi}^{(2)} R_{kbeh, adgj, lcfi}^{(2)} \end{aligned} \right\} \quad (36)$$

where

$$\left. \begin{aligned} Q_{lbeh, adgj, kcfi}^{(1)} &= \frac{1}{\sqrt{T_{lab} T_{kac} T_{bde} T_{cdf} T_{egh} T_{fgi} T_{hjk} T_{ijl}}} \\ Q_{kbeh, adgj, lcfi}^{(2)} &= \frac{1}{\sqrt{T_{kab} T_{lac} T_{bde} T_{cdf} T_{egh} T_{fgi} T_{hjk} T_{ijl}}} \end{aligned} \right\} \quad (37)$$

and

$$\left. \begin{aligned} R_{lbeh, adgj, kcfi}^{(1)} &= \sum_z (-1)^{\sigma+z} (2z+1) S_{akl}^{zhc} S_{dhe}^{zlc} S_{gfi}^{zhi} S_{jhi}^{zlk} \\ R_{kbeh, adgj, lcfi}^{(2)} &= \sum_z (2z+1) S_{alk}^{zhc} S_{dhe}^{zlc} S_{gfi}^{zhi} S_{jhi}^{zlk} \end{aligned} \right\} \quad (38)$$

### Bibliography

- [1] B. L. van der Waerden, *Die Gruppentheoretische Methode in der Quantenmechanik* (Springer-Verlag, Berlin, 1932).
- [2] E. P. Wigner, *On the Matrices which Reduce the Kronecker Products of Representations of  $S$  and  $R$  Groups*, unpublished manuscript (1940), later published in *Quantum Theory of Angular Momentum*, L. C. Biedenharn and H. van Dam, Eds. (Academic Press, New York, 1965, pp. 87-133).
- [3] G. Racah, *Phys. Rev.* **63**, 438 (1942).
- [4] J. P. Elliott, *Proc. R. Soc. A* **218**, 345 (1953).
- [5] H. A. Jahn and J. Hope, *Phys. Rev.* **93**, 318 (1954).
- [6] A. Arima, H. Horie, and Y. Tanabe, *Prog. Theor. Phys.* **11**, 143 (1954).
- [7] R. J. Ord-Smith, *Phys. Rev.* **94**, 1227 (1954).
- [8] J. P. Elliott and B. H. Flowers, *Proc. R. Soc. A* **229**, 536 (1955).
- [9] A. R. Edmonds, *Angular Momentum in Quantum Mechanics* (Princeton University Press, Princeton, NJ, 1957).
- [10] T. Regge, *Nuovo Cimento* **10**, 544 (1958).
- [11] M. Rotenberg, R. Bivins, N. Metropolis, and J. K. Wooten, *The 3-j and 6-j Symbols* (MIT Press, Cambridge, MA, 1959).
- [12] B. R. Judd, *Operator Techniques in Atomic Spectroscopy* (McGraw-Hill, New York, 1963).



- [13] A. P. Jucys and A. A. Bandzaitis, *The Theory of Angular Momentum in Quantum Mechanics* (Mintis, Vilnius, Lithuania, 1965); 2nd ed., (Mokslas, Vilnius, Lithuania, 1977)
- [14] L. C. Biedenharn and J. D. Louck, *Angular Momentum in Quantum Physics, Vol. 8 of Encyclopedia of Mathematics and its Applications*, G. C. Rota, Ed. (Addison-Wesley, Reading, MA, 1981).
- [15] D. A. Varshalovich, A. N. Moskalev, and V. K. Khersonskii, *Quantum Theory of Angular Momentum* (Nauka, Leningrad, 1975), in Russian; (World Scientific Publishing, Singapore, 1988).
- [16] A. J. Stone and C. P. Wood, *Comp. Phys. Comm.* **21**, 195 (1980).
- [17] S. J. Ališauskas and A. P. Jucys, *J. Math. Phys.* **10**, 2227 (1969); **12**, 594 (1971)
- [18] J. Nachamkin, *J. Math. Phys.* **16**, 2391 (1975), Eq. (40).
- [19] D. Zhao and R. N. Zare, *J. Mol. Phys.* **65**, 1236 (1988).
- [20] S.-T. Lai and Y.-N. Chiu, *Comp. Phys. Comm.* **61**, 350 (1990).
- [21] S.-T. Lai and Y.-N. Chiu, *Comp. Phys. Comm.* **70**, 544 (1992).

Received June 23, 1993

# The Diatomic Molecule Project at LMSS 1956–1966: Broken Bottlenecks

BERNARD J. RANSIL

*Department of Medicine, Beth Israel Hospital and Harvard Medical School,  
Boston, Massachusetts 02215*

## Introduction

The title for this brief account of my association with the Laboratory of Molecular Structure and Spectra (LMSS) at Chicago is taken from Chapter 25 of Robert S. Mulliken's autobiography, *Life of a Scientist* [1]. It is apt for two reasons: The dates provide a convenient, although approximate, window of reference for the period, and the term "broken bottlenecks" alludes to the "bottlenecks" that were identified at the historic Shelter Island Conference in 1951 as the most important barriers, at the time, to the computation of accurate analytical molecular wave functions.

As it happens, the dates selected by Mulliken to delimit the period coincide with the year of my arrival at the University of Chicago as a post-doctoral research associate and the year that he was awarded the Nobel Prize in chemistry. But there were many events prior to 1956 that led up to the project, upon which it had been built, and without which it could not have happened. And neither my departure from the project in 1964 nor Mulliken's acceptance of the Nobel Prize in 1966 signaled the project's decline or close, for under Cade and Roothaan it proceeded at a momentum that carried it through to the publication of the extended basis set functions in 1974.

Among the many events that led up to this decade at LMSS and made it possible, let me cite a few of what I consider to be the most significant.

- Publication of Pauling's valence-bond and Hund and Mulliken's MO theories in the 1930s and the subsequent dissemination and discussion of these theories during the next several decades, with many publications on small molecule calculations by workers in Europe, the United States, and Japan.
- The Shelter Island meeting in September 1951, which brought most of the workers in the field together in five sessions, including two that focused on the integrals problem, especially the difficult three- and four-center integrals, and the means of calculating these with existing computers. Individuals presenting papers at the Integrals Session were:

Boys, Cambridge

Herzfeld and Griffing, Catholic University

Roothaan and Ruedenberg, Chicago

Kotani, University of Tokyo  
 Barnett and Coulson, Oxford  
 Kopineck, Max Planck Institute, Göttingen  
 Lundquist and Löwdin, Uppsala  
 Buehler and Hirschfelder, Wisconsin  
 Parr, Carnegie Institute of Technology

- Development of centers for integral calculations: Kotani in Japan; Roothaan, Ruedenberg, and Jaunzemis at Chicago; Barker, Thorne, and Eyring at Salt Lake City; Sklar at Catholic University; Coulson and Barnett at Oxford; Preuss in Göttingen; Sahni and Cooley at New York University.
- Development of early digital computers: Whirlwind at MIT, SEAC at NBS, Washington, DC, ILIAC at University of Illinois, and the Remington Rand Univacs.
- Development of digital computer programs to compute integrals by Barker and Eyring at Utah, Roothaan and Ruedenberg at Chicago with an offshoot at MIT, Nesbet at Boston University, Slater at MIT, Barnett at Oxford, and others; publication of accurate integral tables by several centers.

For myself, a young, inexperienced Ph.D., fresh from a year of post-doctoral work in the Heat Division at the National Bureau of Standards, where, at the suggestion of my chief, Charles Beckett, I had become acquainted with the Bureau's digital computer, SEAC (Standards Eastern Automatic Computer), there was a series of events that led, in random walk fashion, to my decision to go to Chicago. Among these, I recall the following as the most decisive:

- The availability of a home-made analogue computer in the Chemistry Department at Catholic University in the early 1950s, on which my Ph.D. dissertation—an LCAO-MO-SCF treatment of the  $H_3$  complex in open-shell minimal Slater orbital approximation—was done, using self-calculated integral values and values interpolated from Kotani's tables.
- The publication of Roothaan's seminal and breakthrough paper on the LCAO-MO-SCF method for computing wave functions in 1951, just as I entered the Ph.D. program at Catholic University [2].
- A post-doctoral year at NBS 1955–56 during which I learned the theory and elements of digital computing by programming the SEAC, with the assistance of Emilie Haynsworth and Phil Walsh, to solve the Schrödinger wave equation for the  $H_3$  complex; verified the analogue computer results to three-figure agreement, which was one to two figures less than the integral accuracy; and recognized the possibility of generalizing the program to compute wave functions for simple diatomic molecules.
- A letter to Professor Mulliken in the spring of 1956, inquiring about the possibility of doing a post-doctoral at LMSS.
- The gradual coming together of many things involving Mulliken and a grant that he was negotiating with NSF to support such a program; the integrals work by

Roothaan that had been in progress at Chicago for several years; Roothaan's plans for a one-year sabbatical on a Guggenheim in Europe; the decision that Roothaan's graduate students at the time, Doug McLean, Andy Weiss, and Megumu Yoshimine, would contribute their integrals work and programming skills to the construction of a computer program on the Remington Rand Univac 1103 at Wright-Patterson Air Force Base, to which LMSS had contractual access. The program would compute *ab initio* diatomic molecule wave functions in minimal Slater orbital LCAO-MO-SCF approximation, in which the Slater exponents would be iteratively optimized for minimum molecular energy. Three levels of approximation were visualized, distinguished by the orbital exponents: Slater exponents, best optimized atomic exponents, and best optimized molecular exponents. The concept of an *ab initio* computer program had occurred to others as well, e.g., Nesbet at Boston University, working alone, was programming integrals and an SCF routine at the time for selected diatomics.

### Early Days in the Project

When I arrived at LMSS in September 1956 as an NSF Research Associate, the faculty consisted of Professor Robert S. Mulliken, Associate Professor John R. Platt, and Assistant Professor Clemens C. J. Roothaan. Ruedenberg had just departed for Iowa, and Scherr, completing his thesis on  $N_2$ , was about to leave for Texas. Jaunzemis had already been gone a year. Doug McLean and Andy Weiss were research assistants working toward their Ph.D.'s. The computational staff consisted of Tracy Kinyon on a desktop mechanical computer at Chicago, Phil Merryman on the Whirlwind at MIT, and Megumu Yoshimine programming integrals. Bill Lester was an undergraduate student working as a research assistant. Augmented by Doug McLean's dog, Rover, McLean, Weiss, Yoshimine, and I constituted the group working on the diatomic molecule project for the subsequent 18–24 months, with Robert as Big Boss, Clemens as Little Boss, and me as Straw Boss, titles conferred on us one memorable day by Andy, Doug, and Megumu.

### The Project Under Way

[The history of the next 18–24 months is succinctly recounted in Chapter 25 of Mulliken's autobiography from which the following highlights have been adapted.]

Beginning in the fall of 1956, the project moved ahead steadily for the next 18 months with the team of Weiss, Yoshimine, McLean, and Ransil flying back and forth to Dayton in groups of twos, threes, or fours, for two to three evenings and nights of computing, with Ransil assuming responsibility for the overall design of the computer program, the production runs and administrative problems, and Yoshimine, McLean, and Weiss assuming responsibility for programming the integrals and the SCF routine. Everybody on the team did what is now called alpha and beta testing against the very rigorous hand calculations of Tracy Kinyon on his mighty Marchant mechanical desktop calculator, and the Kotani tables. Most

calculational work in those days was done on Monroe, Marchant, or Olivetti calculators.

When Roothaan returned from Europe in December 1957, the minimal-orbital diatomic molecule program was close to production-run status. It was agreed that McLean, Yoshimine, and Weiss would remain on the project until the program was debugged and operational, after which they would spend full time on their doctoral theses.

In the meantime, as Wright-Patterson updated to an 1103 and later to an 1103A, we began to talk of an extended orbital version of the program, and Roothaan recruited a new generation of graduate student assistants and began his accurate atom and molecule calculations. The second generation of graduate student programmers began to trickle in to LMSS beginning the summer and fall of 1958 and continuing into 1960, with Paul Bagus in the vanguard followed by Malli, Miroslav Synek, Chris Wahl, Winifred Huo, and many more during the early sixties.

### Minimal Basis Set Production Runs

But to return to the diatomic molecule program, early in 1958, Serafin Fraga Sanchez arrived from Spain on a Juan March Fund scholarship to join the project, preparatory to a collaboration with Mulliken. When the diatomic molecule program became operational in the spring-summer of 1958 and McLean, Weiss, and Yoshimine undertook their thesis work on Hartree-Fock quality atomic and molecular calculations under Roothaan, Fraga and Ransil began production runs on the first row diatomic homopolar and hydride and selected heteropolars (BF, CO, and LiF). The output consisted of the LCAO-MO wave functions, total molecular and orbital energies, binding energies, ionization potentials, dipole and quadrupole moments, population analysis, spectroscopic constants, limited mixed configuration functions, and potential energy curves for  $H_2$ ,  $He_2^{++}$ , and  $He_2$ . The original output, bound in hard-board covers, still exists.

### Early Fruits of the Project

The early results of the diatomic project and Roothaan's exact atom and molecule work were presented at the Conference on Molecular Quantum Mechanics at Boulder in June 1959 and were subsequently published in the issue of the *Reviews of Modern Physics* dedicated to that meeting [3]. By this time, the prospect of accurate numerical, rather than analytical, solutions to the Schrödinger equation had been seen as realizable and was being actively pursued by Roothaan and Włodzimierz Kolos, on leave from the University of Warsaw.

Also, by this time, LMSS was a beehive of activity with many student technicians, research assistants and research associates, and visitors from all over the world. Among the individuals who came to participate in, and contribute to, the various LMSS activities in this 10-year period as research associates and faculty, the LMSS Technical Reports record the following:

Karl H. Hausser	Max Planck Institute, Heidelberg	9/56-6/57
Takashi Itoh	University of Tokyo	12/56-12/57
James R. Richardson	Purdue University	4/56-9/56
Robert G. Parr	Carnegie Institute of Technology	6/57-7/57
Robert A. Sack	British Rayon Industries	9/58-10/59
Serafin Fraga Sanchez	Juan March Fund Fellow, Spain	6/59-4/61
Sigeru Huzinaga	Kyushu University	6/59-7/61
David Peters	Royal Holloway College, London	10/60-9/61
Charles W. Scherr	University of Texas	6/60-2/61
Paul E. Cade	University of Wisconsin	9/61-8/69
Enrico Clementi	IBM	10/60-7/61, 1/66-12/66
Wlodzimierz Kolos	University of Warsaw	7/57-6/58, 6/61-9/61 also 1966, 1967
Stanton Ehrenson	Brookhaven National Laboratory	9/60-12/62
John B. Greenshields	Duquesne University	9/62-8/64
Roberto Moccia	Instituto Chimico della Universita, Naples	12/60-8/62
Keith Sales	University of London	9/61-1962
John J. Sinai	Purdue University	2/61-7/64
Willis B. Person	University of Iowa	9/60-9/61, also 1966
William Lichten	Sloan Foundation Fellow	1/62-1/63
Sigrid Peyerimhoff	Justus Liebig University Giessen, Germany	-4/64
Lutoslaw Wolniewicz	Nicholas Copernicus University Torun, Poland	-7/64
Juergen M. Hinze	Bielefeld	2/66-1970

### Minimal Basis Set Results

The LMSS contributions to the Boulder meeting earlier that year had included Roothaan's SCF formalism for open-shell atomic systems and accurate calculations on atoms and 2- and 3-body systems, with Kolos, Sack, Sachs, Weiss, McLean, and Yoshimine; Ransil and Fraga's minimal orbital diatomic molecule results; Mulliken and Ransil's systematization of LCAO nomenclature; and Mulliken's study with Fraga of coulomb energy in valence bond theory. Following the meeting, the production runs on the minimal orbital project were completed and were eventually published in eight journal articles and two reports in the LMSS Technical Reports. The first two papers, containing a description of the project and tabulated wave functions, were published in the *Reviews of Modern Physics* in 1960 [4,5]; the remaining six, reporting computed spectroscopic constants, population analyses, potential curves for  $H_2$ ,  $He_2^{++}$ , and selected first row diatomics and limited config-

uration interaction (as it was called then), for selected first row diatomics, appeared at intervals in the *Journal of Chemical Physics* until 1962 [6–13].

The operational success of the atomic calculations and the *ab initio* diatomic molecule program and the results it generated, clearly heralded the dawn of a new era. It seemed at the time that as both computer speed and memory capacity improved, the main obstacle to obtaining accurate analytic wave functions and energies for small molecules would be how to give accurate analytical representation to electron correlation. All other considerations—the nature of the basis sets, basis set expansion limits, and parametric optimization—were perceived as technical problems that would yield to the inexorable advance in computer technology.

In 1959, Mulliken and Roothaan surveyed the progress made since the Shelter Island conference eight years earlier, in breaking the two major bottlenecks that had been identified at that time. The first, the methods of computing difficult integrals, had been solved by Kotani, Amamiya, and Sumose in Japan, Roothaan and Ruedenberg at Chicago, and Coulson and associates at Oxford. The second, the excessively time-consuming process of computing these integrals and solving the Schrödinger wave equation, had been solved by the timely development of high-speed computing machines.

### Moving on to Extended Basis Set Functions

Coincident with the harvesting of the minimal basis set program was the planning, design, and beginning implementation of a second generation, extended basis set diatomic molecular program, with the assistance of the new generation of graduate student programmers recruited by Roothaan. Ransil made plans to enter medical school in September 1960, during which he worked parttime at LMSS to complete the publication of the minimal orbital work, and to relinquish responsibility for the extended basis set work to Paul Cade from Professor Hirschfelder's group at the University of Wisconsin. Cade took over in September of 1961. At that time, it was projected that he would follow a design similar to the minimal orbital study, but would use an extended Slater basis set LCAO-MO-SCF approximation. This effort eventually produced a rich harvest of diatomic molecule studies; tables of the extended basis set functions were published by Cade et al. in 1974 [14].

### Accurate Numerical Functions

As these activities were carried out on the molecular side, Roothaan concentrated largely on accurate numerical calculations on the hydrogen molecule with Kolos. Others involved in Roothaan's accurate atomic and molecular calculations during the decade being remembered were Sack, Weiss, Sachs, and Wolniewicz, a student of Kolos, from Copernicus University in Torun, Poland.

### In Retrospect

Looking back from the perspective of some 30 years, it is my perception that what happened during the first half of that eventful decade at Chicago, as a result

of (1) the mathematical and integrals groundwork laid by Kotani, Roothaan, Ruedenberg, Coulson, and a host of others, (2) the development of the first generation of commercial digital computers, and (3) the emergence of graduate students and post-docs trained in the physics of molecules, mathematics, and early computer science, was the gradual coalescence of all these factors into a new science, in a serendipitous environment that made working together not only possible but fun. It was a privilege to be there at the time and to work with Andy, Doug, Megumu, and Clemens. I have never had the opportunity, and probably never will again, to publicly thank them and to acknowledge my deep and lasting indebtedness to them for being what they were to me in those days: teachers, colleagues, and stalwart friends. It was a once-in-a-lifetime experience, and I thank the organizers of this conference for setting aside time over the coming few days during which we can revisit that era, reflect upon it, catch perhaps some of the optimism and spirit of the period, and appreciate it for what it was: the birth of a new scientific discipline that was neither chemistry nor physics, neither mathematics nor computer science, but a fusion of all of these which produced a prototype tool for exploring and testing theories of molecular binding and interaction.

### Acknowledgments

I wish to thank Clemens C. J. Roothaan, Douglas McLean, and Andrew Weiss for reading the talk version of this memoir and for pointing out several errors in fact. Whatever other errors of omission or commission there may be are the author's, with apologies to those who may be concerned.

### Bibliography

- [1] R. S. Mulliken, *Life of a Scientist*, B. J. Ransil, Ed. (Springer-Verlag, New York, Heidelberg, 1989).
- [2] C. C. J. Roothaan, New developments in molecular orbital theory, *Rev. Mod. Phys.* **23**, 69 (1951)
- [3] *Rev. Mod. Phys.* **32**(2), (1960).
- [4] B. J. Ransil, Studies in molecular structure I. Scope and summary of the diatomic molecule program, *Rev. Mod. Phys.* **32**, 239 (1960).
- [5] B. J. Ransil, Studies in molecular structure. II. LCAO MO SCF wave functions for selected first-row diatomic molecules, *Rev. Mod. Phys.* **32**, 245 (1960).
- [6] S. Fraga and B. J. Ransil, Studies in molecular structure. III. Populations analyses for selected first-row diatomic molecules, *J. Chem. Phys.* **34**, 727 (1961).
- [7] B. J. Ransil, Studies in molecular structure IV. Potential curve for the interaction of two helium atoms in single-configuration LCAO MO SCF approximation, *J. Chem. Phys.* **34**, 2109 (1961).
- [8] S. Fraga and B. J. Ransil, Studies in molecular structure. V. Computed spectroscopic constants for selected diatomic molecules of the first row, *J. Chem. Phys.* **35**, 669 (1961).
- [9] S. Fraga and B. J. Ransil, Studies in molecular structure. VI. Potential curve for the interaction of two hydrogen atoms in the LCAO MO SCF approximation, *J. Chem. Phys.* **35**, 1967 (1961).
- [10] S. Fraga and B. J. Ransil, Studies in molecular structure. V(A). Potential curves of selected first row diatomic molecules, *Lab. Mol. Struct. Spectra Tech. Rep.*, 202 (1961).
- [11] S. Fraga and B. J. Ransil, Formulae for the evaluation of electronic energies in the LCAO MO SCF approximation, *Lab. Mol. Struct. Spectra Tech. Rep.*, 236, (1961).



- [12] S. Fraga and B. J. Ransil, Studies in molecular structure VII. Limited configuration interaction for selected first-row diatomics, *J. Chem. Phys.* **36**, 1127 (1962).
- [13] S. Fraga and B. J. Ransil, Studies in molecular structure VIII.  $\text{He}_2^{++}$  in the single- and many-configuration LCAO MO SCF approximation, *J. Chem. Phys.* **37**, 1112 (1962).
- [14] P. E. Cade, A. C. Wahl, K. Sales, J. B. Greenshields, and G. Malli, *At. Data Nucl. Data Tables* **13**, 339 (1974).

Received May 6, 1993

# Statistical Electron Correlation Coefficients for 29 States of the Heliumlike Ions

NATALIE MARY CANN and RUSSELL J. BOYD

*Department of Chemistry, Dalhousie University, Halifax, Nova Scotia, Canada B3H 4J3*

AJIT J. THAKKAR

*Department of Chemistry, University of New Brunswick, Fredericton, New Brunswick, Canada E3B 6E2*

## Abstract

Statistical electron correlation coefficients provide overall measures of the difference between the electron pair density and the product of one-electron densities. Explicitly correlated wave functions are used to compute radial and angular correlation coefficients for 29 low-lying states ( $n^1S$ ,  $n^3S$ ,  $n^1P$ ,  $n^3P$ ,  $n^1D$ , and  $n^3D$  with  $n < 7$ ) of the two-electron ions from helium through  $\text{Ne}^{8+}$ . This data base of 1566 correlation coefficients permits a systematic study of trends with respect to variation of nuclear charge, degree of excitation, angular momentum, and spin multiplicity. © 1993 John Wiley & Sons, Inc

## Introduction

In contemporary quantum chemistry, those effects neglected by the Hartree-Fock model are normally called electron correlation effects. However, from a statistical standpoint, electron correlation means that the motions of electrons are statistically correlated; that is, the electron pair density is not simply the product of one-electron densities [1]. These two interpretations of electron correlation are different because the antisymmetric Hartree-Fock wave function does account for the Fermi correlation [2] between electrons of like spin. Statistical electron correlation has received only a very tiny fraction of the attention that conventional electron correlation has.

The purpose of this paper is to explore systematically how statistical correlation varies with nuclear charge  $Z$ , degree of excitation, angular momentum  $L$ , and spin multiplicity in the helium isoelectronic series. To this end, we consider statistical electron correlation in 29 low-lying states ( $n^1S$ ,  $n^3S$ ,  $n^1P$ ,  $n^3P$ ,  $n^1D$ , and  $n^3D$  with  $n < 7$ ) for each of the nine ions from He through  $\text{Ne}^{8+}$ . It would be difficult, if not impossible, to assimilate mentally the trends displayed by a series of plots of statistical pair correlation densities for each of 261 states. Therefore, it is natural, and even imperative, to turn to simple measures that give an overall sense of statistical correlation. Convenient indices of this sort, termed statistical correlation coefficients, were introduced by Kutzelnigg et al. [3]. In this work, we use three radial and three

angular correlation coefficients to characterize the statistical electron correlation in each of these states. Even with this simplification, we are left with the task of discerning trends in 1566 correlation coefficients. The method is outlined in the next section, and the results are presented and discussed in the third section. Hartree atomic units are used throughout.

### Method

Standard concepts from mathematical statistics and probability theory led Kutzelnigg et al. [3] to use probe functions  $g(\vec{r})$  of the electronic position vectors to define generalized correlation coefficients in terms of one- and two-electron expectation values:

$$\tau_g = \frac{\langle g(\vec{r}_1)g(\vec{r}_2) \rangle - \langle g(\vec{r}_1) \rangle^2}{\langle g^2(\vec{r}_1) \rangle - \langle g(\vec{r}_1) \rangle^2}. \quad (1)$$

Thakkar and Smith [4] pointed out that Eq. (1) can be rewritten as

$$\tau_g = \frac{2 \int c(\vec{r}_1, \vec{r}_2) g(\vec{r}_1) g(\vec{r}_2) d\vec{r}_1 d\vec{r}_2}{\int D_1(\vec{r}_1) D_1(\vec{r}_2) [g^2(\vec{r}_1) + g^2(\vec{r}_2) - 2g(\vec{r}_1)g(\vec{r}_2)] d\vec{r}_1 d\vec{r}_2}, \quad (2)$$

where

$$c(\vec{r}_1, \vec{r}_2) = D_2(\vec{r}_1, \vec{r}_2) - D_1(\vec{r}_1)D_1(\vec{r}_2) \quad (3)$$

is the statistical pair correlation density in which

$$D_2(\vec{r}_1, \vec{r}_2) = \int \psi^*(\vec{x}_1, \vec{x}_2, \dots, \vec{x}_n) \psi(\vec{x}_1, \vec{x}_2, \dots, \vec{x}_n) d\sigma_1 d\sigma_2 d\vec{x}_3 d\vec{x}_4 \dots d\vec{x}_n \quad (4)$$

is the unit normalized one-electron density. Equations (2) and (3) clearly show that a statistically *uncorrelated* pair density,  $c(\vec{r}_1, \vec{r}_2) = 0$ , is a sufficient, but not

$$D_1(\vec{r}_1) = \int \psi^*(\vec{x}_1, \vec{x}_2, \dots, \vec{x}_n) \psi(\vec{x}_1, \vec{x}_2, \dots, \vec{x}_n) d\sigma_1 d\vec{x}_2 d\vec{x}_3 d\vec{x}_4 \dots d\vec{x}_n \quad (5)$$

is the unit normalized one-electron density. Equations (2) and (3) clearly show that a statistically *uncorrelated* pair density,  $c(\vec{r}_1, \vec{r}_2) = 0$ , is a sufficient, but not necessary, condition for vanishing correlation coefficients. There are two ambiguities in the definition of the  $\tau_g$  coefficients. They depend on the origin of the coordinate system used, and the product of probe functions is ambiguous if the probe is a vector function. These ambiguities are resolved as follows. Since we are concerned only with atoms, the nucleus is the natural origin. The product of probe functions will be interpreted as a scalar product [3].

Radial correlation coefficients are obtained if the probe function is spherically symmetric. The simplest radial probe function is  $g(\vec{r}) = r^k$ , which leads to

$$\tau_{r^k} = \frac{\langle r_1^k r_2^k \rangle - \langle r_1^k \rangle^2}{\langle r_1^{2k} \rangle - \langle r_1^k \rangle^2} \quad (6)$$

The radial coefficients with  $k = +1$  have been studied for the five lowest states of the two-electron ions [3-5] and for the ground and first excited states of the Li-like and Be-like ions [6-8]. The  $k = -1$  coefficient was considered in the latter studies to investigate shell effects. Since the Rydberg states we consider are relatively diffuse, we also examine  $k = 2$ , which should place emphasis on the outer regions. We use the  $k = -1, 1, 2$  coefficients to characterize radial correlation in the K-shell, intermediate, and Rydberg regions, respectively, of the charge cloud.

Angular correlation coefficients result from the probe function  $g(\vec{r}) = \vec{r} r^k$ . Thus,

$$\tau_{\vec{r}r^k} = \frac{\langle r_1^k r_2^k \vec{r}_1 \cdot \vec{r}_2 \rangle}{\langle r_1^{2k+2} \rangle} \quad (7)$$

These angular correlation coefficients cannot exceed 1 in absolute value. Perfect positive correlation ( $\tau = 1$ ) means that the position vectors are expected to coincide whereas perfect negative correlation ( $\tau = -1$ ) means that the position vectors are diametrically opposed with respect to the nucleus. Statistically uncorrelated pair densities lead to  $\tau = 0$  but so do orthogonal position vectors. The case  $k = 0$  is of special interest because  $\tau_r$  can, in principle, be obtained experimentally [4,9]. When  $k = -1$ , the probe function is a unit vector, and the correlation coefficient is simply the expectation value of the cosine of the angle  $\theta_{12}$  subtended at the nucleus by a pair of electron position vectors:  $\tau_{\vec{r}/r} = \langle \cos \theta_{12} \rangle$ . We choose the  $k = -1, 1, 2$  coefficients to characterize angular correlation in the K-shell, intermediate, and Rydberg regions, respectively, of the charge cloud.

Three radial and three angular coefficients were computed for each of the 29 low lying states ( $n^1S, n^3S, n^1P, n^3P, n^1D$ , and  $n^3D$  with  $n < 7$ ) for each of the nine ions from He through  $\text{Ne}^{8+}$ . The computations are based on Cann and Thakkar's systematic collection of very accurate wave functions for these states [10]. Their spin-free wave functions incorporate explicit dependence on the interelectronic distance  $r_{12} = |\vec{r}_1 - \vec{r}_2|$  as follows:

$$\begin{aligned} \Psi = & \sum_{k=1}^N c_k (1 \pm P_{12}) r_1^k \exp(-\alpha_k r_1 - \beta_k r_2 - \gamma_k r_{12}) Y_{L,0}(\Omega_1) Y_{0,0}(\Omega_2) \\ & + \delta_{L,2} \sum_{k=N+1}^{N+M} d_k (1 \pm P_{12}) r_1 r_2 \exp(-\alpha_k r_1 - \beta_k r_2 - \gamma_k r_{12}) Y(\Omega_1, \Omega_2), \quad (8) \end{aligned}$$

where

$$Y(\Omega_1, \Omega_2) = 2Y_{1,0}(\Omega_1)Y_{1,0}(\Omega_2) + Y_{1,1}(\Omega_1)Y_{1,-1}(\Omega_2) + Y_{1,-1}(\Omega_1)Y_{1,1}(\Omega_2). \quad (9)$$

In the above, upper and lower signs correspond to the singlet and triplet states, respectively,  $\vec{r}_i = (r_i, \Omega_i)$ ,  $P_{12}$  is a permutation operator that interchanges  $\vec{r}_1$  and  $\vec{r}_2$ ,  $L$  is the total orbital angular momentum quantum number,  $\delta_{L,2}$  is a Kronecker

delta,  $Y_{L,M}$  are spherical harmonics, and the  $\{c_k, d_k, \alpha_k, \beta_k, \gamma_k\}$  are variational parameters. They each contain 100 terms, with  $N = 70$  and  $M = 30$  for the D states. These wave functions lead to the lowest variational energies published so far except for neutral He and the  $3^1P$  and  $3^3P$  states of the ions. Even in the worst cases, the energies are no more than  $30nE_H$  above the best ones [10]. A fuller discussion of the wave functions may be found elsewhere [10]. Correlation coefficients in the infinite  $Z$  limit were computed from hydrogenic wave functions.

### Results and Discussion

The correlation coefficients are shown graphically; complete tables may be found elsewhere [11]. Figures 1–3 show the K-shell correlation coefficients  $\tau_{1/r}$  and  $\tau_{\bar{r}/r}$  for the  $n = 1, 2, n = 3$ , and  $n = 4$  states, respectively. Figures 4–6 show a similar sequence for the intermediate region correlation coefficients  $\tau_r$  and  $\tau_{\bar{r}}$ , and Figures 7–9 show the Rydberg region correlation coefficients  $\tau_{r^2}$  and  $\tau_{\bar{r}r}$ . The results for the  $n = 5$  and  $n = 6$  states are not shown because they resemble those for  $n = 4$  qualitatively, because the trends observed as  $n$  increases from 3 to 4 persist to larger  $n$ , and because  $\tau_{\bar{r}}$  and  $\tau_{\bar{r}r}$  show some large  $Z$  erratic behavior that is probably a computational artifact.

The ground state is qualitatively different from the excited states; in the orbital model, the two electrons occupy the same orbital in the ground state whereas they occupy different orbitals in the excited states. Moreover, statistical electron correlation in the ground state has been studied previously [3,4], as have some of the coefficients for the  $n = 2$  states [4,5]. Therefore, in this paper, we focus on trends

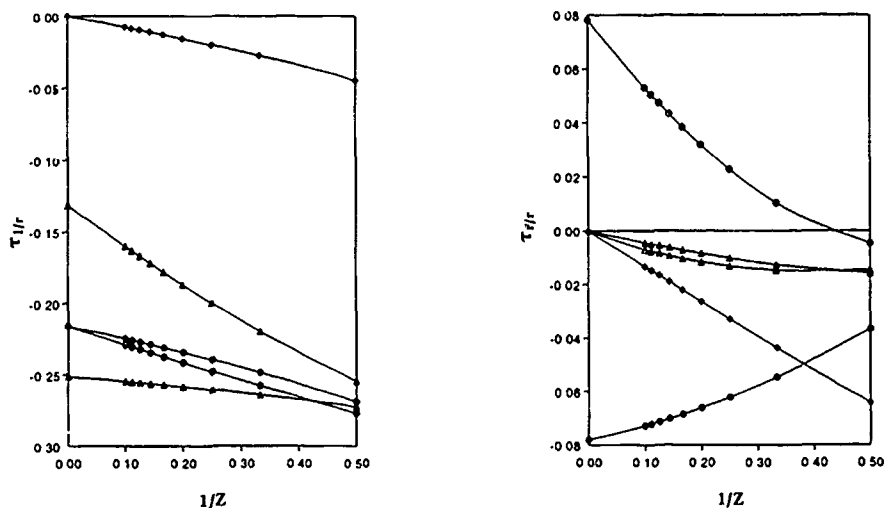


Figure 1.  $\tau_{1/r}$  and  $\tau_{\bar{r}/r}$  as a function of  $1/Z$  for the  $1^1S$  ( $\diamond$ ),  $2^1S$  ( $\Delta$ ),  $2^3S$  ( $\blacktriangle$ ),  $2^1P$  ( $\circ$ ), and  $2^3P$  ( $\bullet$ ) states.

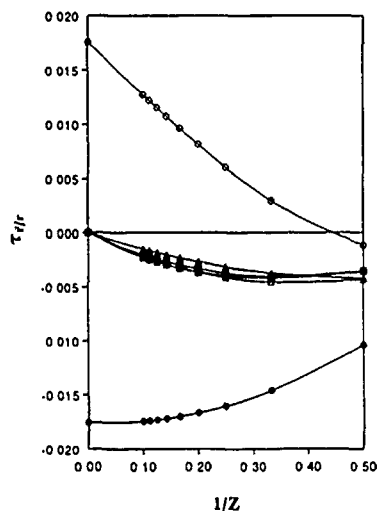
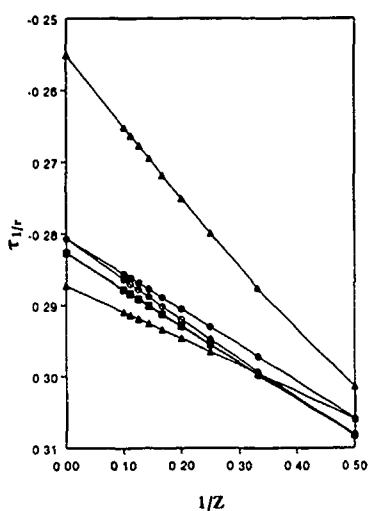


Figure 2.  $\tau_{1/r}$  and  $\tau_{7/r}$  as a function of  $1/Z$  for the  $3^1S$  ( $\Delta$ ),  $3^3S$  ( $\blacktriangle$ ),  $3^1P$  ( $\circ$ ),  $3^3P$  ( $\bullet$ ),  $3^1D$  ( $\square$ ), and  $3^3D$  ( $\blacksquare$ ) states.

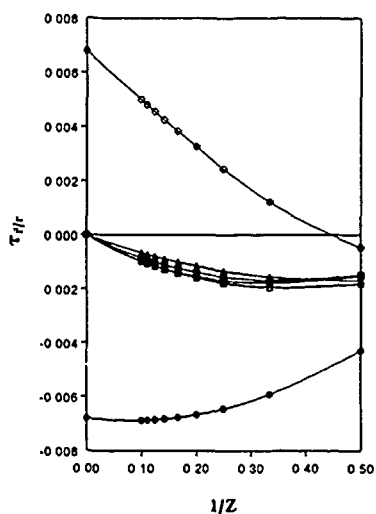
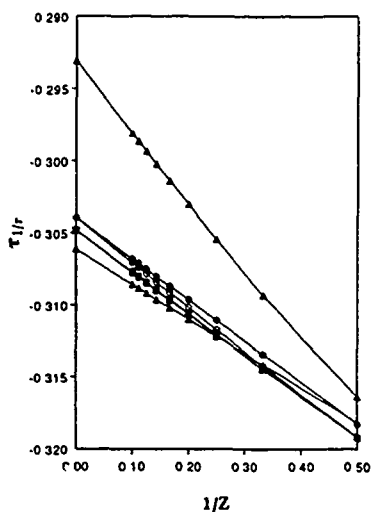


Figure 3.  $\tau_{1/r}$  and  $\tau_{7/r}$  as a function of  $1/Z$  for the  $4^1S$  ( $\Delta$ ),  $4^3S$  ( $\blacktriangle$ ),  $4^1P$  ( $\circ$ ),  $4^3P$  ( $\bullet$ ),  $4^1D$  ( $\square$ ), and  $4^3D$  ( $\blacksquare$ ) states.

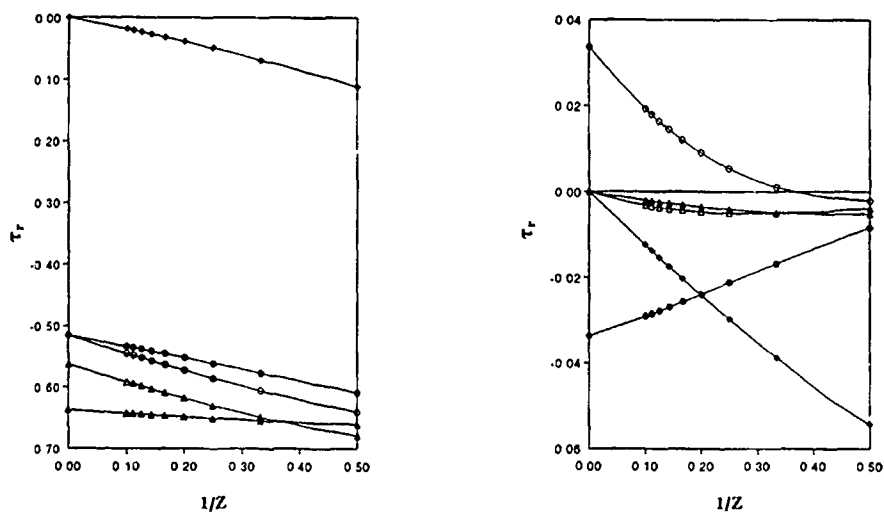


Figure 4.  $\tau_r$  and  $\tau_l$  as a function of  $1/Z$  for the  $1^1S$  ( $\circ$ ),  $2^1S$  ( $\Delta$ ),  $2^3S$  ( $\Delta$ ),  $2^1P$  ( $\circ$ ), and  $2^3P$  ( $\bullet$ ) states.

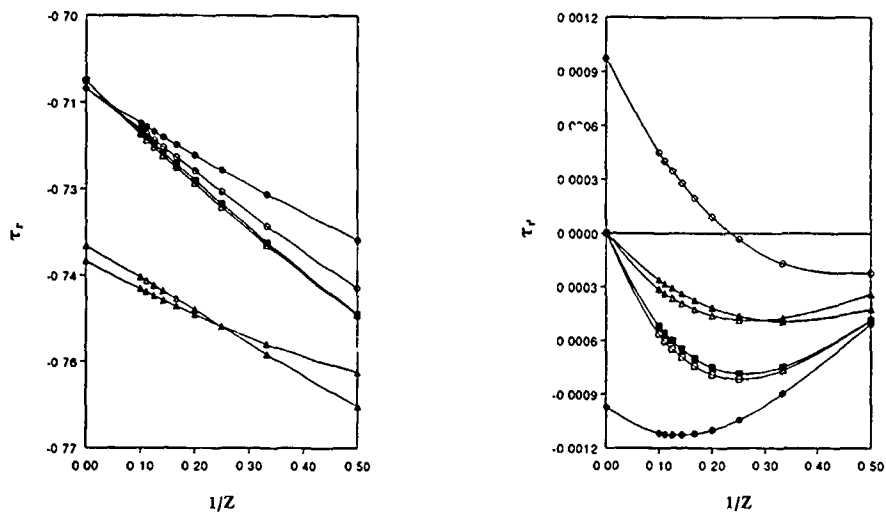


Figure 5.  $\tau_r$  and  $\tau_l$  as a function of  $1/Z$  for the  $3^1S$  ( $\Delta$ ),  $3^3S$  ( $\Delta$ ),  $3^1P$  ( $\circ$ ),  $3^3P$  ( $\bullet$ ),  $3^1D$  ( $\square$ ), and  $3^3D$  ( $\blacksquare$ ) states.

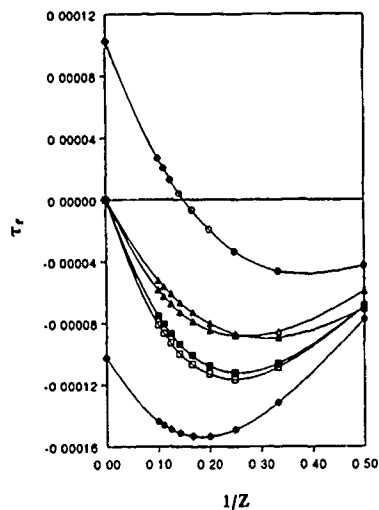
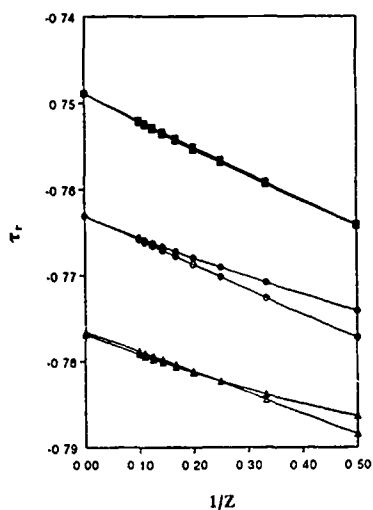


Figure 6.  $\tau_r$  and  $\tau_r$  as a function of  $1/Z$  for the  $4^1S$  ( $\Delta$ ),  $4^3S$  ( $\blacktriangle$ ),  $4^1P$  ( $\circ$ ),  $4^3P$  ( $\bullet$ ),  $4^1D$  ( $\square$ ), and  $4^3D$  ( $\blacksquare$ ) states.

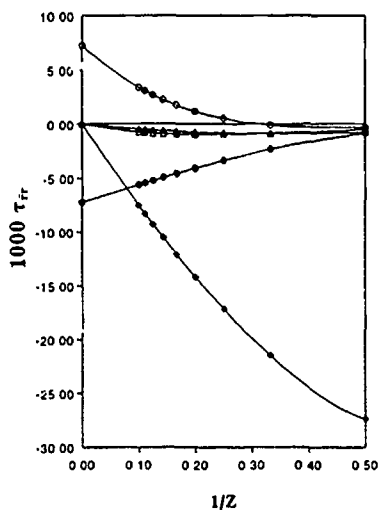
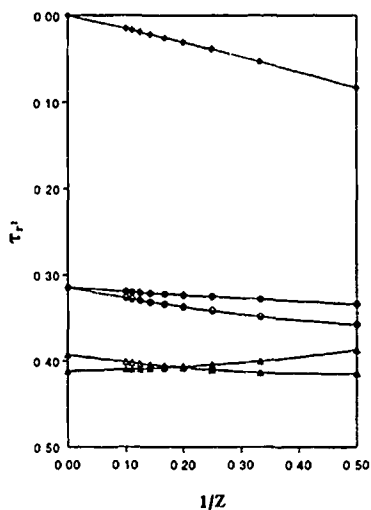


Figure 7.  $\tau_{r'}$  and  $\tau_{r'}$  as a function of  $1/Z$  for the  $1^1S$  ( $\diamond$ ),  $2^1S$  ( $\Delta$ ),  $2^3S$  ( $\blacktriangle$ ),  $2^1P$  ( $\circ$ ), and  $2^3P$  ( $\bullet$ ) states.



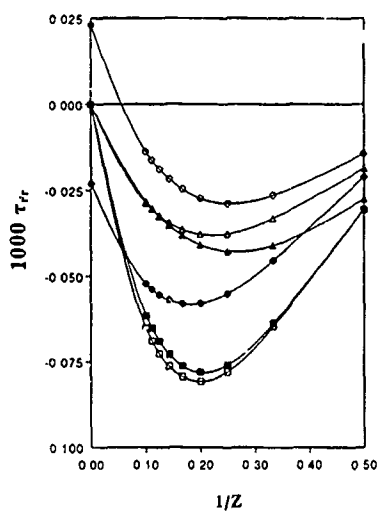
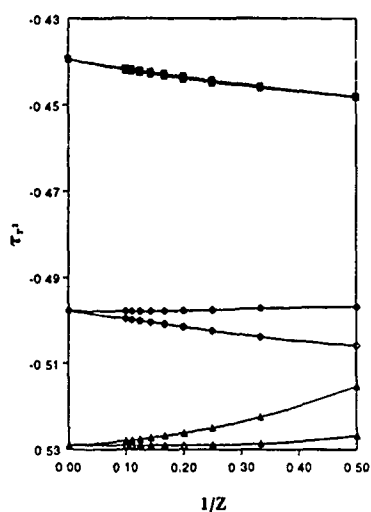


Figure 8.  $\tau_{r^2}$  and  $\tau_{rr}$  as a function of  $1/Z$  for the  $3^1S$  ( $\Delta$ ),  $3^3S$  ( $\blacktriangle$ ),  $3^1P$  ( $\circ$ ),  $3^3P$  ( $\bullet$ ),  $3^1D$  ( $\square$ ), and  $3^3D$  ( $\blacksquare$ ) states.

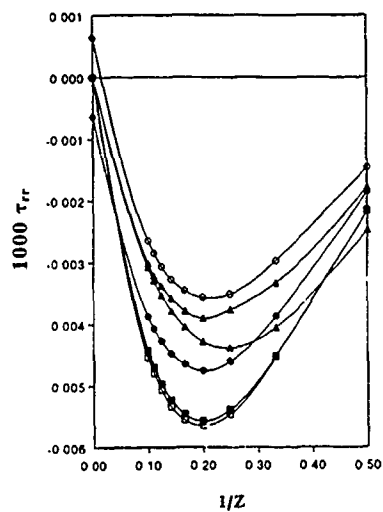
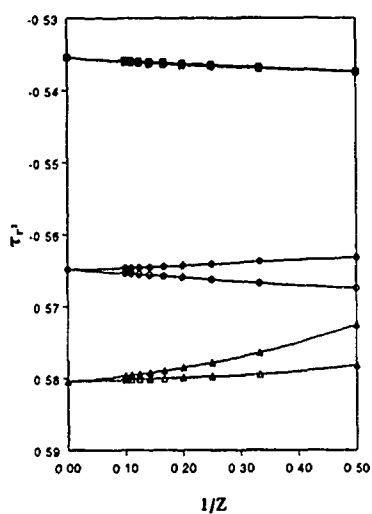


Figure 9.  $\tau_{r^2}$  and  $\tau_{rr}$  as a function of  $1/Z$  for the  $4^1S$  ( $\Delta$ ),  $4^3S$  ( $\blacktriangle$ ),  $4^1P$  ( $\circ$ ),  $4^3P$  ( $\bullet$ ),  $4^1D$  ( $\square$ ), and  $4^3D$  ( $\blacksquare$ ) states.

of the excited state correlation coefficients with variation in nuclear charge  $Z$ , angular momentum  $L$ , degree of excitation  $n$ , and spin  $S$ .

Consider the relative magnitudes of correlation in the three regions. The ratio  $\tau_{1/r}:\tau_r:\tau_{\bar{r}}$  is approximately 3:7:5, indicating that radial correlation is most important in the intermediate region, and least important in the K-shell. Angular correlation, on the other hand, decreases in importance with distance from the nucleus. For  $n = 2$ , the ratio  $\tau_{\bar{r}/r}:\tau_{\bar{r}}:\tau_{\bar{r}r}$  is 4:2:1 but for  $n = 6$  this ratio becomes 100,000:500:1. These ratios can be understood quite simply. In the K-shell, angular correlation is more efficient than radial correlation because of the small size of the K-shell; thus, in the K-shell, correlation energy is obtained primarily through decreased shielding, leading to an increase in electron-nucleus attraction. In the intermediate region, both forms of correlation can be important. In the huge Rydberg region, radial correlation is favored because greater stabilization can be obtained by reduction of interelectronic repulsion than by increase of attraction to the distant nucleus. The probability of finding both electrons in one of these regions is greatest for the intermediate region, and so radial correlation is most significant there.

On the basis of the arguments presented above, one would expect radial correlation to increasingly overshadow angular correlation as the size of the Rydberg region increases with  $n$ . Indeed, the figures show that as  $n$  increases, the radial correlation coefficients increase slightly in magnitude but the angular correlation coefficients decrease dramatically.  $\tau_{\bar{r}/r}$ ,  $\tau_{\bar{r}}$ , and  $\tau_{\bar{r}r}$  decrease by factors of 40, 4000, and 500,000, respectively, as  $n$  increases from 2 to 6.

The behavior of the correlation coefficients, for fixed  $n$ ,  $L$ , and  $S$ , as a function of  $Z$  is described by  $1/Z$  expansions [4]:

$$\tau_R = a_{R,0} + a_{R,1}/Z + a_{R,2}/Z^2 + \dots \quad (10)$$

For each of the correlation coefficients in each of the 29 states, the leading coefficient in the  $1/Z$  expansion was computed from hydrogenic wave functions, and one or two higher order coefficients were obtained by fitting and/or differencing our calculated values; tables of these  $1/Z$  expansion coefficients may be found elsewhere [11]. The figures show that most of the radial  $\tau$  decrease linearly with  $1/Z$ , showing that the higher order terms in Eq. (10) are not significant for  $Z \geq 2$ . By contrast, the angular  $\tau$  show distinctly nonlinear variation with  $1/Z$ .

The variations with  $L$  and  $S$  are not simple. We set aside  $\tau_{\bar{r}r}$  and  $\tau_{1/r}$  because radial correlation in the K-shell and angular correlation in the Rydberg region are less important. The  $\tau_r$  and  $\tau_{\bar{r}}$  show that radial correlation is more important in the S states than in the P and D states. This is reasonable since the spherically symmetric S states are less conducive to angular correlation than the  $L > 0$  states. The  $\tau_{\bar{r}/r}$  and  $\tau_{\bar{r}}$  suggest that angular correlation is most significant in the P states, and confirm [4] that positive angular correlation coefficients are found only for large  $Z$  and only in the 'P states. The only plausible explanation that we can offer for these observations is that they may be artifacts of the probe function used; it may be interesting to test probe functions with more general angular dependence. The triplet is always the more compact state of the singlet-triplet pair associated

with each  $Z$ ,  $n$ , and  $L$  [12]; however, the correlation coefficients do not show behavior that can be attributed to this size effect. Radial correlation seems more important in  $^1P$  states than in  $^3P$  states. Detailed studies of pair correlation densities may help explain some of these features of the  $P$  states.

### Acknowledgments

This work was supported by the Natural Sciences and Engineering Research Council of Canada. The award of a Killam Memorial Scholarship (to N. M. C.) is gratefully acknowledged.

### Bibliography

- [1] R. McWeeny, *Rev. Mod. Phys.* **32**, 335 (1960)
- [2] E. Wigner and F. Seitz, *Phys. Rev.* **43**, 804 (1933); **46**, 509 (1934)
- [3] W. Kutzelnigg, G. Del Re, and G. Berthier, *Phys. Rev.* **172**, 49 (1968).
- [4] A. J. Thakkar and V. H. Smith, Jr., *Phys. Rev. A* **23**, 473 (1981).
- [5] K. E. Banyard and D. J. Ellis, *J. Phys. B* **8**, 2311 (1975).
- [6] K. E. Banyard and M. M. Mashat, *J. Chem. Phys.* **67**, 1405 (1977).
- [7] K. E. Banyard and K. H. Al-Bayati, *J. Phys. B* **19**, 2211 (1986).
- [8] K. E. Banyard, *J. Phys. B* **23**, 777 (1990).
- [9] A. J. Thakkar, *Phys. Rev. A* **25**, 1820 (1982).
- [10] N. M. Cann and A. J. Thakkar, *Phys. Rev. A* **46**, 5397 (1992).
- [11] N. M. Cann, Ph.D. thesis, Dalhousie University, Halifax, Canada (1993).
- [12] R. J. Boyd, *Theor. Chim. Acta* **33**, 79 (1974).

Received June 30, 1993

# Investigation of the Correlation Energy Component of the Intermolecular Interaction Energy

E. KAPUY,\*<sup>†</sup> F. BOGÁR,\* C. KOZMUTZA,<sup>†</sup> and E. TFIRST<sup>†</sup>

\* Department of Theoretical Physics, József Attila University, Széchi vértanúk tere 1, H-6720 Szeged, Hungary and <sup>†</sup>Quantum Theory Group, Physics Institute, Technical University, Budafoki út 8, H-1521 Budapest, Hungary

## Abstract

Supermolecular model of the intermolecular interaction energy is studied. The correlation energy components are calculated by using the many-body perturbation theory (MBPT) in the canonical representation as well as in the localized one. The components of the corrections of the different order are analyzed individually. The effects of the localization procedure and the basis set are also investigated. An H<sub>2</sub>O trimer is used to study the two- and three-body components of the interaction energy. © 1993 John Wiley & Sons, Inc

## Introduction

The difficulties of the determination of the intermolecular interactions in a theoretical way are numerous. The various problems of the quantum chemical calculations are the subject of several excellent review articles (some of them are not restricted to the discussion of two interacting systems). It is well known from experience that a large number of intermolecular interactions behave itself in quite a different way when they are acting in a reaction catalyzed or uncatalyzed. The presence of water molecules, e.g., may effect seriously the interaction energy of reacting systems. The interaction between the molecules CH<sub>2</sub>O and NH<sub>3</sub> is an example for this case [1,2]. It was shown [3] that a single ancillary water molecule interacts favorably with the reacting system. It was also pointed out, in the same study, that the incorporation of a second water molecule leads to a further decrease the distance between the interacting formaldehyde and ammonia molecules.

One can thus conclude that the ancillary water molecules aid the catalysis. The accurate study of this and similar interactions are of incredible importance because of their biological activity. Although the above calculations have been performed on *ab initio* SCF level, some attempts have already been done including the effects of electron correlation, too [4]. It is generally believed that, for serious investigations of intermolecular interaction energies, the correlation component must be taken into account [5].

Tremendous efforts have been made in the past years for shedding light on the understanding the van der Waals bonding, the hydrogen bonding, the solvation effects, etc., using a large variety of quantum chemical methods [Nonadditive po-

tential, configurational interaction (CI), many-body perturbation theory (MBPT), coupled cluster theory (CC)] [6-20].

The theoretical investigations, using *ab initio* methods including the study of correlation energy components are varying from the exhausting analysis of the dipole moments [11], of the dipole-dipole exchange, etc. partitioning [12] up to the discussion of these components in the localized version of the MBPT [13-16]. Some of the present authors also contributed to these investigations [17,18].

The important role of the so called basis set superposition error (BSSE) has also been studied in several papers (see, e.g., Refs. [19-21] and references therein).

As the interaction of water molecules is of basic importance in chemical and biochemical systems many papers have chosen them as model [7,20,21]. Recently various papers have been published on the van der Waals interaction in the ( $H_2O$ ) trimer systems. In Ref. [8] the nonadditive potential of Campbell and Mezei is used to determine the local minima of the energy surface. In Refs. [22,23] the interaction energy is calculated by MBPT with fairly large basis sets. For the water dimer the localized version of the MBPT was successfully applied [24,25].

### Theory

The MBPT in the supermolecular model starts as taking zero-order approximation the HF approximation of the interacting total system. The higher-order terms contain the many-electron effects.

The symmetry adapted perturbation theory (SAPT) (see Ref. [26] and references therein,) starts with the noninteracting monomers as zero-order approximation. It is a double perturbation theory, the perturbations are (1) the intermolecular interaction and (2) many-electron perturbation.

Our method is a version of the supermolecular model [17,18,24]. The occupied ( $\psi_i$ ,  $i = 1, 2, \dots, N$ ) and the virtual ( $\psi_a$ ,  $a = N + 1, N + 2, \dots, M$ ) solutions of the canonical HF equations are localized separately by unitary transformations

$$\varphi_i = \sum_j U_{ij} \psi_j, \quad (1)$$

$$\varphi_a = \sum_b V_{ab} \psi_b. \quad (2)$$

The off-diagonal Lagrangian multipliers are incorporated into the Fock operator of the localized representation (the zero-order Hamiltonian),

$$\hat{F}^{\text{loc}} = \hat{F} - \sum_{\substack{i,j \\ i \neq j}} |i\rangle \epsilon_{ij} \langle j| - \sum_{\substack{a,b \\ a \neq b}} |a\rangle \epsilon_{ab} \langle b| \quad (3)$$

and also appear in the perturbation operator

$$\hat{W}^{\text{loc}} = \hat{W} + \sum_{k=1}^N \left\{ \sum_{\substack{i,j=1 \\ i \neq j}}^N |i\rangle \epsilon_{ij} \langle j| + \sum_{\substack{a,b=N+1 \\ a \neq b}}^M |a\rangle \epsilon_{ab} \langle b| \right\}. \quad (4)$$

The perturbation operator consists of two terms:  $\hat{W}$  is a two-particle interaction, and the second and third terms are single-particle perturbation due to the LMOs. It means that the MBPT in the localized representation is a double perturbation theory. The perturbational energy corrections have two indices:  $E^{(n,m)}$ ,  $n$  denotes the order with respect to the two-particle perturbation, and  $m$  denotes the order with respect to the single-particle perturbation.

Summing over the second indices to infinite order

$$\sum_{m=1}^{\infty} E_{\text{loc}}^{(n,m)} = E_{\text{can}}^{(n)}, \quad (5)$$

we obtain the canonical perturbational series. The localization (1), (2) can be carried out by an ordinary Boys' procedure [27].

It is usually suitable for the occupied orbitals, but, for the virtual subspace particularly in case of larger basis sets, the ordinary Boys' procedure disperses the centroids of the LMOs, and the virtual LMOs are not localized in the same regions as the corresponding occupied ones. As can be seen from Eq. (4), the single-particle perturbation will be small if the LMOs are well separated and the off-diagonal Lagrangian multipliers are small at the same time. These two requirements cannot be satisfied simultaneously by an ordinary Boys' procedure. We are using the following modified procedures. For medium-sized basis sets for the localization of virtual LMOs, taking into account the spatial symmetry of CMOs, we partition them into several groups and localize these groups separately.

In this way the LMOs will be less localized, but the off-diagonal Lagrangian multipliers will be smaller (see Ref. [28]). With these modification we obtained adequate LMOs for many cases. For large basis sets we suggest another modification: localization of the LMOs according to a given localized set of functions (see Ref. [28]).

The essential character of our method that LMOs are used also in the virtual space. As a consequence, every effect can be attributed to a certain "localized" part of the wavefunction.

### Calculations

Our purpose is the investigation of the correlation energy components of the interaction energy as function of the distance of the monomers. Therefore, the geometries have not been optimized. We carried out the calculation for various geometries. Water molecule I and the O atoms of molecule II and III lie in the  $xy$  plane, and the OH bonds of molecule I point towards the lone pairs of molecules II and III. The intramolecular distances are taken as fixed and the intermolecular distances are increased from  $d = 4.0$  a.u. to  $d = 12.0$  a.u. (see the Appendix).

We applied standard 6-31G\* basis set, which is insufficient for small systems but for larger (especially biological) systems is widely used. We think that the standard basis set is suitable to carry out preliminary inquiry in the application of LMOs. For these geometries Hartree-Fock calculations have been carried out for the trimer, dimer, and monomer systems [28-32]. The calculations have been carried out for the corresponding dimer and monomer systems but with trimer, dimer, and mono-

TABLE I The contributions of the correlation energy to the interaction energy of the (H<sub>2</sub>O)<sub>3</sub> trimer at different geometries (in  $\mu$ hartree units).<sup>a</sup>

	4.0	5.0	6.0	8.0	10.0	12.0
$\Delta$ SCF	-550.09	-4241.91	-2329.45	-514.66	-190.34	-85.47
$\Delta E^{(2)}$	-2891.92	-1771.33	-645.426	-50.10	-13.23	-4.85
$\Delta E^{(3)}$	700 714	455.35	1008.08	813.15	4404.02	8536.12
$\Delta E^{(4)}$	9455 90	336 61	1702.89	5 64	29656.49	-15114.48

<sup>a</sup> CP corrected results.

mer basis sets in order to use the full counterpoise (CP) method. For example, the binding energy of the trimer  $\Delta E_{I II III}$  are calculated in the following way:

$$\Delta E_{I II III} = E_{I II III} - E_{(I II III \text{ basis})}^I - E_{(I II III \text{ basis})}^{II} - E_{(I II III \text{ basis})}^{III}.$$

This correction is calculated for every order of the perturbation theory similarly. In the localized representation the BSSE can be taken into account in a different way.

The two-electron integrals are transformed to those in terms of canonical molecular orbitals (CMOs) and the second-, third-, and fourth-order perturbational corrections are calculated by the canonical many-body perturbation theory (CMBPT) [33-38].

The results for the water trimer are shown in Table I. for certain geometries. The contributions to the interaction energy are given in detail ( $\Delta$ SCF,  $\Delta E^{(2)}$ ,  $\Delta E^{(3)}$ , etc.) applying the Boys-Bernardi full counterpoise correction and without it (see Table II.) To show the effect of increasing the basis, we repeated the calculation for water dimer with two *d*-sets (*d* exp: 0.73 and *d'* exp: 0.30). The results are shown in Table III, and compared to those obtained with single *d* set. It can be seen that the CP corrected second order interaction energy component increased by 27%. (The increase of the total energy is much less.) For certain geometries the CMOs were localized by using the modified version of the Boys procedure [28]. As we have already pointed out, the LMOs have very interesting properties.

TABLE II The contributions of the correlation energy to the interaction energy of the (H<sub>2</sub>O)<sub>3</sub> trimer at different geometries (in  $\mu$ hartree units).<sup>a</sup>

	4.0	5.0	6.0	8.0	10.0	12.0
$\Delta$ SCF	-3885.72	-4923.23	-2603.06	-513.18	-1999.42	94.47
$\Delta E^{(2)}$	-5223.23	-2493.15	-830.06	-56.38	-13.26	-4.85
$\Delta E^{(3)}$	1036.28	559.39	-260.11	-394.94	-2195.04	-4260.51
$\Delta E^{(4)}$	-8997.01	-452.71	-1027.68	-879.18	-14800.04	-5957.04

<sup>a</sup> Results without CP correction

TABLE III. The change in the components of the interaction energy of the water dimer when the basis set was increased <sup>a</sup>

	$E^{(2)}$	$E^{(3)}$	$E^{(4)}$
6-31G*	-345.21	-6129.98	-4644.28
6-31G* + $d'$	-468.83	26.32	-97.44

<sup>a</sup> At the geometry  $d = 6.0$  a.u. (in  $\mu$ hartree).

Several contributions of the LMOs for the monomer, dimer, and trimer systems can be investigated. The transferability of the Fock-matrix elements, for example, and of the two-electron integrals over LMOs have advantages. Good results have been obtained for any interacting dimer systems studied so far by our method.

The characterization of the LMOs can be done in different ways. We give the coordinates of centroids for the occupied bond- and lone-pair LMOs as well as the largest centroid lengths of centroids for the virtual LMOs. The centroid vector  $\mathbf{r}_i$  of an LMO is defined as  $\mathbf{r}_i = \langle \varphi_i | \mathbf{r} | \varphi_i \rangle$ . The results obtained for the systems studied at several intermolecular distances are in agreement with our earlier conclusions: All of the LMOs are well separated. The contributions of LMOs are expected, therefore, to show systematic changes when enlarging the intermolecular distances. Up to correlated level, we investigated the correlation energy components of all of the monomer, the dimer, and trimer systems, respectively, at the second and at third order of the MBPT. The results obtained at the MP2 and the MP3 levels both in the canonical (CMBPT) and in the localized (LMBPT) representation make possible a comparison between the corresponding values and thus to get information on the "quality" of the LMBPT. The results are given in Table IV and Table V, respectively. One can see that for all the systems studied the values of CMBPT and LMBPT are close to each other. It is encouraging however, that the deviations between the corresponding canonical and localized correlation energy are less than 10% in each case.

The transferable properties of LMOs as well as the satisfactory agreement between the canonical and localized energy values both at the MP2 and MP3 allowed us to calculate the one-, two-, and three-body interaction energies at the different levels of correlation.

TABLE IV. Interaction energy calculated by the LMBPT in the water trimer at  $d = 5.0$  geometry.

		Uncorrected	BSE: free
2nd order	One-body	-558.30 mhartree	-560.72 mhartree
	Two-body	-971.48 $\mu$ hartree	-993.42 $\mu$ hartree
3rd order	One-body	-15691.36 $\mu$ hartree	-17101.65 $\mu$ hartree
	Two-body	4.66 $\mu$ hartree	27.57 $\mu$ hartree
	Three-body	-0.89 $\mu$ hartree	-0.34 $\mu$ hartree



TABLE V. Interaction energy calculated by the LMBPT in the water trimer at  $d = 6.0$  geometry

		Uncorrected	BSSE free
2nd order	One-body	-557.31 mhartree	-534.42 mhartree
	Two-body	-322.77 $\mu$ hartree	-254.48 $\mu$ hartree
3rd order	One-body	17542.56 $\mu$ hartree	-17599.84 $\mu$ hartree
	Two-body	7.02 $\mu$ hartree	7.57 $\mu$ hartree
	Three-body	-0.21 $\mu$ hartree	-0.21 $\mu$ hartree

It has already been pointed out [18,23]: when the (localized) basis sets are non-overlapping, the intramolecular parts can be assigned to each monomer separately. For a trimer (ABC) system, for example, the intrasystem (one-body) correlation energies can be obtained if we sum over only those occupied and virtual LMOs' indices in the so called pair-correlation energy terms (see details in [24]) which belong only to the monomer A, only to the monomer B, or only to the monomer C, respectively. The two-body terms can be expressed in a similar way: the indices run over only the corresponding LMOs of the monomers A and B, or A and C, etc. The two-body terms can also be named the dispersion energy part of the correlation both at the MP2 and MP3 levels. The results obtained for the intrasystem correlation energies for the water monomer and dimer have already been discussed in [24]. Here we present the values obtained for the many-body terms at the MP2 level (see Table IV, first part). The advantage of using the LMBPT theories lies, furthermore, in the calculation of the three-body interaction terms (in similar manner as described above). The results obtained for the studied trimer system are presented in Table IV and Table V. These values are significantly smaller than the two-body terms, as expected.

The localized representation of the MBPT (LMBPT) are carried out up to third order. As shown in Eq. (5) summing over the single-particle perturbation (order  $m$ ) we obtain the canonical series. In our case if we sum over  $m$  to 2, for  $n = 2$ ,

TABLE VI.

		X	Y	Z
H <sub>2</sub> O (I)	O <sub>1</sub>	0.0	1.1073	0.0
	H <sub>1</sub>	1.4306	0.0	0.0
	H <sub>2</sub>	-1.4306	0.0	0.0
H <sub>2</sub> O (II)	O <sub>2</sub>	4.5937	-2.4483	0.0
	H <sub>3</sub>	4.5937	-1.0178	-1.1073
	H <sub>4</sub>	4.5937	-3.8789	-1.1073
H <sub>2</sub> O (III)	O <sub>3</sub>	-4.5937	-2.4483	0.0
	H <sub>5</sub>	-4.5937	-1.0178	-1.1073
	H <sub>6</sub>	-4.5937	-3.8789	-1.1073

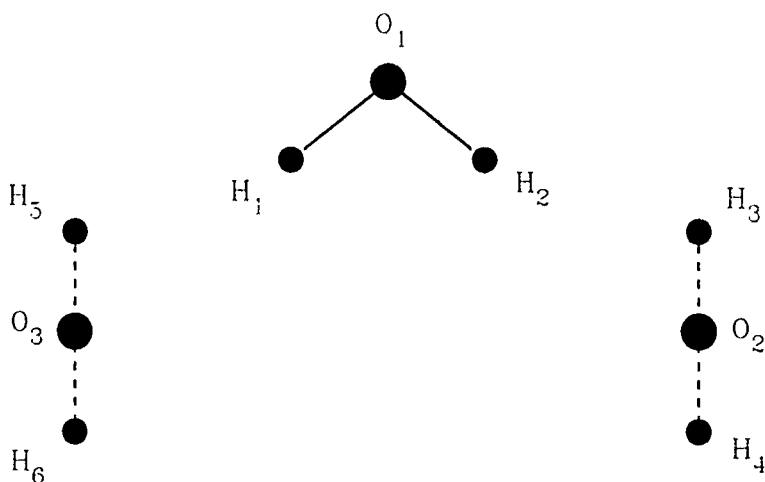


Figure 1. Water trimer (see Appendix).

we obtain the canonical second order correction with an error of 0.28%. If we omit completely the single-particle perturbation, i.e., if we evaluate the canonical diagram with localized orbitals, we obtain 94.96% of the canonical second-order correction. If we sum over  $m$  to 4 for  $n = 3$ , we obtain a corresponding canonical third-order correction with an error of 3.7%. In our calculations we stopped the summations at these orders. Omitting the single-particle perturbation from the third-order terms, we overestimate the canonical value by 10.11%. It means that, in the LMBPT, MP2 level calculations contain a finite summation; consequently, it is, literally, a near MP2 calculation. Also MP3 level calculations are, literally, a near MP3 calculation.

The localized representation has some advantages. The interaction energies can be partitioned according to their source. The occupied orbitals belong uniquely to one of the interacting systems. The interactions accordingly can be partitioned as one-, two-, three-body, etc. interactions. In a trimer system in second order we obtain one- and two-body interactions. In third order we obtain one-, two-, and three-body interactions.

Another advantage of the localized representation is that we can easily find out the source of the BSSE. The LMOs are approximately transferable from the noninteracting monomers to the interacting systems; by utilizing this we can omit the contributions of the LMOs which comes from the other monomer. The BSSE calculated by this method are usually smaller than those calculated by Boys-Bernardi procedure.

#### Appendix: Model Geometry Taken for the System Studied

The intramolecular values ( $\text{O}-\text{H} = 1.809$  bohr,  $\text{HOH} = 104.52^\circ$ ) are the same for the three  $\text{H}_2\text{O}$  molecules. The distance between monomers was systematically

enlarged, starting from an intermolecular distance ( $d$ ) of 4.0 bohr, and then increased through 5.0, 6.0, 8.0, 10.0 up to 12.0 bohr. The coordinates for the first geometry arrangement are given in Table VI.

### Acknowledgment

This work was supported by a grant (OTKA No. 192/90). The calculations have been carried out on the machine of the IBM Academic Initiative in Hungary.

### Bibliography

- [1] S. Scheiner, W. N. Lipscomb, and D. A. Kleier, *J. Am. Chem. Soc.* **98**, 4770 (1976).
- [2] S. F. Abdunur, *Int. J. Quantum Chem. Quantum Biol. Symp.* **7**, 171 (1980).
- [3] I. H. Williams, *J. Am. Chem. Soc.* **109**, 6299 (1987).
- [4] C. Kozmutza, E. M. Evleth, and E. Kapuy, *J. Mol. Structure (Theochem)* **233**, 139 (1991).
- [5] P. Hobza and R. Zahradnik, *Chem. Rev.* **88**, 871 (1988).
- [6] V. Magnasco, G. Figari, and C. Costa, *J. Mol. Structure (Theochem)* **261**, 237 (1992).
- [7] B. J. Yoon, K. Morokuma, and E. R. Davidson, *J. Chem. Phys.* **83**, 1223 (1985).
- [8] D. Belford and E. S. Campbell, *J. Chem. Phys.* **86**, 7013 (1987).
- [9] N. L. Allinger, R. A. Kok, and M. R. Imani, *J. Comput. Chem.* **9**, 591 (1988).
- [10] F. J. Olivares de Valle and M. A. Agnilar, *J. Comput. Chem.* **13**, 115 (1992).
- [11] W. Meyer and L. Frommhold, *Phys. Rev A* **33**, 3807 (1986).
- [12] G. Chalasinski, S. M. Cybulski, M. M. Szczesniak, and S. Scheiner, *J. Chem. Phys.* **91**, 7048 (1989).
- [13] S. Saebo and P. Pulay, *Chem. Phys. Lett.* **113**, 13 (1985).
- [14] P. Pulay and S. Saebo, *Theoret. Chim. Acta* **69**, 357 (1986).
- [15] P. R. Surján, I. Mayer, and I. Lukovits, *Chem. Phys. Lett.* **119**, 538 (1985).
- [16] R. J. Vos, R. Hendriks, and F. B. van Duijneveldt, *J. Comput. Chem.* **11**, 1 (1990).
- [17] E. Kapuy, F. Bartha, F. Bogár, Z. Csépes, and C. Kozmutza, *Int. J. Quantum Chem.* **38**, 139 (1990).
- [18] C. Kozmutza and E. Kapuy, *Int. J. Quantum Chem.* **38**, 665 (1990).
- [19] B. H. Wells, *Mol. Phys.* **50**, 1295 (1983).
- [20] K. Szalewicz, S. J. Cole, W. Kolos, and R. J. Bartlett, *J. Chem. Phys.* **89**, 3662 (1988).
- [21] K. S. Kim, B. J. Mhin, U-Sung Choi, and K. Lee, *J. Chem. Phys.* **97**, 6649 (1992).
- [22] O. Mo, M. Yanez, and J. Elguero, *J. Chem. Phys.* **97**, 6628 (1992).
- [23] G. Chalasinski, M. M. Szczesniak, P. Cieplak, and S. Scheiner, *J. Chem. Phys.* **94**, 2873 (1991).
- [24] E. Kapuy and C. Kozmutza, *J. Chem. Phys.* **94**, 5565 (1991).
- [25] C. Kozmutza and E. Kapuy, *J. Comput. Chem.* **12**, 953 (1991).
- [26] H. L. Williams, K. Szalewicz, B. Jezorski, R. Moszynski, and S. Rybak, *J. Chem. Phys.* **98**, 1279 (1993).
- [27] S. F. Boys, in P. O. Lowdin, Ed., *Quantum Theory of Atoms, Molecules and Solid State* (Academic, New York, 1966), pp. 253-262.
- [28] C. Kozmutza, E. Kapuy, E. M. Evleth, and E. Kassab, *Sanibel Symposium, 1993*, Abstract.
- [29] M. Dupuis, J. D. Wats, H. O. Villar, and G. J. B. Hurst, *Hondo Version 7.0* (1987).
- [30] S. M. Colwell and N. C. Handy, *J. Mol. Structure (Theochem)* **170**, 197 (1988).
- [31] C. Kozmutza, *Theor. Chim. Acta* **60**, 53 (1981).
- [32] F. Bartha, E. Kapuy, and C. Kozmutza, *J. Mol. Str. (Theochem)* **122**, 205 (1985).
- [33] C. Kozmutza and Zs. Ozoróczy, *J. Comput. Chem.* **7**, 494 (1986).
- [34] R. J. Bartlett and G. Purvis, *Int. J. Quantum Chem.* **14**, 561 (1978).
- [35] S. Wilson and D. M. Silver, *Int. J. Quantum Chem.* **15**, 683 (1979).
- [36] I. Hubac and P. Carsky, *Top. Curr. Chem.* **75**, 99 (1978).
- [37] S. Wilson, *Electron Correlation in Molecules* (Clarendon, Oxford, 1984).
- [38] S. A. Kucharski and R. J. Bartlett, *Adv. Quantum Chem.* **18**, 281 (1986).

# Triple Excitations in Coupled-Cluster Theory: Energies and Analytical Derivatives

JOHN D. WATTS and RODNEY J. BARTLETT

*Quantum Theory Project, Departments of Chemistry and Physics,  
University of Florida, Gainesville, Florida 32611-2085*

## Abstract

A review is presented of our recent work which deals with some aspects of the inclusion of connected triple excitations in single reference coupled-cluster theory. We first consider basic aspects of the theory and computational cost, noting the need for accurate and economical approximations to the complete coupled-cluster single, double and triple excitation method (CCSDT). Several such approximations are now available, including the CCSD $\approx$ T (CCSD) and CCSD(T) methods. We have now efficiently implemented analytical derivative methods for these and related methods for open-shell reference determinants, including restricted open-shell Hartree-Fock for CCSD(T). Some results with large basis sets are presented for the HCO radical which further demonstrate the reliability of these methods for the spectroscopic characterization of small open-shell species. The remainder of this article deals with several applications of the complete CCSDT method, a new implementation of which we have recently completed. Like our previous work, this is for general single reference determinants, although we have now incorporated Abelian symmetry. We present a comparison with full configuration interaction data for CH<sub>3</sub>; a study of the N<sub>2</sub> potential curve using restricted and unrestricted Hartree-Fock references, a comparison of the dipole moments and polarizabilities of BeO, and a study of the harmonic force field of  $^2\Sigma_u^+$  C<sub>2</sub><sup>+</sup>. These studies also provide assessments of the accuracy of the approximate schemes for including T<sub>3</sub>. Finally, we present some timing data for some CCSDT calculations with our new implementation. © 1993 John Wiley & Sons, Inc.

## Introduction

Coupled-cluster (CC) methods are now widely used to compute the electronic correlation energy of atoms and molecules, as well as the correlation energy of a wide variety of other physical systems. The theory was introduced by Coester and Kummel to study nuclear matter [1]. It was first formulated for the electronic structure of atoms and molecules by Čížek [2] in the 1960s. These methods were later applied within a semi-empirical framework and to a minimal basis set *ab initio* study of BH<sub>3</sub> [3]. Several years after these pioneering studies, the coupled-cluster doubles (CCD) method was independently implemented in general purpose programs by Bartlett and Purvis [4] and Pople et al. [5]. In the subsequent 15 years there has been intense activity in the field, which has led to clear definitions and efficient computational implementations of a wide variety of CC methods, and there have been many applications. Several reviews [6] document this work.

A wide variety of methods are included by the term *CC methods*. There are several categories, all of whose wave functions, at least in the exact versions of the theories, are obtained through the action of some kind of exponential wave operator

on one or more determinants of orthonormal spin orbitals. When there is just one reference determinant, we have the single reference version of the theory, which is the most highly developed and widely used. There are several kinds of multireference versions of the theory, including the Fock space [7] and Hilbert space [8] theories. These fields are now being actively investigated and applied. As well as the single and multireference methods, there is the *equation-of-motion method* (also termed *linear response CC method*), which may be viewed as a generalization of the single reference theory to excited states [9].

In this article we focus on two aspects of the inclusion of triple excitations in the single reference theory. The first is concerned with the evaluation of analytical derivatives of the energy for several CC methods which include triple excitations *noniteratively*. The second describes some recent research with the complete CC single, double, and triple excitation method (CCSDT). Along with results, we shall include some timings of CCSDT calculations with a new implementation of this method. This will help to assess the degree to which this most rigorous way of including effects of triple excitations can now be applied to chemical problems. The emphasis throughout this article is on the results rather than on the details of the theory. We shall present some basic equations but will not go into details, which are covered in cited literature.

## Basics of CC Theory

### Formal Aspects

Single reference CC theory begins with a reference determinant of orthonormal spin orbitals,  $|\Phi_0\rangle$ . This may be made up of SCF orbitals, but this is not necessary. The CC wave function is obtained by operating on  $|\Phi_0\rangle$  with the exponential wave operator:

$$|\Phi_\alpha\rangle = e^T |\Phi_0\rangle \quad (1)$$

where  $T$  is the sum of one-body, two-body, three-body, etc. cluster operators

$$T = T_1 + T_2 + T_3 + \dots \quad (2)$$

These are given in second-quantized form by

$$T_1 = \sum_{ia} t_i^a \{a^+ i\} \quad (3)$$

$$T_2 = \frac{1}{4} \sum_{ijab} t_{ij}^{ab} \{a^+ i b^+ j\} \quad (4)$$

and so on. The  $t_i^a$ ,  $t_{ij}^{ab}$ , are termed the CC amplitudes, and obtained by solution of the CC equations. The CC equations and energy expression are obtained by inserting  $|\Phi_\alpha\rangle$  in the Schrödinger equation, operating on the left by  $e^{-T}$ , and projecting on the left with either the reference determinant or an excited determinant. Writing the energy as

$$E = \langle \Phi_0 | H | \Phi_0 \rangle + \Delta E_c \quad (5)$$

and defining

$$H_N = H - \langle \Phi_0 | H | \Phi_0 \rangle \quad (6)$$

we obtain equations for the amplitudes [2]

$$\langle \Phi_{ijk}^{abc} | e^{-1} H_N e^1 | \Phi_0 \rangle = \langle \Phi_{ijk}^{abc} | (H_N e^1)_c | \Phi_0 \rangle = 0 \quad (7)$$

and the correlation energy

$$\Delta E_c = \langle \Phi_0 | e^{-1} H_N e^1 | \Phi_0 \rangle = \langle \Phi_0 | (H_N e^1)_c | \Phi_0 \rangle \quad (8)$$

The subscript *c* indicates the restriction to "connected" diagrams [2, 10]. Although presented in this abstract and general form, these equations may readily be written in terms of Fock matrix elements, two-electron integrals, and cluster amplitudes [10]. They are nonlinear in the amplitudes, but by suitable definitions of intermediates may be rewritten so that they are simply a series of contractions of an amplitude and an intermediate, operationally taking on the appearance of equations which are linear in the amplitudes [11, 12], and are thus well-suited to exploiting vector computer architectures.

### *Truncation and Computational Cost*

The formal theory is all well and good, but without approximation it is just the CC representation of the full configuration interaction (FCI) wave function and energy. Therefore in order to obtain computationally feasible CC methods, the cluster operator *T* is truncated, just as CI expansions are truncated. For a system represented by *n* occupied orbitals and *N* virtual orbitals, the costs of the different truncations scale as indicated in Table I. The rapid increase in cost means that in order for these methods to be of practical value, a large fraction of the correlation energy must be recovered by low-order cluster operators. Fortunately, this is the case, with *T*<sub>2</sub> accounting for a considerable fraction of the dynamic correlation energy (i.e. the CCD method [4,5]). Important orbital relaxation effects are accounted for by *T*<sub>1</sub>, so that for many purposes the "singles-and-doubles" model (CCSD) [13] is a very good approximation, much better, for example, than the CISD approximation, even with the usual Langhoff-Davidson unlinked diagram correc-

TABLE I The scaling of the cost of various CC approximations

Truncation of <i>T</i>	Method	Cost/iteration <sup>a</sup>
<i>T</i> <sub>1</sub> + <i>T</i> <sub>2</sub>	CCSD	<i>n</i> <sup>2</sup> <i>N</i> <sup>4</sup> , <i>n</i> <sup>3</sup> <i>N</i> <sup>3</sup> , <i>n</i> <sup>4</sup> <i>N</i> <sup>2</sup>
<i>T</i> <sub>1</sub> + <i>T</i> <sub>2</sub> + <i>T</i> <sub>3</sub>	CCSD1	<i>n</i> <sup>3</sup> <i>N</i> <sup>5</sup> , <i>n</i> <sup>4</sup> <i>N</i> <sup>4</sup> , <i>n</i> <sup>5</sup> <i>N</i> <sup>3</sup>
<i>T</i> <sub>1</sub> + <i>T</i> <sub>2</sub> + <i>T</i> <sub>3</sub> + <i>T</i> <sub>4</sub>	CCSD1Q	<i>n</i> <sup>4</sup> <i>N</i> <sup>6</sup> , <i>n</i> <sup>5</sup> <i>N</i> <sup>5</sup> , <i>n</i> <sup>6</sup> <i>N</i> <sup>4</sup>

<sup>a</sup> *n* and *N* are, respectively, numbers of occupied and virtual orbitals. The exact operation count is proportional to these numbers.

tion [14]. However, in order to achieve high accuracy, one must include  $T_3$ . Judging by comparison with FCI results for small systems, the CCSDT method [15,16,17] does indeed seem to be a rather accurate method. Adding  $T_4$  either through the CCSDTQ model [12] or various approximations thereto [18,19] shows usually small, but sometimes significant, improvements.

Unfortunately, even the CCSDT approximation is somewhat too expensive for most applications. Therefore, a lot of effort has been devoted to finding ways of approximating CCSDT yet reducing the cost. Two approaches have been followed. The first is *iterative* approximations, in which the  $T_3$  equation is truncated but is still iterated. This leads to methods termed CCSDT-1 [20,21], CCSDT-2 [22], and CCSDT-3 [22]. The second approach makes what sounds like an even more drastic approximation, which is not to iterate the  $T_3$  equation at all, but to estimate the contribution of  $T_3$  to the energy from CCSD  $T_1$  and  $T_2$  amplitudes using equations based on perturbation theory [10]. This has led to several methods, including CCSD + T(CCSD) [21], CCSD(T) [23], and CCSD + TQ\*(CCSD) [19]. The first and second of these are rather economical, requiring a CCSD calculation followed by a single evaluation of the  $T_3$  energy, the latter requiring a cost proportional to ( $n^3N^4 + n^4N^3$ ). The third method is more sophisticated and includes connected quadruple excitation ( $T_4$ ) corrections, but is correct through fifth order of many-body perturbation theory and has a  $T_3$  cost proportional to ( $n^3N^5 + n^4N^4 + n^5N^3$ ). The simple *noniterative* approximation CCSD(T) works remarkably well [24–29], although we caution the reader that this is often somewhat fortuitous [30]. It is sufficiently economical to be used with over 200 basis functions when a molecule has  $C_{2v}$  or higher symmetry [31–33]. Accordingly, this and the closely related QCISD(T) approach [34] (which is equivalent through fifth order of MBPT) are being widely used.

### Analytical Derivatives for CC Methods with Noniterative Triple Excitations

As we discussed in the last section, simple noniterative methods of including  $T_3$  are of wide applicability. Therefore efficient analytical evaluation of energy derivatives for these methods is of considerable value. This we now consider.

Methods for the analytical evaluation of derivatives of the CC energy are now at an advanced level. These techniques are essential for exploration of potential energy surfaces, including location and characterization of stationary points, as well as computation of vibrational frequencies and intensities. They may also be used for the computation of first-order properties. Although only first derivatives are routinely available, these may be numerically differentiated to obtain higher derivatives, and this is cheaper and more numerically stable than numerical differentiation of the energy.

At first sight, evaluation of derivatives of the CC energy appears to pose a serious computational problem. Thus, the derivative of the energy with respect to some property  $\alpha$  (for example, a nuclear displacement or electric field) may be written in the general form

$$\frac{\partial E}{\partial \alpha} = f(h^\alpha) \frac{\partial E}{\partial \chi} \frac{\partial \chi}{\partial \alpha} + \frac{\partial E}{\partial c} \frac{\partial c}{\partial \alpha} + \frac{\partial E}{\partial t} \frac{\partial t}{\partial \alpha} \quad (9)$$

when  $f(h^\alpha)$  is a function of the perturbation,  $h^\alpha$ . Here  $\chi$  denotes basis functions,  $c$  denotes MO coefficients, and  $t$  denotes CC amplitudes. For nonvariational (or more precisely nonstationary) methods such as CC methods, all of these terms must be evaluated. For variational methods, however, one or more of these terms vanishes. For example, in SCF and  $\pi$ -SCF methods, the second and third vanish, and for CI methods the third term vanishes. For CC methods the third term must be considered, and this appears to present a significant difficulty. Thus, it appears that in order to evaluate the CC energy derivative, one must explicitly evaluate the derivative of the CC amplitudes, which would require solution of  $3N$  CC-like equations for computation of the force. Fortunately, however, further investigation showed that there was an alternative, much more economical evaluation of the effect of these amplitude derivatives [35–38]. This requires the solution of a *single* perturbation independent set of equations (the  $\Lambda$  equations [38]).

Recent work with expectation value and unitary CC schemes [39] has brought to light a straightforward derivation of these equations, which is more transparent than the original derivations and provides more insight into CC energy derivatives. Consider the functional

$$\Delta E(\Lambda, T) = \langle \Phi_0 | (1 + \Lambda) e^{-T} H_N e^T | \Phi_0 \rangle \quad (10)$$

where  $\Lambda$  is a *de-excitation* operator defined by

$$\Lambda = \sum_a \lambda_a' \{i^+ a\} + \sum_{ab} \lambda_{ab}'' \{i^+ a j^+ b\} + \dots \quad (11)$$

If we attempt to make  $\Delta E(\Lambda, T)$  stationary with respect to  $\Lambda$  amplitudes, then we obtain the CC equations. For example, differentiating with respect a particular amplitude  $\lambda_{ab}''$ , and setting the result equal to zero yields

$$\begin{aligned} \langle \Phi_0 | \{i^+ a j^+ b \dots\} | (P + Q) e^{-T} H_N e^T | \Phi_0 \rangle \\ = \langle \Phi_0 | \{i^+ a j^+ b \dots\} | \mathbf{h} \rangle \langle \mathbf{h} | e^{-T} H_N e^T | \Phi_0 \rangle = 0 \end{aligned} \quad (12)$$

where  $P$  is the reference state projector,  $|\Phi_0\rangle\langle\Phi_0|$  and  $Q$  is the projector for the manifold of excited determinants  $|\mathbf{h}\rangle\langle\mathbf{h}|$ , and we have used  $P + Q = 1$ . It follows that

$$\langle \mathbf{h} | e^{-T} H_N e^T | \Phi_0 \rangle = 0 \quad (13)$$

and we have recovered the CC equations [Eq. (7)]. Similarly, if we attempt to make the functional stationary with respect to  $T$  amplitudes we find

$$\langle \Phi_0 | (1 + \Lambda) e^{-T} H_N e^T | \mathbf{h} \rangle - \Delta E_{cc} \langle \Phi_0 | \Lambda | \mathbf{h} \rangle = 0 \quad (14)$$

which are the  $\Lambda$  equations [38]. If the functional is stationary with respect to  $\Lambda$  and  $T$ , it follows that



$$\frac{\partial \Delta E(\Lambda, T)}{\partial \alpha} = \langle \Phi_0 | (1 + \Lambda) e^{-T} \frac{\partial H_N}{\partial \alpha} e^T | \Phi_0 \rangle \quad (15)$$

From this it is readily apparent that the derivative of the CC (and MBPT) energy has the same general form as that for CI and other methods [40], namely, after transforming to the atomic orbital basis set

$$\frac{\partial E}{\partial \alpha} = D_{\mu\nu} \frac{\partial h_{\mu\nu}}{\partial \alpha} + I_{\mu\nu} \frac{\partial S_{\mu\nu}}{\partial \alpha} + G_{\mu\nu\lambda\sigma} \frac{\partial \langle \mu\nu | \lambda\sigma \rangle}{\partial \alpha} \quad (16)$$

That is, the derivative is expressed in terms of derivatives of one-electron, two-electron, and overlap integrals. The matrices  $D$ ,  $I$ , and  $G$  are independent of the perturbation  $\alpha$ , but of course contain amplitudes of  $\Lambda$ . The derivatives of overlap integrals arise from the orbital response.

As a result of the introduction of  $\Lambda$ , analytical derivatives have now been implemented and are routinely evaluated for several CC methods, including CCSD [41–45], CCSD(T) [46–49], CCSDT-1 [50], as well as for QCISD [51] and QCISD(T) methods [48,52].

For the CCSD(T) method analytical derivatives have been implemented for closed-shell RHF reference determinants [46,47], likewise for QCISD(T) [52]. In recent research we have extended this to the case of UHF reference determinants for the CCSD + T(CCSD), CCSD(T) and QCISD(T) methods, as well as MBPT(4) [48]. This has been implemented in the ACES II program system [53,54], with a vectorized algorithm and Abelian symmetry incorporated along similar lines to previously presented work [55]. The resulting program has been used in several applications, including  $C_4$  [33], HCCO [56], and HOO [48]. The computational effort to evaluate the energy derivative is about twice that required to evaluate the energy.

In related work we have considered derivatives for CCSD(T) when the reference determinant is of the restricted open-shell Hartree-Fock (ROHF) type. While CC methods largely remove the spin contamination of the UHF determinant [6,57], this is not always the case and consequently it is sometimes beneficial to use spin eigenfunction ROHF reference determinants (or other "quasi-RHF" (QRHF) determinants) for open-shell systems [57]. Just defining the energy expression for such a method is not entirely straightforward [45,49], however, and has led to confusion. We earlier presented the formalism and initial results for ROHF-CCSD(T) [45], and expanded on this recently [49]. Of great importance is the need for a transformation to semicanonical orbitals [58] (i.e., the occupied-occupied and virtual-virtual blocks of the spin orbital Fock matrix are diagonal). This removes the equivalence of the  $\alpha$  and  $\beta$  spatial orbitals, but does not alter the spin eigenfunction characteristics of the method. If one does not transform to semicanonical orbitals, it is necessary to iterate the  $T_3$  equation in order to achieve proper invariance properties, which defeats the whole purpose of noniterative methods such as CCSD(T). Building on a previous implementation of ROHF-CCSD gradients [45], we have now implemented analytical derivatives for our ROHF-CCSD(T) method [49]. The cost is essentially the same as in the UHF case.

As an illustration of results that can be obtained with ROHF-CCSD(T) gradients, we show data obtained for HCC with several basis sets [49], compared with experiment [59], in Table II. This is a good example for comparison since this is one of the few open-shell molecules for which *harmonic* frequencies have been deduced from experiment. With the largest basis set, very good agreement with experiment is achieved. This example and work on HOO [48] illustrate that these methods should be suitable for characterizing small transient molecules. It should be emphasized that the basis set used, while large, certainly did not exhaust our capabilities. In this example, for which UHF spin contamination is not large, we also see the equivalence of UHF- and ROHF-based results.

### Some Recent Research with the CCSDT Method

The CCSDT method was first implemented by Noga and Bartlett in 1987 [15], followed by Scuseria and Schaefer in 1988 [16]. These implementations were explicitly restricted to RHF closed-shell reference determinants, and we implemented the method for general closed- and open-shell reference determinants in 1990 [17]. CCSDT is rather an expensive method, and chemical applications are somewhat limited, although there have now been a large number of studies of small systems with DZP or slightly larger basis sets [15-17,27-30,60,61]. Included among the larger CCSDT calculations are our studies of the harmonic force fields of  $C_3^+$  [61] and  $O_3$  [30] and a study of the hyperpolarizabilities of Ne by Rice et al. [62]. Our initial implementation of CCSDT did not exploit point group symmetry, and nor did that of Noga and Bartlett. We have recently completed another implementation which exploits Abelian symmetry by the DPD approach [55], and this has been implemented in ACES II [53,54]. This should enable us to tackle somewhat larger problems with CCSDT than has hitherto been the case. This will be discussed later. First we present results of four series of CCSDT calculations.

TABLE II UHF- and ROHF-CCSD(T) calculated properties of  $\Lambda^2A' HCO$

Ref/Bas <sup>a</sup>	$r_{HC}/\text{\AA}$	$r_{CO}/\text{\AA}$	$\theta/^\circ$	$\omega_1, \omega_2, \omega_3/\text{cm}^{-1}$		
R/421	1.1212	1.1974	124.25	2779	1882	1136
U/421	1.1214	1.1972	124.24	2778	1890	1136
R/532	1.1198	1.1812	124.00	2677	1871	1132
U/532	1.1199	1.1811	124.01	2676	1878	1134
R/5321	1.1174	1.1797	124.41	2727	1896	1134
R/5421	1.1163	1.1804	124.55	2765	1893	1121
Expt	1.119	1.175	124.4	2790	1920	1126

<sup>a</sup> Reference determinant and basis set: R and U denote ROHF and UHF reference determinants, respectively. 421 denotes a 4s2p1d basis set, 532 a 5s3p2d set, and so on.

*FCI Comparison of Bond Stretching in CH<sub>3</sub>*

As bonds in a molecule are stretched, the reference determinant becomes a progressively poorer approximation, and great demands are therefore placed on single reference methods at the stretched geometries. CC methods have been compared with FCI results for several molecules, mostly closed-shell species [15], although there have been some open-shell comparisons [17,34,49]. We now compare the performance of the CCSD, CCSD(T), and CCSDT methods for the simultaneous stretching of the three C—H bonds of CH<sub>3</sub>. The FCI data are from the work of Bauschlicher and Taylor [63]. UHF and ROHF reference determinants are used in the CC calculations. The data are shown in Table III. It is seen that both CCSD and CCSD(T) methods are unable to reproduce the energy at  $2R_e$  very well at all. Moreover, the results obtained with the two reference determinants are quite different. Moving to CCSDT, however, much better agreement with FCI is achieved, with the energies from the two determinants being relatively close (the FCI results will be the same for the two determinants, of course, apart from the small difference due to different dropped core orbitals). The UHF-based results suffer considerably from spin contamination, some of which is removed by the CC methods, especially CCSDT. It is noticeable that the performance of CCSD(T) at stretched geometries appears to be poorer for open-shell molecules (e.g., CH<sub>3</sub>, NH<sub>2</sub>, and SiH<sub>2</sub>) than for closed-shell molecules (e.g., H<sub>2</sub>O), regardless of whether a UHF or ROHF reference determinant is used [49].

*Bond Stretching in N<sub>2</sub>*

This example provides another stern test for single reference CC methods. Some work on this problem was done some time ago by Laidig, Saxe, and Bartlett [64], who investigated the behavior of several single reference CC/MBPT methods, along with MR-CI and a linearized MR-CC method. With an RHF reference, all single reference methods fail in various ways, yielding curves which have a local maximum before falling well below the true curve. At an internuclear distance of about  $2.2a_0$ ,

TABLE III Bond stretching in  $A_1^2CH_3$ . Comparison with full CI for a DZP basis set. Data are deviations from FCI energies in  $10^{-3} E_h$ . The FCI data are from reference 63.

Ref. <sup>a</sup>	Method	$R_e$	$1.5R_e$	$2R_e$
ROHF	CCSD	2.849	8.843	37.322
ROHF	CCSD(T)	0.518	2.113	10.984
ROHF	CCSDT	-0.722	0.138	4.402
UHF	CCSD	2.790	8.768	19.771
UHF	CCSD + T(CCSD)	0.474	2.230	-32.157
UHF	CCSD(T)	0.499	2.669	-28.908
UHF	CCSDT	-0.744	-0.108	1.732

<sup>a</sup> Type of reference determinant.

there is an RHF-UHF instability of  $\sigma_u$  symmetry, and so a UHF determinant of  $C_{\infty v}$  orbitals may be used for larger distances. This greater flexibility in the reference determinant helps the CC/MBPT methods, as shown by Laidig et al. [64]. In particular, it was found that the UHF-CCSD curve was quite reasonable. We have now investigated this problem with the full CCSDT method with both UHF and RHF reference determinants and the same  $4s3p1d$  basis set as used by Laidig et al. The RHF results are shown in Figure 1, and are largely in line with those of Laidig et al., even the full RHF-CCSDT method failing at large enough distances. The UHF results are shown in Figure 2. Here the behavior is much better. Addition of triple excitations improves the CCSD results, and the CCSDT curve is in very good agreement with MR-CI. Note, the CCSD(T) result turns over from spin contamination, although the CCSDT energy does not appear to reflect that, but other properties may. It is seen from this work that UHF-based CC methods can describe the breaking of a triple bond. In fairness it should be mentioned that the UHF reference dissociates approximately into ground state atoms in this case, which is not always the case (for example,  ${}^3\Sigma_g^- \text{O}_2$ ). Further work on a wider class of systems is needed to establish fully the ability of UHF-based single reference CC methods to describe molecular dissociation. Incidentally, when  $T_3$  is included, RHF- and UHF-based CC methods are well known to be able to describe dissociation of single bonds [64]. One practical problem encountered in UHF CC calculations at highly stretched geometries is slow convergence, although RHF-based CC calculations eventually will

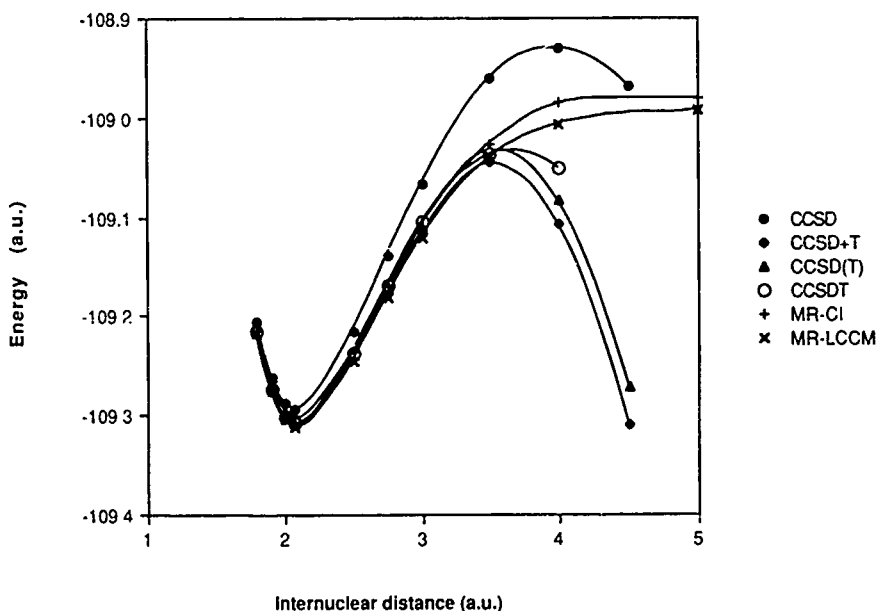


Figure 1. Calculated potential energy curves for various CC methods based on an RHF reference determinant ( $4s3p1d$  basis set,  $D_{2h}$  computational symmetry). The MR-CI and MR-CC data are from the work of Laidig et al

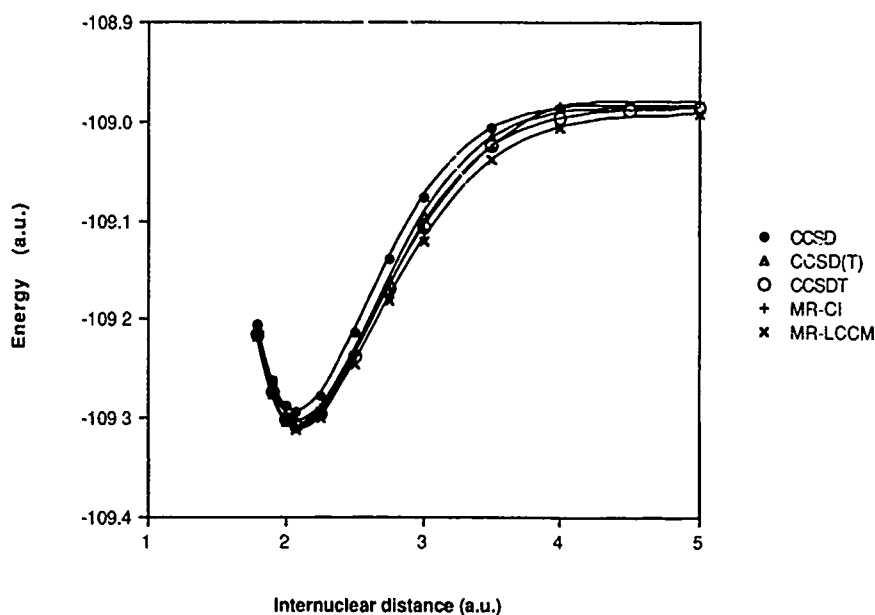


Figure 2. Calculated potential energy curves for various CC methods based on a UHF reference determinant ( $4s3p1d$  basis set,  $C_{2v}$  computational symmetry). The MR-CI and MR-CC data are from the work of Laidig et al.

not converge at all at such geometries, as several amplitudes get very large. Also, in the present work on  $N_2$  the symmetry was relaxed to  $C_{2v}$ , making the calculations more costly than if  $D_{2h}$  symmetry was used.

### *Electrical Properties of $X^1\Sigma$ BeO*

The ground state of BeO is highly polar and provides a challenge to theoretical calculations [65]. Electrical properties have been of interest for some time [66], particularly in view of the stability of various complexes [67] and the dipole bound anion [68]. In recent work we have been comparing different CC methods through calculations of the dipole moment and parallel and perpendicular dipole polarizabilities. A series of calculations were performed with the POL basis of Sadlej [69], which is a  $5s3p2d$  set designed to provide a reasonable description of electrical properties, even though it is only of modest size. For methods for which analytical derivatives were available, the dipole moments were evaluated analytically, and  $\alpha_{zz}$  was obtained from the difference of dipole moments evaluated in the presence of electric field along the molecular axis, while  $\alpha_{xx}$  was obtained from finite differences of energies. For other methods, all results were obtained by taking finite differences of the energy with respect to an electric field. The results are shown in Table IV. Particularly interesting is the fact that the CCSD(T) result for  $\alpha_{zz}$  is so different from the CCSD + T(CCSD) and CCSDT-1 and CCSDT-3 results. Since the three latter meth-

TABLE IV. Electrical properties of BeO.  $R = 1.3308 \text{ \AA}$ ,  $5s3p2d$  basis set. Atomic units.

Method	$\mu$	$\alpha_{xx}$	$\alpha_{zz}$
SCF	2.95	22.4	19.7
MBPT(2)	2.48	32.3	29.3
MBPT(4)	2.30	36.1	37.3
CCSD	2.56	31.3	29.8
CCSD + T(CCSD)	2.26	38.7	45.9
CCSD(T)	2.43	35.1	34.4
CCSDT-1b	2.27	35.3	45.6
CCSDT-3	2.30	34.9	44.6
CCSDT	2.40	34.3	36.0

ods all give somewhat similar results, one would not expect the method of inclusion of triple excitations to affect the results very much. Moreover, through fifth order of MBPT, CCSD(T) is equivalent to CCSDT-1b and CCSDT-3. Somewhat to our surprise, then, we have found that the CCSDT result turns out to be rather close to CCSD(T). The agreement of CCSD(T) with CCSDT is evidently somewhat fortuitous. Moreover, it is not certain in this case how close the CCSDT result is to FCI since a noniterative estimate of  $T_4$  effects indicates a significant value for these [70]. More discussion of results for electrical as well as spectroscopic properties is provided elsewhere [70], along with some interesting results obtained with the QCI methods.

### *Hessian Rank of ${}^2\Sigma_u^+ C_3^+$*

The  $C_3^+$  cation has been the subject of considerable recent theoretical attention [61,71-76]. This has stemmed from the uncertainty of its geometrical structure, experimental data being unable to clearly resolve whether it is bent or is linear but with a low bending frequency [77]. All reliable theoretical work has indicated that a bent structure (electronic state  ${}^2B_2$ ) with a bond angle of about  $70^\circ$  is of lower energy than the  ${}^2\Sigma_u^+$  species with which it correlates in  $D_{\infty h}$ . The exact value of the energy difference differs considerably according to method and basis, although it is likely to be only a few kcal/mol. What has received less attention, but is somewhat intriguing, is the question of whether there is a linear local minimum. Investigation of this point has been hampered by symmetry breaking, and so the imaginary frequencies for  $\sigma_u$  have been regarded with suspicion. Also, there are multiple UHF solutions, and the less contaminated one has several Hartree-Fock instabilities, including one of  $\sigma_u$  symmetry. In our previous work [61] we showed that use of a quasi-RHF reference determinant, consisting of neutral  $C_3$  orbitals, circumvented these problems for the bent species; the reference orbitals are unambiguously determined and do not suffer from symmetry breaking. Another point of interest regarding linear geometries is whether the linear species is stable to bending or not. We have therefore investigated the linear geometries with the QRHF approach and

the full CCSDT method using the same DZP basis set as in our previous work and a  $5s3p2d$  basis set defined by Taylor et al. [75].

We present the data in Table V. The UHF-based results indicate clearly instability along the asymmetric stretching coordinate, and show that the bending frequency is small. It is interesting that the CCSD(T) method predicts a real bending frequency, in line with the findings of Raghavachari and Taylor et al. with the QCISD(T) method, which indicate that there is a local maximum along the path connecting the  $^2B_2$  and  $^2\Sigma_u^+$  states. With CCSDT, however, this seems not to be true. Moving now to the QRHF results, we see that with both basis sets the imaginary  $\sigma_u$  frequency remains, which seems to be strong evidence that this is not an artifact after all. These results also show instability to bending. It is interesting to compare our results with second-order electron propagator [EPT(2)] results of Ortiz [76], which represent the most detailed investigation of the force field of the linear species to date. These, which also are based on neutral  $C_3$  orbitals, predict an imaginary  $\sigma_u$  but a real  $\pi_u$  frequency. Ortiz allowed the two bond lengths to become inequivalent and located the  $^2\Sigma^+$  state, which he finds to be a local minimum. Taylor et al. also located this state at the CASSCF level but appear to regard it as an artifact. Finally, one might ask why the bonds of linear  $C_3^+$  would be inequivalent. A plausible answer may come from the second-order Jahn-Teller theorem. Thus, according to the calculations of Ortiz, the  $^2\Sigma_g^+$  state lies less than 1 eV above the  $^2\Sigma_u^+$  state, and these states may be coupled by the  $\sigma_u$  vibration, leading to a  $^2\Sigma^+$  state.

### *Prospects for Larger CCSDT Calculations*

In Table VI we present preliminary times for CCSDT calculations with our new implementation. Where these are available, we present also times for our previous implementation. The times for the new implementation are roughly a factor of 10 smaller than for the old version for two  $C_{2v}$  examples, and this is a conservative ratio since the  $T_3$  vector was not held in core in the new implementation, while it was in the previous implementation. The use of the DPD algorithm to exploit sym-

TABLE V. Harmonic vibrational frequencies of  $^2\Sigma_u^+ C_3^+$  ( $\text{cm}^{-1}$ ).

Ref/Bas <sup>a</sup>	Method	$\sigma_g$	$\sigma_u$	$\pi_u$
U/421	SCF	1277	2456	190i
U/421	CCSD	1208	2500i	176i
U/421	CCSD(T)	1149	1431i	59
U/421	CCSDT	1158	451i	76i
Q/421	CCSDT	1162	2064i	69i
Q/532	CCSDT	1177	2564i	215i

<sup>a</sup> Reference determinant and basis set (see footnote to Table II). Q denotes a QRHF reference determinant comprising neutral  $C_3$  orbitals.

TABLE VI. Some preliminary timings of CCSDT codes on Cray-3 MP (CPU sec).

System	Ref/Bas <sup>a</sup>	Symmetry <sup>b</sup>	N <sub>bas</sub> <sup>c</sup>	Old <sup>d</sup>	New <sup>e</sup>
<sup>1</sup> A <sub>1</sub> O <sub>3</sub>	R/421	C <sub>2v</sub>	48	15215	1478
<sup>2</sup> B <sub>2</sub> C <sub>3</sub> <sup>+</sup>	U/421	C <sub>2v</sub>	48	9850	795
<sup>2</sup> Σ <sub>u</sub> <sup>+</sup> C <sub>3</sub> <sup>+</sup>	U/532	D <sub>2h</sub>	72		2200
<sup>3</sup> Π <sub>u</sub> C <sub>2</sub>	U/54321	D <sub>2h</sub>	110		3289

<sup>a</sup> Reference determinant and basis set (see footnote to Table II).<sup>b</sup> Computational symmetry.<sup>c</sup> Number of basis functions.<sup>d</sup> Old code had T<sub>3</sub> in core.<sup>e</sup> New code had T<sub>3</sub> out of core. All calculations were run with 6.5 Mwords of memory

metry allows for a theoretical speedup of  $h^2$ , where  $h$  is the order of the computational point group, so a factor of 10 is reasonable given the different modes of T<sub>3</sub> storage. With the new implementation, it is seen that CCSDT calculations with over 100 basis functions (for relatively small numbers of electrons) are quite feasible. Of course, such calculations require of the order of hours of supercomputer time, and one can often achieve similar quality results with approximate methods such as CCSD(T) in a small fraction of the time. However, as seen in some of the examples in this and other articles, there can be significant differences between the methods, and so it is always helpful to be able to compare approximate methods with CCSDT. If there are large differences, it may be true that the approximate method is not appropriate for the problem, although it may (fortuitously) yield good agreement with experiment. If the CCSDT results are in agreement with those of a more approximate method, it is likely that application of the approximate method is appropriate.

### Acknowledgments

This article draws from work supported by both the United States Office of Naval Research and the United States Air Force Office of Scientific Research. Drs. John F. Stanton, Jürgen Gauss, and Walter J. Lauderdale are thanked for major contributions to the ACES II program. The Ohio Supercomputer Center is thanked for supporting the development of ACES II through generous computer resource grants. The Supercomputer Computations Research Institute at Florida State University is thanked for providing computer resources for some of the calculations. Dr. Jürgen Gauss is thanked for contributions to the work on analytical derivatives. Dr. Miroslav Urban is thanked for contributions to the BeO project. John F. Stanton, Jürgen Gauss, and Ajith Perera are thanked for helpful discussions. This article is based on a talk given at the 1993 Sanibel Symposium by JDW, who thanks the Sanibel Conference Organizers for the invitation and support. Dr. Yngve Öhrn is thanked



for inviting us to prepare this article for the Symposium Proceedings. Dr. Ming-Ju Huang is thanked for preparing Figures 1 and 2.

### Bibliography

- [1] F. Coester, *Nucl. Phys.* **1**, 421 (1958); F. Coester and H. Kummel, *ibid.* **17**, 477 (1960); H. Kummel, *Nucl. Phys.* **22**, 177 (1969).
- [2] J. Čížek, *J. Chem. Phys.* **45**, 4256 (1966); *Adv. Chem. Phys.* **14**, 35 (1969).
- [3] J. Paldus and J. Čížek, in *Energy, Structure, and Reactivity*, D. W. Smith and W. B. McRae, Eds. (Wiley, New York, 1973); J. Paldus, J. Čížek, and I. Shavitt, *Phys. Rev. A* **50** (1972).
- [4] R. J. Bartlett and G. D. Purvis III, *Int. J. Quantum Chem., Quantum Chem. Symp.* **14**, 561 (1978).
- [5] J. A. Pople, R. Krishnan, H. B. Schlegel, and J. S. Binkley, *Int. J. Quantum Chem. Quantum Chem. Symp.* **14**, 545 (1978).
- [6] M. Urban, I. Cernusak, V. Kello, and J. Noga, in *Methods in Computational Chemistry* **2**, S. Wilson, Ed. (Plenum, New York, 1987); R. J. Bartlett, *J. Phys. Chem.* **93**, 1697 (1989); J. Paldus, *Methods in Computational Molecular Physics, NATO ASI*, 1991, K. Raghavachari, *Ann. Rev. Phys. Chem.* **42**, 615 (1991).
- [7] Many aspects of the Fock Space CC approach are covered by articles in *Theor. Chim. Acta* **80**, 427-507 (1991).
- [8] B. Jeziorski and H. J. Monkhorst, *Phys. Rev. A* **24**, 1668 (1981); J. Paldus, in *New Horizons in Quantum Chemistry*, (Reidel, Dordrecht, 1983); J. Paldus, L. Pylypow, and B. Jeziorski, *Lecture Notes in Chemistry* **52**, 15, (1989) (U. Kaldor, Ed.); L. Meissner, S. A. Kucharski, and R. J. Bartlett, *J. Chem. Phys.* **91**, 5187 (1989); L. Meissner and R. J. Bartlett, *ibid.* **92**, 561 (1990); S. A. Kucharski and R. J. Bartlett, *ibid.* **95**, 8227 (1991); S. A. Kucharski, A. Balkova, P. G. Szalay, and R. J. Bartlett, *ibid.* **97**, 4289 (1992); A. Balkova, S. A. Kucharski, L. Meissner, and R. J. Bartlett, *J. Chem. Phys.* **95**, 4311 (1991); A. Balkova, S. A. Kucharski, L. Meissner, and R. J. Bartlett, *Theor. Chim. Acta* **80**, 35 (1991); A. Balkova, S. A. Kucharski, and R. J. Bartlett, *Chem. Phys. Lett.* **182**, 511 (1991); A. Balkova and R. J. Bartlett, *Chem. Phys. Lett.* **193**, 364 (1992).
- [9] H. J. Monkhorst, *Int. J. Quantum Chem., Quantum Chem. Symp.* **11**, 421 (1977); H. Nakatsuji and K. Hirao, *J. Chem. Phys.* **68**, 2053 (1978); S. Ghosh, D. Mukherjee, and S. Bhattacharya, *Mol. Phys.* **43**, 173 (1981); H. Seo and R. J. Bartlett, *Int. J. Quantum Chem., Quantum Chem. Symp.* **18**, 255 (1984); J. Geertsen, M. Rittby, and R. J. Bartlett, *Chem. Phys. Lett.* **164**, 57 (1989); H. Koch and P. Jørgensen, *J. Chem. Phys.* **93**, 3333 (1990); H. Koch, H. J. Aa. Jensen, T. Helgaker, and P. Jørgensen, *ibid.* **93**, 3345 (1990); J. F. Stanton and R. J. Bartlett, *J. Chem. Phys.* **98**, 7029 (1993); D. C. Comeau and R. J. Bartlett, *Chem. Phys. Lett.* **207**, 414 (1993).
- [10] S. A. Kucharski and R. J. Bartlett, *Adv. Quantum Chem.* **18**, 281 (1986).
- [11] S. A. Kucharski and R. J. Bartlett, *Theor. Chim. Acta* **80**, 387 (1992).
- [12] S. A. Kucharski and R. J. Bartlett, *J. Chem. Phys.* **97**, 4282 (1992).
- [13] G. D. Purvis III and R. J. Bartlett, *J. Chem. Phys.* **76**, 1910 (1982).
- [14] S. R. Langhoff and E. R. Davidson, *Int. J. Quantum Chem.* **8**, 61 (1974).
- [15] J. Noga and R. J. Bartlett, *J. Chem. Phys.* **86**, 7041 (1987).
- [16] G. E. Scuseria and H. F. Schaefer III, *Chem. Phys. Lett.* **152**, 382 (1988).
- [17] J. D. Watts and R. J. Bartlett, *J. Chem. Phys.* **93**, 6104 (1990).
- [18] S. A. Kucharski and R. J. Bartlett, *Chem. Phys. Lett.* **158**, 550 (1989).
- [19] R. J. Bartlett, J. D. Watts, S. A. Kucharski, and J. Noga, *Chem. Phys. Lett.* **165**, 513 (1990).
- [20] Y. S. Lee, S. A. Kucharski, and R. J. Bartlett, *J. Chem. Phys.* **81**, 5906 (1984).
- [21] M. Urban, J. Noga, S. J. Cole, and R. J. Bartlett, *J. Chem. Phys.* **83**, 4041 (1985).
- [22] J. Noga, R. J. Bartlett, and M. Urban, *Chem. Phys. Lett.* **134**, 126 (1987).
- [23] K. Raghavachari, G. W. Trucks, J. A. Pople, and M. Head-Gordon, *Chem. Phys. Lett.* **157**, 479 (1989).
- [24] T. J. Lee, A. P. Rendell, and P. R. Taylor, *J. Chem. Phys.* **93**, 6636 (1990).
- [25] T. J. Lee and G. E. Scuseria, *J. Chem. Phys.* **93**, 489 (1990).
- [26] T. J. Lee and J. E. Rice, *J. Chem. Phys.* **94**, 1215 (1991).

- [27] G. E. Scuseria and T. J. Lee, *J. Chem. Phys.* **93**, 5851 (1990).
- [28] J. D. Watts and R. J. Bartlett, *J. Chem. Phys.* **95**, 6652 (1991).
- [29] J. D. Watts and R. J. Bartlett, *J. Chem. Phys.* **96**, 6073 (1992).
- [30] J. D. Watts, J. F. Stanton, and R. J. Bartlett, *Chem. Phys. Lett.* **178**, 471 (1991).
- [31] A. P. Rendell, T. J. Lee, and A. Kormonicki, *Chem. Phys. Lett.* **178**, 462 (1991).
- [32] J. D. Watts and R. J. Bartlett, *Chem. Phys. Lett.* **190**, 19 (1992).
- [33] J. D. Watts, J. Gauss, J. F. Stanton, and R. J. Bartlett, *J. Chem. Phys.* **97**, 8772 (1992).
- [34] J. A. Pople, M. Head-Gordon, and K. Raghavachari, *J. Chem. Phys.* **87**, 5968 (1987).
- [35] L. Adamowicz, W. D. Laidig, and R. J. Bartlett, *Int. J. Quantum Chem., Quantum Chem. Symp.* **18**, 245 (1984).
- [36] G. Fitzgerald, R. J. Harrison, and R. J. Bartlett, *J. Chem. Phys.* **85**, 5143 (1986).
- [37] R. J. Bartlett, in *Geometrical Derivatives of Energy Surfaces and Molecular Properties*, P. Jørgensen, and J. Simons, Eds. (Reidel, Dordrecht, 1986).
- [38] E. A. Salter, G. W. Trucks, and R. J. Bartlett, *J. Chem. Phys.* **90**, 1752 (1989).
- [39] P. G. Szalay and R. J. Bartlett, *J. Chem. Phys.*, in press.
- [40] J. E. Rice and R. D. Amos, *Chem. Phys. Lett.* **122**, 585 (1985).
- [41] A. C. Scheiner, G. E. Scuseria, J. E. Rice, T. J. Lee, and H. F. Schaefer III, *J. Chem. Phys.* **87**, 5361 (1987).
- [42] A. P. Rendell and T. J. Lee, *J. Chem. Phys.* **94**, 6219 (1991).
- [43] J. Gauss, J. F. Stanton, and R. J. Bartlett, *J. Chem. Phys.* **95**, 2623 (1991).
- [44] J. Gauss, J. F. Stanton, and R. J. Bartlett, *J. Chem. Phys.* **95**, 2659 (1991).
- [45] J. Gauss, W. J. Lauderdale, J. F. Stanton, J. D. Watts, and R. J. Bartlett, *Chem. Phys. Lett.* **187**, 21 (1991).
- [46] G. E. Scuseria, *J. Chem. Phys.* **94**, 442 (1991).
- [47] T. J. Lee and A. P. Rendell, *J. Chem. Phys.* **94**, 6229 (1991).
- [48] J. D. Watts, J. Gauss, and R. J. Bartlett, *Chem. Phys. Lett.* **200**, 1 (1992).
- [49] J. D. Watts, J. Gauss, and R. J. Bartlett, *J. Chem. Phys.* **98**, 8718 (1993).
- [50] G. E. Scuseria and H. F. Schaefer III, *Chem. Phys. Lett.* **146**, 23 (1988).
- [51] J. Gauss and D. Cremer, *Chem. Phys. Lett.* **150**, 280 (1988).
- [52] J. Gauss and D. Cremer, *Chem. Phys. Lett.* **163**, 549 (1989).
- [53] ACES II is a quantum chemical program package for CC and MBPT energy and gradient calculations. This package includes the SCF, integral transformation, correlation energy, and gradient codes written by J. F. Stanton, J. Gauss, J. D. Watts, W. J. Lauderdale, and R. J. Bartlett, the VMOL integral and VPROPS property integral programs written by P. R. Taylor and J. Almlof, and a modified version of the integral derivative program ABACUS written by T. Helgaker, H. J. Aa. Jensen, P. Jørgensen, J. Olsen, and P. R. Taylor.
- [54] J. F. Stanton, J. Gauss, J. D. Watts, W. J. Lauderdale, and R. J. Bartlett, *Int. J. Quantum Chem., Quantum Chem. Symp.* **26**, 879 (1992).
- [55] J. F. Stanton, J. Gauss, J. D. Watts, and R. J. Bartlett, *J. Chem. Phys.* **94**, 4334 (1991).
- [56] P. G. Szalay, J. F. Stanton, and R. J. Bartlett, *Chem. Phys. Lett.* **193**, 573 (1992).
- [57] M. Rittby and R. J. Bartlett, *J. Phys. Chem.* **92**, 3033 (1988).
- [58] N. C. Handy, J. A. Pople, M. Head-Gordon, K. Raghavachari, and G. W. Trucks, *Chem. Phys. Lett.* **164**, 185 (1989).
- [59] E. Hirota, *J. Mol. Struct.* **146**, 237 (1986); K. K. Murray, T. M. Miller, D. G. Leopold, and W. C. Lineberger, *J. Chem. Phys.* **84**, 2520 (1986).
- [60] C. Sosa, J. Noga, and R. J. Bartlett, *J. Chem. Phys.* **88**, 5974 (1988); G. E. Scuseria, T. P. Hamilton, and H. F. Schaefer III, *J. Chem. Phys.* **92**, 568 (1990); J. D. Watts, I. Cernusak, J. Noga, R. J. Bartlett, C. W. Bauschlicher, Jr., T. J. Lee, A. P. Rendell, and P. R. Taylor, *J. Chem. Phys.* **93**, 8875 (1990); J. M. L. Martin, T. J. Lee, G. E. Scuseria, and P. R. Taylor, *J. Chem. Phys.* **97**, 6549 (1992).
- [61] J. D. Watts, J. F. Stanton, J. Gauss, and R. J. Bartlett, *J. Chem. Phys.* **94**, 4320 (1991).
- [62] J. E. Rice, G. E. Scuseria, T. J. Lee, P. R. Taylor, and J. Almlof, *Chem. Phys. Lett.* **191**, 23 (1992).
- [63] C. W. Bauschlicher, Jr. and P. R. Taylor, *J. Chem. Phys.* **86**, 5600 (1987).
- [64] W. D. Laidig, P. Saxe, and R. J. Bartlett, *J. Chem. Phys.* **86**, 887 (1987).

- [65] H. F. Schaefer III, *J. Chem. Phys.* **55**, 176 (1971).
- [66] G. H. F. Diercksen, A. J. Sadlej, and M. Urban, *Chem. Phys.* **158**, 19 (1991).
- [67] W. Koch, J. R. Collins, and G. Frenking, *Chem. Phys. Lett.* **132**, 330 (1986); W. Koch, G. Frenking, J. Gauss, D. Cremer, and J. R. Collins, *J. Am. Chem. Soc.* **109**, 5917 (1987); G. Frenking, W. Koch, J. Gauss, and D. Cremer, *ibid.* **110**, 8007 (1988); G. Frenking, W. Koch, and J. R. Collins, *J. Chem. Soc., Chem. Commun.* 1147 (1988).
- [68] L. Adamowicz and R. J. Bartlett, *J. Chem. Phys.* **83**, 6268 (1985).
- [69] A. J. Sadlej, *Collect. Czech. Chem. Commun.* **53**, 1995 (1988); A. J. Sadlej, *Theor. Chim. Acta* **79**, 123 (1991).
- [70] J. D. Watts, M. Urban, and R. J. Bartlett, to be published.
- [71] R. S. Grev, I. L. Alberts, and H. F. Schaefer III, *J. Phys. Chem.* **94**, 3379 (1990).
- [72] K. Raghavachari, *Chem. Phys. Lett.* **171**, 249 (1990).
- [73] J. M. L. Martin, J. P. Francois, and R. Gijbels, *J. Chem. Phys.* **93**, 5037 (1990).
- [74] G. E. Scuseria, *Chem. Phys. Lett.* **176**, 27 (1991).
- [75] P. R. Taylor, J. M. L. Martin, J. P. Francois, and R. Gijbels, *J. Phys. Chem.* **95**, 6530 (1991).
- [76] J. V. Ortiz, *J. Chem. Phys.* **97**, 7531 (1992).
- [77] A. Faibis, E. P. Kanter, L. M. Tack, E. Bakke, B. J. Zabransky, *J. Phys. Chem.* **91**, 6445 (1987); Z. Vager and E. P. Kanter, *J. Phys. Chem.* **93**, 7745 (1989).

Received June 24, 1993

# Electron Propagator Theory with the Ground State Correlated by the Coupled-Cluster Method

LESZEK MEISSNER\* and RODNEY J. BARTLETT

*Quantum Theory Project, University of Florida, Gainesville, Florida 32611*

## Abstract

Ground state electron correlation is introduced into the one-particle propagator via coupled cluster theory. This defines a similarity transformation of the Hamiltonian, which leads to the complete separation of the ionization and electron attachment aspects of the propagator. The latter makes it possible to solve for each property independently. Furthermore, the frequency (or energy) dependence which characterizes propagator theory is eliminated by introducing a wave operator formalism. It is shown that this procedure is equivalent to the summation of certain types of terms in the electron propagator perturbation expansion to infinite order. Finally, the resulting equations are found to be equivalent to those of the Fock-space coupled-cluster (or equivalently the equation of motion coupled-cluster) method, which provides an explicit wave function for each state, demonstrating the connection between these different approaches for the calculation of ionization potentials and electron affinities. Understanding this relationship permits new and powerful approximations to be proposed. © 1993 John Wiley & Sons, Inc.

## Introduction

One-particle propagator methods have been employed in molecular theory primarily for the calculation of electron binding energies (ionization potentials and electron affinities). Applications have been presented by Pickup and Goscinski [1] and Purvis and Öhrn [2] using the electron propagator, Simons and Smith using the equation of motion method [3], and Cederbaum employing the Green's function method [4]. All these approaches have been shown to be equivalent [5–8]. Propagator methods depend upon two approximations, one for the reference state which defines the average value of operators, and a largely independent choice of operator manifold that permits the description of ionized, electron attached or excited states. Consequently, hybrid methods have been proposed, where coupled-cluster (CC) theory [9–11] is used to define the reference state solutions together with customary operator choices as in propagator theory. This has been done for the electron propagator [12] and for the polarization propagator [13], however, the exponential nature of the CC wave function invariably requires making rather several approximations to just linear or maybe quadratic terms [12,13] in implementation that jeopardizes the full advantages of the CC method. In this paper, we consider the natural evolution of this idea for the electron propagator and demonstrate its cul-

---

\* Permanent address: Physics Institute, Pedagogical University, PL-42 200 Częstochowa, Poland

mination in Fock space CC [14-16] and the equation-of-motion (EOM-CC) method [18,19].

A characteristic feature of the electron propagator method is that it couples problems of ionization potentials and electron affinities [5-8] (for an overview, see [5]). In this paper, we consider the electron propagator formalism in which electron correlation effects for a reference state are assumed to be known and calculated within the CC framework [9], without truncation of the exponential CC wavefunction, except to excitation levels like CCSD [20]. The cluster operator is used to perform a similarity transformation of the Hamiltonian. Then, in this way, the transformed Hamiltonian replaces the original one in the electron propagator superoperator formalism as similarity transformations do not change the eigenvalue problem. This equivalence holds, however, in the general case and cannot be extended to approximate schemes. The transformed Hamiltonian has a very simple right-hand-side eigenfunction corresponding to the total ground state energy which is the Hartree-Fock determinant. In this way both the transformed and the zero-order Hartree-Fock Hamiltonian have the same right ground state eigenfunction. The use of the transformed Hamiltonian leads to a great simplification in the electron propagator equations. First, it decouples the ionization and electron attachment problems which permits them to be treated separately. Second, we can reduce the superoperator formalism, which is a compact form of commutator and anticommutator algebras, to simpler Fock-space operator considerations. Third, the transparency of the modified theory facilitates introducing new and improved approximations.

Another characteristic of electron propagator theories is that in most formulations the frequency dependence is retained. That suggests a Brillouin-Wigner (B-W) perturbation expansion as a natural way of handling the problem [5-8]. If the transformed Hamiltonian is used, then the perturbation expansion is, of course, expressed in terms of the new transformed Hamiltonian. However, the B-W type expansion has several disadvantages. First, it permits obtaining only a single frequency at a time in spite of the fact that the entire matrix representation of the electron propagator must be constructed. Second, unlike the Rayleigh-Schrödinger expansion (R-S), each calculation must be performed in a self-consistent manner due to the frequency dependence [5-8]. To avoid all these problems one can introduce a correlation operator and effective Hamiltonian (see, for example, [14]) that eliminate the frequency dependence. Once the correlation operator corresponding to a selected part of the spectrum is determined, diagonalization of the effective Hamiltonian provides *all* frequencies due to the universality of the formulation. Moreover, it can be seen that truncation of the correlation operator at some excitation level is equivalent to a summation of certain types of the B-W perturbation diagrams to infinite order.

The electron propagator formalism based on the assumption that the transformed Hamiltonian includes a description of correlation effects for the ground state and on the elimination of frequency dependence, results in a set of equations that can be found to be exactly those given by the Fock-Space CC (FSCC) formalism for ionization and electron attachment calculations with all orbital levels assumed to

be active [15-17]. Furthermore, the equivalence of FSCC and the EOM-CC method for the principal ionization potentials (IPs) and electron affinities (EAs) has also been established [21]. This shows some formal advantage of the FSCC and EOM-CC methods over the electron propagator formulation. It does not necessarily mean that the numerical performance of the standard electron propagator approaches should be worse, since the electron propagator furnishes energy differences, and a poor description of the ground state accompanied by a comparably poor description of ionized or electron attached states can result in a quite reasonable energy differences. Instead, the FSCC or EOM-CC method assumes a higher standard for the description of the reference state and hence a comparable standard would be anticipated for the other states to get adequate IPs and EAs. In the following we will address formal aspects only. The next section is devoted to demonstrating the separation of the ionization and electron attachment problems. Then in the third section the problem of the ionization potential is discussed in detail. The fourth section briefly addresses the electron affinity equations, which differ little, conceptually, from those for ionization potentials.

### The Superoperator Representation of the Electron Propagator with a Correlated Ground State

Superoperators have been employed [1,7] to recast the commutator and anticommutator algebras involved in the standard electron propagator formulation into matrix and vector space techniques. This has been done by introducing a linear space, elements of which are linear combinations of the field operator products [1]:

$$h_1 = \{a_i\}, \{a_a\}, \quad 1 \leq i \leq N < a, \quad (1a)$$

$$h_3 = \{a_a^\dagger a_i a_j\}, \{a_i^\dagger a_a a_b\}, \quad 1 \leq i < j \leq N < a < b, \quad (1b)$$

which could be continued to  $h_5$  or higher.  $N$  is the number of electrons of the system. The above are operators formed from the Hartree-Fock basis where  $i, j, \dots$  indicate occupied spin orbitals while  $a, b, \dots$  are those of unoccupied orbitals.

For  $A$  and  $B$  being general elements of this linear space the superoperator identity  $\hat{I}$  and superoperator Hamiltonian  $\hat{H}$  can be defined as [1,7]

$$\hat{I}A = A, \quad (2a)$$

$$\hat{H}A = [A, H]. \quad (2b)$$

The scalar product then takes the form [1,7]

$$(A|B) = \langle \Phi | [B, A^\dagger]_+ | \Phi \rangle \equiv \langle [B, A^\dagger]_+ \rangle, \quad (3)$$

where  $|\Phi\rangle$  is the Hartree-Fock determinant and  $\langle \rangle$  means the Hartree-Fock average. These definitions permit expressing the electron propagator in the compact matrix form

$$G(E) = (a|(E\hat{I} - \hat{H})^{-1}a), \quad (4)$$

where  $\mathbf{a}$  is a column supermatrix containing all annihilation operators. Employing inner projections and the partitioning technique of Löwdin [22], the superoperator resolvent becomes the matrix inverse [1,7]

$$\mathbf{G}(E) = (\mathbf{a}|\mathbf{h})(\mathbf{h}|(E\hat{I} - \hat{H})\mathbf{h})^{-1}(\mathbf{h}|\mathbf{a}), \quad (5)$$

where the inner projection manifold  $\mathbf{h}$  consists of elements of the linear space. Partitioning of  $\mathbf{h} = \{\mathbf{a}; \mathbf{f}\}$  with  $(\mathbf{a}|\mathbf{f}) = 0$ , where  $\mathbf{a}$  spans the model space while  $\mathbf{f}$  is its orthogonal complement leads to [1,7]

$$\mathbf{G}^{-1}(E) = (\mathbf{a}|(E\hat{I} - \hat{H})\mathbf{a}) - (\mathbf{a}|\hat{H}\mathbf{f})(\mathbf{f}|(E\hat{I} - \hat{H})\mathbf{f})^{-1}(\mathbf{f}|\hat{H}\mathbf{a}). \quad (6)$$

The unperturbed superoperator  $\hat{H}_0$  is chosen and then

$$\hat{H} = \hat{H}_0 + \hat{V}, \quad (7)$$

where  $\hat{V}$  is a perturbation superoperator. One can express  $H_0$  in second quantized form as

$$H_0 = \sum_k \epsilon_k a_k^\dagger a_k. \quad (8)$$

Using the partition of the Hamiltonian, we can write the Dyson equation [23]

$$\mathbf{G}^{-1}(E) = \mathbf{G}_0^{-1}(E) - \Sigma(E), \quad (9)$$

where

$$\mathbf{G}_0^{-1} = (\mathbf{a}|(E\hat{I} - \hat{H}_0)\mathbf{a}), \quad (10)$$

and the self-energy  $\Sigma(E)$  is defined as the remainder in Eq. (6). IPs and EAs are given by the poles of  $\mathbf{G}(E)$ , from

$$\det \mathbf{G}^{-1}(E) = 0. \quad (11)$$

In the following we assume that we are interested in the eigenvalue problem only. It is easy to see that IPs and EAs are invariant with respect to a similarity transformation of  $H$

$$e^{-T} H e^T, \quad (12)$$

where the cluster operator  $T$  is defined as [9-11]

$$T = \sum_{n=1}^N \sum_{a_1 < \dots < a_n} \sum_{i_1 < \dots < i_n} t_{i_1 \dots i_n}^{a_1 \dots a_n} a_{a_1}^\dagger \dots a_{a_n}^\dagger a_{i_n} \dots a_{i_1}. \quad (13)$$

The  $T$  amplitudes are antisymmetric in their upper and lower indices. According to the definition of the superoperator, we can also add some constant term to the operator without causing any change. Hence, we define a new superoperator  $\hat{\tilde{H}}$  instead of  $\hat{H}$ , where

$$\hat{\tilde{H}} = e^{-T} H e^T - E_0. \quad (14)$$

It is assumed that  $T$  amplitudes and  $E_0$  satisfy the equations

$$\langle \Phi | \hat{H} | \Phi \rangle = 0, \quad (15a)$$

$$\langle a_a^\dagger a_i | \Phi | \hat{H} | \Phi \rangle = 0, \quad (15b)$$

$$\langle a_a^\dagger a_i a_b^\dagger a_j | \Phi | \hat{H} | \Phi \rangle = 0, \quad (15c)$$

and so on; hence  $T$  and  $E_0$  can be obtained from these equations [9,10].  $E_0$  is now the total ground state energy. Equation (15) can be equivalently written in the form

$$\hat{H} | \Phi \rangle = 0. \quad (16)$$

$\hat{H}$  is expressed as a second-quantized normal-ordered (with respect to the Hartree-Fock determinant) operator consisting of one-, two-,  $\dots$  particle parts (see, for example, [24]). The zero-particle part does not appear due to the definition (14).

Let us now introduce an additional classification of the elements spanning the orthogonal space. Considering the action of elements of  $f$  on  $\Phi$ , we can obtain two classes of elements,  $f = \{X^\dagger, Y\}$ , defined as

$$f \in X^\dagger \quad \text{if} \quad \langle \Phi | f = 0, \quad (17a)$$

$$f \in Y \quad \text{if} \quad f | \Phi \rangle = 0. \quad (17b)$$

It should be noted here that elements of  $X$  and  $Y^\dagger$  do not belong to the linear space under consideration. The annihilation operators with respect to the physical vacuum can be transformed into a new set of annihilation and creation (quasiparticle or particle-hole) operators but now with respect to the Hartree-Fock determinant as the Fermi vacuum [9]:

$$b_a = a_a. \quad (18a)$$

$$b_i^\dagger = a_i^\dagger. \quad (18b)$$

They fulfill the same anticommutator relations as the  $a$  and  $a^\dagger$  operators. Now it can be seen that each element of  $X^\dagger$  is a product of new creation operators while each element of  $Y$  is a product of the new annihilation operators. It can be noted that  $X^\dagger$  includes 2h-p, 3h-2p,  $\dots$  operators and  $Y^\dagger$  contains 2p-h, 3p-2h,  $\dots$  operators.

Let us show the consequences of using  $\hat{H}$  instead of  $\bar{H}$  for the structure of the  $G^{-1}(E)$  matrix. Consider  $[G^{-1}(E)]_{ia}$  elements. For the first term on the rhs of Eq. (6), we have

$$(a_i | (E\hat{I} - \hat{H}) a_a) = \langle \bar{H} a_a a_i^\dagger - a_a \bar{H} a_i^\dagger + a_i^\dagger \bar{H} a_a - a_i^\dagger a_a \bar{H} \rangle = 0. \quad (19)$$

In a similar way we obtain

$$(X^\dagger | \hat{H} Y) = 0, \quad (20a)$$

$$(X^\dagger | \hat{H} a_a) = 0, \quad (20b)$$

$$(a_i | \hat{H} Y) = 0. \quad (20c)$$



Equations (20a-c) can be used to show that

$$(a_i | \hat{H} f)(f | (E\hat{I} - \hat{H})f)^{-1}(f | \hat{H}a_a) \quad (21)$$

is also zero for any  $i$  and  $a$ . In order to do this, one can use the expansion

$$(f | (E\hat{I} - \hat{H})f)^{-1} = \sum_{k=1}^{\infty} E^{-k} (f | \hat{H}f)^{k-1}. \quad (22)$$

Because of Equations (20a) and (20b), a nonzero contribution from the last two factors in Eq. (21) is

$$\sum_{k=1}^{\infty} E^{-k} (Y | \hat{H}Y)^{k-1} (Y | \hat{H}a_a). \quad (23)$$

Finally we have the following expression for (21)

$$(a_i | \hat{H}Y)(Y | (E\hat{I} - \hat{H})Y)^{-1}(Y | \hat{H}a_a), \quad (24)$$

but it is equal to zero because of Eq. (20c). In this way we have shown that

$$[G^{-1}(E)]_{ia} = 0, \quad (25)$$

for all  $i$  and  $a$ . Hence,  $G^{-1}(E)$  has the structure

$$\begin{array}{cc} & i & a \\ i & \begin{array}{|c|} \hline \text{diagonal} \\ \hline \end{array} & 0 \\ a & \begin{array}{|c|} \hline \text{diagonal} \\ \hline \end{array} \end{array}.$$

Because of this we can write

$$\det G^{-1}(E) = \det[G^{-1}(E)_{ab}] \det[G^{-1}(E)_{ij}], \quad (26)$$

and instead of Eq. (11) one can consider two equations

$$\det[G^{-1}(E)_{ab}] = 0, \quad (27a)$$

$$\det[G^{-1}(E)_{ij}] = 0, \quad (27b)$$

separately. That means that the use of  $\hat{H}$  instead of  $\hat{H}$  decouples the calculation of ionization potentials and electron affinities, or, in other words, the inclusion of correlation effects for the ground state leads to separation of these two problems. One should also notice that the transformation  $\hat{H} \rightarrow \hat{H}^\dagger$  provides the similar effect of eliminating the other off-diagonal block,

$$[G^{-1}(E)]_{ai} = 0, \quad (28)$$

for all  $a$  and  $i$ .

To arrive at Eq. (25) we have taken advantage of the fact that the transformed Hamiltonian has a very simple right eigenfunction which is the Hartree-Fock determinant. That leads to separation of the eigenvalue problems given by Eq. (27). However, one should be aware that this separation does not include properties other than energies. For the eigenvalue problem knowledge of the right ground state eigenvector of  $\hat{H}$  is sufficient for the separation. If one is also interested in

other properties than IPs or EAs, then again the whole matrix of  $G^{-1}(E)$  must be considered. This is because for other properties, a knowledge of the left eigenfunction of  $\hat{H}$  is also necessary. One can introduce the left eigenfunction of  $\hat{H}$  in the electron propagator formalism in an explicit way since the left eigenfunction of  $\hat{H}$  can be obtained as discussed elsewhere [25]. See also Arponen [26]. That would lead to vanishing of the second off-diagonal submatrix of  $G^{-1}(E)$  and complete separation of both subproblems. Very recently such an idea has been explored by Nooijen and Snijders [27]. In the following, we shall concentrate on the eigenvalue problem showing the relation with other approaches designed to calculate IPs and EAs.

### Ionization Potentials

In this section we consider the  $[G^{-1}(E)]_{ii}$  submatrix which corresponds to the ionization potential calculation. In the following we assume that we are interested in principal ionization potentials. From Eq. (6) we have

$$[G^{-1}(L)]_{ii} = (a_i | (E\hat{I} - \hat{H}) a_i) - (a_i | \hat{H} X^\dagger) (X^\dagger | (E\hat{I} - \hat{H}) X^\dagger)^{-1} (X^\dagger | \hat{H} a_i), \quad (29)$$

where  $X^\dagger$  replaces  $f$  because of Eqs. (20c) and (20a). Denoting by

$$(X^\dagger | \hat{\chi} a_i) = (X^\dagger | (E\hat{I} - \hat{H}) X^\dagger)^{-1} (X^\dagger | \hat{H} a_i), \quad (30)$$

we have from (29)

$$[G^{-1}(E)]_{ii} = (a_i | (E\hat{I} - \hat{H}) a_i) - (a_i | \hat{H} X^\dagger) (X^\dagger | \hat{\chi} a_i). \quad (31)$$

It should be noted that  $\chi$  is not explicitly defined by Eq. (30) since it gives only the matrix representation of  $\hat{\chi}$ . Multiplication of Eq. (30) from the left by  $(X^\dagger | (E\hat{I} - \hat{H}) X^\dagger)$  gives

$$(X^\dagger | \hat{H} a_i) + (X^\dagger | \hat{H} X^\dagger) (X^\dagger | \hat{\chi} a_i) - \sum_i (X^\dagger | \hat{\chi} a_i) \delta_{ii} E = 0. \quad (32)$$

It can be seen that by introducing  $\hat{\chi}$  the problem of dealing with the inversion of the matrix  $(X^\dagger | (E\hat{I} - \hat{H}) X^\dagger)$  can be avoided. The possibility of obtaining the inverse matrix directly is limited because the dimension increases rapidly with the size of orbital basis [7]. Some progress in dealing with the matrix inversion problem has been made by Baker and Pickup [28]; however, the most frequent approach in electron propagator theory is to express the inverse matrix through a perturbation expansion. From Eq. (31) we have

$$[G^{-1}(E)]_{ii} = E\delta_{ii} - (a_i | \hat{H} a_i) - (a_i | \hat{H} X^\dagger) (X^\dagger | \hat{\chi} a_i). \quad (33)$$

Let us introduce the following notation:

$$H_{ii}^{\text{eff}} \equiv (a_i | \hat{H} a_i) + (a_i | \hat{H} X^\dagger) (X^\dagger | \hat{\chi} a_i). \quad (34)$$

From (27b) we have that diagonalization of  $H^{\text{eff}}$  at the energy poles gives the desired frequencies

$$\sum_i (H_{ii}^{\text{eff}} - \delta_{ii} E) c_i(L) = 0. \quad (35)$$

where  $c(E)$  is an eigenvector of  $H^{\text{eff}}$  corresponding to the eigenvalue  $E$ . Multiplying Eq. (32) by  $c_j(E)$ , making the summation over  $j$ , using (35), and finally taking into account that the  $c(E)$  are linearly independent, one can get an equation for the matrix elements of  $\hat{\chi}$  which is  $E$ -independent:

$$(\mathbf{X}^\dagger | \hat{H} a_j) + (\mathbf{X}^\dagger | \hat{H} \mathbf{X}^\dagger)(\mathbf{X}^\dagger | \hat{\chi} a_j) - \sum_i (\mathbf{X}^\dagger | \hat{\chi} a_i) H_{ij}^{\text{eff}} = 0. \quad (36)$$

The set of equations (36) and (34) is for  $H_{ij}^{\text{eff}}$  and matrix elements of the superoperator  $\hat{\chi}$ . In this way the  $E$  dependence has been eliminated from the equations. Now diagonalization of  $H^{\text{eff}}$  gives all principal ionization potentials. By inserting (34) into (36), one can see that Eq. (36) is nonlinear in the matrix elements of  $\hat{\chi}$ , and thus has more than one solution. The other solutions provide a description of the satellite ionization potentials (shakeups) [29].

Similar equations are well known from the theory of effective Hamiltonians, where  $H^{\text{eff}}$  is called the matrix representation of the effective Hamiltonian while  $\chi$  is usually called the correlation operator.  $\chi$  can also be expressed as a second-quantized operator (see, for example, [14]). Equations (36) and (34) allow a determination of  $(\mathbf{X}^\dagger | \hat{\chi} a_i)$  iteratively. Equation (36) can be expressed in the form

$$(\mathbf{X}^\dagger | (\epsilon_j \hat{I} - \hat{H}_0) \mathbf{X}^\dagger)(\mathbf{X}^\dagger | \hat{\chi} a_j) = (\mathbf{X}^\dagger | \hat{H} a_j) + (\mathbf{X}^\dagger | \hat{H} \mathbf{X}^\dagger)(\mathbf{X}^\dagger | \hat{\chi} a_j) - \sum_i (\mathbf{X}^\dagger | \hat{\chi} a_i) \Sigma_{ij}, \quad (37)$$

where

$$\Sigma_{ij} = H_{ij}^{\text{eff}} - \epsilon_j \delta_{ij} = (a_i | \hat{H} a_j) + (a_i | \hat{H} \mathbf{X}^\dagger)(\mathbf{X}^\dagger | \hat{\chi} a_j), \quad (38a)$$

and

$$\hat{H} = \bar{H} - \hat{H}_0, \quad \hat{H}_0 = H_0 - \langle H_0 \rangle. \quad (38b)$$

The matrix  $(\mathbf{X}^\dagger | \epsilon_j \hat{I} - \hat{H}_0) \mathbf{X}^\dagger)$  is diagonal and contains the R-S PT energy denominators. For  $\mathbf{X}^\dagger = a_a^\dagger a_k a_l$ , one has the energy denominator  $D = \epsilon_j + \epsilon_a - \epsilon_k - \epsilon_l$ .

One can notice that the superoperator formalism is not too convenient once the ionization and electron attachment problems are separated. Using the definitions (2) and (3) and Eqs. (16) and (17), we have

$$\begin{aligned} \langle \mathbf{X}(\epsilon_j - \hat{H}_0) \mathbf{X}^\dagger \rangle \langle \mathbf{X}[\chi, a_j] \rangle \\ = \langle \mathbf{X} \hat{H} a_j \rangle + \langle \mathbf{X} \hat{H} \mathbf{X}^\dagger \rangle \langle \mathbf{X}[\chi, a_j] \rangle - \sum_i \langle \mathbf{X}[\chi, a_i] \rangle \Sigma_{ij}. \end{aligned} \quad (39a)$$

$$\Sigma_{ij} = \langle a_i^\dagger \hat{H} a_j \rangle + \langle a_i^\dagger \hat{H} \mathbf{X}^\dagger \rangle \langle \mathbf{X}[\chi, a_j] \rangle. \quad (39b)$$

We assume that the operators  $\hat{H}$ ,  $\hat{H}_0$ , and  $\chi$  are in normal order with respect to the Hartree-Fock determinant  $\Phi$  [14-17]. Due to the definitions (14) and (38b),  $\hat{H}$  and  $\hat{H}_0$  do not contain the zero-particle parts (constant terms). Now we can define the  $\chi$  operator explicitly. We argue that  $\chi$  can be expressed by the linear expansion of connected operators

$$\chi = \sum_{n=2}^N \chi(n), \quad (40)$$

with

$$\chi(n) = \sum_{a_1 < \dots < a_{n-1}} \sum_{i_1 < \dots < i_n} \sum_j \chi_{i_1 \dots i_n}^{a_1 \dots a_{n-1}} a_{a_1}^\dagger \dots a_{a_{n-1}}^\dagger a_{i_n} \dots a_{i_1} a_j^\dagger, \quad (41)$$

where the  $\chi$  coefficients are antisymmetric in the  $a$  and  $i$  indices. Connected means here that the equation for  $\chi$  contains connected terms only.

Due to the definition, Eq. (41), we have

$$\langle X[\chi, a_j] \rangle = \langle X\chi a_j \rangle. \quad (42)$$

To obtain an explicit form of the equations, diagrammatic methods can be used [24, 30]. The rules for creating a diagrammatic representation follow from the generalized Wick theorem. The graphical representation of  $\tilde{H}$  is shown in Figure 1(A). Equation (15) is also presented in diagrammatic form in Figure 1(B). Diagrams representing  $\chi$  are shown in Figure 1(C). Since  $\chi$  contains one hole-annihilation operator, then the  $\chi$  diagrams must have precisely one line at the bottom representing  $a_j^\dagger$  and an odd number of lines at the top representing the product of quasiparticle creation operators corresponding to elements of  $X^\dagger$ . The equation for the  $\chi(2)$  operator that represents excitations to the space created by  $X_3^\dagger$  while acting on  $\Phi$  [see Eqs. (1b) and (17a) for the notation] is shown in Figure 1(D). The equation is very simple and identical with those of the Fock-Space CC method for ionization potentials with all active orbital levels [15-17] and the equation of motion CC [18-20]. One can note that only connected diagrams can be obtained. This is because of the fact that disconnected diagrams can be constructed only with those shown in Figure 1(B), but they are equal to zero due to Eq. (15b). This observation can be extended for equations for all components of  $\chi$ , making our assumption of connectedness of the  $\chi$  expansion Eq. (40)-(41) justified. The connected structure of the equations for  $\chi$  is usually sufficient for extensivity (connected structure in terms of the perturbation expansion) for the principal ionization potentials but not for the satellite roots (for details, see [31]).

However, the most frequent approach in the theory of electron propagators is not to employ the correlation operator  $\chi$ , but instead keep the  $E$  dependence through the self-energy term  $\Sigma(E)$  [Eq. (9)] [5-8]. In such a case the Brillouin-Wigner type of perturbation expansion is the most natural choice for generating approximations. Thus the second order or third order as well as some schemes allowing approximate summation of certain types of terms to infinite order have been extensively exploited [5-8]. The importance of different types of diagrams has been investigated showing that it is essential to include ring and ladder diagrams in the third order [4].

The B-W expansion can be easily obtain within our formalism if one uses Eq. (32), where

$$\langle X(E - \tilde{H}_0)X^\dagger \rangle \langle X\chi a_j \rangle = \langle X\tilde{H}a_j \rangle + \langle X\tilde{H}X^\dagger \rangle \langle X\chi a_j \rangle. \quad (43)$$

Then, since  $\langle X(E - \tilde{H}_0)^{-1}X^\dagger \rangle$  is diagonal, one can obtain the simple expansion

$$\langle X\chi a_j \rangle = \sum_{k=0}^{\infty} \langle X(E - \tilde{H}_0)^{-1}\tilde{H}X^\dagger \rangle^k \langle X(E - \tilde{H}_0)^{-1}\tilde{H}a_j \rangle, \quad (44a)$$

$$\tilde{H} = \begin{array}{c} \uparrow \\ \circ \\ \uparrow \end{array} + \begin{array}{c} \downarrow \\ \circ \\ \downarrow \end{array} + \begin{array}{c} \nearrow \\ \circ \\ \searrow \end{array} + \begin{array}{c} \nearrow \downarrow \\ \circ \\ \uparrow \end{array} + \begin{array}{c} \searrow \uparrow \\ \circ \\ \downarrow \end{array} + \dots \quad (\text{A})$$

$$\begin{array}{c} \nearrow \searrow \\ \circ \end{array} = \begin{array}{c} \nearrow \downarrow \searrow \\ \circ \end{array} = \dots = 0 \quad (\text{B})$$

$$\chi = \begin{array}{c} \nearrow \downarrow \searrow \\ \bullet \\ \uparrow \end{array} + \begin{array}{c} \nearrow \downarrow \searrow \\ \bullet \\ \downarrow \end{array} + \dots \quad (\text{C})$$

$$\begin{array}{c} -D \\ \begin{array}{c} \nearrow \downarrow \searrow \\ \bullet \\ \uparrow \end{array} + \begin{array}{c} \nearrow \downarrow \searrow \\ \bullet \\ \downarrow \end{array} + \begin{array}{c} \nearrow \downarrow \searrow \\ \bullet \\ \nearrow \searrow \end{array} + \begin{array}{c} \nearrow \downarrow \searrow \\ \bullet \\ \nearrow \downarrow \searrow \end{array} + \begin{array}{c} \nearrow \downarrow \searrow \\ \bullet \\ \nearrow \downarrow \searrow \end{array} \\ + \begin{array}{c} \nearrow \downarrow \searrow \\ \bullet \\ \nearrow \downarrow \searrow \end{array} + \begin{array}{c} \nearrow \downarrow \searrow \\ \bullet \\ \nearrow \downarrow \searrow \end{array} - \boxed{\Sigma} = 0 \end{array} \quad (\text{D})$$

$$\boxed{\Sigma} = \begin{array}{c} \downarrow \\ \circ \\ \downarrow \end{array} + \begin{array}{c} \nearrow \downarrow \searrow \\ \bullet \\ \uparrow \end{array} + \begin{array}{c} \nearrow \downarrow \searrow \\ \bullet \\ \downarrow \end{array}$$

Figure 1. (A) Graphical representation of  $\tilde{H}$ . (B) Graphical representation of coupled cluster equations (15). (C) Graphical representation of operator  $\chi$ . (D) Graphical representation of equations for  $\chi$  and  $\Sigma$  with the orthogonal space restricted to  $X_3^\dagger$ .

and finally

$$[\Sigma(E)]_{ij} = \langle a_i^\dagger \tilde{H} a_j \rangle + \sum_{k=0}^{\infty} \langle a_i^\dagger \tilde{H} X^k \rangle \langle X(E - \tilde{H}_0)^{-1} \tilde{H} X^k \rangle \langle X(E - \tilde{H}_0)^{-1} \tilde{H} a_j \rangle. \quad (44b)$$

Both approaches are exact in the limit, but they differ in truncation schemes. For FSCC we consider types of  $\chi$  operators that should be included [15-17] (or, equiv-

alently, a truncation scheme for  $X^\dagger$ ) while the order of the perturbation expansion is the natural choice as the truncation criterion for the second approach [5-8].

One can notice that Eqs. (39a-b) and (44b) are equivalent as long as restrictions imposed on  $X^\dagger$  are the same in both approaches. Hence, with a certain approximation for  $X^\dagger$ , FSCC can be regarded as a method that sums contributions from certain types of terms in the perturbation expansion to infinite order. For example, if the orthogonal space is restricted to  $X_3^\dagger$ , FSCC can be considered as a method that sums all 2h-p terms (intermediate states are restricted to those having two holes and one particle) to infinite order. They include the ring and ladder diagrams that have been found to be very important in third-order calculations [4].

The energy can usually be expressed in terms of the perturbation expansion as a sum of connected terms (diagrams) to infinite order. This takes place for the Rayleigh-Schrödinger (R-S) perturbation expansion but usually not for the B-W one. However, in this specific case where the cluster expansion for  $\chi$  is reduced to a linear one, the B-W expansion has this property as well.

The above considerations show how some important contributions appearing in the electron propagator ionization potential perturbation expansion are summed to infinite order by the FSCC method.

### Electron Affinities

Because of the nonhermicity of  $\hat{H}$ , the structure of equations for electron affinities can be different from those for ionization potentials. To have equations for electron affinities similar to those for ionization potentials requires use of  $\hat{H}^\dagger$  instead of  $\hat{H}$  for which the left eigenfunction corresponding to the ground state is known. This leads to the property of Eq. (28) and, again, separation of EAs and IPs. We have

$$[G^{-1}(E)]_{ab} = (a_a | (E\hat{I} - \hat{H}^\dagger) a_b) - (a_a | \hat{H}^\dagger Y) (Y | (E\hat{I} - \hat{H}^\dagger) Y)^{-1} (Y | \hat{H}^\dagger a_b), \quad (45)$$

where now  $f$  is replaced by  $Y$ , because

$$\langle \Phi | \hat{H}^\dagger = 0, \quad (46)$$

and hence

$$(a_a | \hat{H}^\dagger X^\dagger) = 0, \quad (47a)$$

$$(Y | \hat{H}^\dagger X^\dagger) = 0. \quad (47b)$$

Denoting by

$$(Y | \hat{\chi}^\dagger a_b) = (Y | (E\hat{I} - \hat{H}^\dagger) Y)^{-1} (Y | \hat{H}^\dagger a_b), \quad (48)$$

we have from Eq. (45)

$$[G^{-1}(E)]_{ab} = E\delta_{ab} - \langle a_b | \hat{H}^\dagger a_a^\dagger \rangle - \langle [a_b, \chi^\dagger] Y^\dagger \rangle \langle Y | \hat{H}^\dagger a_a^\dagger \rangle, \quad (49)$$

and from Eq. (48)

$$\langle a_b | \hat{H}^\dagger Y^\dagger \rangle + \langle [a_b, \chi^\dagger] Y^\dagger \rangle \langle Y | (\hat{H}^\dagger - E) Y^\dagger \rangle = 0. \quad (50)$$

Taking the Hermitian adjoint of Eq. (50), we get

$$\langle \mathbf{Y} \hat{H} a_b^\dagger \rangle + \langle \mathbf{Y} (\hat{H} - F) \mathbf{Y}^\dagger \rangle \langle \mathbf{Y} [\chi, a_b^\dagger] \rangle = 0, \quad (51)$$

and similarly for Eq. (49)

$$[\mathbf{G}^{-1}(E)]_{ba}^* = E\delta_{ab} - \langle a_a \hat{H} a_b^\dagger \rangle + \langle a_a \hat{H} \mathbf{Y}^\dagger \rangle \langle \mathbf{Y} [\chi, a_b^\dagger] \rangle. \quad (52)$$

That leads to the following expression for the matrix representation of the effective Hamiltonian

$$H_{ab}^{\text{eff}} = \langle a_a \hat{H} a_b^\dagger \rangle - \langle a_a \hat{H} \mathbf{Y}^\dagger \rangle \langle \mathbf{Y} [\chi, a_b^\dagger] \rangle. \quad (53)$$

Diagonalization of  $H^{\text{eff}}$  gives the desired electron affinities if the energy dependence is eliminated from (51) in the way indicated in the previous section. The resulting equations are those of the FSCC [14-17] and EOM-CC [18,21,31,32] methods for electron affinities. Again, the discussion analogous to that for ionization potentials could be presented showing similar relations.

One can also see that Eqs. (51) and (53) can be reached in a different way. Starting with a different definition of the space under consideration

$$\mathfrak{H}_1 = \{a_i^\dagger\}, \{a_a^\dagger\}, \quad 1 \leq i \leq N < a, \quad (54a)$$

$$\mathfrak{H}_2 = \{a_i^\dagger a_j^\dagger a_a^\dagger\}, \{a_i^\dagger a_j^\dagger a_a^\dagger\}, \quad 1 \leq i < j \leq N < a < b, \quad (54b)$$

and higher, the one-electron propagator defined accordingly,

$$G_{ab}(E) = \langle \langle a_a \hat{H} - E | a_b^\dagger \rangle \rangle, \quad (55)$$

one can obtain the equation for electron affinities in the manner indicated in the previous section.

### Conclusion

The electron propagator is potentially capable of simultaneously describing ionization potentials and electron affinities as well as some other properties of the system. Also the frequency dependence that is kept in many approaches complicates calculation since for each of the IPs and EAs separate calculations must be performed.

However, if the correlation effects for the ground state are known, *a priori*, then the formalism can be significantly simplified. We have assumed that the result of a coupled cluster calculation for the ground state is known and we used it to perform a similarity transformation of the Hamiltonian, Eq. (12). The transformed Hamiltonian has, of course, the same eigenvalues in the Fock space, but it has a very simple right-hand-side eigenfunction corresponding to the ground state energy which is the Hartree-Fock determinant. Use of the transformed Hamiltonian  $\tilde{H}$  instead of  $\hat{H}$  results in vanishing of one of the off-diagonal blocks of  $\mathbf{G}^{-1}(E)$ . This asymmetric behavior is caused by the lack of Hermiticity of  $\tilde{H}$ ; however, disappearance of one of the off-diagonal blocks is enough to decouple IP and EA calculations.

Elimination of the energy dependence from the self-energy expression  $\Sigma(E)$  provides a method that is equivalent to the summation of certain types of terms in the

perturbation expansion of  $\Sigma(E)$  to infinite order. It also makes the approach universal in the sense that it furnishes the set of energies simultaneously. The resulting equations are equivalent to those of FSCC or EOM-CC for ionization potentials and electron affinities in spite of the fact that both these formulations represent completely different approaches to the problem. Using the terminology of Oddershede [5], FSCC and EOM-CC are state function methods that start from defining the wavefunctions of states under consideration. The FSCC method is characterized by a valence universal strategy [15] that assumes a hierarchical calculation of the ground state energy, ionization and electron attachment energies, single excitation energies, and so on. In each step results of the previous steps are used to isolate and determine only the genuine changes in the system. The electron propagator method represents a different philosophy in that it attempts to include the effects of the ground state correlation, ionized and electron attached states simultaneously. The derivation presented here demonstrates the link between these approaches that allows a better understanding of the relation between them as well as the evaluation of the quality of particular approximations.

### Acknowledgment

This work was supported by the United States Office of Naval Research under Grant #N00014-92-J-1100.

### Bibliography

- [1] B. T. Pickup and O. Goscinski, *Mol. Phys.* **26**, 1013 (1973).
- [2] G. D. Purvis and Y. Öhrn, *J. Chem. Phys.* **60**, 4063 (1974).
- [3] J. Simons and W. D. Smith, *J. Chem. Phys.* **58**, 4899 (1973).
- [4] L. S. Cederbaum, *J. Phys.* **B8**, 290 (1975).
- [5] J. Oddershede, *Adv. Chem. Phys.* **69**, 201 (1987).
- [6] J. Linderberg and Y. Öhrn, *Propagators in Quantum Chemistry* (Academic, New York, 1973).
- [7] Y. Öhrn and G. Born, *Adv. Quantum Chem.* **13**, 1 (1980).
- [8] L. S. Cederbaum and W. Domcke, *Adv. Chem. Phys.* **36**, 205 (1977).
- [9] J. Čížek, *J. Chem. Phys.* **45**, 4256 (1966); *Adv. Chem. Phys.* **14**, 35 (1969).
- [10] R. J. Bartlett and G. D. Purvis, *Int. J. Quantum Chem.* **14**, 561 (1978).
- [11] R. J. Bartlett, *J. Phys. Chem.* **93**, 1697 (1989).
- [12] V. Ortiz, *Int. J. Quantum Chem. Quant. Chem. Symp.* **25**, 35 (1991).
- [13] J. Geertsen and J. Oddershede, *J. Chem. Phys.* **85**, 2112 (1986).
- [14] I. Lindgren, *J. Phys.* **B7**, 2441 (1974); *Int. J. Quantum Chem. Quantum Chem. Symp.* **12**, 33 (1978).
- [15] A. Haque and D. Mukherjee, *J. Chem. Phys.* **80**, 5058 (1984).
- [16] L. Stolarczyk and H. Monkhorst, *Phys. Rev.* **A32**, 725, 743 (1985).
- [17] S. Pal, M. Rittby, R. J. Bartlett, D. Sinha, and D. Mukherjee, *Chem. Phys. Lett.* **137**, 273 (1987); *J. Chem. Phys.* **88**, 4357 (1988).
- [18] H. Sckino and R. J. Bartlett, *Int. J. Quantum Chem. Quantum Chem. Symp.* **18**, 255 (1984).
- [19] H. Monkhorst, *Int. J. Quantum Chem. Quantum Chem. Symp.* **11**, 421 (1977); K. Emrich, *Nucl. Phys.* **A351**, 392 (1981).
- [20] G. D. Purvis and R. J. Bartlett, *J. Chem. Phys.* **76**, 1910 (1982).
- [21] L. Meissner and R. J. Bartlett, *J. Chem. Phys.* **94**, 6670 (1991).
- [22] P.-O. Lowdin, *Phys. Rev.* **139**, A357 (1967).
- [23] F. J. Dyson, *Phys. Rev.* **75**, 1736 (1949).



- [24] J. Paldus and J. Čížek, *Adv. Quantum Chem.* **9**, 105 (1975).
- [25] P. Szalay and R. J. Bartlett, *J. Chem. Phys.*, to appear; *Int. J. Quantum Chem., Symp.* **26**, 85 (1992).
- [26] J. Arponen, *Ann. Phys.* **151**, 311 (1982).
- [27] R. Chaudhuri, D. Mukhopadhyay, and D. Mukherjee, *Chem. Phys. Lett.* **162**, 393 (1989) and references therein.
- [28] J. Baker and B. T. Pickup, *Chem. Phys. Lett.* **76**, 537 (1980); *Mol. Phys.* **49**, 651 (1983).
- [29] D. Sinha, S. K. Mukhopadhyay, R. Chaudhuri, and D. Mukherjee, *Chem. Phys. Lett.* **154**, 544 (1989).
- [30] S. Kucharski and R. J. Bartlett, *Adv. Quantum Chem.* **18**, 281 (1986).
- [31] D. Mukhopadhyay, S. Mukhopadhyay, R. Chaudhuri, and D. Mukherjee, *Theor. Chim. Acta* **80**, 441 (1991).
- [32] D. C. Comeay and R. J. Bartlett, *Chem. Phys. Lett.* **207**, 414 (1993); J. F. Stanton and R. J. Bartlett, *J. Chem. Phys.* **98**, 7029 (1993).

Received July 21, 1993

# On the Removal of the Exchange Singularity in Extended Systems

GERRARD AISSING and HENDRIK J. MONKHORST

*Quantum Theory Project, University of Florida, Gainesville, Florida 32611-2085*

## Abstract

A serious problem in the *ab-initio* Hartree–Fock calculation for extended systems is a singularity in the exchange contribution to the band energies (the “exchange pathology”). In the homogeneous electron gas this pathology is exactly cancelled by the correlation contribution arising from the sum of all time-ordered ring diagrams (RPA approximation). In this article we show that this cancellation is more general and does also occur in periodically extended systems. © 1993 John Wiley & Sons, Inc.

## Introduction

One of the problems associated with *ab initio* calculations on extended systems at the Hartree–Fock (HF) level is a pathology introduced by the exchange interaction. This pathology has some well-known symptoms: Bandgaps and band widths are too large (both by a factor of two or more), and the density of states at the Fermi level for metals vanishes. As a consequence, results from HF calculations on extended systems are generally considered inferior to those obtained within the local-density approximation. The latter does not suffer from the same drawbacks and gives more realistic values of the properties mentioned above. The exchange-correlation potentials used in local density are all to some extent based on the recognition that exchange and correlation corrections have to be treated on an equal footing to avoid the pathology introduced by exchange alone. For the electron gas Gell-Mann and Brueckner's RPA results shows that this is due to an exact cancellation of this pathology [1,2]. A similar result can be obtained using the dielectric theory in the RPA approximation. This leads to the formulation of a screened interaction. For the homogeneous electron gas this was first worked out by Lindhard [3]. Quinn and Ferrell showed that the same result can be obtained by the study of the self-energy at the Fermi surface [4].

In the early 1960s the problems associated with the unscreened exchange in solids attracted considerable attention [5–7]. These efforts eventually culminated in the work of Hedin, who expanded the self-energy in terms of a screened potential. This expansion is expected to converge faster than the expansion in terms of the unscreened Coulomb interaction [8,9]. However, after the appearance of the landmark articles by Hohenberg and Kohn [10] and Kohn and Sham [11], the attention shifted away from calculations based on *ab initio* methods to density-functional-based methods such as local-density and local-spin-density methods. A more rigorous

approach starting from Hedin's quasi-particle equation has lately attracted considerable attention and has been applied to a number of real systems [12] showing great improvement of the standard local-density methods for excited-state properties in semi-conductors.

For periodically extended systems the situation is more complex than for the homogeneous electron gas. Monkhorst, however, was able to show that the pathology of the exchange in such systems has exactly the same origin as the one in the homogeneous system. In fact, the pathological behavior of the exchange is completely due to the homogeneous part of the charge density in the crystal [13]. The analysis of this pathology and its origin is easiest expressed in the momentum space representation of all quantities involved.

In this article we will revisit part of the proof given in Ref. [13] and continue from there to show that the cancellation of pathologies that occurs in the homogeneous electron gas also occurs independent of the shape of the Fermi surface and consequently independent of the inhomogeneity of a realistic system.

The current analysis will be based on the quasi-particle equation of Hedin [8] and will be expressed in terms of the self-energy contributions from exchange and RPA-like terms. It could be derived just as well using the total energy expression and the Landau liquid theory [14]. We will try to identify the "dangerous" terms, that consequently have to be treated and calculated together, leaving terms that do not introduce any pathologies.

### The Singularity in the Exchange Self-Energy

The exchange contribution to the self-energy does not depend on the energy-parameter and is simply given by the familiar result:

$$\Sigma_{ii}^{\lambda} = - \sum_{\beta} \langle i\beta | r_{12}^{-1} | \beta i \rangle, \quad (1)$$

where  $\beta$  only sums over occupied orbitals. In an extended system the orbital labels are a combination of a band-index ( $\mu$ ) and a  $\mathbf{k}$ -vector, which lies inside the first Brillouin zone (BZ). Eq. (1) then becomes:

$$\Sigma_{\mu\mu}^{\lambda}(\mathbf{k}) = - \sum_{\nu\mathbf{q}} n_{\nu}(\mathbf{k} + \mathbf{q}) \langle \mu\mathbf{k}; \nu(\mathbf{k} + \mathbf{q}) | r_{12}^{-1} | \nu(\mathbf{k} + \mathbf{q}); \mu\mathbf{k} \rangle. \quad (2)$$

Here we have introduced the occupation numbers of the one-particle states

$$n_{\nu}(\mathbf{q}) = \begin{cases} 1 & \text{if } \epsilon_{\nu}(\mathbf{q}) \leq \epsilon_F; \\ 0 & \text{if } \epsilon_{\nu}(\mathbf{q}) > \epsilon_F, \end{cases} \quad (3)$$

where  $\epsilon_F$  is the Fermi energy as obtained from the Hartree (or Hartree-Fock) calculation.

In order to analyze this expression, we express the matrix element in momentum representation (see Appendix A). For the exchange integral we find

$$\Sigma_{\mu\mu}^{\lambda}(\mathbf{k}) = \frac{-4\pi}{V} \sum_{\nu\mathbf{q}} \sum_{\mathbf{G}} n_{\nu}(\mathbf{k} + \mathbf{q}) \frac{\Phi_{\mu\nu}(\mathbf{G} + \mathbf{q}, \mathbf{k}) \Phi_{\nu\mu}(-\mathbf{G} - \mathbf{q}, \mathbf{k} + \mathbf{q})}{(\mathbf{G} + \mathbf{q})^2}. \quad (4)$$

We now immediately realize that the "dangerous" contributions in Eq. (4) come from the terms with  $\mathbf{G} = 0$ . We can therefore split the self-energy into two contributions:

$$\Sigma_{\mu\mu}^{\lambda}(\mathbf{k}) = \Sigma_{\mu\mu}^{\lambda,1}(\mathbf{k}) + \Sigma_{\mu\mu}^{\lambda,2}(\mathbf{k}), \quad (5)$$

where

$$\Sigma_{\mu\mu}^{\lambda,1}(\mathbf{k}) = \frac{-4\pi}{V} \sum_{\mathbf{q}} n_{\nu}(\mathbf{k} + \mathbf{q}) \frac{\Phi_{\mu\nu}(\mathbf{q}, \mathbf{k}) \Phi_{\nu\mu}(-\mathbf{q}, \mathbf{k} + \mathbf{q})}{q^2}, \quad (6)$$

and

$$\Sigma_{\mu\mu}^{\lambda,2}(\mathbf{k}) = \frac{-4\pi}{V} \sum_{\mathbf{q}} \sum_{\mathbf{G} \neq 0} n_{\nu}(\mathbf{k} + \mathbf{q}) \frac{\Phi_{\mu\nu}(\mathbf{G} + \mathbf{q}, \mathbf{k}) \Phi_{\nu\mu}(-\mathbf{G} - \mathbf{q}, \mathbf{k} + \mathbf{q})}{(\mathbf{G} + \mathbf{q})^2}. \quad (7)$$

Equation (7) does not contain any dangerous terms and can therefore be calculated without any further precaution. We can now analyze Eq. (6) further to see what exactly causes the pathology of the exchange.

For orbitals whose band-energy  $\epsilon_{\mu}(\mathbf{k}) > \epsilon_f$ , the summations will not introduce any pathological behavior, because when  $\mathbf{q} \rightarrow 0$ , the numerator vanishes because of Eq. (A7). Therefore, the exchange pathology will only occur for occupied bands, where  $\epsilon_{\mu}(\mathbf{k}) \leq \epsilon_f$ . However, the same argument as used for unoccupied states applies to the occupied ones, unless  $\mu = \nu$ . Therefore, a singular behavior of the integrand only occurs for

$$\Sigma_{\mu\mu}^{\lambda,d}(\mathbf{k}) = \frac{-4\pi}{V} \sum_{\mathbf{q}} n_{\mu}(\mathbf{k} + \mathbf{q}) \frac{\Phi_{\mu\mu}(\mathbf{q}, \mathbf{k}) \Phi_{\mu\mu}(-\mathbf{q}, \mathbf{k} + \mathbf{q})}{q^2}. \quad (8)$$

Because the quantities  $\Phi$  are continuous and smooth across the Fermi surface, the pathology must be caused by the denominator and hence is an end-point singularity associated with the singular behavior of  $1/q^2$  itself. This behavior is independent of the actual shape of the Fermi surface [13]. It leads to the well-known logarithmic behavior of the Hartree-Fock orbital energies at the Fermi surface.

The parts of the exchange self-energy that do not show any pathology can be calculated without any further special treatment. In fact, they can be added to the Hartree-operator to form a modified Hartree-Fock approximation that will have no exchange pathology, but does include most of the exchange contributions. The pathological term in Eq. (8) has to be treated separately. As we will see below, this special treatment of the singular exchange contributions is made redundant by the inclusion of the RPA self-energy into a screened interaction, that does not show any singularity.

### The RPA Self-Energy

The starting point of this work is the quasi-particle equation introduced by Hedin and Lundqvist [8,9]. The single-particle functions  $\phi_k$  and quasi-particle energies  $E_k$  satisfy the equation

$$[h(x) + V(x) - E_k] \phi_k(x) + \int \Sigma(x, x', E_k) \phi_k(x') dx' = 0, \quad (9)$$

where  $x$  and  $x'$  are space- and spin-coordinates  $(\mathbf{r}, \xi)$ . Here  $h$  is the sum of the kinetic energy and the external potential,  $V$  is the effective Coulomb potential, and  $\Sigma$  is the self-energy, containing the effect of exchange and correlation on the quasi-particle energies. As indicated in Eq. (9) the self-energy is generally nonlocal and energy-dependent. Hedin suggested to expand the self-energy in a screened potential  $W$  instead of the unscreened Coulomb potential to improve the convergence of the resulting perturbation series [8]. The lowest-order approximation to  $\Sigma$  is then simply given by the product  $\Sigma = GW$ . The simplest screened potential results from the RPA screening.

We can define the screened interaction in terms of a dielectric response function

$$W(x_1, x_2, \omega) = \int dx_3 v(x_1, x_3) \epsilon^{-1}(x_3, x_2, \omega), \quad (10)$$

where  $\omega$  is the frequency. Note, that in atomic units ( $m = \hbar = e = 1$ ), frequency and energy are expressed in the same units. Note also, that Eq. (9) reduces to the Hartree-Fock approximation when  $W$  is chosen identical to the unscreened interaction. The dielectric response function can be related to the irreducible polarization propagator by

$$\epsilon(x_1, x_2, \omega) = \delta(x_1, x_2) - \int P(x_1, x_3, \omega) v(x_3, x_2) dx_3. \quad (11)$$

The RPA approximation is made by assuming, that  $P$  has the simple form

$$P(x_1, x_2, \omega) = -i \int \frac{d\omega'}{2\pi} G(x_1, x_2, \omega') G(x_2, x_1, \omega' - \omega) e^{i\omega'\eta}. \quad (12)$$

We can now solve the equation for  $\epsilon$  by making a quasi-particle assumption about the Green's function  $G$ , i.e.,

$$G(x_1, x_2, \omega) = \sum_k \frac{\phi_k(x_1) \phi_k^*(x_2)}{\omega - \epsilon_k - i\delta_k}, \quad (13)$$

where the one-particle functions  $\phi_k$  are assumed to be the solution of some suitable one-particle equation, and  $\delta_k$  is defined as

$$\delta_k = \begin{cases} \delta & \text{if } \epsilon_k \leq \epsilon_F; \\ -\delta & \text{if } \epsilon_k > \epsilon_F. \end{cases} \quad (14)$$

Inserting this into the polarization propagator, we obtain

$$P(x_1, x_2, \omega) = \sum_{kk'} \frac{n_k - n_{k'}}{\epsilon_k - \epsilon_{k'} - \omega} \phi_k(x_1) \phi_{k'}^*(x_2) \phi_{k'}(x_2) \phi_k^*(x_1), \quad (15)$$

where  $n_k$  is the occupation number (either 0 or 1) of the state  $\phi_k$ .

In order to facilitate further discussion, we again use momentum space representation for the quantities involved. We will therefore transform all quantities involved to momentum space. For a solid the quasi-particle states  $\phi_k$  are assumed to be Bloch-functions and therefore have the form given in Eq. (A1). This allows us to express all resulting expressions in terms of reciprocal lattice summations only, which will facilitate the analysis of the final result.

Inserting this into the equations for the dielectric response we find

$$\epsilon(\mathbf{q}, \mathbf{q} + \mathbf{K}, \omega) = \delta(\mathbf{q}, \mathbf{q} + \mathbf{K}) - P'(\mathbf{q}, \mathbf{q} + \mathbf{K}, \omega)v(\mathbf{q} + \mathbf{K}) \quad (16)$$

where  $\mathbf{K}$  has to be a reciprocal lattice vector, and  $P'$  is given by

$$P'(\mathbf{q}, \mathbf{q} + \mathbf{K}, \omega) = \frac{2}{(2\pi)^3} \sum_{\mu\nu} \sum_{\mathbf{k}} \frac{n_{\mu}(\mathbf{k}) - n_{\nu}(\mathbf{k} - \mathbf{q} + \mathbf{K}_1)}{\epsilon_{\mu}(\mathbf{k}) - \epsilon_{\nu}(\mathbf{k} - \mathbf{q} + \mathbf{K}_1) - \omega} \Phi_{\mu\nu}^*(\mathbf{q}, \mathbf{k}) \Phi_{\mu\nu}(\mathbf{q} + \mathbf{K}, \mathbf{k}) \quad (17)$$

The factor 2 in the numerator is due to spin, and the reciprocal lattice vector  $\mathbf{K}_1$  has to be chosen such that  $\mathbf{k} - \mathbf{q} + \mathbf{K}_1$  is in the first Brillouin zone. Here we have also used the definition of the Fourier transform of the interaction potential

$$v(\mathbf{q}) = \frac{4\pi}{q^2}. \quad (18)$$

This dielectric function is known as the random phase approximation (RPA) response function. For the homogeneous electron gas it has a relatively simple form due to the fact that the off-diagonal elements of  $\epsilon(\mathbf{k}, \mathbf{k} + \mathbf{K}, \omega)$  vanish. In real metals the off-diagonal elements are related to the so-called local field effects.

In order to examine the analytic behavior of the screened interaction it is sufficient to examine the diagonal approximation to this function only. Wiser has shown that the off-diagonal elements of the RPA response function are often negligible [15]. Moreover, we are mostly interested in the behavior of the dielectric response function at the Fermi surface, where the structure effects are most efficiently screened out by the electron cloud. The diagonal approximation to the dielectric response is:

$$\epsilon(\mathbf{q}, \mathbf{q}, \omega) = 1 - P'(\mathbf{q}, \mathbf{q}, \omega)v(\mathbf{q}) \quad (19)$$

Using this expression in the screened interaction, we find

$$\begin{aligned} W(\mathbf{q}, \mathbf{q}, \omega) &= v(\mathbf{q})\epsilon^{-1}(\mathbf{q}, \mathbf{q}, \omega) \\ &= \frac{4\pi}{V} \frac{1}{q^2 - \frac{4\pi}{V} P'(\mathbf{q}, \mathbf{q}, \omega)} \end{aligned} \quad (20)$$

It is clear that the limiting case for both  $q$  and  $\omega$  vanishing is dominated by the behavior of  $P'$  in that limit. It is now easy to show that

$$\begin{aligned}
\lim_{q \rightarrow 0} P'(\mathbf{q}, \mathbf{q}, 0) &= \lim_{q \rightarrow 0} \frac{1}{4\pi^3} \sum_{\mu\nu} \sum_{\mathbf{k}} \frac{n_{\mu}(\mathbf{k}) - n_{\nu}(\mathbf{k} - \mathbf{q} + \mathbf{K}_1)}{\epsilon_{\mu}(\mathbf{k}) - \epsilon_{\nu}(\mathbf{k} - \mathbf{q} + \mathbf{K}_1)} \\
&\quad \times \Phi_{\mu\nu}^*(\mathbf{q}, \mathbf{k}) \Phi_{\mu\nu}(\mathbf{q}, \mathbf{k}) \\
&= \lim_{q \rightarrow 0} \frac{1}{4\pi^3} \sum_{\mu} \sum_{\mathbf{k}} \frac{n_{\mu}(\mathbf{k}) - n_{\mu}(\mathbf{k} - \mathbf{q})}{\epsilon_{\mu}(\mathbf{k}) - \epsilon_{\mu}(\mathbf{k} - \mathbf{q})} \\
&= \frac{1}{4\pi^3} \sum_{\bar{\mu}\mathbf{k}} \frac{\mathbf{q} \cdot \nabla_{\mathbf{k}} n_{\bar{\mu}}(\mathbf{k})}{\mathbf{q} \cdot \nabla_{\mathbf{k}} \epsilon_{\bar{\mu}}(\mathbf{k})} \quad (21)
\end{aligned}$$

where  $\bar{\mu}$  sums only over those bands that cut through the Fermi surface. This last expression on the right-hand side can be evaluated by realizing that the gradient of the occupation number vanishes everywhere except at the Fermi surface, where it has the value

$$\nabla n_{\bar{\mu}}(\mathbf{k}_F) = -\mathbf{S}_F, \quad (22)$$

where  $\mathbf{S}_F$  is a unit vector normal to the Fermi surface. Then the sum (in the continuous limit an integral) of Eq. (21) becomes a surface sum, which is exactly equal to

$$\frac{1}{4\pi^3} \sum_{\bar{\mu}\mathbf{k} \in \mathbf{S}_F} \frac{-1}{|\nabla_{\mathbf{k}} \epsilon_{\bar{\mu}}(\mathbf{k})|} = -VN_F \quad (23)$$

where  $N_F$  is the density of states at the Fermi surface. We then finally find

$$\lim_{q \rightarrow 0} \epsilon(\mathbf{q}, \mathbf{q}, 0) = 1 + 4\pi VN_F/q^2. \quad (24)$$

This last result is identical to the Thomas-Fermi screening formula, which, of course, is exact in the long wavelength limit. However, it also shows that the use of Hartree-Fock bandstructures as a starting point for correlated quasi-particle band structures is not a good choice, because the density of states at the Fermi surface vanishes in that case. Then, the screening at the Fermi surface vanishes also, leaving an effectively bare interaction at the Fermi surface. The singularity introduced by the exchange will therefore not be lifted, but merely reduced in strength. It is quite easy to prove that the Hartree-Fock singularity in the density of states will in lowest order be reduced to a  $\ln \ln q$  singularity [20]. Moreover, the correction to the band energy at the Fermi surface will be related to an effective potential of the form [21]:

$$W(\mathbf{q}, \mathbf{q}, 0) \sim (\epsilon^{-1}(\mathbf{q}, \mathbf{q}, 0) - 1)v(\mathbf{q}). \quad (25)$$

This expression will vanish in the long-wavelength limit, showing again that little improvement of the bandstructure around the Fermi surface will be obtained.

### Discussion

In this article we have shown that the pathologies introduced by the exchange in density of states are removed by the RPA contribution to the self-energy.

We have, in addition, shown, that the resulting expression does not contain any pathological terms. In fact, it behaves completely regular for long wavelengths. The resulting *effective* potential has the form of a *screened exchange*. This is similar to the situation for the homogeneous electron gas. In fact, all the long wavelength cancellations that characterize the homogeneous electron gas will also occur in the periodically extended systems, because in the long-wavelength limit the structure of the lattice has no influence on the expressions.

Iteration of Eq. (9) will not introduce any new singularities and neither will vertex corrections, because the latter tend to reduce the singularities in the potential by softening the delta-function behavior of the vertex.

In addition we showed that the dielectric response thus calculated will only give a screened potential in the limits  $q \rightarrow 0$  and  $\omega \rightarrow 0$  when non-Hartree-Fock orbitals are used as unperturbed states. The pathology introduced by the exchange will only be lifted if correlation and exchange are combined at every level of theory. This result was also anticipated by those obtained for the homogeneous electron gas.

Although the results in this article are obtained within the quasi-particle approximation, we do not believe this is an important limitation. Calculations on molecules and extended systems have shown that this approximation does not produce serious errors in the determination of electron detachment energies [16-18].

The results derived in this article do not rely in any way on the shape of the Fermi surface. This result is in line with the earlier observation by Monkhorst that the singularities of the exchange interaction are related only to the incomplete integration inside the BZ and not to the actual shape of the enclosing surface(s).

Another noteworthy point is the fact that the results do not in any way depend on the basis set that is used in obtaining the orbitals. The only restriction might be the fact that the basis functions (and hence the orbital set) must have a Fourier transform. In most of the *ab initio* band structure calculations the basis functions are either Gaussian functions or Slater-type functions, which both have easily calculated Fourier transforms. The technique described in this article can therefore without problem be applied to the bandstructures obtained with these basis sets.

### Acknowledgments

We wish to thank Doctors Yngve Öhrn, Vince Ortiz, John Stanton, Leszek Meissner, and Rod Bartlett for many valuable suggestions and discussions during the completion of this work.

### Appendix A: Momentum Space Representation of the Two-Electron Integrals

The solutions of the Hartree equations form an orthonormal set of orbitals for an infinite system. We will denote these orbitals by  $\phi_{\mu\mathbf{k}}(\mathbf{r})$  and the associated orbital energies by  $\epsilon_{\mu}(\mathbf{k})$ . We can expand these orbitals in a complete set of crystal plane waves:

$$\phi_{\mu\mathbf{k}}(\mathbf{r}) = \frac{(2\pi)^{3/2}}{\Omega^{1/2}} \sum_{\mathbf{G}} \phi_{\mu}(\mathbf{G} + \mathbf{k}) \frac{\exp(i(\mathbf{G} + \mathbf{k}) \cdot \mathbf{r})}{V^{1/2}} \quad (\text{A1})$$



where  $\Omega$  is the volume of the unit cell,  $V' = N\Omega$  ( $N$  is the number of unit cells in the total volume), and

$$\phi_{\mu}(\mathbf{G} + \mathbf{k}) = \int \frac{d^3r}{(2\pi)^{3/2}} \phi_{\mu\mathbf{k}}(\mathbf{r}) e^{-i(\mathbf{G}+\mathbf{k}) \cdot \mathbf{r}}. \quad (\text{A2})$$

In these expressions the vector  $\mathbf{G}$  is a reciprocal lattice vector, and the sum in Eq. (A1) runs over all reciprocal lattice vectors. A general two-electron matrix element between four of these Hartree orbitals can then be written

$$\begin{aligned} \langle \mu\mathbf{k}; \nu\mathbf{k}' | r_{12}^{-1} | \rho(\mathbf{k} + \mathbf{q}); \sigma(\mathbf{k}' - \mathbf{q}) \rangle &= \frac{4\pi}{V} \left( \frac{(2\pi)^3}{\Omega} \right) \\ &\times \sum_{\mathbf{G}_{\mu}\mathbf{G}_{\nu}\mathbf{G}_{\rho}\mathbf{G}_{\sigma}} \frac{\phi_{\mu}^*(\mathbf{G}_{\mu} + \mathbf{k}) \phi_{\nu}^*(\mathbf{G}_{\nu} + \mathbf{k}') \phi_{\rho}(\mathbf{G}_{\rho} + \mathbf{k} + \mathbf{q}) \phi_{\sigma}(\mathbf{G}_{\sigma} + \mathbf{k}' - \mathbf{q})}{(\mathbf{G}_{\rho} - \mathbf{G}_{\mu} + \mathbf{q})^2}, \quad (\text{A3}) \end{aligned}$$

with the additional condition on the summations that

$$\mathbf{G}_{\mu} + \mathbf{G}_{\nu} = \mathbf{G}_{\rho} + \mathbf{G}_{\sigma}. \quad (\text{A4})$$

Using this condition, and writing  $\mathbf{G} = \mathbf{G}_{\rho} - \mathbf{G}_{\mu}$ , and using the notation

$$\Phi_{\mu\nu}(\mathbf{Q}, \mathbf{k}) = \frac{(2\pi)^3}{\Omega} \sum_{\mathbf{G}} \phi_{\mu}^*(\mathbf{G} + \mathbf{k}) \phi_{\nu}(\mathbf{G} + \mathbf{Q} + \mathbf{k}), \quad (\text{A5})$$

we finally obtain

$$\begin{aligned} \langle \mu\mathbf{k}; \nu\mathbf{k}' | r_{12}^{-1} | \rho(\mathbf{k} + \mathbf{q}); \sigma(\mathbf{k}' - \mathbf{q}) \rangle & \\ &= \frac{4\pi}{V'} \sum_{\mathbf{G}} \frac{\Phi_{\mu\rho}(\mathbf{G} + \mathbf{q}, \mathbf{k}) \Phi_{\nu\sigma}(-\mathbf{G} - \mathbf{q}, \mathbf{k}')}{(\mathbf{G} + \mathbf{q})^2}. \end{aligned} \quad (\text{A6})$$

Note that Eq. (A5) implies that

$$\Phi_{\mu\nu}(\mathbf{0}, \mathbf{k}) = \frac{(2\pi)^3}{\Omega} \sum_{\mathbf{G}} \phi_{\mu}^*(\mathbf{G} + \mathbf{k}) \phi_{\nu}(\mathbf{G} + \mathbf{k}) = S_{\mu\nu}(\mathbf{k}) = \delta_{\mu\nu} \quad (\text{A7})$$

### Bibliography

- [1] M. Gell-Mann and K. Brueckner, *Phys. Rev.* **106**, 364 (1957).
- [2] M. Gell-Mann, *Phys. Rev.* **106**, 369 (1957).
- [3] J. Lindhard, K. Dan. Vidensk. Selsk. Mat. Fys. Medd. **28**, (8) (1954).
- [4] J. J. Quinn and R. A. Ferrell, *Phys. Rev.* **112**, 812 (1958).
- [5] D. S. Falk, *Phys. Rev.* **118**, 105 (1960).
- [6] G. W. Pratt, *Phys. Rev.* **118**, 462 (1960).
- [7] J. C. Phillips, *Phys. Rev.* **123**, 420 (1961).
- [8] L. Hedin, *Phys. Rev.* **139**, A796 (1965).
- [9] L. Hedin and S. Lundqvist, in *Solid State Physics*, F. Seitz, D. Turnbull, and H. Ehrenreich, Eds. (Academic, New York, 1969), Vol. 23.
- [10] P. Hohenberg and W. Kohn, *Phys. Rev.* **136**, B684 (1964).
- [11] W. Kohn and L. J. Sham, *Phys. Rev.* **140**, A1133 (1965).

- [12] See, e.g., in Adv. Quantum Chem., **21**, 155 (1991).
- [13] H. J. Monkhorst, Phys. Rev. B **20**, 1504 (1979).
- [14] H. J. Monkhorst, unpublished results (1992).
- [15] N. Wiser, Phys. Rev. **126**, 62 (1963).
- [16] L. S. Cederbaum and W. Domcke, Adv. Chem. Phys. **36**, 206 (1977).
- [17] C.-M. Liegener, J. Phys. C: Solid State Phys. **18**, 6011 (1985).
- [18] J. V. Ortiz, Int. J. Quantum Chem., Quantum Chem. Symp. **23**, 321 (1989).
- [19] D. Pines, *The Many-Body Problem* (Benjamin, New York, 1962).
- [20] G. S. Handler, Int. J. Quantum Chem. **33**, 173 (1988).
- [21] N. E. Brener, Phys. Rev. **11**, 929, 1600 (1975).

Received May 3, 1993

## **In Memoriam Michael Andreas Schlüter 1945–1992**

Though not a frequent participant in the Sanibel meetings, Michael Schlüter's work in many-fermion theory, especially density functional theory and studies of complex systems, was so important that he was a presence in many sessions he did not attend. To give but one example, his paper with Lu Sham on the so-called band-gap problem in density functional theory[1] was cited many times in both presentations and discussion.

Two times he gave plenary Sanibel lectures, in 1984 ("Point Defects in Semiconductors with Strong Electron-Lattice Coupling"[2]) and 1988 ("Electronic Structure and Superconductivity of High  $T_c$  Cu Oxides"[3]). Each was a model of his clarity of thought and ability to communicate truly central issues.

Perhaps as remarkable were his comments from the floor. SBT recalls the 1984 Symposium as a particularly lovely example. There had been much discussion on use, in solids, of self-interaction corrections to local density approximations. Eventually Michael asked for the floor, rose quietly to full height, and gave a one-sentence diagnosis of the difficulty: "The problem with self-interaction corrections is that there is no intrinsic scale length over which to localize them in anything but an atom." Equally quietly, he sat down.

Born in Germany, Michael learned fluent French on account of his girlfriend, then wife, now widow. HJM recalls their meeting for the first time at the 1971



Menton Conference, with hikes between sessions devoted to French practice, fundamental problems in semiconductors, and reflections on moving to the USA. (HJM had already emigrated. Years later he and SBT would try, in vain, to persuade Michael to move again, this time to University of Florida.) Michael was already participating as a full peer in luncheon discussions with frequent Sanibel participants such as Norman March, Jan Linderberg, Frank Harris, Jean-Louis Calais, Keith Johnson, et al. One particularly notable event was a dinner in the mountains above Menton that included John Ziman. Michael began his Diplom studies at University of Karlsruhe in LF's group in 1968. Recognized immediately for his innate ability to understand and communicate physics, he became a kind of walking reference. LF recalls dispatching Michael to brief various experimental groups and getting back rave reviews. After the Diplom, Michael confessed his chagrin at not speaking French. In response, LF suggested that Michael could join a friend's group at the new EPFL in Lausanne. He did and, at breathtaking speed, both picked up French and wrote a pseudo-potential code with which he studied layered compounds. In 1972, a Swiss Science Foundation fellowship took him to Marvin Cohen's group at Berkeley as a Postdoc. He went to Bell Labs in 1975 and continued to build the record of achievement noted above.

The three of us are honored to have had the opportunity to give memorial remarks at the outset of the "Michael Schlüter Memorial Session on Density Functional Theory" at the 33rd Sanibel Symposium. We are grateful that our lives were graced by his life and much saddened at the premature loss.

LOTHAR FRITSCHÉ

*Institut für Theoretische Physik, Technische Universität Clausthal*

HENK MONKHORST

SAM TRICKEY

*Quantum Theory Project, University of Florida*

[1] L.J. Sham and M. Schlüter, Phys. Rev. Lett. **51**, 1884 (1983)

[2] G.A. Baraff and M. Schlüter, Int. J. Quantum Chem. **S18**, 737 (1984).

[3] M. Schlüter, Internat. J. Quantum Chem., **S22**, 735 (1988).

# Local Density and Gradient-Corrected Functionals for Short-Range Correlation: Antiparallel-Spin and Non-RPA Contributions

JOHN P. PERDEW

*Department of Physics and Quantum Theory Group, Tulane University,  
New Orleans, Louisiana 70118*

## Abstract

In many situations, the most long-ranged parts of the exchange and correlation holes surrounding an electron cancel one another. Apparently for this reason, local spin density and generalized gradient approximations are more accurate for exchange and correlation together than for either alone. A study is made of the ability of these density functionals, and also the unmodified second-order gradient expansion, to describe various short-range effects in atoms: the correlation contribution to the interacting kinetic energy, the antiparallel-spin correlation energy, and the correction to the random phase approximation. Generalized gradient approximations, constructed with no adjustable parameter from the electron gas of slowly varying density, are found to give results of useful accuracy for real atoms. Prospects are discussed for use of the new functionals to improve the accuracy of electronic-structure calculations.

© 1993 John Wiley & Sons, Inc.

## Introduction

The noninteracting kinetic energy, the exchange energy, and the correlation energy are all functionals of the electron density [1,2]. The first two arise from the exchange hole surrounding an electron, while the third arises from the coupling-constant-averaged correlation hole. The holes may be expanded in powers of the density derivatives at the position of the electron. The resulting gradient expansions have a characteristic structure: When the density does not vary too rapidly over space, the addition of each successive order in  $\nabla$  improves the approximate hole close to its electron, while worsening it far away [3,4].

From this analysis, the local spin density (LSD), second-order gradient expansion (GEA), and generalized gradient (GGA) approximation,

$$E[n_\uparrow, n_\downarrow] = \int d^3r \, e(n_\uparrow, n_\downarrow, \nabla n_\uparrow, \nabla n_\downarrow), \quad (1)$$

are expected to be relatively more accurate for energies that sample the more short-ranged features of the holes. For example, the noninteracting kinetic energy samples only derivatives of the exchange hole at the position of the electron; its GEA makes typical errors of less than 1%, and is its own GGA [5].

This analysis suggests why it is often better to treat exchange and correlation together in the same density functional approximation than to combine an exact (Hartree-Fock) description of exchange with a density functional approximation for correlation. A striking example is the atomization energy of  $C_2$  [6], which is 0.7 eV in Hartree-Fock, 2.3 eV when GGA correlation is added, and 6.55 eV when both exchange and correlation are treated in GGA; the experimental value is 6.36 eV. The explanation seems to be that the exact exchange and correlation holes have long-ranged components which tend to cancel one another. The same cancellation between the most long-ranged components of exchange and parallel-spin correlation occurs in the electron gas of uniform density; each hole has a nonoscillatory  $R^{-4}$  tail, where  $R$  is distance from the electron [3,7]. The residue of this cancellation is plasmon-dominated [3,7] at large  $R$  and falls off like  $R^{-5}$ .

In previous work, accurate generalized gradient approximations for the exchange energy ( $E_x$ ) and correlation energy ( $E_c$ ) have been developed from first principles by cutting off the spurious long-range parts of the second-order gradient expansions for the holes [8,9]. From the GGA for  $E_c$ , a GGA for the correlation contribution  $T_c$  to the interacting kinetic energy has been developed [5,10] and shown [10] to be independent of the most long-ranged part of the correlation hole.

The aim of this work is to develop and test density functionals for two other short-range properties: the antiparallel-spin correlation energy (next section) and the correction to the random phase approximation (third section). Table I compares GGA and nearly exact values [11-15], where available, and confirms the good success that GGA has had for the total correlation energy. Prospects for the practical use of the new functionals are discussed in a later section.

Table II compares LSD, GEA, and GGA results for the neon atom. Note that GEA is typically very unrealistic due to its violation of a sum rule on the correlation hole

TABLE I Comparison between generalized gradient approximation (GGA) and exact values for  $-E_c$  (minus the correlation energy),  $T_c$  (the correlation contribution to the kinetic energy),  $-E_c^{\uparrow\downarrow}$  (the antiparallel-spin contribution to  $-E_c$ ), and  $E_c - E_c^{RPA}$  (the correction to the random phase approximation).<sup>a</sup>

Atom	$-E_c$		$T_c$		$-E_c^{\uparrow\downarrow}$		$E_c - E_c^{RPA}$
	GGA	Exact	GGA	Exact	GGA	Exact	GGA
He	0.046 <sup>a</sup>	0.042 <sup>b,c</sup>	0.038 <sup>a</sup>	0.037 <sup>d</sup>	0.041	0.042 <sup>b,c</sup>	0.031
Be	0.094 <sup>a</sup>	0.094 <sup>b,c</sup>	0.073 <sup>a</sup>	0.074 <sup>d</sup>	0.084	0.091 <sup>e</sup>	0.062
Ne	0.382 <sup>a</sup>	0.39 <sup>b,c</sup>	0.313 <sup>a</sup>	—	0.306	0.31 <sup>e,f</sup>	0.188

<sup>a</sup> Ref. [10]

<sup>b</sup> Ref. [11].

<sup>c</sup> Ref. [12]

<sup>d</sup> Ref. [13].

<sup>e</sup> Ref. [14].

<sup>f</sup> Ref. [15]

TABLE II Comparison among local spin density (LSD), second-order gradient expansion (GEA), and generalized gradient approximation (GGA) results for the neon atom (hartree).<sup>a</sup>

Property	LSD	GEA	GGA	Exact
$T_s$	117.76	127.83	127.83	128.55
$-E_x$	11.033	11.775	12.115	12.108
$-E_c$	0.743	-0.780	0.382	0.39
$T_c$	0.496	0.530	0.313	—
$-E_c^{14}$	0.434	-0.217	0.306	0.31
$E_c - E_c^{RPA}$	0.201	0.174	0.188	—

<sup>a</sup>  $T_s$  (the noninteracting kinetic energy) and  $E_x$  (the exchange energy) from Refs. [5] and [6].

respected by LSD and restored in GGA. LSD is rather unrealistic for the total correlation energy, but less so for the short-range contributions, as expected.

### Antiparallel-Spin Correlation Energy

At least in the uniform electron gas [7], and perhaps more generally, the most long-ranged part of the correlation hole around an electron (which cancels the most long-ranged part of the exchange hole) arises from parallel-spin correlation alone.

The GGA for the *total* correlation energy is [6,9] (in atomic units)

$$E_c[n_\uparrow, n_\downarrow] = \int d^3r n [\epsilon_c(r_s, \zeta) + H(t, r_s, \zeta, \epsilon_c(r_s, \zeta), C_c(r_s))] , \quad (2)$$

where  $n = n_\uparrow + n_\downarrow = \frac{3}{4}\pi r_s^3 = \pi k_F^3/192$ ,  $\zeta = (n_\uparrow - n_\downarrow)/n$ ,

$$t = |\nabla n|/2gk_F n \quad (3)$$

and

$$g = [(1 + \zeta)^{2/3} + (1 - \zeta)^{2/3}]/2 . \quad (4)$$

Note that  $\epsilon_c$ ,  $H$ , and  $g$  are even functions of  $\zeta$ . For a slowly varying density ( $t \rightarrow 0$ ), the right-hand side of Eq. (2) becomes

$$\int d^3r n \epsilon_c(r_s, \zeta) + \int d^3r [C_c(r_s) - 3C_x/7] g |\nabla n|^2 / n^{4/3} + \dots , \quad (5)$$

where  $C_x = -0.001667$ . The first term of Eq. (5) is LSD and the sum of the first two terms is GEA. The second or gradient term depends weakly upon  $\zeta$  since  $g$  varies from 1 at  $\zeta = 0$  to  $2^{1/3}$  at  $\zeta = 1$ , and neglects small [16]  $\nabla\zeta$  contributions to the first-principles GEA. The gradient coefficient  $C(r_s)g$  is dominated by long-wavelength, plasmonlike excitations [3]. In a plasma oscillation, all electrons participate equally without regard to their spins. This observation suggests that the parallel-spin contribution to  $C(r_s)g$  is proportional to the probability that two electron spins are parallel,  $[(1 + \zeta)/2]^2 + [(1 - \zeta)/2]^2$ , which varies from 1/2 at  $\zeta = 0$  to 1 at  $\zeta = \pm 1$ .

The  $H_1$  term of  $H = H_0 + H_1$  is an anomalous [9] parallel-spin contribution which gives rise to the  $-3C_s/7$  piece of the gradient term in Eq. (5). Thus, without the painstaking derivation required by the GEAs for  $E_c$  and  $T_c$ , a guessed GGA for antiparallel-spin correlation is

$$E_c^{\uparrow\downarrow} = \int d^3r n[\epsilon_c^{\uparrow\downarrow}(r_s, \zeta) + H_0(t, r_s, \zeta, \epsilon_c^{\uparrow\downarrow}(r_s, \zeta), C_c^{\uparrow\downarrow}(r_s, \zeta))], \quad (6)$$

with  $\beta = \nu C_c^{\uparrow\downarrow}(r_s, \zeta)$  in Eq. (13) of Ref. [6]. This reduces to

$$\int d^3r n \epsilon_c^{\uparrow\downarrow}(r_s, \zeta) + \int d^3r C_c^{\uparrow\downarrow}(r_s, \zeta) g|\nabla n|^2/n^{4/3} + \dots \quad (7)$$

in the slowly-varying limit. From the high-density limit of the uniform electron gas, the antiparallel-spin correlation energy per electron is approximately\* [7]

$$\epsilon_c^{\uparrow\downarrow}(r_s, \zeta) = \epsilon_c(r_s, \zeta) - \epsilon_c(r_s, 1) \left[ \left( \frac{1+\zeta}{2} \right)^{4/3} + \left( \frac{1-\zeta}{2} \right)^{4/3} \right]. \quad (8)$$

For  $\zeta = 0$  and  $0.01 \leq r_s \leq 2$ , Eq. (8) deviates by no more than about 5% from the estimate of Nozière and Pines [18] who started from second-order perturbation theory and cut off the unconverged small-wavevector contribution; at  $r_s = 5$ , the deviation is still only 12%. From the argument at the end of the preceding paragraph,

$$C_c^{\uparrow\downarrow}(r_s, \zeta) = C_c(r_s) \left[ 1 - \left( \frac{1+\zeta}{2} \right)^2 + \left( \frac{1-\zeta}{2} \right)^2 \right]. \quad (9)$$

For  $\zeta = \pm 1$ ,  $\epsilon_c^{\uparrow\downarrow}$ ,  $C_c^{\uparrow\downarrow}$ , and  $E_c^{\uparrow\downarrow}$  all properly vanish. The integrand of Eq. (6), like that of Eq. (2), is everywhere properly nonpositive and vanishes as  $t \rightarrow \infty$ . The antiparallel-spin correlation potential  $\delta E_c^{\uparrow\downarrow}/\delta n_\sigma(\mathbf{r})$  can be found from Eq. (33) of Ref. [9].

While Eq. (2) is derived, Eq. (6) is only an obvious guess which could be improved by refining the ingredients  $\epsilon_c^{\uparrow\downarrow}$  and  $C_c^{\uparrow\downarrow}$ , and by making a real space cutoff [8,9] on the gradient expansion of the antiparallel-spin correlation hole.

LSD, GEA, and GGA results for 17 spherical atoms or ions with Hartree-Fock densities [19] are presented in Table III. Note that the contribution of antiparallel-spin correlation to  $-E_c$  varies from about 90% for few-electron spin-unpolarized atoms to 74% for the 54-electron atom Xe. Contrast this with the spin-unpolarized uniform electron gas of high density, in which only 60% of the correlation energy arises from antiparallel spins. Preferential suppression of long-range parallel-spin correlation is a characteristic feature of small systems like atoms.

There are two reasons to hope that this GGA for  $E_c^{\uparrow\downarrow}$  might be more accurate than the GGA for  $E_c$ : (1) GGAs are better suited to more short-ranged effects. (2) This GGA for  $E_c^{\uparrow\downarrow}$  is self-interaction-free, i.e., it properly vanishes for a one-electron system.

\* The model pair distribution function which implies this result for the uniform electron gas is supported by results of Pickett [17]



TABLE III. Comparison of LSD, GEA, and GGA results (hartree).<sup>a</sup>

Atom	$-E_c^{LH}$				$E_c-E_c^{RPA}$			
	LSD	GEA	GGA	%	LSD	GEA	GGA	%
H	0.000	-0.000	0.000	0%	0.018	0.007	0.014	210%
He <sup>+</sup>	0.000	-0.000	0.000	0%	0.020	0.007	0.015	204%
He	0.065	-0.035	0.041	88%	0.037	0.018	0.031	67%
Li <sup>+</sup>	0.078	-0.089	0.048	94%	0.039	0.020	0.033	65%
Be <sup>2+</sup>	0.088	-0.147	0.053	99%	0.041	0.022	0.034	64%
Li	0.080	-0.068	0.050	86%	0.054	0.037	0.045	78%
Be <sup>+</sup>	0.091	-0.108	0.057	91%	0.057	0.040	0.048	77%
Be	0.130	-0.099	0.084	89%	0.072	0.049	0.062	66%
Ne <sup>6+</sup>	0.195	-0.454	0.123	100%	0.083	0.063	0.072	59%
N	0.227	-0.145	0.166	83%	0.136	0.111	0.124	62%
Ne	0.434	-0.217	0.306	80%	0.201	0.174	0.188	49%
Ar	0.832	-0.432	0.606	79%	0.365	0.338	0.349	45%
Zn <sup>12+</sup>	1.057	-1.243	0.762	82%	0.393	0.374	0.376	41%
Zn <sup>2+</sup>	1.511	-0.714	1.134	76%	0.598	0.579	0.580	39%
Zn	1.556	-0.636	1.167	76%	0.630	0.614	0.613	40%
Kr	1.916	-0.777	1.450	76%	0.760	0.742	0.743	39%
Xe	3.038	-1.183	2.344	74%	1.153	1.145	1.135	36%

<sup>a</sup> The % column displays the ratio of the GGA for a given property to the GGA for  $-E_c$ .

The self-interaction error of the LSD or GGA approximation for the *total* exchange-correlation energy has several undesirable consequences, which are avoided by approximating only the antiparallel-spin correlation energy. One of the most striking is the self-interaction error of the exchange-correlation potential  $\delta E_{xc}/\delta n_\sigma(\mathbf{r})$ , which is roughly a positive constant over the interior of an atom, but decays like  $+e^2/r$  as  $r \rightarrow \infty$ . This error of the potential is qualitatively similar in the neon [20] and hydrogen atoms. Another error of the GGA potential, its divergence (like  $\nabla^2 n$ ) as  $r \rightarrow 0$ , is probably reduced but not eliminated by approximating only antiparallel-spin correlation.

### Correction to the Random Phase Approximation

The random phase approximation [3] (RPA, sum of ring diagrams, or time-dependent Hartree approximation) is exact for long-range correlation, because it constructs the correlation hole from a density-response function  $\chi(\mathbf{r}, \mathbf{r}', \omega)$  which becomes exact in the limit  $|\mathbf{r}' - \mathbf{r}| \rightarrow \infty$ . However, RPA is poor for short-range correlation. For the uniform electron gas at metallic densities, it produces a correlation hole at the position of the electron ( $\mathbf{r}' = \mathbf{r}$ ) that is much too deep.

The GGA of Eq. (2) is constructed beyond the random phase approximation (RPA). However, it is easy [6] to make an RPA version by using RPA results for the ingredients  $\epsilon_i(r_s, \zeta)$  and  $C_c(r_s)$ . The cutoff parameter [9] in  $H$  should remain unchanged, since RPA should become relatively exact in the high-density limit.

TABLE IV. Parameters of Eq. (10) for the second-order gradient coefficient of the correlation energy, within and beyond the random phase approximation (RPA)

	RPA	Beyond <sup>a</sup>
$\alpha$	0.001254	0.023266
$\beta$	$2.6 \times 10^{-9}$	$7.389 \times 10^{-6}$
$\gamma$	0.444	8.723
$\delta$	0.0071	0.0472

<sup>a</sup> Ref [22].

The Perdew-Wang analytic representation [21] for  $\epsilon_c(r_s, \zeta)$  works equally well within or beyond RPA; only the parameters change, as shown in Table I of Ref. [21]. The Rasolt-Geldart analytic representation [22]

$$C_c(r_s) = -C_c + \frac{0.002568 + \alpha r_s + \beta r_s^2}{1 + \gamma r_s + \delta r_s^2 + 10^4 \beta r_s^3}, \quad (10)$$

may also be used within RPA. Table IV shows the parameters determined here from a fit to the RPA  $C_c(r_s)$  from Ref. [3] at  $r_s = 2, 4, 6$ , and 12.

The difference between Eq. (2) evaluated beyond and within RPA is the GGA for  $E_c - E_c^{\text{RPA}}$ , the correction to the random phase approximation. LSD, GEA, and GGA results for 17 spherical atoms and ions are presented in Table III. [An alternative GGA for  $E_c^{\text{RPA}} - E_c$  could be constructed in the form of Eq. (6), but with "RPA minus exact" inputs for  $\epsilon_c$  and  $C_c$ .]

$E_c - E_c^{\text{RPA}}$  is the only correlation energy studied here for which GEA provides a reasonable estimate,\* and for which LSD is close to GGA. Note that it is an important part of the total correlation energy (67% of  $-E_c$  for He and 36% for Xe). Moreover,  $(E_c - E_c^{\text{RPA}})/N$  (the contribution per electron) is typically close to 0.024 hartree, the second-order exchange constant which corrects the RPA  $\epsilon_c(r_s, \zeta)$  in the high-density limit  $r_s \rightarrow 0$ .

Table III shows that, for spin-unpolarized atoms within LSD,  $E_c - E_c^{\text{RPA}}$  is typically between 40% and 60% of  $-E_c^{\dagger}$ . This result is not unexpected: wavevector analysis of the RPA correlation energy for the uniform electron gas shows [18] that RPA is exact in the small-wavevector limit (long-range, parallel-spin correlation), but is too negative by a factor of two in the large-wavevector limit (short-range, antiparallel-spin correlation).

### Prospects

LSD and GGA density functionals have been constructed and tested for two short-range contributions to the correlation energy: antiparallel-spin and non-RPA. It

\* Vosko and Langreth [23] have suggested that GEA may suffice for the second-order exchange energy, the leading correction to RPA in the high-density limit.

appears that functionals of this kind are potentially more accurate for the short-range contributions than for the total correlation energy. How could these new functionals be used to improve the accuracy of electronic-structure calculations?

The GGA for antiparallel-spin correlation might be combined with some more accurate description of exchange plus parallel-spin correlation energy. Quantum-chemical methods like "coupled cluster" [24] are well suited for this purpose, since they would not be required to build up the cusp of the correlation hole at the position of the electron, which is carried by other electrons with antiparallel spins [7]. This hybrid approach is similar to that of Savin [25], who made a different separation between long-range and short-range correlation. Alternatively, a fully nonlocal weighted density approximation [26] might be used for exchange and parallel-spin correlation [27,28].

The GGA for  $E_c - E_c^{\text{RPA}}$  might be combined [27] with a full RPA calculation of the exchange and correlation energies. RPA-like calculations have been carried out for finite systems [29,30] and for metallic hydrogen [31], but usually in versions of RPA more elaborate than the simple ring sum needed here.

The generally good results obtained from a GGA with no adjustable parameter should finally answer the old question: "What does the electron gas of slowly-varying density have to do with real atoms and molecules?" It is only human beings who draw a distinction between condensed matter physics and quantum chemistry; to Nature, electronic systems form a seamless whole.

### Acknowledgments

This work was supported in part by the National Science Foundation under Grant DMR92-13755. The author thanks A. Savin and J. Oddershede for helpful references.

### Bibliography

- [1] W. Kohn and L. J. Sham, *Phys. Rev.* **140**, A1133 (1965).
- [2] R. O. Jones and O. Gunnarsson, *Rev. Mod. Phys.* **61**, 689 (1989).
- [3] D. C. Langreth and J. P. Perdew, *Phys. Rev. B* **21**, 5469 (1980).
- [4] Y. Wang, J. P. Perdew, J. A. Chevary, L. D. Macdonald, and S. H. Vosko, *Phys. Rev. A* **41**, 78 (1990).
- [5] J. P. Perdew, *Phys. Lett. A* **165**, 79 (1992).
- [6] J. P. Perdew, J. A. Chevary, S. H. Vosko, K. A. Jackson, M. R. Pederson, D. J. Singh, and C. Fiolhais, *Phys. Rev. B* **46**, 6671 (1992).
- [7] J. P. Perdew and Y. Wang, *Phys. Rev. B* **46**, 12947 (1992).
- [8] J. P. Perdew and Y. Wang, *Phys. Rev. B* **33**, 8800 (1986).
- [9] J. P. Perdew, in *Electronic Structure of Solids '91*, P. Ziesche and H. Eschrig, Eds. (Akademie Verlag, Berlin, 1991), p. 11.
- [10] A. Gorling, M. Levy, and J. P. Perdew, *Phys. Rev. B* **47**, 1167 (1993).
- [11] A. Veillard and E. Clementi, *J. Chem. Phys.* **49**, 2415 (1968), H. Stoll and A. Savin, private communication.
- [12] J. B. Lagowski and S. H. Vosko, *J. Phys. B* **21**, 203 (1988).
- [13] C.-O. Almbladh and A. C. Pedroza, *Phys. Rev. A* **29**, 2322 (1984).
- [14] R. K. Nesbet, *Phys. Rev.* **155**, 51 (1967).
- [15] R. K. Nesbet, T. L. Barr, and E. R. Davidson, *Chem. Phys. Lett.* **4**, 203 (1969).

- [16] Y. Wang and J. P. Perdew, Phys. Rev. B **43**, 8911 (1991).
- [17] W. Pickett and J. Q. Broughton, quantum Monte Carlo results (unpublished).
- [18] P. Nozières and D. Pinès, Phys. Rev. **111**, 442 (1958). See Eq. (51).
- [19] E. Clementi and C. Roetti, At. Data Nucl. Data Tables **14**, 177 (1974).
- [20] M. Teter, Int. J. Quantum Chem. Quantum Symp. **27**; C. J. Umrigar and X. Gonze, Bull. Am. Phys. Soc. **38**, 381 (1993).
- [21] J. P. Perdew and Y. Wang, Phys. Rev. **B45**, 13244 (1992).
- [22] M. Rasolt and D. J. W. Geldart, Phys. Rev. **B34**, 1325 (1986).
- [23] S. H. Vosko and D. C. Langreth, private communication.
- [24] G. Stollhoff and A. Heilingbrunner, Z. Phys. **B83**, 85 (1991).
- [25] A. Savin, Int. J. Quantum Chem. Quantum Symp. **22**, 59 (1988); J. Chim. Phys. **86**, 757 (1989).
- [26] O. Gunnarsson, M. Jonson, and B. I. Lundqvist, Phys. Rev. **B20**, 3136 (1979).
- [27] J. P. Perdew, in *Electronic Density Functional Theory of Molecules, Clusters, and Solids*, D. E. Ellis, Ed. (Kluwer Academic, 1993).
- [28] A. Rubio and J. P. Perdew, work in progress.
- [29] A. Szabo and N. S. Ostlund, J. Chem. Phys. **67**, 4351 (1977); J. Oddershede, Adv. Quant. Chem. **11**, 275 (1978).
- [30] F. E. Harris, H. J. Monkhorst, and D. L. Freeman, *Algebraic and Diagrammatic Methods in Many-Fermion Theory* (Oxford University Press, New York, 1992).
- [31] H. J. Monkhorst and J. Oddershede, Phys. Rev. Lett. **30**, 797 (1973).

Received April 21, 1993

# Asymptotic Structure of the Kohn–Sham Effective Potential at Metal Surfaces

MANOJ K. HARBOLA\* and VIRAH T SAHNI

*Department of Physics, Brooklyn College of the City University of New York, Brooklyn, New York 11210, and The Graduate School and University Center of the City University of New York, 33 West 42nd Street, New York, New York 10036*

## Abstract

In this article we calculate the asymptotic structure of the exchange potential for the Fermi level electron in the vacuum region outside a metal surface, and show it to be the image potential. In this asymptotic region the exchange potential due to the Fermi level electron is equivalent to the optimized potential of exchange-only density-functional theory. Thus, the asymptotic Kohn–Sham effective potential at a metal surface is the image potential, and arises solely due to correlations which result from the Pauli exclusion principle © 1993 John Wiley & Sons, Inc

## Introduction

In density-functional theory [1,2], the electrons of a nonuniform system in the presence of an external potential are treated as noninteracting quasi-particles moving in a local effective potential. This effective potential is the sum of the classical Hartree electrostatic and exchange-correlation potentials, with all the many-body effects including those due to the correlation contribution to the kinetic energy being incorporated in the latter. The many-body potential is derived by application of the variational principle for the energy to be the functional derivative of the exchange-correlation energy functional of the density. The asymptotic structure of the effective potential in the classically forbidden region is that of the exchange-correlation potential since the Hartree potential decays exponentially as the density in this region. In this article we address the issue of the structure and physical origin of the effective or equivalently the exchange-correlation potential for asymptotic positions of an electron far in the vacuum outside a metal surface.

In the literature, semiclassical calculations [3–6] obtain the asymptotic structure of the exchange-correlation potential at a metal surface to be the image potential  $-1/4x$  for an electron at a distance  $x$  from the metal surface. In these calculations the asymptotic electron is treated as an external test charge distinct and independent from the inhomogeneous electron gas at the metal–vacuum interface. As a consequence, the asymptotic image-potential structure of the exchange-correlation potential is attributed to being due to Coulomb correlation effects.

---

\* Present address. Center for Advanced Technology, Indore 452013, India.

The asymptotic electron, however, is not separate from but part of the interacting nonuniform electronic system at the surface. In recent work [7,8] the integral equation [6] relating the functional derivative of the exchange-correlation energy to the electron self-energy of many-body perturbation theory has been solved self-consistently within two approximation schemes for the self-energy. The asymptotic structure of the resulting approximate exchange-correlation potential in each case is image-potential-like, and in the latter calculation [8] this structure is shown to be due to the Coulomb correlation contribution to the self-energy. In this calculation [8] the self-energy is replaced by the first term in an expansion [9] in powers of the dynamically screened electron-electron interaction. Further approximations invoked are the replacement of the response function by that within the random phase approximation, and the assumption that the Kohn-Sham and Dyson equation Green functions are the same. On the other hand, the  $-1/r$  asymptotic structure of the effective potential in atoms, as obtained via the integral equation by employing [6] the fact that only the highest occupied orbitals contribute to this structure is shown [6] to be a consequence of Pauli correlations. Thus within this framework, the asymptotic structure of the effective potential of the nonuniform electron gas in atoms and molecules is due to Pauli correlations whereas that at metal surfaces is a result of Coulomb correlations.

In contrast, by application of a physically based many-electron theory [10,11] developed by us, we have shown that both the asymptotic image potential at a metal surface [12,13] as well as the  $-1/r$  asymptotic potential in atoms [10,11,14] are due to Pauli correlation effects. In this theory the local potential representing the correlations due to the Pauli exclusion principle and Coulomb's law is obtained as the work done to move an electron in the force field of its Fermi-Coulomb hole charge distribution. Since the total Coulomb hole charge is zero, Coulomb correlation effects do not contribute to the asymptotic structure of this potential. As such the physical origin of the asymptotic effective potential of *all* nonuniform electronic systems is universal in that it is due only to correlations arising from the Pauli exclusion principle. Thus the asymptotic structure, which arises as a result of the Coulomb interaction between the asymptotic electron and the Fermi hole charge distribution, is exactly known. In the theory the asymptotic electrons are explicitly treated as part of the nonuniform electronic system, and *no approximations* are made in determining the asymptotic structure of the effective potential. The asymptotic image potential structure at a metal surface is obtained from the *delocalized* [15] Fermi hole spread through the crystal, whereas the  $-1/r$  potential in atoms is derived from the Fermi hole *localized* [16] about the nucleus of the atom.

In the present work we show by calculating the asymptotic structure of the rigorously defined [17,6] exchange potential of exchange-only density-functional theory that, as is the case for atoms, the asymptotic effective potential at metal surfaces is an exchange effect. Furthermore, this structure is that of the image potential. Once again, *no approximations* are made in arriving at these conclusions. The calculations, performed within the context of density-functional theory, are distinct from those of our previous work [12,13]. However, the conclusions of the two independent formulations are entirely consistent.

### Exchange-Only Density-Functional Theory

The exchange potential  $\mu_x(\mathbf{r})$  in exchange-only [17] density-functional theory is defined as that obtained by the optimized potential method [18] (OPM). In the OPM, the electrons in an external potential  $V_{\text{ext}}(\mathbf{r})$  are assumed to move in a local effective potential  $V^{\text{OPM}}(\mathbf{r})$  so that the differential equation governing the electronic orbitals  $\phi_i(\mathbf{r})$  is

$$\left[-\frac{1}{2}\nabla^2 + V_{\text{ext}}(\mathbf{r}) + V^{\text{OPM}}(\mathbf{r})\right]\phi_i(\mathbf{r}) = \epsilon_i\phi_i(\mathbf{r}). \quad (1)$$

These orbitals are then employed to determine the Hartree-Fock theory energy which is the expectation value  $\langle H \rangle_{\text{HF}}$  of the nonrelativistic Hamiltonian taken with respect to a Slater determinant of the orbitals  $\phi_i(\mathbf{r})$ . The potential  $V^{\text{OPM}}(\mathbf{r})$  is varied until a minimum of the energy is achieved, i.e., the variation

$$\delta\langle H \rangle_{\text{HF}}/\delta V^{\text{OPM}}(\mathbf{r}) = 0 \quad (2)$$

is performed. The resulting potential is the optimized potential. The exchange part of this potential is obtained by subtracting from it the Hartree potential  $\int d\mathbf{r}' \rho(\mathbf{r}')/|\mathbf{r} - \mathbf{r}'|$ , where the density  $\rho(\mathbf{r}) = \sum_i |\phi_i(\mathbf{r})|^2$ . The variation of Eq. (2) leads [18] to the following integro-differential equation for the exchange potential:

$$\sum_i \int d\mathbf{r}' [\mu_x(\mathbf{r}') - v_{\text{A},i}(\mathbf{r}')] G_i(\mathbf{r}', \mathbf{r}) \phi_i(\mathbf{r}') \phi_i^*(\mathbf{r}) = 0, \quad (3)$$

where  $G_i(\mathbf{r}, \mathbf{r}')$  is the Green function

$$G_i(\mathbf{r}, \mathbf{r}') = \sum_j \phi_j(\mathbf{r}) \phi_j^*(\mathbf{r}') / \epsilon_j - \epsilon_i, \quad (4)$$

and where  $v_{\text{A},i}(\mathbf{r})$  is the Hartree-Fock theory orbital-dependent potential [19,20]

$$v_{\text{A},i}(\mathbf{r}) = - \int \rho_{\text{A},i}(\mathbf{r}, \mathbf{r}') / |\mathbf{r} - \mathbf{r}'| d\mathbf{r}', \quad (5)$$

with

$$\rho_{\text{A},i}(\mathbf{r}, \mathbf{r}') = \sum_j \phi_j^*(\mathbf{r}') \phi_j(\mathbf{r}) \phi_i(\mathbf{r}') / \phi_i(\mathbf{r}) \quad (6)$$

being the orbital-dependent Fermi hole charge at  $\mathbf{r}'$  for an electron at  $\mathbf{r}$ . The OPM has been applied to the nonuniform electronic system at metal surfaces [21] and atoms [22], and leads to properties that are essentially equivalent to those of Hartree-Fock theory [23,24]. The OPM calculations [21] at a metal surface were, however, not carried out for asymptotic positions of the electron in the vacuum. Such a self-consistent solution of the integro-differential equation Eq. (3) for the determination of the asymptotic structure of the exchange potential would be a numerical *tour de force*.

Now it can rigorously be shown [25] that in the asymptotic region (as in the vacuum outside a surface or far from the nucleus of an atom) where the only

contributions to the density come from the highest occupied orbital  $\phi_m(\mathbf{r})$ , the exchange potential  $\mu_e(\mathbf{r})$  is equivalent to the highest occupied orbital-dependent potential  $v_{\lambda, l=m}(\mathbf{r})$  of Hartree-Fock theory [see Eq. (5)]. In other words, the asymptotic structure of the exchange potential at a metal surface arises from the Fermi level electrons. We note that it is only in the asymptotic region where the orbitals decay exponentially is the orbital-dependent potential  $v_{\lambda, m}(\mathbf{r})$  physically meaningful. In other regions, the potential can be singular as at the nodes of the orbitals. From the above, and the fact that the orbital-dependent Fermi hole charge integrates to unity, we see that the asymptotic effective potential in atoms goes as  $-1/r$  and is purely an exchange effect. In order, therefore, to determine the asymptotic structure of the exchange potential  $\mu_e(\mathbf{r})$  at a metal surface, we calculate the asymptotic structure of the orbital-dependent potential  $v_{\lambda, m}(\mathbf{r})$  corresponding to the Fermi level [19].

### Application to the Jellium Metal Surface

In the jellium model of a metal surface, the Hamiltonian of the system is

$$H = -\frac{1}{2} \sum_i \nabla_i^2 + \sum_i V_{\text{ext}}(\mathbf{r}_i) + \frac{1}{2} \sum_{i,j}' \frac{1}{|\mathbf{r}_i - \mathbf{r}_j|}, \quad (7)$$

where the external potential  $V_{\text{ext}}(\mathbf{r}_i) = -\int d\mathbf{r} \rho_+(\mathbf{r})/|\mathbf{r} - \mathbf{r}_i|$  is due to the uniform positive background charge  $\rho_+(\mathbf{r}) = \bar{\rho} \theta(-x + a)$  beginning at the surface at  $x = a$ , and  $\bar{\rho}$  the bulk density of the metal. The constant term corresponding to the self-energy of the jellium charge is not included in the Hamiltonian.

At a jellium metal surface, the translational invariance in the plane of the surface requires the wavefunction of an electron with momentum  $\mathbf{k}$  to be of the form  $\Psi_{\mathbf{k}}(\mathbf{r}) = \Psi_{\mathbf{k}_\parallel}(\mathbf{x}_\parallel) \Phi_k(x)$ ,  $\Psi_{\mathbf{k}_\parallel}(\mathbf{x}_\parallel) = (1/\sqrt{A}) \exp[i\mathbf{k}_\parallel \cdot \mathbf{x}_\parallel]$ ,  $\Phi_k(x) = (-\sqrt{2}/L) \phi_k(x)$ , where  $\phi_k(x)$  is the component of the wavefunction perpendicular to the surface,  $k$  and  $x$  the momentum and position vectors in that direction, and  $\mathbf{k}_\parallel$  and  $\mathbf{x}_\parallel$  the corresponding components in the plane parallel to the surface. This wavefunction is then substituted into Eq. (5) for the orbital-dependent potential which in  $\mathbf{k}$ -notation is

$$v_{\lambda, \mathbf{k}}(\mathbf{r}) = -\int \frac{d\mathbf{r}'}{|\mathbf{r} - \mathbf{r}'|} \sum_{\mathbf{k}'} \frac{\Psi_{\mathbf{k}}^*(\mathbf{r}) \Psi_{\mathbf{k}'}^*(\mathbf{r}') \Psi_{\mathbf{k}'}(\mathbf{r}) \Psi_{\mathbf{k}}(\mathbf{r}')}{\Psi_{\mathbf{k}}^*(\mathbf{r}) \Psi_{\mathbf{k}}(\mathbf{r})}, \quad (8)$$

where we have multiplied the numerator and denominator by  $\Psi_{\mathbf{k}}^*(\mathbf{r})$ . However, since it is only the component of the electron momentum perpendicular to the surface that contributes to the asymptotic structure, we Slater average [20] the potential  $v_{\lambda, \mathbf{k}}(\mathbf{r})$  with respect to the component of the wavefunction in the plane of the surface. This leads to the potential  $v_{\lambda, k}(x)$  which is dependent only on the component  $k$  of the electron momentum. Thus



$$v_{\lambda,k}(\mathbf{r}) = - \frac{\sum_{\mathbf{k}_{||}} \Psi_{\mathbf{k}_{||}}^*(\mathbf{x}_{||}) \Psi_{\mathbf{k}_{||}}(\mathbf{x}_{||}) v_{\lambda,k}(\mathbf{r})}{\sum_{\mathbf{k}_{||}} \Psi_{\mathbf{k}_{||}}^*(\mathbf{x}_{||}) \Psi_{\mathbf{k}_{||}}(\mathbf{x}_{||})} \quad (9)$$

$$\begin{aligned} & \frac{1}{\Phi_{\lambda}^*(x) \Phi_{\lambda}(x)} \int \frac{d\mathbf{r}'}{|\mathbf{r} - \mathbf{r}'|} \\ & \times \left( \Phi_{\lambda}^*(x) \Phi_{\lambda}(x') \sum_{\mathbf{k}_{||}} \Psi_{\mathbf{k}_{||}}^*(\mathbf{x}_{||}) \Psi_{\mathbf{k}_{||}}(\mathbf{x}_{||}') \sum_{\mathbf{k}'} \Psi_{\mathbf{k}'}^*(\mathbf{r}') \Psi_{\mathbf{k}'}(\mathbf{r}) \right) \\ & = - \frac{\sum_{\mathbf{k}_{||}} \Psi_{\mathbf{k}_{||}}^*(\mathbf{x}_{||}) \Psi_{\mathbf{k}_{||}}(\mathbf{x}_{||})}{\sum_{\mathbf{k}_{||}} \Psi_{\mathbf{k}_{||}}^*(\mathbf{x}_{||}) \Psi_{\mathbf{k}_{||}}(\mathbf{x}_{||})}. \end{aligned} \quad (10)$$

On solving the momentum space integrals analytically to the degree possible, and rewriting in terms of the variables  $y = k_F x$ ,  $y' = k_F x'$ ,  $y_{||} = k_F x'_{||}$ ,  $R = |y'_{||}|$ ,  $q = k/k_F$ ,  $q' = k'/k_F$ ,  $Q = (1 - q^2)^{1/2}$  and  $Q' = (1 - q'^2)^{1/2}$  where  $k_F = 1/\alpha r_s [\alpha^{-1} = (9\pi/4)^{1/3}]$  is the Fermi momentum and  $r_s$  the Wigner-Seitz radius, the above expression reduces to

$$\begin{aligned} \frac{v_{\lambda,q}(y)}{(3k_F/2\pi)} &= - \frac{8}{3Q^2 \phi_q(y)} \int_{-\infty}^{\infty} dy' \phi_q(y') \int_0^{\infty} dR \frac{Q J_1(QR)}{R \sqrt{(y - y')^2 + R^2}} \\ &\times \int_0^1 dq' \phi_q^*(y') \phi_q(y') Q' J_1(Q'R), \end{aligned} \quad (11)$$

where  $J_1(z)$  is the first-order Bessel function. At the Fermi level  $q = 1$ , so that Eq. (11) becomes

$$\begin{aligned} \frac{v_{\lambda,1}(y)}{(3k_F/2\pi)} &= - \frac{4}{3\phi_1(y)} \int_{-\infty}^{\infty} dy' \phi_1(y') \int_0^1 dq' \phi_q^*(y') \phi_q(y') Q' \\ &\times \int_0^{\infty} dR \frac{J_1(Q'R)}{\sqrt{(y - y')^2 + R^2}}, \end{aligned} \quad (12)$$

where we have employed  $\lim_{Q \rightarrow 0} J_1(QR) = QR/2$ . Finally, since the  $R$  integral can be done analytically, we have the orbital-dependent potential corresponding to the Fermi level electron with momentum perpendicular to the surface [19] to be

$$\frac{v_{\lambda,1}(y)}{(3k_F/2\pi)} = - \frac{4}{3\phi_1(y)} \int_{-\infty}^{\infty} dy' \frac{\phi_1(y')}{|y - y'|} \int_0^1 dq \phi_q^*(y') \phi_q(y) (1 - e^{-Q|y - y'|}). \quad (13)$$

We have calculated the potential  $v_{\lambda,1}(y)$  for the semi-analytical wavefunctions generated by the finite linear potential model [26] of a metal surface. These wavefunctions are highly accurate and reproduce (see the Appendix of Ref. [13]) the results of fully-self-consistent calculations [3] for the surface energy and work function of simple metals. The wavefunctions which are exponential in the classically forbidden region and oscillatory in the metal bulk are

$$\phi_k(x) = \sin[kx + \delta(k)]\theta(-x) + [B_k Ai(\zeta) + C_k Bi(\zeta)] \\ \times [\theta(x) - \theta(x-b)] + D_k \exp(-\kappa x)\theta(x-b), \quad (14)$$

where  $k = \sqrt{2E}$ ,  $\kappa = \sqrt{2(W-E)}$ ,  $\zeta = (x - E/F)/(2F)^{1/3}$ ,  $E$  is the energy,  $F$  the field strength,  $W$  the barrier height, and  $Ai(\zeta)$  and  $Bi(\zeta)$  are the Airy functions. The phase factor  $\delta(k)$  and the coefficients  $B_k$ ,  $C_k$ , and  $D_k$  are determined by the requirement of continuity of the wavefunction and its logarithmic derivative at  $x=0$  and  $x=b$ . The calculations are performed for a metal of density corresponding to  $r_s = 2.0$ . The wavefunction parameters are the same as those employed in our previous work [12,13] and once again taken from the Appendix of Ref. [13].

In Table I we quote the values of the universal function  $v_{x,1}(y)/(3k_F/2\pi)$  as a function of electron position  $y$  for distances outside the surface ranging from  $y = 10$  to  $y = 20$ . We also quote in Table I the values of the function  $-1/2y \simeq -0.24/x$  for these positions of the electron. A plot of these functions is given in Figure 1. The jellium surface edge is at  $y = 1.33$ . Note that  $y = 2\pi$  corresponds to a Fermi wavelength. Numerical calculations beyond an electron position of  $y = 20$  are difficult due to the delocalized and highly oscillatory nature of the dynamic orbital-dependent Fermi hole charge. The further out beyond the surface the electron, the deeper within the metal this charge distribution is spread. For a study of the orbital-dependent Fermi holes at a metal surface, we refer the reader to Ref. [13]. In the present calculations, the spatial integral has been performed up to approximately 75 Fermi wavelengths inside the metal. It is evident from the results that the potential  $v_{x,1}(y)$  merges with the function  $-1/2y$ . This means that for asymptotic electron positions, the total exchange potential  $\mu_x$  which is equivalent to  $v_{x,1}(y)$  there, will go as the image potential. Thus, when the asymptotic electrons are considered as part of the nonuniform system at the metal surface, the asymptotic effective potential arises solely due to exchange effects and is the image potential.

TABLE I. Values of the universal exchange potential function  $v_{x,1}(y)/(3k_F/2\pi)$  and the function  $1/2y$  for asymptotic electron positions  $y$  (in units of  $\lambda_F/2\pi$ ) in the vacuum region.

$y$	$-v_{x,1}(y)/(3k_F/2\pi)$	$-1/2y$
10	0.0592	0.0500
11	0.0524	0.0455
12	0.0470	0.0417
13	0.0421	0.0385
14	0.0384	0.0357
15	0.0352	0.0333
16	0.0326	0.0313
17	0.0303	0.0294
18	0.0283	0.0278
19	0.0263	0.0263
20	0.0251	0.0250

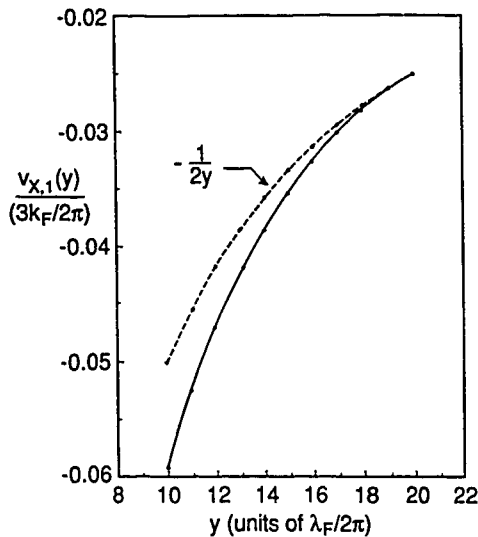


Figure 1. Variation of the universal exchange potential function  $v_{x,1}(y)/(3k_F/2\pi)$  as a function of electron position  $y$ . Here  $v_{x,1}(y)$  is the orbital-dependent exchange potential corresponding to the Fermi level. The function  $-1/2y$  is also plotted.

We also note that although the exchange potential  $v_{x,1}(y)$  due to the Fermi level electron merges with  $-1/2y$  by  $y = 19$ , it does not mean that the effective potential is the image potential from that point on. Rather it indicates that since the potential  $v_{x,1}(y)$  has the image potential structure, the asymptotic structure of the total exchange potential  $\mu_x$  will be the image potential. Near the surface other high energy electrons which lie below the Fermi level also contribute to the total exchange potential so that  $\mu_x \neq v_{x,1}(y)$  there. Therefore, in this region the Kohn-Sham effective potential will not be image-potential-like. It is only by approximately  $y = 40$  that the effective potential at the surface becomes [12,13] the image potential.

### Conclusions

To summarize, we have shown in this article that the asymptotic structure of the density-functional theory effective potential at a metal surface is the image potential, and that it arises solely due to the effects of Pauli correlations between the electrons. The calculations are rigorously quantum-mechanical in that the asymptotic electrons are treated as part of the nonuniform system with the electronic wavefunctions being explicitly employed to determine the potential. These results are entirely consistent with the conclusions of our previous work [12,13] in which the asymptotic effective potential was obtained by calculating the work required to move an electron in the force-field of the (orbital-independent) Fermi hole charge distribution. Thus, we note that *two distinctly different quantum-mechanical formulations* lead to the same conclusions.

We reiterate, however, that there are two schools of thought on the fundamental issue as to the physical origin of the asymptotic image potential at a metal surface. Whereas our present and previous work [12,13] shows this asymptotic structure to be due to Pauli correlations, the work of Eguluz et al. [7,8] indicates it to be a Coulomb-correlation effect. Further research is evidently required to better understand the source of this difference, and on this we are in agreement with these authors (see footnote 23 of Ref. [8]). On the other hand, the conclusions of semiclassical theories have little bearing on this issue. This is because the asymptotic electron is treated in these calculations as an external test charge that is distinct from the inhomogeneous electron gas at the metal surface. The resulting image potential structure of the asymptotic effective potential can therefore only arise as a consequence of correlations due to Coulomb's law.

### Acknowledgment

Acknowledgment is made to the Donors of the Petroleum Research Fund, administered by the American Chemical Society, for the support of this research.

### Bibliography

- [1] P. Hohenberg and W. Kohn, *Phys. Rev.* **136**, B864 (1964); W. Kohn and L. J. Sham, *Phys. Rev.* **140**, A1133 (1965).
- [2] R. M. Dreizler and E. K. U. Gross, *Density-Functional Theory* (Springer-Verlag, Berlin, 1990); R. G. Parr and W. Yang, *Density-Functional Theory of Atoms and Molecules* (Oxford, New York, 1989); N. H. March, *Electron Density Theory of Atoms and Molecules* (Academic, London, 1992).
- [3] N. D. Lang and W. Kohn, *Phys. Rev. B* **1**, 4555 (1970); **3**, 1215 (1971); **7**, 3541 (1973), N. D. Lang, *Solid State Physics* **28**, 225 (1973).
- [4] O. Gunnarsson, M. Jonson, and B. I. Lundqvist, *Phys. Rev. B* **20**, 3136 (1979); C.-O. Almbladh and U. von Barth, *ibid* **31**, 3231 (1985).
- [5] J. Rudnick, Ph.D. thesis, University of California, San Diego, 1970 (unpublished).
- [6] L. J. Sham, *Phys. Rev.* **B32**, 3876 (1985).
- [7] A. G. Eguluz and W. Hanke, *Phys. Rev.* **B39**, 10433 (1989).
- [8] A. G. Eguluz, M. Heinrichsmeier, A. Fleszar, and W. Hanke, *Phys. Rev. Lett.* **68**, 1359 (1992); A. G. Eguluz, J. J. Deisz, M. Heinrichsmeier, A. Fleszar, and W. Hanke, *Int. J. Quantum Chem., Quantum Chem. Symp.* **26**, 837 (1992).
- [9] L. Hedin and S. Lundqvist, *Solid State Physics* **23**, 1 (1969).
- [10] M. K. Harbola and V. Sahni, *Phys. Rev. Lett.* **62**, 489 (1989); V. Sahni and M. K. Harbola, *Int. J. Quantum Chem., Quantum Chem. Symp.* **24**, 569 (1990).
- [11] M. K. Harbola, M. Slamet, and V. Sahni, *Phys. Lett.* **A157**, 60 (1991).
- [12] M. K. Harbola and V. Sahni, *Phys. Rev.* **B39**, 10437 (1989).
- [13] V. Sahni, *Surf. Sci.* **213**, 226 (1989).
- [14] Y. Li, M. K. Harbola, J. B. Krieger, and V. Sahni, *Phys. Rev.* **A40**, 6084 (1989); V. Sahni, Y. Li, and M. K. Harbola, *Phys. Rev.* **A45**, 1434 (1992).
- [15] V. Sahni and K.-P. Bohnen, *Phys. Rev. B* **29**, 1045 (1984), *ibid* **31**, 7651 (1985), M. K. Harbola and V. Sahni, *Phys. Rev.* **B37**, 745 (1988).
- [16] C. J. Nisteruk and H. J. Juretschke, *J. Chem. Phys.* **22**, 2087 (1954), M. K. Harbola and V. Sahni, *J. Chem. Ed.* (to be published).
- [17] V. Sahni, J. Gruenebaum, and J. P. Perdew, *Phys. Rev.* **B26**, 4371 (1982); V. Sahni and M. Levy, *Phys. Rev.* **B33**, 3869 (1986).
- [18] R. T. Sharp and G. K. Horton, *Phys. Rev.* **90**, 3876 (1953); J. D. Talman and W. F. Shadwick, *Phys. Rev.* **A14**, 36 (1976).

- [19] J. Bardeen, Phys. Rev. **49**, 653 (1936).
- [20] J. C. Slater, Phys. Rev. **81**, 385 (1951)
- [21] E. Krotscheck, W. Kohn, and G.-X. Qian, Phys. Rev. **B32**, 5693 (1985).
- [22] K. Aashamar, T. M. Luke, and J. D. Talman, Phys. Rev. **A19**, 6 (1979), Y. Wang, J. P. Perdew, J. A. Chevary, L. D. Macdonald, and S. H. Vosko, Phys. Rev. **A41**, 78 (1990)
- [23] V. Sahni and C. Q. Ma, Phys. Rev. **B22**, 5987 (1980)
- [24] C. F. Fischer, *The Hartree-Fock Method for Atoms* (Wiley, New York, 1977).
- [25] J. B. Krieger, Y. Li, and G. J. Iafrate, Phys. Rev. **A45**, 101 (1992)
- [26] V. Sahni, C. Q. Ma, and J. S. Flamholz, Phys. Rev. **B18**, 3931 (1978).

Received March 17, 1993

# Correlation Corrected Band Structures of Quasi 1D and 2D Periodic Systems and Level Distributions of Disordered Chains; New Method with Correlation for Dynamic Nonlinear Optical Properties of Periodic Polymers

J. LADIK and P. OTTO

*Institute for Theoretical Chemistry and Laboratory of the National Foundation for Cancer Research of the Friedrich-Alexander University Erlangen-Nurnberg, D-8520 Erlangen, Germany*

## Abstract

In this paper, methods of correlation corrections for 1D and 2D periodic systems as well as for 1D nonperiodic polymers are reviewed. These procedures include not only the correlation correction of the total energy per unit cell, but also the recalculation (using the generalized electronic polaron model) of the band structures themselves in the periodic case, as well as the density of states (DOS) in nonperiodic chains. In both cases the inverse Dyson equation was used in an iterative way in the MP/2 and MP/3 level. The programming of the same procedure for the coupled cluster method is in progress. In a number of examples (ground state properties of  $(\text{SN})_x$ , the gap of alternating *trans*-polyacetylene, the exciton spectrum of diacetylene, polyglycine and polyalanine, of a cytosine stack, the bulk modules of polyethylene, the hopping conductivity of insulin), we have obtained quite good agreement with experiment, if a good basis set *ab initio* calculation was supplemented of the correlation correction at the bands or DOS curves, respectively. In the second part of the paper a new method is developed to take into account the simultaneous effect of a static and a periodic time-dependent electric field on the one-electron wave functions and on the total electronic energy of a periodic polymer. The method uses a variational technique (coupled Hartree-Fock equations) instead of perturbation theory for the time-dependent one-electron wave functions. The proper treatment of the potential caused by the field, which in this way does not destroy the periodicity of the polymer, as well as the inclusion of correlation at the MP/2 level of the  $t$ - and  $\omega$ -dependent quasienergy per unit cell is part of the method. Finally, it is shown how one obtains in the usual way the different polarizabilities, second- and third-order hyperpolarizability tensor elements with the help of the derivatives of the quasienergies according to the different field (both static and time-dependent) components. © 1993 John Wiley & Sons, Inc.

## Introduction

The *ab initio* Hartree-Fock (HF) theory (SCF LCAO) crystal orbital (CO) theory has been known since the early work of Löwdin [1]. Our work and the work of André et al. for 1D, 2D, and 3D periodic systems was first published in 1967 [2], and it has become since that time a standard procedure [3(b),(c)]. Closely related work was undertaken also in 1969 by Kunz [3(a)]. Computer codes also for 3D systems have been developed by Pisani's group (Crystal 80, 90, 92) [4].

As the next step, methods based on the generalization of the electronic polaron idea [5] were applied to correct the band structures themselves in the MP/2 [6], MP/3 [7], and in the coupled cluster (CCDD) approximations [8] (with localized orbitals [9]). For these calculations the inverse Dyson equation [10] (see below) was used.

For the determination of the electronic density of states (DOS) of disordered polymers, the so-called negative factor counting (NFC) procedure (based on Dean's negative eigenvalue theorem [11]) was applied both in its simple [12] and matrix block form [13]. The latter method has also been developed in a form that also takes into account correlation [14] and has been applied for several disordered polymers [15].

In all cases, when the calculations could be performed with a good enough basis set and correlation corrections were applied, for unrelated completely different physical properties, results in quite good agreement with experiments were obtained (for several examples, see the next Section).

### Short Review of the Treatment of Correlation in Periodic and Disordered Polymers

We can write the Dyson equation in a matrix form as

$$\mathbf{G} = \mathbf{G}_0 + \mathbf{G}_0 \mathbf{V} \mathbf{G}, \quad (1)$$

where  $\mathbf{G}$  is the Green's matrix of the perturbed and  $\mathbf{G}_0$  the same quantity for the unperturbed system while  $\mathbf{V}$  is the perturbation matrix. Expressing  $\mathbf{G}$  from (1), one obtains

$$\mathbf{G} = (\mathbf{1} - \mathbf{G}_0 \mathbf{V})^{-1} \mathbf{G}_0. \quad (2)$$

The poles of  $\mathbf{G}$  give the quasiparticle (QP) (correlation corrected energies) of the system:

$$0 = [(\mathbf{1} - \mathbf{G}_0 \mathbf{V})^{-1} \mathbf{G}_0]^{-1} \quad (3)$$

Writing out the inverse matrix results in

$$0 = \mathbf{G}_0^{-1} (\mathbf{1} - \mathbf{G}_0 \mathbf{V}) = \mathbf{G}_0^{-1} - \mathbf{V}. \quad (4)$$

In the diagonal approximation [10], one can write for a state  $I(i, k)$

$$0 = \omega_I - \epsilon_I^{\text{HF}} + V_{II} \quad \omega_I = \epsilon_I^{\text{HF}} + V_{II}, \quad (5)$$

which is the inverse Dyson equation where  $\omega_I$  is the QP and  $\epsilon_I$  the HF energy, respectively, and the form of  $V_{II}$  has to be determined by a (size-consistent) approximation used for the correlation, that is,  $\text{MP}_{II}^{(2)}(\omega_I)$ ,  $\text{MP}_{II}^{(2)}(\omega_I) + \text{MP}_I^{(3)}(\omega_I)$  CCSD, CCDD ( $\Sigma_{Ic}^{\text{cc}}(\omega_I) + \Sigma_{Ih}^{\text{cc}}(\omega_I)$ ), etc. Here  $\text{MP}_{II}^{(2)}(\omega_I)$ ,  $\text{MP}_{II}^{(3)}(\omega_I)$  are the Moeller-Plesset [16] expressions for state  $I$ , respectively,  $\Sigma_{Ic}^{\text{cc}}(\omega_I) + \Sigma_{Ih}^{\text{cc}}(\omega_I)$  the electron and hole self-energies obtained for the state  $I$  in a given approximation of

the coupled cluster theory (see Eqs. (9), (10), (21), and (22) of Ref. [9] for the CCDD case [17]).

To keep the discussion simple, we write down explicitly only the expression for  $MP_{1,1}^{(2)}(\omega_1)$  (MP/2):

$$MP_{1,1}^{(2)}(\omega_1) \mp \sum_{\substack{J,A,B \\ J \in \text{occ} \\ A,B \in \text{unocc}}} \frac{V_{IJAB}(2V_{IJ1B} - V_{IJB,1})}{\omega_1 + \epsilon_J^{\text{HF}} - \epsilon_A^{\text{HF}} - \epsilon_B^{\text{HF}}} + \sum_{\substack{J,A,B \\ J \in \text{unocc} \\ A,B \in \text{occ}}} \dots \quad (6)$$

Here  $V_{IJ1B}$  is, in the Bloch orbital basis, the usual two-electron integral

$$V_{IJAB} = \langle \phi_I(1)\phi_J(2) | 1/r_{12} | \phi_A(1)\phi_B(2) \rangle \quad (6')$$

One has to substitute (6) into (5) and iterate until SCF  $\omega_1$  values are obtained.

In this way, for the fundamental gap of alternating *trans*-polyacetylene in the  $MP^{(2)}$  approximation 1.8 eV [7] and in the  $MP^{(2)} + MP^{(3)}$  approximation 2.2 eV were obtained [7] in quite good agreement with experiment.

One should mention that if one is interested only in ground state properties of a polymer near to its equilibrium geometry, one obtains quite good results already with a better basis set HF calculation. Thus we have obtained good agreement with experiment in the case of  $(\text{SN})_x$  [18] for the effective mass and density of states at the Fermi level as well for the charge transfer from S to the N atom using a Gaussian lobe valence-split basis set [19].

Using the above described formalism in the MP level as starting point, Suhai has also obtained, with the aid of a generalized *ab initio* form of the intermediate exciton theory [20,21], quite good agreement with experiment for the exciton energies and intensities for polydiacetylenes, polyethylene, and a cytosine stack (showing the experimentally well-established hyperchromicity of DNA) for polyglycine and polyalanine [22].

We have performed also QP band structure calculations for different periodic 2D systems ( $\text{H}_2$  lattice, graphite, BN layer) [23]. The obtained gaps seem to be again close to the experimentally measured ones (in graphite the part of  $\vec{k}$  space is meant, where the gap is not close to zero).

In the case of polyethylene a good basis (6-31G\*\*) + correlation (MP/2) calculation has provided also very good agreement with experiment for the bulk modulus (theoretical value 303 GPa, experimental ones 250–350 GPa) [24].

Turning now to disordered quasi 1D polymers, the most accurate method seems to be the NFC one [12]. To describe this briefly one starts from the tridiagonal Hückel determinant of a finite but long disordered chain ( $N = 300\text{--}10000$  units)

$$|H(\lambda)| = \begin{vmatrix} \alpha_1 - \lambda & \beta_2 & 0 & 0 & \dots & 0 \\ \beta_2 & \alpha_2 - \lambda & \beta_3 & & & \\ 0 & \beta_3 & \alpha_3 - \lambda & \beta_4 & & \\ \vdots & & & & \ddots & \\ & & & & & \beta_N \alpha_N - \lambda \end{vmatrix} = 0 \quad (7)$$

The Hückel parameters  $\alpha$  and  $\beta$  can be determined on the basis of the band positions ( $\alpha$ ) and bandwidths ( $\beta$ ) of *ab initio* CO calculations of the components of the chain.



repeating them periodically. The determinant (7) (if we would know its roots  $\lambda$ ) could be written in the form

$$|H(\lambda)| = \prod_{j=1}^{\Lambda} (\lambda_j - \lambda). \quad (8)$$

On the other hand, with the help of a successive Gaussian elimination, (7) can be written in a didiagonal form. Then we have, instead of (8),

$$|H(\lambda)| = \sum_{i=1}^{\Lambda} \varepsilon_i(\lambda), \quad (9)$$

where the diagonal elements of the determinant  $\varepsilon(\lambda)$  (at a parameter value  $\lambda$ ) can be computed with the help of the recursion relation (which follows from the Gaussian eliminations)

$$\varepsilon_i(\lambda) = \alpha_i - \lambda - \beta_i^2 / \varepsilon_{i-1}(\lambda), \quad (10a)$$

$$\varepsilon_1(\lambda) = \alpha_1 - \lambda. \quad (10b)$$

This means that if we choose a certain parameter value  $\tilde{\lambda}_1$  in any case when an eigenvalue  $\lambda_j < \tilde{\lambda}_1$ , one obtains a negative factor in (8). Since Eqs. (8) and (9) are equal, the number of negative factors for the same  $\lambda$  has to be the same also in (9) (which can be computed easily). Choosing another trial  $\tilde{\lambda}_2$ , one obtains another number of negative factors in (8) and (9). In this way one can determine the number of eigenvalues  $\lambda_j$  which lie between the two trial values. Scanning in this way the whole spectrum and taking a dense grid, one obtains a good DOS histogram [12].

One can prove [13] that if one has matrix blocks instead of simple matrix elements in (7), relations (10a) and (10b) still hold, if we put into them instead of elements the corresponding blocks:

$$V_i(\lambda) = A_i - \lambda S_i - (B_i^+ - \lambda Q_i^+) U_{i-1}^{-1}(\lambda) (B_i - \lambda Q_i), \quad (11a)$$

$$U_i(\lambda) = A_i - \lambda S_i \quad (11b)$$

Here the  $A_i - s$  are the diagonal blocks which occur in the determinant (since in this case we have an *ab initio* formulation both at the diagonal and off-diagonal part of the determinant not simply  $\lambda$  but its product with the corresponding overlap matrices  $S_i$  and  $Q_i$ , respectively, occurs) and the off-diagonal matrix blocks  $B_i$  describe the interaction with a unit with its first neighbor. For actual calculations in the first neighbor's interactions approximation, one has to perform dimer cluster calculations. For instance, if the chain starts with the units  $AB$ , one has to perform an *ab initio* HF calculation for it:

$$F(AB) - \lambda S(AB) = \begin{pmatrix} F^A - \lambda S^A & F^{AB} - \lambda S^{AB} \\ F^{AB^T} - \lambda S^{AB^T} & F^B - \lambda S^B \end{pmatrix}. \quad (12)$$

Here  $F^A$  and  $F^B$  are  $A_1$  and  $A_2$ , respectively,  $F^{AB} = B_2$ ,  $S^A$  and  $S^B$  stand for  $S_1$  and  $S_2$ , respectively, and finally  $S^{AB} = Q_2$ .

If the chain continues with a unit  $C$ , one has to perform a cluster calculation for the dimer  $BC$ . One can build up in this way the full matrix of the whole chain from the matrix blocks belonging to the consequent dimers. One should mention that to join at  $B$  the  $AB$  and  $BC$  clusters, one has to take, for  $F^B - \lambda S^B$ ,  $\tilde{F}^B - \lambda S^B$ , where  $\tilde{F}^B = \frac{1}{2}(F_1^B + F_2^B)$  (the Fock matrix blocks corresponding to the unit  $B$  in the two different clusters  $AB$  and  $BC$ , respectively, which are not the same). Further if the chain does not show a simple translational symmetry (like in a polynucleotide or polypeptide helix), one has to be careful to perform all dimer calculations in a common coordinate system.

Having built up the  $|F - \lambda S|$  determinant in the described way of the whole chain, one can show that [12,13]

$$|F - \lambda S| = \left( \prod_{i=1}^n s_i \right) \left[ \prod_{j=1}^n (\lambda_j - \lambda) \right] = \prod_{i=1}^N \left[ \prod_{k=1}^{l_i} u_{ik}(\lambda) \right] \quad (13)$$

Here the  $s_i$  are the eigenvalues of the matrix  $S$ , the  $\lambda_j$  those of  $S^{-1/2}FS^{-1/2}$ ,  $N$  is the number of unit cells, the  $l_i$  are the dimensions of the matrices  $U_i(\lambda)$ , and finally  $u_{ik}(\lambda)$  stands for the  $k$ th eigenvalue of the matrix block  $U_i$ . Forming the matrices  $U$  with the help of relation (11), one can diagonalize them and count the number of those  $u_{ik}$  for a given  $\lambda$  that are negative. In this way, one obtains the number of states between two trial  $\lambda$  values originating from all bands. Scanning again the whole spectrum, one obtains now, in contrary to the previous band case, the total DOS.

To test this NCF matrix block method, first a periodic Gly-Gly-Ser chain (in 1:1:1 composition) was calculated, once with the help of the CO method with periodic boundary conditions and once with the matrix block NCF method. The DOS histograms obtained have shown a remarkably good agreement [25]. After this, the sequence of the Gly and Ser units was taken randomly using a Monte Carlo program. In this case the DOS histogram broadened in a very significant amount [25].

Similar calculations were performed for aperiodic DNA sequences [26] (including a part of an oncogene) and also for a larger number of aperiodic polypeptides [27]. If one has at least three or four rather different units, the DOS curves of the random chains show in all cases a very large broadening. This is different to the periodic case (like  $(ABCD)_1$ ), when very narrow nearly  $\delta$ -function-type peaks occurred [26,27]. The explanation of this phenomenon is that if one has a random sequence, a certain unit has four different left and four different right neighbors (16 possibilities with 16 different perturbations, including the two cases when one neighbor is the same as the reference unit and in one case both neighbors of the unit are the same, causing a rather larger perturbation of its level scheme). On the other hand, if one has an  $(ABCD)_1$ -like system a given unit sees always the same two (and different) neighbors.

In the case of the four-component Gly(glycine)-Ser(serine)-Cys(cysteine)-Asn(asparagine) 300 units long polypeptide [27], we have determined, with the

help of the inverse iteration method [28], the physically interesting lowest 25 unfilled levels. Namely, in a DNA-protein complex, due to the negative charge on the  $\text{PO}_4$  units and to some positively charged subunits, like arginine, in nucleohistone, most probably there is a charge transfer from DNA to the protein. The results have shown that all the states being close to the lower edge of the "conduction band" (and therefore below the mobility edge) were completely Anderson-localized on single amino acid residues.

Generalizing the approximate expression given for the primary jump rates of hoppings (hopping frequencies) by Mott and Davis [29] for the case if there are more than one orbitals per site, one can write

$$W_{i \rightarrow B} = V_{phonon} \left( \sum_{r,s} C_{i,r}^A C_{j,s}^B \langle \chi_r^A | \chi_s^B \rangle \right)^2 \exp \left[ - \frac{\Delta E_{ij}}{k_B T} \right], \quad (14)$$

where  $\Delta E_{ij} = \epsilon_j - \epsilon_i$  are the one-electron levels of the orbitals between which the hopping occurs. Finally  $\nu$  is the frequency of acoustic modes which have values in proteins between  $10^{11}$  and  $10^{12} \text{ s}^{-1}$ ; these modes in a polypeptide chain correspond to the relative vibrations of the side chains. Taking hoppings within the same residue and between first and second neighbors, we have obtained values in the order  $10^{12}$ ,  $10^7$ – $10^9$ , and  $10^5$ , respectively [28]. They have the same order of magnitude as the estimated hopping frequencies in good amorphous conductors (silicon or chalcogenides [30]).

We have repeated the whole described calculation (NFC in matrix block form, inverse iteration for the eigenvectors, and determination of the hopping frequencies), taking into account also the disulfur bridges and its experimentally determined geometry for a small protein, the hormone insulin [31]. The hopping frequencies were in order of magnitude the same as for the previously investigated four-component random (artificial) system. Applying these hopping frequencies as input for the random walk theory of Lax and coworkers [32] (after generalizing it again to arbitrary number of orbitals per site), we have determined the frequency-dependent hopping conductivity  $|\sigma(\omega)|$  of this system. We have found that in the frequency range between  $\omega = 10^4$ – $10^8$  (where measurements were performed)  $|\sigma(\omega)|$  has values between  $10^{-7} \Omega^{-1} \text{ cm}^{-1}$  and  $10^{-5} \Omega^{-1} \text{ cm}^{-1}$  [33], which fall between the experimental values found for the different chalcogenides [34].

One should mention that no correlation corrections were taken into account as first approximation in the hopping conductivity calculation of the disordered polypeptide insulin (the treatment of correlation in disordered chains see below). It looks like that, since in the  $\sigma(\omega)$  calculation only hoppings between different excited states was taken into account (the cross gap hoppings would be extremely small due to the very small Boltzmann factor in this case), though their spacing without correlation may be too large, the overall effect is not very large. Anyway, one expects that if one takes into account in a subsequent calculation also correlation, the level spacing would be generally smaller and therefore the Boltzmann factors larger. This could cause easily an increase of  $|\sigma(\omega)|$  at a given  $\omega$  value of 1 or 2 orders of magnitude. Even if this were the case, one would still remain in the upper range of the measured values of chalcogenides [34].

In this way, we could prove that there is a nonnegligible electronic conduction along a disordered polypeptide chain, if it is doped (which *in vivo* easily can happen). This was postulated by Szent-Györgyi [35,36] already in 1941 to explain different biological phenomena (electron transport through proteins at oxidation metabolism and by photosynthesis, fluorescence of a chromophore in proteins which lies far away from another chromophore which has primarily absorbed light, etc.).

We can close this review with the observation that if one performs a good basis HF CO calculation for a periodic system, correcting well enough the resulting bands for correlation, practically all kinds of physical properties of all types of polymers can be computed (using for these properties the right theory) in good agreement with experiment. This opens the possibility of predicting polymers with three to four different unrelated optimal properties ("tailor-made" polymers), which is, of course, of great practical importance. We are working now in cooperation with computer scientists on the acceleration of the different programs (direct SCF + parallelization + vectorization and some other procedures). In this way, we shall also be able to perform the above-described calculations for polymers with larger unit cells.

Returning to the case of nonperiodic polymers, one can combine the matrix-block NFC method also with the inverse Dyson equation. Namely, if

$$FU = SU\varepsilon, \quad (15)$$

where the unitary matrix  $U$  contains the vectors  $u_i$  which fulfill this equation and the diagonal matrix  $\varepsilon$  its eigenvalues, one can write

$$(F + \Delta)U = SU\omega \quad (16a)$$

with

$$\Delta = SUVU^+S \quad (16b)$$

Here the diagonal elements of  $\omega$  are the correlation corrected QP energies of the disordered system. To prove the correctness of Eqs. (16), let us substitute (16b) into (16a), multiply from the left by  $U^+$ , and take into account the normalization condition  $U^+SU = 1$ . In this way we obtain

$$U^+FU + U^+SUVU^+SU = U^+SU\omega \quad (17a)$$

$$\varepsilon + V = \omega, \quad (17b)$$

which is the well-known inverse Dyson equation, for which we can write in the diagonal approximation

$$\varepsilon_i^{\text{HF}} + V_{ii} = \omega_i \quad (i = 1, k_i). \quad (18)$$

This provides in the MP/2 approximation

$$\omega_i = \varepsilon_i^{\text{HF}} + \text{MP}_{ii}^{(2)}(\omega_i). \quad (19)$$

For the actual calculation of aperiodic polymers, one has to perform *ab initio* cluster calculations for dimers. For instance, for an  $AB$  dimer, we have now to write instead of Eq. (12)

$$F(AB) + \Delta(AB) - \lambda S(AB) \\ = \begin{pmatrix} F^A + \Delta^A - \lambda S^A & F^{AB} + \Delta^{AB} - \lambda S^{AB} \\ F^{AB^T} + \Delta^{AB^T} - \lambda S^{AB^T} & F^B + \Delta^B - \lambda S^B \end{pmatrix}. \quad (20)$$

From the dimer clusters matrices, one can construct again the determinant of the whole chain, and, for its diagonal blocks (after successive Gaussian elimination), one has now with the notations  $A_i + \Delta_i = \tilde{A}_i$ ,  $B_i + \Delta_{i+1} = \tilde{B}_i$ ,  $A_i = F^i$ ,  $B_i = F^{i,i+1}$ ,  $\Delta_{i+1} = \Delta^{i,i+1}$ ,

$$\tilde{U}_i(\lambda) = \tilde{A}_i - \lambda S_i - (\tilde{B}_i^T - \lambda Q_i^T) \tilde{U}_{i-1}^{-1} (\tilde{B}_i - \lambda Q_i). \quad (21)$$

Diagonalizing the blocks  $\tilde{U}_i(\lambda)$ , we can count again the negative eigenvalues  $\tilde{n}_i(\lambda)$  at a given  $\lambda$ . Taking a fine grid in  $\lambda$ , we can scan again the whole spectrum and find out again the total DOS, but in this case with correlation.

The described method has been successfully applied to treat several disordered polymer chains (like Li—H chains, disordered polypeptides) with correlation, which resulted again in the decrease of the gap between the "valence levels" and "conduction levels" region and decreased also the width of the allowed energy regions in the DOS histogram.

### A New Correlation Corrected Variation-Perturbation Method for the Calculation of Dynamic Polarizabilities of Polymers

#### General Formalism

In a previous paper [37], a theory for the interaction of a laser pulse with a periodic quasi 1D polymer was developed on the basis of the coupled Hartree-Fock equations. This method has considered the simultaneous effect of the electric and magnetic field of the laser, and therefore the resulting equations have become rather cumbersome. Furthermore, the perturbation term in the Hamiltonian due to the electric field ( $\tilde{E}(\vec{r}, \vec{t})\vec{r}$ ) was not partitioned into a part which shows lattice symmetry and to another one which causes change of  $\vec{k}$  of the electrons [38,39]. This method has been already successfully applied for the calculation of the static (hyper)polarizabilities of different infinite polymers ( $(H_2)_\lambda$ ,  $(H_2O)_\lambda$  and  $(LiH)_\lambda$ ) chains [40].

The other problem that was not addressed in the previous paper was the inclusion of correlation effects in the laser light-polymer interaction. To solve this formidable problem, we return to the case of the perturbation of a periodic polymer by a time-dependent periodic homogeneous electric field\*

\* To simplify the expressions, first we shall not consider in addition to the time-dependent field an additional static electric field.

$$\vec{E}_\omega = \frac{1}{2} \sum_{m=1}^N \vec{E}_0 (e^{im\omega t} + e^{-im\omega t}) \quad (22)$$

but put the magnetic vector potential  $\vec{A} = \vec{0}$ .

It should be pointed out that Rice and Handy [41,42] have already treated the effect of correlation on dynamic polarizabilities, but only for molecules. Furthermore, instead of applying a variational approach, they have used perturbation theory for the determination of the field- and time-dependent one-electron orbitals, which is certainly correct in the case of weak fields, but becomes questionable if one thinks on a later extension of the method for interactions with intense laser pulses. On the other hand, their perturbation theoretical expansion of the one-electron orbitals probably gives more insight into the physical nature of the response at different orders.

The total Hamiltonian of an  $n$ -electron system can be written as

$$\hat{H} = \hat{H}_0 + \hat{H}' \quad (23)$$

where  $\hat{H}_0$  is the usual unperturbed Hamiltonian of a system with  $n$  electrons and  $\hat{H}'$  will become, in the case of the expression (22) of  $\vec{E}$  and  $\vec{A} = \vec{0}$ ,

$$\begin{aligned} \hat{H}'(\vec{r}_1, \dots, \vec{r}_n, \vec{E}_0, \omega, t) &= -\frac{1}{2} |e| \sum_{i=1}^n \sum_{m=1}^N \vec{E}_0 (e^{im\omega t} + e^{-im\omega t}) \vec{r}_i \\ &= -|e| \sum_{i=1}^n \sum_{m=1}^N \cos m\omega t \vec{E}_0 \vec{r}_i \end{aligned} \quad (24)$$

As is well known due to the form

$$\varphi_n(\vec{k}, \vec{r}) = e^{i\vec{k}\vec{r}} u_n(\vec{k}, \vec{r}) \quad (25)$$

of a Bloch orbital, where  $u_n(\vec{k}, \vec{r})$  shows lattice periodicity,  $-|e| \vec{E} \vec{r}$  can be rewritten as [38-40]

$$-|e| \vec{E} \vec{r} = -i|e| \vec{E} e^{i\vec{k}\vec{r}} \vec{\nabla}_{\vec{k}} e^{-i\vec{k}\vec{r}} + i|e| \vec{E} \vec{\nabla}_{\vec{k}} \quad (26)$$

Here the first term on the rhs is invariant under transformations of the symmetry group of the lattice (it can be shown that it does not mix states with different  $\vec{k}$  vectors), while only the second one which has no  $\vec{r}$ -dependence can have nonzero matrix elements between Bloch orbitals with different  $\vec{k}$  vectors [39]. Thus, if one is interested only in the polarization effect of the field (which is usually the case in nonlinear optics), one has to include in  $\hat{H}'$  only the first term of the rhs of (26). Thus we can write

$$\hat{H}' = -i|e| \sum_{i=1}^n \sum_{m=1}^N \cos m\omega t \vec{E}_0 e^{i\vec{k}\vec{r}_i} \vec{\nabla}_{\vec{k}} e^{-i\vec{k}\vec{r}_i} \quad (27)$$

We can now proceed in the usual way applying Frenkel's variational principle [43]\*:

\* Lowdin and Mukherjee [44] have shown that by the variation of the expression in (27), one really obtains a stationary state if the norm of  $\Phi$  exists.

$$J = \frac{1}{T} \int_0^T \frac{\langle \Phi | \hat{H} - \partial/\partial t | \Phi \rangle dt}{\langle \Phi | \Phi \rangle}, \quad \delta J = 0. \quad (28)$$

Here  $\hat{H}$  is defined through Eqs. (23) and (27) and for the field- and time-dependent total  $n$ -electron wave function

$$\Phi(\vec{r}_1, \dots, \vec{r}_n, \vec{E}_0, \omega, t),$$

we apply the Ansatz

$$\Phi(\vec{r}_1, \dots, \vec{r}_n, \vec{E}_0, \omega, t) = e^{-iH_0 t} \hat{A} \prod_{i=1}^n \tilde{\varphi}_i(\vec{r}_i, t, \vec{E}_0, \omega) \quad (29a)$$

with

$$\begin{aligned} \tilde{\varphi}_i(\vec{r}_i, t, \vec{E}_0, \omega) \\ = \varphi_i(\vec{r}_i) + \sum_{m=1}^N [\Delta\varphi_{i,m}^+(\vec{r}_i, \vec{E}_0, \omega)e^{im\omega t} + \Delta\varphi_{i,m}^-(\vec{r}_i, \vec{E}_0, \omega)e^{-im\omega t}]. \end{aligned} \quad (29b)$$

Finally,  $H_0$  is the eigenvalue of  $\hat{H}_0$ .

Substituting (29a) with (29b) into (28) and performing all the operations and the variations according to the unknown one-electron functions  $\Delta\varphi_{i,m}^+$  and  $\Delta\varphi_{i,m}^-$ , respectively, one obtains the following coupled Hartree-Fock (RPA) equations (up to quadratic terms in  $\Delta\varphi_{i,m}^\pm$ ) [45] for their determination

$$\begin{aligned} (\hat{J}_D - \epsilon_i \pm m\omega) |\Delta\varphi_{i,m}^\pm(\vec{r}_i, \vec{E}_0, \omega)\rangle + \hat{h} |\varphi_i(\vec{r}_i)\rangle \\ + \sum_{j=1}^{n/2} \left[ \left( \left\langle \varphi_j(\vec{r}_2) \left| \frac{2 - \hat{P}_{1 \leftrightarrow 2}}{r_{12}} \right| \Delta\varphi_{j,m}^\pm(\vec{r}_2, \vec{E}_0, \omega) \right\rangle_2 \right. \right. \\ \left. \left. + \left\langle \Delta\varphi_{j,m}^\pm(\vec{r}_2) \left| \frac{1 - \hat{P}_{1 \leftrightarrow 2}}{r_{12}} \right| \varphi_j(\vec{r}_2) \right\rangle_2 \right) \right] |\varphi_i(\vec{r}_i)\rangle = 0, \\ i = 1, 2, \dots, n \quad m = 1, 2, \dots, \tilde{N}. \end{aligned} \quad (30)$$

Here  $\hat{P}_{1 \leftrightarrow 2}$  is the exchange operator,  $\epsilon_i$  the eigenvalues of the unperturbed Fock operator of the problem,

$$\hat{J}_D = \sum_{j=1}^{n/2} \left\langle \varphi_j(\vec{r}_2) \left| \frac{2 - \hat{P}_{1 \leftrightarrow 2}}{r_{12}} \right| \varphi_j(\vec{r}_2) \right\rangle_2 + \hat{H}^N, \quad (31a)$$

$$\hat{H}^N = -\frac{1}{2} \Delta_1 - \sum_{l=1}^{2N+1} \sum_{\alpha=1}^{N_n} \frac{z_\alpha}{|\vec{r}_1 - \vec{R}_\alpha^l|}. \quad (31b)$$

[ $(2N+1)$  is the number of unit cells in the polymer,  $N_n$  the number of nuclei in the unit cell,  $z_\alpha$  the charge of the  $\alpha$ th nucleus and  $\vec{R}_\alpha^l$  its position vector in the  $l$ th cell.] Furthermore, in this case,

$$\hat{h} = -\frac{1}{2} \Delta_1 + \sum_{\alpha=1}^{N_n} \frac{z_\alpha}{|\vec{r}_1 - \vec{R}_\alpha^l|}. \quad (32)$$

Introducing an LCAO expansion for the functions

$$\Delta\varphi_{i,m}^{\pm} = \sum_{q=-N}^N \sum_{s=1}^{\tilde{m}} C_{i,m,s}^{q\pm}(\vec{E}_0, \omega) \chi_s^q(\vec{r}), \quad (33)$$

where  $\tilde{m}$  is the number of basis functions in the unit cell,  $\chi_s^q$  is the  $s$ th AO in the  $q$ th cell. Substituting (33) into (30), one easily arrives at the matrix equation

$$\begin{pmatrix} A_{i,m}^- & B_i \\ B_i & A_{i,m}^+ \end{pmatrix} \begin{pmatrix} C_{i,m}^- \\ C_{i,m}^+ \end{pmatrix} = \begin{pmatrix} D_i \\ D_i \end{pmatrix}, \quad (34)$$

where

$$A_{i,m,s,v}^{0,q\pm} = \langle \chi_v^0 | (\hat{f}_D - e_i \pm m\omega) | \chi_s^q \rangle + B_{i,s,v}^{0,q} \quad (35a)$$

$$B_{i,s,v}^{0,q} = \sum_{j=1}^{n/2} \left\langle \chi_v^0(\vec{r}_1) \chi_s^q(\vec{r}_2) \left| \frac{2 - \hat{P}_{1 \rightarrow 2}}{r_{12}} \right| \varphi_i(\vec{r}_1) \varphi_j(\vec{r}_2) \right\rangle, \quad (35b)$$

$$D_{i,s}^q = \langle \chi_s^q | \hat{h} | \varphi_i \rangle. \quad (35c)$$

Equation (34) can be rewritten as

$$A_{i,m}^- C_{i,m}^- + B_i C_{i,m}^+ = D_i, \quad (36a)$$

$$B_i C_{i,m}^- + A_{i,m}^+ C_{i,m}^+ = D_i. \quad (36b)$$

Since the matrices  $A_{i,m}^{\pm}$  and  $B_i$  are, in the case of a linear chain with periodic boundary conditions, cyclic hypermatrices, they can be block-diagonalized with the help of the unitary matrix  $U$  (the  $p, q$ th block of  $U$  is  $U_{p,q} = \exp[i2\pi pq/(2N+1)]$ ) [1]

$$U^{\dagger} A_{i,m}^{-} U U^{\dagger} C_{i,m}^{-} + U^{\dagger} B_i U U^{\dagger} C_{i,m}^{+} = U^{\dagger} D_i, \quad (37a)$$

$$U^{\dagger} B_i U U^{\dagger} C_{i,m}^{-} + U^{\dagger} A_{i,m}^{+} U U^{\dagger} C_{i,m}^{+} = U^{\dagger} D_i. \quad (37b)$$

Using the notations  $A_{i,m}^{-B D} = U^{\dagger} A_{i,m}^{-} U$ , etc.,  $F_{i,m}^{\pm} = U^{\dagger} C_{i,m}^{\pm}$ , and  $G_i = U^{\dagger} D_i$ , we can write

$$A_{i,m}^{-B D} F_{i,m}^{-} + B_i^{B D} F_{i,m}^{+} = G_i, \quad (38a)$$

$$B_i^{B D} F_{i,m}^{-} + A_{i,m}^{+B D} F_{i,m}^{+} = G_i. \quad (38b)$$

This system of equations can be reduced easily to such matrix equations in which each matrix has only the order  $\tilde{m} \times \tilde{m}$ . For  $N \rightarrow \infty$ , one can introduce the continuous variable  $k = 2\pi p/a(2N+1)$  (if  $p$  runs from  $-N$  to  $N$ , the quasicrystal momentum  $k$  will have the range  $-\pi/a \leq k \leq \pi/a$  [1,2] if  $a$  is the elementary translation). In this case we can write [1,2]

$$A_{i,m}(k) F_{i,m}(k) + B_i(k) F_{i,m}^{+}(k) = G_i(k), \quad (39a)$$

$$B_i(k) F_{i,m}(k) + A_{i,m}^{+}(k) F_{i,m}^{+}(k) = G_i(k). \quad (39b)$$



Putting back the two equations in the hypermatrix form, one obtains

$$\begin{pmatrix} A_{i,m}^-(k) & B_i(k) \\ B_i(k) & A_{i,m}^+(k) \end{pmatrix} \begin{pmatrix} F_{i,m}^-(k) \\ F_{i,m}^+(k) \end{pmatrix} = \begin{pmatrix} G_i(k) \\ G_i(k) \end{pmatrix}, \quad (40)$$

which can be solved at each point  $k$  and values  $\vec{E}_0$  and  $\omega$  to obtain the coefficients  $C_{i,m}^{q\pm}(k, \vec{E}_0, \omega)$ . For this we need the back transformation\*

$$C_{i,m}^{\pm}(k, \vec{E}_0, \omega) = \hat{U} F_{i,m}^{\pm}(k, \vec{E}_0, \omega).$$

Furthermore, from the unitary transformations performed in Eqs. (37), it follows [1] that

$$A_{i,m}^{\pm}(k) = \sum_{q=-N}^N e^{ikqa} A_{i,m}^{\pm}(q), \quad (41a)$$

$$B_i(k) = \sum_{q=-N}^N e^{ikqa} B_i(q), \quad (41b)$$

$$G_i(k) = \sum_{q=-N}^N e^{ikqa} G_i(q). \quad (41c)$$

Finally the LCAO crystal orbitals can be written in the presence of the electric field  $\vec{E}_\omega$  as

$$\begin{aligned} \tilde{\varphi}_i(k, \vec{E}_0, \omega, t, \vec{r}) \\ = \frac{1}{2N+1} \sum_{q=-N}^N \sum_{s=1}^{\hat{m}} e^{ikqa} [C_{i,s}(k) + \sum_{m=1}^{\hat{N}} [C_{i,m,s}^+(k, \vec{E}_0, \omega) e^{im\omega t} \\ + C_{i,m,s}^-(k, \vec{E}_0, \omega) e^{-im\omega t}]] \chi_i^q(\vec{r}), \end{aligned} \quad (42)$$

where the coefficients  $C_{i,s}(k)$  belong to the LCAO expansion of the unperturbed crystal orbital  $\varphi_i(k, \vec{r})$ .

We can define  $\vec{E}$  instead of (23) in the more general form

$$\vec{E} = \vec{E}_{st} + \vec{E}_\omega = \vec{E}_{st} + \frac{1}{2} \sum_{m=1}^{\hat{N}} \vec{E}_0 (e^{im\omega t} + e^{-im\omega t}), \quad (43)$$

including the static field  $\vec{E}_{st}$ .

For the determination of the effect of  $\vec{E}_{st}$  on the one-electron wave functions, one can apply perturbation theory [40] with the perturbation operator

\* Actually  $\hat{U}$  and  $\hat{U}^*$  are those blocks of  $U$  and  $U^*$ , respectively, that are necessary for the transformations of these vectors. For instance, in the equation

$$\begin{aligned} U^* C_{i,m}^+(k) &= F_{i,m}^+(k), \\ \hat{U}^* C_{i,m}^+(k) &= \sum_{l=1}^{2N+1} U_l^*(k) C_{i,m,l}(k) = F_{i,m}^+(k), \end{aligned}$$

where  $U_l^*(k)$  stands for the  $l$ ,  $l$ th block (considering  $k$  as a discrete variable which has  $2N+1$  possible values) of the big matrix  $U^*$

$$\hat{H}_{st} = -i|e|\vec{E}_{st}e^{i\vec{k}\vec{r}}\vec{\nabla}_k e^{-i\vec{k}\vec{r}}. * \quad (44)$$

If we apply again an LCAO expansion for the part of the one-electron wave functions due to this perturbation (44) can be written as

$$\varphi_i^{st}(\vec{r}_1, \vec{E}_{st}) = \sum_{q=-N}^N e^{ikqa} \sum_{s=1}^{\hat{m}} \tilde{C}_{i,s}(k, \vec{E}_{st}) \chi_s^q(\vec{r}_1). \quad (45)$$

We can apply again the same formalism for a periodic chain as before to find out the coefficients  $C(k)$  [40].

Thus we can write now for the one-electron wave functions

$$\begin{aligned} \tilde{\varphi}_i = \tilde{\varphi}_i(\vec{r}_1, t, \omega, \vec{E}_{st}, \vec{E}_0) &= \varphi_i(\vec{r}_1, k) + \varphi_i^{st}(\vec{r}_1, \vec{E}_{st}, k) \\ &+ \sum_{m=1}^{\hat{N}} (\Delta\varphi_{i,m}^+(\vec{r}_1, \vec{E}_0, \omega, k)e^{im\omega t} + \Delta\varphi_{i,m}^-(\vec{r}_1, \vec{E}_0, \omega, k)e^{-im\omega t}). \end{aligned} \quad (46)$$

Thus we can finally write

$$\begin{aligned} \tilde{\varphi}_i(\vec{r}, t, \omega, k, \vec{E}_{st}, \vec{E}_0) \\ = \frac{1}{2N+1} \sum_{q=-N}^N \sum_{s=1}^{\hat{m}} e^{ikqa} \left\{ C_{i,s}(k) + \tilde{C}_{i,s}(k, \vec{E}_{st}) \right. \\ \left. + \sum_{m=1}^{\hat{N}} [C_{i,m,s}^+(k, \vec{E}_0, \omega)e^{im\omega t} + C_{i,m}^-(k, \vec{E}_0, \omega)e^{-im\omega t}] \right\}. \end{aligned} \quad (47)$$

### Definition of the Quasi-Hartree-Fock Equations

We can build up the total wave function of the polymer now with the help of the generalized crystal orbitals (46) as

$$\tilde{\Phi}(\vec{r}_1, \dots, \vec{r}_n, k, t, \omega, \vec{E}_{st}, \vec{E}_0) = e^{-iH_0 t} \hat{A} \prod_{i=1}^n \tilde{\varphi}_i(\vec{r}_i, t, k, \omega, \vec{E}_{st}, \vec{E}_0). \quad (48)$$

With the help of (48) we can now define a quasienergy of the polymer in the presence of the static and time-dependent field as

$$W(k, t, \omega, \vec{E}_{st}, \vec{E}_0) = \frac{\langle \tilde{\Phi}(k) | \hat{H} \tilde{\Phi}(k) \rangle}{\langle \tilde{\Phi}(k) | \tilde{\Phi}(k) \rangle}. \quad (49)$$

\* One should point out that if one takes into account also the effect of  $E_{st}$  in the coupled Hartree-Fock equations (30), one has to put instead of  $\varphi_i(\vec{r}_i)$  and  $\epsilon_i$ , respectively,  $\varphi_i(\vec{r}_i) + \varphi_i^{st}(\vec{r}_i, E_{st})$  and  $\epsilon_i + \Delta\epsilon_i^{st}$ , respectively. Here  $\Delta\epsilon_i^{st}$  is the shift of the eigenvalues of the unperturbed Fock operator  $\epsilon_i$  due to the perturbation [45]

Here the brackets mean only integrations according to the spatial variables of the  $n = (2N + 1)\tilde{n}$  electrons ( $\tilde{n}$  is the number of electrons in the unit cell).

Since the crystal orbitals  $\tilde{\varphi}_i$  still have to be orthonormal,  $\langle \tilde{\varphi}_i | \tilde{\varphi}_j \rangle = \delta_{ij}$ ,\* we can write the variational equation

$$\delta[W(k, t, \omega, \vec{E}_{st}, E_0) + \sum_{i,j} \varepsilon_{ij} \langle \tilde{\varphi}_i | \tilde{\varphi}_j \rangle] = 0. \quad (50)$$

where in (49) the total Hamiltonian is defined in the general case as

$$\hat{H} = \hat{H}_0 + \hat{H}',$$

with

$$\hat{H}' = -ie|\sum_{i=1}^n \sum_{m=1}^N [\vec{E}_{st} + \frac{1}{2}\vec{E}_0(e^{im\omega t} + e^{-im\omega t})]e^{i\vec{k}\vec{r}_i}\vec{\nabla}_i e^{-i\vec{k}\vec{r}_i}, \quad (51)$$

and  $\hat{H}_0$  is unperturbed many-electron Hamiltonian of the polymer.

With this definition of  $\hat{H}$ , one can obtain with the help of the usual variational procedure for given  $t$ ,  $\omega$ , and  $k$  values and for vectors  $\vec{E}_{st}$  and  $\vec{E}_0$ , respectively, the quasi Hartree-Fock equations

$$\hat{F}(\vec{E}_{st}, \vec{E}_0, \omega, t, k)\psi_j = \tilde{\varepsilon}_j(\vec{E}_{st}, \vec{E}_0, \omega, t, k)\psi_j(\vec{r}, \omega, t, k, \vec{E}_{st}, \vec{E}_0) \quad (52a)$$

$[\psi_j = \tilde{\varphi}_j$ ; see Eq. (46)] with quasi-Fock operators

$$\hat{F}(\vec{E}_{st}, \vec{E}_0, \omega, t, k) = \hat{H}^N(\vec{E}_{st}, E_0, \omega, t, \vec{r}_1) + \sum_{j=1}^{n/2} (2\hat{J}_j - \hat{K}_j). \quad (52b)$$

Here the quasi-Coulomb operators  $\hat{J}_j$  and quasiexchange operators  $\hat{K}_j$  are defined in the usual way but not with the help of the unperturbed crystal orbitals  $\varphi_j$ , but with the perturbed ones  $\psi_j$ . Furthermore,

$$\hat{H}^N = \hat{H}^A + \sum_{m=1}^N [\vec{E}_{st} + \frac{1}{2}\vec{E}_0(e^{im\omega t} + e^{-im\omega t})]e^{i\vec{k}\vec{r}}\vec{\nabla}_k e^{-i\vec{k}\vec{r}} \quad (52c)$$

( $\hat{H}^N$  is the one-electron operator of the unperturbed polymer).

Substituting the LCAO expression of (46) into (52a) one obtains in the usual way the matrix equation

$$\tilde{F}(k, \omega, t, \vec{E}_{st}, \vec{E}_0)\mathbf{d}_j(k, \omega, t, \vec{E}_{st}, \vec{E}_0) = \tilde{\varepsilon}_j(k, \omega, t, \vec{E}_{st}, \vec{E}_0)\mathbf{S}\mathbf{d}_j. \quad (53a)$$

Here matrix elements of  $\tilde{F}$  are defined as

$$[\tilde{F}(k)]_{r,s} = \sum_{q=1}^N e^{ikqa} \langle \chi_r^0 | \hat{F} | \chi_s^q \rangle \quad (53b)$$

\* Even if the orbitals  $\varphi_i^a$  and  $\tilde{\varphi}$  are orthonormal,  $\langle \varphi_i^a | \varphi_j^a \rangle = \delta_{ij}$ ,  $\langle \tilde{\varphi}_i | \tilde{\varphi}_j \rangle = \delta_{ij}$ , their sum  $\tilde{\varphi}_i$  does not form an orthonormal orbital set. We can apply Schmidt's orthogonalization procedure and renormalize also the orbitals  $\tilde{\varphi}_i$ . In this way we can also write  $\langle \tilde{\varphi}_i | \tilde{\varphi}_j \rangle = \delta_{ij}$ .

with  $\hat{F}$  given in (52b).  $S(k)$  has the elements

$$[S(k)]_{r,v} = \sum_{q=-N}^N e^{ikqa} \langle \chi_r^0 | \chi_v^q \rangle, \quad (53c)$$

and the vectors  $\mathbf{d}_j$  are defined as

$$\begin{aligned} \mathbf{d}_j(k, \dots) &\equiv \mathbf{C}_j(k) + \tilde{\mathbf{C}}_j(k, \tilde{\mathbf{E}}_{st}) \\ &+ \sum_{m=1}^N [\mathbf{C}_{j,m}^+(k, \tilde{\mathbf{E}}_0, \omega) e^{im\omega t} + \mathbf{C}_{j,m}^-(k, \tilde{\mathbf{E}}_0, \omega) e^{-im\omega t}]. \end{aligned} \quad (53d)$$

With these definitions one can solve Eq. (53a) for given  $k$ ,  $\omega$ ,  $t$ ,  $\tilde{\mathbf{E}}_{st}$ , and  $\tilde{\mathbf{E}}_0$  in the same iterative way as one does in the unperturbed case. In this way one can obtain the SCF quasi-Fock operator  $\hat{F}^{\text{SCF}}$  and with the help of (52b) the SCF quasicrystal orbitals

$$\psi_j(\tilde{\mathbf{r}}, \dots)^{\text{SCF}} = \frac{1}{2N+1} \sum_{q=-N}^N e^{ikqa} d_{j,q}(k, t, \omega, \tilde{\mathbf{E}}_{st}, \tilde{\mathbf{E}}_0) \chi_q^j(\tilde{\mathbf{r}}) \quad (54)$$

and the SCF quasi one-electron energies  $\tilde{\epsilon}_j^{\text{SCF}}$ . These quantities are needed in the subsequent treatment of correlation.

One should mention that in the possible case if the iteration procedure for  $\hat{F}$  does not converge, one can still use the orbitals  $\psi_j$  [see Eq. (46)] (after orthogonalization and renormalization) as one-electron orbitals for an MP/2 calculation, and one just can approximate the quasi one-electron energies  $\epsilon$  as

$$\tilde{\epsilon}_j = \langle \psi_j | \hat{F} | \psi_j \rangle. \quad (55)$$

### Moeller-Plesset Perturbation Theory

After having computed the quasi one-electron orbitals  $\psi_j$  and quasi one-electron energies  $\tilde{\epsilon}_j$ , one can apply the MP/2 expression for the second-order correlation correction of the quasitotal energy (49) for given  $k$ ,  $\omega$ ,  $t$ ,  $\tilde{\mathbf{E}}_{st}$ , and  $\tilde{\mathbf{E}}_0$ . In this case the Moeller-Plesset perturbation operator will be

$$\hat{H}_{\text{MP}} = \sum_{i < j} \frac{1}{r_{ij}} - \sum_{\text{occ}} \hat{F}(\tilde{\mathbf{r}}, t, \omega, k, \tilde{\mathbf{E}}_{st}, \tilde{\mathbf{E}}_0) = \sum_{i < j} \frac{1}{r_{ij}} - nF \quad (56)$$

( $n = \tilde{n}(2N+1)$ ). With the definition (56), one can derive in the standard way [46] the second-order correction to the quasitotal energy (for given  $t$ ,  $\omega$ ,  $\tilde{\mathbf{E}}_{st}$ , and  $\tilde{\mathbf{E}}_0$ )

$$\hat{E}_{\text{MP}}^{(2)} = \sum_{I, J, 1, B} \frac{|\langle \psi_I(\tilde{\mathbf{r}}_1, \dots) \psi_J(\tilde{\mathbf{r}}, \dots) | (1/r_{12}) \times (1 - \hat{P}_{1 \rightarrow 2}) | \psi_I(\tilde{\mathbf{r}}_1, \dots) \psi_B(\tilde{\mathbf{r}}_2, \dots) \rangle|}{\tilde{\epsilon}_I + \tilde{\epsilon}_J - \tilde{\epsilon}_1 - \tilde{\epsilon}_B}. \quad (57)$$

Here, of course,  $E_{\text{MP}}^{(2)}(t, \omega, \tilde{\mathbf{E}}_{st}, \tilde{\mathbf{E}}_0)$ , because the perturbed crystal orbitals  $\psi_I(\tilde{\mathbf{r}}, \dots)$  and quasi one-electron energies depend on the same variables (this is meant in the argument of the  $\psi_I$ , etc. by the three points). The  $k$ -dependence is ex-

pressed by the combined indices  $I = i, k_i$ , etc. Therefore, the fourfold summation includes the threefold integration over  $k$  (because of the conservation of momenta  $k_i + k_j = k_a + k_b$ ) (for the details, how one calculates the matrix elements  $\langle \psi_i \psi_j | | \psi_a \psi_b \rangle$  occurring in (57) see again [46]).

After having calculated  $\tilde{E}_{\text{MP}}^{(2)}$ , we can write for the total energy with second-order correlation correction

$$\tilde{E}(t, \omega, \tilde{E}_{\text{st}}, \tilde{E}_0) = \frac{a}{2\pi} \int_{-\pi/a}^{\pi/a} W[k, t, \omega, \tilde{E}_{\text{st}}, \tilde{E}_0] dk + \tilde{E}_{\text{MP}}^{(2)}(t, \omega, \tilde{E}_{\text{st}}, \tilde{E}_0). \quad (58)$$

The development of the program package for the rather complicated formalism developed here and in the previous two subsections is in progress in our laboratory.

### *The Calculation of the Polarizabilities and Hyperpolarizabilities*

Having the quasi total energy (58), we can formally express it in the presence of the electric field

$$\tilde{E} = \tilde{E}_{\text{st}} + \tilde{E}_\omega = \tilde{E}_{\text{st}} + \frac{1}{2} \sum_{m=1}^{\infty} \tilde{E}_0 (e^{im\omega t} + e^{-im\omega t}) = \tilde{E}_{\text{st}} + \sum_{m=1}^{\infty} E_0 \cos m\omega t \quad (59)$$

as

$$\begin{aligned} \tilde{E}(t, \omega, \tilde{E}_{\text{st}}, \tilde{E}_0) = & E_{\text{HF}}^{(0)} + E_{\text{MP}}^{(2)} + \mu_0^+ \mathbf{E}_{\text{st}} + \mathbf{E}^+ \alpha(\omega) \mathbf{E} \\ & + \frac{1}{2} \mathbf{E}^+ \beta \mathbf{E} \mathbf{E} + \frac{1}{3!} \mathbf{E}^+ \gamma E^2 \mathbf{E} + \dots, \end{aligned} \quad (60)$$

where  $E_{\text{HF}}^{(0)}$  and  $E_{\text{MP}}^{(2)}$  are the Hartree-Fock and MP/2 energies of the polymer in the absence of the field and

$$\mu_0 = \mathbf{d}_{\text{st}} \mathbf{E}_{\text{st}} + \frac{1}{2} \mathbf{E}_{\text{st}}^+ \beta_{\text{st}} \mathbf{E}_{\text{st}} + \frac{1}{3!} \mathbf{E}_{\text{st}}^+ \gamma_{\text{st}} \mathbf{E}_{\text{st}} \mathbf{E}_{\text{st}} + \dots \quad (61)$$

is the part of the induced dipole moment due to the static field. It can be easily calculated with the aid of the expression

$$\begin{aligned} \mu_0 = & 2 \frac{a}{2\pi} \sum_{i=1}^n \int_{-\pi/a}^{\pi/a} \left\langle [\varphi_i(\tilde{\mathbf{r}}_i, k) + \varphi_i^{\text{st}}(\tilde{\mathbf{r}}_i, \tilde{E}_{\text{st}}, k)] \right. \\ & \times \sum_{i=1}^n \hat{\mu}_i [\varphi_i(\tilde{\mathbf{r}}_i, k) + \varphi_i^{\text{st}}(\tilde{\mathbf{r}}_i, \tilde{E}_{\text{st}}, k)] \Bigg\rangle dk, \end{aligned} \quad (62)$$

where the dipole moment operator  $\hat{\mu}_i = |e| \tilde{\mathbf{r}}_i$ .

Using expressions (49), (58), and (59), one can apply the time-independent Hellmann-Feynman theorem [46]

$$\frac{\partial \tilde{E}}{\partial \tilde{E}_{\text{st}}} = \langle \tilde{\Phi} | \partial \tilde{H} / \partial \tilde{E}_{\text{st}} | \tilde{\Phi} \rangle \quad (63)$$

(for the conditions of its validity, see [42,44]). Here  $\hat{E}$  is the total energy [see Eq. (59)],  $\Phi$  the many electron wave function [see Eq. (48)] and  $\hat{H}$  the full perturbed Hamiltonian [see Eq. (51)] (if we neglect overtones in the expression of  $\tilde{E}_\omega$ , that is, we put  $m = 1$ ). On the basis of Eq. (63), we can write following [42] but using our notation

$$\mu_0^\lambda = - \frac{\partial \tilde{E}}{\partial E_{st,\lambda}} \bigg|_{\vec{l}=0}, \quad (64a)$$

$$\alpha^{\lambda\mu}(0, 0) = - \frac{\partial^2 \tilde{E}}{\partial E_{st,\lambda} \partial E_{st,\mu}} \bigg|_{\vec{l}=0}, \quad (64b)$$

$$\beta^{\lambda\mu\nu}(0; 0, 0) = - \frac{\partial^3 \tilde{E}}{\partial E_{st,\lambda} \partial E_{st,\mu} \partial E_{st,\nu}} \bigg|_{\vec{l}=0}, \quad (64c)$$

$$\alpha^{\lambda\mu}(-\omega; \omega) \cos \omega t = - \frac{\partial^2 \tilde{E}}{\partial E_{st,\lambda} \partial E_{\omega,\mu}} \bigg|_{\vec{l}=0}, \quad (65a)$$

$$\frac{1}{2} \beta^{\lambda\mu\nu}(0; -\omega, \omega) + \frac{1}{2} \beta^{\lambda\mu\nu}(-2\omega; \omega, \omega) \cos \omega t = - \frac{\partial^3 \tilde{E}}{\partial E_{st,\lambda} \partial E_{\omega,\mu} \partial E_{\omega,\nu}} \bigg|_{\vec{l}=0}, \quad (65b)$$

and finally

$$\beta^{\lambda\mu\nu}(-\omega; 0, \omega) \cos \omega t = - \frac{\partial^3 \tilde{E}}{\partial E_{st,\lambda} \partial E_{\omega,\mu} \partial E_{\omega,\nu}} \bigg|_{\vec{l}=0} \quad (65c)$$

In these equations  $E_{st,\lambda}$  and  $E_{\omega,\mu}$ , respectively, are the  $\lambda$ th component of  $\tilde{E}_{st}$  and the  $\mu$ th one of  $E_\omega$ , respectively. Furthermore, we can determine  $\beta^{\lambda\mu\nu}(0, -\omega, \omega)$  and  $\beta(-2\omega, \omega, \omega)$  separately from Eq. (65b) if we compare the coefficients of the terms containing as factor  $\cos \omega t$  and those of the constant terms. One can deduce also the symmetry relation

$$\beta^{\lambda\mu\nu}(0; \omega, -\omega) = \beta^{\nu\lambda\mu}(\omega; 0, \omega) \quad [42]. \quad (66)$$

There are, of course, more combinations in  $\omega$  in the  $\beta$  possible, but they are not measurable at the present time [42].

Formally one can write also for the elements of  $\gamma$  similar expressions as fourth derivatives of  $\tilde{E}$ . For instance,

$$\gamma^{\lambda\mu\nu\kappa}(-\omega; 0, 0, \omega) \cos \omega t = - \frac{\partial^4 \tilde{E}}{\partial E_{st,\mu} \partial E_{st,\nu} \partial E_{\omega,\lambda} \partial E_{\omega,\kappa}} \quad (67)$$

## Conclusion

It was shown that if the coupled Hartree-Fock equations based on Frenkel's variational principle are applied for the determination of the  $\omega$  depending part of the one-electron wave functions in the presence of  $E_\omega$ , one can easily define a  $\omega$ , and field-dependent quasienergy as Rice and Handy [41,42] did in their per-

turbational theoretical approach to the determination of the orbitals. One can also add to  $E_\omega$  a static field  $E_{st}$  and define the quasienergy with its inclusion. From this quasienergy quasi Hartree-Fock equations were derived with Fock operators  $\hat{F}(t, \omega, E_{st}, E_0)$  which give rise also to one-electron energies  $\tilde{\epsilon}_i$ , which depend on the same quantities as  $\hat{F}$ . The whole formalism was extended from molecules also to periodic polymers. Finally the quasi MP/2 energies for polymers  $\tilde{E}_{MP}^{(2)}$  were also derived. Adding those to the SCF quasitotal energies, one obtains the total energy of a polymer per unit cell  $\tilde{E}(\omega, t, E_{st}, E_0)/(2N + 1)$ .

With the aid of these quantities the polarizability and hyperpolarizability tensor elements can be expressed in the usual way [41,42]. Very probably for the necessary numerical derivatives the same procedures can be applied as before [41,42]. The programming of our coupled HF equations in the presence of  $E = E_{st} + E_\omega$  for a linear polymer as well as the correction of its quasitotal energy per unit cell for correlation is in progress.

As next step we plan to apply a laser pulse instead of  $E(t)$  which means that the magnetic vector potential  $A_\omega \neq 0$ , but

$$A_\omega = \sum_{m=1}^{\infty} [A_0 e^{im\omega t} + A_0^* e^{-im\omega t}]$$

(as it was done before without correlation and without the correct treatment of lattice symmetry in [37]). Finally, we plan to extend the theory to 2D and later also to 3D periodic lattices.

### Acknowledgments

We should like to express our gratitude to Professors J. Čížek, L. Dalton, F. Martino, M. Seel, and S. Suhai and to Drs. A. K. Bakhshi and Y. Ye, who have contributed with their results significantly to this paper, for the fruitful discussions with them. Further the financial support of Siemens AG (by providing free computer time) and of the "Fonds der Chemischen Industrie" is gratefully acknowledged.

### Bibliography

- [1] P.-O. Lowdin, *Adv. Phys.* **5**, 1 (1956).
- [2] G. Del Re, J. Ladik, and G. Biczó, *Phys. Rev.* **155**, 967 (1967); J.-M. André, L. Gouverneur, and G. Leroy, *Int. J. Quant. Chem.* **1**, 427, 451 (1967).
- [3] (a) B. Kunz, *Phys. Stat. Sol.* **36**, 301 (1969). (b) J. Ladik, *Quantum Theory of Polymers as Solids* (Plenum, New York, London, 1988). (c) J.-M. André, J. Delhalle, and J.-L. Brédas, in *Quantum Chemistry: Aided Design of Organic Polymers*, World Scientific, Lecture and Course Notes in Chemistry, S. A. Lin, Ed. (World Scientific, Singapore, London, Hong Kong, 1991), Vol. 2.
- [4] C. Pisani, R. Dovesi, and G. Roetti, *Lecture Notes in Chemistry* **48** (Springer-Verlag, Berlin, Heidelberg, New York, 1988).
- [5] Y. Toyozawa, *Progr. Theor. Phys. (Kyoto)* **12**, 422 (1954).
- [6] S. Suhai, *Phys. Rev. B* **27**, 3506 (1983), Ref. [36], Sec. 5.3.
- [7] C.-M. Liegener, *J. Chem. Phys.* **88**, 6999 (1988).
- [8] W. Forner, *Int. J. Quant. Chem.* **43**, 221 (1992).
- [9] W. Forner, J. Ladik, P. Otto, and J. Čížek, *Chem. Phys.* **97**, 251 (1985).

- [10] L. S. Cederbaum and W. Domcke, *Adv. Chem. Phys.* **36**, 205 (1977).
- [11] P. Dean, *Proc. Roy. Soc. London Ser. A* **254**, 260, 263 (1961); *Rev. Mod. Phys.* **44**, 127 (1972)
- [12] M. Seel, *Chem. Phys.* **43**, 103 (1979); Ref. [36], Chap. 4
- [13] R. S. Day and F. Martino, *Chem. Phys. Lett.* **84**, 86 (1981), Ref. [2], Chap. 4.
- [14] C.-M. Liegener, *Chem. Phys.* **133**, 173 (1989).
- [15] C.-M. Liegener, A. K. Bakhshi, A. Sutjianto, and P. Otto, *Chem. Phys.* **133**, 177 (1989), C.-M. Liegener, A. Sutjianto, and J. Ladik, *Chem. Phys.* **145**, 385 (1990).
- [16] C. Moeller and M. S. Plesset, *Phys. Rev.* **46**, 618 (1934).
- [17] J. Čížek, *J. Chem. Phys.* **45**, 4256 (1966); *Adv. Quant. Chem.* **53**, 35 (1969)
- [18] S. Suhai and J. Ladik, *Solid State Comm.* **22**, 227 (1977).
- [19] B. Roos and P. Siegbahn, *Theor. Chim. Acta (Berlin)* **18**, 209 (1970).
- [20] Y. Takeuti, *Progr. Theor. Phys. (Kyoto)* **18**, 421 (1957).
- [21] S. Suhai, *Phys. Rev.* **B29**, 4570 (1984)
- [22] Ref. [36], Chap. 8, original references and details
- [23] M. Vračko, C.-M. Liegener, and J. Ladik, *Chem. Phys.* **126**, 255 (1988), *Chem. Phys. Lett.* **153**, 166 (1988); *Int. J. Quant. Chem.* **37**, 241 (1990).
- [24] S. Suhai, *J. Polym. Sci. Polym. Phys. Ed.* **21**, 134 (1983)
- [25] S. Suhai, J. Kasper, and J. Ladik, *Int. J. Quant. Chem.* **17**, 995 (1980)
- [26] A. K. Bakhshi, P. Otto, J. Ladik, and M. Seel, *Chem. Phys.* **108**, 223 (1986)
- [27] A. K. Bakhshi, J. Ladik, M. Seel, and P. Otto, *Chem. Phys.* **108**, 233 (1986), A. K. Bakhshi, P. Otto, and J. Ladik, *J. Mol. Struct. (Theochem)* **180**, 113 (1988); A. K. Bakhshi, P. Otto, C.-M. Liegener, E. Rehm, and J. Ladik, *Int. J. Quant. Chem.* **38**, 573 (1990).
- [28] J. H. Wilkinson, *The Algebraic Eigenvalue Problem* (Clarendon, Oxford, 1965), p. 633.
- [29] N. F. Mott and E. A. Davis, *Electronic Processes in Non-Crystalline Materials* (Clarendon, Oxford, 1971).
- [30] M. Silver, G. Schoenherr, and G. Baessler, *Phys. Rev. Lett.* **48**, 352 (1982)
- [31] Y. Ye and J. Ladik, *J. Math. Chem.* (to appear).
- [32] H. Scher and M. Lax, *Phys. Rev. B* **7**, 4491 (1973), T. Odagaki and M. Lax, *Phys. Rev. B* **24**, 5284 (1981); **26**, 6480 (1982).
- [33] Y. Ye and J. Ladik, *Phys. Rev. B* (to appear)
- [34] N. F. Mott and E. A. Davis, *Electronic Processes in Non-Crystalline Materials* (Clarendon, Oxford, 1971), p. 215.
- [35] A. Szent-Gyorgyi, *Science* **93**, 607 (1941).
- [36] A. Szent-Gyorgyi, *Nature* **148**, 157 (1941).
- [37] J. Ladik and L. R. Dalton, *J. Mol. Struct. (Theochem)* **231**, 77 (1991).
- [38] N. F. Mott and H. Jones, *The Theory of the Properties of Metals and Alloys* (Oxford University Press, Oxford, 1936).
- [39] C. Kittel, *Quantenchemie der Festkörper* (Oldenburg, Munich, Vienna, 1970)
- [40] P. Otto, *Phys. Rev.* **B45**, 10876 (1992)
- [41] J. E. Rice and N. C. Handy, *J. Chem. Phys.* **94**, 4959 (1991)
- [42] J. E. Rice and N. C. Handy, *Int. J. Quant. Chem.* **43**, 91 (1992).
- [43] J. Frenkel, *Wave Mechanics, Advanced General Theory* (Dover, New York, 1950).
- [44] P.-O. Lowdin and P. K. Mukherjee, *Chem. Phys. Lett.* **14**, 1 (1972)
- [45] J. Ladik, *J. Mol. Struct. (Theochem)* **199**, 55 (1989).
- [46] Ref. [36], Sec. 5.2.

Received May 13, 1993



# Third-Order Møller–Plesset Perturbation Theory of Electron Correlation in Infinite Systems: A Comparison of Carbon- and Silicon-Based Polymers

S. SUHAI

Molecular Biophysics Department, German Cancer Research Center, Im Neuenheimer Feld 280,  
D-69120 Heidelberg, Federal Republic of Germany

## Abstract

The structural and electronic properties of polysilane,  $(\text{SiH}_2)_n$ , and polysilene,  $(\text{SiH})_n$ , will be compared with their carbon-based analogues polyethylene,  $(\text{CH}_2)_n$ , and polyacetylene,  $(\text{CH})_n$ , as investigated by the *ab initio* crystal orbital method using several, partly highly polarized, atomic basis sets of increasing size at the Hartree–Fock (HF) level and by including electron correlation effects up to the third order of Møller–Plesset perturbation theory. The single-particle energy bands have also been corrected for correlation effects applying the electron polaron quasiparticle (QP) method. Electron correlation plays an essential role in stabilizing the *gauche* conformation of polysilane against the *trans* form. While the *gauche*–*trans* energy difference is about 0.25 eV at the HF level, it will be reduced to about –0.8 eV due to correlation. Also the energy bands and band gaps will be substantially modified in going from the HF to the QP description, resulting in  $\Delta E_{\text{gap}} = 9.5$  and 11.8 eV for *trans* and *gauche* polysilane at HF, and 5.12 and 5.56 eV at the QP level, respectively. Polysilene turns out to be a semiconductor (similar to polyacetylene) for which bond-alternation energetically stabilizes the semiconducting phase (as compared to the equidistant, metallic one) by 1.4 eV at the HF and by 0.6 eV at the MP2 levels, with bond alternations of  $\Delta R = 0.1327$  and 0.0865 Å, respectively. © 1993 John Wiley & Sons, Inc.

## Introduction

Experimental and theoretical research of the past decade convincingly demonstrated several interesting physical and chemical properties of carbon-based organic polymers like polyacetylenes,  $(\text{CH})_n$ , with a wide range of new technological potentials [1]. The experience with this type of materials has led to the common belief that the efficient charge and energy transport phenomena in organic polymers should be related to their extended  $\pi$ -conjugated double-bond system. Some early band structure calculations on the  $\sigma$ -bonded backbone of polypeptides [2,3] indicated, however, that efficient electron delocalization may also result without  $\pi$ -electrons. In fact, theoretical effective mass and mobility values for both electrons and holes indicated more pronounced semiconductive properties in a two-dimensional polypeptide sheet along the  $\sigma$ -bonded backbone of the amino acid residues than in the perpendicular direction, between the  $\pi$ -electron systems of the peptide units.

Recent experimental progress in investigating a relatively new class of silicon-based materials, the polydiorganosilylenes (polysilanes),  $(\text{SiR}_1\text{R}_2)_n$ , with a backbone comprised entirely of Si—Si  $\sigma$ -bonds, has shown, on the other hand,

that  $\sigma$ -bonded polymers are capable of delocalizing their electrons much in the same manner as normally ascribed to the more familiar  $\pi$ -conjugated materials like polyacetylenes, polydiacetylenes, etc. It is a striking observation that, though polysilanes are the structural analogues of polyolefins (e.g., polyethylene), their electronic and optical properties resemble more closely those of quasi-one-dimensional  $\pi$ -conjugated polymers (like polyacetylenes). They exhibit, for instance, a strong and conformationally dependent optical absorption in the near UV [4-17], possess relatively low-lying ionization potentials [18,19], and show an excellent nondispersive photoconductivity [20,21]. Whereas the use of polysilanes as photoconductors depends on their ability to transport charge (they can be doped to about 1 S/cm [22]), their application in nonlinear optical devices [23-25] takes advantage of their unusually high capacity to delocalize electronic excitations. They proved to be valuable as microlithographic contrast enhancement layers in submicron lithography [26] and may replace silicones in some cases [27] due to their higher thermal stabilities and better strength. Unlike many of the carbon-based polymers, polysilanes are almost invariably air-stable and processible by standard industrial techniques. Two recent reviews provide further details on the properties and of the potential applications of these exciting polymers [28-30].

In view of these experimental developments, it seems to be an attractive theoretical problem to systematically compare the structural and physical properties of analogous silicon- and carbon-based materials, respectively, and try to trace back the similarities and differences in their properties to their electronic structure. As a first step towards this goal, the theoretical work to be reported here has mainly concentrated on the Si and C backbones of the corresponding polymers themselves (taking always hydrogen atoms as side groups  $R_1$  and  $R_2$ , respectively). There are, however, several convincing experimental evidences for the importance of the detailed chemical structure of these side groups in governing the physical properties of polysilanes. On the basis of some preliminary calculations applying methyl groups as substituents, we have also obtained some hints for their expected influence through the Si—C orbital mixing but their more accurate investigation has to be the subject of further elaborate investigations. Besides polysilanes, for which a large volume of experimental data are available, we will also report theoretical results on the hypothetical *trans*-polyacetylene analogue (SiH) $_n$ , both in its equidistant and (single-double bond) alternating conformations, respectively. Though it seems to be very intricate to synthesize stable compounds containing silicon-silicon double bonds [31], the first successful synthesis of such a compound [32] induced theoretical work on silicon-containing polymers containing unsaturated bonds [33-36].

Most of the earlier theoretical investigations aiming at the prediction of the structural parameters of polysilanes used small oligosilanes (up to pentasilane) as model compounds apart from empirical force field calculations [37-40] that could use chains up to 30 Si atoms. Among the semiempirical methods, CNDO/2 has been used to compute the structure and ionization potentials [41] as well as low-lying excitation energies [42], MNDO [43,44] and MNDO/2 [45] calculations predicted

reasonable Si—Si bond lengths for different *trans* and *gauche* conformations, respectively, while AM1 and PM3 [46] have been used to analyze the conformational effect of various substituent groups. In the first *ab initio* HF cluster calculations, Mintmire and Ortiz [47,48] utilized a polarized (3-21G\*) atomic basis set and obtained reasonable bond lengths and valence angles, respectively, and provided vertical ionization potentials of the first four oligosilanes in good agreement with experiment. At the same level of theory, Nelson and Pietro [49] studied the evolution of the valence band of polysilanes from cluster energy levels, while Balaji and Michl [50] performed CI calculations with a double-zeta + *d* + Rydberg-type basis set to obtain the singlet excitation energies of the  $\text{Si}_n\text{H}_{2n+2}$ ,  $n = 2 - 5$  series. Finally, Kirtman and Hasan computed in a recent study [51] linear and nonlinear static electronic polarizabilities of  $\text{H}_3 - (\text{SiH}_2)_n - \text{SiH}_3$  oligomers until  $n = 13$  in the *trans* conformation.

The most sensitive part of the abovementioned conformational studies is the computation of the dihedral angles of the Si backbone that play a decisive role in determining the photophysical properties of these materials [52]. *trans* and *gauche* conformations have generally been identified as local minima of the potential energy surface but the location of the absolute minimum remained, due to the small energy differences obtained, mostly beyond the credibility limit of the methods applied. Methods applying empirical potential functions usually favored the *gauche* over the *trans* form, while single determinant MO methods (neglecting dispersion forces) predicted mostly the less compact *trans* form as the absolute minimum. A very important hint for the need of including electron correlation in these investigations came from the MP2/6-31G\* calculation of Mintmire and Ortiz [47] who found that the MP2 energy (computed for the HF optimized geometry) slightly inverts the stability order in tetrasilane (favoring the *gauche* form by 0.04 kcal/mol).

Theoretical work on infinite polysilanes concentrated mostly on the computation of the band structures by using semiempirical [41,53,54] or local density functional [55–58] methods and standard geometrical parameters. *Ab initio* crystal orbital geometry optimizations have been performed at the HF level, however, for the *trans* conformer using a minimal basis set [59], for both of the *trans* and *gauche* conformers, respectively, with a double-zeta basis [60], and for different mixed composites of the two structures again at the minimal basis level [61]. The linear polarizability of *trans*-polysilane has been investigated with STO-3G and 4-31G basis sets recently [62] without geometry optimization.

The present article will give a short review of a first principles method for the calculation of electron correlation effects on the total and single particle energies in infinite polymers and it will present new results concerning the geometrical structure and the electronic band indices of several infinite polyene models. The next two sections will summarize the methodological aspects related to the computation of the correlated ground state in the second order of PT and of its HF part, respectively, while the fourth section will provide the necessary working expressions to compute (correlated) quasiparticle energies. Finally, we will present our new results for five different infinite polyene models.

### Computational Method: Hartree-Fock and Møller-Plesset Schemes for Infinite Regular Polymers

Our *ab initio* computational procedure to calculate electron correlation effects for infinite polymers has been recently described [63,64]. Here, we only summarize the basic expressions to define the various theoretical levels as applied to polysilanes. The zeroth-order (Hartree-Fock)  $N$ -electron wavefunction,  $\Phi_0$ , will be written as a Slater-determinant built, utilizing the translational symmetry of the polymer, from doubly filled Bloch functions,  $\phi(\vec{r})$ , in the form

$$\Phi_0 = (N!)^{-1/2} \det[\cdots \phi_n^{\vec{k}}(\vec{r}_i) \alpha(\sigma_i) \phi_n^{\vec{k}}(\vec{r}_{i+1}) \beta(\sigma_{i+1}) \cdots]. \quad (1)$$

$\phi_n^{\vec{k}}(\vec{r})$  stands here for a one-electron state with quasi-momentum  $\vec{k}$  in band  $n$ . The Bloch functions themselves will be expressed as linear combinations of symmetry adapted Bloch basis orbitals in the form

$$\phi_n^{\vec{k}}(\vec{r}) = \sum_{a=1}^{\nu} C_{an}^{\vec{k}} \psi_a^{\vec{k}}(\vec{r}), \quad (2)$$

where  $\nu$  is the number of basis orbitals per elementary cell of the polymer and the Bloch orbitals  $\psi_a^{\vec{k}}(\vec{r})$  are themselves linear combinations of (Gaussian-type) atomic orbitals:

$$\psi_a^{\vec{k}}(\vec{r}) = N_c^{-1/2} \sum_{j=1}^{N_c} \exp\{i\vec{k}\vec{R}_j\} \chi_a^j(\vec{r}). \quad (3)$$

$N_c$  stands here for the number of elementary cells and the atomic orbital  $\chi_a^j(\vec{r}) = \chi_a(\vec{r} - \vec{R}_a - \vec{R}_j)$  is centered in the cell  $j$  at  $\vec{R}_a + \vec{R}_j$ . The nonrelativistic electronic Hamiltonian of the polymer (in atomic units) has the form

$$\hat{H} = -\frac{1}{2} \Delta_{\vec{r}} - \sum_{h=1}^{N_c} \sum_{A=1}^{n_A} \frac{Z_A}{|\vec{r} - \vec{R}_h - \vec{R}_A|} + \sum_{l < m} \frac{1}{|\vec{r}_l - \vec{r}_m|}. \quad (4)$$

$n_A$  is here the number of atoms per unit cell and  $Z_A$  is the core charge of the atom  $A$  at position  $\vec{R}_A$ , respectively. Variation of the expectation value  $\langle \Phi_0 | \hat{H} | \Phi_0 \rangle$  leads to the polymer HF equation

$$\hat{F}(\vec{r}_l) \phi_n^{\vec{k}}(\vec{r}_l) = \epsilon_n^{\vec{k}} \phi_n^{\vec{k}}(\vec{r}_l), \quad (5)$$

with the Fock-operator

$$\begin{aligned} \hat{F}(\vec{r}_l) = & -\frac{1}{2} \Delta_{\vec{r}_l} - \sum_{h=1}^{N_c} \sum_{A=1}^{n_A} \frac{Z_A}{|\vec{r}_l - \vec{R}_h - \vec{R}_A|} + \int d^3\vec{r}_m \frac{\rho(\vec{r}_m, \vec{r}_m)}{|\vec{r}_l - \vec{r}_m|} \\ & - \int d^3\vec{r}_m \frac{\rho(\vec{r}_l, \vec{r}_m)}{|\vec{r}_l - \vec{r}_m|} \hat{P}(\vec{r}_l, \vec{r}_m), \end{aligned} \quad (6)$$

where the permutation operator  $\hat{P}$  interchanges the variables  $\vec{r}_l$  and  $\vec{r}_m$ , respectively.

before integration for the function standing behind him. The first-order density matrix  $\rho(\vec{r}_l, \vec{r}_m)$  is constructed from the occupied Bloch orbitals as

$$\rho(\vec{r}_l, \vec{r}_m) = \sum_n^{\text{occ}} \sum_{\vec{k}}^{\{BZ\}} \phi_n^{\vec{k}}(\vec{r}_l) [\phi_n^{\vec{k}}(\vec{r}_m)]^* . \quad (7)$$

For the computation of the correlation energy, we will apply the Møller-Plesset partitioning scheme [65] of the Rayleigh-Schrödinger many-body perturbation theory (RS-MBPT) [66] by writing the full many-particle Hamiltonian (4) in the form

$$\hat{H} = \hat{H}_o + \hat{Q} . \quad (8)$$

$$\hat{H}_o = \sum_I \epsilon_I c_I^\dagger c_I \quad (9)$$

$$\begin{aligned} \hat{Q} = & 1/2 \sum_I \sum_J \sum_L \sum_M \langle IJ|LM \rangle c_I^\dagger c_J^\dagger c_M c_L \\ & - \sum_I \sum_J \sum_L \langle LJ||LJ \rangle n_L c_I^\dagger c_J \end{aligned} \quad (10)$$

$c_I^\dagger$  and  $c_I$  are here creation and annihilation operators, respectively, referring to the Bloch spin orbitals  $\phi_I$  (the compound index  $I$  refers to the band index  $i$  and quasi-momentum  $\vec{k}_i$ ),  $n_L$  is the occupation number, and the four-center repulsion integrals are defined by

$$\langle IJ|LM \rangle = \int d\vec{r}_1 \int d\vec{r}_2 \phi_{i'}^{\vec{k}_i}(\vec{r}_1)^* \phi_{j'}^{\vec{k}_j}(\vec{r}_2)^* r^{-1} \phi_{l'}^{\vec{k}_l}(\vec{r}_1) \phi_{m'}^{\vec{k}_m}(\vec{r}_2) \quad (11)$$

Integrals of the type  $\langle \dots || \dots \rangle$  are in their structure analogous to Eq. (11) with the difference that the Coulomb operator is multiplied in them by the factor  $(1 - \hat{P}_{12})$  to take account of exchange. The zeroth order many-electron wavefunctions are eigenfunctions of  $\hat{H}_o$ :

$$\hat{H}_o \Phi_\lambda = E_\lambda \Phi_\lambda . \quad (12)$$

The working expressions of MBPT can be written in a compact form using the reduced resolvent of  $\hat{H}_o$  belonging to its lowest eigenvalue,  $E_o$ :

$$\hat{G}_o = \sum_{\lambda=1}^{\infty} (E_o - E_\lambda)^{-1} |\Phi_\lambda\rangle \langle \Phi_\lambda| \equiv \hat{G} \quad (13)$$

In terms of  $\hat{G}$ , the first three orders of the RS-MBPT are given by

$$E_1 = \langle \Phi_o | \hat{Q} | \Phi_o \rangle \quad (14)$$

$$E_2 = \langle \Phi_o | \hat{Q} \hat{G} \hat{Q} | \Phi_o \rangle \quad (15)$$

$$E_3 = \langle \Phi_o | \hat{Q} \hat{G} \hat{Q} \hat{G} \hat{Q} | \Phi_o \rangle - \langle \Phi_o | \hat{Q} \hat{G} \hat{G} \hat{Q} | \Phi_o \rangle \langle \Phi_o | \hat{Q} | \Phi_o \rangle \quad (16)$$

Since  $E_{\text{HF}} = E_o + E_1$ , the correlation energy, defined as the difference between the exact eigenvalue of  $\hat{H}$  and  $E_{\text{HF}}$ , can be obtained as the sum of all higher order terms

in the perturbation series starting by  $E_2$ . If we take into account the translational symmetry of the polymer, substitute the resolvent operator from Eq. (13) and make use of diagrammatic techniques [66], we straightforwardly arrive at the expressions

$$E_2 = \sum_{i < j} \sum_{a < b} \sum_{\bar{k}_i} \sum_{\bar{k}_j} \sum_{\bar{q}} \frac{|\langle \phi_i^{\bar{k}_i} \phi_j^{\bar{k}_j} \| \phi_a^{\bar{k}_i + \bar{q}} \phi_b^{\bar{k}_j - \bar{q}} \rangle|^2}{(\varepsilon_i^{\bar{k}_i} + \varepsilon_j^{\bar{k}_j} - \varepsilon_a^{\bar{k}_i + \bar{q}} - \varepsilon_b^{\bar{k}_j - \bar{q}})} \quad (17)$$

$$\begin{aligned} E_3 = & \sum_{i < j} \sum_{a < b} \sum_{c < d} \sum_{\bar{k}_i} \sum_{\bar{k}_j} \sum_{\bar{q}} \sum_{\bar{r}} \\ & \times \frac{\langle \phi_i^{\bar{k}_i} \phi_j^{\bar{k}_j} \| \phi_a^{\bar{k}_i + \bar{q}} \phi_b^{\bar{k}_j - \bar{q}} \rangle \langle \phi_a^{\bar{k}_i + \bar{q}} \phi_b^{\bar{k}_j - \bar{q}} \| \phi_c^{\bar{k}_i + \bar{r}} \phi_d^{\bar{k}_j - \bar{r}} \rangle}{(\varepsilon_i^{\bar{k}_i} + \varepsilon_j^{\bar{k}_j} - \varepsilon_a^{\bar{k}_i + \bar{q}} - \varepsilon_b^{\bar{k}_j - \bar{q}})} \\ & \times \frac{\langle \phi_c^{\bar{k}_i + \bar{r}} \phi_d^{\bar{k}_j - \bar{r}} \| \phi_i^{\bar{k}_i} \phi_j^{\bar{k}_j} \rangle}{(\varepsilon_i^{\bar{k}_i} + \varepsilon_j^{\bar{k}_j} - \varepsilon_c^{\bar{k}_i + \bar{r}} - \varepsilon_d^{\bar{k}_j - \bar{r}})} \\ & + \sum_{i < j} \sum_{a < b} \sum_{k < l} \sum_{\bar{k}_i} \sum_{\bar{k}_j} \sum_{\bar{q}} \sum_{\bar{r}} \frac{\langle \phi_i^{\bar{k}_i} \phi_j^{\bar{k}_j} \| \phi_a^{\bar{k}_i + \bar{q}} \phi_b^{\bar{k}_j - \bar{q}} \rangle}{(\varepsilon_i^{\bar{k}_i} + \varepsilon_j^{\bar{k}_j} - \varepsilon_a^{\bar{k}_i + \bar{q}} - \varepsilon_b^{\bar{k}_j - \bar{q}})} \\ & \times \frac{\langle \phi_a^{\bar{k}_i + \bar{q}} \phi_b^{\bar{k}_j - \bar{q}} \| \phi_k^{\bar{k}_i} \phi_l^{\bar{k}_j} \rangle \langle \phi_k^{\bar{k}_i} \phi_l^{\bar{k}_j} \| \phi_i^{\bar{k}_i} \phi_j^{\bar{k}_j} \rangle}{(\varepsilon_k^{\bar{k}_i} + \varepsilon_l^{\bar{k}_j} - \varepsilon_a^{\bar{k}_i + \bar{q}} - \varepsilon_b^{\bar{k}_j - \bar{q}})} \\ & + \sum_{i < j} \sum_{k < l} \sum_{a < b} \sum_{c < d} \sum_{\bar{k}_i} \sum_{\bar{k}_j} \sum_{\bar{q}} \sum_{\bar{r}} \\ & \times \frac{\langle \phi_i^{\bar{k}_i} \phi_j^{\bar{k}_j} \| \phi_a^{\bar{k}_i + \bar{q}} \phi_b^{\bar{k}_j - \bar{q}} \rangle \langle \phi_a^{\bar{k}_i + \bar{q}} \phi_b^{\bar{k}_j - \bar{q}} \| \phi_k^{\bar{k}_i + \bar{r}} \phi_l^{\bar{k}_j - \bar{r}} \rangle \langle \phi_k^{\bar{k}_i + \bar{r}} \phi_l^{\bar{k}_j - \bar{r}} \| \phi_i^{\bar{k}_i} \phi_j^{\bar{k}_j} \rangle}{(\varepsilon_i^{\bar{k}_i} + \varepsilon_j^{\bar{k}_j} - \varepsilon_a^{\bar{k}_i + \bar{q}} - \varepsilon_b^{\bar{k}_j - \bar{q}})(\varepsilon_k^{\bar{k}_i} + \varepsilon_l^{\bar{k}_j} - \varepsilon_c^{\bar{k}_i + \bar{r}} - \varepsilon_d^{\bar{k}_j - \bar{r}})} \quad (18) \end{aligned}$$

The notation follows here the convention that indices  $i, j, \dots$  denote energy bands occupied in the ground state and  $a, b, \dots$  stand for virtual bands.

The termination of the perturbation expansion at the second order has two major advantages. At first, in this case only matrix elements between the ground state and doubly excited configurations will have to be computed. (Starting at third order, also matrix elements between doubly excited states will be required, whose list substantially exceeds that of the former elements, since even with the use of basis sets of moderate size the number of virtual bands exceeds by far that of the occupied ones.) At second,  $E_2$  can be thought of as a sum of separate electron-pair contributions if it is written in the form

$$E_2 = \sum_I \sum'_J \varepsilon_{IJ} \quad (19)$$

where the pair-correlation energies  $\varepsilon_{IJ}$  are defined by the comparison of Eqs. (17) and (19). In this way, the particle concept can also be preserved beyond the HF theory, and one can define quasiparticle states (and energy bands) that incorporate correlation effects at the given level of approximation.

The HF method is especially efficient if the Bloch orbitals are calculated in the form of a linear combination of atomic orbitals (LCAO) [67,68] since in this case

the large amount of experience collected in the field of molecular quantum mechanics can be used in polymer studies. In post-HF computations (like correlation and excitonic effects, impurity levels, etc.), however, the transformation from the Bloch basis to that of Wannier functions [69] turned out to be a very efficient procedure. The connection between the two basis sets is given by the Fourier transformation

$$w_n^I \equiv w_n(\vec{r} - \vec{R}_I) = N_c^{-1/2} \sum_{\vec{k}} \exp(-i\vec{k}\vec{R}_I) \phi_n^{\vec{k}}(\vec{r}), \quad (20)$$

where the Wannier function  $w_n^I(\vec{r}) = w_n(\vec{r} - \vec{R}_I)$  is centered around the monomer at  $\vec{R}_I$ . From the point of view of the accuracy and economy of the above mentioned calculations, the optimal (minimal) extension of  $w_n$  over neighboring unit cells in the polymer is of great importance. The originally undetermined phase of the Bloch functions, represented by the transformation  $\bar{\phi}_n^{\vec{k}}(\vec{r}) = \phi_n^{\vec{k}}(\vec{r}) \exp[i\lambda_n(\vec{k})]$  (where  $\lambda_n(\vec{k})$  can be any analytic function of  $\vec{k}$  possessing the symmetry of the BZ) can be utilized to determine the phase factor  $\exp\{i\lambda_n(\vec{k})\}$  in such a way that the Wannier functions will be localized [70]. After transformation (20), the Wannier functions are obtained in the same AO basis, in which the Bloch functions are calculated:

$$w_n^I(\vec{r} - \vec{R}_I) = \sum_h \sum_p d_{pn}^h \chi_p(\vec{r} - \vec{R}_I - \vec{R}_h). \quad (21)$$

The variational optimization of the phase factors reduces first the sum  $h$  over a few neighboring cells. For a given cell, the Wannier function components  $\sum_p d_{pn}^h(\vec{r} - \vec{R}_I - \vec{R}_h)$  are similar to molecular orbitals (MOs). It is not surprising, therefore, that methods worked out for MO localization may also provide excellent tools in polymer theory. The Wannier transformation is, unfortunately, not feasible in the case of metallic systems. For this case, a special numerical procedure has been developed [71] that starts from Bloch functions in tight-binding form

$$\phi_n^{\vec{k}}(\vec{r}) = N_c^{-1/2} \sum_{j=1}^{N_c} \exp\{i\vec{k}\vec{R}_j\} \Lambda_n^{\vec{k}}(\vec{r} - \vec{R}_j), \quad (22)$$

with

$$\Lambda_n^{\vec{k}}(\vec{r} - \vec{R}_j) = \sum_{a=1}^v C_{an}^{\vec{k}} \chi_a^I(\vec{r}), \quad (23)$$

and expands the  $\Lambda$  factors into a series of trigonometrical functions according to  $\vec{k}$  within the BZ. In this way, the four-index transformation will have to be performed only on the expansion coefficients (and not on the  $\Lambda$  functions themselves at a large number of  $\vec{k}$  values in the BZ). It turned out that also for metallic polyene (as found previously for simpler model systems [71]) the leading terms of the  $\Lambda$ -expansion until second power provide enough numerical stability to compute the correlation terms.

Electron correlation influences, besides the ground state total (binding) energy of the system, other observables as well. Within an approximate physical model,

the so-called electron polaron theory [72,73], one can reasonably correct for such effects, for instance, the single-particle energies of the valence and conduction bands, respectively. The physical meaning of the energy bands is given by Koopman's theorem stating that the band energies, as calculated by Eq. (5), are in fact the momentum-dependent electron affinities (EAs) and ionization potentials (IPs) of the HF  $N$ -electron system, respectively. Generalizing this statement to the correlation problem (at second order MP perturbation theory [71]), the corresponding quasiparticle (QP) energies can be obtained as EAs and IPs, respectively, of the correlated  $N$ -particle wavefunction

$$\epsilon_C(\text{QP}) = \epsilon_C(\text{HF}) + \Sigma_C^{(N+1)}(e) + \Sigma_C^{(N+1)}(h), \quad (24)$$

$$\epsilon_V(\text{QP}) = \epsilon_V(\text{HF}) + \Sigma_V^{(N)}(e) + \Sigma_V^{(N)}(h). \quad (25)$$

The correction terms appearing in Eqs. (24, 25), in addition to the HF band energies, are the electron and hole self-energies,  $\Sigma(e)$  and  $\Sigma(h)$ , respectively. The physical origin of these self-energy corrections is a cloud of virtual excitons accompanying the HF particles in analogy to the lattice polaron problem where virtual (optical) phonons dress the polarizing particle. A more detailed analysis of the structure of the corresponding expressions reveals [71–73] that the various  $\Sigma(\epsilon)$ -type terms tend to stabilize and the  $\Sigma(h)$ -type terms tend to destabilize the corresponding quasiparticle states, respectively. As a net effect, the correlated IPs and EAs will be reduced, as compared with their HF values; the valence bands will move upwards and the conduction bands downwards, respectively. Since the upper and lower band limits will be usually influenced to a different extent, a Franck–Condon type band narrowing effect can also be observed (as in the case of phonon polaron states).

### Conformational Properties: A Comparison of Carbon- and Silicon-Based Polymers

The conformational parameters of the simplest silane polymer,  $(\text{SiH}_2)_n$ , have been investigated both at the HF and MP2 levels of theory, respectively. To understand the dependence of the physical properties of these polymers (especially those strongly depending on correlation effects) on the size of the atomic basis set, we have employed in these studies several such sets starting from the minimal-type STO-3G, through double-zeta (DZ) [74] up to several polarized sets like DZ( $p$ ), DZ( $d, p$ ), DZ( $2d, p$ ), and DZ( $2df, p$ ). The exponents and contraction coefficients of these basis sets have been taken from the Gaussian suite of quantum chemical programs [75]. Our crystal orbital program package also uses several parts of the Gaussian system including all integral routines. Table I summarizes the structural parameters obtained for the three basic rotamers of polysilane, the *trans*, *eclipsed*, and *gauche* structures, respectively. Small cluster calculations [47,48] also indicate the presence of a fourth (*eclipsed*) conformer at the dihedral angle  $\theta = 0^\circ$  but our SCF program could not converge to this solution.

We can see that, apart from trivial deviations, all basis sets for both methods properly locate these structures around the  $\Theta$  values of  $180^\circ$ ,  $120^\circ$ , and  $60^\circ$ , re-



TABLE I. Structural parameters of three polyhydrosilane,  $(\text{SiH}_2)_n$ , structures (*trans*, *gauche*, and *eclipsed*, respectively) as optimized at the Hartree-Fock (HF) and second-order Møller-Plesset (MP2) levels of theory using different atomic basis sets. These structures are characterized by the dihedral angle  $\theta$  as defined by four consecutive Si atoms of the polymer (the *trans* form corresponds to the fully extended chain). The potential surface of the polymer has been scanned for  $\theta$  values around the expected local minima of the *trans* and *gauche* structures ( $\theta = 180^\circ$  and  $\theta = 60^\circ$ , respectively), and in the neighborhood of the expected maximum for an eclipsed structure ( $\theta = 120^\circ$ ).<sup>a</sup> (Distances are given in Å, angles in degrees.)

Method/basis set	R(Si—Si)	R(Si—H)	$\alpha(\text{Si—Si—Si})$	$\beta(\text{Si—Si—H})^b$	$\theta(\text{Si—Si—Si—Si})$
HF/DZ	2.3917	1.4848	111.93	109.83	180.
HF/DZ ( <i>d,p</i> )	2.3793	1.4835	112.04	110.12	180.
HF/DZ (2 <i>df,p</i> )	2.3728	1.4805	112.14	110.16	180.
MP2/DZ	2.3977	1.4984	112.02	109.61	180.
MP2/DZ ( <i>d,p</i> )	2.3591	1.4813	111.92	110.28	180.
MP2/DZ (2 <i>df,p</i> )	2.3559	1.4782	111.92	110.28	180.
HF/DZ	2.4012	1.4849	112.02	109.89	120.29
HF/DZ ( <i>d,p</i> )	2.3912	1.4830	112.38	110.18	120.09
HF/DZ (2 <i>df,p</i> )	2.3878	1.4802	112.35	110.23	120.15
MP2/DZ	2.4070	1.4985	110.85	109.76	120.84
MP2/DZ ( <i>d,p</i> )	2.3734	1.4809	111.75	109.88	121.21
MP2/DZ (2 <i>df,p</i> )	2.3706	1.4776	111.78	110.07	120.66
HF/DZ	2.3925	1.4849	111.79	109.65	64.50
HF/DZ ( <i>d,p</i> )	2.3807	1.4801	112.18	109.96	61.29
HF/DZ (2 <i>df,p</i> )	2.3736	1.4782	112.24	109.98	60.65
MP2/DZ	2.3986	1.4982	111.38	109.50	61.63
MP2/DZ ( <i>d,p</i> )	2.3610	1.4812	111.06	110.18	58.13
MP2/DZ (2 <i>df,p</i> )	2.3582	1.4786	111.04	110.39	60.24

<sup>a</sup> There is another expected local maximum for an eclipsed structure with  $\theta = 0^\circ$ . Due to convergence problems of the SCF procedure for small  $\theta$  values, our program could not reach this point on the potential surface.

<sup>b</sup> The H—Si—H plane is perpendicular to the Si—Si—Si plane and bisects the corresponding backbone angle  $\alpha$ .

spectively. The bond angles obtained for the polymer are also in good agreement with those obtained earlier for small clusters using 3-21 G\* and 6-31G\*\* basis sets, respectively [47-49,51]. The Si—Si bond length is, however, very sensitive to both basis set and correlation effects varying by 0.03 to 0.04 Å from the DZ to the DZ(2*df,p*) levels. Since the binding energy of the conformers very sensitively depends on this distance, even its small variations as functions of the dihedral angle are important. It elongates by about 0.015 Å (both for HF and MP2) in going from the *trans* to the *eclipsed* conformation and relaxes nearly back to its *trans* value at the *gauche* conformation.

The energetic changes accompanying the torsional motion of polysilane are shown in Table II. It is interesting to note first that even the use of the DZ(*d,p*) basis

TABLE II. Hartree-Fock ( $E_{\text{HF}}$ ), second- and third-order correlation ( $E_2$  and  $E_3$ ), and total energies ( $E_{\text{MP2}}$  and  $E_{\text{MP3}}$ ), respectively, obtained (using different atomic basis sets) per unit cell of polyhydrosilane,  $(\text{SiH}_2)_n$ , in different conformations: *trans* (dihedral angle  $\theta = 180^\circ$ ), *gauche* ( $\theta = 60^\circ$ ), and *eclipsed* ( $\theta = 120^\circ$ ). The absolute energies for the *trans* conformer are given in hartree, the relative energies for the *gauche* and *eclipsed* structures, respectively, are measured in millihartree from the corresponding *trans* value.

Energy	STO-3G	DZ	DZ (d)	DZ ( $d_{\text{VT}}$ )	DZ (2d,p)	DZ (2d,p)
$E_{\text{HF}}^a$ ( <i>trans</i> )	-286.792048	-290.043384	-290.081176	-290.083897	-290.088803	-290.090847
$E_2^b$ ( <i>trans</i> )	-0.038940	-0.115122	-0.143169	-0.161810	-0.165908	-0.178680
$E_3^c$ ( <i>trans</i> )	—	-0.055776	—	-0.074992	—	—
$E_{\text{MP2}}^d$ ( <i>trans</i> )	-286.830842	-290.158340	-290.224223	-290.245618	-290.254322	-290.269219
$E_{\text{MP3}}^e$ ( <i>trans</i> )	—	-290.214616	—	-290.320010	—	—
$\Delta E_{\text{HF}}^a$ ( <i>eclipsed</i> )	1.229	1.215	1.684	1.687	1.818	1.738
$\Delta E_{\text{MP2}}^b$ ( <i>eclipsed</i> )	—	1.217	1.626	1.645	1.542	1.708
$\Delta E_{\text{MP3}}^c$ ( <i>eclipsed</i> )	—	1.149	—	1.629	—	—
$\Delta E_{\text{HF}}^a$ ( <i>gauche</i> )	0.415	0.172	0.230	0.207	0.242	0.267
$\Delta E_{\text{MP2}}^b$ ( <i>gauche</i> )	—	-0.218	-0.494	-0.551	-0.631	-0.810
$\Delta E_{\text{MP3}}^c$ ( <i>gauche</i> )	—	-0.234	—	-0.546	—	—
$\Delta E_{\text{HF}}^a$ ( <i>gauche-trans</i> )	0.234	0.063	—	0.092	—	—
$\Delta E_{\text{MP2}}^b$ ( <i>gauche-trans</i> )	—	-0.105	—	-0.245	—	—

<sup>a</sup> Energy at the optimized HF geometry.

<sup>b</sup> Energy at the optimized MP2 geometry.

<sup>c</sup> Single-point calculation at the MP2 optimized geometry.

<sup>d</sup> The Si backbone dihedral angles have been taken alternating as  $60^\circ$  and  $180^\circ$ , respectively. The unit cell consists in this case of two  $\text{SiH}_2$  formula units but the corresponding energies have been divided by 2 to facilitate the comparison with the other structures.

(comparable to the 6-31 G\*\* basis set) does not completely saturate the HF energy per SiH<sub>2</sub> unit in polysilane. The additional set of *d*- and *f*-functions further decreases the HF energy by 20 and 8 millihartrees, respectively. This is in striking difference to its structural carbon analogue, polyethylene, for which the DZ( *d*,*p*) basis is very close to the estimated HF limit (Table III). The relative HF energies are, however, less sensitive to polarization functions also for polysilane. The height of the *eclipsed* torsional barrier (1.7–1.8 millihartree) is, for instance, reasonably described by using one set of *d*-functions for the Si atom [DZ( *d*)]. This situation is similar to polyethylene though the barrier height is substantially larger for the carbon backbone (6.8–6.9 millihartree). Since the correlation contribution is very similar in the *trans* and *eclipsed* conformers of polysilane, respectively, the MP2 level barrier values are nearly equal to the HF ones (1.6–1.7 millihartree). Furthermore, though the third-order correlation contribution, *E*<sub>3</sub>, substantially lowers the total energy (its value is about 46–43% of *E*<sub>2</sub> in polysilane and 37–44% in polyethylene, respectively), its influence is relatively small on the conformational energy difference since it changes quite slowly as a function of  $\theta$ .

Since the *gauche* conformation is much more compact than the two previously discussed ones, dispersion interactions become more important for it. In polysilane, the *trans*-*gauche* barrier is about 0.25 millihartree at the HF level but it diminishes at the MP2 and MP3 levels, respectively, and the *gauche* structure will be stabilized by about -0.8 millihartree relative to the *trans* conformation. This differs again from polyethylene where, though the corresponding barrier is also reduced by correlation, it seems to be stabilized at about 1.4 to 1.6 millihartree, i.e., the *trans*

TABLE III Hartree-Fock (*E*<sub>HF</sub>), second- and third-order correlation (*E*<sub>2</sub> and *E*<sub>3</sub>), and total energies (*E*<sub>MP2</sub> and *E*<sub>MP3</sub>), respectively, obtained (using different atomic basis sets) per unit cell of polyethylene in different conformations, *trans* (dihedral angle  $\theta = 180^\circ$ ), *gauche* ( $\theta = 60^\circ$ ), and *eclipsed* ( $\theta = 120^\circ$ ) The absolute energies for the *trans* conformer are given in hartree, the relative energies for the *gauche* and *eclipsed* structures, respectively, are measured in millihartree from the corresponding *trans*-value

Energy	STO-3G	DZ	DZ (d)	DZ (d,p)	DZ (2d,p)	DZ (2d,f,p)
<i>E</i> <sub>HF</sub> <sup>a</sup> ( <i>trans</i> )	-38 580150	-39.022111	-39 039101	-39 042697	-39 043195	-39.043797
<i>E</i> <sub>2</sub> <sup>b</sup> ( <i>trans</i> )	-0.052657	-0.101050	-0.142073	-0.155058	-0.166158	-0.178008
<i>E</i> <sub>3</sub> <sup>c</sup> ( <i>trans</i> )	—	-0.045211	—	-0.057358	—	—
<i>E</i> <sub>MP2</sub> <sup>b</sup> ( <i>trans</i> )	-38.632689	-39.123008	-39.181045	-39.197612	-39.209208	-39.221652
<i>E</i> <sub>MP3</sub> <sup>c</sup> ( <i>trans</i> )	—	-39.168219	—	-39.254970	—	—
$\Delta E$ <sub>HF</sub> <sup>a</sup> ( <i>eclipsed</i> )	6.250	6.482	6.864	6.921	6.874	6.862
$\Delta E$ <sub>MP2</sub> <sup>b</sup> ( <i>eclipsed</i> )	—	5.736	5.981	6.030	6.152	6.968
$\Delta E$ <sub>MP3</sub> <sup>c</sup> ( <i>eclipsed</i> )	—	5.642	—	5.881	—	—
$\Delta E$ <sub>HF</sub> <sup>a</sup> ( <i>gauche</i> )	1.617	1.599	1.657	1.691	1.624	1.334
$\Delta E$ <sub>MP2</sub> <sup>b</sup> ( <i>gauche</i> )	—	0.377	0.381	0.353	0.328	0.330
$\Delta E$ <sub>MP3</sub> <sup>c</sup> ( <i>gauche</i> )	—	0.386	—	0.247	—	—

<sup>a</sup> Energy at the optimized HF geometry.

<sup>b</sup> Energy at the optimized MP2 geometry

<sup>c</sup> Single-point calculation at the MP2 optimized geometry.

configuration remains the energetically favored one. Since the conformation energy differences obtained here are comparable to the thermal energy at room temperature ( $kT$  is about 1 millihartree at  $300^\circ\text{K}$ ), these polymer backbones will be extremely flexible against conformational excitations at higher temperatures. Furthermore, since interchain interactions in the corresponding polymer crystals will also play an important role in determining the most stable single chain structure, a final conclusion on relative stabilities will be possible only after their inclusion. The available experimental structural parameters also refer to polysilanes with more complicated side chains so that a more serious comparison with experiments will have to await their inclusion into the computations. (More details on these potential surfaces and on the corresponding zero-point vibrational corrections will be published elsewhere.)

Table IV presents the HF and MP2 energies, respectively, for the hypothetical polymer *trans*-(SiH)<sub>n</sub>, optimized first as a bond-alternating and then as an equidistant zig-zag chain. The development of the bond alternating geometry in polysilene is very similar to the case of *trans*-polyacetylene [64,71]. While the increasing quality of the HF description [STO-3G, DZ, and DZ(*d,p*) basis sets, respectively], produces bond alternation values (difference in the lengths of single and double bonds, respectively) of  $\Delta R = 0.1438, 0.1074$ , and  $0.1167 \text{ \AA}$  for polyacetylene [71], the corresponding  $\Delta R$  values for polysilene are  $0.1529, 0.1159$ , and  $0.1327 \text{ \AA}$ . As correlation reduces  $\Delta R$  to  $0.1105, 0.0834$ , and  $0.0816 \text{ \AA}$  for polyacetylene, it has the same effect in polysilene leading to  $0.1121, 0.0990$ , and  $0.0865 \text{ \AA}$ , respectively. Though the energy barrier of about 1.4 millihartree between the alternating and equidistant chains at the HF level will be reduced to approximately 0.6 millihartree at the MP2 level, it definitively persists and favors the bond-alternating (semiconducting) phase as the energetically stable one.

TABLE IV Hartree-Fock ( $E_{\text{HF}}$ ), second-order correlation ( $E_2$ ), and total energies ( $E_{\text{MP2}}$ ), respectively, obtained (using different atomic basis sets) per SiH unit of polyhydrosilene, (SiH)<sub>n</sub>, in *alternating trans* (alt) and *equidistant trans* (equ.) conformations, respectively. The absolute energies ( $E$ ) are given in hartree, the relative energies ( $\Delta E$ ) in millihartree.

	STO-3G	DZ	DZ ( <i>d,p</i> )	DZ (2 <i>df,p</i> )
$E_{\text{HF}}^a$ (alt.)	-286.154454	-289.446521	-289.476705	-289.498665
$E_2^b$ (alt.)	-0.049050	-0.114584	-0.156216	-0.172212
$E_{\text{MP2}}^b$ (alt.)	-286.203000	-289.560313	-289.476016	-289.670768
$E_{\text{HF}}^a$ (equ.)	-286.152922	-289.445485	-289.475306	-289.497253
$E_2^b$ (equ.)	-0.050179	-0.115073	-0.157010	-0.172788
$E_{\text{MP2}}^b$ (equ.)	-286.201808	-289.559785	-289.631699	-289.670200
$\Delta E_{\text{HF}}^a$ (alt-equ.)	-2.380	-1.036	-1.399	-1.412
$\Delta E_{\text{MP2}}^b$ (alt-equ.)	-1.192	-0.528	-0.533	-0.568

<sup>a</sup> Energy at the optimized HF geometry.

<sup>b</sup> Energy at the optimized MP2 geometry.

TABLE V. HF and quasiparticle (QP) energy levels at the limits of the valence and conduction bands, respectively, of *trans*-polyhydrosilane, *t*-(SiH<sub>2</sub>)<sub>x</sub>, computed with double-zeta (DZ) and polarized atomic basis sets, respectively (in eV)

	DZ		DZ ( <i>d,p</i> )		DZ (2 <i>d</i> / <i>f,p</i> )	
	HF	QP	HF	QP	HF	QP
$\epsilon_{v, \min}$	-13.652	-12.588	-13.816	-12.246	-13.829	-12.067
$\epsilon_{v, \max}$	-8.473	-7.612	-8.588	-7.386	-8.677	-7.138
$\epsilon_{c, \min}$	1.276	0.942	1.224	-1.471	0.919	-2.012
$\epsilon_{c, \max}$	9.501	8.902	9.408	6.912	9.308	5.942
$\Delta E_{\text{gap}}$	9.749	8.554	9.812	5.915	9.516	5.126

### Energy Bands in Hartree-Fock and Quasiparticle Theory

Tables V and VI contain the limits of the valence and conduction bands, and the width of the forbidden gap computed for the *trans* and *gauche* conformations of (SiH<sub>2</sub>)<sub>x</sub> using selected basis sets at the HF and electron polaron levels, respectively. The HF bands seem to be quite stabilized at the DZ basis set level including the band energy shifts due to the backbone torsion. The valence band of the *gauche* modification will be stabilized by about 0.8 eV compared with the *trans* one, and it becomes narrower by 1 to 1.2 eV. A similar shift to lower energies occurs for the HF conduction band in going from *trans* to *gauche* but its width will be reduced by 2.5 eV. The formation of correlated quasiparticle states according to Eqs. (24, 25) shifts the valence band for both systems upwards by an amount depending on the magnitude of the correlation energy associated with the basis set in question (ranging from 0.8–2.2 eV for different basis sets). The lower edges are shifted somewhat stronger (by 0.4–0.8 eV) resulting in the previously mentioned Franck-Condon type band narrowing. Similar observations can be made, in the opposite energetic direction, for the conduction bands. As a net effect, the semiconducting band gap will be substantially reduced due to correlation: its *trans* HF value of 9.5 eV diminishes to 5.12 eV and the *gauche* value from 11.8 eV to 5.56 eV.

TABLE VI. HF and quasiparticle (QP) energy levels at the limits of the valence and conduction bands, respectively, of *gauche*-polyhydrosilane, *g*-(SiH<sub>2</sub>)<sub>x</sub>, computed with double-zeta (DZ) and polarized atomic basis sets, respectively (in eV).

	DZ		DZ ( <i>d,p</i> )		DZ (2 <i>d</i> / <i>f,p</i> )	
	HF	QP	HF	QP	HF	QP
$\epsilon_{v, \min}$	-14.602	-13.208	-14.588	-12.711	-14.617	-12.208
$\epsilon_{v, \max}$	-10.486	-9.216	-10.512	-9.002	-10.590	-8.422
$\epsilon_{c, \min}$	1.530	0.948	1.406	-2.200	1.192	-2.862
$\epsilon_{c, \max}$	7.105	6.287	6.997	3.067	6.872	2.433
$\Delta E_{\text{gap}}$	12.016	10.164	11.918	6.802	11.782	5.560

TABLE VII HF and quasiparticle (QP) energy levels at the limits of the valence and conduction bands, respectively, of alternating *trans*-polysilene,  $t\text{-(SiH)}_x$ , computed with double-zeta (DZ) and polarized atomic basis sets, respectively (in eV).

	DZ		DZ ( <i>d,p</i> )		DZ (2 <i>df,p</i> )	
	HF	QP	HF	QP	HF	QP
$\epsilon_{i, \min}$	-9.428	-8.108	-9.506	-8.426	-9.544	-8.166
$\epsilon_{i, \max}$	-5.924	-5.088	-5.987	-4.909	-6.062	-4.720
$\epsilon_{c, \min}$	-1.802	-2.617	-1.969	-3.188	-1.980	-3.392
$\epsilon_{c, \max}$	2.716	1.420	2.646	1.289	2.579	0.822
$\Delta E_{\text{gap}}$	4.122	2.471	4.018	1.721	4.082	1.328

Table VII summarizes the analogous band indices for the energetically more stable bond-alternating model of *trans* polysilene. Besides similar observations as above in the case of polysilane, it is important to emphasize here that, though correlation again substantially reduces the band gap, with  $\Delta E_{\text{gap}} = 1.3$  eV polysilene still remains a semiconductor. The energy band structures obtained here for a number of different silicon-based polymers form the starting point for the computation and structure-dependent analysis of their optical spectra making use of the intermediate exciton model [76,77]. The corresponding results will be published elsewhere [78].

### Acknowledgments

The author is indebted to Dr. Hiroyuki Teramae for providing a CRAY version and new geometry optimization routines to the authors crystal orbital program and to Ms. Beate Hübner and Sabine Attinger for programming assistance. The generous support with computer time on the CONVEX and CRAY supercomputers of DKFZ and of the University of Stuttgart will be also gratefully acknowledged.

### Bibliography

- [1] *Conjugate Conducting Polymers*, H. G. Kiess, Ed. (Springer-Verlag, Berlin, 1992).
- [2] S. Suhai, *Theor. Chim. Acta (Berl.)* **34**, 157 (1974).
- [3] S. Suhai, *Biopolymers* **13**, 1731 (1974).
- [4] R. West, L. D. David, P. I. Djurovich, K. L. Stearley, K. S. V. Srinivasan, and H. Yu, *J. Am. Chem. Soc.* **94**, 3806 (1972).
- [5] R. D. Miller, D. Hofer, J. Rabolt, and G. N. Fickes, *J. Am. Chem. Soc.* **107**, 2172 (1985).
- [6] L. A. Harrah and J. M. Zeigler, *J. Polym. Sci., Polym. Lett. Ed.* **23**, 209 (1985).
- [7] P. Trefonas III, J. R. Damewood, Jr., R. West, and R. D. Miller, *Organometallics* **4**, 1318 (1985).
- [8] K. A. Klingensmith, J. W. Downing, R. D. Miller, and J. Michl, *J. Am. Chem. Soc.* **108**, 7438 (1986).
- [9] Y. Moritomo, Y. Tokura, H. Tachibana, Y. Kawabata, and R. D. Miller, *Phys. Rev.* **B43**, 14746 (1991).
- [10] H. Tachibana, Y. Kawabata, S. Koshihara, T. Arima, Y. Moritomo, and Y. Tokura, *Phys. Rev.* **B44**, 5487 (1991).

- [11] Z. G. Soos and R. G. Kepler, *Phys. Rev.* **B43**, 11908 (1991).
- [12] Y.-P. Sun, Y. Hamada, L.-M. Huang, J. Maxka, J.-S. Hsiao, R. West, and J. Michl, *J. Am. Chem. Soc.* **114**, 6301 (1992).
- [13] Y.-P. Sun and J. Michl, *J. Am. Chem. Soc.* **114**, 8186 (1992).
- [14] Z. V. Vardeny, X. Wei, S. G. Han, K. S. Wong, L. X. Zheng, and G. S. Kanner, *Synth. Met.* **49-50**, 453 (1992).
- [15] H. S. Platt and J. Michl, *Chem. Phys. Lett.* **198**, 400 (1992).
- [16] T. Hasegawa, Y. Iwasa, H. Sunamura, T. Koda, Y. Tokura, H. Tachibana, M. Matsumoto, and S. Abe, *Phys. Rev. Lett.* **69**, 668 (1992).
- [17] S. Abe, J. Yu, and W. P. Su, *Phys. Rev.* **B45**, 8264 (1992).
- [18] H. Bock, W. Ensslin, F. Feher, and R. Freund, *J. Am. Chem. Soc.* **98**, 668 (1976).
- [19] H. Bock, W. Kaim, M. Kira, and R. West, *J. Am. Chem. Soc.* **101**, 7667 (1979).
- [20] R. G. Kepler, J. M. Zeigler, and L. A. Harrah, *Bull. Am. Phys. Soc.* **29**, 509 (1984).
- [21] R. G. Kepler, J. M. Zeigler, L. A. Harrah, and S. R. Kurtz, *Phys. Rev.* **B35**, 2818 (1987).
- [22] R. West, L. D. David, P. I. Djurovich, K. L. Stearley, K. S. V. Srinivasan, and H. Yu, *J. Am. Chem. Soc.* **103**, 7352 (1981).
- [23] F. Kajzar, J. Messier, and C. Rosilio, *J. Appl. Phys.* **60**, 3040 (1986).
- [24] J.-C. Baumert, G. C. Bjorklund, D. H. Jundt, M. C. Jurich, H. Looser, R. D. Miller, J. Rabolt, R. Sooriyakumaran, J. D. Swalen, and R. J. Twieg, *Appl. Phys. Lett.* **5**, 1147 (1988).
- [25] L. Wang, Q. Z. Wang, P. P. Ho, R. Dersinville, R. R. Alfano, W. K. Zou, and N. L. Yang, *Appl. Phys. Lett.* **53**, 1245 (1988).
- [26] D. C. Hofer, R. D. Miller, C. G. Wilson, and A. Neureuther, *SPIE Advances in Resist Technology*, **469**, 108 (1984).
- [27] J. M. Zeigler, L. A. Harrah, and A. W. Wilson, *SPIE Advances in Resist Technology*, **539**, 166 (1985).
- [28] R. West, *J. Organomet. Chem.* **300**, 327 (1986).
- [29] R. D. Miller and J. Michl, *Chem. Rev.* **89**, 1359 (1989).
- [30] J. M. Zeigler, *Mol. Cryst. Liq. Cryst.* **190**, 265 (1990).
- [31] L. E. Gusel'nikov and N. S. Nametkin, *Chem. Rev.* **79**, 529 (1979).
- [32] R. West, M. J. Fink, and J. Michl, *Science* **214**, 1343 (1981).
- [33] K. Takeda and S. Kagoshima, *Phys. Rev.* **B37**, 6406 (1988).
- [34] K. Tanaka, H. Kobayashi, T. Koike, T. Tamabe, Y. Osawa, S. Niwa, and N. Yasuda, *Synth. Met.* **25**, 289 (1988).
- [35] M. Springborg, *Phys. Rev.* **B40**, 7839 (1989).
- [36] H. Teramae, *Phys. Rev.* **B46**, 12788 (1992).
- [37] J. R. Damewood, Jr. and R. West, *Macromolecules* **18**, 159 (1985).
- [38] J. R. Damewood, Jr., *Macromolecules* **18**, 1795 (1985).
- [39] W. J. Welsch, L. DeBolt, and J. E. Mark, *Macromolecules* **19**, 2978 (1986).
- [40] B. L. Farmer, J. F. Rabolt, and R. D. Miller, *Macromolecules* **20**, 1167 (1987).
- [41] K. Takeda, N. Matsumoto, and M. Fukuchi, *Phys. Rev.* **B30**, 5871 (1984).
- [42] R. W. Bigelow, *Chem. Phys. Lett.* **126**, 63 (1986).
- [43] W. S. J. Verwoerd, *J. Comput. Chem.* **3**, 445 (1982).
- [44] R. W. Bigelow and K. M. McGrane, *J. Polymer Sci.: Part B. Polymer Phys.* **24**, 1233 (1986).
- [45] W. J. Welsch and W. D. Johnson, *Macromolecules* **23**, 1881 (1990).
- [46] M. Jalali-Heravi, S. P. McManus, S. E. Zuttaut, and J. K. McDonald, *Chem. Mater.* **3**, 1024 (1991).
- [47] J. W. Mintmire and J. V. Ortiz, *Macromolecules* **21**, 1189 (1988).
- [48] J. W. Mintmire and J. V. Ortiz, *J. Am. Chem. Soc.* **110**, 4522 (1988).
- [49] J. T. Nelson and W. J. Pietro, *J. Phys. Chem.* **92**, 1365 (1988).
- [50] V. Balaji and J. Michl, *Polyhedron* **10**, 1265 (1991).
- [51] B. Kirtman and M. Hasan, *J. Chem. Phys.* **96**, 470 (1992).
- [52] J. Michl and V. Balaji, in *Computational Advances in Organic Chemistry: Molecular Structure and Reactivity*, C. Orgetir and I. G. Csizmadia, Eds. (Kluwer Acad. Publ., 1991), pp. 323-354.
- [53] K. Takeda, H. Teramae, and N. Matsumoto, *J. Am. Chem. Soc.* **108**, 8166 (1986).
- [54] K. Takeda, M. Fujino, K. Seki, and H. Inokuchi, *Phys. Rev.* **B36**, 8129 (1987).

- [55] J. W. Mintmire, Phys. Rev. B39, 13350 (1989).
- [56] K. Takeda and K. Shiraishi, Phys. Rev. B39, 11028 (1989).
- [57] K. Takeda, K. Shiraishi, and N. Matsumoto, J. Am. Chem. Soc. 112, 5043 (1990).
- [58] K. Takeda and K. Shiraishi, Phil. Mag. B65, 535 (1992).
- [59] H. Teramae, T. Yamabe, and A. Imamura, Theor. Chim. Acta (Berl.) 64, 1 (1983).
- [60] H. Teramae and K. Takeda, J. Am. Chem. Soc. 111, 1281 (1989).
- [61] N. Matsumoto and H. Teramae, J. Am. Chem. Soc. 113, 4481 (1991).
- [62] B. Champagne and J.-M. André, Int. J. Quantum Chem. 42, 1009 (1992).
- [63] S. Suhai, "Collective Excitations in Biological Macromolecules. Photoelectron and Exciton Spectra of Polyene, Polypeptides, and Polynucleotides," in *Molecules in Physics, Chemistry, and Biology*, J. Maruani, Ed. (Kluwer Acad. Publ., 1989), Vol. IV, pp. 133-194.
- [64] S. Suhai, Int. J. Quantum Chem. 42, 193 (1992).
- [65] C. Moller and M. S. Plesset, Phys. Rev. 46, 618 (1934).
- [66] N. H. March, W. H. Young, and S. Sampanthar, *The Many-Body Problem in Quantum Mechanics* (Cambridge University Press, 1967).
- [67] G. Del Re, J. Ladik, and G. Biczko, Phys. Rev. 155, 967 (1967).
- [68] J. M. Andre, L. Gouverneur, and G. Leroy, Int. J. Quantum Chem. 1, 427 (1967).
- [69] G. H. Wannier, Phys. Rev. 52, 191 (1937).
- [70] E. I. Blount, Solid State Phys. 13, 305 (1963).
- [71] S. Suhai, Phys. Rev. B27, 3506 (1983).
- [72] Y. Toyozawa, Progr. Theor. Phys. 12, 422 (1954).
- [73] S. T. Pantelides, D. J. Mickish and A. B. Kunz, Phys. Rev. B10, 2602 (1974).
- [74] T. H. Dunning and P. J. Hay, *Modern Theoretical Chemistry*, (Plenum, New York, 1976), pp. 1-28.
- [75] Gaussian 92, M. J. Frisch et al., (Gaussian, Inc., Pittsburgh PA, 1992).
- [76] S. Suhai, Int. J. Quantum Chem, Quantum Biol. Symp. 18, 161 (1984).
- [77] S. Suhai, J. Chem. Phys. 84, 5071 (1986).
- [78] S. Suhai, J. Chem. Phys. (in press)

Received May 27, 1993



# Spin-Polarized LCGTO-FF Band Structure Technique: Application to 3d Transition Metal Monolayers

J. C. BOETTGER

*Theoretical Division, Los Alamos National Laboratory, Los Alamos, New Mexico 87545*

## Abstract

The linear combinations of Gaussian-type orbitals-fitting function (LCGTO-FF) technique, as embodied in the program package FILMS, has been extended to include spin-polarization effects. The spin-polarized LCGTO-FF method is described here. Test results are presented for square monolayers of seven 3d-transition metals (Ti, V, Cr, Mn, Fe, Co, and Ni) at the lattice constant of Ag(001). The LCGTO-FF results compare favorably with previous results obtained with the FLAPW technique © 1993 John Wiley & Sons, Inc

## Introduction

During the past decade, the linear combinations of Gaussian type orbitals-fitting function (LCGTO-FF) technique [1] has been used to calculate the properties of a number of ultra-thin films (UTF); see Ref. [2] for a review. Most of those calculations have been restricted to UTFs composed of relatively small atoms ( $Z \leq 20$ ); although there have been some exceptions [3]. This focus on small systems has been due, in part, to two basic limitations of the program package (FILMS) used for those calculations: (1) neglect of relativistic effects, and (2) neglect of spin-polarization.

Here, the program FILMS has been modified to incorporate spin-polarization effects into the LCGTO-FF technique. This extension of the method is straightforward but has potential pitfalls due to the particular formalism used by FILMS to fit the local spin-density approximation (LSDA) exchange-correlation (XC) kernels ( $\epsilon_{xc}$  and  $V'_{xc}$ ). For this reason, the new spin-polarized version of FILMS has been tested carefully by calculating the spin magnetic moments for square lattice monolayers of seven 3d transition metals (Ti, V, Cr, Mn, Fe, Co, and Ni), all at the theoretical lattice constant of Ag(001);  $a = 5.51$  a.u. [4]. This particular test allows direct comparison with previously published results obtained with the FLAPW technique [5] using the same LSDA model as is used in FILMS (that proposed in Ref. [4]).

The basic LCGTO-FF method and its extension to include spin-polarization effects are described in the next section. Results will then be presented for the cohesive energies, spin magnetic moments, and work functions of the 3d transition metals. Brief concluding remarks are given in the final section.

## Methodology

### *The LCGTO-FF Technique*

The LCGTO-FF technique is an all-electron, full-potential, electronic structure method which is characterized by its use of three independent Gaussian basis sets to expand the one-electron orbitals, the charge density, and the LSDA XC energy density and potential. The current implementation of the LCGTO-FF technique in FILMS is derived from a fitting function UTF electronic structure code due to Mintmire, Sabin, and Trickey [6], which in turn was related to a fitting function based cluster code [7]. Although FILMS is directly related to these other GTO fitting function based methods, the present implementation of the LCGTO-FF technique has several distinctive features (see below).

The purpose of fitting the charge density with GTOs is to reduce the number of Coulomb integrals required in the calculations by ensuring that only three-center integrals appear in the total energy expression and the one-electron equations, instead of the usual four-center integrals. Thus, the total number of Coulomb integrals required for a system will scale as  $N_o^2 N_c$  (where  $N_o$  = the number of orbital basis functions and  $N_c$  = the number of charge fit functions), instead of the usual  $N_o^4$ . Since the charge density is a nodeless function, unlike the orbitals,  $N_c$  is generally less than  $N_o$ ; thereby providing an additional reduction in the total number of Coulomb integrals. In all of the extant GTO fitting function codes, the expansion coefficients of the charge density fitting functions are determined by variationally minimizing the error in the Coulomb energy due to the fit [6,7]. Once all the necessary Coulomb integrals have been evaluated analytically, the variational charge fit can be accomplished by solving a simple linear matrix equation [6,7].

The calculation of the three-center Coulomb integrals involves lengthy lattice summations over a pair of orbitals and a charge fitting function plus a neutralizing array of nuclei [6]. To improve convergence, the integral sums for the very diffuse orbitals are calculated with mixed real and reciprocal space techniques [6]. The remaining integral sums are accelerated via multipole expansion techniques [6]. In FILMS, the pure real-space integral summations for the *s*-type fitting functions plus their neutralizing point charge arrays are further accelerated by splitting the sums into a short-range part consisting of the fitting function and a single neutralizing positive point charge and a long-range part formed from the nuclear array and a single negative point charge [8]. This procedure is both faster and more stable than the original method used in Ref. [6].

The XC fitting function procedure can be understood best as a rather sophisticated numerical quadrature scheme which allows a highly accurate evaluation of the XC integrals on a relatively sparse integration mesh by fitting of the integral kernels with GTOs. The expansion coefficients of the XC fitting functions are obtained from a weighted least squares fit to the energy density or potential on the numerical integration mesh. This least squares fit can be expressed as a linear matrix equation whose elements are obtained via numerical integration. The fitted energy density and potential then can be used to evaluate the XC matrix elements of the secular equation and total energy analytically to a much higher level of precision (and in

less time) than would be possible with direct numerical integration. The accuracy of the XC matrix elements is also improved by constraining the fit procedure to ensure that the numerical integral of the charge density times the difference between the fitted and exact energy densities (or potentials) vanishes [9].

In FILMS, the numerical XC integrals are carried out with an integration technique specifically designed to exploit the UTF geometry [8]. The UTF unit cell (which has infinite extent in the  $z$ -direction) is divided into three distinct regions: (1) a collection of touching spheres centered on the atomic sites in the cell, (2) a vacuum region which lies outside of two horizontal planes which just touch the outermost atomic spheres, and (3) an interstitial region. In the spheres, the numerical integrals are factored into a radial integral on an exponential mesh and an angular integral using Gaussian quadrature including all spherical harmonics through  $l = 12$ . In the vacuum region, the integral is divided into a  $z$ -integral on an exponential mesh and an  $x, y$  integral on a uniform mesh exhibiting the symmetry of the 2d lattice. In the interstitial region, the integral is calculated with a simple histogram technique on a very dense uniform mesh whose  $x, y$  coordinates exhibit the symmetry of the 2d lattice. This numerical integration scheme is substantially more accurate (and requires less time) than the numerical integration scheme used in Ref. [6].

The most important difference between the present implementation of the LCGTO-FF technique and other GTO fitting function methods is in the XC fitting. In FILMS, the XC fitting procedure is referenced to the fitted charge density  $[\tilde{\rho}(\vec{r})]$  in place of the exact density  $[\rho(\vec{r})]$  [1]; i.e., once  $\tilde{\rho}(\vec{r})$  has been found, it is used in place of  $\rho(\vec{r})$  in all XC expressions. This approximation produces a significant speedup in the calculations. Forming  $\tilde{\rho}(\vec{r})$  at a given point on the numerical integration mesh only requires summing over  $N_c$  fitting functions, whereas forming  $\rho(\vec{r})$  requires summing over  $N_o^2$  products of orbital basis functions for  $N_k$  inequivalent Bloch vectors ( $\vec{k}$ ) in the Brillouin zone. Thus using  $\tilde{\rho}(\vec{r})$  in place of  $\rho(\vec{r})$  reduces the time required for the XC fit by a factor of  $(N_o^2 N_k / N_c)$ ; typically more than two orders of magnitude. As an added benefit, the use of  $\tilde{\rho}(\vec{r})$  also produces a more stable XC energy calculation by replacing the usual rather slowly converging numerical Brillouin zone integrations with analytical real space integrals.

Unfortunately, the use of  $\tilde{\rho}(\vec{r})$  in the XC fit introduces a source of potential difficulties in the LCGTO-FF calculations. The variational charge fitting procedure ensures that the error in the Coulomb energy will be minimized. However, there is no proven way to constrain the fitted density to be positive everywhere. Thus, in some cases, the charge fit procedure will yield a fitted density which is negative in the far vacuum region (in essence sacrificing the far region to get a better description closer to the nucleus). Although this negative density has negligible impact on the Coulomb energy, it can alter the work function  $\Phi$  of a film significantly by spuriously reducing the dipole barrier. In addition, there is no meaningful way to calculate the XC kernels for a negative  $\tilde{\rho}(\vec{r})$ . For these reasons, it has been found that the best solution to this problem is to be careful to select a charge fit basis which does not produce any negative density. If a charge basis does produce a negative density, it can usually be removed by using a slightly larger exponent for the most diffuse  $s$ -type Gaussian. It has been found generally that the work function

and cohesive energy for a given system are relatively insensitive to the choice of the charge fit basis provided there is no negative density.

The generalization of the LCGTO-FF technique just described to include spin-polarization effects is straightforward. Instead of fitting only the total charge density, the spin-up and spin-down densities must be fitted independently. Then spin-up and spin-down parts of the XC energy density and potential can be formed and fitted on the numerical integration mesh. The only significant concern in this procedure lies in the fact that the minority spin charge density will generally be more localized than the majority spin or total charge density. Thus the fitted minority spin charge density is more apt to have regions of negative density. Although such a result would not affect the Coulomb energy or the work function, provided the total charge density is positive everywhere, it could adversely affect the XC energy. This point will be discussed further below.

### *Basis Sets*

It has been found that for atoms in the outer layer of a UTF, the  $s$ -type and  $p_z$ -type orbital basis sets should be atomic-like (diffuse), while the  $p_x$ -type and  $p_y$ -type basis sets should be crystalline-like (well localized) [10]. Similar guidelines for  $d$ -states can be inferred. For the seven 3d transition metals considered here (Ti, V, Cr, Mn, Fe, Co, and Ni), the orbital basis sets used are derived from Huzinaga's [11] (14s9p5d) atomic basis sets.

For each system, the  $s$ -type orbital basis is formed by contracting the five most local GTOs in the atomic basis using the expansion coefficients of the 1s atomic orbital as contraction coefficients. For the  $p$ -type orbital bases, the four most local atomic GTOs have been contracted using the 2p orbital coefficients. Because the highest occupied  $p$ -state in the atom (3p) is quite local, the  $p$ -type bases for the monolayers have been augmented with a GTO whose exponent is 0.14 for all atoms, except Ni for which an exponent of 0.15 was preferred. The  $p_z$  manifold was further augmented with a GTO of exponent 0.06. For the  $d$ -type orbital basis, the four most local atomic GTOs were contracted using 3d orbital coefficients. All of the  $d$ -type bases used were augmented with one additional GTO whose exponent depended on the atom under consideration (0.16—Ti, V, Cr; 0.18—Mn; 0.20—Fe, Co, Ni). To avoid linear dependencies, the exponent of the most diffuse  $d$ -type atomic GTO for Ti and V was replaced with 0.32; twice the value of the exponent used to augment the basis. For all of the monolayers, the final orbital basis set used was a (14s10p6d+1 $p_z$ ) primitive basis contracted to a (10s7p3d+1 $p_z$ ) basis.

In keeping with previous experience, the fitting function basis sets for the charge fit and XC fit have been chosen to be identical (the fit basis) [12]. The symmetries of the monolayer dictate that only two types of GTOs (with  $l \leq 2$ ) can appear in the fit basis;  $s$  and  $d_{z^2-1/2(x^2-y^2)}$ . A single 11 GTO  $s$ -type basis has been used for all of the monolayers considered here. Three distinct 3 GTO  $d$ -type basis sets were used depending on the atom under consideration. All of the fit function exponents used here are given in Table I. Note that for the lighter atoms, the  $d$ -type exponents used are larger. Localization of the  $d$  basis set was necessary for those systems to

TABLE I. Fitting function exponents for the seven transition metal monolayers. One *s*-type basis was used for all seven systems. Three distinct *d*-type bases were used depending on the specific atom.

<i>s</i> -type	<i>d</i> -type		
All monolayers	Ti, V, Cr, Mn	Fe	Co, Ni
30000.00	3.80	3.00	3.00
4500.00	1.80	1.20	0.90
750.00	0.80	0.50	0.30
240.00			
80.00			
27.00			
9.00			
3.00			
0.90			
0.27			
0.08			

avoid negative values of the minority spin density, as discussed above. Test calculations on Mn using the most diffuse and the most local of the three *d*-type fit bases produced roughly a 10 mRy shift in the total energy (an acceptable variation for these systems) and roughly a 20 mRy shift in  $\Phi$ . The shift in  $\Phi$  is larger than would generally be considered acceptable. However, this shift is not indicative of the imprecision of the final value used for  $\Phi$  because the more diffuse basis produces negative electron density in the far vacuum region which, as was noted above, has disastrous consequences for  $\Phi$ .

#### Additional Computational Details

The real-space numerical integration mesh used in these calculations was of the general form described earlier. The atomic sphere region included 91 exponentially spaced radial points and 28 nonequivalent angular points. In each vacuum region, 15 exponentially spaced *z*-points and 36 nonequivalent symmetrically distributed (*x*, *y*) points were used. A total of 3673 uniformly distributed points were used for the interstitial integration. Thus, the real-space numerical integration mesh included a total of 7274 points in the UTF unit cell.

In all of these calculations, the irreducible triangle of the Brillouin zone (BZ) was sampled at 36 uniformly distributed Bloch vectors. The necessary BZ integrations were carried out using the linear triangle technique. The SCF cycle was iterated until the total energy was converged to less than 0.01 mRy. In all cases, the spin magnetic moment  $\mu$  was converged to 0.001  $\mu_B$ .

#### Results

The most fundamental quantity yielded by any LSDA calculation is the total energy. For this reason, it is important to obtain the cohesive energy ( $E_{c,l}$ ) of the

TABLE II. Atomic energies ( $E_a$ ), monolayer cohesive energies ( $E_{c,1}$ ), and bulk cohesive energies ( $E_{c,b}$ ) from Ref. [4]; all in eV.

System	$E_a$	$E_{c,1}$	$E_{c,b}$
Ti	23055.438	4.04	6.12
V	25625.982	3.27	6.12
Cr	28358.633	2.27	4.82
Mn	31254.251	2.66	4.95
Fe	34317.464	3.35	6.26
Co	37553.985	3.30	6.48
Ni	40968.036	2.78	5.70

monolayers even though they have not been geometry optimized. Table II lists total LSDA energies for isolated atoms of Ti, V, Cr, Mn, Fe, Co, and Ni calculated using the same orbital basis sets as were used for the monolayers; except that the  $p_x$  and  $p_y$  basis sets are augmented to make them identical to the  $p_z$  basis. The atomic configurations were assumed to be identical to those given in Ref. [4]. The largest sources of error in  $E_{c,1}$  are two inconsistencies between the atomic and monolayer calculations: (1) the atom calculation did not use fitting functions and (2) the atom calculation did not include off-site orbital basis functions. These inconsistencies may introduce an error in  $E_{c,1}$  on the order of a few tenths of an eV. In Table II, the present values of  $E_{c,1}$  are compared with bulk cohesive energies ( $E_{c,b}$ ) reported by Ref. [4]. The ratios  $E_{c,1}/E_{c,b}$  for these systems all lie in the range 0.47 to 0.66; smaller than has been found in other monolayer systems [3]. Given the fact that the monolayers are calculated at expanded nearest neighbor distances, these values for  $E_{c,1}$  are quite sensible.

In Table III, the total spin magnetic moments obtained here for the 3d transition metal monolayers are compared with those reported by Ref. [5] at the same lattice

TABLE III. The total spin magnetic moments ( $\mu_t$ ) and muffin-tin-sphere spin magnetic moments ( $\mu_{mts}$ ) found here for the transition metal monolayers using the LCGTO-FF method are compared to the values of  $\mu_{mts}$  found in Ref. [5] with the FLAPW method and the bulk values of  $\mu_t$  from Ref. [4]; all in  $\mu_B$ .

System	LCGTO-FF		FLAPW	Bulk
	$\mu_t$	$\mu_{mts}$	$\mu_{mts}$	$\mu_t$
Ti	2.05	1.62	1.72	—
V	3.10	2.70	2.87	—
Cr	5.04	4.52	4.50	—
Mn	4.57	4.33	4.32	—
Fe	3.32	3.27	3.29	2.15
Co	2.13	2.15	2.20	1.56
Ni	0.96	0.98	1.02	0.59

TABLE IV. The theoretical work functions ( $\Phi_1$ ) for the transition metal monolayers are compared with experimental surface work functions ( $\Phi_s$ ) given in Ref. [13]. Theoretical values of  $\Phi_s$  obtained in Ref. [14] with the surface Green's function method are also given. (All values are in eV).

System	$\Phi_1$	$\Phi_s$ , exp.	$\Phi_s$ , theo.
Ti	5.01	4.33	—
V	5.30	4.3	—
Cr	5.08	4.5	—
Mn	4.11	4.1	—
Fe	4.73	4.67	4.50
Co	5.24	5.0	5.52
Ni	5.41	5.22	5.75

constant using the same LSDA. Since the values given in Ref. [5] are calculated inside of muffin-tin spheres, equivalent muffin-tin values are given for the present calculations. In all cases there is good agreement between the FLAPW and LCGTO-FF muffin-tin sphere values, demonstrating the high quality of the present results. It is also worth noting that the muffin-tin sphere values of  $\mu$  seriously underestimate the total values for Ti, V, Cr, and Mn. This result is due to the rather diffuse character of the majority spin d-states for the lighter transition metals. Table III, also includes theoretical bulk values of  $\mu$  reported by Ref. [4] for Fe, Co, and Ni; using the same LSDA as was used here. Comparison of the monolayer and bulk values reveals the now standard enhancement of the spin magnetic moment of the monolayer relative to the bulk.

One additional calculated quantity which bears a careful examination is the work function ( $\Phi$ ). In Table IV, values of  $\Phi$  are reported for all of the systems studied here, together with experimental surface values [13]. Table IV also includes theoretical values of  $\Phi$  for Fe, Co, and Ni surfaces (with square symmetries) obtained with a surface Green's function technique [14]. Given the differences in the types of systems considered (expanded monolayer versus surface), the present results are in reasonable agreement with the experimental values, except for the lighter Z systems. The larger difference for Ti, V, and Cr may be due to the fact that the monolayer is spin-polarized while the surface is not. Overall, there is no evidence of difficulties with the new spin-polarized version of FILMS.

### Conclusions

The calculations presented here demonstrate that the new spin-polarized version of FILMS is capable of producing reliable results for transition metals. This method could be further improved by allowing different fitting function basis sets to be used for the majority spin and minority spin charge and XC functions. A further useful development would be inclusion of relativistic effects.

The present calculations have also demonstrated the need to include the interstitial contributions to the spin magnetic moment. For highly polarized materials, using only the muffin-tin sphere portion of the magnetic moment may result in as much as a 20% underestimate of  $\mu$ .

### Acknowledgments

I am grateful to S. B. Trickey for numerous conversations during the course of this research. This work was supported in part by the U. S. Department of Energy.

### Bibliography

- [1] J. C. Boettger and S. B. Trickey, Phys. Rev. B32, 1356 (1985); J. C. Boettger and S. B. Trickey, J. Phys. F: Met. Phys. 16, 693 (1986); J. C. Boettger and S. B. Trickey, unpublished.
- [2] J. C. Boettger, Int. J. Quantum Chem., Quantum Chem. Symp. 26, 633 (1992).
- [3] J. C. Boettger and S. B. Trickey, J. Phys.: Condens. Matter 1, 4323 (1989); U. Birkenheuer, N. Roesch, S. B. Trickey, and J. Nozke, Z. Phys. B83, 267 (1991).
- [4] V. L. Moruzzi, J. F. Janak, and A. R. Williams, *Calculated Electronic Properties of Elemental Solids* (Pergamon, New York, 1978).
- [5] S. Blugel, B. Drittler, R. Zeller, and P. H. Dederichs, Appl. Phys. A49, 547 (1989).
- [6] J. W. Mintmire, J. R. Sabin, and S. B. Trickey, Phys. Rev. B26, 1743 (1982); J. W. Mintmire, Ph.D thesis, Univ. of Florida, unpublished (1980).
- [7] B. I. Dunlap, J. W. D. Connolly, and J. R. Sabin, J. Chem. Phys. 71, 3396 (1979).
- [8] J. C. Boettger (unpublished).
- [9] J. Andzelm, E. Radzio-Andzelm, and D. R. Salahub, J. Comput. Chem. 6, 520 (1985).
- [10] J. C. Boettger and S. B. Trickey, Phys. Rev. B45, 1363 (1992).
- [11] S. Huzinaga, J. Chem. Phys. 66, 4245 (1977).
- [12] J. C. Boettger, Int. J. Quantum Chem., Quantum Chem. Symp. 25, 629 (1991).
- [13] H. B. Michaelson, J. Appl. Phys. 48, 4729 (1977).
- [14] M. Alden, S. Mirbt, H. L. Skriver, N. M. Rosengaard, and B. Johansson, Phys. Rev. B46, 6303 (1992).

Received March 16, 1993



# Density-Functional Theory in Glass Chemistry

MICHAEL P. TETER

*Research Department, Corning, Inc. Sullivan Park, Corning, New York 14831*

The development of new inorganic materials at Corning, Inc. has a long and distinguished history. A short and necessarily incomplete list of important materials discoveries at Corning includes low expansion borosilicate glasses such as Pyrex,<sup>®</sup> ultra-low expansion titanium-silicate glasses made by flame hydrolysis, silicones, fiberglass<sup>®</sup>, the complex field of glass-ceramics which ranges from ultra-high strength materials to machinable mica-based forms, photochromic glasses, x-ray absorbing television glasses, extrudable oriented ceramics, and the ultra-pure materials for optical fibers. While extremely successful, the development of new materials at Corning has been a difficult process. From the start of a research project until the manufacture of a commercial product can take from 5 to 10 years, and the vast majority of research projects fail. One important factor at the heart of the long development times and the high failure rate is a lack of fundamental understanding concerning reactions and structure in amorphous materials. New materials are developed by a mixture of intuition and empiricism.

From the time of Zachariason [1], we have had reasonable ideas about glass structure. In summary, first neighbor environments look almost exactly the same as they do in crystals, but these building blocks of first neighbor configurations are put together in a continuous random network. Electro-neutrality is preserved in the smallest possible volume consistent with ion sizes. Unfortunately, the bonding differences between a glass such as fused silica and the crystal structure of quartz are reasonably subtle. We know the structure of quartz through the analysis of x-ray diffraction experiments. The repeating nature of the quartz crystal gives many diffraction peaks which allow the structure to be unambiguously extracted. Fused silica has no repeating units other than the  $\text{SiO}_4$  tetrahedra and the strong diffraction peaks are related to these. The bonding differences between crystalline and amorphous silica occur primarily at third neighbors and beyond, and it is precisely this information which is washed out by diffraction from the amorphous structure. Most other probes again give strong information about first neighbors, weak results about second, and are washed out by third neighbors. Thus we are not certain about the structure of the most prototypical of all glasses, fused silica, which serves as a backbone for most of the silicate glasses.

Doris Evans, an x-ray crystallographer at Corning, built a model of fused silica in the mid 1960s [2] to see if a model could be built with the constraint that the only construction variable was the bonding angle between  $\text{SiO}_4$  tetrahedra. She

built a model of over 1200 tetrahedra and was able to convince herself that the procedure could be continued indefinitely. A careful analysis of the model showed that it could nearly reproduce most of the known properties of fused silica. The most important discrepancy was in the density. A careful study of variations in the density showed that it could be varied over 10% without rearranging the bonding or violating the constraint of perfect tetrahedra [3]. There had to be something other than a geometric constraint which determined the final values of the physical properties. Clearly structures arrange themselves to minimize the free energy at elevated temperatures. At low temperatures, the product of temperature and entropy becomes negligible and the free energy converges to the potential energy. Fused silica is a child of the elevated temperatures at which its bonding arrangements are formed and the relaxation in geometry but not bonding at lower temperatures. Consequently it was felt that the only way to attack the problem of molecular structure of glasses was through molecular dynamical modeling at high temperatures which could properly account for the dynamic effects of entropy coupled with a slow decrease in temperature to relax the geometry.

Born-Meyer-Huggins pair potentials were created for silicon ions and oxygen ions, and I performed molecular modeling for fused silica for over 1,000 ions. This led to a model which resembled the model of Evans but was different in many of the details. She then asked me if my potentials could reproduce the structure of the crystalline polymorphs of silica, i.e., quartz, cristobalite, coesite, tridymite, and stishovite. Since I was claiming to be able to model amorphous  $\text{SiO}_2$ , I should be able to reproduce the periodic structures that silica found to be the most natural ways to arrange itself. I found to my dismay that I could not reproduce such structures. This led to Evans Law of Glass Structure: "Accept no model of glass structure which cannot reproduce as stable structures the underlying crystalline polymorphs of similar composition."

In the early 1980s, the need for a first principles treatment of glass chemistry was becoming more urgent, and I undertook a new survey of the field to find changes and opportunities. At MIT, talks with Professor John Joannopoulos convinced me that the state of the art of density-functional quantum mechanics developed by Kohn and Sham [4] had reached the point where solids could be realistically modeled without parameterization.

The typical condensed matter calculation modeled a semiconductor with a few atoms in a periodic cell. Planewaves and pseudopotentials were used, and to model silicon required approximately 50 to 100 planewaves per atom. The diagonalization of matrices a few hundred square was not a demanding task, but since the computational effort to carry out diagonalization grew as the number of planewaves cubed, much bigger problems were computationally intractable. Because of the deep nonlocal pseudopotentials required to accurately model oxygen, oxygen requires ten times as many planewaves per atom as silicon. To simulate quartz would require the diagonalization of 10,000 by 10,000 matrices.

Douglas Allan and I at Corning had the opportunity to develop a new code from scratch. The first analysis we performed was with respect to basis sets. Table I shows

TABLE I. Properties of various bases.

	Planewaves	Orbitals	Muffin tins	Finite elements
Orthonormal complete	Yes	No	No	No
Fast transform	Yes	No	No	Yes
H <sub>1</sub> resolution with small number	No	Yes	Yes	Yes
Easy solution to Poisson's eqn	Yes	No	No	No
Exact density	Yes	No	No	Yes
No Pulay corrections	Yes	No	No	No
All-electron for all Z	No	Yes	Yes	Yes
Easy periodic implementation	Yes	No	Yes	No
Fast iterative solution methods	Yes	No	No	No
Natural X — C integration grid	Yes	No	No	Yes
Easy to code	Yes	No	No	No

the various basis sets in common use at the time and their relative advantages and disadvantages. The ideal basis set would clearly have no defects.

We generated simple plane-wave, gaussian, and finite-element codes and began comparing performances on model problems. In 1985, Car and Parrinello [5] wrote an article on quantum-mechanical molecular dynamics which emphasized the iterative approach to matrix diagonalization and showed how to derive an eigenvector by a method which scaled nearly linearly with the number of planewaves. The new method required local pseudopotentials which would not work for oxygen and was still too slow, but we began a systematic development of a planewave program because the possibility of major performance improvement was significant. The nonlocal pseudopotentials of Hamann, Schluter and Chiang [6] were generating physical properties whose errors were at the few percent level and looked extremely promising. We began a program to see if we could utilize these nonlocal pseudo-

TABLE II.  $\alpha$ -Quartz structure (trigonal  $P3_221$ )

Parameter	Experiment	Theory	$\Delta$ (%)
$a$ (nm)	0.49134	0.4880	-0.68
$c$ (nm)	0.54052	0.5270	-0.65
Si ( $\lambda$ )	0.46987 (9)	0.4638	-1.3
O ( $\lambda$ )	0.4141 (2)	0.4081	-1.4
O ( $y$ )	0.2681 (2)	0.2758	+2.9
O ( $z$ )	0.2855 (1)	0.2782	-2.6

TABLE III.  $\alpha$ -Cristobalite structure (tetragonal  $P4_12_12$ ).

Parameter	Experiment	Theory	$\Delta$ (%)
$a$ (nm)	0.49570 (1)	0.495	0.04
$c$ (nm)	0.68903 (2)	0.6906	0.23
Si ( $x = y$ )	0.3047 (2)	0.3030	-0.56
O ( $x$ )	0.2381 (2)	0.2380	-0.04
O ( $y$ )	0.1109 (2)	0.1112	0.27
O ( $z$ )	0.1826 (1)	0.1825	-0.05

potentials in a Car-Parrinello approach. We were aided by an article by Kleinman and Bylander who showed how to generate nonlocal pseudopotentials which were separable in momentum space and which scaled linearly in the number of plane waves. Unfortunately their article came out before the advent of fast iterative solution methods, so the initial advantages of using their methods were minimal since solution time dominated matrix setup time. The real importance of their approach was developed later.

Using the new separable pseudopotentials, Allen and Teter [7] showed how oxides could be modeled successfully, and Teter, Payne, and Allen [8] showed how eigenvectors could be extracted most efficiently. The details of the resulting iterative diagonalization along with a review of the planewave pseudopotential method may be found in the review article by Payne et al. [9]. For the first time, this made the planewave pseudopotential treatment of oxides viable. We then began the systematic treatment of silicates using *ab initio* methods and have fulfilled Doris Evans' challenge that all crystalline polymorphs of silica be faithfully modeled by this method. The tables below show the calculated versus measured structural parameters for several silica and titania crystals [10]. These are reproduced in Tables II through V.

After developing a general response functional capability within the planewave code, the optical phonons in quartz were simulated [11]. The results were with a few percent of experiment, but more importantly, the interaction between ions could be quantitatively measured. A study of the Born Effective-Charge Tensor for oxygen shows that no model which treats oxygen ions as charged balls can effectively model the dynamics in oxides. The polarization of the ions is at least as important as their charge in determining the correct interactions, and this is fundamentally a quantum-mechanical effect.

TABLE IV. Stishovite structure (tetragonal  $P4_2/mnm$ ).

Parameter	Experiment	Theory	$\Delta$ (%)
$a$ (nm)	0.41773 (1)	0.4255	1.9
$c$ (nm)	0.26655 (1)	0.2604	-2.3
O ( $x = y$ )	0.30614 (3)	0.3082	0.67

TABLE V. Rutile ( $\text{TiO}_2$ ) structure (tetragonal  $P4_2/mnm$ ).

Parameter	Experiment	Theory	$\Delta$ (%)
$a$ (nm)	0.4594	0.4584	-0.22
$c$ (nm)	0.2958	0.2961	0.10
O ( $x = y$ )	0.305	0.3044	-0.20

Having generated an *ab initio* code for studying oxides we began the study of defects in crystalline structures such as oxygen vacancies and interstitials. We found interesting dynamic reactions involving these defects whose barriers were of the order of a few tenths of an eV. The question naturally arose as to whether either LDA or the pseudopotentials were really this accurate. Since the solutions methods were now really fast for hundreds of thousands of grid points we began a systematic investigation of the all-electron behavior of carbon. The finding was that under compression, the norm-conserving pseudopotentials had deviations in the total energy versus lattice constant curves when compared with the all electron results of the order of 1.5 eV. These results are shown in Table VI. This was clearly too much error in the pseudopotential approximation to trust the earlier results. As a consequence, a great deal of effort was expended to determine the major source of error remaining in the pseudopotential approximation. This was determined to be

TABLE VI. Energies for diamond under isostatic compression for norm-conserving pseudopotential, all-electron and extended norm and hardness-conserving pseudopotential. A constant has been subtracted from both pseudopotential calculations to make their average energies the same as the all-electron case. Also included are the standard deviations of the differences from the all-electron case, the equilibrium lattice constant  $a_0$ , the bulk modulus  $B$ , and the pressure derivative of the bulk modulus.

Lattice constant (bohr)	Norm-cons. -63.112325 (hartree)	All-electron (hartree)	ENHC -62.361247 (hartree)
5.0	-73.559096	-73.679091	-73.677824
5.8	-74.206141	-74.242149	-74.240666
6.0	-74.281435	-74.301995	-74.300981
6.2	-74.334449	-74.342446	-74.340841
6.4	-74.360408	-74.364967	-74.364244
6.6	-74.389790	-74.374818	-74.374361
6.8	-74.398456	-74.373822	-74.373871
7.0	-74.397801	-74.364842	-74.365143
7.2	-74.389796	-74.348265	-74.350026
8.0	-74.313485	-74.247460	-74.251898
$\sigma$ (hartree)	0.0492		0.0018
$a_0$ (bohr)	6.882	6.678	6.689
$B$ (hartree/bohr <sup>3</sup> )	0.01362	0.01628	0.01571
$\partial B/\partial P$	3.728	3.599	3.648

TABLE VII. Structure of  $\alpha$ -quartz for norm-conserving, hardness and extended norm-conserving pseudopotentials and experiment.

Parameter	Norm-cons.	HENC	Experiment
$a$ (bohr)	9.363	9.285	9.290
$c$ (bohr)	10.304	10.209	10.215
Si $x$	.4638	.4688	.4697
O $x$	.4081	.4140	.4135
O $y$	.2758	.2699	.2669
O $z$	.2782	.2839	.2858

a difference between the responses of the atom and pseudoatom with regard to changes in occupancies of the valence states. A prescription for forcing the pseudopotential to mimic the correct response as well as fulfill the earlier constraints led to more than an order of magnitude reduction in the pseudopotential error, and typical differences between the all-electron results and the pseudopotential results were .05 eV [12]. Because these pseudopotentials give response correct to second order in arbitrary occupancy changes in the valence states, they are called Hardness-Conserving pseudopotentials. The structure of quartz was relaxed using the new pseudopotentials with the basis set taken to energy convergence well below the millihartree level. The results are in Table VII. You will notice that the experimental numbers are different from those in Table II. For the earlier work, a room temperature measurement for the silica structure was used. Since we had every reason to believe that we had significantly reduced the error in the structure, we found a zero degree kelvin measurement. The error when compared with experiment has been reduced by over an order of magnitude. The same pseudopotentials were then used to regenerate the optical phonon frequencies and it was found that the errors dropped from around 5% to below 1%. For the first time we were able to see systematic deviations in the frequency errors. The lower the optical frequency mode, the more the harmonic frequency fell below the experimental result. It is currently conjectured that this difference is due to anharmonic corrections which are expected to be greater for lower frequency modes, and this is being tested. The summary of these results seems to be that for structural properties in solids, the LDA is better than previously believed, and most of the error seems to be pseudopotential error. I also expect some improvement for isolated molecules, versus earlier pseudopotential calculations, but in these cases, the self-interaction in the tails of the wavefunction probably dominates the error more than in a solid where the density never really goes to zero.

Having generated a reference plane-wave code and a new generation of pseudopotentials, we are now ready to attack realistic glass-chemistry problems. Unfortunately, this tool cannot be used directly. Glass is unique in that the major unknown in glass structure is the bonding topology. The differences between bonding topologies in fused silica, and the normal silica crystals begin at about third neighbors. Clearly the correct bonding arrangement is that which minimizes the free

energy at the glass formation temperature. If one wants to simulate infinite amorphous structures by using very large periodic cells, then the minimum cell size which allows freedom for third neighbors to bond without interference with periodic images is about 400 atoms. More realistically 1,000 to 10,000 atoms should be modeled. The upper limit on the plane-wave code is about 100 to 200 atoms, for a few dozen dynamic steps. We need millions of dynamic steps to achieve a reasonably annealed structure. The reference code must then be used to generate models which can go much faster. We have a few rudimentary ones under development with a few simple calculations, but it is clear that a new generation of molecular modeling which allows dynamic bond forming and breaking is needed to realistically model glass chemistry.

In the spirit of the Sanibel conference, I would like to close with a few words concerning my view of the future of density-functional-based molecular modeling:

- 1) First, with regard to basis sets, I believe that plane-waves and pseudopotentials will probably vanish like dinosaurs in the coming meteoric collision of computational methods with wavelet representations. Professor Joannopoulos's group at MIT has recently shown that it is possible to represent accurately the 1S state of uranium as well as its adjustment under any reasonable perturbation with a few hundred three-dimensional wavelets [13]. It takes over 1,000 plane-waves to accurately represent the 3D state of titanium, and over a billion to represent the 1S state of uranium in a box large enough to simulate a significant molecule. Wavelets seem to represent that ideal representation with no defects, at least within the list shown in Table I. At the moment both our optimism and ignorance are unbounded, and to quote the immortal Murphy, "The best thing about a new idea is that we don't know what's wrong with it."
- 2) We in solid state physics are seeing the development of new *ab initio* solution methods which scale linearly in the number of atoms. These are, at the moment, ponderous and represent no threat to current methods. As a prognosticator, I feel that these methods will dominate *ab initio* calculations in large systems within 5 years.
- 3) New density functionals hold the promise of reducing the LDA errors by an order of magnitude, without a corresponding increase in computational effort. Some of these are based on gradient corrections. Careful comparison between gradient-corrected LDA calculations and exact results from diffusion Monte Carlo calculations show that the gradient corrections still have serious difficulties. I personally believe that the most promising new functionals are based on an improved weighted density approach utilizing a nonlocal integral formulation of the exchange-correlation hole.
- 4) Lastly, I believe that a new generation of accurate molecular modeling is coming which will include electron degrees of freedom and allow not only reactions, but be fast enough to handle systems of 10,000 atoms for millions of time steps. These models will be parameterized directly from the density-functional codes. While we have one of these under development for glass chemistry, it is too early to speak of results other than qualitatively it seems to work.

**Bibliography**

- [1] W. H. Zachariasen, J. Am. Chem. Soc. **54**, 3841 (1932).
- [2] D. L. Evans and S. V. King, Nature **212**, 1353 (1966).
- [3] D. L. Evans and M. P. Teter, *The Structure of Non-Crystalline Materials*, P. H. Gaskell, Ed. (Taylor and Francis, London, 1977), p. 53.
- [4] W. Kohn and L. J. Sham, Phys. Rev. A **140**, 1133 (1965).
- [5] R. Car and M. Parrinello, Phys. Rev. Lett. **55**, 2471 (1985).
- [6] D. R. Hamann, M. Schluter, and C. Chiang, Phys. Rev. Lett. **43**, 1494 (1979).
- [7] D. C. Allan and M. P. Teter, Phys. Rev. Lett. **59**, 1136 (1987).
- [8] M. P. Teter, M. C. Payne, and D. C. Allan, Phys. Rev. **B40**, 12255 (1989).
- [9] M. C. Payne, M. P. Teter, D. C. Allan, T. A. Arias, and J. D. Joannopoulos, Rev. Mod. Phys. **64**, 1045 (1992).
- [10] D. C. Allan and M. P. Teter, J. Am. Ceram. Soc. **73**, 3309 (1990).
- [11] X. Gonze, D. C. Allan, and M. P. Teter, Phys. Rev. Lett. **68**, 3603 (1992).
- [12] M. P. Teter, to be published in Phys. Rev. B.
- [13] K. Cho, T. A. Arias, J. D. Joannopoulos, and P. K. Lam, submitted to Phys. Rev. Lett.

Received March 14, 1993



# ***Ab Initio* Investigation of Void Stabilization: Oxygen in Nickel**

RANDALL C. BOEHM and AJIT BANERJEE

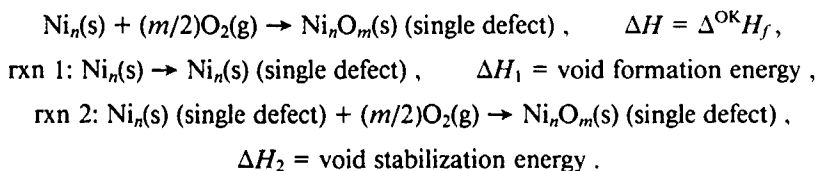
*Theory Project, Materials Chemistry, Idaho National Engineering Laboratory, EG&G of Idaho, Inc., Idaho Falls, Idaho 83415-2208*

## **Abstract**

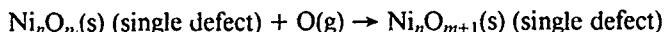
We have used the *ab initio* technique of UHF/LANLMB to study the interactions between absorbed oxygen atoms and molecules with their host nickel lattice. The host lattice is approximated by a small cluster of nickel atoms that are arranged as face-centered-cubic, except for a tubular void described by the absence of three or four lattice elements. The oxygen absorbates are placed, one at time, within this cavity. We conclude that, for tubular cavities, the interaction between the nickel lattice and the oxygen absorbates is stronger than the interactions between pairs of oxygen atoms, suggesting that the absorbates are mostly atomic (as apposed to diatomic) in character, while the (energetically) most preferred number of oxygen atoms to reside inside an  $n$ -site, tubular hollow of nickel is simply  $(n - 1)$  © 1993 John Wiley & Sons, Inc

## **Introduction**

The stabilization of microcavity voids in face-centered cubic (fcc) solids is believed to result in an increase in the homogeneity of the material as well as an increase in the microstructure stability [1,2]. In turn, these changes are believed to result in an improvement of bulk properties such as tensile strength, fatigue strength, and creep resistance [3]. We have undertaken this study in order to gain fundamental understanding of void stabilization and its relation to the microstructure of a material. The lattice of nickel was selected, with oxygen (atomic and molecular) impurities, as a specific system to study because of a collaboration we have with experimentalists from this lab who are analyzing the properties of this system. The term "void stabilization" taken by itself is ambiguous in that it is not inherently clear what is taken as the reference point. Ultimately, one would like to compare the energies of void defects, with and without absorbates, to the energy of the pure metal plus molecular  $O_2$  and to the energies of other kinds of defects (stacking fault or dislocation loop) with and without absorbates. We feel the best way to progress toward this comparison is to make a tendency toward their standard heats of formation in the following manner:



The body of this report is concerned only with reaction 2, the heat of which we define as the void stabilization energy. An alternative view is presented as an appendix. Namely, a definition of void stabilization is given by the following equation:



### Method

The host lattice is approximated by a small cluster of nickel atoms that are arranged as face-centered cubic, except for a tubular void described by the absence of three or four lattice elements. The oxygen absorbates are placed, one at time, within this cavity. Elucidation of the electronic structure was accomplished at the spin-unrestricted Hartree-Fock (UHF) level with the LANL1MB basis. The full basis set description has been published elsewhere [4] but will be reviewed here briefly for completeness. Each electron's orbital around oxygen is described by three gaussian primitives, contracted into each of the 1s and 2sp shells. The 1s through 3p electrons on Ni, taken to be core electrons, are described by a single pseudopotential, while the remaining 4s and 3d valence electrons go into orbitals that are described by single sets (three primitives per set) of s-, (five) p-, and d-type functions.

In the interest of easing computational demands, while maintaining computational integrity, the optimized nuclear configurations which are shown in Figure 1 were determined under the following constraints based upon the symmetry of the cluster or the bulk. For the reference structure all Ni—Ni bonds were constrained to be of the same length ( $R$ ) and all Ni—Ni—Ni bond angles were fixed at  $180^\circ$  or  $120^\circ$  as shown in Figure 1. The so-optimized structure was then taken as the host lattice, which remained rigid for all subsequent calculations. In structure A1, the oxygen atom resides at a distance ( $R_2$ ) of 4.126 Å from the edge of the cavity. A full description of the potential as a function of the  $z$ -coordinate of oxygen is shown in Figure 2. For structure B1, the  $\text{O}_2$  bond distance ( $R_0$ ) was reoptimized to 1.268 Å from its gas phase, UHF/LANL1MB value of 1.217 Å [5]. Concurrent to this optimization, the distance from the center of the  $\text{O}_2$  bond to the edge of the cavity ( $R_3$ ) was determined. For structure A2 a  $D_{2h}$  symmetry constraint was enforced throughout the optimization of  $R_2$ , the distance between atomic oxygen and the edge of the cavity. However, once determined, the energy of this structure was compared to the energy of an alternative structure that has one oxygen atom in the center of the cavity and the other a distance of  $R_2$  from the edge of the cavity, as well as several others.

The structure A2 shown in Figure 1 is the lowest energy configuration. The values of  $R_2$  and  $R_3$  were optimized in a similar manner for structures B2, B3, and A3. Structure A4 is simply an fcc layer with four nickel atoms displaced by four oxygen atoms. Finally, a single point energy calculation was completed for structure B4 as a check on our presumption that the  $\Delta H_f$  of these clusters will increase quickly as the number of atoms inside the void exceeds the number of vacancies defining the cavity.

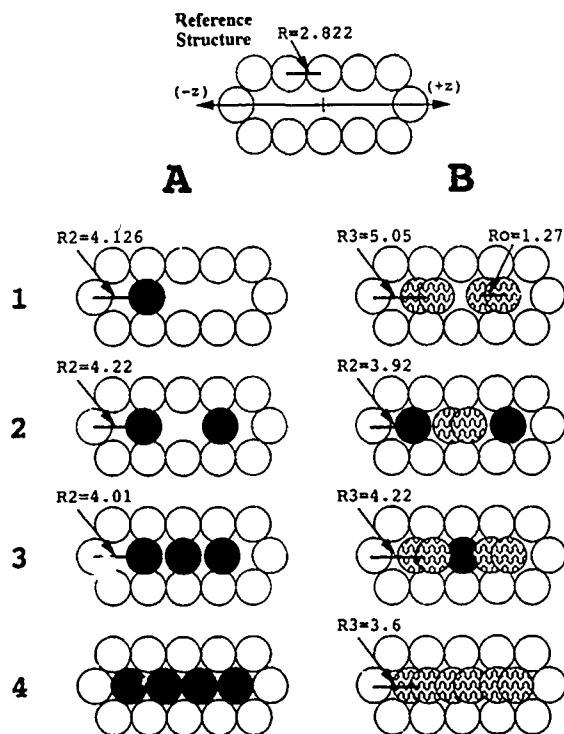


Figure 1. (a) The layout of this figure is something like a table in that the structures are delineated by rows and columns. Structure B2, for example, is in column B and row 2. (b) The open circles represent nickel. The plain shaded circles represent atomic oxygen. The wavy shaded circles represent molecular oxygen. (c) All structures shown belong to the  $D_{2h}$  point group, except for structure A1 which belongs to the  $C_{2v}$  point group. (d)  $R$  is the distance between adjacent nickels.  $R_0$  is the distance between oxygens, and  $R_2$  is the  $z$ -position of oxygen, relative to the edge of the box.  $R_3$  is the  $z$ -position of the midpoint of  $O_2$ , relative to the edge of the box.

## Results

### One Oxygen Atom

The behavior of a single oxygen atom trapped inside a tubular void of an fcc solid is interesting not only because it lays the foundation for understanding void stabilization, but also because it displays at once several fundamental aspects of all physical systems. Its behavior is influenced by symmetry, by a periodicity of the field generated by the host metal, and by edge effects which are akin to the particle-in-a-box model. It was shown many years ago [6] that any molecular system, characterized by a nondegenerate electronic state which is at a stationary point within point group  $G$ , will also be at a stationary point within any subgroup of  $G$ . The highest-order point group to which this Ni/O cluster (oxygen trapped within a four-

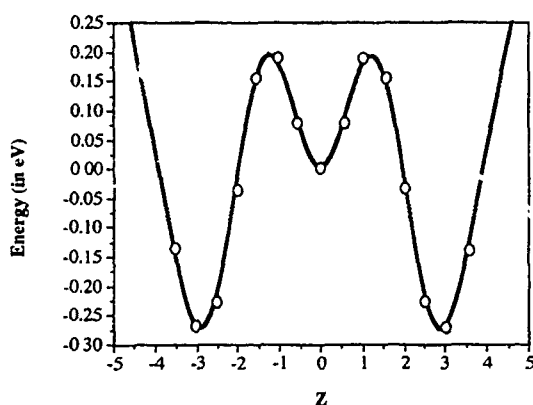


Figure 2. The solid line represents a fit to the *ab initio* data; represented by open circles.

site tubular cavity in nickel) conceivably could belong is  $D_{2h}$ . This conformation has oxygen at the center of the void, and it must correspond to a local stationary point. In the bulk system, that we are simulating, the potential along the ( $x$ ) direction is exactly the same as the potential along the ( $y'$ ) direction, where the  $y'$  direction is perpendicular to the  $z$ -axis while it makes an angle of  $60^\circ$  with the  $x$ -axis, and the  $z$ -axis runs along the length of the void. In our model, the width of the void is 4.887 Å, just 10% more than twice the UHF/LANL1MB bond length (2.208 Å) of NiO gas. Because of these two points, it is unlikely that the energy of system would decrease as oxygen moves, within the  $xy$ -plane, away from the geometric center.

TABLE I. Absolute energies (hartrees).

Species	UHF energy	$S(S+1)\hbar^2$	$R_2$ , or bond (Å)
O	-73.8042	2.000	
Ni	-38.9803	2.000	
NiO	-112.7492	2.854	2.208
O <sub>2</sub>	-147.6342	2.000	1.217
Ni <sub>2</sub>	-77.9527	2.004	2.742
Ni <sub>10</sub>	-389.6730	10.129	2.822
Ni <sub>10</sub> O <sub>2</sub>	-537.4486	10.762	4.18
Ni <sub>12</sub>	-467.7216	10.700	2.822
Ni <sub>12</sub> O	-541.5954	11.295	4.13
Ni <sub>12</sub> O <sub>2</sub>	-615.4290	12.206	4.22
Ni <sub>12</sub> O <sub>3</sub>	-689.2588	13.494	4.01
Ni <sub>12</sub> O <sub>4</sub>	-763.0271	—	—
Ni <sub>12</sub> O <sub>2</sub> (O <sub>2</sub> )	-763.0382	13.710	3.92
Ni <sub>12</sub> (O <sub>2</sub> ) <sub>2</sub>	-763.0665	12.653	4.42
Ni <sub>12</sub> O(O <sub>2</sub> ) <sub>2</sub>	-836.3584	13.394	3.59
Ni <sub>12</sub> (O <sub>2</sub> ) <sub>3</sub>	-910.6624	—	3.00

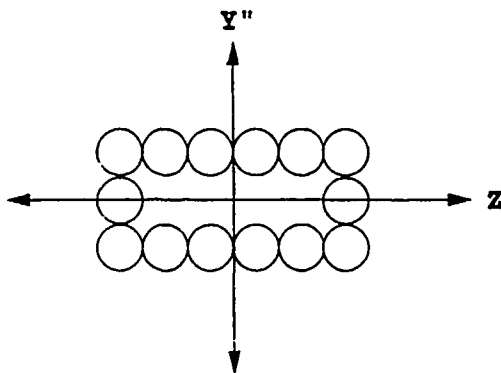
TABLE II. Off-center energies of  $\text{Ni}_{12}\text{O}$ .

Distance off center ( $\text{\AA}$ )	$\Delta E$ (eV)
$y = 0.05$	0.07
$y = 0.00$	0.00
$y = -0.05$	0.07

The results shown in Table II validate this presumption for the one oxygen case, and we presume that such a condition also holds for multiple absorbates.

Now that we have established that oxygen should lie somewhere on the  $z$ -axis, we may defend our decision to include a single plane for our model by simply noting that the  $xz$  and  $yz$  planes are exactly equivalent while a third plane ( $y''z$ ) is shown in Figure 3. Deletion of the ( $y'z$ ) and ( $y''z$ ) planes is expected to effect no influence on the qualitative predictions of our model, as the kinds of interactions that are prevalent in the ( $y''z$ ) plane are outweighed by the closer, shifted interactions prevalent in each of the ( $y'z$ ) and ( $xz$ ) planes. The quantitative predictions are, however, likely to be compromised, but this kind of result is already compromised by computational level and basis set size. Therefore, we feel nothing significant is lost by considering a single plane.

For displacement of oxygen along the  $z$ -axis, we reiterate that the  $D_{2h}$  structure corresponds to a minimum or a maximum by symmetry. In this direction, however, there exists  $4.85 \text{ \AA}$  (as apposed to  $0.23 \text{ \AA}$  in the ( $x$ ) or ( $y$ ) directions) of "free" range before the boundary of the box is first impeded upon. Any potential energy curve covering this much distance, through chemically significant regions, is likely to encompass several extrema. Certainly the periodic Ni/O system we are simulating will exhibit three or four local minima (with two unique well depths) in which the oxygen atom could reside. Our model gives three minima (see Fig. 2). The  $D_{2h}$  structure is slightly higher in energy than shown in Figure 1 (A1), as well as (of course) is mirror image reflection through the ( $xy$ ) plane.

Figure 3. A four-site cavity in nickel: the ( $Y''Z$ ) plane.

The potential energy curve (Fig. 2) can be divided conceptually into three distinct partitions. Empirical fits to each of these partitions are shown in Figure 4. The periodic part [Fig. 4(a)] is due to interactions of oxygen with the Ni cores. The edge effect [Fig. 4(b)] is due to the physical boundary of the box. The delocalized partition [Fig. 4(c)] is due to a propagated and progressive difference in the valence region of the Ni atoms from the edge to the center. Such a decomposition may be useful for making projections of the behavior of one oxygen atom in progressively larger tubular voids. We, however, have employed it as a guide in our characterization and analyses of multiple oxygen atoms within the same, four-site hollow.

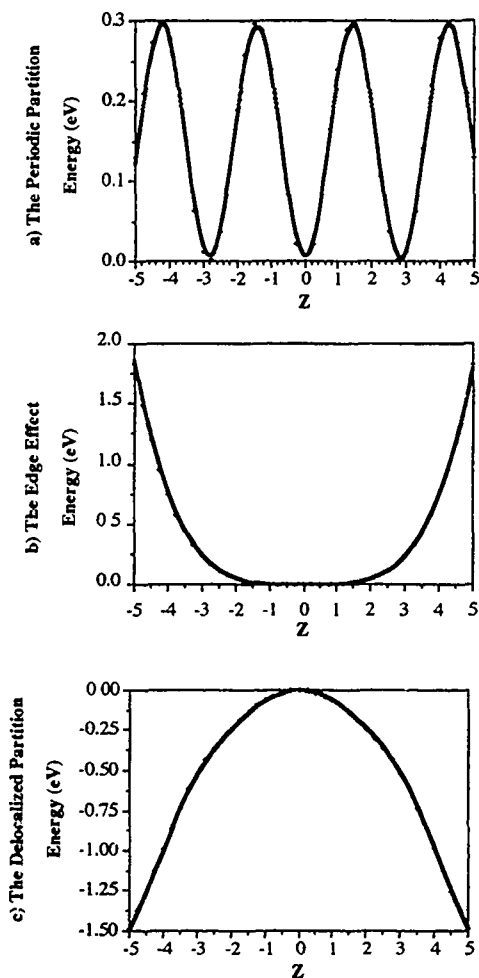


Figure 4. (a)  $E = A_0 \sin^2(bz)$ ,  $A_0 = 0.29835$  eV,  $b = 1.1134$  Å<sup>-1</sup>; (b)  $E = k_2(bz)^4$ ,  $k_2 = 0.00190$  eV Å<sup>-4</sup>; (c)  $E = E_0 + A' + k_1(bz)^2$ ,  $k_1 = -0.04641$  eV Å<sup>-2</sup>,  $E_0 = -0.00073$  eV,  $A' = c'[(bz) \sin(bz)]^2$ ,  $c' = -0.00383$ .

### *Two Oxygen Atoms*

For two oxygen atoms inside the void, there exists four physically distinct nuclear configurations that may correspond to local minima on the ground electronic surface. There may be one oxygen atom in each of the wells near  $\pm 3$  Å [Figs. 2 and 4(a)], there maybe one oxygen atom at either of these locations while the second oxygen is near the geometric center, or there may be two oxygen atoms in any one of the wells shown in Figure 2. Each of these configurations was explored in some detail.

We have found no local minimum corresponding to a pair of oxygen atoms (i.e., an oxygen molecule) inside a single well. This indicates that oxygen-oxygen attractions are overwhelmed by oxygen-lattice interactions, at the UHF/LANL1MB level. Each of the remaining two configurations do correspond to local minima. The minimum at ( $z_1 = 2.83$ ,  $z_2 = -2.83$ ) is 0.29 eV lower in energy than the local minimum at ( $z_1 = 2.63$ ,  $z_2 = 0.01$ ), which is about the same as the difference in energy between the two distinguishable structures for  $\text{Ni}_{12}\text{O}$ . The position of the first oxygen in the higher energy structure (of  $\text{Ni}_{12}\text{O}_2$ ) is, however, shifted by 0.2 Å relative to the position of oxygen in the lowest energy structure of  $\text{Ni}_{12}\text{O}$  and relative to the first oxygen in the global minimum for  $\text{Ni}_{12}\text{O}_2$ . Of course, the second oxygen atom, in the higher energy structure, is also shifted somewhat from the geometric center, as expected within the laws governed by  $C_{2v}$  symmetry rules. These shifts indicate that oxygen-oxygen attractions are exerting some influence on the relative positions of each oxygen within the void. Taken with our earlier said conclusion, this influence is propagated through a barrier rather than within a single well.

### *Three Oxygen Atoms*

Using our results for the two oxygen case as a guide, we doubt that more than one (locally) minimum energy configuration exists for the three oxygen case. The arrangement of the single, expected minimum energy structure is  $D_{2h}$ , as shown in Figure 1, structure A3. The direct (and indirect) force exerted by the center oxygen on the two "edge" oxygens is divided equally between them, thereby diminishing its magnitude relative to the higher energy structure of the two oxygen case. At the UHF/LANL1MB level this direct force is insufficient (relative to oxygen-lattice interactions) to effect an appreciable influence on the relative positions of each oxygen within the void. On the contrary, the electron withdrawing character of the oxygen atoms appears to affect the host lattice in such a way as to increase the magnitude [the curvature of curve 4(c), if you will] of the propagated difference in the valence region of the Ni atoms, resulting in a net increase in the skew of the edge oxygen atoms toward the edge of the cavity.

The resultant void stabilization of this structure is the greatest that we compiled during the four-site hollow portion of this study (the compilation is given in Table III). It is interesting to note that most of the volume of the Ni cavity is occupied by the three oxygen atoms, distributed throughout the void so that the largest unoccupied hollow is just 4.01 Å in length (and 4.89 Å in diameter). The results in Table III also suggest that the change in stabilization energy decreases as more

TABLE III. Void stabilization energies.

Figure	Stabilization energy (no. of impurities in cavity)	
	Pattern A	Pattern B
1	1.54 (1.1) <sup>a,b</sup>	2.08 (2.4)
2	1.99 (2.2)	1.31 (3.4)
3	2.34 (3.3)	1.39 (3.5)
4	1.01 (4.4)	1.1 (3.6)

<sup>a</sup> Energies are in units of eV.

<sup>b</sup> The first number in parentheses is the total number of (atomic and/or molecular) impurities, while the second number is the total number of atoms.

oxygen atoms are stuffed into the void:  $\text{Ni}_{12}\text{O}_2$  is more stable than  $\text{Ni}_{12}\text{O}$ , while  $\text{Ni}_{12}\text{O}_4$  is 0.26 eV less stable than  $\text{Ni}_{12}\text{O}_3$ , etc.

#### Four Oxygen Atoms

The four oxygen case is interesting because it has more oxygen atoms confined within the cavity than the cavity has wells into which the atoms may reside. It follows then that at least one well will have to accommodate two oxygen atoms (an oxygen molecule), provided that the analysis of the PES shown in Figure 2 remains qualitatively correct. We have explored those regions of the PES near the equilibrium geometries of each of the structures shown in Figure 1, A4, B1, and B2, as well as an additional structure which is described later in this section.

Structure A4 is expected to correspond to saddle point configuration because each of the four absorbed oxygen atoms reside at a maximum on the periodic portion of the PES [see Fig. 4(a)]. Further, we observe that there exist four ways that each of the two interior oxygen atoms may fall off these maxima. These are represented by structures B1 and B2 and by a doubly degenerate structure with a molecule in one of the outer wells and a single atom each of the remaining two wells. Note that the pair of outer oxygen atoms is presumed to fall inward due to the edge effect that becomes strongly repulsive as " $z$ " surpasses 4.2 Å (as  $R_2$  drops below 2.8 Å).

Each of these nuclear configurations were found to be lower energy structures than that of A4, as expected. Hence we observe four directions that lead to lower energy than that of structure A4. Therefore, the energy of structure A4 represents an upper bound of the barrier to conversion between structure B1 and B2 (or any couple of the four minima described above) [7]. At the LANLMB level, structure B1 is more stable than structure B2 by 0.77 eV, while the barrier to conversion of B2 to B1 is less than 0.30 eV. The doubly degenerate  $C_{2v}$  structure, not shown, has an energy only slightly lower than that of structure B2. This is surprising as we



expected (based upon the arguments presented in the next section) the energy of this structure to be about half that of structure B2, taking the energy of structure B1 as zero (possibly, we missed the minimum by a significant amount as our search was somewhat limited).

Apparently the effect shown in Figure 4(c) continues to increase in magnitude as the number of oxygen absorbates continue to increase. We say this for two reasons: The first is that the difference in energy between the global minimum and the next lowest minimum increases steadily from the one oxygen case to the two oxygen case to the four oxygen case. The other reason is that degree of skew of the outer oxygen atoms in the three oxygen case toward the edge of the box points to an increase in this effect, as discussed in the section devoted to the three oxygen case. In the four oxygen case this skew loses its meaning as it is impractical to distinguish between those effects which result from oxygen-oxygen interactions and those which result from delocalized lattice-oxygen interactions.

Finally, let us speak to the probability of finding two oxygen molecules inside a four-site, nickel lattice hollow. Table III shows that the greatest stabilization is effected by the three atomic oxygen absorbates. If such cavities at first form quickly around impurities, rather than by diffusion of impurities into preformed cavities, then three atomic oxygen absorbates is an unlikely number, as is any odd number of atomic oxygen absorbates in any cavity. The exception to this rule is the event which includes the collapse of a large cavity during a latter stage of solidification, after the molecular oxygen absorbates have dissociated and dispersed throughout the void. The question we have answered is whether a four-site hollow is more likely to form initially around one oxygen molecule or two oxygen molecules. The results in Table III indicate that the net stabilization energy, defined as the energy of the naked nickel cluster ( $\text{Ni}_{12}$ ) plus  $n$  times the energy of gaseous  $\text{O}_2$  minus the minimum energy of  $\text{Ni}_{12}\text{O}_{2n}$ , is nearly the same for each case. On this basis, one cannot determine which of the above scenarios is more probable. However, the rapid solidification of nickel is a process that occurs at high temperature; thus entropy is expected to be an important factor in the determination of most probable void sizes and nucleation sites. Usually this factor will favor the channel with more translational degrees of freedom, and there is no reason to expect anything different here. Hence, the scenario which describes nucleation of a void around a single molecular impurity, followed by dissociation into a pair of trapped oxygen atoms, is expected to be the most probable.

#### *Five and Six Oxygen Atoms*

The supersaturated case studies were performed primarily to determine the maximum number of oxygen atoms that could be placed inside a four-site Ni hollow without effecting a net positive  $\Delta H_2$ . This number is six, or a pair of atoms per natural well of the system. We propose the maximum number of oxygen absorbates in any tubular void is governed by the same physical circumstance. Hence,  $(2n - 2)$  is the maximum number of oxygen absorbates that can be packed into any  $n$ -site tubular Ni hollow.

### *Three-Site Hollow*

Those results in Table III that point to "three" as the optimal number of trapped oxygen absorbates inside the four-site Ni hollow already suggest that it is energetically favorable to have each natural well of the void be occupied by exactly one atomic absorbate. The results for two oxygen atoms inside a three-site hollow strongly reinforce this suggestion. The stability of  $\text{Ni}_{10}\text{O}_2$  is 1.86 eV greater than that of  $\text{Ni}_{12}\text{O}_2$ . Taken alone, this suggests that number of vacancies defining a tubular void in nickel is not persuaded by energy to exceed  $(2n + 1)$ , where  $n$  is the number of  $\text{O}_2$  molecules around which Ni is solidifying. There are, of course, many other components that need to be evaluated (such as the energy required to create an  $n$ -site hollow from a perfect fcc lattice, for example) before one can say definitively that the creation of one cavity size, in the presence of oxygen, is preferred over another. We feel the comparison above is one very important component toward this end.

### **Conclusion**

We have shown that  $n$ -site tabular hollows in nickel exhibit  $(n - 1)$  natural wells into which oxygen might reside. The interaction energy between the nickel lattice and these oxygen absorbates is greater than the interaction energy between pairs of oxygen atoms. This implies that the absorbates exist in a form which is predominantly atomic, as opposed to diatomic. The most preferred number of these atomic absorbates is  $(n - 1)$ , exactly matching the number of natural wells resulting from the structure of the host lattice. The maximum number of oxygen atoms within a single  $n$ -site hollow is  $2(n - 1)$ , or one molecule per natural well. Finally let us remind the reader that each of the stated conclusions apply, at the UHF/LANL1MB level, only to tubular (i.e., linear) cavities. Substantially different conclusions may result from studies of 2D and 3D cavities, especially for larger cavities that begin to share more characteristics with adsorption, than with typical absorption.

### **Appendix**

Let us alternatively define void stabilization as the binding energy of an oxygen atom inside a nickel/void complex that is already occupied by  $m$  oxygen atoms,  $m = 0-5$  (see the first section). Using this definition, we find that void stabilization decreases steadily from 1.89 eV at  $m = 0$  to  $-0.33$  eV at  $m = 4$  before increasing slightly again at  $m = 5$ . From this approach we find that  $m = 4$  is the maximum number of oxygen atoms that can be inserted into the cavity before the void stabilization energy (VSE) changes sign. This contrasts with the previous answer of (at least) six absorbates before the sign of  $\Delta H_2$  changes. Clearly this difference is the result of differing definitions of void stabilization. The binding energy (BE) equal to zero marks the point at which it is no longer energetically favorable to bind the nickel/void/oxygen complex with another oxygen atom. Thus, the BE definition of VSE would also suggest that  $m = 4$  is the most favorable number of oxygen absorbates to insert into the nickel/void complex. However,  $m = 4$  is only slightly favored

over  $m = 3$  so that we cannot determine definitively which number is most preferred. This is again in sharp contrast to the  $\Delta H_2$  definition of VSE which leads to  $m = 3$  as a clear favorite, with  $m = 2$  and  $m = 4$  being too close to call. These differences prove that great attention must be paid to which definition of void stabilization has been invoked, a number of which have been seen in the literature [8-10].

### Acknowledgments

The authors would like to thank the INEL supercomputer center for its generous allocation of time on the Cray X-MP and Dr. John Flinn for many helpful discussions concerning the experiments which led to this study. This work was partially supported through the EG&G of Idaho, Long Term Research Initiative program under the DOE Idaho Field Office Contract DE-AC07-761DO1570.

### Bibliography

- [1] M. Cohen, B. H. Kear, and R. Mehrabian, in *Proceedings of the 2nd International Conference of Rapid Solidification Processing—Principles Technologies II* (Claitors, Baton Rouge, LA, 1980), pp. 1-23.
- [2] J. E. Flinn, *Rapid Solidification for Reduced Consumption of Strategic Advedds* (Noyes, Park Ridge, NJ, 1985).
- [3] J. E. Flinn, J. C. Bae, and T. F. Kelly, *Heat Resistant Materials*, K. Nateson, and D. J. Tilladi, Eds. (ASM International, Metals Park, OH, 1991) pp. 35-44.
- [4] P. J. Hay and W. R. Wadt, *J. Chem. Phys.* **82**, 270-310 (1985).
- [5] R. C. Weast, M. J. Astle, and W. H. Beyer, Eds. *CRC Handbook of Chemistry and Physics*, 68th ed. (CRC, Boca Raton, FL, 1987).
- [6] H. Jahn and E. Teller, *Proc. Roy. Soc. London Ser. A* **161**, 220 (1937).
- [7] L. L. Lohr, private communication.
- [8] J. B. Adam and W. G. Wolfer, to appear.
- [9] S. J. Kinkle and E. H. Lee, *Metall. Trans. A* **21A**, 1037 (1990).
- [10] L. E. Seitzman, G. L. Kulcinski, and R. A. Dodd, in *Radiation-Induced Changes in Microstructure 13th International Symposium (Part 1)*, ASTM STP 955, F. A. Gamer, N. H. Packan, and A. S. Kumer, Eds. (American Society for Testing and Materials, Philadelphia, 1987), p. 279.

Received April 6, 1993

# V<sup>4+</sup> Doping into SiO<sub>2</sub>, ZrO<sub>2</sub> and ZrSiO<sub>4</sub> Structures. An *Ab Initio* Perturbed Ion Study

J. ANDRÉS, A. BELTRÁN, J. CARDA, and G. MONRÓS

*Department of Experimental Sciences, Universitat Jaume I, Box 242, 12080 Castelló, Spain*

## Abstract

An *ab initio* perturbed ion study using X-ray diffraction data has been carried out for ZrSiO<sub>4</sub> (zircon), ZrO<sub>2</sub> (monoclinic zirconia, baddeleyite), and SiO<sub>2</sub> ( $\alpha$ -cristobalite) crystal lattice structures. The different substitutions of V<sup>4+</sup> for Zr<sup>4+</sup> and Si<sup>4+</sup> occurring in these host lattices have been analyzed. Geometry optimizations have been performed with the aim of determining the relative stability, cell parameters, and force constants of radial displacement associated with the local relaxation for pure and doped structures. Numerical results are confronted against experimental data and compared with previous results. The geometrical cell parameters of different structures obtained by computer simulation and the results of the X-ray diffraction studies agree with previous experimental data. For the zircon lattice, the substitution of V<sup>4+</sup> for Zr<sup>4+</sup> at an eightfold-coordinated site is energetically favorable while the substitution of V<sup>4+</sup> for Si<sup>4+</sup> at a fourfold-coordinated site is unstable. For ZrO<sub>2</sub>, the substitution of V<sup>4+</sup> for Zr<sup>4+</sup> is energetically favorable while the substitution of V<sup>4+</sup> for Si<sup>4+</sup> in SiO<sub>2</sub> is energetically unfavorable. There is less sensitive influence of the crystal lattice parameters for substitutions occurring at the eightfold-coordinated ion site in ZrSiO<sub>4</sub> and SiO<sub>2</sub> structures. The doping process produces a decrease of force constant (*k*) values associated with the breathing fundamental vibrational mode for all structures. The *k* associated with the radial displacement in dodecahedral substitution in the ZrSiO<sub>4</sub> structure is especially high. The force constants for this movement in tetrahedral substitution in the ZrSiO<sub>4</sub>, ZrO<sub>2</sub>, and SiO<sub>2</sub> structures have a lower value. The differences between ionic radii reported by Shannon and Prewitt of the species concerned in the doping process are not capable of explaining the relaxation of crystal lattice parameters in the ZrO<sub>2</sub> and SiO<sub>2</sub> structures. © 1993 John Wiley & Sons, Inc

## Introduction

It is well known that there is considerable interest within the ceramics industry in the zircon structure, ZrSiO<sub>4</sub>, due to its natural capacity to accept replacements of its cations by foreign cations in a substitutional solid solution [1]. In particular, the discovery of the vanadium-zircon blue pigment with high stability and comparatively low cost was a fundamental advance in the ceramic pigments field [2–4].

The principal structural unit of zircon is a chain of alternating edge-sharing SiO<sub>4</sub> tetrahedra and ZrO<sub>8</sub> triangular dodecahedra extending parallel to the *c*-axis. The chains are joined laterally by edge-sharing dodecahedra. In zircon, octahedral sites are present but contain no cations [5]. Therefore, the foreign cations could occupy the Si<sup>4+</sup> position and/or the Zr<sup>4+</sup> in the zircon structure.

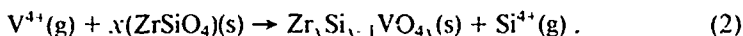
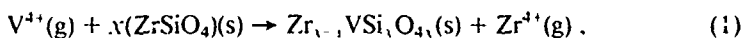
From an experimental point of view, it is difficult to assess spectroscopically the exact substitutional site because both positions have the same, D<sub>2h</sub>, symmetry. This

fact has produced an interesting controversy in the literature: Demiray et al. [6] have concluded that the  $V^{4+}$  ion only occupies the dodecahedral sites in the lattice, replacing the  $Zr^{4+}$  ion. Di Gregorio and Greenblatt [7] conclude that the  $V^{4+}$  ion would preferentially occupy the tetrahedral environments, replacing the  $Si^{4+}$ . Lastly, Hong et al. [8], using the previous experimental results and calculating the distribution of energy levels, have concluded that  $V^{4+}$  replaces both  $Si^{4+}$  and  $Zr^{4+}$  in the zircon lattice. Recently, Chandley and Clark [9] suggest that vanadium occupies either the  $Si^{4+}$  alone or both the  $Zr^{4+}$  and  $Si^{4+}$  sites but predominantly the  $Si^{4+}$  site in  $ZrSiO_4$ .

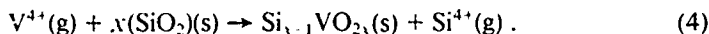
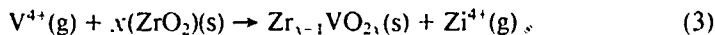
Our interest in the zircon structure has existed for a considerable time, and we initiated our experimental research by examining the synthesis of different kinds of solid solutions by a sol-gel process and their characterization [10]. From a theoretical point of view, two studies have been carried out by us [11] and Chandley et al. [12] in order to determine the site at which vanadium prefers to be doped in the zircon structure. From this aspect, the present paper can be considered as a prolongation of these works.

There are several ways to address the problem of substitution of  $V^{4+}$  into the  $ZrSiO_4$  lattice, depending upon which mode of synthesis is being analyzed. We can consider two procedures:

(i) In a flux-grown crystal, the most simple analysis involves two possible substitutions, as defect reactions show:



(ii)  $ZrSiO_4$  can be formed by the reaction of  $V^{4+}$  with  $ZrO_2$  (monoclinic zirconia, baddeleyite) and  $SiO_2$  ( $\alpha$ -cristobalite) that act as precursors [9,10], then the incorporation of  $V^{4+}$  into  $ZrSiO_4$  is therefore dependent on the defect reactions:



In conclusion, depending on the chemical environment present during the synthesis of  $ZrSiO_4$ ,  $V^{4+}$  can be readily substituted either for  $Zr^{4+}$ , via direct substitution [Eq. (1)] or via  $ZrO_2$  doping [Eq. (3)], or for  $Si^{4+}$ , via direct substitution [Eq. (2)] or via  $SiO_2$  doping [Eq. (4)].

The *ab initio* perturbed ion (aiPI) method has been successfully applied to the calculation of the electronic structure of different structures like halides [13], hydrides [14], binary oxides [15], different oxo, and fluoropervskites [16]. This method gives detailed information on the ionic wavefunctions and the microscopic interactions determining the relative stability of pure or/and doped structures.

Following recent achievements in applying this methodology in order to acquire an understanding of the physical and chemical properties relevant to condensed matter, the present work has been launched with the aim of investigating theoretically the following aspects:

(i) Calculation of different properties like lattice energy, equilibrium cell parameters of ZrSiO<sub>4</sub>, ZrO<sub>2</sub>, SiO<sub>2</sub>, Zr<sub>1-1</sub> VSi<sub>1</sub>O<sub>4</sub>, Zr<sub>1</sub>Si<sub>1-1</sub> VO<sub>4</sub>, Zr<sub>1-1</sub> VO<sub>2</sub>, and Si<sub>1-1</sub> VO<sub>2</sub> structures.

(ii) Calculation of force constants associated with breathing or radial vibrational modes of pure and doped structures.

(iii) Numerical results are analyzed and compared against other theoretical results and experimental data.

The method and model are summarized in the next section. The results and discussion are presented in the third section. A short section of conclusions closes this paper.

### Method and Model

#### *aiPI method*

The aiPI method [17] provides an adequate quantum-mechanical treatment of the atom-in-the-lattice structure. The particular features of this method have been described by Luaña and Flórez [18], and it is suitable for studying crystal defects in terms of clusters whose size and characteristics can properly simulate the effects induced by the presence of impurity ions.

Effective energies and optimized structures are reported for clusters of the pure crystals, ZrSiO<sub>4</sub>, ZrO<sub>2</sub>, and SiO<sub>2</sub>, and of the vanadium-doped structures, Zr<sub>1-1</sub> VSi<sub>1</sub>O<sub>4</sub>, Zr<sub>1</sub>Si<sub>1-1</sub> VO<sub>4</sub>, Zr<sub>1-1</sub> VO<sub>2</sub>, and Si<sub>1-1</sub> VO<sub>2</sub>. The impurity ions occupying cationic vacancies in the crystal are simulated assuming that the substitution occurs in a single center, which is the reference origin in the construction of the clusters. The clusters have been built successively adding shells of ions that are symmetrically distributed around the origin.

#### *Model*

To avoid undesirable effects related to the cluster-lattice interface as have been previously noted in other theoretical studies by Luaña and Flórez [18], the different structures and the impurity center (V<sup>4+</sup>) are simulated by a large cluster. In this work, we have self-consistently computed the electronic structure of eight different clusters that includes a total number of atoms from 53 to 117 (20–46 shells of neighbors). Zr<sub>23</sub>Si<sub>14</sub>O<sub>80</sub>, Zr<sub>22</sub>VSi<sub>14</sub>O<sub>80</sub>, Si<sub>23</sub>Zr<sub>14</sub>O<sub>76</sub>, and Si<sub>22</sub>VZr<sub>14</sub>O<sub>76</sub> (around 4% molar of doping) clusters embedded in a zircon lattice have been used. Zr<sub>17</sub>O<sub>36</sub> and Zr<sub>16</sub>VO<sub>36</sub> (around 6% of doping) clusters embedded in a monoclinic zirconia lattice while Si<sub>29</sub>O<sub>58</sub> and Si<sub>28</sub>VO<sub>58</sub> (around 4% of doping) clusters embedded in a  $\alpha$ -cristobalite lattice have been employed.

Large STO basis sets are used on every ion: (5s5p) for O<sup>2-</sup>, (5s4p) for Si<sup>4+</sup>, (8s6p5d) for V<sup>4+</sup>, and (10s9p5d) for Zr<sup>4+</sup> [19]. The wavefunctions and effective potentials, used to represent the lattice environment on each cluster, have been obtained from a previous aiPI calculation on the pure, infinite cluster. The Madelung potential, responsible for the largest part of the interaction energies, has been analytically integrated. The quantum mechanical contributions to the interaction energies have

been counted for a large number of neighboring shells until a convergence of  $10^{-6}$  hartrees is achieved in the effective energy of the clusters. The effective energy includes correlation estimated by means of the unrelaxed Coulomb-Hartree-Fock formalism [20]. The term unrelaxed is used because the *aiPI* wavefunctions are not affected by this correction.

The geometry of the different crystal structures was optimized, varying the structure and calculating the effective energy. The optimized distances were calculated in the following way: The geometry of the first shell was varied until a minimum effective energy was obtained; with the first shell fixed at the minimum, we proceed to optimize to the second shell, and so on. A schematic representation of  $\text{ZrSiO}_4$ ,  $\text{ZrO}_2$ , and  $\text{SiO}_2$  are presented in Figures 1, 2, and 3, respectively.

## Results and Discussion

### Structures

The calculated crystal lattice parameters for  $\text{ZrSiO}_4$ ,  $\text{Zr}_{1-x}\text{VSi}_x\text{O}_4$ ,  $\text{Zr}_{1-x}\text{Si}_x\text{O}_4$ ,  $\text{VO}_2$ , and  $\text{SiO}_2$  obtained from an X-ray diffraction study [10] using the Rietveld method [21,22] are listed in Table I. In Tables IIa and IIb are given the calculated bond lengths for pure and vanadium-doped zircon at  $\text{Zr}^{4+}$  and  $\text{Si}^{4+}$  sites, respectively. The experimental distances are obtained from the values presented in Table I, considering the tetragonal  $I4_1/\text{amd}$  space group.

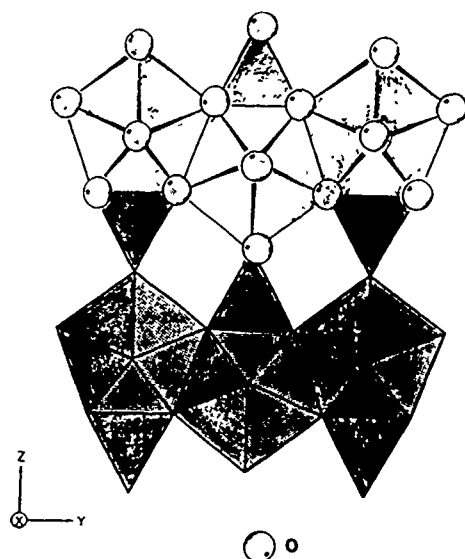


Figure 1. Schematic representation of zircon structure. The chains of alternating edge-sharing  $\text{SiO}_4$  tetrahedra and  $\text{ZrO}_6$  triangular dodecahedra extending parallel to *c* and joined laterally by edge-sharing dodecahedra.

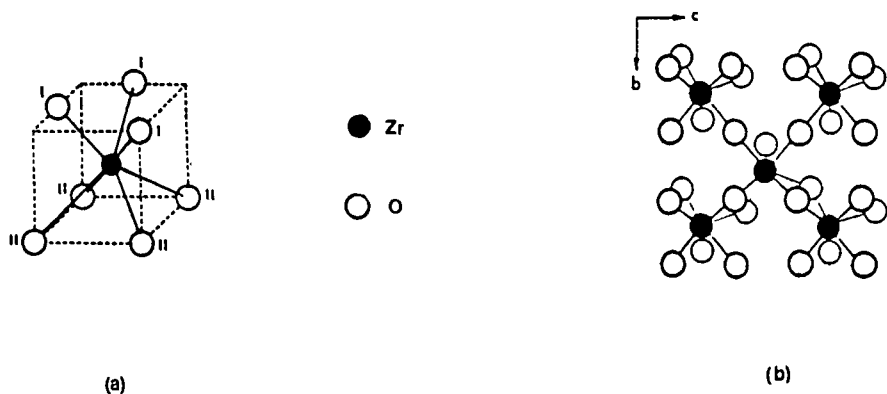


Figure 2. Schematic representation of monoclinic zirconia (baddeleyite) (a) 7-coordination of Zr<sup>4+</sup> (idealized); (b) projection of atomic dispositions

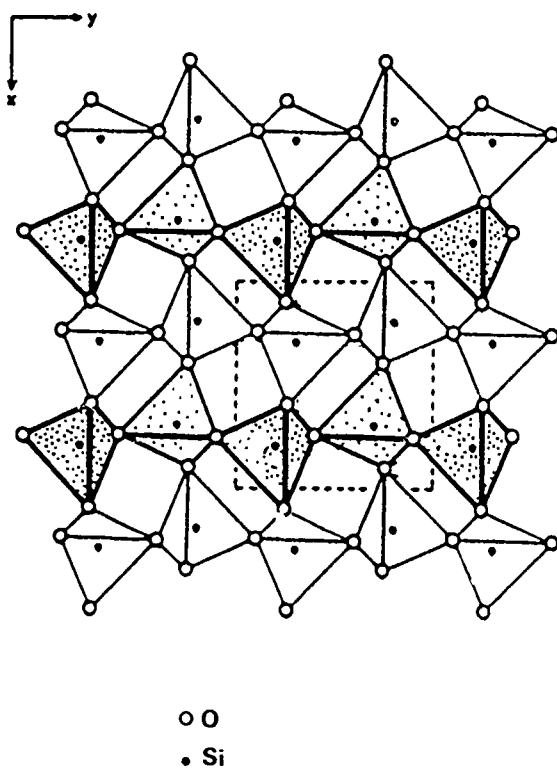


Figure 3. Schematic representation of  $\alpha$ -cristobalite structure.



TABLE I. Lattice calculation data: crystal lattice parameters.

Lattice	<i>a</i> (bohr) <sup>a</sup>	<i>b</i> (bohr) <sup>a</sup>	<i>c</i> (bohr) <sup>a</sup>	<i>V</i> (bohr <sup>3</sup> ) <sup>a</sup>	<i>b</i> (deg)	Origin
ZrSiO <sub>4</sub>	12.485	12.485	11.304	1762.19	90	Ref. [23]
	12.4609	12.4609	11.2854	1752.32	90	This work
	(12.4741)	(12.4741)	(11.2968)	(1757.81)	90	This work
ZrO <sub>2</sub>	9.7234	9.8408	10.0358	947.87	99.23	Ref. [23]
	9.7330	9.8485	10.0482	950.71	99.23	This work
SiO <sub>2</sub>	9.407	9.407	13.130	1163.41	90	Ref. [23]
	9.4089	9.4089	13.1506	1164.20	90	This work

Doped structure values in parentheses.

In Tables IIc and IId the corresponding bond distances for pure ZrO<sub>2</sub>, SiO<sub>2</sub> and doped Zr<sub>1-x</sub>VO<sub>2x</sub>, and Si<sub>1-x</sub>VO<sub>2x</sub> structures are summarized, and the experimental distances are obtained from the values presented in Table I, considering the monoclinic P2<sub>1</sub>/c and tetragonal P4<sub>1</sub>2<sub>1</sub>2<sub>1</sub> space groups, respectively.

For the zircon structure, a comparison of the optimized and experimental values reported by us and Hyde and Andersson [23] (Tables IIa and IIb) shows a good agreement, around 2% and 5% difference for geometrical parameters related to Zr<sup>4+</sup> and Si<sup>4+</sup> sites, respectively. The effect of doping vanadium into the zirconium site is to shorten the four equatorial metal oxygen bonds and to lengthen the four axial metal oxygen bonds. The presence of the impurity center in the lattice produces a change of equatorial oxygen ions that are moved 0.0944 a.u. closer to the metal ion, altering the bond distance from 4.2087 (Zr<sup>4+</sup>—O<sup>2-</sup>) to 4.1143 a.u. (V<sup>4+</sup>—O<sup>2-</sup>). The effect of doping vanadium into the silicon site is that the four oxygen ions bonded to the vanadium ion move away from their original positions, altering the lattice ion to oxygen bond lengths from 3.1881 (Si<sup>4+</sup>—O<sup>2-</sup>) to 3.4332 a.u. (V<sup>4+</sup>—O<sup>2-</sup>), a difference of 0.2451 a.u. This is compensated for by moving the zirconium and silicon ions bonded to those oxygen ions further away from the dopant ion, and by small changes in Zr<sup>4+</sup>—O<sup>2-</sup> and Si<sup>4+</sup>—O<sup>2-</sup> bond lengths. Thus the greatest

TABLE IIa. Calculated bond lengths (a.u.) for pure and vanadium-doped zircon at Zr<sup>4+</sup> site.

Metal ion	Ion	Optimized distance	Experimental distance	From the literature
Pure structure				
Zr <sup>4+</sup>	4x O <sup>2-</sup> (axial)	4.0351	4.0351	4.025 [23]
	4x O <sup>2-</sup> (equatorial)	4.2087	4.2997	4.288 [23]
Vanadium-doped structure				
V <sup>4+</sup>	4x O <sup>2-</sup> (axial)	4.0394	4.0394	3.855 [12]
	4x O <sup>2-</sup> (equatorial)	4.1143	4.3041	4.301 [12]

TABLE IIb. Calculated bond lengths (a.u.) for pure and vanadium-doped zircon at Si<sup>4+</sup> site

Metal ion	Ion	Optimized distance	Experimental distance	From the literature
Pure structure Si <sup>4+</sup>	4λ O <sup>2-</sup> (1)	3.1881	3.0315	3.065 [23]
	2λ Zr <sup>4+</sup>	5.6427	5.6427	
	4λ O <sup>2-</sup> (2)	6.2310	6.2310	
Vanadium-doped structure V <sup>4+</sup>	4λ O <sup>2-</sup> (1)	3.4332	3.0346	3.322 [12]
	2λ Zr <sup>4+</sup>	5.8745	5.6484	
	4λ O <sup>2-</sup> (2)	6.3251	6.2374	

TABLE IIc. Calculated bond lengths (a.u.) for pure and vanadium-doped ZrO<sub>2</sub>.

Metal ion	Anion	Optimized distance	Experimental distance	Ref. [24]
Pure structure Zr <sup>4+</sup>	O <sup>2-</sup> (1)	3.6837	3.8776	3.91
	O <sup>2-</sup> (2)	3.7037	3.8986	
	O <sup>2-</sup> (3)	3.8648	4.0682	
	Average	3.75	3.95	
	O <sup>2-</sup> (4)	3.8719	4.0757	
	O <sup>2-</sup> (5)	3.9073	4.1129	
	O <sup>2-</sup> (6)	4.0246	4.2364	
	O <sup>2-</sup> (7)	4.0693	4.2835	
	Average	3.96	4.18	
Vanadium-doped structure V <sup>4+</sup>	O <sup>2-</sup> (1)	3.2960		4.18
	O <sup>2-</sup> (2)	3.3138		
	O <sup>2-</sup> (3)	3.4580		
	Average	3.36		
	O <sup>2-</sup> (4)	3.4643		
	O <sup>2-</sup> (5)	3.4960		
	O <sup>2-</sup> (6)	3.6009		
	O <sup>2-</sup> (7)	3.6410		
	Average	3.55		

TABLE IIId Calculated bond lengths (a.u.) for pure and vanadium-doped  $\text{SiO}_2$ .

Metal ion	Ion	Optimized distance	Experimental distance	Ref. [23]
<b>Pure structure</b>				
$\text{Si}^{4+}$	$2 \times \text{O}^{2-}$ (1)	2.9485	3.0392	
	$2 \times \text{O}^{2-}$ (2)	3.0566	3.0400	
	Average	3.003	3.040	3.04
	$4 \times \text{Si}^{4+}$	5.8160	5.8160	
Vanadium-doped structure	$2 \times \text{O}^{2-}$ (3)	6.6234	6.6157	
	$2 \times \text{O}^{2-}$ (1)	3.1007		
	$2 \times \text{O}^{2-}$ (2)	3.1015		
	Average	3.101		
$\text{V}^{4+}$	$4 \times \text{Si}^{4+}$	5.8160		
	$2 \times \text{O}^{2-}$ (3)	6.6234		

distortion of the lattice on doping occurs with vanadium doping into the  $\text{Si}^{4+}$  site. These results agree with the data reported by Chandley et al. [12]

For the  $\text{ZrO}_2$  structure, a comparison of optimized and experimental distances shows a 5% difference (Table IIc). In this lattice the  $\text{Zr}^{4+}$  is 7-coordinated (Fig. 2), and three oxygen ions have a practically coplanar arrangement while the remaining four oxygen ions present a tetrahedral coordination with a larger mean distance from the metal ion. The effect of doping vanadium into the zirconium site is to shorten the two groups of metal oxygen bonds. The three coplanar oxygen ions are moved in an average of 0.39 a.u. closer to the metal ion while the tetrahedral oxygen ions are displaced in an average of 0.41 a.u. closer to the metal ion. The doping process produces a noticeable compression.

For the  $\text{SiO}_2$ , a comparison of optimized and experimental distances shows a 3% difference (Table IIId). The effect of doping vanadium into the silicon site is to lengthen the four metal oxygen bonds while the remaining bond distances are unaffected.

### Energetics

The defect reaction ( $\Delta E$ ) energies to substitute  $\text{Zr}^{4+}$  and  $\text{Si}^{4+}$  in the host materials  $\text{ZrSiO}_4$  for  $\text{V}^{4+}$ :  $\text{V}_{\text{Zr}}\text{:ZrSiO}_4$  [Eq. (1)] and  $\text{V}_{\text{Si}}\text{:ZrSiO}_4$  [Eq. (2)], respectively, are listed in Table III, together with  $\Delta E$  to substitute vanadium for  $\text{Zr}^{4+}$  in  $\text{ZrO}_2$ ,  $\text{V}_{\text{Zr}}\text{:ZrO}_2$  [Eq. (3)] as well as vanadium for  $\text{Si}^{4+}$  in  $\text{SiO}_2$ ,  $\text{V}_{\text{Si}}\text{:SiO}_2$  [Eq. (4)]. In this table,  $\Delta E$  (experimental structure) is the calculated defect reaction energy associated with experimental geometry without optimization procedure while  $\Delta E$  (optimized struc-

TABLE III. Defect reaction energies (a.u.).

Impurity center	$\Delta L$ (experimental structure)	$\Delta E$ (optimized structure)
V <sub>Zr</sub> :ZrSiO <sub>4</sub>	-0.2021	-0.2212
V <sub>Si</sub> :ZrSiO <sub>4</sub>	1.3564	0.2509
V <sub>Zr</sub> :ZrO <sub>2</sub> (m)	-0.2513	-0.5723
V <sub>Si</sub> :SiO <sub>2</sub> ( $\alpha$ )	0.7587	0.7505

ture) corresponds to the value obtained optimizing the geometry as described in the previous section.

The  $\Delta E$  values show that V<sup>4+</sup> ion would substitute more easily for Zr<sup>4+</sup> than for Si<sup>4+</sup>. The substitution of V<sup>4+</sup> on the Zr<sup>4+</sup> site is favored throughout by -0.22 and -0.57 a.u. in ZrSiO<sub>4</sub> and ZrO<sub>2</sub> structures, respectively. Considering that ZrSiO<sub>4</sub> is not formed by the reaction of a V<sup>4+</sup>-bearing melt with ZrSiO<sub>4</sub>, [9,10] but rather by the reaction of doped ZrO<sub>2</sub> and SiO<sub>2</sub>, Zr<sup>4+</sup> can be readily substituted for V<sup>4+</sup> via ZrO<sub>2</sub> doping.

It is important to note that the geometry optimization process for the V<sub>Si</sub>:ZrSiO<sub>4</sub> structure significantly modifies the value of  $\Delta E$  from 1.36 to 0.25 a.u. For the V<sub>Zr</sub>:ZrO<sub>2</sub> structure, this change is minor, from -0.25 to -0.57 a.u. This results can be explained due to large changes of crystal lattice parameters when the optimization of geometry is carried out (see Tables IIb and IIc).

### Force Constants

The aim of this section is to simulate lattice relaxation around a point defect and to use this to evaluate the energy and force constant ( $k$ ) associated with the symmetric breathing (radial) fundamental vibrational mode. The  $k$  value was studied by means of the calculation of the effective energy as function of the crystallographic displacement which was changing in a stepwise fashion; a fitting method to a fifth potential polynomial is used.

The  $k$  values for pure and doped ZrSiO<sub>4</sub>, ZrO<sub>2</sub>, and SiO<sub>2</sub> structures are listed in Table IV. These numerical values can be summarized as follows: (i) The doping process produces a decrease of  $k$  values for all structures; (ii) the  $k$  value associated with the dodecahedral site in the zircon structure is especially high; (iii) the  $k$  values for the tetrahedral site in the zircon structure, ZrO<sub>2</sub> and SiO<sub>2</sub> crystal lattices render similar values; (iv) the doping in tetrahedral substitution for zircon structure produces a considerable decrease of  $k$  value. This fact agrees with the appreciable geometrical distortion after this substitution occurs at the tetrahedral site in the zircon structure and with the experimental values on compressibility studies reported by Hazen and Finger [25].

If we try to rationalize our results on the basis of a comparison of the ionic radii of the species concerned in the doping process, taking ionic radii from Shannon and Prewitt [26] the differences in size between the substituent V<sup>4+</sup> and the ion in the host lattices are:  $R(V^{4+}) - R(Si^{4+}) = 1.380 - 0.756 = 0.624$  bohr and  $R(V^{4+})$

TABLE IV. Force constants (a.u.).

	Tetrahedral site	Dodecahedral site
ZrSiO <sub>4</sub>		
Pure structure	1.86	82.62
(V-doped)	(0.64)	(68.80)
SiO <sub>2</sub> ( $\alpha$ )		
Pure structure		2.51
(V-doped)		(2.38)
ZrO <sub>2</sub> (m)		
Pure structure		1.82
(V-doped)		(1.64)

$-R(\text{Zr}^{4+}) = 1.380 - 1.625 = -0.245$  bohr. For the zircon structure, the geometry relaxation following substitution on the dodecahedral site is expected to be less sensitive if we consider the similar ionic radii of  $\text{Zr}^{4+}$  and  $\text{V}^{4+}$  as our data show. However, for the doping process in  $\text{ZrO}_2$  and  $\text{SiO}_2$  structures, this argument does not work. The use of the relative size of ions and volume of the crystal cells (see Table I) do not reproduce theoretical and experimental evidence for these crystal lattices.

### Conclusions

Cluster-in-the-lattice simulations of pure and doped  $\text{ZrSiO}_4$ ,  $\text{ZrO}_2$ , and  $\text{SiO}_2$  structures and X-ray diffraction studies appear to be an appropriate procedure to systematically characterize the energy, the changes or distortions of cell parameters, and force constant for these crystal lattices associated with the doping process.

The results of the present study can be summarized as follows:

(i) The calculated crystal lattice parameters obtained from a X-ray diffraction study using the Rietveld method for these structures are similar to these reported by Hyde and Andersson.

(ii) Less sensitive influence of the crystal lattice parameters for substitutions occurring at the eightfold-coordinated ion site in  $\text{ZrSiO}_4$  and  $\text{SiO}_2$  structures.

(iii) Substitutions of  $\text{V}^{4+}$  for  $\text{Zr}^{4+}$  at the dodecahedral site in zircon structure and  $\text{V}^{4+}$  for  $\text{Zr}^{4+}$  in  $\text{ZrO}_2$  structure are energetically favorable.

(iv) Our stability results disagree with Chandley's et al. [12] conclusions; however, the structural data and distortion of the lattice which take place on substitution are similar.

(v) An analysis of the defect energy and the breathing fundamental vibrational mode for substitutions of  $\text{V}^{4+}$  for  $\text{Si}^{4+}$  at the tetrahedral site in the  $\text{ZrSiO}_4$  and  $\text{SiO}_2$  structures does not reveal any indication of energy stabilization for this doped structure. This behavior confirms previous findings [6] while being at variance with others [7,9].

(vi) The doping process produces a decrease of force constant values associated with the breathing fundamental vibrational mode for all structures.

(vii) The  $k$  associated with the breathing displacement in dodecahedral substitution for the ZrSiO<sub>4</sub> structure is especially high. The force constants for this movement in tetrahedral substitution for the ZrSiO<sub>4</sub>, the ZrO<sub>2</sub>, and SiO<sub>2</sub> structures have a lower value.

(viii) The differences between ionic radii of the species concerned in the doping process do not explain the relaxation of crystal lattice parameters for the ZrO<sub>2</sub> and SiO<sub>2</sub> structures.

### Acknowledgments

Financial support from research funds of Bancaixa and Universitat Jaume I is gratefully acknowledged. We are most indebted to V. Luaña and A. Martín Pendás for sending us their latest version of the aiPI method and S. Böhm for technical support which allowed us to carry out the calculations. Use of a cluster of workstations HP series Apollo 9000/730 of the Centre de Procesament de Dades, Universitat Jaume I, Castelló is also gratefully acknowledged.

### Bibliography

- [1] F. T. Both and G. N. Peel, *Trans. Brit. Ceram. Soc.* **61**, 359 (1962).
- [2] (a) C. A. Seabright, *Ceramics Pigments U.S. Pat.* 2, 441, 407 (May 1948). (b) C. A. Seabright, *Br. Pat.* 625, 448 (1949).
- [3] A. A. Balman and R. A. Laudise, *J. Am. Chem. Soc.* **48**, 130 (1965).
- [4] R. Carter, *Ceram. Ind. J.*, 19 (1985).
- [5] K. Robinson, G. V. Gibbs, and P. H. Ribbe, *Am. Mineral.* **56**, 782 (1971).
- [6] T. Demirey, D. K. Nath, and F. A. Hummel, *J. Am. Chem. Soc.* **53**, 1 (1970).
- [7] S. Di Gregorio and M. Greenblatt, *J. Chem. Phys.* **76**, 2931 (1982).
- [8] Hong Xiayou, Bai Gui-Ku, and Zhao Ming-Guang, *J. Phys. Chem. Solids* **46**, 719 (1985).
- [9] P. Chandley and R. J. H. Clark, *J. Crystal Growth* **116**, 151 (1992).
- [10] (a) G. Monrós, J. Carda, P. Escobano, and J. Alarcón, *J. Mater. Sci. Lett.* **9**, 184 (1990). (b) G. Monrós, J. Carda, M. A. Tena, P. Escobano, and J. Alarcón, *Br. Ceram. Trans. J.* **90**, 157 (1991); (c) G. Monrós, J. Carda, P. Escobano, M. A. Tena, and J. Alarcón, *J. Mater. Sci.* **27**, 351 (1992); (d) G. Monrós, J. Carda, M. A. Tena, P. Escobano, V. Cantavella, and J. Alarcón, *Mater. Res. Bull.* **27**, 753 (1992). (e) G. Monrós, J. Carda, M. A. Tena, P. Escobano, M. Sales, and J. Alarcón, *J. Eur. Ceram. Soc.* **11**, 77 (1993).
- [11] A. Beltrán, S. Böhm, A. Flores-Riveros, J. A. Igualada, G. Monrós, J. Andrés, V. Luaña, and A. Martín Pendás, *J. Phys. Chem.*, (1993), to appear.
- [12] P. Chandley, R. J. H. Clark, R. J. Angel, and G. D. Price, *J. Chem. Soc. Dalton Trans.*, 1579 (1992).
- [13] V. Luaña and L. Pueyo, *J. Mol. Struct. (Theochem)* **166**, 215 (1988).
- [14] V. Luaña and L. Pueyo, *Phys. Rev.* **B41**, 3800 (1990).
- [15] V. Luaña, J. M. Recio, and L. Pueyo, *Phys. Rev.* **B42**, 1791 (1990).
- [16] M. Flórez, E. Francisco, V. Luaña, A. M. Pendás, J. M. Recio, M. Bermejo, and L. Pueyo, in *Cluster Models for Surface and Bulk Phenomena*, G. Pacchioni, P. S. Bagus, and F. Parmigiani, Eds. (Plenum, New York, 1992), p. 619.
- [17] (a) L. Pueyo, V. Luaña, M. Flórez, and E. Francisco, in *Structure, Interactions and Reactivity*, S. Fraga, Ed. (Elsevier, Amsterdam, 1992), Vol. B, p. 504; (b) V. Luaña, M. Flórez, E. Francisco, A.

- M. Pendás, J. M. Recio, M. Bermejo, and L. Pueyo, in *Cluster Models for Surface and Bulk Phenomena*, G. Pacchioni, P. S. Bagus, and F. Parmigiani Eds. (Plenum, New York, 1992), p. 605.
- [18] V. Luaña and M. Flórez, *J. Chem. Phys.* **97**, 6544 (1992)
- [19] E. Clementi and C. Roetti, *At. Data Nucl. Data Tables* **14**, 177 (1974)
- [20] S. J. Chakravorty and E. Clementi, *Phys. Rev. A* **39**, 2290 (1989).
- [21] H. M. Rietveld, *J. Appl. Cryst.* **2**, 65 (1969).
- [22] Full Prof Computer Program, Version 2.1 Mar92-ILLJRC, J. Rodriguez-Carvajal, Institut Laue-Langevin, France.
- [23] B. G. Hyde and S. Andersson, *Inorganic Crystal Structures* (Wiley, New York, 1989).
- [24] A. F. Wells, *Structural Inorganic Chemistry*, 5th ed. (Clarendon, Oxford, 1991).
- [25] R. M. Hazen and L. W. Finger, *Am. Miner.* **64**, 196 (1979).
- [26] (a) R. D. Shannon and C. T. Prewitt, *Acta Crystallogr. B* **25**, 925 (1969), (b) R. D. Shannon, *Acta Crystallogr. A* **32**, 751 (1976)

Received April 22, 1993

# Towards an Understanding of the Electronic Structure of Mott-Insulating Transition Metal Oxides

CHANGJIANG MEI and VEDENE H. SMITH, JR.

*Department of Chemistry, Queen's University, Kingston, Ontario, Canada, K7L 3N6*

## Abstract

Due to suggestions that Self Interaction Corrections (SIC), gradient corrections, and short-range electron-electron interactions in the Local (Spin) Density Approximation (L(S)DA) scheme may significantly influence the computed electronic structure for the Mott-insulating (MI) transition metal oxides (TMOs), a comparative study has been made of Hartree Fock (HF) and L(S)DA computations for NiO. Since HF lacks electronic correlation, it overestimates band width (in conductors) and/or band gaps (in insulators). It gives the band gap for NiO two times larger than that in experiment, while LSDA gives the gap one order of magnitude smaller than the experimental value. We demonstrate that the HF results are consistent with some previously believed to be well-understood experiments, while the L(S)DA results are not. It is suggested that HF may offer a better reference state for the development of a LSDA scheme. © 1993 John Wiley & Sons, Inc.

## Introduction

The discovery of the high- $T_c$  superconductors (HTSCs) [1] based on copper oxide layer structures has re-opened interest in the study of the (MI) TMOs, a class of materials to which the HTSCs also belong, and for which the theoretical computation of their electronic structure has been always a challenge. In order to understand all important properties of these materials including the high- $T_c$  superconductivity, detailed knowledge of their electronic structures is essential.

Due to the relatively poor computers available at the time and the imperfections of the computational methods, early electronic structure studies on the (MI) TMOs [2] obtained electronic structures which compared poorly with experiments in some very critical features, such as magnetic properties, band gaps and widths, relative positions of bands, etc.

Recently, there have been many attempts to improve the understanding of these problems. Singh and Pickett [3] added gradient corrections to the exchange-correlation potential within the L(S)DA [4]. Yu and Freeman [5] included a short-range electron-electron interaction in addition to the normal L(S)DA potential in order to describe the electronic correlations of the localized electrons more properly. Svane and Gunnarsson [6] added to the L(S)DA scheme the SIC which result from the approximate treatment of the exchange. On the other hand, Shen et al. [7] reported recently experimental band structures for NiO. In the  $\Gamma - X$  direction,



there are bands at about  $-11$  eV below the Fermi energy ( $\epsilon_F$ ) which cannot be identified as any of the L(S)DA bands, no matter which corrections have been made.

In order to find out how these deviations come about, the electronic structure has been calculated in the present study within both HF and LDA approximations for NiO, which is a typical (MI) TMO. Comparison has been made between results from both methods, and with typical previous LSDA results [8]. It should be mentioned that Wilson (1970) [9] and Kunz (1981) [10] studied the (MI) TMOs with approximate HF methods and obtained valuable physical insight but their studies were ignored in the literature.

### Methods

The presumably most advanced method for electronic structure calculations of solids is the Density Functional (DF) theory with the use of the Kohn and Sham [11] one-electron Hamiltonian. It includes, along with the kinetic and Hartree terms, an effective exchange and correlation potential,  $W_{xc}(\rho)$ , which is in turn a functional of the electronic density  $\rho(r)$ . The exact form of this functional for almost all realistic systems is unknown. The L(S)DA has to be made by evaluating  $W_{xc}(\rho)$  at the local density, i.e.,  $W_{xc}(\rho)|_r \equiv W_{xc}(\rho(r))$ . In practice, the explicit form of the functional  $W_{xc}(\rho(r))$  is usually considered not to be critical, except that it should be exact in the limit of the homogeneous electron gas [12].

The HF method [13], on the other hand, does not suffer from the local approximations on the exchange-correlation potential. The corresponding single determinant wavefunction is a clearly defined quantity which takes account of the different nodal structures of the different orbitals via its non-local, exact exchange term. In principle, it is known what is missing from the HF state and how it can be improved by introducing correlation either through perturbational or variational procedures [14]. As a result, HF calculations can be used as a good reference for other computations. In fact, Kohn and Sham in their original article [11] suggested an alternative LDA scheme by using HF as the reference rather than the usual non-interacting system.

With the HF method, it is known that because the non-local exchange term is not compensated due to the lack of electronic correlation, calculated conducting band structures, especially for metals where screening is important, are about twice as wide as those from experiments, as are band gaps for insulators and semiconductors. However, HF calculations may be considered as the lower limit of approximate screening in insulators while the L(S)DA is the upper limit. Generally, the HF method overestimates band widths and band gaps while L(S)DA underestimates.

Another important fact is that in the presence of strong correlations, as in the TMOs with their quite localized  $d$  electrons, both methods may lead to large deviations because in the HF approximation, by definition, correlation is not included at all while in the L(S)DA, the very inhomogeneous charge distribution, which is far from that of the electron gas, invalidates the approximation. Although L(S)DA

considers electronic correlation to some extent, it is really not known which effect is larger. In this study for NiO, both methods were employed and it is hoped that comparison between the results from these two methods and with that of experiments may reveal which effect is more important for the calculated electronic structures of these materials. In the present study, the restricted HF calculation was done with CRYSTAL [13] because there is still no facility in the present laboratory to do a spin polarized HF calculation, and a corresponding non-magnetic LDA calculation was carried out with WIEN which is a Full Potential LAPW LDA program [15].

The NiO crystal has the NaCl structure of space group  $O_h^2(Fm3m)$  [16],  $a = 4.17 \text{ \AA}$ , and atomic positions Ni(0.0, 0.0, 0.0) and O(0.5, 0.0, 0.0). For the present HF study, a He-core pseudopotential for O [17], an Ar-core pseudopotential for Ni [18] are used. For Ni-3d valence orbitals, TZ GTOs are used with 4s basis [19]. For O, a DZ GTO basis for the 2p valence orbitals are employed [17].

### Results and Discussions

Electronic structure studies for MITMOS, as well as for the parent materials of HTSCs [20], show that the uppermost band, the O- $p$  and metal- $d$   $\sigma$ -antibonding band, is half-filled. Because of the strong on-site Coulomb repulsion, a gap opens between the lower- and the upper-half bands and the system undergoes a metal-insulator transition. Therefore, these materials exhibit antiferromagnetism (AF) below the Néel temperature and poor conductivity. As discussed in Ref. [6], LSDA electronic structure calculations for NiO and MnO with artificially dimerized unit cells result in AF insulating ground states, as they should, but fail to give such a ground state for CuO, CoO, and FeO. LSDA gave the other non-bonding metal  $t_{2g}$   $d$ -bands slightly (ca. 1 eV) below the bonding metal  $e_g$   $d$ -band(s) and above the O  $p$ -bands. However, the recent LSDA calculations by Svane and Gunnarsson [6] with SIC included successfully found AF insulating ground states for CuO, FeO, and CoO as well, in contrast to usual LSDA scheme [6]. Unfortunately, bands and DOS's were not published from these calculations. For comparison, the band gap for NiO, which is one of the most critical criteria, as listed in Ref. [6], is 4.3 eV as from experiment, 0.2 eV given by traditional LSDA, 2.5 eV given by Svane and Gunnarsson, but 14.4 given by Unrestricted HF [21].

In Figure 1, the non-magnetic HF band structures of NiO are shown, in comparison with the corresponding LDA results, as can be seen for the  $\Gamma - L$  portion also in Ref. [22]. The corresponding HF densities of states (DOSS) are shown in Figure 2; a previous LSDA DOS by Terakura et al. [8] is given as an insert. It can be seen from Figure 1 that the LDA and HF results are very consistent with each other for bands around  $\epsilon_F$ . The crossing points of the partially filled  $p - d$  antibonding band (marked with "A - B") with  $\epsilon_F$  from both methods are in good agreement. The splitting and dispersion of the partially filled band from both calculations are very similar. However, it should be emphasized again that for a non-magnetic study, all band structure methods fail to give a gap in the partially filled band. The comparison given shows that both methods yield similar features in the considered energy regions under similar conditions.

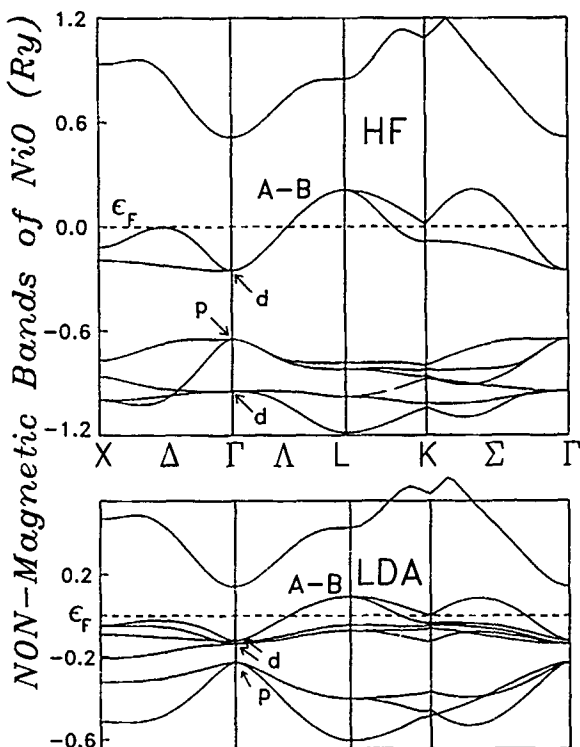


Figure 1. Non-magnetic band structures of NiO calculated with both HF(CRYSTAL) and LDA(WIEN) methods. The Fermi energies are set at 0.0. The antibonding  $\text{Ni}_d\text{—O}_p$  band is marked with "A-B".

It is not surprising that the HF band dispersion is about two times larger than the LDA because the two methods differ by the treatment of exchange and correlation. The most significant difference is, however, that HF predicts the metal  $d_{i_z}$  to lie below all other valence bands. Yet the typical L(S)DA result leaves them only 1 eV or less under the uppermost occupied band (referring to the LDA parts of Fig. 1). This difference can also be seen from the DOSS in Figure 2, where LSDA predicts all metal  $d$ -states to be concentrated to give one single peak lying within 3 eV below the  $\epsilon_F$ , while HF gives three peaks, one around  $\epsilon_F$ , one far below  $\epsilon_F$  and all other valence bands ( $d_{i_z}$  non-bonding bands), and another in between (which is from the pure  $\text{O}_p$  bands and the metal- $d$  -  $\text{O-p}$  bonding bands).

Traditionally [2], the  $d_{i_z} - d_{e_g}$  splitting was considered to be a *pure* crystal field effect. The two sets of orbitals were believed to differ by roughly an energy of the order of magnitude of the overlap integral between  $d_{e_g}$  and the ligands, which is about ca. 1 eV. The  $d_{i_z}$  is considered to be unchanged. But in this understanding, an important effect, *relaxation*, was missed. In reality, however, once the  $d_{e_g}$  electrons

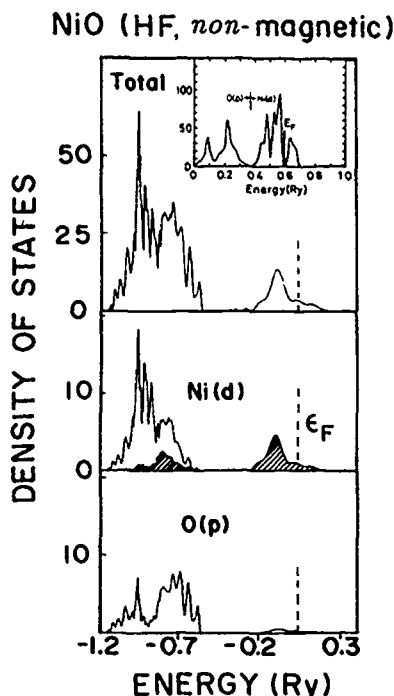


Figure 2. HF DOS of NiO corresponding to Figure 1. The shaded part in the HF Ni(*d*) DOS is the contributions of Ni— $d_{x^2-y^2}$  + Ni— $d_{z^2}$  states which take part in the Ni<sub>*d*</sub>—O<sub>*p*</sub>  $\sigma$ -bonding. It is clear that the DOS around the Fermi energy is predominantly of Ni—*d* character. The spin polarized LDA total DOS by Terakura et al. [8] is shown as the insert.

form bonds with ligand electrons and become delocalized, they will leave space for the  $d_{t_{2g}}$  electrons, and the latter see a less screened core and drop to an even lower energy. This process results in a splitting much larger than the overlap integral with the leading term due to the difference in electron-core interactions. This feature can hardly be reproduced by the standard LDA scheme because in such a scheme there is usually a physical boundary between core and valence regions, into which the valence electrons can never penetrate. But this is not true for 3*d* electrons as they can be very close to the core in reality. It was shown by an *ab initio* correlated electronic structure calculation for Cu—O clusters [23] that the HF results are very close to experimentally determined metal *d* and O *p* occupations, which are critical to explain the magnetic momentum and on-site Coulomb interaction. Recently, Anisimov et al. showed that in an *improved* LSDA model band structure calculation, the metal non-bonding *d* band lies below all other valence bands [24].

Recently, angle-resolved photoemission experiments by Shen et al. [7] provided an experimental band structure for NiO. The uppermost antibonding band and the O-*p* bands confirm both the L(S)DA and HF results. But in the  $\Gamma - X$  direction (referring to Fig. 25 in Ref. [7]), there are two very weakly dispersed experimental

bands below the O-*p* bands, which cannot be assigned to any of the LDA and/or LSDA bands. However, these two bands fit fairly well with the metal  $d_{t2g}$ -bands from the HF! In fact, if we look back at some old experiments, believed to be well understood, we can see that they can be interpreted very well by HF calculations but not by LDA.

The satellites in the photoemission spectrum of TMOs and their assignment first proposed by Wertheim and Hüfner [25] is the first of such widely discussed topics. From L(S)DA computations, all metal *d* states are concentrated (see the insert in Fig. 2, from Terakura et al. [8]) within 3 eV below  $\epsilon_F$ . It is very difficult to interpret the satellite structure within L(S)DA without invoking complicated many-particle processes. But, these satellites are located just at the positions of the non-bonding metal  $d_{t2g}$  states predicted by HF, and it is straightforward to assign the satellites to these states. Comparison of the HF DOS of NiO in Figure 2 with Figure 1 (NiO) of Ref. [25] shows good agreement.

In the early 70s, Powell reported the photoabsorption spectrum for a NiO crystal (Fig. 3 in Ref. [26]). This spectrum can be understood also very well by referring to the HF DOS of NiO in Figure 2. In Figure 3, the theoretical photoabsorption spectra are shown in comparison with the experiment. They were calculated by

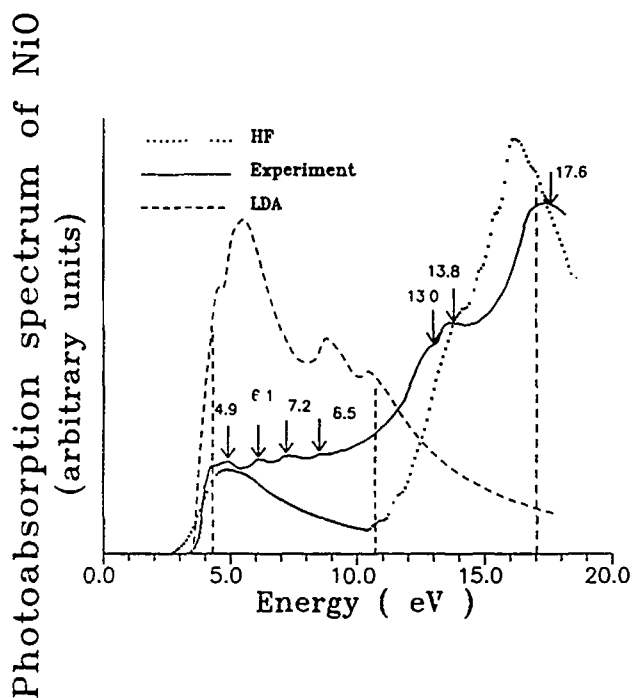


Figure 3 The theoretical HF and LDA photoabsorption spectra are shown in comparison with the experiment by Powell [26]. A shift was made to position the edge of the platform at about 4.3 eV in order to compare with the experimental result.

integrating the HF and the LSDA DOS's weighted with the X-ray absorption cross sections from  $\epsilon_F$  to the bottom of the metal  $d$  and O  $p$  bands. The HF spectrum reproduces all the basic structure of the experimental spectrum! If one keeps in mind that the inclusion of electronic correlation will open a gap in the half-filled band across the  $\epsilon_F$ , which will result in a "steeper" stepping-up for the spectrum at the beginning, and a higher platform between 4.3 to 9.1 eV. The narrowing of the bands due to correlation will open up gaps and thus leave shoulders at 13.1 and 14.3 eV. On the other hand, it is difficult to see any similarity of the LSDA spectrum with the experiment.

### Conclusions

From the calculations discussed above, it is clear that the computational techniques for the electronic structures of (MI) TMOs still need essential improvements. In LSDA, because of the shortcomings of its approximations, the computed band gaps of the MI TMOs and the magnetic moments are not quantitatively, in some cases even not qualitatively, consistent with experiments. The magnetic correlation effect above the Néel temperature is not necessarily commensurate [23], so that the current treatment of magnetism by simply dimerizing the unit cell cannot hope to fit experiments in every detail. HF, on the other hand, does not include correlation at all by definition, and thus cannot hope to give a *correlated* electronic structure. It should be emphasized though that a UHF computation *can* give a band gap and an AF insulating ground state for NiO with artificially dimerized unit cell [21]. The results shown above imply that the HF state may offer a better reference state for further improvements as Kohn and Sham suggested in their first article [11].

### Acknowledgments

The authors would like to acknowledge the support by the Natural Sciences and Engineering Research Council of Canada. The authors would like also to thank the Torino group for help with the CRYSTAL-HF calculation; Z.-X. Shen for communicating his new experimental results, and M. Stott and J. Chen for stimulating discussions. We especially thank P. Blaha for help with the WIEN LDA calculations.

### Bibliography

- [1] K. A. Müller and J. G. Bednorz, *Z. Phys.* **B64**, 189 (1986).
- [2] J. B. Goodenough, *Progress in Solid State Chemistry*, Vol. 5, H. Reiss, Ed. (Pergamon Press Ltd., Oxford, 1971).
- [3] D. J. Singh and W. E. Pickett, *Physica* **B163**, 470 (1990).
- [4] D. C. Langreth and M. J. Mehl, *Phys. Rev.* **B28**, 1809 (1983).
- [5] J. Yu and A. J. Freeman, *Bull. APS*, **36**, K23 5, 770 (1991).
- [6] A. Svane and O. Gunnarsson, *Eur. Phys. Lett.* **7**, 171 (1988); *Phys. Rev. Lett.* **65**, 1148 (1990); *Phys. Rev.* **B41**, 4811 (1990).
- [7] Z.-X. Shen, et al., *Phys. Rev.* **B44**, 3604 (1991).
- [8] K. Terakura, T. Oguchi, A. R. Williams, and A. R. Kübler, *Phys. Rev.* **B30**, 4734 (1984).
- [9] T. M. Wilson, *Int. J. Quantum Chem.: Quantum Chem. Symp.* **3**, 757 (1970).

- [10] A. B. Kunz, *Int. J. Quantum Chem.: Quantum Chem. Symp.* **15**, 487 (1981).
- [11] W. Kohn and L. J. Sham, *Phys. Rev.* **140**, A1133 (1965).
- [12] O. K. Andersen, O. Jepsen, and D. Glötzl, in *Highlights of Condensed Matter Theory*, Proceedings of the International School of Physics, Enrico Fermi, Varenna, July 1983, F. Bassani et al., Eds., (Elsevier, Amsterdam, 1985); and references therein.
- [13] C. Pisani, R. Dovesi, and C. Roetti, *Lecture Notes in Chemistry* **48**, *Hartree-Fock ab initio Treatment of Crystalline Systems*, (Springer, Berlin, 1988); CRYSTAL 88, QCPE program No. 577; R. Dovesi, V. R. Saunders, and C. Roetti, *CRYSTAL 92 USER DOCUMENTATION* (University of Torino and Daresbury Laboratory, 1992).
- [14] Correlation can be added to the HF state by using, for example the Local Ansatz, see, e.g.: B. Kiel, G. Stollhoff, C. Weigel, P. Fulde, and H. Stoll, *Z. Phys.* **B46**, 1 (1982).
- [15] P. Blaha, K. Schwarz, and P. Sorantin, *Comp. Phys. Comm.* **59**, 399 (1990).
- [16] R. W. G. Wyckoff, *Crystal Structures*, Ch. III. (Interscience, New York, 1948).
- [17] H. Preuss, H. Stoll, U. Wedig, and Th. Krüger, *Int. J. Quantum Chem.* **19**, 113 (1981).
- [18] P. J. Hay and W. R. Wadt, *J. Chem. Phys.* **82**, 270 (1985).
- [19] M. Dolg, U. Wedig, H. Stoll, and H. Preuss, *J. Chem. Phys.* **86**, 866 (1987).
- [20] W. E. Pickett, *Rev. Mod. Phys.* **61**, 433, 749 E (1989).
- [21] E. Apra', et al., *Proceedings of the CECAM workshop*—Orsay, Paris, France, October 1991.
- [22] B. Szpunar and V. H. Smith, Jr., in *Electronic Structure and Mechanisms for High-T<sub>c</sub> Superconductivity*, J. Ashkenazi and G. Vezzoli, Eds. (Plenum, New York, 1991).
- [23] C.-J. Mei and G. Stollhoff, *Z. Phys.* **B77**, 353 (1989); *Phys. Rev.* **B43**, 3065 (1991).
- [24] V. I. Anisimov, J. Zaanen, and O. K. Andersen, *Phys. Rev.* **B44**, 943 (1991).
- [25] G. K. Wertheim and S. Hüfner, *Phys. Rev. Lett.* **28**, 1028 (1972).
- [26] R. J. Powell, Stanford Electronics Laboratory Technical Report No. 5220-1 1967 (unpublished), cited in D. Adler and J. Feinleib, *Phys. Rev.* **B2**, 3112 (1970).

Received March 14, 1993

# Electronic and Geometric Characteristics of Precrystalline Structures in Highly Dispersed Rh Catalysts

GUILLERMINA LUCIA ESTIU\* and MICHAEL C. ZERNER

*Quantum Theory Project, University of Florida, Gainesville, Florida 32611*

## Abstract

The structure of small Rh clusters compatible in size with the particles that are present in highly dispersed supported catalysts are studied at the SCF level by means of intermediate neglect of differential orbital (INDO) calculations. In agreement with experimental determinations and calculations on other metals, we have found nonperiodic (precristalline) structures of  $C_{3v}$  and  $D_{3d}$  symmetry the most stable ones. An analysis of these geometries suggest that they result from first- and second-order Jahn-Teller distortions of icosahedra. Although higher multiplicities characterize higher symmetry structures, we find that the lower symmetry structures are characterized by low multiplicities. The electronic characteristics of the surface sites are analyzed at the CI level. In contrast to extended periodic surfaces, which are characterized by negative charge density on the metal atoms, the surfaces of the small clusters appear as electron deficient structures, with negative charge localized on the internal atoms. This may be a key factor in understanding the different catalytic activity of metal surfaces and supported metal catalysts.

© 1993 John Wiley & Sons, Inc.

## Introduction

The field of metal cluster chemistry has reached a particularly exciting point in its development because the size of the cluster being characterized may be large enough for meaningful comparison of their physical and chemical properties with bulk metal and metal surfaces, and, on the other hand, sufficiently small as to be able to examine by quantum chemical techniques [1].

A metal cluster compound has been defined as a group of two or more metal atoms where direct and substantial metal bonding is present [2]. The size of the arrangement can, thence, vary from two to several hundred atoms, and most of the research in this field has focused on the way several properties, such as chemical hardness [3], ionization potentials [4], electron affinities [4], binding energies (BEs) [5], and polarizabilities [6], change with size, allowing an examination of the transition from molecular to metallic behavior [7]. The geometry of a metal cluster also changes from a polyhedron (precristalline) structure to a reticular, lattice-based one, defining a transition for a certain number of atoms that depends

---

\* Permanent address. Proyecto Quinor, Facultad de Ciencias Exactas, Universidad Nacional de la Plata, Casilla de Correo 962, (1900) La Plata, Argentina.



on the element under consideration [4-8]. In this framework, the structure of a cluster is one of the most controversial subjects, because it is both difficult to probe experimentally and hard to calculate. This is especially the case with transition metal atoms, and their agglomerates, many of which are of great industrial importance.

Cluster sizes of particular stability are often revealed in a mass spectrum by striking maxima in the envelope of peak intensities. The number of atoms associated with the maxima which defines the most stable structures (magic numbers) [9] depends on the bonding character of the atoms forming the cluster [10]. The van der Waals bonded rare gas clusters have magic numbers of a complete icosahedra [6,9,10], whereas the smallest magic numbers of alkali and noble metals correspond to the shell structure of the valence electrons [6,9,10]. Magic numbers corresponding to icosahedral packing of Na, K, Ca, Ba, Sr, Mg, Ni, Co, and Cu atoms have been also found [8-10]. However, the icosahedral clusters have the same magic numbers as the cubooctahedral structures, and the question then naturally arises as to which one is formed more easily.

Transition metal clusters are important in catalytic research, where highly dispersed metal catalysts, of particle size small enough to be considered precrystalline structures, are associated with the higher activity due to the occurrence of a larger concentration of active sites. In order to understand their particular reactivity, the geometric and electronic characteristics of the different sites must be accurately determined. Modern quantum chemical technologies that include gradient-driven geometry optimizing algorithms are particularly suited to examine the individual bonding behavior of the elements that make up precrystalline structures, and, in turn, can be used for the calculation of the electronic descriptors on the different sites of a given optimized structure.

When dealing with systems of catalytic importance, mainly associated with elements of the second and third transition series, only small clusters (three or four atoms) have been treated in configuration interaction calculations [11-15]. Molecular dynamics [10], as well as Monte Carlo [11] simulations, however, have been used in an interesting fashion to analyze the precrystalline to reticular transition in extended systems as a function of the number of atoms required for the transition structure.

Because of our interest in reaction mechanisms on supported catalysts, we are looking for an accurate and quantitative description of the geometric and electronic characteristics of the different reaction sites in the smallest structures compatible with those that can be found in the real support.

Rhodium clusters have industrial uses as catalysts in a variety of hydrocarbon oxidation reactions, perhaps the best known use that in automotive exhaust anti-pollution systems [16-18]. Considerable progress has been made in the knowledge of the influence of the particle size, surface structure, and surface composition on the reactivity of Rh clusters. Particle sizes as small as 1 nm have been characterized in supported catalysts [19], a size that is associated with precrystalline structures. Surface atoms represent the majority of the atoms in these particles, and sites of different topologies (kinks, edges, and corners) are defined. Theoretical investigation

is, however, a challenging task, primary due to the large number of incomplete d shells of the metal atoms, which lead to a great number of low lying states and associated structures. The presence of so many states causes serious convergency problems when self-consistent field (SCF) techniques are applied, and most often necessitates a treatment that includes electron correlation. These concerns make examination of open-shell clusters using SCF-based techniques that can address questions of structure and multiplicity difficult to apply.

In this work we apply a version of the intermediate neglect of differential overlap (INDO) model [20], at both the SCF and the configuration interaction (CI) level, using the ZINDO program [21] to determine the structure as well as the electronic characteristics of the different sites in the small Rh particles that *may* be present in highly dispersed supported catalysts. We stress *may* here, for in this preliminary study we have not considered the interesting possibility that the support itself might influence structure as well as electronic properties.

### Computational Details

Most often each calculation starts as configuration-averaged Hartree-Fock (CAHF), with an average multiplicity for the number of electrons considered [22a]. A small CI using these orbitals on several interesting multiplicities then indicates which states should, in general, be pursued through the restricted open-shell Hartree-Fock (ROHF) procedure [22b]. For each structure and possible multiplicity, a separate geometry search is made using the ROHF procedure as described below.

The geometry optimization step of the calculation is particularly important in obtaining a proper description of the geometric and electronic parameters that are responsible for and, at the same time may justify, the different catalytic activity of the surface sites defined on a given structure. The calculated geometries are the result of a full optimization of the coordinates (interatomic distances and angles) without any constrain on their variation. The Head and Zerner technique [23,24] has been used, with the Broyden-Fletcher-Goldfarb-Shanno (BFGS) algorithm to update the inverse Hessian matrix. For a complete search of the structure of minimum energy on the potential energy surface, different initial geometries, associated with different symmetries of the cluster, have been defined as initial guesses for the geometry optimization routines, including both polygonal structures and pieces of the bulk. In this way, the relative stability of different stable geometries that may be present in the precrystalline structures are also compared. The number of atoms in the cluster has to be, then, compatible with the definition of octahedral, icosahedral, fcc, and hcp structures free of undesirable effects of nonregular environments on the atoms of the borders.  $Rh_{13}$  and  $Rh_{19}$  match these requirements; the latter are close in size to the 1 nm particles characteristic of highly dispersed catalysts. Although pieces of bulk (fcc and hcp) structures may be *a priori* ruled out for precrystalline structures, because the precrystalline to reticular transition would occur for a cluster size larger than 1 nm, it is nevertheless interesting to compare the energy of the crystalline structures with those of the precrystalline ones for the different cluster sizes.

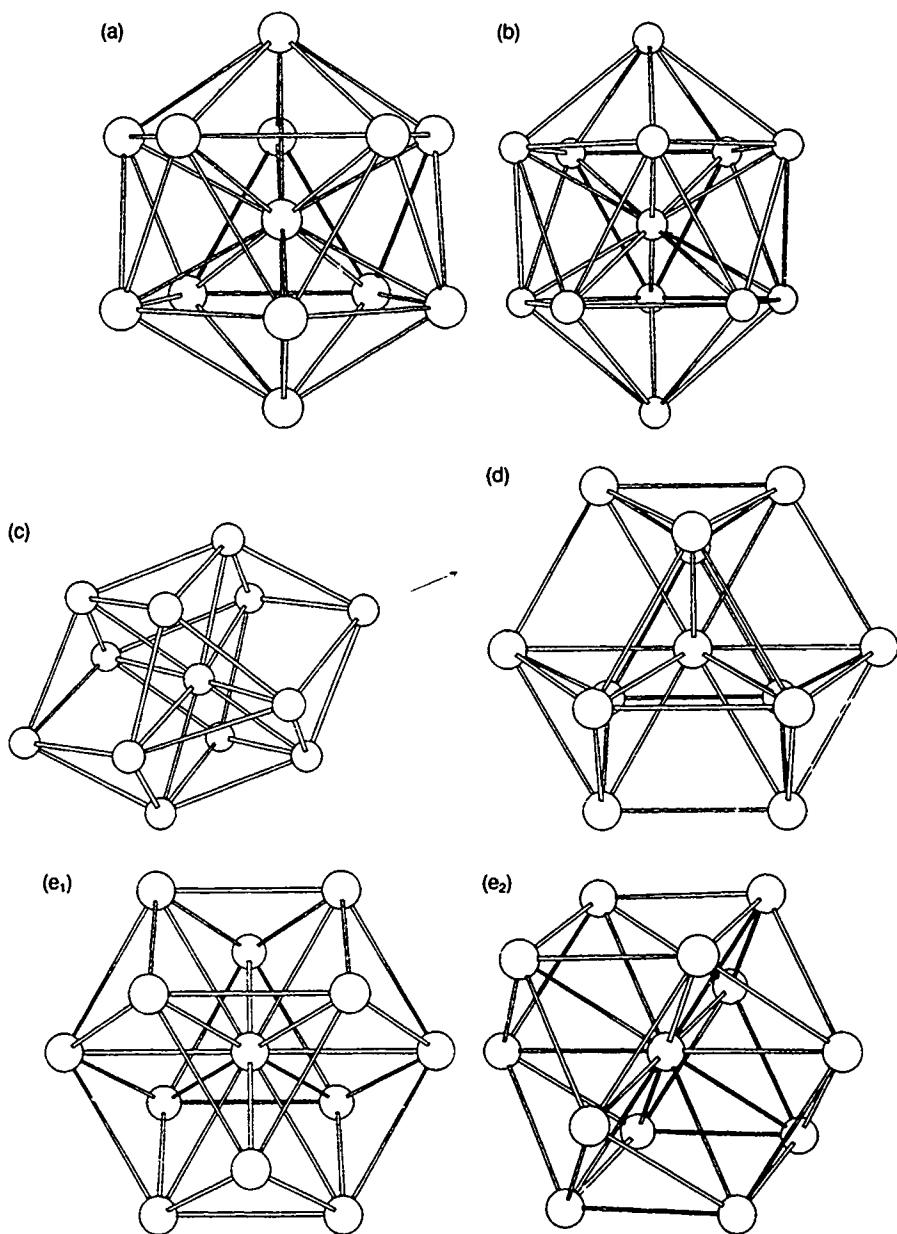


Figure 1. Starting  $Rh_{13}$  structures for the geometry optimization procedure. (a) icosahedral symmetry,  $I_h$ ; (b) "d<sub>4h</sub>" symmetry,  $D_{3d}$ ; (c) octahedral symmetry,  $O_h$ ; (d) close-packed  $D_{3h}$ . (e) close-packed fcc structure (e<sub>1</sub>, e<sub>2</sub> are different views of the same structure),  $D_{3d}$ . Starting geometries represented by Figures (a), (b), and (c) evolve into the same final structure depicted in Figure 2.

TABLE I. Total energies (a.u.) associated with the most stable multiplicities of the different  $Rh_{13}$  geometries after a full optimization procedure.\*

$M$	hcp	fcc	Oc	$D_5$	Ic
2	-294.81	-294.87	-294.69	-294.87	-294.87
4	-294.76	-294.86	-294.67	-294.86	-294.85
6	-294.72	-294.81	-294.62	-294.84	-294.83

\* Only the hexagonal and distorted octahedral does not change to a  $D_5$  symmetry.

The open-shell structure of the Rh atom ( $d^8s^1$ ) defines a certain number of unpaired electrons for the  $Rh_{13}$  and  $Rh_{19}$  systems. The stabilities of the different multiplicities ( $M$ ) have been compared at the ROHF level for the different starting geometries. This procedure is complex, for we find that different multiplicities form different structures, or, perhaps, vice versa.

Two parameterizations of the INDO theory are used in these studies: one for geometry, which utilizes two-center two-electron integrals that are calculated *ab initio*, and one to calculate the electronic descriptors at fixed geometries, which obtains these integrals empirically from atomic spectroscopy [20,25-27]. The calculation of the electronic descriptors as well as the analysis of the molecular orbital interactions has been done, in the framework of this parameterization, at the CI level. The resonance integrals " $\beta$ " are chosen according to a formula that takes into account different electron negativities [28]. This parameterization reproduces the available experimental geometries and excited state manifold of  $Rh_2$  and  $Rh_4$ , but does incorporate a correction for overbinding proportional to the calculated bond index [28]. Other aspects of the method are given elsewhere [20,25].

## Results and Discussion

### $Rh_{13}$ Structures

We first compare the stability of regular but nonperiodic structures with that of pieces of bulk, represented by means of the same number of atoms, whose repetition

TABLE II. Total energies (a.u.) associated with the different multiplicities for the different calculated  $Rh_4$  geometries.\*

$M$	Square planar	Tetrahedral	Tetrahedral (2.69 Å)
1	-90.311	-90.371	-90.038
3	-90.308	-90.337	-90.019
5	-90.248	-90.282	-90.030
7	-90.161	-90.168	-90.045

\* First and second columns refers to the full optimized square planar and tetrahedral geometries. The third column gives the total energy of the tetrahedral structure for the bulk Rh-Rh interatomic distances.

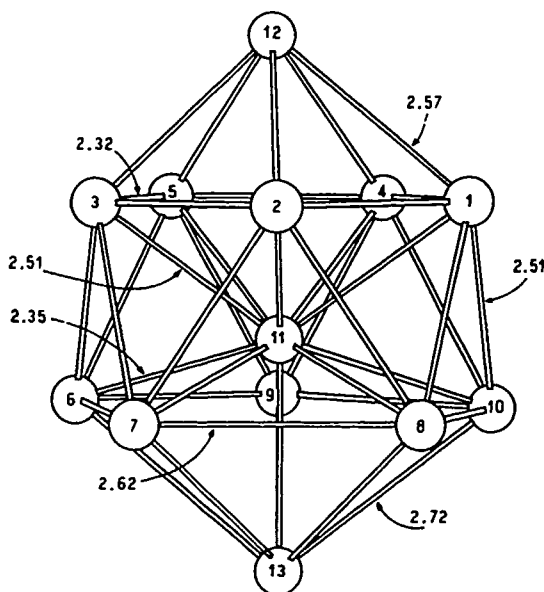


Figure 2. Most stable  $\text{Rh}_{13}$  structure as the result of a full geometry optimization procedure,  $C_{3v}$ . Geometric parameters are indicated. Electronic parameters = local density charges on the atomic centers [ $q$  (a.u.)] are as follows:  $q_1 = q_2 = q_3 = q_4 = q_5 = -0.128$ ,  $q_6 = q_7 = q_8 = q_9 = q_{10} = +0.197$ ,  $q_{11} = -0.919$ ,  $q_{12} = +0.366$ ,  $q_{13} = +0.201$ .

in three dimensions would develop the three-dimensional periodic structures characteristic of the bulk metal.

Among the regular structures, icosahedral and cuboctahedral structures can be constructed by means of either 12 or 13 rhodium atoms which occupy only the vertices of the icosahedron or both the vertices and the center of the structure, respectively. However, 12 atoms is not an appropriate number to construct pieces of fcc or hcp bulk structures. In addition, a comparison of the BE per metal atom for the  $\text{Rh}_{12}$  and  $\text{Rh}_{13}$  structures gives a higher stability to the latter (0.5 eV for the icosahedron and 0.25 eV for the octahedral geometry), making  $\text{Rh}_{13}$  a much more attractive structure to examine.

For these reasons, we have chosen a  $\text{Rh}_{13}$  cluster size to build up structures of icosahedral of  $D_5$  and cuboctahedral symmetry, as well as fcc and hcp pieces of bulk [Figs. 1(a)–(e)] as starting structures for a full geometry optimization procedure. The fcc and hcp structures can also be described as centered cuboctahedral and anticuboctahedral symmetries [1]. Because they are characteristic of close-packed metallic lattices, we have chosen this related nomenclature. The octahedral structures depicted in Figures 1(c) and 1(d) are almost equivalent, as can easily be seen from a comparison of these figures. However, the structure referred to as cuboctahedral (1c) has a distortion along the  $z$ -axis that increases the distance from the apex atoms to the center by 40% of its regular value. Different Rh–Rh

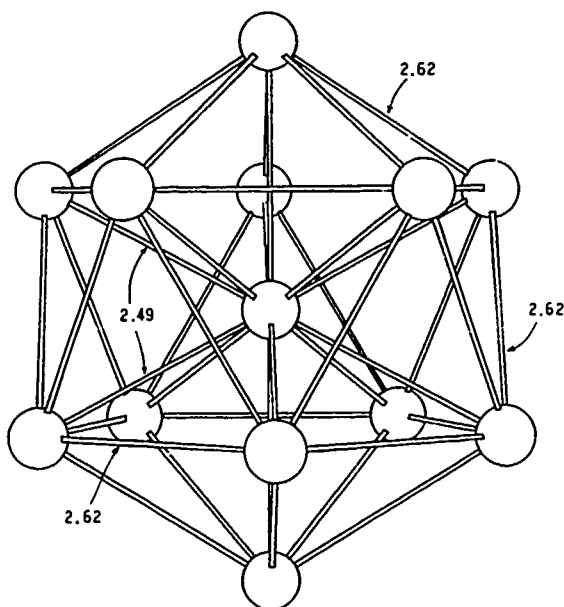


Figure 3. Most stable  $\text{Rh}_{13}$  "icosahedral" structure after a full geometry optimization. The Rh-Rh interatomic distances  $R(4-5)$ ,  $R(3-6)$ ,  $R(7-8)$ ,  $R(1-10)$ ,  $R(2,12)$ ,  $R(9,13)$  are 3% longer than the others (see text).

interatomic distances, between 2.0 and 2.7 Å, have been used to build up the initial structures. The lowest energies are always achieved for closest interatomic distances of about 2.5 Å, which appears to represent a compromise between the interatomic distance in the diatomic (2.20 Å [28]) and that in the bulk (2.69 Å [29]).

$\text{Rh}_{13}$  clusters are open-shell structures characterized by a multiplicity ( $M$ ) larger than 1. Each structure has been examined for different  $M$  values. Results in Table I demonstrate that the occupation of low-lying energy levels stabilizes the lowest multiplicity. We stress that each structure, associated with a given  $M$ , has been derived from a full optimization of all distances, without imposing any geometry or symmetry constraints. When symmetry results, it results as a consequence of the optimization.

The same result, related to the higher stability of the lower  $M$  values, has been found for  $\text{Rh}_4$  clusters, which show an interesting behavior relative to the importance of the geometry optimization in the definition of the multiplicity and vice versa. Starting from either square planar or tetrahedral structures, the optimization of both multiplicities and bond lengths gives a regular close-shell structure, either square-planar, with Rh-Rh bond distances of 2.1056 Å, or tetrahedral, with bond length 2.2728 Å. These smaller structures yield interatomic distances that are close to that in the diatomic. On the other hand, if the distance is kept frozen to that observed in the bulk (2.69 Å), the most stable structure is associated with 6 unpaired electrons (Table II). This result is in agreement with density functional calculations

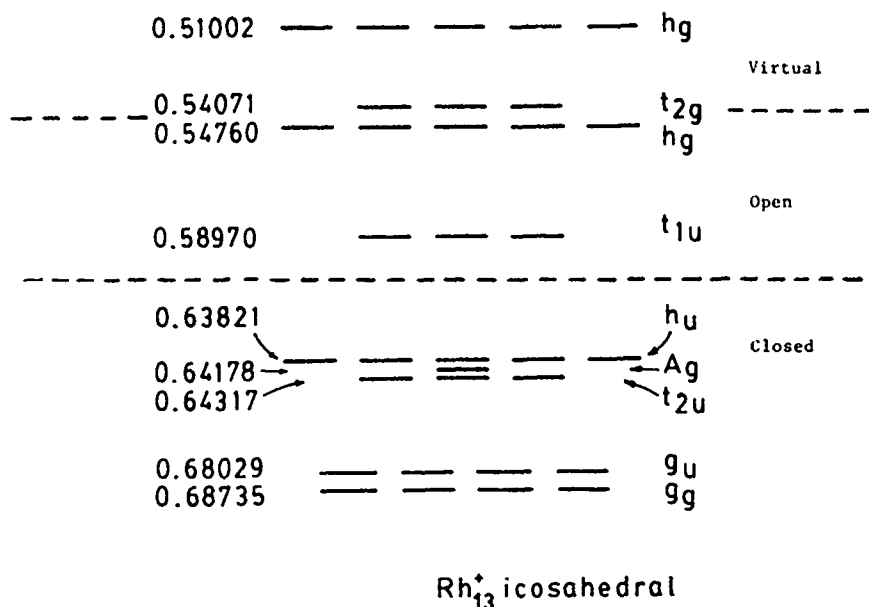


Figure 4. The frontier molecular orbitals obtain for  $Rh_{13}^+$  in  $I_h$  symmetry from a CAHF calculation with four electrons in eight orbitals. Note that the closeness in energy of these orbitals leads to very many nearly degenerate states. Energies are in hartrees. The dashed lines indicate the doubly occupied space, the "open" space, and the virtual space.

[30] that model the Rh(111) surface structures by means of regular tetrahedron constructed with four Rh atoms separated by the bulk interatomic distance. Six unpaired electrons give the lowest energy under these conditions. However, when the bond length is allowed to relax to the equilibrium interatomic distances, the electronic configuration changes from ( ${}^7A_2$ )  $1a_1^2 1t_2^6 1e^4 2t_2^3 3t_2^2 2e^4 2a_1^1 1t_1^3 1t_2^3$ , to lowest energy ( ${}^1A_1$ )  $1a_1^2 1t_2^6 1e^4 2t_2^3 3t_2^2 2e^4 2a_1^1 1t_1^6$ . The decrease in multiplicity is clearly associated with the relaxation of the interatomic distances, leading to larger spin-pairing due to the more efficient overlap of the atomic orbitals, and the resulting stronger interactions. The comparison of the Mülliken populations on the Rh atoms for both interatomic distances shows a larger population of the d orbitals in the septet ( $5s^{0.58}5p^{0.27}4d^{8.15}$  vs.  $5s^{0.59}5p^{0.54}4d^{7.94}$ ). The higher occupation of the more diffuse sp orbitals favors the more efficient overlap in the close-shell structure. The shortening of the bond distances in small metal clusters is not surprising on the basis of the well-known contractions of the lattice parameters in small particles associated with surface stress that has been experimentally determined for several transition metal atoms [5,31], and which are easily confirmed in these calculations.

Table I summarizes our results for  $Rh_{13}$ , and indicates that the most stable geometry (Fig. 2) is one of near  $C_{5v}$  symmetry and is achieved after the optimization of the initial  $D_{5d}$  symmetry structure. The same final geometry is obtained from full optimization of the fcc and the icosahedral starting structures. The fcc structure,

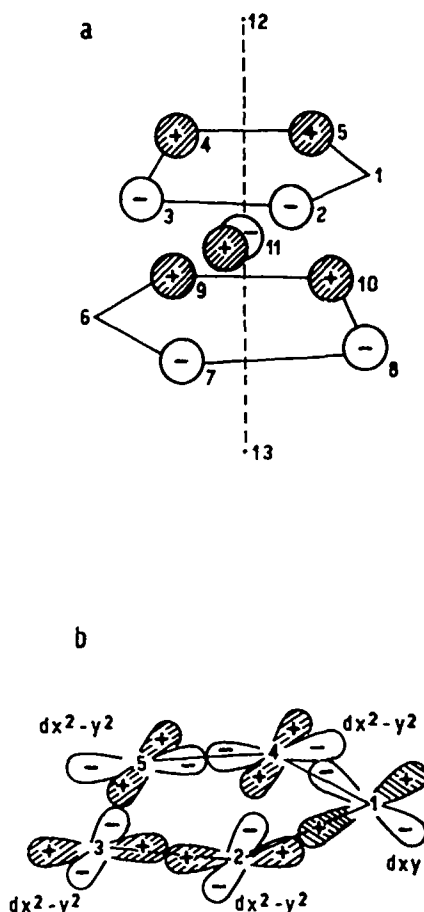


Figure 5. Molecular orbital interactions that involve the unpaired electron of the  $Rh_{13}$  structure. (a) Bonding interactions between opposite atoms on the alternate pentagons. Antibonding interactions are between the s orbitals on the pentagons and the p on the central atom. (b) Bonding interactions between the d orbitals of the atoms on one of the pentagons.

in particular, goes through a remarkable modification of its geometry, requiring a large number of cycles in the geometry search to finally reach the structure of Figure 2. An energy barrier is associated with the transition from hexagonal and from a distorted cuboctahedral to the final structure depicted in Figure 2, and thus these structures represent proper minima on the potential energy surface. In these two cases, the change in geometry from the initial one assumed to begin the optimization procedure involves a shortening of the interatomic distances approximately 4%, again favoring bond lengths closer to that in the diatomic.

Icosahedral structures have been identified in several inorganic Rh compounds, as  $[Rh_{12}Sb(CO)_{27}]^{-3}$  [32]. Cuboctahedral geometries have also been found in,



	0.43321	—	—	—	—	—	hg
VIRTUAL	0.45255		—	—	—		t <sub>2g</sub>
-----							
	0.47976		—	—	—		t <sub>1u</sub>
OPEN	0.50034						hg
	0.50613	==	==	==	==	==	h <sub>u</sub>
	0.51453						Ag
CLOSED	0.52618		—	—	—		t <sub>2u</sub>
	0.55397						g <sub>u</sub>
	0.55536	==	==	==	==		g <sub>g</sub>

### Rh<sub>13</sub> icosahedral

Figure 6. The frontier molecular orbitals obtained for Rh<sub>13</sub> in *I<sub>h</sub>* symmetry from a CAHF calculation with five electrons in eight orbitals. Note that the closeness in energy of these orbitals leads to very many nearly degenerate states. Energies are in hartrees. The dashed lines indicate the doubly occupied space, the "open" space, and the virtual space.

for example, [Rh<sub>13</sub>(CO)<sub>24</sub>H<sub>3</sub>]<sup>-3</sup> and [Rh<sub>12</sub>Pt(CO)<sub>24</sub>]<sup>-4</sup> [33]. The presence of the carbonyl ligand, which is known to involve important charge transfer interactions with the metal [1], preclude, unfortunately, any inference from these structures to that of the naked Rh<sub>13</sub> clusters. Rather both icosahedral and cubooctahedral are made plausible.

According to our calculations, the structure of Rh<sub>13</sub> clusters (Fig. 2) can be described as distorted icosahedron, defined by 12 fivefold axis and 20 triangular faces. Ten of the 12 vertices, on the other hand, define two alternate pentagons, while the others are aligned with the center of the structure, perpendicular to them. It is distorted in the sense that the edges are no longer of equal length and the inversion center is lost. The full symmetry characteristic of the icosahedra [34], with 120 symmetry operations, does not apply.

In this particular case the distortion from a regular icosahedra involves mainly (Fig. 2):

- A change of the relative sizes of the alternate pentagons, from two equal in a regular icosahedra [Fig. 1(a)], to a larger and a smaller one, of interatomic distances of 2.31 and 2.62 Å, respectively.
- An asymmetric lengthening of the distances along the z-axis, more important between the larger pentagon and the adjacent apex atom.
- A change in the distance from the atom in the center to the atoms in the pentagons which, instead of equidistant as in a regular icosahedra, is closer to the larger pentagon.

*Origin of the Distortion:* According to the Jahn-Teller (JT) theorem [35,36], any nonlinear system where there is orbital degeneracy has a vibrational mode which

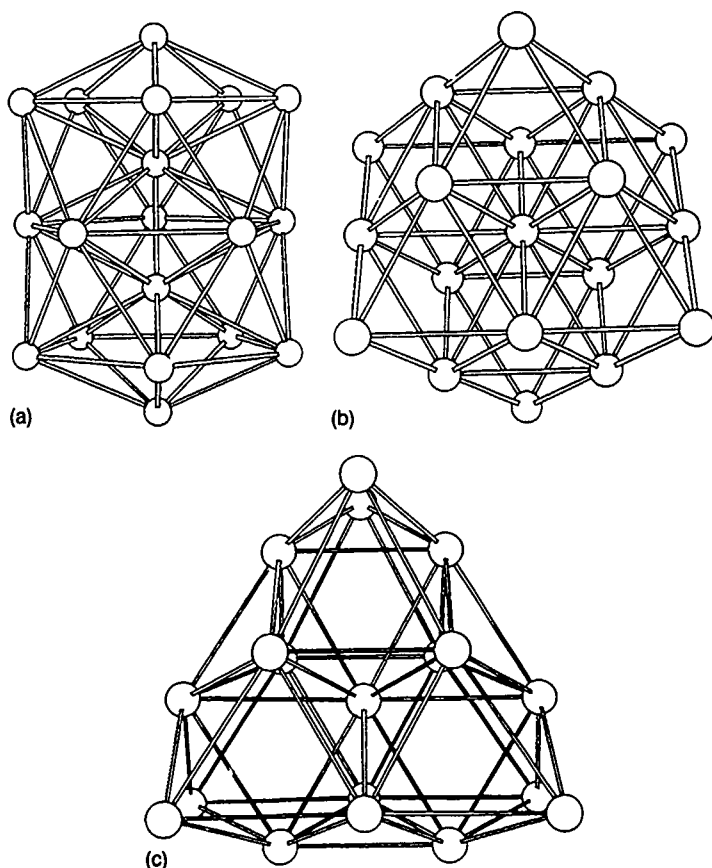


Figure 7. Starting  $Rh_{19}$  structures for the geometry optimization procedure. (a)  $D_{5h}$  symmetry; (b) closed packed fcc structure; (c) close packed hexagonal structure. Both the  $D_{5h}$  symmetry and the fcc structure evolves to the same final structure depicted in Figure 6.

will lower the symmetry and also lower the energy of the system. A Jahn-Teller distortion would, then, change the geometry of the system in order to decrease its symmetry in such a fashion that the electronic state is no longer spatially degenerate. Calculations by other authors [11,37-39] have shown that the most stable structure of a metal cluster is strongly influenced by the JT effect, as we find here. Because of the nature of the distortion in  $Rh_{13}$  we examine the structure of  $Rh_{13}^+$ . The hope here is that the positive ion has states that are further separated in energy than the neutral and the results could guide our thinking on the neutral. Starting from an icosahedron, a geometry optimization is made for each multiplicity. The lowest energy of all these structures is a singlet of  $C_{2h}$  symmetry (see caption in Fig. 3). This structure might be understood as resulting from an  $^1H_u$  state from an idealized  $I_h$  structure obtained from a CAHF calculation in which four electrons are averaged over eight orbitals, the  $t_{1u}$  and  $h_g$  orbitals of Figure 4. Other schemes we tried either

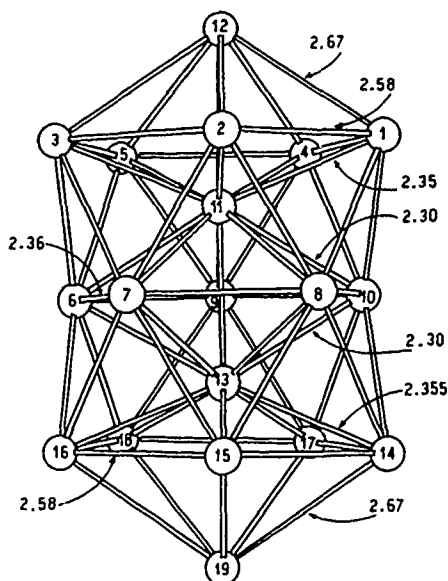


Figure 8. The most stable  $Rh_{19}$  structure ( $D_{5h}$ ) calculated from a full geometry optimization. Geometry parameters are indicated. Electronic parameters = local density charges on the atomic centers [ $q$  (a.u.)] are as follows.  $q_1 = q_2 = q_3 = q_4 = q_5 = q_{14} = q_{15} = q_{16} = q_{17} = q_{18} = +0.360$ ,  $q_6 = q_7 = q_8 = q_9 = q_{10} = -0.480$ ,  $q_{11} = q_{13} = -1.200$ ,  $q_{12} = q_{19} = +0.690$ .

did not lead to icosahedron, or led to orbitals which did not have the symmetry of the nuclear framework. This  $^1H_u$  state undergoes a distortion along an  $h_g$  mode and gives a  $^1E_{2u}$  state in  $D_{5d}$  which further undergoes a first order JT distortion to  $C_{2h}$  along an  $e_{1g}$  mode. As is usually found for highly symmetric structure with a large number of degenerate orbitals, the lowest  $I_h$  structure is not a singlet but a  $^5H_g$  state. We calculate that the  $^1H_u$  state lies 0.03 eV above the  $^5H_g$  one for the  $I_h$  geometry. The lowest quintet, however, lies considerably higher than the singlet in the final  $C_{2h}$  structure. Within 0.1 eV of our lowest calculated  $^5H_g$  state lie more than 350 states.\*

In the  $C_{2h}$  structure the  $t_{1u}$  and  $h_g$  orbitals (the frontier orbitals active in the CAHF) are calculated nearly degenerate, with an energy difference obtained from

\* The idealized  $I_h$  structure we start with corresponds to a perfect icosahedron that results after symmetrizing the  $C_{2v}$  structure obtained from the geometry optimization. Because of the large number of molecular orbitals very close in energy, pure states are very hard to separate, as they tend to mix during the SCF cycles. Molecular orbitals characteristic of an icosahedron can only be kept by means of CAHF calculation. In order to properly choose a good set of orbitals to be averaged, we started by the analysis of the orbital that result from extended Hückel (EHT) calculations. From the EHT results we first averaged four electrons in the  $t_{1u}$  orbital. However, when the pure spin states were projected by means of multi-reference CI calculations, the  $h_u$  orbitals were always involved. We therefore extend the CAHF calculations of four electrons in eight orbitals. Calculations using the resultant basis gives a reasonable explanation of the JT distortion as discussed

the CAHF procedure of only 0.001 eV (Fig. 3). The three Lowest Unoccupied Molecular Orbital (LUMO) orbitals are mainly formed from contributions of the s (and some d) orbitals of the Rh atoms of the pentagonal rings, and the  $p_x$ ,  $p_y$ ,  $p_z$  orbitals on the central atom.

The occupation of one of these eight nearly degenerate orbitals to form the neutral molecule brings about a new interaction, which is:

- bonding on the s orbitals of opposite atoms of different rings [Fig. 5(a)]
- antibonding between the s orbitals on the atoms of the rings and the p orbitals on the central atom [Fig. 5(a)]
- bonding on the d orbitals on the atoms 1, 2, 3, 4, and 5 (Fig. 3) on one of the pentagons [Fig. 5(b)].

The first interaction shortens the interatomic distances between adjacent atoms on different pentagons by 0.1 Å, from 2.62 in the cation to 2.52 Å in the neutral molecule. The d interaction, on the other hand, shortens the interatomic distances between the atoms of one of the rings from 2.62 to 2.32 Å, leading to a more effective overlap of the s and p orbitals on the central atom. This interaction moves the central atom closer to the other pentagon, due to the antibonding character of the sp interaction.

In spite of considerable work, and our experience learned from  $\text{Rh}_{13}^+$ , we have not been able to track the reason for the distortion of  $\text{Rh}_{13}$  from  $I_h$ . Our final state is a doublet with  $C_v$  symmetry, a structure which is very nearly  $C_{5v}$ .

CAHF calculations with five electrons in eight orbitals ( $t_{1u}$  and  $h_g$ ) does yield an  $I_h$  structure. After CI our lowest state is a  $^6A_{1g}$  state which should be JT stable. The lowest octet,  $^8G_g$ , is calculated 310  $\text{cm}^{-1}$  higher in energy, than a quartet,  $^4H_g$ , 1990  $\text{cm}^{-1}$  above  $^6A_{1g}$ . The lowest doublet  $^2H_g$ , is calculated some 3000  $\text{cm}^{-1}$  higher in energy, but this is the parent that leads to the lowest energy  $C_v$  structure. Some 250 states lie within 0.1 eV of the  $^6A_{1g}$  state. A feasible chain for the distortion is  $^2H_g(I_h) \rightarrow ^2A_{1g}(D_{5d}) \rightarrow ^2A_{1g}(C_{5v})$ . The first step is first-order JT through an  $h_g$  mode. The second is a second-order JT distortion along an  $a_{1u}$  mode that mixes the  $^2A_{1g}(D_{5d})$  state with a  $^2A_{1u}(D_{5d})$  state that we calculate nearly degenerate. Indeed, the lower of the two depends on the size of the CI. We have not proven this—a mathematical problem, but not a physical one. Starting from nearly any structure, we obtain the same lowest energy structure and multiplicity.

Returning for the moment to the density of states of near lying energy, it may be that many doublets are sampled at any reasonable temperature, each with somewhat differing geometries leading to a somewhat flexible structure.

*Consequences of the Distortion.* In the resulting  $\text{Rh}_{13}$  structure there are several surface sites (Fig. 2). Because of the different electronic environment and local density charges, each one can be associated with a different catalytic activity. Single coordination sites may correspond to atoms on the pentagons or to apex atoms, having a different local density due to the different environment. In the same way, bicoordinated sites may be defined between atoms on one pentagon, between an apex and an atom of a pentagon or between atoms of two different pentagons,

and three coordinated sites between two atoms of one of the pentagons and the adjacent apex or between atoms of different pentagons. The interactions of an adsorbate will be different on each of the different sites, and they have to be analyzed separately if we assume the structure is fairly rigid, or that absorption may lock in the different sites.

Although positive and negative local charges are defined on the surface atoms, the surface of the cluster is, on the average, electron deficient, bearing a 0.91 a.u. positive charge (0.076/surface atom). A charge of the same magnitude and opposite sign is concentrated on the atom in the center.

The positive charge density on the surface of the cluster contrasts with the local negative charge density on the terrace atoms in the bulk [28], and is a key factor in understanding the different catalytic activity of both structures.

### *Rh<sub>19</sub> Structures*

Larger  $D_5$  structures can be grown from the 13 atom icosahedron by adding pentagonal rings around each vertex [40]. The arrangement  $Rh_{19}$  is obtained by adding one pentagonal ring around a fivefold axis and one additional atom on it [40] (see Fig. 6). This double icosahedron [Fig. 7(a)] is formed by two interpenetrating icosahedra sharing two central atoms and one pentagonal ring. This cluster size is also compatible with fcc and hcp pieces of bulk [Figs. 7(b) and 7(c)].

Nineteen Atom  $D_5$  structures have been found in Pt and Au compounds [1,40]. The "double icosahedron" structure has also been characterized for laser-evaporated  $Ni_{19}$  clusters [9c]. Because of the small size of the cluster, it seems reasonable that the lower energy be associated to the precrystalline structure rather than the reticular one.

The structures depicted in Figures 7(a)–(c), constructed with Rh–Rh interatomic distances of 2.5 Å, form starting geometries for a full geometry optimization, free of constraints on the variation of any of the coordinates or symmetry constraints. The lowest energy structure we obtain is given in Figure 8. It is of  $D_{5h}$  symmetry.

The behavior of the  $Rh_{19}$  cluster is very similar to that of  $Rh_{13}$  in two main aspects:

1. The final structure results from the same kind of distortion described for  $Rh_{13}$ , which stabilizes a smaller central pentagon with Rh–Rh distances of 2.3 Å and two larger pentagons with Rh–Rh distances of 2.56 Å. However, there is no change in the  $D_{5h}$  symmetry from the initial [Fig. 5(a)] to the final (Fig. 6) structures, and the complications we encountered in the smaller structure are avoided.

2. The fcc starting structure goes to the same distorted  $D_5$  one upon geometry optimization, while the hcp keeps its original symmetry, decreasing the bond length to an average value of 2.3 Å, giving a structure 2.08 eV less stable than the  $D_{5h}$  one.

In the same way previously described for  $Rh_{13}$  clusters, the distorted geometry is associated with a distribution of positive and negative charges on the surface, negative on the atoms of the smaller pentagon and positive on the others (Fig. 6).

The surface charge is positive, 2.4 a.u. A negative charge of the same magnitude is uniformly distributed between the two central Rh atoms. Different surface sites, and in particular electron-deficient ones, are obtained for these structures, and characterize the structural and electronic properties of the active sites in the small particles of highly dispersed catalysts.

The larger stability of the structures of fivefold symmetry for both  $\text{Rh}_{13}$  and  $\text{Rh}_{19}$  clusters lead us to infer that these may be the preferred symmetry of the small Rh particules that are present in highly dispersed supported catalysts, and the sites defined in these structures might be the surface sites of catalytic activity.

The energy of the different structures for a particular cluster size is the result of a balance between the surface and the bulk energy. The structure of the crystalline habit is the most stable for a bulk metal (fcc for Rh). In the small clusters, on the other hand, most of the atoms are surface atoms, and the surface energy becomes the dominant contribution to the total energy. Icosahedral symmetries are characterized by a large concentration of triangular faces, which are the minimum part of an fcc(111) structure, associated with the larger packing density and the lower total energy. This gives a plausible explanation for the larger stability of the icosahedral-like structures in small clusters of fcc metals.

Previous studies of the structure of transition metal clusters also seem to favor icosahedral structures. However, distortions of a lower symmetry are not often discussed, as the structures obtained are often the results of geometry optimization with symmetry constraints. *Ab initio* multireference calculations suggest an  $I_h$  symmetry with a lowest  $^6A_g$  state of icosahedral symmetry for both  $\text{Li}_{13}$  [41] and  $\text{Cu}_{13}$  structures [42]. Dynamical calculations on the structure of  $\text{Ni}_n$  clusters ( $n = 4-13$ ), minimizing the BE using a near first principle-corrective effective medium theory (CEM) yield an  $I_h$  symmetry 0.1 eV more stable than the  $O_h$  or  $D_{3h}$  ones for  $\text{Ni}_{13}$  [43].

The results presented in this paper show the solution of the structure of small transition metal cluster when the coordinates are allowed to completely relax. One might expect that only after this relocation can a proper description of the electronic feature that characterizes the different surface sites be determined. We might add, however, that with so many low lying states, the actual sites might be characterized by an average, or be determined by a specific interaction with an adsorbate.

In general agreement with systematic calculations of the properties of metal clusters as a function of size [43], we find an increase of the BE per atom from 1.10 eV for  $\text{Rh}_4$ , 2.97 eV for  $\text{Rh}_{12}$ , 3.55 eV for  $\text{Rh}_{13}$ , and 4.48 eV for  $\text{Rh}_{19}$ .

### Conclusion

We have calculated at the SCT-CI level the most stable structures of the small Rh clusters,  $\text{Rh}_{13}$  and  $\text{Rh}_{19}$ , that may be present in highly dispersed supported catalysts, as well as the structural and electronic characteristics that helps define the particular reactivity of the different surface sites.

In agreement with previous calculations and experimental research on other transition metal atoms [8-11], a lower energy is found for the structures of fivefold

symmetry. As has been described for the  $Rh_{13}$  molecule, Jahn-Teller distortions play an important role in the determination of the final geometries. In addition, we note that the final structures generally form lower multiplicities, rather than the higher multiplicities that seem to characterize the higher symmetry structures.

In the final structure, different surface sites are defined that might show a different reactivity towards a given adsorbate. The surface as a whole is characterized, for both  $Rh_{11}$  and  $Rh_{10}$  by an electron deficiency, which will help determine the nature of the interactions with a given adsorbate.

In the final analysis we caution, however, that the support, itself, might effect the electronic characteristics of the surface sites. Preliminary studies suggest sizable barriers for CO migration on the various surface sites, and that, in fact, each site might be expected to have a somewhat different reactivity [44].

The characteristics of the resulting structure demonstrate the importance of a careful geometry optimization procedure in the analysis of the reactivity of a given metal cluster, capable of differentiating the surface sites whose structural and electronic characteristics are far from those that may be present in regular structures of a higher symmetry.

#### Acknowledgments

This work was supported in part from a grant from the Office of Naval Research. G.L.E. is grateful to the Consejo Nacional de Investigaciones Científicas y Técnicas (CONICET), República Argentina, for a postdoctoral fellowship, and the Fundacio Antorchas for travel support.

#### Bibliography

- [1] (a) D. M. P. Mingos and D. J. Wales, *Introduction to Cluster Chemistry Organic and Organometallic Chemistry Series*, Prentice Hall Advanced Reference Series, Physical and Life Sciences (Prentice-Hall, Englewood Cliffs, NJ, 1990); (b) see also *Computational Chemistry: The Challenge of d and f Electrons*, ACS Proceedings Series, D. Salahub and M. C. Zerner, Eds. (American Chemical Society, Washington, DC, 1989).
- [2] F. A. Cotton and R. A. Walton, *Multiple Bonds between Metal Atoms* (Wiley, New York, 1982).
- [3] M. K. Harbola, *Proc. Natl. Acad. Sci. USA* **89**, 1036 (1992).
- [4] K. J. Taylor, C. L. Pettiette-Hall, O. Cheshnovsky, and R. E. Smalley, *J. Chem. Phys.*, to appear.
- [5] H. P. Cheng, R. S. Berry, and R. L. Whetten, *Phys. Rev. B* **43**, 10,647 (1991).
- [6] M. D. Morse, *Chem. Rev.* **86**, 1049 (1986).
- [7] J. Jortner, *Z. Phys. D. Atoms, Molecules Clusters* **24**, 247 (1992).
- [8] L. P. Martin, I. Bergmann, H. Gohlich, and T. Lange, *Chem. Phys. Lett.* **176**, 343 (1991).
- [9] (a) T. D. Klots, B. J. Winter, E. K. Parks, and S. J. Riley, *J. Chem. Phys.* **92**, 2110 (1990); (b) B. J. Winter, T. D. Klots, E. K. Parks, and S. J. Riley, *Z. Phys. D* **19**, 375 (1991); (c) B. J. Winter, E. K. Parks, and S. J. Riley, *J. Chem. Phys.* **94**, 8618 (1991).
- [10] S. Valkealahti and M. Manninen, *Phys. Rev. B* **45**, 9459 (1992).
- [11] O. B. Christensen, K. W. Jacobsen, J. K. Nørskov, and M. Manninen, *Phys. Rev. Lett.* **66**, 2219 (1991).
- [12] K. K. Das and K. Balasubramanian, *J. Chem. Phys.* **93**, 625 (1990).
- [13] K. Balasubramanian, *J. Chem. Phys.* **91**, 307 (1989).
- [14] V. Bonacic-Koutecky, P. Fantucci, and J. Koutecky, *Chem. Rev.* **91**, 1035 (1991).
- [15] F. Illas, J. Rubio, and J. Canellas, *J. Chem. Phys.* **93**, 2603 (1990).

- [16] J. C. Schlatter and K. C. Taylor, *J. Catal.* **49**, 42 (1977).
- [17] N. W. Cant and W. K. Hall, *J. Catal.* **27**, 80 (1972).
- [18] K. Kunimatsu, R. O. Lezna, and M. Enyo, *J. Electroanal. Chem.* **258**, 115 (1989).
- [19] (a) B. Coq, A. Goursot, T. Tazi, F. Figueras, and D. Salahub, *J. Am. Chem. Soc.* **113**, 148 (1991); (b) A. Goursot, B. Coq, L. C. de Menorval, T. Tazi, F. Figueras, and D. R. Salahub, *Z. Phys. D* **19**, 367 (1991).
- [20] (a) J. A. Pople, D. L. Beveridge, and P. A. Dobosh, *J. Chem. Phys.* **47**, 2026 (1967); (b) J. E. Ridley and M. C. Zerner, *Theor. Chim. Acta (Berl.)* **42**, 223 (1976); (c) M. C. Zerner, G. H. Loew, R. F. Kirchner, and U. T. Mueller-Westerhoff, *J. Am. Chem. Soc.* **106**, 589 (1984); (d) A. D. Bacon and M. C. Zerner, *Theoret. Chim. Acta* **53**, 21 (1979).
- [21] M. C. Zerner, ZINDO package, Quantum Theory Project, Williamson Hall, University of Florida.
- [22] (a) M. C. Zerner, *Int. J. Quant. Chem.* **35**, 567 (1989); (b) W. D. Edwards and M. C. Zerner, *Theoret. Chim. Acta* **72**, 347 (1987).
- [23] (a) J. D. Head and M. C. Zerner, *Chem. Phys. Lett.* **122**, 264 (1985); (b) J. D. Head and M. C. Zerner, *Chem. Phys. Lett.* **131**, 359 (1986).
- [24] J. D. Head, B. Weiner, and M. C. Zerner, *Int. J. Quantum Chem.* **33**, 177 (1988).
- [25] W. P. Anderson, T. R. Cundari, and M. C. Zerner, *Int. J. Quantum Chem.* **34**, 31 (1991).
- [26] M. C. Zerner, in *Reviews in Computational Chemistry*, K. B. Lipkowitz and B. Boyd, Eds. (VCH Publishers, New York, 1990), Vol. 2.
- [27] J. P. Stewart, in *Reviews in Computational Chemistry*, K. B. Lipkowitz and B. Boyd, Eds. (VCH Publishers, New York, 1990), Vol. 1.
- [28] G. L. Estiu and M. C. Zerner, *Int. J. Quantum Chem. Quantum Chem. Symp.* **26**, 587 (1992).
- [29] D. R. Lide, Ed., *CRC Handbook of Chemistry and Physics*, (CRC Press, Boca Raton, FL, 1990-1991).
- [30] A. Goursot, I. Papai, and D. R. Salahub, *J. Am. Chem. Soc.* **114**, 7452 (1992).
- [31] G. Apai, J. F. Hamilton, J. Stohr, and A. Thompson, *Phys. Rev. B* **43**, 165 (1979).
- [32] J. L. Vidal and J. M. Troup, *J. Organometall. Chem.* **213**, 238 (1981).
- [33] V. G. Albano, A. Ceriotti, P. Chini, S. Martinengo, and W. M. Anker, *J. Soc. Chem. Commun.*, 859 (1975).
- [34] B. Bruce King, *Inorg. Chim. Acta* **198-200**, 841 (1992).
- [35] F. A. Cotton and G. Wilkinson, *Introduction to Advanced Inorganic Chemistry*, 3rd. ed. (Wiley, New York, 1972).
- [36] A. F. Williams, *A Theoretical Approach to Inorganic Chemistry* (Springer-Verlag, Berlin, 1979).
- [37] J. Koutecky and P. Fantucci, *Chem. Rev.* **86**, 539 (1986) and references therein.
- [38] B. K. Rao, S. N. Khanna, and P. Jena, *Phys. Rev. B* **36**, 953 (1987).
- [39] J. A. Cocordan, R. Virkkunen, and M. Manninen, *Phys. Scr.* **38**, 758 (1988).
- [40] P. Jena, B. K. Rao, and N. Khanna, Eds., *The Physics and Chemistry of Small Clusters*, NATO ASI Series (Plenum, New York, 1986).
- [41] G. Pacchioni and J. Koutecky, *J. Chem. Phys.* **81**, 3588 (1984).
- [42] G. Demuyck, M. M. Rohemer, A. Strich, and A. Veillard, *J. Chem. Phys.* **75**, 3443 (1981).
- [43] K. Raghavan, M. S. Stave, and A. E. DePristo, *J. Chem. Phys.* **91**, 1904 (1989).
- [44] G. Estiu and M. C. Zerner, work in progress.

Received June 2, 1993



# Electronic States Induced by a Ga Vacancy in the $\text{GaAs}_{1-x}\text{P}_x$ Alloy

L. M. R. SCOLFARO, R. PINTANEL, A. FAZZIO, and J. R. LEITE

*Instituto de Física da Universidade de São Paulo, C.P. 20516, 01498-970 São Paulo, SP, Brazil*

## Abstract

Self-consistent one-electron state calculations are carried out, for the first time, for a gallium vacancy in the  $\text{GaAs}_{1-x}\text{P}_x$  alloy. The cluster model, within the framework of the multiple-scattering  $X\alpha$  theory, is used to calculate several charge states of the vacancy. Suitable clusters have been considered in order to simulate the phosphorous concentration  $x$  in the alloy and how the nearest-neighbors configurations affect the vacancy-related levels. It is found that the defect introduces a deep energy level into the band gap which follows the host-valence band edge as  $x$  varies. The same trend in donor and acceptor levels is observed, with a very small Mott-Hubbard potential energy. © 1993 John Wiley & Sons, Inc

## Introduction

Among the native defects which appear in III-V semiconductor compounds, vacancies are the most common ones. They are usually mobile and can thus migrate in the material, being trapped by other defects or impurities and forming complexes. They introduce deep localized states into the fundamental band gap of the semiconductor and may appear as neutral, positively or negatively charged depending on the position of the Fermi level.

It has been shown that an alternative way of investigating the electronic properties of localized defects in III-V semiconductors is to gradually vary the host material, for example, by alloying or applying hydrostatic pressure, and then to study the changes induced in the defect properties [1,2].

Experiments where the host band structure of GaAs is continuously altered through chemical alloying with P, have been proposed to investigate the particular case of transition metal impurities in the  $\text{GaAs}_{1-x}\text{P}_x$  alloy [3,4]. Due to perturbation, band edges of the host band structure are shifted and impurity states are affected differently depending on their detailed nature. The same trend observed in the impurities acceptor binding energies along the alloy has been recently confirmed by us through calculations performed within the framework of the multiple-scattering  $X\alpha$  cluster model [5].

In the present work we apply the molecular cluster model and the multiple-scattering  $X\alpha$  theory to investigate the electronic properties of a Ga, unrelaxed vacancy in  $\text{GaAs}_{1-x}\text{P}_x$ . Self-consistent electronic state calculations are carried out for the neutral, positively, and negatively charge states of the defect ( $V^0$ ,  $V^+$ ,  $V^-$ ).

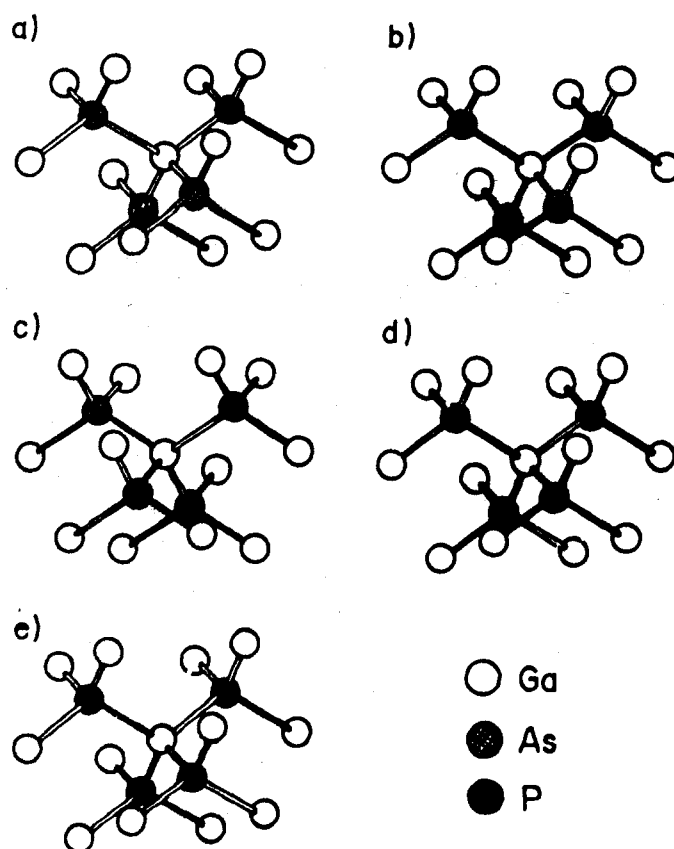


Figure 1. Schematic representation of the 17-atom cluster models used to simulate the  $\text{GaAs}_{1-x}\text{P}_x$  host alloy for (a)  $x = 0$ ; (b)  $x = 0.25$ ; (c)  $x = 0.5$ ; (d)  $x = 0.75$ ; (e)  $x = 1$ .

We analyze the trends in the vacancy energy levels and discuss the stability of charge states as  $x$  varies along the alloy.

### Theoretical Model

The results presented here for the Ga vacancy in the  $\text{GaAs}_{1-x}\text{P}_x$  alloy were obtained through Watson-sphere terminated 17-atom clusters centered at the substitutional Ga site [6,7]. The cluster models consist of a central atom surrounded by 4 nearest neighbors and 12 next-nearest neighbors. By starting with the perfect host alloy and considering the extremum  $x = 0$ , i.e., the GaAs, the cluster then comprises a central Ga atom, the first shell of 4As atoms, and the second shell of 12Ga atoms. The P concentration  $x$  in the alloy is simulated by replacing some of the 4 As nearest neighbors by P, keeping the second shell of 12 Ga atoms unchanged. Within the molecular cluster model, if  $n$  of the 4 nearest neighbors atoms are As, then  $(4 - n)$  atoms are P. This configuration will correspond to a P concentration  $x = (4 - n)/4$  in the alloy. Therefore, by changing the configuration of the nearest neighbors, we simulate the undoped  $\text{GaAs}_{1-x}\text{P}_x$  alloy for  $x = 0, 0.25, 0.5, 0.75$ ,

and 1. The correspondent calculated clusters are GaAs ( $x = 0$ ),  $3\text{As} + 1\text{P}$  ( $x = 0.25$ ),  $2\text{As} + 2\text{P}$  ( $x = 0.5$ ),  $1\text{As} + 3\text{P}$  ( $x = 0.75$ ), and GaP ( $x = 1$ ). The cluster models are schematically shown in Figure 1. The group symmetries are  $T_d$ ,  $C_{3v}$ ,  $C_{2v}$ ,  $C_{3v}$ , and  $T_d$  for clusters GaAs,  $3\text{As} + 1\text{P}$ ,  $2\text{As} + 2\text{P}$ ,  $1\text{As} + 3\text{P}$  and GaP, respectively. In order to simulate the Ga vacancy in the alloy (system  $\text{GaAs}_{1-x}\text{P}_x$ :  $\text{V}_{\text{Ga}}$ ) the central Ga atom is removed in each of the five configurations above, and all other parameters are kept the same as in the perfect host alloy. The radii of the muffin-tin spheres utilized for the GaAs and GaP clusters are the covalent radii as reported in previous works [6,7]. For the  $3\text{As} + 1\text{P}$  and  $2\text{As} + 2\text{P}$  clusters we have used the same muffin-tin parameters as for GaAs; for the  $1\text{As} + 3\text{P}$  cluster the GaP parameters have been adopted. The model, as it has been applied to study defects in GaAs [8,9] and GaP [7] is described elsewhere. Recently, we have also used the cluster models adopted here to describe impurity levels induced by copper and manganese in the  $\text{GaAs}_{1-x}\text{P}_x$  alloy [5].

The calculations carried out here were performed within the framework of the spin-unrestricted approximation, by including all the electrons except those filling inner atomic shells, up to 3d in As and Ga which were kept frozen. Electronic levels were calculated by taking into account the Slater transition-state concept [10].

## Results and Discussion

We start by analyzing the results obtained for the extrema of the alloy. The neutral Ga vacancy in GaAs and GaP gives rise to a deep threefold degenerate  $t_2$  level within the band gap. Since three valence electrons are removed from the lattice when a Ga vacancy is created, this level is partially occupied with three holes and therefore the defect can act as deep acceptor and/or donor centers. Its electrical, optical, and magnetic properties are then related to the broken  $\text{sp}^3$  chemical bonds which originate  $a_1$  and  $t_2$  defect levels, the former appearing as a resonance below the top of the valence band while the latter is introduced into the band gap. For the  $3\text{As} + 1\text{P}$  cluster ( $x = 0.25$ ) the  $t_2$  level splits into two levels,  $a_1$  and  $e$  of the  $C_{3v}$  group symmetry which are occupied with two and one electrons, respectively. In the case of the  $2\text{As} + 2\text{P}$  cluster ( $x = 0.5$ ) in  $C_{2v}$  symmetry, three levels  $a_1$ ,  $b_1$ , and  $b_2$  appear within the band gap, with the uppermost occupied being a  $b_2$  level with one electron. For the  $1\text{As} + 3\text{P}$  cluster, again in  $C_{3v}$  symmetry, an  $a_1$  level fully occupied and an  $e$  level occupied by one electron are found within the band gap. The charge distributions obtained for the vacancy  $t_2$  gap level, and  $t_2$ -derived gap levels, show that they are mostly localized in the first shell of nearest neighbors, with practically the same percentage of charge in all cluster configurations (52% inside the first shell). Similar results have been predicted by previous theoretical calculations for the Ga vacancy in GaAs [11,12] and GaP [13].

The trend observed for the highest occupied  $t_2$ -derived energy level indicates that the vacancy gap level remains nearly constant, in relation to the top of the valence band, as  $x$  the concentration of P in the alloy varies from 0 to 1. This practically independent behavior of the vacancy defect gap level with  $x$  is consistent with its bonding state character of a Ga  $p$ -atomic orbital. It is worth mentioning that a

completely different picture is obtained for transition-metal impurities replacing Ga atoms in the  $\text{GaAs}_{1-x}\text{P}_x$  alloy. It has been shown that the deep transition-metal impurity levels in III-V compounds do not follow any of the host band-edges; instead, they are pinned to the vacuum level, due to their antibonding nature with respect to the impurity-host orbital bondings [14]. Contrary to previous suggestions [15], our results for vacancies in  $\text{GaAs}_{1-x}\text{P}_x$  reveal a host valence-band pinning of the deep vacancy-related levels.

In Figure 2 we present the trend in the donor ( $0/+$ ) and acceptor ( $-/0$ ) energy levels as a function of  $x$  in  $\text{GaAs}_{1-x}\text{P}_x$ . The calculated electronic levels shown, evaluated through the transition-state concept [10], do not include spin-polarization effects. We should mention, however, that all eigenvalues within the gap are lowered by less than 0.2 eV, for all cluster configurations, when spin-unrestricted calculations are performed. As can be seen in the figure, a similar trend for ( $-/0$ ) and ( $0/+$ ) levels along the alloy is observed. The difference in energy between the ( $-/0$ ) and ( $0/+$ ) levels, which accounts for the Mott-Hubbard potential energy  $U$ , is of the order of 0.05 eV. This is consistent with the expected multiple charge states character of the vacancy [16]. According to our results, at least three charge states ( $V^+$ ,  $V^0$ ,  $V^-$ ) are predicted for the Ga vacancy in  $\text{GaAs}_{1-x}\text{P}_x$ , which can occur stable depending on the position of the Fermi level. However, it is interesting to note that due to the valence-band pinning of the donor and acceptor transition energies, for a fixed Fermi level position the vacancy charge state is independent of the alloy composition  $x$ .

In summary, we have shown theoretically that the donor and acceptor energy levels induced by an ideal Ga vacancy in the  $\text{GaAs}_{1-x}\text{P}_x$  alloy are pinned to the host valence band edge. Therefore, these levels cannot be used to determine GaAs/GaAs<sub>x</sub>P<sub>x</sub> heterostructures band offsets, as has been the case of transition metal impurity levels [14].

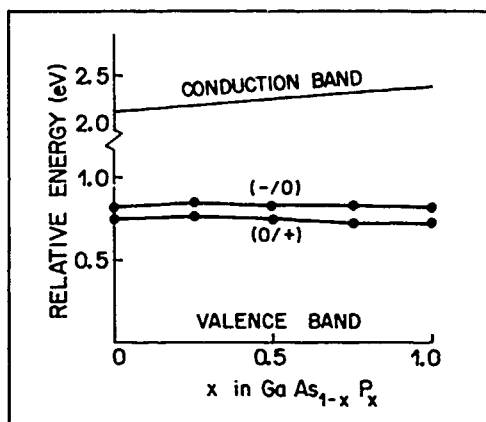


Figure 2. Calculated donor ( $0/+$ ) and acceptor ( $-/0$ ) energy levels for the Ga vacancy in  $\text{GaAs}_{1-x}\text{P}_x$  as a function of the alloy concentration  $x$ . Energies are related to the top of the valence band. The solid lines were drawn to guide the eyes.

### Acknowledgments

The authors thank the Brazilian Agency Conselho Nacional de Desenvolvimento Científico e Tecnológico (CNPq) for partial support.

### Bibliography

- [1] L. Samuelson, M. Gerling, X. Liu, S. Nilsson, P. Omling, M.-E. Pistol, and P. Silverberg, in *Proc 19th Int. Conf Phys Semic*, Vol. 2, W. Zawadzki, Ed. (Poland, 1988), p. 967.
- [2] S. Nilsson and L. Samuelson, in *Defects in Semiconductors*, Vols. 10-12 of *Materials Science Forum*, H. J. von Bardeleben, Ed. (Trans Tech. Switzerland, 1986), p. 615.
- [3] L. Samuelson, S. Nilsson, Z.-G. Wang, and H. G. Grmmeiss, *Phys. Rev. Lett* **53**, 1501 (1984).
- [4] M.-E. Pistol, S. Nilsson, and L. Samuelson, *Phys. Rev.* **B38**, 8293 (1988).
- [5] R. Pintanel, L. M. R. Scolfaro, and J. R. Leite, in *Defects in Semiconductors*, Vols. 83-87 of *Materials Science Forum*, G. Davies, G. G. DeLeo, and M. Stavola, Eds. (Trans Tech. Switzerland, 1992), p. 707.
- [6] A. Fazzio and J. R. Leite, *Phys. Rev.* **B21**, 4710 (1980).
- [7] A. Fazzio, L. M. Brescansin, and J. R. Leite, *J. Phys.* **C15**, L1 (1982).
- [8] L. M. R. Scolfaro, R. Pintanel, V. M. S. Gomes, J. R. Leite, and A. S. Chaves, *Phys. Rev.* **B15**, 7135 (1986).
- [9] L. M. R. Scolfaro, E. A. Meneses, C. A. C. Mendonça, J. R. Leite, and J. M. V. Martins, in *Defects in Semiconductors*, Vols. 65-66 of *Materials Science Forum*, G. Davies, Ed. (Trans Tech Switzerland, 1991), p. 369.
- [10] J. C. Slater, *The Self-Consistent Field for Molecules and Solids*, (McGraw-Hill, New York, 1974).
- [11] H. Xu and U. Lindefelt, *Phys. Rev.* **B41**, 5979 (1990).
- [12] G. B. Bachelet, G. A. Baraff, and M. Schlüter, *Phys. Rev.* **B24**, 915 (1981).
- [13] H. Xu, *J. Appl. Phys.* **68**, 4077 (1990).
- [14] M. J. Caldas, A. Fazzio, and A. Zunger, *Appl. Phys. Lett.* **45**, 671 (1984); A. Zunger, *Phys. Rev. Lett.* **54**, 849 (1985).
- [15] H. P. Hjalmarson, P. Vogl, D. J. Wolford, and J. D. Dow, *Phys. Rev. Lett.* **44**, 810 (1980).
- [16] See, for example, G. A. Baraff, E. O. Kane, and M. Schlüter, *Phys. Rev.* **21**, 5662 (1980).

Received March 15, 1993

# Electronic Stopping Power for Protons in an LiF Monolayer

J. Z. WU, S. B. TRICKEY, and J. R. SABIN

*Quantum Theory Project, University of Florida, Gainesville, Florida 32611*

## Abstract

In our previous work, the stopping properties of metallic and covalent films were investigated. Here we consider an ionically bound film. The energy loss of a proton in an LiF monolayer (LiF-1L) is calculated in orbital fashion, based on kinetic theory. The required momentum density and mean excitation energy are obtained from the local density approximation and local plasma approximation respectively. For comparison, the LiF molecule is treated by use of a large intermolecular distance in the film. We find the stopping cross section of the LiF molecule to be only slightly larger than that for the LiF-1L. The Bragg rule (additivity of stopping for the corresponding atoms) is not valid for the ionically bound molecule nor the corresponding extended system, but may be valid if additivity of stopping of atomic ions is assumed. © 1993 John Wiley & Sons, Inc.

## Introduction

While many stopping calculations have been performed in the last half century, so far as we know none has treated stopping in an ionically bound crystal or molecule, except by using Bragg's rule [1]. Mean excitation energies have been calculated from the local plasma approximation (LPA) [2], but the electron densities  $\rho(\vec{r})$  were estimated roughly from the  $\rho(\vec{r})$ s of corresponding atomic neutral states and ionic bond parameters. Some experimental stopping results for LiF are also known (that of Bader et al. [3] is rather old; Biersack et al. [4] measured 1–2 MeV alpha stopping powers in LiF; Kubo [5] measured the depths of regions damaged by a proton in an LiF crystal). In our previous work, the stopping properties for ultrathin metallic and covalent films were investigated [6,7]. Here we extend consideration to an ionically bound film. Since the alkali halides are the prototypes of ionically bound systems, and the calculated structural and electronic properties for the ground state of an LiF-1L are available [8], we considered the electronic stopping powers for a proton in an LiF monolayer and in isolated LiF molecules. Electron capture by the proton (charge state changes), and ionic dissociation of LiF were neglected. The section next describes the method which we used, with results and discussion in the section after next.

## Methodology

The linear energy loss of a swift, massive, charged particle in matter is known as

$$-\frac{1}{N} \frac{dE}{dx} = S(\vec{v}), \quad (1)$$

where  $N$  is the number density of scatterers (here the unit scatterer is an LiF ion pair),  $S$  is the stopping cross section per scatterer,  $\vec{v}$  is the velocity of the incident particle,  $E$  its energy, and  $x$  its path length. We use Hartree atomic units in Eq. (1) and throughout this paper. Because electrons in different energy levels have different stopping properties, the stopping cross section must be calculated in a state-dependent fashion (that is, via an energy-based decomposition [9]). Following Sabin and Oddershede, we employed Sigmund's kinetic theory of stopping [10] in the form

$$S(\vec{v}) = \frac{4\pi e^4 Z_1^2 Z_2}{mv^2} L(\vec{v}), \quad (2)$$

$$L(\vec{v}) = \sum_l L_l(\vec{v}), \quad (3)$$

$$L_l(\vec{v}) = \sum_{\vec{v}_{2z}} \int_{-\infty}^{\infty} dv_{2z} \frac{1}{\eta_l N_{\text{cell}}} \rho_l(\vec{v}_2) L_l^0(|\vec{v} - \vec{v}_2|) \frac{\vec{v} \cdot (\vec{v} - \vec{v}_2)}{|\vec{v} - \vec{v}_2|^3} v. \quad (4)$$

In Eqs. (2), (3), and (4),  $Z_1$  is the projectile charge,  $Z_2$  the number of electrons per molecule,  $\rho_l(\vec{v}_2)$  is the momentum density of the  $l$ th energy subband and  $1/(\eta_l N_{\text{cell}})$  is the normalization factor for  $\rho_l(\vec{v}_2)$ . We discuss the choices of subband below.

In Eq. (4)  $L_l^0$  is of Bethe form with a low energy cutoff

$$L_l^0(v) = \frac{\eta_l}{nZ_2} \ln\left(\frac{2mv^2}{I_l}\right) \theta\left(v^2 - \frac{I_l}{2m}\right), \quad (5)$$

where  $n$  is the number of molecules per unit cell. The orbital mean excitation energy  $I_l$  is determined solely from the orbital charge density through the orbital local plasma approximation (OLPA)

$$\ln I_l = \frac{1}{\eta_l} \int_{-\infty}^{\infty} dz \int_A d\sigma \rho_l(\vec{r}) \ln \left[ \chi \hbar \left( \frac{4\pi e^2 \rho(\vec{r})}{m} \right)^{1/2} \right]. \quad (6)$$

For simplicity and clarity the scaling parameter  $\chi$  was chosen to be unity throughout.

The required momentum density is constructed from the Fourier transform of the Kohn-Sham (KS) eigenfunctions in real space:

$$\rho_l(\vec{p}) = \sum_{\vec{k} \in BZ}^{\text{occ}} n_{l,\vec{k}} |\psi_{l,\vec{k}}(\vec{p})|^2, \quad (7)$$

$$\Psi_{l,\vec{k}}(\vec{p}) = \frac{1}{[2\pi N_{\text{cell}} A]^{1/2}} \int_{-\infty}^{\infty} dz \int_{NA} d\sigma e^{i\vec{p} \cdot \vec{r}} \psi_{l,\vec{k}}(\vec{r}).$$

The Lam-Platzman correction [11] was omitted. The KS functions were obtained in the local density approximation (LDA) utilizing the Hedin-Lundqvist (HL) model. The atomic calculations used the same OLPA and LDA but were spin-polarized in the central field approximation.

The electronic structure calculations used the code FILMS [12,13]. In it the KS functions are expanded in a linear combination of Gaussian-type orbitals, the "KS"

basis [14]. The charge density and exchange-correlation energy density are expanded in two auxiliary Gaussian bases sets, the "Q" and "XC" fitting bases. The various basis sets are tabulated in Ref. [8].

The lattice structure utilized corresponds to the (100) plane of the NaCl structure. The irreducible triangle is  $1/8$  of the Brillouin zone (BZ); ten  $\vec{k}$  points in that irreducible triangle were used [8].

The energy subbands were chosen as follows: Atomic stopping was used for the 1s bands (in tests, the discrepancy between atomic and 1L stopping for this band is in the second decimal place of the stopping cross section at its maximum). The three energy bands of 2p-like character are all in a similar energy range, and hence were grouped as one energy subband. This grouping was tested by dividing the energy range of those three energy bands into three windows ( $E_{l-1}$  to  $E_l$ ) according to

$$E_l = E_{\min}^{2p} + l[(E_{\max}^{2p} - E_{\min}^{2p})/3], \quad l = 1, 2, 3, \quad (8)$$

and then calculating the stopping cross section at one velocity (near the maximum position of the stopping cross section). Again the discrepancy between the two calculations is only in the second decimal place in the stopping cross section at that  $v$ .

In the momentum integral [Eq. (4)], the domain can be reduced to an irreducible region in momentum space by use of symmetry properties. Since the KS functions are only available within the irreducible part of the BZ, one must rotate the wave vector into the irreducible part and make the corresponding rotation for the corresponding momentum based on the symmetry properties to evaluate the momentum density. A useful result (for computational speed) is that  $\psi_{i,\vec{k}}(\vec{p})$  is a nonvanishing function if and only if  $\vec{p} = \vec{K}_m - \vec{k}$ , where  $\{\vec{K}_m\}$  are reciprocal lattice vectors.

To treat the isolated molecule, we used FILMS but with a large distance (15.0 a.u.) between the molecules in a square lattice. The molecular orientation was along the edge of the square. We refer to this calculation as the LiF "quasimolecule."

## Results

For convenience, the relevant basis set parameters, total energies, structural parameters, energy subbands, mean excitation energies, and stopping cross sections for the LiF-1L, the LiF quasimolecule, the Li atom, and the F atom are all shown in Table I. The structural properties and energy bands reported here are from Ref. [8].

Figure 1 shows the stopping cross section as a function of proton velocity. An interesting qualitative feature is that the stopping cross section for the LiF-1L is very close to that of the LiF molecule. The molecular cross section is only slightly bigger, about 3% at most. This is very different from the behavior of both metallic and covalent systems. However, it is unsurprising since the total energy of the molecule is close to the total energy per formula unit of the 1L and the valence band for the 1L is rather flat. These features all reflect the fact that most of the cohesive energy with respect to isolated atoms is in the molecular ionic bonding.



TABLE I Comparison of the phase difference in proton stopping by the targets of LiF-1L, LiF molecule, and Li atom+ F atom.\*

	Li atom + F atom		LiF	LiF monolayer
	F atom	Li atom	quasimolecule; molecule along $x$ direction	
KS bases	13s8p	13s	13s8p1pz for F 13s4p for Li	13s8p1pz for F 12s4p for Li
Q and XC bases			13s7d3p <sub>x</sub> for F 12s4d2p <sub>x</sub> for Li	13s7d for F 11s4d for Li
Distance between Li and F (a.u.)	Infinity		2.80	3.50
$E_{\text{tot}}$ (H)	-106.47322		-106.71320	-106.81508
F-like 1s band				
Energy range (H)	-24.19804 -24.16738 <sup>b</sup>		-23.92276	From -24.00958 to -24.00958
$I$ (eV)	483.498		483.682	483.651
$S$ at $v = 2.25$ a.u.	0.160		0.160	0.160
Li-like 1s band				
Energy range (H)		-1.87535 -1.86729 <sup>b</sup>	-1.81928	From -1.75448 to -1.75041
$I$ (eV)		71.424	72.493	72.580
$S$ at $v = 2.25$ a.u.		2.745	2.745	2.778 (film) 2.745 (atom)
2s band				
Energy range (H)	-1.11586 -1.05527 <sup>b</sup>	-0.12463 -0.04807 <sup>b</sup>	-0.89822	From -0.99472 to -0.97130
$I$ (eV)	62.550	3.420	62.943	62.465
$S$ at $v = 2.25$ a.u.	3.991	8.072	4.054	4.108
2p band				
Energy range (H)	-0.44410 -0.38525 <sup>b</sup>		From -0.25208 to -0.22604	From -0.38650 to -0.28574
$I$ (eV)	54.363		48.184	50.688
$S$ at $v = 2.25$ a.u.	8.034		11.314	10.923
$I^{\text{total}}$	91.148	25.935	79.308	81.134
$S^{\text{tot}}$ at $v = 2.25$ a.u.		23.002	18.273	17.969
$S_{\text{max}}$		40.489	18.290	17.962
$v$ at $S_{\text{max}}$		0.61	2.32	2.33

\* The unit of  $S$  is  $10^{-15}$  eV cm<sup>2</sup>/molecule.<sup>b</sup> Two energy levels are for two spins.

This dramatic influence of binding upon stopping also is illustrated in Figures 1 and 2. There we have applied the Bragg rule for a compound, say AB, to wit

$$S_{AB}(v) \approx S_A(v) + S_B(v), \quad (9)$$

with A and B chosen as the Li and F atoms, respectively. The Bragg rule stopping drastically overestimates both the 1L and isolated molecule stopping, as shown in

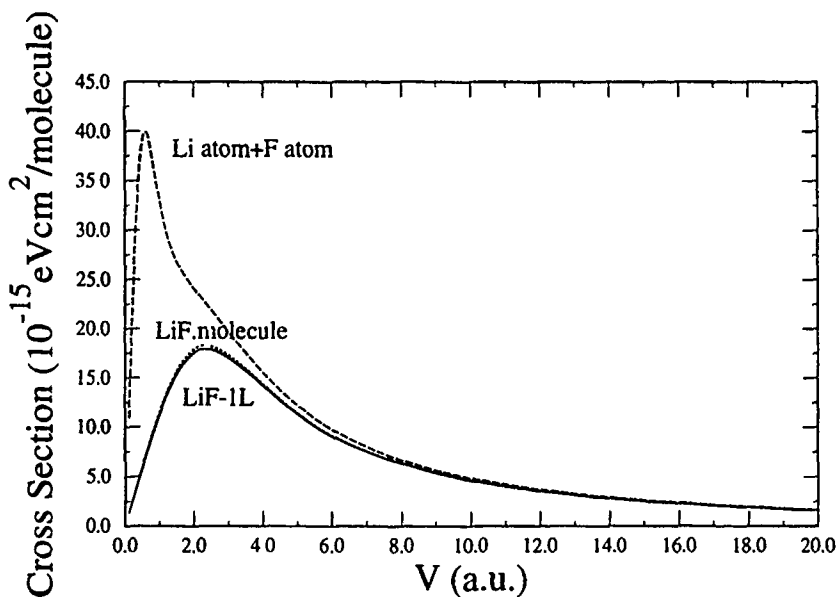


Figure 1. The comparison for the stopping cross sections for the LiF-1L, LiF quasimolecule, and Bragg rule (Li atom + F atom).

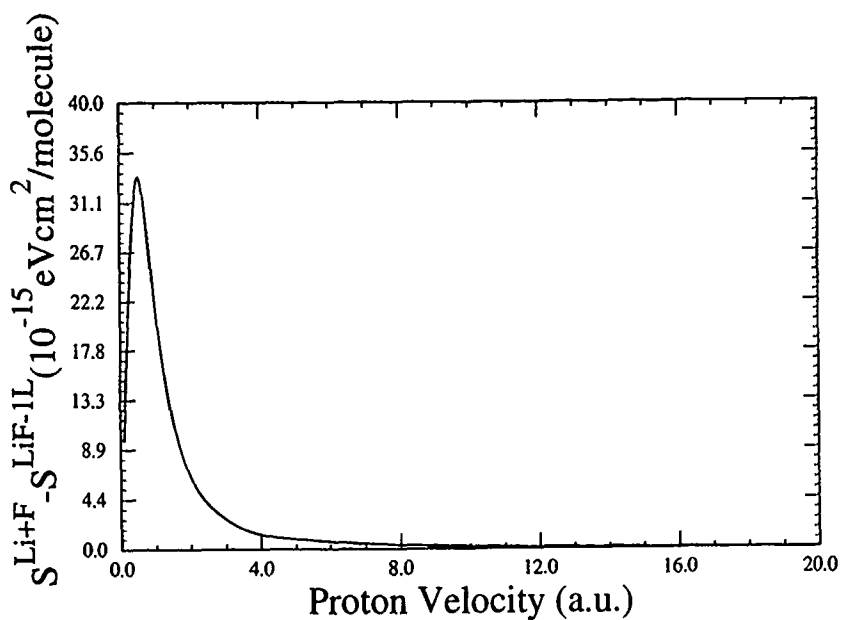


Figure 2. Isolated atom/monolayer difference of the stopping cross section for LiF.

Figure 2. which displays the difference. Since the latter two are close, it is clearly molecular binding effects (missing from the Bragg rule) which are the cause of the large suppression of stopping.

Application of Bragg's rule with A and B as ionic species is another matter. Experimental results [4] for the stopping power for boron-doped LiF, in thin evaporated layers, are found to agree with Andersen and Ziegler's [15] predictions within a few percentage points, if the validity of Bragg's rule for ions is assumed. We could not perform a similar test using addition of isolated constituent ions because of a well-known problem in LDA. As a consequence of improper self-interaction cancellation, LDA does not yield a properly bound negative ion without introduction of some arbitrary confining potential. However, since the LiF-1L has a very localized charge distribution which is quite similar to that for the LiF molecule, it is reasonable to predict that Bragg rule additivity based upon the corresponding ions will be valid for both ionically bound films and molecules, consistent with the experimental results just mentioned.

Further insight may be obtained by comparison of the 2s and 2p stopping for the F and Li atoms with that of the LiF-1L as shown in Figure 3. The figure makes apparent how much the 2s and 2p orbitals of LiF are dominated by F contributions. The 2s-like stopping for the LiF-1L is almost the same as that of the F atom. The 2p-like stopping in the 1L has the same behavior but is bigger than that for the F atom, a consequence of charge transfer, (there are six electrons involved for the 1L whereas there are five for the isolated F atom).

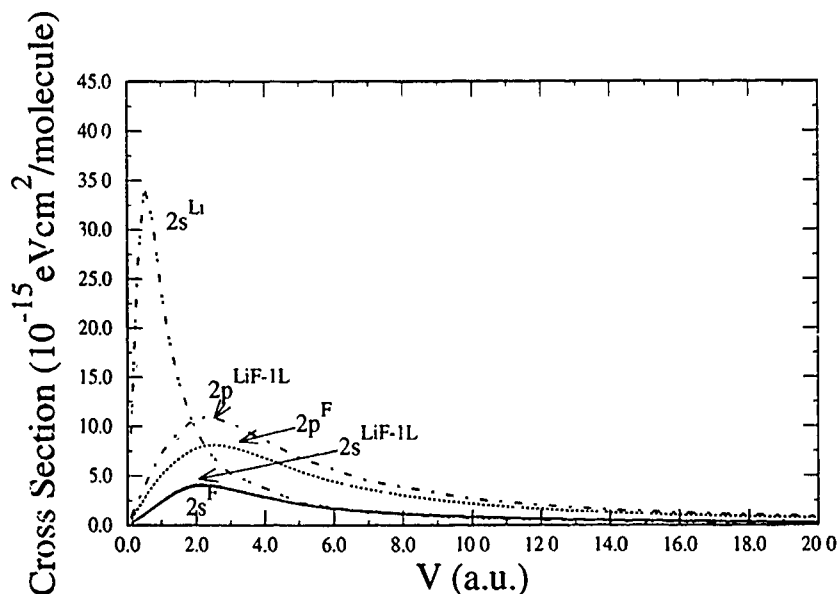


Figure 3. Comparison of the 2s stopping and 2p stopping for the atom F, atom Li, and LiF-1L.

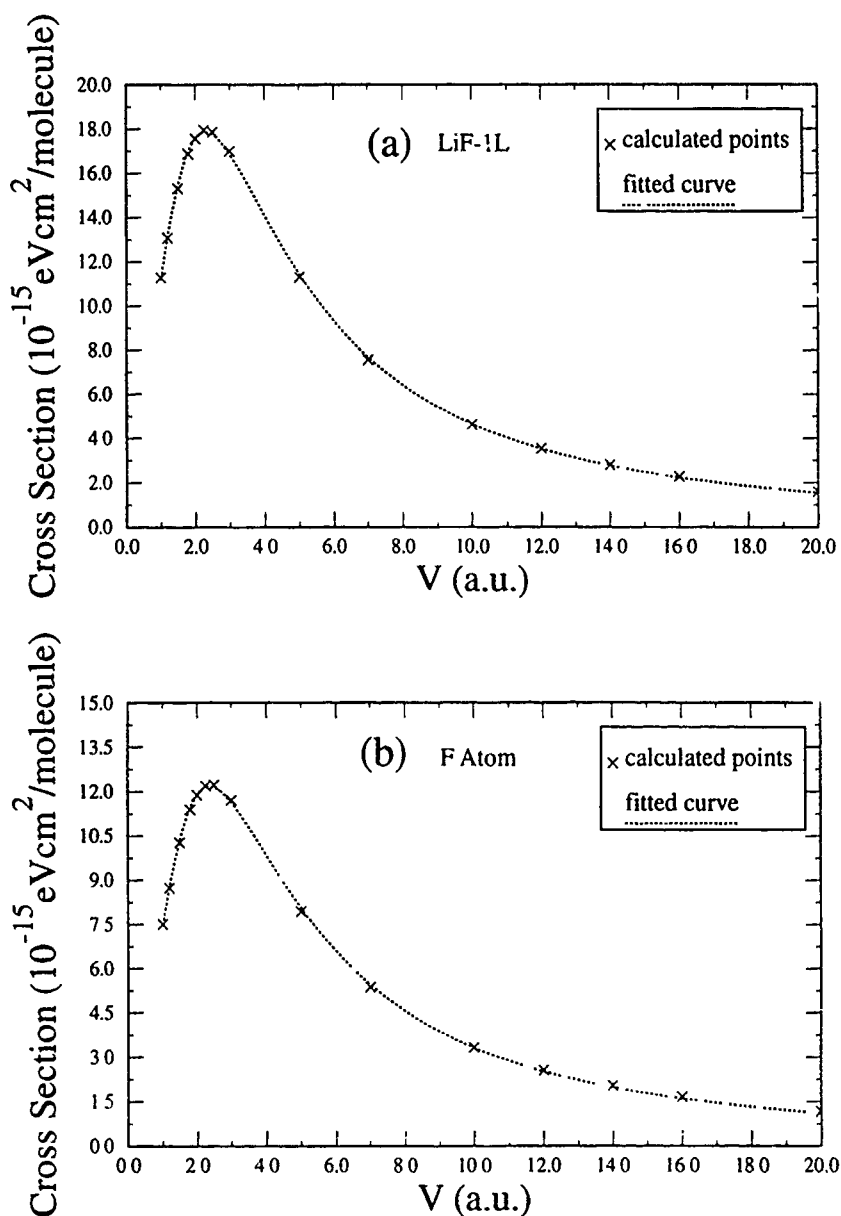


Figure 4. Calculated and fitted stopping curves: (a) LiF-1L; (b) F atom.

TABLE II. Analytic fitting parameters and standard deviations for LiF-1L, F atom, and Li-atom 2s orbital.

	Range (a.u.)	$a_1$	$a_2$	$a_3$	$a_4$	Standard deviation
LiF-1L	1.0-20.0	0.617	6.490	97.317	76.429	0.09
F atom	1.0-20.0	0.622	7.103	69.998	57.256	0.06
Li atom 2s	0.35-20.0	0.0579	0.168	9.735	0.00283	0.28

As another means of tabulating stopping and to provide an efficient summary of our calculated points, we consider analytic fitting. As shown in Figure 4, a simple four-parameter fit modeled on the Bethe logarithm works quite well. The fit is so good for the Li 2s atomic stopping that the original and fitted curves are essentially indistinguishable. The general form is

$$S(v) = \left( \frac{1}{v^2 + a_2} \right) \left( a_3 + \frac{a_4}{v^6} \right) \left( \ln \frac{v^2}{a_1} \right). \quad (10)$$

When fit over the range  $1.0 \text{ a.u.} \leq v \leq 20.0 \text{ a.u.}$  (or  $0.35 \text{ a.u.} \leq v \leq 20.0 \text{ a.u.}$  for the Li 2s atomic stopping). We get the parameters and standard deviations tabulated in Table II.

### Acknowledgments

This work was supported in part by the U.S. Army Research Office under contract DAA L03-91-G-0119.

### Bibliography

- [1] G. N. Potetyunko, *Sov. At. Energy* **52**, 137 (1980).
- [2] J. W. Wilson, C. K. Chang, Y. J. Xu, and E. Kamaratos, *J. Appl. Phys.* **53**(2), 828 (1982).
- [3] M. Bader, R. E. Pixley, F. S. Mozer, and W. Whaling, *Phys. Rev.* **103**, 32 (1956).
- [4] J. P. Biersack, D. Fink, W. Miekeley, and K. Tjan, *Nucl. Instrum. Meth.* **B15**, 96 (1986).
- [5] K. Kubo, *J. Phys. Soc. Jpn.* **36**, 1593 (1974).
- [6] J. Z. Wu, S. B. Trickey, J. R. Sabin, and D. E. Meltzer, *Nucl. Instrum. Meth.* **B56**, 340 (1991).
- [7] J. Z. Wu, S. B. Trickey, and J. R. Sabin, *Nucl. Instrum. Meth. B* (1993), to appear
- [8] J. Z. Wu, S. B. Trickey, J. R. Sabin, and J. C. Boettger, unpublished.
- [9] J. Oddershede and J. R. Sabin, *Phys. Rev. A* **26**, 3209 (1982).
- [10] P. Sigmund, *Phys. Rev. A* **26**, 2497 (1982).
- [11] L. Lam and P. M. Platzman, *Phys. Rev. B* **9**, 5122 (1974).
- [12] J. C. Boettger and S. B. Trickey, *J. Phys.: Condensed Matter* **1**, 4323 (1989).
- [13] J. C. Boettger and S. B. Trickey, *J. Phys. F: Met. Phys.* **16**, 693 (1986).
- [14] J. W. Mintmire, J. R. Sabin, and S. B. Trickey, *Phys. Rev. B* **26**, 1743 (1982).
- [15] H. H. Andersen and J. F. Ziegler, *The Stopping Power and Ranges of Ions in Matter* (Pergamon, New York, 1977), Vol. 3, p. 4.

Received April 16, 1993

# Some Density-Functional LMTO Studies of Electronic Properties of Quasi-One-Dimensional Systems

MICHAEL SPRINGBORG

*Fakultät für Chemie, Universität Konstanz, D-W-7750 Konstanz, Federal Republic of Germany*

## Abstract

Results of first-principles, density-functional, LMTO calculations on quasi-one-dimensional systems are presented. Special emphasis is put on the problems related with studying the properties of real materials by means of electronic structure calculations. As examples we discuss undoped and doped *trans* polyacetylene, an MX chain compound, CaNiN, and a comparison between polycarbonitrile and hydrogen cyanide. It is argued that single-chain calculations on undoped polyacetylene predict a bond-length alternation, whereas this may be suppressed in multichain calculations. For an MX chain we demonstrate the importance of including the full ligand structure, whereas many properties of CaNiN can be understood as intrinsic to single chains. A comparison between the covalently bonded polycarbonitrile and the hydrogen-bonded hydrogen cyanide reveals differences between delocalized and localized electrons but also inaccuracies in the relative total energies. Finally, results for doped *trans* polyacetylene indicate relatively large electronic dopant-polymer hopping integrals as well as problems in describing electron transfers for weakly interacting systems when using a local-density approximation. In total it is demonstrated that reliable and useful informations are obtained in most cases, but also that one has to be careful in choosing the idealized system that is to represent the real material and that certain aspects of the local-density approximation should be improved. © 1993 John Wiley & Sons, Inc.

## Introduction

One of the goals of materials science is to understand the physical and chemical properties of materials with the purpose of being able to predict the properties of new materials and to select materials with predefined properties. This requires development of general models that describe the properties and/or materials of interest. These models may be derived by analyzing experimental or theoretical results for a number of specific materials. However, the interpretation of the experimental outcomes may not be simple or obscured by unwanted effects like those of inhomogeneities, impurities, surfaces, etc. Similarly, detailed theoretical studies of realistic materials are often beyond the limits of any computer facility, and one has to study idealized systems that may or may not be related to the real systems.

We shall here report results of theoretical studies of the electronic properties of quasi-one-dimensional materials. We shall concentrate on general problems related to theoretical studies of materials properties by discussing some few typical examples. The focus is not on the chosen examples but on the general problems. The materials of our interest are characterized by being extended in at least one dimension and having interatomic interactions that typically are substantially stronger in this di-

reaction than in the other two. We have previously developed a first-principles method for quasi-one-dimensional, periodic, infinite systems [1]. This method will be briefly reviewed in the next section. There we also discuss a procedure for studying the properties of the material when the periodicity is disrupted. The third through seventh sections contain various examples of applications. In the third section the well-known and thoroughly studied conjugated polymer *trans* polyacetylene is discussed. We shall here concentrate on whether the material can be idealized as one- or three-dimensional and on problems associated with estimating the size of correlation effects. The fourth section is devoted to a so-called mixed-valence halogen-bridged transition-metal linear chain compound which has features resembling those of polyacetylene. This is chosen as an example of the systems for which omitting apparently less important aspects may lead to significant effects. In the fifth section we discuss another metal-containing material CaNiN. A comparison between a hydrogen-bonded polymer (hydrogen cyanide) and a conjugated polymer (polycarbonitrile) is the topic of the sixth section, and the seventh section is devoted to doped polyacetylene. These two systems exemplify problems of the local-density approximation but it is also demonstrated that useful information can be obtained despite these problems. A conclusion is presented in the last section.

## Computational Method

### Periodic Chains

Using the Born-Oppenheimer approximation and the Hohenberg-Kohn [2] density functional formalism, we calculate the ground-state properties of the system of our interest by solving the Kohn-Sham equations [3]

$$\left[ -\frac{\hbar^2}{2m} \nabla^2 + V_{\text{eff}}(\vec{r}) \right] \psi_i(\vec{r}) = \epsilon_i \cdot \psi_i(\vec{r}). \quad (1)$$

The exchange-correlation parts of the effective potential  $V'_{\text{eff}}$  are approximated using a local approximation. Thereby the potential  $V_{\text{eff}}$  becomes a well-defined functional of the total electron density which in turn is the sum of the single-particle densities,

$$\rho(\vec{r}) = \sum_{i=1}^{\text{occ}} |\psi_i(\vec{r})|^2. \quad (2)$$

Equations (1) and (2) are solved by expanding the eigenfunctions  $\psi_i(\vec{r})$  in a basis consisting of linearized muffin-tin orbitals (LMTOs) defined as follows. The nuclei are assumed occupying the centers of nonoverlapping (muffin-tin) spheres. An LMTO centered at the nucleus at  $\vec{R}$  is outside all spheres defined as a Hankel function times a harmonic,  $i\kappa^{l+1}[(2l-1)!!]^{-1}h_l^{(1)}(\kappa|\vec{r}-\vec{R}|)Y_L(\widehat{r-\vec{R}})$  with  $L \equiv (l, m)$  and  $\kappa^2 < 0$ . Inside any sphere this function is augmented with linear combinations of the so-called  $\phi$  and  $\dot{\phi}$  functions such that the resulting function becomes continuous and differentiable everywhere. The functions  $\phi$  of a specific

site are obtained by replacing  $V_{\text{eff}}$  of Eq. (1) with its spherically symmetric component. In that case Eq. (1) can be transformed into a one-dimensional differential equation that can be solved numerically when choosing  $\epsilon = \epsilon_v$ , "reasonable" (i.e., in the energy region for which that particular function has its largest components).  $\dot{\phi}$  is the derivative of  $\phi$  with respect to the energy  $\epsilon_v$ .  $\phi$  and  $\dot{\phi}$  are specific for the atom at  $\vec{R}$  and the angular quantum number  $l$  and depends parametrically on  $\epsilon_v$ . For more details the reader is referred to Refs. [1,4-8].

Since the LMTOs are unfamiliar to many and only rarely depicted, we show in Figure 1 the LMTO  $s$  and  $p_z$  basis functions for a CO molecule placed along the  $z$ -axis. Especially the augmentation inside "other" spheres makes the LMTO basis set different from many basis sets. Thereby the well-known basis-set superposition error is essentially lacking. In this figure we also show the potential and its spherically symmetric part inside the spheres. Since the deviations from spherical symmetry is only small, we expect the LMTOs per construction to be good approximations to the true eigenfunctions of the Kohn-Sham equations inside the spheres.

Before proceeding it may be worthwhile discussing advantages and disadvantages of the present approach. This discussion may be separated into two parts: the use of the density functional formalism and the choice of the LMTOs as basis functions.

The density-functional formalism is in principle exact, but, due to the local approximation, one introduces right from the beginning an approximation that may or may not be good. On the other hand, the single-particle form of Eq. (1) allows for larger systems a much more accurate solution than the exact many-particle Schrödinger equation does.

By choosing LMTOs as basis functions these are to a large extent potential-adapted such that the basis set may be kept at a limited size without loss of accuracy. Using Gaussians or plane waves instead of LMTOs would correspond to approximating the potential by harmonic potentials or constants, respectively, which clearly is a worse approximation than the potential used in constructing the LMTOs. On the other hand, since we are including the full potential (and not only its muffin-tin parts) the calculations become more evolved, partly due to the separation of space into two parts, for which, furthermore, all quantities are given analytically inside one part (the interstitial region) and numerically inside the other part (the muffin-tin spheres).

Finally, for a quasi-one-dimensional system that is assumed being infinite and periodic in one dimension, we form Bloch waves from the atom-centered basis functions. This procedure can with advantage be applied also for polymers with a general helical symmetry (see, e.g., Refs. [1,5,8]).

### *Structural Defects*

Structural defects may have crucial impacts on transport properties (e.g., charge and proton conductivities) of the materials, and it would therefore be highly desirable to include these in the first-principles description of the systems. However, they destroy the periodicity, and one would have to study systems of finite size, to consider periodically repeated defects, or to use a Greens function technique. As a simpler



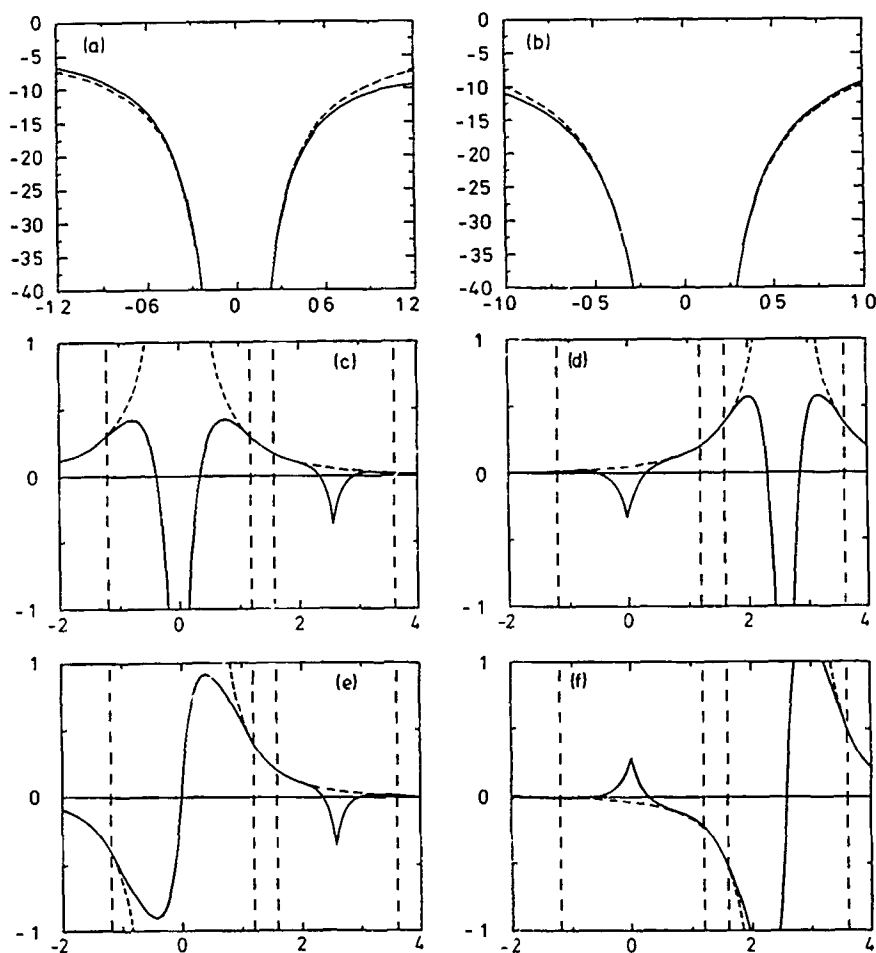


Figure 1. (a,b) Potentials and (c-f) basis functions for a CO molecule. The C atom is placed at the origin and the O atom at (0,0,2.3) a.u. All quantities are depicted along the molecular axis and in a.u. In (a,b) we show the full potential (the solid curve) and its spherically symmetric part (the dashed curve) inside (a) the carbon and (b) the oxygen muffin-tin sphere. (c,d) and (e,f) show  $s$  and  $p_z$ , respectively, basis functions centered on (c,e) the carbon atom and (d,f) the oxygen atom. Here, the vertical dashed lines mark the borders of the muffin-tin spheres, the full curves are the basis functions, and the dashed curves the Hankel functions

alternative, we have decided to use model calculations in the study of the structural defects, for which the models are based on results of first-principles calculations on defect-free systems.

In Figure 2, we show a chain consisting of a number of almost identical units. These units may have internal structure and will in most cases consist of a smaller number of atoms. The internal structure is in that case related to the relative position

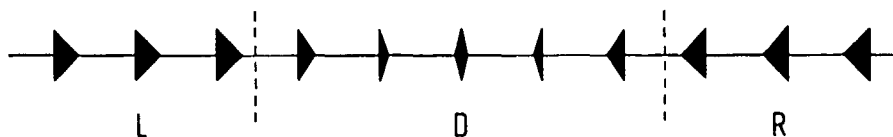


Figure 2. Schematic representation of an infinite chain consisting of repeated units with internal structure. The regions *R* and *L* are each regular, whereas *D* corresponds to a domain wall (a defect region).

of the atoms. In order to describe the structure of the chain, we will ascribe a single structural parameter  $x_n$  to the  $n$ th unit. It is thereby assumed that all other structural parameters of the  $n$ th unit are relaxed upon variation of  $x_n$  and are irrelevant in describing the defect-containing system.

The central region in Figure 2 (denoted "D") separates two parts ("R" and "L") where the chain is regular. Thus,  $x_n$  is a constant in each of the regular parts and varies from one value to the other inside the D region. If the R and L regions are different but energetically degenerate, the D region is a domain wall that can easily move up and down the chain. D is in that case often denoted a soliton. If the R and L regions are identical, D is a polaron, and also this is highly mobile. The importance of the defects stems from the fact that they may be the carriers of charge, energy, protons, etc. For certain systems they occur, moreover, in the ground-state configuration of the charged system.

In all cases  $x_n$  varies inside the D region smoothly between two values  $x_l$  and  $x_u$ . In order to study the system of Figure 2, we perform first-principles calculations on periodic chains, i.e.,  $x_n = x_0 = \text{const}$ ,  $x_l \leq x_0 \leq x_u$ . The results of these are subsequently mapped onto a suitable model Hamiltonian with which we finally study the defect-containing system. Since doping or low-energy photoexcitation leads to changes only in the occupation of the frontier orbitals, the model Hamiltonian will typically contain a tight-binding part for their description plus a simple function of the structural parameters describing the remaining part of the total energy. The on-site energies and hopping integrals of the first part will depend on the local environment as given by  $\{x_n\}$ . A typical example is *trans* polyacetylene to be discussed in the next section. It should be stressed that the success of this approach depends on a number of assumptions including that, for a given  $x_n$ , all other structural parameters are relaxed in the same way independent of whether the  $n$ th unit is a part of a periodic chain or of a defect-containing chain, and that effects specific for the defects (e.g., long-range Coulomb effects or effects due to an increased localization of electrons) can largely be ignored. This is discussed in detail in Ref. [9].

### *Trans* Polyacetylene

*Trans* polyacetylene (Fig. 3) is the prototype of the conjugated polymers/synthetic metals that exhibit large changes in their properties upon doping or photoexcitation (see, e.g., Ref. [10]). There is accordingly a vast literature dealing with this material.

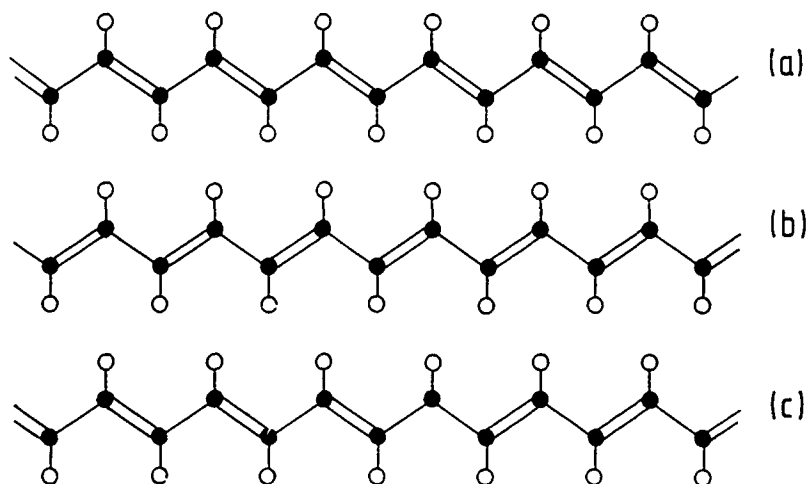


Figure 3. *Trans* polyacetylene. (a) and (b) show the regular, energetically degenerate phases. (c) a soliton. The black and white circles represent carbon and hydrogen atoms, respectively.

From a theoretical point of view it is an ideal compound since its unit cell—when considering only one isolated infinite chain—contains only four atoms,  $C_2H_2$ .

The doping or photoexcitation is supposed to lead to the creation of solitons [Fig. 3(c)] which are the domain walls in the language of Figure 2. The two regular chains (R and L in Fig. 2) differ only in the way the C—C double and single bonds alternate, and each unit in Figure 2 consists of one CH unit.

The experimentally studied material is far from homogeneous. It contains longer and shorter chains that are arranged partly parallel and partly at random. On the other hand, in the parameter-free studies idealizations are investigated. These are either infinite, isolated, periodic chains; infinite, periodic, three-dimensional crystals; or isolated, finite molecules. This may be one reason for the scattered agreement between theory and experiment regarding the C—C bond-length alternation. Whereas experiment finds a clear alternation (bond lengths alternating equal to 2.57 and 2.72–2.73 a.u. [11,12]), the theoretical results range from good agreement with this to a vanishing bond-length alternation (see, e.g., Ref. [6] and references therein). In our own study [6] on an isolated, infinite chain we found bond lengths equal to 2.58 and 2.76 a.u. which are seen to agree well with experiment. Moreover, it turns out that the (almost) vanishing bond-length alternation mainly has been found with local-density calculations on three-dimensional crystals. Since the local-density approximation tends to overestimate the strength of chemical bonds [13], one may speculate that also the interchain interactions are overestimated, which in turn may lead to smaller inaccuracies in the intrachain interactions. This might ultimately lead to the (almost) lacking bond-length alternation. On the other hand, all density-functional calculations on single, finite or infinite chains have predicted a bond-length alternation.

In Figure 4 we show our calculated [6] total energy as a function of C—C bond-length alternation for a single chain with the unit-cell length kept fixed at the value of the optimized structure. We see here that the energy gain upon bond-length alternation indeed is small and thus that it may be strongly modified upon smaller changes in the assumptions. Therefore, the results may depend crucially on whether one studies an isolated chain or one embedded in a multichain environment.

We next turn to the discussion of the solitons and apply the procedure outlined in the previous section. We accordingly map results of first-principles calculations on periodic chains with different C—C bond-length alternations onto a suitable model Hamiltonian. To this end, it is useful to follow the ideas of Su et al. [14–16]. They realized that the orbitals split into energetically low-lying  $\sigma$  orbitals formed by carbon  $sp^2$  hybrids and hydrogen  $s$  functions as well as  $\pi$  orbitals generated by carbon  $p$  functions around the Fermi level. This separation is recovered in Figure 5, where we show our calculated band structures of *trans* polyacetylene [6].

Su et al. included a tight-binding description of the  $\pi$  orbitals (the frontier orbitals) whereas the remainder of the total Hamiltonian was written as a harmonic function of nearest-neighbor bond lengths. This corresponds for the periodic, neutral chain to separating the total energy as done in Figure 4. Applying this model on a doped chain (i.e., a chain with more or fewer electrons), Su et al. found that chains containing one soliton per charge were the stabler ones in the dilute doping limit. The solitons lead according to their model to gap states exactly at midgap. However, according to experiments the gap states are found somewhat off (about 0.2 eV) the

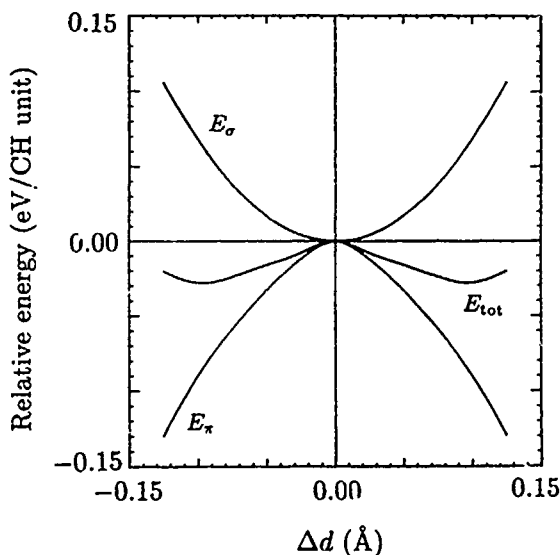


Figure 4. Total energy, the  $\pi$  electron energy (defined as the sum of the single-particle energies of the occupied  $\pi$  orbitals), and the remainder (the  $\sigma$  energy) in eV/ $C_2H_2$  unit as functions of C—C bond-length alternation  $\Delta d$  (defined as the difference in the lengths of the two nearest-neighbor C—C bonds).

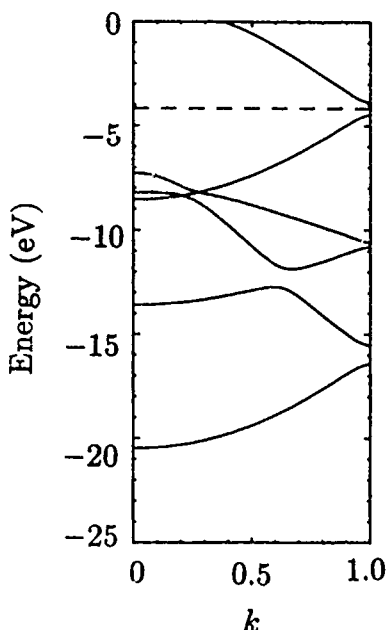


Figure 5 The band structures of the optimized *trans* polyacetylene chain. The dashed line marks the Fermi level, and  $k = 0$  and  $k = 1$  is the zone center and zone edge, respectively.

midgap position [17–19]. The origin of this discrepancy is far from clear. It has been argued that correlation effects are the reason [20], but also single-particle effects may explain at least parts of the difference [6]. The first-principles calculations can be used in refining the model and its parameters. Thereby, we showed [6] that one may extend the simplest model of Su et al. with some realistic single-particle effects that ultimately lead to a shift of the gap states. The thereby obtained shift was, however, only half as large (about 0.1 eV) as that observed by experiments.

### An MX Chain

Another class of materials that recently has attracted considerable attention (see, e.g., Ref. [10]) is the so-called mixed-valence transition-metal halogen-bridged linear-chain MX compounds. As a prototype of those we shall here focus on  $\text{Pt}_2\text{Br}_6(\text{NH}_3)_4$ . This material consists of linear parallel chains with alternating Pt and Br atoms along the chain axis. To each Pt atom are two further Br atoms and two  $\text{NH}_3$  molecules attached as sideligands.

According to experiments the Br atoms of the chain backbone are placed pairwise closer to every second Pt atom resulting in an alternating valence of the Pt atoms. We may now relate the structure to that of Figure 2 with every unit being one  $\text{Pt}_2\text{Br}_6(\text{NH}_3)_4$  unit. The occurrence of two energetically degenerate structures—differing in the valence alternation—leads hence to the possibility of the existence of solitons, as originally proposed by Baeriswyl and Bishop [21].

The present interest in this class of materials stems from the possibility of tuning the properties by using different types of metal atoms (e.g., Pd, Ni, Pt) and/or halogen atoms (e.g., Cl, I, Br) (see, e.g., Refs. [10,22,23]). Also by varying the sideligands or applying pressure the properties can be changed.

We have studied the  $\text{Pt}_2\text{Br}_6(\text{NH}_3)_4$  compound using both single-chain calculations (with the method of the second section) and full-potential LMTO calculations on a three-dimensional material [24]. Model calculations as described in the second section have not yet been carried through, but it was shown [24] that the parameters extracted from the first-principles calculations agree well with those usually assumed realistic for these materials.

According to the simplest picture, one would expect the frontier orbitals to be generated by Pt  $d_{z^2}$  and Br  $p_z$  orbitals, where the  $z$ -axis is assumed parallel to the chain axis. The alternation in valence is then ascribed to a Peierls distortion which doubles the unit cell. This picture is only partly verified by calculations on PtBr chains for which all sideligands have been neglected. Both according to the single-chain calculations and according to the crystal calculations, the optimized Pt-Br distance was roughly 13% too small compared with experiments [25] (i.e., 9.14 a.u. vs. 10.49 a.u.). Moreover, several bands were found to cross the Fermi level, and there was no sign of a dimerization.

One might expect that these results were obscured by the exclusion of the Br sideligands. Since Br is an electronegative, open-shell atom, these atoms may remove orbitals of the PtBr chain from the region around the Fermi level. Although this was confirmed by the calculations, the lowest total energy was still found for an undimerized structure. Only by including also the  $\text{NH}_3$  sideligands was the experimentally observed dimerization found, as shown in Figure 6. Moreover, only then we found Pt  $d_{z^2}$  and Br  $p_z$  orbitals as the only frontier orbitals. Although  $\text{NH}_3$  is a closed-shell molecule, it is polarized, and one may understand the result as due to interactions between nitrogen lone pairs and Pt orbitals.

### CaNiN

CaNiN [Fig. 7(a)] was synthesized some few years ago [26] and is interesting since it combines one-, two-, and three-dimensional features. Thus, it consists of two-dimensional layers of one-dimensional NiN chains separated by layers of Ca atoms such that the whole system becomes three-dimensional [Fig. 7(a)]. The question we here shall address is whether the basic features can be understood "within a one-dimensional picture." If so, the material would be interesting as a polymer based to a large extent on transition metals.

We first performed single-chain calculations on an isolated NiN chain [27]. This gave an optimized NiN bond length equal to 3.28 a.u., which is somewhat smaller than the experimental value of 3.38 a.u. [26]. Including one Ca atom per NiN unit as shown in Figure 7(b) led to an optimized Ni-N bond length of 3.50 a.u., i.e., larger than given by experiment. According to Mulliken gross populations, 0.4 electrons have been transferred from Ca to NiN, but due to the presence of the Ca atoms the electrons of the NiN chains have to some extent been redistributed and

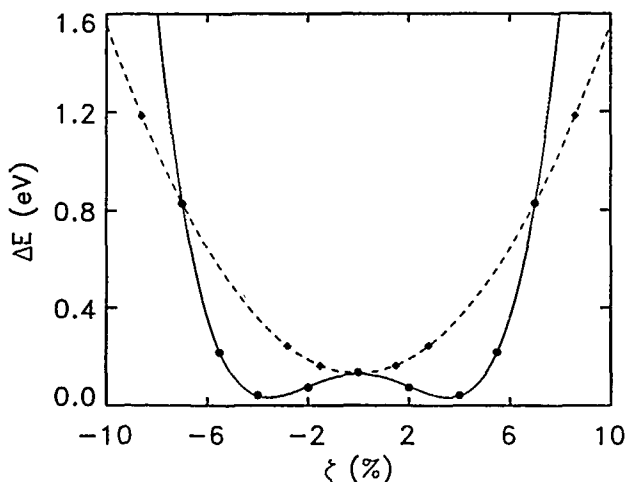


Figure 6. Relative total energy per  $\text{Pt}_2\text{Br}_6$  unit as a function of the dimensionization amplitude  $\zeta$  for the MX chain without (dashed curve) and with (solid curve) inclusion of the  $\text{NH}_3$  sideligands.  $\zeta$  is the shift of the Br atoms of the chain away from the midpoint measured in units of the Pt-Pt interatomic distance.

the transferred electrons do accordingly not only enter empty orbitals of the NiN chain. The distance between the Ca atoms and the NiN chains is found to be much larger (6.05 a.u.) than the experimental value (4.72 a.u.). Due to the fairly large Ca—NiN distance, the main interactions are of electrostatic nature. Since these are long-ranged, the relative position of the Ca atoms and the NiN chains becomes

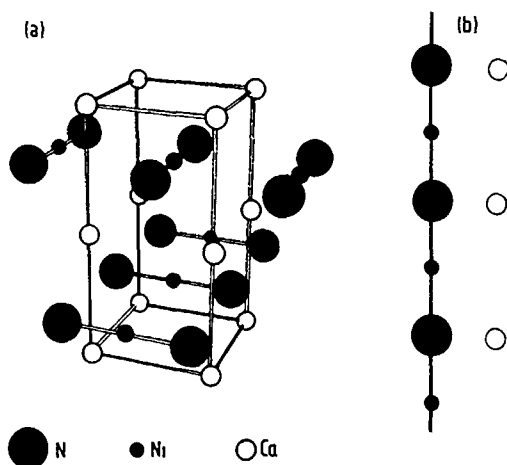


Figure 7. Schematic representation of (a) the crystal structure of  $\text{CaNiN}$  and (b) of one  $\text{CaNiN}$  chain.

very sensitive to treating a single chain or the complete crystal, explaining the difference between theory and experiment.

In order to compare the single-chain results with those of the crystalline material, we finally performed one calculation for the experimental geometry using the LMTO-ASA programs for crystals [4,28-30]. In Figure 8 we show the densities of states as obtained for the NiN chain, the CaNiN chain, and the CaNiN crystal. We observe here close similarities for all three systems. Thus, the low-energy region in Figure 8(c) resembles those of Figures 8(a) and 8(b) except for some shoulders due to

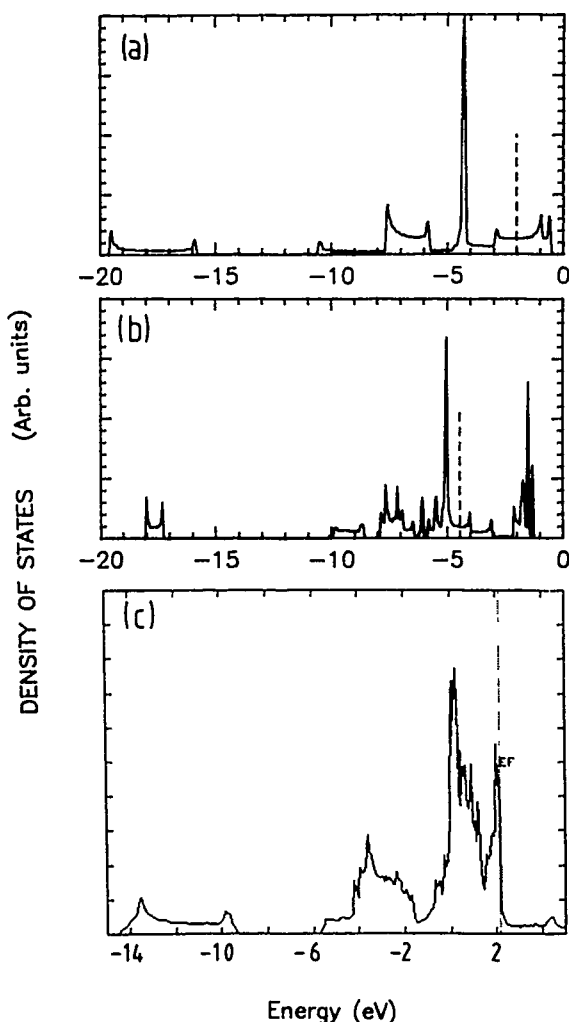


Figure 8. Total density of states of (a) a single NiN chain, (b) a single CaNiN chain, and (c) a CaNiN crystal. The vertical dashed lines mark the Fermi level. Only in (a) and (b) is an energy-zero defined (infinitely far away from the system).



three-dimensional effects. Also closer to the Fermi level there are similarities: the peak around  $-8$ – $-6$  eV ( $-5$  eV) in Figures 8(a) and 8(b) corresponds to that around  $-4$ – $-2$  eV ( $0$  eV) in Figure 8(c). However, the band structures for the crystal (not shown) reveal also some dispersion (i.e., interactions) in the direction perpendicular to the chains especially for the upper valence bands. This is responsible for the differences in the density of states closest to the Fermi level. Finally, the differences in the width of the lowest shown peak can be related to different lattice constants.

### Polycarbonitrile vs. Hydrogen Cyanide

Upon replacing every second CH unit of trans polyacetylene with an N atom, one arrives at polycarbonitrile which may be classified as another conjugated polymer. The unit cell of this polymer contains the same three atoms (H, C, and N) as hydrogen cyanide, which is a hydrogen-bonded polymer consisting of covalently bonded linear HCN monomers linked through weak hydrogen bonds (cf. Fig. 9). A comparison between these two thus gives information on the differences between systems with delocalized electrons and those with localized electrons. As a third polymer that can be included in this comparison, we include the hydrogen-bonded  $(\text{CNH})_x$  polymer of Figure 9 [31]. We shall here concentrate on the first-principles results and refer the reader to Ref. [31] for a discussion of the structural defects which were studied using methods as described in the second section.

The optimized structure of polycarbonitrile was found to be very realistic, although precise experimental information was lacking. On the other hand, the unit cell length of  $(\text{HCN})_x$  was found to be about 8% smaller than the experimental value (7.62 a.u. vs. 8.20 a.u.), and, moreover, the polymer was found to be only metastable compared with dissociation into isolated monomers. A similar metastability was

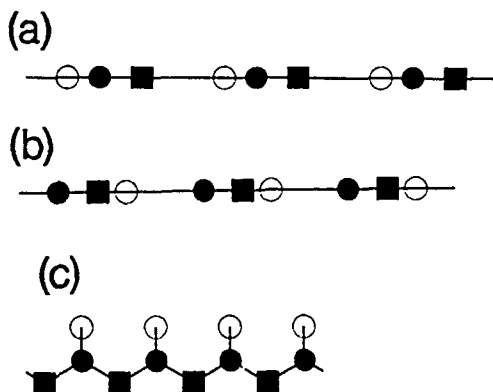


Figure 9. Schematic representation of (a) hydrogen cyanide  $(\text{HCN})_x$ , (b)  $(\text{CNH})_x$ , and (c) polycarbonitrile  $(\text{CHN})_x$ . (c) is a conjugated polymer; the other two hydrogen-bonded. The filled circles and squares represent carbon and nitrogen atoms, respectively, and the empty circles hydrogen atoms.

obtained for  $(\text{CNH})_x$  for which we found no experimental information. We believe this to be a consequence of the tendency of the local-density approximation to overestimate strengths of chemical bonds, i.e., also of a small covalent component of the otherwise weak hydrogen bonds. This overestimate may lead to too short hydrogen bonds and in turn modify the covalent bonds of the  $\text{HCN}$  and  $\text{CNH}$  monomers, thereby interchanging the energetic order of the monomers and the polymers. Some recent results [32,33] have indicated that this failure is relatively general for local-density calculations on hydrogen-bonded systems, although calculations on hydrogen halides have given very realistic results (see, e.g., Ref. [8]). However, by using a so-called nonlocal-density approximation proper structural properties are obtained [32,33]. We have not yet studied this for the present systems.

We believe the local-density approximation also to be responsible for our finding that the conjugated polymer is the stablest isomer [31]. We shall discuss this finding in some detail. In Figure 10 we show our calculated relative energies. However, the overestimate in the strength of a covalent bond due to the local-density approximation depends mainly on the type of bond and is between less than 1 and more than 2 eV per bond [13]. For the sake of simplicity, we shall here assume it to be  $2 \pm 0.5$  eV per covalent bond. For the conjugated  $(\text{CHN})_x$  polymer, we have three covalent bonds per unit cell (one  $\text{C}-\text{H}$  and two  $\text{C}-\text{N}$  bonds), giving an overestimate in the binding energy of about 6 eV. For the other two systems, the number of covalent bonds per unit cell is only two, giving an overestimate of roughly 4 eV. Thereby the relative total energies get modified as indicated in Figure 10. In total, we thus see that the calculations do not permit us to make any reliable statements of the relative stability of these compounds due to the different types of bonds of the different systems. Related arguments should also be applicable for the relative stability of the hydrogen-bonded polymers and the corresponding isolated monomers for which we find the total energies of the polymers to be about 0.4–0.8 eV per monomer above those of the isolated monomers.

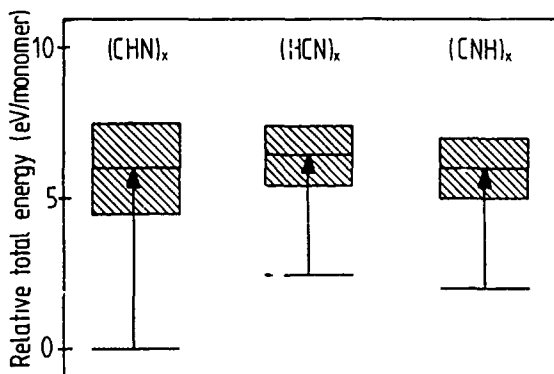


Figure 10. Relative total energies per monomer of the different  $\text{H}-\text{C}-\text{N}$  compounds as calculated (lower part) and when modified as described in the text (upper part).

Despite the problems related to obtaining accurate structural informations, the calculations can be used in providing insight into differences between localized and delocalized electrons. In Figure 11 we show the band structures of the three polymers. The localization in the hydrogen-bonded systems results in considerably smaller band widths, which show up in the density of states and photoelectron spectra as significantly narrower peaks (see Ref. [31]). Nevertheless, similarities are observed. Thus, the lowest band for the conjugated polymer is due to C—N  $\sigma$  orbitals and is to some extent recovered for the other two polymers. The uppermost  $\sigma$  valence band in Figure 11(c) is due to  $N$  lone pairs and can also be found for the HCN polymer. Also the  $\pi$  band in Figure 11(c)—due to C—N  $\pi$  bands—is observed for the other two systems.

The discussion of localization versus delocalization can be extended to include electron densities in position and momentum spaces. We shall not discuss this point further here but refer to Ref. [31]. Moreover, a similar comparison can be carried through for polyacetylene and polycarbonitrile [34].

### Doped Polyacetylene

In the third section, we mentioned that the properties of polyacetylene can be changed significantly upon doping. Within models such as that of Su et al., the dopants are merely treated as a passive electron reservoir donating or accepting electrons to or from the polyacetylene chains, and all changes are intrinsic to the polymers. However, electron spin resonance (ESR) experiments [35–37] on doped polyacetylene have indicated that the role of the dopant is more active. We therefore

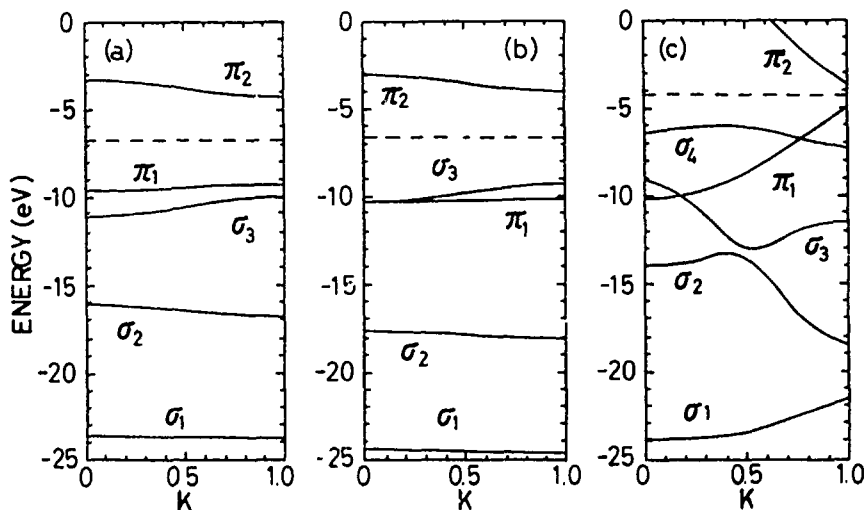


Figure 11. Band structures of (a,b) the hydrogen-bonded (a)  $(\text{HCN})_x$  and (b)  $(\text{CNH})_x$  polymer and (c) the conjugated  $(\text{CHN})_x$  polymer. The dashed lines represent the Fermi level, and  $k = 0$  and  $k = 1$  are the zone center and zone boundary, respectively.

studied a single polyacetylene chain doped periodically 33% with monatomic dopants ranging from Li to Na (i.e.,  $Z = 3-11$ ) [38]. Although the dopant concentration is higher than experimentally achievable (up to 15–20%, see, e.g., Ref. [10]), dopant-dopant interactions are largely excluded such that the results should also be relevant for lower dopant concentrations.

Our main interest was to see at which energies dopant orbitals occurred (i.e., whether they could be expected to be important in the transport processes) and to estimate the electronic dopant-polymer hopping integrals. However, due to inaccuracies in the local-density calculations, this was related with some uncertainties as we shall see.

It turned out that the frontier orbitals for all systems except for the Ne-doped polymer had large components on the dopants. Moreover, the Mulliken populations indicated a fractional electron transfer ( $-0.3$ – $+0.8$  electrons) between the dopants and the polymer. This implies that the dopant-polymer interactions have a significant covalent component. Whereas most transfers in principle agree with chemical intuition, we found—surprisingly—that Li and Na receive electrons instead of donating them.

In principle, the eigenvalues  $\epsilon_i$  of the Kohn-Sham equations (1) are not related to electronic excitation energies except for the uppermost occupied orbital which—for the exact density functional—should be related to the first ionization potential  $V_{IP}$  [39]. However, the local-density approximation gives a much too weak dependence of this as a function of the atomic number  $Z$  [40,13] for isolated atoms. Therefore, the uppermost occupied orbitals of weakly interacting systems will tend to have noteworthy components on all subsystems, as we found for doped polyacetylene. Moreover, small changes in  $V_{IP}$  as a function of atomic number—as, for instance, caused by effects due to the presence of more than one atom—will easily lead to an electron transfer in the wrong direction. We believe that this explains our results for Li and Na.

These results imply that some features for weakly interacting systems may be related with significant uncertainties when calculated with a local-density method. On the other hand, we believe the occurrence of fractional electron transfers and of significant dopant-polymer hopping integrals (we estimated them to be  $\sim 0.5$  eV [38]) to be true such that our results also may be considered a theoretical verification of the experimental ESR results of Bernier and coworkers [35–37].

### Conclusions

In the present paper we have discussed how first-principles, density-functional calculations—mainly on quasi-one-dimensional systems and when using an LMTO approach—can be used in understanding the chemical and physical properties of specific materials. These results may in turn be used in developing more general descriptions of larger classes of materials and/or properties. Most real materials are, however, too complicated to be the subject of any parameter-free study, and one has accordingly to examine idealized systems. The main result of the present paper was that the outcome of such studies might depend critically on the choice

of the model system. Thus, the bond-length alternation observed experimentally for *trans* polyacetylene was not reproduced by some other theoretical studies. We suggested this to be related to differences in treating three-dimensional structures vs. single chains. As another result the simplest chemical picture of the MX chain was only recovered when including the full ligand structure. On the other hand, the electronic properties of CaNiN were well described as a quasi-one-dimensional metal-containing material but three-dimensional effects were important when addressing the question of the position of the Ca atoms relative to the NiN chains.

As a further example of the importance of having the proper description, we considered models for investigating the soliton-induced gap states for *trans* polyacetylene. The simplest single-particle model of Su et al. predicted these to appear exactly at midgap whereas experiments found these off midgap. Effects beyond those of a single-particle picture can describe this but also further single-particle effects can be (parts of) an explanation of the discrepancy.

In the last two sections, we addressed some more fundamental problems of the local-density approximation. We found that the structural properties of the covalently bonded polycarbonitrile were well described but those of the hydrogen-bonded systems were less accurate. Moreover, the relative stabilities were not well described. Results of some recent studies indicate, however, that a nonlocal approximation within the density-functional formalism may solve this problem. Despite these inaccuracies the calculations could give interesting information on localization vs. delocalization of the electrons.

Finally, the results for doped polyacetylene indicated nonnegligible dopant-polymer interactions but also problems for local-density calculations in obtaining reliable electron transfers for weakly interacting systems. This problem may be related to the fundamental problem of local-density calculations in describing the gap between occupied and unoccupied orbitals accurately.

### Bibliography

- [1] M. Springborg and O. K. Andersen, *J. Chem. Phys.* **87**, 7125 (1987).
- [2] P. Hohenberg and W. Kohn, *Phys. Rev.* **136**, B864 (1964).
- [3] W. Kohn and L. J. Sham, *Phys. Rev.* **140**, A1133 (1965).
- [4] O. K. Andersen, *Phys. Rev. B* **12**, 3060 (1975).
- [5] M. Springborg, *J. Chim. Phys.* **86**, 715 (1989).
- [6] M. Springborg, J.-L. Calais, O. Goscinski, and L. A. Eriksson, *Phys. Rev.* **B44**, 12713 (1991).
- [7] S. Yu. Savrasov and D. Yu. Savrasov, *Phys. Rev.* **B46**, 12181 (1992).
- [8] M. Springborg, *Int. Rev. Phys. Chem.*, to appear.
- [9] M. Springborg, *Physica B* **172**, 225 (1991).
- [10] *Proceedings of International Conference of Science and Technology of Synthetic Metals*, Gothenburg, Sweden, August 1992. *Synth. Met.* **55-57**.
- [11] C. R. Fincher, Jr., C.-E. Chen, A. J. Heeger, A. G. MacDiarmid, and J. B. Hastings, *Phys. Rev. Lett.* **48**, 100 (1982).
- [12] C. S. Yannoni and T. C. Clarke, *Phys. Rev. Lett.* **51**, 1191 (1983).
- [13] R. O. Jones and O. Gunnarsson, *Rev. Mod. Phys.* **61**, 689 (1989).
- [14] W. P. Su, J. R. Schrieffer, and A. J. Heeger, *Phys. Rev. Lett.* **42**, 1698 (1979).
- [15] W. P. Su, J. R. Schrieffer, and A. J. Heeger, *Phys. Rev. B* **22**, 2099 (1980).
- [16] A. J. Heeger, S. Kivelson, J. R. Schrieffer, and W.-P. Su, *Rev. Mod. Phys.* **60**, 781 (1988).

- [17] M. Tanaka, A. Watanabe, and J. Tanaka, *Bull. Chem. Soc. Japan* **53**, 645 (1980).
- [18] A. Feldblum, J. H. Kaufman, S. Etemad, A. J. Heeger, T.-C. Chung, and A. G. MacDiarmid, *Phys. Rev. B* **26**, 815 (1982).
- [19] Z. Vardeny, J. Orenstein, and G. L. Baker, *Phys. Rev. Lett.* **50**, 2032 (1983).
- [20] D. K. Campbell and A. R. Bishop, *Phys. Rev. B* **24**, 4859 (1981).
- [21] D. Baeriswyl and A. R. Bishop, *Phys. Scr.* **T19**, 239 (1987).
- [22] J. T. Gammel, A. Saxena, I. Batistić, A. R. Bishop, and S. R. Phillpot, *Phys. Rev. B* **45**, 6408 (1992).
- [23] S. M. Weber-Milbrodt, J. T. Gammel, A. R. Bishop, and E. Y. Loh, Jr., *Phys. Rev. B* **45**, 6435 (1992).
- [24] M. Alouani, R. C. Albers, J. M. Wills, and M. Springborg, *Phys. Rev. Lett.* **69**, 3104 (1992).
- [25] H. J. Keller, B. Keppler, G. Ledezma-Sanchez, and W. Steiger, *Acta Crystallogr. B* **37**, 674 (1981).
- [26] M. Y. Chern and F. J. Disalvo, *J. Solid State Chem.* **88**, 459 (1990).
- [27] M. Springborg and R. C. Albers, *Synth. Met.* **56**, 3383 (1993).
- [28] O. K. Andersen, O. Jepsen, and D. Glotzel, *Proceedings of the International School of Physics "Enrico Fermi,"* F. Bassani, F. Fumi, and M. P. Tosi, Eds., (North-Holland, New York 1985), Vol. 89, p. 59.
- [29] O. K. Andersen, O. Jepsen, and M. Sob, in *Electronic Band Structure and Its Applications*, M. Yussouf, Ed. (Springer-Verlag, Berlin, 1987), p. 1.
- [30] M. van Schilfgaarde, T. A. Paxton, O. Jepsen, and O. K. Andersen, Max-Planck-Institut für Festkörperforschung, Stuttgart, Germany (private communication).
- [31] M. Springborg, *Ber. Bunsenges. Phys. Chem.* **95**, 1238 (1991).
- [32] F. Sim, A. St-Amand, I. Papai, and D. R. Salahub, *J. Am. Chem. Soc.* **114**, 4391 (1992).
- [33] C. Lee, D. Vanderbilt, K. Laasonen, R. Car, and M. Parrinello, *Phys. Rev. Lett.* **69**, 462 (1992).
- [34] M. Springborg, *Z. Naturforsch. A*, **48**, 159 (1993).
- [35] F. Rachdi and P. Bernier, *Phys. Rev. B* **33**, 7817 (1986).
- [36] A. El-Khodary and P. Bernier, *J. Chem. Phys.* **85**, 2243 (1986).
- [37] C. Fite, A. El Khodary, and P. Bernier, *Solid State Commun.* **62**, 599 (1987).
- [38] L. A. Eriksson and M. Springborg, *Phys. Rev. B* **46**, 15833 (1992).
- [39] C.-O. Almbladh and U. von Barth, *Phys. Rev. B* **31**, 3231 (1985).
- [40] S. B. Trickey, *Phys. Rev. Lett.* **56**, 881 (1986).

Received April 16, 1993

# Rules for Intrinsically (Super) Conducting Polymers

GERRARD AISSING and HENDRIK J. MONKHORST

*Quantum Theory Project, University of Florida, Gainesville, Florida 32611-2085*

CHENGZHENG HU

*Physics Department, Wuhan University, Wuhan, People's Republic of China*

## Abstract

We propose a number of rules based on topological and structural considerations for the synthesis of intrinsically conducting polymeric materials. These rules can be summarized as follows: (i) The polymer has to have a glide plane or a twofold screw axis when infinitely extended; (ii) the unit cell must contain  $4N + 2$  valence electrons; (iii) the packing into the solid is restricted by symmetry rules that conserve the twofold degeneracy caused by rule (i). These rules are necessary (but not sufficient) for superconductivity. The inorganic polymer poly(sulfur-nitride), which is a metallic superconductor with a critical temperature of  $T_c = 0.33$  K, is identified as a striking example of these rules. © 1993 John Wiley & Sons, Inc.

In 1964 Little [1] proposed the attractive idea that there may exist certain organic polymers which can become superconducting at high temperatures. Such organic molecules should, according to Little's original proposal, consist of two parts: a conducting chain (the backbone) and a series of side groups attached to this backbone. If these side groups are easily polarized, the electrons in the spine can be coupled by the polarization-induced interaction of the side groups. This interaction can provide the attractive coupling necessary for superconductivity [2]. In spite of many attempts to synthesize conducting polymers based on conjugated backbones, no significant progress has been made in the synthesis of intrinsically conducting polymers. Most of the organic conductors synthesized to date are semiconductors that become conducting only after heavy doping (see, e.g., the recent publications in Ref. [3]). Unfortunately, the structural and mechanical properties of these doped polymers are not always useful for large scale application. More progress has been made in the field of molecular organic (super-) conductors [4]. Values of  $T_c$  have now reached a value of 12.5 K [5] and will likely continue to rise. The discovery of the superconducting properties of Li-, Cs-, and Rb-doped Buckminster-Fullerenes also indicates that superconductivity of organic materials is far more common than originally believed [6-9] (Ref. [9] gives results for mixed-Cs, Rb compounds).

So far, only one intrinsically conductive polymer has been synthesized. There are several possible reasons for this fact. First, there is a technical one: Up to now the techniques for synthesis of polymers with high crystallinity have been insufficient to create conductive polymers in which the charge carrier mobility is comparable to that in metals or semiconductors. Second, a one-dimensional conductor is sup-

posed to undergo a Peierls distortion, which will result in a gap at the Fermi level [10]. In that case, the density of states at the Fermi level will vanish and so will the metallic conductivity. The resulting polymer will only become conducting after doping. However, doped polymers usually do not crystallize in well-defined crystal structures due to the disorder caused by the doping. It therefore seems worthwhile to investigate the possibility of the existence of a class of intrinsically conducting polymers that do not undergo a Peierls distortion.

If we consider an isolated polymer chain, we can immediately state the conditions under which it will be conducting.

1. The polymer structure should have an almost rigid backbone, with glide plane symmetry and/or twofold screw axis symmetry when infinitely extended. This rule is a consequence of Herring's theorem. This theorem implies that a one-dimensional system with a glide plane or a twofold screw axis along its spine will show a double degeneracy at the zone boundary for all one electron levels [11,12]
2. There should be  $4N + 2$  electrons per unit cell. Under this condition the highest occupied MO will be filled exactly up to the zone boundary. This rule could be called a *superaromaticity rule*, as it is the polymer extension to the Hückel stabilization rule for aromatic molecules. It is this degeneracy at the Fermi level that may offset a Peierls distortion [10]. Moreover, it assures a high density of states at the Fermi level.

A polymer that obeys both rules, and does not undergo a Peierls distortion, is a conductor. If we crystallize this polymer into a solid and succeed in packing the polymer in such a way that the above-mentioned rules still apply, then the resulting system will still be conducting. In that case the interchain interaction will not reduce the polymer to a semiconductor. This represents our third rule.

In fact, the interchain interaction may be important for more than one reason. If these interactions are strong enough, so that the resulting solid polymer is not a one-dimensional system, but has to be regarded as a highly anisotropic three-dimensional system, a Peierls distortion may be avoided.

This seems to be the case with poly(sulfur-nitride). From calculations and experiments one can conclude that this remarkable polymer obeys the two rules stated above. The crystal symmetry is  $P2_1/c$  [13]. The S-N chains are oriented along the *b*-axis, which happens to be the twofold screw axis of the unit cell. There are two crystallographically equivalent chains per unit cell, which are related by screw axis symmetry around the *b*-axis of the monoclinic unit cell. Moreover, there is proof that the interchain interaction is almost as strong as the intrachain interaction due to the close proximity of S and N atoms in neighboring chains, and therefore  $(SN)_x$  has to be seen as an anisotropic three-dimensional solid and not a one-dimensional polymer [14]. This strong interchain interaction is apparently the reason  $(SN)_x$  does not undergo a Peierls distortion, although *ab initio* LCAO-CO calculations by Dovesi et al. show that the energy difference between the symmetric and the symmetry broken state is exceedingly small, indicating that the absence of a Peierls distortion may also be an intrinsic quality of  $(SN)_x$  [15]. The conductivity parallel



to the molecular axes at room temperature is  $\sigma_{\parallel} = 4 \times 10^3 (\Omega \text{ cm})^{-1}$  [16,17]. At 4.2 K this value is about 1000 times as high. At low temperatures the ratio  $\sigma_{\parallel}/\sigma_{\perp}$  is of the order of 1000 [18]. Furthermore,  $(\text{SN})_x$  undergoes a transition to a superconducting state at 0.33 K. It is believed—at this moment—to be a “normal” type II BCS superconductor. Both  $\sigma$  and  $T_c$  increase under pressure [19–21].

A key issue is the preparation of conducting polymers with a high degree of crystallinity. Experiments with doped polyacetylenes show that high crystallinity increases the conductivity dramatically by increasing the effective conjugation of the chains. In these systems the crystallinity can be improved by annealing techniques [22].

Further possibilities for achieving high crystallinity lie in the synthesis of soluble polymers, which can be crystallized from solution.

Finally, the question has to be asked: Can conducting polymers that obey our two rules be superconductors? According to Little's model, this is certainly a possibility [1]. We can imagine that the conductive backbone has a number of side groups that are highly polarizable, thus inducing attractive interaction between the conduction electrons, leading to a BCS-type pairing [2]. Due to the one-dimensionality of the polymers, the density of states at the Fermi level will be high, leading to a stronger coupling of the electrons and hence a higher  $T_c$ . This situation can be compared to that observed in the A-15 compounds, where the one-dimensionality of the transition metal chains is considered to be responsible for the rather high values of  $T_c$  [23]. On the other hand, a mechanism involving the interactions between the conduction electrons in one chain with the neighboring chains could also occur. A similar mechanism was recently discussed as a possible explanation of the high- $T_c$  superconductivity in the layered cuprates [24,25]. This additional fourth rule is more quantitative than the first three. The actual unit cell composition and chemical structure must be involved, and a predictive theory must recognize these factors explicitly [26].

Polymers that contain large side groups and sheet (2D) materials that resemble the Cu-O type materials in structure and meet the original topological requirements of Little's model for excitonic superconductivity are currently being investigated. The main focus of these studies is, however, on organometallic systems [27]. Also, a number of sandwich materials have been produced. They are, however, very hard to process because of their air sensitivity, involatility, and insolubility [28]. At this moment, a number of experimental groups are studying the possibilities of synthesizing polymers that obey the rules presented in this paper. The results of these efforts will give us opportunity to test and, if needed, tune our rules. We believe the three rules, stated here, are qualitatively correct. Feedback from experimental results will be important to turn these qualitative rules into a quantitatively predictive theory of (super) conductive polymers.

In summary, we propose a number of simple topological and structural rules, that will lead to intrinsically conducting polymers. If these polymers, in addition to our rules, have side chains of high polarizability, they can become superconducting at fairly high temperatures. Because the proposed class of polymers is intrinsically conducting, none of the disorder problems arising from the usually applied heavy

doping occurs. In addition, our rules can be used as practical guidelines in the search for intrinsically conducting polymers.

### Bibliography

- [1] W. A. Little, *Phys. Rev. A* **134**, 1415 (1964).
- [2] J. Bardeen, L. Cooper, and J. R. Schrieffer, *Phys. Rev.* **108**, 1175 (1957).
- [3] M. G. Kanatzidis, *C&EN* (December 3, 1990) p. 36.
- [4] V. Z. Kresin and W. A. Little, Eds., *Organic Superconductors* (Reidel, New York, 1991).
- [5] A. M. Kini, U. Geiser, H. H. Wang, K. D. Carlson, J. Williams, W. K. Kwok, K. G. Vandervoort, J. E. Thompson, D. L. Stupka, D. Jung, M.-H. Wangbo, *Inorg. Chem.* **29**, 2555 (1990).
- [6] A. F. Hebard, M. J. Rosseinsky, R. C. Haddon, D. W. Murphy, S. H. Glarum, T. T. M. Palstra, A. P. Ramirez, and A. R. Kortan, *Nature* **350**, 600 (1991).
- [7] K. Holczer, O. Klein, S.-M. Huang, R. B. Kaner, K.-J. Fu, R. L. Whetten, and F. Diederich, *Science* **252**, 1154 (1991).
- [8] M. J. Rosseinsky, A. P. Ramirez, S. H. Glarum, D. W. Murphy, R. C. Haddon, A. F. Hebard, T. T. M. Palstra, A. R. Kortan, S. M. Zahurak, and A. V. Makhija, *Phys. Rev. Lett.* **66**, 2830 (1991).
- [9] For the highest  $T_c$  values, see K. Tanigaki, T. W. Ebbesen, S. Saito, J. Mizuki, J. S. Tsai, Y. Kubo and S. Kurishina, *Nature* **352**, 222 (1991).
- [10] R. E. Peierls, *Quantum Theory of Solids* (Oxford University Press, Oxford, 1955).
- [11] C. Herring, *Phys. Rev.* **52**, 361, 365 (1937); *J. Franklin Inst.* **233**, 525 (1942).
- [12] W. L. McCubbin, in *Electronic Structure of Polymers and Molecular Crystals*, J.-M. André and J. Ladik, Eds. (Plenum, New York, 1974), p. 171.
- [13] M. J. Cohen, A. F. Garito, A. J. Heeger, A. G. MacDiarmid, C. M. Mikulski, M. S. Saran, and J. Kleppinger, *J. Am. Chem. Soc.* **98**, 3844 (1976).
- [14] W. I. Friesen, A. J. Berlinsky, B. Bergersen, L. Weiler, and T. M. Rice, *J. Phys. C Solid State Phys.* **8**, 3549 (1975).
- [15] R. Dovesi, C. Pisani, C. Roetti, and V. R. Saunders, *J. Chem. Phys.* **81**, 2839 (1984).
- [16] G. B. Street and R. L. Greene, *IBM J. Res. Dev.* **21**, 99 (1977).
- [17] R. L. Greene and G. B. Street, in *Chemistry and Physics of One-Dimensional Metals*, H. J. Keller, Ed. (Plenum, New York, 1977), p. 167.
- [18] P. M. Grant, R. L. Greene, W. D. Gill, W. E. Rudge, and G. B. Street, *Mol. Cryst. Liq. Cryst.* **32**, 171 (1976).
- [19] W. D. Gill, R. L. Greene, G. B. Street, and W. A. Little, *Phys. Rev. Lett.* **35**, 1732 (1975).
- [20] W. H. Muller, F. Baumann, G. Dammer, and L. Pitschovius, *Solid State Commun.* **25**, 119 (1978).
- [21] R. Clarke, *Solid State Commun.* **25**, 333 (1978).
- [22] R. L. Elsenbaumer, in *Organic Superconductivity*, V. Z. Kresin and W. A. Little, Eds. (Plenum, New York, 1991), p. 341, and references therein.
- [23] J. C. Phillips, *Physics of High- $T_c$  Superconductors* (Academic, New York, 1991), Chapter II and references therein.
- [24] W. A. Harrison, *Phys. Rev. B* **38**, 270 (1988); **44**, 7768 (1991).
- [25] W. A. Harrison, in *Novel Superconductivity*, S. A. Wolf and V. Z. Kresin, Eds. (Plenum, New York, 1987), p. 507.
- [26] G. Aissing and H. J. Monkhurst, unpublished results (1991).
- [27] J. P. Collman and W. A. Little, NTIS AD-769 630.
- [28] B. Bush and J. J. Lagowski, in *Organic Superconductivity*, V. Z. Kresin and W. A. Little, Eds. (Plenum, New York, 1991), p. 347.

Received May 13, 1993

# Energetics of Small Clusters of Stabilized Jellium: Continuum and Shell-Structure Effects

MARTA BRAJCZEWSKA and CARLOS FIOLEHAIS

*Departamento de Física da Universidade de Coimbra, P-3000 Coimbra, Portugal*

JOHN P. PERDEW

*Department of Physics and Quantum Theory Group, Tulane University,  
New Orleans, Louisiana, 70118*

## Abstract

We evaluate binding energies, ionization energies, and second-order energy differences as functions of valence electron number for small spherical clusters of stabilized jellium, using the Kohn-Sham equations with the local-spin-density (LSD) approximation. Cohesive energies are also reported. A comparison is made with semiclassical formulas (liquid drop model and Padé approximant, with surface and curvature coefficients derived from first principles). These formulas nicely average the shell-structure oscillations of the energy, which are found to be almost the same as for ordinary jellium. Spherical clusters with 1, 7, and 9 electrons have binding energies very close to those of the semiclassical predictions.

© 1993 John Wiley & Sons, Inc.

## Introduction

In the simple metals, the delocalized valence electrons experience a weak ionic pseudopotential, which in simplified treatments is often replaced by the potential of a uniform positive background with a sharp boundary (jellium).

The stabilized jellium model [1] for surface and cohesive properties of simple metals is intended to cure well-known deficiencies of the ordinary jellium model: unrealistic results for the binding energies at all densities, for the compression properties at low densities (negative bulk modulus for the density of cesium), and for the surface properties at high densities (negative surface tension for the density of aluminum). All these unrealistic results follow from the fact that jellium is unstable, except at a density close to that of sodium. At that density, jellium and stabilized jellium have identical surface properties. The stabilized jellium model retains the simplicity and universality of jellium. With only two inputs, the density and valence, this model provides an accurate overall description of the binding energies of all simple metals, in the framework of density-functional methods. Given only the density, it delivers reasonable overall surface properties (work function, surface tension, etc.). This result is achieved by subtracting from the energy functional of the jellium model the spurious self-interaction of the bulk positive charge and by introducing inside the solid a constant potential, the average value in the Wigner—

TABLE I Liquid drop model coefficients  $a_v$ ,  $a_s$ , and  $a_c$ . The surface and curvature coefficients are from a Kohn-Sham calculation for the planar surface of stabilized jellium [8]. Also indicated are the work function  $W$  and the distance  $x_0$  from the image plane to the jellium edge of the planar surface, from [9].

	$r_s$ (bohr)	$a_v$ (eV)	$a_s$ (eV)	$a_c$ (eV)	$W$ (eV)	$x_0$ (bohr)
Al	2.07	-10.58	0.87	0.65	4.27	1.01
Na	3.99	-6.26	0.59	0.24	2.94	1.27
Cs	5.63	-4.64	0.42	0.13	2.26	1.55

Seitz cell of the difference between a local pseudopotential and the jellium background potential.

The jellium model should have the same drawbacks for metallic clusters as for the bulk system. For example, it does not yield realistic binding energies, and it is completely inadequate to describe compression effects of finite systems. Notwithstanding these deficiencies, the jellium model with the help of density-functional methods has been extensively used for understanding metallic clusters [2,3,4]. Those studies support the image of the cluster as a system of electrons bound in a one-particle potential due to the spherical (or deformed) jellium background and the other electrons. Clusters with "magic" numbers of electrons (2, 8, 18, 20, etc.) are more stable than their neighbors, due to the presence of larger gaps above the highest occupied level. The occurrence of ionization energies with local maxima for magic systems corroborates that picture.

Here we shall evaluate the effect of the "stabilization" of jellium on static properties of clusters, such as binding energies, ionization energies and second-order energy differences. In other work [5], the stabilized jellium model will be applied to describe compression effects for clusters at any density.

This work calculates energies of small spherical stabilized jellium clusters, as functions of electron number, using the Kohn-Sham equations of density-functional theory (within the local-spin-density approximation, LSD). By "small," we mean that the number of valence electrons is  $N \leq 20$ . The quantal energy of the cluster is compared with a classical liquid drop formula. A variant of the liquid drop formula, using a Padé approximant, which has been proposed recently for the study

TABLE II. Padé coefficients for the stabilized jellium model [5]. The  $r_s$  values are those of Table I

	$b_1$	$b_2$	$b_3$
Al	0.742	6.326	0.123
Na	0.399	0.284	0.146
Cs	0.308	0.227	0.147

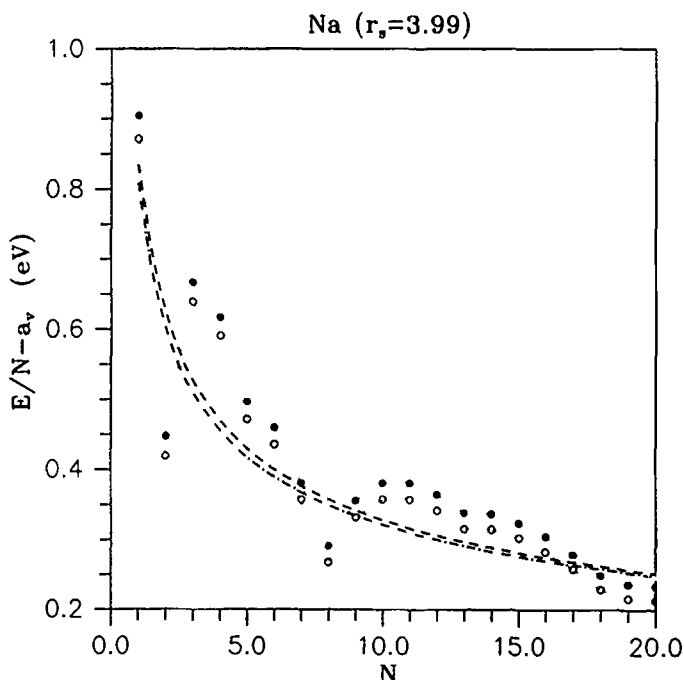


Figure 1. Non-bulk binding energy per valence electron  $E/N - a_v$  for clusters of sodium ( $r_s = 3.99$ ), within the stabilized jellium model. The symbols  $\bullet$  and  $\circ$  represent, respectively, the Kohn-Sham results for stabilized and ordinary jellium. The dashed line represents the liquid drop model, and the dashed-dotted line the Padé approximant. The bulk binding energy is  $a_v = -6.26$  eV for stabilized jellium and  $a_v = -2.10$  eV for jellium.

of small voids inside solids [6], is also considered. The enhancement of stability due to shell effects, which is known for jellium, is examined for stabilized jellium. Ionization energies of stabilized jellium clusters are evaluated. Finally, the energies of stabilized jellium atoms are used together with bulk binding energies to obtain cohesive energies.

In the next section, we present the Kohn-Sham equations applied to spherical clusters of stabilized jellium. Results are then displayed for the energetics of three metals (Al, Na and Cs), which cover the whole range of metallic densities. In the last section, further work with stabilized jellium is proposed.

### Kohn-Sham Equations for a Cluster of Stabilized Jellium

Let us adopt the atomic system of units ( $e = m = \hbar = 1$ ). We consider a spherical uniform positive background of finite density  $n_+$  such that

$$n_+(\mathbf{r}) = \bar{n} \Theta(R - r), \quad \Theta(R - r) = \begin{cases} 1 & (r \leq R) \\ 0 & (r \geq R) \end{cases}, \quad (2.1)$$

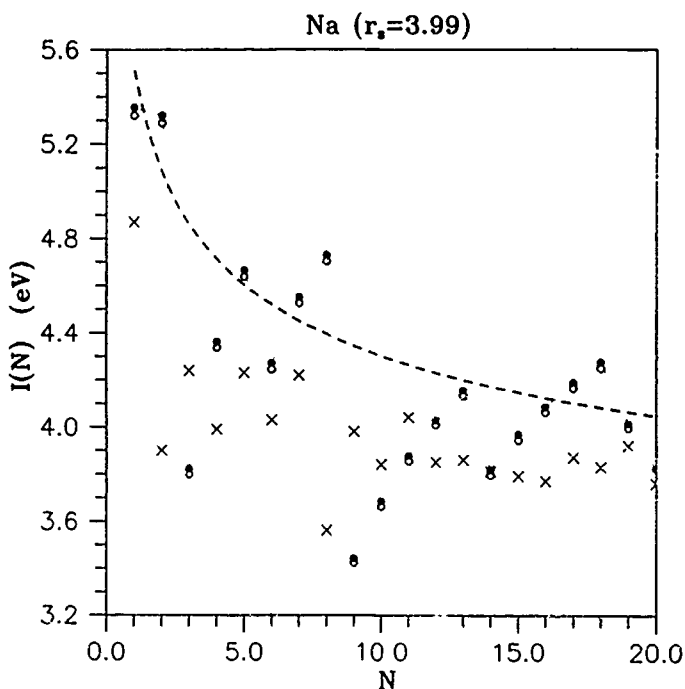


Figure 2. Ionization energies for clusters of sodium. The symbols ● and ○ represent, respectively, stabilized and ordinary jellium results. The dashed line represents the result of formula (2.22) for the stabilized jellium model. Experimental data are indicated by X [22].

with

$$\bar{n} = \frac{3}{4\pi r_s^3} = \frac{k_F^3}{3\pi^2}, \quad (2.2)$$

and  $R$  the cluster radius. From the neutrality condition

$$\int d^3r n_+(r) = N, \quad (2.3)$$

the radius of the background sphere must be

$$R = N^{1/3} r_s. \quad (2.4)$$

The self-consistent Kohn-Sham equation is

$$\left[ -\frac{1}{2} \nabla^2 + v_{\text{eff}}(r, \sigma) \right] \psi_{\alpha\sigma}(r) = \epsilon_{\alpha\sigma} \psi_{\alpha\sigma}(r), \quad (2.5)$$

where  $\alpha$  denotes a set of quantum numbers and  $\sigma$  is a spin number (up  $\uparrow$  or down  $\downarrow$ ).

In Eq. (2.5), the effective potential is

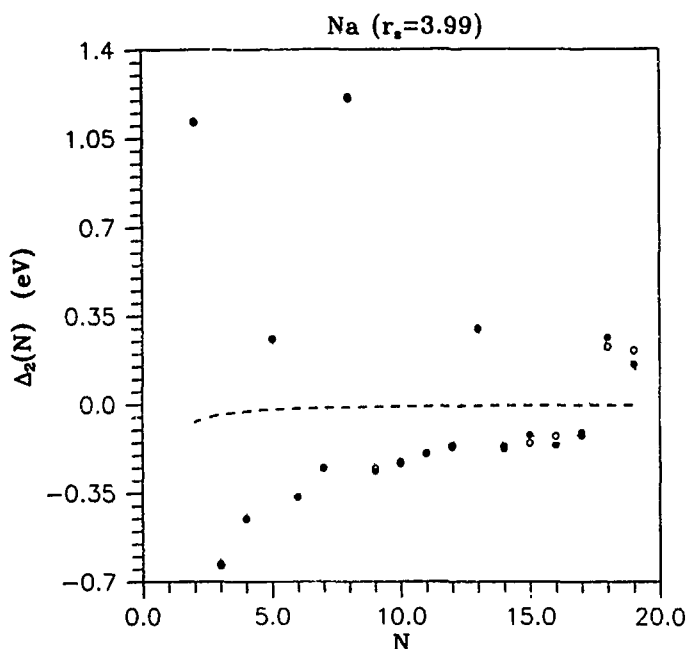


Figure 3. Second-order energy differences for clusters of sodium. The symbols ● and ○ represent, respectively, stabilized and ordinary jellium results. The dashed line represents the liquid drop model for stabilized jellium.

$$v_{\text{eff}}(\mathbf{r}, \sigma) = v_+(\mathbf{r}) + \int d^3r' \frac{n(\mathbf{r}')}{|\mathbf{r} - \mathbf{r}'|} + \mu_{xc}^{\sigma}(\mathbf{r}), \quad (2.6)$$

where  $v_+$  is the electrostatic potential for the interaction between the background and the electrons,  $n(\mathbf{r})$  is the total electronic density, and  $\mu_{xc}^{\sigma}(\mathbf{r})$  the spin-dependent exchange-correlation potential. We have

$$v_+(\mathbf{r}) = \begin{cases} -\frac{N}{2R} \left[ 3 - \left( \frac{r}{R} \right)^2 \right] + \langle \delta v \rangle_{\text{WS}} & (r < R) \\ -\frac{N}{r} & (r > R), \end{cases} \quad (2.7)$$

with

$$\langle \delta v \rangle_{\text{WS}} = -\frac{k_F^2}{5} + \frac{k_F}{4\pi} + \frac{r_s}{3} \frac{d\epsilon_c}{dr_s}, \quad (2.8)$$

the average potential difference which appears in the stabilized jellium model [1]. ( $\epsilon_c$  is the correlation energy per electron of the uniform electron gas [7].) The second term in (2.6) is the Hartree potential. The last term is the exchange-correlation potential

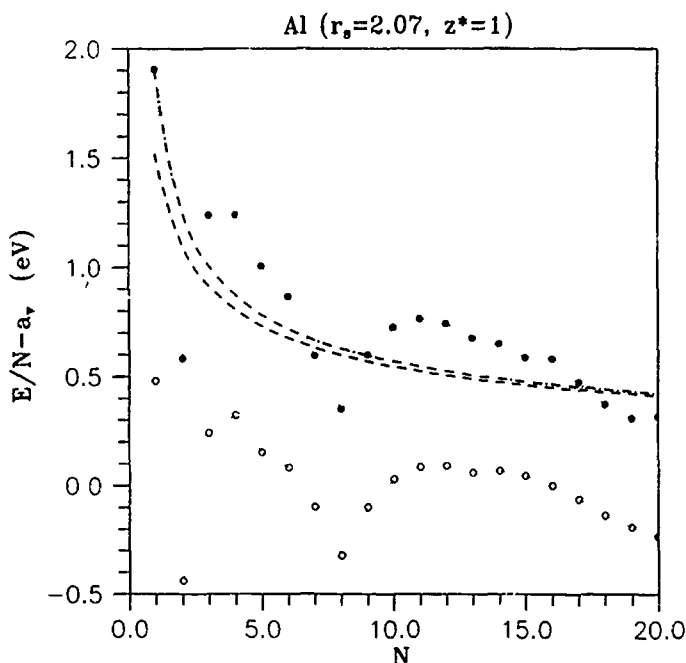


Figure 4. The same as Figure 1 for aluminum ( $r_s = 2.07$ ). The bulk binding energy is  $a_v = -10.59$  eV for stabilized jellium and  $a_v = -0.21$  eV for jellium.

$$\mu_{xc}^s(n_\uparrow(\mathbf{r}), n_\downarrow(\mathbf{r})) = \frac{\partial}{\partial n_s} [n \epsilon_{xc}(n_\uparrow, n_\downarrow)], \quad (2.9)$$

where  $n_\uparrow(\mathbf{r})$  and  $n_\downarrow(\mathbf{r})$  are the up and down spin densities, respectively. Here  $\epsilon_{xc} = \epsilon_x + \epsilon_c$ , with  $\epsilon_x = -3k_F/4\pi$  the exchange energy per electron of the uniform gas.

The total electronic density is given by

$$n(\mathbf{r}) = \sum_{\sigma=\uparrow,\downarrow} n_\sigma(\mathbf{r}), \quad (2.10)$$

with

$$n_\sigma(\mathbf{r}) = \sum_{\alpha} f_{\alpha\sigma} |\psi_{\alpha\sigma}(\mathbf{r})|^2. \quad (2.11)$$

The  $f_{\alpha\sigma}$  are occupation numbers of the orbitals defined by the quantum numbers  $\alpha\sigma$  ( $f_{\alpha\sigma} = \Theta(\epsilon_F - \epsilon_{\alpha\sigma})$ , with  $\epsilon_F$  the Fermi energy, and  $\sum_{\alpha\sigma} f_{\alpha\sigma} = N$ ).

The total energy of the stabilized jellium cluster is

$$\begin{aligned} E(N) = & \sum_{\alpha\sigma} f_{\alpha\sigma} \epsilon_{\alpha\sigma} - \left( U[n] + \sum_{\sigma} \int d^3r \mu_{xc}^s(n_\uparrow, n_\downarrow) n_\sigma(\mathbf{r}) \right) + U_B[n_+] \\ & + \int d^3r \epsilon_{xc}(n_\uparrow, n_\downarrow) n(\mathbf{r}), \end{aligned} \quad (2.12)$$



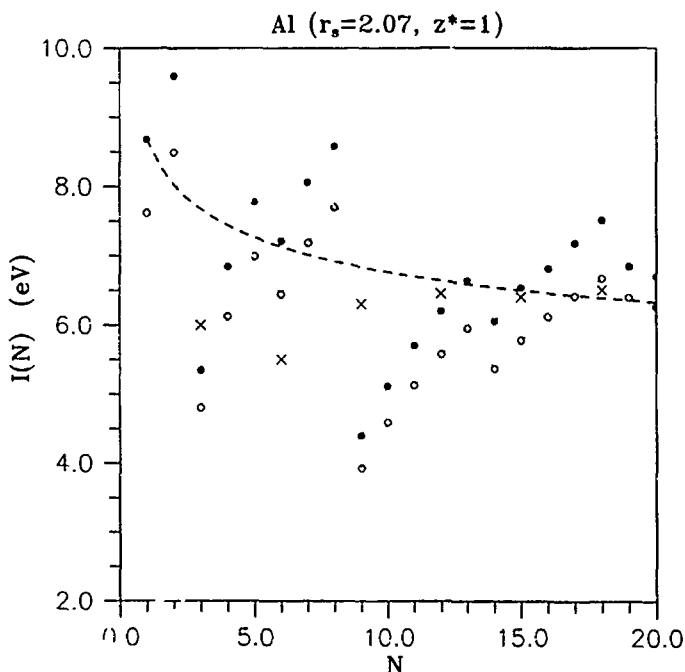


Figure 5. The same as Figure 2 for aluminum. Note that only  $N = 3, 6, 9, 12, 15, 18$  are physically meaningful. Experimental data are taken from [23].

where

$$U[n] = \frac{1}{2} \int d^3r \int d^3r' \frac{n(\mathbf{r})n(\mathbf{r}')}{|\mathbf{r} - \mathbf{r}'|} \quad (2.13)$$

is the electronic Coulomb repulsion energy, and

$$U_B[n_+] = \frac{3}{5} \frac{N(N - N^{1/3})}{R} \quad (2.14)$$

is the background Coulomb repulsion minus the self-repulsion energy within each Wigner-Seitz cell. We have adopted the version of stabilized jellium in which the effective valence is unity ( $z^* = 1$ ), since this version gives the more realistic bulk modulus. The ordinary jellium model is recovered by dropping the last term of Eqs. (2.7) ( $r < R$ ) and (2.14).

For a spherical system, the self-consistent Eq. (2.5) is

$$-\frac{1}{2r^2} \frac{d}{dr} \left( r^2 \frac{d\mathcal{R}_{nlm}}{dr} \right) + \left( v_{\text{eff}}(r, \sigma) + \frac{l(l+1)}{2r^2} - \epsilon_{nl} \right) \mathcal{R}_{nlm} = 0, \quad (2.15)$$

where  $\mathcal{R}_{nlm} = \mathcal{R}_{nlm\sigma}$  is the radial wave function. As an approximation and to oblige the system to have spherical symmetry, we replace the true electronic spin density by the spherical average

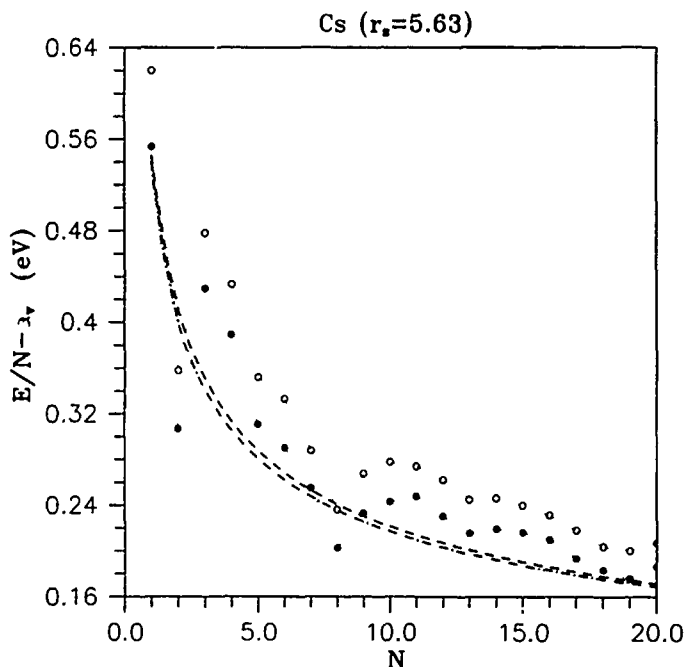


Figure 6. The same as Figure 1 for cesium ( $r_s = 5.63$ ). The bulk binding energy is  $a_v = -4.64$  eV for stabilized jellium and  $a_v = -1.98$  eV for jellium.

$$n_o(\mathbf{r}) = \frac{1}{4\pi} \sum_{nlm} |\mathcal{R}_{nlmo}(\mathbf{r})|^2. \quad (2.16)$$

In order to solve (2.15), with the approximation (2.16), we have used an atomic code where the nucleus with constant charge has been expanded to the desired cluster radius.

It is known that the energy of a finite quantal system, such as a cluster, can be described in an average way by the liquid drop model (LDM)

$$E_{\text{LDM}}(N) = a_v N + a_s N^{2/3} + a_c N^{1/3} + \dots \quad (2.17)$$

The coefficients  $a_v$  (volume),  $a_s$  (surface), and  $a_c$  (curvature) for the stabilized jellium model have been obtained with the aid of the so-called "leptodermous expansion" [8]. They are given in Table I for Al, Na, and Cs.

We can write (2.17) in the form

$$E_{\text{LDM}}(N) = a_v N + a_s(N) N^{2/3}. \quad (2.18)$$

The Padé formula for a stable cluster is [6]

$$a_s(N) = a_s [1 - b_1 N^{-1/3} + b_2 N^{-2/3} - b_3 N^{-1}]^{-1}. \quad (2.19)$$

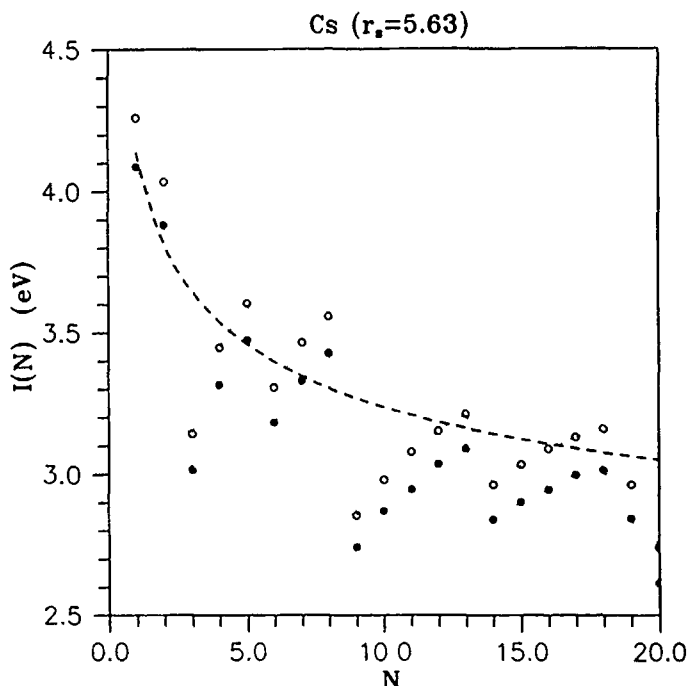


Figure 7. The same as Figure 2 for cesium.

The coefficients  $b_1$ ,  $b_2$ , and  $b_3$  are given in Table II. This formula was developed to connect the liquid drop expansion for a spherical void of large radius with the perturbation expansion for a void of small radius. It effectively sums the leptodermous expansion to all orders, and has been adapted to clusters by changing the sign of the curvature  $R^{-1}$ .

We compare the liquid drop prediction with the quantal result, looking for special stability (shell closures) for numbers  $N$  such that

$$E(N) < E_{\text{LDM}}(N). \quad (2.20)$$

Relative stability is also indicated by local maxima of the ionization energy

$$I(N) = E_N(N-1) - E_N(N), \quad (2.21)$$

where the subscript  $N$  denotes the fixed positive charge. A smooth formula for the ionization energy is

$$I(N) = W + \frac{1}{2(r_s N^{1/3} + x_0)}, \quad (2.22)$$

with  $W$  the work function and  $x_0$  the location of the image plane for the planar surface. (The values in Table I are taken from [9].) Eq. (2.22) is an approximation

TABLE III. Cohesive energies for the stabilized jellium (SJ) and jellium (J) models (in eV), using different approximations. "LSD" means local-spin-density, "LDA" local-density approximation, "SIC" self-interaction correction, "LDM" liquid drop model, "Padé" Padé approximant, and "Exp" experiment (from [18]). Here we use densities which are slightly different from those of Table I. The values in this table refer to zero temperature, while the previous ones are room temperature values.

	$r_s$ (bohr)		LSD	LDA	SIC	LDM	Padé	Exp.
Al ( $N = 3$ )	2.07	SJ	3.79	3.93	3.21	2.75	3.02	3.34
		J	0.72	0.84	0.21	-0.25	-0.07	
Al ( $N = 1$ )	2.07	SJ	1.91	2.41	1.61	1.52	1.90	—
		J	0.48	0.91	0.24	0.08	0.19	
Na	3.93	SJ	0.92	1.18	0.81	0.85	0.82	1.13
		J	0.88	1.15	0.78	0.82	0.78	
Cs	5.62	SJ	0.56	0.74	0.51	0.59	0.54	0.83
		J	0.62	0.81	0.57	0.66	0.76	

to the liquid drop expression [10], in which a weakly size-dependent LDM chemical potential  $\mu(R) \approx -W$  appears.

A third measure of stability is the second-order energy difference, which has been used to interpret mass spectra of metallic clusters:

$$\Delta_2(N) = E(N+1) + E(N-1) - 2E(N). \quad (2.23)$$

A peak of this quantity means an enhancement of stability with respect to neighboring values of  $N$ . In the liquid drop model, Eq. (2.23) becomes  $\Delta_2(N) = \partial^2 E_{\text{LDM}}(N)/\partial N^2$ . We shall see whether the criteria for relative stability based on (2.20), (2.21), and (2.23) agree.

## Results

Bulk jellium is stable at the density  $r_s = 4.2$ , where  $\langle \delta v \rangle_{\text{WS}} = 0$ . Sodium ( $r_s = 3.99$ ) has therefore been used as an application of the jellium model [11,12]. Since the stabilized jellium model yields a small value of  $\langle \delta v \rangle_{\text{WS}}$  for Na, the surface properties of jellium and stabilized jellium should be practically the same for this metal, although the bulk binding energy per particle  $a_v$  is very different in the two models. Small clusters of Na are more bound in the stabilized jellium description than in jellium (see Fig. 1, noting the different  $a_v$  for stabilized jellium and jellium). Nevertheless, the shell structure, i.e., the oscillation around the smooth curve given by the liquid drop formula, is essentially the same, with magic numbers  $N = 2, 8, 18, 20$ . The binding energy is also well below the LDM curve for  $N = 19$ , where the  $2s$  shell is half-filled. For the electron numbers  $N = 1, 7, 9, 17$ , the quantal result agrees closely with the LDM prediction. These "tell-tale" numbers might be used to estimate the exact (beyond LSD) surface and curvature energies from careful quantum-chemical calculations for small spherical clusters. For Na, the Padé representation practically coincides with the liquid drop formula.

The shell structures of jellium and stabilized jellium are also displayed by the ionization energies. The ionization energies of the two models agree closely (Fig. 2). The ionization energy for  $N = 19$  is bigger than that for  $N = 20$ ; this fact, known for jellium in LSD [13], holds for stabilized jellium as well. The local maxima at half-filled shells ( $N = 5, 13$ ) are a characteristic of LSD, and are not seen in the local-density-approximation (LDA) [14]. (LDA is LSD with  $n_t, n_i$  replaced by  $n/2, n/2$ .)

Figure 2 also presents experimental ionization energies for Na clusters. For the smallest clusters, the spherical stabilized jellium results are not in good agreement with experiment. In fact, clusters of five or fewer atoms are typically planar [15,16]. Moreover, the instability of many spherical open-shell clusters is evident from the total energies of Figure 1. For example, the total energy for  $N = 3$  is greater than the sum of total energies for  $N = 2$  and 1. These unstable clusters will start to deform away from spherical shape toward fission. In many cases, they will reach energy minima before fission occurs. Spheroidal distortions can correct most of the difference between our ionization energies and experimental ones [17].

The second-order energy difference is almost identical in jellium and stabilized jellium (Fig. 3). The liquid drop result for  $\Delta_2(N)$  is practically constant ( $\Delta_2(N) \approx 0$ ), providing a good average of the quantal values.

Turning to Al, we find that the shell fluctuations are bigger than for sodium, although the two patterns are similar (Fig. 4). The Padé approximant and the LDM formula agree, except for the smallest clusters ( $N \leq 8$ ). For  $N = 1$ , the Padé formula reproduces the quantal energy; recall that  $N$  is the number of valence electrons and not the number of atoms. The ionization energies of stabilized jellium (Fig. 5) are bigger than those of jellium, although the peak structure is the same. For  $N \geq 12$ , our results agree with experiment.

In the case of Cs (Figs. 6 and 7), the nonbulk binding energies  $E/N - a_v$  and the ionization energies of stabilized jellium are below those of jellium. As expected, a negative value of  $\langle \delta v \rangle_{ws}$  (as in Al) increases the nonbulk binding energy  $E/N - a_v$ , the ionization energy, and the amplitude of  $\Delta_2(N)$  oscillations, while a positive value (as in Cs) has the opposite effects.

The cohesive energy is the energy difference between the free atom and an atom in the bulk. It can be written as

$$\epsilon_{coh} = -a_v z + E(N = z), \quad (3.1)$$

where  $z$  is the valence of the atom. This quantity can be read directly from Figures 1, 4, and 6. Table III gives values for the cohesive energy of stabilized and ordinary jellium, in different approximations.

In the case of Al, an atom of stabilized jellium is a cluster with  $\langle \delta v \rangle_{ws}$  constructed from an effective valence  $z^* = 1$ , but with  $N = 3$  electrons (real valence). We have also included in Table III the case  $N = 1$ , since this provides a fair test of the LDM and Padé formulas.

We see from Table III that stabilization of jellium drastically improves the cohesive energy of Al, in comparison with experiment. Table III also shows that the Padé successfully predicts the LSD cohesive energies of monovalent metals ( $N = 1$ ); the

discrepancy for  $N = 3$  may be attributed to shell effects. Our LDA values agree with the "ideal metal" results of Rose and Shore [18]. The surface and cohesive properties of the ideal metal are the same as those of stabilized jellium; the small difference we find arises from the use of a different correlation energy. We note that the LDA cohesive energies are close to experimental ones. However, this close agreement is due to a cancellation of errors between the LDA and the stabilized jellium approximation. The *exact* cohesive energy for monovalent stabilized jellium is given by the self-interaction correction (SIC) [19], and is smaller than the LSD value.

### Conclusions

We have analyzed the properties of small clusters of stabilized jellium. Stabilized jellium is similar to the pseudojellium model of Utreras-Díaz and Shore [20], but unlike the latter it does not use phenomenological information other than the density. Binding energies, ionization energies, second-order energy differences, and cohesive energies have been calculated. The shell structure is essentially the same for ordinary and stabilized jellium. The various measures of stability tend to agree. The cohesive energies are more realistic in the stabilized jellium model than in the ordinary one, particularly for Al.

Future work with stabilized jellium could investigate different breakup channels for charged clusters (a problem which has been studied within the ordinary jellium model [14]), self-compression effects (since a cluster should have a central density bigger than the bulk value [5]), large clusters (e.g., the analysis of supershells [21]), and the static and optical response of clusters.

### Acknowledgments

The work of two of the authors (C.F. and J.P.) was supported by NATO collaborative research Grant 910623. That of one of the authors (J.P.) was supported by the U.S. National Science Foundation under Grant DMR92-13755. C.F. acknowledges a travel grant from the Calouste Gulbenkian Foundation, which made possible the presentation of this work at the 1993 Sanibel Meeting.

### Bibliography

- [1] J. P. Perdew, H. Q. Tran, and E. D. Smith, *Phys. Rev.* **B42**, 11627 (1990).
- [2] W. de Heer, W. Knight, M. Chou, and M. Cohen, *Solid State Physics*, Vol. 40, H. Ehrenreich and O. Turnbull, Eds. (Academic, New York, 1987), p. 93.
- [3] M. Brack, *Rev. Mod. Phys.* (1993), to appear in July.
- [4] W. de Heer, *Rev. Mod. Phys.* (1993), to appear in July.
- [5] J. P. Perdew, C. Fiolhais, and M. Bralczevska, unpublished.
- [6] J. P. Perdew, P. Ziesche, and C. Fiolhais, *Phys. Rev.* **B47** (1993).
- [7] S. H. Vosko, L. Wilk, and M. Nusair, *Can. J. Phys.* **58**, 1200 (1980).
- [8] C. Fiolhais and J. P. Perdew, *Phys. Rev.* **B45**, 6207 (1992).
- [9] A. Kiejna, *Phys. Rev.* **B47**, 7361 (1993).
- [10] J. P. Perdew, in *Condensed Matter Theories*, Vol. 4, J. Keller, Ed. (Plenum, NY, 1989).
- [11] D. R. Snider and R. S. Sorbello, *Solid State Comm.* **47**, 845 (1983).
- [12] D. E. Beck, *Solid State Comm.* **49**, 381 (1984).

- [13] P. Ballone, C. J. Umrigar, and P. Delaly, *Phys. Rev.* **B45**, 6293 (1992).
- [14] Y. Ishii, S. Ohnishi, and S. Sugano, *Phys. Rev.* **B33**, 5271 (1986).
- [15] U. Röthlisberger and W. Andreoni, *J. Chem. Phys.* **94**, 8129 (1991).
- [16] R. O. Jones, *Phys. Rev. Lett.* **67**, 224 (1991).
- [17] W. Ekardt and Z. Penzar, *Phys. Rev.* **B38**, 4273 (1988).
- [18] J. H. Rose and H. B. Shore, *Phys. Rev.* **B43**, 11605 (1991).
- [19] J. P. Perdew and A. Zunger, *Phys. Rev.* **B23**, 5048 (1981).
- [20] C. A. Utreras-Diaz and H. B. Shore, *Phys. Rev.* **B40**, 10345 (1989).
- [21] J. Meyer, unpublished.
- [22] M. M. Kappes, M. Schär, U. Rothlisberger, Ch. Yeretzian, and E. Schumacher, *Chem. Phys. Lett.* **143**, 251 (1988).
- [23] M. F. Jarrold, J. E. Bower, and J. S. Kraus, *J. Chem. Phys.* **86**, 3876 (1987).

Received April 29, 1993

# Density-Functional and *Ab Initio* Computational Studies of Palladium Clusters

JORGE M. SEMINARIO, MONICA C. CONCHA, and PETER POLITZER

*Department of Chemistry, University of New Orleans, New Orleans, Louisiana 70148*

## Abstract

Nonlocal density-functional and correlated *ab initio* methods have been used to compute singlet-triplet separations for the Pd atom and Pd<sub>2</sub>, as well as the dissociation energies of the latter in its ground and first excited states. The results are in good agreement with the available experimental data and with other high-level calculations. Single-point local density-functional computations were carried out for Pd clusters up to Pd<sub>22</sub> (1012 electrons). The interaction energy per Pd— bond appears to be approaching a limiting value for Pd<sub>22</sub>. © 1993 John Wiley & Sons, Inc.

## Introduction

We are interested in applying density-functional theory (DFT) to small clusters of transition metal atoms. One of our objectives is to determine how large a cluster is needed to realistically simulate a metal surface, in order to permit the investigation of chemisorption and catalytic processes; and to determine the ground state atomic and electronic structure of small transition metal clusters.

In the present work, we have focused specifically upon palladium, and have proceeded on two levels: (a) We have compared sophisticated nonlocal DFT and *ab initio* methods in computing the singlet-triplet separations for the palladium atom and the Pd<sub>2</sub> molecule, as well as the bond length and dissociation energy of the latter in each state; and (b) we have used a local DFT approach to carry out single-point runs on clusters as large as Pd<sub>22</sub> (1012 electrons).

## Methods

Density-functional theory [1–4], as it has been applied in this investigation, is based on the Hohenberg–Kohn theorem [5] and the Kohn–Sham procedure [6]. In the latter, the total energy of an N-electron system (as would be obtained by solving the Schrödinger equation exactly) is found by minimizing, with respect to the electronic density  $\rho(\mathbf{r})$ , the total energy functional  $E[\rho]$ ,

$$E[\rho] = \int v_{\text{ext}}(\mathbf{r})\rho(\mathbf{r}) d\mathbf{r} + T_s[\rho] + V_{\text{class}}[\rho] + E_{\text{xc}}[\rho]. \quad (1)$$

$V_{\text{ext}}(\mathbf{r})$  is the external potential due to the nuclei,  $T_s[\rho]$  is the kinetic energy of a hypothetical set of non-interacting electrons having the same density  $\rho(\mathbf{r})$  as the



system under consideration, and  $V_{\text{class}}[\rho]$  is the classical energy calculated using the density  $\rho(\mathbf{r})$ .

$$V_{\text{class}}[\rho] = \frac{1}{2} \int \frac{\rho(\mathbf{r})\rho(\mathbf{r}') d\mathbf{r} d\mathbf{r}'}{|\mathbf{r} - \mathbf{r}'|} \quad (2)$$

The exchange–correlation functional,  $E_{\text{xc}}[\rho]$ , is expressed exactly in terms of the adiabatic connection variable  $\lambda$  by Eq. (3):

$$E_{\text{xc}}[\rho] = \int_0^1 \langle \Psi_\lambda | V_{\text{ee}} | \Psi_\lambda \rangle d\lambda - V_{\text{class}}[\rho]. \quad (3)$$

The functions  $\Psi_\lambda$  are the solutions of,

$$\hat{H}_\lambda \Psi_\lambda = E_\lambda \Psi_\lambda \quad (4)$$

where,

$$\hat{H}_\lambda = \hat{T} + \hat{v}_\lambda + \lambda \hat{V}_{\text{ee}}. \quad (5)$$

In Eq. (5), the electron–electron interaction operator,  $\hat{V}_{\text{ee}}$ , is linearly scaled from zero to one by the variable  $\lambda$  in a manner such that  $\nu_\lambda$  yields the same  $\rho(\mathbf{r})$  for any  $\lambda$  in the interval  $[0,1]$ . (According to the Hohenberg–Kohn theorem, the potential determines the density [5].)

The energy quantity  $E_{\text{xc}}$  as given by Eq. (3) is clearly not equivalent to the sum of the exchange and correlation energies as defined in *ab initio* formalism. Unfortunately, the expression for  $E_{\text{xc}}[\rho]$  in Eq. (3) can only be evaluated in special cases. One of these is an uniform electron gas (jellium), for which exact ground-state solutions have been obtained by stochastic simulations [7], from which functionals have been constructed, primarily by fitting procedures [8]. These functionals correspond to the local density approximation. First-order corrections can be made using gradients of the density, resulting in so-called nonlocal approximations [1,2].

For the Pd atom and for  $\text{Pd}_2$ , we have used the sophisticated nonlocal exchange–correlation functional of Perdew and Wang, the generalized-gradient approximation (GGA) [11,12]. This was developed entirely from first principles, and has no fitted parameters. We have recently coded this functional into the DFT program deMon [13,14]. The single-point runs on Pd clusters were carried out with the DFT program DMol [15], which uses a local-density approximation [16]. We have used the standard double numerical (DN) basis set. The *ab initio* results that we report were obtained with Gaussian 92 [17].

## Results

### Pd Atom

The standard deMon Gaussian DZVPP basis set for Pd, (18s, 12p, 9d) contracted to (6s, 5p, 3d), yields a singlet–triplet separation of 33.5 kcal/mol, which differs considerably from the experimental 18.8 kcal/mol [18]. Accordingly we used Huzinaga's (17s, 11p, 8d) basis set [19], uncontracted, to compute the singlet–triplet

separation by both *ab initio* and DFT procedures. The two DFT calculations were carried out with the Perdew-Wang  $E_{xc}[\rho]$  functionals GGA-PW86 [9,10] and GGA-PW91 [11,12]. The results are in Table I.

Most of the *ab initio* correlated results and both of the DFT are within 3 kcal/mol of the experimental value. It is seen that the effect of including the core electrons can be quite significant, as much as 5.3 kcal/mol. It is relevant to mention that a QCI (full core) calculation was terminated after having used more than one hour of CPU time on a CRAY C-90 for only two iterations (out of possibly 15) of the triple substitutions; in contrast, the DFT calculations despite slow convergence (more than 1500 iterations for the triplet) required only about 10 min.

### *Pd<sub>2</sub>*

Initial results obtained with the DZVPP basis set were qualitatively incorrect, so we have continued with the Huzinaga [19]. Our computed bond lengths, total energies and dissociation energies for the triplet ground state and the first singlet excited state of  $Pd_2$  are given in Table II, as are the singlet-triplet separations,  $T_e$ . Experimental and other calculated data are also included. Our DFT-GGA-PW86 ground state dissociation energy and triplet-singlet separation are in good agreement with the MCSCF(CASSCF)MRSDCI results and with one of the experimental values for  $D_e$ .

### *Pd Clusters*

The Pd clusters that were investigated are shown in Figure 1. They were given geometries corresponding to the [111] surface of the metal, with the closest inter-

TABLE I. Calculated energies of the singlet ground state and first excited triplet state of the palladium atom, using the Huzinaga (17s, 11p, 8d) basis set.

Method	Singlet (hartrees)	Triplet (hartrees)	Separation (kcal/mol)
Hartree-Fock	-4937.79120	-4937.78582	3.4
MP2 (frozen core)	-4937.91174	-4937.87904	20.5
MP2 (full core)	-4938.75759	-4938.71649	25.8
MP3 (frozen core)	-4937.90090	-4937.87540	16.0
MP3 (full core)	-4938.68426	-4938.66039	15.0
MP4SDQ (frozen core)	-4937.90689	-4937.87748	18.5
MP4SDQ (full core)	-4938.71916	-4938.68446	21.7
QCISDt (frozen core)	-4937.90824	-4937.87999	17.7
DFT-GGA-PW86	-4940.67375	-4940.64130	20.4
DFT-GGA-PW91	-4940.66042	-4940.62611	21.5
Experimental <sup>a</sup>			18.8
MCSCF(CASSCF)/FOCI + RCI <sup>b</sup>			13.8

<sup>a</sup> Reference [18].

<sup>b</sup> Reference [20].

TABLE II. Results for the palladium dimer ground state triplet and first excited state singlet using the (17s, 11p, 8d) basis set.

Method	Triplet			Singlet			Separation $T_e$ (kcal/mol)
	Energy (hartrees)	$R_e$ (Å)	$D_e$ (kcal/mol)	Energy (hartrees)	$R_e$ (Å)	$D_e$ (kcal/mol)	
Hartree-Fock	-9875.57302	2.78	5.9				
MP2 (frozen core)	-9875.81501	2.46	-5.3	-9875.82866	2.9	3.3	-8.6
DFT-GGA-PW86	-9881.37740	2.62	18.8	-9881.36716	2.7, -2.8 <sup>d</sup>	12.3	6.4
Experimental <sup>a</sup>			16.9, 26.0				
MCSCF(CASSCF)MRSDCI <sup>b</sup>		2.48	19.6		2.87		3.6
DFT (model core potential) <sup>c</sup>		2.46	31.3		2.64	21.9	9.5

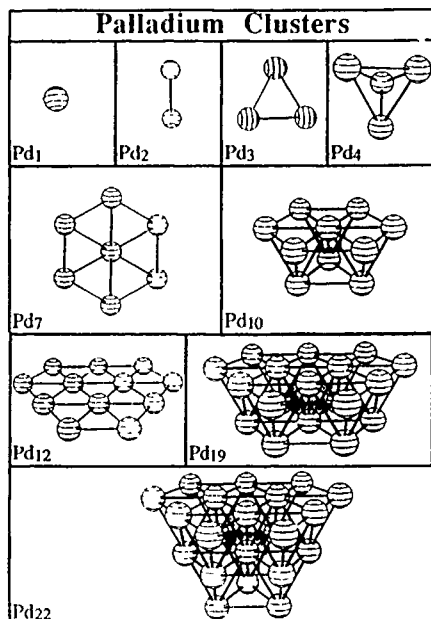
<sup>a</sup> Reference [21].<sup>b</sup> Reference [22].<sup>c</sup> Reference [23].<sup>d</sup> A very shallow minimum was obtained

Figure 1. Palladium clusters that were studied using a local density-functional theory approach.

TABLE III. Local density-functional theory results for palladium clusters.

Cluster	Number of Pd—Pd bonds	Energy (hartrees)	$\Delta E = E(\text{Pd}_n) - nE(\text{Pd})$		$\Delta E$ per Pd—Pd bond (kcal/mol)
			(hartrees)	(kcal/mol)	
Pd <sub>1</sub>	0	-4935.1926	-0.0	0.0	—
Pd <sub>2</sub>	1	-9870.4412	-0.056	-35.1	-35.1
Pd <sub>3</sub>	3	-14805.7079	-0.130	-81.6	-27.2
Pd <sub>4</sub>	6	-19741.0160	-0.2456	-154.1	-25.7
Pd <sub>7</sub>	12	-34546.8208	-0.4724	-296.5	-24.7
Pd <sub>10</sub>	24	-49352.7822	-0.8561	-537.2	-22.4
Pd <sub>12</sub>	24	-59223.2213	-0.9099	-571.0	-23.8
Pd <sub>19</sub>	57	-93770.5585	-1.8988	-1191.5	-20.9
Pd <sub>22</sub>	69	-108576.53	-2.29	-1438.5	-20.8

atomic distance in each case being set equal to the experimentally determined 2.75 Å [24]. The calculated total and interaction energies are given in Table III.

The dissociation energy of Pd<sub>2</sub> is predicted from Table III to be 35.1 kcal/mol, which is considerably greater than our DFT-GGA-PW86 value in Table II, 12.3 kcal/mol. This could reflect both the difference in bond length and also the well-known tendency of local-density approximations to overestimate dissociation energies [25-27]. However a key point that emerges from Table III is that the interaction energy per bond appears to be nearing a limiting value for Pd<sub>22</sub>. This suggests that clusters of this size may be reasonable models for a metal surface (including the underlying atoms).

### Discussion

We have demonstrated the feasibility of local density-functional calculations on systems having as many as 1012 electrons (Pd<sub>22</sub>). At the local/DN level, 660 basis functions are required for the latter computation. The total energy is in the neighborhood of -108576 hartrees. At this order of magnitude, the error in the energy due to the use of REAL\*8 precision is about 6 kcal/mol. The use of REAL\*16, which would solve the problem due to truncation in the floating point operations, is not practical because there are not commercial floating point processors of 128 bytes; accordingly the REAL\*16 arithmetic must be software-implemented. Machines like the CRAY YMP then require about 10 times more CPU time to process REAL\*16 operations. This is in addition to the inherent problem, in these Pd clusters, of a large number of low-lying states near the ground state, which makes the SCF convergence very slow and tedious. The convergence problem is independent of the program. On the CRAY YMP8-864, each SCF cycle required 764 seconds of CPU time; the number of cycles needed for a respectable energy was about 20, and much more for a good density. About 500 Mbytes of scratch disk space were required, which is not excessive in view of the size of the system.

Despite these figures, there is reason for optimism. With massively parallel computers, turn-around times are reduced by at least one order of magnitude. DFT

codes are more vectorizable than are *ab initio*, and run more efficiently by a factor of 3 to 5. This efficiency can be made much higher in massively parallel computers. DFT codes are still in development, and improvements can be anticipated.

### Acknowledgment

We thank Dr. Jane S. Murray for help in preparing this manuscript. We greatly appreciate the Pittsburgh Supercomputing Center for a grant to use the state-of-the-art Cray YMP C-90 where the deMon and Gaussian-92 programs were run, and the San Diego Supercomputing Center for a grant to use the Cray YMP-864 where the program DMol was run.

### Bibliography

- [1] E. S. Kryachko and E. Ludeña, *Energy Density Functional Theory of Many-Electron Systems* (Academic, New York, 1990).
- [2] R. M. Dreizler and E. K. U. Gross, *Density Functional Theory* (Springer-Verlag, Berlin, 1990).
- [3] R. G. Parr and W. Yang, *Density Functional Theory of Atoms and Molecules* (Oxford University Press, Oxford, 1989).
- [4] J. K. Labanowski and J. W. Andzelm, Eds., *Density Functional Methods in Chemistry* (Springer, New York, 1991).
- [5] P. Hohenberg and W. Kohn, *Phys. Rev.* **B136**, 864 (1964).
- [6] W. Kohn and L. J. Sham, *Phys. Rev.* **A140**, 1133 (1965).
- [7] D. M. Ceperley and B. J. Alder, *Phys. Rev. Lett.* **45**, 566 (1980).
- [8] S. H. Vosko, L. Wilk, and M. Nussair, *Can. J. Phys.* **58**, 1200 (1980).
- [9] J. P. Perdew, *Phys. Rev.* **B33**, 8822 (1986); **34**, 7406(E) (1986).
- [10] J. P. Perdew and Y. Wang, *Phys. Rev.* **B33**, 8800 (1986).
- [11] J. P. Perdew and Y. Wang, *Phys. Rev.* **B45**, 13244 (1992).
- [12] J. P. Perdew, J. A. Chevary, S. H. Vosko, K. A. Jackson, M. R. Pederson, D. J. Singh, and C. Fiolhais, *Phys. Rev.* **B46**, 6671 (1992).
- [13] A. St-Amant and D. R. Salahub, *Chem. Phys. Lett.* **169**, 387 (1990).
- [14] A. St-Amant, Ph.D. Thesis, Université de Montréal (1992).
- [15] B. Delley, *J. Chem. Phys.* **92**, 508 (1990).
- [16] U. von Barth and L. Hedin, *J. Phys.* **C5**, 1629 (1972).
- [17] Gaussian 92, Revision C, M. J. Frisch, G. W. Trucks, M. Head-Gordon, P. M. W. Gill, M. W. Wong, J. B. Foresman, B. G. Johnson, H. B. Schlegel, M. A. Robb, E. S. Replogle, R. Gomperts, J. L. Andres, K. Raghavachari, J. S. Binkley, C. Gonzalez, R. L. Martin, D. J. Fox, D. J. Defrees, J. Baker, J. J. P. Stewart, and J. A. Pople, Gaussian, Inc., Pittsburgh PA, 1992.
- [18] C. E. Moore, *Table of Atomic Energy Levels* (U.S. National Bureau of Standards, Washington, D.C., 1971).
- [19] S. J. Huzinaga, *Chem. Phys.* **66**, 4377 (1977).
- [20] Y. Sakai, H. Tatewaki, and S. J. Huzinaga, *Comput. Chem.* **2**, 278 (1982).
- [21] S. S. Lin, B. Strauss, and A. Kant, *J. Chem. Phys.* **51**, 2282 (1969).
- [22] K. Balasubramanian, *J. Chem. Phys.* **89**, 6310 (1988).
- [23] A. Goursot, I. Papai, and D. R. Salahub, *J. Am. Chem. Soc.* **114**, 7452 (1992).
- [24] Y. Kuk, L. C. Feldman, and P. J. Silverman, *Phys. Rev. Lett.* **50**, 511 (1983).
- [25] J. P. Perdew and A. Zunger, *Phys. Rev.* **B23**, 5048 (1981).
- [26] J. M. Seminario, M. C. Concha, and P. Politzer, *Int. J. Quantum Chem. S* **25**, 249 (1991).
- [27] O. Gunnarsson and R. O. Jones, *Phys. Rev.* **B31**, 7588 (1985).

Received March 15, 1993

# Multiconfigurational Spin-Adapted Single-Reference Coupled Cluster Formalism

X. LI and J. PALDUS\*

*Quantum Theory Group, Department of Applied Mathematics, University of Waterloo,  
Waterloo, Ontario, Canada N2L 3G1*

## Abstract

We exploit the unitary group formalism in formulating a multiconfigurational single-reference coupled cluster method for cases involving one or two electrons in open shells. The linear version of CCSD theory for the simple open shell case and for low lying singlet states of closed shell systems are considered in detail. The entire formalism is related to the unitary group based CISD method, and explicit expressions for size-extensivity corrections, leading to the L-CCSD formalism, are given. An illustrative example of the minimum basis set model of the BeH radical is also presented. © 1993 John Wiley & Sons, Inc.

## Introduction

The connected cluster structure of an exact wave function [1], describing a non-degenerate closed shell ground state, is well known from many-body perturbation theory (MBPT) (see, e.g., Ref. [2]). This result, often referred to as the connected cluster theorem [2] (in contrast to a better known linked cluster theorem), immediately implies the standard coupled cluster (CC) exponential Ansatz for the corresponding wave operator. This cluster Ansatz proved to be very useful when designing size extensive methods that efficiently account for many-electron correlation effects in atomic, molecular, and even in extended (solid state or polymer) systems.

An extension of the CC formalism to degenerate or quasidegenerate closed shell states, or in fact to general open shell systems, proved to be most exacting. Although the spin-not-adapted, single reference CC formalism exploiting the unrestricted Hartree-Fock (UHF) reference can often provide very useful results, even in open shell situations, it cannot be regarded as a *bona fide* theory in view of its inherent limitations (spin contamination of the resulting wave functions, inability to distinguish various components of more complex multiplet systems, nonanalytic behavior of potential energy hypersurfaces, etc.). It has been generally recognized that a proper account of quasidegeneracy effects requires a multireference (MR) version of a standard single reference (SR) approach, based on the effective Hamiltonian concept and the generalized Bloch equation. Two different types of generalized MR

---

\* Also at Department of Chemistry and Guelph-Waterloo Center for Graduate Work in Chemistry, Waterloo Campus, University of Waterloo, Waterloo, Ontario, Canada N2L 3G1.

CC Ansätze were proposed, leading, respectively, to the so-called valence universal or Fock space and state universal or Hilbert space MR CC approaches (see, e.g., Refs. [2-4]). While initially only various versions of the former approach were exploited in actual applications (see, e.g., Ref. [5]), lately the state universal formalism is also being explored [6-9]. Unfortunately, our knowledge of cluster structure in the general open shell case is very limited, in contrast to the closed shell case where the situation is much simpler, since this structure can considerably vary from case to case [e.g., states of different multiplicity, covalent vs. ionic type states in the sense of the valence bond (VB) theory, multiradicals or transition complexes far away from equilibrium geometry, etc.]. Nonetheless, it seems plausible that a satisfactory description may be achieved in most cases by considering only pair clusters with respect to each reference considered, as in the closed shell case, as long as a suitably large model space is employed. However, since a given configuration has generally a different excitation order with respect to different reference configurations, the truncation scheme for the MR approaches is much more complex than in SR methods and much has yet to be learned concerning this topic.

In any case, the available limited experience with MR CC approaches leaves little doubt that they are much more demanding than the SR methods, and the computational difficulties and complexity grow with the increasing dimensionality of the model space employed. For this reason, much attention has been paid to approaches based on incomplete model spaces [10,11] (it should be noted that practically all existing applications of valence universal approaches were carried out with incomplete model spaces and often with different ones for different geometries). Thus, for purely pragmatic reasons, it seems important to explore the capabilities of SR CC approaches employing an open shell—generally multideterminantal or multiconfigurational (MC)—reference. Such an approach naturally arises when we apply the SR CC formalism to a spin-adapted reference configuration, such as given, for example, by the electronic Gel'fand state of the unitary group approach (UGA) [12-16]. This approach can be particularly useful for various special cases, such as, e.g., the ground states of radicals (when in fact a single determinantal reference suffices) or the low-lying excited singlet or triplet states of molecules having a closed shell ground state. In designing this type of MC-SR open-shell CC theories, the UGA [12-16] or Clifford algebra UGA (CAUGA) [17] formalism may be very helpful [18-20], since a chosen reference may be simply characterized as an electronic Gel'fand state, a CAUGA VB-type state or yet another MC state, while the required cluster operator can be expressed in terms of unitary group  $U(n)$  generators or, more generally, in terms of replacement operators from a universal enveloping algebra of  $U(n)$ , forming the so-called external algebra [4,18-20]. The derivation of appropriate CC equations and of the energy expression then reduces to a repeated application of basic commutation rules for  $U(n)$  generators or replacement operators and the rules for the action of these operators on a reference state. One of the first exploitations of this idea [21] was recently encoded for the high-spin reference states by Janssen and Schaefer [22], who designed general symbol manipulation code (written in C) that generates the appropriate CC equations and automatically produces the required FORTRAN code. However, these authors employed the so-

called generator basis [15], which produces a set of nonorthogonal, overcomplete, and unnormalized states which, in our view, may lead to various divergence problems when iteratively solving CC equations. A similar program, based on the UGA-type MC-SR CC approach [23] and employing spin-adapted and orthonormal excited state manifold, was designed very recently and is currently being tested [24].

In this paper we shall present a preliminary description of our implementation of the CAUGA formalism in MC-SR CC approaches, concentrating on a few special—though very important—cases of simple open shell doublets and singlet and triplet excited states of closed shell systems. Following a brief outline of a general formalism in the next section, we illustrate our approach on the simplest open shell case at the linear level of approximation in the third section. The required explicit expressions for the open shell singlet case are also given in this section. An application of this level of theory to a simple minimum basis set (MBS) model of BeH may be found in the fourth section, and the conclusions concerning general MC-SR CC approaches that can be drawn at this stage are presented in the last section.

### Basic Formalism

In our implementation of the general MC-SR CC formalism, we first construct a set of excitation operators  $\{G_i\}$  that generate spin-adapted and orthonormal configurations when applied to the reference, namely,

$$|\Phi_i\rangle = G_i |\Phi_0\rangle, \quad \langle \Phi_i | \Phi_j \rangle = \delta_{ij}. \quad (1)$$

Since these operators generate spin-adapted configurations when acting on various states arising through the action of  $G_i$ 's and/or of a spin-independent Hamiltonian  $H$  on  $|\Phi_0\rangle$ , the whole formalism is spin-adapted and no spin-contamination can arise. The cluster Ansatz employed takes the standard SR form,

$$|\Psi\rangle = \exp(T) |\Phi_0\rangle, \quad (2)$$

and the cluster operator  $T$  is represented as a linear combination of excitation operators  $G_i$ ,

$$T = \sum_i t_i G_i, \quad (3)$$

where the  $t_i$  designate the corresponding cluster amplitudes. Note that, in general, with  $|\Phi_0\rangle$  representing an MC reference, the excitation order of each  $G_i$  is not well defined. Nonetheless, we have to truncate the connected cluster components in (3) at some reasonable level, namely, an essentially biexcited level, so that we obtain an approximation corresponding to the CCSD method of a standard SR case, when we use the approximation  $T = T_1 + T_2$ . Thus, in cases considered by us, there are at most two orbitals in  $|\Phi_0\rangle$  that are not doubly occupied (we shall refer to them loosely as active or valence orbitals in analogy with the general MR case). However, in contrast to the general MR situation, all active orbitals (though not the spin orbitals) are singly occupied in every configuration or Slater determinant constituting our MC reference  $|\Phi_0\rangle$ .



Thus, in our developments, we shall consider all genuine mono- and biexcitations from  $|\Phi_0\rangle$ , as well as the so-called pseudomono- and pseudobiexcitations involving core-active and active-virtual excitations. With this generalization in mind, we can again classify our approximations using the standard acronyms CCSD, CCSDT, etc., as in the SR case. Relying on UGA, we then express the excitation operators  $G_i$ , corresponding to single and double excitations from  $|\Phi_0\rangle$  in the above-mentioned generalized sense, in terms of linear combinations of  $U(n)$  generator products. Clearly, each reference  $|\Phi_0\rangle$  will require a specific definition of such an operator set.

We shall rely on a standard algebraic derivation (see, e.g., Refs. [2] and [4]) of SR CC equations, obtaining for the energy

$$E = \langle \Phi_0 | \exp(-T) H \exp(T) | \Phi_0 \rangle \quad (4a)$$

or

$$\begin{aligned} \Delta E = E - \langle \Phi_0 | H | \Phi_0 \rangle &= \langle \Phi_0 | [H, T] | \Phi_0 \rangle \\ &+ \frac{1}{2} \langle \Phi_0 | [[H, T], T] | \Phi_0 \rangle + \dots, \end{aligned} \quad (4b)$$

with the cluster amplitudes given by a solution of CC equations

$$a_i + \sum_j b_{ij} t_j + \frac{1}{2} \sum_{j,k} c_{ijk} t_j t_k + \dots = 0, \quad (5)$$

where the coefficients have the form

$$a_i = \langle \Phi_i | H | \Phi_0 \rangle = \langle \Phi_0 | G_i^\dagger H | \Phi_0 \rangle, \quad (6)$$

$$b_{ij} = \langle \Phi_i | [H, G_j] | \Phi_0 \rangle = \langle \Phi_0 | G_i^\dagger [H, G_j] | \Phi_0 \rangle, \quad (7)$$

$$c_{ijk} = \langle \Phi_i | [[H, G_j], G_k] | \Phi_0 \rangle = \langle \Phi_0 | G_i^\dagger [[H, G_j], G_k] | \Phi_0 \rangle, \quad \text{etc.} \quad (8)$$

Assuming that  $|\Phi_0\rangle$  represents the RHF reference for a given state, we can interpret  $\Delta E$ , Eq. (5), as the correlation energy for that state. Note also that the excited state manifold, onto which we project, is given as a linear span of configurations  $|\Phi_i\rangle$ ,  $i \neq 0$ , defined by excitation operators  $G_i$ ,  $|\Phi_i\rangle = G_i |\Phi_0\rangle$ . For the sake of brevity, we shall illustrate this formalism in the next section on the simplest possible case, involving one singly occupied orbital outside the closed shell, restricting ourselves to the linear level of the CC theory. The open shell singlet case (involving two active orbitals) was briefly described in Ref. [20] and the explicit expressions for the linear level of the theory are also given in the next section. A complete formulation for all three cases mentioned above will be given elsewhere.

### L-CCSD Formalism for Simple Open Shells

For the sake of brevity, we restrict ourselves to the linear form of CC theory. Thus, the development presented below parallels the recent work by Neogrády et al. [25], employing, however, a very different formalism. For near equilibrium geometries, the linear approach represents already a useful approximation. An ex-

tension of this approach to a fully quadratic case, as well as to other cases mentioned above, has been carried out [26] and is presently being tested.

When considering the linear approximation,

$$a_i + \sum_j b_{ij} t_j = 0, \quad (9)$$

we can evaluate the required coefficients  $a_i$  and  $b_{ij}$  either directly, using expressions (6) and (7), respectively, or we can exploit the relationship between the L-CCSD and CISD methods [2,27]. The latter approach has the advantage that we can exploit existing codes for various CISD implementations, not to mention a certain pedagogical value that indicates explicitly the corrections for unlinked cluster contributions that are present in the CISD approach, and are responsible for its lack of size extensivity. While no corrections arise for the absolute terms, Eq. (6), so that

$$a_i = H_{i0} = \langle \Phi_i | H | \Phi_0 \rangle, \quad (10)$$

we have for the linear coefficients that

$$b_{ij} = H_{ij} - \Delta_{ij}, \quad (11)$$

where  $H_{ij} = \langle \Phi_i | H | \Phi_j \rangle$  are standard CI matrix elements and  $\Delta_{ij}$  represent size extensivity corrections,

$$\Delta_{ij} = \langle \Phi_0 | G_i^\dagger G_j H | \Phi_0 \rangle. \quad (12)$$

Noting that the product  $G_i^\dagger G_j$  represents a linear combination of  $U(n)$  generator products of the type

$$E_{l_1}^{u_1} E_{l_2}^{u_2} \cdots E_{l_k}^{u_k}, \quad (13)$$

where the difference between the subscript and superscript index sets  $L \equiv \{l_1, l_2, \dots, l_k\}$  and  $U \equiv \{u_1, u_2, \dots, u_k\}$ , respectively, is uniquely determined by the given product  $G_i^\dagger G_j$ , we can give the size extensivity corrections  $\Delta_{ij}$  the following more explicit form. Since  $H$  involves at most two-body terms, the index sets  $U$  and  $L$  can differ in at most two orbital labels (cf., e.g., Ref. [4]), so that we can distinguish the following three nonvanishing cases:

(i)  $U = L$ , when

$$\Delta_{ij} = \langle \Phi_0 | H | \Phi_0 \rangle \delta_{ij} = E_0 \delta_{ij}. \quad (14)$$

(ii)  $U \Delta L = (U \cup L) \setminus (U \cap L) = \{u, l\}$ , when

$$\begin{aligned} \Delta_{ij} = & [f_l^u + (ll|lu)\delta_{l,n_l}] \langle \Phi_0 | G_i^\dagger G_j E_u^l | \Phi_0 \rangle \\ & + \sum_{m(\neq u,l)} (ml|mu) \langle \Phi_0 | G_i^\dagger G_j E_m^l E_u^m | \Phi_0 \rangle, \end{aligned} \quad (15)$$

where  $n_l$  is the occupation number of the  $l$ th orbital in  $\Phi_0$  and the sum over  $m$  extends over all singly occupied orbitals in  $\Phi_0$  that are distinct from  $u$  and  $l$ . Finally,

(iii)  $U \Delta L = \{u_1 = u, u_2 = v, l_1 = l, l_2 = k\}$ , when

$$\Delta_{ij} = [(1 + \delta_{uv})(1 + \delta_{lk})]^{-1} \mathcal{S}_{uv}(lu|kv) \langle \Phi_0 | G_i^\dagger G_j E_u^l E_v^k | \Phi_0 \rangle, \quad (16)$$

where  $\mathcal{S}_{uv}$  is a symmetrizer in  $u$  and  $v$  labels,

$$\mathcal{S}_{uv} = 1 + (uv), \quad (17)$$

with  $(uv)$  designating the transposition of  $u$  and  $v$ . Further, we defined that

$$f_i^u = z_i^u + \sum_m [n_m(mm|lu) - (ml|mu)], \quad (18)$$

with the sum extending over all orbitals occupied in  $|\Phi_0\rangle$  and  $z_i^u$  designating the one-electron integral  $\langle u|\hat{z}|l\rangle$ . Finally, we note that we employ here Mulliken notation for two electron integrals,  $(ij|kl) = \langle ik|\hat{v}|jl\rangle$ . Thus, once the excitation operators  $G_i$  are defined, we can calculate the size-extensivity corrections  $\Delta_j$  as mean values of multigenerator products in the reference state  $|\Phi_0\rangle$ . Indeed, this is the case for all coefficients arising in CC equations, as Eqs. (6)–(8) indicate. The explicit expressions for these quantities in terms of cluster amplitudes and one- and two-electron integrals can be worked out either "by hand" or with the help of a computer program. Our results, including those shown below, were obtained in both ways.

As mentioned above, we shall present the relevant excitation operators  $G_i$  and the corresponding correction terms  $\Delta_j$  for the simple open shell case, i.e., for a doublet state with one electron outside the closed shell. Thus, schematically, we have that

$$|\Phi_0\rangle = |[core]\phi_p\rangle. \quad (19)$$

Obviously, there is a great flexibility in defining the excitation operators  $G_i$ , since our singly and doubly excited configurations involve, generally, three and five singly occupied orbitals and we are free to choose any coupling scheme we like. In view of the fact that we are using the CI–CC connection, as well as UGA formalism, to formulate the L-CCSD equations, we shall systematically employ the Gel'fand–Tsetlin basis and thus define our excitation operators in such a way that they produce electronic Gel'fand states when acting on our reference configuration. In this way the existing CI programs, employing Gel'fand–Tsetlin basis, can be simply modified to obtain L-CCSD formalism once the corrections  $\Delta_j$  are known.

To simplify our notation, we designate core orbitals by the letters from the beginning of the alphabet, i.e., as  $a, b, c$ , etc., while reserving the letters  $r, s, t$ , etc. from the end of the alphabet for virtual orbitals. The only valence (active) orbital is labeled by  $p$  as already indicated in Eq. (19). Moreover, we shall assume that our reference  $|\Phi_0\rangle$ , Eq. (19), represents an ROHF wave function and that the SCF orbitals are numbered in the order [core] [virtual] [active]. The desired excitation operators then take the form:

(i) Single and pseudosingle excitations:

$$G_p^r = E_p^r, \quad (20a)$$

$$G_a^p = -E_a^p, \quad (20b)$$

$${}^mG_a^r = \begin{cases} (1/\sqrt{2})E_a^r & (m=1), \\ (1/\sqrt{6})(E_a^r E_p^r + E_p^r E_a^r) & (m=3). \end{cases} \quad (20c)$$

Here and in the following, the intermediate spin multiplicity, designated by  $m$  ( $m = 1, 3$ ), is employed to label different components of the same multiplet.

(ii) Double and pseudodouble excitations:

$${}^m G_{ab}^p = (-1)^{\delta_{ab}+1} {}^m \mathcal{S}_{ab} E_a^p E_b^r / \sqrt{2m(1+\delta_{ab})} \quad (m = 1 \text{ for } a = b; m = 1, 3 \text{ for } a < b), \quad (20d)$$

$${}^m G_{ap}^r = (-1)^{\delta_{ap}+1} \sqrt{1+\delta_r} [E_a^r E_p^s + (m-1)E_a^s E_p^r] / \sqrt{2m} \quad (m = 1 \text{ for } r = s; m = 1, 3 \text{ for } r < s), \quad (20e)$$

$${}^1 G_{aa}^r = \frac{1}{2} E_a^r E_a^r, \quad (20f)$$

$${}^m G_{aa}^s = \begin{cases} (1/\sqrt{2}) E_a^s E_a^s & (m = 1) \\ -(1/\sqrt{6}) {}^3 \mathcal{S}_r E_a^p E_p^r E_a^s & (m = 3) \end{cases} \quad (20g)$$

$${}^m G_{ab}^n = \begin{cases} -(1/\sqrt{2}) E_a^r E_b^r & (m = 1) \\ -(1/\sqrt{6}) {}^3 \mathcal{S}_{ab} E_a^p E_p^r E_b^r & (m = 3) \end{cases} \quad (20h)$$

$${}^m G_{ab}^r = \begin{cases} -\frac{1}{2} {}^1 \mathcal{S}_{ab} E_a^r E_b^r & (m = 1) \\ (1/2\sqrt{3}) {}^3 \mathcal{S}_r {}^1 \mathcal{S}_{ab} E_a^p E_p^r E_b^r & (m = 2) \\ (1/2\sqrt{3}) {}^3 \mathcal{S}_{ab} E_a^r E_b^r & (m = 3) \\ (1/6) {}^3 \mathcal{S}_{ab} (E_a^r E_b^r + 2E_a^r E_b^p E_p^r) & (m = 4) \\ (1/6\sqrt{2}) {}^3 \mathcal{S}_{ab} (-E_a^r E_b^r + E_a^r E_b^p E_p^r + 3E_a^s E_b^p E_p^r) & (m = 5) \end{cases} \quad (20i)$$

In the last case, when five singly occupied orbitals are involved, we distinguish the five resulting doublets by the superscript  $m$ ,  $m = 1, 2, 3, 4, 5$ . The spin-adapted symmetrizer  ${}^m \mathcal{S}_{ij}$  is defined as

$${}^m \mathcal{S}_{ij} = 1 + (2 - m)(ij) \quad (m = 1, 3). \quad (21)$$

The corrections  $\Delta_{ij}$ , associated with excitation operators (20), are given in Table I, while the required coefficients, appearing in these expressions, may be found in Tables II and III. It should be noted that these expressions reflect the symmetry that is involved in the excitation operators employed. Consider, for example, the most complicated case of doubly excited states involving five open-shell orbitals,  $|{}^m \Phi_{ab}^r\rangle = {}^m G_{ab}^r |\Phi_0\rangle$ . The resulting five doublets may be characterized by the following Young or Weyl tableaux

$$\begin{array}{|c|c|} \hline 1 & 2 \\ \hline 3 & 4 \\ \hline 5 & \\ \hline \end{array} \quad \begin{array}{|c|c|} \hline 1 & 2 \\ \hline 3 & 5 \\ \hline 4 & \\ \hline \end{array} \quad \begin{array}{|c|c|} \hline 1 & 3 \\ \hline 2 & 4 \\ \hline 5 & \\ \hline \end{array} \quad \begin{array}{|c|c|} \hline 1 & 3 \\ \hline 2 & 5 \\ \hline 4 & \\ \hline \end{array} \quad \begin{array}{|c|c|} \hline 1 & 4 \\ \hline 2 & 5 \\ \hline 3 & \\ \hline \end{array} \quad (22)$$

where, for greater simplicity, we designated the singly occupied orbitals  $a, b, r, s$ , and  $p$  by 1, 2, 3, 4, and 5. The symmetry, or transformation properties, of these states with respect to transpositions ( $ab$ ) and ( $rs$ ) of core and virtual orbitals, respectively, are summarized in Table IV. Note that the symbol [31] implies the transformation property characterized by [31] partition, namely,

TABLE I Size extensivity correction term  $\Delta_{ij}$  for the simple open shell doublet case <sup>a</sup>

$G_i$	$G_j$	$\Delta_{ij}$	Footnote
${}^m G_{aa}^t$	$G_p^t$	$\sqrt{m/2} [f_a^p + \langle ap pp\rangle]$	
	$G_a^p$	$(2-m)\sqrt{m/2} f_p^t$	
${}^m G_{ab}^{tp}$	$G_p^t$	$N_{ab} \sqrt{m/2} [f_b^t - (2-m)\langle bp rp\rangle]$	b
	${}^n G_a^t$	$N_{ab} \alpha_{mn} [f_b^t + \langle bp pp\rangle]$	b
${}^m G_{ap}^{ts}$	$G_p^t$	(i) $t = r = s$ : $-[f_a^s + 2\langle ap rp\rangle]$ (ii) $t = r < s$ : $\sqrt{m/2}[(m-2)f_a^s + \langle ap sp\rangle]$ (iii) $t = s > r$ : $\sqrt{2}\delta_{m1} f_a^r + \sqrt{m/2}\langle ap rp\rangle$	
	${}^n G_a^t$	(i) $t = r = s$ : $-(1/\sqrt{2n})f_p^t$ (ii) $t = r < s$ : $\delta_{m1} (1/\sqrt{n})f_p^t$ (iii) $t = s > r$ : $(n-2)\alpha_{mr} f_p^t$	
${}^1 G_{aa}^{rr}$	$G_p^r$	$\langle ar ap\rangle$	
	$G_a^p$	$\langle ar rp\rangle$	
	${}^n G_a^r$	$\sqrt{n/2} [2\delta_{n1} f_a^r + (2-n)\langle ap rp\rangle]$	
	${}^1 G_{aa}^{rp}$	$f_p^r$	
	${}^1 G_{ap}^{rr}$	$-[f_a^p + \langle ap pp\rangle]$	
${}^m G_{aa}^{rs}$	$G_p^t$	$(2-m)\sqrt{m/2} \langle as up\rangle$	c
$(r < s)$	$G_a^p$	$\sqrt{m/2} [(2-m)\langle ar sp\rangle + \langle as rp\rangle]$	
	${}^n G_a^t$	$(2-m)[\delta_{mn} f_a^s - t_{mn}\langle ap sp\rangle]$	c
	${}^1 G_{aa}^{tp}$	$(2-m)\sqrt{m/2} f_p^t$	c
	${}^n G_{ap}^{rr}$	$(2-m)(n-2)t_{mn} [f_a^p + \langle ap pp\rangle]$	
${}^m G_{ab}^{rr}$	$G_p^r$	$-\sqrt{m/2} [(2-m)\langle ar bp\rangle + \langle ap br\rangle]$	
$(a < b)$	$G_a^p$	$-(2-m)\sqrt{m/2} \langle br rp\rangle$	b
	${}^n G_a^t$	$-\delta_{mn} f_b^r - (2-m)(2-n)(\sqrt{mn/2})\langle bp rp\rangle$	b
	${}^n G_{ab}^{rp}$	$\delta_{mn} (2-m) f_p^r$	
	${}^1 G_{ap}^{rr}$	$(2-m)\sqrt{m/2} [f_b^p + \langle bp pp\rangle]$	c
${}^m G_{ab}^{rs}$	$G_p^t$	(i) $t = r$ : $\sqrt{2} D_{m1} [\langle as bp\rangle + a_m \langle ap bs\rangle]$ (ii) $t = s$ : $\sqrt{2} C_{m1} [\langle ar bp\rangle + a_m \langle ap br\rangle]$ (i) $c = a$ : $\sqrt{2} a_m b_m [C_{m1} \langle br sp\rangle + D_{m1} \langle bs rp\rangle]$ (ii) $c = b$ : $\sqrt{2} \delta_{m1} [C_{m1} \langle ar sp\rangle + D_{m1} \langle as rp\rangle]$ (i) $c = a, t = r$ : $A_{mn} f_b^s + C_{mn} \langle bp sp\rangle$ (ii) $c = a, t = s$ : $B_{n,1n} f_b^s + D_{mn} \langle bp rp\rangle$ (iii) $c = b, t = r$ : $a_m [A_{mn} f_a^s + C_{mn} \langle ap sp\rangle]$ (iv) $c = b, t = s$ : $a_m [B_{mn} f_a^s + D_{mn} \langle ap rp\rangle]$	
	${}^n G_{ab}^{rp}$	(i) $t = r$ : $E_{mn} f_p^t$ (ii) $t = s$ : $F_{mn} f_p^t$	
	${}^n G_{ap}^{rs}$	(i) $c = a$ : $G_{mn} [f_b^s + \langle bp pp\rangle]$ (ii) $c = b$ : $a_m G_{mn} [f_a^s + \langle ap pp\rangle]$	

<sup>a</sup> We define  $N_{ab} = (-1)^{b_{ab}+1} \sqrt{1 + \delta_{ab}}$ .<sup>b</sup> When  $c = a$ . Symmetric to  $(a, b)$  when  $m = 1$  and antisymmetric to  $(a, b)$  when  $m = 3$ .<sup>c</sup> When  $t = r$ . Symmetric to  $(r, s)$  when  $m = 1$  and antisymmetric to  $(r, s)$  when  $m = 3$ .

TABLE II. Coefficients appearing in size extensivity correction terms  $\Delta_n$  of Tables I and V.

<i>n</i>	1		3	
	1	3	1	3
$t_{mn}$	-1	1	1	1
$l_{mn}$	-1/2	$\sqrt{3}/2$	$\sqrt{3}/2$	1/2
$\alpha_{mn}$	1/2	$-\sqrt{3}/2$	$-1/2\sqrt{3}$	1/2
$\tilde{\alpha}_{mn}$	1/2	$-\sqrt{3}/2$	$1/\sqrt{3}$	0
$\beta_{mn}$	1	0	$1/2\sqrt{3}$	1/2
$\tilde{\gamma}_{mn}$	-1/2	$\sqrt{3}/2$	$1/2\sqrt{3}$	1/2

$$(34) \begin{array}{|c|c|} \hline 1 & 3 \\ \hline 2 & 5 \\ \hline 4 & \\ \hline \end{array} = -\frac{1}{3} \begin{array}{|c|c|} \hline 1 & 3 \\ \hline 2 & 5 \\ \hline 4 & \\ \hline \end{array} + \frac{2\sqrt{2}}{3} \begin{array}{|c|c|} \hline 1 & 4 \\ \hline 2 & 5 \\ \hline 3 & \\ \hline \end{array} \quad (23)$$

and similarly for the last Young tableau in (22). We thus see immediately that the symmetry with respect to the transposition (*ab*) is represented by the coefficients  $a_m$  of Table III. To understand the symmetry with respect to the transposition of virtual orbitals, (*rs*), we define the following matrix T,

$$\mathbf{T} = \begin{bmatrix} 1 & 0 & 0 & 0 & 0 \\ 0 & -1 & 0 & 0 & 0 \\ 0 & 0 & -1 & 0 & 0 \\ 0 & 0 & 0 & -1/3 & 2\sqrt{2}/3 \\ 0 & 0 & 0 & 2\sqrt{2}/3 & 1/3 \end{bmatrix}. \quad (24)$$

TABLE III. Coefficients appearing in size extensivity correction terms  $\Delta_n$  of Tables I and V.<sup>a</sup>

<i>n</i>	1					3				
	1	2	3	4	5	1	2	3	4	5
$a_m$	1	1	-1	-1	-1					
$b_m$	1	-1	1	-1	-1					
$A_{mn}$	$-x_1$	0	$\lambda_2$	0	0	0	$x_1$	0	$x_3$	$-\lambda_4$
$B_{mn}$	$-\lambda_1$	0	$-\lambda_2$	0	0	0	$-\lambda_1$	0	$-\lambda_2$	0
$C_{mn}$	$-\lambda_5$	$-\lambda_6$	$\lambda_6$	$x_7$	0	$\lambda_6$	$-\lambda_5$	$\lambda_5$	$-\lambda_8$	$-\lambda_4$
$D_{mn}$	$-\lambda_5$	$\lambda_6$	$-\lambda_6$	$-\lambda_5$	1	$\lambda_6$	$\lambda_5$	$-\lambda_5$	$-\lambda_9$	$-\lambda_{10}$
$\tilde{C}_{mn}$	$-\lambda_5$	$-\lambda_6$	$\lambda_6$	$x_7$	0	$\lambda_6$	$\lambda_5$	$\lambda_5$	$x_8$	$-\lambda_{10}$
$\tilde{D}_{mn}$	$-\lambda_5$	$\lambda_6$	$-\lambda_6$	$-\lambda_5$	1	$\lambda_6$	$-\lambda_5$	$-\lambda_5$	$-\lambda_6$	0
$E_{mn}$	$\lambda_1$	$-x_2$	0	0	0	0	0	$x_1$	$-x_2$	0
$F_{mn}$	$\lambda_1$	$\lambda_2$	0	0	0	0	0	$-\lambda_1$	$x_1$	$-\lambda_4$
$G_{mn}$	$-\lambda_5$	$-\lambda_6$	$\lambda_6$	$\lambda_7$	0	$-\lambda_6$	$\lambda_5$	$-\lambda_5$	$\lambda_8$	$\lambda_4$

<sup>a</sup> The following definitions are used to simplify the table.  $x_1 = 1/\sqrt{2}$ ;  $\lambda_2 = \sqrt{3}/2$ ;  $x_3 = 1/\sqrt{6}$ ;  $\lambda_4 = 2/\sqrt{3}$ ;  $\lambda_5 = 1/2\sqrt{2}$ ;  $\lambda_6 = \sqrt{3}/2\sqrt{2}$ ;  $\lambda_7 = 3/2\sqrt{2}$ ;  $\lambda_8 = 1/2\sqrt{6}$ ;  $\lambda_9 = 5/2\sqrt{6}$ ;  $\lambda_{10} = 1/\sqrt{3}$ .

TABLE IV. Transformation properties of five doublets, characterized by Young tableaux, Eq. (22), with respect to transpositions (12) = (ab) and (34) = (rs).<sup>a</sup>

<i>m</i>	(12) = (ab)	(34) = (rs)
1	<i>S</i>	<i>S</i>
2	<i>S</i>	<i>A</i>
3	<i>A</i>	<i>A</i>
4	<i>A</i>	[31]
5	<i>A</i>	[31]

<sup>a</sup> *S* and *A* designate the symmetric and antisymmetric behavior, while [31] indicates the transformation property of [31] partition, Eq. (23). See the text for details.

as implied by Table IV and Eq. (23). It is then easily verified that the  $5 \times 2$  matrices  $\mathbf{A} = [A_{mn}]$ ,  $\mathbf{B} = [B_{mn}]$ , etc., with entries given in Table III, satisfy the following relations

$$\mathbf{TA} = \mathbf{B}, \quad \mathbf{TC} = \mathbf{D}, \quad \text{and} \quad \mathbf{TE} = \mathbf{F}. \quad (25)$$

The symmetry properties involved in the remaining  $\Delta_{ij}$  terms can be found in an analogous way.

At this stage it is worthwhile to observe that the above results immediately imply the size extensivity corrections for the closed shell case. The only possible one- and two-body excitation operators that arise in this case are  ${}^1G_a'$ ,  ${}^1G_{aa}''$ ,  ${}^1G_{aa}^r$ ,  ${}^1G_{ab}''$  and  ${}^mG_{ab}^r$  ( $m = 1, 3$ ). Thus, disregarding the cases involving other types of excitation operators and eliminating any integrals involving the active label  $p$ , we arrive at  $\Delta_{ij}$  corrections pertaining to the closed shell case. It is thus easily seen that besides the most important diagonal terms  $\Delta_{ii} = E_0$ , the only nonvanishing  $\Delta_{ij}$  terms arise between double and single excitation operators. Thus, for example, for  $G_i = {}^mG_{ab}^r$  and  $G_j = {}^1G_a'$ , we get

$$\Delta_{ij} = \langle \Phi_0 | ({}^mG_{ab}^r)^\dagger {}^1G_a' H | \Phi_0 \rangle = -(2 - m) \sqrt{m/2} f_b^i. \quad (26)$$

In this case, the result is symmetric with respect to transpositions (ab) and (rs) for  $m = 1$  and antisymmetric when  $m = 3$ . Note that when using RHF orbitals, all these correction terms vanish, since  $f_a^r = 0$  for any  $r$  and  $a$ . Finally, in the L-CCD case, the only nonvanishing correction terms are the diagonal ones,  $\Delta_{ii} = E_0$ .

The above-presented scheme may be easily—at least in principle—extended to other open shell cases, provided that we can define a suitable set of excitation operators. For the simplest open shell singlet case, describing low energy excited states of closed shell systems, the required set of excitation operator may be found in Ref. [20]. The size extensivity corrections  $\Delta_{ij}$  corresponding to this set of excitation operators is given in Table V. We have also formulated the same formalism for simple open-shell triplet states.

TABLE V. Size extensivity correction terms  $\Delta_\eta$  for the open shell singlet case.\*

$G_i$	$G_j$	$\Delta_\eta$	Footnote
$G_k^i$	$G_k^i$	$2[f_k^i + (k\bar{k} \bar{k}\bar{k})]$	
$G_a^k$	$G_a^k$	$-2[f_k^i + (k\bar{k} \bar{k}\bar{k})]$	
${}^mG_a^r$	$G_k^i$	$\phi_k^m \sqrt{m/2} [f_a^i + (ak kk) - (a\bar{k} k\bar{k})]$	
	$G_a^k$	$\phi_k^m \sqrt{m/2} [f_r^i + 2(k\bar{k} \bar{k}r)]$	
	$G_{ak}^i$	$\delta_{m,1} \sqrt{2} [f_k^i + (k\bar{k} k\bar{k})]$	
$G_{ab}^{pq}$	$G_c^i$	$N_{ab} [f_c^i + (b\bar{c} \bar{k}\bar{k}) - (bk k\bar{k})]$	b
$G_{pq}^r$	$G_k^i$	$\sqrt{1 + \delta_{rs}} [f_s^i + 2(sk k\bar{k})]$	c
$G_{ak}^i$	$G_k^i$	$-[f_k^i + (a\bar{k} \bar{k}\bar{k}) - (ak k\bar{k})]$	
	$G_a^k$	$f_r^i + 2(k\bar{k} r\bar{k})$	
	${}^nG_a^r$	$\sqrt{2/n} [f_k^i + (k\bar{k} \bar{k}\bar{k})]$	
${}^mG_{ab}^k$	$G_k^i$	$(-1)^{k\omega} \delta_{m,1} \sqrt{2/(1 + \delta_{ab})} [(ak b\bar{k}) + (a\bar{k} bk)]$	
	$G_c^i$	$N_{ab} \sqrt{m/2} [f_r^i - (2 - m)(bk rk) + 2\delta_{m,1}(b\bar{k} r\bar{k})]$	d
	$G_c^i$	$N_{ab} \sqrt{m/2} [(bk r\bar{k}) - 2(br k\bar{k})]$	d
	${}^nG_c^r$	$\phi_k^r (-1)^{k\omega} \sqrt{1 + \delta_{ab}} \tilde{\alpha}_{mn} [f_k^i + (bk kk) - (b\bar{k} k\bar{k})]$	d
	$G_{ab}^{pq}$	$\delta_{m,1} (1/\sqrt{2}) [f_r^i + 2(rk k\bar{k})]$	
	${}^nG_{ab}^k$	$-\delta_{mn} 2 [f_k^i + (k\bar{k} k\bar{k})]$	
	$G_{ck}^i$	$(N_{ab}/\sqrt{2}) \tilde{\alpha}_{m,1} [f_k^i + (b\bar{k} \bar{k}\bar{k})] - (bk k\bar{k})]$	d
${}^mG_{ak}^r$	$G_k^i$	$-[f_r^i + 2(ak rk) - (a\bar{k} r\bar{k})]$	e
		$\sqrt{2} [\tilde{\gamma}_{m,1} f_s^i + \sqrt{m/2} (ak sk) - \tilde{\beta}_{m,1} (a\bar{k} s\bar{k})]$	f
		$\sqrt{2} [\tilde{\beta}_{m,1} f_r^i + \sqrt{m/2} (ak rk) - \tilde{\gamma}_{m,1} (a\bar{k} r\bar{k})]$	g
	$G_k^i$	$-[2(ar k\bar{k}) - (a\bar{k} rk)]$	e
		$\sqrt{2} \tilde{\gamma}_{m,1} [2(as k\bar{k}) - (a\bar{k} sk)]$	f
		$\sqrt{2} \tilde{\beta}_{m,1} [2(ar k\bar{k}) - (a\bar{k} rk)]$	g
	$G_a^k$	$-\sqrt{m} (1 + \delta_{rs})/2 [(rk s\bar{k}) + (r\bar{k} sk)]$	
	${}^nG_a^r$	$-\sqrt{2} \tilde{\alpha}_{1n} [f_r^i + 2(k\bar{k} r\bar{k})]$	e
		$\tilde{\beta}_{mn} [f_s^i + 2(k\bar{k} s\bar{k})]$	f
		$\tilde{\gamma}_{mn} [f_r^i + 2(k\bar{k} r\bar{k})]$	g
	$G_{pq}^r$	$(1 + \delta_{rs})/2 \sqrt{m/2} [f_k^i + (a\bar{k} \bar{k}\bar{k}) - (ak k\bar{k})]$	
	${}^nG_{ak}^r$	$\delta_{mn} 2 [f_k^i + (k\bar{k} \bar{k}\bar{k})]$	
	$G_{ak}^i$	$(-1/2) [f_r^i + 2(k\bar{k} rk)]$	e
		$(1/\sqrt{2}) \tilde{\beta}_{m,1} [f_s^i + 2(k\bar{k} sk)]$	f
		$(1/\sqrt{2}) \tilde{\gamma}_{m,1} [f_r^i + 2(k\bar{k} rk)]$	g
${}^1G_{aa}^r$	$G_k^i$	$(ar ak)$	
	$G_a^k$	$(ar rk)$	
	${}^nG_a^r$	$\sqrt{n/2} [\delta_{n,1} 2 f_r^i + (2 - n)(ap rp) + (aq rq)]$	
	$G_{aa}^{rr}$	$-\sqrt{2} (rp rq)$	
	$G_{pq}^{rr}$	$\sqrt{2} (ap aq)$	
	${}^1G_{aa}^k$	$[f_r^i + 2(r\bar{k} k\bar{k})]$	
	${}^1G_{ak}^r$	$-[f_k^i + (ak kk) - (a\bar{k} k\bar{k})]$	
	$G_{ak}^i$	$[2(ar k\bar{k}) - (ak r\bar{k})]$	
${}^mG_{aa}^r$	$G_k^i$	$\phi_k^m \sqrt{m/2} (as ak)$	h
$(r < s)$	$G_a^k$	$\phi_k^m \sqrt{m/2} [(2 - m)(ar sk) + (as rk)]$	
	${}^nG_a^i$	$(2 - m) \{ \delta_{mn} f_s^i + \epsilon_{mn} \epsilon_{mn} [(2 - n)(2 - m)(ap sp) + (aq sq)] \}$	h

(Continued)



TABLE V. (Continued)

$G_i$	$G_j$	$\Delta_{ij}$	Footnote
	$G_{aa}^{pa}$	$-\delta_{m1}\{(rp sq) + (rq sp)\}$	
	$G_{pq}^{pa}$	$\delta_{m1}\sqrt{2}(ap aq)$	
	${}^1G_{aa}^{ik}$	$\phi_k^m\sqrt{m/2}[f_s^k + 2(s\bar{k} k\bar{k})]$	<sup>h</sup>
	${}^nG_{ak}^{pa}$	$\phi_k^m(2-n)t_{mn}[f_k^a + (ak kk) - (a\bar{k} k\bar{k})]$	
	$G_{ak}^{ia}$	$\delta_{m1}(1/\sqrt{2})[2(as k\bar{k}) - (ak s\bar{k})]$	<sup>h</sup>
${}^mG_{ah}^{ra}$	$G_k^i$	$-\phi_r^m\sqrt{m/2}[(2-m)(ar bk) + (ak br)]$	
$(a < b)$	$G_c^i$	$-\phi_k^m\sqrt{m/2}(br rk)$	<sup>d</sup>
	${}^nG_c^i$	$-(\delta_{mn}f_r^b + t_{mn}t_{mn}[(2-n)(2-m)(bp rp) + (bq rq)])$	<sup>d</sup>
	$G_{ab}^{pq}$	$-\delta_{m1}\sqrt{2}(rp rq)$	
	$G_{pq}^{ra}$	$-\delta_{m1}[(ap bq) + (aq bp)]$	
	${}^nG_{ab}^{rk}$	$\phi_k^m\delta_{mn}[f_r^k + 2(r\bar{k} k\bar{k})]$	
	${}^1G_{ck}^{ra}$	$\phi_k^m\sqrt{m/2}[f_k^k + (bk kk) - (b\bar{k} k\bar{k})]$	<sup>d</sup>
	$G_{ck}^{rk}$	$-\delta_{m1}(1/\sqrt{2})[2(br k\bar{k}) - (bk r\bar{k})]$	<sup>d</sup>
${}^mG_{ah}^{ra}$	$G_k^i$	$\eta_k^m\sqrt{2}\hat{C}_{m1}(as bk) + a_m(ak bv)]$	<sup>f</sup>
		$\eta_k^m\sqrt{2}\hat{D}_{m1}(ar bk) + a_m(ak br)]$	<sup>g</sup>
	$G_c^k$	$\eta_k^m\sqrt{2}a_m[\hat{D}_{m1}(br sk) + \hat{C}_{m1}(bv rk)]$	<sup>i</sup>
		$\eta_k^m\sqrt{2}[\hat{D}_{m1}(ar sk) + \hat{C}_{m1}(as r\bar{k})]$	<sup>j</sup>
	${}^nG_c^i$	$A_{mn}f_s^b + \hat{C}_{mn1}(bp sp) + (2-n)b_m(bq sq)]$	<sup>if</sup>
		$B_{mn}f_r^b + \hat{D}_{mn1}(bp rp) + (2-n)b_m(bq rq)]$	<sup>ig</sup>
		$a_m\{A_{mn}f_s^a + \hat{C}_{mn1}(ap sp) + (2-n)b_m(aq sq)]\}$	<sup>jf</sup>
		$a_m\{B_{mn}f_r^a + \hat{D}_{mn1}(ap rp) + (2-n)b_m(aq rq)]\}$	<sup>ig</sup>
	$G_{ab}^{pq}$	$-\delta_{m1}\{(rp sq) + (rq sp)\}$	
	$G_{pq}^{pa}$	$-\delta_{m1}[(ap bq) + (aq bp)]$	
	${}^nG_{ab}^{ik}$	$\eta_k^m E_{mn}[f_s^k + 2(s\bar{k} k\bar{k})]$	<sup>f</sup>
		$\eta_k^m F_{mn}[f_r^k + 2(r\bar{k} k\bar{k})]$	<sup>g</sup>
	${}^nG_{ck}^{ra}$	$\eta_k^m G_{mn}[f_k^k + (bk kk) - (b\bar{k} k\bar{k})]$	<sup>i</sup>
		$\eta_k^m a_m G_{mn}[f_k^a + (ak kk) - (a\bar{k} k\bar{k})]$	<sup>j</sup>
	$G_{ck}^{rk}$	$A_{m1}[2(bv k\bar{k}) - (bk s\bar{k})]$	<sup>if</sup>
		$a_m A_{m1}[2(br k\bar{k}) - (bk r\bar{k})]$	<sup>ig</sup>
		$a_m A_{m1}[2(as k\bar{k}) - (ak s\bar{k})]$	<sup>jf</sup>
		$A_{m1}[2(ar k\bar{k}) - (ak r\bar{k})]$	<sup>ig</sup>

\* The label  $k$  designates either  $p$  or  $q$  open shell orbitals. We also use a convention that  $\bar{k} = q$  when  $k = p$  and  $\bar{k} = p$  when  $k = q$ . The phase factors  $\phi_k^m$  and  $\eta_k^m$  are defined as follows:  $\phi_p^m = 1$ ,  $\phi_q^m = (2-m)$ ;  $\eta_p^m = 1$ ,  $\eta_q^m = b_m$ . We also define  $N_{ab} = (-1)^{b+1}\sqrt{1 + \delta_{ab}}$ .

<sup>b</sup> When  $c = a$ . Symmetric to  $(a, b)$ .

<sup>c</sup> When  $t = r$ . Symmetric to  $(r, s)$ .

<sup>d</sup> When  $c = a$ . Symmetric to  $(a, b)$  when  $m = 1$  and antisymmetric to  $(a, b)$  when  $m = 3$ .

<sup>e</sup>  $t = r = s$ .

<sup>f</sup>  $t = r < s$ .

<sup>g</sup>  $t = s > r$ .

<sup>h</sup> When  $t = r$ . Symmetric to  $(r, s)$  when  $m = 1$  and antisymmetric to  $(r, s)$  when  $m = 3$ .

<sup>i</sup>  $c = a < b$ .

<sup>j</sup>  $c = b > a$ .



As we approach the dissociation limit, the L-CCSD approximation suffers a singular behavior at about 4 a.u., similarly as observed in quasidegenerate closed shell situations [27,29,30]. In fact, this region corresponds to a singular behavior of the ROHF ground state: Between approximately 3.5 and 4.5 a.u., we can obtain two distinct ROHF solutions whose energies cross at about 4 a.u. (see Fig. 1) [31]. The ROHF solution that can be continued when proceeding from the equilibrium geometry towards the dissociation limit corresponds to a mixture of covalent and ionic structures, similarly as the RHF solution for the  $H_2$  molecule. The solution that one obtains for large internuclear separations corresponds then to the proper dissociation limit, the closed shell part describing essentially the Be atom and the open shell orbital being almost exclusively localized on the H atom [31]. It is worthwhile to note that this difficult "transition" region is the source of various difficulties even when one employs the VB- rather than MO-based approaches [31].

Although this singular behavior of the L-CCSD approach is overcome when we include at least quadratic terms in the CCSD equations [32], a more thorough investigation of the character of this singular behavior would be desirable. We note that the L-CCSD potential energy curve was obtained by employing the lowest energy ROHF solution throughout. In other words, the ROHF reference is switched at  $\sim 4$  a.u., where the crossing occurs (cf. Fig. 1). When we employ the ROHF solution continued from the bonded region, much more complex singularity pattern of the L-CCSD energy arises.

It is of interest to note that the  $\Delta = [\Delta_{ij}]$  matrix of size extensivity corrections is much sparser than the CISD matrix  $\mathbf{H} = [H_{ij}]$ . In fact, if we only consider the most important and simplest diagonal terms,  $\Delta_{ii} = E_0$  (which, in fact, would vanish if we employ a properly defined normal product form of the Hamiltonian,  $H_N = H - E_0$  [2,33]) and neglect all the remaining off-diagonal terms, the resulting change in the energy, at least in the neighborhood of the equilibrium geometry, is very small. Thus, using a simplified version of the L-CCSD theory based on the CISD matrix, namely, defining

$$a_i = H_{i0}, \quad b_{ij} = H_{ij} - E_0 \delta_{ij}, \quad (27)$$

will yield very close result to the exact L-CCSD. This is reminiscent of a procedure advocated by Hoffmann and Simons (cf., Eq. (2.5a) or [34]), assuming that we employ a multiconfigurational reference, such as given by a solution of the MC SCF equations or by a suitable linear combination of Gel'fand states. Clearly, such a method will not be exactly size-extensive; however, minor violations of size extensivity may be outbalanced by the simplicity of such an approach.

### Discussion

In this paper we attempted to explore the possibilities offered by SR, but not necessarily single determinantal, CC approaches. We have also seen that when aiming for a spin-adapted version of the theory, the UGA- or CAUGA-based formalism can be very useful. Although the two simplest open shell cases presented here, namely, a single electron outside a closed shell and a singlet excited state of closed shell

systems, can be handled directly, without employing special computer codes, the complexity of the formalism rapidly increases with the number of open shells. For this reason, a special program (in FORTRAN) was written that is capable of handling more complex open shell systems. A similar program was also designed to produce the nonlinear form of CC equations and a required code. These programs were tested on the above presented special cases and are further being simplified in order to achieve greater efficiency. The description of these codes and their capabilities will be given elsewhere.

Concerning the linear version of the CC theory considered here, we must stress again its limitations when applied to general situations that do not correspond to a bonding region characterizing equilibrium geometries. Nonetheless, even the L-CCSD results can be very useful if properly employed. It is certainly very dangerous to make any conclusions when considering only one fixed nuclear conformation. However, when used over a wide range of geometries, the range of its validity is easily established. In fact, this region of applicability is already implied by the character of one-electron MOs and of the reference configuration employed, even though for more general open shell cases this problem should be investigated in greater detail.

Let us, finally, address one additional aspect of the formalism described in this paper. We recall that in order to classify and label the excitation operators  $G_i$  or, equivalently, the corresponding excited states  $|\Phi_i\rangle = G_i|\Phi_0\rangle$  that span the excited state manifold defining the level of the CC approximation employed, we rely, generally, on some suitable chain of subgroups. In this paper we have defined our excitation operators in such a way that they produce Gel'fand-Tsetlin states, which are adapted to the well-known canonical chain

$$U(n) \supset U(n-1) \supset \dots \supset U(1). \quad (28)$$

As already mentioned, the advantages of this choice are (i) the possibility to exploit UGA formalism and, at least for the linear level of theory, (ii) to rely on the existing CI codes and algorithms.

Recalling the orthogonally spin-adapted formalism for the closed shell case [33], we see that the coupling scheme implied by the canonical chain (28), or by the Gel'fand-Tsetlin states, leads to a rather awkward symmetry properties with respect to permutation of hole or particle labels, as exemplified by Eq. (23). It is thus preferable to exploit the following subgroup chain [76,35]

$$U(n) \supset U(n_{\text{core}}) \times U(n_{\text{virtual}}) \times U(n_{\text{active}}), \quad (29)$$

which is presently being explored. Since in any practically viable scheme we have to restrict ourselves to single and double excitations, the resulting configurations will involve at most two singly occupied orbitals in the core and at most two singly occupied virtuals. It is then convenient to couple these orbitals into a symmetric and an antisymmetric pairs (cf.  $pp$ - $hh$  coupling used in the closed shell case [33]). Clearly, this cannot be done when relying on the canonical chain (28), as seen by the examples given above, e.g., Eq. (23). Using such a coupling scheme leads to CC equations having much simpler symmetry properties than when exploiting the

canonical chain (28). The details of these developments will be presented elsewhere [26,35].

### Acknowledgments

Continued support by NSERC (J. P.) is gratefully acknowledged.

### Bibliography

- [1] J. Hubbard, Proc. Roy. Soc. (London) A **244**, 199 (1958) and references therein.
- [2] J. Paldus, in *Methods in Computational Molecular Physics*, NATO ASI Series, Series B, Vol. 293, S. Wilson and G. H. F. Diercksens, Eds. (Plenum, New York, 1992), p. 99-194.
- [3] D. Mukherjee and S. Pal, Adv. Quantum Chem. **20**, 292 (1989).
- [4] J. Paldus, in *Relativistic and Correlation Effects in Molecules and Solids*, NATO ASI Series, G. L. Malli, Ed. (Plenum, New York, 1993), to appear.
- [5] U. Kaldor, Theor. Chim. Acta **80**, 427 (1991).
- [6] J. Paldus, L. Pylypow, and B. Jeziorski, in *Many-Body Methods in Quantum Chemistry*, Lecture Notes in Chemistry, Vol. 52, U. Kaldor, Ed. (Springer-Verlag, Berlin, 1989), pp. 151-170.
- [7] A. Balková, S. A. Kucharski, L. Meissner, and R. J. Bartlett, Theor. Chim. Acta **80**, 335 (1991); A. Balková, S. A. Kucharski, and R. J. Bartlett, Chem. Phys. Lett. **182**, 511 (1991); A. Balková, S. A. Kucharski, L. Meissner, and R. J. Bartlett, J. Chem. Phys. **95**, 4311 (1991).
- [8] J. Paldus, P. Piecuch, B. Jeziorski, and L. Pylypow, in *Recent Progress in Many-Body Theories*, Vol. 3, T. L. Ainsworth, C. E. Campbell, B. E. Clements, and E. Krotscheck, Eds. (Plenum, New York, 1992), pp. 287-303.
- [9] J. Paldus, P. Piecuch, L. Pylypow, and B. Jeziorski, Phys. Rev. A **47**, 2738 (1993); P. Piecuch and J. Paldus, unpublished work.
- [10] I. Lindgren, Phys. Scr. **32**, 291, 611 (1985); D. Mukherjee, Chem. Phys. Lett. **125**, 207 (1986).
- [11] S. A. Kucharski and R. J. Bartlett, J. Chem. Phys. **95**, 8227 (1991) and references therein.
- [12] J. Paldus, J. Chem. Phys. **61**, 5321 (1974); in *Theoretical Chemistry: Advances and Perspectives*, H. Eyring and D. Henderson, Eds. (Academic, New York, 1976), Vol. 2, pp. 131-290.
- [13] I. Shavitt, Int. J. Quantum Chem. Quantum Chem. Symp. **11**, 131 (1977); **12**, 5 (1978).
- [14] J. Hinze, Ed., *The Unitary Group for the Evaluation of Electronic Energy Matrix Elements*, Lecture Notes in Chemistry, Vol. 22 (Springer-Verlag, Berlin, 1981).
- [15] F. A. Matsen and R. Pauncz, *The Unitary Group in Quantum Chemistry* (Elsevier, Amsterdam, 1986).
- [16] J. Paldus, in *Mathematical Frontiers in Computational Chemical Physics*, IMA Series, Vol. 15, D. G. Truhlar, Ed. (Springer-Verlag, New York, 1988), pp. 262-299; I. Shavitt, *ibid.*, pp. 300-349.
- [17] J. Paldus and C. R. Sarma, J. Chem. Phys. **83**, 5135 (1985); J. Paldus, M.-J. Gao, and J.-Q. Chen, Phys. Rev. A **35**, 3197 (1987).
- [18] J. Paldus and B. Jeziorski, Theor. Chim. Acta **73**, 81 (1988).
- [19] B. Jeziorski and J. Paldus, J. Chem. Phys. **88**, 5673 (1988); **90**, 2714 (1989).
- [20] J. Paldus and X. Li, in *Symmetries in Science VI: From the Rotation Group to Quantum Algebras*, B. Gruber, Ed. (Plenum, New York, 1993), to appear.
- [21] M. R. Hoffmann and J. Simons, J. Chem. Phys. **88**, 993 (1988); **90**, 3671 (1989) and references therein.
- [22] C. L. Janssen and H. F. Schaefer III, Theor. Chim. Acta **79**, 1 (1991).
- [23] B. Jeziorski, P. Jankowski, and J. Paldus, unpublished results.
- [24] P. Jankowski, unpublished results.
- [25] P. Neogrády, M. Urban, and I. Hubač, J. Chem. Phys. **97**, 5074 (1992).
- [26] X. Li and J. Paldus, unpublished results.
- [27] J. Paldus, P. E. S. Wormer, F. Visser, and A. van der Avoird, J. Chem. Phys. **76**, 2458 (1982).

- [28] M. Dupuis, D. Spangler, and J. J. Wendoloski, GAMESS system of programs, National Resource for Computations in Chemistry, *Software Catalog* (University of California, Berkeley, 1980), Program QG 01; M. W. Schmidt, K. K. Baldridge, J. A. Boatz, J. H. Jensen, S. Koseki, M. S. Gordon, K. A. Nguyen, T. L. Windus, and S. T. Elbert, *QCPE Bull.* **10**, 52 (1990).
- [29] K. Jankowski and J. Paldus, *Int. J. Quantum Chem.* **18**, 1243 (1980).
- [30] J. Paldus, M. Takahashi, and R. W. H. Cho, *Phys. Rev. B* **30**, 4267 (1984).
- [31] R. S. Mulliken, *Int. J. Quantum Chem. Quantum Chem. Symp.* **5**, 95 (1971); J. Gerratt and M. Raimondi, *Proc. Roy. Soc. (London) A* **371**, 525 (1980).
- [32] J. Paldus and J. Čížek, *Adv. Quantum Chem.* **9**, 105 (1975).
- [33] J. Paldus, *J. Chem. Phys.* **67**, 303 (1977); P. Piecuch and J. Paldus, *Int. J. Quantum Chem.* **36**, 429 (1989).
- [34] M. R. Hoffmann and J. Simons, *J. Chem. Phys.* **90**, 3671 (1989).
- [35] B. Jeziorski, J. Paldus, and P. Jankowski, unpublished results.

Received May 24, 1993

# Computation and Analysis of the Full Configuration Interaction Wave Function of Some Simple Systems

GIAN LUIGI BENDAZZOLI and STEFANO EVANGELISTI

*Dipartimento di Chimica Fisica ed Inorganica, Università di Bologna, Viale Risorgimento 4,  
40136 Bologna, Italy*

## Abstract

A recently developed Full Configuration Interaction method is discussed and used to compute wave functions for  $N_2$  and  $H_8$  on an IBM RISC 6000 workstation. As a further application of the formalism a cluster and natural orbital analysis of the wave functions is performed for the  $N_2$  molecule at various internuclear distances and for the  $H_8$  model. © 1993 John Wiley & Sons, Inc.

## Introduction

The Full Configuration Interaction (Full CI or FCI) method is the simplest among quantum chemical methods and has the property of giving the best possible wave function once a one-particle basis set is given. It is not a practical tool for studying even moderate size molecules, because of the factorial growth of the dimensions of the CI space with the number  $N$  of orbitals and the number  $n$  of electrons. However it is extremely important to assess the validity of approximate methods [1], and also to get a general insight into the structure of the wave function in small molecules and in model systems. There are two approaches to Full CI. The first one uses Slater determinants as basis functions [2–10], in the second spin adapted configuration state functions [11,12]. In the second approach the dimensions of the CI space are smaller, but the computer code is more complex and difficult to vectorize. The first approach seems to allow for better efficiency, in spite of the longer expansions and the lack of complete spin adaptation. We have recently developed a CI method belonging to the first class [13], which has been used to compute wave functions with up to 73 million components [14]. In this article we present medium size computations on an IBM RISC 6000 workstation and perform a cluster and natural orbital analysis of the full CI wave functions of  $N_2$  and  $H_8$ . In order to test the performance of the method on a vector supercomputer, a few tests on CRAY machines are also presented.

## Description of the CI Method

Although the method is described in detail in [13], we briefly review here its essential features. According to an idea which goes back to N. C. Handy [2], a

Slater determinant is represented by a product of two strings  $s_1$  and  $s_2$  specifying the alpha and beta occupation numbers. If we write down an  $a_i^\dagger$  for each 1 in position  $i$  of the string, we have an ordered product of creation operators defining the Slater determinant completely, including its phase. If we order the strings in some way, e.g., in lexical order, the CI vector can be addressed as a two-dimensional array  $X(s_1, s_2)$ . As usual in direct CI methods, we try to compute an eigenvector of a huge Hamiltonian matrix  $H$  by an iterative procedure in which, at each step, we have to compute the vector  $Y = HX$  directly from the two electron integrals and the vector  $X$  from the previous cycle. Our approach is very simple. From the second quantized form of the Hamiltonian, one can see that  $H$  is a sum of elementary operators like:

$$\langle i|j\rangle a_{i\mu}^\dagger a_{i\mu} \quad (1)$$

$$\langle ij|kl\rangle a_{i\mu}^\dagger a_{j\mu}^\dagger a_{l\mu} a_{k\mu} \quad (2)$$

$$\langle ij|kl\rangle a_{i\mu}^\dagger a_{j\nu}^\dagger a_{l\nu} a_{k\mu} \quad (3)$$

$$\mu, \nu = \alpha \text{ or } \beta, \quad \mu \neq \nu$$

Equations (1) and (2) induce a mapping between strings of the same spin, while eq. (3) induces a product mapping involving both alpha and beta strings. The idea is to construct, for each operator, two lists of strings mapped one into another element by element under the action of the operator. Consider as an example  $a_i^\dagger a_l$ , which appears in eq. (1). We generate all strings in lexical order, incrementing a counter  $c$  at each step. As soon as a string is constructed, we examine it. If we find that orbital  $i$  is empty and orbital  $l$  is populated, we add the string (or, better, the value of the counter  $c$ ) to the list labeled by orbital indexes  $l$  and  $i$ , in order. At the end of the process we have a list of all strings having orbital  $i$  empty and orbital  $l$  populated. This list will be put in an array  $OV(m; i, l)$  where  $m$  labels the string,  $i$  the occupied, and  $l$  the empty orbital (the name  $OV$  comes from the words occupied and virtual). The numbers of strings accumulated in the  $OV$  lists are also computed and stored in an array  $NOV(i, l)$ . Now, as shown in [13], one can prove that the operator  $a_i^\dagger a_l$  sends the string  $OV(m; l, i)$  in the string  $OV(m; i, l)$  multiplied by a sign factor or phase. The proof relies upon lexical order and extends to operators of type (2). These operators will use lists of strings having two orbitals,  $k$  and  $l$ , populated and  $i, j$  empty; we call these lists  $OOVV(m; l, k, j, i)$ . In order to realize the correspondence induced by type (3) operators, we use the  $OV$  lists twice. Since the lists actually contain addresses or pointers, the mapping in determinant space is realized as follows:

$$Y(OV(m; i, l), I) \leftarrow X(OV(m; l, i), I) * \text{phase} * \text{integral} \quad (4)$$

for type (1) operators, or:

$$Y(OOVV(m; j, i, k, l), I) \leftarrow X(OOVV(m; k, l, j, i), I) * \text{phase} * \text{integral} \quad (5)$$

$$Y(OV(m; i, k), OV(n; j, l)) \leftarrow X(OV(m; k, i), OV(n; l, j)) * \text{phase} * \text{integral} \quad (6)$$



for type (2) and (3) operators, respectively. The phase factors can be stored as separate arrays, or can be incorporated into the addresses. These phases are actually the nonzero values of coupling coefficients [5].

Our method is essentially integral driven and the strategy is to scan the two electron integral supermatrix, to pick up for each  $(ik|jl)$  all the corresponding  $X$  values, and accumulate the product in the proper location of  $Y$  array. In this way, integrals which are zero by symmetry or for some other reason are easily skipped. We will consider the implementation of the two electron loops only. In its simplest implementation, we keep in memory  $X$ ,  $Y$ , the lists, and the two electron integrals. The dimensions of  $X$ ,  $Y$  grow very fast with the number  $N$  of orbitals and the number  $n$  of electrons; the length of the lists also grows fast, but less rapidly than the FCI vector. It becomes something like 10% or so already for vectors of dimensions  $10^7$  [13]. As a second step, in order to treat larger problems, we can exploit symmetry and divide the strings in blocks. In such a case, we collect all strings of a given symmetry in the same block and order them lexically within each block. A third step consists in dividing  $X$  and  $Y$  arrays in arbitrary blocks simply according to the length of the array, according to how much memory is available in the computer. This extension can be coupled to the symmetry blocking and requires no essential modification of the lists. We will not examine this possibility here.

Consider the structure of the two main loops  $\beta\beta$  and  $\alpha\beta$ , originating from operators given in eqs. (2) and (3), respectively. The simplest one is the  $\beta\beta$ , which, in the case of no symmetry, reads:

#### $\beta\beta$ LOOP

```

loop over orbitals  $i, j, k, l$ 
   $v = (ik|jl) - (il|jk)$ 
  loop  $m = 1$ , length of list  $OOVV(i, j, k, l)$ 
     $I = OOVV(m; k, l, j, i)$ 
     $S = v * \text{phase}$ 
     $J = OOVV(m; j, i, k, l)$ 
    loop  $K = 1$ , number of  $\alpha$  strings.
       $Y(K, J) = Y(K, J) + X(K, I) * S$ 
    endloop  $K$ 
  endloop  $m$ 
endloop  $i, j, k, l$ 

```

The inner loop vectorizes at unit stride; its length is the  $\alpha$  dimension of  $X$ ,  $Y$  arrays; it can be implemented using BLAS routines SAXPY or DAXPY. The characteristic feature of our loop is the use of the two-electron four index list  $OOVV$ . The overall operation count is essentially the same as other schemes, like Olsen's [6] or Zarrabian's [7,8]; however the structure is simpler and the intermediate states are completely bypassed. The structure of the  $\alpha\alpha$  loop is similar. In this case the inner loop would vectorize at nonunit, although constant, stride. One can perform a transposition of the  $X$ ,  $Y$  arrays before the loop in order to have stride 1, which gives better vector performance. In the case  $S_z = 0$ , as pointed out by Olsen

[6], the contribution of the  $\alpha\alpha$  loop is simply given by that of  $\beta\beta$  times  $(-1)^S$ , where  $S$  is the total spin. This means that we can halve the number of operations and force a definite spin reversal symmetry from the outset.

Consider now the case when we group in the same block all strings of a given (abelian) symmetry. The strings are in lexical order within the block and we have a list for each operator and symmetry block. The addresses stored in the lists are relative to the blocks. Moreover, any operator has a definite symmetry, so strings of a given block are sent to strings of another block of definite symmetry. The structure of  $\beta\beta$  loop is now embedded in an external loop over symmetry indices of  $Y$  and  $X$  blocks; at each step we read block  $X$  of symmetries  $x_\alpha, x_\beta$  and compute its contribution to block  $Y$  of symmetries  $y_\alpha, y_\beta$ ; once a block  $Y$  is completed, we write it on disk. Furthermore, the four index lists need to be computed only for those quadruples of indices which are totally symmetrical. Therefore the string symmetry is not changed and this loop will be done only in the "diagonal case" when  $x_\alpha = y_\alpha, x_\beta = y_\beta$ . The dimensions of blocks tend to be quite balanced, even when the orbitals are quite unevenly distributed among the various symmetries.

As far as the  $\alpha\beta$  loop is concerned, one should remind it is the most time-consuming part of the algorithm, due to an higher operation count and to its intrinsic complexity. The mapping induced by  $a_{i\alpha}^\dagger a_{j\beta}^\dagger a_{l\beta} a_{k\alpha}$  is a product of an  $\alpha$  and a  $\beta$  mapping of the type described for the  $\beta\beta$  loop. The lists used are the shorter one-electron two-index lists. In this case the inner loop will not run over all strings in a block, but on those contained in the one-electron list: this means that components of  $X, Y$  arrays are not scanned one by one in sequence, but there are in general random jumps, although some structure is preserved. In order to achieve efficient vectorization, one must use gather-scatter operations as pointed out by [6]. In our scheme we use two auxiliary arrays of dimensions that can accomodate as many rows of  $X$  and  $Y$  array as there are elements in an  $OV$  list. The loop structure is given in the following ( $\odot$  denotes the group multiplication, and we use the index of an orbital to indicate also its symmetry):

### $\alpha\beta$ LOOP

loop over block indexes  $x_\beta, y_\beta$

$x_\alpha = \text{Symmetry of CI vector } \odot x_\beta^{-1}$ ,

$y_\alpha = \text{Symmetry of CI vector } \odot y_\beta^{-1}$ ,

loop over  $i, k$  orbitals ( $\alpha$  spin)

skip when  $(x_\alpha \odot i \odot k \odot y_\alpha)$  not totally symmetrical.

gather rows of  $X$  array in a scratch  $XS$  multiplied by the  $\alpha$  phase; the rows correspond to the entries in  $OV(k, i; x_\alpha)$  (vectorized at constant stride).

define  $NLEN$  = number of rows transferred.

loop over  $j, l$  orbitals ( $\beta$  spin).

skip when  $(x_\beta \odot j \odot l \odot y_\beta)$  not totally symmetric.

loop  $m = 1$ , length of  $OV(l, j; x_\beta)$

$S = \text{phase} \star (ik|jl)$

```

      I = OV(m; l, j; xβ); J = OV(m; j, l, yβ)
      loop K = 1, NLEN
        YS(K, J) = YS(K, J) + X(K, I)*S
      endloop K
    endloop m
  endloop j, l

```

scatter *NLEN* rows from *YS* array to *Y* array; the rows correspond to the entries *OV*(*i*, *k*; *x<sub>α</sub>*) (vectorized at constant stride).

```

endloop i, k
endloop xβ, yβ

```

Lists of all symmetries are needed, i.e., no reduction of list length takes place. The length of the inner loop *NLEN* affects the efficiency on vector machines. We group together two columns of *X* and *Y*, in order to have maximum *NLEN*, i.e., the columns corresponding to the terms  $a_i^\dagger a_j^\dagger j a_i a_k$  and  $a_i^\dagger a_k^\dagger a_i a_j$  of the Hamiltonian.

In order to assess the effectiveness of the method we present here some computations carried out on a workstation IBM RISC 6000, plus a few tests on CRAY Y-MP and C90. The symmetry adapted version of the program was used. In Table I we report energy values computed for water with DZ basis [3] at equilibrium geometry. It is a small computation performed in order to test the program and to illustrate all the possibilities offered by spatial and spin reversal symmetry. A preliminary SCF computation on the ground state of water was performed by using the program CADPAC [15]; the MO's obtained were used to expand the FCI wavefunctions for all cases reported in the table.

A larger and more interesting test case is given by the Ne atom in a [5s3p2d] AO basis and with eight active electrons, because it can be compared with earlier

TABLE I. FCI energies (a.u.) of water with DZ basis [3] with  $C_{2v}$  geometry. Eight different states are reported (the lowest states for each symmetry). For the four different spatial symmetries both singlets (spin rev. = +1) and triplets (spin rev. = -1) are considered.

Symmetry	Spin rev.	$F_{\text{tot}}$	$N_{\text{det}}$
$A_1$	+1	-76.157866	1,002,708
	-1	-75.797148	
$A_2$	+1	-75.761016	1,017,744
	-1	-75.779894	
$B_1$	+1	-75.670399	1,001,536
	-1	-75.721598	
$B_2$	+1	-75.742374	1,002,016
	-1	-75.867480	

calculations by Bauschlicher et al. [16] and by Olsen et al. [10]. The basis set used in our computation is slightly different from that of Refs. [16] and [10], because we used 6-component  $d$ -functions and discarded the two highest SCF orbitals of  $s$ -symmetry, in order to have exactly the same number of orbitals as a  $[5s3p2d]$  basis with 5-component  $d$  orbitals. The only difference between our basis and that of Ref. [16] and [10] is in the radial part of the  $s$  functions, not in their number. For this reason we get a correlation energy slightly different from that reported in Ref. [16], i.e.  $-0.245093$  hartrees instead of  $-0.244864$ . Various timings are reported in Table II. The values reported for the IBM RISC were obtained by using the function MCLOCK() and include the contribution of I/O, which amounts to about 10%. It is remarkable that on a workstation we have essentially the same time per iteration as on a CRAY 2. An all-in-core version of our program was run also a CRAY Y-MP and on a CRAY C90, giving the times reported which of course do not include any I/O. These results demonstrate that medium size full CI computations can be efficiently carried out on a workstation.

Encouraged by this result, we decided to consider a larger case, i.e.,  $N_2$  in a split-valence or VDZ basis. Using 18 active orbitals and 14 correlated electrons, the dimension of FCI space is 126,608,256 determinants, distributed in 8 blocks of 16 millions each in  $D_{2h}$  symmetry. The iterative process requires a large amount of I/O (about 9.5 Gbytes per iteration), and therefore the use of asynchronous I/O routines (BUFFER IN/OUT) is recommended. The efficiency of the parallelization of our code can be judged from the following data. A preliminary calculation performed on CRAY Y-MP (4 cpu, 64 MW core memory) gave a total cpu time of about 1125 s per iteration using the 4 cpu, with an elapsed time of 910 s. By running the same calculation on a single cpu, we obtained a cpu time of 1060 s per iteration, and an elapsed time of 1675 s. Therefore, as far as cpu time is concerned, the parallelization efficiency is 94%, the contribution of I/O being essentially the same in both cases (about 600 s).

This problem was however too large for our RISC workstation. Therefore we discarded the two highest MO's of  $\sigma$  symmetry and got a dimension of 16,631,136 determinants, partitioned in eight nearly equal blocks in  $D_{2h}$ . In Table III we summarize timing data on the RISC 6000 for this and other smaller cases, measured by

TABLE II. Comparison of iteration time (in seconds and seconds per million determinants) for Ne 'S, ( $5s3p2d$ ) basis set, eight active electrons.  $G$  is the symmetry group used for the calculation,  $N_{det}$  the number of determinants of the FCI vector using this group, and  $T_{it}$  the iteration cpu time.  $T_{it}$  is given in seconds and  $T_{it}/N_{det}$  in seconds per million determinants.

Reference	$G$	$N_{det}$	Computer	$T_{it}$	$T_{it}/N_{det}$
Bauschlicher et al. [16]	$D_{2h}$	9,805,897	CRAY 2	1368	139.5
Olsen et al. [10]	$D_{\sigma h}$	5,502,533	IBM 3090/VF	360	65.4
Present work	$D_{2h}$	9,805,897	IBM RISC 6000/950	1482	151.1
	$D_{2h}$	9,805,897	CRAY Y-MP	85	8.7
	$D_{2h}$	9,805,897	CRAY C90	45	4.6

TABLE III. Timing data (in seconds and seconds per million determinants) on IBM RISC 6000/950 for different systems.

System:	H <sub>2</sub> O	Ne	N <sub>2</sub>	H <sub>8</sub>
State:	<sup>1</sup> A <sub>1</sub>	<sup>1</sup> S	X <sup>1</sup> Σ <sub>g</sub> <sup>+</sup>	<sup>1</sup> A <sub>1g</sub>
Basis set:	DZ	[5s3p2d]	VDZ	DZ
Active orbitals:	14	23	16	16
Correlated electrons:	10	8	14	8
Symmetry group:	C <sub>2v</sub>	D <sub>2h</sub>	D <sub>2h</sub>	D <sub>2h</sub>
Symmetry blocks:	4	8	8	4
Number of dets (N <sub>det</sub> )	1,002,708	9,805,897	16,361,136	828,688
Iteration time (T <sub>it</sub> ):	126	1480	1810	90
T <sub>it</sub> /N <sub>det</sub>	126.0	151.2	110.6	108.4

the AIX function MCLOCK(). They are average values including the contributions of all CPU time used during an iteration (HX, I/O, normalization, . . .) in the presence of another concurrent job. The CPU time per million determinants is frequently reported as an indicator of the efficiency of the program; in our case it is in the range 100–150 s/million determinants. The time values reported for N<sub>2</sub> are lower than those given in Ref. [13] for a similar computation, due to the use of the BLAS routine DAXPY.

### Analysis of the Wavefunction

Natural orbital analysis [17] is a well-known procedure to get some insight into the structure of the wave function. The one-electron density-matrix (one-matrix)  $\rho$  in the MO basis is easily computed from the CI vector and the one electron lists OV. The  $ij$  element of the spinless one-matrix is simply given by:

$$\rho_{ij} = \sum_{m=1, \text{NOV}(i,j)} \sum_{K=1, \text{Nstrings}} X[OV(m; i, j), K] X[OV(m; j, i), K] + X[K, OV(m; i, j)] X[K, OV(m; j, i)] \quad (7)$$

when  $S_z = 0$  and the wave function is totally symmetric in an abelian group; it has no  $\alpha\beta$  contribution. The eigenvectors of the one-matrix are the natural orbitals of the system, and the eigenvalues are the corresponding natural orbital occupation numbers.

An important underlying structure of the wave function is associated with the cluster expansion. This was discovered long ago [18], and constitutes the basis of the various coupled cluster methods [19] which appear to be powerful and promising tools at our disposal for computing molecular properties [20]. The cluster expansion of a closed-shell FCI wave function can be written as:

$$|\text{FCI}\rangle = \exp(T_1 + T_2 + T_3 + \dots)|\text{SCF}\rangle \quad (8)$$

where  $T_1, T_2, T_3, \dots$  are cluster operators defined as

$$T_k = \sum_{i_1, \dots, i_k \in \text{occ}} \sum_{p_1, \dots, p_k \in \text{virt}} t_k(i_1, \dots, i_k; p_1, \dots, p_k) a_{i_1}^\dagger \cdots a_{i_k}^\dagger a_{p_1} \cdots a_{p_k} \quad (9)$$

They fulfill the following equations:

$$[T_k, T_l] = 0 \quad (10)$$

$$T_k^{[n/k]} = 0 \quad (11)$$

where  $n$  is the number of electrons and  $[n/k]$  is the ratio rounded to the nearest integer  $\geq n/k$ .

A cluster analysis of the FCI vector can be performed along the following lines (see for instance [21]). First of all, the matrix elements of the cluster operators are extracted from the coefficients of single, double, triple,  $\dots$  excitations of the FCI vector in the following way. Denote  $C_1, C_2, C_3, \dots$  the operators transforming the SCF vector in the FCI one:

$$|\text{FCI}\rangle = (1 + C_1 + C_2 + C_3 + \dots)|\text{SCF}\rangle \quad (12)$$

in such a way that the matrix elements of  $C_1, C_2, C_3$  are the coefficients of single, double, triple,  $\dots$  excitations, respectively, in the intermediate normalization  $\langle \text{FCI} | \text{SCF} \rangle = 1, \langle \text{SCF} | \text{SCF} \rangle = 1$ . The operators  $C_k$  are therefore given by expressions analogous to those of the  $T_k$ .

$$C_k = \sum_{i_1, \dots, i_k \in \text{occ}} \sum_{p_1, \dots, p_k \in \text{virt}} c_k(i_1, \dots, i_k; p_1, \dots, p_k) a_{i_1}^\dagger \cdots a_{i_k}^\dagger a_{p_1} \cdots a_{p_k} \quad (13)$$

By equating eqs. (12) and (8) we obtain the chain of equations [22]:

$$T_1 = C_1, \quad (14)$$

$$\frac{1}{2} T_1^2 + T_2 = C_2 \quad (15)$$

and so on. These equations are easily solved, and they give

$$t_1(i; p) = c_1(i; p), \quad (16)$$

$$t_2(i, j; p, q) = c_2(i, j; p, q) + 1/2(1 - P_{i,j})(1 - P_{p,q})c_1(i; p)c_1(j; q) \quad (17)$$

and so on. Here  $P_{i,j}$  and  $P_{p,q}$  are permutation operators exchanging the indexes  $i, j$  and  $p, q$ , respectively. Once the matrix elements of the cluster operators are known, we can compute the vector resulting from the application of any polynomial in  $T_1, T_2, T_3, \dots$  to an arbitrary vector of the FCI space. If we restrict ourselves to  $T_1$  and  $T_2$ , this requires nothing but the same algorithm described for the application of the Hamiltonian operator. The computer time required in this case is much smaller than a FCI iteration because the number of nonzero matrix elements of  $T_1$  and  $T_2$  is much less than the number of nonzero two-electron integrals. This can be seen from the values of indexes  $i, j, \dots$  and  $p, q, \dots$  which do not span

TABLE IV. Computed values of energies and related quantities for the ground state  $X^1\Sigma_g^+$  of  $\text{N}_2$  at various levels of approximation.  $R$  is the internuclear distance ( $R_0 = 2.12$ , close to the equilibrium distance). Method represents the level of approximation (see text);  $E_{\text{tot}}$  is the total energy;  $E_{\text{corr}}$  is the difference with the SCF energy,  $\cos_{\text{SCF}}$  is the cosine between the approximate vector and the SCF vector;  $\cos_{\text{FCI}}$  is the analogous cosine with the exact FCI vector. All values are in atomic units.

$R$	Method	$E_{\text{tot}}$	$E_{\text{corr}}$	% $E_{\text{FCI}}$	$\cos_{\text{FCI}}$	$\cos_{\text{SCF}}$
$0.5 R_0$	SCF	-104.905525	0.000000	0.0%	0.988201	1.000000
	FCI	-104.989179	-0.083654	100.0%	1.000000	0.988201
	SD	-104.986737	-0.081213	97.1%	0.999803	0.988396
	exp SD	-104.988142	-0.082617	98.8%	0.999886	0.988315
$R_0$	SCF	-108.818276	0.000000	0.0%	0.947271	1.000000
	FCI	-109.022844	-0.204568	100.0%	1.000000	0.947271
	SD	-108.999695	-0.181419	88.7%	0.996714	0.950394
	exp SD	-109.014873	-0.196597	96.1%	0.998655	0.948893
$1.5 R_0$	SCF	-108.518520	0.000000	0.0%	0.797811	1.000000
	FCI	-108.897984	-0.379464	100.0%	1.000000	0.797811
	SD	-108.791008	-0.272489	71.8%	0.969170	0.823185
	exp SD	-108.871607	-0.353087	93.0%	0.993576	0.803943
$2.0 R_0$	SCF	-108.226273	0.000000	0.0%	0.442780	1.000000
	FCI	-108.825898	-0.599626	100.0%	1.000000	0.442780
	SD	-108.588260	-0.361988	60.4%	0.847671	0.522335
	exp SD	-108.769450	-0.543177	90.6%	0.970143	0.387482
$10.0 R_0$	SCF	-107.750890	0.000000	0.0%	0.243124	1.000000
	FCI	-108.815249	-1.064359	100.0%	1.000000	0.243124
	SD	-108.351849	-0.600959	56.5%	0.694635	0.350011
	exp SD	-108.672174	-0.921285	86.6%	0.908307	0.157619

the full range of  $N$  orbitals, but only the occupied and the virtual orbitals in the SCF determinant, respectively. We can also easily compute the vector

$$|\text{exp SD}\rangle = \exp(T_1 + T_2)|\text{SCF}\rangle \quad (18)$$

because the exponential series breaks down to a polynomial in  $T_1$  and  $T_2$  thanks to the nilpotency property eq. (11). This vector can be compared to the FCI solution, and to the other vector

$$|\text{SD}\rangle = (1 + C_1 + C_2)|\text{SCF}\rangle \quad (19)$$

i.e., with the FCI solution projected on the space of those determinants which are at most double excitations from the SCF. We note that both  $|\text{SD}\rangle$  and  $|\text{exp SD}\rangle$  are in the intermediate normalization. The vector (18) contains all unlinked higher order excitations coming from the connected single- and double-excitations of the FCI vector.

From an approximate vector  $|\tilde{\Psi}\rangle$ , either  $|\text{SD}\rangle$  or  $|\text{exp SD}\rangle$ , we can compute the "variational" upper bound to the energy:

TABLE V. Occupation numbers of the natural orbitals of  $N_2$  at various internuclear distances. The occupation numbers of  $1\sigma_g$  and  $1\sigma_u$  natural orbitals differ from 2.0000 by less than  $5 \cdot 10^{-5}$  at all internuclear distances.

a) $R = 0.5 R_0$			
Symmetry	$ FCI\rangle$	$ SD\rangle$	$ \exp SD\rangle$
$2\sigma_g$	1.9925	1.9928	1.9927
$3\sigma_g$	1.9976	1.9977	1.9976
$2\sigma_u$	1.9882	1.9885	1.9884
$1\pi_u$	1.9875	1.9878	1.9877
$1\pi_g$	0.0150	0.0146	0.0148
$3\sigma_u$	0.0078	0.0076	0.0077
$4\sigma_u$	0.0025	0.0024	0.0024
$2\pi_u$	0.0017	0.0016	0.0016
$4\sigma_g$	0.0017	0.0015	0.0016
$2\pi_g$	0.0007	0.0007	0.0007
b) $R = R_0$			
Symmetry	$ FCI\rangle$	$ SD\rangle$	$ \exp SD\rangle$
$2\sigma_g$	1.9896	1.9910	1.9903
$2\sigma_u$	1.9796	1.9815	1.9807
$3\sigma_g$	1.9733	1.9773	1.9754
$1\pi_u$	1.9227	1.9307	1.9266
$1\pi_g$	0.0809	0.0728	0.0770
$3\sigma_u$	0.0234	0.0201	0.0219
$4\sigma_u$	0.0093	0.0082	0.0088
$2\pi_u$	0.0058	0.0050	0.0052
$4\sigma_g$	0.0041	0.0036	0.0038
$2\pi_g$	0.0010	0.0008	0.0008
c) $R = 1.5 R_0$			
Symmetry	$ FCI\rangle$	$ SD\rangle$	$ \exp SD\rangle$
$2\sigma_g$	1.9883	1.9921	1.9900
$2\sigma_u$	1.9816	1.9862	1.9835
$3\sigma_g$	1.8753	1.9217	1.8929
$1\pi_u$	1.6596	1.7348	1.6756
$1\pi_g$	0.3386	0.2653	0.3262
$3\sigma_u$	0.1249	0.0790	0.1083
$2\pi_u$	0.0083	0.0048	0.0048
$4\sigma_u$	0.0066	0.0043	0.0054
$4\sigma_g$	0.0050	0.0028	0.0034
$2\pi_g$	0.0027	0.0015	0.0018
d) $R = 2.0 R_0$			
Symmetry	$ FCI\rangle$	$ SD\rangle$	$ \exp SD\rangle$
$2\sigma_g$	1.9941	1.9980	1.9960
$2\sigma_u$	1.9916	1.9966	1.9945
$3\sigma_g$	1.4836	1.7257	1.3424
$1\pi_u$	1.1719	1.4185	0.9671
$1\pi_g$	0.8211	0.5783	1.0320
$3\sigma_u$	0.5132	0.2738	0.6585



TABLE V. (Continued)

d) $R = 2.0 R_0$ (Continued)			
Symmetry	$ FCI\rangle$	$ SD\rangle$	$ \exp SD\rangle$
$2\pi_u$	0.0065	0.0033	0.0017
$4\sigma_g$	0.0057	0.0021	0.0021
$4\sigma_u$	0.0048	0.0014	0.0024
$2\pi_g$	0.0041	0.0011	0.0012
e) $R = 10.0 R_0$			
Symmetry	$ FCI\rangle$	$ SD\rangle$	$ \exp SD\rangle$
$2\sigma_g$	1.9961	1.9995	1.9984
$2\sigma_u$	1.9961	1.9995	1.9984
$3\sigma_g$	0.9969	1.4174	0.6086
$1\pi_u$	0.9969	1.4174	0.6085
$1\pi_g$	0.9969	0.5802	1.3911
$3\sigma_u$	0.9969	0.5802	1.3911
$2\pi_u$	0.0044	0.0007	0.0007
$4\sigma_g$	0.0044	0.0020	0.0007
$4\sigma_u$	0.0044	0.0007	0.0007
$2\pi_g$	0.0044	0.0020	0.0007

$$\bar{E} = \langle \bar{\Psi} | H | \bar{\Psi} \rangle / \langle \bar{\Psi} | \bar{\Psi} \rangle \quad (20)$$

which gives information about the ability of the vectors (18) and (19) to approximate the FCI solution. Another measure of the same property is given by

$$\cos_{FCI} = \frac{\langle \bar{\Psi} | FCI \rangle}{\| \bar{\Psi} \| \| FCI \|} \quad (21)$$

i.e., the cosine of the angle between vector  $|\bar{\Psi}\rangle$  and  $|FCI\rangle$ .

Remember that our cluster analysis is only partial: the importance of connected excitations of order higher than 2 can be obtained only indirectly by comparison with the FCI results.

### Applications to $N_2$ and $H_8$

With this technique we have investigated two systems. The first is the  $N_2$  molecule at five internuclear distances and using the VDZ basis [23] truncated to 16 MO's. The results are collected in Tables IV and V. In Table IV we collect total and correlation energies for the following functions:  $|SCF\rangle$ ,  $|FCI\rangle$ , the projection of  $|FCI\rangle$  in the space of singles and doubles, denoted by  $|SD\rangle$ , and the exponential  $|\exp SD\rangle$  defined in eq. (18). The cosines of the angles of any vector with  $|FCI\rangle$  and  $|SCF\rangle$  are also reported. From these data one can follow the increase of correlation energy with the internuclear distance. It is remarkable how the  $|\exp SD\rangle$  manages to recover a large fraction of the correlation energy: 85.4% of FCI at ten times the equilibrium internuclear distance, i.e., 21.2 bohr. At this distance the

TABLE VI Computed values of energies and related quantities for the ground state  $^1A_{1g}$  of  $H_8$  at various levels of approximation  $\alpha$  is the distortion from the  $D_{8h}$  symmetry, Method represents the level of approximation (see text),  $E_{tot}$  is the total energy;  $E_{corr}$  is the difference with the SCF energy;  $\cos_{SCF}$  is the cosine between the approximate vector and the SCF vector;  $\cos_{FCI}$  is the analogous cosine with the exact FCI vector. All values are in atomic units.

$\alpha$	Method	$E_{tot}$	$E_{corr}$	% $E_{FCI}$	$\cos_{FCI}$	$\cos_{SCF}$
1.0000	SCF	-4.284048	0.000000	0.0%	0.936431	1.000000
	FCI	-4.416537	-0.132489	100.0%	1.000000	0.936431
	SD	-4.404999	-0.120951	91.3%	0.997102	0.939153
	exp SD	-4.415626	-0.131579	99.3%	0.999768	0.936703
0.1000	SCF	-4.167991	0.000000	0.0%	0.836074	1.000000
	FCI	-4.315812	-0.147821	100.0%	1.000000	0.836074
	SD	-4.291160	-0.123169	83.3%	0.991633	0.843129
	exp SD	-4.308775	-0.140784	95.2%	0.996730	0.838160
0.0100	SCF	-4.149155	0.000000	0.0%	0.687678	1.000000
	FCI	-4.308362	-0.159206	100.0%	1.000000	0.687678
	SD	-4.265770	-0.116614	73.2%	0.983508	0.699209
	exp SD	-4.289768	-0.140613	88.3%	0.991195	0.691383
0.0010	SCF	-4.147195	0.000000	0.0%	0.666401	1.000000
	FCI	-4.308064	-0.160869	100.0%	1.000000	0.666401
	SD	-4.263109	-0.115913	72.1%	0.982443	0.678309
	exp SD	-4.287676	-0.140481	83.3%	0.990397	0.670158
0.0001	SCF	-4.146999	0.000000	0.0%	0.664227	1.000000
	FCI	-4.308040	-0.161041	100.0%	1.000000	0.664227
	SD	-4.262846	-0.115847	71.9%	0.982336	0.676171
	exp SD	-4.287467	-0.140468	87.2%	0.990316	0.667987

triple bond is completely broken, as can be seen from the occupation numbers of natural orbitals reported in Table V. However, the absolute error in correlation energy is very large, i.e., 0.155826 hartrees. These data clearly indicate the importance of connected triples, quadruples, and higher excitations in the FCI vector at large internuclear distances in  $N_2$ . These data also suggest that a "variational" single reference SD coupled cluster wave function is not adequate to compute a quantitatively correct dissociation curve for  $N_2$  molecule, even though a variational optimization of the matrix elements of  $T_1$  and  $T_2$  would increase the percentage of predicted correlation energy. In this connection it should be reminded that the usual Restricted Hartree-Fock Coupled Cluster truncated to Single and Double excitations (RHF-CCSD) gives for this molecule qualitatively incorrect results. The potential energy curve computed by Laidig et al. shows indeed an unphysical maximum in the region of  $R = 4$  a.u. [24], and seems to decrease to very low values at large  $R$ . The usual procedure to compute the energy in CC methods uses the transition formula:

$$\frac{\langle \text{exp SD} | H | \text{SCF} \rangle}{\langle \text{exp SD} | \text{SCF} \rangle} \quad (22)$$

which is not variationally bounded; both  $|\text{exp } SD\rangle$  and  $|SD\rangle$  give back to the exact FCI energy at any distance when plugged into eq. (22). Our results confirm the usefulness of the extension of CC methods to higher excitations [25] or to multireference functions [26].

In Table V we report the natural orbitals occupation numbers of  $N_2$  at the same five internuclear distances, for the three wave functions  $|FCI\rangle$ ,  $|SD\rangle$  and  $|\text{exp } SD\rangle$ . The first four orbitals (two  $\sigma_g$  and two  $\sigma_u$  orbitals) are practically doubly occupied at any distance. The triple bond is formed by the orbitals  $3\sigma_g$ ,  $1\pi_{xu}$ , and  $1\pi_{yu}$ , while  $3\sigma_u$ ,  $1\pi_{xg}$ , and  $1\pi_{yg}$  are the corresponding antibonding orbitals. It is therefore possible to follow the dissociation of the triple bond with the internuclear distance. At long distance, at FCI level, both the three bonding orbitals and the three antibonding orbitals are populated with a single electron. Since at large distance they are mainly formed by  $p$  atomic orbitals, this corresponds to the correct dissociation of the molecule, with a single electron in each one of the  $2p_x$ ,  $2p_y$ , and  $2p_z$  AO of the two N atoms. The  $|SD\rangle$  vector, on the contrary, has the bonding orbitals more occupied than the antibonding orbitals. This is a consequence of the incorrect dissociation of the closed shell SCF, since double excitations are unable to produce two neutral atoms starting from the closed-shell reference. Quite remarkably, the occupation numbers corresponding to the  $|\text{exp } SD\rangle$  vector are unbalanced exactly on the opposite way, with the antibonding orbitals more occupied than the bonding orbitals. This is due to the absence of linked higher order excitations, which would partially cancel the products of diexcitations.

Similar computations and analysis were performed on the  $H_8$  system (see Table VI), originally studied by Jankowski et al. [27] with a minimal basis set, and later investigated by Bartlett and co-workers at DZ and DZP level [28]. In this model four  $H_2$  molecules with fixed internuclear distance (2.0 a.u.) are initially arranged into an octagonal  $D_{8h}$  structure. Two  $H_2$  molecules are then symmetrically displaced from their initial positions by an amount  $\alpha$ , and the symmetry is lowered to  $D_{2h}$ . The level of degeneracy is controlled by the parameter  $\alpha$ , which represents the distortion from the symmetric  $D_{8h}$  structure, which corresponds to  $\alpha = 0$ . When  $\alpha$  goes to zero, the highest occupied and lowest unoccupied MO's become quasi-degenerate, and two configurations are dominant in the FCI wave function. In fact, as we can see from Table VI, the weight of the SCF determinant in the FCI vector, which is given by  $\cos^2_{SCF}(FCI)$ , is close to  $1/2$  as  $\alpha$  goes to zero.

We used the DZ basis set of Paldus et al. [29], and we performed FCI calculations followed by cluster analysis for five values of the parameter  $\alpha$ . This is a less degenerate system than a dissociating  $N_2$  molecule, and the difference between the exact correlation energy and that associated with  $|\text{exp } SD\rangle$  is smaller. However when we examine the percent of correlation energy recovered by  $|\text{exp } SD\rangle$ , we find for small  $\alpha$  a value very similar to the corresponding percent for  $N_2$  at  $R = 10R_0$ . This indicates that even in this simple case connected triple and quadruple excitations are important, as already pointed out by Bartlett and co-workers in the case of single reference CC approach for this system.

### Acknowledgments

This work has been supported by the Italian National Research Council CNR partly within "Progetto Finalizzato Sistemi Informatici e Calcolo Parallelo" and partly within "Calcolo Avanzato in Chimica." Free computer time on CRAY Y-MP was provided by CINECA (Bologna, Italy), Grant No. 93110310. The authors thank Prof. N. C. Handy FRS for suggesting the cluster analysis of the wave functions, and for useful comments and discussions; Dr. R. Ansaloni of CRAY Research Italia and Dr. E. Rossi of CINECA for performing the tests on CRAY Y-MP and C90; and Prof. P. Palmieri for useful suggestions in the implementation on IBM workstation.

### Bibliography

- [1] C. W. Bauschlicher, Jr. and S. R. Langhoff, *Adv. Chem. Phys.* **LXXVII**, 103 (1990), and references therein.
- [2] N. C. Handy, *Chem. Phys. Lett.* **74**, 280 (1980).
- [3] P. Saxe, H. F. Schaefer III, and N. C. Handy, *Chem. Phys. Lett.* **79**, 202 (1981).
- [4] P. E. M. Siegbahn, *Chem. Phys. Lett.* **109**, 417 (1984).
- [5] P. J. Knowles and N. C. Handy, *Chem. Phys. Lett.* **111**, 315 (1984); P. J. Knowles and N. C. Handy, *Comput. Phys. Commun.* **54**, 75 (1989).
- [6] J. Olsen, B. O. Roos, P. Jorgensen, and H. J. Aa. Jensen, *J. Chem. Phys.* **89**, 2185 (1988).
- [7] S. Zarrabian, C. R. Sarma, and J. Paldus, *Chem. Phys. Lett.* **155**, 183 (1989).
- [8] R. J. Harrison and S. Zarrabian, *Chem. Phys. Lett.* **158**, 393 (1989).
- [9] P. J. Knowles, *Chem. Phys. Lett.* **155**, 513 (1989); P. J. Knowles and N. C. Handy, *J. Chem. Phys.* **91**, 2396 (1989).
- [10] J. Olsen, P. Joergensen, and J. Simons, *Chem. Phys. Lett.* **169**, 463 (1990).
- [11] See, e.g. "The unitary group," J. Hinze, Ed. in *Lecture Notes in Chemistry*, vol. 22 (Springer-Verlag, Berlin, 1981).
- [12] See e.g. R. McWeeny, *Methods of Molecular Quantum Mechanics*, 2nd ed. (Academic Press, London, 1989).
- [13] G. L. Bendazzoli and S. Evangelisti, *J. Chem. Phys.* **98**, 3141 (1993).
- [14] G. L. Bendazzoli and S. Evangelisti, *Chem. Phys. Lett.* **185**, 125 (1991); R. Ansaloni, S. Evangelisti, G. Paruolo, and E. Rossi, *Int. J. Supercomputer Applications* **6**, 351 (1992).
- [15] R. D. Amos and J. E. Rice, *The Cambridge Analytical Derivative Package* (Cambridge, U.K., 1987).
- [16] C. W. Bauschlicher, Jr., S. R. Langhoff, P. R. Taylor, and H. Partridge, *Chem Phys Lett.* **126**, 436 (1986).
- [17] P. O. Lowdin, *Phys. Rev.* **97**, 1474 (1955).
- [18] J. Hubbard, *Proc. R. Soc. London Ser. A* **240**, 539 (1957); F. Coester, *Nucl. Phys.* **7**, 421 (1958); F. Coester and H. Kümmel, *Nucl. Phys.* **17**, 477 (1960).
- [19] J. Čížek, *J. Chem. Phys.* **45**, 4256 (1966); J. Paldus, J. Čížek, and I. Shavitt, *Phys. Rev. A* **5**, 50 (1972); J. Paldus and J. Čížek in *Energy, Structure and Reactivity*, D. W. Smith and W. B. McRae, Eds. (Wiley, New York, 1973).
- [20] R. J. Bartlett, *Ann. Rev. Phys. Chem.* **32**, 359 (1981); R. J. Bartlett, *J. Phys. Chem.* **93**, 1697 (1989).
- [21] J. Paldus and M. J. Boyle, *Int. J. Quantum Chem.* **XXII**, 1281 (1982).
- [22] J. Čížek, J. Paldus, and L. Šroubková, *Int. J. Quantum Chem.* **III**, 149 (1969).
- [23] T. H. Dunning, Jr. and P. J. Hay, in *Modern Theoretical Chemistry*, vol. 3, *Methods of Electronic Structure Theory*, H. F. Schaefer III, Ed. (Plenum Press, New York and London, 1977), chap. 1.
- [24] W. D. Laidig, P. Saxe, and R. J. Bartlett, *J. Chem. Phys.* **82**, 887 (1987).

- [25] N. Oliphant and L. Adamowicz, *J. Chem. Phys.* **95**, 6645 (1991); S. A. Kucharski and R. J. Bartlett, *J. Chem. Phys.* **97**, 4282 (1992).
- [26] See, e.g., "Aspects of many-body effects in molecules and extended systems," *Lecture Notes in Chemistry*, vol. 50, D. Mukherjee, Ed. (Springer-Verlag, Berlin, 1989); *Many-body methods in quantum chemistry*, in *Lecture Notes in Chemistry*, vol. 52, U. Kaldor, Ed. (Springer-Verlag, Berlin, 1989).
- [27] K. Jankowski, L. Meissner, and J. Wasilewski, *Int. J. Quantum Chem.* **XXVIII**, 931 (1985); L. Meissner, K. Jankowski, and J. Wasilewski, *Int. J. Quantum Chem.* **XXXIV**, 535 (1988); K. Jankowski, J. Paldus, and J. Wasilewski, *J. Chem. Phys.* **95**, 5349 (1991).
- [28] S. A. Kucharski, A. Balková, P. G. Szalay, and R. J. Bartlett, *J. Chem. Phys.* **97**, 4289 (1992).
- [29] J. Paldus, P. E. S. Wormer, and M. Benard, *Coll. Czech. Chem. Commun.* **53**, 1919 (1988).

Received August 2, 1993

# A Note on the Calculation of Some Transformation Coefficients

ZHENYI WEN\*

*Department of Chemistry, Indiana University, Bloomington, Indiana 47405*

## Abstract

This article gives an improved derivation for  $U(n_1 + n_2) \supset U(n_1) \times U(n_2)$ ,  $S_{\Lambda_1 + \Lambda_2} \supset S_{\Lambda_1} \times S_{\Lambda_2}$ , and other transformation coefficients by using a series of elementary Racah transformations. These transformation coefficients can be expressed generally in terms of a product of segments containing 6j symbols and easily calculated. Possible segment factors are given in Table I. © 1993 John Wiley & Sons, Inc

Due to their importance in applications, the  $U(n_1 + n_2) \supset U(n_1) \times U(n_2)$  and  $S_{\Lambda_1 + \Lambda_2} \supset S_{\Lambda_1} \times S_{\Lambda_2}$  transformation coefficients have attracted numerous studies [1–11]. A motivation for these studies is to exploit the possibility of partitioning a large system into smaller subsystems in actual calculations. For this purpose it is obviously desirable to find a simple and effective approach of evaluating the coefficients. For a electron system, with which quantum chemists are particularly concerned, the spin algebra approach based on the spin characteristic of electron spin-adapted functions might be conceptually the simplest one. By using the graphic technique of the spin algebra the author of this note in an earlier publication gave the closed formulae for  $S_{\Lambda_1 + \Lambda_2} \supset S_{\Lambda_1} \times S_{\Lambda_2}$  and  $U(n_1 + n_2) \supset U(n_1) \times U(n_2)$  transformation coefficients [10]. These formulae seem quite easy to handle and have been involved in the program of ligand field calculations. [12].

Although the application of the spin graph approach is straightforward, the procedure obtaining a general expression is often tedious because a series of graph transformations should be carried out. In this note we shall show that in some cases the complex procedure of graph transformations may be avoided.

Let us take  $U(n) \supset U(n_1) \times U(n_2)$  ( $n = n_1 + n_2$ ) transformation coefficient as an example. Suppose that  $|s(d_r)m(d_r)\rangle$  is the spin function associated with an orbital. Its explicit form depends on the step number  $d_r$  and can be written as

$$|s(d_r)m(d_r)\rangle = \begin{cases} 1, & d = 0 \\ \left| \frac{1}{2} m_r \right\rangle, & d = 1 \text{ or } 2 \\ \left\{ \frac{1}{2} \sum_{m'_r, m''_r} \left| \frac{1}{2} m'_r \right\rangle \left| \frac{1}{2} m''_r \right\rangle \left\langle \frac{1}{2} m'_r \frac{1}{2} m''_r \right| 00 \right\}, & d = 3 \end{cases} \quad (1)$$

\* Permanent address: Institute of Modern Physics, Northwest University, Xian, Shaanxi 710069, P.R. China.

According to the  $SU(2)$  scheme, and  $U(n)$  Gelfand state (so-called canonical basis) can be constructed by gradual coupling of individual orbital spin, i.e.,

$$\begin{aligned}
 |[\lambda]d_1 \cdots d_{n_1} \cdots d_n\rangle &= |[\lambda]\bar{S}_1 \cdots \bar{S}_{n_1} \cdots \bar{S}_n\rangle \\
 &= f \sum_{\{m(d_r)\}} \sum_{\{\bar{M}_r\}} \prod_{r=2}^n |\bar{S}_{r-1} \bar{M}_{r-1}\rangle |s(d_r)m(d_r)\rangle \\
 &\quad \times \langle \bar{S}_{r-1} \bar{M}_{r-1} s(d_r)m(d_r) | \bar{S}_r \bar{M}_r \rangle \quad (2)
 \end{aligned}$$

where  $\bar{S}_r$  is the intermediate spin generated by coupling the first  $r$  orbitals,  $\bar{M}_r$  is the corresponding component, and  $f$  is a phase factor. This coupling scheme can be symbolized by

$$(\cdots((s(d_1)s(d_2))\bar{S}_2s(d_3))\bar{S}_3\cdots)\bar{S}_{n_1}\cdots)\bar{S}_{n-1}s(d_n))\bar{S}_n = S \quad (3)$$

or illustrated by labeled binary tree [13] (Fig. 1).

We can similarly construct the noncanonical basis or the basis function symmetry-adapted to  $U(n_1) \times U(n_2)$  by coupling  $U(n_1)$  and  $U(n_2)$  Gelfand states into the state having total spin  $S$ ,

$$\begin{aligned}
 |[\lambda_1]d_1 \cdots d_{n_1}; [\lambda_2]d'_{n_1+1} \cdots d'_n\rangle \\
 = \sum_{\bar{M}_{n_1}, \bar{M}'_n} |[\lambda_1]\bar{S}_1 \cdots \bar{S}_{n_1}\rangle |[\lambda_2]\bar{S}'_{n_1+1} \cdots \bar{S}'_n\rangle \langle \bar{S}_{n_1} \bar{M}_{n_1} \bar{S}'_n \bar{M}'_n | SM \rangle \quad (4)
 \end{aligned}$$

The coupling scheme for the noncanonical basis is

$$\begin{aligned}
 (\cdots((s(d_1)s(d_2))\bar{S}_2\cdots s(d_{n_1}))\bar{S}_{n_1}(\cdots(s(d_{n_1+1})s(d_{n_1+2}))\bar{S}'_{n_1+2}\cdots) \\
 \times \bar{S}'_{n-1}s(d_n)\bar{S}'_n)\bar{S}_n = S \quad (5)
 \end{aligned}$$

and the corresponding labeled tree diagram is shown in Figure 2.

As is well known that the  $U(n) \supset U(n_1) \times U(n_2)$  transformation coefficients are contained in the following expansion,

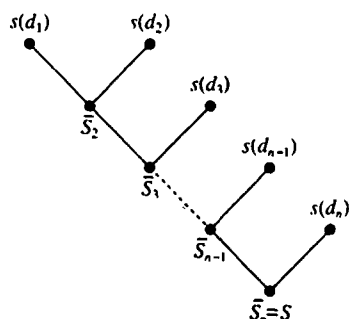


Figure 1. Canonical basis.

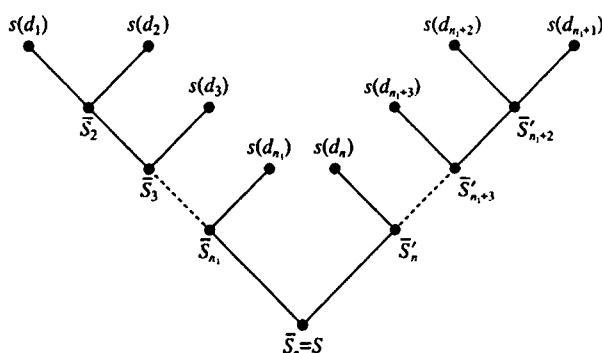


Figure 2. Noncanonical basis.

$$\begin{aligned}
 & |[\lambda_1]d_1 \cdots d_{n_1}; [\lambda_2]d'_{n_1+1} \cdots d'_n \rangle \\
 &= \sum_{d_1 \cdots d_n} |[\lambda]d_1 \cdots d_n \rangle \langle [\lambda]d_1 \cdots d_n | [\lambda_1]d_1 \cdots d_{n_1}; \\
 & \quad [\lambda_2]d'_{n_1+1} \cdots d'_n \rangle \quad (6)
 \end{aligned}$$

Comparing the coupling schemes we find that the transformation from (3) to (5) can be realized by a series of similar elementary transformations,

$$\begin{aligned}
 & \cdots ((\bar{S}_{n_1} s(d'_{r-1})) \bar{S}'_{r-1} s(d'_r)) \bar{S}'_r \cdots \xrightarrow{R_r} \cdots ((\bar{S}_{n_1} (s(d'_{r-1}) s(d'_r)) \bar{S}'_r) \bar{S}'_r \cdots \\
 & \quad r = n_1 + 2, n_1 + 3, \cdots n \quad (7)
 \end{aligned}$$

Each elementary transformation corresponds a Racah's recoupling transformation,

$$((j_1 j_2) j_{12} j_3) J \rightarrow ((j_1 (j_2 j_3) j_{23}) J \quad (8)$$

and contributes a  $6j$  symbol factor to the  $U(n) \supset U(n_1) \times U(n_2)$  transformation coefficient,

$$(-1)^{\bar{S}_{n_1} + s'(d_{r-1}) + \bar{S}_r + s(d_r)} [\bar{S}_{r-1}, \bar{S}'_r]^{1/2} \begin{Bmatrix} \bar{S}_n & \bar{S}_r & \bar{S}'_r \\ s(d_r) & s(d'_{r-1}) & \bar{S}'_{r-1} \end{Bmatrix} \quad (9)$$

where

$$[\bar{S}_{r-1}, \bar{S}'_r] = (2\bar{S}_{r-1} + 1)(2\bar{S}'_r + 1)$$

and

$$s(d'_{r-1}) = \begin{cases} s(d_{n_1+1}), & r = n_1 + 2 \\ \bar{S}'_{r-1}, & r \neq n_1 + 2 \end{cases} \quad (10)$$

Thus the  $U(n) \supset U(n_1) \times U(n_2)$  transformation coefficient is obtained by multiplying  $(n - n_1 - 1)$   $6j$  factors together. The transformation process from (3) to (5) is shown in Figure 3.



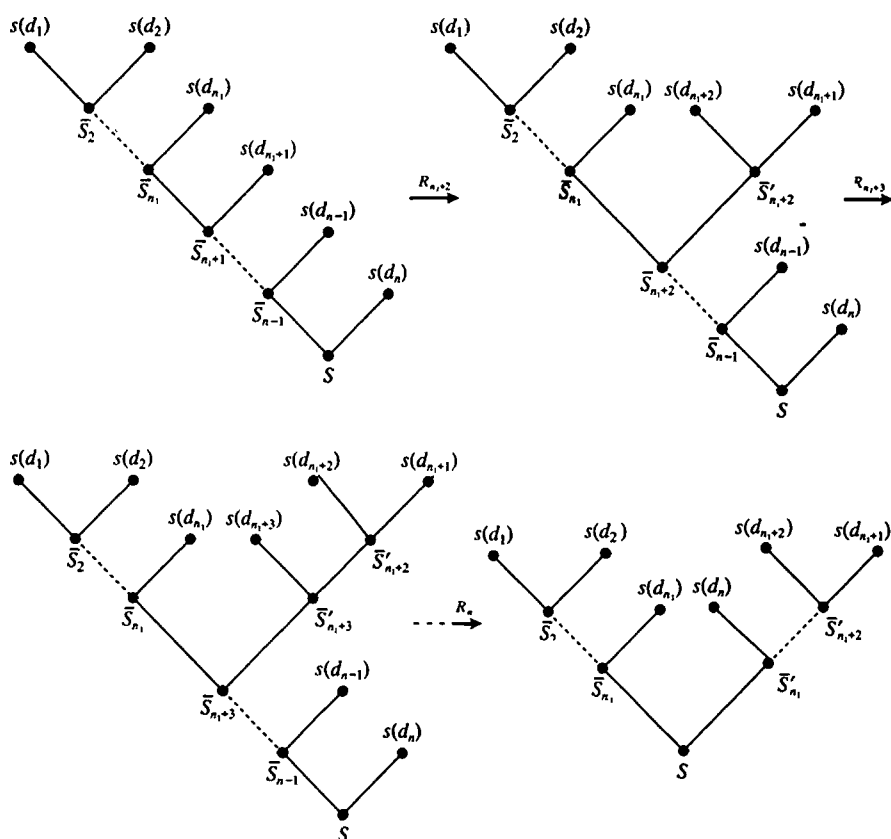


Figure 3. Transformation from canonical basis to noncanonical basis.

The coefficient can also be written into the product of segments, i.e.,

$$\langle (d_1 \cdots d_n) | (d_1 \cdots d_{n_1}) (d'_{n_1+1} \cdots d'_n) \rangle = \prod_{r=n_1+2}^n S(d_r d'_r; b_{n_1}, b_r b'_r) \quad (11)$$

The values of segment factors are given in Table I.

Another example is the transformation between Yamanauchi-Kotani functions and Jahn-Serber functions. The former coupling is represented into

$$(\cdots ((S_1 S_2) \bar{S}_2 S_3) \bar{S}_3 \cdots S_N) S \quad (12)$$

while the latter

$$(\cdots ((S_1 S_2) \bar{S}'_2 (S_3 S_4) \bar{S}'_3) \bar{S}'_4 \cdots (S_{N-1} S_N) \bar{S}'_{N-1}) \bar{S}'_N) S \quad (13)$$

Again we found  $(N-2)/2$  elementary transformations which will change (11) into (12). The elementary transformation is

TABLE I.  $S(d, d'; b_{n_1}, b_r, b'_r)$ .

$d, d'$	$S(d, d'; b_{n_1}, b_r, b'_r)$
0 0	$\varphi$
1 1	$\varphi \left[ \frac{(b_{n_1} + b_r + b'_r + 2)(-b_{n_1} + b_r + b'_r)}{4(b_r + 1)b'_r} \right]^{1/2}$
2 1	$\varphi(-1)^{b_r} \left[ \frac{(b_{n_1} + b_r - b'_r + 2)(b_{n_1} - b_r + b'_r)}{4(b_r + 1)b'_r} \right]^{1/2}$
1 2	$\varphi(-1)^{b_r+1} \left[ \frac{(b_{n_1} - b_r + b'_r + 2)(b_{n_1} + b_r - b'_r)}{4(b_r + 1)(b'_r + 2)} \right]^{1/2}$
2 2	$\varphi(-1)^{b_r+b'_r} \left[ \frac{(b_{n_1} + b_r + b'_r + 4)(-b_{n_1} + b_r + b'_r + 2)}{4(b_r + 1)b'_r} \right]^{1/2}$
3 3	$\varphi(-1)^{b_r+b'_r}$

$$\varphi = \begin{cases} 1, & d_{n_1} = 1 \\ (-1)^{b_{n_1}+1}, & d_{n_1} = 2, 3 \end{cases}$$

$$\cdots (\bar{S}_{2i} S_{2i+1}) \bar{S}_{2i+1} S_{2i+2} \bar{S}_{2i+2} \cdots \xrightarrow{R_i} \cdots (\bar{S}_{2i} (S_{2i+1} S_{2i+2}) \bar{S}'_{2i+1}) \bar{S}'_{2i+2} \cdots$$

$$i = 1, 2, \cdots, (N-2)/2$$

and provides a factor

$$\delta(\bar{S}_{2i+2}, \bar{S}'_{2i+2}) (-1)^{\bar{S}_{2i} + \bar{S}_{2i+1} + S_{2i+2} + \bar{S}_{2i+2}} [\bar{S}_{2i+1}, \bar{S}'_{2i+1}]^{1/2} \begin{Bmatrix} \bar{S}_{2i} & S_{2i+1} & \bar{S}_{2i+1} \\ S_{2i+2} & \bar{S}_{2i+2} & \bar{S}'_{2i+1} \end{Bmatrix}$$

Multiplying these factors together, we obtain the transformation coefficient [14],

$$\prod_{i=1}^{N/2-1} (-1)^{\bar{S}_{2i} + \bar{S}_{2i+2} + 1} [\bar{S}_{2i+1}, \bar{S}'_{2i+1}]^{1/2} \begin{Bmatrix} \bar{S}_{2i} & 1/2 & \bar{S}_{2i+1} \\ 1/2 & \bar{S}_{2i+2} & \bar{S}'_{2i+1} \end{Bmatrix} \quad (14)$$

The coefficients derived above are only two examples of a big family of transformation coefficients between different angular momentum coupling schemes. The matrix elements of  $U(n)$  generators and their products can also be put under this family. It is generally proven that the transformation coefficient between a pair of coupling schemes is expressible in terms of sums over products of  $6j$  symbol factors or Racah's coefficients [13]. This conclusion clearly reveals the close relationship between transformation coefficients and  $3nj$  symbols. As an explanation of this fact we point out that the overlap part of a matrix element  $\langle d' | e_{ij,kl} | d \rangle = \langle d' | (E_{ij} E_{kl} - \delta_{jk} E_{il}) | d \rangle$  is exactly the first or second kind of  $3nj$  symbol. It is easy to see that the exchange-type and direct-type matrix elements correspond to the first and second kind of  $3nj$  symbols, respectively. Based on this correspondence

we can prove the relation between the two kinds of matrix elements, which is of course useful for improving the efficiency of the CI program [15].

### Acknowledgment

The author would like to express his thanks to Professor E. R. Davidson for his hospitality.

### Bibliography

- [1] H. Hori, J. Phys. Soc., Jpn. **19**, 1783 (1964).
- [2] L. J. Somers, J. Math. Phys. **24**, 772 (1983).
- [3] Chen Jinquan, D. F. Collinson, and Gao Meijuan, J. Math. Phys. **24**, 2695 (1983).
- [4] I. G. Kaplan, *Symmetry of Many-Electron Systems*, (Academic, New York, 1975).
- [5] C. Suryanarayana and M. K. Rao, J. Phys. **A15**, 2013 (1982).
- [6] C. W. Patterson and W. G. Harter, Phys. Rev. **A15**, 2372 (1977).
- [7] C. R. Sarma and K. V. Dinesha, Int. J. Quantum Chem. **16**, 1195 (1979).
- [8] K. V. Dinesha, C. R. Shama, and S. Rettrup, Adv. Quantum Chem. **14**, 125 (1981).
- [9] M. D. Gould and J. Paldus, Int. J. Quantum Chem. **25**, 327 (1986).
- [10] Wen Zhenyi, Int. J. Quantum Chem. **28**, 1779 (1986).
- [11] H. Lin, Theor. Chim. Acta **79**, 43 (1991).
- [12] Y. Dou, Z. Wen, Z. Liu, D. Zhang, and Y. Wang, Chem. J. of Chinese Uni. **10**, 1229 (1989).
- [13] L. C. Biedenharn and J. D. Louck, *Encyclopedia of Mathematics*, Vol. 9 (Addison-Wesley, Reading, MA, 1981).
- [14] S. Wilson, Chem. Phys. Lett. **49**, 168 (1977).
- [15] Y. Wang, Z. Wen, Z. Zhang, and Q. Dou, J. Comput. Chem. **13**, 187 (1982).

Received March 15, 1993

# Rigorous Interpretation of Electronic Wavefunctions. IV. Origins of the Unusual Stability of the 1,3-Dimethylimidazol-2-Ylidene Carbene

JERZY CIOSLOWSKI

Department of Chemistry and Supercomputer Computations Research Institute,  
Florida State University, Tallahassee, Florida 32306-3006

## Abstract

*Ab initio* electronic structure calculations, carried out in conjunction with rigorous analysis of the resulting wavefunctions, demonstrate that the electronic factors responsible for the unusual stability of the 1,3-dimethylimidazol-2-ylidene carbene are directly related to the substantial  $\sigma$ -backdonation from the carbenic carbon to the adjacent nitrogen atoms. The  $\pi$ -donation is found to play only a minor role, ruling out the presence of significant stabilization due to ylidic resonance structures. The unusually large proton affinity of the carbene is explained by the extra  $\pi$ -electron stabilization of the corresponding 1,3-dimethylimidazolium cation. The MP2/6-311++G\*\* level of theory is found to be sufficient for accurate predictions of the geometries of the imidazol-2-ylidene carbenes. © 1993 John Wiley & Sons, Inc

## Introduction

The accuracy achieved by electronic structure calculations on  $|\text{CH}_2$ , the prototype carbene, is widely regarded as one of the triumphs of modern quantum chemistry (for a recent review, see Ref. [1]). For larger carbenes, such calculations are too expensive to be practical, as it takes over 700,000 configurations in the CI procedure and very large basis sets to compute the singlet-triplet splitting in  $|\text{CH}_2$  within 0.1 [kcal/mol] [2]. In light of this fact, the necessity of understanding the general factors influencing stability of carbenes becomes urgent.

Following several unsuccessful attempts by Wanzlick and Schönherr [3], very recently Arduengo and coworkers have succeeded in isolating several stable carbenes for the first time [4,5]. These compounds, many of which have been crystallized and have had their structures analyzed by means of X-ray diffraction, are alkyl and aryl derivatives of imidazol-2-ylidene. Despite the obvious importance of this discovery, very little effort has been directed by theoretical chemists toward explaining the unusual stability of the imidazol-2-ylidene carbenes, with the early low-grade EHT calculations [6] and the recent *ab initio* study [7] being the only relevant electronic structure investigations available in the chemical literature.

Several researchers extended conflicting arguments concerning the mechanisms responsible for the wide variation in the singlet-triplet energy gaps in carbenes (for a recent review and an attempt to reconcile the different theories, see Ref. [8]). Regrettably, most of the previously published analyses rely heavily on nonrigorous

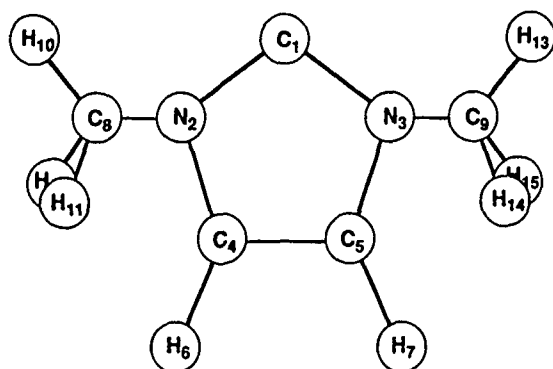


Figure 1. The molecular skeleton of  $C_5H_6N_2$ .

interpretive tools, such as the notoriously unreliable Mulliken atomic charges. Although the arguments arising from application of such tools are often qualitatively correct (note, however, some recent examples to the contrary [9,10]), reliable and theoretically consistent interpretation of electronic wavefunctions can only be achieved with techniques that do not invoke the notion of basis functions as "atomic orbitals." Building upon the topological theory of atoms in molecules [11], we have recently proposed bias-free definitions of localized natural orbitals [12], covalent bond orders [13], measures of steric crowding [14], and electronegativities of atoms and functional groups in molecules [15]. In this paper, we employ these rigorous interpretive tools in order to pinpoint the origins of the unusual stability of 1,3-dimethylimidazol-2-ylidene (Fig. 1), which is the simplest stable carbene reported

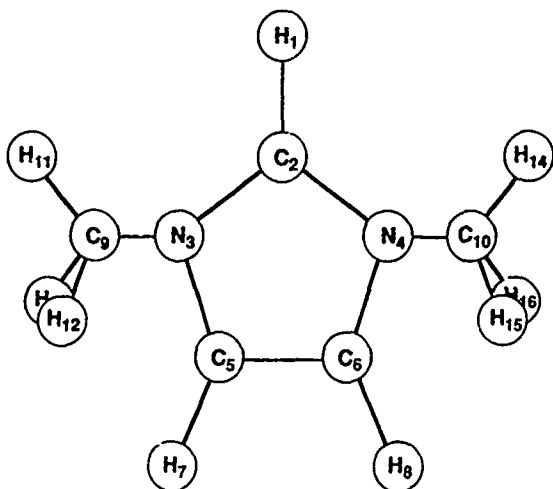


Figure 2. The molecular skeleton of  $C_5H_9N_2^+$ .

thus far [5]. We also report the results of a similar analysis for its parent carbenium ion, the 1,3-dimethylimidazolium cation (Fig. 2).

### Computational Techniques

The geometries of the systems under study were optimized at both the HF/6-311++G\*\* and MP2/6-311++G\*\* levels using the GAUSSIAN 90 suite of programs [16]. The minima on the respective potential energy hypersurfaces were characterized with the HF/6-311++G\*\* vibrational frequencies. The total and relative energies obtained from these calculations are listed in Table I.

The one-electron density matrices were computed at both the HF and MP2 [17] levels. The atomic overlap matrices (AOMs) [18] were calculated with the VECAIM program [19]. The LOSSES program [20] was employed in computations of the localized natural orbitals [12] and covalent bond orders [13].

### Results and Discussion

In the singlet  $|\text{CH}_2$  with a linear geometry, the degeneracy of Slater determinants that result from occupying the perpendicular  $\pi$  orbitals necessitates invoking a two-configurational wavefunction as the correct zeroth-order description. However, decreasing the H—C—H angle to its equilibrium value of ca.  $105^\circ$  significantly lessens the severity of the degeneracy, making the singly-configurational description reasonable [21]. Therefore, despite relatively large errors in the calculated singlet-triplet splittings, one expects the MP2 level of theory to yield geometries and electron densities accurate enough for a reliable analysis of the electronic structures of singlet carbenes. The results of calculations on the  $\text{C}_5\text{H}_8\text{N}_2$  carbene (Fig. 1, Table II) confirm these expectations. When compared with the experimental values for the 1,3,4,5-tetramethyl derivative, the calculated bond lengths and bond angles are found to be as accurate as the corresponding quantities obtained with the two-configurational SCF [7]. The analogous comparison for the geometrical parameters of the  $\text{C}_5\text{H}_9\text{N}_2^+$  cation (Fig. 2, Table III) is hindered by the unavailability of sufficiently accurate experimental data.

The C—N bonds in both the carbene and the carbenium cation are strongly polarized, as reflected by the calculated atomic charges (Tables IV and V). As

TABLE I. The total and relative HF/6-311++G\*\* and MP2/6-311++G\*\* energies of  $\text{C}_5\text{H}_8\text{N}_2$  and  $\text{C}_5\text{H}_9\text{N}_2^+$ .

System	$E_{\text{HF}}$ [a.u.]	$E_{\text{MP2}}$ [a.u.]	$\Delta E_{\text{HF}}$ [kcal/mol]*	$\Delta E_{\text{MP2}}$ [kcal/mol]*
$\text{C}_5\text{H}_8\text{N}_2$	-302.915711	-304.108346	0.0 (0.0)	0.0 (0.0)
$\text{C}_5\text{H}_9\text{N}_2^+$	-303.346434	-304.537389	-270.1 (-260.8)	-269.2 (-259.9)

\* Values corrected for the zero-point energies (at 298 [K] with vibrational frequencies calculated at the HF/6-311++G\*\* level) in parentheses.

TABLE II The calculated vs. experimental bond lengths [Å] and bond angles [°] in  $C_5H_8N_2$ .

Bond length or angle <sup>a</sup>	Calculated <sup>b</sup>	Experimental	
		c	d
C <sub>1</sub> N <sub>2</sub>	1.371 (1.349) [1.352]	1.363	1.370
C <sub>4</sub> N <sub>2</sub>	1.380 (1.384) [1.397]	1.394	1.384
C <sub>4</sub> C <sub>5</sub>	1.370 (1.334) [1.350]	1.352	1.338
C <sub>8</sub> N <sub>2</sub>	1.453 (1.446) [n/a]	1.454	1.484
C <sub>4</sub> H <sub>6</sub>	1.080 (1.069) [n/a]	n/a	0.964
C <sub>8</sub> H <sub>10</sub>	1.089 (1.079) [n/a]	n/a	n/a
C <sub>8</sub> H <sub>11</sub>	1.093 (1.085) [n/a]	n/a	n/a
N <sub>2</sub> C <sub>1</sub> N <sub>3</sub>	101.5 (103.0) [101.9]	101.5	102.2
C <sub>1</sub> N <sub>2</sub> C <sub>4</sub>	113.4 (112.2) [113.5]	113.5	112.2
N <sub>2</sub> C <sub>4</sub> C <sub>5</sub>	105.8 (106.3) [105.6]	105.8	106.7
C <sub>1</sub> N <sub>2</sub> C <sub>8</sub>	122.6 (123.7) [n/a]	122.9	122.8
N <sub>2</sub> C <sub>4</sub> H <sub>6</sub>	123.4 (123.1) [n/a]	n/a	123.5
N <sub>2</sub> C <sub>8</sub> H <sub>10</sub>	107.2 (108.0) [n/a]	n/a	n/a
N <sub>2</sub> C <sub>8</sub> H <sub>11</sub>	110.4 (110.8) [n/a]	n/a	n/a

<sup>a</sup> See Figure 1 for atom numbering.<sup>b</sup> MP2/6-311++G\*\* values followed by the HF/6-311++G\*\* data in parentheses and the TCSCF/DZP data from Ref. [7] in square brackets<sup>c</sup> Experimental values for the 1,3,4,5-tetramethylimidazol-2-ylidene [5].<sup>d</sup> Experimental values for the 1,3-di-1-adamantylimidazol-2-ylidene [4, 5]TABLE III. The calculated vs. experimental bond lengths [Å] and bond angles [°] in  $C_5H_9N_2^+$ .

Bond length or angle <sup>a</sup>	Calculated <sup>b</sup>	Experimental <sup>c</sup>
C <sub>2</sub> H <sub>1</sub>	1.080 (1.070) [n/a]	n/a
C <sub>2</sub> N <sub>3</sub>	1.342 (1.314) [1.316]	1.330
C <sub>5</sub> N <sub>3</sub>	1.374 (1.378) [1.384]	1.380
C <sub>5</sub> C <sub>6</sub>	1.374 (1.341) [1.345]	n/a
C <sub>9</sub> N <sub>3</sub>	1.469 (1.467) [n/a]	n/a
C <sub>5</sub> H <sub>7</sub>	1.079 (1.068) [n/a]	n/a
C <sub>9</sub> H <sub>11</sub>	1.089 (1.080) [n/a]	n/a
C <sub>9</sub> H <sub>12</sub>	1.090 (1.080) [n/a]	n/a
N <sub>3</sub> C-N <sub>4</sub>	108.4 (109.8) [108.2]	109.7
C <sub>2</sub> N <sub>3</sub> C <sub>5</sub>	108.8 (108.0) [109.4]	n/a
N-C	107.0 (107.1) [106.5]	n/a
C-N	125.5 (126.3) [n/a]	n/a
N	122.2 (122.2) [n/a]	n/a
N <sub>3</sub> C <sub>9</sub> H <sub>11</sub>	108.5 (108.8) [n/a]	n/a
N <sub>3</sub> C <sub>9</sub> H <sub>12</sub>	109.1 (109.3) [n/a]	n/a

<sup>a</sup> See Figure 2 for atom numbering.<sup>b</sup> MP2/6-311++G\*\* values followed by the HF/6-311++G\*\* data in parentheses and the HF/DZP data from Ref. [7] in square brackets.<sup>c</sup> Experimental values for the (1,3-di-1-adamantylimidazolium)<sup>+</sup> · B(C<sub>6</sub>H<sub>5</sub>)<sub>4</sub><sup>-</sup> [4].

TABLE IV. The HF/6-311++G\*\* and MP2/6-311++G\*\* Bader atomic charges and AOM-based covalent bond orders in  $C_5H_8N_2$ .

Atom <sup>a</sup>	$Q_{\text{Bader}}^b$	Bond	$P_{\text{cov}}^b$
C <sub>1</sub>	0.707 (1.038)	C <sub>1</sub> —N <sub>2</sub>	1.108 (1.034)
N <sub>2</sub>	-1.254 (-1.620)	C <sub>4</sub> —N <sub>2</sub>	1.012 (0.981)
C <sub>4</sub>	0.366 (0.496)	C <sub>4</sub> —C <sub>5</sub>	1.609 (1.702)
H <sub>6</sub>	0.033 (0.067)	C <sub>4</sub> —H <sub>6</sub>	0.949 (0.984)
C <sub>8</sub>	0.363 (0.598)	C <sub>8</sub> —N <sub>2</sub>	0.886 (0.871)
H <sub>10</sub>	0.079 (0.029)	C <sub>8</sub> —H <sub>10</sub>	0.916 (0.943)
H <sub>11</sub>	0.022 (-0.027)	C <sub>8</sub> —H <sub>11</sub>	0.936 (0.959)

<sup>a</sup> See Figure 1 for atom numbering.<sup>b</sup> MP2/6-311++G\*\* values followed by the HF/6-311++G\*\* data in parentheses.

expected [22], the ionicity of bonds is grossly overestimated at the HF level. For this reason, all the subsequent discussion is limited here to atomic and bond properties derived from the MP2 density matrices. The covalent bond orders indicate the presence of single bonds, except for those linking two carbon atoms in the imidazole rings, which have bond orders close to 2.

In accordance with the predominantly singly-configurational character of both  $C_5H_8N_2$  and  $C_5H_9N_2^+$ , the occupation numbers of the strongly occupied localized natural orbitals (LNOs) do not deviate significantly from the limiting value of 2 (Tables VI and VII). The LNOs make it possible to analyze the electronic structures of the species under study on an orbital-by-orbital basis. Discarding those describing the core electrons, there are 27 strongly occupied localized natural orbitals in the 1,3-dimethylimidazol-2-ylidene carbene. The presence of  $C_2$  symmetry reduces this number to only 10 distinct LNOs (Table VI, Fig. 3). Taking into account the

TABLE V. The HF/6-311++G\*\* and MP2/6-311++G\*\* Bader atomic charges and AOM-based covalent bond orders in  $C_5H_9N_2^+$ .

Atom <sup>a</sup>	$Q_{\text{Bader}}^b$	Bond	$P_{\text{cov}}^b$
H <sub>1</sub>	0.160 (0.144)	C <sub>2</sub> —H <sub>1</sub>	0.886 (0.904)
C <sub>2</sub>	0.995 (1.401)	C <sub>2</sub> —N <sub>3</sub>	1.180 (1.117)
N <sub>3</sub>	-1.226 (-1.580)	C <sub>5</sub> —N <sub>3</sub>	0.985 (0.955)
C <sub>5</sub>	0.418 (0.527)	C <sub>5</sub> —C <sub>6</sub>	1.522 (1.626)
H <sub>7</sub>	0.147 (0.121)	C <sub>5</sub> —H <sub>7</sub>	0.920 (0.955)
C <sub>9</sub>	0.323 (0.508)	C <sub>9</sub> —N <sub>3</sub>	0.848 (0.829)
H <sub>11</sub>	0.081 (0.042)	C <sub>9</sub> —H <sub>11</sub>	0.919 (0.947)
H <sub>12</sub>	0.091 (0.055)	C <sub>9</sub> —H <sub>12</sub>	0.919 (0.948)

<sup>a</sup> See Figure 2 for atom numbering.<sup>b</sup> MP2/6-311++G\*\* values followed by the HF/6-311++G\*\* data in parentheses.



TABLE VI. The valence MP2/6-311++G\*\* strongly occupied localized natural orbitals in  $C_3H_5N_2$ .

Orbital <sup>a</sup>	Occupancy	Description
8 (9)	1.963	61.0% ionic C—N $\sigma$ bond, 96.8% localized
10 (11)	1.960	46.9% ionic C—N $\sigma$ bond, 96.5% localized
12 (13)	1.959	46.6% ionic C—N $\sigma$ bond, 96.4% localized
14	1.965	Purely covalent C—C $\sigma$ bond, 95.4% localized
15 (16)	1.941	Tricentric C—N—C $\pi$ bond, 93.9% localized
17	1.964	$\sigma$ lone pair, 90.4% localized on C
18 (19)	1.971	11.3% ionic C—H $\sigma$ bond, 97.4% localized
20 (21)	1.971	8.8% ionic C—H $\sigma$ bond, 95.6% localized
22	1.930	Purely covalent C—C $\pi$ bond, 85.2% localized
23 (24, 25, 26, 27)	1.971	4.2% ionic C—H $\sigma$ bond, 96.1% localized

<sup>a</sup> LNOS ordered according to increasing negative kinetic energies (see Fig. 3) with orbitals related by symmetry given in parentheses.

local symmetries, eight of these orbitals are of the  $\sigma$  type. With the exception of the  $\sigma$  lone pair, the  $\sigma$  LNOS are strongly localized, with the localization numbers (calculated as the sums of the pertinent atomic occupancies) in excess of 95%. The imidazole ring is described by the LNOS 8, 10, 14, and their symmetry-related counterparts (Fig. 3). The bonds between the formally divalent (carbenic) carbon and the neighboring nitrogens (LNOS 8 and 9) are particularly ionic, resulting in a large positive charge on the carbon atom (Table IV). The ionicities of the remaining C—N bonds (LNOS 10 and 11 for the intraring C—N bonds, and LNOS 12 and 13 for the ring-CH<sub>3</sub> C—N bonds) are markedly smaller. The C—H bonds of the bonds CH (LNOS 18 and 19) and CH<sub>3</sub> groups (LNOS 20, 21, 23–27) are almost completely covalent. Finally, the C—C bond of the imidazole ring (LNO 14) is purely covalent due to the underlying molecular symmetry.

TABLE VII. The valence MP2/6-311++G\*\* strongly occupied localized natural orbitals in  $C_3H_5N_2^+$ .

Orbital <sup>a</sup>	Occupancy	Description
8 (9)	1.962	51.7% ionic C—N $\sigma$ bond, 96.5% localized
10 (11)	1.961	52.1% ionic C—N $\sigma$ bond, 97.0% localized
12 (13)	1.961	53.4% ionic C—N $\sigma$ bond, 97.1% localized
14	1.965	Purely covalent C—C $\sigma$ bond, 95.0% localized
15 (16)	1.931	Tricentric C—N—C $\pi$ bond, 94.8% localized
17	1.972	18.8% ionic C—H $\sigma$ bond, 96.3% localized
18 (19)	1.972	17.9% ionic C—H $\sigma$ bond, 97.2% localized
20	1.920	Purely covalent C—C $\pi$ bond, 80.7% localized
21 (22, 23, 24)	1.971	10.1% ionic C—H $\sigma$ bond, 95.9% localized
25 (26)	1.971	9.1% ionic C—H $\sigma$ bond, 95.7% localized

<sup>a</sup> LNOS ordered according to increasing negative kinetic energies (see Fig. 4) with orbitals related by symmetry given in parentheses.

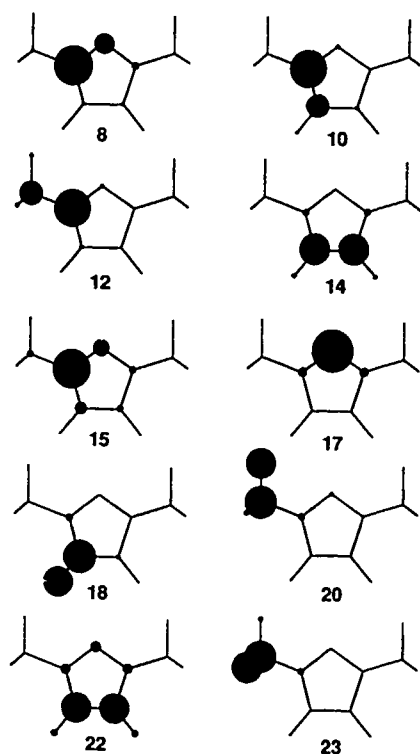


Figure 3. Atomic occupancies (represented by areas of the shaded circles) of the strongly occupied localized natural orbitals (LNOS) of the  $C_3H_8N_2$  molecule.

The system of the  $\pi$ -type orbitals consists of just two distinct LNOS. The LNO number 14, which pertains to the intraring C—C  $\pi$ -bond, is partially delocalized over the neighboring nitrogen atoms. The other symmetry-related pair of the  $\pi$ -type LNOS (LNOS 15 and 16) describes tricentric C—N—C bonds. Despite the delocalized character of these LNOS, their occupancies on the carbenic carbon atom are rather small, amounting to only 12%. This implies only a marginal  $\pi$ -donation from the nitrogens to the carbon atom, especially when compared with the massive  $\sigma$ -backdonation. This  $\sigma$ -backdonation also plays some role for the carbon lone pair (LNO 17), which is only 90.4% localized (Table VI, Fig. 3).

Protonation of  $C_3H_8N_2$  is a strongly exothermic process. In agreement with the previous calculations [7], we find the imidazol-2-ylidene system to be a much stronger base than other carbenes. We attribute this increased basicity to the extra  $\pi$ -electron stabilization enjoyed by the corresponding carbenium cation, for which there is the following evidence: First, the excess electric charge of the proton is efficiently distributed over the entire imidazol moiety (compare the data in Tables IV and V). Therefore, the increase (by 0.288) in the atomic charge of the carbenic carbon is much smaller than what one would expect from the loss of the lone pair

electrons that are now shared with the hydrogen atom. The protonation almost completely equalizes the ionicities of the three distinct C—N bonds (LNOS 8, 10, and 12; Table VII), which now span a narrow range of 51.7–53.4%. The newly formed C—H bond (described by LNO 17) is very similar in its very moderate ionicity to the other C—H bonds (LNOS 18 and 19) of the imidazole ring.

Second, although the  $\sigma$ -type LNOS (including those describing the C—H bonds of the CH<sub>3</sub> groups and the C—C bond of the imidazole ring) remain strongly localized in the carbenium cation, localization of the  $\pi$ -type orbitals decreases markedly upon protonation. In particular, the localization index of the LNO pertaining to the C—C  $\pi$ -bond falls by ca. 5%, mostly due to the increased delocalization over the formerly carbenic carbon atom (Fig. 4). The same carbon atom also enjoys an increased  $\pi$ -donation from the neighboring nitrogens, due to changes in atomic occupancies of the tricentric LNOS 15 and 16 (compare Figs. 3 and 4).

When comparing two chemical systems, the increase (decrease) in the strength of an analogous bond, as evidenced by its shortening (lengthening), can be attributed to either increased (decreased) covalent interactions or increased (decreased) bond ionicity. Which mechanism is the major driving force in a given case can be easily

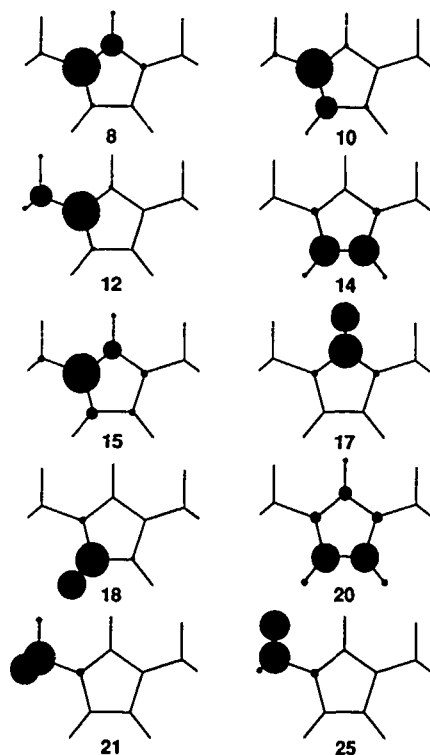


Figure 4. Atomic occupancies (represented by areas of the shaded circles) of the strongly occupied localized natural orbitals (LNOS) of the C<sub>5</sub>H<sub>9</sub>N<sub>2</sub><sup>+</sup> cation.

decided by examining the changes in the relevant covalent bond orders. The decrease (increase) in the bond strength accompanied by the decrease (increase) in the covalent bond order indicates the predominant decrease (increase) in the covalent interactions, which can often be explained by delocalization effects. On the other hand, the decrease (increase) in the bond strength in conjunction with the increase (decreased) covalent bond order points to the predominant decrease (increase) in the bond ionicity.

Applying the aforescribed criterion, one finds that the significant shortening upon protonation of the bonds linking the carbenic carbon with the neighboring nitrogens is mostly due to increased conjugation in the carbenium cation. The accompanying slight shortening of the two other C—N bonds of the imidazole ring can be attributed to the increased bond ionicity. The C—C bond lengthens somewhat upon protonation. This, together with the corresponding drop in the covalent bond order, indicates decreased covalent interactions as the result of the increased  $\pi$ -electron delocalization (see above).

What are the origins of the unusual stability of the 1,3-dimethylimidazol-2-ylidene carbene? The factors related to the substituents on the imidazole ring have to be spelled out first. Among them, the absence of hydrogen atoms in the 1,3- positions is obviously important, as it prevents rapid isomerization to imidazole through a 1,2-proton shift. Blocking of the 4,5- positions appears to be less critical, although 1,3-dimethyl-imidazol-2-ylidene is much less stable than its 1,3,4,5-tetramethyl analog [4].

The electronic factors are directly traced to the large singlet-triplet energy gap of  $C_5H_8N_2$  [7]. In principle, two alternative explanations of this large splitting are possible [8]. First, in line with the original ideas of Wanzlick [3], one would expect the  $\pi$ -donation to stabilize the singlet state through bonding with the vacant  $\pi$  orbital of the carbenic carbon [23]. Another possibility is that the  $\sigma$ -backdonation favors the singlet state by increasing the positive charge on the carbon atom [24]. In light of the analysis described above, the first explanation does not appear credible, taking into account the small degree of  $\pi$ -donation present in the carbene under study. On the other hand, the second explanation is fully compatible with the large  $\sigma$ -donation due to the large electronegativity difference between the carbenic carbon and the adjacent nitrogens.

It is proper at this point to comment on the relative importance of the two aforementioned mechanisms to the *energetics* of the singlet-triplet gap. In principle, it is possible (although not very likely) for the  $\pi$ -donation to play, in spite of its small relative magnitude, the dominant role in determining the singlet-triplet splitting. The only way to entirely rule out this possibility is to correlate the calculated splittings with the extents of  $\pi$ -donation and  $\sigma$ -backdonation. Such correlation, which has been recently attempted [8], is not without serious dangers of misinterpretation. First of all, the use of the Mulliken atomic charges, with their well-known deficiencies (see, for example, Ref. [25]), may easily result in misleading conclusions. This is well illustrated by the previous calculations [7] which, on the basis of the Mulliken population analysis, found the stabilization of the singlet state of imidazol-2-ylidene due to the  $\pi$ -donation relatively insignificant. At the same time,

the Mulliken charge on the carbenic carbon atom was found to be very close to zero, ruling out stabilization due to the  $\sigma$ -backdonation and leaving the unusual stability of the imidazol-2-ylidene carbene completely unexplained.

Second, even when rigorously derived atomic charges are correlated with the singlet-triplet energy gaps, one may expect the proportionality factor to be significantly different from that for an isolated carbon atom. This is so because the potentials around the carbenic carbon atoms are no longer spherically symmetrical. This means that the singlet-triplet splitting is expected to depend not only on the charge on the pertinent carbon atom, but also on its higher multipole moments, which often have quite large magnitudes. For example, our calculations show that the carbenic carbon atom in the 1,3-dimethylimidazol-2-ylidene molecule bears the dipole moment of ca. 1.88 [a.u.], which corresponds to the mean displacement of the atomic charge density equal to about 0.15 [Å]. Therefore, any empirical correlation between the splitting and the atomic charge must include in an effective manner variability of these moments with the atomic charge, thus altering the proportionality factor.

Finally, we would like to bring the reader's attention to a particular feature of the calculated 1,3-dimethylimidazol-2-ylidene geometry for which we *do not* have a simple explanation. As revealed by the data listed in Table II, the bond angle  $\text{N}_2\text{C}_8\text{H}_{10}$  (Fig. 1, Table II) between the nitrogen atom, the carbon of the methyl group, and the hydrogen facing the lone pair of the carbenic carbon is much smaller (by ca.  $3^\circ$ ) than the analogous angles ( $\text{N}_2\text{C}_8\text{H}_{11}$  and  $\text{N}_2\text{C}_8\text{H}_{11}$ ) for the other hydrogens. The difference in angles disappears almost completely upon protonation. We speculate that the tilting of the C—H bond toward the carbon lone pair is caused by attractive interactions between the C—H dipole and strongly dipolar electron distribution around the carbenic carbon.

### Conclusions

One can expect the geometries of imidazol-2-ylidene carbenes and the corresponding imidazolium cations to be accurately predicted at the MP2/6-311++G\*\* level of theory. Rigorous analysis of the one-electron density matrices calculated within the same approximation affords a clear-cut description of the electronic structures of these systems in terms of localized natural orbitals. Taking into account the results of such an orbital-by-orbital analysis, the unusual stability of the imidazol-2-ylidene carbenes can be directly related to the substantial  $\sigma$ -backdonation from the carbenic carbon to the adjacent nitrogen atoms, with the resulting large positive charge on the carbon atom strongly favoring the singlet state over the triplet one. The  $\pi$ -donation is expected to be marginal and therefore to play only a minor role, ruling out the presence of significant stabilization due to ylidic resonance structures. The unusually large proton affinity of the imidazol-2-ylidene carbenes can be readily explained by the extra  $\pi$ -electron stabilization of the corresponding imidazolium cations.

### Acknowledgments

This work was partially supported by the National Science Foundation under the Contract CHE-9015566, the Camille and Henry Dreyfus Foundation New Fac-

ulty Award Program, the Florida State University through time granted on its Cray Y-MP digital computer, and the donors of The Petroleum Research Fund administered by ACS (Grant PRF 25076-G6). The author thanks Dr. S. T. Mixon for critical comments.

### Bibliography

- [1] H. F. Schaefer, III, *Science* **231**, 1100 (1986).
- [2] C. W. Bauschlicher, Jr., S. R. Langhoff, and P. R. Taylor, *J. Chem. Phys.* **87**, 387 (1987).
- [3] H. Schonherr and H. Wanzlick, *Chem. Ber.* **103**, 1037 (1970).
- [4] A. J. Arduengo, III, R. L. Harlow, and M. Kline, *J. Am. Chem. Soc.* **113**, 361 (1991).
- [5] A. J. Arduengo, III, H. V. Raska Dias, R. L. Harlow, and M. Kline, *J. Am. Chem. Soc.* **114**, 5530 (1992).
- [6] R. Gleiter and R. J. Hoffmann, *J. Am. Chem. Soc.* **90**, 5457 (1968).
- [7] D. A. Dixon and A. J. Arduengo, III, *J. Phys. Chem.* **95**, 4180 (1991).
- [8] K. K. Inkura, W. A. Goddard, III, and J. L. Beauchamp, *J. Am. Chem. Soc.* **114**, 48 (1992).
- [9] K. B. Wiberg and K. E. Laidig, *J. Am. Chem. Soc.* **109**, 5935 (1987).
- [10] J. Cioslowski and P. R. Surjan, *J. Mol. Struct. (Theorchem)* **255**, 9 (1992).
- [11] R. F. W. Bader, *Atoms in Molecules: A Quantum Theory* (Clarendon, Oxford, 1990).
- [12] J. Cioslowski, *J. Math. Chem.* **8**, 169 (1991); *Int. J. Quant. Chem.* **S24**, 15 (1990).
- [13] J. Cioslowski and S. T. Mixon, *J. Am. Chem. Soc.* **113**, 4142 (1991).
- [14] J. Cioslowski and S. T. Mixon, *J. Am. Chem. Soc.* **114**, 4382 (1992).
- [15] J. Cioslowski and S. T. Mixon, *J. Am. Chem. Soc.* **115**, (1992).
- [16] M. J. Frisch, M. Head-Gordon, G. W. Trucks, J. B. Foresman, H. B. Schlegel, K. Raghavachari, M. Robb, J. S. Binkley, C. Gonzalez, D. J. Defrees, D. J. Fox, R. A. Whiteside, R. Seeger, C. F. Melius, J. Baker, R. L. Martin, L. R. Kahn, J. J. P. Stewart, S. Topiol, and J. A. Pople, *GAUSSIAN 90*, Revision F, (GAUSSIAN, Pittsburgh, PA, 1990).
- [17] E. A. Salter, G. W. Trucks, G. Fitzgerald, and R. J. Bartlett, *Chem. Phys. Lett.* **141**, 61 (1987).
- [18] F. W. Biegler-König, R. F. W. Bader, and T. H. Tang, *J. Comput. Chem.* **3**, 317 (1982).
- [19] J. Cioslowski, *Chem. Phys. Lett.* **194**, 73 (1992).
- [20] J. Cioslowski, *LOSSES: Localized Orbitals for Systematic Studies of Electronic Structures*, 1991.
- [21] S. J. Kim, T. P. Hamilton, and H. F. Schaefer, III, *J. Chem. Phys.* **94**, 2063 (1991).
- [22] J. Cioslowski, *J. Am. Chem. Soc.* **111**, 8333 (1989); K. B. Wiberg, C. M. Hadad, T. J. LePage, C. M. Breneman, and M. J. Frisch, *J. Phys. Chem.* **96**, 671 (1992).
- [23] A. C. Hopkinson and M. H. Lien, *Can. J. Chem.* **63**, 3582 (1985); D. Feller, W. T. Borden, and E. R. Davidson, *Chem. Phys. Lett.* **71**, 22 (1980); P. H. Mueller, N. G. Rondan, K. N. Houk, J. F. Harrison, D. Hooper, B. H. Willen, and J. F. Liebman, *J. Am. Chem. Soc.* **103**, 5049 (1981).
- [24] C. W. Bauschlicher, Jr., H. F. Schaefer, III, and P. S. Bagus, *J. Am. Chem. Soc.* **99**, 7106 (1977).
- [25] J. Cioslowski, P. J. Hay, and J. P. Ritchie, *J. Phys. Chem.* **94**, 148 (1990).

Received March 30, 1993

# Molecular SCF Calculations Using a Basis of Numerical Orbitals

JAMES D. TALMAN

*Departments of Applied Mathematics and Physics and Centre for Chemical Physics,  
University of Western Ontario, London, Ontario, Canada N6A 5B7*

## Abstract

Techniques for computing the multicenter integrals required for molecular calculations for orbitals for which the radial factors are given numerically are described. The methods make extensive use of a numerical algorithm for computing spherical Bessel transforms. The feasibility of using these methods is demonstrated by applying them to SCF calculations for the methane molecule. © 1993 John Wiley & Sons, Inc

## Introduction

In atomic structure calculations, both numerical or finite difference approximation and finite basis expansion methods have proved to be of great value and have lead to successful theoretical calculations. The former approach has been pioneered in large part by Froese Fischer [1], and the application of the latter in atomic physics is associated to considerable extent with Clementi and Roetti [2]. The situation is, of course, considerably different in molecular physics, where, apart from some calculations for diatomic molecules, essentially all calculations employ finite basis expansion methods, as pioneered by Roothaan. Moreover, practically all finite basis expansion methods employ expansions in Gaussian type orbitals (GTOs). The reason for this is obvious; the calculation of the necessary matrix elements is almost trivial for GTOs and is practically intractible for other functional forms.

Despite the fact that GTO expansion methods have been widely successful in describing molecular properties, there still seems to be interest in developing alternative methods for approximating molecular wave functions. This stems in part from the fact that GTOs are not particularly suited to describing the behavior of the wave function close to the nuclei and at large distances. This problem is overcome in part by superposing several GTOs to give a more realistic orbital (the method of contraction), but this sacrifices part of the virtue of the simplicity of the matrix element calculation. It is also a difficult computational challenge to optimize the nonlinear parameters in the GTOs, and this is usually done only partially, using so-called even-tempered nonlinear parameters. The interest in using basis functions other than GTOs has led to considerable effort to develop techniques for computing matrix elements for other forms of basis functions, namely, Slater orbitals (STOs) or more general forms of exponential basis functions (ETOs). Techniques for such

orbitals in the two-center case have been developed some 30 years ago by Barnett and Coulson [3] and Geller [4]. A variety of approaches have been reviewed in 1981 at a conference devoted to these problems [5].

As commented above, relatively little work has been done on applying purely numerical techniques in molecular calculations, although some aspects of this have been reviewed at a conference in 1988 [6].

Since numerically determined wave functions offer more generality than wave functions constructed as linear combinations of analytic basis functions, it remains of interest to try to incorporate such functions in molecular calculations. In this article some progress in this direction will be described and results of applying the methods to the  $\text{CH}_4$  molecule are reported.

The calculations that have been carried out are SCF calculations using molecular orbitals that are linear combinations of atomic orbitals that are obtained numerically as atomic orbitals. It would appear that the use of such orbitals should be optimal, in that all the energy to be obtained by orbital optimization for the isolated atomic systems is obtained, and resulting energy differences should represent chemical bonding energies. In other words, errors from basis set incompleteness should be very small in this approach. It could also be hoped that, by using more realistic orbitals, the required number of orbitals to obtain satisfactory results might be substantially reduced. The extra computational complexity of using numerical orbitals could then possibly be compensated by a reduction in the number required.

The numerical methods used are based on an effective method for computing spherical Bessel transforms numerically [7,8]. Since these transforms are essentially the Fourier transforms of angular momentum eigenfunctions, and translation in position space corresponds to multiplication by a complex exponential in momentum space, this facilitates the calculation of multicenter integrals for numerically determined orbitals. This transform method will be reviewed in the next section, and its application to overlap integrals, nuclear attraction integrals, and two-electron integrals will be described in the following sections. The results of the application of the method to  $\text{CH}_4$  will be given, and the limitations and outlook for other applications will be discussed.

Momentum space methods for STOs have been studied extensively by Silverstone and coworkers; these methods have been reviewed by Todd et al. [9]. Similarly, techniques using so-called *B* functions which are equivalent to STOs have been extensively studied by Steinborn and coworkers. This work has been recently reviewed by Steinborn et al. [10].

### Numerical Spherical Bessel Transforms

The basis functions to be considered are taken to be angular momentum functions of the form

$$f_{lm}(\mathbf{r}) = f_l(r)Y_{lm}(\hat{\mathbf{r}}), \quad (1)$$

where  $Y_{lm}(\hat{\mathbf{r}})$  is the usual spherical harmonic. The Fourier transform of  $f$  is defined to be

$$\tilde{f}_{lm}(\mathbf{k}) = \int e^{i\mathbf{k}\cdot\mathbf{r}} f_{lm}(\mathbf{r}) d\mathbf{r}. \quad (2)$$



The familiar expansion of a plane wave in spherical harmonics

$$e^{i\mathbf{k}\cdot\mathbf{r}} = 4\pi \sum l^l j_l(kr) Y_{lm}(\hat{\mathbf{k}}) Y_{lm}(\hat{\mathbf{r}})^* \quad (3)$$

can be readily applied to show that

$$\tilde{f}_{lm}(\mathbf{k}) = 4\pi i^l \tilde{f}_l(k) Y_{lm}(\hat{\mathbf{k}}), \quad (4)$$

where

$$\tilde{f}_l(k) = \int_0^\infty j_l(kr) f_l(r) r^2 dr. \quad (5)$$

If new variables  $\kappa = \ln k$  and  $\rho = \ln r$  are introduced, this equation can be written as

$$\begin{aligned} \tilde{f}_l(e^\kappa) &= \int_{-\infty}^\infty j_l(e^{\rho+\kappa}) f_l(e^\rho) e^{3\rho} d\rho \\ &= e^{-3\kappa/2} \int_{-\infty}^\infty j_l(e^{\rho+\kappa}) e^{3\rho/2} f_l(e^\rho) e^{3(\rho+\kappa)/2} d\rho. \end{aligned} \quad (6)$$

The integral in the right-hand side of Eq. (6) can be recognized as a convolution of a function of  $\rho$  and function of  $\rho + \kappa$ . It is therefore possible to compute it in terms of the inverse Fourier transform of the product of the Fourier transform of each factor; this gives the convolution as a function of  $-\kappa$ .

In the calculations described here, the Fourier transform of  $e^{3\rho/2} f_l(e^\rho)$  is computed numerically using the fast Fourier transform method, and the transform of  $e^{3\rho/2} j_l(e^\rho)$  is obtained analytically. The inverse transform of the product is again computed using the fast Fourier transform. Complete details of the numerical method are given in Ref. [8].

The expansion of an angular momentum function centered at one point in terms of angular momentum functions centered at another point can easily be effected using Fourier transforms. We write

$$\begin{aligned} f_{lm}(\mathbf{r} - \mathbf{a}) &= \frac{1}{(2\pi)^3} \int e^{-i\mathbf{k}\cdot(\mathbf{r}-\mathbf{a})} \tilde{f}_{lm}(\mathbf{k}) d\mathbf{k} \\ &= \frac{1}{(2\pi)^3} \int e^{-i\mathbf{k}\cdot\mathbf{r}} e^{i\mathbf{k}\cdot\mathbf{a}} \tilde{f}_{lm}(\mathbf{k}) d\mathbf{k}. \end{aligned} \quad (7)$$

Expanding each factor in the last expression in spherical harmonics, using Eqs. (3) and (4) gives

$$f_{lm}(\mathbf{r} - \mathbf{a}) = \sum_{LL'MM'} (-1)^m \begin{pmatrix} L & L' & l \\ -M & -M' & m \end{pmatrix} Y_{LM}(\hat{\mathbf{a}}) Y_{L'M'}(\hat{\mathbf{r}}) f_{LL'}(r, a), \quad (8)$$

where

$$f_{LL'}(r, a) = 8i^{l+l'-l} \sqrt{\frac{(2l+1)(2L+1)(2L'+1)}{4\pi}} \begin{pmatrix} L & L' & l \\ 0 & 0 & 0 \end{pmatrix} \times \int_0^\infty j_L(ka) j_{L'}(kr) \hat{f}_l(k) k^2 dk. \quad (9)$$

The functions  $f_{LL'}(r, a)$ , which are the Löwdin alpha-functions in the case of STOS [11], can therefore be tabulated on the logarithmic mesh by computing  $\hat{f}_l(k)$ , multiplying by  $j_L(ka)$  and computing the  $L'$  spherical Bessel transform of the product.

The overlap integral of two angular momentum functions can be computed in momentum space [12] as

$$\begin{aligned} & \int f_{l'm'}(\mathbf{r} - \mathbf{a})^* g_{lm}(\mathbf{r}) d\mathbf{r} \\ &= \frac{1}{(2\pi)^3} \int \int e^{i\mathbf{k} \cdot (\mathbf{r} - \mathbf{a})} f_{l'm'}(\mathbf{k})^* g_{lm}(\mathbf{r}) d\mathbf{k} d\mathbf{r} \\ &= \frac{1}{(2\pi)^3} \int e^{-i\mathbf{k} \cdot \mathbf{a}} \hat{f}_{l'm'}(\mathbf{k})^* \hat{g}_{lm}(\mathbf{k}) d\mathbf{k} \\ &= 8 \sum_{LM} i^{l+l'-l} \sqrt{\frac{(2l+1)(2l'+1)(2L+1)}{4\pi}} \\ & \quad \times (-1)^m \begin{pmatrix} l & l' & L \\ 0 & 0 & 0 \end{pmatrix} \begin{pmatrix} l & l' & L \\ m & -m' & -M \end{pmatrix} \times Y_{LM}(\hat{\mathbf{a}}) \int_0^\infty j_L(ka) \hat{f}_{l'}(k) \hat{g}_l(k) k^2 dk. \end{aligned} \quad (10)$$

The sum on  $L$  is in this case finite. Matrix elements of the kinetic energy operator are readily obtained by replacing  $k^2$  by  $k^4$  in the integrand.

### Nuclear Attraction Integrals

The calculation of the nuclear attraction energy requires the evaluation of integrals of the form

$$I = \int f_{l'm'}(\mathbf{r} - \mathbf{a})^* \frac{1}{|\mathbf{r} - \mathbf{R}|} g_{lm}(\mathbf{r} - \mathbf{a}) d\mathbf{r}. \quad (11)$$

These have been computed by translating each factor to a common origin which is chosen to optimize the convergence rate of the infinite sums [13]. The Coulomb factor is expanded using the usual expansion

$$\frac{1}{|\mathbf{r} - \mathbf{R}|} = 4\pi \sum_{\lambda\mu} \frac{1}{2\lambda+1} [r_{<}^\lambda / r_{>}^{\lambda+1}] Y_{\lambda\mu}(\hat{\mathbf{r}})^* Y_{\lambda\mu}(\hat{\mathbf{R}}). \quad (12)$$

The maximum value of  $L'$  in Eq. (8) and of  $\lambda$  in Eq. (12) will be denoted by  $L_{N,\max}$ .

The angular factor in the integral is expressible in terms of  $3 - j$  coefficients. The radial integral is obtained using the trapezoidal rule on the logarithmic mesh. However, the integrand has a discontinuous derivative at  $r = R$ , and a correction has been included to account for this.

It can be shown [13] that the convergence of the angular momentum sums is geometric in the ratios of the distances of the three centers from the expansion center. With the optimum choice of the expansion center the largest possible value of this ratio is 0.618, the reciprocal of the golden mean. The disadvantage of this approach is that the angular momentum sum is twofold infinite whereas it is singly-infinite if the expansion center is one of the three centers in the integrand. However, with the latter choice, the convergence may be only algebraic, rather than geometric if the centers lie on an equilateral triangle.

### Two-Electron Integrals

The most time consuming part of the SCF calculation is to compute the two-electron or four-center integrals of the form

$$I_2 = \iint f_{l_1 m_1}(\mathbf{r} - \mathbf{a})^* g_{l_2 m_2}(\mathbf{r} - \mathbf{b}) \frac{1}{|\mathbf{r} - \mathbf{r}'|} \times f_{l'_1 m'_1}(\mathbf{r}' - \mathbf{a}')^* g_{l'_2 m'_2}(\mathbf{r}' - \mathbf{b}') d\mathbf{r} d\mathbf{r}'. \quad (13)$$

These integrals are the interaction energy between two charge density distributions which are the products of a pair of orbitals [14]. If the number of orbitals is  $N$ , there are of the order of  $N^2/2$  charge distributions and of the order of  $N^4/8$  two-electron integrals. Although the integral is sixfold in position space, it is only threefold in momentum space [15]; it is therefore more convenient to do the integration in momentum space. The technique that has been employed is to expand the product of two orbitals in a multipole expansion of angular momentum functions centered at the midpoint points  $\mathbf{c}$  and  $\mathbf{c}'$  between the centers of each factor. This expansion may be rather slowly convergent; however, if the centers are separated, the product will be small, and less accuracy is required than when the orbitals are on the same center.

The interaction energy of charge distributions  $F_{\Lambda\sigma}(\mathbf{r})$  centered at  $\mathbf{c}$  and  $G_{\Lambda'\sigma'}(\mathbf{r})$  centered at  $\mathbf{c}'$  is

$$I_2 = \iint F_{\Lambda\sigma}(\mathbf{r} - \mathbf{c}) \frac{1}{|\mathbf{r} - \mathbf{r}'|} G_{\Lambda'\sigma'}(\mathbf{r}' - \mathbf{c}') d\mathbf{r} d\mathbf{r}'. \quad (14)$$

In momentum space this becomes

$$I_2 = \frac{1}{2\pi^2} \int e^{i\mathbf{k} \cdot (\mathbf{c} - \mathbf{c}')} \tilde{F}_{\Lambda\sigma}(\mathbf{k}) \tilde{G}_{\Lambda'\sigma'}(\mathbf{k}) \frac{1}{k^2} d\mathbf{k}. \quad (15)$$

This integral is essentially the same as the integral in Eq. (10) so that

$$I_2 = 32\pi \sum_{LM} i^{\Lambda+\Lambda'-L} \sqrt{\frac{(2\Lambda+1)(2\Lambda'+1)(2L+1)}{4\pi}} \\ \times (-1)^M \begin{pmatrix} \Lambda & \Lambda' & L \\ 0 & 0 & 0 \end{pmatrix} \begin{pmatrix} \Lambda & \Lambda' & L \\ \sigma & \sigma' & -M \end{pmatrix} \\ \times Y_{LM}(\hat{\mathbf{R}}) \int_0^\infty j_L(kR) \tilde{F}_\Lambda(k) \tilde{G}_{\Lambda'}(k) dk, \quad (16)$$

where  $\mathbf{R} = \mathbf{c} - \mathbf{c}'$ .

The product of angular momentum functions centered at  $\mathbf{a}$  and  $\mathbf{b}$  can be expressed in terms of angular momentum functions centered at the midpoint  $\mathbf{c} = (\mathbf{a} + \mathbf{b})/2$  as

$$f_{l_1 m_1}(\mathbf{r} - \mathbf{a})^* g_{l_2 m_2}(\mathbf{r} - \mathbf{b}) = \sum_{\Lambda \sigma} F_{\Lambda \sigma}(R) Y_{\Lambda \sigma}(\Theta \Phi), \quad (17)$$

where  $R\Theta\Phi$  are the spherical polar coordinates of  $\mathbf{r} - \mathbf{c}$ . However, it is more satisfactory [16] to express the product as

$$f_{l_1 m_1}(\mathbf{r} - \mathbf{a})^* g_{l_2 m_2}(\mathbf{r} - \mathbf{b}) = \sum_{j\lambda\Lambda\mu\sigma} (-1)^{m_1} \sqrt{\frac{(2l_1+1)(2l_2+1)}{(2\lambda+1)(2\Lambda+1)}} \\ \times \begin{pmatrix} l_1 & l_2 & j \\ -m_1 & m_2 & m \end{pmatrix} \begin{pmatrix} j & \lambda & \Lambda \\ m & \mu & \sigma \end{pmatrix} Y_{\lambda\mu}(\hat{\mathbf{c}}) Y_{\Lambda\sigma}(\hat{\mathbf{r}}) F_{j\lambda\Lambda}(r), \quad (18)$$

where

$$F_{j\lambda\Lambda}(r) = \sum_{L_1 L'_1 L_2 L'_2} (2\lambda+1)(2\Lambda+1)(2j+1)(-1)^{L_2} \\ \times \begin{pmatrix} L_1 & L_2 & \lambda \\ 0 & 0 & 0 \end{pmatrix} \begin{pmatrix} L'_1 & L'_2 & \Lambda \\ 0 & 0 & 0 \end{pmatrix} \begin{Bmatrix} l_1 & l_2 & j \\ L_1 & L_2 & \lambda \\ L'_1 & L'_2 & \Lambda \end{Bmatrix} f_{L_1 L'_1}(r, d) g_{L_2 L'_2}(r, d) \quad (19)$$

and  $d = |\mathbf{a} - \mathbf{b}|/2$ . The sum in Eq. (19) is singly infinite.

The two-electron integrals are therefore given by

$$I_2 = \sum_{j''} (-1)^{m_1+m_2} \begin{pmatrix} l_1 & l_2 & j \\ -m_1 & -m_2 & m \end{pmatrix} \begin{pmatrix} l'_1 & l'_2 & j' \\ m'_1 & m'_2 & m' \end{pmatrix} S(jm, j'm'), \quad (20)$$

where

$$\begin{aligned}
 S(jm, j'm') = & \sum_{j\lambda\Lambda\sigma} \sum_{j'\lambda'\Lambda'\sigma'} \sum_L \begin{pmatrix} j & \lambda & \Lambda \\ m & \mu & \sigma \end{pmatrix} \begin{pmatrix} j' & \lambda' & \Lambda' \\ m' & \mu' & \sigma' \end{pmatrix} Y_{\lambda\mu}(\hat{\mathbf{e}}) Y_{\lambda'\mu'}(\hat{\mathbf{e}}') Y_{LM}(\hat{\mathbf{R}}) \\
 & \times (-1)^{(\Lambda-\Lambda'+L)/2+M} (2L+1) \begin{pmatrix} \Lambda & \Lambda' & L \\ 0 & 0 & 0 \end{pmatrix} \begin{pmatrix} \Lambda & \Lambda' & L \\ \sigma & \sigma' & -M \end{pmatrix} \\
 & \times h(\lambda\Lambda j, \lambda'\Lambda' j', L)
 \end{aligned} \quad (21)$$

and

$$h(\lambda\Lambda j, \lambda'\Lambda' j', L) = 32\pi \int_0^\infty j_L(kR) \tilde{F}_{j\lambda\Lambda}(k) \tilde{G}_{j'\lambda'\Lambda'}(k) dk. \quad (22)$$

The two-electron integrals have been calculated using the spherical Bessel transforms of the functions  $F_{j\lambda\Lambda}(r)$  in Eq. (16). The integrals were calculated using Gauss-Laguerre integration on a mesh of  $N_{GL}$  points. The functions  $\tilde{F}_{j\lambda\Lambda}(k)$  for  $0 \leq \Lambda \leq \Lambda_{\max}$  are calculated initially, interpolated onto the Gauss-Laguerre mesh and stored. The maximum value of  $L'_1$  and  $L'_2$  in the sum in Eq. (19) will be denoted by  $L'_{\max}$ . Since the calculation of the transforms of the product functions requires only  $N^2/2$  steps, it is possible to use a considerably refined mesh and a reasonably large value of  $L'_{\max}$  for the calculations with a relatively small expenditure of computer time. Since the Gauss-Laguerre mesh is relatively small, of the order of 20-40 mesh points, the storage requirements were tolerable in the present calculations.

The advantage of the expansion (18) over (17) is that fewer functions need to be stored. For example, in the case  $l_1 = l_2 = 0$ , it is necessary to store  $\Lambda_{\max} + 1$  functions  $\tilde{F}_{j\lambda\Lambda}(k)$  arising in Eq. (18) compared with  $(\Lambda_{\max} + 1)^2$  functions  $\tilde{F}_{\Lambda\sigma}(k)$  that arise in Eq. (17). Similarly, there is a large reduction in the number of integrals of the type defined in Eq. (22) using the formulation of Eq. (18).

### Numerical Accuracy

The accuracy obtained in the calculations depends on a number of parameters governing the numerical approximations. These are:

- $\rho_{\min}$ ,  $\kappa_{\min}$ ,  $h$ ,  $N_{\log}$ , defining the logarithmic meshes in  $r$  and  $k$ ;
- $N_{GL}$ ,  $k_{\max}$  defining the mesh for the Gauss-Laguerre integration;
- $L_{N,\max}$ , the maximum of  $L'$  and  $\lambda$  in the nuclear attraction integrals;
- $L_{2,\max}$ , the maximum of  $L'_1$  and  $L'_2$  in Eq. (19);
- $\Lambda_{\max}$ , the maximum of  $\Lambda$  and  $\Lambda'$  in Eq. (21).

The calculations have been made with  $\rho_{\min} = -14$ ,  $\kappa_{\min} = -11$ ,  $h = 0.14$  and  $N_{\log} = 128$ . The results change by only a few parts in  $10^{-5}$  if  $N_{\log}$  is doubled and  $h$  is halved.

Results of calculations for various choices of the other parameters in the minimal basis set calculation are given in Table I. It is seen that results accurate to a few

TABLE I. Calculated energies for the methane molecule in a.u. using the minimal basis for various values of the parameters determining the numerical procedure.\*

$N_{GL}$	$k_{max}$	$L_{N,max}$	$L_{2,max}$	$\Lambda_{max}^{(1)}$	$\Lambda_{max}^{(2)}$	$E$
20	40.0	6	14	6	2	-40.04680
30	40.0	6	14	6	2	-40.04678
40	40.0	6	14	6	2	-40.04680
40	50.0	6	14	6	2	-40.04680
30	40.0	7	14	6	2	-40.04702
30	40.0	8	14	6	2	-40.04701
30	40.0	8	16	6	2	-40.04697
30	40.0	8	14	7	2	-40.04964
30	40.0	8	14	8	2	-40.04974
30	40.0	8	14	9	2	-40.05055
30	40.0	8	14	10	2	-40.05058
30	40.0	8	14	10	3	-40.04456
30	40.0	8	14	10	4	-40.04395
30	40.0	8	14	10	5	-40.04342
30	40.0	8	14	10	6	-40.04335

\* The parameters are defined in the text. The C—H bond length is 2.0665 bohr.

parts in  $10^{-5}$  are obtained for reasonably small values of  $N_{GL}$  of the order of 20–40. The parameter  $k_{max}$  is the maximum value of  $k$  in the Gauss–Laguerre mesh and should be determined so that the integrand in Eq. (22) is negligible at  $k_{max}$ . If the orbitals in the integrand are  $s$  orbitals, which is the worst case, the integrand, apart from the factor  $j_L(kR)$ , decreases like  $k^{-8}$  for large  $k$  and should be less than  $10^{-6}$  for  $k_{max}$  of the order of 5. This should, however, be multiplied by  $Z_{max}$ , the largest nuclear charge, since this determines the scale of the momentum variable. Therefore, a value of  $k_{max}$  of the order of 30 or 40 should provide accuracy of better than  $10^{-5}$ . The results confirm that this is reasonable.

It is seen that accuracy of a few parts in  $10^{-5}$  is obtained with  $L_{N,max} = 8$ . Comparable accuracy is obtained for  $L_{2,max} = 14$ .

It has been found that the sum on  $\Lambda$  and  $\Lambda'$  for the two-electron integrals converges more slowly if either of the separations  $c$  or  $c'$  is zero. (If both separations are zero, the sum is finite.) Since these integrals are also larger, it is necessary to treat them more carefully. On the other hand, the sum in this case is only singly, rather than doubly infinite. The calculation has therefore been arranged so that the summation is truncated at a larger value,  $\Lambda_{max}^{(1)}$ , in the case  $c = 0$  or  $c' = 0$  and at a smaller value,  $\Lambda_{max}^{(2)}$ , otherwise. It appears that accuracy of a few parts in  $10^{-5}$  is obtained for  $\Lambda_{max}^{(1)} = 10$  and  $\Lambda_{max}^{(2)} = 6$ . It is the latter parameter that governs the most time consuming part of the two-electron integral calculation. It can be shown that the number of terms in the calculation behaves like  $\Lambda_{max}^4$  so that in going from  $\Lambda_{max} = 4$  to  $\Lambda_{max} = 6$ , the time requirement increases fivefold. Thus accuracy of the order of  $10^{-3}$  is much more readily obtainable than  $10^{-4}$ .

### Results Including Polarization Orbitals

The variational SCF calculation can be improved by going beyond the minimal basis set, in this case 1s, 2s, and 2p orbitals on C and 1s orbitals on H, to include so-called polarization orbitals. These can be either excited orbitals centered on each atom, or "floating orbitals" which may be GTOs. Calculations have been carried out using the former approach, including up to 4s, 3p, and 3d orbitals on C and up to 2p on H. It should be noted that the orbitals that have been used are not exactly Hartree-Fock atomic orbitals; for the C orbitals they are obtained from the optimized potential model [17], which yield orbitals essentially the same as Hartree-Fock orbitals for the occupied states [18], but can also generate orthogonal orbitals for unoccupied states.

These results have been obtained using the numerical parameters from the last line of Table I. No further tests have been made on the effect of changing these parameters. It can be expected, however, that the effect on the contributions of the polarization orbitals will be small since these are already small. Furthermore, most of the computational inaccuracy arises from large momentum components in the orbitals, and these should be much smaller in the more diffuse unoccupied orbitals.

Results are given in Table II and compared with similar calculations using GTOs [19]. The results are rather disappointing in that the GTO calculations yield a lower energy than the result using optimized atomic orbitals in each case. On the other hand, the results are obtained with no orbital optimization, whereas the results using GTOs are obtained with searches over the parameters determining the unoccupied orbitals.

### Discussion

The results obtained from these calculations indicate that, perhaps contrary to expectation, atomic Hartree-Fock orbitals do not provide a particularly good basis for molecular SCF calculations. The reason for this may be that the molecule is more tightly bound than the constituent atoms. The behavior of the C 2p orbitals

TABLE II. Calculated energies in a.u. for the methane molecule using various basis sets.<sup>a</sup>

Basis		<i>E</i>	<i>E</i> <sub>GTO</sub> <sup>b</sup>
C	H		
1s,2s,2p	1s	-40.0433	-40.1282
+3s,4s,3p	2s	-40.1397	-40.1801
+3d	—	-40.1632	-40.1982
+—	2p	-40.1775	-40.2039

<sup>a</sup> Corresponding results for Gaussian bases are denoted *E*<sub>GTO</sub>.

<sup>b</sup> Ref. [19].

at large  $r$  is governed by the single-particle energy eigenvalue which is  $-0.431$  a.u., whereas the  $\text{CH}_4$  ionization potential as given by the valence electron eigenvalue in the present calculation is  $-0.548$  a.u. Further evidence of this is that there are very large mixings of the polarization orbitals, with amplitudes comparable to those of the occupied orbitals.

On the other hand, the results indicate that it is quite feasible to carry out SCF calculations for small molecules using these momentum space techniques. The minimum basis set calculation required 14 s on a CYBER 2000U and the two-electron integrals required about 2.5 ms per integral. This could also be carried out on a PC. The largest calculation reported, using 35 basis functions, required 1600 s. The calculation of the approximately 200,000 two-electron integrals required 1400 s or about 7 ms per integral. With  $\Lambda_{\text{max}}^{(2)}$  reduced from 6 to 4, this is reduced to about 2.7 ms per integral.

The success of these calculations suggests that it may be possible to develop a variational approach to compute numerically the basis orbitals entering the calculation. This could permit the use of the finite difference approximation methods that give accurate Hartree-Fock wave functions for atoms in molecular calculations.

### Acknowledgments

This research has been supported by the Natural Science and Engineering Research Council of Canada and by Nordita.

### Bibliography

- [1] C. Froese Fischer, *The Hartree-Fock Method for Atoms* (Wiley-Interscience, New York, 1978).
- [2] E. Clementi and C. Roetti, *At. Data. Nucl. Data Tables* **14**, 177 (1974).
- [3] M. P. Barnett and C. A. Coulson, *Phil. Trans. Roy. Soc. A* **243**, 221 (1951).
- [4] M. Geller, *J. Chem. Phys.* **39**, 84 (1963).
- [5] C. A. Weatherford and H. W. Jones, Eds., *ETO Multicenter Molecular Integrals* (Reidel, Dordrecht, 1982).
- [6] M. Defranceschi and J. Delhalle, Eds., *Numerical Determination of the Electronic Structure of Atoms, Diatomic and Polyatomic Molecules*, NATO ASI Series 271 (Kluwer, Dordrecht, 1989).
- [7] J. D. Talman, *J. Comput. Phys.* **29**, 35 (1978).
- [8] J. D. Talman, *Comput. Phys. Comm.* **30**, 93 (1983).
- [9] H. D. Todd, K. C. Daiker, R. D. Cloney S. J., R. K. Moats, and H. J. Silverstone, in Ref. [5].
- [10] E. O. Steinborn, H. H. H. Homeier and E. J. Weniger, *J. Mol. Struct. (Theochem.)* **260**, 207 (1992).
- [11] P. O. Löwdin, *Adv. Phys.* **5**, 1 (1956).
- [12] F. P. Prosser and C. H. Blanchard, *J. Chem. Phys.* **36**, 1112 (1962).
- [13] J. D. Talman, *J. Chem. Phys.* **84**, 6879 (1986).
- [14] C. C. J. Roothaan, *J. Chem. Phys.* **19**, 1445 (1951).
- [15] M. Geller, *J. Chem. Phys.* **39**, 854 (1963).
- [16] J. D. Talman, *J. Chem. Phys.* **80**, 2000 (1984).
- [17] J. D. Talman and W. F. Shadwick, *Phys. Rev. A* **14**, 36 (1976).
- [18] K. Aashamar, T. M. Luke, and J. D. Talman, *Phys. Rev. A* **19**, 6 (1979).
- [19] S. Rothenberg and H. F. Shaeffer III, *J. Chem. Phys.* **54**, 2764 (1971).

Received May 11, 1993



# Basis Set Dependence of *Ab-Initio* Calculated Vibration Frequencies

MICHAELA FLOCK and MICHAEL RAMEK

*Institut für Physikalische und Theoretische Chemie, Technische Universität Graz,  
A-8010 Graz, Austria*

## Abstract

Vibration frequencies for 2-aminoethanol, neutral glycine, glycolic acid, *n*-propylamine, *n*-propanol, and propionic acid were calculated on the *ab-initio* RHF level with a variety of standard basis sets including polarization and diffuse functions. Experimental frequencies, if available, are compared with these data and basis set suitability is discussed on the basis of this comparison. © 1993 John Wiley & Sons, Inc.

## Introduction

The calculation of vibration frequencies in variational *ab-initio* programs is usually carried out by diagonalizing the Hessian matrix of second derivatives. Frequencies calculated this way are consistently too large; in the case of stretch vibrations the excess may reach the order of some hundred  $\text{cm}^{-1}$ . At first glance it appears that this deviation is caused by considering the second derivatives only, which corresponds to the assumption of harmonic oscillator behavior. It is a striking fact, however, that this straightforward looking consideration is wrong: the deviation from the harmonic oscillator behavior can be calculated rather accurately by variational *ab-initio* methods at the Hartree-Fock level as well as at the post-Hartree-Fock level [1]. The differences between experimental and calculated frequencies therefore must be due to intrinsic deficiencies of the description of the potential energy surface near the local minimum.

Since calculated vibration frequencies allow a direct link to experiments, the correlation between calculated and experimental values has been a topic of interest for several years. The main emphasis depends mostly upon the intended use of the calculated values: either as a help in the assignment of normal modes to experimentally measured frequencies, or as a prediction of experimentally inaccessible data. The first case is best covered by scaling not the frequencies, but the elements of the Hessian matrix with a number of individual scale factors [2]. In the latter case oftentimes one global scale factor is used to adjust the calculated frequency values. (Some recent applications may be found in Ref. [3-6].)

We have investigated several compounds at the Hartree-Fock level with a variety of basis sets in the last years in the course of a study of amino acids and related species. In some cases considerable differences between the various basis sets have been encountered, especially regarding the number and the nature of stationary

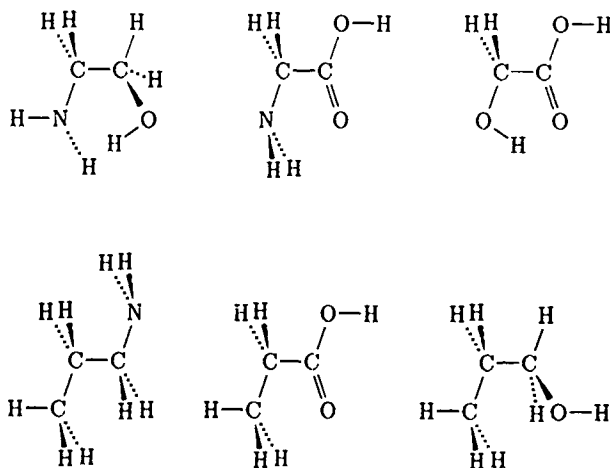
points in the potential energy surface [7-10]. The purpose of this contribution is to exploit the basis set dependence of the calculated frequencies of some of these compounds, namely 2-aminoethanol, glycine, glycolic acid, *n*-propylamine, propionic acid, and *n*-propanol. All of these combine one or two of the functional groups  $\text{—NH}_2$ ,  $\text{—OH}$ , and  $\text{—COOH}$  to organic molecules with four main chain atoms. These molecules may be considered as model compounds for larger systems which are partly affected by intramolecular interactions, e.g., biologically important species.

## Results

For all compounds the global minimum of the potential energy surface, or, in the case of *n*-propylamine and *n*-propanol, the one, which is the global minimum with most basis sets, is considered here. These conformers are depicted in Scheme 1.

The wavenumbers of these conformers, which were calculated at the RHF level [11] for the respective optimized geometries with a number of standard basis sets, are shown in Figures 1 to 6. The following basis sets have been used: 3-21G [12], 4-21G [13], UQ10 [14], 4-31G [15], 6-31G [16], 6-311G [17], and Dunning's 10s,5p/4s basis set [18] (denoted DH in the following). The 6-31G and the 6-311G basis sets have also been augmented by polarization functions [19] and diffuse functions [20].

It has to be noted explicitly that some vibration modes change significantly upon basis set variation. All frequencies, for which the associated mode of vibration remains essentially unchanged, are connected in Figures 1 to 6 with straight lines. Figure 7 exemplifies this using the specific example of modes 6 and 7 of *n*-propylamine with the basis sets 6-311+G and 6-31G\*: mode 7 with the 6-311+G basis set is identical with mode 6 in the 6-31G\* description, but mode 6/6-311+G has



Scheme 1

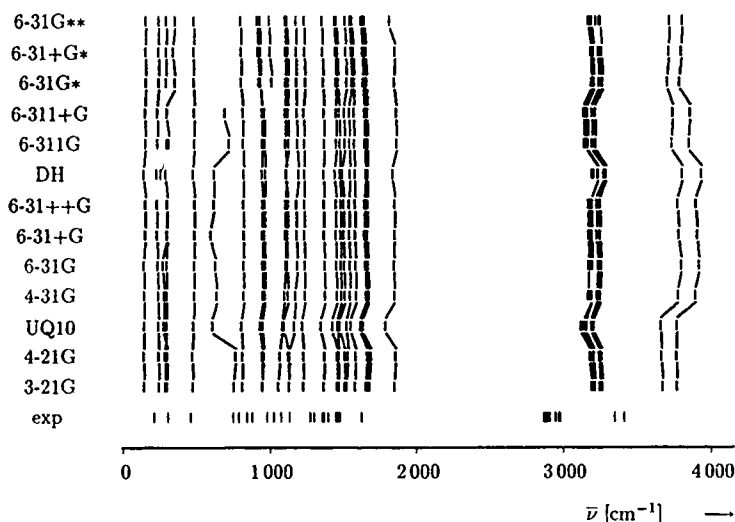


Figure 1 Experimental [22] and calculated wave numbers (*ab-initio* RHF, harmonic approximation) for *n*-propylamine with various basis sets.

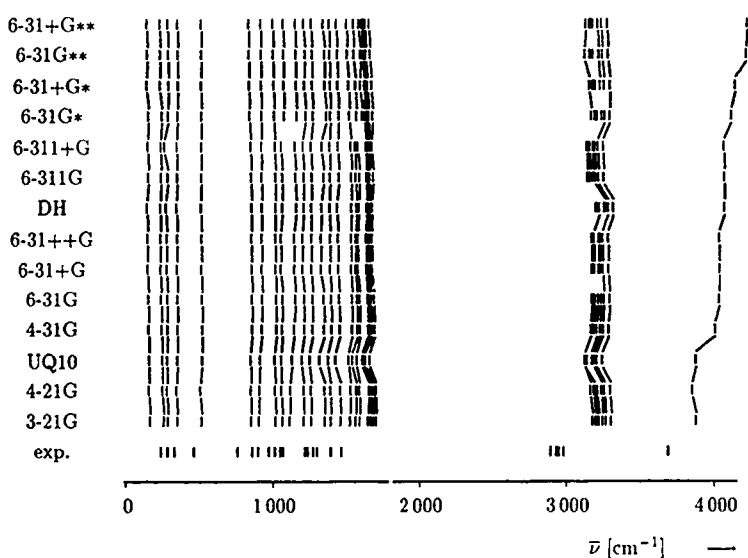


Figure 2. Experimental [28] and calculated wave numbers (*ab-initio* RHF, harmonic approximation) for *n*-propanol with various basis sets.

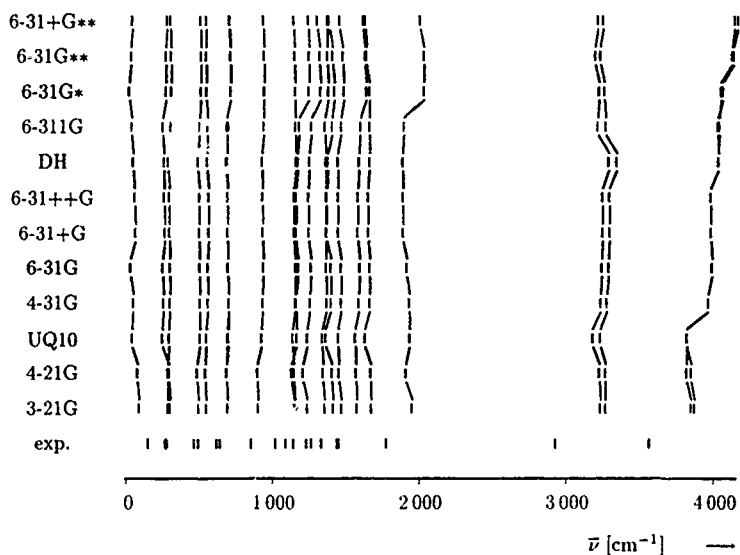


Figure 3. Experimental [24] and calculated wave numbers (*ab-initio* RHF, harmonic approximation) for the global minimum in the PES of glycolic acid with various basis sets.

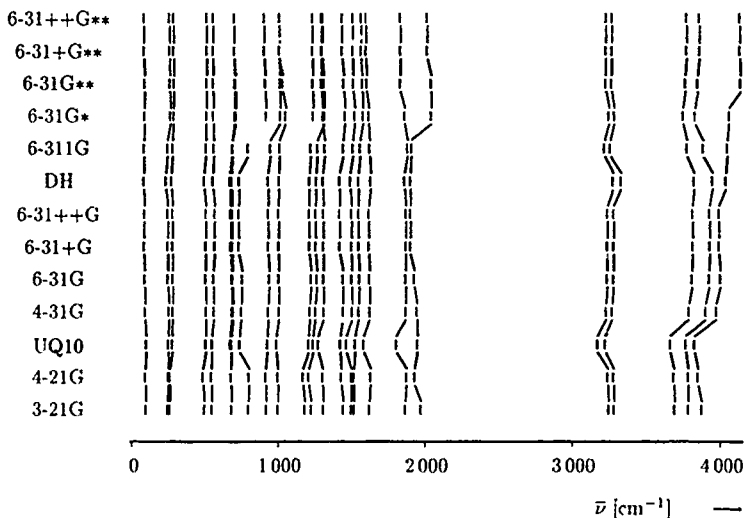


Figure 4. Calculated wave numbers (*ab-initio* RHF, harmonic approximation) for the global minimum in the PES of neutral glycine with various basis sets.

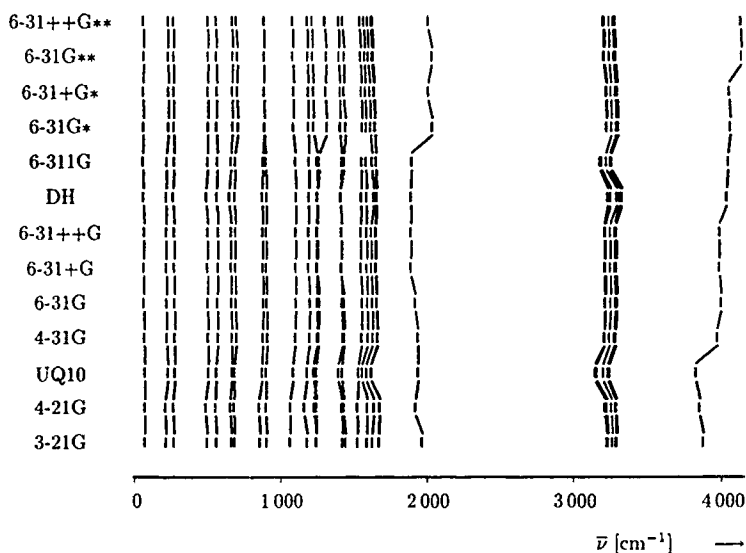


Figure 5. Calculated wave numbers (*ab-initio* RHF, harmonic approximation) for the global minimum in the PES of propionic acid with various basis sets.

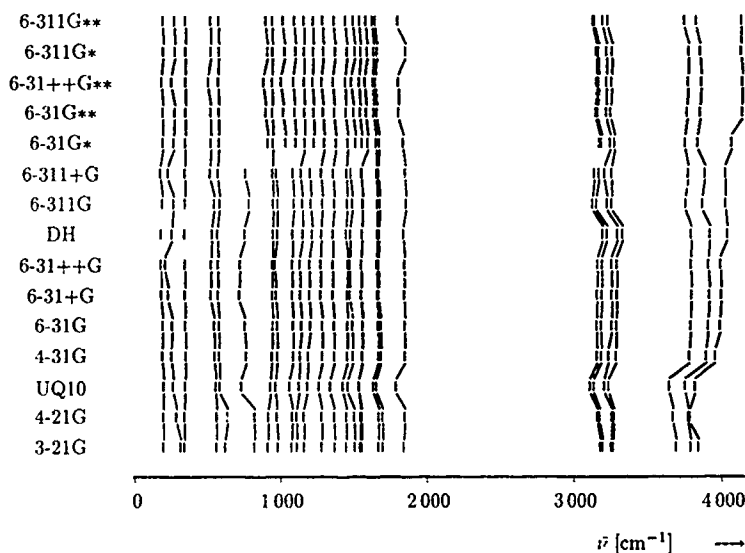


Figure 6. Calculated wave numbers (*ab-initio* RHF, harmonic approximation) for the global minimum in the PES of 2-aminoethanol with various basis sets.

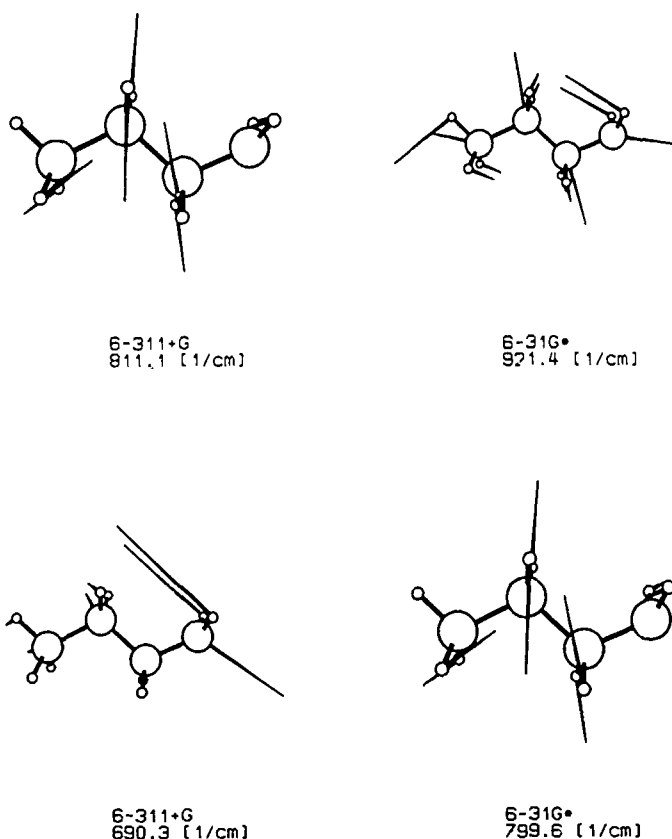


Figure 7. The vibration modes 6 and 7 of *n*-propylamine with the basis sets 6-311+G and 6-31G\*. Mode 7/6-311+G is identical with mode 6/6-31G\*, but mode 6/6-311+G has no equivalent in the 6-31G\* description nor has mode 7/6-31G\*.

no equivalent in the 6-31G\* description nor has mode 7/6-31G\*. This effect seems to be specific for the C—C—NH<sub>2</sub> fragment, because the same situation also occurs in the case of glycine and 2-aminoethanol.

Another trend, which may be gathered from Figures 2 to 6, is the increase of the C=O stretch vibration frequency upon inclusion of polarization functions on the atoms C, N, and O, and the increase of the O—H stretch vibration frequency upon inclusion of polarization functions on hydrogen. Since there are only minor changes in the position of the C—H and N—H stretch vibrations, both of these effects point to the *d*-type polarization function on oxygen as the sole reason. The variation of the exponent of this *d*-type function leads to energy minima for exponents between 0.85 to 0.95 (Fig. 8). (The standard value proposed by Hariharan and Pople [19] for this exponent is 0.8.) A slight increase, but no significant change of the O—H frequency values is correlated with an increase of the exponent.

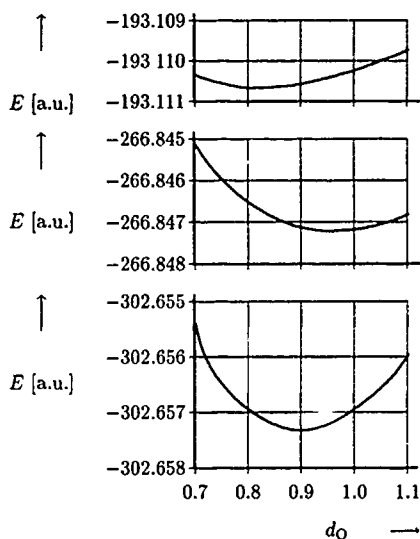


Figure 8. The electronic energy (6-31G\*) of *n*-propanol (top), propionic acid (middle), and glycolic acid (bottom) as a function of exponent of the  $d$ -type polarization function on oxygen.

Frequencies calculated at the MP2 level were not considered in this study, because the deviation between these and the experimental data has no systematic trend; MP2 frequencies are much closer to the experimental ones, but either greater or less than them.

### Discussion

Figures 1 to 6 allow the distinction of three groups of basis sets: group A, which consists of the basis sets 3-21G, 4-21G, and UQ10; group B, which contains the split and triple valence basis sets 4-31G, 6-31G, DH, and 6-311G, with and without diffuse functions; and group C, which covers all basis sets with polarization functions. This classification agrees with one based on the geometry data of all local minima of glycolic acid and glycine [9,21].

For the purpose of judging the widely used global scaling of calculated frequency values, the experimental frequencies of *n*-propylamine, *n*-propanol, and glycolic acid [20-24] are compared with the calculated values for all three basis set groups in Figures 9 to 11. The experimental values are drawn in these figures on different scales (which corresponds to the application of one common scale factor). If the lowest frequencies, which are extremely difficult to detect experimentally, are ignored in the comparison of experimental and calculated values, a good agreement is given for the oxygen containing compounds *n*-propanol and glycolic acid only in the case of basis set group B, whereas for *n*-propylamine agreement is best with the polarized basis sets.

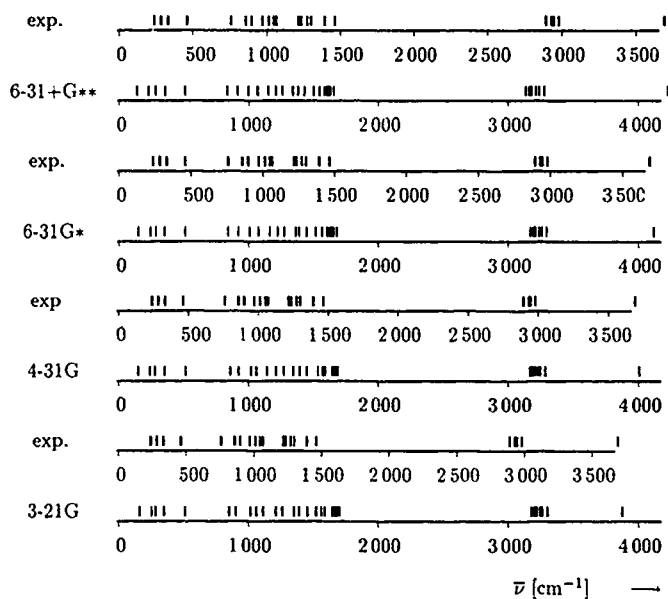


Figure 9. Experimental [28] and scaled calculated vibration frequencies for *n*-propanol. The different length of the abscissae corresponds to a uniform scale factor.

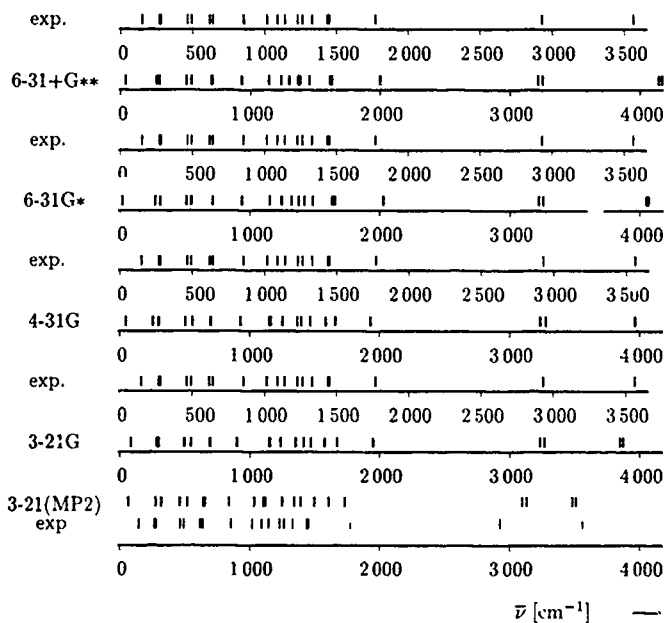


Figure 10. Experimental [24] and scaled calculated vibration frequencies for glycolic acid. The different length of the abscissae corresponds to a uniform scale factor.



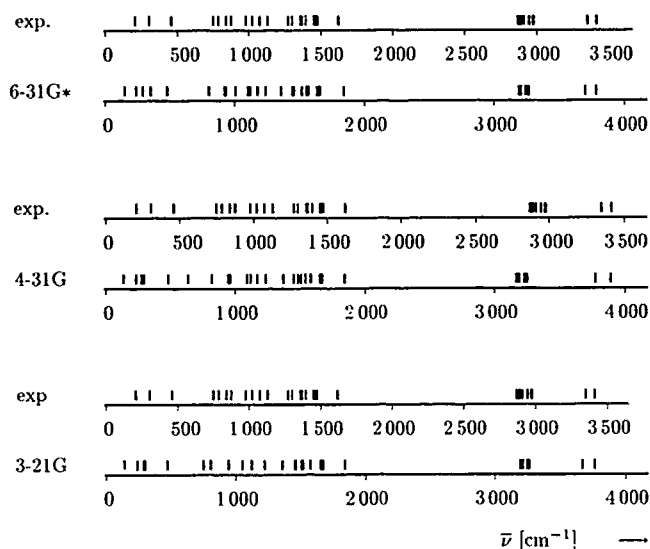


Figure 11. Experimental [22] and scaled calculated vibration frequencies for *n*-propylamine. The different length of the abscissae corresponds to a uniform scale factor.

The effect of the significant changes, which are to be observed in Figures 1 to 6 when going from basis set group B to group C, is therefore opposite for oxygen and nitrogen. For nitrogen it brings the calculated frequencies in better agreement with the experimental ones if proper scaling is employed. For oxygen it causes a mismatch that increases when polarization functions are added on hydrogen atoms. The relation between bond lengths and calculated vibration frequencies should be pointed out specifically. The C=O data for glycolic acid, which are displayed in Figure 12, show that there is an almost perfect linear dependence between these quantities, when the results for *different conformers* are considered which were obtained with the *same basis set*. This corresponds well with the observation that was made for O—H in water [25]. In contrast, data of the *same conformer* obtained with *different basis sets* do not show specific regularities.

The good agreement between experimental and calculated frequencies, which were obtained with group B basis sets for glycolic acid matches the observation that the optimized geometry of the global minimum of the potential energy surface, when calculated with group B basis sets, is in much better agreement with experimental data than with group C basis sets. This seems to be generalizable for organic compounds which contain only oxygen hetero atoms (c.f. [26]).

The conclusion, which can be drawn at least for species similar to the ones discussed here, is to avoid the use of *d*-type polarization functions on oxygen. In contrast, basis sets of the type used by Sato et al. [20] and Batista de Carvalho et al. [27], i.e., split valence basis sets with additional *d*-polarization functions only on nitrogen, appear to be quite reasonable in this context.

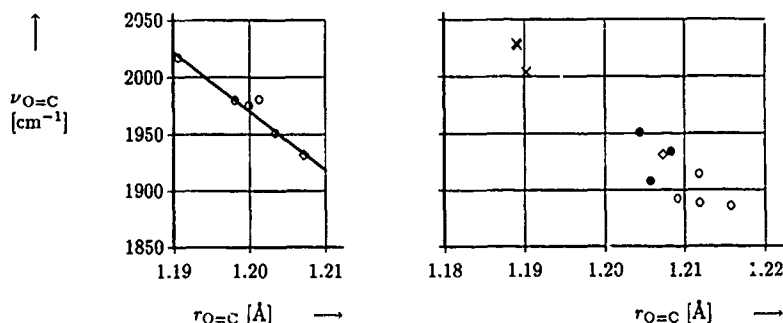


Figure 12. The correlation of C=O distance and frequency for all glycolic acid minima, calculated with the 4-31G basis set (left), where the H-bonded minimum (III in [9]) can be recognized as the one outside the fitted curve. The global minimum (◇) was calculated with different standard basis sets (right), where ● marks double zeta basis sets and ○ triple zeta basis sets with and without diffuse functions. All basis sets including polarization functions are marked by ×. The experimental C=O bond length, obtained from microwave data, is 1.210 Å [29].

### Acknowledgment

This work was supported by the Austrian Fonds zur Förderung der wissenschaftlichen Forschung (projects P8053 and P9095). The authors are grateful for this support and the constant support by the EDV-Zentrum der Technischen Universität Graz. Thanks are due to Mike W. Schmidt (Iowa State University) for a copy of GAMESS and to Anne-Marie Kelterer (TU Graz) for contributing 2-aminoethanol data prior to publication.

### Bibliography

- [1] W. B. De Almeida, *Spectrochim. Acta* **48A**, 1445 (1992).
- [2] P. Pulay, G. Fogarasi, G. Pongor, J. E. Boggs, and A. Vargha, *J. Am. Chem. Soc.* **105**, 7037 (1983).
- [3] J. L. Brum, R. D. Johnson III, and J. W. Hudgens, *J. Chem. Phys.* **98**(5), 3732 (1993).
- [4] M. Schütz, T. Bürgi, and S. Leutwyler, *J. Mol. Struct. (Theochem)* **276**, 17 (1992).
- [5] S. C. Smith, P. F. Wilson, P. Sudkeaw, R. G. A. R. MacLagan, M. J. McEwan, V. G. Anicich, and W. T. Huntress, *J. Chem. Phys.* **98**(3), 1944 (1993).
- [6] J. Breidung and W. Thiel, *J. Comp. Chem.* **13**, 165 (1992).
- [7] M. Ramek, V. K. W. Cheng, R. F. Frey, S. Q. Newton, and L. Schäfer, *J. Mol. Struct. (Theochem)* **235**, 1 (1991).
- [8] M. Ramek and V. K. W. Cheng, *Int. J. Quantum Chem., Quantum Biol. Symp.* **19**, 15 (1992).
- [9] M. Flock and M. Ramek, *Int. J. Quantum Chem., Quantum Chem. Symp.* **26**, 505 (1992).
- [10] A.-M. Kelterer, M. Ramek, R. F. Frey, M. Cao, and L. Schäfer, *J. Mol. Struct. (Theochem)* (Submitted).
- [11] C. C. J. Roothaan, *Rev. Mod. Phys.* **23**, 69 (1951).
- [12] J. S. Binkley, J. A. Pople, and W. J. Hehre, *J. Am. Chem. Soc.* **102**, 939 (1980).
- [13] P. Pulay, G. Fogarasi, F. Pang, and J. E. Boggs, *J. Am. Chem. Soc.* **101**, 2550 (1979).
- [14] P. G. Mezey and I. G. Csizmadia, *Can. J. Chem.* **55**, 1181 (1977).
- [15] R. Ditchfield, W. J. Hehre, and J. A. Pople, *J. Chem. Phys.* **54**, 724 (1971).
- [16] W. J. Hehre, R. Ditchfield, and J. A. Pople, *J. Chem. Phys.* **56**, 2257 (1972).

- [17] R. Krishnan, J. S. Binkley, R. Seeger, and J. A. Pople, *J. Chem. Phys.* **72**, 650 (1980).
- [18] T. H. Dunning Jr. and P. J. Hay, in *Methods of Electronic Structure Theory*, H. F. Schaefer III, Ed. (Plenum Press, New York, 1977), p. 1.
- [19] P. C. Hariharan and J. A. Pople, *Theor. Chim. Acta* **28**, 213 (1973).
- [20] T. Clark, J. Chandrasekhar, G. W. Spitznagel, and P. v. Ragué Schleyer, *J. Comp. Chem.* **4**, 294 (1983).
- [21] M. Ramek, unpublished results.
- [22] N. Sato, Y. Hamada, and M. Tsuboi, *Spectrochim. Acta* **43A**, 943 (1987).
- [23] K. Fukushima and B. Zwolinski, *J. Mol. Spectrosc.* **26**, 368 (1968).
- [24] H. Hollenstein, R. W. Schär, N. Schwizgebel, G. Grassi, and H. H. Gunthard, *Spectrochim. Acta* **39A**, 193 (1983).
- [25] K. Hermansson, *Int. J. Quantum Chem.* **45**, 747 (1993).
- [26] E. Honegger and S. Leutwyler, *J. Chem. Phys.* **88**(4), 2582 (1988).
- [27] L. A. E. Batista De Carvalho, A. M. Amorim Da Costa, M. L. Duarte, and J. J. Teixeira-Dias, *Spectrochim. Acta* **44A**, 723 (1988).
- [28] E. K. Plyler, *J. Res. Natl. Bur. St.* **A48**, 281 (1952).
- [29] C. E. Blom and A. Bauder, *J. Am. Chem. Soc.* **104**, 2993 (1982).

Received July 9, 1993

# Double and Quadruple Zeta Contracted Gaussian Basis Sets for Hydrogen through Neon

AJIT J. THAKKAR

*Department of Chemistry, University of New Brunswick, Fredericton,  
New Brunswick, Canada E3B 6E2*

TOSHIKATSU KOGA and MAKI SAITO

*Department of Applied Chemistry, Muroran Institute of Technology, Muroran, Hokkaido 050, Japan*

RUTH E. HOFFMEYER

*Department of Chemistry, University of New Brunswick, Fredericton,  
New Brunswick, Canada E3B 6E2*

## Abstract

Koga and Thakkar's reoptimized (9s5p) and (12s7p) Gaussian basis sets for the atoms Li to Ne are contracted to [4s2p] and [7s4p], respectively, and their (4s) and (6s) sets for H and He are contracted to [2s] and [4s], respectively. The basis sets are tested by performing self-consistent-field (SCF) geometry optimizations on LiH, BeH<sub>2</sub>, B<sub>2</sub>H<sub>6</sub>, CH<sub>4</sub>, NH<sub>3</sub>, H<sub>2</sub>O, and HF. The equilibrium geometries of hydrogen peroxide and hydrazine are determined at both the SCF and fourth-order many-body perturbation theory level. © 1993 John Wiley & Sons, Inc.

## Introduction

Most contemporary quantum chemical calculations use basis sets of Gaussian-type functions (GTF). There are many good reviews and compendia [1–8] of GTF basis sets. Dunning's double zeta [4s2p/2s] contractions [9] of Huzinaga's variationally optimized (9s5p/4s) GTF sets [10] are among the most popular basis sets for hydrogen and the first row atoms from B through F. Huzinaga's basis sets for H to Ne were variationally reoptimized and larger sets for Li to Ne were constructed [11] and contracted [12] by van Duijneveldt; these have also been widely used.

Recently, Koga and Thakkar [13] obtained further variational improvements in (9s5p) and (12s7p) GTF sets for Li to Ne, and (4s) and (6s) sets for H and He. Their (9s5p) basis sets [13] for Li to Ne are in complete agreement with the very recent work of Schafer et al. [14], who independently reoptimized Huzinaga's (9s5p) sets. Koga and Thakkar's basis sets for Li to Ne yield atomic energies lower than those of van Duijneveldt [11] by amounts ranging from  $6.1 \times 10^{-6}$  to  $1.5 \times 10^{-4} E_H$ . These energy improvements are rather small in the context of molecular calculations. However, the reoptimized exponents of the tight GTF differ by as much as 25% from the previous ones [11], and this may be of some significance for properties other than the energy. We report double and quadruple zeta contractions of Koga

TABLE I. Atomic energies, with signs reversed, from various GTF basis sets

	HD <sup>a</sup>	VD <sup>b</sup>	B0 <sup>c</sup>	B1 <sup>c</sup>	B2 <sup>c</sup>	(9s5p) <sup>d</sup>
Li (2P)			7.3647293	7.3647293	7.3647293	7.3647293
Be (3P)			14.509918	14.510791	14.510812	14.510815
B (2P)	24.526415	24.52687	24.526304	24.527471	24.527527	24.527546
C (3P)	37.684508	37.68519	37.684687	37.685561	37.685665	37.685700
N (4S)	54.394392	54.39535	54.395093	54.395655	54.395829	54.395885
O (3P)	74.798837	74.80040	74.800333	74.800635	74.800912	74.800995
F (2P)	99.393300	99.39557	99.395769	99.395937	99.396285	99.396402
Ne (1S)		128.52711	128.52752	128.52793	128.52811	128.52827

<sup>a</sup> HD is Dunning's [4s2p] contraction [9] of Huzinaga's (9s5p) set [10].

<sup>b</sup> VD is (9s5p)/[4s2p] set of van Duijneveldt [11,12].

<sup>c</sup> B0, B1, and B2, respectively, are [4s2p] contractions of Koga and Thakkar's (9s5p) set [13] using 0, 1, and 2 repeated primitives

<sup>d</sup> (9s5p) is the uncontracted set from Ref [13].

and Thakkar's basis sets [13] for use in molecular calculations. The contraction procedure is described in the next section, and the basis sets are tested in the third section. Hartree atomic units are used except where explicitly stated otherwise.

### Contraction of the Basis Sets

Basis sets of contracted Gaussian type functions (CGTFs) can be of either the segmented [9] or generalized [15] type. In the elegant general contraction scheme of Raffennetti [15], the CGTFs can be constructed from atomic calculations in the parent uncontracted GTF basis set without any further complications. However, a "primitive" GTF will generally appear in many CGTFs, and this will lead to many

TABLE II. Atomic energies, with signs reversed, from various GTF basis sets.

	C0 <sup>a</sup>	C1 <sup>a</sup>	(12s7p) <sup>b</sup>	NHF <sup>c</sup>
Li (2P)	7.3650363	7.3650363	7.3650363	7.3650697
Be (3P)	14.511439	14.511443	14.511444	14.511502
B (2P)	24.528939	24.528953	24.528953	24.529061
C (3P)	37.688397	37.688422	37.688423	37.688619
N (4S)	54.400561	54.400602	54.400603	54.400934
O (3P)	74.808783	74.808842	74.808846	74.809398
F (2P)	99.408404	99.408490	99.408492	99.409349
Ne (1S)	128.54573	128.54584	128.54584	128.54710

<sup>a</sup> C0 and C1, respectively, are [7s4p] contractions of Koga and Thakkar's (12s7p) set [13] using 0 and 1 repeated primitives.

<sup>b</sup> (12s7p) is the uncontracted set from Ref. [13]

<sup>c</sup> NHF is the Hartree-Fock limit from Ref. [21].

TABLE III. Exponents ( $\alpha$ ) and contraction coefficients ( $c$ ) of the (4s)/[2s] CGTF basis sets for H and He.<sup>a</sup>

H		He	
$\alpha$	$c$	$\alpha$	$c$
13.011	0.033484	38.355	0.040183
1.9623	0.234719	5.7689	0.261395
0.44454	0.813774	1.2399	0.793038
	-----		-----
0.12195	1.000000	0.29758	1.000000

<sup>a</sup> Dashed lines separate the contracted functions. A scale factor of 1.2 should be used for H in molecular calculations by multiplying the  $\alpha$  by 1.44.

unnecessary integral evaluations unless the integral program specifically takes this into account. Unfortunately, many popular integral programs do not have the capability to use generalized contractions efficiently.

The alternative is segmented contraction [9] in which primitive GTFs, with the possible exception of one or two crucial ones, appear in only one CGTF. Ideally, one should variationally optimize the contraction coefficients, the exponents, and the grouping pattern. We are not aware of any such work. Segmented CGTF basis sets with both exponents and contraction coefficients variationally optimized for a predetermined contraction pattern can be found in Refs. [14,16], for example. More common are segmented basis sets in which the contraction pattern (splitting)

TABLE IV. Exponents ( $\alpha$ ) and contraction coefficients ( $c$ ) of the (6s)/[4s] CGTF basis sets for H and He.<sup>a</sup>

H		He	
$\alpha$	$c$	$\alpha$	$c$
82.921	0.022940	234.06	0.024379
12.452	0.175491	35.174	0.184036
2.8330	0.864756	7.9911	0.857623
	-----		-----
0.80001	1.000000	2.2124	1.000000
	-----		-----
0.25859	1.000000	0.66707	1.000000
	-----		-----
0.089969	1.000000	0.20895	1.000000

<sup>a</sup> Dashed lines separate the contracted functions. No scaling of the H basis set is recommended for molecular calculations.

TABLE V Exponents ( $\alpha$ ) and contraction coefficients ( $c$ ) of the (9s5p)/[4s2p] CGTF basis sets for Li, Be, B, and C.<sup>a</sup>

Li		Be		B		C	
$\alpha$	$c$	$\alpha$	$c$	$\alpha$	$c$	$\alpha$	$c$
s							
1.4990(+3)	0.001042	2.9330(+3)	0.001046	4.7108(+3)	0.001133	6.7799(+3)	0.001222
2.2491(+2)	0.008024	4.4002(+2)	0.008066	7.0674(+2)	0.008740	1.0172(+3)	0.009430
5.1184(+1)	0.040590	1.0015(+2)	0.041001	1.6088(+2)	0.044488	2.3157(+2)	0.048023
1.4453(+1)	0.150484	2.8304(+1)	0.154551	4.5518(+1)	0.168530	6.5547(+1)	0.182197
4.6303	0.393278	9.1146	0.416999	1.4724(+1)	0.458573	2.1253(+1)	0.496064
1.5900	0.529439	3.1694	0.499759	5.1823	0.440665	7.5339	0.385105
-----	-----	-----	-----	-----	-----	-----	-----
1.5900	0.217740	3.1694	0.316393	5.1823	0.409712	7.5339	0.471311
5.6547(-1)	0.812720	1.1439	0.721799	1.9068	0.632099	2.8031	0.571296
-----	-----	-----	-----	-----	-----	-----	-----
7.3410(-2)	1.000000	1.8648(-1)	1.000000	3.3302(-1)	1.000000	5.2151(-1)	1.000000
-----	-----	-----	-----	-----	-----	-----	-----
2.8042(-2)	1.000000	6.5912(-2)	1.000000	1.0434(-1)	1.000000	1.5957(-1)	1.000000
p							
3.2665	0.012169	7.4498	0.014399	1.2053(+1)	0.017293	1.8734(+1)	0.018170
6.5119(-1)	0.067015	1.5796	0.084345	2.6120	0.105484	4.1362	0.112687
1.6963(-1)	0.295830	4.3604(-1)	0.332582	7.4689(-1)	0.365660	1.2004	0.376170
5.5778(-2)	0.745417	1.4436(-1)	0.701899	2.3873(-1)	0.663256	3.8346(-1)	0.648667
-----	-----	-----	-----	-----	-----	-----	-----
2.0500(-2)	1.000000	5.0195(-2)	1.000000	7.7218(-2)	1.000000	1.2129(-1)	1.000000

<sup>a</sup> Dashed lines separate the contracted functions.  $A(\pm n)$  means  $A \times 10^{\pm n}$ .

is optimized by trial and error, and the contraction coefficients are either taken from atomic calculations in the parent set as in Ref. [9], or variationally optimized as in Ref. [17].

In this work, we examined up to 11 contraction patterns for each basis set, and the use of 0, 1, and 2 primitive GTFs appearing in two CGTFs. For each pattern, the contraction coefficients were variationally optimized to minimize the spin-restricted Roothaan-Hartree-Fock (RHF) atomic energy [18]. The contraction pattern leading to the lowest energy was chosen with *no attempt* to impose a uniform pattern for all first-row atoms. All atomic self-consistent-field (SCF) calculations were done with the ATOM program [19] modified to allow the optimization of contraction coefficients by the conjugate direction algorithm of Powell [20].

The lightest atoms pose a few special problems. Hydrogen and helium have only one occupied atomic orbital (AO), and hence contraction imposes no penalty on the atomic RHF energy. Thus the contraction coefficients are simply taken from uncontracted calculations and renormalized. The contraction pattern is chosen so that the tightest GTFs are grouped in one CGTF and all the other primitive GTFs are left uncontracted. This procedure is, of course, equivalent to a generalized contraction scheme for H and He.

Lithium and beryllium have only s-type AOs occupied in their ground states but a basis set without p-type GTF would be useless for meaningful molecular calculations. This problem is solved for Be by contracting wave functions [13] for the

TABLE VI. Exponents ( $\alpha$ ) and contraction coefficients ( $c$ ) of the (9s5p)/[4s2p] CGTF basis sets for N, O, F, and Ne.\*

	N		O		F		Ne	
	$\alpha$	$c$	$\alpha$	$c$	$\alpha$	$c$	$\alpha$	$c$
s	9.1556(+3)	0.001327	1.1852(+4)	0.001445	1.4846(+4)	0.001915	1.8135(+4)	0.001966
	1.3736(+3)	0.010240	1.7782(+3)	0.011147	2.2274(+3)	0.014770	2.7210(+3)	0.015165
	3.1273(+2)	0.052146	4.0486(+2)	0.056764	5.0714(+2)	0.075268	6.1951(+2)	0.077257
	8.8547(+1)	0.197926	1.1466(+2)	0.215473	1.4364(+2)	0.285328	1.7548(+2)	0.292825
	2.8756(+1)	0.538041	3.7279(+1)	0.584655	4.6740(+1)	0.710267	5.7133(+1)	0.701811
	1.0246(+1)	0.320789	1.3334(+1)	0.246860	-----	-----	-----	-----
	-----	-----	-----	-----	4.6740(+1)	0.032103	5.7133(+1)	0.045089
	1.0246(+1)	0.524498	1.3334(+1)	0.569590	1.6766(+1)	0.634574	2.0538(+1)	0.633958
	3.8443	0.517846	5.0385	0.471791	6.3699	0.379011	7.8363	0.368695
	-----	-----	-----	-----	-----	-----	-----	-----
	7.4650(-1)	1.000000	1.0136	1.000000	1.3164	1.000000	1.6548	1.000000
	-----	-----	-----	-----	-----	-----	-----	-----
	2.2475(-1)	1.000000	3.0250(-1)	1.000000	3.9009(-1)	1.000000	4.8755(-1)	1.000000
p	2.6667(+1)	0.018796	3.4493(+1)	0.020236	4.3907(+1)	0.021053	5.4752(+1)	0.021555
	5.9557	0.117689	7.7562	0.126799	9.9298	0.132049	1.2440(+1)	0.135355
	1.7440	0.383034	2.2820	0.394680	2.9313	0.400866	3.6819	0.404588
	5.5629(-1)	0.638961	7.1691(-1)	0.624014	9.1433(-1)	0.615513	1.1444	0.610111
	-----	-----	-----	-----	-----	-----	-----	-----
	1.7315(-1)	1.000000	2.1461(-1)	1.000000	2.6783(-1)	1.000000	3.3084(-1)	1.000000

\* Dashed lines separate the contracted functions.  $A(\pm n)$  means  $A \times 10^{\pm n}$ .

1s<sup>2</sup>2s2p (<sup>3</sup>P) state. The problem is a bit more subtle for Li because the excited 1s<sup>2</sup>2p (<sup>2</sup>P) state has no occupied valence s-type AO. In previous work, such as Ref. [1], the s-GTFs were taken from the ground 1s<sup>2</sup>2s (<sup>2</sup>S) state and the p-GTFs from the <sup>2</sup>P state. We follow a similar method. The exponents of the s- and p-GTF were taken from the <sup>2</sup>S and <sup>2</sup>P states, respectively, and the contraction coefficients and pattern of the resulting basis set were optimized for the <sup>2</sup>P state.

## Results and Discussion

### Atomic Energies

Consider the (9s5p)/[4s2p] double zeta sets first. Table I compares atomic RHF energies predicted by the Huzinaga-Dunning (HD) basis sets [9,10], the van Duijneveldt (VD) basis sets [11,12], and our B0, B1 and B2 basis sets which are contractions of the Koga-Thakkar sets [13] allowing 0, 1, and 2 primitive GTFs to occur in two different CGTFs. Despite the fact that the uncontracted basis sets of Koga and Thakkar always predict lower energies than the uncontracted sets of Huzinaga [10] and van Duijneveldt [11], the B0 sets do not always yield the lowest atomic energy. The HD set for B and the VD sets for B, C, N, O, and F predict lower energies than B0. Perhaps this is because the lower energy in the uncontracted sets of Ref. [13] is achieved by more efficient sharing of the primitive GTFs between AOs. The B1 sets



TABLE VII. Exponents ( $\alpha$ ) and contraction coefficients ( $c$ ) of the (12s7p)/[7s4p] CGTF basis sets for Li, Be, B, and C.<sup>a</sup>

Li		Be		B		C		
$\alpha$	$c$	$\alpha$	$c$	$\alpha$	$c$	$\alpha$	$c$	
s	7 2056(+3)	0 001377	1 4726(+4)	0.000649	2.3831(+4)	0.000677	3 5088(+4)	0.000670
	1.0797(+3)	0 010690	2 2064(+3)	0.005039	3 5706(+3)	0.005258	5.2574(+3)	0.005202
	2.4575(+2)	0 055804	5 0211(+2)	0.026338	8 1263(+2)	0.027495	1.1965(+3)	0.027207
	6.9591(+1)	0 229711	1 4216(+2)	0.108941	2.3012(+2)	0 113855	3.3884(+2)	0.112759
	2.2677(+1)	0 774239	4.6333(+1)	0 372164	7.5026(+1)	0.390462	1.1048(+2)	0.387704
	-----	-----	1.6653(+1)	0.584765	2.7001(+1)	0 561959	3.9785(+1)	0.565654
	8.1342	0.399797	-----	-----	-----	-----	-----	-----
	3.1007	0.638965	1 6653(+1)	0.175059	2.7001(+1)	0.190582	3 9785(+1)	0.188092
	-----	-----	6 3909	0.847351	1 0405(+1)	0.833209	1.5366(+1)	0.835353
	3.1007	0 136977	-----	-----	-----	-----	-----	-----
	1 2284	0 880219	2.5611	1.000000	4 2062	1.000000	6.2406	1.000000
	-----	-----	-----	-----	-----	-----	-----	-----
	4 9392(-1)	1 000000	1 0431	1.000000	1 7351	1 000000	2 5893	1.000000
	-----	-----	-----	-----	-----	-----	-----	-----
	9 3051(-2)	1 000000	2.6381(-1)	1.000000	4.7134(-1)	1.000000	7.4105(-1)	1.000000
	-----	-----	-----	-----	-----	-----	-----	-----
	4.5938(-2)	1.000000	1.1902(-1)	1.000000	1.9016(-1)	1.000000	2.9334(-1)	1.000000
	-----	-----	-----	-----	-----	-----	-----	-----
	2.1487(-2)	1 000000	4 9993(-2)	1.000000	7 4118(-2)	1 000000	1 1187(-1)	1.000000
p	1 1280(+1)	0 009365	2 5176(+1)	0.008491	3 9999(+1)	0 008421	6 1636(+1)	0.008244
	2 5963	0 059879	5.8681	0.058808	9 3406	0 059974	1 4444(+1)	0.060288
	7 4764(-1)	0 226884	1.7584	0.238068	2.8358	0.252929	4.4412	0.258479
	2.4245(-1)	0 807339	5.9700(-1)	0.793234	9.9115(-1)	0.776731	1 5716	0.770226
	-----	-----	-----	-----	-----	-----	-----	-----
	9.0648(-2)	1.000000	2.2804(-1)	1.000000	3.7600(-1)	1 000000	5 9804(-1)	1 000000
	-----	-----	-----	-----	-----	-----	-----	-----
	3.7362(-2)	1.000000	9.2477(-2)	1 000000	1.4581(-1)	1.000000	2.3019(-1)	1.000000
	-----	-----	-----	-----	-----	-----	-----	-----
	1.6037(-2)	1.000000	3 7652(-2)	1.000000	5.6094(-2)	1.000000	8.6596(-2)	1 000000

<sup>a</sup> Dashed lines separate the contracted functions.  $A(\pm n)$  means  $A \times 10^{\pm n}$ .

with one duplicated primitive give consistently lower energies than the HD, VD, and B0 sets. The B1 energies are higher than the uncontracted ones by amount ranging between 0.02 and 0.47 mhartrees. The B2 energies are lower still. We think the B1 sets are a good compromise and choose them to be our double zeta sets.

Consider the "quadruple" zeta sets next. Table II compares atomic RHF energies predicted by the C0 and C1 basis sets, which are our [7s4p] contractions of the Koga-Thakkar sets [13] allowing 0 and 1 primitive GTF to occur in two different CGTFs, with the uncontracted (12s7p) set [13] and the numerical Hartree-Fock limits [21]. The C1 energies are within 1  $\mu$ hartree of the uncontracted ones, whereas the C0 energies can be as much as 0.11 mhartrees above the uncontracted ones. The C1 sets are our chosen quadruple zeta sets.

TABLE VIII. Exponents ( $\alpha$ ) and contraction coefficients ( $c$ ) of the (12s7p)/[7s4p] CGTF basis sets for N, O, F, and Ne<sup>a</sup>

	N		O		F		Ne	
	$\alpha$	$c$	$\alpha$	$c$	$\alpha$	$c$	$\alpha$	$c$
s	4.8335(+4)	0.001342	6.3655(+4)	0.000659	8.0955(+4)	0.001338	1.0024(+5)	0.000652
	7.2421(+3)	0.010419	9.5376(+3)	0.005115	1.2130(+4)	0.010395	1.5020(+4)	0.005062
	1.6482(+3)	0.054507	2.1707(+3)	0.026762	2.7606(+3)	0.054388	3.4184(+3)	0.026486
	4.6676(+2)	0.226001	6.1472(+2)	0.111012	7.8177(+2)	0.225664	9.6806(+2)	0.109907
	1.5220(+2)	0.778370	2.0045(+2)	0.382771	2.5493(+2)	0.778747	3.1569(+2)	0.379532
	-----	-----	7.2230(+1)	0.572099	-----	-----	1.1379(+2)	0.576290
	5.4828(+1)	0.370936	-----	-----	9.1880(+1)	0.372275	-----	-----
	2.1209(+1)	0.665560	7.2230(+1)	0.183965	3.5612(+1)	0.664141	1.1379(+2)	0.181356
	-----	-----	2.7972(+1)	0.838955	-----	-----	4.4134(+1)	0.841240
	2.1209(+1)	0.106526	-----	-----	3.5612(+1)	0.111996	-----	-----
	8.6404	0.906538	1.1423(+1)	1.000000	1.4568(+1)	0.901547	1.8079(+1)	1.000000
	-----	-----	-----	-----	-----	-----	-----	-----
	3.5990	1.000000	4.7730	1.000000	6.1013	1.000000	7.5847	1.000000
	-----	-----	-----	-----	-----	-----	-----	-----
	1.0622	1.000000	1.4400	1.000000	1.8691	1.000000	2.3498	1.000000
	-----	-----	-----	-----	-----	-----	-----	-----
	4.1529(-1)	1.000000	5.5984(-1)	1.000000	7.2310(-1)	1.000000	9.0531(-1)	1.000000
	-----	-----	-----	-----	-----	-----	-----	-----
	1.5609(-1)	1.000000	2.0807(-1)	1.000000	2.6649(-1)	1.000000	3.3148(-1)	1.000000
p	8.7205(+1)	0.008156	1.1154(+2)	0.008325	1.4099(+2)	0.008401	1.7499(+2)	0.008433
	2.0478(+1)	0.060642	2.6206(+1)	0.062300	3.3151(+1)	0.063288	4.1180(+1)	0.063903
	6.3463	0.262389	8.1556	0.269698	1.0356(+1)	0.274073	1.2905(+1)	0.276881
	2.2624	0.765702	2.9196	0.757895	3.7182	0.753122	4.6434	0.750009
	-----	-----	-----	-----	-----	-----	-----	-----
	8.6191(-1)	1.000000	1.1047	1.000000	1.4022	1.000000	1.7483	1.000000
	-----	-----	-----	-----	-----	-----	-----	-----
	3.2978(-1)	1.000000	4.1368(-1)	1.000000	5.1932(-1)	1.000000	6.4347(-1)	1.000000
	-----	-----	-----	-----	-----	-----	-----	-----
	1.2205(-1)	1.000000	1.4810(-1)	1.000000	1.8225(-1)	1.000000	2.2294(-1)	1.000000

<sup>a</sup> Dashed lines separate the contracted functions.  $A(\pm n)$  means  $A \times 10^{\pm n}$ 

### Molecular Tests

The double and quadruple zeta basis sets for H and He are listed in Tables III and IV. The double zeta (DZ) sets for the first row atoms are given in Tables V and VI whereas the quadruple zeta (QZ) sets are in Tables VII and VIII. Note that the contraction pattern is not uniform across the first row. Following Dunning [9], we recommend that in molecular calculations the double zeta set for H be scaled by factor of 1.2, that is, the exponents for H in Table III be multiplied by  $(1.2)^2 = 1.44$ . The quadruple zeta set for H is sufficiently flexible that we recommend it not be scaled.

TABLE IX. Exponents of polarization functions: p-GTF for H, spherical harmonic (five-membered) d-GTF for first-row atoms

	Pa	Pb	Pc	2P
H	1.0	1.0	0.727	(1.05, 0.35)
Li	0.18	0.18		
Be	0.32	0.32		
B	0.70	0.388	0.343	(0.187, 0.822)
C	0.75	0.600	0.550	(0.288, 1.335)
N	0.80	0.864	0.817	(0.412, 1.986)
O	0.85	1.154	1.185	(0.535, 2.704)
F	0.90	1.496	1.640	(0.682, 3.559)
Ne		1.888	2.202	(0.852, 4.550)

Polarization functions are needed in molecular calculations. Dunning and Hay [1] recommended exponents for a p-GTF in H, and d-GTF in B to F, and d-GTF exponents for Li and Be can be obtained from a formula of Ahlrichs and Taylor [2]. This set of polarization functions is listed as Pa in Table IX. A different set of d-GTF for B to Ne [3], and the same polarization functions for H, Li, and Be are listed in Table IX as Pb. Dunning's [22] correlation consistent polarization functions, listed as Pc, are quite close to the Pb set. Any one of Pa, Pb, and Pc could be used with the DZ sets. The QZ sets can be supplemented by a pair of p-GTF for H, and two sets of d-GTF for B to Ne [3] as listed in Table IX under 2P, or by the (2d1f) or (3d2f1g) correlation consistent sets of Dunning [22].

As a test, self-consistent-field (SCF) geometry optimizations were performed with Gaussian 90 [23] for seven molecules: LiH, HF, BeH<sub>2</sub> in *D<sub>∞h</sub>* symmetry, CH<sub>4</sub> in *T<sub>d</sub>* symmetry, NH<sub>3</sub> in *C<sub>3v</sub>* symmetry, H<sub>2</sub>O in *C<sub>2v</sub>* symmetry, and B<sub>2</sub>H<sub>6</sub> in *D<sub>2h</sub>* symmetry. The basis sets used are the Huzinaga-Dunning (HD) [9,10] double zeta sets and our DZ and QZ sets, with and without polarization functions. There are no HD double zeta sets for Li and Be, and the Dunning-Hay (9s5p)/[3s2p] split valence sets [1] were used instead.

In all cases, the molecular SCF energies (not tabulated) at the equilibrium geometry, both experimental and predicted, obeyed the following ordering: HD > DZ > QZ > HD + Pa > DZ + Pa > QZ + Pb > QZ + 2P. Table X compares the resulting geometries and dipole moments with experiment [24-29]. Our DZ sets give essentially the same results as the standard HD sets, although in most cases the DZ results are slightly closer to the largest basis results than the HD ones. As expected, polarization functions affect dipole moments and bond angles much more than bond lengths. In most cases, the QZ + 2P basis set predicts dipole moments noticeably closer to the experimental ones than either the HD + Pa or DZ + Pa sets.

Finally, as nontrivial tests of these basis sets, we consider the equilibrium geometries of hydrogen peroxide (H<sub>2</sub>O<sub>2</sub>) and hydrazine (N<sub>2</sub>H<sub>4</sub>) assuming *C<sub>2</sub>* symmetry. Both require the determination of dihedral angles that are very sensitive to details of the basis set, as Table XI shows clearly. Geometry optimizations were also carried

TABLE X. SCE equilibrium geometries and dipole moments  $\mu$  for HF, LiH, CH<sub>4</sub>, BeH<sub>2</sub>, H<sub>2</sub>O, NH<sub>3</sub>, and B<sub>2</sub>H<sub>6</sub>.<sup>a</sup>

	HF		LiH		CH <sub>4</sub>	BeH <sub>2</sub>
	$r(\text{HF})$	$\mu(\text{HF})$	$r(\text{LiH})$	$\mu(\text{LiH})$	$r(\text{CH})$	$r(\text{BeH})$
HD	0.9196	2.383	1.6318	5.998	1.0834	1.3359
DZ	0.9218	2.391	1.6332	6.034	1.0829	1.3366
QZ	0.9174	2.373	1.6061	6.035	1.0810	1.3306
HD + <i>Pa</i>	0.9032	2.027	1.6236	5.949	1.0846	1.3357
DZ + <i>Pa</i>	0.9037	2.030	1.6265	5.984	1.0844	1.3358
QZ + <i>Ph</i>	0.8985	2.068	1.6061	6.013	1.0831	1.3308
QZ + 2P	0.9002	1.927	—	—	1.0819	—
Expt	0.9168	1.803	1.5957	5.829	1.085	—

	H <sub>2</sub> O		NH <sub>3</sub>		$\mu(\text{NH}_3)$
	$r(\text{OH})$	$\angle\text{HOH}$	$\mu(\text{H}_2\text{O})$	$r(\text{NH})$	$\angle\text{HNH}$
HD	0.9514	112.51	2.530	0.9944	116.28
DZ	0.9519	112.49	2.526	0.9939	116.26
QZ	0.9502	112.10	2.553	0.9935	115.15
HD + <i>Pa</i>	0.9439	106.71	2.177	1.0011	108.18
DZ + <i>Pa</i>	0.9438	106.72	2.174	1.0008	108.09
QZ + <i>Ph</i>	0.9410	106.93	2.246	0.9987	108.68
QZ + 2P	0.9414	106.38	2.010	0.9990	107.88
Expt	0.9575	104.51	1.847	1.0124	107.07

	B <sub>2</sub> H <sub>6</sub>			
	$r(\text{BB})$	$r(\text{BH}_t)$	$r(\text{BH}_s)$	$\angle\text{H}_t\text{BH}_t$
HD	1.8303	1.1826	1.3402	123.00
DZ	1.8209	1.1831	1.3358	122.62
QZ	1.8003	1.1802	1.3213	122.30
HD + <i>Pa</i>	1.7944	1.1865	1.3284	122.48
DZ + <i>Pa</i>	1.7901	1.1866	1.3265	122.28
QZ + <i>Ph</i>	1.7309	1.1839	1.3209	122.04
QZ + 2P	1.7773	1.1833	1.3180	121.99
Expt	1.743	1.184	1.314	121.5

<sup>a</sup> Bond lengths ( $r$ ) are in Å, bond angles in degrees, and dipole moments in debyes. The bridging and terminal hydrogens in B<sub>2</sub>H<sub>6</sub> are denoted H<sub>t</sub> and H<sub>s</sub>, respectively. Experimental data are from Refs. [24–29].

out using fourth-order many-body perturbation theory with triple substitutions neglected, that is, SDQ-MP4 [30].

First, consider hydrogen peroxide. Inclusion of polarization functions reduces the dihedral angle  $\beta$  by 30–45°. A previous complete MP4/HD + *Pa* calculation [31] gave  $r(\text{OO}) = 1.471$  Å,  $r(\text{OH}) = 0.970$  Å,  $\angle\text{HOO} = 99.3^\circ$ , and  $\beta = 116.3^\circ$  in reasonable agreement with our SDQ-MP4/DZ + *Pa* results. An MP2/6-311G(3d,2p)

TABLE XI. SCF and SDQ - MP4 geometries for  $\text{H}_2\text{O}_2$  and  $\text{N}_2\text{H}_4$ .<sup>a</sup>

	$\text{H}_2\text{O}_2$			
	$r(\text{OO})$	$r(\text{OH})$	$\angle\text{HOO}$	$\beta$
SCF/HD	1.4438	0.9564	102.77	144.3
SCF/DZ	1.4461	0.9571	102.72	142.9
SCF/QZ	1.4396	0.9542	102.06	163.1
SCF/HD + $P_a$	1.3922	0.9467	102.73	112.5
SCF/DZ + $P_a$	1.3931	0.9466	102.69	112.1
SCF/QZ + $P_b$	1.3888	0.9431	102.74	118.2
SCF/QZ + $2P$	1.3966	0.9431	102.68	111.2
SDQ - MP4/DZ + $P_a$	1.4615	0.9688	99.74	114.2
SDQ - MP4/QZ + $2P$	1.4652	0.9630	99.77	113.8
Expt [33]	1.4645	0.965	99.4	111.8

	$\text{N}_2\text{H}_4$						
	$r(\text{NN})$	$r(\text{NH}_a)$	$r(\text{NH}_b)$	$\angle\text{H}_a\text{NH}_b$	$\angle\text{H}_a\text{NN}$	$\angle\text{H}_b\text{NN}$	$\beta(\text{H}_a\text{NNH}_b)$
SCF/HD	1.4064	0.9952	0.9984	115.13	113.01	116.67	92.1
SCF/DZ	1.4044	0.9947	0.9978	115.14	113.08	116.72	92.0
SCF/QZ	1.4099	0.9933	0.9967	114.15	112.07	115.77	92.1
SCF/HD + $P_a$	1.4117	0.9989	1.0015	108.94	108.53	112.67	89.8
SCF/DZ + $P_a$	1.4107	0.9986	1.0013	108.87	108.48	112.64	89.7
SCF/QZ + $P_b$	1.4111	0.9963	0.9993	109.25	108.71	112.73	90.2
SCF/QZ + $2P$	1.4166	0.9957	0.9984	108.67	108.24	112.17	90.1
SDQ - MP4/DZ + $P_a$	1.4419	1.0152	1.0185	106.99	106.51	111.37	89.6
SDQ - MP4/QZ + $2P$	1.4476	1.0091	1.0119	107.44	106.58	111.05	90.9
Expt [35]	1.449	1.021	1.021	(106.6)	106	112	91

<sup>a</sup> Bond lengths are in Å and angles in degrees.  $\beta$  is a dihedral angle. The hydrogens on each N in hydrazine are nonequivalent and are denoted by  $\text{H}_a$  and  $\text{H}_b$ , respectively.

calculation [32] led to  $r(\text{OO}) = 1.450$  Å,  $r(\text{OH}) = 0.962$  Å,  $\angle\text{HOO} = 99.5^\circ$ , and  $\beta = 111.1^\circ$ . Good agreement with an experimental geometry of Koput [33] is obtained by our SDQ - MP4/QZ +  $2P$  calculation: The bond distances agree within 0.002 Å, the  $\angle\text{HOO}$  to  $0.4^\circ$ , and the dihedral angle to  $2^\circ$ .

Next consider hydrazine. All calculations show that the two hydrogens, labelled  $\text{H}_a$  and  $\text{H}_b$ , on each nitrogen are nonequivalent. A CISD(Q), configuration interaction with all single and double substitutions approximately corrected for unlinked clusters, calculation [34] in a  $6 - 31\text{G}^*$  basis led to  $r(\text{NN}) = 1.448$  Å,  $r(\text{NH}_a) = 1.018$  Å,  $r(\text{NH}_b) = 1.021$  Å,  $\angle\text{H}_a\text{NH}_b = 106.64^\circ$ ,  $\angle\text{H}_a\text{NN} = 105.94^\circ$ ,  $\angle\text{H}_b\text{NN} = 110.82^\circ$ , and  $\beta(\text{H}_a\text{NNH}_b) = 90.05^\circ$ . An experimental equilibrium structure is not known but a thermally averaged  $r_g$  structure has been determined by Kohata et al. [35]. They were unable to match the nonequivalent NH bonds with the corresponding angles and therefore reported an average  $r(\text{NH})$ . Moreover, they fixed  $\angle\text{HNNH}$  at  $106.6^\circ$  from the CISD(Q) calculation [34]. Our SDQ - MP4/QZ +  $2P$  calculation may be the best equilibrium geometry available to date.

We hope the basis sets presented in this paper will be generally useful to the quantum chemistry community.

### Acknowledgment

This work was supported in part by the Natural Sciences and Engineering Research Council of Canada.

### Bibliography

- [1] T. H. Dunning, Jr. and P. J. Hay, in *Methods of Electronic Structure Theory*, H. F. Schaefer, III Ed. (Plenum, New York, 1977), pp. 1-27.
- [2] R. Ahlrichs and P. R. Taylor, *J. Chim. Phys.* **78**, 315 (1981).
- [3] J. Andzelm, S. Huzinaga, M. Klobukowski, E. Radzio-Andzelm, Y. Sakai, and H. Tatewaki, *Gaussian Basis Sets for Molecular Calculations* (Elsevier, Amsterdam, 1984).
- [4] R. Poirier, R. Kar, and I. G. Csizmadia, *Handbook of Gaussian Basis Sets* (Elsevier, New York, 1985).
- [5] S. Huzinaga, *Comput. Phys. Rep.* **2**, 279 (1985).
- [6] E. R. Davidson and D. Feller, *Chem. Rev.* **86**, 681 (1986).
- [7] W. J. Hehre, L. Radom, P. v. R. Schleyer, and J. A. Pople, *Ab Initio Molecular Orbital Theory* (Wiley, New York, 1986).
- [8] S. Wilson, *Adv. Chem. Phys.* **67**, 439 (1987).
- [9] T. H. Dunning, Jr., *J. Chem. Phys.* **53**, 2823 (1970).
- [10] S. Huzinaga, *J. Chem. Phys.* **42**, 1293 (1965).
- [11] F. B. van Duijneveldt, *Gaussian Basis Sets for the Atoms H-Ne for Use in Molecular Calculations*, IBM Research Report RJ945, (IBM, San Jose, CA, 1971).
- [12] J. G. C. M. van Duijneveldt-van de Rijdt and F. B. van Duijneveldt, *J. Mol. Struct. (Theochem)* **89**, 185 (1982).
- [13] T. Koga and A. J. Thakkar, *Theor. Chim. Acta*, to appear.
- [14] A. Schafer, H. Horn, and R. Ahlrichs, *J. Chem. Phys.* **97**, 2571 (1992).
- [15] R. C.affenetti, *J. Chem. Phys.* **58**, 4452 (1973).
- [16] R. Ditchfield, W. J. Hehre, and J. A. Pople, *J. Chem. Phys.* **54**, 724 (1971).
- [17] A. D. McLean and G. S. Chandler, *J. Chem. Phys.* **72**, 5639 (1980).
- [18] C. C. J. Roothaan, *Rev. Mod. Phys.* **32**, 179 (1960); C. C. J. Roothaan and P. S. Bagus, *Methods Comput. Phys.* **2**, 47 (1963).
- [19] B. Roos, C. Salez, A. Veillard, and E. Clementi, *A General Program for Calculation of Atomic SCF Orbitals by the Expansion Method*, IBM Report (IBM, San Jose, CA, 1968).
- [20] M. J. D. Powell, *Comput. J.* **7**, 155 (1964).
- [21] C. Froese-Fischer, *The Hartree-Fock Method for Atoms* (Wiley, New York, 1977).
- [22] T. H. Dunning, Jr., *J. Chem. Phys.* **90**, 1007 (1989).
- [23] M. J. Frisch, M. Head-Gordon, G. W. Trucks, J. B. Foresman, H. B. Schlegel, K. Raghavachari, M. Robb, J. S. Binkley, C. Gonzalez, D. J. Defrees, D. J. Fox, R. A. Whiteside, R. Seeger, C. F. Melius, J. Baker, R. L. Martin, L. R. Kahn, J. J. P. Stewart, S. Topiol, and J. A. Pople, *Gaussian 90*, Revision J (Gaussian, Inc., Pittsburgh, PA, 1990).
- [24] K. P. Huber and G. Herzberg, *Molecular Spectra and Molecular Structure IV Constants of Diatomic Molecules* (Van Nostrand, New York, 1979).
- [25] K. H. Hellwege and A. M. Hellwege, Eds., *Landolt-Börnstein, New Series, Group II* (Springer-Verlag, Berlin, 1976), Vols. 4, 6, 7.
- [26] J. L. Duncan and J. Harper, *Mol. Phys.* **51**, 371 (1984).
- [27] D. L. Gray and A. G. Robiette, *Mol. Phys.* **37**, 1901 (1979).
- [28] S. A. Clough, Y. Beers, G. P. Klein, and L. S. Rothman, *J. Chem. Phys.* **59**, 2254 (1973).
- [29] J. F. Ogilvie, W. R. Radwell, and R. H. Tipping, *J. Chem. Phys.* **73**, 5221 (1980).
- [30] R. J. Bartlett, *Annu. Rev. Phys. Chem.* **32**, 359 (1981).

- [31] D. Christen, H. Mack, and H. Oberhammer, *Tetrahedron* **44**, 7363 (1988).
- [32] J. E. Carpenter and F. Weinhold, *J. Phys. Chem.* **90**, 6405 (1986).
- [33] J. Koput, *J. Mol. Spectrosc.* **115**, 438 (1986).
- [34] N. Tanaka, Y. Hamada, Y. Sugawara, M. Tsuboi, S. Kata, and K. Morokuma, *J. Mol. Spectrosc.* **99**, 245 (1983).
- [35] K. Kohata, T. Fukuyama, and K. Kuchitsu, *J. Phys. Chem.* **86**, 602 (1982).

Received April 8, 1993



# Kinetic Energy Component in the Divide-and-Conquer Method

ZHONGXIANG ZHOU

Department of Chemistry, University of North Carolina, Chapel Hill, North Carolina 27599-3290

## Abstract

The kinetic energy component is shown to be a well-defined quantity in the divide-and-conquer method. This kinetic energy converges to the conventional Kohn–Sham kinetic energy when the numbers of the “buffer atoms” for subsystems increase. Numerical results from sample calculations confirm that the kinetic energy component converges to the Kohn–Sham value as the basis set increases. © 1993 John Wiley & Sons, Inc

## Introduction

Accurate computation of the kinetic energy is essential to *ab initio* calculations. In the density-functional formalism the common practice is to represent the kinetic energy in terms of the Kohn–Sham orbitals. This representation recovers most of the kinetic energy. The residue of the kinetic energy, conventionally denoted by  $T_c$ , is included in the exchange-correlation component  $E_{xc}$  of the Kohn–Sham energy. The result is in principle exact [1–4]. The introduction of the auxiliary Kohn–Sham orbitals increases the size dependence of the density-functional computations while alleviating the problem of the unavailability of the explicit form of the kinetic energy density functional. The Kohn–Sham kinetic energy is a functional of the density, as is the exchange-correlation energy and so the total energy. All ground-state properties can be calculated accurately as long as the density is computed accurately.

In the conventional Kohn–Sham scheme the global Kohn–Sham orbitals are expanded in terms of a proper basis set. The coefficients of the expansion are obtained via a Rayleigh–Ritz variational principle. The divide-and-conquer method solves the Kohn–Sham equation differently [5]. It uses the density as its basic variational variable. No global molecular orbitals are involved. This reduces the size dependence of the computation from  $N^3$  for the conventional Kohn–Sham method to  $N$  (or at most  $N^2$ ), where  $N$  is the number of electrons in the system. The kinetic energy was not calculated separately. Instead it was computed together with a potential term as a whole. Since the global Kohn–Sham orbitals are not used in the divide-and-conquer method the kinetic energy has to be redefined. The main objective of this article is to define the kinetic energy within the divide-and-conquer formulation starting from a recent *ab initio* construction of the divide-and-conquer method



[6], and to show that this definition conforms to the conventional Kohn-Sham definition.

### Theory

The Kohn-Sham equation is the operational equation in density-functional computations. For an electronic system it reads

$$\left[ -\frac{1}{2} \nabla^2 + v(\vec{r}) + \phi_s(\vec{r}) + v_{xc}(\vec{r}) \right] \psi_i = \epsilon_i \psi_i \quad (1)$$

with

$$\rho(\vec{r}) = \sum_i n_i |\psi_i|^2 \quad (2)$$

$$\phi_s(\vec{r}) = \int \frac{\rho(\vec{r}_1)}{|\vec{r} - \vec{r}_1|} d\vec{r}_1 \quad (3)$$

$$v_{xc}(\vec{r}) = \frac{\delta E_{xc}[\rho]}{\delta \rho(\vec{r})} \quad (4)$$

$v(\vec{r})$  is the external potential acting on the electronic system;  $\psi_i$  and  $\epsilon_i$  are the Kohn-Sham orbitals and eigenvalues, respectively. The total energy is

$$E = \mathcal{G} + Q[\rho] + \sum_{\lambda > \nu} \frac{Z_\lambda Z_\nu}{R_{\lambda\nu}} \quad (5)$$

where

$$\mathcal{G} = \sum_i n_i \epsilon_i \quad (6)$$

$$Q[\rho] = \int \rho(\vec{r}) \left\{ -\frac{1}{2} \phi_s(\vec{r}) - v_{xc}(\vec{r}) \right\} d\vec{r} + E_{xc}[\rho] \quad (7)$$

The last term in Eq. (5) is the nuclear interaction energy.

The self-consistent solution of Eqs. (1) to (4) involves the expansion of the  $\psi_i(\vec{r})$  as a linear combination of basis functions, usually atomic orbitals, or other functions such as Slater-type or Gaussian-type functions centered on atoms. There exists inefficiency here. When the density or total energy is computed not every term in the linear-combination-of-basis-function summation of the Kohn-Sham orbitals contributes because of the exponential decay of the basis functions. Suppose that one uses a basis set with functions centered at one point one would expect very bad result unless very big basis set is used. One-center functions represent the region near the center well, and the region far away from the center poorly. One way to improve this bad representation is of course to use the basis set mentioned above, that is the one with functions from all atoms in the molecule. Another way to achieve this improvement is to divide a large system into several regions such that each region has its own basis set with functions centered only within or near

the region. And a Kohn-Sham equation is solved for each region. This way each region has been represented reasonably accurately by a set of equations and its associated basis set. The global solution is obtained by assembling solutions from all subsystems. Weighting functions can be used for this purpose. The weighting functions are designed in such a way that they are big within the regions they are associated with and small away from the regions. This is exactly the philosophy behind the recently developed divide-and-conquer method [5,6]. The advantage of this divide-and-conquer approach is that the auxiliary Kohn-Sham orbitals can be completely eliminated and hence the size dependence of the computations is reduced, without any loss of accuracy.

Consider a molecular system. Each subsystem  $\alpha$  can be thought of as consisting of several atoms. Let  $\{p^\alpha(\vec{r})\}$  be the weighting functions mentioned above, previously called partition functions. The  $\{p^\alpha(\vec{r})\}$  satisfies the relations:  $\sum_\alpha p^\alpha(\vec{r}) = 1$  and  $p^\alpha(\vec{r}) \geq 0$ . Let  $\{\phi_i^\alpha(\vec{r})\}$  be the basis set associated with the subsystem  $\alpha$ . The Kohn-Sham equation (1) can be solved using this basis set. Denote the solution as  $\{\psi_\alpha^\alpha(\vec{r}), \epsilon_\alpha^\alpha\}$ . The density generated is

$$\tilde{\rho}^\alpha(\vec{r}) = \sum_{i_\alpha} n_{i_\alpha} |\psi_{i_\alpha}^\alpha(\vec{r})|^2 \quad (8)$$

For closed shell  $n_{i_\alpha} = 2$ . The global density can be composed as following

$$\rho(\vec{r}) = \sum_\alpha p^\alpha(\vec{r}) \tilde{\rho}^\alpha(\vec{r}) = \sum_\alpha \sum_{i_\alpha} 2 f_\beta(\epsilon_F - \epsilon_{i_\alpha}^\alpha) p^\alpha(\vec{r}) |\psi_{i_\alpha}^\alpha(\vec{r})|^2 \quad (9)$$

where  $f_\beta(x) = 1/[1 + \exp(-\beta x)]$  is the fermi function. The substitution of  $n_{i_\alpha} = 2$  with a fermi function comes from a simple technical consideration which will manifest itself in the following normalization relation:

$$N = \int \rho(\vec{r}) d\vec{r} = 2 \sum_\alpha \sum_{i_\alpha} f_\beta(\epsilon_F - \epsilon_{i_\alpha}^\alpha) \langle \psi_{i_\alpha}^\alpha | p^\alpha(\vec{r}) | \psi_{i_\alpha}^\alpha \rangle \quad (10)$$

$\epsilon_F$  is the parameter to be used to normalize the electron density as given by the above equation. The fermi function makes this normalization process possible.  $f_\beta(x)$  approaches a step function as  $\beta$  becomes bigger.

To compose  $\mathcal{E}$  a local form of it has to be used

$$\tilde{\mathcal{E}}^\alpha(\vec{r}) = \sum_{i_\alpha, j_\alpha} n_{i_\alpha} \langle \psi_{i_\alpha}^\alpha | H | \psi_{j_\alpha}^\alpha \rangle \psi_{j_\alpha}^{*\alpha}(\vec{r}) \psi_{i_\alpha}^\alpha(\vec{r}) \quad (11)$$

where  $H$  is the Kohn-Sham Hamiltonian. Another form of this local quantity is

$$\tilde{\mathcal{E}}^\alpha(\vec{r}) = \sum_{i_\alpha} n_{i_\alpha} \psi_{i_\alpha}^{*\alpha}(\vec{r}) H \psi_{i_\alpha}^\alpha(\vec{r}) \quad (11a)$$

Subtle differences between these two forms exist. They are the same if the basis set used is complete. The global  $\mathcal{E}$  is

$$\mathcal{E} = \sum_\alpha \int p^\alpha(\vec{r}) \tilde{\mathcal{E}}^\alpha(\vec{r}) d\vec{r} = 2 \sum_\alpha \sum_{i_\alpha} f_\beta(\epsilon_F - \epsilon_{i_\alpha}^\alpha) \epsilon_{i_\alpha}^\alpha \langle \psi_{i_\alpha}^\alpha | p^\alpha(\vec{r}) | \psi_{i_\alpha}^\alpha \rangle \quad (12)$$

or

$$\mathcal{E} = 2 \sum_{\alpha} \sum_{i_{\alpha}} f_{\beta}(\epsilon_F - \epsilon_{i_{\alpha}}^{\alpha}) \int p^{\alpha}(\vec{r}) \psi_{i_{\alpha}}^{\alpha*}(\vec{r}) H \psi_{i_{\alpha}}^{\alpha}(\vec{r}) d\vec{r} \quad (12a)$$

Again  $n_{i_{\alpha}}$  has been replaced by the fermi function. Equation (12) is the formula used in the previous publications [5-9] and will be used here.

Suppose that the limit  $\beta \rightarrow \infty$  is taken. The divide-and-conquer formulation as described by Eqs. (8) to (12) reduces to the conventional Kohn-Sham formulation if the basis set  $\{\phi_i^{\alpha}(\vec{r})\}$  covers the same function space for all  $\alpha$ . The divide-and-conquer method results from the discriminate truncations of complete basis sets in different subsystems [6].

The self-consistent solution of the divide-and-conquer formulas (1), (3) through (5), (9), (10), (12) does not require the construction of the global Kohn-Sham orbitals. Complete Hamiltonian and overlap matrices are not needed here.

A local kinetic energy can be defined similar to the definition of  $\tilde{\mathcal{E}}^{\alpha}(\vec{r})$  in Eq. (11)

$$\tilde{T}^{\alpha}(\vec{r}) = \sum_{i_{\alpha} j_{\alpha}} n_{i_{\alpha}} \langle \psi_{i_{\alpha}}^{\alpha} | \hat{T} | \psi_{j_{\alpha}}^{\alpha} \rangle \psi_{j_{\alpha}}^{\alpha*}(\vec{r}) \psi_{i_{\alpha}}^{\alpha}(\vec{r}) \quad (13)$$

The kinetic energy in the divide-and-conquer method is

$$\begin{aligned} T &= \sum_{\alpha} \int p^{\alpha}(\vec{r}) \tilde{T}^{\alpha}(\vec{r}) d\vec{r} \\ &= 2 \sum_{\alpha} \sum_{i_{\alpha} j_{\alpha}} f_{\beta}(\epsilon_F - \epsilon_{i_{\alpha}}^{\alpha}) \langle \psi_{i_{\alpha}}^{\alpha} | \hat{T} | \psi_{j_{\alpha}}^{\alpha} \rangle \langle \psi_{j_{\alpha}}^{\alpha} | p^{\alpha}(\vec{r}) | \psi_{i_{\alpha}}^{\alpha} \rangle \end{aligned} \quad (14)$$

An definition of  $\tilde{T}^{\alpha}(\vec{r})$  analogous to the definition of  $\tilde{\mathcal{E}}^{\alpha}(\vec{r})$  in Eq. (11a) will result in the total kinetic energy definition

$$T = 2 \sum_{\alpha} \sum_{i_{\alpha}} f_{\beta}(\epsilon_F - \epsilon_{i_{\alpha}}^{\alpha}) \int p^{\alpha}(\vec{r}) \psi_{i_{\alpha}}^{\alpha}(\vec{r}) \hat{T} \psi_{i_{\alpha}}^{\alpha}(\vec{r}) d\vec{r} \quad (14a)$$

These two definition of the kinetic energy become the same if a complete basis set is used. The kinetic energy from both Eq. (14) and (14a) becomes the conventional Kohn-Sham kinetic energy when  $\beta \rightarrow \infty$  and  $\{\phi_i^{\alpha}(\vec{r})\}$  covers the same function space as the Kohn-Sham basis set does for all  $\alpha$ .

Equation (14) is used in the following computations of kinetic energy because of its numerical simplicity. Equation (14) is compatible with Eq. (12) not with Eq. (12a).

## Results and Discussion

In the present calculations the  $X_{\alpha}$  approximation with  $\alpha = 0.7$  for the exchange-correlation energy functional  $E_{xc}[\rho]$  has been used. The standard techniques for

the multicenter three-dimensional numerical integrations are taken from the literature [7,10]. The partition function  $\{p^a(\vec{r})\}$  is built from the spherical atomic densities:  $p^a(\vec{r}) = \sum_{a \in \alpha} [\rho_0^a(|\vec{r} - \vec{R}_a|)]^2 / \sum_{\beta} \sum_{b \in \beta} [\rho_0^b(|\vec{r} - \vec{R}_b|)]^2$ . The basis set consists of the projected and optimized atomic orbitals [7]. For the divide-and-conquer calculation two ways are used to enlarge the subsystem basis sets: to add more atomic orbitals from atoms within the subsystems and to include atomic orbitals contributed by the neighboring atoms, the so-called "buffer atoms" [7]. The density-functional programs developed in Yang's Laboratory, modified as appropriate, is used [5,7].

Sample calculations are carried out for benzene and a tetrapeptide. The benzene geometry used is  $D_{6h}$  symmetry with  $d_{CC} = 1.397$  Å and  $d_{CH} = 1.084$  Å. The tetrapeptide geometry is taken from Ref. [7]. In the divide-and-conquer calculation benzene is divided into six subsystems, each consisting of a CH piece. The tetrapeptide is divided into 13 pieces, each consisting of a heavy backbone atom and the side atoms attached to it. Numerical results are reported in Table I and Table II.

TABLE I. Total energy and kinetic energy component from both the Kohn-Sham method and the divide-and-conquer method for benzene. *mn*, *./m'n'*, stands for the numerical atomic basis set used: *m* s-type and *n* p-type atomic orbitals for C atom and *m'* s-type and *n'* p-type atomic orbitals for H atom. *bn* stands for that *n*th nearest neighbors have been used as "buffer atoms". Atomic unit is used.

Basis C/H	$-E$		$T$	
	$\beta = 100$	$\beta = 150$	$\beta = 100$	$\beta = 150$
21/10				
b0	230.080	230.068	224.303	224.432
b1	228.268	228.281	225.259	225.253
b2	228.228	228.256	225.618	225.627
b3	228.336	228.336	225.217	225.217
KS	228.338		225.221	
32/21				
b0	229.067	229.121	231.982	232.030
b1	228.972	228.976	229.010	229.027
b2	228.838	228.840	229.230	229.254
b3	228.930	228.930	229.154	229.154
KS	228.930		229.211	
431/32				
b0	229.508	230.451	230.533	231.550
b1	229.026	229.028	228.328	228.310
b2	228.911	228.911	229.106	229.109
b3	228.994	228.994	229.041	229.043
KS	228.994		229.097	

TABLE II. Total energy and kinetic energy for tetrapeptide.  $\beta = 156$ . And atomic unit is used.  $E_{\text{Harrs}}$  is from Harris-type calculation and  $E_{\text{SCF}}$  is the self-consistent result. See Table I for the notations of basis set.

Basis NCO/H	$-E_{\text{Harrs}}$	$-E_{\text{SCF}}$	$T$
21/10			
b0	900.162	899.484	888.420
b1	896.205	895.620	894.240
b2	896.627	896.105	894.121
b3	896.656	896.128	893.773
b4	896.658	896.129	893.791
b5	896.658	896.131	893.759
KS	896.658	896.129	893.772

Given in Table I are the total electronic energy and the kinetic energy component from both the divide-and-conquer method and the conventional Kohn-Sham method for benzene. The results show that both the total energy and the kinetic energy component converge to the Kohn-Sham (KS) results when more buffer atoms are included. Similar results were reported for the total energy by Yang et al. [5,7-9]. Particularly the divide-and-conquer method gives the right kinetic energy component. This is true for different level of basis sets. The same conclusion is reached from calculations for the tetrapeptide as shown in Table II. To see the error introduced by the fermi function substitution two different  $\beta$  values have been used for the benzene calculations. As can be seen from Table I that the  $\beta$  value plays a very minor role here. This means that the introduction of the fermi function brings in a negligible error as far as  $\beta$  is sufficiently large (see also ref. [5]). Also given in Table II is the energy from Harris type calculations [11]. The same convergence pattern is found in  $E_{\text{Harrs}}$  as in  $E_{\text{SCF}}$ . This may be very important in large molecule calculation since the Harris type calculation is much easier to carry out.

The conclusion is that the divide-and-conquer method can give the correct energy components as well as the total energy though their convergence may be slower than that of the total energy.

#### Acknowledgment

This research is supported by a grant to the University of North Carolina at Chapel Hill from the National Science Foundation. A CPU time grant from North Carolina Supercomputer Center is warmly acknowledged. I thank Professor Weitao Yang of Duke University for helpful discussion and for allowing me to use his programs, and Professor Robert G. Parr of the University of North Carolina for support and especially stressing to us the importance of the problem here addressed.

### Bibliography

- [1] P. Hohenberg and W. Kohn, Phys. Rev. **136**, B864 (1964).
- [2] W. Kohn and L. J. Sham, Phys. Rev. **140**, A1133 (1965).
- [3] R. G. Parr and W. Yang, *Density-Functional Theory of Atoms and Molecules* (Oxford University Press, New York, 1989).
- [4] R. M. Dreizler and E. K. U. Gross, *Density Functional Theory* (Springer-Verlag, Berlin, 1990)
- [5] W. Yang, Phys. Rev. Lett. **66**, 1438 (1991)
- [6] Z. Zhou, Chem. Phys. Lett. **203**, 396 (1993).
- [7] W. Yang, Phys. Rev. A **44**, 7823 (1991).
- [8] C. Lee and W. Yang, J. Chem. Phys. **96**, 2408 (1992).
- [9] W. Yang, J. Mol. Struct. **255**, 461 (1992).
- [10] B. Delley, J. Chem. Phys. **92**, 508 (1990).
- [11] J. Harris, Phys. Rev. B **31**, 1770 (1985)

Received March 15, 1993

# Statistical Microdynamics of Extended Systems in Natural Function Spaces

ROBERT G. BROWN AND MIKAEL CIFTAN

*Duke University Physics Department, Durham, North Carolina 27708-0305*

## Abstract

An approximate numerical method of solving the Generalized Master Equation for a many-body problem is presented, with examples of its application. This method involves the construction from the full Hamiltonian (of the system plus the "bath") of a set of unitary Langevin equations that combine deterministic microcanonical, stochastic canonical (heat bath), and stochastic nonthermal dynamics in a single time-integration scheme. If implemented in a representation that captures the essential physics and repeatedly run from a given initial condition, this method evaluates stochastic representatives from the actual fiber bundle of system worldlines that flow from the initial condition and, hence, numerically evaluates the path integral. © 1993 John Wiley & Sons, Inc.

## I. Introduction

In a many-body problem, selecting the "right" generalized (functional) coordinates for the description of the system is very important. A good choice can make a problem relatively straightforward, can teach us about the key physics of the problem, and can even make our approximations and omissions less important. A bad choice can confuse the physics of the problem or lead to inconsistent or unphysical results even while it appears to be working perfectly. More often than not, the choice of representation is connected to the method of solution so that one more or less determines the other, although there are some representations that admit more than one method of solution.

Unfortunately, there is no *prescription* for selecting the best functional representation for a problem—it remains more art than science. In addition, there are well-known approaches based on representations that poorly describe the problem but that compensate for this by being easy to evaluate and integrate. These methods can be counted on to at least yield an answer at the end of a calculation (although there is no guarantee that the answer is even approximately correct). Given the grant-funded ecology of scientific research, there is thus a temptation and a tendency to repeatedly study a given problem to ever-higher order with a poorly convergent representation rather than invest the time (and take the risk) of studying the problem carefully and selecting a representation that may (or may *not*) be numerically or analytically difficult but that embraces the actual physics well and converges in application rapidly.

Some problems, of course, do yield to a heavy-handed approach at modest cost and frequently with "standard" codes so that even programming time is minimized. For these problems, art has become science (or even engineering) and we do not consider them further. Other problems, however, do not, and these "complex" problems are almost by definition among the most interesting problems available for study. Examples of complex problems are studies of phase transitions and critical phenomena for various systems, relaxation phenomena, reaction dynamics, and turbulence; generally, almost any system that exhibits macroscopically nonlinear behavior (static or dynamic, in open or closed systems) is microscopically complex, as some sort of fundamental reorganization of the microscopically linear system into self-consistent structures is associated with the macroscopic nonlinearity. These structures are rarely easily understood in terms of simple, linearized models of their microscopic components or modes.

A specific example of the importance of the correct generalized coordinates is found by studying the role of vortices or defect structures in general in Kosterlitz-Thouless transitions [1] such as occur in the  $2d/2D$  (planar, or  $xy$ -model) Heisenberg ferromagnet. This kind of phase transition is characterized by the unbinding of defect pairs (spin vortices of opposite twist) that are perturbatively disconnected from linearized (spin wave) descriptions. These defects are not just simple linear combinations of spin-wave modes—they have an identity, a structure, and an effective interaction all their own. It is difficult, if not impossible, to understand the planar ferromagnet without *first* recognizing that these defects are the relevant structures and implementing their coordinatization in the method used.

For researchers in many fields, then, it is useful to study as many examples of successful and unsuccessful descriptions of complex problems as possible, so that one's "bag of tricks" may contain the trick that one needs when one needs it and so that one can avoid methods unlikely to yield a correct answer. It is also worthwhile to understand the rationale underlying the descriptions that *do* work so that we may find new ones and even eventually reduce the art of discovering such a description to a science of implementing a prescription.

In this spirit, therefore, we present a uniform approach, based on numerically solving stochastic, unitary, integrodifferential equations that has worked well for us in certain many-body problems in the past. The equations solved are a Langevin realization of the Generalized Master Equation (GME)\* or path integral [3] for the problem, and the approach itself can be applied to a wide range of systems and phenomena. As such, it combines methods of microcanonical "molecular dynamics" (although we have not applied it to molecular problems) with methods of importance sampling heat bath Monte Carlo based on Glauber canonical thermalization "dynamics" [4,5].

To solve problems in quantum optics [6,7], magnetism [8], and even lattice gauge theory [9], we

---

\* For a discussion of the Generalized Master Equation in the context of quantum optics and Langevin equations, see, e.g., [2].



1. Select a system description that is simple enough that it can be worked with numerically and complex enough that it can describe all evaluated moments and quantities accessible by the actual system. The system description *can* be fully quantum-correlated (entangled), but if it is, there are distinct limits on the size of the systems that can be studied. In magnetic problems involving spin  $1/2$ , e.g., a fully entangled  $N$  spin description requires  $\sim \mathcal{O}(2^N)$  real number coordinates for the system alone. On the other hand, if one assumes a semiclassical spin-spin interaction, the spins do not entangle (so that the system can be in a simple product state) a system description scales like  $\sim \mathcal{O}(N)$ .

The fully entangled description is quantum mechanically "exact" but only small systems can be studied, so that many-body effects, especially on macroscopic scales, may be represented rather poorly. On the other hand, the simpler description can be scaled to rather large lattices (we reach  $N = 2^{14}$ – $2^{15}$  routinely, and  $2^{20}$ – $2^{21}$  are accessible on parallel supercomputers) and thus exhibit a full range of macroscopically nonlinear behaviors, but may or may not represent the local quantum theory very accurately. In between, there are various ways of constructing clustered or coarse-grained representations with a limited range of entanglement that should improve the quantum description but still allow statistically meaningful and scale-extensible macroscopic behavior to be studied, although this has yet to be proven (by us, at least).

Experience suggests that in many cases the semiclassical or classical coordinatization captures most of the essential quantum physics and describes experiment rather well because of the short correlation times of the entangled states in systems at a finite temperature.

2. With a numerically tractable representation in hand, we then solve for its explicit coherent time evolution by deriving and integrating (numerically) appropriate coupled differential equations from the system Hamiltonian.
3. Simultaneously (while the system undergoes its natural conservative and coherent microscopic motions) simulate its incoherent time evolution by treating its incoherent bath interaction as a random series of delta-correlated *unitary* transition processes. Each transition carries the system from one coherent, time-reversible system worldline to another (generally quite near by). In the process, information is irreversibly lost (explicitly, to the bath) and energy may or may not be conserved.

The essential feature of our approach is that we separate out the coherent and incoherent components of the motion of the system and treat the intrinsically unitarity-preserving coherent time evolution "exactly" (analytically or numerically) and *force* the incoherent components of the motion to be unitary transitions driven by stochastic interactions with the rest of the universe in such a way that the damping/decay rate equations are satisfied on the average. The various mechanisms and fields that contribute directly to the incoherent time evolution we call the "bath," with the understanding that it is we who decide which part of nature makes up the "system" and which part the bath.

In the GME, once one decides on the system, the bath is everything else (all the coordinates traced over in the projection to system-only coordinates). In

our approach, the same thing is very nearly true, except that we absorb the unitary contributions of the nonsystem coordinates to system motion into the reversible deterministic evolution and treat only the nonunitary (damping) contributions as being the stochastic bath (which may or may not be a thermal bath in the classic sense).

4. Finally, accumulate or record in each time step "measurements" performed on the system. As the *full microscopic state* of the system is always available, arbitrary moments and quantities that are generalized functions of the system coordinates can be studied.
5. Depending on what one is studying in a particular problem, the forward time evolution of the system from a given initial state can be repeatedly solved. The set of trajectories thus accumulated constitute a sampling of the actual fiber bundle of trajectories from which the path integral of the problem gets its weight. The moments of this bundle of trajectories (for a nonequilibrium system) are also of general interest.

The time evolution thus generated has several remarkable features: It allows for or includes both microcanonical, canonical, and pure stochastic time flow. Both pure molecular dynamics and pure (static) importance sampling Monte Carlo are thus completely embedded subsets of the general scheme and can be implemented by simply setting certain rate parameters to zero or unity. This method is, however, much more general and can be applied to far more complex and realistic problems in addition to the already vast body of problems accessible to the two embedded methods.

It can describe (thermal) equilibrium problems, relaxation models, and general nonequilibrium problems. Open (damped, driven) systems can thus be microscopically treated. The hysteresis cycle of absorptive optical bistability obtained in [6] and described below is the trace of a first-order dynamical phase transition in an open, damped, driven system.

The microdynamic method is non-Markovian. When a many-body system makes a "quantum jump" from one worldline to a nearby worldline (when the optical state of a single atom of the system changes, e.g.), most of the information required to describe the original worldline is left intact. In fact, this method can be viewed (from the point of view of information theory) as solving for the finite difference dynamics of entropy flow into or out of the system from the bath. In practice, the behavior of the system is distinguishably connected to its past-time history for times much longer than the time scale of microscopic motion or local stochastic relaxation, especially when strongly nonlinear or critical behavior is macroscopically observed, i.e., structures in the system can have extremely long lifetimes, many times longer than the "memory time" of a single component in the structure. Obvious examples of this are critical slowing down in general and metastable configurations "frozen in" to a system during a rapid quench from high-temperature initial conditions through a second-order critical point.

In Figures 4 and 5, we offer numerical evidence that including system dynamics interleaved with the heat bath thermalization process can alter the longitudinal

relaxation rates when the spin-spin relaxation rates exceed the rates of the spin-bath interaction (i.e., when the spin waves have a long thermal coherence time). This is not unreasonable, but is completely invisible in any Monte Carlo approach that does not include microdynamics explicitly. On the other hand, when the thermalization process is fast with respect to the spin-spin relaxation rate, then the time scales associated with Glauber dynamics are essentially real time and dynamical scaling laws obtained with this tool are valid.

A final appealing feature of this approach is that it is based on implementing, as faithfully as possible, a numerical realization of what we believe to actually be occurring in the system in nature. It is more than "just a simulation"—it is a numerical solution to the (admittedly stochastic) equations of motion. As a consequence, we expect that the method will respect detailed balance *and* broken ergodicity [10] when appropriate (as when the system undergoes a phase transition) but will also respect the kind of broken ergodicity that *supersedes* detailed balance when appropriate. Not all simulation methods respect broken ergodicity even when it occurs in the actual physical model, so this is an important consideration [11].

It is not possible in a short paper to present more than a brief outline of some of the results successfully obtained in this approach. This list is constantly changing, as well, as we are currently actively involved in implementing it to a variety of problems. We urge interested readers to obtain the original papers or to contact us for more detailed discussions.

## II. Optics

We deduced this method in work leading to its original application in studies of the nonlinear quantum optics of "two level atoms" in a tuned cavity and stimulated with a coherent, resonant optical field (see [6] and the copious references therein). Phenomena exhibited by such a collection include photon echoes, superradiance, and absorptive optical bistability (a dynamical first-order phase transition). At the time of our work, there were semiheuristic descriptions of photon echoes, several competing explanations for superradiance (or superfluorescence) at various levels of quantum entanglement, and a mean-field-based understanding of absorptive optical bistability at the level of nonlinear equations describing the equilibrium. None of the methods used to understand these specific problems could also describe more than one of the other two in the same coordinatization.

We realized that if we treated the ensemble of two-level atoms as being semi-classically coupled via the total cavity field (after extracting the atom-field entangling that leads to the spontaneous emission rates in QED), that free quantum time evolution from a simple product state would leave the atoms in a simple product state. If we treated the spontaneous emission process physically as a stochastic, delta-correlated transition from an arbitrary superposition state to the ground state, we could obtain unitary Langevin equations that precisely reproduce the single-atom expectation values in the appropriate limit but that fully allow for classically correlated (collective) field emission and absorption. It was natural to add other generic-phase interrupting processes (such as elastic or inelastic collisions) as an additional unitarity preserving stochastic transition term in the time-evolution loop.

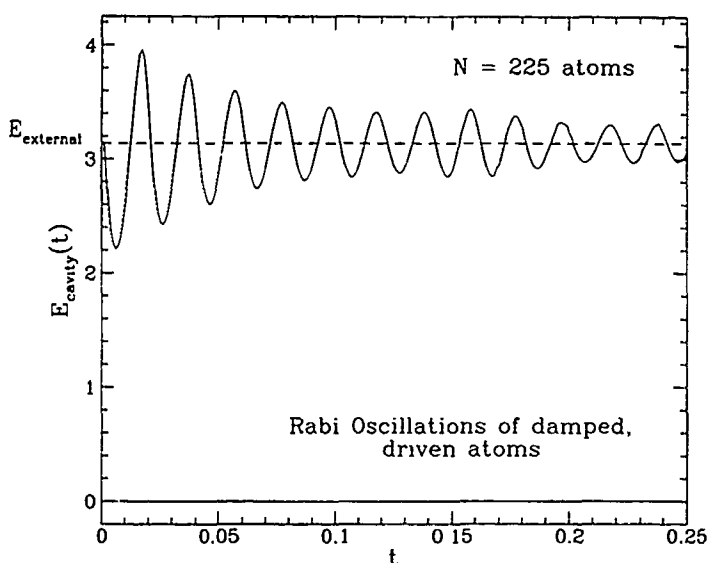


Figure 1. The modulation of the driving external field by Rabi oscillations in a collection of  $N = 225$  two-level, resonant atoms enclosed in a "cavity." As the atoms are driven through the Rabi cycle, they coherently absorb and re-emit radiation in phase with the driving field. At the same time, however, incoherent processes destroy the collective phase of the atoms so that eventually they absorb as much as they decay and the cavity becomes transparent.

The resulting system of  $3N + 1$  coupled *linear* ordinary differential equations for the system of atoms plus the field was readily integrable in time. The stochastic elements preserved the unitarity of the description and, hence, the post-transition integrability. Accurate numerical results were easily obtained for  $N \sim 10^2$ – $10^3$  even on modest computers.

This method proved capable of describing photon echoes, self-initiated superradiance, and absorptive optical bistability within a single approach, by simply altering the appropriate parameters of the model in much the same way that they would be varied in the different experiments required to measure them in a single collection of atoms. In Figure 1 we present the modulation of a transmitted radiation pulse by Rabi oscillations in resonant two-level atoms.<sup>†</sup> This shows that the atoms in our numerical example correctly exhibit damped, driven motion that can be obtained analytically for this simple case.

In Figure 2 we present a typical superradiance curve produced by the numerical model, with an inset closeup of the initiating spontaneous emission event. This picture is entirely consistent with the observations of MacGillivray and Feld [13], who also proposed that the full apparatus of quantum entangled atomic states was not really necessary to quantitatively or qualitatively describe superradiance ex-

<sup>†</sup> See a discussion of Rabi oscillations, together with figures, in, e.g., [12].

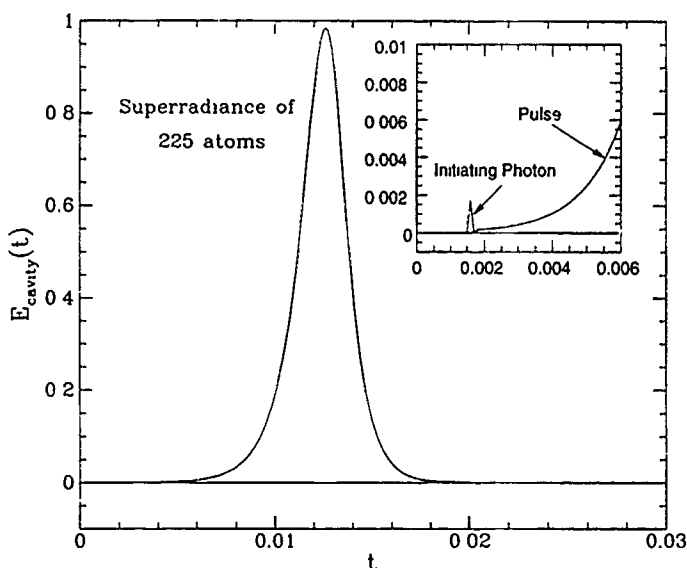


Figure 2. The collective, superradiant emission of  $N = 225$  two-level atoms prepared at time  $t = 0$  in the completely inverted state. The system is quiescent for a delay time after inversion, at which point a single spontaneous decay photon emission with overlap in the cavity mode initiates the growth of the superradiant pulse (see inset). The pulse itself develops the characteristic hyperbolic secant shape. The delay time itself has been physically observed (see MacGillivray and Feld [13]).

periments. Note that this is considered a *nonlinear* macroscopic phenomenon that we are obtaining from a strictly *linear* microscopic model, exactly as it obtains in nature.

Finally, in Figure 3, we present a photon echo as produced by the numerical model. This phenomenon, while well understood on an heuristic level, is remarkably difficult to get from a deterministic or semideterministic algebraic model. It verifies that the atoms are being driven precisely as we expect them to be on a fully microscopic basis. There are several interesting features of this curve that are more fully discussed in [6].

The  $N$ -atom optical Bloch equations (our numerical model) also gave, for the first time, a complete microscopic picture of what was happening inside the system as it was driven through a complete hysteresis cycle in absorptive optical bistability. The macroscopic nonlinearity was thus illuminated as a simple, intuitively understandable microscopic behavior resulting from the collective interaction of the atoms with the driving mode and the cavity. Also, the approach does not yield the non-physical middle branch that results from the cubic mean field equations for the equilibrium—it allows, instead, a direct probe of the size-extensivity of the stability of the fluctuation-induced phase transition at the branch points of the state curve. A full time trace of the hysteresis cycle is given in [6], as well as the resulting hysteresis curve itself.

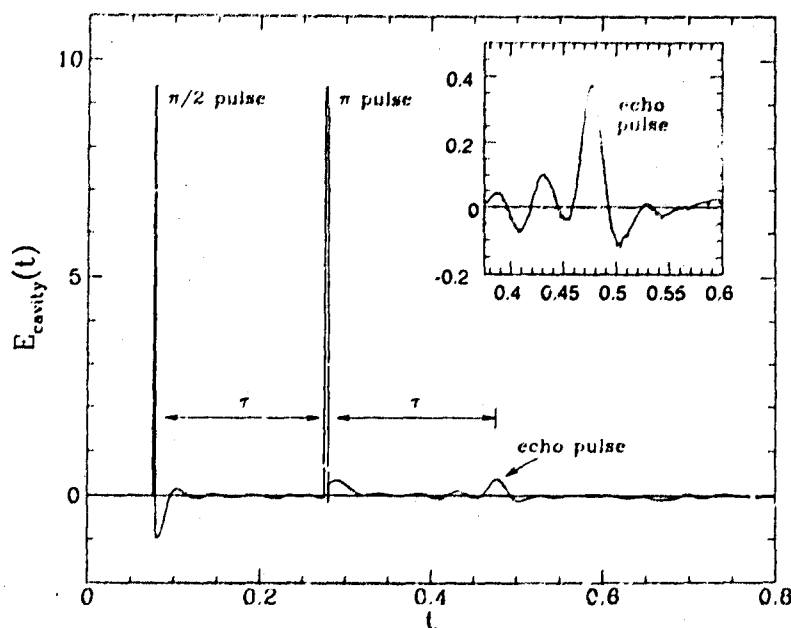


Figure 3. The same collection of  $N = 225$  atoms being driven through a "photon echo" experiment. The atoms are initially in the ground state. They are then briefly exposed to a " $\pi/2$ "-pulse that coherently polarizes them. The atoms start to radiate away the energy that they absorbed, but this process is cut off by their inhomogeneous dephasing. After a delay  $\tau$ , they are exposed to an applied " $\pi$ "-pulse that inverts their moments with respect to the polarization plane. After an additional delay  $\tau$ , the atoms rephase, producing the clearly visible collective emission pulse in the cavity field.

### III. Magnetism

Our original studies of the optics problem were conducted at zero temperature. This is because it is *very* difficult to include temperature *and* time evolution in an open many-body problem. From some of our initial studies [7], however, it became clear that we needed to be able to treat finite temperature bath interactions, as they could lead to a fundamentally new kind of organization of the optical states. Since the role of temperature in many-body physics is nowhere as well understood as it is in magnetism, and since in any event spin dynamics in magnetism is closely allied to the pseudospin dynamics that we studied in optics, we turned to magnetism to learn how to implement canonical heat baths in our optical method.

The natural extension of the method that we used to treat spontaneous emission and collisions in the optics problem was to induce unitarity-preserving transitions from arbitrary superposition states to new superpositions states selected from the canonical distribution of available states at the given temperature. We therefore implemented this in our code after converting it into a form suitable for studying magnetism. As we studied Monte Carlo methods for the first time (to learn how to accumulate appropriate averages so that we could check our results), we learned that this is the Glauber or heat bath thermalization method [4,5] that we had reinvented with a somewhat different motivation.

In ordinary Monte Carlo, the time scale of Glauber thermalization dynamics is arbitrary—"Monte Carlo time" is not necessarily related to real time, although it is frequently treated as if it were in studies of dynamic scaling. In the unitary Langevin method that we describe herein, Monte Carlo time is directly and uniquely related to real time by the presence of the relative time scales of the various physical processes being directly integrated over in the deterministic evolution. It is not necessary to confine oneself to studies of models where the thermalization time is much smaller than the spin-spin dynamics time scale or vice versa. Instead, one can study both of these possibilities as well as the possibility that spin-wave relaxation and Glauber thermalization proceed on commensurate time scales. In this case, the combination of microcanonical spin-wave relaxation and the canonical thermal relaxation rates can, at least in principle, alter the dynamic susceptibilities of the system being studied.

Using our method, we directly study the spin autocorrelation function  $\langle \mathbf{S}(0) \cdot \mathbf{S}(t) \rangle$  (where the average is over multiple time trajectories and all lattices sites on an  $8 \times 8 \times 8$  simple cubic Heisenberg ferromagnet with periodic boundary conditions). The spin autocorrelation has two components: The "longitudinal" component measures how rapidly the spin component parallel to the bulk magnetization vector at  $t = 0$  changes; the "transverse" component measures how rapidly the short-range structure in the components perpendicular to the initial magnetization vector decays in time. The longitudinal component, for a system in equilibrium, is expected to undergo a random walk on the surface of the (order parameter) sphere with an angular step size that scales like  $\sqrt{n}$ . The transverse autocorrelation relaxation time is expected to diverge at the critical point and a dynamical critical exponent is associated with this.

We find that the full inclusion of dynamics *does* alter the transverse relaxation rates of the system under certain, readily understandable circumstances. We also find that it *does not* alter the longitudinal relaxation or in any way affect detailed balance or the averages of thermodynamic (static) quantities.

In the case of classical Heisenberg spins interacting via a nearest-neighbor interaction, the classical free motion is for each spin to instantaneously precess around the instantaneous "field" produced by its nearest neighbors at a rate determined by the field strength. This is simply described by a set of coupled ordinary differential equations that can be explicitly (numerically) integrated very accurately. The time required to produce a single  $2\pi$  precession around the largest internal field possible can be larger than, smaller than, or comparable to the time required to make a Monte Carlo time step (i.e., apply the heat bath algorithm to each spin in the system one time). This can be adjusted in the code by interspersing several smaller integration time steps inside the thermalization loop or by performing several thermalization loops per integration time step.

Figure 4 is a comparison of a typical ordinary heat bath Monte Carlo autocorrelation (no dynamics at all) with the autocorrelation produced when dynamics are included but with spin-spin relaxation rates that are comparable to or slower than the thermal Monte Carlo relaxation rates; i.e., each spin can precess only a small distance around its local site field before being "thermalized," even in the

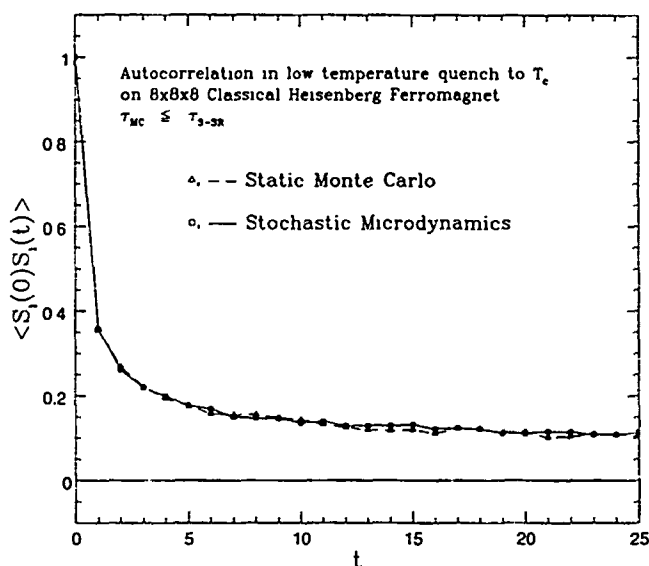


Figure 4. The decay of total autocorrelation in an  $8 \times 8 \times 8$  simple cubic lattice of Heisenberg spins at their critical temperature. In one case, dynamical spin-spin relaxation occurs, but at a rate the same than or slower than the thermal relaxation rate. In the other case, thermal relaxation only is present. The two relaxation rates are indistinguishable.

strongest local fields that can exist in the system. The thermalizing bath interactions (Monte Carlo steps) destroy the local-phase angles of the spins with respect to their local instantaneous field. This results in a characteristic fast decay of the transverse component of its spin autocorrelation to the residual slowly decaying longitudinal component. Clearly, the transverse relaxation rates are equal for both situations (with or without the dynamics) or nearly so. The same is true for the longitudinal rates. The scatter observed is due to relatively small number (100) of short runs being averaged and should not be interpreted as a structure of any sort.

On the other hand, in Figure 5, we set the time scales so that each spin could precess through angles comparable to  $2\pi$  due to the Hamiltonian spin-spin interaction (spin wave motion) during the intervals between thermalizing bath interactions. This spin motion has the effect of destroying transverse correlations independent of the bath. As a consequence, transverse relaxation is greatly accelerated on the time scale of the Monte Carlo process ( $t$  counts Monte Carlo "sweeps" or time steps). Indeed, one would expect that even if no random processes whatsoever were present, the spin-spin interaction would generally suffice to destroy transverse correlation in the system via wavelike dispersion processes. Longitudinal correlation, however, is a constant of the motion for the Heisenberg Hamiltonian and only the bath breaks this symmetry, inducing gradual longitudinal relaxation.

Clearly, this is a very simple case that is readily understandable—after the simulation reveals the phenomenon. On the other hand, it also shows how far more



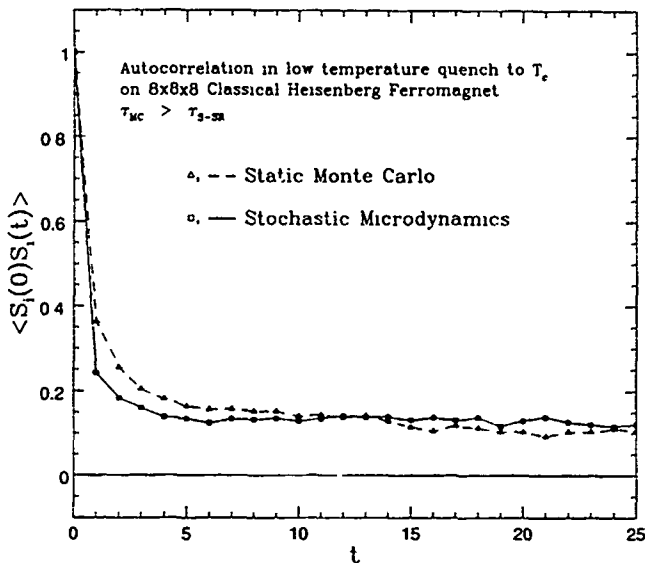


Figure 5. The same as in Figure 4, but now the spin-spin relaxation for the "fastest" modes proceeds  $\sim 10\times$  faster than the thermal relaxation rate. This clearly affects the transverse decay rate, as spin-spin relaxation alone would destroy transverse autocorrelation. The decay of longitudinal autocorrelation, however, is still dominated by the Monte Carlo (thermal) relaxation process, as this kind of autocorrelation is nearly conserved by Hamiltonian motion.

complex behavior can be simulated for an open system that cannot be so easily understood. It also provides, at last, a formal process for validating the notion of "Monte Carlo time" and its relevance to dynamic scaling laws. In systems where the thermal spin-wave coherence time is short, Monte Carlo time as used in heat bath simulations should yield meaningful dynamical exponents. In systems where the thermal relaxation process is slow with respect to the time constants of the internal motion, however, this is not guaranteed to be the case.

The continuing study of both dynamics and static critical properties in open and closed systems is the focus of our current research efforts [8]. In addition, we are involved on an advisory level with the extensions of this method in lattice gauge calculations being conducted here [9]. It is our belief that this method will eventually prove to be a powerful tool in the arsenal of the many-body theorist.

#### IV. Conclusions

We have presented a description of a method that, supplemented by a perusal of our published and unpublished work, should suffice to enable interested researchers to implement a generically similar scheme in a wide range of dynamics or static many-body problems. We have also presented evidence that this scheme

leads to physically reasonable and intuitively understandable results in a very natural way.

To conclude, we want to present the logic of this approach in more complex (and complete) representations, including both the full  $N$ -body representation and coherent states. The former leads to a problem that is numerically intractable as it stands except for very small  $N$ ; the latter has functional extensions that may make it very useful in this sort of approach.

In the specific examples discussed above, the spins or atoms were assumed to be in a simple product state—no quantum entangling of the spin-spin interaction was allowed.

Note that in magnetism this makes a quantum spin model into a semiclassical spin model equivalent to the classical model ( $S = \infty$ ). The spins are still semiclassical in that quantum transitions are still allowed; this can lead to some interesting and unique new physics that we are still studying.

In optics this means that we are not using the fully entangled Dicke states [14] or atomic coherent states [15] (the spin-state equivalents of the coherent states of the radiation field [16]) but a representation intermediate between these entangled representations and the neoclassical picture of Jaynes and Cummings [17]. This representation treats the single atom-field entangling in QED (extracting the actual spontaneous emission rate and Lamb shift) but leaves the atom-atom interaction disentangled. This works remarkably well for most problems.

If, however, one is faced with a problem where many-body entangling is a necessary evil with significant physical consequences, all is not lost. The method can still be applied, although one will have to work much harder and strain one's computational resources.

The essential elements to applying this method to entangled problems are

1. Identifying the best representation, i.e., the smallest and most tractable representation that still contains the essential features of the model.
2. Deriving microreversible equations of motion for the coordinates of this description.
3. Deriving, deducing, or even guessing the appropriate unitary transitions induced by the "bath" (thermal or otherwise).
4. Implementing the equations of motion and stochastic bath interactions in a single piece of code with appropriate statistical hooks and accumulators.

By using clustering and scaling arguments in the first step, it may be possible to embed this algorithm at the heart of a real-space real-time numerical renormalization scheme applicable to entangled open systems. This would open a new range of extremely interesting problems up to detailed study and is one of the chief goals of our current research.

We are also very interested in synthesizing the results from these physically motivated Langevin equation calculations with the concepts and results obtained with the functional integral method [18]. The microdynamic method, when applied carefully, may give us insight into the correct form of the "mean field" results (or a related Landau theory) that can be corrected for fluctuations by functional integral

methods. We have obtained [19] the real-space, real-time, dynamical evolution equations in the functional integral approach using the coherent state representation [16]).

### Acknowledgment

We wish to acknowledge the support the Army Research Office, which sponsored this research.

### Bibliography

- [1] J. M. Kosterlitz and D. J. Thouless, *J. Phys.* **C6**, 1181 (1973)
- [2] G. S. Agarwal, *Quantum Optics*, Springer Tracts in Modern Physics, Vol. 70 (Springer-Verlag, New York, 1974).
- [3] R. P. Feynman and A. R. Hibbs, *Quantum Mechanics and Path Integrals* (McGraw-Hill, New York, 1964).
- [4] R. J. Glauber, *Jour. Math. Phys.* **4**, 294 (1963).
- [5] K. Binder and D. W. Heermann, *Monte Carlo Simulation in Statistical Physics*, Springer Series in Solid-State Sciences 80 (Springer-Verlag, New York, 1988).
- [6] R. G. Brown and M. Cifan, *Phys. Rev. A* **40**, 3080 (1989).
- [7] R. G. Brown and M. Cifan, in *Condensed Matter Theories 3*, J. S. Arponen, R. G. Bishop, and M. Manninen, Eds. (Plenum, New York, 1987), p. 339.
- [8] R. G. Brown and M. Cifan, unpublished (work in progress on the semiclassical/classical Heisenberg model).
- [9] B. Müller and A. Trayanov, *Phys. Rev. Lett.* **68**, 3387 (1992).
- [10] R. G. Palmer, *Adv. Phys.* **32**, 669 (1982).
- [11] See, e.g., the discussion in O. G. Mountsen, *Computer Studies of Phase Transitions and Critical Phenomena*, Springer-Verlag Series in Computational Physics (Springer-Verlag, New York, 1984) p. 7 and ff.
- [12] R. Loudon, *The Quantum Theory of Light* (Clarendon, Oxford, 1983)
- [13] J. C. MacGillivray and M. S. Feld, *Phys. Rev. A* **14**, 1169 (1976).
- [14] R. H. Dicke, *Phys. Rev.* **93**, 99 (1954).
- [15] F. T. Arecchi, E. Courtens, R. Gilmore, and H. Thomas, *Phys. Rev. A* **6**, 2211 (1972).
- [16] R. Glauber, *Phys. Rev.* **131**, 2766 (1963).
- [17] E. T. Jaynes and F. W. Cummings, *Proc. IEEE* **51**, 89 (1963).
- [18] J. W. Negele and H. Orland, *Quantum Many-Particle Systems* (Addison-Wesley, New York, 1988).
- [19] W. Poetz and M. Cifan, unpublished (1993).

Received July 1, 1993

# Determinantal Inequalities among $\langle r^n \rangle$

P. CSAVINSZKY

*Department of Physics and Astronomy, University of Maine, Orono, Maine 04469-5709*

## Abstract

This paper considers two types of  $2 \times 2$ ,  $3 \times 3$ , and  $4 \times 4$  determinantal inequalities. The elements of one type are  $\langle r^n \rangle$ , while the elements of the other type are  $c\langle r^n \rangle$ , where  $c = 3 + n$ . The  $2 \times 2$ ,  $3 \times 3$ , and  $4 \times 4$  determinantal inequalities involve  $n = -1, 0, 1$ ,  $n = -1, 0, 2, 3, 4$ , and  $n = -1, 0, 1, 2, 3, 4, 5$ . The two types of  $2 \times 2$ ,  $3 \times 3$ , and  $4 \times 4$  inequalities are used to obtain lower bound estimates of  $\langle r \rangle$ ,  $\langle r^3 \rangle$ , and  $\langle r^5 \rangle$  for the noble gas atoms He, Ne, Ar, Kr, and Xe. The values of these quantities obtained from the inequalities are compared with the quantum mechanical values of Boyd, who calculated them with the near Hartree-Fock analytical wave functions of Clementi and Roetti. © 1993 John Wiley & Sons, Inc.

## Introduction

The establishment of inequalities involving  $\langle r^n \rangle$ , where  $r$  is the distance from the atomic nucleus, poses the question: To what accuracy can one calculate an expectation value of  $r^n$  in terms of other expectation values of powers of  $r$ ? Several  $N \times N$  determinantal inequalities involving  $\langle r^n \rangle$  were given by Gadre and Matcha [1]. The  $2 \times 2$  inequalities involve  $\langle r^n \rangle$  with  $n = -1, 0, 1$ . The  $3 \times 3$  inequalities involve  $\langle r^n \rangle$  with  $n = -1, 0, 1, 2, 3$ . One of the  $2 \times 2$  and one of the  $3 \times 3$  inequalities involve  $c\langle r^n \rangle$ , where  $c = 3 + n$ .

In the present work, two  $4 \times 4$  determinantal inequalities are established. One of these involves  $\langle r^n \rangle$ , while the other one involves  $c\langle r^n \rangle$  with  $c = 3 + n$  and  $n = -1, 0, 1, 2, 3, 4, 5$ .

The motivation for establishing  $N \times N$  determinantal inequalities is simple. The  $2 \times 2$  case, for instance, permits one to obtain a lower bound estimate of  $\langle r \rangle$  in terms of  $\langle r^{-1} \rangle$ . Similarly, the  $3 \times 3$  case permits one to obtain a lower bound estimate of  $\langle r^3 \rangle$  in terms of  $\langle r^{-1} \rangle$ ,  $\langle r \rangle$ , and  $\langle r^2 \rangle$ . In a similar manner, in the  $4 \times 4$  case, one can obtain a lower bound estimate of  $\langle r^5 \rangle$  in terms of  $\langle r^{-1} \rangle$ ,  $\langle r \rangle$ ,  $\langle r^2 \rangle$ ,  $\langle r^3 \rangle$ , and  $\langle r^4 \rangle$ . In the present work,  $\langle r \rangle$ ,  $\langle r^3 \rangle$ , and  $\langle r^5 \rangle$  are calculated from two types of determinantal inequalities for the noble gas atoms He, Ne, Ar, Kr, and Xe. In these calculations, the  $\langle r^n \rangle$  values of Boyd [2] are used who obtained them from the near Hartree-Fock (HF) analytical wave functions of Clementi and Roetti [3].\*

\* It should be mentioned here that a large body of literature exists on (per electron) momentum expectation values  $\langle p^n \rangle$ . Some of this literature deals with inequalities involving expectation values of powers of  $p$ , while another part of the literature deals with inequalities involving both  $\langle p^n \rangle$  and  $\langle r^n \rangle$ . None of the relevant publications will be referred to in the present paper.

In what follows, atomic units will be used. (The unit of length is the bohr, the unit of energy is the hartree.)

### Determinantal Inequalities

A type of determinantal inequalities was obtained by Gadre and Matcha [1], who made use of the Gram inequality, namely [4] of

$$\left| \int f_{\lambda}(x) f_{\mu}(x) dx \right| \geq 0 \quad (\lambda, \mu = 1, 2, \dots, N). \quad (1)$$

Defining  $f_n(x)$  by [1]\*

$$f_n(x) = [4\pi r^{2n-1} \rho(r)]^{1/2} \quad (n = 1, 2, \dots, N), \quad (2)$$

where  $\rho(r)$  is the position electron density, and noting that

$$\rho(r) = (1/4\pi) r^{-2} D(r), \quad (3)$$

where  $D(r)$  is the position radial electron density, normalized to unity [2], one obtains with

$$\langle r^n \rangle = \int_0^{\infty} r^n D(r) dr \quad (4)$$

the  $2 \times 2$ ,  $3 \times 3$ , and  $4 \times 4$  inequalities

$$\begin{vmatrix} \langle r^{-1} \rangle & 1 \\ 1 & \langle r \rangle \end{vmatrix} \geq 0, \quad (5)$$

$$\begin{vmatrix} \langle r^{-1} \rangle & 1 & \langle r \rangle \\ 1 & \langle r \rangle & \langle r^2 \rangle \\ \langle r \rangle & \langle r^2 \rangle & \langle r^3 \rangle \end{vmatrix} \geq 0, \quad (6)$$

and

$$\begin{vmatrix} \langle r^{-1} \rangle & 1 & \langle r \rangle & \langle r^2 \rangle \\ 1 & \langle r \rangle & \langle r^2 \rangle & \langle r^3 \rangle \\ \langle r \rangle & \langle r^2 \rangle & \langle r^3 \rangle & \langle r^4 \rangle \\ \langle r^2 \rangle & \langle r^3 \rangle & \langle r^4 \rangle & \langle r^5 \rangle \end{vmatrix} \geq 0. \quad (7)$$

Putting the  $2 \times 2$ ,  $3 \times 3$ , and  $4 \times 4$  determinants in Eqs. (5)–(7) equal to zero, the calculated lower bound values of  $\langle r \rangle$ ,  $\langle r^3 \rangle$ , and  $\langle r^5 \rangle$ , for the noble gas atoms He, Ne, Ar, Kr, and Xe, are displayed in the second columns of Tables I, II, and III.

Another type of determinantal inequalities was obtained by Gadre and Matcha [1] by making use of a theorem by Pólya and Szegő [5], namely,

\* There is a misprint in Ref. [1]. The quantity  $f_n$  there is given as  $f_n = [4\pi\rho(r)^{2n-1}]^{1/2}$  ( $n = 1, 2, 3, \dots$ ), whereas the correct expression is that displayed in Eq. (2) of the present paper.

TABLE I. Calculated lower bound (LB) and quantum mechanical (QM) values of  $\langle r \rangle$  (in a.u.) and their ratios.\*

Atom	$\langle r \rangle_{\text{LB}}$	$\langle r \rangle_{\text{QM}}$	$\langle r \rangle_{\text{LB}}/\langle r \rangle_{\text{QM}}$
He	0.59	0.93	0.64
Ne	0.32	0.79	0.41
Ar	0.26	0.89	0.29
Kr	0.20	0.73	0.27
Xe	0.17	0.72	0.24

\* The calculated values of  $\langle r \rangle$  were obtained from the  $2 \times 2$  determinant in Eq. (5) by putting it equal to zero. The quantum mechanical values of  $\langle r \rangle$  were taken from Ref. [2].

$$\left| (a_\lambda + a_\mu + 1) \int_0^\infty x^{a_\lambda + a_\mu} f(x) dx \right| \geq 0 \quad (\lambda, \mu = 1, 2, \dots, N). \quad (8)$$

Defining  $f(x)$  by  $4\pi\rho(r)$  [1],\* and setting  $a_1 = 1/2$ ,  $a_2 = 3/2$ ;  $a_1 = 1/2$ ,  $a_2 = 3/2$ ,  $a_3 = 5/2$ ; and  $a_1 = 1/2$ ,  $a_2 = 3/2$ ,  $a_3 = 5/2$ , and  $a_4 = 7/2$ , one obtains the  $2 \times 2$ ,  $3 \times 3$ , and  $4 \times 4$  inequalities

$$\begin{vmatrix} 2\langle r^{-1} \rangle & 3 \\ 3 & 4\langle r \rangle \end{vmatrix} \geq 0, \quad (9)$$

$$\begin{vmatrix} 2\langle r^{-1} \rangle & 3 & 4\langle r \rangle \\ 3 & 4\langle r \rangle & 5\langle r^2 \rangle \\ 4\langle r \rangle & 5\langle r^2 \rangle & 6\langle r^3 \rangle \end{vmatrix} \geq 0, \quad (10)$$

\* The  $4\pi$  factor is missing in Ref. [1]. The introduction of this factor is, however, necessary if one wants to reproduce Eq. (6) of Ref. [1].

TABLE II. Calculated lower bound (LB) and quantum mechanical (QM) values of  $\langle r^3 \rangle$  (in a.u.) and their ratios.\*

Atom	$\langle r^3 \rangle_{\text{LB}}$	$\langle r^3 \rangle_{\text{QM}}$	$\langle r^3 \rangle_{\text{LB}}/\langle r^3 \rangle_{\text{QM}}$
He	1.72	1.94	0.89
Ne	1.29	1.44	0.90
Ar	2.54	3.11	0.82
Kr	1.82	2.44	0.74
Xe	2.03	2.82	0.72

\* The calculated values of  $\langle r^3 \rangle$  were obtained from the  $3 \times 3$  determinant in Eq. (6) by putting it equal to zero. The quantum mechanical values of  $\langle r^3 \rangle$  were taken from Ref. [2].

TABLE III. Calculated lower bound (LB) and quantum mechanical (QM) values of  $\langle r^5 \rangle$  (in a.u.) and their ratios.<sup>a</sup>

Atom	$\langle r^5 \rangle_{\text{LB}}$	$\langle r^5 \rangle_{\text{QM}}$	$\langle r^5 \rangle_{\text{LB}} / \langle r^5 \rangle_{\text{QM}}$
He	7.02	9.20	0.76
Ne	5.93	6.24	0.95
Ar	19.87	24.42	0.81
Kr	20.91	22.27	0.94
Xe	29.67	31.75	0.94

<sup>a</sup> The calculated values of  $\langle r^5 \rangle$  were obtained from the  $4 \times 4$  determinant in Eq. (7) by putting it equal to zero. The quantum mechanical values of  $\langle r^5 \rangle$  were taken from Ref. [2].

and

$$\begin{vmatrix} 2\langle r^{-1} \rangle & 3 & 4\langle r \rangle & 5\langle r^2 \rangle \\ 3 & 4\langle r \rangle & 5\langle r^2 \rangle & 6\langle r^3 \rangle \\ 4\langle r \rangle & 5\langle r^2 \rangle & 6\langle r^3 \rangle & 7\langle r^4 \rangle \\ 5\langle r^2 \rangle & 6\langle r^3 \rangle & 7\langle r^4 \rangle & 8\langle r^5 \rangle \end{vmatrix} \geq 0. \quad (11)$$

Putting the  $2 \times 2$ ,  $3 \times 3$ , and  $4 \times 4$  determinants in Eqs. (9)–(11) equal to zero, the calculated lower bound values of  $\langle r \rangle$ ,  $\langle r^3 \rangle$ , and  $\langle r^5 \rangle$ , for the noble gas atoms He, Ne, Ar, Kr, and Xe, are displayed in the second columns of Tables IV, V, and VI.

TABLE IV. Calculated lower bound (LB) and quantum mechanical (QM) values of  $\langle r \rangle$  (in a.u.) and their ratios.<sup>a</sup>

Atom	$\langle r \rangle_{\text{LB}}$	$\langle r \rangle_{\text{QM}}$	$\langle r \rangle_{\text{LB}} / \langle r \rangle_{\text{QM}}$
He	0.67	0.93	0.72
Ne	0.36	0.79	0.46
Ar	0.29	0.89	0.33
Kr	0.22	0.73	0.31
Xe	0.19	0.72	0.26

<sup>a</sup> The calculated values of  $\langle r \rangle$  were obtained from the  $2 \times 2$  determinant in Eq. (9) by putting it equal to zero. The quantum mechanical values of  $\langle r \rangle$  were taken from Ref. [2].

TABLE V. Calculated lower bound (LB) and quantum mechanical (QM) values of  $\langle r^3 \rangle$  (in a.u.) and their ratios.<sup>a</sup>

Atom	$\langle r^3 \rangle_{\text{LB}}$	$\langle r^3 \rangle_{\text{QM}}$	$\langle r^3 \rangle_{\text{LB}} / \langle r^3 \rangle_{\text{QM}}$
He	1.79	1.94	0.92
Ne	1.25	1.44	0.86
Ar	2.64	3.11	0.85
Kr	1.90	2.44	0.78
Xe	2.13	2.82	0.75

<sup>a</sup> The calculated values of  $\langle r^3 \rangle$  were obtained from the  $3 \times 3$  determinant in Eq. (10) by putting it equal to zero. The quantum mechanical values of  $\langle r^3 \rangle$  were taken from Ref. [2].

Finally, it is noted that Eq. (9), in the form of  $(8/9)\langle r \rangle \langle r^{-1} \rangle > 1$ , has already been obtained by Gadre [6].\*

\* There is a misprint in Ref [6]. The right-hand side of the inequality [Eq. (1)] is written as

$$1 - \left( \frac{a-b}{a+b+1} \right)^2 \int_0^\infty x^{2a} \phi(x) dx \int_0^\infty x^{2b} \phi(x) dx,$$

whereas the correct expression is

$$\left[ 1 - \left( \frac{a-b}{a+b+1} \right)^2 \right] \int_0^\infty x^{2a} \phi(x) dx \int_0^\infty x^{2b} \phi(x) dx.$$

The inequalities in Ref [6] have been derived on the assumption that the electronic charge density  $\rho(r)$  is monotonically decreasing with  $r$ . There is no general proof of this, but there is numerical evidence by Sperber [7] and by Simas et al. [14] that HF charge densities are monotonically decreasing functions of  $r$ . In Ref. [14] this has been established for the neutral atoms H through U by making use of the near HF analytical wave functions of Clementi and Roetti [3] and those of MacLean and MacLean [15].

TABLE VI. Calculated lower bound (LB) and quantum mechanical (QM) values of  $\langle r^5 \rangle$  (in a.u.) and their ratios.<sup>a</sup>

Atom	$\langle r^5 \rangle_{\text{LB}}$	$\langle r^5 \rangle_{\text{QM}}$	$\langle r^5 \rangle_{\text{LB}} / \langle r^5 \rangle_{\text{QM}}$
He	9.01	9.20	0.98
Ne	6.01	6.24	0.96
Ar	23.28	24.42	0.95
Kr	21.10	22.27	0.95
Xe	30.01	31.75	0.95

<sup>a</sup> The calculated values of  $\langle r^5 \rangle$  were obtained from the  $4 \times 4$  determinant in Eq. (11) by putting it equal to zero. The quantum mechanical values of  $\langle r^5 \rangle$  were taken from Ref. [2].



### Discussion

It is seen from the second column of Table I that the value of  $\langle r \rangle_{\text{LB}}$  decreases as one goes from He to Xe. The second column of Table II does not show a regular behavior in the values of  $\langle r^3 \rangle_{\text{LB}}$ . The second column of Table III shows that, with the exception of Ne, the value of  $\langle r^5 \rangle_{\text{LB}}$  increases as one goes from He to Xe. Inspection of the  $\langle r \rangle_{\text{QM}}$  (QM means quantum mechanical) values in the third column of Table I shows that the decreasing trend in this quantity is broken with Ar. One can see from the third column of Table II that there is no systematic trend in the values of  $\langle r^3 \rangle_{\text{QM}}$  as one goes from He to Xe. A look at the values of  $\langle r^5 \rangle_{\text{QM}}$  in the third column of Table III reveals no systematic trend in this quantity either. The fourth columns of Tables I and II reveal that, for all noble gas atoms,  $\langle r \rangle_{\text{LB}} / \langle r \rangle_{\text{QM}}$  and  $\langle r^3 \rangle_{\text{LB}} / \langle r^3 \rangle_{\text{QM}}$  is smaller than unity. This is also the case for  $\langle r^5 \rangle_{\text{LB}} / \langle r^5 \rangle_{\text{QM}}$ , as can be seen from the fourth column of Table III.

Moving now to Table IV, one sees that the values of  $\langle r \rangle_{\text{LB}}$ , in the second column of Table IV, exhibit a decreasing trend. The  $\langle r \rangle_{\text{LB}} / \langle r \rangle_{\text{QM}}$  values, in the fourth column of Table IV, show a decreasing trend too. A glance at the  $\langle r^3 \rangle_{\text{LB}}$  values in the second column of Table V shows an irregular behavior. Inspection of the  $\langle r^3 \rangle_{\text{LB}} / \langle r^3 \rangle_{\text{QM}}$  values in the fourth column of Table V shows a decreasing behavior as one moves from He to Xe. One can see from the second column of Table VI that there is no systematic trend in the values of  $\langle r^5 \rangle_{\text{LB}}$  as one moves from He to Xe. It is interesting to note that the values of  $\langle r^5 \rangle_{\text{LB}} / \langle r^5 \rangle_{\text{QM}}$ , in the fourth column of Table VI, show a near constancy.

One more point should be mentioned in connection with Tables I–VI. In Ref. [2] the quantities  $\langle r^{-1} \rangle_{\text{QM}}$ ,  $\langle r \rangle_{\text{QM}}$ ,  $\langle r^2 \rangle_{\text{QM}}$ , and  $\langle r^3 \rangle_{\text{QM}}$  are displayed to an accuracy of five numbers following the decimal point. The quantity  $\langle r^4 \rangle_{\text{QM}}$  is displayed to an accuracy of four numbers following the decimal point, while for  $\langle r^5 \rangle_{\text{QM}}$  the accuracy drops to three numbers following the decimal point. For this reason, the present calculations were carried out to an accuracy of three numbers following the decimal point and the results shown in Tables I–IV are rounded to two numbers following the decimal point.

### Conclusion

It does not seem promising to enter into speculation about the reason for the trends exhibited in Tables I–VI by  $\langle r \rangle_{\text{LB}}$ ,  $\langle r^3 \rangle_{\text{LB}}$ , and  $\langle r^5 \rangle_{\text{LB}}$ . About the only safe statement is that the trends are connected with the increasing number of electrons distributed in an increasing number of shells, as one moves from He to Xe.

Another question may be asked: Which  $2 \times 2$ ,  $3 \times 3$ , and  $4 \times 4$  determinantal inequalities give "better" bounds? Are the inequalities in Eqs. (5)–(7) better than those in Eqs. (9)–(11), or is it the other way around? One may attempt to answer this question by calculating the quantities

$$\frac{\text{column 4 of Table I}}{\text{column 4 of Table IV}}, \quad (11)$$

$$\frac{\text{column 4 of Table II}}{\text{column 4 of Table V}}, \quad (12)$$

TABLE VII. Comparison of the two sets of  $2 \times 2$ ,  $3 \times 3$ , and  $4 \times 4$  determinantal inequalities [Eqs (5)–(7) and (9)–(11)]

Atom	Column 4 of Table I	Column 4 of Table II	Column 4 of Table III
	Column 4 of Table IV	Column 4 of Table V	Column 4 of Table VI
He	0.89	0.97	0.78
Ne	0.89	1.05	0.99
Ar	0.88	0.96	0.85
Kr	0.87	0.95	0.99
Xe	0.92	0.96	0.99

and

$$\frac{\text{column 4 of Table III}}{\text{column 4 of Table VI}} \quad (13)$$

for He, Ne, Ar, Kr, and Xe. These quantities are tabulated in Table VII.

Inspection of Table VII reveals that, for all noble gas atoms, the values in the second column of the table are remarkably constant, whereas those in the third and fourth columns show deviations from constancy. It is also seen from Table VII that, in most cases, the values displayed in the second, third, and fourth columns are smaller than unity. Looking at these columns of Table VII, it appears safe to say that both sets of determinantal inequalities are equally "good." One might add that the second set [Eqs. (9)–(11)] is "better" for  $\langle r \rangle_{\text{LB}} / \langle r \rangle_{\text{QM}}$  than the first set [Eqs. (5)–(7)], while no such clear-cut behavior is exhibited by  $\langle r^3 \rangle_{\text{LB}} / \langle r^3 \rangle_{\text{QM}}$  and  $\langle r^5 \rangle_{\text{LB}} / \langle r^5 \rangle_{\text{QM}}$ .

It should be mentioned here for the sake of completeness that some inequalities involving  $\langle r^n \rangle$  have been established for two-electron systems. The papers by Tsapline [8], Blau et al. [9], and Gálvez [10] deal with this subject.\* It should also be mentioned that Weinhold [11] used determinantal inequalities for obtaining bounds to various quantum mechanical quantities such as energy eigenvalues, scattering phase shifts and several other quantities.

In closing, two recent papers (not dealing with two-electron atoms) should also be mentioned. The first paper is by Angulo and Dehesa [12], who obtained inequalities for  $\langle r^n \rangle \langle r^{n-2} \rangle$ . The second paper is by Gálvez and Porras [13], who obtained the inequalities  $\langle r^{k-3} \rangle \leq (2Z/k) \langle r^{k-2} \rangle$  ( $Z$  is the atomic number) with  $k = 1, 2, 3$ . Gálvez and Porras [13] have also obtained more complicated inequalities that involve  $\langle r^{k-3} \rangle$  (on the left-hand side of the inequality), and  $\langle r^{k-2} \rangle$ ,  $\langle r^{k-1} \rangle$ ,  $\langle r^k \rangle$ , and  $k$  (on the right-hand side of the inequality).

\* References [8–10] gave general  $N$ -electron inequalities. In Refs. [8] and [10] they were applied to one-electron and two-electron systems

### Acknowledgments

The author wishes to thank Dr. R. J. Boyd for sending him the analytical approximations for the radial electron density  $D(r)$  used by him in the calculations of  $\langle r^n \rangle$  ( $n = -2, -1, 1, 2, 3, 4, 5$ ) for the neutral atoms from He to Xe.

### Bibliography

- [1] S. R. Gadre and R. L. Matcha, *J. Chem. Phys.* **74**, 589 (1981).
- [2] R. J. Boyd, *Can. J. Phys.* **55**, 452 (1977).
- [3] E. Clementi and C. Roetti, *At. Data Nucl. Data Tables* **14**, 177 (1974).
- [4] R. Courant and D. Hilbert, *Methods of Mathematical Physics* (Wiley-Interscience, New York, 1955), Vol. I, p. 62.
- [5] G. Pólya and G. Szego, *Problems and Theorems in Analysis* (Springer-Verlag, New York, 1976), Vol. II, p. 109.
- [6] S. R. Gadre, *J. Chem. Phys.* **71**, 1510 (1979).
- [7] G. Sperber, *Int. J. Quantum Chem.* **5**, 189 (1971).
- [8] B. Tsapline, *Chem. Phys. Lett.* **6**, 596 (1970).
- [9] R. Blau, A. R. P. Rau, and L. Spruch, *Phys. Rev. A* **8**, 119 (1973).
- [10] F. J. Gálvez, *Phys. Rev. A* **39**, 501 (1989).
- [11] F. Weinhold, *Adv. Quantum Chem.* **6**, 299 (1972).
- [12] J. C. Angulo and J. S. Dehesa, *Phys. Rev. A* **44**, 1516 (1991).
- [13] F. J. Gálvez and I. Porras, *Phys. Rev. A* **44**, 144 (1991).
- [14] A. M. Simas, R. P. Sagar, A. C. T. Ku, and V. H. Smith, Jr., *Can. J. Chem.* **66**, 1923 (1988).
- [15] A. D. MacLean and R. S. MacLean, *At. Data Nucl. Data Tables* **26**, 197 (1981).

Received May 11, 1993

# Relativistic Quantum Defect Orbital Calculations of Singlet-Singlet Transitions in the Zinc and Cadmium Isoelectronic Sequences

C. LAVÍN, P. MARTIN, and I. MARTIN

*Departamento de Química Física, Facultad de Ciencias, Universidad de Valladolid,  
47005 Valladolid, Spain*

J. KARWOWSKI

*Instytut Fizyki, Uniwersytet Mikołaja Kopernika, 87-100 Toruń, Poland*

## Abstract

Relativistic quantum defect orbital (RQDO) calculations, with and without explicit account for core-valence correlation, have been performed on several electron transitions in the zinc and cadmium isoelectronic sequences, which are of interest in astrophysics and fusion plasma research. A comparative study with other theoretical results and experimental measurements has also been carried out. © 1993 John Wiley & Sons, Inc.

## Introduction

Spectroscopic investigations on the structure of highly ionized atoms have undergone significant developments in recent years. The experimental progress is largely due to the introduction of several powerful light sources, such as laser-produced plasmas, Tokamak fusion reactors, and beams of fast, excited ions. The results obtained with these laboratory devices complement the data from astrophysical observations of the solar corona and solar flares. Experimental and theoretical data for highly ionized atoms are needed for the diagnostics of astrophysical and laboratory plasmas. For more than 40 years it has been possible to record the spectrum of the sun in the UV and x-ray regions by means of spacecraft-based observations. These observations have revealed a large number of radiative transitions, not previously observed in the laboratory, thereby stimulating much activity in theoretical and experimental atomic spectroscopy.

Highly ionized atoms appear in magnetically confined high-temperature fusion plasmas, such as those created with Tokamaks, stellarators, magnetic mirrors, etc., as well as in inertially confined plasmas, produced with powerful lasers of particle beams. The presence of heavy, ionized atoms results in energy losses and plasma cooling. However, there are also positive aspects, since the radiation emitted from the impurities provides detailed information about the physical processes in these plasmas [1].

To provide the atomic data necessary for plasma diagnostics, such as transition probabilities and oscillator strengths, is still a challenge for experimentalists and theoreticians. Nevertheless, cosmic and Tokamaks-oriented spectroscopy can also supply valuable tests of atomic model calculations [2]. The most reliable results for both energy levels and transition probabilities are obtained with the multiconfiguration Dirac-Fock method [3]. However, this approach becomes prohibitively time-consuming if the number of transitions to be studied is very large. According to Curtis [4], the spectroscopic classification of the relevant lines exceeds the general capability of *ab initio* methods, and sometimes requires the application of semiempirical methods. This conforms with the earlier remarks by Hafner and Schwarz [5] in their application of a relativistic pseudopotential approach to the calculation of a large number of atomic transition probabilities. Very recently, Laughlin [6] has pointed out, after comparing lifetimes obtained with a numerical Coulomb approximation and a model potential with accurate experimental measurements for some alkali-like systems, that high accuracy may be achieved with relatively simple computational procedures, as long as they are appropriate to the problem.

The quantum defect orbital (RQDO) method [7] and its relativistic (RQDO) formulation [8] have proven to be both simple and reliable procedures to predict oscillator strengths. Moreover, being simple and analytically solvable models, these methods may give a deeper insight into the physical nature of the problems than sophisticated numerical techniques do. A special feature of the QDO and RQDO methods is that the computational effort does not increase as the atomic system becomes heavier.

The principal resonance lines of the Zn and Cd isoelectronic sequences are important spectral features for the diagnostics and modeling of high-temperature magnetically confined plasmas. These ions contain two valence electrons outside core electrons in tightly-bound closed shells, and their spectra remain simple, even for very highly ionized species. The spectral transitions most commonly observed in fusion-type plasmas are transitions to the ground state from low-lying excited states having the same principal quantum number [9]. In the zinc and cadmium sequences, these transitions are of the types  $4s^2-4s4p$  and  $5s^2-5s5p$ , respectively, which give prominent spectral lines. Some other transitions, such as  $4s4p-4s4d$  and  $5s5p-5s5d$  are also of practical interest. Unfortunately, experimental data for these transitions exist only for the lower sequence members, and are mainly restricted to the resonance lines.

In this work, we have calculated oscillator strengths for the above transitions in ions belonging to the Zn and Cd isoelectronic sequences with both the QDO and RQDO procedures, with and without explicit inclusion of core-valence correlation through two forms of the core-polarization corrected transition operator, as described in the next section. The relativistic calculations have been performed in the intermediate coupling scheme. A comparative study of the results obtained with other theoretical and experimental (where available)  $f$ -values will also be carried out.

### Method of Calculation

The relativistic quantum defect orbitals corresponding to a state characterized by its experimental energy  $E^x$  are the analytical solutions of the quasirelativistic second-order Dirac-like equation [8]

$$\left[ -\frac{d^2}{dr^2} + \frac{\Lambda(\Lambda + 1)}{r^2} - \frac{2Z'_{\text{net}}}{r} \right] \Psi_k^{RD} = 2e^{RD} \Psi_k^{RD} \quad (1)$$

where,

$$\Lambda = \tilde{n} - n + 1 - \delta' + c, \quad (2)$$

$$Z'_{\text{net}} = Z_{\text{net}}(1 + \alpha^2 E^x), \quad (3)$$

$$e^{RD} = -\frac{(Z'_{\text{net}})^2}{2(\tilde{n} - \delta')^2} = E^x \frac{(1 + \alpha^2 E^x/2)}{(1 + \alpha^2 E^x)^2}, \quad (4)$$

where  $\tilde{n}$  is the relativistic principal quantum number,  $n$  and  $l$  are the principal and orbital angular momentum quantum numbers,  $\delta'$  is the relativistic quantum defect,  $c$  is an integer chosen to ensure the normalizability of the wavefunction and its correct nodal structure,  $Z_{\text{net}}$  is the nuclear charge acting on the valence electrons at large radial distance, and  $\alpha$  is the fine structure constant. Atomic units are used throughout. To determine the wavefunctions,  $\delta'$  is first obtained empirically from Eq. (4). Then the model potential parameter  $\Lambda$  is obtained from Eq. (2) and substituted into Eq. (1) which can be solved analytically. Since the effective Hamiltonian in Eq. (1) includes a screening term, the quantum defect orbitals are approximately valid in the core region of space.

The non-relativistic QDO equation is obtained by setting  $\alpha$  equal to zero. Then  $E^x$  becomes the experimental term energy, averaged over its fine structure components.

Both the relativistic and non-relativistic quantum defect orbitals lead to closed-form analytical expressions for the transition integrals. This allows us to calculate transition probabilities and oscillator strengths by simple algebra and with little computational effort.

The radial part of the transition integrals involved in the computation of transition probabilities and oscillator strengths is defined as

$$\tilde{M}_{if} = \int_0^\infty R_i \tilde{Q}(r) R_f r^2 dr \quad (5)$$

where the simplest form of the transition operator is  $Q(r) = r$ , in its dipole-length formulation.

One aspect of the computational procedure which has to be investigated is how to correct the transition operator for the neglect of explicit core-valence correlation in the quantum defects orbitals. It is well known that core-valence correlation significantly contributes to certain transition matrix elements. The model potential parameter given by Eq. (2) implicitly accounts for core-valence correlation, also

known as core-valence polarization. This partly avoids the addition of a core-polarization term to the model potential, depending on free parameters, as done in some relevant procedures [10,11]. An additional and much simpler explicit introduction of core-valence polarization can be achieved by writing the dipole-length transition operator in the first-order corrected form originally proposed by Hameed et al. [12]

$$\tilde{Q}(r) = \tilde{r}[1 - \alpha_c/r^3 f(r)] \quad (6)$$

where  $\alpha_c$  is the electric dipole polarizability of the atomic core, and  $f(r)$  is a cut-off function which tends to unity for  $r \rightarrow \infty$  and presents divergence for  $r \rightarrow 0$ . It is difficult to derive a general expression for  $f(r)$ . In previous works [13] we have used that proposed by Caves and Dalgarno [14]:

$$f(r) = 1 - \exp(-r/r_c)^3 \quad (7)$$

where  $r_c$  is a suitable chosen cut-off parameter, which we have always taken to be approximately equal to twice the core mean radius.

Very recently [15] a new form for  $f(r)$  has been successfully tested within the QDO/RQDO context:

$$f(r) = [1 - \exp(-r/r_c)]^3 \quad (8)$$

This expression offers the great advantage, unlike Eq. (6), of retaining total analyticity in the QDO/RQDO transition integrals.

In the present calculations the above three forms of  $Q(r)$ ,  $r$ , and those given by Eq. (6) combined with Eqs. (7) and (8), respectively, have been employed throughout. The core polarizabilities have been taken from Refs. [16] and [17]. A much greater consistency has been obtained with the choice of Eq. (8) over the choice of Eq. (7) for the cut-off function, in the sense that the dependence of the resulting oscillator strengths on the value of  $r_c$  is much smaller with the former than with the latter. Hence, in the next section we shall only present the RQDO oscillator strengths calculated with  $Q(r) = r$  and with  $Q(r)$  given by Eqs. (6) and (8).

For obtaining the quantum defects as well as the transition energies, the empirical energy data that we consider as most reliable have been employed [18–25].

### Results and Analysis

The relativistic quantum defect orbital (RQDO) oscillator strengths, calculated within the intermediate coupling scheme, for the zinc and cadmium isoelectronic sequences, are displayed in Tables I to IV. Two sets of RQDO  $f$ -values are shown, those computed with the standard dipole-length operator,  $Q(r) = r$ , and those where core-valence correlation has been explicitly introduced by using the core-polarization transition operator given by Eqs. (6) and (8). We have studied as many atomic systems as those for which empirical energy data were available. Other oscillator strengths, from theoretical calculations and experimental measurements, found in the literature, have been included in the tables for a comparative analysis.

TABLE I. Oscillator strengths for the  $4s^2\ ^1S_0-4s4p\ ^1P_1$  transition in zinc-like ions.

	RQDO <sup>a</sup>	RQDO <sup>b</sup>	RHF <sup>c</sup>	RRPA <sup>d</sup>	MCRRPA <sup>e</sup>	HF <sup>f</sup>	MCHF <sup>g</sup>	MCHF <sup>h</sup>	Exp.
ZnI	1.96	1.86		1.97		2.02	1.77	1.56	$1.50 \pm 0.05^i$ $1.46 \pm 0.8^j$ $1.18 \pm 0.14^k$ $1.43 \pm 0.15^l$ $1.45 \pm 0.16^m$
GaII	2.63	2.38		1.97	1.98	2.58	2.01	1.76	$1.39 \pm 0.17^n$ $1.85 \pm 0.15^o$
GeIII	2.32	2.04		1.98	1.98	2.56	2.00	1.74	$1.38 \pm 0.22^n$ $1.85 \pm 0.2^o$
AsIV	2.06	1.73			1.94	2.46	1.94	1.71	$1.12 \pm 0.11^n$ $1.56 \pm 0.23^o$
SeV	1.86	1.53				2.36	1.89	1.68	$0.96 \pm 0.18^n$ $1.30 \pm 0.13^p$
BrVI	1.70	1.48		1.84	1.83	2.27	1.84	1.64	$0.82 \pm 0.12^q$ $0.82 \pm 0.07^r$
KrVII	1.57	1.35			1.78	2.19	1.79	1.61	$0.81 \pm 0.09^s$ $0.94 \pm 0.04^t$
RbVIII	1.46	1.26	1.72		1.73				
SrIX	1.39	1.25	1.67						
YX	1.39	1.24	1.63						
ZrXI	1.33	1.21	1.59	1.61					
NbXII	1.28	1.16	1.55		1.56				
MoXIII	1.24	1.13	1.51	1.54	1.53	1.86	1.57	1.43	
TcXIV	1.17	1.11	1.48						
RuXV	1.12	1.03	1.44						
RhXVI	1.07	1.01	1.41						
PdXVII	1.02	0.97	1.38						
AgXVIII	0.98	0.93	1.36		1.37				
CdXIX	0.95	0.90	1.33		1.35				
InXX	0.91	0.88	1.30						
SnXXI	0.89	0.85	1.28			1.68	1.39	1.29	
SbXXII	0.86	0.83	1.26						
TeXXIII	0.83	0.81	1.24			1.70	1.37	1.28	
IXXIV	0.81	0.79	1.22		1.24				
XcXXV	0.79	0.78	1.25	1.24	1.23				

<sup>a</sup> RQDO.<sup>b</sup> RQDO, with polarization.<sup>c</sup> Biémont et al. (1989) [30].<sup>d</sup> Shorer and Dalgarno (1977) [28].<sup>e</sup> Cheng and Huang (1992) [31].<sup>f,g,h</sup> Froese Fischer and Hansen (1978) [26].<sup>i</sup> Landman and Novick (1964) [41].<sup>j</sup> Lurio et al. (1964) [42].<sup>k</sup> Baumann and Smith (1970) [43].<sup>l</sup> Andersen and Sorensen (1973) [33].<sup>m</sup> Abjean and Johannin-Gilles (1975) [44].<sup>n</sup> Sorensen (1973) [34].<sup>o</sup> Andersen et al. (1979) beam-foil, corrected for cascading [35].<sup>p</sup> Bahr et al. (1982) beam-foil, corrected for cascading [36].<sup>q</sup> Pinnington et al. (1977) [37].<sup>r</sup> Knystautas and Drouin (1977) [38].<sup>s</sup> Druetta and Buchet (1976) [39].<sup>t</sup> Irwin et al. [40].



TABLE II. Oscillator strengths for the  $4s4p\ ^1P_1-4s4d\ ^1D_2$  transition in zinc-like ions.

Ion	RQDO <sup>a</sup>	RQDO <sup>b</sup>	MCHF <sup>c</sup>	MCDHF <sup>d</sup>	MCDHF <sup>e</sup>	RHF <sup>f</sup>	MP <sup>g</sup>
SeV	1.33	1.20	1.66	1.65			
BrVI	1.35	1.21	1.60	1.60			
KrVII	1.33	1.16	1.54	1.53	1.59		
RbVIII	1.27	1.11				1.66	1.68
SrIX	1.23	1.08				1.59	1.62
YX	1.23	1.10				1.53	1.63
ZrXI	1.19	1.08				1.47	1.49
NbXII	1.14	1.03				1.41	1.94
MoXIII	1.09	1.00	1.21	1.19	1.26	1.36	1.38
TcXIV	1.02	0.95				1.31	
RuXV	0.96	0.90				1.27	
RhXVI	0.91	0.85				1.23	
PdXVII	0.86	0.81				1.19	
AgXVIII	0.81	0.77				1.15	
CdXIX	0.77	0.73				1.12	
InXX	0.73	0.70				1.09	
SnXXI	0.70	0.67	0.93	0.9	0.98	1.06	
SbXXII	0.66	0.64				1.03	
TeXXIII	0.63	0.61				1.02	
IXXIV	0.60	0.58					
XeXXV	0.57	0.55	0.83	0.8	0.88	0.95	

<sup>a</sup> RQDO.<sup>b</sup> RQDO, with polarization.<sup>c</sup> Froese Fischer and Hansen (1979) [27].<sup>d</sup> Froese Fischer and Hansen, intermediate coupling with polarization (1979) [27].<sup>e</sup> Froese Fischer and Hansen, intermediate coupling with polarization and approximate correction relativistic (1979) [27].<sup>f</sup> Biémont et al. (1989) [30].<sup>g</sup> Victor and Taylor (1983) [29].

Prior to analyzing the results presented for each individual isoelectronic sequence, a few general comments on the main features of the comparative theoretical and experimental procedures are in order.

The main concerns of the authors whose theoretical results for the zinc-like ions are included in Tables I and II, can be summarized as follows. Most of them have taken into account intrashell correlation within the valence shell (or outer correlation, in the terminology of Froese Fischer and Hansen [26,27]) [26–31], and some of them emphasize the importance of relativistic effects, particularly for the heavier and more highly ionized atoms. Shorer and Dalgarno [28], Victor and Taylor [29], Biémont et al. [30] and Cheng and Huang [31] follow theoretical procedures into which relativistic effects are directly incorporated, whereas Froese Fischer and Hansen only estimate these effects by using observed energies and allowing for spin-orbit interaction [26], or by using multiconfiguration Dirac-Hartree-Fock energies and an intermediate coupling scheme [27] in their multi-

TABLE III Oscillator strengths for the  $5s^2\ ^1S_0-5snp\ ^1P_1$  ( $n = 5, 6$ ) and  $5s5p\ ^1P_1-5snd\ ^1D_2$  transitions in cadmium.

Ion	Transition	RQDO <sup>a</sup>	RQDO <sup>b</sup>	CI <sup>c</sup>	RHFIC <sup>d</sup>	MCRHF <sup>e</sup> + CP	CIRHF <sup>f</sup> + CP	Exp.
CdI	$5s^2\ ^1S_0-5s5p\ ^1P_1$	1.32	1.19	1.85	2.13	1.36	1.35	$1.42 \pm 0.04^g$ $1.12 \pm 0.08^h$ $1.30 \pm 0.1^i$
InII		1.61	1.44	1.64	2.73	1.58	1.57	$1.26 \pm 0.20^j$ $1.43 \pm 0.09^k$
SnIII		1.62	1.46		2.75	1.61	1.60	$1.30 \pm 0.20^j$ $1.36^l$ $1.47 \pm 0.15^m$ $1.50 \pm 0.1^n$
SbIV		1.57	1.40		2.71	1.62	1.62	$0.88 \pm 0.15^j$
TeV		1.54	1.39		2.66	1.63	1.57	$0.88 \pm 0.15^j$ $1.39 \pm 0.13^m$ $1.31 \pm 0.1^o$
IVl		1.48	1.33	1.49	2.60	1.61	1.57	$1.10 \pm 0.15^p$
XeVII		1.51	1.36	1.48	2.54	1.60	1.57	$1.1 \pm 0.1^q$ $1.22 \pm 0.07^r$ $1.45 \pm 0.10^o$
CsVIII		1.49	1.35		2.56	1.70	1.60	
BaIX		1.45	1.33		2.51	1.70	1.70	
CdI	$5s^2\ ^1S_0-5s6p\ ^1P_1$	0.124	0.106					
XeVII		0.009	0.014					
CsVIII		0.015	0.020					
BaIX		0.022	0.027					
CdI	$5s5p\ ^1P_1-5s5d\ ^1D_2$	0.692	0.672					
XeVII		0.872	0.808					
CsVIII		0.85	0.791					
BaIX		0.82	0.764					

<sup>a</sup> RQDO.<sup>b</sup> RQDO, with polarization.<sup>c</sup> Hibbert (1982) [47].<sup>d</sup> Migdalek and Baylis (1986) [46].<sup>e</sup> Migdalek and Bojara (1988) [48].<sup>f</sup> Lurio and Novick (1964) [42].<sup>g</sup> Baumann and Smith (1970) [43].<sup>h</sup> Andersen and Sorensen (1973) [33].<sup>i</sup> Andersen et al. (1973) [51].<sup>j</sup> Ansbacher et al. (1986), beam-foil, corrected for cascading [52].<sup>k</sup> Pinnington et al. (1985) beam-foil, corrected for cascading [53].<sup>l</sup> Pinnington et al. (1987b) beam-foil, corrected for cascading [54].<sup>m</sup> Pinnington et al. (1987a) corrected for cascading [55].<sup>n</sup> O'Neill et al. (1979) [24].<sup>o</sup> Pinnington (1976) [56].<sup>p</sup> Kernahan et al. (1980) [57].

TABLE IV Oscillator strengths for the  $5s^2\ ^1S_0$ - $5s5p\ ^1P_1$ ,  $5s5p\ ^1P_1$ - $5snp\ ^1S_0$ ,  $5s5p\ ^1P_1$ - $5snd\ ^1D_2$  transitions in cadmium.

	RADO <sup>a</sup>	RQDO <sup>b</sup>	Semiemp. <sup>c</sup>	SCHF <sup>d</sup>	Exp.
$5s^2\ ^1S_0$ - $5s5p\ ^1P_1$	1.32	1.19	2.05	1.95	$1.42 \pm 0.04^e$ $1.12 \pm 0.08^f$ $1.30 \pm 0.1^g$
$5s^2\ ^1S_0$ - $5s6p\ ^1P_1$	0.124	0.106	0.124	0.33	
$5s^2\ ^1S_0$ - $5s7p\ ^1P_1$	0.375 (-1)	0.31 (-1)	0.309 (-1)		
$5s^2\ ^1S_0$ - $5s8p\ ^1P_1$	0.166 (-1)	0.136 (-1)	0.125 (-1)		
$5s^2\ ^1S_0$ - $5s9p\ ^1P_1$	0.885 (-2)	0.72 (-2)	0.632 (-2)		
$5s^2\ ^1S_0$ - $5s10p\ ^1P_1$	0.523 (-2)	0.423 (-2)			
$5s^2\ ^1S_0$ - $5s11p\ ^1P_1$	0.341 (-2)	0.275 (-2)			
$5s5p\ ^1P_1$ - $5s6s\ ^1S_0$	0.179	0.176	0.173	0.014	
$5s5p\ ^1P_1$ - $5s7s\ ^1S_0$	0.926 (-2)	0.883 (-2)	0.108 (-1)		
$5s5p\ ^1P_1$ - $5s8s\ ^1S_0$	0.275 (-2)	0.259 (-2)	0.34 (-2)		
$5s5p\ ^1P_1$ - $5s9s\ ^1S_0$	0.124 (-2)	0.117 (-2)	0.158 (-2)		
$5s5p\ ^1P_1$ - $5s10s\ ^1S_0$	0.665 (-3)	0.621 (-3)	0.86 (-3)		
$5s5p\ ^1P_1$ - $5s11s\ ^1S_0$	0.401 (-3)	0.374 (-3)	0.524 (-3)		
$5s5p\ ^1P_1$ - $5s12s\ ^1S_0$	0.277 (-3)	0.259 (-3)			
$5s5p\ ^1P_1$ - $5s5d\ ^1D_2$	0.692	0.672	0.778		
$5s5p\ ^1P_1$ - $5s6d\ ^1D_2$	0.973 (-1)	0.922 (-1)	0.951 (-1)		
$5s5p\ ^1P_1$ - $5s7d\ ^1D_2$	0.310 (-1)	0.289 (-1)	0.268 (-1)		
$5s5p\ ^1P_1$ - $5s8d\ ^1D_2$	0.135 (-1)	0.125 (-1)	0.105 (-1)		
$5s5p\ ^1P_1$ - $5s9d\ ^1D_2$	0.752 (-2)	0.692 (-2)	0.56 (-2)		
$5s5p\ ^1P_1$ - $5s10d\ ^1D_2$	0.464 (-2)	0.425 (-2)	0.338 (-2)		

<sup>a</sup> RQDO.<sup>b</sup> RQDO, with polarization.<sup>c</sup> Zilitis (1971) [49].<sup>d</sup> Helliwell (1968) [50].<sup>e</sup> Lurio and Novick (1964) [42].<sup>f</sup> Baumann and Smith (1970) [43].<sup>g</sup> Andersen and Sorensen (1973) [33].

configuration Hartree-Fock (MCHF) treatments. However, the better agreement between theory and experiment brought about by the explicit inclusion of core-valence correlation (or full correlation [26,27], although recognized by some of the authors, such as Cheng and Huang [31], is only carried out by Froese Fischer and Hansen [26,27]. Regarding the experimental  $f$ -values, which are in most cases lower than the oscillator strengths calculated by the above authors, their small magnitude has been attributed [32,31] to an inadequate treatment of cascading effects in the measurement of lifetimes with beam-foil techniques which result in longer lifetimes for the excited levels than the actual ones and too small oscillator strengths. Some of the most recent measurements have already been corrected for cascading. When this is the case, we have made a remark at the foot of the tables.

In Table I we display, together with the RQDO results, the oscillator strengths calculated by Biémont et al. [30] with the relativistic Hartree-Fock (RHF) method. These authors claim to have accounted for the most important relativistic effects, as well as for valence electron correlation by including all the configurations within the  $n = 4$  complex. Also shown are the relativistic random-phase-approximation (RRPA) and multiconfiguration RRPA (MCRRPA) results by Shorer and Dalgarno [28] and Cheng and Huang [31], respectively, the three sets of  $f$ -values reported by Froese Fischer and Hansen [26] with the approximate relativistic Hartree-Fock (HF), multiconfiguration Hartree-Fock (MCHF) with account for outer correlation only, and with full correlation, respectively. The experimental data found in the literature are also shown in the table. Although most of the available measurements are the result of beam-foil experiments [33-40], some others come from Hanle effect [41,42], phase-shift [43] and absorption in atomic beam [44] observations. Large discrepancies between the observed and most of the calculated oscillator strengths are apparent, the discrepancies increasing with increasing degree of ionization. In their extensive study of this transition, Froese Fischer and Hansen [26] conclude that outer shell or intravalence correlation brings the largest change in the  $f$ -values at the lower  $Z$  end of the sequence. The present RQDO results with explicit account for polarization are in fairly good accordance with the experimental results, considering the overall degree of agreement between the other theoretical  $f$ -values and the measurements. In particular, the RQDO  $f$ -values agree best with the most recent experimental values [35,36] which are claimed to have reduced the influence of cascading in the lifetimes. Except for the less ionized species, the RQDO oscillator strengths, when corrected for polarization, agree rather well with the MCHF, full correlation, results of Froese Fischer and Hansen [26]. For ZnI, GaII, and GeIII the correlation within the valence shell is expected to be most important. These effects, which lead to a reduction in the magnitude of oscillator strengths, are not explicitly accounted for in the RQDO procedure. For the higher ions for which experimental data are available, the best coincidence between theory and experiment is achieved with the RQDO values.

Table II contains the oscillator strengths for the  $4s4p\ ^1P_1-4s4d\ ^1D_2$  transition in the zinc sequence. The empirical energy data available for this transition in the low  $Z$  end of the sequence [45] suffered from significant uncertainties, and, hence, the RQDO results reported in this table begin with SeV. No experimental  $f$ -values have been found in the literature for the ions studied, and our analysis must rest on the comparative theoretical results that are available. These comprise the multiconfiguration Hartree-Fock (MCHF) with core-polarization  $f$ -values by Froese Fischer and Hansen [27], the multi-configuration Dirac-Hartree-Fock (MCDHF) with polarization, and within the intermediate coupling scheme, respectively, by the same authors [27], the RHF results by Biémont et al. [30], obtained with the same technique as for the resonance transition, and the  $f$ -values calculated by Victor and Taylor [29] using a semiempirical model potential and Dirac-Hartree-Fock (DHF) orbitals for describing the core. In this transition it is observed, as in the previous one, that the influence of core-valence polarization in the oscillator strengths decreases with the degree of ionization. The RQDO results, even without explicit account

for polarization, are lower in magnitude than the remaining theoretical data, but, they show the best overall accordance with the MCDHF with polarization  $f$ -values of Froese Fischer and Hansen [27]. Whether the experimental measurements, if available, would also yield lower oscillator strengths than most of the theoretical results and would show a reasonable agreement with the RQDO values is hard to predict. The uncertainties in the empirical energy data employed in our calculations may partly account for the RQDO  $f$ -values not having attained a better agreement with the MCDHF results.

The resonance,  $5s^2\ ^1S_0$ - $5s5p\ ^1P_1$ , transition of cadmium-like ions has also been the object of several theoretical studies, as well as experimental measurements. Migdalek and Baylis [46] have also been concerned, with correctly accounting for intravalence correlation, core-valence polarization and relativistic effects for the cadmium isoelectronic sequence, as were the aforementioned authors who studied the zinc isoelectronic sequence. Previous calculations of similar nature are those by Hibbert [47] on a few Cd-like ions. Hibbert [47] derived configuration interaction (CI) wavefunctions to represent the intravalence correlation, keeping the core frozen. He, then, estimated empirical factors to correct for errors in the calculated transition energies, for core-polarization effects, and for relativistic spin dependent interactions. These factors demonstrated the importance of both relativistic effects and core-valence correlation. Migdalek and Baylis [46], with an approach that combines limited relativistic mixing to represent intravalence correlation with a polarization model to account for core-valence correlation, report results for many of the ions studied by us with two specific methods, the relativistic Hartree-Fock in intermediate coupling, RHFIC, and the multiconfiguration Hartree-Fock with a polarization correction (MCRHF+CP). The calculations of Migdalek and Bojara [48] followed a relativistic configuration interaction procedure with explicit core-polarization (CIRHF+CP). These authors claim to have obtained reliable oscillator strengths, at a far smaller computational expense than required by similar scale multiconfiguration calculations. Their results are also displayed in Table III. The RQDO  $f$ -values for the resonance transition of Cd-like systems, without explicit core polarization correction, agree quite well with both the MCRHF+CP and CIRHF+CP results of Refs. [46] and [48]. When explicit polarization correction is introduced, the RQDO oscillator strengths become smaller than the previous ones, but better approach the experimental values. Which of the two RQDO sets of results is more correct is hard to decide. Admitting that core-valence correlation is important, it may happen that their implicit account in the RQDO  $f$ -values calculated with  $Q(r) = r$  suffice.

Also included in Table III are the RQDO oscillator strengths for the  $5s^2\ ^1S_0$ - $5s6p\ ^1P_1$  and  $5s5p\ ^1P_1$ - $5s5d\ ^1D_2$  transitions for the only few ions for which experimental energy data were available. Given the reduced number of results, we have not built independent tables for them. No comparative data have been found in the literature. The RQDO  $f$ -values for these transitions are lower in magnitude than for the resonance transition, a feature that was to be expected.

And, finally, in Table IV we display the oscillator strengths for transitions belonging to the principal ( $5s^2\ ^1S_0$ - $5snp\ ^1P_1$ ), sharp ( $5s5p\ ^1P_1$ - $5sns\ ^1S_0$ ) and diffuse ( $5s5p\ ^1P_1$ - $5snd\ ^1D_2$ ) spectral series of neutral cadmium, for which some empirical

energy data were available. As comparative results we have found those calculated by a semiempirical method by Zilitis [49], and those by Helliwell [50] with a semiempirically modified self-consistent-field (SCF) method. A few experimental measurements are also included in the table. For the resonance transition, a fairly good agreement between the RQDO results without explicit polarization and the measurement is apparent, while the other two theoretical results are appreciably higher. For the remaining transitions in the table and overall good agreement between the RQDO and the semiempirical  $f$ -values [49] is observed. The explicit account for core-valence polarization has less influence in the RQDO  $f$ -values for the higher transitions in the three spectral series than for the lower ones. The effects of explicitly neglecting intrashell correlation are hard to establish, given the nature of the comparative data.

### Concluding Remarks

The RQDO oscillator strengths calculated for the resonance  $4s^2\ ^1S_0$ – $4s4p\ ^1P_1$  and the  $4s4p\ ^1P_1$ – $4s4d\ ^1D_2$  transitions in the zinc isoelectronic sequence are in fairly good agreement with the results of the rather more sophisticated MCRRPA [31] and MCHF [26,27] calculations, which account for inner and outer correlation, as well as for relativistic effects. The RQDO  $f$ -values conform with the experimental results better than those of much more complex theoretical procedures, although the accuracy of some of the measurements has not been completely established.

For the cadmium isoelectronic sequence, similar comments could be made regarding the correctness of the RQDO oscillator strengths for the resonance transition. For this sequence, the most complete calculations reported are those of the MCRHF+CP [46] and CIRHF+CP [48] procedures, with which results the RQDO values conform reasonably well. For neutral cadmium, the correctness of the RQDO oscillator strengths in transition belonging to the principal, sharp and diffuse spectral series, is more difficult to establish, given the scarcity of comparative data.

Overall, we seem to find reasons to be hopeful about the possibilities of the RQDO formalism for predicting spectral properties of interest in astrophysics and nuclear fusion research. These reason rest on the correctness of the results so far achieved, and the low computational expense and avoidance of the numerous convergence problems which are common in the multiconfigurational approaches.

### Acknowledgments

This work has been supported by the D.G.I.C.Y.T. of the Spanish Ministry of Education and Science, under Projects No. PB88-0343 and No. PB91-0207-C02-01.

### Bibliography

- [1] I. Martinson, Rep. Prog. Phys. **52**, 157 (1989).
- [2] S. Johansson, Com. At. Mol. Phys. **24**, 159 (1990).
- [3] K. G. Dyall, I. P. Grant, C. T. Johnson, F. A. Parpia, and E. P. Plummer, Comput. Phys. Commun. **55**, 425 (1989).

- [4] L. J. Curtis, Phys. Scr. **35**, 805 (1987).
- [5] P. Hafner and W. H. E. Schwarz, J. Phys. B: At. Mol. Phys. **17**, 2975 (1978).
- [6] C. Laughlin, Phys. Scr. **45**, 238 (1992).
- [7] G. Simons, J. Chem. Phys. **60**, 645 (1974); I. Martin and G. Simons, J. Chem. Phys. **62**, 4799 (1975); Mol. Phys. **32**, 1017 (1976).
- [8] I. Martin and J. Karwowski, J. Phys. B: At. Mol. Opt. Phys. **24**, 1539 (1991).
- [9] J. Reader and N. Acquista, Phys. Rev. Lett. **39**, 184 (1977).
- [10] A. Dalgarno, C. Bother, and G. A. Victor, Chem. Phys. Lett. **7**, 265 (1970).
- [11] M. Szulkin and J. Karwowski, J. Phys. B: At. Mol. Phys. **14**, 4729 (1981).
- [12] S. Hameed, A. Herzenberg, and M. G. James, J. Phys. B: At. Mol. Phys. **1**, 822 (1968).
- [13] I. Martin, C. Barrientos, and I. Gútiérrez, Int. J. Quantum Chem. **37**, 221 (1990).
- [14] T. C. Caves and A. Dalgarno, J. Quant. Spectrosc. Radiat. Transfer **12**, 1539 (1972).
- [15] D. Bielinska-Waz, Master of Science Thesis; Institute of Physics, University Nicholas Copernicus, Toruń, Poland (1992).
- [16] V. P. Shevelko and Vinogradov, Phys. Scr. **19**, 275 (1979).
- [17] S. Fraga, J. Karwowski, and K. M. A. Saxena, *Handbook of Atomic Data* (1976 Amsterdam, Elsevier).
- [18] I. Johansson and R. Contreras, Ark Fys **37**, 513 (1968).
- [19] C. E. Moore, "Atomic Energy Levels" NSRDS-NBS No. 35 (Washington, DC: US Govt Printing Office) 1971.
- [20] Y. N. Joshi and T. A. M. Van Kleef, Phys. Scr. **34**, 135 (1986).
- [21] S. S. Churilov, A. N. Ryabtsev, and J. F. Wyart, Phys. Scr. **38**, 326 (1988).
- [22] N. Acquista and J. Reader, J. Opt. Soc. Am. **B1**, 649 (1984).
- [23] C. Breton, G. De Michelis, W. Hecq, M. Mattioli, J. Ramette, and B. Saoutic, Phys. Scr. **37**, 33 (1988).
- [24] J. A. O'Neill, E. H. Pinnington, K. E. Donnelly, and R. L. Brooks, Phys. Scr. **20**, 60 (1979).
- [25] V. Kaufman and J. Sugar, J. Op. Soc. Am. **B4**, 1919 (1987).
- [26] C. Froese Fischer and J. E. Hansen, Phys. Rev. **A17**, 1956 (1978).
- [27] C. Froese Fischer and J. E. Hansen, Phys. Rev. **A19**, 1819 (1979).
- [28] P. Shorer and A. Dalgarno, Phys. Rev. **A16**, 1502 (1977).
- [29] G. A. Victor and W. R. Taylor, At. Data Nucl. Data Tables **28**, 167 (1983).
- [30] E. Diémont, P. Quinet, and B. C. Fawcett, Phys. Scr. **39**, 562 (1989).
- [31] T.-C. Cheng and K.-N. Huang, Phys. Rev. **A45**, 4367 (1992).
- [32] S. M. Younger and W. L. Wiese, Phys. Rev. **18**, 2366 (1978).
- [33] T. Andersen and G. Sorensen, J. Quant. Spectrosc. Radiat. Transfer **13**, 369 (1973).
- [34] G. Sorensen, Phys. Rev. **A 7**, 85 (1973).
- [35] T. Andersen, P. Eriksen, O. Poulsen, and P. S. Ramanujan, Phys. Rev. **A20**, 2621 (1979).
- [36] J. L. Bahr, E. H. Pinnington, J. A. Kernahan, and J. A. O'Neill, Can. J. Phys. **60**, 1108 (1982).
- [37] E. H. Pinnington, J. A. Kernahan, and K. E. Donnelly, J. Op. Soc. Am. **67**, 162 (1977).
- [38] E. J. Knystautas and R. Drouin, J. Quant. Spectrosc. Radiat. Transfer. **17**, 551 (1977).
- [39] M. Druetta and J. P. Buchet, J. Op. Soc. Am. **B 66**, 433 (1976).
- [40] D. J. G. Irwin, J. A. Kernahan, E. H. Pinnington, and A. E. Livingston, J. Op. Soc. Am. **B66**, 1396 (1976).
- [41] A. Landman and R. Novick, Phys. Rev. **134**, A 56 (1964).
- [42] A. Lurio, R. L. Zafra, and R. J. Goshen, Phys. Rev. **134**, A 1198 (1964).
- [43] S. R. Baumann and W. H. Smith, J. Op. Soc. Am. **60**, 345 (1970).
- [44] R. Abjean and A. Johannin-Gilles, J. Quant. Spectrosc. Radiat. Transfer, **15**, 25 (1975).
- [45] R. L. Kelly, J. Phys. Chem. Ref. Data **16**, Supp. No. 1, Part II (1987).
- [46] J. Migdalek and W. E. Baylis, J. Phys. B: At. Mol. Phys. **19**, 1, (1986).
- [47] A. Hibbert, Nuclear Instruments and Methods **202**, 323 (1982).
- [48] J. Migdalek and A. Bojara, J. Phys. B: At. Mol. Phys. **21**, 2221 (1988).
- [49] V. A. Zilitis, Opt. Spectrosc. **31**, 86 (1971).
- [50] T. M. Helliwell, Phys. Rev. **175**, 50 (1968).
- [51] T. Andersen, A. K. Nielsen, and G. Sorensen, Phys. Scr. **6**, 122 (1973).

- [52] W. Ansbacher, E. H. Pinnington, J. A. Kernahan, and K. N. Gosselin, *Can. J. Phys.* **64**, 1365 (1986).
- [53] E. H. Pinnington, W. Ansbacher, J. A. Kernahan, and A. S. Inamdar, *J. Op. Soc. Am B2*, 331 (1985).
- [54] E. H. Pinnington, J. A. Kernahan, and W. Ansbacher, *Can. J. Phys.* **65**, 7 (1987b).
- [55] E. H. Pinnington, W. Ansbacher, J. A. Kernahan, *J. Op. Soc. Am B4*, 696 (1987a).
- [56] E. H. Pinnington, *Beam Foil Spectroscopy Vol 1* (Plenum, New York, 1976), p. 235.
- [57] J. A. Kernahan, E. H. Pinnington, J. A. O'Neill, J. L. Bahr, and K. E. Donnelly, *J. Op. Soc. Am.* **70**, 1126 (1980).

Received March 13, 1993



# Properties of the Two-Electron Ionization Ladder and Related Good Quantum Numbers

YANNIS KOMNINOS, SPYROS THEMELIS, MICHAEL CHRYSOS,\*  
and CLEANTHES A. NICOLAIDES

*Theoretical and Physical Chemistry Institute, National Hellenic Research Foundation, 48,  
Vas. Constantinou Ave., 116 35 Athens, Greece*

## Abstract

In recent publications we have presented a general theory for the identification and computation of correlated wavefunctions of a particular class of doubly excited states which constitute a two-electron ionization ladder (TEIL) leading smoothly to the so-called Wannier state at  $E = 0$ . In this work, we examine further the properties of these wavefunctions for two-electron atoms of  $^1S$  and  $^1P$  symmetry, especially as regards their analysis in terms of hydrogenic basis sets and good quantum numbers. We find that the Herrick-Sinanoglu ( $K, T$ ) classification loses accuracy as we move toward threshold and we show that, when single as well as double excitations are considered, a better quantum number for the TEIL is  $F = N - 1 - K$ , where  $N, K$  are not good numbers anymore. The extent of the breakdown of the ( $K, T$ ) representation depends on the system and on the level of excitation (more serious in negative ions and for high lying states). © 1993 John Wiley & Sons, Inc.

## Introduction

According to a recently developed theory [1–3], the wavefunctions of a class of doubly excited states (DES) which leads smoothly to the Wannier state at threshold, i.e., to the state where the two electrons are ejected with zero energy in opposite directions, can be identified *a priori* and computed from first principles with great accuracy. This class has been called the *Wannier two-electron ionization ladder* (TEIL). The concepts, the formalism, and the computational methods are general, and allow practical applications to polyelectronic atoms and to large values of the principal quantum number  $n$ . By now, we have predicted the TEILs of  $H^-$ ,  $He$ ,  $Li^+$  ( $^1P$  symmetry),  $H^-$  ( $^1S$ ),  $He^-$  ( $^2S$ ), and  $Li^-$  ( $^1S$ ) [1–3]. Correlated wavefunctions up to  $n = 10$  have been obtained and a number of conclusions have been drawn from their analysis [1–3].

In this article we proceed further with the study of the TEIL wavefunctions, in two directions.

- (1) Since many of the arguments and computations in the literature of DES are based on configuration–interaction calculations with hydrogenic functions, e.g. [4–6], we have related the information obtained from our state-specific

\* Present address. Laboratoire de Photophysique Moléculaire, CNRS, Université de Paris Sud, 91405, Orsay, CEDEX, France.

TEIL wavefunctions and energies to the information obtained in terms of hydrogenic basis sets. The conclusions are drawn from calculations on the  $^1S$  and  $^1P^o$  symmetry of a two-electron system with  $Z = 1, 2, 3$ , and hydrogenic quantum numbers  $n = 6-15$ .

- (2) Wulfman [8] and Sinanoglu and Herrick [4] have pioneered the use of group theory for the approximate treatment of the structure of DES and for the establishment of new classification schemes. The quantum numbers  $K, T$  [4] have since been used repeatedly in the phenomenology and qualitative analysis of DES [6,9,10]. Given that our theory yields correlated wavefunctions for low as well as for high  $n$ —previously not available—the accuracy of the  $(K, T)$  classification for the TEIL can be tested as a function of energy and nuclear charge.

### The $^1S$ and $^1P^o$ TEIL Wavefunctions—Comparison with Hydrogenic Basis Set Calculations

The theory of Refs. [1-3] shows how correlated wavefunctions of the TEIL in polyelectronic atoms can be computed from first principles. We have demonstrated that these highly correlated systems can be treated in terms of orbitals and configurations, provided the state-specific approach to the electronic structure of excited states is employed (e.g. [11,12]). High  $n$  states ( $n$  up to 10) became amenable to calculation for the first time. The demonstration [1] that the TEIL states correspond to the lowest energy in each manifold of hydrogenically degenerate states and that they satisfy the quantum mechanical version of  $\bar{r}_1 = -\bar{r}_2$  has recently also been used [6] for the identification of such states in He  $^1P^o$ —albeit of low  $n$  only—from CI wavefunctions with hydrogenic orbitals. (Other orbitals, such as Sturmians or numerical, can, of course, also be used in such truncated diagonalization procedures for two-electron atoms).

In this article we analyze further the TEILs of  $^1S$  and  $^1P^o$  symmetries. For small  $n$  (up to 6), the wavefunction corresponding to the square integrable part of the resonance [1-3,12,13], for each shell  $n$ , is given by

$$W_n = W_n^o + X_n \quad (1)$$

where  $W_n^o$  is obtained from a multiconfigurational Hartree-Fock (MCHF) calculation and  $X_n$  is obtained variationally. Both  $W_n^o$  and  $X_n$  are subjected to specific orthogonality constraints [1-3,12,13].  $W_n$  may correspond to a dielectronic or to a polyelectronic system and is composed of configurations which are symmetry adapted.

For small atoms, the configurations which enter  $W_n^o$  are of the intrashell type, i.e.,  $n_1 = n_2 = n$  for the two-valence electrons. The self-consistent calculation takes into account angular as well as radial correlation. The MCHF solution for the lowest energy results in positive coefficients, provided the Condon and Shortley sign convention of the Clebsch-Gordon coefficients is followed. For  $n > 6$  the MCHF solutions do not converge and we proceed as follows: (a) We diagonalize the Hamiltonian in a hydrogenic basis with  $N_0 \leq n, n' \leq N_0 + 3$ ; (b) We reexpress the resulting eigenvectors in the basis of the natural orbitals [7]. This brings the wavefunction again in the form (1). We have confirmed that for  $n \leq 6$ , this procedure yields

orbitals and coefficients identical to the MCHF ones. Thus, the two procedures are equivalent.

### The TEIL and its Good Quantum Numbers—The Importance of Double Excitations

It has been emphasized in the literature of DES that the  $O(3)$ , single configuration approximation (SCA) breaks down. It is important to remind the reader that this fact characterizes other situations as well, such as valence-Rydberg mixings or molecular structure in the dissociation region. Its remedy does not necessarily imply, at least not yet, the abandonment of the orbital concept and configuration mixing. It is true that it looks simpler—and perhaps more elegant—to have only one “configuration” in order to describe in zeroth order the state of a system. However, this does not mean that the method used to obtain it is more practical and easily extendable to incorporate the remaining electron correlation. On the other hand, for a theory of DES which defines and computes consistently a multiconfigurational zeroth order vector as well as its important corrections, the resulting information can be quantitative as well as conceptual. Having said this, we turn to the problem of optimizing the zeroth order representation of DES in terms of “configurations” with good quantum numbers.

Given the multitude of closely lying DES and the related complexities of the standard CI methods, the group theoretic analyses of Wulfman [8] and of Herrick and Sinanoglu [4,9] have shed new light from a different angle to the problem of the economical qualitative description and meaningful classification of DES in two-electron atoms. In these, the concept of the doubly excited symmetry basis (DESB) was introduced, which is defined in terms of hydrogenic solutions. The DESB states are represented by a specific linear combination of configurations of a given  $L$  and  $M_L$ , for various allowed values of  $l_1$  and  $l_2$ . The coefficients of the expansion depend on the principal quantum numbers  $n_1$  and  $n_2$  as well as on  $L$  and two additional quantum numbers  $J_1$  and  $J_2$  whose range of values is

$$\frac{n - N}{2} \leq J_i \leq \frac{n + N - 2}{2} \quad i = 1, 2$$

$$\text{where} \quad n = \max(n_1, n_2), \quad N = \min(n_1, n_2) \quad (2a)$$

with the additional restriction

$$|J_1 - J_2| \leq L \leq J_1 + J_2 \quad (2b)$$

In the expressions for the eigenvalues of certain operators, the quantum numbers  $J_1$  and  $J_2$  appear only as sums or as differences. Thus, Wulfman [8] defined  $P = J_1 + J_2$  and  $Q = J_1 - J_2$  as the appropriate quantum numbers. On the other hand, Herrick and Sinanoglu define  $T = |Q|$  and  $K = P - n + 1$  as the pair of the new quantum numbers. The first choice is due to the fact that only simple  $\pm$  admixtures of  $+|Q|$  and  $-|Q|$  states have definite parity. The second is born out of numerical

TABLE I. Analysis of the configuration-interaction wavefunctions corresponding to the lowest energy of each manifold in terms of DESB vectors. The  $KT$  fraction contains all the intrashell  $n_1 = n_2 = N_0$  DESB configurations plus all the intershell ones resulting from it through double excitation. The  $FT$  fraction includes the double excitations with a higher  $K_{\max} = N - 1 - T$ . The most important by far is that with  $N = N_0 + 1$ .

N	L	H <sup>-</sup>		He		Li <sup>+</sup>	
		KT fraction	FT fraction	KT fraction	FT fraction	KT fraction	FT fraction
6	0	0.98777	0.99519	0.99879	0.99886	0.99839	0.99845
	1	0.97470	0.98761	0.99700	0.99724	0.99782	0.99786
7	0	0.98432	0.99499	0.99884	0.99902	0.99867	0.99871
	1	0.97116	0.98764	0.99711	0.99755	0.99811	0.99814
8	0	0.98015	0.99469	0.99872	0.99911	0.99893	0.99895
	1	0.96668	0.98734	0.99695	0.99770	0.99839	0.99843
9	0	0.97537	0.99431	0.99845	0.99913	0.99914	0.99916
	1	0.96149	0.98683	0.99656	0.99772	0.99863	0.99869
10	0	0.97006	0.99390	0.99801	0.99910	0.99929	0.99934
	1	0.95572	0.98619	0.99595	0.99763	0.99880	0.99890
11	0	0.96428	0.99347	0.99741	0.99902	0.99937	0.99947
	1	0.94950	0.98547	0.99514	0.99746	0.99889	0.99906
12	0	0.95812	0.99302	0.99665	0.99890	0.99940	0.99957
	1	0.94289	0.98471	0.99414	0.99722	0.99890	0.99918
13	0	0.95163	0.99257	0.99573	0.99875	0.99935	0.99963
	1	0.93599	0.98393	0.99295	0.99692	0.99881	0.99924
14	0	0.94486	0.99212	0.99466	0.99858	0.99923	0.99967
	1	0.92885	0.98314	0.99160	0.99658	0.99864	0.99926
15	0	0.93787	0.99169	0.99345	0.99839	0.99905	0.99968
	1	0.92153	0.98235	0.99008	0.99620	0.99838	0.99923

results. It is useful because, in this way, a whole Rydberg series can be assigned the same  $K, T$ . Their allowed values are [4.9]

$$T = 0, 1, \dots, \min(L, N - 1) \quad (3a)$$

and

$$-(N - 1 - T) \leq K \leq N - 1 - T \quad \text{in steps of 2} \quad (3b)$$

Robaux [6] has subjected hydrogenic basis CI wavefunctions for He 'P' DES ( $N = 2-6$ ) to a  $(K, T)$  analysis, where configurations are made up of fixed  $N$  and a variable  $n$ , according to the Herrick and Sinanoglu prescription [4]. Her main findings and conclusions are:

- (1) In accordance with the results of Ref. [1], the lowest energy state within an  $N$  manifold yields  $\langle r_1 \rangle = \langle r_2 \rangle$ . The set of these states defines the TEIL.

TABLE II. Purity of the  $F$  quantum number in the first three intrashell  $^1S$  states ( $T = 0$ ) of the  $N = 6$  manifold. It is best for the lowest state, the TEIL state, studied here and in our earlier work. It deteriorates for the other roots.

$N = 6 \quad ^1S$			
$F$	$H^-$	He	$Li^+$
First intrashell state			
0	0.99519	0.99886	0.99845
2	0.00478	0.00112	0.00153
4	0.00004	0.00002	0.00002
Second intrashell state			
0	0.00368	0.00011	0.00090
2	0.96606	0.99253	0.99550
4	0.02953	0.00728	0.00353
6	0.00072	0.00009	0.00008
Third intrashell state			
0	0.00008	0.00002	0.00002
2	0.04900	0.00251	0.00010
4	0.85820	0.96300	0.98441
6	0.08722	0.03364	0.01521
8	0.00522	0.00080	0.00024

- (2) For the TEIL,  $K$  and  $T$  are good numbers (see Table III of Ref. [6]). Given that the ideas of DESB states and  $K$ ,  $T$  or molecular classification schemes [4,6,9,10,15] have thus far been applied only to low-lying DES, it is important to establish the degree of validity of the goodness of the  $K$ ,  $T$  classification as  $N$  increases. Our TEIL wavefunctions reach  $N = 15$  and offer a good possibility for such an analysis.

We have expanded our TEIL functions in terms of DESB states, without the restriction of fixed  $N$ , a restriction implying that only single excitations are included. Instead, we introduce a lowest value  $N_0$ , which corresponds to the  $W'_{\Lambda_0}$  MCHF vector, and then expand in terms of DESB states whose quantum numbers  $N$  and  $n$  satisfy  $n \geq N \geq N_0$ . In this way, double excitations are included in the expansion, while the whole state remains orthogonal to the lower threshold channels. Let

$$W'_{\Lambda_0} = \sum_n \sum_{\Lambda} \sum_K \sum_T C_{\Lambda n}^{K T} |N n K T (L S) \rangle \quad n \geq N \geq N_0 \quad (4)$$

First we examine  $T$ . For  $^1S$  states,  $T$  can have only one value,  $T = 0$ . Therefore, no conclusions can be drawn from this case. On the other hand, for the  $^1P^o$  states,  $T = 1$  for the intrashell DESB states ( $n = N$ ) but it can assume two values,  $T = 0$  and 1, for the intershell DESB states ( $n \neq N$ ). Therefore, the  $^1P^o$  states offer the

TABLE III. Energies, in atomic units, of the configuration-interaction wavefunctions corresponding to the lowest root of each manifold for  $^1S$  and  $^1P$  symmetries of  $H^-$ , He and  $Li^+$ . The energies are well approximated by the values produced from the formula, Ref. [1c]  $E_n = -C(Z) [n(n-1)/n^4]$ .

$^1S$			
N	$H^-$	He	$Li^+$
6	-0.01824	-0.09074	-0.21863
7	-0.01352	-0.06693	-0.16102
8	-0.01042	-0.05140	-0.12352
9	-0.00828	-0.04072	-0.09775
10	-0.00674	-0.03305	-0.07928
11	-0.00560	-0.02737	-0.06560
12	-0.00472	-0.02303	-0.05518
13	-0.00404	-0.01966	-0.04706
14	-0.00349	-0.01697	-0.04061
15	-0.00305	-0.01480	-0.03540

$^1P$			
N	$H^-$	He	$Li^+$
6	-0.01756	-0.08902	-0.21577
7	-0.01311	-0.06590	-0.15932
8	-0.01016	-0.05074	-0.12243
9	-0.00810	-0.04027	-0.09701
10	-0.00661	-0.03274	-0.07876
11	-0.00550	-0.02714	-0.06521
12	-0.00465	-0.02286	-0.05489
13	-0.00398	-0.01952	-0.04683
14	-0.00345	-0.01687	-0.04043
15	-0.00301	-0.01472	-0.03526

opportunity of testing whether  $T$  is a good quantum number. It turns out that intershell DESB functions with  $T = 0$  have negligible overlap with  $W_{\lambda_0}^{\lambda_0}$ . Therefore, our numerical results show that  $T$  is a good number.

Next, let us examine  $K$ , given a value of  $T$ . The intrashell DESB function with the lowest energy has  $K = K_{\max} = N - 1 - T$  ( $N = N_0$ ). Our computations show that it gives the highest contribution to the expansion (4). When only single excitations are added,  $K_{\max}$  remains a good quantum number. Things change when an improvement of the total wavefunction is made, by including double excitations as well. Considering the first double excitation, ( $N = N_0 + 1$ ), we see that it does not contain  $K_{\max}$  ( $K$  runs in steps of two). On the other hand, our calculations show that the highest contribution comes from the term with  $K = K_{\max} = N - 1 - T$ , ( $N = N_0 + 1$ ).

We note that the same analysis of the other roots of each manifold  $N_0$  shows characteristics very similar to the ones discussed above for the lowest energy state (the TEIL state).

Taking into account the aforementioned findings, we have looked for a new quantum number to replace  $K$ , given that  $N$  cannot be kept fixed anymore. Indeed, such a number exists and is defined by

$$F = N - 1 - K_{\max} = T, \quad (5)$$

for the lowest energy state of each  $N_o$  manifold. Here, neither  $N$  or  $K(K_{\max})$  are good quantum numbers.

Eq. (5) refers to the lowest energy state of each manifold  $N_o$ . In general,

$$F = N - 1 - K \quad (5a)$$

Since the range of  $K$  is given by (3b), the corresponding range of  $F$  is

$$T \leq F \leq 2N - 2 - T, \quad \text{in steps of } 2 \quad (6)$$

This proposal extends and revises the scheme of Herrick and Sinanoglu where both  $N$  and  $K$  are considered to be good quantum numbers. If this is assumed to be the case, then, of course, the definition and use of  $F$  is redundant.

Given the above, the appropriate representation of  $W_{N_o}^o$  is

$$W_{N_o}^o \approx \sum_n \sum_N C_{Nn}^{FT} |NnFT(LS) > n \geq N \geq N_o \quad (7)$$

Thus, having found through computation based on our TEIL wavefunctions that for high-lying DES the  $(K, T)$  representation loses accuracy, we have identified the cause of the breakdown in the importance of the double excitations. The magnitude of their effect depends on the system and on the level of excitation.

The numerical demonstration of these conclusions is given in Table I. The importance of DESB states with doubly excited configurations manifests itself in  $H^-$  already for small  $N_o$ . For He and the positive ions we must move to higher values of  $N_o$ , close to 10, for their contribution to become important.

Thus, the  $FT$  scheme provides approximately good quantum numbers for relatively high values of  $N_o$  even for the difficult case of  $H^-$ . Nevertheless, for sufficiently high values of  $N_o$  all quantum numbers are expected to cease being good ones. For the other intrashell states of each  $N$ -manifold, matters deteriorate for lower values of  $N_o$ . The extent of the breakdown of the  $F$  quantum number depends on the system and on the level of excitation (more serious in low values of  $Z$  and for high-lying states) as well as on the value of  $F$  (more serious for high values), as it is shown in Table II. For the sake of completeness, the energies of the wavefunctions computed for this work are given in Table III.

### Conclusion

The computation of the correlated TEIL wavefunctions [1-3] in the regime of high principal quantum numbers has allowed for the first time the quantitative examination of assumptions and group theoretic results obtained using hydrogenic basis sets. The  $^1S$  and the  $^1P^o$  symmetries were studied for  $Z = 1, 2, 3$ . One conclusion is that the Herrick-Sinanoglu  $(K, T)$  representation for two electron DES [4,9] loses its accuracy as we move up in energy. It is found that neither  $N$  nor  $K$  are good numbers. The reason that this breakdown is not seen in the low-lying states

is the fact that in this case, the relative importance of the double excitations (with hydrogenic functions) is small. We have explained this breakdown in terms of the spatial characteristics of the wavefunctions and have shown why it is more important in  $H^-$ , i.e., the negative ions.

Finally, we have proposed a new quantum number,  $F = N - 1 - K$ , [Eqs. (5), (5a), (6)] which remains "good" (not exact of course) for low- as well as for high-lying DES. We note that  $F$  is numerically the same quantity as  $\nu_2$ , the number of bending quanta in the molecular picture of DES (Refs. [15,9]).

Therefore, the results of Table II provide a physical picture of the relative importance of the vibration-bending modes  $\nu_2 = 0, 2$ , and 4 in the first three intrashell states of  $^1S$  symmetry.

### Bibliography

- [1] Y. Komninos and C. A. Nicolaides, *J. Phys.* B19, 1701 (1986); C. A. Nicolaides and Y. Komninos, *Phys. Rev.* A35, 999 (1987); C. A. Nicolaides, M. Chrysos, and Y. Komninos, *J. Phys.* B21, L73 (1988).
- [2] Y. Komninos, M. Chrysos, and C. A. Nicolaides, *J. Phys.* B20, L791 (1987); M. Chrysos, Y. Komninos, and C. A. Nicolaides, *J. Phys.* B25, 1977 (1992).
- [3] C. A. Nicolaides and Y. Komninos, *J. Phys.* B23, L571 (1990); C. A. Nicolaides, M. Chrysos, and Y. Komninos, *Phys. Rev.* A39, 1523 (1989).
- [4] D. R. Herrick and O. Sinanoglu, *Phys. Rev.* A11, 97 (1975); O. Sinanoglu and D. R. Herrick, *J. Chem. Phys.* 62, 886 (1975).
- [5] M. J. Conneely and L. Lipsky, *J. Phys.* B11, 4135 (1978).
- [6] O. Robaux, *J. Phys.* B20, 2347 (1987).
- [7] C. Froese-Fischer, *The Hartree-Fock Method for Atoms* (Wiley Interscience, New York, 1977).
- [8] C. Wulfman, *Phys. Lett.* A26, 397 (1968); *Chem. Phys. Lett.* 23, 370 (1973).
- [9] D. R. Herrick and M. E. Kellman, *Phys. Rev.* A21, 418 (1980); D. R. Herrick, *Adv. Chem. Phys.* 52, 1 (1982).
- [10] C. D. Lin and J. H. Macek, *Phys. Rev.* A29, 2317 (1984); C. D. Lin, *Phys. Rev.* A29, 1019 (1984).
- [11] C. A. Nicolaides, in *Advanced Theories and Computational Approaches to the Electronic Structure of Molecules*, C. E. Dykstra, Ed. (Reidel, Dordrecht, 1984), p. 161, and in *Giant Resonances in Atoms, Molecules and Solids*, J. P. Connerade, J. M. Esteve, and R. C. Karnatak, Eds. (Reidel, Dordrecht, 1987), p. 213.
- [12] Y. Komninos, N. Makri, and C. A. Nicolaides, *Z. Phys.* D2, 105 (1986); C. A. Nicolaides, N. Makri, and Y. Komninos, *J. Phys.* B20, 4963 (1987).
- [13] C. A. Nicolaides, *Phys. Rev.* A6, 2078 (1972); C. A. Nicolaides and D. R. Beck, *Int. J. Quantum Chem.* 14, 457 (1978).
- [14] M. Crance and L. Armstrong, *Phys. Rev.* A26, 694 (1982).
- [15] G. S. Ezra and R. S. Berry, *Phys. Rev. Lett.* 52, 1252 (1984); C. D. Lin, *Phys. Rev. Lett.* 52, 1253 (1984).

Received May 27, 1993



# A Comparison of Ground-State Averages in Electron Propagator Theory

J. V. ORTIZ

*Department of Chemistry, University of New Mexico, Albuquerque, New Mexico 87131 and  
Department of Chemistry, University of Utah, Salt Lake City, Utah 84112*

## Abstract

In the Dyson equation, the self-energy describes all relaxation and correlation corrections to Koopmans's theorem. Energy-independent contributions to the self-energy depend on the one-electron reduced density matrix of the reference state. Three formalisms for calculating these terms are considered: perturbation theory, coupled-cluster theory, and contour integral theory. In one method, combinations of coupled-cluster singles and doubles amplitudes are substituted for first-order double excitation coefficients and for second-order single excitation coefficients. Another approach generates a description of reference state correlation through the evaluation of approximate contour integral expressions. Calculations on electron binding energies of closed-shell molecules and anions reveal that the coupled-cluster results for the energy-independent self-energy terms are closer to the perturbative results than to the contour integral values. © 1993 John Wiley & Sons, Inc

## Introduction

Applications of electron propagator theory [1–7] in quantum chemistry have been confined chiefly to the calculation of ionization energies and electron affinities at a fixed nuclear geometry. Recent developments have extended the scope of applications to effective densities and energy gradients for initial,  $N$ -electron states and final states with  $N \pm 1$  electrons [8]. At the heart of these procedures lie choices for the treatment of correlation in propagator reference states. These choices ideally are matched with operator manifolds that produce a balanced description of many states. While the choice of operator manifolds is determined principally by the kinds of final states under study, there is comparatively greater license in reference state approximations. In the context of diagrammatic approaches, these approximations generally originate from perturbative improvements to a Hartree–Fock wavefunction. Recent attempts to achieve renormalized descriptions of reference state correlation have employed coupled-cluster wavefunctions [9]. In addition, there have been many applications of multiconfigurational SCF wavefunctions and related operator manifolds [10]. All of these methods depend on separate determinations of reference state wavefunctions that are essentially independent of the propagator formalism. Separate calculations on reference state correlation can be avoided entirely by systematic improvements to the operator manifold; an uncorrelated reference state suffices for such an approach [4]. A disadvantage of methods of this type is that they require large operator manifolds to compensate for the

absence of reference state correlation. An intermediate method, one which makes limited use of correlated reference states, can be derived from propagator expressions for the density matrices of these states [6,11]. Self-consistent descriptions of density matrices and electron binding energies can be achieved in this manner.

In this article, three methods for calculating contributions to the electron propagator's self-energy matrix are compared. This matrix, which contains all correlation corrections to Koopmans's theorem electron binding energies, has contributions which depend on the one-electron density matrix of the reference state. Correlated density matrices are obtained from perturbation theory on a Hartree-Fock wavefunction, from a coupled-cluster wavefunction and from contour integrals involving the self-energy matrix. Numerical results on ionization energies and electron affinities complete the comparison.

### Electron Propagator Theory

Elements of the electron propagator matrix contain information about the  $N$ -electron reference state and final states with  $N \pm 1$  electrons. The  $p, q$  element of this matrix, where  $p$  and  $q$  are general spin-orbital indices, is given by

$$\lim_{\eta \rightarrow 0} \left\{ \sum_n \frac{\langle N | a_p^\dagger | N-1, n \rangle \langle N-1, n | a_q | N \rangle}{E + E_n(N-1) - E_0(N) - i\eta} + \sum_n \frac{\langle N | a_q | N+1, n \rangle \langle N+1, n | a_p^\dagger | N \rangle}{E - E_n(N+1) + E_0(N) + i\eta} \right\}.$$

Poles are values of  $E$  that produce singularities, for they equal an ionization energy or an electron affinity. Another useful expression of the electron propagator matrix employs superoperator theory [12]. The superoperator metric, defined by

$$(\mathbf{Y} | \mathbf{Z}) = \langle 0 | [\mathbf{Y}^\dagger, \mathbf{Z}]_+ | 0 \rangle,$$

depends on the choice of the  $N$ -electron reference state,  $|0\rangle$ , and on the space of ionization operators. The identity and Hamiltonian superoperators operate on the latter; the defining equations are

$$\hat{\mathbf{I}}\mathbf{X} = \mathbf{X},$$

and

$$\hat{\mathbf{H}}\mathbf{X} = [\mathbf{X}, \mathbf{H}].$$

In this notation, the electron propagator matrix is

$$\mathbf{G}(E) = (\mathbf{a} | (E\hat{\mathbf{I}} - \hat{\mathbf{H}})^{-1} \mathbf{a}),$$

but a more useful form that avoids an inverse operator in favor of a matrix inversion is

$$\mathbf{G}(E) = (\mathbf{a} | \mathbf{h}) (\mathbf{h} | (E\hat{\mathbf{I}} - \hat{\mathbf{H}}) \mathbf{h})^{-1} (\mathbf{h} | \mathbf{a}).$$

where  $\mathbf{h}$  stands for the full space of ionization operators. After partitioning this space into the primary space of simple field operators,  $\mathbf{a}$ , and an orthogonal secondary space,  $\mathbf{f}$ , one obtains

$$\begin{aligned} \mathbf{G}(E) &= [(\mathbf{a}|\mathbf{a})(\mathbf{a}|\mathbf{f})] \begin{bmatrix} (\mathbf{a}|(E\hat{I} - \hat{H})\mathbf{a}) & (\mathbf{a}|(E\hat{I} - \hat{H})\mathbf{f}) \\ (\mathbf{f}|(E\hat{I} - \hat{H})\mathbf{a}) & (\mathbf{f}|(E\hat{I} - \hat{H})\mathbf{f}) \end{bmatrix}^{-1} \begin{bmatrix} (\mathbf{a}|\mathbf{a}) \\ (\mathbf{f}|\mathbf{a}) \end{bmatrix} \\ &= [\mathbf{1} \ \mathbf{0}] \begin{bmatrix} E\mathbf{1} - (\mathbf{a}|\hat{\mathbf{H}}\mathbf{a}) & -(\mathbf{a}|\hat{\mathbf{H}}\mathbf{f}) \\ -(\mathbf{f}|\hat{\mathbf{H}}\mathbf{a}) & E\mathbf{1} - (\mathbf{f}|\hat{\mathbf{H}}\mathbf{f}) \end{bmatrix}^{-1} \begin{bmatrix} \mathbf{1} \\ \mathbf{0} \end{bmatrix}. \end{aligned}$$

The Dyson equation can be derived at this point by observing that only the upper-left block of the inverse matrix is relevant and by considering the inverse propagator matrix. One obtains

$$\mathbf{G}^{-1}(E) = E\mathbf{1} - (\mathbf{a}|\hat{\mathbf{H}}\mathbf{a}) - (\mathbf{a}|\hat{\mathbf{H}}\mathbf{f})[E\mathbf{1} - (\mathbf{f}|\hat{\mathbf{H}}\mathbf{f})]^{-1}(\mathbf{f}|\hat{\mathbf{H}}\mathbf{a}).$$

The second term's elements depend on the reference state's one-electron reduced density matrix,  $\rho$ ,

$$(a_p|\hat{\mathbf{H}}a_q) = h_{pq} + \sum_{rs} (pq\|rs) \langle 0|a_r^\dagger a_s|0 \rangle = h_{pq} + \sum_{rs} (pq\|rs) \rho_{rs}.$$

It is possible to separate the correlated and uncorrelated contributions to the density matrix by writing the reference state as Hartree-Fock plus corrections. In the canonical orbital basis, the uncorrelated part is diagonal:

$$\epsilon_p \delta_{pq} = h_{pq} + \sum_{rs} (pq\|rs) \langle HF|a_r^\dagger a_s|HF \rangle = h_{pq} + \sum_r (pq\|rr) n_r,$$

where the occupation numbers,  $n$ , are unity for occupied spin-orbitals and zero for virtual spin-orbitals. A separation of correlated and uncorrelated terms in the Dyson equation is thereby effected by writing

$$\begin{aligned} \mathbf{G}^{-1}(E) &= E\mathbf{1} - \epsilon - (\mathbf{a}|\hat{\mathbf{H}}\mathbf{a})_{\text{correlation}} - (\mathbf{a}|\hat{\mathbf{H}}\mathbf{f})[E\mathbf{1} - (\mathbf{f}|\hat{\mathbf{H}}\mathbf{f})]^{-1}(\mathbf{f}|\hat{\mathbf{H}}\mathbf{a}) \\ &= \mathbf{G}_0^{-1}(E) - \Sigma(E). \end{aligned}$$

The first two terms, which are diagonal in the canonical orbital basis, constitute the inverse of the uncorrelated electron propagator matrix, whose poles are identical to the ionization energies and electron affinities of Koopmans's theorem:

$$\mathbf{G}_0^{-1}(E)_{pq} = (E - \epsilon_p) \delta_{pq}.$$

The subscript below the  $(\mathbf{a}|\hat{\mathbf{H}}\mathbf{a})_{\text{correlation}}$  term stipulates that the Hartree-Fock contribution to the one-electron density matrix has been omitted. The elements of this term have the following form:

$$(\mathbf{a}_p|\hat{\mathbf{H}}\mathbf{a}_q)_{\text{correlation}} = \sum_{rs} (pq\|rs) \rho'_{rs}.$$

In the Dyson equation, correlation corrections to the uncorrelated inverse propagator matrix arise from the energy-independent term just discussed or from the energy-dependent final term. These corrections, also known as the self-energy matrix, do

not vanish when  $E$  becomes positively or negatively infinite, for the constant terms remain. Because of this limiting behavior, the constant parts of the self-energy matrix,  $\Sigma(E)$ , are often symbolized by  $\Sigma(\infty)$ , where

$$\Sigma(E) = \Sigma(\infty) + \Sigma'(E).$$

The energy-dependent part of the self-energy is denoted by the prime superscript:

$$\Sigma'(E) = (\mathbf{a}|\hat{\mathbf{H}}\mathbf{f})[E\mathbf{1} - (\mathbf{f}|\hat{\mathbf{H}}\mathbf{f})]^{-1}(\mathbf{f}|\hat{\mathbf{H}}\mathbf{a}).$$

The energy-independent part is defined by

$$\Sigma(\infty) = (\mathbf{a}|\hat{\mathbf{H}}\mathbf{a})_{\text{correlation}}.$$

### Perturbative Arguments

In order to define an approximate self-energy expression, various investigators have advocated a variety of choices for the operator manifold  $\mathbf{f}$  and the reference state. For example, the burden of calculating accurate poles (but not residues) can be placed entirely on the operator space by choosing a Hartree-Fock reference for all superoperator matrix elements [4]. To a lesser extent, one can dispense with the operator manifold  $\mathbf{f}$  and rely solely on reference state corrections in the matrix  $\Sigma(\infty)$  [13]. For the lowest ionization energy, this is a satisfactory approach in the limit of a complete basis. A mixed strategy, relying on improvements of both kinds, has been applied more often. Justifications for various choices generally involve counting orders of the fluctuation potential in the self-energy. For example, the second order self-energy is obtained when

$$\Sigma'^{(2)}(E) = (\mathbf{a}|\hat{\mathbf{H}}\mathbf{f}_3)^{(1)}[E\mathbf{1} - (\mathbf{f}_3|\hat{\mathbf{H}}\mathbf{f}_3)^{(0)}]^{-1}(\mathbf{f}_3|\hat{\mathbf{H}}\mathbf{a})^{(1)},$$

where the superscripts in parentheses refer to the highest order in the fluctuation potential that is included in the superoperator matrices and  $\mathbf{f}_3$  refers to the space of triple field operator products. Only Hartree-Fock contributions to ground-state averages are needed at this level. A renormalized theory which recovers all second-order terms is obtained when the matrix  $(\mathbf{f}|\hat{\mathbf{H}}\mathbf{f})$  is evaluated in first order. This replacement, operative in the so-called 2p-h TDA approximation [3], includes ring and ladder diagrams through all orders. To obtain all terms through third order in  $\Sigma'(E)$ , the following form is sufficient:

$$\Sigma'^{(3+)}(E) = (\mathbf{a}|\hat{\mathbf{H}}\mathbf{f}_3)^{(2)}[E\mathbf{1} - (\mathbf{f}_3|\hat{\mathbf{H}}\mathbf{f}_3)^{(1)}]^{-1}(\mathbf{f}_3|\hat{\mathbf{H}}\mathbf{a})^{(2)}.$$

Beginning in third order, correlation corrections to the ground-state averages are needed [14]. In this case, they arise in  $(\mathbf{a}|\hat{\mathbf{H}}\mathbf{f}_3)$  and  $(\mathbf{f}_3|\hat{\mathbf{H}}\mathbf{a})$  through first-order double excitations. This approximate  $\Sigma'$  has been called extended 2p-h TDA and ADC(3) in the literature [6]. It contains many terms that are higher than third order and therefore the notation 3+ is used in the superscript. Because superoperator matrix elements that couple  $\mathbf{a}$  and  $\mathbf{f}_3$  first appear in second order, the  $\mathbf{f}_3$  portion of the operator manifold is not needed until fourth order in the self-energy matrix.

For the constant part of the self-energy, contributions of order  $n$  require  $\rho^c$  in order  $n - 1$ . Because single excitation corrections to the Hartree-Fock wavefunction

vanish in first order, there are no first-order corrections in the correlation density matrix. Therefore, there are no constant self-energy terms in second order.  $\Sigma(\infty)$  appears in third-order through first-order double excitations and second-order single excitations in the reference state. The former excitations contribute to the occupied-occupied and virtual-virtual blocks of the density matrix and the latter contribute to the occupied-virtual block. If third-order  $\Sigma(\infty)$  is added to  $\Sigma^{(3+)}(E)$ , the resulting self-energy matrix is complete through third order [15].

### Coupled-Cluster Reference States

The perturbative approach discussed above rests on systematic improvements in ground-state averages and operator manifolds. Infinite order corrections can be obtained by retaining the full inverse matrix that occurs in the energy-dependent part of the self-energy matrix. (Finite order terms can be identified by expanding the inverse in powers of its uncorrelated, diagonal part and its correlated, nondiagonal part.) Instead of relying on finite order improvements to the reference state's wavefunction or density matrices, one can employ a description that contains infinite order corrections [9]. The usual coupled-cluster ansatz for the reference state has several properties that make it convenient for this purpose. The most common coupled-cluster wavefunction [16]

$$|CC\rangle = e^T |HF\rangle.$$

where

$$T = T_1 + T_2 + T_3 + \dots$$

$$T_1 = \sum_i \sum_a t_i^a a_i^\dagger a_i$$

$$T_2 = \sum_{i>j} \sum_{a>b} t_{ij}^{ab} a_a^\dagger a_b^\dagger a_i a_j$$

$$T_3 = \sum_{i>j>k} \sum_{a>b>c} t_{ijk}^{abc} a_a^\dagger a_b^\dagger a_c^\dagger a_i a_j a_k$$

has amplitudes that are easily related to the usual configuration interaction ansatz,

$$|CI\rangle = (1 + C_1 + C_2 + C_3 + \dots) |HF\rangle,$$

where

$$C_1 = \sum_i \sum_a c_i^a a_i^\dagger a_i$$

$$C_2 = \sum_{i>j} \sum_{a>b} c_{ij}^{ab} a_a^\dagger a_b^\dagger a_i a_j$$

$$C_3 = \sum_{i>j>k} \sum_{a>b>c} c_{ijk}^{abc} a_a^\dagger a_b^\dagger a_c^\dagger a_i a_j a_k.$$

By equating terms with different degrees of excitation with respect to the Hartree-Fock reference, one concludes that the single and double excitation coefficients

that are implicit in a coupled-cluster singles and doubles wavefunction [17] are given by

$$c_i^a = t_i^a$$

and

$$c_{ij}^{ab} = t_{ij}^{ab} + t_i^a t_j^b - t_j^a t_i^b.$$

Of special interest to this discussion is the inclusion of all first-order doubles contributions and all second-order singles contributions to the configuration interaction coefficients generated in this manner. Substitution of these coefficients for the usual perturbative values in the expressions for  $\rho^c$  in second order recovers all third-order self-energy contributions while including many higher order terms. While it is possible to restrict these substitutions to the constant part of the self-energy matrix, recent implementations have extended these replacements to the second-order superoperator matrices,  $(\mathbf{a}|\hat{\mathbf{H}}\mathbf{f}_3)^{(2)}$  and  $(\mathbf{f}_3|\hat{\mathbf{H}}\mathbf{a})^{(2)}$ , required for the third-order energy-dependent self-energy [9].

### Contour Integral Theory

The energy-independent part of the self-energy matrix depends on the one-electron reduced density matrix. This matrix, in turn, can be evaluated through the contour integral relation

$$\rho = \frac{1}{2\pi i} \int_C \mathbf{G}(E) dE,$$

where  $C$  denotes a contour that encloses all ionization energy poles in the complex plane [1]. From iterations on an alternative form of the Dyson equation,

$$\mathbf{G}(E) = \mathbf{G}_0(E) + \mathbf{G}_0(E)\Sigma(E)\mathbf{G}(E),$$

it is clear that the propagator matrix can be expressed in powers of the self-energy matrix:

$$\mathbf{G}(E) = \mathbf{G}_0(E) + \mathbf{G}_0(E)\Sigma(E)\mathbf{G}_0(E) + \mathbf{G}_0(E)\Sigma(E)\mathbf{G}_0(E)\Sigma(E)\mathbf{G}_0(E) + \dots,$$

These relations suggest an iterative procedure in which density matrices obtained from the contour integral are used to obtain new elements of the self-energy matrix, which, in turn, are used to evaluate the propagator matrix. The cycle is completed when the new propagator matrix produces a new density matrix. Because  $\Sigma(\infty)$  depends linearly on  $\rho^c$ , various powers of latter matrix are implicitly contained in the contour integral relation. By truncating the Dyson expansion so that

$$\mathbf{G}_0(E)\Sigma(E)\mathbf{G}_0(E)\Sigma(E)\mathbf{G}_0(E)$$

and subsequent terms are omitted, one obtains a linearized expression for the density matrix [6,11]. Because the uncorrelated contribution to the density is given by

$$\rho^{\text{HF}} = \frac{1}{2\pi i} \int_C \mathbf{G}_0(E) dE,$$

the correlated contribution,  $\rho^c$ , is involved in the following relation:

$$\rho^c = \frac{1}{2\pi i} \int_C \mathbf{G}_0(E) \{ \Sigma(\infty) + \Sigma'(E) \} \mathbf{G}_0(E) dE.$$

The first term on the right side of this equation is easily evaluated through

$$\frac{1}{2\pi i} \int_C \mathbf{G}_{0pp}(E) \Sigma(\infty)_{pq} \mathbf{G}_{0qq}(E) dE = \frac{1}{2\pi i} \int_C \mathbf{G}_{0pp}(E) \sum_{rs} (pq||rs) \rho_{rs}^c \mathbf{G}_{0qq}(E) dE.$$

The last expression vanishes for  $\epsilon_p = \epsilon_q$ ; for  $\epsilon_p \neq \epsilon_q$ , one obtains

$$\frac{n_p - n_q}{\epsilon_p - \epsilon_q} \sum_{rs} (pq||rs) \rho_{rs}^c.$$

By defining

$$V_{pq,rs} = (pq||rs),$$

and

$$d_{pq} = \begin{cases} 0 & \text{if } \epsilon_p = \epsilon_q \\ \frac{n_p - n_q}{\epsilon_p - \epsilon_q} & \text{if } \epsilon_p \neq \epsilon_q \end{cases},$$

one can write the following equation for the correlated part of the density matrix:

$$(1 - dV)\rho^c = \frac{1}{2\pi i} \int_C \mathbf{G}_0(E) \Sigma'(E) \mathbf{G}_0(E) dE.$$

The most taxing aspect of this calculation is evaluation of the contour integral matrix

$$\frac{1}{2\pi i} \int_C \mathbf{G}_0(E) \Sigma'(E) \mathbf{G}_0(E) dE.$$

In effect, the energy-dependent self-energy matrix must be calculated at energies equal to the canonical orbital energies. For  $\Sigma'^{(3+)}(E)$ , calculation of

$$[E1 - (\mathbf{f}_3|\hat{\mathbf{H}}\mathbf{f}_3)^{(1)}]^{-1}(\mathbf{f}_3|\hat{\mathbf{H}}\mathbf{a})^{(2)}$$

is the crucial step. The inverse matrix is expanded in powers of its diagonal, zeroth-order part and its first-order part:

$$\begin{aligned} & \{ [E1 - (\mathbf{f}_3|\hat{\mathbf{H}}_0\mathbf{f}_3)]^{-1} + [E1 - (\mathbf{f}_3|\hat{\mathbf{H}}_0\mathbf{f}_3)]^{-1}(\mathbf{f}_3|\hat{\mathbf{V}}\mathbf{f}_3)[E1 - (\mathbf{f}_3|\hat{\mathbf{H}}_0\mathbf{f}_3)]^{-1} \\ & + [E1 - (\mathbf{f}_3|\hat{\mathbf{H}}_0\mathbf{f}_3)]^{-1}(\mathbf{f}_3|\hat{\mathbf{V}}\mathbf{f}_3)[E1 - (\mathbf{f}_3|\hat{\mathbf{H}}_0\mathbf{f}_3)]^{-1}(\mathbf{f}_3|\hat{\mathbf{V}}\mathbf{f}_3)[E1 - (\mathbf{f}_3|\hat{\mathbf{H}}_0\mathbf{f}_3)]^{-1} \\ & + \dots \} (\mathbf{f}_3|\hat{\mathbf{H}}\mathbf{a})^{(2)}. \end{aligned}$$

TABLE I. 6-311++G(2df,2pd) anion ionization energies (eV).

Anion	Third order		Coupled cluster		Contour integral		Expt. [23]
	$\Sigma(\infty)_n$	Pole	$\Sigma(\infty)_n$	Pole	$\Sigma(\infty)_n$	Pole	
F <sup>-</sup>	-0.827	-4.337	-0.769	-4.155	-0.231	-3.797	3.40
OH <sup>-</sup>	-0.384	-2.450	-0.365	-2.306	-0.014	-2.119	1.83
NH <sub>2</sub> <sup>-</sup>	0.137	-0.884	0.096	-0.850	0.197	-0.830	0.78

The convergence criterion for these matrix elements is  $10^{-6}$  atomic units. The most demanding summations scale as  $O^2V^4$ , where  $O$  is the number of occupied orbitals and  $V$  is the number of virtual orbitals. (Identical scaling factors occur in a variety of methods, such as singles and doubles configuration interaction, third-order many-body perturbation theory and coupled-cluster singles and doubles [16].) By rearranging the linear equations and expanding  $(1 - dV)^{-1}$ , it is possible to identify terms of various orders:

$$\rho^c = (1 + dV^{(1)} + dV^{(1)}dV^{(1)} + \dots)$$

$$\frac{1}{2\pi i} \int_C G_0(E) \{ \Sigma'^{(2)}(E) + \Sigma'^{(3)}(E) + \dots \} G_0(E) dE.$$

Derivation of the correlated density matrix through second-order (and the corresponding third-order constant diagrams) requires the second-order self-energy and the identity term from the expansion of  $(1 - dV)^{-1}$ . Retention of the full inverse introduces higher order corrections. For third-order  $\rho^c$ , second- and third-order contributions to  $\Sigma'(E)$  are required. Because the lowest order contributions to the self-energy matrix are second order, the lowest order terms that are neglected in the approximation

$$G(E) \approx G_0(E) + G_0(E)\Sigma(E)G_0(E)$$

occur in the fourth-order density matrix. Insertion of  $\Sigma'^{(3+)}(E)$  in contour integral expressions that ignore quadratic and higher terms in the self-energy matrix provides

TABLE II. 5s4p1d N<sub>2</sub> ionization energies (eV)

Final state	Third order		Coupled cluster		Contour integral		Expt. [23]
	$\Sigma(\infty)_n$	Pole	$\Sigma(\infty)_n$	Pole	$\Sigma(\infty)_n$	Pole	
<sup>2</sup> II <sub>u</sub>	0.685	-16.628	0.624	-16.806	0.445	-16.850	16.98
<sup>2</sup> $\Sigma_g^-$	0.798	-15.482	0.787	-15.429	0.559	-15.694	15.60
<sup>2</sup> $\Sigma_u^-$	0.679	-18.790	0.688	-18.711	0.482	-18.951	18.78



TABLE III. 6-311++G(2df,2pd) H<sub>2</sub>O ionization energies (eV)

Final state	Third order		Coupled cluster		Contour integral		Expt. [23]
	$\Sigma(\infty)_n$	Pole	$\Sigma(\infty)_n$	Pole	$\Sigma(\infty)_n$	Pole	
<sup>2</sup> B <sub>1</sub>	0.048	-13.064	0.006	-13.046	0.111	-13.006	12.62
<sup>2</sup> A <sub>1</sub>	0.021	-15.331	-0.021	-15.334	0.091	-15.266	14.74
<sup>2</sup> B <sub>2</sub>	0.012	-19.262	-0.026	-19.307	0.084	-19.194	18.51

a full fourth-order description of  $\Sigma(\infty)$ . Many, but not all, fifth-order and higher terms in the self-energy matrix are implicitly included. One source of these terms is the renormalized character of  $\Sigma^{(3+)}(E)$ . Another source is the infinite order expansion of  $(1 - dV)^{-1}$  that is implicit in solving

$$\rho^c = (1 - dV)^{-1} \frac{1}{2\pi i} \int_C G_0(E) \Sigma^{(3+)}(E) G_0(E) dE.$$

The latter equation is used to produce  $\rho^c$  and the resulting elements of  $\Sigma(\infty)$  in the calculations that are presented in the next section. Linear equations for  $\rho^c$  are solved with a direct inversion of iterative subspaces procedure [18], where the convergence criterion is  $10^{-8}$ .

### Numerical Examples

The three methods discussed above have been programmed as part of an extension of EPT90, an electron propagator program [19]. Hartree-Fock calculations and integral transformations to the canonical molecular orbital basis are performed with Gaussian 90 [20]. Coupled-cluster singles and doubles calculations have been implemented separately [9].

6-311++G(2df,2pd) basis sets [21] are used in calculations on anions, H<sub>2</sub>O and H<sub>3</sub>N. Bond lengths are 0.965 Å in OH<sup>-</sup> and 1.030 Å in NH<sub>2</sub><sup>-</sup>; the bond angle in the latter anion is 101.3°. In the H<sub>2</sub>O calculations, the bond length is 0.959 Å and the bond angle is 103.5°; for H<sub>3</sub>N, the corresponding data are 1.013 Å and 107.4°. Core molecular orbitals are dropped in all summations pertaining to the propagator and coupled-cluster singles and doubles calculations. The basis and geometry for

TABLE IV. 6-311++G(2df,2pd) H<sub>3</sub>N ionization energies (eV).

Final state	Third order		Coupled cluster		Contour integral		Expt. [23]
	$\Sigma(\infty)_n$	Pole	$\Sigma(\infty)_n$	Pole	$\Sigma(\infty)_n$	Pole	
<sup>2</sup> A <sub>1</sub>	0.333	-10.961	0.310	-10.978	0.284	-11.005	10.85
<sup>2</sup> E	0.257	-16.740	0.231	-16.807	0.224	-16.769	15.8

$N_2$  have been previously employed [22]. No molecular orbitals are dropped from the latter calculation.

Results on anions in Table I include ionization energies and diagonal elements of the constant self-energy matrix whose indices match the index of the highest occupied canonical orbital. The basis sets are typical of accurate electron affinity calculations, for they include diffuse s and p functions, a triple  $\zeta$  valence set, and double polarization functions. In the columns labeled third order, constant terms of third order are combined with  $\Sigma^{(3+)}(E)$ . Coupled-cluster substitutions for perturbative reference state corrections are made in the following two columns. The next two columns are results from the contour integral procedure. The present set of anions is a severe test of electron affinity methods, for the highly electronegative central atoms possess electrons that are confined to a small volume. For  $F^-$  and  $OH^-$ , the coupled-cluster results effect clear improvements over third order. Experimental values for the anion ionization energies are still a few tenths of an electron Volt away [23]. Changes in the constant self-energy terms explain only part of the differences between the poles. Coupled cluster improvements to the  $(a|\hat{H}f_3)$  and  $(f_3|\hat{H}a)$  matrices may have a greater effect. The difference between third-order and contour integral results, however, lies entirely in the treatment of the constant self-energy matrix. There is a marked contrast between the contour integral values and the third-order values that leads to a similar set of shifts in the poles. This is an indication that higher-order terms in the constant self-energy matrix can be large.

Calculations on  $N_2$  with the model basis of Table II disclose a similar set of trends. Discrepancies between third-order and coupled-cluster results are small. Contour integral descriptions of the constant self-energy matrix improve the third-order results somewhat better.

For calculations on  $H_2O$  (Table III), the coupled-cluster values for the constant self-energy terms do not lie between the third-order and contour integral results. The latter treatment gives a qualitatively superior set of improvements to third order. The remaining deficiencies of third order probably originate from the absence of quintuple products in the operator manifold.

Results on  $H_3N$  (Table IV) demonstrate that a third-order description of the constant self-energy matrix can be accurate. The coupled-cluster poles lie between the third-order and contour integral results.

### Conclusions

Fourth- and higher-order corrections to the constant self-energy matrix can be important in the calculation of electron binding energies. The requisite improvements in the one-electron density matrix can be obtained through perturbative corrections to reference state wavefunctions, through coupled-cluster wavefunctions or through contour integrals. With the use of  $\Sigma^{(3+)}(E)$  and the truncation of the Dyson equation after the term that is linear in the self-energy matrix, the most difficult summation has a scaling factor,  $O^2V^4$ , identical to that of its counterpart in a coupled-cluster singles and doubles optimization. (The most difficult step in

the evaluation of the constant third-order diagrams has an  $O^3V^3$  scaling factor.) The contour integral procedure sometimes produces large corrections to the third-order constant self-energy matrix. In the coupled-cluster approach, discrepancies with the third-order constant terms are smaller. Based on these preliminary results, the contour integral procedure appears to be a more efficient sixth-power method than the coupled-cluster approach for improving the constant contributions to the self-energy. In order to take full advantage of the coupled-cluster reference state, it may be necessary to calculate additional contributions to  $\rho'$  with the same singles and doubles amplitudes. Another promising possibility is abandonment of the Dyson expansion of the propagator matrix in powers of the self-energy matrix in favor of direct integration over the Coulson contour.

### Acknowledgments

Part of this work was done during a sabbatical visit to the laboratory of Prof. J. Simons at the University of Utah. Discussions with Prof. Simons and Dr. J. Nichols have been useful and illuminating. This work was partially supported by the National Science Foundation under Grants CHE-9101777 and by the Petroleum Research Fund under Grant 24512-AC6.

### Bibliography

- [1] J. Linderberg and Y. Öhrn, *Propagators in Quantum Chemistry* (Academic Press, New York, 1973).
- [2] B. T. Pickup and O. Goscinski, *Mol. Phys.* **26**, 1013 (1973).
- [3] L. S. Cederbaum and W. Domcke, *Adv. Chem. Phys.* **26**, 206 (1977).
- [4] Y. Öhrn and G. Born, *Adv. Quantum Chem.* **13**, 1 (1981).
- [5] M. F. Herman, K. F. Freed, and D. Yeager, *Adv. Chem. Phys.* **48**, 1 (1981).
- [6] W. von Niessen, J. Schirmer, and L. S. Cederbaum, *Comput. Phys. Rep.* **1**, 57 (1984).
- [7] J. Simons, *Theor. Chem. Adv. Persp.* **3**, 1 (1978).
- [8] J. Cioslowski and J. V. Ortiz, *J. Chem. Phys.* **96**, 8379 (1992); J. V. Ortiz, *J. Chem. Phys.* **97**, 7531 (1992); J. V. Ortiz, *Int. J. Quantum Chem., Quantum Chem. Symp.* **26**, 1 (1992).
- [9] J. V. Ortiz, *Chem. Phys. Lett.* **199**, 530 (1992); J. V. Ortiz, *Int. J. Quantum Chem., Quantum Chem. Symp.* **25**, 35 (1992).
- [10] J. A. Nichols, D. L. Yeager, and P. Jorgensen, *J. Chem. Phys.* **80**, 293 (1984); J. T. Golab and D. L. Yeager, *J. Chem. Phys.* **87**, 2925 (1987).
- [11] J. Schirmer and G. Angonoa, *J. Chem. Phys.* **91**, 1754 (1989).
- [12] O. Goscinski and B. Lukman, *Chem. Phys. Lett.* **7**, 573 (1970).
- [13] D. W. Smith and O. W. Day, *J. Chem. Phys.* **62**, 113 (1975).
- [14] J. Simons and S. Smith, *J. Chem. Phys.* **58**, 4899 (1973).
- [15] J. Baker and B. T. Pickup, *Chem. Phys. Lett.* **76**, 537 (1980).
- [16] R. J. Bartlett, *J. Phys. Chem.* **93**, 1697 (1989).
- [17] G. D. Purvis and R. J. Bartlett, *J. Chem. Phys.* **76**, 1910 (1982).
- [18] J. A. Pople, R. Krishnan, H. B. Schlegel, and J. S. Binkley, *Int. J. Quantum Chem., Quantum Chem. Symp.* **13**, 225 (1979); G. D. Purvis and R. J. Bartlett, *J. Chem. Phys.* **75**, 1284 (1981).
- [19] J. V. Ortiz, EPT90, an *ab initio* electron propagator program, J. V. Ortiz, *Int. J. Quantum Chem., Quantum Chem. Symp.* **23**, 321 (1989).
- [20] Gaussian 90, Revision F, M. J. Frisch, M. Head-Gordon, G. W. Trucks, J. B. Foresman, H. B. Schlegel, K. Ragavachari, M. Robb, J. S. Binkley, C. Gonzalez, D. J. Defrees, D. J. Fox, R. A.

- Whiteside, R. Seeger, C. F. Melius, J. Baker, R. L. Martin, L. R. Kahn, J. J. P. Stewart, S. Topiol, and J. A. Pople, Gaussian, Inc., Pittsburgh, PA, 1990.
- [21] R. Krishnan, J. S. Binkley, R. Seeger, and J. A. Pople, *J. Chem. Phys.* **72**, 650 (1980); T. Clark, J. Chandrasekhar, G. W. Spitznagel, and P. v. R. Schleyer, *J. Comp. Chem.* **4**, 294 (1983); M. J. Frisch, J. A. Pople, and J. S. Binkley, *J. Chem. Phys.* **80**, 3265 (1984).
- [22] G. Angonoa, O. Walter, and J. Schirmer, *J. Chem. Phys.* **87**, 6789 (1987).
- [23]  $F^-$ : H. Hotop and W. C. Lineberger, *J. Phys. Chem. Ref. Data* **4**, 539 (1975).  $OH^-$ : F. A. Schulz, R. D. Mead, P. L. Jones, and W. C. Lineberger, *J. Chem. Phys.* **77**, 1153 (1982).  $NH_2^-$ : R. J. Celotta, R. A. Bennett, and J. L. Hall, *J. Chem. Phys.* **60**, 1740 (1974). Neutrals: K. Kimura, S. Katsumata, Y. Achiba, T. Yamazaki, and S. Iwata, *Handbook of He I Photoelectron Spectra of Fundamental Organic Molecules* (Japan Scientific Societies Press, Tokyo, 1981).

Received March 13, 1993

# Comparison of Ground and Triplet State Geometries of Malonaldehyde

KARL LUTH and STEVE SCHEINER

*Department of Chemistry & Biochemistry, Southern Illinois University, Carbondale, Illinois 62901*

## Abstract

The geometries of the ground and first triplet excited state of malonaldehyde are compared for two distinct configurations of the molecule. The first represents the equilibrium geometry and the second structure corresponds to the transition state for the intramolecular hydrogen transfer. The ground state computations utilize both self-consistent field and Moller-Plesset second-order perturbation theory. The excited state computations employ several different theoretical methods, unrestricted Hartree-Fock (UHF), unrestricted second-order Moller-Plesset perturbation theory (UMP2), CI Singles (CIS), and complete active space self-consistent field (CAS). The geometric parameters obtained for the two configurations are contrasted in both the ground and excited state. The structural differences are related to the extent of hydrogen bonding present, which is compared to the calculated proton transfer barrier. © 1993 John Wiley & Sons, Inc.

## Introduction

In contrast to proton transfers which take place in the ground electronic state, the study of such reactions occurring in excited electronic states is in its infancy. The sensitivity of the properties of the proton-transfer reaction to the nature of the solvent suggests gas-phase work would be required in order to understand the intrinsic behavior of a given system. Some relevant work is being reported in the gas phase [1-8], as well as in low-temperature matrices [9,10].

On the theoretical side, only a couple of *ab initio* studies have been reported for excited state proton transfer at this time [11,12]. Since the computational methods available to study excited states are somewhat limited, especially for states that are not the lowest energy of a given symmetry type, it is important to determine which of the available methods are dependable and how the results obtained from different methods compare with one another. The most logical point to begin the comparison concerns the optimized structures obtained using various methods. This comparison is crucial because electronic properties depend on the quality of the geometry considered.

This article systematically compares the geometries obtained for the lowest excited triplet state of malonaldehyde using a number of theoretical methods. These methods were chosen less for purposes of rigorous accuracy but rather as a means of comparing the results of various computationally tractable procedures. Unrestricted Hartree-Fock (UHF) is a historically popular means of investigating some of the

lower excited states. While it does not yield a state which is an eigenfunction of the spin operator, it is usually possible to draw a direct connection with the correct state. A common follow-up to UHF which introduces dynamic correlation in an efficient manner is unrestricted Moller-Plesset perturbation theory (UMP2) which has been investigated here as well. Pople and coworkers have recently introduced a CI Singles scheme (CIS) which permits one to obtain a first approximation of various excited states, even those of the same symmetry as the ground state. This method would appear quite promising for purposes of studying excited state proton transfers and warrants some scrutiny. As a last procedure, we test the complete active space self-consistent field (CAS) method which removes much of the arbitrariness of MCSCF and has proven rather dependable.

Malonaldehyde was chosen due to its relatively small size and simplicity. This molecule has itself been studied both experimentally [13-17] and theoretically in the ground state [18-20], which provide valuable benchmarks in determining the accuracy of the computational methods tested.

### Computational Details

All of the computations relevant to this communication, except for the complete active space self-consistent field calculations (CAS), were performed using the Gaussian 90 *ab initio* package [21]. The CAS calculations [22] utilized the General Atomic and Molecular Electronic Structure System (GAMESS) [23]. The CI singles (CIS) method [24] was utilized as implemented in Gaussian 90. Electron correlation was incorporated into some of the ground and excited state computations via a second-order Moller-Plesset correction to either the SCF or CIS energy. Three basis sets are considered, split valence 4-31G [25], polarized triple valence 6-311G\*\* [26,27], and another containing diffuse functions, 6-31+G\*\* [28].

Two configurations of malonaldehyde are investigated as illustrated in Figure 1. The first, designated **M**, represents the equilibrium geometry. The hydrogen is covalently bonded to one oxygen and interacts with the other via a hydrogen bond. The second configuration corresponds to the midpoint or transition state, **TS**, of the proton transfer process and has the hydrogen equidistant from the two oxygens. Both structures were initially found, and in subsequent calculations constrained, to be planar. **M** has  $C_s$  symmetry and the point group of **TS** is  $C_{2v}$ . All harmonic

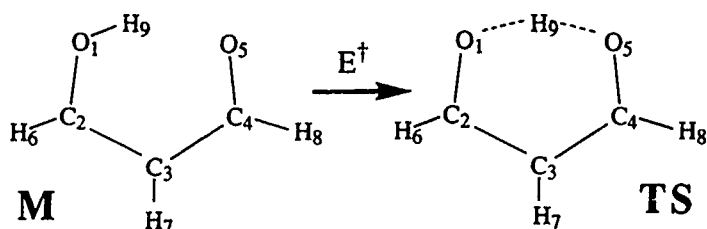


Figure 1. Structures of the two forms of malonaldehyde investigated. **M** represents the equilibrium form and **TS** represents the transition state of the proton transfer.

frequencies of the former are positive while the latter has associated with it a single imaginary frequency, corresponding to the transfer of the proton. The proton transfer barrier is calculated as the energy difference between the **M** and **TS** structures.

### Ground State

In contrast to the excited states which have been largely unexplored by *ab initio* computations, there is a significant body of theoretical as well as experimental data concerning the ground state of malonaldehyde. These earlier results can serve as a valuable measure of the reliability of some of the computational methods employed here. The salient features of the geometries optimized at various levels of theory are reported in Table I, along with the total energy.

All the data confirm a number of structural changes caused by the half transfer of the proton. The  $O_1C_2$  hydroxyl bond of **M** shortens as it acquires more of the carbonyl character it will have following completion of the proton transfer. The opposite trend is noted in the originally carbonyl  $C_4O_5$  bond. The formally double  $C_2C_3$  bond in **M** elongates while the single  $C_3C_4$  bond contracts. Most of these bond length changes are in the neighborhood of 0.05 Å. Also important are the parameters relevant to the H-bond connecting the two oxygens. The interoxygen distance is reduced by perhaps 0.3 to 0.4 Å when the bridging hydrogen is moved midway between them. This change is accomplished largely by reductions of up to 7° in some of the internal bond angles. The shrinking  $R(OO)$  is accompanied by a more linear H-bond in the sense that this proton lies closer to the  $O \cdots O$  axis.

The MP2/6-311G\*\* data agree nicely with the MP2/6-31G\*\* values reported by Frisch et al. [20]. The results also correspond nicely to those determined experimentally by Wilson and coworkers [17]. In addition, the partial transfer of the hydrogen affects the other geometric properties as observed experimentally by Roubin and coworkers, who noted that the relative C—C and C—O bond orders vary as the hydrogen transfers [13].

With regard to the effect of the level of theory upon the geometry, the larger basis set yields shorter C—O and longer C—C bonds than does 4-31G at the SCF level. There is evidence that 6-311G\*\* provides a weaker H-bond in the **M** conformer:  $r(O_1H)$  is shorter by 0.01 Å and the interoxygen distance longer by 0.02 Å. (The diffuse functions of 6-31+G\*\* induce very little change in the geometrical parameters.) The same indicators suggest that correlation strengthens the H-bond considerably.

### Excited State

The lowest lying excited state of malonaldehyde is a triplet derived from an excitation from the highest occupied molecular orbital (HOMO) into the lowest unoccupied molecular orbital (LUMO). The HOMO has  $\pi$  symmetry and is primarily of C—C bonding character along with some C—O antibonding, and the LUMO is almost entirely C—O  $\pi^*$ . The transition is denoted  ${}^3\pi - \pi^*$ .

Before discussing the geometries in detail, a brief mention should be made of the details of the methods used. For each method investigated, except CAS, the

TABLE I. Optimized geometries<sup>a</sup> and energies of ground state of malonaldehyde, M, and the transition state of the proton transfer, TS.

	M					TS					
	SCF 4-31G	SCF 6-311G**	SCF 6-31+G**	MP2 6-311G**	MP2 <sup>b</sup> 6-31G**	Exp. <sup>c</sup>	SCF 4-31G	SCF 6-311G**	SCF 6-31+G**	MP2 6-311G**	MP2 <sup>b</sup> 6-31G**
O <sub>1</sub> C <sub>2</sub>	1.335	1.310	1.312	1.322	1.328	1.320	1.281	1.251	1.256	1.277	1.285
C <sub>2</sub> C <sub>3</sub>	1.338	1.341	1.344	1.365	1.362	1.348	1.388	1.394	1.395	1.400	1.396
C <sub>3</sub> C <sub>4</sub>	1.441	1.455	1.453	1.444	1.439	1.454	1.388	1.394	1.395	1.400	1.396
C <sub>4</sub> O <sub>5</sub>	1.230	1.200	1.208	1.239	1.248	1.234	1.281	1.251	1.256	1.277	1.285
C <sub>2</sub> H <sub>6</sub>	1.066	1.076	1.075	1.087	1.083	1.089	1.074	1.083	1.082	1.094	1.089
C <sub>3</sub> H <sub>7</sub>	1.068	1.073	1.073	1.081	1.077	1.091	1.066	1.070	1.071	1.079	1.075
C <sub>4</sub> H <sub>8</sub>	1.081	1.093	1.091	1.103	1.098	1.094	1.074	1.083	1.082	1.094	1.089
O <sub>1</sub> H <sub>9</sub>	0.963	0.953	0.956	0.991	0.994	0.969	1.209	1.186	1.189	1.197	1.203
O <sub>5</sub> ...H <sub>9</sub>	1.917	1.895	1.897	1.678	1.694	1.680	1.209	1.186	1.189	1.197	1.203
O <sub>1</sub> ...O <sub>5</sub>	2.671	2.689	2.689	2.581	2.589	2.553-2.576	2.331	2.321	2.323	2.355	2.361
θ(C <sub>2</sub> C <sub>3</sub> C <sub>4</sub> )	125.79	126.37	126.15	124.40	124.5	124.5	121.26	121.89	121.65	121.89	121.9
θ(C <sub>3</sub> C <sub>4</sub> O <sub>5</sub> )	121.49	121.08	121.24	119.16	119.5	119.4	116.30	114.91	115.22	115.58	115.9
θ(C <sub>2</sub> C <sub>3</sub> H <sub>6</sub> )	123.62	124.19	123.93	123.51	123.5	123.0	121.26	121.89	121.65	121.89	121.9
θ(C <sub>3</sub> C <sub>4</sub> H <sub>7</sub> )	122.32	121.18	121.30	122.29	122.5	122.3	121.69	120.86	121.08	121.24	
θ(C <sub>3</sub> C <sub>4</sub> H <sub>8</sub> )	119.04	119.54	119.45	120.78	120.0	128.1	121.84	122.54	122.39	122.21	
θ(C <sub>2</sub> O <sub>1</sub> H <sub>9</sub> )	117.15	116.23	116.60	117.38	117.6	117.6	121.69	120.86	121.08	121.24	
θ(C <sub>3</sub> O <sub>1</sub> H <sub>9</sub> )	113.92	109.46	110.11	104.62	105.4	106.3	106.08	102.67	103.08	100.66	
θ(O <sub>5</sub> O <sub>1</sub> H <sub>9</sub> )	31.52	27.43	27.84	19.52			15.49	12.02	12.34	10.34	
E <sup>SCF</sup>	-265.24118	-265.70629	-265.65279	-265.70142			-265.22197	-265.68903	-265.63630	-265.68655	
E <sup>MP2</sup>	-265.75058	-266.50772		-266.60608	-266.41851		-265.73996	-266.50403		-266.60063	

<sup>a</sup> Distances in Å, angles in degrees, energies in hartree.<sup>b</sup> Reference [20].<sup>c</sup> Reference [17].



utilization of the method is straightforward. One need only specify which state is to be explored. For CAS, an additional step must be performed; the active space must be defined. In this study, two different CAS active spaces were investigated. The first included the two singly occupied  $\pi$  orbitals and one additional virtual orbital of  $\pi$  symmetry (the lowest energy virtual  $\pi$ ), giving two active electrons in three active orbitals, this prescription is designated CAS-1. CAS-2 added two doubly occupied  $\pi$  orbitals and the next lowest unoccupied  $\pi$  orbital, totalling six active electrons and six active orbitals.

For the excited state, relaxation to a lower energy state of the same symmetry is not a problem. However, for excited state calculations in general, such as  $S_1$ , this collapsing to a lower state can be a significant concern. It should be noted that of the methods used, only CIS does not suffer from this problem.

The geometries obtained for the equilibrium orientation, **M**, are provided in Table II. Initially, the excited state geometries will be compared to the values obtained for the ground state. Generally, each method provides similar results resulting from excitation. Understanding the differences in the geometry of the excited state is predicated on the molecular orbitals that are involved in the excitation. The HOMO and the LUMO are shown in Figure 2 for both the **M** and **TS** structures. The characters of the orbitals are similar for each orientation, although the interactions are cleaner in the **TS** form due to the increased symmetry. The phases of the  $\pi$  orbitals in the HOMO are such that bonding interactions exist primarily between like atoms (C—C or O—O) while those between unlike atoms are  $\pi^*$  in character. The LUMO introduces a second nodal plane such that most interactions are antibonding, except those involving  $C_3$ .

The  $O_1$ — $C_2$  bond lengthening can be understood simply via the placement of an electron in the LUMO which is strongly antibonding between the two pertinent atoms. A large stretch occurs in the  $C_2C_3$  bond upon excitation from HOMO to LUMO since the interaction between these two atoms changes from bonding in the HOMO to antibonding in the LUMO for both arrangements. The appearance of a bonding interaction between  $C_3$  and  $C_4$  in the LUMO of the **M** form accounts for the shorter  $C_3$ — $C_4$  bond in the  ${}^3\pi - \pi^*$  state. The strong antibond between  $C_4$  and  $O_5$  in the LUMO is largely responsible for the stretch in this bond upon electronic excitation.

The excited state results indicate that the hydrogen bond is weakened by the excitation. This change manifests itself in several geometric adjustments. First, the  $O_5$ — $H_9$  distance is lengthened by roughly 0.2 Å. Second, the O—O separation is also increased by a similar amount. Finally, the hydrogen bond is more linear in the ground state.

Now the discrepancies between the various methods of calculating excited state geometries can be addressed. First, for the **M** form, the most notable differences occur in the variables related to the bridging hydrogen atom. The deviation of this hydrogen from the O—O axis is around 35° for the UHF, UMP2, and CIS methods, but is only 14.6° and 17.5° for the two CAS calculations. The  $O_5$ — $H_9$  and the  $O_1$ — $O_5$  separations are also shorter in the CAS calculations, although in this case

TABLE II. Optimized geometries<sup>a</sup> and energies of the first excited triplet state of malonaldehyde in the M configuration.

	4-31G				6-311G**				6-31+G**
	UHF	UMP2	CIS	CAS 1 <sup>b</sup>	CAS 2 <sup>c</sup>	UHF	UMP2	CIS	
O <sub>1</sub> C <sub>2</sub>	1.373	1.399	1.371	1.357	1.363	1.350	1.362	1.351	1.350
C <sub>2</sub> C <sub>3</sub>	1.380	1.376	1.441	1.440	1.441	1.382	1.367	1.461	1.384
C <sub>3</sub> C <sub>4</sub>	1.385	1.392	1.397	1.330	1.356	1.389	1.384	1.424	1.390
C <sub>4</sub> O <sub>5</sub>	1.380	1.396	1.268	1.394	1.381	1.349	1.345	1.217	1.349
C <sub>2</sub> H <sub>6</sub>	1.066	1.080	1.062	1.064	1.064	1.071	1.076	1.067	1.071
C <sub>3</sub> H <sub>7</sub>	1.072	1.086	1.072	1.073	1.072	1.075	1.078	1.076	1.075
C <sub>4</sub> H <sub>8</sub>	1.069	1.084	1.073	1.067	1.068	1.073	1.081	1.087	1.073
O <sub>1</sub> H <sub>9</sub>	0.952	0.982	0.953	0.955	0.954	0.943	0.966	0.943	0.943
O <sub>3</sub> ...H <sub>9</sub>	2.175	2.126	2.089	2.045	2.066	2.185	2.074	2.052	2.205
O <sub>1</sub> ...O <sub>5</sub>	2.862	2.877	2.808	2.782	2.801	2.909	2.850	2.825	2.919
#(O <sub>1</sub> C <sub>2</sub> C <sub>3</sub> )	126.37	126.70	123.51	124.19	124.30	126.84	128.78	122.54	126.76
#(C <sub>2</sub> C <sub>3</sub> C <sub>4</sub> )	127.74	127.49	126.81	127.86	127.38	128.34	126.94	126.20	128.59
#(C <sub>3</sub> C <sub>4</sub> O <sub>5</sub> )	121.74	122.08	121.26	120.25	120.65	122.52	122.80	122.34	122.56
#(C <sub>3</sub> C <sub>2</sub> H <sub>6</sub> )	122.29	122.93	122.63	122.20	122.37	121.06	121.77	121.89	121.14
#(C <sub>4</sub> C <sub>3</sub> H <sub>7</sub> )	115.88	115.86	117.35	117.32	117.35	115.50	116.04	117.34	115.39
#(C <sub>3</sub> C <sub>4</sub> H <sub>8</sub> )	125.39	125.54	119.54	123.93	123.33	124.77	124.80	117.12	124.70
#(C <sub>2</sub> O <sub>1</sub> H <sub>9</sub> )	117.02	113.23	114.80	114.63	114.72	112.79	110.14	110.34	113.53
#(O <sub>5</sub> O <sub>1</sub> H <sub>9</sub> )	36.76	33.28	34.10	14.64	17.54	33.45	30.30	29.01	34.27
E	-265.18117	-265.62666	-265.14006	-265.16071	-265.20583	-265.56544	-266.26700	-265.59780	-265.57495

<sup>a</sup> Distances in Å, angles in degrees, energies in hartree.<sup>b</sup> Using smaller active space, 2 single occupied orbitals and 1 unoccupied orbital.<sup>c</sup> Using larger active space, 2 doubly occupied orbitals, 2 singly occupied orbitals, and 2 unoccupied orbitals.

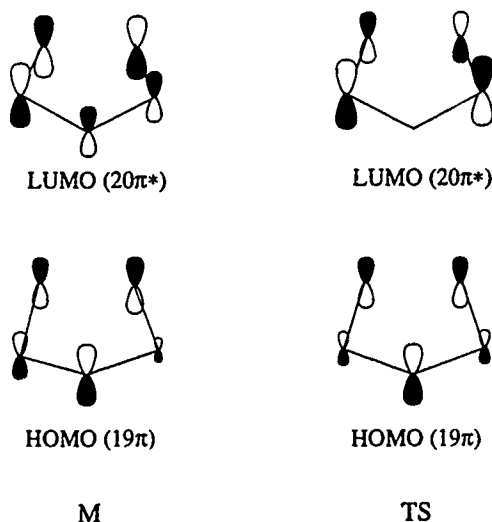


Figure 2. Schematic diagram of the orbital structure of the HOMO and LUMO of the M and TS forms of malonaldehyde, calculated using 6-311G\*\* basis set. The size of each lobe corresponds to the magnitude of the molecular orbital coefficient.

the CIS values are nearly as short. There thus appears to be significantly more hydrogen bonding in the CAS computations, especially with the smaller active space.

Another significant difference concerns the bond lengths around the ring. The carbonyl  $C_4-O_5$  distance in the CIS computation is much shorter than the other methods, and the  $C_3-C_4$  bond is longer than the CAS values. These differences result in much more distinct single and double bond character for  $C_3-C_4$  and  $C_4-O_5$ , respectively, using CIS. Also, the UMP2 bond lengths are generally longer than those from any of the other methods. Similar comparisons are evident from the data available using the larger basis set.

The optimized parameters for the transition state of the transfer are given in Table III. In comparison to the ground state, the results correspond to those discussed for the M form, not surprisingly since the character of the HOMO and LUMO are roughly the same for both configurations. The main variation from the M results is that like bonds are now equivalent due to the inclusion of the  $C_2$  symmetry axis.

Before comparing the excited state TS geometries, the magnitude of the changes expected compared to those for the M structure should be addressed. The TS structure should not change as much when the excited state is optimized due to the  $C_{2v}$  constraint that requires the hydrogen to be equidistant from both oxygens. This condition prevents the hydrogen from having a strong covalent bond to either oxygen atom. Therefore, the stability of the molecule is directly related to both hydrogen bonding interactions and the oxygens cannot move too far apart without destroying these hydrogen bonding interactions. On the other hand, the M configuration does possess a covalent O—H interaction, allowing the hydrogen bond to

TABLE III. Optimized geometries<sup>a</sup> and energies of the first excited triplet state of malonaldehyde in the transition state, TS, configuration.

	4-31G				6-311G**				6-311G**	
	UHF	UMP2	CIS	CAS 1 <sup>b</sup>	CAS 2 <sup>c</sup>	UHF	UMP2	CIS	UHF	UMP2
O <sub>1</sub> C <sub>2</sub>	1.387	1.405	1.309	1.308	1.318	1.356	1.356	1.281	1.356	1.356
C <sub>2</sub> C <sub>3</sub>	1.382	1.383	1.410	1.421	1.417	1.384	1.374	1.415	1.385	1.385
C <sub>3</sub> C <sub>4</sub>	1.382	1.383	1.410	1.421	1.417	1.384	1.374	1.415	1.385	1.385
C <sub>4</sub> O <sub>5</sub>	1.387	1.405	1.309	1.308	1.318	1.356	1.356	1.281	1.356	1.356
C <sub>3</sub> H <sub>6</sub>	1.066	1.082	1.066	1.067	1.066	1.071	1.079	1.075	1.071	1.071
C <sub>3</sub> H <sub>7</sub>	1.069	1.084	1.071	1.071	1.071	1.072	1.077	1.075	1.073	1.073
C <sub>4</sub> H <sub>8</sub>	1.066	1.082	1.066	1.067	1.066	1.071	1.079	1.075	1.071	1.071
O <sub>1</sub> ...H <sub>9</sub>	1.191	1.184	1.219	1.219	1.218	1.168	1.154	1.195	1.169	1.169
O <sub>5</sub> ...H <sub>6</sub>	1.191	1.184	1.219	1.219	1.218	1.168	1.154	1.195	1.169	1.169
O <sub>1</sub> ...O <sub>5</sub>	2.278	2.264	2.363	2.364	2.364	2.261	2.230	2.348	2.262	2.262
θ(O <sub>1</sub> C <sub>2</sub> C <sub>3</sub> )	118.81	118.87	117.29	117.14	117.03	119.13	119.50	117.55	119.01	119.01
θ(C <sub>2</sub> C <sub>3</sub> C <sub>4</sub> )	118.37	117.94	121.29	120.97	121.33	117.36	116.47	120.27	117.51	117.51
θ(C <sub>3</sub> C <sub>4</sub> O <sub>5</sub> )	118.81	118.87	117.29	117.14	117.03	119.13	119.50	117.55	119.01	119.01
θ(C <sub>3</sub> C <sub>2</sub> H <sub>6</sub> )	127.81	127.92	123.39	123.19	124.07	127.19	126.85	122.34	127.21	127.21
θ(C <sub>3</sub> C <sub>3</sub> H <sub>7</sub> )	120.81	121.03	119.36	119.51	119.34	121.32	121.76	119.91	121.24	121.24
θ(C <sub>3</sub> C <sub>4</sub> H <sub>8</sub> )	127.81	127.92	123.39	123.19	124.07	127.19	126.85	122.34	127.21	127.21
θ(O <sub>5</sub> O <sub>1</sub> H <sub>9</sub> )	17.14	17.04	14.20	14.04	13.90	14.53	14.91	10.80	14.67	14.67
E	-265.12837	-265.60094	-265.10050	-265.11463	-265.14808	-265.51065	-266.24535	-265.56320	-265.51912	-265.51912

<sup>a</sup> Distances in Å, angles in degrees, energies in hartree.<sup>b</sup> Using smaller active space, 2 single occupied orbitals, and 1 unoccupied orbital.<sup>c</sup> Using larger active space, 2 doubly occupied orbitals, 2 singly occupied orbitals, and 2 unoccupied orbitals.

be any strength without destroying the main covalent interactions which hold the molecule together, which allows more significant rearrangement.

The main feature of the comparison between methods for the excited TS orientation, is the categorization of the results into two distinct groups. The UHF and UMP2 results are very similar, but markedly different from the other methods. Meanwhile, the CIS and both CAS computations give essentially identical structures; the largest variations are 0.01 Å and 0.3°. Quite remarkably, the O—H and O—O separations are all within 0.001 Å.

The major differences between the two groups of data concern the bonding arrangement around the ring and the O—O—H relationships. The UHF and UMP2 computations both give much longer C—O bonds and slightly shorter C—C bonds than the other methods, indicating more delocalization remains, especially using UHF where all four bonds are nearly equivalent. The O—O separation and the O—H distances are smaller by approximately 0.1 Å and 0.03 Å, respectively, in the UHF and UMP2 computations. This adjustment would result in greater hydrogen bonding. However, this potential increase is counteracted by the linearity of the hydrogen bond. The CIS and CAS results indicate a more linear bonding arrangement by roughly 3°. Therefore, even though there are changes in the TS structures, the overall effect on the strength of the hydrogen bond is minimal, as expected. Once again, the 6-311G\*\* and 6-31+G\*\* data confirm the trends observed using the smaller basis set. The primary difference is that the larger bases produce structures that have more hydrogen bonding. This is evident in the increased linearity of the H-bond, by 3°, and shorter O—O and O—H distances.

The barrier for proton transfer is defined as the difference in energy between the TS and M structures. The barriers for each of the excited state methods discussed are listed in Table IV. Of most interest is that each method has a transfer barrier higher by a factor of approximately two to three than the ground state, except UMP2 which is only slightly above the ground state value. Comparison of the rows illustrates a fairly minor basis set sensitivity. In addition, the barriers correlate well with the relative hydrogen bonding strengths discussed earlier. The greater the amount of hydrogen bonding; the smaller the proton transfer barrier. This relationship also explains why the excited state barriers are so much higher than the ground state values, which have indications of much stronger hydrogen bonding. Of course, this

TABLE IV. Energy barriers (kcal/mol) computed for proton transfer in excited triplet state of malonaldehyde.

	UHF	UMP2	CIS	CAS 1 <sup>a</sup>	CAS 2 <sup>b</sup>
4-31G	33.1	16.1	24.8	28.9	36.2
6-311G**	34.4	13.6	21.7		
6-31+G**	35.0				

<sup>a</sup> Using smaller active space: 2 single occupied orbitals and 1 unoccupied orbital.

<sup>b</sup> Using larger active space: 2 doubly occupied orbitals, 2 singly occupied orbitals, and 2 unoccupied orbitals.

conclusion remains subject to results that might be obtained with better account of electron correlation.

### Summary and Conclusions

The lowest excited electronic state of malonaldehyde is  ${}^3\pi - \pi^*$  resulting from an excitation from the highest occupied to the lowest unoccupied MO. The geometries of both the equilibrium and transition state forms of malonaldehyde reveal a change in character of the bonding interactions as excitation from the  $\pi$  to  $\pi^*$  orbital occurs, independent of the computational method utilized. The excitation produces more delocalization of the bonding around the ring and a larger separation between the oxygens and central hydrogen atoms, resulting in weakened hydrogen bonding.

The proton transfer barrier for the excited state is consistently higher than for the ground state, by a factor of two to three. This result is in accord with the relative strengths of the intramolecular H-bond: a stronger interaction is associated with a low barrier. Also, there is little sensitivity to the basis set chosen. On the other hand, an estimate of the true proton transfer barrier would be premature without more complete treatment of electron correlation with more flexible basis sets.

While the levels of theory discussed here are inadequate to provide a definitive answer as to the particulars of the true geometry, the consistency of certain trends observed with these methods serves to reinforce their validity. For example, the qualitative aspects of the differences between the ground and excited state geometries of malonaldehyde are similar for all the methods investigated. The structure of the excited state contains less hydrogen bonding than the ground state and the resulting barrier to proton transfer is larger.

The quantitative aspects of the geometric parameters studied for the excited state methodologies are somewhat less consistent. The results for the equilibrium configuration (M) vary depending on the method. There are no clear indications as to which method produces the best values, although some UMP2 bond lengths appear long and the CAS H-bond is seemingly too linear. On the other hand, the CIS and CAS results for the transition state configuration (TS) are virtually identical, indicating much less sensitivity to the actual method employed.

### Acknowledgments

This work was supported by the National Institutes of Health (GM29391) and National Science Foundation (CHE-9123824).

### Bibliography

- [1] Th. Arthen-Engeland, T. Bultmann, N. P. Ernstring, M. A. Rodriguez, and W. Thiel, *Chem. Phys.* **163**, 43 (1992).
- [2] J. A. Syage and J. Steadman, *J. Chem. Phys.* **95**, 2497 (1991); J. Steadman and J. A. Syage, *J. Am. Chem. Soc.* **113**, 6786 (1991).
- [3] O. Cheshnovsky and S. Leutwyler, *J. Chem. Phys.* **88**, 4127 (1988).
- [4] K. Fuke, T. Yabe, N. Chiba, T. Kohida, and K. Kaya, *J. Phys. Chem.* **90**, 2309 (1986).

- [5] H. Sekiya, Y. Nagashima, T. Tsuji, Y. Nishimura, A. Mori, and H. Takeshita, *J. Phys. Chem.* **95**, 10311 (1991).
- [6] T. Tsuji, H. Sekiya, Y. Nishimura, R. Mori, and H. Takeshita, *J. Chem. Phys.* **97**, 6032 (1992).
- [7] N. P. Ernsting, Th. Arthen-Engeland, M. A. Rodriguez, and W. Thiel, *J. Chem. Phys.* **97**, 3914 (1992).
- [8] M. F. Hineman, G. A. Brucker, D. F. Kelley, and E. R. Bernstein, *J. Chem. Phys.* **97**, 3341 (1992).
- [9] C. Crepin and A. Tramer, *Chem. Phys.* **156**, 281 (1991).
- [10] T. C. Swinney and D. F. Kelley, *J. Phys. Chem.* **95**, 2430 (1991); D.-J. Jang, G. A. Brucker, and D. F. Kelley, *Ibid* **90**, 6808 (1986).
- [11] S. Roszak, U. Kaldor, D. A. Chapman, and J. J. Kaufman, *J. Phys. Chem.* **96**, 2123 (1992).
- [12] H. Tanaka and K. Nishimoto, *J. Phys. Chem.* **88**, 1052 (1984).
- [13] T. Chiavassa, P. Roubin, L. Pizzala, A. Verlaque, A. Allouche, and F. Marinelli, *J. Phys. Chem.* **96**, 10659 (1992).
- [14] D. W. Firth, K. Beyer, M. A. Dvorak, S. W. Reeve, A. Grushow, and K. R. Leopold, *J. Chem. Phys.* **94**, 9606 (1991).
- [15] S. L. Baughcum, Z. Smith, E. B. Wilson, and R. W. Duerst, *J. Am. Chem. Soc.* **106**, 2260 (1984).
- [16] P. Turner, S. L. Baughcum, S. L. Coy, and Z. Smith, *J. Am. Chem. Soc.* **106**, 2265 (1984).
- [17] S. L. Baughcum, R. W. Duerst, W. F. Rowe, Z. Smith, and E. B. Wilson, *J. Am. Chem. Soc.* **98**, 4021 (1976).
- [18] Z. Latajka and S. Scheiner, *J. Phys. Chem.* **96**, 9764 (1992).
- [19] N. Shida, P. F. Barbara, and J. E. Almlof, *J. Chem. Phys.* **91**, 4061 (1989).
- [20] M. J. Frisch, A. C. Scheiner, and H. F. Schaefer, III, *J. Chem. Phys.* **82**, 4194 (1985).
- [21] Gaussian 90, M. J. Frisch, M. Head-Gordon, G. W. Trucks, J. B. Foresman, H. B. Schlegel, K. Raghavachari, M. A. Robb, J. S. Binkley, C. Gonzalez, D. J. Defrees, D. J. Fox, R. A. Whiteside, R. Seeger, C. F. Melius, J. Baker, R. L. Martin, L. R. Kahn, J. J. P. Stewart, S. Topiol, and J. A. Pople, (Gaussian, Inc., Pittsburgh, PA, 1990).
- [22] B. O. Roos, in *Advances in Chemical Physics*, K. P. Lawley, Ed. (Wiley Interscience, New York, 1987), **69**, 339.
- [23] General Atomic and Molecular Electronic Structure System, M. Dupuis, D. Spangler, and J. J. Wendoloski, National Resource for Computational Chemistry, Lawrence Berkeley Laboratory, Berkeley, CA, 1980, as modified by M. W. Schmidt, North Dakota State University; S. T. Elbert, Iowa State University.
- [24] J. B. Foresman, M. Head-Gordon, J. A. Pople, and M. J. Frisch, *J. Phys. Chem.* **96**, 135 (1992).
- [25] W. J. Hehre, R. Ditchfield, and J. A. Pople, *J. Chem. Phys.* **56**, 2257 (1972).
- [26] R. Krishnan, J. S. Binkley, R. Seeger, and J. A. Pople, *J. Chem. Phys.* **72**, 650 (1980).
- [27] A. D. McLean and G. S. Chandler, *J. Chem. Phys.* **72**, 5639 (1980).
- [28] T. Clark, J. Chandrasekhar, G. W. Spitznagel, and P. v. R. Schleyer, *J. Comput. Chem.* **4**, 294 (1983).

Received May 28, 1993

# Electric Multipole Moment Integrals Evaluated over Slater-Type Orbitals

XUEHE ZHENG and MICHAEL C. ZERNER

*Quantum Theory Project, University of Florida, Gainesville, Florida 32611*

## Abstract

We study integrals that arise in the calculation of electric multipole moments. A computational approach is developed to evaluate these integrals in an STO basis set in a straightforward, yet somewhat untraditional fashion. The computation involves a simple three-step procedure: translation of all Cartesian parts to one center, local evaluation, and a single one-sided rotation into the molecular frame. Some assessment on this method is discussed. An implementation of the method is presented in this paper to compute overlap, dipole, quadrupole, octopole, and hexadecapole moment integrals in a basis set that includes up to  $g$  orbitals. © 1993 John Wiley & Sons, Inc.

## Introduction

Electric multipole moments have been of both experimental and theoretical interest for some time. While direct measurements are usually limited to dipole and quadrupole moments [1], molecular electronic structure theory has lately made investigations on electric moments exceeding tenth order [2,3]. Due to experimental limitations, studies of higher moments are not aimed at confirmation of measured result; rather they are driven by the needs of recent advances in molecular dynamics [4], computation of high order polarizabilities [5–7], molecular optical and magnetic properties [8–10], intermolecular interactions in terms of the London series [7,10–15], and quantum mechanical solvent effect in the formalism of the self-consistent reaction field theory [16–18].

The challenge here, then, is to calculate electric moments useful to develop some of the above-mentioned fields. This challenge is currently being addressed utilizing methods based on electronic structure theory of varying sophistication. A molecular orbital description can often give molecular dipole moments with greater assurance than it can give the quadrupole moments. For moments higher than quadrupole we know that basis set choice is very important [19], for high moments are very sensitive to electronic distributions in the outer molecular region, which can only be better described by extended basis sets. Basis set effects are believed to be more important than correlation on these high moments [20,3]. On the other hand, most multipole-moment studies are carried out using Gaussian basis sets; in fact, we are not aware of any recent Slater-type orbital (STO) basis set calculations on moments higher than quadrupole for polyatomic molecules (we note an early paper [21]). The drawback of Gaussian basis sets is apparent here: High moments expansion of electrostatic interactions is a good approximation only at long range,



where the Gaussian functions are known to fall too sharply. For this reason there have even been *ab initio* calculations using Gaussian basis sets that are then fitted to STOs to study long-range interactions [22].

The introduction of Gaussian basis sets into molecular orbital theory is to facilitate integration. Multipole moment integrals are conveniently worked out in Gaussian basis sets by Matsuoka [23], Augspurger and Dykstra [24], and Mikkelsen et al. [17]. A study of these moments using numerical techniques can be found in the calculation of Sundholm and Pyykko [3]. High moment integrals over STO basis sets are not well studied, although they would not appear to be particularly intractable. Originally molecular orbital theory of polyatomic molecules was formulated using STO basis sets and a series of now classical work on STO integrals was carried out by Mulliken et al. [25], Roothaan [26], Ruedenberg [27], and Ruedenberg et al. [28]. Local dipole moment integrals were formulated by Hamilton [29] using *C* functions. Quadrupole moment integrals were included in the study by Wahl et al. [30], and implemented by Bagus et al. [31] for linear molecules. A specific and detailed treatment of dipole moment integrals for polyatomic molecules was presented by Rein et al. [32], which was extended to handle quadrupole moment integrals by Rabinowitz and Rein [33], and octopole moment integrals by Swisler and Rein [21]. Higher-order moment integrals have not been studied in detail in extended STO basis sets for polyatomic molecules.

Electric moment integrals are of one-electron and, at most, three-center. A method of evaluating integrals of this nature is generally outlined by Harris and Michels [34], Steinborn and Ruedenberg [35], and Guseinov and Sadichov [36]. These traditional approaches all invoke translational, rotational, and combinational properties of spherical harmonics of various kinds that are nicely examined in the works of Steinborn and Ruedenberg [37] and Steinborn [38]. This paper presents a novel method of evaluating multipole moment integrals over STO basis sets. We will show explicit formulas for up to hexadecapole moment in a basis set that includes up to *g* orbitals. The method, although somewhat tedious, is completely generalizable and results in very fast computer code.

### Preliminary Considerations

#### *Cartesians and Tesseral Harmonics*

An STO is usually given by

$$\chi_{n,l,m} = \left[ \frac{(2\zeta)^{2n+1}}{(2n)!} \right]^{1/2} r^{n-1} e^{-\zeta r} \bar{Y}_l^m(\theta, \phi), \quad (1a)$$

where  $\bar{Y}_l^m(\theta, \phi)$  are the normalized real spherical harmonics [39] and the square root factor is the normalization constant for the radial component. We regroup these terms as

$$\chi_{n,l,m} = \left[ \frac{(2\zeta)^{2n+1}}{(2n)!} \right]^{1/2} r^{n-l-1} e^{-\zeta r} [r^l \bar{Y}_l^m(\theta, \phi)], \quad (1b)$$

which allows a convenient representation of the angular part in terms of Cartesian components. The quantities in the second bracket are known as Tesseral harmonics [40], which we note as

$$l_{\bar{m}} = [r' \bar{Y}^m(\theta, \phi)],$$

where  $l$  has its usual meaning ( $l = 0, 1, 2, 3 \dots$  for  $s, p, d, f, \dots$ ) and  $\bar{m}$  enumerates the real components obtained from adding  $Y_l^m \pm Y_l^{-m}$ .

We define a product of the powers of  $x$ ,  $y$ , and  $z$  to be a Cartesian,

$$(i, j, k) = x^i y^j z^k, \quad (2)$$

where  $i, j$ , and  $k$  are integers. In this notation the normalized Tesseral harmonics are written below for up to  $g$  type (we follow Pauling and Wilson [41]):

*s Harmonic:*

$$s = \sqrt{(1/4\pi)}(0,0,0).$$

*p Harmonics:*

$$p_x = \sqrt{(3/4\pi)}(1,0,0), \quad p_y = \sqrt{(3/4\pi)}(0,1,0), \quad p_z = \sqrt{(3/4\pi)}(0,0,1).$$

*d Harmonics:*

$$d_{z^2} = \sqrt{(5/16\pi)}[2(0,0,2) - (2,0,0) - (0,2,0)],$$

$$d_{x^2-y^2} = \sqrt{(15/16\pi)}[(2,0,0) - (0,2,0)],$$

$$d_{xy} = \sqrt{(15/4\pi)}(1,1,0), \quad d_{xz} = \sqrt{(15/4\pi)}(1,0,1), \quad d_{yz} = \sqrt{(15/4\pi)}(0,1,1).$$

*f Harmonics:*

$$f_{z^3} = \sqrt{(63/16\pi)}[\frac{2}{3}(0,0,3) - (2,0,1) - (0,2,1)],$$

$$f_{xz^2} = \sqrt{(21/32\pi)}[4(1,0,2) - (3,0,0) - (1,2,0)],$$

$$f_{yz^2} = \sqrt{(21/32\pi)}[4(0,1,2) - (2,1,0) - (0,3,0)],$$

$$f_{z(x^2-y^2)} = \sqrt{(105/16\pi)}[(2,0,1) - (0,2,1)], \quad f_{xyz} = \sqrt{(105/4\pi)}(1,1,1),$$

$$f_{x^3-3xy^2} = \sqrt{(35/32\pi)}[(3,0,0) - 3(1,2,0)],$$

$$f_{3x^2y-y^3} = \sqrt{(35/32\pi)}[3(2,1,0) - (0,3,0)].$$

*g Harmonics:*

$$g_{z^4} = (9/16\sqrt{\pi})[(4,0,0) + 2(2,2,0) + (0,4,0)$$

$$- 8(2,0,2) - 8(0,2,2) + \frac{8}{3}(0,0,4)],$$

$$g_{xz^3} = \frac{9}{8}\sqrt{(10/\pi)}[\frac{4}{3}(1,0,3) - (3,0,1) - (1,2,1)],$$

$$g_{yz^3} = \frac{9}{8}\sqrt{(10/\pi)}[\frac{4}{3}(0,1,3) - (2,1,1) - (0,3,1)],$$

$$g_{z^2(x^2-y^2)} = \frac{3}{8}\sqrt{(5/\pi)}[-(4,0,0) + (0,4,0) + 6(2,0,2) - 6(0,2,2)],$$

$$g_{xyz^2} = \frac{3}{4}\sqrt{(5/\pi)}[6(1,1,2) - (3,1,0) - (1,3,0)],$$

$$g_{z(x^3-3xy^2)} = \frac{3}{8}\sqrt{(70/\pi)}[(3,0,1) - 3(1,2,1)],$$

$$g_{z(3x^2y-y^3)} = \frac{3}{8}\sqrt{(70/\pi)}[3(2,1,1) - (0,3,1)],$$

$$g_{x^2y^2} = \frac{3}{16}\sqrt{(35/\pi)}[(4,0,0) - 6(2,2,0) + (0,4,0)],$$

$$g_{xy(x^2-y^2)} = \frac{3}{4}\sqrt{(35/\pi)}[(3,1,0) - (1,3,0)].$$

### The Multipole Moment Operator

There has been two ways of defining multipole moments in the literature. The earlier, and perhaps, simpler, definition (see, for example, Ref. [42]) is

$$M_{l,m} = r^l \left[ \frac{4\pi}{2(l+1)} \right]^{1/2} Y_{l,m}(\theta, \phi), \quad (3)$$

where the  $Y_{l,m}(\theta, \phi)$  are the spherical harmonics. An alternative definition, following Buckingham [43], is

monopole	$q = 1$ ,	
dipole	$\mu_\alpha = r_\alpha$ ,	
quadrupole	$\theta_{\alpha\beta} = \frac{1}{2}(3r_\alpha r_\beta - r^2 \delta_{\alpha\beta})$ ,	(4)
octopole	$\Omega_{\alpha\beta\gamma} = \frac{1}{2}(5r_\alpha r_\beta r_\gamma - r_\alpha r_\beta^2 \delta_{\beta\gamma} - r_\beta r_\delta^2 \delta_{\gamma\alpha} - r_\gamma r_\delta^2 \delta_{\alpha\beta})$ ,	
etc.		

where we omit all charges. The tensor operators of the first several moments in Eq. (4) take the following form:

*Dipole:*

$$\mu_x = (1,0,0), \quad \mu_y = (0,1,0), \quad \mu_z = (0,0,1).$$

*Quadrupole:*

$$\begin{aligned} Q_{xx} &= \frac{1}{2}[2(2,0,0) - (0,2,0) - (0,0,2)], \\ Q_{yy} &= \frac{1}{2}[2(0,2,0) - (2,0,0) - (0,0,2)], \\ Q_{zz} &= \frac{1}{2}[2(0,0,2) - (2,0,0) - (0,2,0)], \quad Q_{xy} = \frac{3}{2}(1,1,0), \\ Q_{xz} &= \frac{3}{2}(1,0,1), \quad Q_{yz} = \frac{3}{2}(0,1,1). \end{aligned}$$

*Octopole:*

$$\begin{aligned} \Omega_{xxx} &= \frac{1}{2}[2(3,0,0) - 3(1,2,0) - 3(1,0,2)], \\ \Omega_{yyy} &= \frac{1}{2}[2(0,3,0) - 3(2,1,0) - 3(0,1,2)], \\ \Omega_{zzz} &= \frac{1}{2}[2(0,0,3) - 3(2,0,1) - 3(0,2,1)], \\ \Omega_{xxy} &= \frac{1}{2}[4(2,1,0) - (0,3,0) - (0,1,2)], \\ \Omega_{xxz} &= \frac{1}{2}[4(2,0,1) - (0,2,1) - (0,0,3)], \\ \Omega_{xyy} &= \frac{1}{2}[4(1,2,0) - (3,0,0) - (1,0,2)], \\ \Omega_{xzz} &= \frac{5}{2}(1,1,1) \quad \Omega_{xzz} = \frac{1}{2}[4(1,0,2) - (3,0,0) - (1,2,0)], \\ \Omega_{yyz} &= \frac{1}{2}[4(0,2,1) - (2,0,1) - (0,0,3)], \\ \Omega_{yzz} &= \frac{1}{2}[4(0,1,2) - (2,1,0) - (0,3,0)], \end{aligned}$$

*Hexadecapole:*

$$\begin{aligned}
\Gamma_{xxxx} &= (4,0,0) - 3[(2,2,0) + (2,0,2)] + \frac{3}{8}[(0,0,4) + (0,4,0)] + \frac{3}{4}(0,2,2), \\
\Gamma_{xxxy} &= \frac{5}{2}(3,1,0) - \frac{15}{8}[(1,3,0) + (1,1,2)], \\
\Gamma_{xxxz} &= \frac{5}{2}(3,0,1) - \frac{15}{8}[(1,2,1) + (1,0,3)], \\
\Gamma_{xyyy} &= \frac{3}{8}[9(2,2,0) - (2,0,2) - (0,2,2)] - \frac{1}{2}[(4,0,0) + (0,4,0)] + \frac{1}{8}(0,0,4), \\
\Gamma_{xyyz} &= \frac{3}{8}(2,1,1) - \frac{5}{8}[(0,1,3) + (0,3,1)], \\
\Gamma_{xzzz} &= \frac{3}{8}[9(2,0,2) - (2,2,0) - (0,2,2)] - \frac{1}{2}[(0,0,4) + (4,0,0)] + \frac{1}{8}(0,4,0), \\
\Gamma_{xyxx} &= \frac{5}{2}(1,3,0) - \frac{15}{8}[(1,1,2) + (3,1,0)], \\
\Gamma_{xyyz} &= \frac{15}{4}(1,2,1) - \frac{5}{8}[(1,0,3) + (3,0,1)], \\
\Gamma_{xzzz} &= \frac{15}{4}(1,1,2) - \frac{5}{8}[(1,3,0) + (3,1,0)], \\
\Gamma_{yzzz} &= \frac{5}{2}(1,0,3) - \frac{15}{8}[(1,2,1) + (3,0,1)], \\
\Gamma_{yyyy} &= (0,4,0) + \frac{3}{8}[(0,0,4) + (4,0,0)] - 3[(0,2,2) + (2,2,0)] + \frac{3}{4}(2,0,2), \\
\Gamma_{yyyz} &= \frac{5}{2}(0,3,1) - \frac{15}{8}[(0,1,3) + (2,1,1)], \\
\Gamma_{yzzz} &= \frac{3}{8}[9(0,2,2) - (2,0,2) - (2,2,0)] - \frac{1}{2}[(0,0,4) + (0,4,0)] + \frac{1}{8}(4,0,0), \\
\Gamma_{yzzz} &= \frac{5}{2}(0,1,3) - \frac{15}{8}[(0,3,1) + (2,1,1)], \\
\Gamma_{zzzz} &= (0,0,4) + \frac{3}{4}(2,2,0) + \frac{3}{8}[(0,4,0) + (4,0,0)] - 3[(2,0,2) + (0,2,2)].
\end{aligned}$$

Following Rabinowitz and Rein [33], we can define a primitive multipole moment operator as

$$M_{i,j,k} = x^i y^j z^k = (i, j, k), \quad (5)$$

with its expectation values giving all the integrals necessary to compute the multipole moment tensors defined above. The computation of the nuclear contribution to the multipole moments is straightforward, simply replacing the electronic coordinates  $x, y, z$  in  $M_{i,j,k}$  with the nuclear ones  $X, Y, Z$ . We therefore consider only the electronic contribution in this paper.

*Coordinate Systems and the Rotational Matrix*

The STO basis functions are generally associated with centers (usually on nuclei) denoted as  $A, B, \dots$ . The center of a primitive moment operator of Eq. (5) is denoted as  $O$ . Lower-case subscripts  $a, b$ , and  $o$  specify the vector components measured from the centers  $A, B$ , and  $O$ , respectively. Unlike Cartesian Gaussians, STO two-center integrals are generally evaluated over a local system (see Fig. 1) with the axis between the two centers defining the local  $Z, Z_a$ , and  $Z_b$  axes, with the local  $X, X_a, X_b$  and  $Y, Y_a, Y_b$  axes parallel. Here the upper-case notations  $X, Y, Z$  represent axes in the local system. The  $Z_a$  and  $Z_b$  axes are either pointing at each other, or are directed in the same direction. We adapt the latter, as shown in Figure 1.

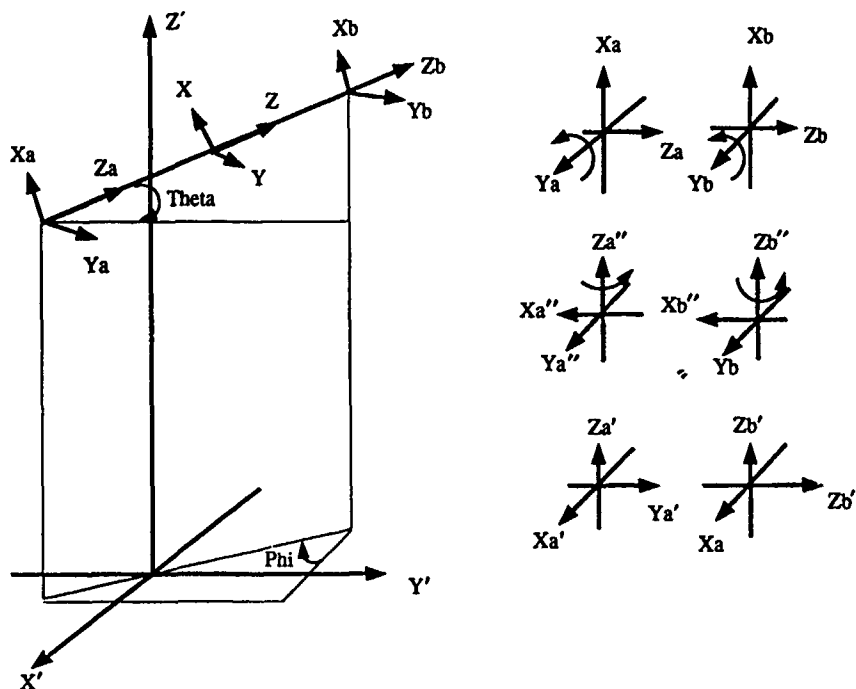


Figure 1. Rotation from Ellipsoidal Coordinate to Molecular Frame.

With the origin of the Cartesian coordinate system  $[X, Y, Z]$  placed halfway between the two basis function centers  $A$  and  $B$ , the local system described above is used to define a prolated spheroidal, or ellipsoidal coordinate system focused on  $A$  and  $B$ , respectively [35]. Adapting the definition and notations of reference [35], we list some important relations below for an ellipsoidal coordinate system,

$$\begin{aligned}
 r_a &= (R/2)(\xi + \eta), & r_b &= (R/2)(\xi - \eta), \\
 x_a &= x_b = (R/2)\sqrt{(\xi^2 - 1)(1 - \eta^2)}\cos\phi, \\
 y_a &= y_b = (R/2)\sqrt{(\xi^2 - 1)(1 - \eta^2)}\sin\phi, \\
 z_a &= (R/2)(1 + \xi\eta), & z_b &= (R/2)(1 - \xi\eta), \\
 d\tau &= (R^3/8)(\xi^2 - \eta^2) d\xi d\eta d\phi.
 \end{aligned} \tag{6}$$

The integrals evaluated in a local ellipsoidal coordinate system then need to be back-transformed into a laboratory, or molecular-based coordinate system, which we define to be the molecular frame  $[x', y', z']$ . The rotation necessary for this transformation is based on the directional cosines (see Fig. 1),

$$\begin{aligned}
 \cos\theta &= \Delta z'/R, \\
 \cos\phi &= \Delta y'/\sqrt{\Delta x'^2 + \Delta y'^2},
 \end{aligned} \tag{7}$$

and the rotation matrix  $R(\theta, \phi)$  can be obtained in two steps:

(i) Rotate about the  $y$  axis to align the  $z$  axis:  $R_1(\theta)$ ,

$$\begin{pmatrix} X'' \\ Y'' \\ Z'' \end{pmatrix} = R_1(\theta) \begin{pmatrix} X \\ Y \\ Z \end{pmatrix} = \begin{pmatrix} \cos \theta & 0 & \sin \theta \\ 0 & 1 & 0 \\ -\sin \theta & 0 & \cos \theta \end{pmatrix} \begin{pmatrix} X \\ Y \\ Z \end{pmatrix}. \quad (8)$$

(ii) Rotate about the  $z''$  axis to align the  $x''$  and  $y''$  axes:  $R_2(\phi)$ ,

$$\begin{pmatrix} X' \\ Y' \\ Z' \end{pmatrix} = R_2(\phi) \begin{pmatrix} X'' \\ Y'' \\ Z'' \end{pmatrix} = \begin{pmatrix} \cos \phi & -\sin \phi & 0 \\ \sin \phi & \cos \phi & 0 \\ 0 & 0 & 1 \end{pmatrix} \begin{pmatrix} X'' \\ Y'' \\ Z'' \end{pmatrix}. \quad (9)$$

The final rotation matrix based on Eqs. (8) and (9) is therefore

$$R(\theta, \phi) = R_2(\phi)R_1(\theta) = \begin{pmatrix} \cos \theta \cos \phi & -\sin \phi & \sin \theta \cos \phi \\ \cos \theta \sin \phi & \cos \phi & \sin \theta \sin \phi \\ -\sin \theta & 0 & \cos \theta \end{pmatrix}. \quad (10)$$

### Method

#### Translation of Centers

The most common way to proceed from here is, assuming the moment definition of Eq. (3), to evaluate the integrals such as

$$I = \int d\Omega Y_{l''}^{m''}(\theta_a, \phi_a) Y_{l'''}^{m'''}(\theta_o, \phi_o) Y_{l'''}^{m'''}(\theta_b, \phi_b) \quad (11a)$$

and to translate the center  $O$  to the center  $A$  or  $B$  with the lowest  $l$  value, say, center  $B$  with  $l''$ . Making use of the translational property of spherical harmonics [44] and Gaunt coefficients [45], this yields an integral with sigma ( $m = 0$ ), pi ( $m = 1$ ), delta ( $m = 2$ ), phi ( $m = 3$ ), etc., components. The maximum  $m$  component required is then the lesser of  $l'' + l'''$  and  $l'$ , i.e.,

$$I = \sum_{m=0}^{\min(l''+l''', l')} R_m I_m = R_\sigma I_\sigma + (R_\pi + R_{\pi'}) I_\pi + (R_\delta + R_\delta) I_\delta + \dots \quad (11b)$$

where the  $R_m$ 's are the factors due to rotating the integral back to the molecular frame, and the  $I_m$ 's are the appropriate integrals evaluated in the local frame. Note that  $R_m = R_{m(A)m(B)}$ —each center must be rotated, and there are two pi components, two delta components, etc.

In this study we will translate the angular components of both the operator and the orbital centered on  $A$  to  $B$ . By doing so, center  $A$  will only have a sigma component and Eq. (11b) will have the simple appearance of

$$I = R_{\sigma(B)} \tilde{I}_\sigma. \quad (11c)$$

We will show that the evaluation of  $\tilde{I}_\sigma$  and the rotation  $R_{\sigma(A)} R_{\sigma(B)} = R_{\sigma(B)}$  are very simple. The use of Eq. (11c) rather than Eq. (11b), and its simplicity, are at the heart of this work.

Considering a general laboratory coordinate system  $[x, y, z]$  and a particular one  $[x_a, y_a, z_a]$  centered at  $A(a_x, a_y, a_z)$ , we have

$$\begin{aligned}x_a &= x - a_x, \\y_a &= y - a_y, \\z_a &= z - a_z.\end{aligned}\quad (12)$$

To translate the coordinate system  $[x_a, y_a, z_a]$  to another one  $[x_b, y_b, z_b]$  centered at  $B(b_x, b_y, b_z)$ , we write

$$\begin{aligned}x_a &= x_b + (b_x - a_x) = x_b + \bar{b}a_x, \\y_a &= y_b + (b_y - a_y) = y_b + \bar{b}a_y, \\z_a &= z_b + (b_z - a_z) = z_b + \bar{b}a_z.\end{aligned}\quad (13)$$

An arbitrary Cartesian defined in the previous section is therefore translated from center  $A$  to center  $B$  by way of

$$\begin{aligned}x_a^i y_a^j z_a^k &= \sum_{r=0}^i \binom{i}{r} \bar{b}a_x^{i-r} x_b^r \sum_{s=0}^j \binom{j}{s} \bar{b}a_y^{j-s} y_b^s \sum_{t=0}^k \binom{k}{t} \bar{b}a_z^{k-t} z_b^t \\&= \sum_{\substack{(i,j,k) \\ (r,s,t)=(0,0,0)}} C_{r,s,t}(\bar{b}a_x, \bar{b}a_y, \bar{b}a_z) x_b^r y_b^s z_b^t.\end{aligned}\quad (14)$$

The translations in terms of Eq. (14) enable a multipole moment integral, apart from a normalization factor, to assume the following form,

$$\begin{aligned}\langle M_{l,m,n} \rangle &= \langle r_a^{n_a-l_a-1} x_a^i y_a^j z_a^k e^{-\zeta_a r_a} | x_o^l y_o^m z_o^n | r_b^{n_b-l_b-1} x_b^e y_b^f z_b^g e^{-\zeta_b r_b} \rangle \\&= \sum_{\substack{(i,j,k) \\ (r,s,t)=(0,0,0)}} C_{r,s,t}(\bar{b}a_x, \bar{b}a_y, \bar{b}a_z) \sum_{\substack{(l,m,n) \\ (u,v,w)=(0,0,0)}} C_{u,v,w}(\bar{b}o_x, \bar{b}o_y, \bar{b}o_z) \\&\quad \times \langle r_a^{n_a-l_a-1} e^{-\zeta_a r_a} | r_b^{n_b-l_b-1} x_b^{e+r+u} y_b^{f+s+v} z_b^g e^{-\zeta_b r_b} \rangle,\end{aligned}\quad (15)$$

where center  $O(O_x, O_y, O_z)$  places the origin from which the multipole moment integral is evaluated.

In this development it is clear that a moment integral is a combination of overlap integrals, which, in terms of Eq. (15), are always between an  $s$  orbital and a higher-order orbital. The translation to achieve this is straightforward. However, the sixfold sum that appears in Eq. (15), if directly implemented, is computationally inefficient, as was first experienced by Taketa et al. in their work on Gaussian integrals [46]. For this reason we translate an STO centered at  $A(x_a, y_a, z_a)$  and the moment operator centered on  $O(x_o, y_o, z_o)$  separately onto the center  $B(x_b, y_b, z_b)$  using two sets of predetermined formulas. With the convention that all left-hand quantities in a formula are centered on  $A$ , and those on the right-hand side are centered on  $B$ , we list these formulas as follows:

*Master Formulas for STO Translation:*

$$l_m^A = \sum_{\mu} g_{\mu}^A(\bar{b}a_x, \bar{b}a_y, \bar{b}a_z)(i, j, k)_{\mu}^B,$$

$$\begin{aligned}
p_x &= \sqrt{3/4\pi} [\bar{b}a_x(0,0,0) + (1,0,0)], \\
p_y &= \sqrt{3/4\pi} [\bar{b}a_y(0,0,0) + (0,1,0)], \\
p_z &= \sqrt{3/4\pi} [\bar{b}a_z(0,0,0) + (0,0,1)], \\
d_{z^2} &= \sqrt{5/16\pi} [(2\bar{b}a_z^2 - \bar{b}a_x^2 - \bar{b}a_y^2)(0,0,0) - 2\bar{b}a_x(1,0,0) - 2\bar{b}a_y(0,1,0) \\
&\quad + 4\bar{b}a_z(0,0,1) - (2,0,0) - (0,2,0) + 2(0,0,2)], \\
d_{x^2-y^2} &= \sqrt{15/16\pi} [\bar{b}a_x^2 - \bar{b}a_y^2](0,0,0) - 2\bar{b}a_y(0,1,0) \\
&\quad + 2\bar{b}a_x(1,0,0) + (2,0,0) - (0,2,0)], \\
d_{xy} &= \sqrt{15/4\pi} [\bar{b}a_x\bar{b}a_y(0,0,0) + \bar{b}a_y(1,0,0) + \bar{b}a_x(0,1,0) + (1,1,0)], \\
d_{xz} &= \sqrt{15/4\pi} [\bar{b}a_x\bar{b}a_z(0,0,0) + \bar{b}a_z(1,0,0) + \bar{b}a_x(0,0,1) + (1,0,1)], \\
d_{yz} &= \sqrt{15/4\pi} [\bar{b}a_y\bar{b}a_z(0,0,0) + \bar{b}a_z(0,1,0) + \bar{b}a_y(0,0,1) + (0,1,1)], \\
f_{z^3} &= \sqrt{7/16\pi} [(2\bar{b}a_z^3 - 3\bar{b}a_x^2\bar{b}a_z - 3\bar{b}a_y^2\bar{b}a_z)(0,0,0) - 6\bar{b}a_x\bar{b}a_z(1,0,0) \\
&\quad - 6\bar{b}a_y\bar{b}a_z(0,1,0) + (6\bar{b}a_z^2 - 3\bar{b}a_x^2 - 3\bar{b}a_y^2)(0,0,1) \\
&\quad - 3\bar{b}a_z(2,0,0) - 6\bar{b}a_x(1,0,1) - 3\bar{b}a_z(0,2,0) - 6\bar{b}a_y(0,1,1) \\
&\quad + 6\bar{b}a_z(0,0,2) - 3(2,0,1) - 3(0,2,1) + 2(0,0,3)], \\
f_{xz^2} &= \sqrt{21/32\pi} [(4\bar{b}a_x\bar{b}a_z^2 - \bar{b}a_x^3 - \bar{b}a_y\bar{b}a_z^2)(0,0,0) \\
&\quad + (4\bar{b}a_z^2 - 3\bar{b}a_x^2 - \bar{b}a_y^2)(1,0,0) - 2\bar{b}a_x\bar{b}a_y(0,1,0) \\
&\quad + 8\bar{b}a_x\bar{b}a_z(0,0,1) - 3\bar{b}a_x(2,0,0) - 2\bar{b}a_y(1,1,0) - \bar{b}a_x(0,2,0) \\
&\quad + 8\bar{b}a_z(1,0,1) + 4\bar{b}a_x(0,0,2) - (3,0,0) - (1,2,0) + 4(1,0,2)], \\
f_{yz^2} &= \sqrt{21/32\pi} [(4\bar{b}a_y\bar{b}a_z^2 - \bar{b}a_x^2\bar{b}a_y - \bar{b}a_y^3)(0,0,0) - 2\bar{b}a_x\bar{b}a_y(1,0,0) \\
&\quad + 8\bar{b}a_y\bar{b}a_z(0,0,1) + (4\bar{b}a_z^2 - \bar{b}a_x^2 - 3\bar{b}a_y^2)(0,1,0) \\
&\quad - \bar{b}a_y(2,0,0) - 2\bar{b}a_x(1,1,0) - 3\bar{b}a_y(0,2,0) + 8\bar{b}a_z(0,1,1) \\
&\quad + 4\bar{b}a_y(0,0,2) - (2,1,0) - (0,3,0) + 4(0,1,2)], \\
f_{z(\lambda^2-\nu^2)} &= \sqrt{105/16\pi} [\bar{b}a_z(\bar{b}a_x^2 - \bar{b}a_y^2)(0,0,0) + 2\bar{b}a_x\bar{b}a_z(1,0,0) \\
&\quad - 2\bar{b}a_y\bar{b}a_z(0,1,0) + (\bar{b}a_x^2 - \bar{b}a_y^2)(0,0,1) \\
&\quad + \bar{b}a_z(2,0,0) + 2\bar{b}a_x(1,0,1) - \bar{b}a_z(0,2,0) \\
&\quad - 2\bar{b}a_y(0,1,1) + (2,0,1) - (0,2,1)], \\
f_{xyz} &= \sqrt{105/4\pi} [\bar{b}a_x\bar{b}a_y\bar{b}a_z(0,0,0) + \bar{b}a_y\bar{b}a_z(1,0,0) + \bar{b}a_x\bar{b}a_z(0,1,0) \\
&\quad + \bar{b}a_x\bar{b}a_y(0,0,1) + \bar{b}a_z(1,1,0) + \bar{b}a_y(1,0,1) \\
&\quad + \bar{b}a_x(0,1,1) + (1,1,1)], \\
f_{\lambda^3-3\lambda\nu^2} &= \sqrt{35/32\pi} [(\bar{b}a_x^3 - \bar{b}a_x\bar{b}a_y^2)(0,0,0) + 3(\bar{b}a_x^2 - \bar{b}a_y^2)(1,0,0) \\
&\quad - 6\bar{b}a_x\bar{b}a_y(0,1,0) + 3\bar{b}a_x(2,0,0) - 6\bar{b}a_y(1,1,0) \\
&\quad - 3\bar{b}a_x(0,2,0) + (3,0,0) - 3(1,2,0)],
\end{aligned}$$



$$f_{3\lambda^2, y^{-3}} = \sqrt{(35/32\pi)} [(3\bar{b}a_x^2\bar{b}a_y - \bar{b}a_y^3)(0,0,0) + 6\bar{b}a_x\bar{b}a_y(1,0,0) \\ + 3(\bar{b}a_x^2 - \bar{b}a_y^2)(0,1,0) + 3\bar{b}a_y(2,0,0) + 6\bar{b}a_x(1,1,0) \\ - 3\bar{b}a_y(0,2,0) + 3(2,1,0) - (0,3,0)],$$

$$g_{z^4} = (3/16\sqrt{\pi}) \{ (3\bar{b}a_x^4 + 6\bar{b}a_x^2\bar{b}a_y^2 + 3\bar{b}a_y^4 - 24\bar{b}a_x^2\bar{b}a_z^2 + 8\bar{b}a_z^4 \\ - 24\bar{b}a_x^2\bar{b}a_z^2)(0,0,0) + (12\bar{b}a_x^3 + 2\bar{b}a_x\bar{b}a_z^2 - 48\bar{b}a_x\bar{b}a_z^2)(1,0,0) \\ + 12(\bar{b}a_x^2\bar{b}a_y + \bar{b}a_y^3 - 4\bar{b}a_y\bar{b}a_z^2)(0,1,0) + 16(2\bar{b}a_z^3 - 3\bar{b}a_x^2\bar{b}a_z \\ - 3\bar{b}a_y^2\bar{b}a_z)(0,0,1) + 6(3\bar{b}a_x^2 + \bar{b}a_y^2 - 4\bar{b}a_z^2)(2,0,0) \\ + 24\bar{b}a_x\bar{b}a_y(1,1,0) - 96\bar{b}a_x\bar{b}a_z(1,0,1) + 6(\bar{b}a_x^2 + 3\bar{b}a_y^2 \\ - 4\bar{b}a_z^2)(0,2,0) - 96\bar{b}a_y\bar{b}a_z(0,1,1) - 24(\bar{b}a_x^2 + \bar{b}a_y^2 \\ - 2\bar{b}a_z^2)(0,0,2) + 12\bar{b}a_x[(3,0,0) + (1,2,0) + 4(1,0,2)] \\ + 12\bar{b}a_y[(2,1,0) + (0,3,0) - 4(0,1,2)] - 16\bar{b}a_z[3(2,0,1) \\ + 3(0,2,1) - 2(0,0,3)] + 3(4,0,0) + 6(2,2,0) \\ - 24(2,0,2) + 3(0,4,0) - 24(0,2,2) + 8(0,0,4) \},$$

$$g_{xz^3} = \frac{3}{8}\sqrt{(10/\pi)} \{ (4\bar{b}a_x\bar{b}a_z^3 - 3\bar{b}a_x^3\bar{b}a_z - 3\bar{b}a_x\bar{b}a_z^2\bar{b}a_z)(0,0,0) \\ + (4\bar{b}a_z^3 - 9\bar{b}a_x^2\bar{b}a_z - 3\bar{b}a_y^2\bar{b}a_z)(1,0,0) \\ - 6\bar{b}a_x\bar{b}a_y\bar{b}a_z(0,1,0) + 3(4\bar{b}a_x\bar{b}a_z^2 - \bar{b}a_x^3 - \bar{b}a_y\bar{b}a_z^2)(0,0,1) \\ + 3(4\bar{b}a_z^2 - 3\bar{b}a_x^2 - \bar{b}a_y^2)(1,0,1) - 3\bar{b}a_x\bar{b}a_z[3(2,0,0) \\ + (0,2,0) - 4(0,0,2)] - 6\bar{b}a_y\bar{b}a_z(1,1,0) - 6\bar{b}a_x\bar{b}a_y(0,1,1) \\ + 3\bar{b}a_z[4(1,0,2) - (3,0,0) - (1,2,0)] + \bar{b}a_x[4(0,0,3) \\ - 3(0,2,1) - 9(2,0,1)] - 6\bar{b}a_y(1,1,1) - 3(3,0,1) \\ - 3(1,2,1) + 4(1,0,3) \},$$

$$g_{yz^3} = \frac{3}{8}\sqrt{(10/\pi)} \{ (4\bar{b}a_y\bar{b}a_z^3 - 3\bar{b}a_y^3\bar{b}a_z - 3\bar{b}a_y^2\bar{b}a_z\bar{b}a_z)(0,0,0) \\ + (4\bar{b}a_z^3 - 9\bar{b}a_y^2\bar{b}a_z - 3\bar{b}a_x^2\bar{b}a_z)(0,1,0) - 6\bar{b}a_x\bar{b}a_y\bar{b}a_z(1,0,0) \\ + 3(4\bar{b}a_y\bar{b}a_z^2 - \bar{b}a_y^3 - \bar{b}a_x^2\bar{b}a_y)(0,0,1) + 3(4\bar{b}a_z^2 - 3\bar{b}a_y^2 \\ - \bar{b}a_x^2)(0,1,1) - 3\bar{b}a_y\bar{b}a_z[(2,0,0) + 3(0,2,0) - 4(0,0,2)] \\ - 6\bar{b}a_x\bar{b}a_z(1,1,0) - 6\bar{b}a_x\bar{b}a_y(1,0,1) + 3\bar{b}a_z[4(0,1,2) \\ - (0,3,0) - (2,1,0)] + \bar{b}a_y[4(0,0,3) - 3(2,0,1) - 9(0,2,1)] \\ - 6\bar{b}a_x(1,1,1) - 3(0,3,1) - 3(2,1,1) + 4(0,1,3) \},$$

$$g_{z^2(x^2-y^2)} = \frac{3}{8}\sqrt{(5/\pi)} \{ (\bar{b}a_y^4 - \bar{b}a_x^4 + 6\bar{b}a_x^2\bar{b}a_z^2 - 6\bar{b}a_y^2\bar{b}a_z^2)(0,0,0) \\ + 4(3\bar{b}a_x\bar{b}a_z^2 - \bar{b}a_x^3)(1,0,0) - 4(3\bar{b}a_y\bar{b}a_z^2 - \bar{b}a_y^3)(0,1,0) \\ + 12(\bar{b}a_x^2\bar{b}a_z - \bar{b}a_y^2\bar{b}a_z)(0,0,1) - 6(\bar{b}a_x^2 - \bar{b}a_z^2) \cdot (2,0,0) \}$$

$$\begin{aligned}
& + 24\bar{b}a_x\bar{b}a_z(1,0,1) + 6(\bar{b}a_y^2 - \bar{b}a_z^2)(0,2,0) \\
& - 24\bar{b}a_y\bar{b}a_z(0,1,1) + 6(\bar{b}a_x^2 - \bar{b}a_y^2)(0,0,2) \\
& + 4\bar{b}a_x[3(1,0,2) - (3,0,0)] + 12\bar{b}a_z[(2,0,1) - (0,2,1)] \\
& + 4\bar{b}a_y[(0,3,0) - 3(0,1,2)] - (4,0,0) \\
& + 6(2,0,2) + (0,4,0) - 6(0,2,2) \},
\end{aligned}$$

$$\begin{aligned}
g_{xyz^2} = \frac{3}{4} \sqrt{(5/\pi)} \{ & (6\bar{b}a_x\bar{b}a_y\bar{b}a_z^2 - \bar{b}a_x^3\bar{b}a_y - \bar{b}a_x\bar{b}a_y^3)(0,0,0) \\
& + (6\bar{b}a_y\bar{b}a_z^2 - 3\bar{b}a_x^2\bar{b}a_y - \bar{b}a_y^3)(1,0,0) + (6\bar{b}a_x\bar{b}a_z^2 - \bar{b}a_x^3 \\
& - 3\bar{b}a_x\bar{b}a_y^2)(0,1,0) + 12\bar{b}a_x\bar{b}a_y\bar{b}a_z(0,0,1) + 3(2\bar{b}a_z^2 - \bar{b}a_z^2 \\
& - \bar{b}a_y^2)(1,1,0) - 3\bar{b}a_x\bar{b}a_y[(2,0,0) + (0,2,0) - 2(0,0,2)] \\
& + 12\bar{b}a_y\bar{b}a_z(1,0,1) + 12\bar{b}a_x\bar{b}a_z(0,1,1) - \bar{b}a_y[(3,0,0) \\
& + 3(1,2,0) - 6(1,0,2)] - \bar{b}a_x[3(2,1,0) \\
& + (0,3,0) - 6(0,1,2)] + 12\bar{b}a_z(1,1,1) \\
& - (3,1,0) - (1,3,0) + 6(1,1,2) \},
\end{aligned}$$

$$\begin{aligned}
g_{z(x^3-3xy^2)} = \frac{3}{8} \sqrt{(70/\pi)} \{ & (\bar{b}a_x^3\bar{b}a_z - 3\bar{b}a_x\bar{b}a_y^2\bar{b}a_z)(0,0,0) \\
& + 3(\bar{b}a_x^2\bar{b}a_z - \bar{b}a_y^2\bar{b}a_z)(1,0,0) - 6\bar{b}a_x\bar{b}a_y\bar{b}a_z(0,1,0) \\
& + (\bar{b}a_x^3 - 3\bar{b}a_x\bar{b}a_y^2)(0,0,1) - 6\bar{b}a_y\bar{b}a_z(1,1,0) \\
& + 3\bar{b}a_x\bar{b}a_z[(2,0,0) - (0,2,0)] + 3(\bar{b}a_x^2 - \bar{b}a_y^2)(1,0,1) \\
& - 6\bar{b}a_x\bar{b}a_y(0,1,1) + \bar{b}a_z[(3,0,0) - 3(1,2,0)] \\
& + 3\bar{b}a_x[(2,0,1) - (0,2,1)] - 6\bar{b}a_y(1,1,1) \\
& + (3,0,1) - 3(1,2,1) \},
\end{aligned}$$

$$\begin{aligned}
g_{z(3x^2y-y^3)} = \frac{3}{8} \sqrt{(70/\pi)} \{ & (3\bar{b}a_x^2\bar{b}a_y\bar{b}a_z - \bar{b}a_y^3\bar{b}a_z)(0,0,0) \\
& + 3(\bar{b}a_x^2\bar{b}a_z - \bar{b}a_y^2\bar{b}a_z)(0,1,0) + 6\bar{b}a_x\bar{b}a_y\bar{b}a_z(1,0,0) \\
& + (3\bar{b}a_x^2\bar{b}a_y - \bar{b}a_y^3)(0,0,1) + 6\bar{b}a_x\bar{b}a_z(1,1,0) \\
& + 3\bar{b}a_y\bar{b}a_z[(2,0,0) - (0,2,0)] + 3(\bar{b}a_x^2 - \bar{b}a_y^2)(0,1,1) \\
& - 5\bar{b}a_x\bar{b}a_y(1,0,1) + \bar{b}a_z[3(2,1,0) - (0,3,0)] \\
& + 3\bar{b}a_y[(2,0,1) - (0,2,1)] + 6\bar{b}a_x(1,1,1) \\
& - (0,3,1) + 3(2,1,1) \},
\end{aligned}$$

$$\begin{aligned}
g_{x^2y^2} = \frac{3}{16} \sqrt{(35/\pi)} \{ & (\bar{b}a_x^4 - 6\bar{b}a_x^2\bar{b}a_y^2 + \bar{b}a_y^4)(0,0,0) + 4(\bar{b}a_x^3 - 3\bar{b}a_x\bar{b}a_y^2)(1,0,0) \\
& + 4(\bar{b}a_y^3 - 3\bar{b}a_x^2\bar{b}a_y)(0,1,0) + 6(\bar{b}a_x^2 - \bar{b}a_y^2)[(2,0,0) \\
& - (0,2,0)] - 24\bar{b}a_x\bar{b}a_y(1,1,0) + 4\bar{b}a_x[(3,0,0) \\
& - 3(1,2,0)] + 4\bar{b}a_y[(0,3,0) - 3(2,1,0)] \\
& + (4,0,0) - 6(2,2,0) + (0,4,0) \},
\end{aligned}$$

$$\begin{aligned}
g_{xy}(x^2-y^2) = \frac{1}{4} \sqrt{(35/\pi)} \{ & (\overline{ba_x^3 \overline{ba_y}} - \overline{ba_x \overline{ba_y^3}})(0,0,0) + (3\overline{ba_x^2 \overline{ba_y}} - \overline{ba_y^3})(1,0,0) \\
& + (\overline{ba_x^3} - 3\overline{ba_x \overline{ba_y^2}})(0,1,0) \\
& + 3\overline{ba_x \overline{ba_y}}[(2,0,0) - (0,2,0)] + 3(\overline{ba_x^2} - \overline{ba_y^2})(1,1,0) \\
& + \overline{ba_y}[(3,0,0) - 3(1,2,0)] + \overline{ba_x}[3(2,1,0) - (0,3,0)] \\
& + (3,1,0) - (1,3,0) \} .
\end{aligned}$$

*Master Formulas for Operator Translation:*

$$(n, l, m)^O = \sum_i f_i^O(\overline{bo_x}, \overline{bo_y}, \overline{bo_z})(i, j, k)_v^B,$$

$$(1,0,0) = \overline{bo_x}(0,0,0) + (1,0,0),$$

$$(0,1,0) = \overline{bo_y}(0,0,0) + (0,1,0),$$

$$(0,0,1) = \overline{bo_z}(0,0,0) + (0,0,1),$$

$$(2,0,0) = \overline{bo_x^2}(0,0,0) + 2\overline{bo_x}(1,0,0) + (2,0,0),$$

$$(1,1,0) = \overline{bo_x \overline{bo_y}}(0,0,0) + \overline{bo_y}(1,0,0) + \overline{bo_x}(0,1,0) + (1,1,0),$$

$$(1,0,1) = \overline{bo_x \overline{bo_z}}(0,0,0) + \overline{bo_z}(1,0,0) + \overline{bo_x}(0,0,1) + (1,0,1),$$

$$(0,2,0) = \overline{bo_y^2}(0,0,0) + 2\overline{bo_y}(0,1,0) + (0,2,0),$$

$$(0,1,1) = \overline{bo_y \overline{bo_z}}(0,0,0) + \overline{bo_z}(0,1,0) + \overline{bo_y}(0,0,1) + (0,1,1),$$

$$(0,0,2) = \overline{bo_z^2}(0,0,0) + 2\overline{bo_z}(0,0,1) + (0,0,2),$$

$$(3,0,0) = \overline{bo_x^3}(0,0,0) + 3\overline{bo_x^2}(1,0,0) + 3\overline{bo_x}(2,0,0) + (3,0,0),$$

$$(1,2,0) = \overline{bo_x \overline{bo_y^2}}(0,0,0) + \overline{bo_y^2}(1,0,0) + 2\overline{bo_x \overline{bo_y}}(0,1,0)$$

$$+ 2\overline{bo_y}(1,1,0) + \overline{bo_x}(0,2,0) + (1,2,0),$$

$$(1,0,2) = \overline{bo_x \overline{bo_z^2}}(0,0,0) + \overline{bo_z^2}(1,0,0) + 2\overline{bo_x \overline{bo_z}}(0,0,1)$$

$$+ 2\overline{bo_z}(1,0,1) + \overline{bo_x}(0,0,2) + (1,0,2),$$

$$(2,1,0) = \overline{bo_x^2 \overline{bo_y}}(0,0,0) + 2\overline{bo_x \overline{bo_y}}(1,0,0) + \overline{bo_x^2}(0,1,0)$$

$$+ 2\overline{bo_x}(1,1,0) + \overline{bo_y}(2,0,0) + (2,1,0),$$

$$(2,0,1) = \overline{bo_x^2 \overline{bo_z}}(0,0,0) + 2\overline{bo_x \overline{bo_z}}(1,0,0) + \overline{bo_x^2}(0,0,1)$$

$$+ 2\overline{bo_x}(1,0,1) + \overline{bo_z}(2,0,0) + (2,0,1),$$

$$(1,1,1) = \overline{bo_x \overline{bo_y \overline{bo_z}}}(0,0,0) + \overline{bo_y \overline{bo_z}}(1,0,0) + \overline{bo_x \overline{bo_z}}(0,1,0) + \overline{bo_x \overline{bo_y}}(0,0,1)$$

$$+ \overline{bo_z}(1,1,0) + \overline{bo_y}(1,0,1) + \overline{bo_x}(0,1,1) + (1,1,1),$$

$$(0,3,0) = \overline{bo_y^3}(0,0,0) + 3\overline{bo_y^2}(0,1,0) + 3\overline{bo_y}(0,2,0) + (0,3,0),$$

$$(0,1,2) = \overline{bo_y \overline{bo_z^2}}(0,0,0) + \overline{bo_z^2}(0,1,0) + 2\overline{bo_y \overline{bo_z}}(0,0,1)$$

$$+ 2\overline{bo_z}(0,1,1) + \overline{bo_y}(0,0,2) + (0,1,2),$$

$$\begin{aligned}
(0,2,1) &= \overline{bo}_x^2 \overline{bo}_z(0,0,0) + 2\overline{bo}_y \overline{bo}_z(0,1,0) + \overline{bo}_y^2(0,0,1) \\
&\quad + 2\overline{bo}_y(0,1,1) + \overline{bo}_z(0,2,0) + (0,2,1), \\
(0,0,3) &= \overline{bo}_z^3(0,0,0) + 3\overline{bo}_z^2(0,0,1) + 3\overline{bo}_z(0,0,2) + (0,0,3), \\
(4,0,0) &= \overline{bo}_x^4(0,0,0) + 4\overline{bo}_x^3(1,0,0) + 6\overline{bo}_x^2(2,0,0) + 4\overline{bo}_x(3,0,0) + (4,0,0), \\
(3,1,0) &= \overline{bo}_x^3 \overline{bo}_y(0,0,0) + 3\overline{bo}_x^2 \overline{bo}_y(1,0,0) + \overline{bo}_x^3(0,1,0) + 3\overline{bo}_x \overline{bo}_y(2,0,0) \\
&\quad + 3\overline{bo}_x^2(1,1,0) + \overline{bo}_y(3,0,0) + 3\overline{bo}_x(2,1,0) + (3,1,0), \\
(3,0,1) &= \overline{bo}_x^3 \overline{bo}_z(0,0,0) + 3\overline{bo}_x^2 \overline{bo}_z(1,0,0) + \overline{bo}_x^3(0,0,1) + 3\overline{bo}_x^2(1,0,1) \\
&\quad + 3\overline{bo}_x \overline{bo}_z(2,0,0) + \overline{bo}_z(3,0,0) + 3\overline{bo}_x(2,0,1) + (3,0,1), \\
(2,2,0) &= \overline{bo}_x^2 \overline{bo}_y^2(0,0,0) + 2\overline{bo}_x \overline{bo}_y^2(1,0,0) + 2\overline{bo}_x^2 \overline{bo}_y(0,1,0) \\
&\quad + \overline{bo}_y^2(2,0,0) + 4\overline{bo}_x \overline{bo}_y(1,1,0) + \overline{bo}_x^2(0,2,0) \\
&\quad + 2\overline{bo}_x(1,2,0) + 2\overline{bo}_y(2,1,0) + (2,2,0), \\
(2,1,1) &= \overline{bo}_x^2 \overline{bo}_y \overline{bo}_z(0,0,0) + 2\overline{bo}_x \overline{bo}_y \overline{bo}_z(1,0,0) + \overline{bo}_x^2 \overline{bo}_z(0,1,0) \\
&\quad + \overline{bo}_x^2 \overline{bo}_y(0,0,1) + \overline{bo}_y \overline{bo}_z(2,0,0) + 2\overline{bo}_x \overline{bo}_z(1,1,0) \\
&\quad + 2\overline{bo}_x \overline{bo}_y(1,0,1) + \overline{bo}_x^2(0,1,1) + \overline{bo}_z(2,1,0) \\
&\quad + \overline{bo}_y(2,0,1) + 2\overline{bo}_x(1,1,1) + (2,1,1), \\
(2,0,2) &= \overline{bo}_x^2 \overline{bo}_z^2(0,0,0) + 2\overline{bo}_x \overline{bo}_z^2(1,0,0) + 2\overline{bo}_x^2 \overline{bo}_z(0,0,1) \\
&\quad + 4\overline{bo}_x \overline{bo}_z(1,0,1) + \overline{bo}_z^2(2,0,0) + \overline{bo}_x^2(0,0,2) \\
&\quad + 2\overline{bo}_x(1,0,2) + 2\overline{bo}_z(2,0,1) + (2,0,2), \\
(1,3,0) &= \overline{bo}_x \overline{bo}_y^3(0,0,0) + 3\overline{bo}_x \overline{bo}_y^2(0,1,0) + \overline{bo}_y^3(1,0,0) + 3\overline{bo}_x \overline{bo}_y(0,2,0) \\
&\quad + 3\overline{bo}_y^2(1,1,0) + \overline{bo}_x(0,3,0) + 3\overline{bo}_y(1,2,0) + (1,3,0), \\
(1,2,1) &= \overline{bo}_x \overline{bo}_y^2 \overline{bo}_z(0,0,0) + 2\overline{bo}_x \overline{bo}_y \overline{bo}_z(0,1,0) + \overline{bo}_y^2 \overline{bo}_z(1,0,0) \\
&\quad + \overline{bo}_x \overline{bo}_y^2(0,0,1) + \overline{bo}_x \overline{bo}_z(0,2,0) + 2\overline{bo}_y \overline{bo}_z(1,1,0) \\
&\quad + 2\overline{bo}_x \overline{bo}_y(0,1,1) + \overline{bo}_y^2(1,0,1) + \overline{bo}_z(1,2,0) \\
&\quad + \overline{bo}_x(0,2,1) + 2\overline{bo}_y(1,1,1) + (1,2,1), \\
(1,1,2) &= \overline{bo}_x \overline{bo}_y \overline{bo}_z^2(0,0,0) + \overline{bo}_y \overline{bo}_z^2(1,0,0) + \overline{bo}_x \overline{bo}_z^2(0,1,0) \\
&\quad + 2\overline{bo}_x \overline{bo}_y \overline{bo}_z(0,0,1) + \overline{bo}_z^2(1,1,0) + 2\overline{bo}_y \overline{bo}_z(1,0,1) \\
&\quad + 2\overline{bo}_x \overline{bo}_z(0,1,1) + \overline{bo}_x \overline{bo}_y(0,0,2) + \overline{bo}_y(1,0,2) \\
&\quad + 2\overline{bo}_z(1,1,1) + \overline{bo}_x(0,1,2) + (1,1,2), \\
(1,0,3) &= \overline{bo}_x \overline{bo}_z^3(0,0,0) + \overline{bo}_z^3(1,0,0) + 3\overline{bo}_x \overline{bo}_z^2(0,0,1) + 3\overline{bo}_z^2(1,0,1) \\
&\quad + 3\overline{bo}_x \overline{bo}_z(0,0,2) + 3\overline{bo}_z(1,0,2) + \overline{bo}_x(0,0,3) + (1,0,3), \\
(0,4,0) &= \overline{bo}_y^4(0,0,0) + 4\overline{bo}_y^3(0,1,0) + 6\overline{bo}_y^2(0,2,0) + 4\overline{bo}_y(0,3,0) + (0,4,0),
\end{aligned}$$

$$\begin{aligned}
(0,3,1) &= \overline{b\sigma}_y^3 \overline{b\sigma}_z(0,0,0) + 3\overline{b\sigma}_y^2 \overline{b\sigma}_z(0,1,0) + \overline{b\sigma}_y^3(0,0,1) + 3\overline{b\sigma}_y^2(0,1,1) \\
&\quad + 3\overline{b\sigma}_y \overline{b\sigma}_z(0,2,0) + \overline{b\sigma}_z(0,3,0) + 3\overline{b\sigma}_y(0,2,1) + (0,3,1), \\
(0,2,2) &= \overline{b\sigma}_y^2 \overline{b\sigma}_z^2(0,0,0) + 2\overline{b\sigma}_y \overline{b\sigma}_z^2(0,1,0) + 2\overline{b\sigma}_y^2 \overline{b\sigma}_z(0,0,1) \\
&\quad + 4\overline{b\sigma}_y \overline{b\sigma}_z(0,1,1) + \overline{b\sigma}_z^2(0,2,0) + \overline{b\sigma}_y^2(0,0,2) \\
&\quad + 2\overline{b\sigma}_y(0,1,2) + 2\overline{b\sigma}_z(0,2,1) + (0,2,2), \\
(0,1,3) &= \overline{b\sigma}_y \overline{b\sigma}_z^3(0,0,0) + \overline{b\sigma}_z^3(0,1,0) + 3\overline{b\sigma}_y \overline{b\sigma}_z^2(0,0,1) + 3\overline{b\sigma}_z^2(0,1,1) \\
&\quad + 3\overline{b\sigma}_y \overline{b\sigma}_z(0,0,2) + 3\overline{b\sigma}_z(0,1,2) + \overline{b\sigma}_y(0,0,3) + (0,1,3), \\
(0,0,4) &= \overline{b\sigma}_z^4(0,0,0) + 4\overline{b\sigma}_z^3(1,0,0) + 6\overline{b\sigma}_z^2(0,0,2) + 4\overline{b\sigma}_z(0,0,3) + (0,0,4).
\end{aligned}$$

With this accomplishment we can now write the sixfold sum of Eq. (15) in terms of a twofold sum over the two Cartesians, both centered on  $B$ , in the following fashion:

$$\begin{aligned}
\langle M_{I,m,n} \rangle &= \langle r_a^{n_a-l_a-1} x_a^l y_a^j z_a^k e^{-i\sigma_a} | x_o^l y_o^m z_o^n | r_b^{n_b-l_b-1} x_b^f y_b^g z_b^g e^{-i\sigma_b} \rangle \\
&\quad \cdot \langle r_a^{n_a-l_a-1} \left( \sum_u g_u^a(\overline{b\sigma}_x, \overline{b\sigma}_y, \overline{b\sigma}_z) x_b^{l_x^a} y_b^{l_y^a} z_b^{l_z^a} \right) e^{-i\sigma_a} | \\
&\quad \cdot \left( \sum_v f_v^a(\overline{b\sigma}_x, \overline{b\sigma}_y, \overline{b\sigma}_z) x_b^{l_x^a} y_b^{l_y^a} z_b^{l_z^a} \right) | r_b^{n_b-l_b-1} x_b^e y_b^f z_b^g e^{-i\sigma_b} \rangle \\
&= \sum_{u,v} g_u^a(\overline{b\sigma}_x, \overline{b\sigma}_y, \overline{b\sigma}_z) f_v^a(\overline{b\sigma}_x, \overline{b\sigma}_y, \overline{b\sigma}_z) \\
&\quad \cdot \langle r_a^{n_a-l_a-1} e^{-i\sigma_a} | r_b^{n_b-l_b-1} x_b^{e+l_x^a} y_b^{f+l_y^a} z_b^{g+l_z^a} e^{-i\sigma_b} \rangle, \quad (16)
\end{aligned}$$

where the coefficients  $g_u^a(\overline{b\sigma}_x, \overline{b\sigma}_y, \overline{b\sigma}_z)$  and  $f_v^a(\overline{b\sigma}_x, \overline{b\sigma}_y, \overline{b\sigma}_z)$  are taken from the master formulas through two computational do loops.

### Local Integral Evaluation

*One-Center Integrals:* After the translations described by Eq. (16), all one-center integrals, apart from a normalization factor, take the form

$$\begin{aligned}
I_1 &= \langle r_b^{n_b+n_b-l_a-l_b-2} x_b^l y_b^j z_b^k e^{-(i\sigma_a+i\sigma_b)r_b} \rangle = \int_0^\infty r_b^{n_b+n_b-l_a-l_b-1+j+k} e^{-(i\sigma_a+i\sigma_b)r_b} dr_b \\
&\quad \times \int_0^\pi \sin^{i+j+1} \theta_b \cos^k \theta_b d\theta_b \int_0^{2\pi} \sin^l \phi \cos^j \phi d\phi \quad (17)
\end{aligned}$$

and we proceed to evaluate the nonvanishing angular part of  $I_1$  first.

Assuming  $m$  and  $n$  to be integers, we have, in general,

$$\int_0^{\pi, 2\pi} \cos^m \phi \sin^n \phi d\phi = \frac{m-1}{m+n} \int_0^{\pi, 2\pi} \cos^{m-2} \phi \sin^n \phi d\phi. \quad (18)$$

Applying Eq. (18) in a recursive manner, we get

$$\begin{aligned}\int_0^{\pi, 2\pi} \cos^m \phi \sin^n \phi d\phi &= \frac{m-1}{m+n} \cdot \frac{m-3}{m+n-2} \int_0^{\pi, 2\pi} \cos^{m-4} \phi \sin^n \phi d\phi \\ &= \frac{m-1}{m+n} \cdot \frac{m-3}{m+n-2} \cdot \frac{m-5}{m+n-4} \\ &\quad \times \int_0^{\pi, 2\pi} \cos^{m-6} \phi \sin^n \phi d\phi = \dots \\ &= \frac{(m-1)!!n!!}{(m+n)!!} \int_0^{\pi, 2\pi} \sin^n \phi d\phi. \quad (19)\end{aligned}$$

In Eq. (19) we need to examine two cases of the sine integral. First, if  $n$  is even,

$$\begin{aligned}\int_0^{\pi, 2\pi} \sin^n \phi d\phi &= \frac{n-1}{n} \int_0^{\pi, 2\pi} \sin^{n-2} \phi d\phi \\ &= \frac{n-1}{n} \cdot \frac{n-3}{n-2} \int_0^{\pi, 2\pi} \sin^{n-4} \phi d\phi = \dots \\ &= \frac{(n-1)!!}{n!!} (\pi, 2\pi). \quad (20)\end{aligned}$$

Therefore, for even  $m$  and even  $n$ , Eqs. (19) and (20) give the closed formulae

$$\int_0^{\pi} \cos^m \phi \sin^n \phi d\phi = \frac{(m-1)!!(n-1)!!\pi}{(m+n)!!}, \quad (21a)$$

$$\int_0^{2\pi} \cos^m \phi \sin^n \phi d\phi = \frac{(m-1)!!(n-1)!!}{(m+n)!!} (2\pi) = F(m, n). \quad (21b)$$

We then examine the sine integrals with odd  $n$  in Eq. (19):

$$\begin{aligned}\int_0^{\pi} \sin^n \phi d\phi &= -\cos \phi \frac{2^{2(n-1)/2} \left(\frac{n-1}{2}\right)! \left(\frac{n-1}{2}\right)!}{n!} \Bigg|_0^{\pi} \\ &= \frac{2^n \left(\frac{n-1}{2}\right)! \left(\frac{n-1}{2}\right)!}{n!} \quad (22a)\end{aligned}$$

$$\int_0^{2\pi} \sin^n \phi d\phi = 0. \quad (22b)$$

Finally Eqs. (19) and (22) give, for even  $m$  and odd  $n$ , the closed formulae

$$\int_0^{\pi} \cos^m \phi \sin^n \phi d\phi = \frac{(m-1)!!n!!}{(m+n)!!} \cdot \frac{2^n \left(\frac{n-1}{2}\right)! \left(\frac{n-1}{2}\right)!}{n!} \quad (23)$$

All the angular integrals necessary for  $I_1$  are given by Eqs. (21) and (23). The radial part of  $I_1$  is simply  $\int_0^\infty r^n e^{-ar} = n!/\alpha^{n+1}$ .

*Two-Center Integrals:* In an ellipsoidal coordinate system we use Eq. (6) noted in the previous section to express a two-center integral that evolves from the translation of Eq. (16),

$$\begin{aligned} I_2 &= \langle r_a^{n_a-l_a-1} e^{-\zeta_a r_a} | r_b^{n_b-l_b-1} x_b^i y_b^j z_b^k e^{\zeta_b r_b} \rangle \\ &= \int_1^\infty d\xi \int_{-1}^1 d\eta \int_0^{2\pi} d\phi (R/2)^{n_a+n_b-l_a-l_b+i+j+k+1} (\xi + \eta)^{n_a+1} (\xi - \eta)^{n_b+1} \\ &\quad \times [(\xi^2 - 1)(1 - \eta^2)]^{(i+j)/2} (1 - \xi\eta)^k e^{-\rho\xi - \tau\eta} \cos^i \phi \sin^j \phi \\ &= \int_1^\infty d\xi \int_{-1}^1 d\eta (R/2)^{n_a+n_b-l_a-l_b+i+j+k+1} (\xi + \eta)^{n_a+1} (\xi - \eta)^{n_b+1} \\ &\quad \times [(\xi^2 - 1)(1 - \eta^2)]^{(i+j)/2} (1 - \xi\eta)^k e^{-\rho\xi - \tau\eta} \cdot F(i, j), \end{aligned} \quad (24)$$

where

$$\begin{aligned} \rho &= (R/2)(\zeta_a + \zeta_b), \\ \tau &= (\zeta_a - \zeta_b)/(\zeta_a + \zeta_b) \end{aligned}$$

and  $F(i, j)$  is given by Eq. (21b).

At this point, we feel it is convenient if a new function is introduced as

$$\begin{aligned} Z_{\alpha,\beta,\gamma,\delta}(\rho, \tau) &= \int_1^\infty d\xi \int_{-1}^1 d\eta (\xi + \eta)^\alpha (\xi - \eta)^\beta \\ &\quad \times [(\xi^2 - 1)(1 - \eta^2)]^\gamma (1 - \xi\eta)^\delta e^{-\rho\xi - \tau\eta}, \end{aligned} \quad (25)$$

which we shall call "Z functions." The recursion formulas of Z are simpler than those derived by Ruedenberg et al. [28]. In this work we adapt an algorithm proposed by Stevens [47,48] based on the binomial theorem,

$$\begin{aligned} Z_{\alpha,\beta,\gamma,\delta}(\rho, \tau) &= \sum_{i,j,k,l,m} \binom{\alpha}{i} \binom{\beta}{j} \binom{\gamma}{k} \binom{\gamma}{l} \binom{\delta}{m} (-)^{j+k+l+m} \\ &\quad \times A_{\alpha+\beta+2\gamma+\delta-i-j-2k-m}(\rho) B_{i+j+l+m}(\rho, \tau), \end{aligned} \quad (26)$$

where the  $A$  and  $B$  functions are as defined by Mulliken et al. [25], and have been well studied by, among others, Miller et al. [49] and Harris [50].

In this formalism, the two-center integral of Eq. (24) is evaluated as the product of Z and F functions,

$$\begin{aligned} I_2 &= \langle r_a^{n_a-l_a-1} e^{-\zeta_a r_a} | r_b^{n_b-l_b-1} x_b^i y_b^j z_b^k e^{\zeta_b r_b} \rangle \\ &= Z_{n_a-l_a, n_b-l_b, (i+j)/2, k}(\rho, \tau) F(i, j). \end{aligned} \quad (27)$$

### Rotational Transform into Molecular Frame

As discussed in the previous section, all integrals evaluated in this section need to be back-transformed into molecular frame  $[x', y', z']$  (see Fig. 1) through a matrix rotation

$$R(\theta, \phi) \begin{pmatrix} x \\ y \\ z \end{pmatrix} = \begin{pmatrix} r_{11} & r_{12} & r_{13} \\ r_{21} & r_{22} & r_{23} \\ r_{31} & 0 & r_{33} \end{pmatrix} \begin{pmatrix} x \\ y \\ z \end{pmatrix} = \begin{pmatrix} x' \\ y' \\ z' \end{pmatrix}, \quad (28)$$

where the matrix elements are given by Eq. (10). We now let the rotation described by Eq. (28) act on an arbitrary Cartesian in the ellipsoidal coordinate system,

$$\begin{aligned} Rx^i y^j z^k &= (r_{11}x + r_{12}y + r_{13}z)^i (r_{21}x + r_{22}y + r_{23}z)^j (r_{31}x + r_{33}z)^k \\ &= \sum_{(r,s,t)(u,v,w)(p,q)} c_{r,s,t}^i(r_{11}, r_{12}, r_{13}) c_{u,v,w}^j(r_{21}, r_{22}, r_{23}) c_{p,q}^k(r_{31}, r_{33}) \\ &\quad \times x^{r+u+p} y^{s+v} z^{t+w+q}, \end{aligned} \quad (29)$$

where

$$\begin{aligned} c_{r,s,t}^i(r_{11}, r_{12}, r_{13}) &= (i!/r!s!t!) r_{11}^r r_{12}^s r_{13}^t \\ c_{u,v,w}^j(r_{21}, r_{22}, r_{23}) &= (j!/u!v!w!) r_{21}^u r_{22}^v r_{23}^w \\ c_{p,q}^k(r_{31}, r_{33}) &= (k!/p!q!) r_{31}^p r_{33}^q \end{aligned} \quad (30)$$

Considering  $I_2$  of Eq. (24), we now have

$$\begin{aligned} RI_2 &= R \langle r_a^{n_a} e^{-\zeta_a r_a} | r_b^{n_b} x_b^i y_b^j z_b^k e^{-\zeta_b r_b} \rangle \\ &= \langle r_a^{n_a} e^{-\zeta_a r_a} | r_b^{n_b} (Rx_b^i y_b^j z_b^k) e^{-\zeta_b r_b} \rangle \\ &= \sum_{(r,s,t)(u,v,w)(p,q)} c_{r,s,t}^i c_{u,v,w}^j c_{p,q}^k \langle r_a^{n_a} e^{-\zeta_a r_a} | r_b^{n_b} x_b^{r+u+p} y_b^{s+v} z_b^{t+w+q} e^{-\zeta_b r_b} \rangle, \end{aligned} \quad (31)$$

where we have applied Eq. (29) and used the rotational equivalence of coordinate systems  $[x, y, z]$  and  $[x_b, y_b, z_b]$  (see, again, Fig. 1).

In this approach it is remarkable that the rotation  $R(\theta, \phi)$  needs to act only on the right-hand side of Eq. (24) to rotate the integral  $I_2$  into the molecular frame.

### Computational Procedure

The method presented here proceeds as follows:

(i) For two orbitals on the same center, the operator is translated, the symmetry is checked, and if nonzero, integral evaluation proceeds as outlined two subsections ago.

(ii) For orbitals on different centers:

- (1) Choose the orbital with bigger  $l$  in Eq. (1a) to be centered on  $B$ .
- (2) Translation is made in two do loops of Eq. (16) by using the master formulas.
- (3) Determine the order  $L = e + f + g + t_{x,u}^e + t_{x,v}^e + t_{y,u}^e + t_{y,v}^e + t_{z,u}^e + t_{z,v}^e$  of the Cartesian on the righthand side of Eq. (16).
- (4) Sort out the angular symmetry "allowed" Cartesians of the order  $L$  determined in step (3) by way of the  $F(i, j)$  functions shown two subsections ago.
- (5) Compute the necessary  $Z$  functions [Eq. (26)], and then the local integrals [Eq. (27)] required by step (4).
- (6) Rotate the computed local integrals into the molecular frame by using Eq. (31).



### Discussion and Conclusions

A general method of evaluating electric moment integrals over Slater-type orbitals is developed. A program that implements the procedure just described above has been in use in this laboratory for some time. We have been using these moments for studies on solvation using the self-consistent reaction field model, and for examining the long-range interactions between molecules.

The method we outline is somewhat unusual in that the Cartesian components of one orbital and the operator are both translated to the center of another orbital and thus only a single sigma symmetry integration remains between an  $s$  orbital on one center and a complex Cartesian orbital of the form  $x^i y^j z^k r^l e^{-\xi r}$  on the other. The local evaluation of this integral is easy, as is the rotation back into the molecular frame. Although the method is quite general, the price we pay for this computational simplicity is formal complexity. Generating explicit formula for higher moments, or higher angular momentum atomic-like orbitals, is tedious. We do not maintain the "symmetry" of the spherical harmonics, and we pay a penalty for this.

A definite advantage of the method described is that we need to consider the  $z$  component of one atomic orbital, and the  $Z$  function we need (Eq. (25)) is simpler than the traditional  $L$  function [30],

$$L_{\alpha,\beta}^{\gamma,\delta,\epsilon}(\rho, \tau) = \int_1^\infty d\xi \int_{-1}^1 d\eta (\xi + \eta)^\alpha (\xi - \eta)^\beta (1 + \xi\eta)^\gamma \\ \times (1 - \xi\eta)^\delta [(\xi^2 - 1)(1 - \eta^2)]^\epsilon e^{-\rho\xi - \tau\rho\eta} \quad (32)$$

or the  $C$  function [28],

$$C_{\alpha,\beta}^{\gamma,\delta,\epsilon}(\rho, \tau) = (\frac{1}{2} \xi_b R)^{\alpha+\beta+\gamma+\delta+2\epsilon+1} L_{\alpha,\beta}^{\gamma,\delta,\epsilon}(\rho, \tau). \quad (33)$$

TABLE I. Percentage of Cartesians needed to integrate with

Order	Number of Cartesians (A)	Number of Cartesians with nonzero angular integral (B)	B/A
0	1	1	1.00
1	3	1	0.33
2	6	3	0.50
3	10	3	0.30
4	15	6	0.40
5	21	6	0.29
6	28	10	0.36
7	36	10	0.28
8	45	15	0.33
9	55	15	0.27
10	66	21	0.32
11	78	21	0.27
12	91	28	0.31

Both  $L$  and  $C$  functions, if evaluated in the fashion of Eq. (26) require a sixfold sum, while the evaluation of  $Z$  functions needs a fivefold sum, a saving of the innermost do loop in computation. It would be worthwhile to further investigate the  $Z$  function recursion relations.

Before concluding, we further note that the "Cartesian STOs" are prescreened based on angular symmetry before the integration takes place. Note that  $i$  and  $j$  in the Cartesian  $(i, j, k)$  that occurs in Eq. (24) must both be even or the integral vanishes. For example, a typical nonvanishing quadrupole integral between  $d$  orbitals contains on average 18 different terms of 64 possible, but only five or six are nonzero. In Table I we list the number of Cartesians for a given order, and the number of Cartesians that have nonvanishing angular integral based on the prescreening of  $F(i, j)$ . This table shows that in the integration with Cartesian STOs, there is a saving of about 70%.

### Acknowledgments

This work is supported in part through a grant from the Office of Naval Research. The authors also enjoyed discussions on this work with Professor Paul E. Wormer (University of Nijmegen) on several occasions.

### Bibliography

- [1] A. D. Buckingham, *J. Chem. Phys.* **30**, 1580 (1959).
- [2] D. G. Bounds and S. Wilson, *Mol. Phys.* **54**, 445 (1985).
- [3] D. Sundholm and P. Pyykko, *Mol. Phys.* **56**, 1411 (1985).
- [4] M. P. Allen and D. J. Tildesley, *Computer Simulation of Liquids* (Clarendon, Oxford, 1987).
- [5] A. D. Buckingham and K. L. Clarke, *Chem. Phys. Lett.* **57**, 321 (1978).
- [6] Peter D. Dacre, *J. Chem. Phys.* **80**, 5677 (1984).
- [7] K. Wolinski and A. J. Sadlej, *Mol. Phys.* **75**, 221 (1992).
- [8] R. M. Stevens and M. Karplus, *J. Chem. Phys.* **49**, 1094 (1968); R. Rein, G. R. Pack, and J. R. Rabinowitz, *J. Magnet. Reson.* **6**, 360 (1972).
- [9] P. A. Tanner and G. G. Siu, *Mol. Phys.* **75**, 233 (1992).
- [10] F. London, *Trans. Faraday Soc.* **33**, 8 (1937).
- [11] F. London, *J. Phys. Chem.* **46**, 305 (1942).
- [12] J. R. Rabinowitz, T. J. Swisler, and R. Rein, *Int. J. Quantum Chem.* **6**, 353 (1972).
- [13] R. Rein and G. P. Pack, *Nature* **242**, 526 (1973).
- [14] K.-C. Ng, W. J. Meath and A. R. Allnatt, *Mol. Phys.* **32**, 177 (1976).
- [15] W. A. Sokalski, M. Shibata, R. L. Ornstein, and R. Rein, *J. Comput. Chem.* **13**, 883 (1992).
- [16] O. Tapia and O. Goscinski, *Mol. Phys.* **29**, 1653 (1975).
- [17] K. V. Mikkelsen, H. Agren, H. J. A. Jensen, and T. Helgaker, *J. Chem. Phys.* **89**, 3086 (1988).
- [18] M. Karelson and M. C. Zerner, *J. Phys. Chem.* **96**, 6949 (1992).
- [19] E. A. McCullough Jr., *Mol. Phys.* **42**, 943 (1981).
- [20] S. Wilson, in *Methods in Computational Molecular Physics*, G. H. F. Diercksen and S. Wilson, Eds. (Reidel, Dordrecht, 1983), p. 71.
- [21] T. J. Swisler and R. Rein, *Chem. Phys. Lett.* **15**, 617 (1972).
- [22] S. Larsson, K. Stahl, and M. C. Zerner, *Inorg. Chem.* **25**, 3033 (1986).
- [23] O. Matsuoka, *Int. J. Quant. Chem.* **5**, 1 (1971).
- [24] J. D. Augspurger and C. E. Dykstra, *J. Comput. Chem.* **11**, 105 (1990).
- [25] R. S. Mulliken, C. A. Rieke, D. Orloff, and H. Orloff, *J. Chem. Phys.* **17**, 1248 (1949).
- [26] C. C. J. Roothaan, *J. Chem. Phys.* **19**, 1445 (1951), **24**, 947 (1956).
- [27] K. Ruedenberg, *J. Chem. Phys.* **19**, 1459 (1951).

- [28] K. Ruedenberg, C. C. J. Roothaan, and W. Jaunzemis, *J. Chem. Phys.* **24**, 201 (1956).
- [29] W. C. Hamilton, *J. Chem. Phys.* **26**, 1018 (1957).
- [30] A. C. Wahl, P. E. Cade, and C. C. J. Roothaan, *J. Chem. Phys.* **41**, 2578 (1964).
- [31] P. S. Bagus, B. Li, A. D. McLean, and M. Yoshimine, *ALCHEMY* (IBM Research Lab., San Jose, CA).
- [32] R. Rei, G. A. Clarke, and F. E. Harris, in *Quantum Aspects of Heterocyclic Compounds in Chemistry and Biology* (The Israel Academy of Science and Humanities, 1970), p. 86.
- [33] J. R. Rabinowitz and R. Rein, *Int. J. Quant. Chem.* **6**, 669 (1972).
- [34] F. E. Harris and H. H. Michels, *Adv. Chem. Phys.* **13**, 205 (1967).
- [35] E. O. Steinborn and K. Ruedenberg, *Int. J. Quantum Chem.* **6**, 413 (1972).
- [36] I. I. Guseinov and F. S. Sadichov, *J. Phys. B* **10**, L261 (1977).
- [37] E. O. Steinborn and K. Ruedenberg, *Adv. Quantum Chem.* **7**, 1 (1973).
- [38] E. O. Steinborn, *Adv. Quantum Chem.* **7**, 83 (1973).
- [39] J. C. Slater, *Phys. Rev.* **36**, 57 (1930).
- [40] J. A. Detrio, *J. Chem. Phys.* **57**, 5012 (1972).
- [41] L. Pauling and E. B. Wilson, *Introduction to Quantum Mechanics* (McGraw-Hall, New York, 1935).
- [42] J. O. Hirschfelder, C. F. Curtis, and R. B. Bird, *Molecular Theory of Gases and Liquids* (Wiley, New York, 1954).
- [43] A. D. Buckingham, *Quart. Rev. Chem. Soc.* **13**, 183 (1959).
- [44] E. W. Hobson, *The Theory of Spherical and Ellipsoidal Harmonics* (Cambridge University Press, Cambridge, 1931).
- [45] L. C. Biedenharn and J. D. Louck, *Angular Momentum in Quantum Physics Theory and Application* (Addison-Wesley, Reading, MA, 1981).
- [46] H. Taketa, S. Huzinaga, and K. O-Ohata, *J. Phys. Soc. Japan* **21**, 2313 (1966).
- [47] R. M. Stevens, *J. Chem. Phys.* **52**, 1397 (1970).
- [48] R. M. Stevens, *J. Chem. Phys.* **55**, 1725 (1972).
- [49] J. Miller, J. M. Gerhauser, and F. A. Matsen, *Quantum Chemistry Integrals and Tables* (University of Texas Press, Austin, 1959).
- [50] F. Harris, *Computation Methods of Quantum Chemistry*, Summer Institute in Quantum Chemistry, Solid State Physics and Quantum Biology, Uppsala, Sweden (1973).

Received May 11, 1993

# Success and Pitfalls of the Dielectric Continuum Model in Quantum Chemical Calculations

ALEX H. DE VRIES,\*<sup>†</sup> PIET TH. VAN DUIJNEN,<sup>†</sup>  
and ANDRÉ H. JUFFER<sup>‡§</sup>

<sup>†</sup>Department of Organic and Molecular Inorganic Chemistry and <sup>‡</sup>Department of Biophysical Chemistry, State University of Groningen, Nijenborgh 4, 9747 AG Groningen, The Netherlands

## Abstract

Recently we presented an extension of the direct reaction field (DRF) method, in which a quantum system and a set of point charges and interacting polarizabilities are embedded in a continuum that is characterized by a dielectric constant  $\epsilon$  and a finite ionic strength. The reaction field of the continuum is found by solving the (linearized) Poisson-Boltzmann equation by a boundary element method for the complete charge distribution in a cavity of arbitrary size and form. Like many other authors, we found that the results depend critically on the choice of the size of the cavity, in the sense that the continuum contribution to the solvation energy decreases rapidly with the relative cavity size. The literature gives no clues for the definition of the cavity size beyond "physical intuition" or implicit fitting to experimental or otherwise desired results. From theoretical considerations, a number of limitations on the position of the boundary are derived. With a boundary defined within these limitations, the experimental hydration energies cannot be reproduced, mainly because of the neglected specific interactions. In addition, we found that the description of the solute's electronic states also depends on the solvation model. We suggest that one or more explicit solvent layers are needed to obtain reliable solvation and excitation energies. © 1993 John Wiley & Sons, Inc.

## Introduction

Dielectric continuum models have become quite popular in the calculation of solvation free energies and solvation effects on equilibria and electronic spectra, combining them with quantum theoretical [1-5], semiempirical [6,7], and entirely classical treatments [8-10] of a solute. The methods are based on the notion that electrostatic behavior of solvent bulk can approximately be described by a single parameter, viz., the dielectric constant [11]. Some methods also allow for a finite ionic strength of the bulk, introducing an additional parameter for description of the bulk, the Debye screening length  $\kappa^{-1}$ .

The popularity of the dielectric model is based on the success in reproducing solvation energies with relatively little computational cost. For hydration energies, good agreement is found with more explicit water models, as used in molecular

\* To whom correspondence should be addressed (e-mail address: alexxx@chem.rug.nl).

<sup>†</sup> Present address: EMBL Heidelberg, Meyerhofstrasse 1, 6900 Heidelberg, Germany.

dynamics (MD) [12] and Monte Carlo (MC) [13-15] simulations, which are comparatively rather expensive.

In this paper, the theoretical foundations of the continuum approach are revisited, in order to derive criteria for the appropriateness of the dielectric model and for the location of the boundary separating solute and dielectric from the limitations set by theory. It is shown that most current models do not correctly apply these criteria. As a result, these models are not general in the sense that they can be extended to nonaqueous solutions without reparameterization.

### Theoretical Framework

Consider a macroscopic volume described on the quantum chemical level (nuclei and electrons as the constituent particles). The properties of the system follow from the wave function  $\Psi$  of the system, a function of the coordinates of all particles, and time, defining a state of the system. In the case of stationary states, time enters only as a phase factor. Then the wave function can be found by solving the time-independent Schrödinger equation  $\hat{H}\Psi = E\Psi$ , where the Hamiltonian  $\hat{H}$  contains the kinetic and interaction operators of all particles. Assuming  $\Psi$  is known, properties of the system can be calculated by integrating  $\Psi^* \hat{A} \Psi$  over all space, where  $\hat{A}$  is the operator connected with the property of interest. The effort needed for this integration can be reduced enormously if  $\Psi$  vanishes for certain coordinates in large parts of space. One then deals with localized particles.

If a group of particles is localized in the same region in space, say  $S$ , the integration may be carried out separately over the particles of this group and is confined to the selected volume  $S$  in space. If no other particle outside the group has a contribution inside the volume, the part of the wave function describing the particles of the group,  $\Psi_S$ , may be factored out of the total wave function, leaving  $\Psi_A$  for the rest of the particles:

$$\Psi = \Psi_A \otimes \Psi_S. \quad (1)$$

Because of the indistinguishability of electrons, this can never be done in principle, but no error is made if the scalar product of the component functions equals zero (i.e., if the component functions "do not overlap").

If the property of interest is the energy, the result of integrating the  $A$ - $S$  interaction part of the Hamiltonian,  $\hat{V}_{AS}$ , over  $S$  is the potential of the particles constituting group  $S$  in space:

$$\hat{H} = \hat{H}_A^0 + \hat{H}_S^0 + \hat{V}_{AS}, \quad \hat{V}_{AS} = \sum_{a \in A} \sum_{s \in S} \frac{z_a z_s}{|\mathbf{r}_a - \mathbf{r}_s|}, \quad (2)$$

$$E = \langle \Psi_A | \hat{H}_A^0 | \Psi_A \rangle_A + \langle \Psi_S | \hat{H}_S^0 | \Psi_S \rangle_S + \Delta E_{\text{int}},$$

$$\Delta E_{\text{int}} = \left\langle \Psi_A \left| \sum_{a \in A} z_a \left\langle \Psi_S \left| \sum_{s \in S} \frac{z_s}{|\mathbf{r}_a - \mathbf{r}_s|} \right| \Psi_S \right\rangle_S \right| \Psi_A \right\rangle_A = \left\langle \Psi_A \left| \sum_{a \in A} z_a \Phi_S(\mathbf{r}_a) \right| \Psi_A \right\rangle_A, \quad (3)$$

where  $z_i$  and  $\mathbf{r}_i$  are the charge and position vector of particle  $i$ , respectively. Here the regions of integration are indicated by the italic capitals  $S$  and  $A$ . Solving the Schrödinger equation (SE) for the whole system can now be partitioned into smaller problems, for which the SE is to be solved in an external potential. This is the group-function approach advocated by McWeeny [16] in which the energy  $E$  is minimized in an iterative scheme. Starting from some trial functions for subsystems  $A$  and  $S$ , the potential in  $A$  due to  $S$  is calculated as in (3). The energy of  $A$  in this potential

$$E_A = \left\langle \Psi_A \left| \hat{H}_A^0 + \sum_{a \in A} z_a \Phi_S(\mathbf{r}_a) \right| \Psi_A \right\rangle_A \quad (4)$$

is minimized, giving a new wave function  $\Psi_A$ . Next, the potential due to  $A$  in  $S$  is calculated, and in turn  $\Psi_S$  is optimized in this potential. A new potential due to  $S$  in  $A$  is found and applied, etc., until self-consistency is reached.

In a perturbation formalism, where the starting functions for  $\Psi_A$  and  $\Psi_S$  are the vacuum (ground) state functions  $\Psi_A^0$  and  $\Psi_S^0$  of the subsystems  $A$  and  $S$  and the optimized functions are expanded in the orthogonal set of solutions to the vacuum problem  $\hat{H}_A^0 \Psi_A^m = E_A^m \Psi_A^m$  for subsystem  $A$  (and similarly for  $S$ ), it is easily seen that  $\Phi_S$  can be split into two contributions, resulting from the vacuum charge density and the density change induced by subsystem  $A$ . The former is called the static potential and the latter the response potential. To second order in the perturbation  $\hat{V}_{AS}$ ,

$$\begin{aligned} \Phi_S(\mathbf{r}_a) &= \left\langle \Psi_S \left| \sum_{s \in S} \frac{z_s}{|\mathbf{r}_a - \mathbf{r}_s|} \right| \Psi_S \right\rangle_S \\ &= \left\langle \Psi_S^0 \left| \sum_{s \in S} \frac{z_s}{|\mathbf{r}_a - \mathbf{r}_s|} \right| \Psi_S^0 \right\rangle_S + \left\{ 2 \sum_{k \neq 0} c_k \left\langle \Psi_S^0 \left| \sum_{s \in S} \frac{z_s}{|\mathbf{r}_a - \mathbf{r}_s|} \right| \Psi_S^k \right\rangle_S \right. \\ &\quad \left. + \sum_{k, m \neq 0} c_k \left\langle \Psi_S^k \left| \sum_{s \in S} \frac{z_s}{|\mathbf{r}_a - \mathbf{r}_s|} \right| \Psi_S^m \right\rangle_S c_m \right\} \\ &= \Phi_S^0(\mathbf{r}_a) + \Phi_S^{\text{response}}(\mathbf{r}_a) \end{aligned} \quad (5)$$

In (5) the coefficients  $c_k$  and wave functions are taken to be real. Expanding the perturbation operator  $\hat{V}_{AS}$  around a representative point  $\mathbf{r}_s^0$  in  $S$ ,  $c_k$  can be written as

$$\begin{aligned} c_k &= \frac{\left\langle \Psi_S^k \left| \sum_{a \in A} \sum_{s \in S} \frac{z_a z_s}{|\mathbf{r}'_a - \mathbf{r}_s|} \right| \Psi_S^0 \right\rangle_S}{E_0 - E_k} \\ &= \sum_{a \in A} \frac{-z_a (\mathbf{r}'_a - \mathbf{r}_s^0)}{|\mathbf{r}'_a - \mathbf{r}_s^0|^3} \frac{\left\langle \Psi_S^k \left| \sum_{s \in S} z_s \mathbf{r}'_s \right| \Psi_S^0 \right\rangle_S}{E_0 - E_k} + \dots, \end{aligned} \quad (6)$$

using the orthogonality of the zeroth-order functions. The field operator of subsystem  $A$  at the representative point in  $S$  and the dipole operator of subsystem  $S$  with

respect to the representative point are now recognized. Inserting (6) in the second term of (5) and making the same expansion for the potential operator, truncating at the dipole term, the second-order expression for the dipole polarizability of subsystem  $S$  emerges, thus showing the connection of the second term in (5) to the linear response functions of subsystem  $S$ :

$$\begin{aligned}
 2 \sum_{k \neq 0} c_k \left\langle \Psi_S^0 \left| \sum_{s \in S} \frac{z_s}{|\mathbf{r}_a - \mathbf{r}_s|} \right| \Psi_S^k \right\rangle_S &= \sum_{a \in A} \frac{-z_a(\mathbf{r}'_a - \mathbf{r}_s^0)}{|\mathbf{r}'_a - \mathbf{r}_s^0|^3} 2 \sum_{k \neq 0} \frac{\left\langle \Psi_S^k \left| \sum_{s \in S} z_s \mathbf{r}'_s \right| \Psi_S^0 \right\rangle_S}{E_0 - E_k} \\
 &\times \left\langle \Psi_S^0 \left| \sum_{s \in S} z_s \mathbf{r}'_s \right| \Psi_S^k \right\rangle_S \frac{-(\mathbf{r}_a - \mathbf{r}_s^0)}{|\mathbf{r}_a - \mathbf{r}_s^0|^3} + \dots \\
 &= \hat{E}_A(\mathbf{r}_s^0) \alpha_S(\mathbf{r}_s^0) \frac{-(\mathbf{r}_a - \mathbf{r}_s^0)}{|\mathbf{r}_a - \mathbf{r}_s^0|^3} + \dots \quad (7)
 \end{aligned}$$

The meaning of (7) is evident: the field due to a source in  $A$  at  $\mathbf{r}_s^0$  induces a dipole proportional to the polarisability  $\alpha_S$  at  $\mathbf{r}_s^0$ , which in turn gives rise to a (response) potential at the source in subsystem  $A$ . Higher order responses follow similarly from the continued expansion of the second term, and from the third term in (5), connecting to the quadratic response functions of  $S$ .

In order to reduce the number of degrees of freedom of the system, the static and response potentials due to  $S$  should be mapped on some functional form containing far less parameters than the original number of particles in  $S$ . The reduction is achieved by truncating the expansions in the Taylor series of the operators and the order of response theory. In practice, the Taylor series are usually truncated at the dipole level and the responses at second order in the perturbation, as shown here. Apart from these truncations, the size of the subsystems of which the properties are determined is also reflected in the sophistication of the mapping on classical models [17].

The great advantage of the treatment outlined above is that both the permanent moments and the response functions are defined entirely in terms of the subsystem(s)  $S$ , and can be obtained from explicit calculation at any level, or from experiment. The permanent moments and the response functions may be regarded as parameters describing the *collective* properties of the particles comprising subsystem  $S$ .

The theoretical development so far requires solute/solvent separation for more or less formal reasons, and linear response of the solvent for practical reasons. In the next section we will analyze various model response functions with respect to these requirements.

### Dielectric Models Scrutinized

The separation of two or more systems and the (non)linearity of their mutual interactions are, of course, strongly connected. For example, the interactions between the three atoms in a single water molecule are highly nonlinear because their charge distributions overlap strongly *and* the electric potentials and fields are too large to

expect linear response. As far as the energy is concerned, the only way to deal with this problem is to describe the system in terms of electrons and (effective) nuclei, and solve a set of coupled equations which contain all of the nonlinear problems. One of the properties of the resulting charge distribution is its (dipole) polarizability describing the linear response of this collection of atoms.

In the water dimer at its optimal geometry, the largest overlap between two MOs is about 0.05 (this was calculated with program suites SYMOL and GNOME [18], with optimized orbitals in the water dimer). Whether or not this is a "large" overlap depends on the context in which the overlap criterion is used. One may wonder if the electrostatic interaction between the molecules can be described with a linear response model at this distance, or more generally: Up to what distance is this model acceptable? One possible answer comes from simple electrostatics given, e.g., by Thole [19]. Consider two isotropic interacting polarizabilities  $\alpha_i$  and  $\alpha_j$  at distance  $r$ . The effective polarizability along the axis is

$$\alpha_{\parallel} = \frac{\alpha_i + \alpha_j + 4\alpha_i\alpha_j/r^3}{1 - 4\alpha_i\alpha_j/r^6}. \quad (8)$$

When  $r$  approaches  $(4\alpha_i\alpha_j)^{1/6}$ ,  $\alpha_{\parallel}$  tends to infinity, caused by the cooperative interaction between the two induced dipoles along the axis. The trouble starts obviously already when the polarizability volumes—i.e., spheres with radius  $\alpha^{1/3}$ —start overlapping. Such a situation should either be avoided, or one must account for the nonlinearities, e.g., by screening the interactions. In our model for reaction potentials we have adopted Thole's method for defining an effective "many-body" polarizability, in which  $d_{ij} = 1.662 (\alpha_i\alpha_j)^{1/6}$  is the minimum distance for two interacting polarizabilities without screening function, where the factor 1.662 and the polarizabilities are model parameters fitted to (experimental or calculated) molecular dipole polarizabilities. If the polarizabilities come closer, the fields of the induced dipoles are damped to account for the overlap of the electronic densities connected to the polarizabilities. In the water dimer we may put the monomer electronic polarizabilities of 10 bohr<sup>3</sup> on the oxygen atoms, which are in the equilibrium geometry about 6 bohr apart. Thole's criterion shows that already at this distance the treatment of mutual induction effects may be treated completely classical [20], provided the inducing fields correspond to charge distributions, which are correct up to at least the dipole term [21]. Apparently both the separation and the linearity requirements are satisfied in this situation.

The dielectric continuum model maps the electric behavior of a bulk volume onto a single nonvanishing parameter, the dielectric constant, describing its linear response [11]. Jackson [22] has shown on experimental grounds that the size of representative bulk volumes in which the solvent is partitioned should be at least 10<sup>7</sup> bohr<sup>3</sup>, being macroscopic on an atomic scale, but microscopic on an everyday experimental scale. On this scale, the bulk is homogeneous and structureless, resulting in vanishing electric moments, so that the bulk has no static potential contribution.

In continuum models for solvation it is necessary to define a cavity in the dielectric to contain the solute. The solute's response potential is found by solving Poisson's



equation, which is practicable only if no higher order than linear response is allowed. In practice, two types of method for solving the Poisson equation are in use: one based on spatial integration (on some grid) [9], the other based on (numerical) integration on the surface enveloping the solute (usually built from small adjacent polygons) [8,10]. The surface defines the boundary between the solute cavity and the solvent bulk. Of the second type, analytic methods exist [1,3,7,23], but they are only possible for spherical and elliptical cavities, making them less useful for general purposes.

The necessity of defining a cavity around the solute immediately poses the problem of where to put its boundary. Because the reaction potential is very sensitive to the solute-boundary distance, getting "physically plausible results" strongly depends on the careful definition of the boundary. The surfaces employed in most models resemble a Connolly surface [24], which is defined by rolling a probe sphere with the size of a solvent molecule over a set of overlapping spheres centred on the solute's atomic sites. If the atomic spheres are given the atomic van der Waals radii, Connolly's "van der Waals surface" is defined by the "contact points" between probe and atomic spheres. The surface traced by the center of the probe is usually called the "solvent accessible" surface.

We want the boundary first to be consistent with the nonoverlap requirement, meaning that no significant part of solute's (electronic) charge is to be found outside the cavity. Regarding this, Miertuś et al. [2] tell us that this requirement leads to "unrealistically small" reaction potentials. Indeed they found with the standard van der Waals radii that a sizable amount of electronic density (for water about 1%) extends over the boundary. This means that the overlap of 0.05, mentioned above, is here too large. To remedy this effect, a correction was made for the "charge leakage," and at the same time the atomic radii were scaled up by 20%, to keep the charge distribution within the cavity to within 0.5%. The analytic methods employ a cavity with a volume derived from the density of the solute, which leads to a cavity of approximately the same size as defined by the Connolly van der Waals radii [3,7], so that they may suffer from the same defect. Choices published so far are all of the type "van der Waals plus something" or "van der Waals times something" to arrive at "realistic" solvation energies.

At this point we conclude that the van der Waals surfaces are too close to the solute to be consistent with the nonoverlap criterion, and we suggest increasing the "atomic spheres" by adding at least one solvent radius. In case of a water solute in bulk water, this means that the boundary is located 7.3 bohr from the center of mass of the solute. Already here we note that by this procedure the experimental hydration energy cannot be reproduced.

Next we look into the combined overlap/nonlinearity problem. Obviously, no source charge or (induced) dipole may ever be positioned precisely on the boundary, because its reaction potential will then be infinitely large. A measure for the minimal distance can be obtained—at least for a neutral, polarizable solute—by repeating Thole's reasoning for two polarizabilities.

The dielectric constant of the bulk is, via the dielectric susceptibility,  $\chi_e = (\epsilon - 1)/4\pi$ , connected to the polarizability density, which includes, apart from the elec-

tronic polarization, vibrational and rotational contributions. For polar solvents the rotational contribution, i.e., the effect of the permanent dipoles orienting themselves along the applied field, dominates. By simply multiplying the dielectric susceptibility by the volume of one solvent molecule (assuming that the dielectric is homogeneous to a microscopic limit), one gets an effective molecular polarizability. Again taking water as an example, we obtain (from the density and susceptibility at 298 K) an effective polarizability of  $1240 \text{ bohr}^3$  per molecule. Applying Thole's criterion for the interacting polarizabilities of the central water ( $10 \text{ bohr}^3$ ) and an effective neighboring bulk molecule, the minimum distance should be 8.0 bohr, which is slightly larger than that derived from the first criterion. This second criterion is not always the strongest. For benzene in benzene, e.g., the first criterion (no overlap) would put the boundary at 12.4 bohr from the center of mass, the interacting polarizabilities criterion at only 7.2 bohr.

The last possible test regards the linearity of the response per se. If the solute's field strength is too large, nonlinear effects will give rise to an enhanced or reduced polarization of the bulk, depending on the type of effect [11, Chap. 7]. For polar solvents, the main nonlinear effect is saturation: The molecular dipoles become more or less fixed in space with respect to the solute, strongly reducing the orientational contribution to the local polarizability.

At the macroscopic level this can be remedied quite satisfactorily by introducing a correction function to the dielectric constant proportional to the square of the field strength, but at microscopic level the dielectric model breaks down and at least the first solvent layer should be included in a more detailed way in the description. From experiment it is known that nonlinear effects show up at field strengths of about  $2 \cdot 10^{-6} \text{ a.u.}$  ( $10^4 \text{ V/cm}$ ), which is, for example, generated by a unit dipole (2.54 D) at 100 bohr *in vacuo*! Considering again water in water, with a solute dipole moment equal to 1.85 D, the previous criteria look pallid. If the boundary would be put at the required distance (73 bohr), many layers of solvent water would have to be included to make the model still look like a condensed phase.

In practice, one can probably do with a smaller number of solvent layers, as the collective field of solute and solvent layers will fall off faster than the field of the solute alone. Insight in the minimum number of solvent layers to be included can be gained from the radial distribution functions of the solvent. A typical radial distribution for bulk water after Narten et al. [25] is schematically shown in Figure 1. It is clear that at least the first two layers should be considered in detail, since the requirement of homogeneity is not fulfilled. The problem of smoothing the transition from explicit to continuum description of the bulk molecules has recently been addressed by one of us [26].

### Computational Methods

Our model of the condensed phase [5] is illustrated in Figure 2. The part of interest is treated quantum mechanically, and is called the "quantum system." This may be the active site of an enzyme or a solute molecule, or a small cluster of

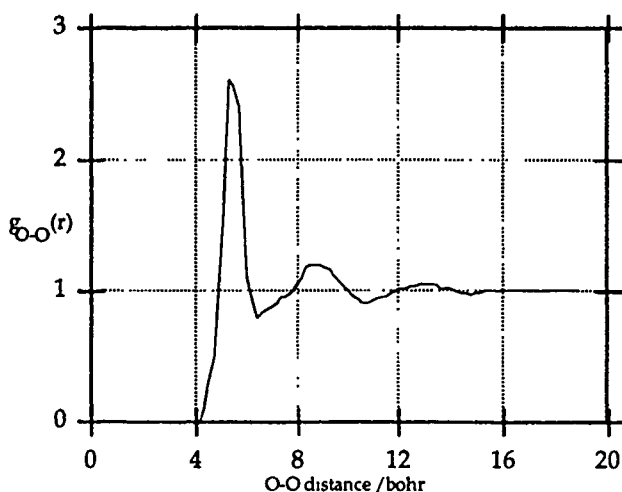


Figure 1. O—O radial distribution function of bulk water.

molecules. A number of subsystems may be defined, which are treated in a discrete classical way. The vacuum static potential of the subsystems is reproduced by an expanded monopole representation (usually charges at the nuclei of the subsystems are sufficient to obtain accurate fields), whereas the response potential is mediated through (anisotropic) dipole polarizabilities (usually one per subsystem).

The "quantum + discrete classical" system is enveloped by a surface, defining the boundary between discrete and continuum systems. The system outside the

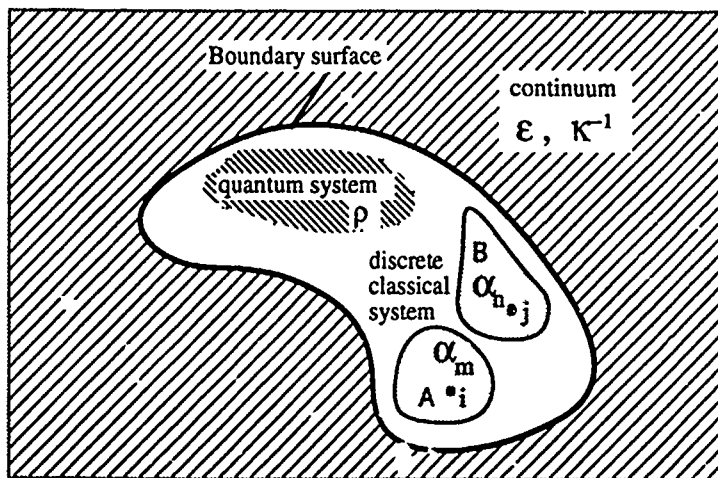


Figure 2. General condensed phase model.

boundary is modeled by a single response parameter, viz., the dielectric constant. The response potential in the region of the quantum system is found by solving Poisson's equation for the system of interacting charges and polarizabilities inside the boundary. The method allows for an additional response parameter for the continuum, the Debye screening length  $\kappa^{-1}$ , in order to model an ionic bulk solution.

The free energy change of solvation contains three contributions associated, respectively, with the solute's loss of translational freedom [27], the creation of a cavity in the solvent, and the solute/solvent interactions:

$$\Delta G_{\text{solv}} = \Delta G_{\text{tr}} + \Delta G_{\text{cav}} + \Delta G_{\text{int}}. \quad (9)$$

We take

$$\Delta G_{\text{tr}} = \Delta A_{\text{tr}} + \Delta(pV) \approx -RT \left( \ln \frac{V_l}{V_g} + 1 \right) \quad (10)$$

where the volumes  $V_l$  and  $V_g$  are calculated from the liquid and gas phase densities, respectively, under standard conditions, and the gas is assumed to obey the perfect gas law.

For the cavitation free energy the semiempirical method based on a hard sphere model due to Pierotti [28] is used. The expression for the cavitation free energy is rooted in statistical mechanics and needs only solute and solvent diameter and solvent number density as parameters. The molecular radii may be calculated from density, reducing the number of parameters by one, or fitted to experimentally determined cavitation free energies:

$$\begin{aligned} \Delta G_{\text{cav}} &= K_0 + K_1 \sigma_{12} + K_2 \sigma_{12}^2 + K_3 \sigma_{12}^3, \\ K_0 &= RT \left\{ -\ln(1-y) + \frac{9}{2} [y/(1-y)]^2 \right\} - \frac{\pi P \sigma_1^3}{6}, \\ K_1 &= -\frac{RT}{\sigma_1} \left\{ 6[y/(1-y)] + 18[y/(1-y)]^2 \right\} + \pi P \sigma_1^2, \\ K_2 &= \frac{RT}{\sigma_1^2} \left\{ 12[y/(1-y)] + 18[y/(1-y)]^2 \right\} - 2\pi P \sigma_1, \\ K_3 &= \frac{4}{3} \pi P, \quad y = \frac{\pi \sigma_1^3 \rho L}{6M}, \quad \sigma_{12} = \frac{1}{2}(\sigma_1 + \sigma_2). \end{aligned} \quad (11)$$

In (11)  $\sigma_1$  and  $\sigma_2$  are the solvent and solute diameter, respectively,  $P$  is the pressure and  $\rho$ , and  $M$  the solvent density and molecular weight, respectively. On the beneficiary side there is the energy gained from interaction of the solute with the solvent molecules,  $\Delta G_{\text{int}}$ .

In our implementation (currently within HONDO8 [29]), the static and response potentials may be added to the Hamiltonian of the quantum system, giving access to the electronic properties of the quantum system in the presence of the classical discrete and/or continuum environment, either in a perturbation treatment, or variationally, within the self-consistent field approximation. For the short range

repulsion energies between the discrete classical parts and the quantum system we used a model adapted from the CHARMM [30] programs. Further computational details may be found elsewhere [5,31].

### Results: Solvation (Free) Energies

#### *Water in Water*

In Figure 3 we have collected  $\Delta G_{\text{int}}$  values for water in a dielectric continuum with  $\epsilon = 78.5$ , for different sizes of the cavity.

Clearly the sensitivity of the stabilization energy to the position of the boundary emerges. At the distance we feel the requirements of nonoverlapping systems and prevention of the polarization catastrophe are met (7.3 bohr), the stabilization energy ( $\approx 6 \text{ kJ mol}^{-1}$ ), which reasonably reflects the *bulk* contribution, is far too small to be considered as the electrostatic part of the solvation free energy.

As a next step, the first solvation layer is taken into account explicitly by our classical model. The four water molecules surrounding the central water are each modeled by point charges at the nuclei (so as to reproduce the vacuum water dipole moment [21]) and a group polarizability (reproducing the experimental water polarizability [19]) at the center of charge.

The geometrical arrangement is such that each central water-classical water is at the water dimer optimum distance and orientation. The various contributions to the interaction energy are presented in Table I.

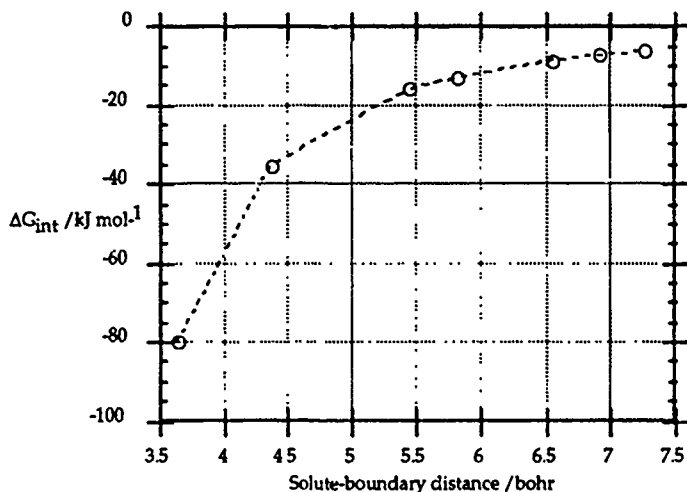


Figure 3. Continuum reaction field stabilization energy as a function of water-boundary distance in the range of van der Waals (3.65 bohr) to twice the van der Waals radius (7.3 bohr) of water. The boundary was Connolly's van der Waals surface with probe radius 2.64 bohr and the dielectric constant was 78.5.

TABLE I. Partitioning of interaction energy between a quantum mechanically treated water<sup>a</sup> and four classical water molecules.<sup>b</sup>

Type of interaction	$\Delta E_{\text{int}}$ (kJ mol <sup>-1</sup> )
Electrostatic	-65
Induction	-6
Dispersion <sup>c</sup>	-21
	-92
$\Delta G_{\text{tr}} + \Delta G_{\text{cav}}$	+29
Total	-63

<sup>a</sup> DZP basis set, optimized vacuum geometry.

<sup>b</sup> The water molecules are represented by point charges at the nuclei (-0.796 for O, to give the vacuum dipole moment) and an anisotropic group polarisability constructed from atomic polarisabilities.

<sup>c</sup> This is an estimate, see Refs. [20,21,31,32].

The numbers in Table I are enthalpies rather than free energies, and therefore a modest Monte Carlo (MC) sampling [14] was performed of the part of phase space connected with rotations of the classical waters. Translations were excluded at this point because we have not yet developed a satisfactory model for the short-range repulsions consistent with the electrostatic part of our model. In two further calculations, the bulk beyond the first solvation shell was added in the dielectric continuum description. Again, calculations were done on the reference configuration, as well as the Monte Carlo sampling of the rotational freedom. The results of all these calculations are presented in Table II.

The final result for  $\Delta G_{\text{solv}}$  in Table II (-48 kJ mol<sup>-1</sup>) is already close to the experimental value (-42 kJ mol<sup>-1</sup>), and adding the translation freedom would most likely bring the two values closer together.

### *Benzene in Benzene, Hexane, and Methanol: Transfer Free Energies*

A test of the generality of the continuum model is the transfer free energy of benzene, which has been determined experimentally [33]. The transfer free energy is defined as the free energy of transferring a solute molecule from one solvent to another. The solvation free energy of benzene in benzene, hexane, and methanol is calculated by the same procedure as used for water in water by the continuum model alone. The results are presented in Table III.

If the boundary surface is Connolly's van der Waals surface of benzene, the dispersion interaction (which is the dominant contribution) is calculated to be 340-390 kJ mol<sup>-1</sup>.

This is far too large, probably due to "charge leakage," and overshooting the solvation energy by a factor of 10 for benzene. These problems are not encountered

TABLE II. Total interaction energies between a quantum mechanically treated water and four classical water molecules for reference geometry and Monte Carlo sampling of rotational configuration space with and without a dielectric.<sup>a</sup>

Solvent model	$\Delta E_{\text{int}}$ (kJ mol <sup>-1</sup> ) <sup>b</sup>
Four classical waters	
Reference geometry	-92
Monte Carlo of rotations	-71 ± 9
Ref. geometry + dielectric	-103
Monte Carlo of rotations	-77 ± 9
$\Delta G_{\text{solv}} = \Delta E_{\text{int}} + 29 \text{ kJ mol}^{-1}$	

<sup>a</sup> The boundary is approximately the solvent accessible surface of the QM water + four classical water cluster; the dielectric constant is 78.5.

<sup>b</sup> The dispersion term is assumed to be constant for all configurations and is not explicitly calculated in the Monte Carlo run for each configuration.

with the boundary surface suggested by us in the third section. following the no-overlap criterion, taking both solute and solvent microscopic structure into account. On the other hand, with the surface advocated by us, the interaction energy is too small to reproduce the experimental solvation free energy, as well as the transfer free energy, even in a qualitative sense.

### Results: Electronic Properties

Apart from energy, (electronic) properties of the solutes are of interest. Indeed, the whole point of maintaining a quantum mechanical description of some part of the condensed phase is to have access to electronic properties.

TABLE III. Solvation and transfer free energies of benzene.

Solvent <sup>a</sup>	Solvation energy (kJ mol <sup>-1</sup> )		Transfer energy (kJ mol <sup>-1</sup> )	
	Calcd	Exptl	Calcd	Exptl
Benzene	+27	-31	+17	-5.0
Hexane	+30		+20	-3.8
Methanol	+10		0	0

<sup>a</sup> The boundary is approximately the solvent accessible surface of benzene; the static and optical dielectric constants for benzene, hexane, and methanol are 2.3 and 2.253, 1.9 and 1.89, 32.6 and 1.766, respectively.

The electronic spectrum of water is not particularly exciting, but some aspects will be considered briefly to point out the differences between the continuum model and the explicit classical model for the first solvation layer. Table IV contains the shifts of the HOMO orbital energy (Koopmans' ionization energy), the dipole moment and the polarizability of the quantum mechanically treated water molecule going from vacuum to solution, for the different models. Most strikingly, the HOMO is destabilized if the explicit water model is used, and stabilized by about the same amount in the continuum model.

Closer inspection of the polarizability shows that, although the overall polarizability is not very sensitive to the solvent model, the individual contributions are, as may be seen from the oscillator strengths, which for brevity here are omitted. Placing the dielectric at the distance advocated by us leaves the properties of the water molecule almost unchanged.

The electronic spectrum of water is not spectacularly solvent-dependent and therefore not a good test for the applicability of the continuum approach for electronic properties. More marked solvent effects are seen for conjugated systems, whose transitions often serve as solvent polarity scales [35]. Unfortunately, these systems are mostly too large for easy quantum chemical computations. A less successful solvent polarity scale was derived from the  $n \rightarrow \pi^*$  transition of acetone [36], which is a tractable molecule for quantum chemical computations. In the experimental transition energy is  $35.850 \text{ cm}^{-1}$ . The solvent effect on this transition is some  $2000 \text{ cm}^{-1}$  on going from hexane to water.

The same solvent models as for water in water were tested, only for the atomic radii the van der Waals + 20% radii were chosen, and a larger number of explicit water molecules were taken into account (17 instead of four).

In order to reflect the short lifetime of the excited states, they were calculated in the static reaction field of the ground state, which is not in equilibrium with the excited state charge density. The reason for this is the slow relaxation associated with the orientational component of the dielectric response [37,38], so that the excited state "sees" the polarization of the environment in equilibrium with the ground state. The electronic part of the dielectric response is much faster and is in equilibrium with the excited state density. This last part is treated here as a perturbation (for both ground and excited states), which usually makes little difference

TABLE IV Dependence of water properties on solvent model.<sup>a</sup>

Solvent model	$\Delta\epsilon \text{ (kJ mol}^{-1}\text{)}^b$	$\Delta\mu \text{ (a.u.)}$	$\Delta\alpha \text{ (a.u.)}^c$
Dielectric at van der Waals distance	-23	+0.19	-0.7
Four classical waters, reference geometry	+19	+0.22	-0.8
Four class. waters, ref. geom + dielectric	+18	+0.23	-0.8
Dielectric at vdW + water distance	-2	+0.02	-0.07

<sup>a</sup> The shifts w.r.t. the vacuum properties are shown.

<sup>b</sup> HOMO orbital energy shift; this is Koopmans' ionization energy shift.

<sup>c</sup> Calculated by second-order perturbation theory, with nonempirical Unsold approximation [34]



to the interaction energy. Work is in progress to treat the different frequency components of the dielectric response in a more sophisticated way. The results for the calculated transition energies, as well as the nuclear and electronic contributions to the interaction with the nonequilibrium reaction field are presented in Table V. The difference between continuum approach and explicit treatment of solvent water molecules in the first (and part of the second) shell is for acetone decidedly more marked than for water in water. Although the calculated excitation energy shifts are almost equal in both approaches, the causes are entirely different. With the explicit water treatment, the nuclei are stabilized more in the static field than are the electrons, whereas with the dielectric response field, the reverse is found.

### Discussion and Conclusions

Dielectric continuum models have been successful in calculating the interaction energy between solute and solvent based on one solute molecule in a dielectric. It has been shown that the results of the continuum models compare well with results obtained by models that include a more explicit description of the solvent, in MC, MD, and free energy perturbation (FEP) calculations, for water as solvent. Although the results may be comparable when interaction energy is concerned, the origin of the interaction energy is totally different in the continuum and more explicit models. Modeling other solvents than water by a dielectric is a rather unexplored area of research [39,40].

In the dielectric continuum approach, the interaction is solely due to a linear response of the collective solvent molecules, whereas the explicit models show clear saturation effects of the first solvent layers, a fact that is confirmed experimentally. The molecules in the first solvation shell of water in water are strongly hydrogen bonded to the central water and there is a strong dipole-dipole interaction, keeping the orientation of the molecules rather fixed. This effect is certainly not described by the dielectric constant, for this behavior is strongly nonlinear.

The favorable interactions of water in water thus find their root in very specific dipole-dipole and hydrogen bonding interactions, with electronic induction playing a minor role, as can be seen from Table I. The success of the continuum model must therefore be explained by a fortuitous choice of boundary regarding experimental hydration energies only.

TABLE V.  $n \rightarrow \pi^*$  transition energies of acetone *in vacuo* and in water<sup>a</sup> and interaction energies of nuclei and electrons with nonequilibrium reaction field in the excited state.

Type and solvent model	$\nu (n \rightarrow \pi^*)$ (cm <sup>-1</sup> )	$\Delta E$ (nuc) (hartree)	$\Delta E$ (el) (hartree)
Vacuum	25,321		
Dielectric at van der Waals + 20% distance	28,030	+0.198	-0.214
17 classical waters, reference geometry	28,066	-0.183	+0.157

<sup>a</sup> The standard STO4-31G basis was used throughout.

The results for the solvation and transfer energies of benzene in various solvents clearly show that the dielectric model is not easily extendable to other solvents. Retaining the van der Waals surface gives problems in the dispersion term.

In an attempt to extend the dielectric continuum approach to any solvent, one could envisage the following procedure for each solvent: Vary the solute-boundary distance to reproduce the experimental solvation energy, and derive some atomic radii for the solute atoms in that solvent. To calculate the solvation energy of other solutes in that solvent, use those solvent dependent atomic radii as parameters. This procedure has been very successful for water [2,4,6], and may be for other solvents. Such a procedure must, however, be considered as engineering, and one must be very reluctant to attach any physical meaning to the radii and to calculated properties other than the energies.

Considering the electronic properties of water as they change from vacuum to solvent, as shown in Table IV, most striking are the different HOMO orbital energy shifts between the explicit water model and the continuum models. Closer inspection of the polarizability shows that, although the overall polarizability is not very sensitive to the solvent model, the individual contributions are, as could be seen from the oscillator strengths. Placing the dielectric at the distance advocated by us, leaves the properties of the water molecule almost unchanged.

The case of the  $n \rightarrow \pi^*$  transition of acetone (Table V) shows that, although overall energies may correspond, the partitioning of different contributions may drastically differ, giving rise to a physically different interpretation of the causes and effects. Here, again, some saturation in the first shell sets up a static field that influences the electronic properties of the ground and  $n \rightarrow \pi^*$  state. This effect is clearly reversed by a dielectric response only description.

Although the dielectric continuum model for water as a solvent is satisfactory for hydration free energy calculations, it does not accurately describe the bulk solvent influence on electronic properties of the solute. For this, a more microscopically detailed description is required, to account for nonlinear effects in the first solvation shell(s).

Also, the same procedure for modeling water is not applicable when modeling other solvents, necessitating a new definition of the solute-solvent boundary distance for each solvent. Rather than such an ad hoc treatment, we advocate the more detailed description of solvent molecules in the first solvation shells. We could short-circuit all of our arguments for this approach by looking at Figure 1 again, and assume indeed that the dielectric constant can only represent a homogeneous and structureless continuum. This will put directly the boundary where all requirements are fulfilled at once, albeit that the region where the solvent shows structure must be taken into account explicitly.

### Bibliography

- [1] K. V. Mikkelsen, E. Dalgaard, and P. Swanström, *J. Phys. Chem.* **91**, 3081 (1987).
- [2] S. Miertus, E. Scrocco, and J. Tomasi, *Chem. Phys.* **55**, 117 (1981).
- [3] K. V. Mikkelsen, H. Ågren, H. J. Aa Jensen, and T. Helgaker, *J. Chem. Phys.* **89**, 3086 (1988).

- [4] M. W. Wong, M. J. Frisch, and K. B. Wiberg, *J. Am. Chem. Soc.* **113**, 4776 (1991).
- [5] P. Th. van Duijnen, A. H. Juffer, and J. P. Dijkman, *J. Mol. Struct. (Theocchem)* **260**, 195 (1992).
- [6] C. J. Cramer and D. G. Truhlar, *J. Am. Chem. Soc.* **113**, 8305 (1991).
- [7] M. M. Karelson, T. Tamm, A. R. Katritzky, M. Szefran, and M. C. Zerner, *Int. J. Quantum Chem.* **37**, 1 (1990).
- [8] R. J. Zauhar and R. S. Morgan, *J. Comput. Chem.* **9**, 171 (1988).
- [9] M. K. Gilson, K. A. Sharp, and B. H. Honig, *J. Comput. Chem.* **9**, 327 (1988).
- [10] A. H. Juffer, E. F. F. Botta, B. A. M. Van Keulen, A. van der Ploeg, and H. J. C. Berendsen, *J. Comput. Phys.* **97**, 144 (1991).
- [11] C. J. F. Böttcher, *Theory of Electric Polarisation*, 2nd ed. (Elsevier, Amsterdam, 1973).
- [12] A. Jean-Charles, A. Nicholls, K. Sharp, B. Honig, A. Tempczyk, T. F. Hendrickson, and W. C. Still, *J. Am. Chem. Soc.* **113**, 1454 (1991).
- [13] J. A. C. Rullmann and P. Th. van Duijnen, *Mol. Phys.* **61**, 293 (1987).
- [14] J. A. C. Rullmann and P. Th. van Duijnen, *Mol. Phys.* **63**, 451 (1988).
- [15] A. H. de Vries and P. Th. van Duijnen, *Biophys. Chem.* **43**, 139 (1992).
- [16] R. McWeeny, *Methods of Molecular Quantum Mechanics*, 2nd ed. (Academic, London, 1992), Chap. 14.
- [17] J. A. C. Rullmann and P. Th. van Duijnen, *CRC Rep. Mol. Theory* **1**, 1 (1990).
- [18] G. A. van der Velde, Ph.D. Thesis, University of Groningen, 1974, SYMOL; R. Broer, Ph.D. Thesis, University of Groningen, 1981, GNOME.
- [19] B. T. Thole, *Chem. Phys.* **59**, 341 (1981).
- [20] B. T. Thole and P. Th. van Duijnen, *Chem. Phys.* **71**, 211 (1982).
- [21] B. T. Thole and P. Th. van Duijnen, *Theor. Chim. Acta* **63**, 209 (1983).
- [22] J. D. Jackson, *Classical Electrodynamics*, 2nd ed. (Wiley, New York, 1975), Chap. 6.
- [23] L. Onsager, *J. Am. Chem. Soc.* **58**, 1486 (1936).
- [24] M. L. Connolly, *Science* **221**, 709 (1983).
- [25] A. H. Narten, W. E. Thiessen, and L. Blum, *Science* **217**, 1033 (1982).
- [26] A. H. Juffer and H. J. C. Berendsen, *Mol. Phys.*, in press.
- [27] H. Eyring, J. Walter, and G. E. Kimball, *Quantum Chemistry* (Wiley, New York, 1944).
- [28] R. A. Pierotti, *Chem. Rev.* **76**, 717 (1976).
- [29] M. Dupuis and S. A. Maluendes, in *Modern Techniques in Computational Chemistry*, E. Clementi, Ed. (ESCOM, Leiden, 1991), Chap. 8.
- [30] B. R. Brooks, R. E. Bruccoleri, B. D. Olafson, D. J. Staes, S. Swaminathan, and M. Karplus, *J. Comput. Chem.* **4**, 187 (1983).
- [31] B. T. Thole and P. Th. van Duijnen, *Theor. Chim. Acta* **55**, 307 (1980).
- [32] J. G. Ángyan and G. Jansen, *Chem. Phys. Lett.* **175**, 313 (1990).
- [33] K. A. Connors, *Chemical Kinetics, The Study of Reaction Rates in Solution* (VCH, New York, 1990), p. 421.
- [34] F. Mulder, M. C. van Hemert, P. E. S. Wormer, and A. van der Avoird, *Theor. Chim. Acta* **46**, 39 (1977).
- [35] C. Reichardt, *Angew. Chem. Int. Ed. Eng.* **18**, 98 (1979).
- [36] W. P. Hayes and C. J. Timmons, *Spectrochim. Acta* **21**, 529 (1965).
- [37] H. Ågren and K. V. Mikkelsen, *J. Mol. Struct. (Theocchem)* **234**, 425 (1991).
- [38] M. M. Karelson and M. C. Zerner, *J. Phys. Chem.* **96**, 6949 (1992).
- [39] H. J. Kim and J. T. Hynes, *J. Am. Chem. Soc.* **114**, 10508 (1992).
- [40] K. B. Wiberg and M. W. Wong, *J. Am. Chem. Soc.* **115**, 1078 (1993).

Received May 12, 1993

# Quantum Field Theoretical Methods in Chemically Bonded Systems. V. Potential Energy Curves for $N_2(X^1\Sigma_g^+) \rightarrow 2N(^4S)^*$

THOMAS E. SORENSEN and WALTER B. ENGLAND

*Department of Chemistry and Laboratory for Surface Studies, University of Wisconsin-Milwaukee, Milwaukee, Wisconsin 53201*

DAVID M. SILVER

*Applied Physics Laboratory, Johns Hopkins University, Laurel, Maryland 20723*

## Abstract

Many-body perturbation theory is applied to the nitrogen triple bond for bond distances ranging from the atomic regime to about  $0.6a_0$  shorter than equilibrium. A full-optimized reaction space model is used to compute orbital spaces with an even-tempered gaussian-type basis set and also with a nominal Bagus-Gilbert Slater-type basis set. Conservation of orbital angular momentum in the atomic regime leads to perturbative theory for Hartree-Fock plus proper dissociation. Angular momentum conservation can also be enforced with a scaled Slater-Condon parameter. Third-order dissociation energies and spectroscopic constants approach limits of the chosen basis sets. © 1993 John Wiley & Sons, Inc.

## Introduction

The methods of quantum field theory differ from those of first-quantized theory. Quasiparticles and a quasiparticle vacuum describe the single-particle characteristics of a many-particle system. Many-particle conservation theorems such as particle number are side conditions placed on observables and enter as Lagrange multipliers such as chemical potential. Many-particle interactions are defined by Feynman diagrams (FDs). FDs describe scattering events among the quasiparticles. Correlation is defined by FDs that furnish an exact order-by-order series expansion for many-body perturbation theory (MBPT). Particles and holes and the Hartree-Fock (HF) vacuum describe *normal* fermion problems. They are defined by a single-particle Schrödinger equation with a potential set up according to Poisson's equation (Hartree potential) and correct quantum statistics (exchange interaction). Binding among particles and holes is described by *paired* quasiparticles and the Bardeen-Cooper-Schrieffer (BCS) vacuum. For historical reasons, paired quasiparticles are associated with superfluid and superconducting fermion problems; however, paired quasipar-

---

\* This work was supported in part by IBM RSP 3112 and in part by the U.S. Department of the Navy, Space and Naval Warfare Systems Command under Contract N00039-89-C-0001. It was presented, in part, at the Midwest Theoretical Chemistry Conference, East Lansing, Michigan, May 1992.

ticles are also needed to represent chemical bonds in molecules. Paired quasiparticles and side conditions for chemical problems may be based on chemical intuition and adiabatic symmetry correlation. The 1-particle Schrödinger equation for paired quasiparticles includes a generalized HF potential which allows fractionally occupied 1-particle levels, 2-particle binding interactions between particles and holes (pairing interactions), and terms from the side conditions (for example, chemical potential). The potential treats particles and holes associated with chemical bonds as paired quasiparticles and all others as normal quasiparticles. Quasiparticles, quasiparticle energies, and Lagrange multipliers for side conditions are determined self-consistently. Many-body corrections are FD for self-consistent quasiparticles. They are computed with low-order MBPT.

Second-quantized methods for particles and holes can be readily transposed to  $n$ -particle Hilbert space because the HF vacuum is a determinant that lies within one such space. However, because the BCS vacuum has components in more than one such space (see the next section), FD for paired quasiparticles must be formulated in Fock space. As is typical of the many-body problem, there is a simple formulation based on field-theoretic methods.

Field-theoretic methods for paired quasiparticles were applied to chemical bonds in a series of papers. The Heitler-London (HL) model of bonding and side conditions for particle-number conservation and proper dissociation were used to set up the model problems. Spectroscopic constants were reported in Paper I [1] for  $H_2$ , LiH, FH,  $F_2$ , and  $N_2$ . Formulae for FDs were derived in Paper II [2]. Paper III [3] reported ground-state energy curves for the four single-bonded diatomic molecules  $H_2$ , LiH, FH, and  $F_2$ . Paper IV [4] analyzed the perturbative corrections which were the basis for the energy curves reported in Paper III.

Papers I-IV were concerned mainly with particle-number conservation. An additional side condition is required for description of multiple chemical bonds. The foundations for the present work have been established in earlier work [5] in which a field-theoretic model Hamiltonian had been developed for the proper dissociation of multiple bonds, with  $N_2$  used as an illustration. Additionally, the broad background and specific theoretical treatment can be found in Paper II [2] and the detailed description and analysis of correlation energy terms can be found in Paper IV [4].

The present work reports calculations for  $N_2$  where the side condition is conservation of orbital angular momentum along the transition from  $N_2(X^1\Sigma_g^+)$  to two  $N(^4S)$  atoms. Additional conditions needed to describe the multiple bonding structure of  $N_2$  are described in the next section. The computational methods and details are presented in the third section. The perturbative results for  $N_2$  and a discussion of their accuracy are given in the fourth section.

### Perturbation Theory for the $N_2$ Ground State

The foundations for the present work have been established in earlier work [5] and Paper II [2]. Additional conditions needed to describe the multiple bonding structure of  $N_2$  are described in this section.

### Quasiparticles

Fractionally occupied full-optimized reaction-space (FORS) orbitals [6-8] which become degenerate at long bond distances are *paired levels*. They are in 1-to-1 correspondence with filled (hole) and empty (particle) levels of the normal HF determinant.

#### Paired levels for $N_2(X^2\Sigma_g^-)$

Hole	Particle	(1)
$z_h = 3\sigma_g$	$z_u = 3\sigma_u$	
$x_h = 1\pi_{xu}$	$x_u = 1\pi_{xg}$	
$y_h = 1\pi_{yu}$	$y_u = 1\pi_{yg}$	

Pairing removes degeneracy at long bond distances by diagonalizing a model Hamiltonian. A special Bogoliubov-Valatin (BV) transformation is the transformation to the diagonal representation. The BV transformation coefficients may be determined by solving the HL problem in the FORS. In that case, and with 1 standing for  $\zeta_b$  and 2 standing for  $\zeta_a$  for  $\zeta = x, y, z$ , the BV transformation is the same as Eq. (3) of Paper IV. Overlapping orbitals, normalization conditions, the particle-number conservation condition, and phase choices for the BV transformation in the FORS are the same as Eqs. (4)-(7), respectively, of Paper IV.

Equation (4) of Paper IV in the FORS is a "pairing" transformation [9, Eq. (3.42)]. Second-quantized operators for overlapping orbitals are defined by the same transformation

$$\begin{aligned}\hat{c}_{li} &= v_{ib}\hat{a}_{ib} + u_{ib}\hat{a}_{ia}, \\ \hat{c}_{ir} &= v_{ib}\hat{a}_{ib} - u_{ib}\hat{a}_{ia}\end{aligned}\quad (2)$$

and satisfy anticommutation conditions like those for overlapping atomic orbitals [10, Eq. (9.3)]:

$$\hat{c}_{li}^\dagger\hat{c}_{ir} + \hat{c}_{ir}\hat{c}_{li}^\dagger = S_i, \quad S_i = 2v_{ib}^2 - 1. \quad (3)$$

$S_i$  is the inner product or overlap in the FORS defined by Eq. (4) of Paper IV and is a type of "paired" inner product [9, Eq. (3.44)].  $\hat{a}_k$  is an annihilation operator for the FORS orbital  $\phi_k$ . At long bond distances, the FORS becomes the atomic HF space for  $2N(^4S)$ , and  $\hat{c}_{li}$  and  $\hat{c}_{ir}$  become annihilation operators for atomic HF  $2p_i$  orbitals on the atoms  $N_l$  and  $N_r$ , respectively. In the molecular regime,  $\hat{c}_{li}$  and  $\hat{c}_{ir}$  are annihilation operators for paired vestiges of atomic  $2p$  orbitals.

### Unperturbed Ground State

Equation (9) of Paper IV becomes a product of operators for FORS subshells which correspond to *unpaired holes*  $1\sigma_g, 2\sigma_g, 1\sigma_u, 2\sigma_u$ :

$$\hat{K} = \prod_{p=g,u} \prod_{k=1}^2 \hat{a}_{k\sigma_p}^\dagger \hat{a}_{k\sigma_p}^\dagger. \quad (4)$$

$k(\bar{k})$  stands for spin  $\frac{1}{2}(-\frac{1}{2})$ . Equation (8) of Paper IV becomes

$$\hat{M}_f = -\left(\frac{1}{v_{fb}^2}\right) \hat{\alpha}_{fb} \hat{\alpha}_{fb} \hat{\alpha}_{fa} \hat{\alpha}_{fa} \quad (5)$$

$$= (u_{fb} v_{fb} [1 + \hat{B}_f^2] + [u_{fb}^4 + v_{fb}^4]^{1/2} \hat{B}_f), \quad (6)$$

$$\hat{B}_f = \left[ \frac{1}{u_{fb}^4 + v_{fb}^4} \right]^{1/2} (v_{fb}^2 \hat{a}_{fb}^+ \hat{a}_{fb}^+ - u_{fb}^2 \hat{a}_{fa}^+ \hat{a}_{fa}^+). \quad (7)$$

Equations (10) and (13) of Paper IV become

$$|\mathcal{HL}\rangle = \prod_{f=x,y,z} \hat{M}_f \hat{K} | \rangle, \quad (8)$$

$$\hat{a}_k^+ |\mathcal{HL}\rangle = 0 \quad \text{for filled levels}, \quad (9)$$

$$\hat{\alpha}_k |\mathcal{HL}\rangle = 0 \quad \text{for paired levels}, \quad (10)$$

$$\hat{a}_k |\mathcal{HL}\rangle = 0 \quad \text{for empty levels}, \quad (11)$$

while Eqs. (17) and (18) become

$$|\text{HL}\rangle = \prod_{f=x,y,z} \hat{B}_f \hat{K} | \rangle. \quad (12)$$

$|\text{HL}\rangle$  is the HL *Ansatz* in the FORS. It is a sum of eight closed-shell determinants.  $|\mathcal{HL}\rangle$  is the corresponding BCS *Ansatz* in the FORS. It is a sum of 64 closed-shell determinants.

Unperturbed excited states are defined in §2.4 of Paper II and §2.1.2 of Paper IV. Excited states with manifestly incorrect particle-number are not allowed. Spurious excited states are eliminated.

### Model Hamiltonian

In the FORS, Eq. (23) of Paper IV generalizes to

$$\begin{aligned} \hat{H} &= \hat{H} - \hat{L}^{[\text{PN}]} - \hat{L}^{[\text{AM}]} \\ \hat{L}^{[\text{PN}]} &= \lambda_1^{[\text{PN}]} (\hat{N} - 6) + \frac{1}{2} \lambda_2^{[\text{PN}]} (\hat{N} - 6)^2 \\ &= \hat{L}_2^{[\text{PN}]} + \hat{L}_1^{[\text{PN}]} + \lambda_0^{[\text{PN}]}, \\ \hat{L}^{[\text{AM}]} &= \lambda_2^{[\text{AM}]} (\hat{L}_f^2 + \hat{L}_r^2) \\ &= \hat{L}_2^{[\text{AM}]} + \hat{L}_1^{[\text{AM}]} + \lambda_0^{[\text{AM}]}. \end{aligned} \quad (13)$$

$\hat{H}$  is the ordinary Hamiltonian. The  $L$  operator  $\hat{L}^{[\text{PN}]}$  ( $\hat{L}^{[\text{AM}]}$ ) enforces particle-number (atomic-fragment angular momentum) symmetry for the fractionally occupied shells.  $\hat{N}$  is the number operator [10, Eq. (8.7)] for the fractionally occupied shells. At long bond distances,  $\hat{L}_p$  is the second-quantized orbital angular momentum operator for the 2p shell on nitrogen atom  $p$  expressed in a real cartesian basis [10, Eqs. (8.7) and (9.19)]. In general,  $\hat{L}_l$  and  $\hat{L}_r$  are vestiges of total orbital angular momentum in the paired bases  $\hat{c}_{fi}$ ,  $\hat{c}_{fr}$  [Eq. (2)].

### Parameters

$\hat{L}_1^{[PN]}$ ,  $\hat{L}_2^{[PN]}$  and  $\lambda_0^{[PN]}$  are generalizations of the operators discussed in §2.2 of Paper IV.  $\lambda$  parameters depend on the FORS but not on a specific orbital basis for the FORS. Equation (35) of Paper IV is used to calculate  $\lambda_0^{[PN]}$ . The gap equation is used to calculate "chemical potential" [11, Eq. (62)]. As functions of bond distance, parameters for  $N_2$  appear similar to those for  $F_2$  (see Fig. 4 of Paper IV).

Formulae for normally ordered orbital angular momentum operators of Eq. (13) have not been reported previously:

$$\lambda_0^{[AM]} = \lambda_2^{[AM]} \langle \hat{\vec{L}}_l^2 + \hat{\vec{L}}_r^2 \rangle, \quad (14)$$

$$\begin{aligned} \hat{L}_1^{[AM]} = \lambda_2^{[AM]} \sum_{k=b,a} \sum_{\zeta=x,y,z} \sum_{m_s=-\frac{1}{2}, \frac{1}{2}} [\mathcal{L}_{\zeta k}^{(1,1)} : \hat{a}_{\zeta k m_s}^+ \hat{a}_{\zeta k m_s} : \\ + \mathcal{L}_{\zeta k m_s}^{(2,0)} (: \hat{a}_{\zeta k m_s}^+ \hat{a}_{\zeta k \bar{m}_s}^+ : + : \hat{a}_{\zeta k \bar{m}_s} \hat{a}_{\zeta k m_s} :)], \end{aligned} \quad (15)$$

$$\begin{aligned} \hat{L}_2^{[AM]} = \lambda_2^{[AM]} \sum_{k,k'=b,a} \sum_{\zeta \neq \zeta'=x,y,z} [h_{\zeta k} h_{\zeta' k'} \sum_{m_s=-\frac{1}{2}, \frac{1}{2}} (: \hat{a}_{\zeta k m_s}^+ \hat{a}_{\zeta' k' m_s}^+ \hat{a}_{\zeta k m_s} \hat{a}_{\zeta' k' m_s} : \\ + : \hat{a}_{\zeta k m_s}^+ \hat{a}_{\zeta' k' \bar{m}_s}^+ \hat{a}_{\zeta k \bar{m}_s} \hat{a}_{\zeta' k' m_s} : - : \hat{a}_{\zeta k m_s}^+ \hat{a}_{\zeta' k' \bar{m}_s}^+ \hat{a}_{\zeta k \bar{m}_s} \hat{a}_{\zeta' k' \bar{m}_s} :)] \end{aligned} \quad (16)$$

$$\langle \hat{\vec{L}}_l^2 + \hat{\vec{L}}_r^2 \rangle = 2 \sum_{k=b,a} \sum_{\zeta=x,y,z} \left( 2h_{\zeta k}^2 - h_{\zeta k} \sum_{k'=b,a} \sum_{\zeta' \neq \zeta} h_{\zeta' k'} (h_{\zeta k} h_{\zeta' k'} + \chi_{\zeta k} \chi_{\zeta' k'}) \right), \quad (17)$$

$$\mathcal{L}_{\zeta k}^{(1,1)} = h_{\zeta k} \left( 1 - 2 \sum_{k'=b,a} \sum_{\zeta' \neq \zeta} h_{\zeta' k'}^2 \right), \quad (18)$$

$$\mathcal{L}_{\zeta k m_s}^{(2,0)} = -h_{\zeta k} \sum_{k'=b,a} \sum_{\zeta' \neq \zeta} h_{\zeta' k'} \chi_{\zeta' k' m_s}. \quad (19)$$

Normal ordering with respect to  $|\mathcal{HL}\rangle$  [12, § 11.4] is denoted by  $: \dots :$ , where  $\dots$  stands for a product of second-quantized operators.  $h_{\zeta k}$  and  $\chi_{\zeta k m_s}$  are occupation and pairing numbers, respectively, for the fractionally occupied subshells of the FORS. They are defined as in §2.1.3 of Paper IV.

The FORS at infinity connects to the HF model of the atoms. The simplest molecular model that properly connects to the atoms is used to enforce angular momentum conservation for the atoms. This model is known as HFPD for HF plus proper dissociation [13]. Enforcing the connection yields conditions for  $\lambda_0^{[AM]}$ ,

$$\lambda_0^{[AM]} = E_{HL} - E_{HFPD}, \quad (20)$$

and the unperturbed energy,

$$\langle HL | \hat{\mathbf{H}} | HL \rangle = \langle \mathcal{HL} | \hat{\mathbf{H}} | \mathcal{HL} \rangle = E_{HFPD}. \quad (21)$$

$E_{HFPD}$  is computed with the HFPD *Ansatz* [13, Table I] in the FORS. In the language of FD, HFPD sums to every order all diagrams needed to enforce angular momentum symmetry for  $2N(^4S)$  relative to HL. All orders are needed because symmetries cannot be enforced by finite-order perturbation theory [14, p. 431].

$\lambda_0^{[AM]}$  varies between  $\frac{9}{25}F^2$  at long bond distances and (approximately) zero, where  $F^2$  is the Slater–Condon electron–repulsion integral for the 2p subshell of nitrogen



atom. This is expected because orbital angular momentum symmetry is quenched in the molecular regime. Association of  $\lambda_0^{[AM]}$  with  $F^2$  may be treated as a condition for model building:

$$\lim_{R \rightarrow \infty} \lambda_0^{[AM]} = \frac{9}{25} F^2. \quad (22)$$

In the latter case, quenching of orbital momentum is approximated by  $\frac{9}{25} F^2$  multiplied times the occupation number of the  $1\pi_a$  natural orbital.

$$\lambda_0^{[AM]}(F^2) = 2n_{\pi_a} \frac{9}{25} F^2. \quad (23)$$

(The  $1\pi_a$  natural orbital is chosen because it maintains 2p character without appreciable hybridization.)

$F^2$  can be assigned its value at  $R \rightarrow \infty$  ( $F^2$ ) for all  $R$  values, or can be computed for each  $R$  value as an appropriately weighted average of integrals involving only fractionally occupied levels ( $F_R^2$ ). If  $E_{HL}$  is given, Eq. (20) yields two corresponding approximations to  $E_{HFPD}$  ( $E_{F^2}$  and  $E_{F_R^2}$ , respectively). Perturbative corrections can be computed for  $E_{F^2}$  and  $E_{F_R^2}$ .

### Perturbative Corrections

One-body terms of the model Hamiltonian are identified by the normally ordered expansion of  $\tilde{H}$  in the canonical representation. This is described in Paper II. The unperturbed Hamiltonian is defined by Eq. (39) of Paper IV. The diagonalization condition for the generalized Fock operator (self-consistent energy) placed on Eq. (39) of Paper IV is also enforced here. *This diagonalization condition uniquely defines a canonical FORS representation. It does not mix filled, fractionally occupied, or empty spaces defined by the FORS.*

The perturbation is the two-body operator in the canonical representation. It is defined in Paper II and §3 of Paper IV. Nonbubble diagrams are calculated with the formulae of Paper II. Formulae for bubble diagrams are reported elsewhere [15, 16].

Diagrammatic overcount for HFPD and  $F^2$  models is the same as for HL. Overcount for HL is described in Papers II and IV of this series, and is the same for  $N_2$  with the understanding that three sets of paired levels must be counted. FDs are then counted in this work as in Papers II and IV.

### Computational Details

#### Basis Sets, FORS and Software

Two basis sets were selected to test the model. An even-tempered gaussian contraction (ETGC) (10s6p2d1f)/[4s3p2d1f] [17–19] and a polarized (4s3p1d1f) nominal Bagus–Gilbert basis of Slater-type atomic functions (STF) [20] were taken from the literature. The ETGC s and p sets were augmented with the most diffuse primitives. The basis sets are capable of approximating the dissociation energy of

nitrogen to within about 0.5 eV [21]. This error is about six times as large as that for the total energy of He in a comparable basis [22, Table 1, p. 11]. Errors associated with the basic two-body interaction scale upward to the error in dissociation energy for  $N_2$  because errors in the six two-body bonding interactions make no contributions to N atoms.

Integrals, 4-index transformations, and FORS calculations were carried out with ALIS [17] and ALCHEMY2 [23] for the ETGC and STF basis sets, respectively. In each case, the FORS is defined by completely filled shells  $1\sigma_g, 2\sigma_g, 1\sigma_u, 2\sigma_u$ , fractionally occupied shells  $3\sigma_g, 3\sigma_u, 1\pi_u, 1\pi_g$ , and empty shells all others allowed by the basis.

ALIS was supplemented by BIGGMOLI [24] f-orbital integral programs, square-canonical and symmetry supermatrix ordering programs, and symmetry-adapted self-consistent-field and 4-index transformation code, all provided by Dr. R. C. Raffanetti. ALCHEMY2 was supplemented by software for a real transformation [25] and generalized valence bond diagonalization [26] and 4-index transformation [27] codes. Except for the f-orbital integral code, the supplements were required for preprocessing.

Accuracy of FORS results is established by comparison with exact FORS results [28, numerical MCSCF in Table 1]. Spectroscopic constants are compared in Table

TABLE I. FORS and perturbative spectroscopic constants for  $N_2(X^1\Sigma_g^+)$ . HFPD was computed with ETGC.  $F^2$  and  $F_R^2$  above (below) HFPD were computed with ETGC(STF).

Model		$D_e$ (eV)	$R_e$ (Å)	$\omega_e$ (cm <sup>-1</sup> )	$\omega_e x_e$ (cm <sup>-1</sup> )	$B_e$ (cm <sup>-1</sup> )	$\alpha_e$ (cm <sup>-1</sup> )	$\bar{D}_e$ (cm <sup>-1</sup> × 10 <sup>6</sup> )
FORS	ETGC	8.79	1.103	2337	14.1	1.963	0.017	5.5
	STF	8.69	1.103	2341	14.1	1.965	0.017	5.5
	limit <sup>a</sup>	8.911	1.102	2353	14.1			
f o	$F^2$	7.26	1.098	2337	17.1	1.983	0.019	5.7
i r	$F_R^2$	7.25	1.097	2344	17.0	1.985	0.019	5.7
r d	HFPD	7.24	1.096	2363	16.3	1.989	0.018	5.6
s e	$F^2$	7.19	1.097	2342	17.0	1.985	0.019	5.7
t r	$F_R^2$	7.16	1.097	2349	16.9	1.987	0.019	5.7
s o	$F^2$	12.34	1.074	2610	13.4	2.072	0.015	5.2
e r	$F_R^2$	12.33	1.074	2616	13.4	2.074	0.015	5.2
c d	HFPD	12.33	1.072	2633	12.9	2.078	0.015	5.2
n e	$F^2$	12.19	1.075	2604	13.2	2.067	0.015	5.2
d r	$F_R^2$	12.16	1.075	2610	13.2	2.069	0.015	5.2
t o	$F^2$	9.54	1.083	2457	15.8	2.039	0.018	5.6
h r	$F_R^2$	9.53	1.082	2463	15.7	2.041	0.018	5.6
i d	HFPD	9.53	1.082	2476	15.1	2.043	0.017	5.5
r e	$F^2$	9.33	1.084	2443	16.0	2.034	0.018	5.6
d r	$F_R^2$	9.31	1.083	2450	16.0	2.036	0.018	5.6

<sup>a</sup> [28].

1. The unperturbed ground state is accurately represented in the ETGC and STF bases. The unperturbed excited states are probably equally accurately represented. Nevertheless, small errors accumulate in the dissociation energy because of the multiple bond.

FDs calculated through third order in the STF basis with closed-shell single-determinant code [29–31] require about one IBM 3090 CPU minute for each value of the bond distance. FDs calculated through third order in the STF (ETGC) basis with general block-driven code require about 12 (26) Convex C220 CPU s.

### *Spectroscopic Constants*

Dunham's method [32] was used to calculate spectroscopic constants [33]. Polynomial<sup>4</sup> of degree 9 were fitted. The grid has 22 points and is shown in Table II. Step sizes around the minimum internuclear distance are  $0.05a_0$ . Uncertainties in equilibrium bond distance due to fitting the calculated energies are of order  $\pm 0.0005a_0$  [34<sup>25</sup>]. Dissociation energies ( $D_e$ ) were computed with Eq. (2) of Paper III.

## **Results**

### *Perturbative Calculations*

Perturbative calculations have been performed corresponding to the three models described in the second section. Where the model building for  $\lambda_0^{[AM]}$  uses  $F^2$  evaluated at the separated atom limit, the results are designated  $F^2$ . If the HFPD value is used as indicated in Eq. (20), the results are designated HFPD. If  $F^2$  is evaluated at each  $R$  value, then the results are designated  $F_R^2$ . The calculations for  $F^2$  and  $F_R^2$  were performed using ETGC and STF basis sets. The HFPD has been calculated using ETGC. The values can be compared in Table II (total energies), Figure 1 (binding energies), and Table I (spectroscopic constants). Agreement is excellent. Curves for model FD and perturbative corrections for  $N_2$  appear overall the same as those shown for  $F_2$  on Figures 5–7 of Paper IV.

### *Accuracy of the Perturbative Results*

Second-order accuracy is not sufficient over the range of spectroscopic properties, as demonstrated in Table I. In Table III, spectroscopic constants are reported for models of  $N_2$  near limits of comparably chosen basis sets. By third order,  $D_e$ ,  $R_e$ , and  $\omega_e$  differ by about 0.1 eV,  $-0.02 \text{ \AA}$  and  $130 \text{ cm}^{-1}$ , respectively, from the aforementioned limits. In larger basis sets such as those of Almlöf et al. [21], it is probable that third-order dissociation energies will fall within 0.1 eV of experiment. (Unfortunately, we cannot preprocess such extensive calculations at present.) The conclusion is that third-order accuracy is useful for many purposes. In addition, the third-order HFPD value for  $D_e$  (in Table I) is comparable to the  $D_e$  obtained from the fourth-order calculation MP4 (in Table III), where the MP4 is derived from a single-determinantal zeroth-order expansion.

TABLE II HFPD total energies and energy differences of  $F^2$  and  $F_R^2$  models relative to HFPD (ETGC basis). To compute model energies, subtract energy differences from HFPD. Units are hartrees.

$R(a_0)^b$	First order			Third order <sup>a</sup>		
	HFPD	$F^2$	$F_R^2$	HFPD	$F^2$	$F_R^2$
1.40	-108.15866	-0.00098	-0.00094	-108.40314	-0.00027	-0.00025
1.50	-108.49987	-0.00103	-0.00103	-108.73628	-0.00032	-0.00032
1.60	-108.72982	-0.00104	-0.00110	-108.95915	-0.00039	-0.00041
1.70	-108.87992	-0.00098	-0.00111	-109.10300	-0.00045	-0.00051
1.75	-108.93240	-0.00094	-0.00111	-109.15263	-0.00046	-0.00055
1.80	-108.97288	-0.00086	-0.00109	-109.19041	-0.00046	-0.00058
1.85	-109.00324	-0.00076	-0.00104	-109.21821	-0.00044	-0.00060
1.90	-109.02509	-0.00064	-0.00098	-109.23762	-0.00039	-0.00060
1.95	-109.03981	-0.00049	-0.00090	-109.25000	-0.00032	-0.00058
2.00	-109.04859	-0.00031	-0.00079	-109.25655	-0.00021	-0.00054
2.05	-109.05238	-0.00008	-0.00064	-109.25812	-0.00006	-0.00045
2.10	-109.05216	0.00012	-0.00051	-109.25581	0.00009	-0.00038
2.15	-109.04859	0.00039	-0.00033	-109.25017	0.00030	-0.00025
2.20	-109.04237	0.00070	-0.00011	-109.24195	0.00055	-0.00009
2.25	-109.03401	0.00104	0.00014	-109.23160	0.00085	0.00011
2.30	-109.02401	0.00143	0.00043	-109.21965	0.00120	0.00036
2.35	-109.01279	0.00184	0.00074	-109.20652	0.00157	0.00063
2.40	-109.00069	0.00230	0.00110	-109.19254	0.00200	0.00095
2.50	-108.97506	0.00328	0.00189	-109.16325	0.00295	0.00170
2.60	-108.94897	0.00439	0.00281	-109.13359	0.00403	0.00258
2.70	-108.92385	0.00552	0.00379	-109.10498	0.00518	0.00355
2.80	-108.90056	0.00664	0.00479	-109.07824	0.00631	0.00455
2.90	-108.87967	0.00766	0.00573	-109.05392	0.00736	0.00551
3.00	-108.86144	0.00846	0.00652	-109.03227	0.00822	0.00633
3.10	-108.84593	0.00909	0.00716	-109.01343	0.00888	0.00699
3.20	-108.83300	0.00945	0.00758	-108.99725	0.00930	0.00746
3.30	-108.82240	0.00956	0.00779	-108.98351	0.00946	0.00771
3.40	-180.81383	0.00943	0.00778	-108.97195	0.00937	0.00774
3.50	-108.80701	0.00905	0.00757	-108.96229	0.00903	0.00755
3.60	-108.80167	0.00846	0.00714	-108.95425	0.00845	0.00713
3.70	-108.79754	0.00768	0.00653	-108.94755	0.00768	0.00653
3.80	-108.79442	0.00673	0.00575	-108.94197	0.00675	0.00576
4.00	-108.79038	0.00461	0.00390	-108.93342	0.00461	0.00390
4.50	-108.78702	-0.00015	-0.00041	-108.92129	-0.00015	-0.00044
5.00	-108.78666	-0.00235	-0.00246	-108.91553	-0.00234	-0.00245
5.50	-108.78666	-0.00269	-0.00271	-108.91240	-0.00269	-0.00271
6.00	-108.78665	-0.00227	-0.00226	-108.91053	-0.00227	-0.00226
6.50	-108.78662	-0.00168	-0.00166	-108.90936	-0.00167	-0.00166
7.00	-108.78659	-0.00116	-0.00115	-108.90862	-0.00116	-0.00115
7.50	-108.78656	-0.00078	-0.00077	-108.90812	-0.00078	-0.00076

<sup>a</sup> Second-order shows the same behavior.<sup>b</sup> The grid  $1.60a_0 \leq R \leq 3.00a_0$  was used to fit the energy to a polynomial for Dunham analysis.

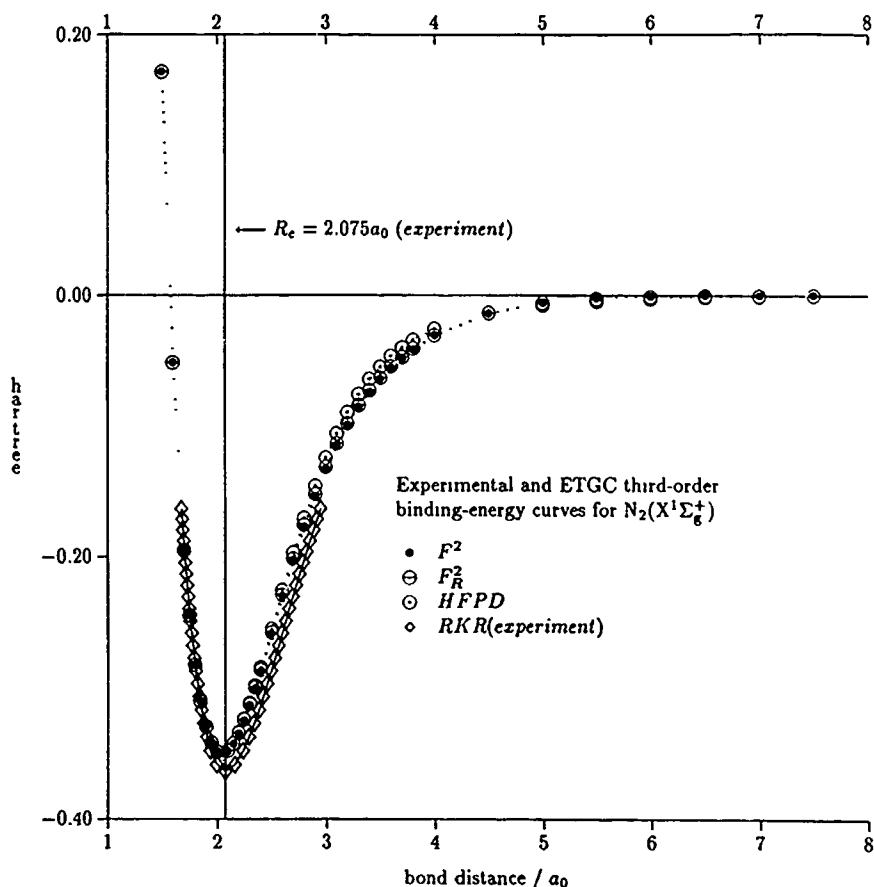


Figure 1. Experimental and ETGC third-order binding-energy curves for  $N_2(X^1\Sigma_g^+)$ .

The enforcement of angular momentum conservation for  $N_2$  in Paper I was based on Eqs. (14) and (23), with Eqs. (15) and (16) neglected. At third order, this approximation yields  $D_e$  about 0.4 eV above the limit of the chosen basis. This accuracy is insufficient for most purposes. It is noteworthy that inclusion of the terms in Eqs. (15) and (16) enable the attainment of the limit in the chosen basis set from the perturbative approach. This level of accuracy extends to  $D_e$  as well, as seen in Table III.

$R_e$  and  $\omega_e$  at third order differ from the achievable limits a bit more than might have been guessed. This is also true of  $F_2$  and FH in Paper III. Perhaps it is true whenever second-order corrections are "large."

HL models for  $F_2$  and FH are the same as HF PD models. Supplementary configurations needed for a more extensive unperturbed model are of the "split-shells" type. "Split shells" for  $F_2$  and FH require solving non-HL problems to determine BV transformation coefficients in the FORS (see §3.3–3.4 of Paper III and references

TABLE III. Comparison of third-order spectroscopic constants for  $N_2(X^1\Sigma_g^+)$  with accurate theoretical models in similar basis sets.

Model	$D_e$ (eV)	$R_e$ (Å)	$\omega_e$ (cm <sup>-1</sup> )	$\omega_e x_e$ (cm <sup>-1</sup> )	Basis set
Contracted CI <sup>a</sup>	9.46	1.101	2345		(11s7p2d1f)/[6s5p2d1f]
MP4 <sup>b</sup>	9.60				6-311G(2df,p)
MRCI + $Q^c$	9.37				(13s8p6d4f)/[4s3p2d1f] GC
$F^2$	9.54	1.083	2457	15.8	ETGc(present)
CI-SDQ <sup>d</sup>	9.34-9.41 <sup>e</sup>	1.095	2416	12.0	(6s4p3d2f) STF
$F^2$	9.33	1.084	2443	16.0	STF(present)
Expt <sup>f</sup>	9.91	1.098	2359	14.3	

<sup>a</sup> [36].<sup>b</sup> [37].<sup>c</sup> [21].<sup>d</sup> [38].<sup>e</sup> [39]: (5s4p3d) STF VCI + first and second orders.<sup>f</sup> [40].

therein), whereas angular momentum conservation includes available "split shells" in  $N_2$ . Perhaps this explains why third order based on the BV transformation determined by the HL problem is generally more accurate for  $N_2$  than for either  $F_2$  or  $FH$ .

### Acknowledgment

Professors W. C. Ermler and J. Hinze and Drs. S. Wilson, S. T. Elbert and R. C. Raffanetti are thanked for software.

### Bibliography

- [1] T. E. Sorensen, W. B. England, and D. M. Silver, *J. Phys.* **B22**, L539 (1989) (Paper I).
- [2] T. E. Sorensen, W. B. England, D. M. Silver, and E. O. Steinborn, *Theor. Chim. Acta* **84**, 1 (1992) (Paper II).
- [3] T. E. Sorensen, W. B. England, and D. M. Silver, *Theor. Chim. Acta* **84**, 21 (1992) (Paper III).
- [4] T. E. Sorensen, W. B. England, and D. M. Silver, *Theor. Chim. Acta* **84**, 37 (1992) (Paper IV).
- [5] W. B. England, D. M. Silver, and E. O. Steinborn, *J. Chem. Phys.* **81**, 4546 (1984).
- [6] K. R. Sundberg and K. Ruedenberg, *Quantum Science*, (Plenum, New York, 1976), p. 505.
- [7] M. Gilbert-Dombek, Ph.D. thesis, Iowa State University, 1977.
- [8] L. M. Cheung, K. R. Sundberg, and K. Ruedenberg, *Int. J. Quantum Chem.* **16**, 1103 (1979).
- [9] R. Pauncz, *Alternant Molecular Orbital Method* (Saunders, Philadelphia, 1967).
- [10] J. Linderberg and Y. Öhrn, *Propagators in Quantum Chemistry* (Academic, New York, 1973).
- [11] W. B. England, *J. Phys. Chem.* **86**, 1204 (1982).
- [12] D. J. Rowe, *Nuclear Collective Motion: Models and Theory* (Methuen, London, 1970).
- [13] G. C. Lie and E. Clementi, *J. Chem. Phys.* **60**, 1275 (1974).
- [14] J.-P. Blaizot and G. Ripka, *Quantum Theory of Finite Systems* (MIT Press, Cambridge, 1986).
- [15] T. E. Sorensen, Ph.D. thesis, University of Wisconsin-Milwaukee, 1989.
- [16] T. E. Sorensen and W. B. England, (1993), in preparation.

- [17] S. T. Elbert, Alis4.2, private communication (1990).
- [18] M. W. Schmidt and K. Ruedenberg, *J. Chem. Phys.* **71**, 3951 (1979).
- [19] T. H. Dunning, *J. Chem. Phys.* **90**, 1007 (1989).
- [20] A. D. McLean and M. Yoshimine, *IBM J. Res. Dev. Suppl.* **12**, 206 (1968); *Notes* p. 198.
- [21] J. Almlof, B. L. DeLeeuw, P. R. Taylor, C. W. Bauschlicher, and P. Siegbahn, *Int. J. Quantum Chem. Quantum Chem. Symp.* **23**, 345 (1989).
- [22] R. G. Parr, *The Quantum Theory of Molecular Structure* (Benjamin, New York, 1964).
- [23] P. S. Bagus, B. Liu, A. D. McLean, and M. Yoshimine, Alchemy2, private communication (1986).
- [24] R. C. Raffanetti, *J. Chem. Phys.* **58**, 4452 (1973).
- [25] Y. S. Lee, Transformation from integrals based on complex spherical harmonics to integrals based on real spherical harmonics (1980).
- [26] W. J. Hunt, P. J. Hay, and W. A. Goddard, *J. Chem. Phys.* **57**, 738 (1972).
- [27] N. W. Winter, D. M. Pitzer, and T. H. Dunning, Four-index integral transformation program (1973).
- [28] W. C. Ermler and C. W. Huang, *Chem. Phys. Lett.* **120**, 159 (1985).
- [29] D. M. Silver, *Comput. Phys. Commun.* **14**, 71 (1978).
- [30] D. M. Silver, *Comput. Phys. Commun.* **14**, 81 (1978).
- [31] S. Wilson, *Comput. Phys. Commun.* **14**, 91 (1978).
- [32] J. L. Dunham, *Phys. Rev.* **41**, 721 (1932).
- [33] J. Hinze, Dunham analysis (1975).
- [34] U. Wahlgren, J. Pacansky, and P. S. Bagus, *J. Chem. Phys.* **63**, 2874 (1975).
- [35] P. R. Taylor, G. B. Bacskay, N. S. Husin, and A. C. Hurley, *J. Chem. Phys.* **70**, 4481 (1979).
- [36] P. E. M. Siegbahn, *Int. J. Quantum Chem.* **23**, 1869 (1983).
- [37] M. J. Frisch, J. A. Pople, and J. S. Binkley, *J. Chem. Phys.* **80**, 3265 (1984).
- [38] W. C. Ermler and A. D. McLean, *J. Chem. Phys.* **73**, 2297 (1980).
- [39] W. C. Ermler, A. D. McLean, and R. S. Mulliken, *J. Phys. Chem.* **86**, 1305 (1982).
- [40] K. P. Huber and G. Herzberg, *Molecular Spectra and Molecular Structure, Vol. 4, Constants of Diatomic Molecules* (Van Nostrand, Princeton, NJ, 1979).

Received March 1, 1993

# ***Ab Initio* SCF Investigation of the Potential Energy Surface of 4-Aminobutanol**

ANNE-MARIE KELTERER and MICHAEL RAMEK

*Institut für Physikalische und Theoretische Chemie, Technische Universität Graz,  
A-8010 Graz, Austria*

## **Abstract**

Results of an *ab initio* SCF (4-31G) study of the potential energy surface of 4-aminobutanol are reported. Four different intramolecular hydrogen bonds are present in the various local minima:  $N \cdots H-O$ ,  $N-H \cdots O$ ,  $C_4-H \cdots O$ ,  $N \cdots H-C_1$ . These interactions are discussed and compared with those present in the homologues 3-aminopropanol and 2-aminoethanol. © 1993 John Wiley & Sons, Inc

## **Introduction**

$\omega$ -Amino-*n*-alkanols form an interesting class of compounds, because the chemical importance of its members covers the whole range of the traditional branches of chemistry. 2-Aminoethanol has a biological function in the most important phosphatides, which play an important role in cell membranes [1-4], of blood [5,6], brain [7-9], heart [10], and liver [11]. Both 2-aminoethanol and 3-aminopropanol may act as inhibitors in various surface [12,13] and enzyme reactions [14] by forming complexes with one of the hetero atoms N and O. Complex formation of 2-aminoethanol and 3-aminopropanol with Cu(II) [15-17], Ni(II) [18,19], aluminum oxides [20,21],  $TiO_2$  [22], and barium aryl oxides [23] has been investigated over years. Both 2-aminoethanol and 3-aminopropanol were also studied as part of Schiff base complexes [19,16]. Except for studies of the dehydration and deamination [24-27] and of the silver complexes [28] of all amino alcohols up to five carbon atoms, 4-aminobutanol has appeared in the literature in the last years as part of antitumor DNA intercalators [29].

We became interested in  $\omega$ -amino-*n*-alkanols as part of an *ab initio* investigation of amino acids and related compounds. 2-Aminoethanol has been the target of a number of quantum chemical calculations in the past [30-34]. The potential energy surfaces (PES) of 3-aminopropanol and 4-aminobutanol were characterized in our group. The results for 3-aminopropanol [35,36] and the three 4-aminobutanol conformers of lowest energy have been reported already [34]. It is the purpose of this contribution to give an overview over all local minima in the PES of 4-aminobutanol, to discuss selected details, and to compare 4-aminobutanol with its homologues 3-aminopropanol and 2-aminoethanol.



The 4-31G basis set [37] and the RHF formalism [38] were used in all calculations of this study for two main reasons. First, optimized geometries obtained in this manner correlate well with experimentally determined structures for 2-aminoethanol and 3-aminopropanol. Second, the same method and basis set have been employed by our group in the past; hence the results for 4-aminobutanol can be compared with those of past work at one consistent level. Calculations were performed with the program GAMESS [39]. All local minima were fully optimized to a rms gradient less than  $1.6 \times 10^{-4}$  H/Bohr or H/rad and verified to have positive eigenvalues of the Hessian matrix only.

### Local Minima

One hundred ten symmetry unique local minima were located in the potential energy surface of 4-aminobutanol. In accordance with earlier work, a positive torsion angle N—C—C—C was chosen as the criterion for symmetry uniqueness. Figure 1 displays the relative energy of all of these minima as a function of the dihedral angles of the molecular backbone, Figure 2 shows the various orientations of the amino group. These displays show that with one exception three standard positions per internal rotation may be distinguished. This allows an extended version of the nomenclature used by Radom et al. in previous work on 2-aminoethanol [30]: each local minimum will be denoted by a five letter symbol  $vWXYZ$ , in which  $v$  describes the orientation of the amino group via the torsion angle between the lone electron pair and the carbon chain,  $W$  gives the N—C—C—C torsion angle,  $X$  gives the C—C—C—C torsion angle,  $Y$  indicates the C—C—C—O torsion angle, and  $z$  gives the C—C—O—H torsion angle.  $G$  and  $g$  denote torsion angles around  $+60^\circ$ ,  $G'$  and  $g'$  denote torsion angles around  $-60^\circ$ , and  $T$  and  $t$  denote torsion angles around  $180^\circ$ . The C—C—O—H angle close to  $0^\circ$ , which occurs in one conformer, will be denoted  $s$ . The global minimum, e.g., for which the dihedral angles are  $H_1-N-C-C = 59.2^\circ$ ,  $H_2-N-C-C = -171.4^\circ$ ,  $N-C-C-C = 76.8^\circ$ ,  $C-C-C-C = -71.5^\circ$ ,  $C-C-C-O = 73.3^\circ$ , and  $H-O-C-C = -61.6^\circ$ , is thus labeled  $g'GG'Gg'$ .

Table I lists the labels of all symmetry unique local minima together with relative energies ( $E_{rel} = 0$  corresponds to  $-286.755020$  a.u.), vibrational zero point energies, and rotation constants. The detailed geometry data (bond lengths, valence, and torsion angles) and the Cartesian coordinates are available from the authors or by electronic mail (F5351DAA@AWIUNI11.BITNET).

Four different intramolecular hydrogen bonds,  $N \cdots H-O$ ,  $N-H \cdots O$ ,  $N \cdots H-C_1$ , and  $C_4-H \cdots O$ , occur in a number of 4-aminobutanol conformers. The first of these,  $N \cdots H-O$ , is much stronger than the others. It is present in the conformers  $g'GG'Gg'$ ,  $g'GG'G'g$ , and  $g'GGG's$  (with  $N \cdots H$  distances of 1.902, 2.057, and 1.990 Å, respectively). Some aspects of this interaction, namely, its influence on bond lengths and vibration frequencies, have been discussed previously [34]. The  $N \cdots H-O$  hydrogen bond also has significant influence on the energetics: The three conformers, which contain this bond, are much lower in

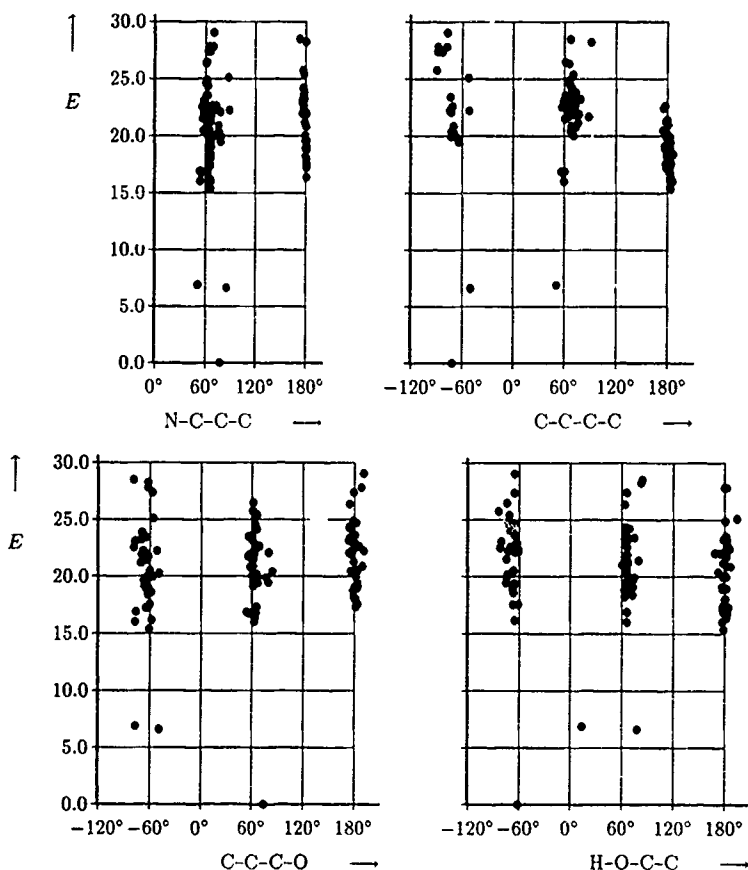


Figure 1. The relative energy (kJ/mol) of all symmetry unique local minima in the PES of 4-aminobutanol as a function of the dihedral angles of the molecular backbone.

energy than all other conformers (cf. Fig. 1). This stabilization has considerable effect on the topology of the PES of 4-aminobutanol, because it fixes the amino group in one position: No local minima are present, which differ from  $g'GG'Gg'$ ,  $g'GG'G'g$ , and  $g'GGG's$  in the orientation of the amino group only. Furthermore, no local minima exist, which differ from the global minimum  $g'GG'Gg'$  in the orientation of the hydroxy group. In the case of  $g'GGG's$  only one conformer ( $g'GGG't$ ) with a different orientation of the hydroxy group is formed.

A comparison of the number of local minima, which are actually present in the 4-aminobutanol PES, with the number of conformations that results from the structural principle of three orientations per internal rotation ( $3^5 = 243$ ), reveals the dominant nature of the  $N \cdots H-O$  hydrogen bond. One out of the 110 symmetry unique local minima is of  $C_s$  symmetry; hence a total of 219 local minima is present

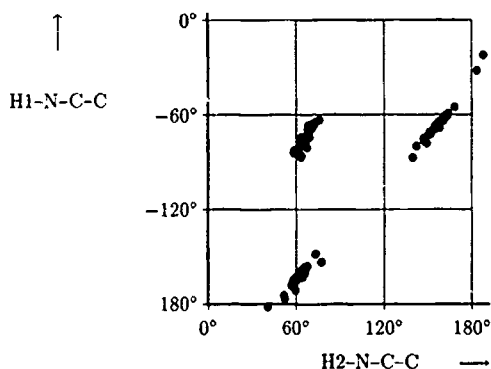
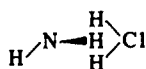


Figure 2. The plot of the two dihedral angles H—N—C—C against each other for all symmetry unique local minima in the PES of 4-aminobutanol shows that three major orientations of the amino group occur.

in the 4-aminobutanol PES. Hence a total of 24 conformers, i.e., 12 symmetry unique conformers, are "missing." The stability of  $g'GG'Gg'$ ,  $g'GG'G'g$ , and  $g'GGG's$  explains the absence of nine of these 12 missing symmetry unique conformers. The remaining three conformers are  $gGG'Tg$ ,  $gGG'Tg'$ , and  $gGG'Tt$ , which are not formed due to a steric hindering of the type

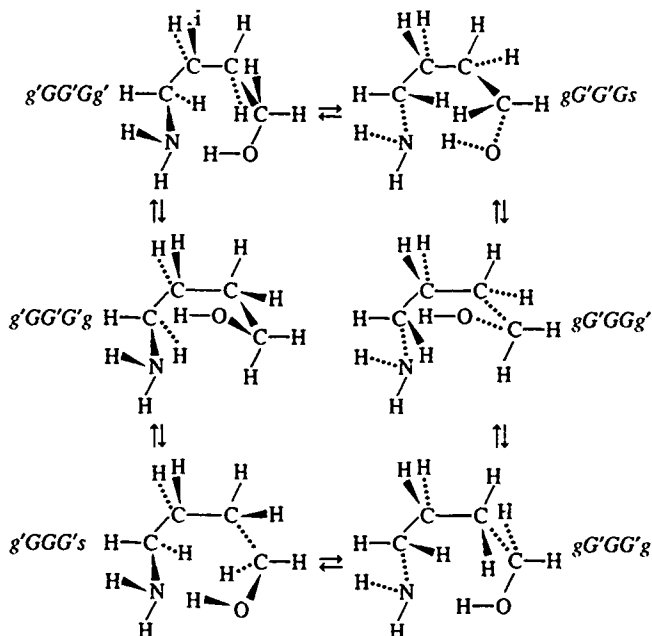


The intramolecular hydrogen bond  $\text{N}-\text{H} \cdots \text{O}$  is present in the conformers  $gGG'Gt$  ( $\text{H} \cdots \text{O}$  distance: 2.055 Å),  $gGG'Gg$  (2.061 Å),  $tGG'Gg$  (2.090 Å),  $tGG'Gt$  (2.114 Å),  $gGG'G'g'$  (2.178 Å),  $gGG'G't$  (2.263 Å),  $gGGG't$  (2.355 Å),  $tGGG't$  (2.395 Å), and  $gGGG'g'$  (2.469 Å). The  $\text{N} \cdots \text{H}-\text{C}_1$  hydrogen bond is present in  $g'GG'G'g'$  ( $\text{N} \cdots \text{H}$  distance 2.462 Å),  $g'GG'G't$  (2.502 Å),  $g'GG'Tg'$  (2.574 Å),  $g'GG'Tg$  (2.591 Å), and in  $g'GG'Tt$  (2.616 Å). The  $\text{C}_4-\text{H} \cdots \text{O}$  hydrogen bond is present in  $g'GGG't$  ( $\text{H} \cdots \text{O}$  distance: 2.398 Å),  $tTGG't$  (2.409 Å),  $g'TGG't$  (2.426 Å),  $tTGG'g'$  (2.436 Å),  $g'TGG'g'$  (2.447 Å),  $gTGG't$  (2.447 Å), and  $gTGG'g'$  (2.470 Å). None of the intramolecular interactions  $\text{N}-\text{H} \cdots \text{O}$ ,  $\text{N} \cdots \text{H}-\text{C}_1$ , and  $\text{C}_4-\text{H} \cdots \text{O}$  has an influence on energetics, bond lengths, or vibration frequencies. Analyses of the electron densities along these interactions, however, prove that each of them is associated with a critical point of the electron density with two negative eigenvalues. Such critical points represent chemical bonds [40]; the classification of these interactions as hydrogen bonds is therefore correct.

In addition to these intramolecular hydrogen bonds two conformers contain interactions, which lead to five-membered ring structures:  $\text{C}_3-\text{H} \cdots \text{O}$  in  $g'GG'G't$  (with an  $\text{H} \cdots \text{O}$  distance of 2.515 Å) and  $\text{N} \cdots \text{H}-\text{C}_2$  in  $g'GGG't$  (with an  $\text{N} \cdots \text{H}$  distance of 2.607 Å). Inspection of the electron density shows that these interactions are not hydrogen bonds but mainly of electrostatic origin.

## Reaction Paths

The minima  $g'GG'Gg'$ ,  $g'GG'G'g$ , and  $g'GGG's$ , which are stabilized by the intramolecular  $N \cdots H-O$  hydrogen bond, and their mirror images are directly interconnected in the reaction sequence



The  $N \cdots H-O$  bond is preserved along this reaction sequence: The  $N \cdots H$  distance is 1.906 Å in the transition state  $g'GG'Gg' \rightleftharpoons g'GG'G'g$ , 1.923 Å in the transition state  $g'GG'G'g \rightleftharpoons g'GGG's$ , and 1.911 Å in the transition state  $g'GG'Gg' \rightleftharpoons g'G'Gs$ . As a consequence of this bond preservation, some of the internal rotations are coupled in these reactions as shown in Figure 3. The energy profile along one of these reaction, namely,  $g'GG'Gg' \rightleftharpoons g'GG'G'g$ , is displayed in Figure 4. This profile is noteworthy because it contains a flat region near the conformation  $g'GG'Gs$ , which is also a consequence of the  $N \cdots H-O$  hydrogen bond. In contrast to similar situations, which occur in the PES of 3-aminopropanol, the point of inflexion, which is associated with this flat region, does not have zero gradients.

Table II lists the potential barriers of all internal rotations of the global minimum together with the final conformer of each of these rotations.

## Discussion

A comparison of Figure 1 with the corresponding plots for 2-aminoethanol and 3-aminopropanol (Figs. 1 and 2 in [35]) shows increasing scatter in the series 2-

TABLE I Relative and vibrational zero point energies (kJ/mol) and rotation constants (GHz) for all symmetry unique local minima in the PES of 4-aminobutanol. The absolute energy of the global minimum is -286.755020 a.u.

Conformer	Relative energy	Rotation constants			Zero point energy
<i>g'</i> GG' <i>G'</i> <i>g'</i>	20.235	1.9823	2.4500	4.8861	437.421
<i>g'</i> GG' <i>G'</i> <i>g</i>	6.606	2.0484	2.8453	4.4951	441.012
<i>g'</i> GG' <i>G'</i> <i>t</i>	19.951	1.9249	2.3219	5.0383	437.353
<i>g'</i> GG' <i>Gg'</i>	0.000	1.9519	2.8492	4.4927	441.255
<i>g</i> GG' <i>Gi</i>	20.371	1.9080	2.7406	4.5571	438.178
<i>g'</i> GG' <i>Tg'</i>	22.217	1.5115	1.7859	6.3962	435.964
<i>g'</i> GG' <i>Tg</i>	22.587	1.5173	1.8051	6.3466	436.350
<i>g'</i> GG' <i>Tt</i>	20.860	1.5187	1.8027	6.4301	436.819
<i>g'</i> GGG' <i>s</i>	6.876	2.0774	2.8578	4.5231	441.286
<i>g'</i> GGG' <i>t</i>	21.684	1.8100	2.0465	5.6946	436.005
<i>g'</i> GGG' <i>g'</i>	21.513	1.8240	1.8309	6.2137	436.073
<i>g'</i> GGG' <i>g</i>	16.835	1.9227	1.9456	5.8506	437.575
<i>g'</i> GGG' <i>t</i>	16.732	1.9322	1.9211	5.9836	437.287
<i>g'</i> GGT' <i>g'</i>	22.348	1.5096	1.6256	6.9352	435.922
<i>g'</i> GGT' <i>g</i>	20.419	1.5181	1.6502	6.8161	436.537
<i>g'</i> GGT' <i>t</i>	22.020	1.5249	1.6438	6.9395	435.850
<i>g'</i> GTG' <i>g'</i>	16.149	1.3731	1.4767	9.5897	436.025
<i>g'</i> GTG' <i>g</i>	18.373	1.3652	1.4700	9.5892	435.893
<i>g'</i> GTG' <i>t</i>	15.351	1.3828	1.4908	9.6783	436.062
<i>g'</i> GTG' <i>g'</i>	20.151	1.4877	1.5953	7.7394	435.600
<i>g'</i> GTG' <i>g</i>	15.995	1.5057	1.5879	7.3455	436.552
<i>g'</i> GTG' <i>t</i>	16.761	1.5181	1.5801	7.6013	435.890
<i>g'</i> GTT' <i>g'</i>	17.544	1.2732	1.3664	9.2636	435.768
<i>g'</i> GTT' <i>g</i>	18.793	1.2732	1.3624	9.3050	435.722
<i>g'</i> GTT' <i>t</i>	18.917	1.2811	1.3727	9.3493	435.013
<i>g'</i> TG' <i>G'</i> <i>g</i>	23.414	1.4836	1.5875	7.1202	435.978
<i>g'</i> TG' <i>Gg'</i>	25.733	1.5460	1.8254	6.3449	436.373
<i>g'</i> TGG' <i>g'</i>	23.842	1.5376	1.8271	6.2704	436.395
<i>g'</i> TGG' <i>g</i>	28.232	1.5225	1.7738	6.4675	435.730
<i>g'</i> TGG' <i>t</i>	23.207	1.5370	1.8152	6.4227	436.157
<i>g'</i> TGG' <i>g'</i>	25.378	1.4794	1.5828	7.1611	435.526
<i>g'</i> TGG' <i>g</i>	21.912	1.5126	1.6309	6.9231	436.434
<i>g'</i> TGG' <i>t</i>	21.960	1.5167	1.6281	7.0458	436.377
<i>g'</i> TGT' <i>g'</i>	23.590	1.2383	1.2985	11.2167	435.675
<i>g'</i> TGT' <i>g</i>	24.202	1.2364	1.2919	11.3292	435.523
<i>g'</i> TGT' <i>t</i>	23.236	1.2412	1.2991	11.4938	435.507
<i>g'</i> TTG' <i>g'</i>	18.877	1.2815	1.3792	9.2827	435.697
<i>g'</i> TTG' <i>t</i>	17.181	1.2893	1.3899	9.4151	435.819
<i>g'</i> TTG' <i>g</i>	19.589	1.2810	1.3720	9.3463	435.474
<i>g</i> GG' <i>G'</i> <i>g'</i>	22.206	2.0012	2.6990	4.5942	437.746
<i>g</i> GG' <i>G'</i> <i>t</i>	25.092	1.9989	2.6602	4.6676	436.653
<i>g</i> GG' <i>Gg</i>	19.444	1.9551	2.8134	4.4527	437.855
<i>g</i> GGG' <i>g'</i>	22.516	1.9889	2.6451	4.6244	436.771
<i>g</i> GGG' <i>t</i>	16.858	2.0219	2.6731	4.6972	437.667
<i>g</i> GGG' <i>g'</i>	26.452	1.7914	1.8093	6.3200	436.331
<i>g</i> GGG' <i>g</i>	23.482	1.7873	1.8058	6.3971	436.272

TABLE I. (Continued)

Conformer	Relative energy	Rotation constants			Zero point energy
<i>gGGGt</i>	23.522	1.7978	1.8171	6.4228	436.278
<i>gGGTg'</i>	24.682	1.5154	1.6502	6.8174	436.114
<i>gGGTg</i>	26.344	1.5010	1.6255	6.9422	434.724
<i>gGGTt</i>	24.856	1.5143	1.6376	6.9535	435.912
<i>gGTG'g'</i>	20.463	1.3662	1.4766	9.6294	436.051
<i>gGTG'g</i>	21.398	1.3566	1.4709	9.6826	436.009
<i>gGTG't</i>	19.06 <sup>a</sup>	1.3742	1.4888	9.7382	436.035
<i>gGTGg'</i>	22.616	1.4630	1.5032	7.9175	435.667
<i>gGTGg</i>	20.991	1.4964	1.5326	7.7031	435.356
<i>gGTGt</i>	22.424	1.4879	1.5185	8.0528	434.969
<i>gGTTg'</i>	20.489	1.2588	1.3587	9.5305	435.495
<i>gGTTg</i>	21.230	1.2586	1.3515	9.5708	435.189
<i>gGTTt</i>	19.946	1.2682	1.3669	9.5718	435.687
<i>gTGG'g'</i>	22.217	1.5401	1.8486	6.2973	435.895
<i>gTGG't</i>	21.172	1.5394	1.8397	6.4165	435.943
<i>gTGGg</i>	23.181	1.4890	1.5857	7.2267	435.737
<i>gTGGt</i>	22.687	1.4990	1.5892	7.3396	436.146
<i>gTGTg'</i>	22.514	1.2384	1.3080	11.2433	435.836
<i>gTGTg</i>	23.370	1.2355	1.2994	11.3460	435.564
<i>gTGTt</i>	21.968	1.2404	1.3067	11.5193	435.547
<i>gTTG'g</i>	19.599	1.2633	1.3493	9.6519	436.009
<i>gTTG't</i>	18.890	1.2885	1.3760	9.5597	435.517
<i>gTTGg'</i>	19.416	1.2670	1.3690	9.4677	435.980
<i>gTTTg'</i>	19.080	1.0977	1.1360	16.6300	434.994
<i>gTTTg</i>	18.741	1.0978	1.1364	16.6275	435.276
<i>gTTTt</i>	17.948	1.1042	1.1452	16.7998	435.289
<i>tGG'G'g'</i>	27.360	1.8024	2.0574	5.3532	435.801
<i>tGG'G't</i>	27.794	1.7671	1.9739	5.6258	435.520
<i>tGG'Gg</i>	19.857	1.9318	2.7804	4.4276	437.685
<i>tGG'Gt</i>	22.062	1.8964	2.7180	4.5176	437.716
<i>tGG'Tg'</i>	29.020	1.4813	1.7414	6.4150	434.027
<i>tGG'Tg</i>	27.384	1.5012	1.7599	6.3445	434.881
<i>tGG'Tt</i>	27.799	1.4891	1.7551	6.4587	434.227
<i>tGGG'g'</i>	23.060	1.9589	2.5545	4.6649	436.359
<i>tGGG't</i>	16.005	2.0061	2.6569	4.6631	437.513
<i>tGGGg'</i>	24.525	1.7120	1.7402	6.6377	435.824
<i>tGGGg</i>	21.744	1.7727	1.7891	6.4084	435.872
<i>tGGGt</i>	20.899	1.7158	1.7490	6.7842	436.044
<i>tGGTg'</i>	22.766	1.5000	1.6284	6.8122	435.717
<i>tGGTg</i>	24.325	1.4775	1.5880	7.0303	435.690
<i>tGGTt</i>	22.201	1.4934	1.6053	7.0299	435.738
<i>tGTG'g'</i>	18.573	1.3562	1.4601	9.5787	435.343
<i>tGTG'g</i>	19.883	1.3472	1.4529	9.6124	435.175
<i>tGTG't</i>	17.378	1.3668	1.4761	9.6428	435.424
<i>tGTGg'</i>	19.899	1.4694	1.5034	7.7458	435.761
<i>tGTGg</i>	19.114	1.4785	1.5318	7.5514	435.667
<i>tGTGt</i>	17.294	1.4971	1.5560	7.5573	435.599
<i>tGTTg'</i>	19.400	1.2573	1.3506	9.3091	435.383

(Continued)

TABLE I. (Continued)

Conformer	Relative energy	Rotation constants			Zero point energy
<i>IGTTg</i>	18.998	1.2588	1.3469	9.3318	435.407
<i>IGTTi</i>	18.027	1.2656	1.3591	9.3779	435.440
<i>ITGG'g'</i>	22.115	1.5412	1.8417	6.2151	435.900
<i>ITGG'g</i>	28.484	1.4978	1.7809	6.3938	434.686
<i>ITGG'i</i>	21.886	1.5442	1.8368	6.3492	435.712
<i>ITGGg'</i>	24.110	1.4739	1.5813	7.1335	435.462
<i>ITGGg</i>	20.797	1.4958	1.6112	6.9751	436.003
<i>ITGGi</i>	20.030	1.5096	1.6281	6.9906	436.143
<i>ITGTg'</i>	22.907	1.2343	1.3007	11.1295	435.298
<i>ITGTg</i>	23.102	1.2321	1.2932	11.2092	435.374
<i>ITGTi</i>	21.933	1.2371	1.3013	11.3789	435.259
<i>ITTG'g'</i>	17.515	1.2721	1.3636	9.2731	435.525
<i>ITTG'g</i>	19.087	1.2577	1.3488	9.5059	435.532
<i>ITTGi</i>	16.344	1.2832	1.3802	9.3580	435.574
<i>ITTTg</i>	18.182	1.0921	1.1276	16.4923	434.990
<i>ITTTi</i>	17.305	1.0986	1.1364	16.6482	435.131

aminoethanol, 3-aminopropanol, and 4-aminobutanol, which is paralleled by an increasing energy gap between the global minimum and the bulk of conformers without intramolecular interactions. The increasing energy gap and the corresponding potential barriers prove that the seven-membered ring, which is formed in 4-aminobutanol, is more stable than the six-membered ring of 3-aminopropanol and the five-membered ring of 2-aminoethanol. This increase of stability with ring size is in good agreement with the effect of the  $N \cdots H-O$  hydrogen bond on the  $O-H$  bond length and vibration frequency [34,41,42]. Furthermore, the larger amount of scatter indicates that the conformers of 4-aminobutanol are more flexible than those of 3-aminopropanol and 2-aminoethanol. This is an interesting conclusion: On the one hand, it provides an explanation for the increase of stability with the ring size, because the two functional groups can arrange themselves with less hindering by the rest of the molecule. On the other hand, however, the same is valid for all other 4-aminobutanol conformers too, which makes the greater stability of the global minimum of 4-aminobutanol even more remarkable.

For the global minima of the homologues 2-aminoethanol, 3-aminopropanol, and 4-aminobutanol it has to be noted that for none of them the potential barrier for H-bond preserving reactions is the lowest one. In any case there is one internal rotation, which destroys the intramolecular  $N \cdots H-O$  hydrogen bond, but requires less activation energy than those internal rotations that preserve the H-bond.

Upon comparing the various intramolecular hydrogen bonds in 4-aminobutanol and 3-aminopropanol, one encounters that the  $C_4-H \cdots O$  and  $N \cdots H-C_1$  interactions in 4-aminobutanol have no counterparts in 3-aminopropanol and 2-aminoethanol. This seems to be not so much a consequence of the greater flexibility in 4-aminobutanol, but one of the fact that these interactions form six-membered

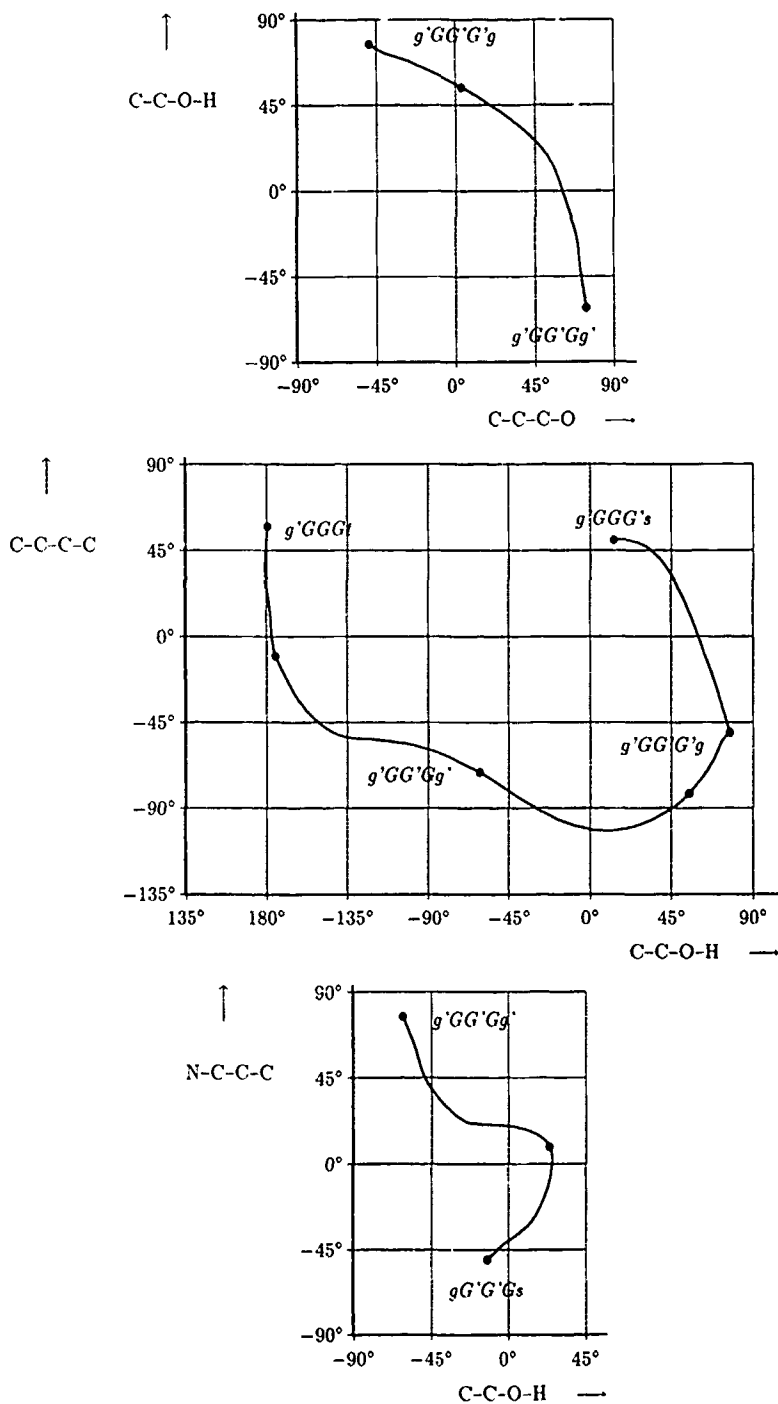


Figure 3. Various internal rotations are coupled with each other in the reactions of the global minimum  $g'GG'Gg'$  as a consequence of the intramolecular hydrogen bond  $N \cdots H-O$ . (●) Stationary points (local minima and saddle points) of the PES.



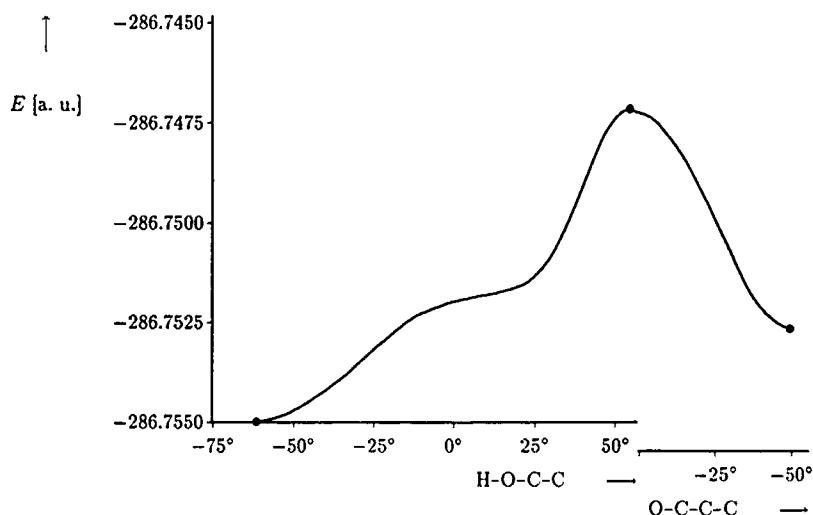


Figure 4. The energy profile of the reaction  $g'GG'Gg' \rightleftharpoons g'GG'G'g$  contains a flat region due to the  $N \cdots H-O$  hydrogen bond. (●) Stationary points (local minima and saddle points) of the PES.

rings of the chair type in 4-aminobutanol. The analogous five membered rings in 3-aminopropanol would require drastic deviations from the "standard"  $C-C-C-O$  and  $C-C-C-N$  orientations of  $-60^\circ$ ,  $60^\circ$ , and  $180^\circ$ .

### Acknowledgments

This work was supported by the Austrian Fonds zur Förderung der wissenschaftlichen Forschung (Project P 6856). Many calculations were done on the IBM 3090 VF operated by the EDV-Zentrum der Universität Wien within IBM's European

TABLE II Final geometries and potential barriers (kJ/mol) of the various reaction paths of the most stable 4-aminobutanol conformer  $g'GG'Gg'$ .

Internal rotation	Final conformer	Potential barrier
Decreasing angle $C-C-C-C$	$g'GTGg$	19.16
Increasing angle $C-C-O-H$	$g'GG'G'g$	20.60
Increasing angle $N-C-C-C$	$g'TG'Gg'$	29.32
Increasing angle $C-C-C-O$	$g'GG'Tg'$	31.60
Decreasing angle $C-C-O-H$	$g'GGGt$	39.01
Increasing angle $C-C-C-C$		
Decreasing angle $C-C-C-O$	$g'GG'G'g'$	41.00
Decreasing angle $N-C-C-C$	$gG'G'G\ddagger$	26.06

Academic Supercomputing Initiative. The authors are grateful for this support and the constant support by the EDV-Zentrum der Technischen Universität Graz. Thanks are due to Dr. Mike W. Schmidt (Iowa State University) for a copy of GAMESS.

### Bibliography

- [1] L. Milakofsky, R. A. Hare, J. M. Miller, and W. H. Vogel, *Life Sci.* **36**, 753 (1985).
- [2] G. A-Wen Pu and R. E. Anderson, *J. Neurochem.* **42**, 185 (1984).
- [3] S. McNulty, R. Sayner, and M. Rumsby, *Biochem. Soc. Trans.* **19**, 153 (1991).
- [4] K. Lohner, P. Balgavy, A. Hermetter, F. Paltauf, and P. Laggnier, *Biochim. Biophys. Acta* **1061**, 132 (1991).
- [5] M. L. Nieto, M. E. Venable, S. A. Bauldry, D. G. Greene, M. Kennedy, D. A. Bass, and R. L. Wykle, *J. Biol. Chem.* **266**, 18699 (1991).
- [6] K. E. H. El Tahir, M. A. S. El-Naser, A. M. Ageel, H. A. El-Obeid, and K. A. Al-Rashood, *Arch. Int. Pharmacodyn.* **306**, 162 (1990).
- [7] J. Strosznajder, A. Radomska-Pyrek, and L. A. Horrocks, *Biochim. Biophys. Acta* **574**, 48 (1979).
- [8] T. Kunishita, L. K. Vaswani, C. R. Morrow, G. P. Novak, and R. W. Ledeen, *J. Neurochem.* **48**, 1 (1987).
- [9] C. Andnamampandry, L. Freysz, J. N. Kanfer, H. Dreyfus, and R. Massarelli, *J. Neurochem.* **56**, 1845 (1991).
- [10] T. A. Zelinski and P. C. Choy, *Can. J. Biochem.* **60**, 827 (1982).
- [11] R. R. Dils and G. Hubscher, *Biochim. Biophys. Acta* **46**, 505 (1961).
- [12] T. Lippert, A. Wokaun, and D. Lenoir, *Environ. Sci. Technol.* **25**, 1485 (1991).
- [13] J. M. Costa and J. M. Lluch, *Corros. Sci.* **24**, 929 (1984).
- [14] M. Iwama, T. Takahashi, N. Inokuchi, T. Koyama, and M. Ine, *J. Biochem.* **98**, 341 (1985).
- [15] R. Lingren, R. Sillanpää, K. Rissanen, L. K. Thompson, C. J. O'Connor, G. A. Van Albada, and J. Reedijk, *Inorgan. Chim. Acta* **171**, 95 (1990).
- [16] N. A. Bailey, D. E. Fenton, and J. R. Tate, *Inorg. Chim. Acta* **112**, 17 (1986).
- [17] G. A. Lawrence, M. Maeder, M. A. O'Leary, B. W. Skelton, and A. H. White, *Aust. J. Chem.* **44**, 1227 (1991).
- [18] J. M. Antelo, F. Arce, J. Casado, and A. Varela, *Ann. Chim. (Rome)* **70**, 167 (1980).
- [19] G. Cros and J.-P. Laurent, *Inorg. Chim. Acta* **142**, 113 (1988).
- [20] N. M. D. Brown, R. J. Turner, and D. G. Walmsley, *J. Mol. Struct.* **79**, 163 (1982).
- [21] S. D. Williams and K. W. Hipps, *J. Catal.* **78**, 96 (1982).
- [22] T. Karah and S. Okazaki, *Bull. Chem. Soc. Jpn.* **54**, 3259 (1981).
- [23] K. G. Caulton, M. H. Chisholm, S. R. Drake, and K. Folting, *Inorg. Chim. Acta* **30**, 1500 (1991).
- [24] V. H. Wysocki, D. J. Burnksy, and R. G. Cooks, *J. Org. Chem.* **50**, 1287 (1985).
- [25] H. E. Audier, A. Milliet, C. Perret, J. C. Tabet, and P. Varenne, *Org. Mass Spectrom.* **13**, 315 (1978).
- [26] T. Naota and S.-I. Murahashi, *Synlett* **10**, 693 (1991).
- [27] J.-F. Pilard, B. Klein, F. Texier-Boullet, and J. Hamelin, *Synlett* **3**, 219 (1992).
- [28] D. J. Alner, R. C. Lansbury, and A. G. Smeeth, *J. Chem. Soc. (A)* **1968**, 417.
- [29] K. W. Bair, R. L. Tuttle, V. C. Knick, M. Cory, and D. D. McKee, *J. Med. Chem.* **33**, 2385 (1990).
- [30] L. Radom, W. A. Lathan, W. J. Hehre, and J. A. Pople, *J. Am. Chem. Soc.* **95**, 693 (1973).
- [31] M. Rasanen, A. Aspiala, L. Homanen, and J. Murto, *J. Mol. Struct. (Theochem)* **96**, 81 (1982).
- [32] C. van Alsenoy, K. Siam, J. D. Ewbank, and L. Schafer, *J. Mol. Struct. (Theochem)* **136**, 77 (1986).
- [33] L. G. Vanquickenborne, B. Coussens, C. Verlindé, and C. de Ranter, *J. Mol. Struct. (Theochem)* **201**, 1 (1989).

- [34] A.-M. Kelterer and M. Ramek, *J. Mol. Struct. (Theochem)* **232**, 189 (1991).
- [35] A.-M. Kelterer, M. Flock, and M. Ramek, *J. Mol. Struct. (Theochem)* **276**, 35 (1992).
- [36] M. Ramek, M. Flock, A.-M. Kelterer, and V. K. W. Cheng, *J. Mol. Struct. (Theochem)* **276**, 61 (1992).
- [37] R. Ditchfield, W. J. Hehre, and J. A. Pople, *J. Chem. Phys.* **54**, 724 (1971).
- [38] C. C. J. Roothaan, *Rev. Mod. Phys.* **23**, 69 (1951).
- [39] M. W. Schmidt, K. K. Baldridge, J. A. Boatz, J. H. Jensen, S. Koseki, M. S. Gordon, K. A. Nguyen, T. L. Windus, and S. T. Elbert, *QCPE Bull* **10**, 52 (1990).
- [40] R. W. F. Bader, *Atoms in Molecules* (Clarendon, Oxford, 1990), p. 19.
- [41] R. Mathis, M. Maurette, Ch. Godechot, and A. Lattes, *Bull. Soc. Chim. Fr.*, 3047 (1970).
- [42] Y. Y. Kharitonov, È. G. Khoshabova, M. N. Rodnikova, K. T. Dudnikova, and A. B. Razumova, *Dokl. Akad. Nauk SSSR* **304**, 917 (1989).

Received June 24, 1993

# Solvent Effect on the Potential Surface of the Proton Transfer in $[\text{H}_3\text{N}-\text{H}-\text{NH}_3]^+$

JIALI GAO

Department of Chemistry, State University of New York at Buffalo, Buffalo, New York 14214

## Abstract

Statistical mechanics Monte Carlo simulations of the proton transfer in  $[\text{H}_3\text{N}-\text{H}-\text{NH}_3]^+$  in aqueous solution have been carried out using the combined quantum mechanical and molecular mechanical AM1/TIP3P potential. As in the gas phase, squeezing and stretching motions of the donor-acceptor distance have profound effects on the proton transfer. Solvation increases the activation free energy of the proton transfer by 3 kcal/mol over that in the gas phase. The results suggest that the combined QM/MM potential may be used in models that treat the proton motion quantum mechanically and the solvent dynamics classically. © 1993 John Wiley & Sons, Inc.

## Introduction

In a recent study, McCammon and coworkers constructed the potential energy surface for the proton transfer reactions of  $[\text{H}_3\text{N}-\text{H}-\text{NH}_3]^+$  and  $[\text{H}_3\text{N}-\text{H}-\text{OH}_2]^+$  in the gas phase through *ab initio* calculations at the MP2/6-31G(d) level [1]. The effort was a prelude to modeling the quantum mechanical tunneling effect in proton transfer process [2], which has also been observed in enzymatic reactions [3]. The authors found that the barrier heights for these reactions are sensitive to the squeezing and stretching motions of the donor-acceptor fragments, suggesting that a dynamic model should be used for the proton transfer [1]. In addition, the analytical potential function obtained by fitting to the *ab initio* data provides the necessary information needed in the quantum mechanical treatment of proton transfer in proteins. However, a full description of the proton transfer process requires specific consideration of the environmental solvent effects [4]. Unfortunately, most theoretical studies to date have been limited to model systems in the gas phase or phenomenological approaches due to the lack of proper potential functions for solute-solvent interactions [5-7].

A viable approach to the determination of the potential surface for the proton transfer in solution is to use a combined quantum mechanical and molecular mechanical (QM/MM) method by treating the solute quantum mechanically and the solvent molecules classically [4]. Consequently, the solute-solvent interaction as well as the proton-transfer potential surface is evaluated by the quantum mechanical calculations in fluid simulations. The quantum tunneling effect is then obtained through the time-dependent Schrödinger equation for the propagation of the proton on the potential surface approximated by the QM/MM model. This idea has been

pioneered by many researchers [8–11]. Warshel and coworkers used the empirical valence bond theory to study the hydrogen transfer reactions in proteins including lysozyme, trypsin, and lactate dehydrogenase [8], while Kollman [9], Karplus, and coworkers combined *ab initio* and semiempirical molecular orbital theory with the classical dynamics method [10]. Our own effort on the use of the hybrid QM/MM potential in statistical mechanics Monte Carlo simulations has demonstrated that the combined semiempirical AM1 theory and the TIP3P model for water can provide adequate description of the solvation of biomolecular systems in aqueous solution [11]. Furthermore, our results showed that the solvent polarization effects, which are of the primary concern on the use of the empirical potentials, can be quantitatively determined a priori in these calculations [12,13].

In this article, we examine the solvent effect on the Born–Oppenheimer potential surface for the proton transfer of  $[\text{H}_3\text{N}—\text{H}—\text{NH}_3]^+$  in water using the hybrid AM1/TIP3P potential via Monte Carlo simulations. Comparison with the gas phase results from Ref. [1] will be made. The dynamics and contributions to the rate constant from the quantum mechanical nuclear tunneling will be presented in a future publication. In the following, computational details will be first given followed by results and discussion.

### Computational Details

In the present study, the combined QM/MM potential is partitioned into a quantum mechanical region consisting of the proton donor and acceptor molecules,  $[\text{H}_3\text{N}—\text{H}—\text{NH}_3]^+$ , and a molecular mechanical region of the solvent molecules approximated by the three-site TIP3P model for water [14]. Clearly, in order to compute the energies of the QM solute molecules throughout the condensed-phase simulation, a computationally efficient method must be used. The semiempirical Austin Model 1 (AM1) theory developed by Dewar and coworkers [15] is employed to form the AM1/TIP3P force field [12]. Thus, the solute,  $[\text{H}_3\text{N}—\text{H}—\text{NH}_3]^+$ , is represented by valence electrons and nucleus cores in the Monte Carlo simulation. The restricted Hartree–Fock (HF) wave function,  $\Phi$ , is used with a single Slater determinant of all doubly occupied molecular orbitals (MO), which are linear combinations of a minimum basis set [15]. The total effective Hamiltonian of the system is given by:

$$\hat{H}_{\text{eff}} = \hat{H}^o + \hat{H}_{\text{qm/mm}} + \hat{H}_{\text{mm}}, \quad (1)$$

where  $\hat{H}^o$  is the AM1 Hamiltonian for the solute molecules,  $\hat{H}_{\text{mm}}$  is the molecular mechanical solvent energy, and  $\hat{H}_{\text{qm/mm}}$  is the solute–solvent interaction Hamiltonian defined previously [10–12]. Therefore, the total potential energy in the combined QM/MM force field is computed using Eq. (2),

$$E_{\text{tot}} = \langle \Phi | \hat{H}_{\text{eff}} | \Phi \rangle = E_{\text{qm}} + E_{\text{qm/mm}} + E_{\text{mm}}. \quad (2)$$

Here,  $\Phi$  is the wave function of the solute in aqueous solution,  $E_{\text{mm}}$  is the MM pair-interaction energy for the solvent molecules enumerated with the empirical TIP3P

potential, and  $(E_{qm} + E_{qm/mm})$  are determined through the Hartree-Fock self-consistent-field MO calculations. In particular, the solute-solvent interaction energy is

$$E_{qm/mm} = \langle \Phi | \hat{H}_{qm/mm}^{el} | \Phi \rangle + \sum_i \sum_s^{\text{solute water}} 4\epsilon_{is} [(\sigma_{is}/R_{is})^{12} - (\sigma_{is}/R_{is})^6], \quad (3)$$

where  $\hat{H}_{qm/mm}^{el}$  is the electronic portion of the solute-solvent interaction Hamiltonian, and the Lennard-Jones terms account for dispersion interactions between the QM and MM regions, which are omitted in the hybrid QM/MM approximation [10,12]. The Lennard-Jones parameters are taken from our previous work [12].

The potential energy surface for the proton transfer in  $[\text{H}_3\text{N}-\text{H}-\text{NH}_3]^+$  is determined as a function of the internuclear distance between the nitrogen atoms,  $R$ , and the position of the proton,  $x$ , measured from the geometrical center of the two nitrogens. The model as defined in Ref. [1] is shown in Figure 1. Note that only the linear arrangement is considered here, while McCammon and coworkers also investigated the off-axis displacement [1]. In the gas phase, the  $C_{3v}$  structure is the minimum configuration at a fixed  $R$ , which was used in the energy calculations. However, the rotation of the  $\text{NH}_3$  groups along the  $\text{N}-\text{N}$  axis is sampled through the dihedral sampling procedure in the Monte Carlo calculations. So, the model system takes a  $C_3$  symmetry in general in the computation of the free energies of solvation in water.

The free energy of solvation was computed via statistical perturbation theory [16] using the MCQUB/BOSS program [17], in which the quantum mechanical energies were evaluated with the MOPAC program modified to include the  $\hat{H}_{qm/mm}$  terms [18]. The calculations were performed at  $R = 2.50$  to  $3.00$  Å with an increment of  $0.05$  Å. For each value of  $R$ ,  $x$  was transformed from  $0.00$  to  $0.45$  Å using the "double-wide" sampling technique [19] with  $\Delta x = \pm 0.05$  Å to compute the relative free energies of solvation [Eq. (4)]:

$$\Delta G(x_1 \rightarrow x_2, R) = -k_B T \ln \langle e^{-\Delta E(x_1 \rightarrow x_2, R)/k_B T} \rangle_1 \quad (4)$$

where  $k_B$  is Boltzmann's constant,  $\langle \rangle_1$  represents the ensemble average using the Hamiltonian  $\hat{H}_{eff}(x_1, R)$ , and  $\Delta E(x_1 \rightarrow x_2, R)$  is the energy difference between proton positions  $x_1$  and  $x_2$ . Finally, the relative free energy between two adjacent lines was connected through an additional perturbation of  $R$  at  $x = 0.00$  Å. Therefore, the data for the solvation effect on the proton transfer came from a total of

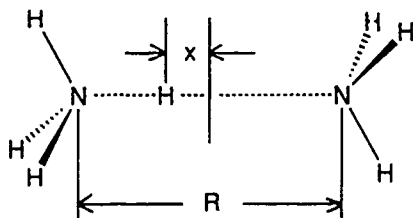


Figure 1. Geometrical definition for the model proton bound dimer.

60 simulations, each consisting of  $1 \times 10^6$  configurations for equilibration followed by  $1.5 \times 10^6$  configurations of averaging, and each requiring about 10 h of CPU time on an IBM RS/6000 Model 560 computer. All simulations were carried out in a rectangular box (ca.  $18.5 \times 18.5 \times 27.8 \text{ \AA}^3$ ) containing 321 water molecules plus  $[\text{H}_3\text{N}-\text{H}-\text{NH}_3]^+$ . The isothermal-isobaric (NPT) ensemble at  $25^\circ\text{C}$  and 1 atm was used along with the periodic boundary conditions. A spherical cutoff of  $9.5 \text{ \AA}$  was adopted for solute-solvent and solvent-solvent interactions. Standard deviations were estimated by computing separate averages over blocks of  $10^5$  configurations. The accumulative error was about 0.2 kcal/mol from the center of the free energy map.

### Results and Discussion

To verify the performance of the semiempirical AM1 method for the proton transfer in  $[\text{H}_3\text{N}-\text{H}-\text{NH}_3]^+$ , the computed barrier heights at fixed values of the nitrogen separation are compared with the results obtained by McCammon and coworkers using the MP2/6-31G(d) method (Table I); the agreement with the *ab initio* data is good, suggesting that the AM1 method may be used to study the present proton transfer reaction. The MP2/6-31G(d) optimizations yield an equilibrium distance of  $R = 2.72 \text{ \AA}$  [1], which is close to the AM1 value of  $2.74 \text{ \AA}$ . At  $R = 2.75 \text{ \AA}$ , the computed barriers are, respectively, 2.6 and 3.3 kcal/mol at the MP2 and AM1 levels, while squeezing the system to  $R = 2.5 \text{ \AA}$  results in a single minimum of symmetric configuration, which has an energy equal to the barrier height at  $R = 2.75 \text{ \AA}$ . The barrier height is raised to 10.2 and 12.4 kcal/mol for the MP2/6-31G(d) and AM1 models upon stretching the N—N distance to  $R = 3.00 \text{ \AA}$ . The potential energy surface obtained from the AM1 calculations is similar to that from the *ab initio* calculations, and is displayed in Figure 2, in which the energy has been anchored to zero at the global minimum. The feature of the combined motion of the proton and heavy-atom positions for the proton transfer along the classical path observed in the *ab initio* calculations are clearly seen in Figure 2. The transition state at  $R = 2.62 \text{ \AA}$  ( $x = 0.00$ ) is 1.4 kcal/mol above the global minimum, a result in good agreement with the MP2/6-31G(d) result ( $\Delta E^\ddagger = 0.9 \text{ kcal/mol}$  at  $R = 2.62 \text{ \AA}$ ) [1].

The free energy surface for the proton transfer in aqueous solution is shown in Figure 3. The solvent effect is apparent in comparison with the potential surface in the gas phase displayed in Figure 2. First, the solvation effect increases the barrier

TABLE I. Computed activation energies for the proton transfer of  $[\text{H}_3\text{N}-\text{H}-\text{NH}_3]^+$  in the gas phase (kcal/mol)

$R(\text{N}-\text{N}), \text{ \AA}$	$\Delta H^\ddagger$ (AM1)	$\Delta E^\ddagger$ (MP2/6-31G*)
2.50	0	0
2.75	3.3	2.6
3.00	12.4	10.2





of the proton transfer in  $[\text{H}_3\text{N}-\text{H}-\text{NH}_3]^+$  by ca. 3 kcal/mol. Apparently, at the transition state where the transferring proton is situated in the middle of the donor and acceptor molecules, the positive charge is more delocalized than the ion-dipole complex. Consequently, the transition state is not as strongly stabilized by the solvent as that of the ion-dipole structure. The results emphasize the importance of specific consideration of the environmental solvation contributions to the rate constant in theoretical models for the proton transfer in enzymatic systems. Secondly, the ion-dipole complex is a very stable species in the gas phase, which requires much more energy to dissociate into separate ammonium ion and ammonia monomers than that needed to cross the barrier of the proton transfer process (the binding energy of  $\text{NH}_4^+$  and  $\text{NH}_3$  is about 27 kcal/mol) [6]. In aqueous solution, however, the competition between the intrinsic binding of the ion-dipole complex and the solute-solvent interaction yields a delicacy on the details of the potential surface. Figure 3 shows that the ion-dipole complex is only about 1 kcal/mol lower in energy than the species with a N—N separation of 2.95 Å. The feature is similar to that observed in the  $\text{S}_\text{N}2$  reaction of  $\text{Cl}^- + \text{CH}_3\text{Cl}$  in water, where the gas-phase ion-dipole minimum is completely smeared out in aqueous solution, leading to a unimodal reaction profile [20].

Structural details on the solute-solvent interactions are further characterized by the computed radial distribution functions (rdfs),  $g_{xy}(r)$ , which give the probability of finding an atom of type  $y$  a distance  $r$  from an atom of type  $x$ . The results for the simulation at  $R = 2.75$  Å and  $x = 0.30$  Å, corresponding to the minimum in Figure 3, are given in Figures 4 through 6. In these figures the first atom for an  $xy$  distribution, refers to an atom of the solute and the second atom is either the oxygen or the hydrogen of water.

Figure 4 shows the  $\text{NH}_3$  hydrogen-water oxygen rdfs. For the donor molecule ( $\text{NH}_4^+$ , solid curve), hydrogen bonding interactions are clearly revealed by the first peak at 1.9 Å, which is in exact agreement with a previous study of the solvation of methylammonium ion in water [21]. Integration of this peak to 2.5 Å yields 1.4 water molecules per hydrogen. Thus, the total number of nearest-neighbor water

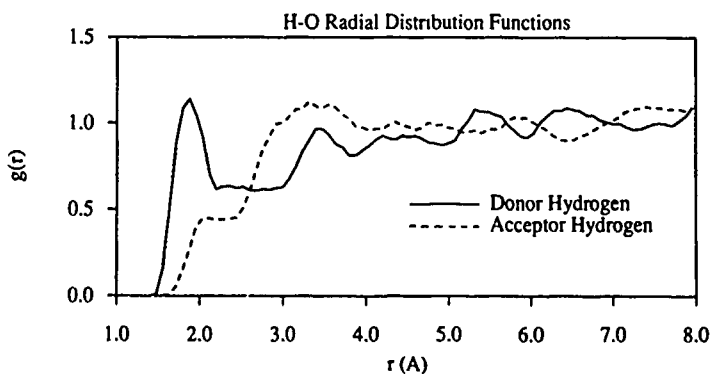


Figure 4. Amino hydrogen-water oxygen radial distribution functions.

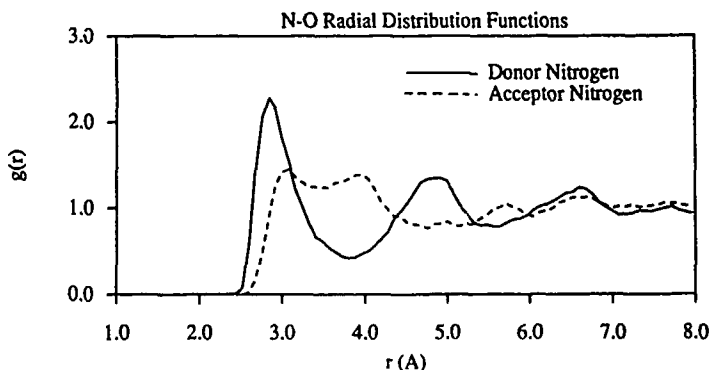


Figure 5. Nitrogen-water oxygen radial distribution functions.

molecules for the donor is 4.2, which may be compared with the value of 3.9 for methylammonium ion [21]. Hydrogen bonding interactions between the acceptor ammonia hydrogen and water are much weaker as expected. The dashed curve in Figure 4 displayed only a small shoulder in the H—O rdf. The hydrogen-bond donating ability of  $\text{NH}_3$  is known to be poor from *ab initio* calculations and gas-phase microwave experiments [22]. The N—O rdfs in Figure 5 confirm the pattern of hydrogen bonding interactions noted above with a sharp first peak for the donor monomer (solid curve) and a broad distribution for the acceptor nitrogen (dashed curve).

Finally, the rdfs for the transferring proton with water are shown in Figure 6. Due to steric congestions from the donor and acceptor  $\text{NH}_3$  groups in  $[\text{H}_3\text{N}-\text{H}-\text{NH}_3]^+$ , the migrating proton is not well hydrated by the solvent

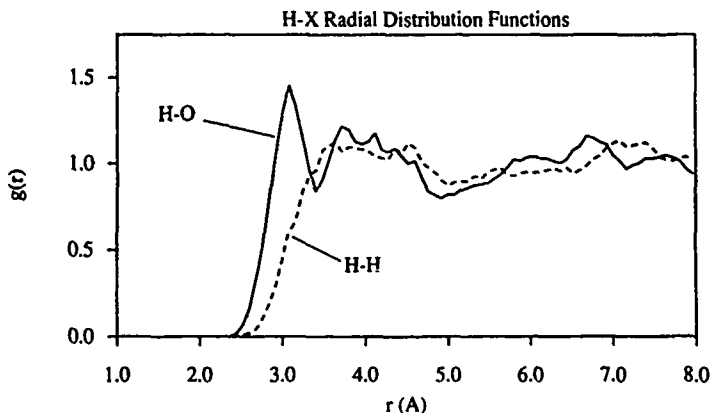


Figure 6. Radial distribution functions for the migrating proton with water oxygen (solid curve) and hydrogen (dashed curve).

molecules. Thus, the peaks occur at larger distances than those shown in Figure 4. Furthermore, the broad, structureless distribution for the H—H rdf indicates that the water hydrogens have considerable orientational freedom in forming hydrogen bonds with the solute.

### Conclusion

We have presented the results from Monte Carlo simulations of the proton transfer in  $[\text{H}_3\text{N}-\text{H}-\text{NH}_3]^+$  in water using the combined QM/MM-AM1/TIP3P method. The solvent effect was found to significantly increase the classical activation free energy over that in the gas phase. The barrier to proton transfer is sensitive to the distance between the donor and acceptor nitrogen atoms. Although the quantum-mechanical nuclear tunneling was not specifically considered, the present study shows that the hybrid QM/MM-AM1/TIP3P potential can provide adequate description of the solute-solvent interaction for the proton transfer process in solution, and the method may be used in a model that treats the proton motion quantum mechanically and the solvent dynamics classically.

### Acknowledgments

Gratitude is expressed to the donors of the Petroleum Research Fund, administered by the American Chemical Society, and to the National Institutes of Health through a Shannon Award for support of our research. The author is grateful to A. Auerbach for computational assistance.

### Bibliography

- [1] L. Jaroszewski, B. Lesyng, J. J. Tanner, and J. A. McCammon, *Chem. Phys. Lett.* **175**, 282 (1990).
- [2] R. P. Bell, *The Proton in Chemistry* (Chapman and Hall, London, 1973); R. P. Bell, *The Tunnel Effect in Chemistry* (Chapman and Hall, London, 1980).
- [3] Y. Cha, C. J. Murray, and J. P. Klinman, *Science* **243**, 1325 (1989); K. L. Grant and J. P. Klinman, *Biochemistry* **28**, 6597 (1989); J. Rucker, Y. Cha, T. Jonsson, K. L. Grant, and J. P. Klinman, *Biochemistry* **31**, 11489 (1992).
- [4] A. Warshel, *Computer Modeling of Chemical Reactions in Proteins and Solutions* (John Wiley, New York, 1991).
- [5] J. R. de la Vega, *Acc. Chem. Res.* **15**, 185 (1982); J. Bicerano, H. F. Schaefer, III, and W. H. Miller, *J. Am. Chem. Soc.* **105**, 2550 (1983); N. Makri and W. H. Miller, *J. Chem. Phys.* **91**, 4026 (1989); N. Shida, P. F. Barbara, and J. E. Almlof, *J. Chem. Phys.* **91**, 4061 (1989); S. Wolfe, S. Hoz, C.-K. Kim, and K. Yang, *J. Am. Chem. Soc.* **112**, 4186 (1990); E. Bosch, M. Moreno, and J. M. Lluch, *J. Am. Chem. Soc.* **114**, 2072 (1992).
- [6] S. Scheiner, *Acc. Chem. Res.* **18**, 174 (1985); E. A. Hillenbrand and S. Scheiner, *J. Am. Chem. Soc.* **107**, 7690 (1985).
- [7] R. A. Marcus, *Ann. Rev. Phys. Chem.* **15**, 155 (1964); B. C. Garrett and D. G. Truhlar, *J. Phys. Chem.* **95**, 10374 (1991); P. P. Schmit, *J. Phys. Chem.* **93**, 6610 (1989); D. C. Borgis, S. Lee, and J. T. Hynes, *Chem. Phys. Lett.* **162**, 19 (1989); S. Chapman, D. P. Ali, and J. T. Hynes, *Chem. Phys.* **136**, 297 (1989).

- [8] A. Warshel and S. Russell, *J. Am. Chem. Soc.* **108**, 6569 (1986); A. Warshel and Z. T. Chu, *J. Chem. Phys.* **93**, 4003 (1990); J.-K. Hwang, Z. T. Chu, A. Yadav, and A. Warshel, *J. Phys. Chem.* **95**, 8445 (1991).
- [9] U. C. Singh and P. A. Kollman, *J. Comput. Chem.* **7**, 718 (1986); S. J. Weiner, G. L. Seibel, and P. A. Kollman, *Proc. Natl. Acad. Sci.* **83**, 649 (1986).
- [10] M. J. Field, P. A. Bash, and M. Karplus, *J. Comput. Chem.* **11**, 700 (1990); P. A. Bash, M. J. Field, and M. Karplus, *J. Am. Chem. Soc.* **109**, 8192 (1987).
- [11] J. Gao, *J. Phys. Chem.* **96**, 537 (1992); J. Gao and J. J. Pavelites, *J. Am. Chem. Soc.* **114**, 1912 (1992).
- [12] J. Gao and X. Xia, *Science* **258**, 631 (1992).
- [13] J. Gao, *J. Chem. Phys.* **98**, 2975 (1993).
- [14] W. L. Jorgensen, J. Chandrasekhar, J. D. Madura, R. W. Impey, and M. L. Klein, *J. Chem. Phys.* **79**, 926 (1983).
- [15] M. J. S. Dewar, E. G. Zoebisch, E. F. Healy, and J. J. P. Stewart, *J. Am. Chem. Soc.* **107**, 3902 (1985).
- [16] R. W. Zwanzig, *J. Chem. Phys.* **22**, 1420 (1954).
- [17] W. L. Jorgensen, *BOSS, Version 2.9*, (Department of Chemistry, Yale University; 1990); J. Gao, *MCQUB*, (Department of Chemistry, State University of New York at Buffalo; 1992).
- [18] J. J. P. Stewart, *MOPAC, Version 5; Quantum Chemistry Program Exchange 455*, Vol. 6, No. 391 (1986).
- [19] W. L. Jorgensen and C. Ravimohan, *J. Chem. Phys.* **83**, 6548 (1985).
- [20] J. Chandrasekhar, S. F. Smith, and W. L. Jorgensen, *J. Am. Chem. Soc.* **107**, 154 (1985).
- [21] W. L. Jorgensen and J. Gao, *J. Phys. Chem.* **90**, 2174 (1986).
- [22] D. D. Nelson, Jr., G. T. Fraser, and Klemperer, *Science*, **238**, 1670 (1987); M. J. Frisch, J. E. Del Bene, J. S. Binkley, and H. F. Schaefer, III, *J. Chem. Phys.* **84**, 2279 (1986).

Received March 15, 1993

# Instability in Chemical Bonds. II. Theoretical Studies of Exchange-Coupled Open-Shell Systems

K. YAMAGUCHI,\* M. OKUMURA, K. TAKADA, and S. YAMANAKA

*Department of Chemistry, Faculty of Science, Hokkaido University, Sapporo, 060, Japan*

## Abstract

The electronic and geometrical structures of exchange-coupled open-shell systems such as bis(methylene)methane and the chromium-methylene cation were investigated by the molecular orbital and its extended methods: RHF, UHF, UNO-CAS, RMP, UMP, PUMP, APUMP, UCCSD(T), UNO-CI and QCISD(T). The fully optimized geometries of these species by the energy gradients of UMP/CI solutions are consistent with the experimental values. The total energies of the lowest and highest spin states were calculated in order to elucidate the effective exchange integrals in the Heisenberg model for methylene and bis(methylene)methane. The spin projection is necessary for the UHF-based wavefunctions in the lowest spin state of the species. The binding energies for the chromium cation-methylene double bond were calculated by both spin-unprojected and -projected methods. It was found that the binding energy between  $\text{Cr}^+$  and  $^3\text{CH}_2$  by APUHF QCISD(T) is in accord with the experimental value. © 1993 John Wiley & Sons, Inc.

## Introduction

Recently electronic and geometrical structures of unstable molecules and their clusters have received particular interest, since computational methods for stable closed-shell molecules and concerted reactions are rather established. One of the remarkable features of unstable molecules such as diradical and polyradicals is that the restricted Hartree-Fock (RHF) and open-shell RHF (ORHF) solutions for these systems suffer, respectively, from the so-called triplet instability and/or spin-flip (SF) instability [1]. Then the spin and electron correlations are nondynamically important, indicating the necessity of beyond Hartree-Fock theories and computations [2]. As a continuation of the previous work [1] (hereafter it is referred to as the Part I), we here summarize our recent theoretical approaches to unstable chemical bonds involved in exchange-coupled open-shell systems.

We first summarize theoretical backgrounds in the next section, where advanced MO techniques are examined in relation to chemical pictures and models for unstable molecules [1]. Both spin-restricted and unrestricted post-Hartree-Fock methods are briefly reviewed in the next section. In order to explain practical aspects in *ab initio* computations, we investigate the electronic structures of methylene and bis(methylene)methane in the third and fourth sections. The effective exchange integrals for these species in the Heisenberg model are calculated by the total energy

\* Also at Department of Chemistry, Faculty of Science, Osaka University, Osaka 560, Japan.

difference between the lowest-spin (LS) and highest-spin (HS) states. The direct exchange-coupling energies between chromium cation and triplet methylene are examined by several computational methods in the fifth section.

## Theoretical Backgrounds

### *Instability of Chemical Bonds in Open-Shell Systems*

The *ab initio* restricted Hartree-Fock (RHF) molecular orbital (MO) method [3] has been utilized for elucidation of electronic structures of closed-shell organic molecules such as homopolar and polar nonradical species. In order to elucidate geometrical parameters such as bond lengths and angles, together with electronic structures, a variety of *ab initio* RHF and RHF-based post Hartree-Fock calculations have already been carried out for organic molecules and organic reaction intermediates [4].

However, the intrinsic deficiency of the RHF MO method is that it cannot describe a dissociation process of a covalent bond even in a qualitative sense. An approach to this problem within the Hartree-Fock (HF) MO framework is to use the unrestricted HF (UHF) theory [5]. The bifurcation of the RHF MOs into the DODS MOs occurs at the triplet (T) instability threshold where the lowest eigenvalue ( $\lambda_0 = 0$ ) of the T-instability matrix is zero [3,6-8]. This means chemically that a molecule under consideration has a singlet diradical character [9]. Generally, the UHF MO method offers a qualitatively correct orbital picture and orbital correlation diagram for the dissociation of a covalent bond, being applicable to diradical and polyradical species [10]. However, the UHF-based wavefunctions for singlet diradicals and low-spin species suffer from the spin contaminations arising from high-spin states [5], leading to spin-projection or spin-restricted procedures described below [11-13].

### *UNO-CASCI and CASSCF Methods*

A spin-restricted method for the elucidation of electronic structures of unstable molecules, particularly of open-shell species such as diradical and polyradical species, is the multiconfiguration self-consistent-field (MCSCF) method [2]. As an extension of the MO-theoretical approach to unstable molecules, we have investigated the utility of approximate natural orbitals and their occupation numbers determined by the UHF calculations for selections of active orbitals and for rapid convergence of the multireference (MR) configuration interaction (CI) and MCSCF calculations [14,15]. Recently, Pulay and his coworkers [16,17] have also demonstrated that the UHF solutions can be used for determining approximate natural orbitals that are starting trial orbitals for effective MCSCF calculations of complex open-shell species.

In order to elucidate the open-shell characters, the UHF solution is expressed by the corresponding molecular orbitals (CMOs) [5,18]:

$$\Psi(\text{UHF}) = |X_1\bar{\eta}_1 X_2\bar{\eta}_2 \cdots X_N\bar{\eta}_N|, \quad (1)$$

where  $\chi_i$  and  $\eta_i$  are CMOS, which are related to the UHF natural orbitals (UHF NO = UNO) $\varphi_j$ ,

$$\chi_{\text{HO}-i} = \cos \omega \varphi_{\text{HO}-i} + \sin \omega \varphi_{\text{LU}+i} \quad (\text{HO} = \text{HOMO}, \text{LU} = \text{LUMO}), \quad (2a)$$

$$\eta_{\text{HO}-i} = \cos \omega \varphi_{\text{HO}-i} - \sin \omega \varphi_{\text{LU}+i}, \quad (2b)$$

where  $\omega$  is the orbital mixing parameter. The localized natural orbitals (LNO) and magnetic orbitals are defined as the corresponding MOS at the strong correlation limit  $\omega = 45^\circ$  [19]:

$$\chi_{\text{HO}-i}(\text{LNO}) = (\varphi_{\text{HO}-i} + \varphi_{\text{LU}+i})/\sqrt{2} \quad (\text{HO} = \text{HOMO}, \text{LU} = \text{LUMO}), \quad (2c)$$

$$\eta_{\text{HO}-i}(\text{LNO}) = (\varphi_{\text{HO}-i} - \varphi_{\text{LU}+i})/\sqrt{2}. \quad (2d)$$

The LNOs are useful for the valence-bond (VB)-like explanations of the UNO complete active space (CAS) configuration interaction (CI) wavefunctions [1,14].

The natural orbital pairs  $(\varphi_{\text{HO}-i}, \varphi_{\text{LU}+i})$  in Eq. (2) are usually the bonding and antibonding MOS, and these are spatially symmetry-adapted orbitals in contrast to generalized valence bond (GVB) natural orbitals [1], which are often bond orbitals. The occupation numbers ( $n_i$ ) of these NOs are given by the orbital overlap between the corresponding orbital pairs  $(\chi_{\text{HO}-i}$  and  $\eta_{\text{HO}-i})$  as

$$n_{\text{HO}-i}(\text{UHF}) = 1 + T_i, \quad n_{\text{LU}+i}(\text{UHF}) = 1 - T_i, \quad (3a)$$

where

$$T_{ij} = \int \chi_i \eta_j dr = \delta_{ij}, \quad T_{ii} = T_i. \quad (4)$$

Judging from the magnitude of the occupation numbers, we can select the active natural orbitals for the full valence (FV) CI or CAS CI calculations for the ground and lower excited states [15,20,21]. When the UNO and CAS(FV) CI vector are utilized as trial orbitals [15] for the more refined FV-type MCSCF calculations [15] for a state under consideration, the procedure is often called as UNO-CASSCF or UNO-CAS [18].

The interrelationship between the UHF, spin-projected UHF (PUHF) and UNO CASSCF methods is clear. As an example, let us consider the case of diradical species in which the corresponding orbitals are essentially equivalent to the closed-shell MOS  $\varphi$  except for a diradical pair [1,22,23]:

$$\chi_i = \eta_i \approx \varphi_i \quad (i = 0, 1, 2, \dots, \text{HO} - i). \quad (5)$$

The singlet UHF orbital configuration  $|\chi_{\text{HO}}\eta_{\text{HO}}|$  for diradicals does not express the pure singlet state. The spin projection of the configuration into the singlet state (PUHF) is necessary for a quantitative purpose:

$$\Psi(\text{PUHF}) = |\varphi_1\bar{\varphi}_1\varphi_2\bar{\varphi}_2\{\chi_{\text{HO}}\bar{\eta}_{\text{HO}} + \eta_{\text{HO}}\bar{\chi}_{\text{HO}}\}| \quad (6a)$$

$$= \cos^2 \omega |\varphi_1\bar{\varphi}_1\varphi_2\bar{\varphi}_2 \cdots \varphi_{\text{HO}}\bar{\varphi}_{\text{HO}}| \\ - \sin^2 \omega |\varphi_1\bar{\varphi}_1\varphi_2\bar{\varphi}_2 \cdots \varphi_{\text{LU}}\bar{\varphi}_{\text{LU}}|, \quad (6b)$$

where  $\omega$  is defined by Eq. (2). The PUHF wavefunction is the  $2 \times 2$  multiconfiguration wavefunction constructed from the ground and doubly excited state functions.

The diradical character  $y$  is defined by the weight ( $W_d$ ) of the doubly excited configuration in the MCSCF theory and it is formally expressed by the orbital overlap  $T_i$  in the case of the PUHF theory [1,5,23,24]:

$$y_i = 2W_d = 1 - 2T_i/(1 + T_i^2). \quad (7a)$$

The diradical characters by the PUHF method are 0% and 100% for closed-shell and pure diradical states, respectively. The occupation numbers of UNO for polyradicals in the PUHF state are generally given by

$$n_{\text{HO}-i}(\text{PUHF}) = [n_{\text{HO}-i}(\text{UHF})]^2/(1 + T_i^2), \quad (3b)$$

$$n_{\text{LU}+i}(\text{PUHF}) = [n_{\text{LU}+i}(\text{UHF})]^2/(1 + T_i^2). \quad (3c)$$

Therefore, the occupation number of an antibonding UNO is nothing but the diradical character for a chemical bond  $i$ :

$$n_{\text{LU}+i}(\text{PUHF}) = y_{\text{LU}+i}. \quad (7b)$$

Generally, the UNO CASSCF method should involve at least all the active pairs of UNOs, which are responsible for di- and polyradical states. Therefore, the UNO CAS wavefunction includes the nondynamical part of electron correlation correction.

### *Single Reference (SR) Post-Hartree-Fock Methods*

The R(U)HF and UNO-CASSCF wavefunctions do not involve the so-called dynamical electron correlation effect. Several post Hartree-Fock approaches have been successfully used for simple and efficient computations of electron correlation energies [24,25]. For closed-shell molecules and singlet species without strong diradical characters, the reference wavefunction is usually for the RHF type:

$$\Psi(\text{RHF } X) = \Psi(\text{RHF}) + \Psi(X \text{ correction}), \quad (8)$$

where the  $X$ 's mean the post Hartree-Fock methods:  $n$ th-order Møller-Plesset perturbation (MP $n$ ), coupled-cluster double (CCD), CC single double (CCSD), CCD plus single and triple perturbation (CCDST4), quadratic SD configuration interaction (QCISD), and QCISD plus triple excitation [QCISD(T)], etc. [25]. The RHF-based wavefunctions are quite acceptable wavefunctions for closed-shell species and singlet species with weak diradical characters. However, they often over(under) estimate the correlation correction for singlet species with strong diradical characters, indicating the breakdown of the RHF-based approaches [26].

For open-shell molecules and singlet species with strong diradical characters, the reference wavefunction is of the UHF type:

$$\Psi(\text{UHF } X) = \Psi(\text{UHF}) + \Psi(X \text{ correction}), \quad (9)$$

where the  $X$ 's are the same as those in Eq. (8). The UHF-based wavefunctions are acceptable wavefunctions for doublet radicals, triplet diradicals, and high-spin



polyradicals at or close to the equilibrium geometries. For singlet diradicals and low-spin polyradicals, however, they are often heavily contaminated by higher spin states. The MP, CC, and QCI theories do not remove these contaminations involved in the UHF reference function in Eq. (9).

Schlegel [12] has proposed a spin annihilation procedure for the UMP $n$  ( $n = 2-4$ ) wavefunctions based on Löwdin's projection operator  $\mathbf{O}$  [27]:

$$\mathbf{O} = \prod_{S=J+1}^{S=J+l} \{S^2 - J(J+1)\} / \{S(S+1) - J(J+1)\}, \quad (10)$$

where  $S$  is given by the difference between up ( $N_a$ ) and down ( $N_b$ ) spins. i.e.,  $S = \frac{1}{2}(N_a - N_b)$  and where the cases of  $l = 1$  and  $l = 2$  correspond, respectively, to Schlegel [12] and Handy [13] projections. Generally speaking, the spin projection is necessary for all the split pairs ( $T_i < 1.0$ ) in Eq. (2). The incomplete projection often suffers from the so-called size inconsistent problem: The size inconsistency means that the total energy of a cluster consisted of  $n$  molecules is not equal to  $n$  times the energy of one molecule even at the dissociation limit.

#### *Approximate but Size-Consistent Spin Projection Procedure*

A size-consistent but approximate spin projection procedure was also proposed [10,11]. Let us first consider the diradical case given by Eq. (6). If the contamination of the singlet wavefunction is assumed to be arisen only from the triplet state in the case of the singlet diradical, then the singlet UHF-based wavefunctions can be written as

$$^1\Psi(\text{UHF } X) = C_s \, ^1\Phi(\text{PUHF } X) + C_t \, ^3\Phi(\text{PUHF } X), \quad (11)$$

where  $^q\Phi(\text{PUHF } X)$  denotes the UHF  $X$  wavefunction for the pure  $q$  spin state and  $C_s$  and  $C_t$  are the coefficients of the pure singlet and triplet components, respectively. Because of the second term in Eq. (11), the  $^1\Psi(\text{UHF } X)$  wavefunction will have an expectation value  $^1\langle S^2 \rangle$  of the total spin operator different from zero. Therefore, the coefficient of the triplet component can be calculated by

$$C_t^2 = ^1\langle S^2 \rangle (\text{UHF } X) / ^3\langle S^2 \rangle (\text{UHF } X). \quad (12a)$$

The total energy of the pure singlet state is approximately given by

$$^1E(\text{APUHF } X) = ^1E(\text{UHF } X) + f \times [^1E(\text{UHF } X) - ^3E(\text{UHF } X)], \quad (13a)$$

where APUHF  $X$  denotes the approximate PUHF  $X$  and  $^W E(Z)$  denotes the total energy for the  $W$  spin state by the method  $Z$ . The correction factor  $f$  is given by

$$f = C_t^2 / (1 - C_t^2) = ^1\langle S^2 \rangle (\text{UHF } X) / [^3\langle S^2 \rangle (\text{UHF } X) - ^1\langle S^2 \rangle (\text{UHF } X)]. \quad (14a)$$

Equation (13a) is applicable to polyradicals [11,28] where the  $f$ -factor is approximately given by

$$f = [^{1S}\langle S^2 \rangle (\text{UHF } X) - S(S+1)] / [^{HS}\langle S^2 \rangle (\text{UHF } X) - ^{1S}\langle S^2 \rangle (\text{UHF } X)], \quad (14b)$$

where LS and HS mean the lowest spin and highest spin states, respectively. Since the computation of  ${}^N\langle S^2 \rangle(\text{UHF } X)$ -value is not easy, it is estimated by the extrapolation from the UMP2 value

$${}^N\langle S^2 \rangle(\text{UHF } X) = {}^N\langle S^2 \rangle(\text{UMP2}) + g \times [{}^N\langle S^2 \rangle(\text{UMP2}) - {}^N\langle S^2 \rangle(\text{UHF})], \quad (15)$$

$$g = [{}^N E(\text{UHF } X) - {}^N E(\text{UMP2})] / [{}^N E(\text{UMP2}) - {}^N E(\text{UHF})]. \quad (16)$$

The approximate spin projection procedure is applicable to all UHF-based post Hartree-Fock wavefunctions in the strong correlation regime.

### *Multireference (MR) Post Hartree-Fock Methods*

The multireference (MR) methods are inevitable for very accurate descriptions of unstable molecules in the intermediate correlation regime and excited states in general [1]. In principle, the MR zero-order wavefunction can be constructed by the UHF CI within active UHF MOs, which are responsible for diradical and poly-radicals [15]. For example, two occupied and two unoccupied MOs are selected as active UHF orbitals for diradicals; the number of active MOs are twice as compared with the spin-restricted approach. The MR UHF CI and related methods are useful for heavy atom systems, where spin-dependent interactions such as the spin-orbit interaction are particularly important.

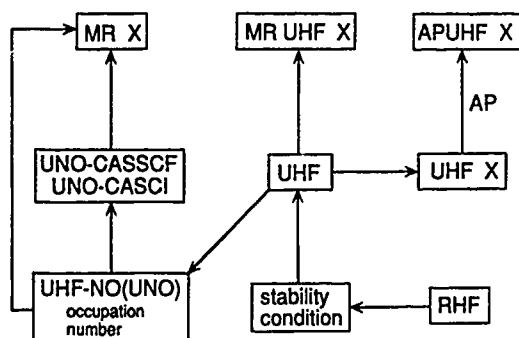
In order to reduce the number of active orbitals, we have proposed the use of symmetry-adapted UHF NO for MR post HF calculations in the case of spin-free molecular systems [1,14,15], where the UNO CASCI wavefunction is taken as the zero-order wavefunction:

$$\Psi(\text{MR } X) = \Psi(\text{UNO-CASCI}) + \Psi(X \text{ correction}), \quad (17)$$

where  $X$  is given in Eq. (8). If the coupled-cluster (CC) single excitation operator is employed for  $X$ , the resulting solution is equivalent to the UNO CASSCF wavefunction as discussed previously [15]. The UNO CASCI reference is also used for the UNO many-body perturbation (PT $n$ ) and UNO coupled-cluster single and double (CCSD) method [15]. The second-order UNO-PT method can be applicable to relatively larger systems for which UNO-CASSCF and MR SD CI calculations are not practical. Recently several partitioning schemes of effective Hamiltonians are proposed for efficient PT computations [29,30]. Figure 1 illustrates computational schemes for the ground and excited states of unstable molecules.

### **Singlet-Triplet Energy Separation of Methylene**

Methylene is usually investigated as a calibration of several levels of computations [31]. The RHF solution of methylene is triplet-unstable [5,9], being reorganized into the singlet UHF solution, where the split HOMOs for the up and down spins are given by



X = MP, CC(S)D, QCISD(T)

Figure 1. Schematic illustrations of theoretical approaches to unstable molecules such as singlet diradicals and polyradicals. The constructions of appropriate UHF solutions are particularly important in this approach. To this end, UHF MOS for fragments are useful as starting orbitals for SCF cycles. The natural orbital analysis of the UHF solutions is also important to perform the spin-restricted post HF calculations.

$$\chi_{\text{HO}} = \cos \omega \sigma + \sin \omega \pi, \quad (2c)$$

$$\eta_{\text{HO}} = \cos \omega \sigma - \sin \omega \pi. \quad (2d)$$

Figure 2(A) illustrates the shapes of molecular orbitals in the  $^1\text{RHF}$ ,  $^1\text{UHF}$ , and  $^3\text{UHF}$  solutions. The orbital overlap  $T_{\text{HO}}$  between the split MOS in the  $^1\text{UHF}$  solution is 0.537 at the singlet optimized geometry (see below), and therefore the diradical character  $y$  is only 17%. The PUHF solution for the singlet state is expressed by the  $2 \times 2$  UNO CI form as

$$\Psi(\text{PUHF}) = |\{\chi_{\text{HO}}\overline{\eta_{\text{HO}}} + \eta_{\text{HO}}\overline{\chi_{\text{HO}}}\}| = \cos^2 \omega |\sigma\overline{\sigma}| - \sin^2 \omega |\pi\overline{\pi}|. \quad (6c)$$

Therefore, APUHF post HF wavefunctions such as APUHF CCSD are approximately equal to those of two-reference post HF methods in Eq. (17).

The post HF calculations were carried out for the calculated geometries [31]: (A)  $R(\text{C}-\text{H}) = 1.0832 \text{ \AA}$  and  $\langle \text{HCH} = 132.3^\circ$  for the triplet methylene and (B)  $R(\text{C}-\text{H}) = 1.1118 \text{ \AA}$  and  $\langle \text{HCH} = 102.4^\circ$  for the singlet methylene. Table I summarizes the total energies by the RHF- and UHF-based 6-31G\* calculations and the adiabatic energy differences between the singlet (S) and triplet (T) states.

From Table I, the following should be noted: (1) The singlet UHF 6-311G\*\* solution is more stable by 11.6 kcal/mol than the RHF solution in accord with the triplet instability of the RHF solution. (2) The spin projected UHF (APUHF) solution is less stable by 3.7 kcal/mol than the UHF solution because of the removal of the ground-triplet contaminant. (3) The  $\langle S^2 \rangle$ -values for singlet UHF-based methods are about 0.7, indicating the necessity of the spin projection, whereas they are about 2.0 for the triplet UHF-based methods. (4) The energy correction for UHF QCISD(T) by the approximate spin projection is 0.9 kcal/mol. The energy difference between

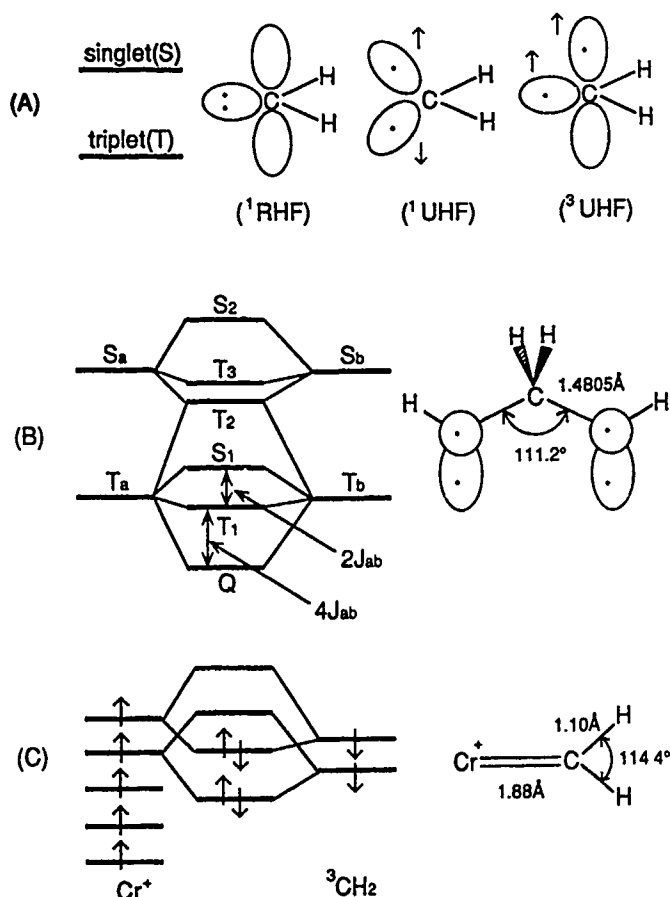


Figure 2. (A) Energy levels are diradical orbital configurations for methylene. (B) energy levels of bis(methylene)methane constructed of triplet methylenes via the through-bond coupling and the optimized geometry by the UMP2 6-31G\* method. (C) Exchange-coupling between chromium cation and triplet methylene and the partial optimized geometry by the UMP4 method.

the RHF QCISD(T) and APUHF QCISD(T) is only 0.5 kcal/mol. This means that RHF QCISD(T) works well in the case of weak singlet diradicals. (5) The S-T separation is calculated to be 29 kcal/mol by the energy difference between singlet RHF and triplet UHF energies, whereas it is 21 kcal/mol by the energy difference between  $^1\text{APUHF}$  and  $^3\text{UHF}$ . (6) The S-T gap is 12.6 kcal/mol by the difference between  $^1\text{RHF}$ - and  $^3\text{UHF}$  QCISD(T) total energies, whereas it is 12.7 kcal/mol by the total energy difference between  $^1\text{APUHF}$  and  $^3\text{UHF}$  QCISD(T).

The S-T separation at the QCISD(T) level is the same as that of extensive CASSCF MBPT calculations [30]. However, it is still larger by 0.7 kcal/mol than the full CI value [31].

TABLE I. Energy gaps between HS and LS states calculated for methylene<sup>a</sup> by several computational methods.<sup>b</sup>

Method	LS $E_{\text{total}}$	HS $E_{\text{total}}$	$\Delta E^c$ (kcal/mol)
RHF	-38.869754	*	(29.2)
UHF	-38.905961	-38.933894	17.7
APUHF	-38.882616	-38.933894	21.4
PUHF ( $l = 1$ ) <sup>d</sup>	-38.892119	-38.936661	19.4
PUHF ( $l = 2$ )	-38.887879	-38.936655	20.5
RMP2	-38.985493	*	(18.0)
UMP2	-39.009446	-39.033121	14.0
APUMP2	-38.987899	-39.033121	16.0
PUMP2 ( $l = 1$ ) <sup>d</sup>	-38.995325	-39.034977	15.1
PUMP2 ( $l = 2$ )	-38.990961	-39.034971	16.3
RMP4	-39.010397	*	(13.8)
UMP4	-39.031977	-39.053149	12.3
APUMP4	-39.012708	-39.053149	13.5
PUMP4 ( $l = 1$ ) <sup>d</sup>	-39.017608	-39.054290	13.0
PUMP4 ( $l = 2$ )	-39.013148	-39.054284	14.2
RHF CCD	-39.011107	*	(13.4)
UHF CCD	-39.035334	-39.051619	12.0
APUCC	-39.020513	-39.051619	13.0
RHF CCDST4	-39.015589	*	(12.5)
UHF CCDST4	-39.041659	-39.054460	11.6
APUHF CCDST4	-39.030009	-39.054460	12.4
RHF QCISD	-39.011953	*	(13.4)
UHF QCISD	-39.037480	-39.052614	12.0
APUHF QCISD	-39.023706	-39.052614	13.0
RHF QCISD(T)	-39.015763	*	(12.6)
UHF QCISD(T)	-39.045098	-39.054735	11.8
APUHF QCISD(T)	-39.036327	-39.054735	12.7

<sup>a</sup>  $R(\text{CH}) = 1.0832 \text{ \AA}$ ;  $\angle \text{HCH} = 132.3^\circ$ .<sup>b</sup> 6-311G\*\* basis set.<sup>c</sup>  $\Delta E = E(\text{LS}) - E(\text{HS})$ .<sup>d</sup> Level of spin projection.

### Through-Bond Interaction between Triplet Methylene

As shown previously [32], the merit of the APUHF QCISD(T) is applicable to relatively larger clusters of open-shell species. As a simple example of tetradicals, here we examine bis(methylene)methane 2 ( $\text{H}\ddot{\text{C}}-\text{CH}_2-\ddot{\text{C}}\text{H}$ ) which is formally formed by the through-bond coupling of two triplet methylenes via the methylene bridge. There are two singlet, three triplet, and one quintet states for 2 as illustrated in Figure 2(B). The lower-lying singlet ( $S_1$ ), triplet ( $T_1$ ), and quintet (Q) states for 2 arise from the exchange coupling between the ground triplet methylene units as illustrated in Figure 2(B). The UHF wavefunctions for the Q state are approximately given by the symmetry adapted UHF NOS as

$$\Psi(Q) = |\varphi_1 \varphi_{-1} \varphi_{-2}|, \quad (18)$$

where UHF NO are given by the bonding and antibonding  $\sigma$  and  $\pi$  MOs constructed of the linear combination of the  $\sigma$  and  $\pi$  radical orbitals of methylenes a and b:

$$\varphi_{\pm 1} = (\sigma_X \pm \sigma_Y)/\sqrt{2}, \quad \varphi_{\pm 2} = (\pi_X \pm \pi_Y)/\sqrt{2}, \quad (19)$$

where  $X$  ( $Y$ ) denotes the site a or b. Therefore the corresponding MOs for the singlet UHF solution  $|\chi_a \bar{\xi}_a \chi_b \bar{\xi}_b|$  are approximately given by

$$\chi_X = \cos \omega_1 \varphi_1 + \sin \omega_1 \varphi_{-1} = \cos(\omega_1 - \pi/4) \sigma_X + \cos(\omega_1 + \pi/4) \sigma_Y, \quad (20a)$$

$$\xi_X = \cos \omega_1 \varphi_2 + \sin \omega_2 \varphi_{-2} = \cos(\omega_2 - \pi/4) \pi_X + \cos(\omega_2 + \pi/4) \pi_Y. \quad (20b)$$

The natural orbital (NO) analysis of the singlet UHF 6-31G\* solution for **2** shows that the orbital overlaps for  $\sigma$ - and  $\pi$ -type corresponding MOs are 0.0019 and 0.0331, respectively: namely,  $\omega_1 = \omega_2 \cong \pi/4$ , and therefore  $\chi_a \cong \sigma_a$ ,  $\xi_a \cong \pi_a$ ,  $\chi_b \cong \sigma_b$  and  $\xi_b \cong \pi_b$ . The corresponding MOs are essentially equivalent to the  $\sigma$  and  $\pi$  radical MOs of methylenes a and b, respectively.

Full geometry optimizations of the quintet state of **2** have been carried out by using the energy gradient of the UMP2 6-31G\* wavefunction. Figure 2(B) shows the fully optimized geometry of **2**. The total energies of the lowest spin (LS =  $S_1$ ) and highest spin (HS = Q) states of **2** at the optimized geometry were calculated by several post HF methods, and the refinements of the total energies for the LS state were conducted by the spin projection procedure in the second section. The energy gaps between the LS and HS states were determined from these total energies, being equivalent to  $6J_{ab}$  values in the Heisenberg Hamiltonian as illustrated in Figure 2(B):

$$\mathbf{H}_{\text{HB}} = - \sum 2J_{ab} \mathbf{S}_a \cdot \mathbf{S}_b, \quad (21a)$$

$$J_{ab} = [{}^{\text{LS}}E_{\text{UHF}\lambda} - {}^{\text{HS}}E_{\text{UHF}\lambda}] / [{}^{\text{HS}}\langle \mathbf{S}^2 \rangle (\text{UHF } X) - {}^{\text{LS}}\langle \mathbf{S}^2 \rangle (\text{UHF } X)], \quad (21b)$$

where  $S_c$  denotes the spin at the site  $c$  ( $=a$  or  $b$ ).

Table II summarizes the calculated results. From this table, the following conclusions can be drawn: (1) The LS–HS energy differences are positive by all computational methods. Then bis(methylene)methane with the  $C_{2v}$  symmetry is the HS ground-state molecule. (2) The energy differences by the spin-unprojected UHF CCD (UCCD), QCISD, QCISD(T), and UMP4 methods are quite similar. (3) The  $\langle \mathbf{S}^2 \rangle$  values for the singlet post UHF wavefunctions are about 2.0, showing the necessity of the spin projection to obtain the pure singlet state wavefunctions. (4) The energy differences by UMP $n$ , QCISD, and QCISD(T) increase by 40–50% after the approximate spin projection of the LS (singlet) solution. (5) The energy difference by the UHF-based post HF methods are close to those of the spin-symmetry adapted post HF calculations: namely, UNO-CASSCF by the use of the four-active orbitals and four-electrons {4,4} and MRSDCI based on UNO-CASSCF {4,4}. (6) The energy difference after Schlegel's spin projection, PUMP $n$  ( $l=1$ ), becomes abnormally large, indicating that the single annihilation procedure breaks down in this system, and Handy's double projection scheme [13], PUMP $n$  ( $l=2$ ), also leads to the overestimation of

TABLE II. Energy gaps between HS and LS states calculated for  $\dot{\text{C}}\text{HCH}_2\dot{\text{C}}\text{H}^a$  by several computational methods.<sup>b</sup>

Method	LS <sub>E<sub>total</sub></sub>	HS <sub>E<sub>total</sub></sub>	$\Delta E^c$ (cm <sup>-1</sup> )
RHF	-115.606953	*	*
UHF	-115.726823	-115.731980	1132
APUHF	-115.724216	-115.731980	1704
PUHF ( <i>l</i> = 1) <sup>d</sup>	-115.076390	-115.736351	144810
PUHF ( <i>l</i> = 2)	-115.714942	-115.736316	4690
PUHF ( <i>l</i> = 3)	-115.730817	-115.736316	1207
CASSCF {4,4}	-115.632879	-115.637639	1045
RMP2	-115.928650	*	*
UMP2	-116.011102	-116.016101	1097
APUMP2	-116.008583	-116.016101	1650
PUMP2 ( <i>l</i> = 1) <sup>d</sup>	-115.360641	-116.019048	144469
PUMP2 ( <i>l</i> = 2)	-115.999185	-116.019017	4352
PUMP2 ( <i>l</i> = 3)	-116.015094	-116.019017	861
MRSDCI	-115.938403	-115.994575	1355
RMP4	-115.984004	*	*
UMP4	-116.057428	-116.061969	996
APUMP4	-116.055141	-116.061969	1499
PUMP4 ( <i>l</i> = 1) <sup>d</sup>	-115.406948	-116.063810	144130
PUMP4 ( <i>l</i> = 2)	-116.045485	-116.063782	4015
PUMP4 ( <i>l</i> = 3)	-116.061418	-116.063782	519
MRSDCI <sup>e</sup>	-115.969039	-115.975804	1485
RHF CCD	-115.978510	*	*
UHF CCD	-116.049360	-116.053758	965
APUCCD	-116.047115	-116.053758	1452
RHF CCDST4	-115.994211	*	*
UHF CCDST4	-116.060536	-116.064864	950
APUHF CCDST4	-116.058356	-116.064864	1429
RHF QCISD	-115.982453	*	*
UHF QCISD	-116.053440	-116.057786	954
APUHF QCISD	-116.051251	-116.057786	1435
RHF QCISD(T)	-115.994910	*	*
UHF QCISD(T)	-116.061562	-116.065875	946
APUHF QCISD(T)	-116.059390	-116.065875	1424

<sup>a</sup> At the optimized geometry for quintet state.<sup>b</sup> 6-31G\* basis set<sup>c</sup>  $\Delta E = E(\text{LS}) - E(\text{HS})$ .<sup>d</sup> \* of spin projection.<sup>e</sup> \* Davidson correction.

the energy gaps, as compared with those of QCISD and MR SD CI, because of the multiple bond splittings. The triple projection, PUMP<sub>*n*</sub> (*l* = 3), rather underestimates the energy gaps because of the overstabilization of the LS state.

From these conclusions, the LS-HS energy gaps by the UHF-based post HF methods (for example, UHF QCISD) followed by the approximate spin projection are almost

equivalent to those of the spin-restricted post HF methods such as MR SD CI// CASSCF. Judging from the numerical data in Table II, the APUMP2 method is practically useful for semiquantitative calculations of the LS-HS gaps [ $J_{ab}$  in Eq. (21b)] in larger systems.

### Chromium-Methylene Complex

Carter and Goddard [33] have shown that the high-spin ( $^6B_1$ ) state of the chromium-methylene ion 3 is calculated to be more stable than the low-spin ( $^4B_1$ ) state when the open-shell RHF method is employed. Their perfect-pairing (PP) generalized valence bond (GVB) calculations have also failed to reproduce the greater stability of the  $^4B_1$  state. Thus, the nature of the naked chromium-methylene bond appears to be much different from that of the corresponding carbene complexes  $(CO)_5Cr = CXX'$  satisfying the 18-electron rule, for which the closed-shell RHF description is reasonable. In other words, the  $\sigma$ - and  $\pi$ -bonds between  $Cr^+$  and  $^3CH_2(^3B_1)$  in the  $^4B_1$  state are not so strong as described by the closed-shell bonding pairs [33], showing the triplet-type instability [1].

The highest-spin (HS) UHF solution for the  $^8B_1$  state is given by the bonding and antibonding  $\sigma$  and  $\pi$  natural orbitals (NOS) as

$$\Psi(^8B_1) = |K\varphi_\sigma\varphi_{\sigma^*}\varphi_\pi\varphi_{\pi^*}|, \quad (22)$$

where  $K$  denotes the high-spin d-electron part ( $dx^2 - y^2 dx^2 - y^2 dxy$ ). The spin-polarized corresponding  $\sigma$ - and  $\pi$ -orbitals are given by the orbital mixings as

$$\chi_\sigma = \cos \omega \varphi_\sigma + \sin \omega \varphi_{\sigma^*}, \quad \eta_\sigma = \cos \omega \varphi_\sigma - \sin \omega \varphi_{\sigma^*}, \quad (6e)$$

$$\chi_\pi = \cos \omega \varphi_\pi + \sin \omega \varphi_{\pi^*}, \quad \eta_\pi = \cos \omega \varphi_\pi - \sin \omega \varphi_{\pi^*}. \quad (6f)$$

The intermediate ( $^6B_1$ ) and lowest-spin ( $^4B_1$ ) UHF solutions are therefore given by

$$\Psi(^6B_1) = |K\chi_\sigma\bar{\eta}_\sigma\varphi_\pi\varphi_{\pi^*}|, \quad \Psi(^4B_1) = |K\chi_\sigma\bar{\eta}_\sigma\chi_\pi\bar{\eta}_\pi|. \quad (23)$$

These UHF solutions were obtained by the use of the basis sets: Tatewaki-Huzinaga MIDI-1 supplemented by the 4p-AO with the same exponent as that for the 4s-AO and by the Hay's diffuse d-orbital ( $\alpha = 0.0912$ ) for Cr and MIDI-1 plus diffuse orbital for C and 4-31G for H. The orbital overlap  $T_\sigma$  for the  $\sigma$ -corresponding MOs in the  $^4B_1$  state is 0.952, whereas it is 0.302 for the  $\pi$ -corresponding MOs; note that  $T_\pi$  is 0.342 by GVB PP. The  $\sigma$ -bond is regarded as a stable covalent bond. On the other hand, the  $\pi$ -bond is a diradical pair with the moderate diradical character (45%). The  $^4B_1$  state is calculated to be more stable by 15.1 kcal/mol than the  $^6B_1$  state even at the UHF level, in contrast to the GVB PP result [34]. The  $^4B_1$ - $^6B_1$  energy gap becomes 19.0 kcal/mol after the approximate spin projection (APUHF) by the use of the  $^8B_1$  UHF energy. The latter value is in accord with the MCSCF value (17.7 kcal/mol) [35].

Figure 2(C) illustrates the energy optimized geometry of  $(CrCH_2)^+$  by UMP4. The binding energy between  $Cr^+$  and  $^3CH_2$  has been calculated by the UHF-based post HF methods by adding the  $f$  ( $\alpha = 0.9$ ),  $d$  ( $\alpha = 0.6$ ), and  $p$  ( $\alpha = 0.164$ ) polarization functions for Cr, C, and H, respectively. Table III summarizes the



TABLE III. Total energies of chromium-methylene cation and methylene and binding energy between chromium cation and triplet methylene by post-Hartree-Fock methods.

Method	(CrCH <sub>2</sub> ) <sup>+</sup>	CH <sub>2</sub>	BE <sup>a</sup> (kcal/mol)
UHF	-1081.590694	-38.732592	10.8
APUHF	-1081.596224	-38.732592	14.3
PUHF ( <i>l</i> = 1)	-1081.588557	-38.735148	7.89
PUHF ( <i>l</i> = 2)	-1081.588764	-38.735143	8.02
PUHF ( <i>l</i> = 3)	-1081.588754	-38.735143	8.02
PUHF ( <i>l</i> = 4)	-1081.588754	-38.735143	8.02
UNOCAS {7,7}	-1081.614535	-38.735148	25.8
UMP2	-1081.783325	-38.822338	36.6
APUMP2	-1081.791261	-38.822338	44.6
PUMP2 ( <i>l</i> = 1)	-1081.781178	-38.823986	34.2
PUMP2 ( <i>l</i> = 2)	-1081.781385	-38.823981	34.4
PUMP2 ( <i>l</i> = 3)	-1081.781375	-38.823981	34.3
PUMP2 ( <i>l</i> = 4)	-1081.781375	-38.823981	34.3
UMP4	-1081.811054	-38.838798	39.5
APUMP4	-1081.819342	-38.838798	44.7
PUMP4 ( <i>l</i> = 1)	-1081.808911	-38.839782	37.6
PUMP4 ( <i>l</i> = 2)	-1081.809118	-38.839777	37.7
PUMP4 ( <i>l</i> = 3)	-1081.809107	-38.839777	37.7
PUMP4 ( <i>l</i> = 4)	-1081.809107	-38.839777	37.7
UHF CCSD	-1081.814276	-38.838552	42.3
APUHF CCSD	-1081.822728	-38.838552	47.6
UHF QCISD	-1081.817769	-38.838585	44.3
APUHF QCISD	-1081.826810	-38.838585	50.0
CCSD(T)	-1081.823399	-38.839856	46.5
APUHF CCSD(T)	-1081.832696	-38.839856	52.4
UHF QCISD(T)	-1081.825574	-38.839871	47.8
APUHF QCISD(T)	-1081.835054	-38.839871	53.8

<sup>a</sup> Binding energy.

total energies of the chromium-methylene cation and triplet methylene and the calculated binding energies.

From Table III, the following conclusions may be drawn: (1) The binding energies (BEs) are 11 and 14 kcal/mol by UHF and APUHF, respectively, whereas it is 26 kcal/mol by UNO-CASSCF {7,7}. (2) The  $\langle S^2 \rangle$ -values for the quartet UHF-based wavefunctions are about 4.7, being larger than the exact value (3.75). (3) The BE-values are 37 and 40 kcal/mol by UMP2 and UMP4, respectively. The binding energy is 45 kcal/mol by APUMP4, indicating that the spin projection effect is significant, as expected from the  $\langle S^2 \rangle$ -value. (4) The BE-values are 47 and 48 kcal/mol by UHF CCSD(T) and QCISD(T), respectively. After the approximate spin projection, they are 52 and 54 kcal/mol, respectively.

The binding energy by APUMP4 is similar to the GVB CI value (44 kcal/mol) [33]. The BE-value by APUHF QCISD(T) is close to the experimental value (53.6

kcal/mol) by Armentrout et al. [36]. The present result indicates the importance of both dynamical correlation and spin-projection corrections for unstable  $d\pi-p\pi$  bonds.

### Concluding Remarks

The spin projection is necessary for UHF-based post Hartree-Fock wavefunctions [37] if systems under consideration have unstable chemical bonds with significant diradical and polyradical characters. The approximately spin-projected UHF (APUHF) QCISD(T) and CCSD(T) methods are applicable to qualitative computations of the LS-HS energy gaps in exchange-coupled open-shell systems and naked transition-metal carbon bonds. The APUHF MP2 (APUMP2) method is useful for qualitative purpose [11]. The UNO-CASSCF method is applicable to rather complex systems such as organo transition-metal systems.

The UHF-based post HF methods are particularly useful for theoretical investigations of exchange-coupled organic systems such as clusters of triplet carbenes [38], high-spin oligomers, clusters of stable nitroxides, etc., for which the spin polarization effects play important roles in spin alignments [39-42]. These systems are receiving current interest from the view point of molecular magnetism, for example, organic ferromagnet [43,44]. The present computational schemes are used for molecular design of organic magnetic materials [45].

### Acknowledgments

This work was carried out by the aid of a Grant-in-Aid for Scientific Research on Priority Area "Molecular Magnetism" (Area No. 228/04242104) from the Ministry of Education, Science and Culture and a Grant from the Inamori Foundation (Kyoto).

### Bibliography

- [1] K. Yamaguchi, in *Self-Consistent Field. Theory and Applications*, (K. Carbo and M. Klobukowski, Eds. (Elsevier, Amsterdam, 1990), p. 727.
- [2] K. P. Lawley, Ed., *Adv. Chem. Phys.* **67**, (1987) (Vols. I and II).
- [3] C. C. J. Roothaan, *Rev. Mod. Phys.* **23**, 69 (1951).
- [4] W. J. Hehre, L. Radom, P. v. R. Schleyer, and J. A. Pople, *Ab Initio Molecular Orbital Theory* (Wiley, New York, 1986).
- [5] K. Yamaguchi, *Chem. Phys. Lett.* **33**, 330 (1975); **35**, 230 (1975).
- [6] D. J. Thouless, *The Quantum Mechanics of Many-Body Systems* (Academic, New York, 1961).
- [7] J. Cizek and J. Paldus, *J. Chem. Phys.* **47**, 3976 (1967).
- [8] H. Fukutome, *Prog. Theoret. Phys.* **47**, 1156 (1972).
- [9] K. Yamaguchi, T. Fueno, and H. Fukutome, *Chem. Phys. Lett.* **22**, 466 (1973).
- [10] K. Yamaguchi et al., *Theoret. Chim. Acta* **73**, 337 (1988).
- [11] K. Yamaguchi, Y. Takahara, and T. Fueno, in *Applied Quantum Chemistry*, V. H. Smith et al., Eds. (Reidel, Dordrecht, 1986), p. 155.
- [12] H. B. Schlegel, *J. Chem. Phys.* **84**, 4530 (1986).
- [13] P. J. Knowles and N. C. Handy, *J. Chem. Phys.* **88**, 6991 (1988).
- [14] K. Yamaguchi, K. Ohta, S. Yabushita, and T. Fueno, *Chem. Phys. Lett.* **49**, 555 (1977).
- [15] K. Yamaguchi, *Int. J. Quant. Chem. Quantum Chem. Symp.* **14**, 269 (1980).

- [16] P. Pulay and T. P. Hamilton, *J. Chem. Phys.* **88**, 4926 (1988).
- [17] J. M. Bofill and P. Pulay, *J. Chem. Phys.* **90**, 3657 (1989).
- [18] A. T. Amos and G. G. Hall, *Proc. Roy. Soc. (London)* **A263**, 483 (1961).
- [19] K. Yamaguchi, K. Ohta, and T. Fueno, *Chem. Phys. Lett.* **50**, 266 (1977).
- [20] K. Rudenberg, L. M. Cheung, and S. T. Elbert, *Int. J. Quant. Chem.* **16**, 1069 (1979).
- [21] B. Roos, *Int. J. Quantum Chem. Quantum Chem. Symp.* **14**, 175 (1980).
- [22] K. Yamaguchi, *J. Mol. Struct. (Theochem)* **103**, 101 (1983).
- [23] K. Takatsuka, K. Yamaguchi, and T. Fueno, *Theoret. Chim. Acta* **48**, 175 (1978).
- [24] C. Møller and M. S. Plesset, *Phys. Rev.* **46**, 618 (1934).
- [25] J. A. Pople, M. Head-Gordon, and K. Raghavachan, *J. Chem. Phys.* **87**, 5968 (1987).
- [26] N. C. Handy, P. J. Knowles, and K. Somasundram, *Theoret. Chim. Acta* **68**, 87 (1985).
- [27] P. O. Lowdin, *Phys. Rev.* **97**, 1509 (1955).
- [28] K. Yamaguchi et al., *Chem. Phys. Lett.* **149**, 537 (1988).
- [29] K. Wolinski and P. Pulay, *J. Chem. Phys.* **90**, 36497 (1989).
- [30] K. Andersson et al., *J. Chem. Phys.* **96**, 1218 (1992).
- [31] C. W. Bauschlicher, Jr. and P. R. Taylor, *J. Chem. Phys.* **85**, 6510 (1986).
- [32] M. Okumura et al., *Mol. Cryst. Liq. Cryst.* **233**, 41 (1993).
- [33] Y. Takahara, K. Yamaguchi, and T. Fueno, *Chem. Phys. Lett.* **158**, 95 (1989).
- [34] E. A. Carter and W. A. Goddard, *J. Phys. Chem.* **88**, 1485 (1984).
- [35] A. E. Alvarado-Swaisgood, J. Allison, and J. F. Harrison, *J. Phys. Chem.* **89**, 2517 (1985).
- [36] P. B. Armentrout, L. S. Sunderlin, and E. R. Fisher, *Inorg. Chem.* **28**, 4437 (1989).
- [37] M. Frish et al., GAUSSIAN 92 series, Carnegie-Mellon Quantum Chemistry Publishing Unit: Carnegie-Melon University, Pittsburgh, PA 15213.
- [38] K. Yamaguchi, Y. Toyoda, and T. Fueno, *Chem. Phys. Lett.* **159**, 459 (1989).
- [39] K. Yamaguchi, H. Fukui, and T. Fueno, *Chem. Lett.* 625 (1986).
- [40] K. Yamaguchi, H. Namimoto, and T. Fueno, *Mol. Cryst. Liq. Cryst.* **176**, 151 (1989).
- [41] K. Yamaguchi, *Int. J. Quant. Chem.* **37**, 167 (1990).
- [42] K. Yamaguchi et al., *Chem. Phys. Lett.* **190**, 459 (1992); **191**, 237 (1992).
- [43] K. Awaga and Y. Maruyama, *Chem. Phys. Lett.* **158**, 556 (1989).
- [44] M. Kinoshita et al., *Chem. Lett.*, 1225 (1991).
- [45] J. S. Miller et al., *Mol. Cryst. Liq. Cryst.* **176** (1989).

Received July 8, 1993

# Quantum Wavepacket Dynamics for the $^1\Sigma^+$ States of Boron Hydride

J. BROECKHOVE, B. FEYEN,\* and P. VAN LEUVEN

*Universitair Centrum Antwerpen (RUC), Department of Mathematics and Computer Sciences,  
Groenenborgerlaan 171, B2020 Antwerpen, Belgium*

R. CIMIRAGLIA and M. PERSICO

*Istituto di Chimica Fisica dell'Università di Pisa, 56100 Pisa, Italy*

## Abstract

We investigate the intramolecular dynamics of the ground state and the first three singlet  $^1\Sigma^+$  excited states of boron hydride (BH) using the split-operator method. *Ab initio* calculations show that these states have strong nonadiabatic couplings, resulting in a complex topology of avoided crossing regions and double well potentials. We attempt to find a method to populate the second minimum of  $B\ ^1\Sigma^+$  enabling experimental observation of its vibrational states. © 1993 John Wiley & Sons, Inc.

## Introduction

The first four  $^1\Sigma^+$  states of BH have been studied spectroscopically by various authors [1]. For each of the states, at least one vibrational level has been observed. There are several *ab initio* studies of BH [2]. These *ab initio* calculations show that the  $B\ ^1\Sigma^+$  potential curve has a double minimum. The vibrational levels which are localized in the outer minimum, however, have not yet been observed experimentally. In this contribution we are looking for a method to populate vibrational levels in the second minimum of the  $B\ ^1\Sigma^+$  state. The frequencies associated with transitions from these states are sufficiently different from those originating from the inner minimum that they can be easily discriminated.

The next section presents the FFT split-operator method and the Hamiltonian used in our calculations. In the third section, we give short description of the electronic states involved and the method used to calculate them. We will discuss our results in the fourth section. It appears that a direct excitation process cannot create the required population of the outer minimum. The procedure we investigate consists of three steps. In the first one we create an electronic excitation. The fifth section contains the conclusions to be drawn from this contribution.

## Time Propagation

We consider a one-dimensional model for BH, neglecting effects of rotation. Four electronic states of the diatom are included: the  $X\ ^1\Sigma^+$  electronic ground state

---

\* Research associate IIKW, Belgium.

and three (closely) coupled excited electronic states,  $B^1\Sigma^+$ ,  $C^1\Sigma^+$ , and  $E^1\Sigma^+$  in order of increasing dissociation energy. We study the interaction of the vibronic degrees of freedom BH with an ultraviolet laser and a strong infrared laser (applied both separately and simultaneously). In what follows, we will use atomic units unless stated explicitly.

The time evolution associated with the nuclear motion is obtained as a solution of the time-dependent Schrödinger equation (TDSE):

$$i \frac{\partial \Psi}{\partial t} = (\hat{T}_N + \hat{H}_{el} + \hat{H}_{int}) \Psi, \quad (1)$$

where  $\Psi$  is a four-component wave function, one for each of the four electronic states mentioned above,

$$\Psi(\mathbf{X}, R, t) = \sum_{i=1}^4 \psi_i(R, t) \eta_i(\mathbf{X}; R). \quad (2)$$

Each  $\Psi_i$  represents the nuclear motion on the associated electronic potential. Projecting on the electronic states  $\eta_i$  leads to the set of four coupled equations

$$i \frac{\partial}{\partial t} \psi_i = \sum_j (\hat{H}_{ij} + \hat{\mu}_{ij} E a(t) \cos(\omega t)) \psi_j, \quad (3)$$

where  $\mathbf{X}$  represents all the electronic coordinates and  $R$  is the internuclear distance. The different matrix elements are given by

$$\hat{H}_{ii} \left( R, \frac{\partial}{\partial R} \right) = -\frac{1}{2m} \frac{\partial^2}{\partial R^2} + U_{ii}(R) + g_{ii}(R), \quad (4)$$

$$\hat{H}_{ij} \left( R, \frac{\partial}{\partial R} \right) = U_{ij}(R) + 2f_{ij}(R) \frac{\partial}{\partial R} + g_{ij}(R), \quad (5)$$

$$\hat{H}_{ij} = \hat{H}_{ji}, \quad (6)$$

The various potentials and coupling are given by the formulae

$$g_{ij}(R) = (1/2m) \langle \eta_i(R) | \partial^2 / \partial R^2 | \eta_j(R) \rangle_{\mathbf{X}}, \quad (7)$$

$$f_{ij}(R) = (1/2m) \langle \eta_i(R) | \partial / \partial R | \eta_j(R) \rangle_{\mathbf{X}}, \quad (8)$$

$$U_{ij}(R) = \langle \eta_i(R) | \hat{H}_{el} | \eta_j(R) \rangle_{\mathbf{X}}, \quad (9)$$

with  $m$  the reduced mass of the molecule and  $\mu_{ij}$  the matrix elements of the dipole operator.  $\langle \rangle_{\mathbf{X}}$  means integration over  $\mathbf{X}$ .

The equation will be solved numerically on a one-dimensional grid with the initial condition that one component  $\psi_i$  is an adiabatic vibrational state  $\chi'_i$  and the other components are zero. The vibrational eigenstates are obtained using a shooting method [3] based on the Numerov algorithm.

The propagation is done using the FFT split-operator method (for comparison with other methods, see Refs. [4]). The key concept in the split-operator technique

is to approximate the evolution operator over a small time interval as a product of exponentials

$$U(t, t + \epsilon) = T \exp\left(-i \int_t^{t+\epsilon} H(s) ds\right) \quad (10)$$

$$\approx \exp\left(-i \frac{\epsilon}{2} T\right) \exp\left(-i \int_{t-1}^t ds V(s)\right) \exp\left(-i \frac{\epsilon}{2} T\right), \quad (11)$$

which is correct up to second order in  $\epsilon$  [5]. This way, one can use a different electronic basis set for the kinetic energy operator and the potential energy operator, each one optimal for the exponentiation of the respective operator. While for the case of two electronic states special formulae exist [6,7], the exponentiation of the matrix operators in general is most effectively done by straightforward diagonalization [8,9].

The Born–Oppenheimer or adiabatic basis is the most natural to use. However, the nonvanishing derivative coupling terms  $f_{ij}$  inhibit exponentiation since there is no transformation on nuclear coordinates which can diagonalize a matrix containing these terms. It is also known that the functions  $g_{ij}$  and  $f_{ij}$  are sharply peaked when evaluated in the Born–Oppenheimer basis. In order to correctly represent them, one either has to use very dense or nonequidistant grids. Neither of both alternatives is computationally efficient [10]. To solve these problems, one can introduce an alternative set of electronic functions, a so-called diabatic basis. In this basis, the multiplicative coupling functions vary smoothly with  $R$  and the derivative couplings are negligible. Without the derivative couplings, the kinetic energy operator can be exponentiated by Fourier transformation to the momentum representation where it becomes a multiplicative operator. In our calculations we use the quasidiabatic basis as defined by Cimraglia et al. [11,12].

### The BH Potentials

The calculations in this paper are performed using *ab initio* potentials. Other authors have used *ab initio* potentials, e.g., to study the dissociation dynamics of CINO [13], FNO [14,15], and H<sub>2</sub>O [16]. The potentials, coupling functions and dipole moments, were described in Ref. [12]. As can be seen in Figure 1, the first excited state appears to have a double minimum. It dissociates into B(<sup>2</sup>S, 3s) and H(<sup>2</sup>S) but acquires a strong ionic character in the outermost well. The second excited state exhibits an avoided crossing and a double minimum. It dissociates into B(<sup>2</sup>D, 2s2p<sup>2</sup>) and H(<sup>2</sup>S). In the outer minimum its character is a mixture of B<sup>+</sup>H<sup>-</sup> and B(<sup>2</sup>P, 3p) while in the interior region it has the same character as in the dissociation region. The third excited state undergoes two avoided crossings, one with the ionic state and one with the B(<sup>2</sup>P, 3p) state.

As mentioned in the previous section, our calculations are performed in the quasidiabatic basis. The first step in the construction of this basis is the calculation of a zeroth order adiabatic basis. The adiabatic basis was obtained by a SCF-CI calculations at some 20 internuclear distances, starting from 1.2 a.u. A gaussian

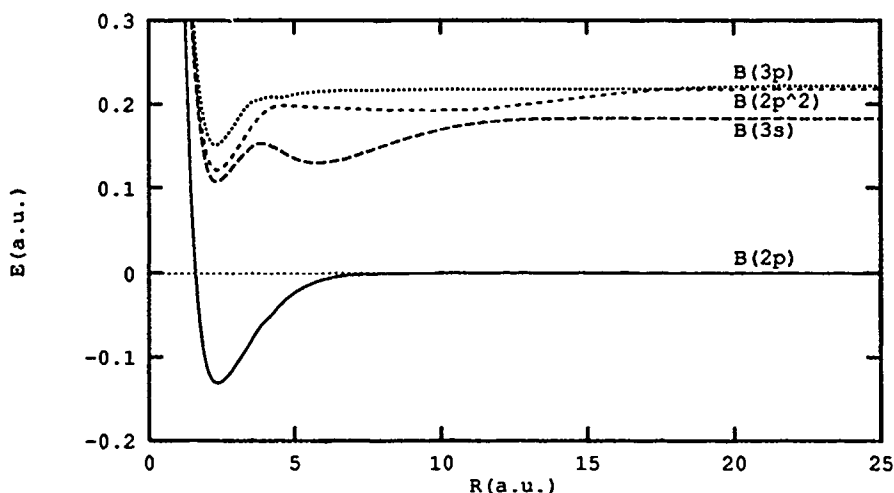


Figure 1. Adiabatic potentials for the first four  $1\Sigma^+$  states of BH. Values in atomic units.

atomic basis set was used, similar to that of Jaszunski et al. [17]. Some diffuse s and p functions were added to correctly represent higher Rydberg terms of the B atom and the  $H^-$  anion. Electron correlation was treated by the CIPSI multireference perturbation algorithm [18,19]. Spline interpolation was used to obtain the calculated functions at intermediate values of  $R$ . For further details we refer to Ref. [20]. The zeroth-order diabatic basis is obtained by unitary transformation. The transformation is such that it maximizes the overlap of the zeroth-order diabatic

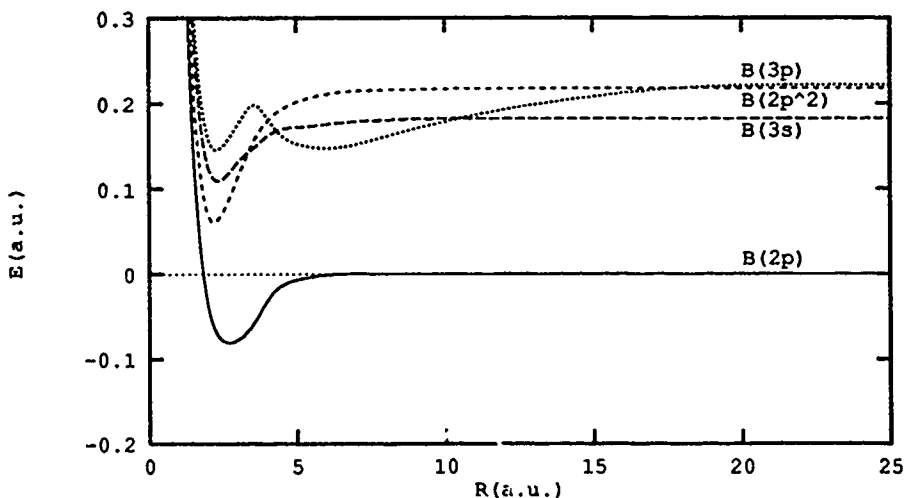


Figure 2. Diabatic potentials for the first four  $1\Sigma^+$  states of BH. Values in atomic units.

functions with a set of independent diabatic reference functions. Quasidegenerate perturbation theory is then applied to obtain the final diabatic basis set. For a detailed description we refer to Refs. [11,12].

In comparing Figures 1 and 2, respectively, one notices the rather large differences between adiabatic and diabatic potentials. The diabatic ground state minimum is less deep and less tight than the corresponding adiabatic one. The order of the second and the third state is interchanged between the two representations. The rather large interaction energies (Fig. 3), in particular  $h_{13}$ , are consistent with this.

The dipole moments  $\mu_{ii}$  and the dipole transition matrix elements  $\mu_{ij}$  are also *ab initio* results. The presence of the ionic contribution in the electronic wavefunction is clearly visible in these quantities. In the regions where the electronic states are characterized as ionic, the dipole moment is large and varies almost linearly with distance.

### Results and Discussion

In what follows, we investigate several possibilities to populate the second minimum of  $B^1\Sigma^+$  by combination of electromagnetic and nonadiabatic interactions. Experimentally the population of vibrational states in the outer well should be observable. We assume that the electric field is parallel to the molecular axis and that the electric dipole approximation is valid. Two types of fields are used throughout the calculations: monochromatic fields (instantaneously switched on) and gaussian pulses. The parameters of the field are chosen using physical arguments. We did not use any technique to optimise the field as, e.g., developed by Tannor and Rice [21,22] and also by Rabitz and coworkers [23-26].

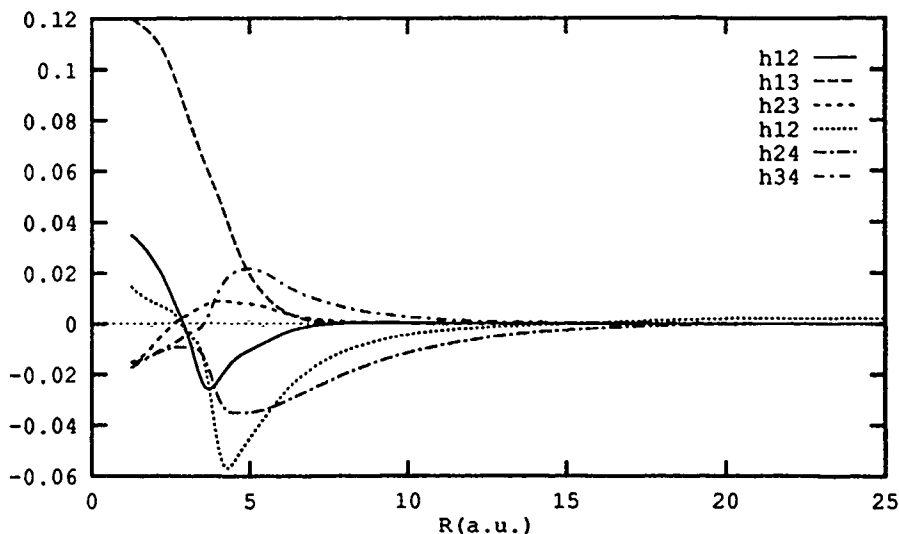


Figure 3. Off-diagonal matrix elements of the Hamiltonian in the diabatic basis. Values in atomic units.



It appears that one cannot directly excite a vibrational state of the outer minimum. The Franck-Condon factors are too small: there is no appreciable overlap between the respective wavefunctions due to the difference in position of the minima ( $R_{\text{inner}}^1 \approx 2.3$  a.u.,  $R_{\text{outer}}^2 \approx 5.8$  a.u.). Only the vibrational states of  $B^1\Sigma^+$ , which are significantly localized in the inner well, can be excited directly from the ground state. To create population in both wells, we will have to consider highly excited vibrational states of  $B^2\Sigma^+$ . The oscillator strengths  $f$  [27] of the corresponding transitions show, however, that these states are also not accessible by direct EM excitation from the vibronic ground state ( $f \approx 10^{-10}$ ).

An alternative pathway of occupying  $B^1\Sigma^+$  is through excitation to the other electronic states and subsequent nonadiabatic population transfer. From our calculations we see that excitations to vibrational states of  $C^1\Sigma^+$  are effective in populating  $B^1\Sigma^+$  appreciably, starting from  $\nu = 4$ . Again the oscillator strengths [27] do not permit direct transitions. They vary in magnitude from  $10^{-9}$  to  $10^{-5}$ . The only remaining possibility is an electronic excitation to  $E^1\Sigma^+$ . Oscillator strengths leave us no choice but to make a transition to the vibrational ground state ( $f \approx 10^{-2}$  for this transition). We performed a first calculation, modeling an instantaneous monochromatic transition from  $X^1\Sigma^+$  to  $E^1\Sigma^+$ , by taking  $\psi = (0, 0, 0, \chi_4^0)$  as initial condition. The calculation does not include an explicit interaction with an external field. Figure 4 shows the time evolution of the occupation probability of the electronic states. One can see that the maximum of  $P_2(t)$  is about 20% of the initial occupation probability of  $E^1\Sigma^+$ . It is also clear that there is a large recurrence of the system to its initial state after approximately 1 ps. To approach more realistic experimental conditions, which will use a pulsed laser to perform this excitation, we performed a second calculation. Here we used  $\psi = (\chi_1^0, 0, 0, 0)$  as an initial condition, and we included explicitly the interaction with the external

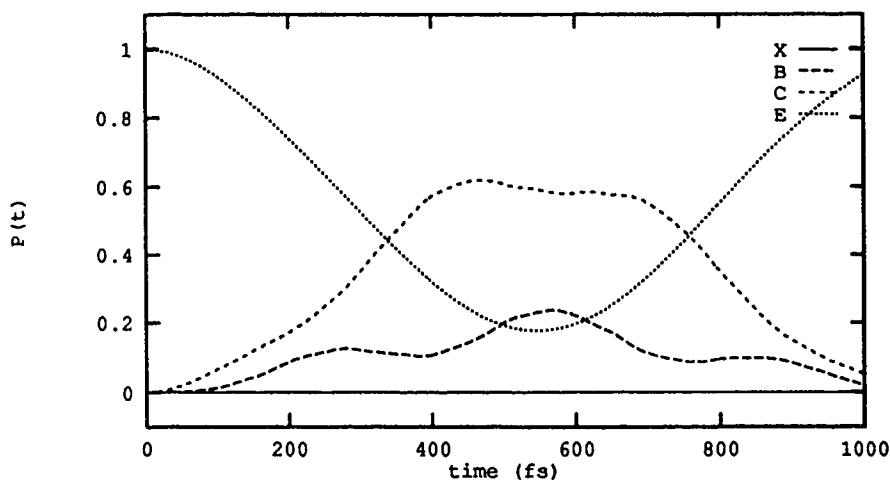


Figure 4. Occupation probability of electronic states as a function of time. No interaction with an external field.

field ( $\omega = 0.28$  a.u.). The pulse we use is a Gaussian with an FWHM of 50 fs and a peak intensity of  $0.4 \text{ GW/cm}^2$ . The pulse is centered at  $t = 100$  fs. Figure 5 shows the occupation probabilities of the electronic states as a function of time. Clearly the behavior is similar to the previous calculation, apart from a time delay and a scale factor reflecting the oscillator strength for the transition. Also  $P_4(t)$  starts from zero and grows to its maximum during the time the field is active instead of starting from its maximum value as in Figure 4. The order of magnitude of  $P_2$  ( $\approx 10^{-4}$ ) seems small but is nevertheless sufficient for spectroscopic purposes. So far, we only studied the time evolution of the total occupation probability of the electronic states. By projecting  $\psi_2(t)$  on the adiabatic vibrational states of  $B^1\Sigma^+$ , we learn that  $\psi_2 \approx \chi_2^{16}$ . The populations of the other vibrational states are at least 2 orders of magnitude smaller.  $\chi_2^{16}$  is not localized in one of the two wells exclusively. Our purpose is, however, to create a nonnegligible population of some vibrational states located in the outer well only.

Next we will investigate the adiabatic vibrational deexcitation of the  $B^1\Sigma^+$  state through an applied IR field. Collisional deexcitation is not a relevant process in view of the time scales involved. The highest vibrational state which is located clearly in the outer well is the  $\chi_2^{10}$  state. Transitions to this state create the required population. Therefore, we focus momentarily on  $\chi_2^{16}$  to optimize our field parameters. The selected transition can be induced with and without the use of intermediate levels. Also the number of intermediate levels can be varied: The transition frequency can be chosen to be resonant to a single photon transition ( $\Omega = E_{16} - E_{10}$ ) or to an  $n$ -photon process [ $\Omega = (E_{16} - E_{10})/n$ ]. Testing various possibilities, we found that the 2-photon process was more effective than the 3- or 6-photon process. This we investigated using monochromatic radiation. Figure 6 shows the evolution of the occupation probability of  $\chi_2^{16}$  and  $\chi_2^{10}$  under the application of a gaussian laser

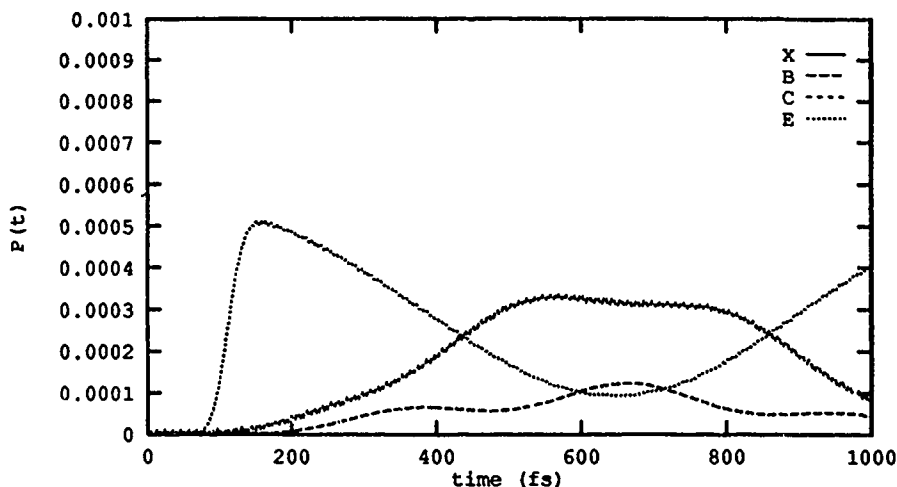


Figure 5. Occupation probability of electronic states as a function of time. Interaction with gaussian laser pulse.

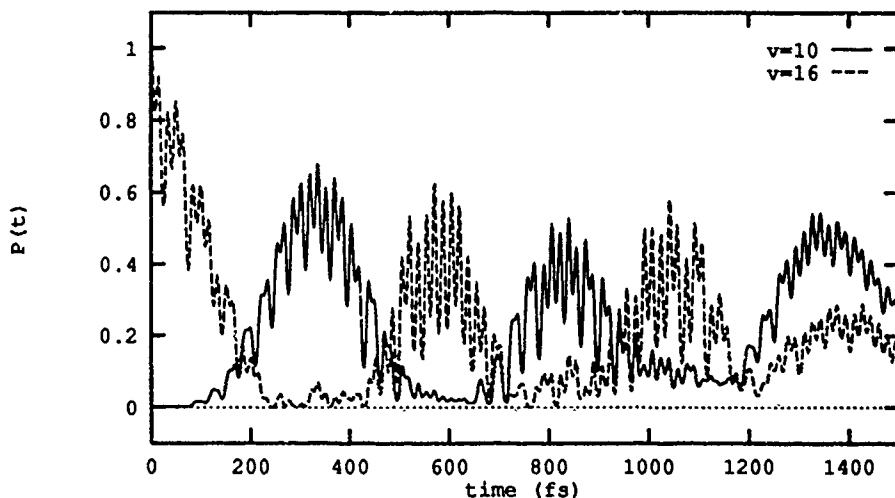


Figure 6. Time evolution of the occupation probabilities of vibrational states using a gaussian pulse.

pulse with an FWHM of 500 fs, a peak intensity of 40 GW/cm<sup>2</sup>, centered at  $t = 750$  fs. The main difference with the monochromatic results is a decrease of the maximum of the curve by about 10% and a decrease in the global period. The maximum in the curve still reaches about 70% of the initial occupation of  $\chi_2^{16}$ , which is sufficiently high for the purpose of observation.

Until now we have studied the effect of excitation, deexcitation and nonadiabatic coupling of the electronic states separately. Here we will present the results of a combined calculation. The initial condition is  $\psi = (\chi_1^0, 0, 0, 0)$ . We used two gaussian pulses. The UV pulse has the same characteristics as in the calculation presented previously. The IR deexcitation pulse ( $\omega = 0.0045$  a.u.) has an FWHM of 400 fs and is centered at  $t = 750$  fs. From Figure 7 we see that we have succeeded in populating  $\chi_2^{10}$  to  $\approx 10^{-5}$ . Moreover, we can see that after the IR pulse has died out, the population of  $\chi_2^{10}$  stays constant while the population of  $\chi_2^{16}$  starts to oscillate again due to the nonadiabatic interactions with the other electronic states. The population of  $\chi_2^{10}$  is 4% of the total population of the outer minimum on the average. The interaction with the IR field also causes the total population of the outer minimum to be increased by about a factor of 2 (Fig. 8), reaching a time averaged value of  $1.2 \times 10^{-4}$ . From these two facts we may conclude that it should be possible to observe the vibrational states of the second minimum experimentally.

### Conclusions

Using *ab initio* potentials, coupling functions and dipole functions we have examined the intramolecular dynamics BH of the first four  $^1\Sigma^+$  electronic states. Looking for a procedure to populate the second minimum of  $^1\Sigma^+$ , we found that

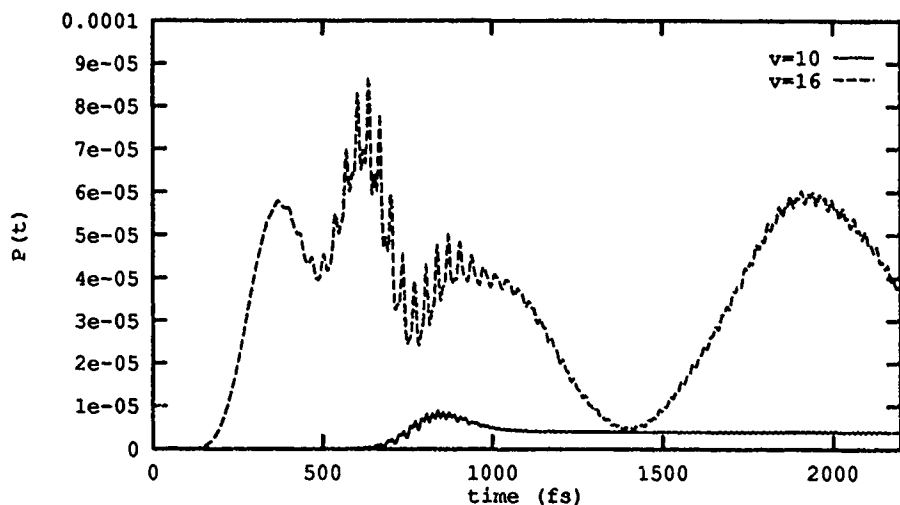


Figure 7. Time evolution of the occupation probabilities of vibrational states using a gaussian UV (excitation) pulse and a gaussian IR pulse (deexcitation).

it is not possible to perform a one-step excitation to the outer minimum. We proposed the following procedure: excitation by a UV laser pulse to the  $E {}^1\Sigma^+$  state. The nonadiabatic interactions cause the  $B {}^1\Sigma^+$  to be populated in a high vibrational state. The second step in our procedure is a vibrational deexcitation by an infrared laser pulse. We succeed in increasing the total population of the outer well and

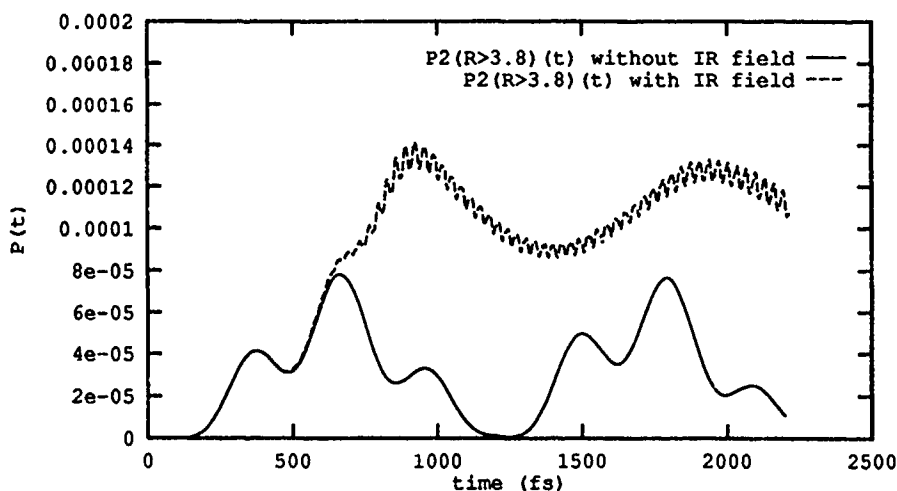


Figure 8. Time evolution of the occupation probabilities of the outer minimum using a gaussian UV (excitation) pulse with and without a gaussian IR pulse (deexcitation).

creating a stable population of vibrational states which are predominantly localized in it. From the results of the combined calculation, however, we can see that there is still much to be done on the optimisation of the parameters (e.g., width of the IR pulse, maximum intensities of and time delay between the pulses).

### Bibliography

- [1] S. Bauer, G. Herzberg, and W. C. Johns, *J. Mol. Spectrosc.* **13**, 256 (1964); W. C. Johns, F. A. Griem, and R. F. Porter, *J. Mol. Spectrosc.* **22**, 435 (1967); F. S. Pianalto, L. C. O'Brien, P. C. Keller, and P. F. Bernath, *J. Mol. Spectrosc.* **129**, 248 (1988).
- [2] J. C. Browne and E. M. Greenawalt, *Chem. Phys. Lett.* **7**, 363 (1970); P. K. Pearson, C. F. Bernder, and H. F. Shaefer, *J. Chem. Phys.* **55**, 5235 (1971); S. A. Houlden and I. G. Csizmadia, *Theor. Chim. Acta* **35**, 173 (1974); W. Meyer and P. Rosmus, *J. Chem. Phys.* **63**, 2356 (1975); M. Jaszunski, B. O. Roos, and P.-O. Widmark, *J. Chem. Phys.* **75**, 306 (1981); P. Botschwina, *Chem. Phys. Lett.* **129**, 279 (1986).
- [3] B. R. Johnson, *J. Chem. Phys.* **67**, 4086 (1977).
- [4] C. Leforestier, R. H. Bisseling, C. Cerjan, M. D. Feit, R. Friesner, A. Guldberg, H. Hammerich, G. Jolicard, W. Karlein, H. D. Meyer, N. Lipkin, O. Roncero, and R. Kosloff, *J. Comput. Phys.* **94**, 59 (1991).
- [5] J. A. Fleck, J. R. Morris, and M. D. Feit, *Appl. Phys.* **10**, 129 (1976).
- [6] J. Aivarillos and H. Metiu, *J. Chem. Phys.* **88**, 4957 (1988).
- [7] J. Broeckhove, B. Feyen, L. Lathouwers, F. Arickx, and P. Van Leuven, *Chem. Phys. Lett.* **174**, 504 (1990).
- [8] C. Moler and C. Van Loan, *SIAM Rev.* **20**, 801 (1978).
- [9] F. M. Hernandez and D. A. Micha, *J. Chem. Phys.* **97**, 8173 (1992).
- [10] I. Cacelli, *J. Chem. Phys.* **96**, 8439 (1992).
- [11] R. Cimiraglia, J.-P. Malrieu, M. Persico, and F. Spiegelmann, *J. Phys. B: At. Mol. Phys.* **18**, 3073 (1985).
- [12] R. Cimiraglia, in *Time-Dependent Quantum Molecular Dynamics*, Vol. 299 of Nato ASI Series and Series B: Physics, J. Broeckhove and L. Lathouwers, Eds (Plenum, New York, 1992), pp 11-26.
- [13] A. Veguri, A. Untch, and R. Schinke, *J. Chem. Phys.* **96**, 3688 (1992).
- [14] A. Ogai, J. Brandon, H. Reisler, H. U. Suter, J. R. Huber, M. v. Dirker, and R. Schinke, *J. Chem. Phys.* **96**, 6643 (1992).
- [15] H. U. Suter, J. R. Huber, M. v. Dirke, A. Untch, and R. Schinke, *J. Chem. Phys.* **96**, 6727 (1992).
- [16] J. Senson, R. Brudzynski, B. R. Hudson, J. Zhang, and D. G. Imre, *J. Chem. Phys.* **141**, 393 (1990).
- [17] M. Jaszunski, B. O. Roos, and P.-O. Widmark, *J. Chem. Phys.* **75**, 306 (1981).
- [18] B. Huron, J.-P. Malrieu, and P. Rancurel, *J. Chem. Phys.* **58**, 5745 (1973).
- [19] R. Cimiraglia and M. Persico, *J. Comput. Chem.* **39**, 39 (1987).
- [20] R. Cimiraglia, M. Persico, and F. Spiegelmann, to appear.
- [21] D. J. Tannor, R. Kosloff, and S. A. Rice, *J. Chem. Phys.* **85**, 5805 (1986).
- [22] R. Kosloff, S. A. Rice, P. Gaspard, S. Tersigni, and D. J. Tannor, *Chem. Phys.* **139**, 201 (1989).
- [23] R. S. Judson and H. Rabitz, *Phys. Rev. Lett.* **68**, 1500 (1992).
- [24] P. Gross, D. Neuhauser, and H. Rabitz, *J. Chem. Phys.* **96**, 2834 (1992).
- [25] S. Shi and H. Rabitz, *J. Chem. Phys.* **97**, 276 (1992).
- [26] G. B. Beumee and H. Rabitz, *J. Chem. Phys.* **97**, 1353 (1992).
- [27] M. Persico, private communication

Received May 13, 1993

# An Improved Eikonal Treatment of Rotationally Inelastic He—H<sub>2</sub> Scattering

JOEL M. COHEN\* and GEORGE R. FAMINI

*U.S. Army Chemical and Biological Defense Agency, SMCCR-RSP-C, Aberdeen, Maryland 21010*

## Abstract

A variation of the usual semiclassical short wavelength (eikonal) method was recently applied to model calculations of electronically diabatic atom-atom collisions. Microreversibility was computationally imposed on the dynamics by following trajectories initiating in the ground and excited states simultaneously. When improved transition probabilities for several two-state systems were obtained in this manner, a multistate application was selected. Self-consistent eikonal/averaged effective potential (SCE/AEP) state to state calculations are performed for rotationally inelastic HeH<sub>2</sub> scattering at total energies of .1 and .9 eV. using an (8,2) basis (7 states). Phase shifted amplitudes are introduced that add constraints to the coupled differential equations and reduce cpu time. Definite parity partial and total cross sections compare favorably to the previous semiclassical coupled states (SCS) results of Billing (1978) as well as to both the quantum ADP<sub>J<sub>z</sub></sub> and CC results of Shimon and Kouri (1977). © 1993 John Wiley & Sons, Inc.

## Introduction

For several decades the difficulty of applying purely quantum dynamical methods to all but a handful of chemical systems has inspired the development of various semiclassical and quasiclassical approaches [1]. Among the more serious semiclassical attempts is an eikonal formalism presented with some clarity by Michels in 1983 [2]. This method, with refinements, has been applied to polyatomic photodissociation [3], electronically diabatic gas-surface scattering with [4] and without [5] surface motion, rotationally and electronically inelastic scattering of NO from an Ag(111) surface [6], atom-atom elastic scattering angular distributions [7], and atom-atom collision electronic transitions [8].

Near quantitative agreement with formally exact methods was achieved in the electronically active atom-atom investigation by strictly imposing microreversibility on the semiclassical calculations. The improvement was initially demonstrated with three different electronically diabatic two-state models. It was accomplished by running the excitation and de-excitation calculations simultaneously along a near classical trajectory formed by combining the two processes. Because a major advantage of the eikonal method is that it can be extended without any fundamental changes to accommodate a theoretically unlimited number of degrees of freedom, the natural next step is to apply the improved version to generic multistate systems.

\* National Research Council Postdoctoral Associate.

A select case is rotationally inelastic atom-diatomic scattering. This is the simplest case where the matrix elements are well known [9], having been exactly derived from the laws of vector addition [10]. It has a further advantage that the energy levels are closely spaced, a condition generally favoring semiclassical treatments.

As far back as 1977 Billing performed similar calculations for He—H<sub>2</sub> at collision energies below the threshold for vibrational excitation [11]. His efforts even included an ad hoc means for dealing with microreversibility. The initial velocity was taken to be the mean of the velocities for the initial and final states. While this approach does not achieve genuine microreversibility as the forward and reverse probabilities are *not* identical, it does come close. It is highly effective and, along with related variations, has been found useful [12]. Using the same potential and general development as Billing allows us to directly compare results.

Billing endorsed what he called the semiclassical coupled states method (SCS) based on three assumptions:

- (i) decoupling of the rotational projection,  $m$ , states;
- (ii) classical treatment of translation;
- (iii) an effective potential and velocity is used.

The eikonal treatment presented here departs from these assumptions only in that it uses an improved effective potential and no effective velocity. The advantage is that microreversibility is precisely achieved while eliminating choices based on intuition. Also, the formalism is developed in a way that allows uniform application, avoiding the need for reinterpretation with each new problem.

Assumption (i) refers simply to the coupled states (CS) approximation itself. We do not take a position on that here, since the purpose is to explore an improved semiclassical approach to dynamics which could be applied in *either* a coupled states or close coupling (CC) context. The literature is replete with discussions of CS calculations [13]. While the savings in cpu time is expected to be less dramatic, some savings may be obtained by using a variable time step differential equation solver and semiclassical solutions in place of exact solutions in a CC calculation. This is left for future investigation.

Assumption (ii) is the minimalist semiclassical approximation. Quantization of translational motion is least likely to change the results in a practical sense. Eikonal treatments generally include this feature, as do most semiclassical methods.

Assumption (iii) considers two approximations, the effective potential and effective velocity. An effective potential is used to self-consistently couple quantum coefficients and the classical motion. This provides a method for step-wise generation of the coefficients from initial conditions and the progress of the modified (near-) classical trajectory that proceeds from the modified (effective) potential. While there may be some variation in the expressions used for the coefficients, and differences in the differential equations also may appear, the effective potential is seminal to both SCS and Self-Consistent Eikonal (SCE) calculations. The present work uses the recently developed averaged effective potential (AEP) in place of the usual effective potential (EP) used in SCE calculations.

The effective velocity is another matter. In the SCS approach, the initial velocity is chosen to be the average of the initial and final state velocities, which is imposed as an initial condition of the differential equations. In SCE calculations the initial potential energy subtracted from the total energy gives the initial kinetic energy, which has the initial velocity. No effective velocity is imposed.

This article is divided into seven sections. Following the introduction, the semiclassical formalism originally employed in Billing's work is presented and the CS equations and some simple insights are given. Eikonal formalism and the modifications to Billing's approach that were used in the present calculations are then discussed followed by parameters and various other details of the potential. Some results are shown and discussed, including alternative eikonal equations that reduce the consumption of cpu time. The final section presents conclusions, general discussion, and plans for future applications.

### Semiclassical Equations (Billing)

Following Billing [11], using assumptions (i), (ii), and (iii) gives the following set of equations for the amplitudes  $a_\alpha$

$$i\hbar \dot{a}_\alpha = \sum_{\alpha'} V_{\alpha\alpha'} \exp\left[\frac{i}{\hbar}(E_\alpha - E_{\alpha'})t\right] a_{\alpha'} \quad (2-1)$$

where  $E_\alpha$  represents the vibrational/rotational eigenstate, and  $\alpha$  is the collection of quantum numbers ( $v, j, m$ ).

The potential matrix elements are expressed

$$V_{\alpha\alpha'} = \left(\frac{2j'+1}{2j+1}\right)^{1/2} \sum_{i,k} \langle v|(r-\bar{r})^i|v'\rangle f_{ki}[R(t)] X \langle kj'00|j0\rangle \langle j'km'0|jm\rangle \quad (2-2)$$

where  $R$  is the  $A$  to  $BC$  (He to H<sub>2</sub>) separation,  $r$  the  $BC$  (H<sub>2</sub>) bond length, and  $\bar{r}$  the equilibrium value of  $r$ . The first bracket on the right describes vibrational transitions and the other two are Clebsh-Gordon coefficients, for rotations. The  $f_{ki}(R)$  were obtained by expanding the Krauss-Mies potential surface [14]:

$$V(R, r, \gamma) = \sum_{i,k} f_{ki}(R) (r-\bar{r})^i P_k(\cos \gamma) \quad (2-3)$$

where  $P_k$  is a Legendre polynomial and  $\gamma$  is the angle between  $R$  and  $r$ .

The effective potential combines transition amplitudes and potential elements:

$$V_{\text{eff}}(R, t) = \sum_{\alpha\alpha'} a_\alpha a_{\alpha'}^* V_{\alpha\alpha'} \exp\left[\frac{i}{\hbar}(E_\alpha - E_{\alpha'})t\right]. \quad (2-4)$$

Because  $V_{\alpha\alpha'} = V_{\alpha'\alpha}$ ,  $V_{\text{eff}}$  is real and determines the relative motion, where  $\mu$  is the reduced mass of  $A + BC$  (He + H<sub>2</sub>),  $P$  is the relative momentum,  $l$  is the orbital angular momentum quantum number and



$$\begin{aligned}\dot{R} &= \partial H_{\text{eff}} / \partial R = \mu^{-1} P, \\ \dot{P} &= -\partial H_{\text{eff}} / \partial R = -\frac{\partial V_{\text{eff}}}{\partial R} + \frac{\left(l + \frac{1}{2}\right)^2}{\mu R^3},\end{aligned}\quad (2-5)$$

$(l + 1/2)^2$  is the Langer modification for  $l(l+1)$  [15], and

$$\begin{aligned}H_{\text{eff}} &= \frac{P^2}{2\mu} + V_{\text{eff}}(R, t) \\ &= (1/2\mu)(P_R^2 + P_\theta^2) + V_{\text{eff}}(R, t),\end{aligned}$$

where

$$P_\theta^2 = \frac{\left(l + \frac{1}{2}\right)^2}{R^2}. \quad (2-6)$$

Billing uses an effective velocity ( $\bar{v}$ ) to determine the initial value of  $P$ ,

$$\begin{aligned}P(t_{\text{initial}}) &\approx P_R(t_{\text{initial}}) = \mu \bar{v}, \\ \bar{v} &= (2U/\mu)^{1/2},\end{aligned}$$

where

$$U = \frac{1}{4} \{ 2E - E_v - E_{v'} + 2[(E - E_v)(E - E_{v'})]^{1/2} \}. \quad (2-7)$$

This is the semiclassical approach presented by Billing for rotationally inelastic He—H<sub>2</sub> in 1977. In a 1976 article [16] he gave simpler expressions for the coefficient derivatives and effective potential that are consistent with those presented by this author. The more involved equations were probably developed for computational efficiency, which this author handles in a slightly different manner. The effective velocity does seem somewhat problematic. If there is to be an effective velocity there will be an effective energy ( $U$ ) of some sort so the first two lines in (2-7) follow naturally. The particular form given to  $U$  in the third line of (2-7) was determined in some sense by intuition. Under different circumstances one might devise a different choice for  $U$  that gave better results, leaving the overall concept less grounded in generality. Other effective velocity treatments have similar problems.

The notion, moreover, that microreversibility should lead to some kind of average velocity is genuinely insightful. The trajectory ought not only to commence with that description, but conclude that way as well. While this approach ensures that things start out right, there is nothing in the calculations design to *compel* average trajectory behavior at the detector. In spite of this, the amazing stability of these kinds of semiclassical calculations allows the effective velocity method to produce vastly more useful results than the entirely unmodified one. This is particularly

remarkable in light of the fact that the initial amplitudes are in no way adjusted to conform to the radically compromised initial velocity. The extended Hamilton-like equations [(2-1) and (2-5)] are symmetrically balanced so as to gravitate away from any strong deviations. In what follows, a very small number of additional modifications give a significantly enhanced account of semiclassical scattering.

### Coupled States Equations (ADP<sub>j<sub>z</sub></sub>)

One adaptation of the coupled states approach is the ADP<sub>j<sub>z</sub></sub> method of Shimoni and Kouri [17]. Each total angular momentum (*J*) cross section is taken as the sum of even and odd parity contributions,

$$\sigma^J(J \rightarrow j') = \sigma_{\text{even}}^J(j \rightarrow j') + \sigma_{\text{odd}}^J(j \rightarrow j'). \quad (3-1)$$

The even parity cross section is

$$\sigma_{\text{even}}^J = \frac{\pi(2J+1)}{k_{vj}^2(2j+1)} X \sum_{\lambda=0}^{j_m} \sum_{L=J-j_m}^{J+j_m} \frac{1}{j_m+1} |\delta_{\alpha\alpha'} - a_{\alpha\alpha'}|^2, \quad \Delta L = 2; \quad (3-2)$$

and the odd parity cross section is

$$\sigma_{\text{odd}}^J = \frac{\pi(2J+1)}{k_{vj}^2(2j+1)} X \sum_{\lambda=0}^{j_m} \sum_{L=J-j_m+1}^{J+j_m-1} \frac{1 - \delta_{\lambda,0}}{j_m} |\delta_{\alpha\alpha'} - a_{\alpha\alpha'}|^2, \quad \Delta L = 2. \quad (3-3)$$

where

$$k_{vj}^2 = \frac{2\mu}{\hbar^2} (E - E_{vj}), \quad j_m = \min(j, j'), \text{ and } j_M = \max(j, j').$$

While a thorough discussion of these equations would be quite lengthy, the general intent is readily encapsulated:

Parity is familiar from quantum mechanics. Transitions between parity states may or may not be allowed. It is useful therefore, in determining state-to-state cross sections, to take parity into account.

The square modulus of the amplitude,  $|\delta_{\alpha\alpha'} - a_{\alpha\alpha'}|^2$ , is the transition probability. Cross sections are intuitive physical representations of the likelihood of a transition. They are proportional to the probability.

The appearance of  $\pi$  results from integration over the azimuthal angle. Intuitively, the cross section is the area of a circle. That area is given by  $\pi$  times the square of the radius in which collisions are determined to have occurred.

Cross sections are inversely proportional to the square of initial relative momentum (in this case the wave number  $k_{vj}$ ). This is clear because the slower the projectile, the longer it spends in the interaction region, the greater the chance for the target to be influenced, and the larger the cross section. The converse applies to faster projectiles.

Each *J* state is  $(2J+1)$  degenerate. Each of these degenerate states has the same energy, but may have a different orientation (spatial representation) and/or com-

bination of orbital ( $l$ ) and rotational ( $j$ ) components from the rest. The factor  $(2J + 1)$  is included to weight the cross sections accordingly.

The precise mathematics that places  $(2j + 1)$  in the denominator is beyond the scope of this discussion, but the idea is to keep from over counting the  $j$  degeneracy. Remember,  $J$  and  $j$  are related, each  $j$  state leads to a different  $J$  state, so the  $j$  states are already included once in the  $J$  states. Some of them explicitly reappear in the sum over  $\lambda$  (degenerate  $j$  states are  $m$  states;  $m$  states contributing to the CS representation are labeled  $\lambda$ ). The  $j$  (and  $j'$ ) degeneracy is also taken into account in the expression for  $V_{\alpha\alpha'}$  [eq. (2-2)]. Apparently if not placed in the denominator, it would appear once too often.

The sum over  $\lambda$  relates directly to the coupled states approximation. In close coupling calculations all possible  $m \rightarrow m'$  transitions are explicitly taken into account. This means that different solutions are required for every set of  $(m, m')$  quantum numbers, all  $(2j_{\max} + 1)^2/2$  of them [18]!  $j \rightarrow j'$  cross sections are obtained by adding over all of these  $m \rightarrow m'$  contributions. The coupled states approach postulates that the details of the  $m \rightarrow m'$  transitions are relatively unimportant in looking at  $j \rightarrow j'$  transitions. Setting the total magnetic quantum number to zero,  $M = m + m' = 0$ , decouples the  $m$  states and eliminates these details. Nullifying  $M$  means that  $m = -m'$  and by convention  $\lambda = |m| = |m'|$ . There are only  $(2j_{\max} + 1)/2$  values of  $\lambda$  and only that many solutions are used (recall that  $V_{\alpha\alpha'} = V_{\alpha'\alpha}$ ). When CS calculations are appropriate they save tremendous amounts of computer time.

The sum over alternate values of  $L$  amounts to a pre-averaging or smoothing technique. Before it was developed individual transition probabilities were directly summed over  $\lambda$ . The problem was that these tended to vary irregularly leading to unstable results. For  $\sigma_{\text{even}}^J(\sigma_{\text{odd}}^J)$  there are  $j_M + 1$  ( $j_M$ ) values of  $L$  included in the  $\Delta L$  sum. Inclusion of the factor  $1/(j_M + 1)$  for even parity states and  $(1 - \delta)/j_M$  for odd parity states simply produces local (in  $L$  or  $J$ ) averages of subsets of probability elements. Taking an even parity example with, say,  $j_M = 5$  and  $J = 6$ , there is an average over 6 alternate probability elements ranging from  $L = 1$  to  $L = 11$  instead of the single  $L = 6$  element. After the summation over alternate values of  $L$  is performed, every entry presents an average rather than a single datum. This clearly does stabilize.

Finally, the identical coupled states equations are applied in either the exact or semiclassical context. If the amplitudes ( $a_{\alpha\alpha'}$ ) are obtained by exact methods one has the usual CS calculation; if they are obtained semiclassically one has an SCS calculation. That is the entire difference.

Virtually limitless volumes of scientific literature have been devoted to the coupled states approximation and its application. The interested reader is enthusiastically referred to these.†

### Eikonal Formalism

Integrating over the electronic variables leaves an  $R$ -dependent form of Schroedinger's equation,

† Kouri's chapter on approximate rotational methods, Ref. [18], lists 156 articles.

$$\left[ \frac{1}{2m} \left( \frac{\hbar}{i} \frac{\partial}{\partial R} \right)^2 + V(R) - E \right] \psi(R) = 0, \quad (4-1)$$

where  $V$  refers to the classical potential and  $R$  is the interparticle separation. The eikonal wave function is defined in two steps. First, separate  $\psi$  into exponential and pre-exponential factors,

$$\psi = \chi(R) \exp \left[ \frac{i}{\hbar} S(R) \right]. \quad (4-2)$$

Then associate  $S$  with the classical action,

$$S(R) = \int P(R) dR,$$

so

$$P = dS/dR. \quad (4-3)$$

Putting eqs. (4-2) and (4-3) in eq. (4-1) gives

$$\begin{aligned} & -\frac{\hbar^2}{2m} \frac{d^2 \chi}{dR^2} - i\hbar \frac{P}{m} \frac{d\chi}{dR} \\ & -i \frac{\hbar}{2m} \frac{dP}{dR} \chi + \frac{P^2}{2m} \chi + V\chi - E\chi = 0. \end{aligned} \quad (4-4)$$

A simplified form of this equation may be obtained by introducing diagonal matrices  $W(P, R)$  and  $K(R)$ :

$$W_{qu}(P, R) = V_{qu}(R) + iU(R) - K(R),$$

$$(K)_{\Gamma'\Gamma} = \delta_{\Gamma'\Gamma} \left( -\frac{\hbar^2}{2m} \right) \frac{d^2 \chi_{\Gamma}}{dR^2} \chi_{\Gamma},$$

$$U(R) = \frac{\hbar}{2m} \frac{dP}{dR}. \quad (4-5)$$

Equation (4-4) becomes

$$\left[ \frac{P}{m} \frac{\hbar}{i} \frac{d}{dR} + V(R) - W_{qu}(P, R) \right] \chi(R) = 0 \quad (4-6)$$

which is still exact.

The effective potential,  $V_{qu}(P, R)$ , is obtained exactly by left multiplying eq. (4-4) by  $\chi^+$ , adding the adjoint of the resulting expression to itself, and solving for  $E$ . Since  $E$  is the total energy and  $P^2/2m$  is the kinetic energy the remaining term is the effective potential:

$$E = \frac{P^2}{2m} + V_{qu}(P, R),$$

$$V_{qu}(P, R) = (\chi^+ \chi)^{-1} \left[ \chi^+ \mathbf{V} \chi + \frac{i\hbar}{2m} P \left( \frac{\partial \chi^+}{\partial R} \chi - \chi^+ \frac{\partial \chi}{\partial R} \right) - \frac{\hbar^2}{2m} \left( \frac{\partial^2 \chi^+}{\partial R^2} \chi + \chi^+ \frac{\partial^2 \chi}{\partial R^2} \right) \right]. \quad (4-7)$$

In practice one uses a short wavelength approximation. As the momentum increases at higher energies the wavelength, which is inversely proportional to the momentum, decreases and

$$|d^2\chi/dR^2| \ll |d\chi/dR(P/\hbar)| \ll |\chi(P/\hbar)^2|. \quad (4-8)$$

Applying these inequalities to eq. (4-6) gives

$$\left[ \frac{P}{m} \frac{\hbar}{i} \frac{d}{dR} + \mathbf{V}(R) - \mathbf{W}(R) \right] \chi(R) = 0.$$

$$\mathbf{W}(R) = V_q(R)1 + i\mathbf{U}(R),$$

$$V_q(R) = (\chi^+ \chi)^{-1} \chi^+ \mathbf{V}(R) \chi. \quad (4-9)$$

Since  $R = R(t)$  the function  $\chi(R)$  may be expressed as some function of time. The row matrix  $\mathbf{A}(t)$  is defined to satisfy

$$\chi[R(t)] = \mathbf{A}(t) e^{i/\hbar \int \mathbf{W}[R(t')] dt'}. \quad (4-10)$$

Also  $V(R) = V[R(t)]$ , so placing eq. (4-10) in eq. (4-9) gives

$$\left\{ \frac{\hbar}{i} \frac{d}{dt} + \mathbf{V}[R(t)] \right\} \mathbf{A}(t) = 0. \quad (4-11)$$

The initial value of  $A_j(t) = 1$  in the initial channel and zero in all others. Since  $V$  is Hermitian

$$d(\mathbf{A}^+ \mathbf{A})/dt = 0$$

and

$$\mathbf{A}^+ \mathbf{A} = 1 \quad (4-12)$$

at all times.  $\mathbf{A}$  is the general probability amplitude in the eikonal formalism. If  $\mathbf{V}$  corresponds to the rotationally inelastic potential, i.e.,

$$V_{ii} = V_{\alpha\alpha'} + \delta_{\alpha\alpha'} E_{\alpha}, \quad (4-13)$$

then  $\mathbf{A}$  corresponds to  $a$  from above [see eqs. (2-1) and (2-4)],

$$\mathbf{A} = \mathbf{a}, \quad (4-14)$$

so

$$i\hbar \dot{a}_\alpha = \sum_{\alpha'} (V_{\alpha\alpha'} + \delta_{\alpha\alpha'} E_\alpha) a_{\alpha'} . \quad (4-15)$$

Notice since

$$V_q = \frac{\chi^+ V \chi}{\chi^+ \chi} = \frac{\mathbf{A}^+ \mathbf{V} \mathbf{A}}{\mathbf{A}^+ \mathbf{A}} = \mathbf{A}^+ \mathbf{V} \mathbf{A} . \quad (4-16)$$

the effective potential for rotationally inelastic scattering becomes

$$V_{\text{eff}} = \sum_{\alpha\alpha'} a_\alpha^* V_{\alpha\alpha'} a_{\alpha'} . \quad (4-17)$$

These coefficient and effective potential equations, sans the complex exponential factors, conserve energy precisely and are more directly evaluated.

The discussion up to now concerned the SCE/EP formalism (Self-Consistent Eikonal/Effective Potential). The SCE/AEP equations (Self-Consistent Eikonal/Averaged Effective Potential) were developed to impose microreversibility on the calculations. To do this, the excitation and de-excitation calculations are combined. The potential governing this new calculation, the AEP, is the mean of the usual effective potential for the forward reaction and the usual effective potential for the reverse reaction at time  $t$ ,

$$\begin{aligned} \nu_{\alpha\alpha'} &= \frac{\mathbf{a}_{\alpha\alpha'}^+ \mathbf{V} \mathbf{a}_{\alpha\alpha'}}{\mathbf{a}_{\alpha\alpha'}^+ \mathbf{a}_{\alpha\alpha'}} ; \\ \nu_{\alpha'\alpha} &= \frac{\mathbf{a}_{\alpha'\alpha}^+ \mathbf{V} \mathbf{a}_{\alpha'\alpha}}{\mathbf{a}_{\alpha'\alpha}^+ \mathbf{a}_{\alpha'\alpha}} ; \\ \nu &= \frac{\nu_{\alpha\alpha'} + \nu_{\alpha'\alpha}}{2} \end{aligned} \quad (4-18)$$

Notice that there are now two complete sets of coefficients,  $a_{\alpha\alpha'}$  and  $a_{\alpha'\alpha}$ . One set starts with an amplitude of unity in the  $\alpha$  state and zero in all others while the other set starts with unity amplitude in the  $\alpha'$  state and zero in the rest. In the diabatic representation, where this work is done, the high symmetry of the SCE/AEP equations allows the calculations to be performed in about the same cpu time as SCE/EP calculations, despite the increased number of differential equations. The improved quality of results is remarkable. SCE/AEP calculations demonstrate semi-quantitative to quantitative agreement with calculations based on exact methods.

### The Potential

When Billing expanded the Krauss-Mies potential as in eq. (2-3), the following  $f_{ki}$ 's were obtained [11]:

$$\begin{aligned}
 f_{00} &= aCe^{-\alpha_0 R}, & f_{01} &= Ce^{-\alpha_0 R}(a\alpha_1 R - c), \\
 f_{21} &= Ce^{-\alpha_0 R}(ab\alpha_1 R + cd), & f_{20} &= abCe^{-\alpha_0 R}, \\
 f_{02} &= Ce^{-\alpha_0 R}\left(\frac{1}{2}\alpha_1^2 aR^2 - \alpha_1 cR\right), \\
 f_{22} &= Ce^{-\alpha_0 R}\left(\frac{1}{2}\alpha_1^2 abR^2 + \alpha_1 cdR\right).
 \end{aligned}$$

where

$$\begin{aligned}
 a &= 1.10041, & b &= 0.1825, & C &= 198.378 \text{ eV.}, \\
 c &= 0.9855 \text{ \AA}^{-1}, & d &= 0.27506, & \alpha_0 &= 3.518 \text{ \AA}^{-1},
 \end{aligned}$$

and

$$\alpha_1 = 1.145 \text{ \AA}^{-2}.$$

In general one might evaluate

$$E_{v,j} = \hbar\omega_e \left[ \left( v + \frac{1}{2} \right) - x_e \left( v + \frac{1}{2} \right)^2 \right] + E_j, \quad (5-1)$$

where  $\omega_e$  and  $\omega_e x_e$  are Morse parameters for the diatomic and  $E_j$  is the rotational state spacing. In the present work correct spectroscopic values were preferred [19].

Since collision energies were taken below the vibrational threshold (and also vibrational transitions were not considered) it was feasible to evaluate the vibrational factors,  $\langle v | (r - \bar{r})^i | v' \rangle$ , see eq. (2-2), within a rigid rotor approximation. This is the limit where vibrational and rotational motions are decoupled. Billing's hydrogen molecule values for the matrix elements defined [20]

$$\begin{aligned}
 M_{v'v}^{(i)} &= \int_{-\infty}^{\infty} \phi_v^0(u) \phi_{v'}^0(u) (u/\bar{r})^i du, \\
 u &= r - \bar{r},
 \end{aligned} \quad (5-2)$$

are given in Table I. The  $\phi_v^0$  are eigenfunctions in the vibrational equation

$$H_v \phi_v^0 = \left[ -\frac{\hbar^2}{2m} \frac{\partial^2}{\partial r^2} + v(r) \right] \phi_v^0 = E_v \phi_v^0 \quad (5-3)$$

TABLE I.  $M_{v'v}^{(i)}$  for  $H_2$  [19].

$v$	$v'$	$i = 0$	$i = 1$	$i = 2$
0	0	1.00	0.0304	0.0152
0	1	0.0	0.119	0.0122
1	1	1.00	0.0944	0.0527

where  $m$  is the reduced mass of H<sub>2</sub> and  $v(r)$  is the intramolecular (Morse H<sub>2</sub>) potential. The mathematics for evaluating  $M_{v'v}^{(i)}$  is described in Ref. [21]. It is helpful to keep in mind that the  $M_{v'v}^{(i)}$  need be multiplied by  $\bar{r}^i$  to recover the length in nonreduced units. In the vibrating rotor model the  $M_{v'v}^{(i)}$  represent unperturbed states which are subsequently modified with correction (perturbation) terms. This is necessary to describe vibrational transitions and some purely rotational transitions, exs., large basis set calculations, large  $\Delta j$ , collision energy above vibrational threshold.

Clebsh-Gordon coefficients convert to  $3j$  symbols,

$$\begin{pmatrix} j_1 & j_2 & J \\ m_1 & m_2 & M \end{pmatrix} = (-1)^{j_1-j_2-M} (2J+1)^{-1/2} \langle j_1 j_2 m_1 m_2 | J-M \rangle, \quad (5-4)$$

where  $M = m_1 + m_2$ . Subroutines for evaluating  $3j$  symbols are fairly common.

The potential elements are now

$$V_{\alpha\alpha'}(R) = (2j' + 1) \sum_{i,k} M_{v'v}^{(i)} \bar{r}^i f_{ki}(R) \\ X(-1)^\lambda \begin{pmatrix} j & k & j' \\ 0 & 0 & 0 \end{pmatrix} \begin{pmatrix} j & k & j' \\ -\lambda & 0 & \lambda \end{pmatrix}. \quad (5-5)$$

Figure 1 shows the diagonal elements,  $V_{\alpha\alpha} + E_\alpha$ , used in these HeH<sub>2</sub> calculations. For an (8,2) basis, that is,  $j$  equals 0, 2, 4, 6, and 8 in the ground vibrational state ( $v = 0$ ) and  $j$  equals 0 and 2 for the first excited vibrational state ( $v = 1$ ), there are seven diagonal elements. Quite noticeable is the near degeneracy of the ( $vj$ ) = 08 and 10 surfaces. This follows because the spectroscopic states are separated by only 8.3 cm<sup>-1</sup> (Table II).

Since coupling between rotational states disappears for  $|\Delta j| > 2$  the combination of diagonal and off-diagonal elements within a vibrational level form a tri-diagonal matrix. In addition there is nonzero coupling between both like and adjacent rotational states in different vibrational levels. Figure 2 shows, for example, nonzero coupling between the 02 state and the adjacent, 00 and 04, states and the 02 state and the vibrationally excited, 10 and 12, elements. For an (8,2) basis there are 22 off-diagonal nonzero potential elements. Of course, since  $V_{\alpha\alpha'} = V_{\alpha'\alpha}$ , only 11 of these are unique. There are 19 different potential elements for this particular basis, which happens to be quite small.

## Results

Rotationally inelastic SCE scattering calculations were performed on the HeH<sub>2</sub> system in the body fixed frame at total energies of .1 and .9 eV. (neglecting ground-state vibrational energy) using an (8,2) basis. The standard choice function  $\bar{l}(J, j) = J$  was used, as it was for the original semi-classical calculations performed by Billing [11]. The selection of choice function is a very intricate matter, but apparently within the ADP<sub>Jz</sub> formalism there is little effect other than a small shift of  $\sigma^J$  along the  $J$  axis. Since the purpose was to test the applicability of the SCE/



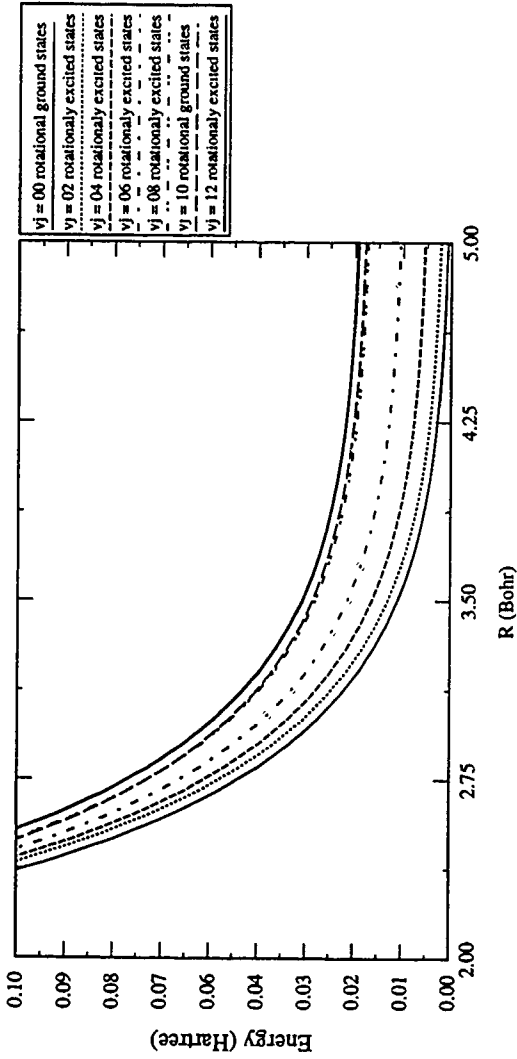


Figure 1. Diagonal He—H<sub>2</sub> potential elements,  $V_{aa} + E_a$ , for an (8,2) basis.

TABLE II. Molecular constants and vibrotational eigenstates of H<sub>2</sub> [19].

$m$ 0.504 a.u.		
$\bar{r}$ 0.7438 Å		
$\omega_e$ 4416.7 cm <sup>-1</sup>		
$\omega_e x_e$ 127.4 cm <sup>-1</sup>		
$v$	$J$	Spectroscopic states (cm <sup>-1</sup> )
0	0	2176.5
0	2	2530.9
0	4	3345.3
0	6	4591.4
0	8	6229.4
1	0	6337.7
1	2	6674.4

AEP method to rotationally inelastic collisions, previously developed parameters and constants were left unchanged.

An Adams–Basforth–Moulton predictor corrector type differential equation solver with documented reliability, DE [21], was used with both error parameters set to  $1 \times 10^{-9}$ . These could have been adjusted to as large as  $10^{-7}$  or  $10^{-6}$  without much effect, but these particular calculations are not very time consuming so extra care

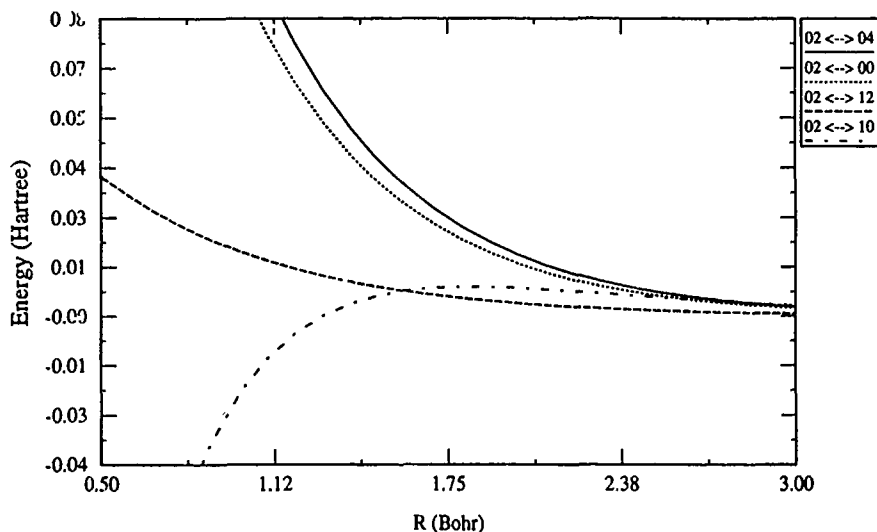


Figure 2. Off-diagonal He—H<sub>2</sub> potential elements,  $V_{aa}$ , for an (8,2) basis. Coupling to the 02 state.

could be afforded the testing stage. A micro-Vax II was selected because code development is more facile than with more massive computers and, again, the model calculations are abbreviated. Experience has enabled the addition of a number of nice touches to the code, but it has never been fully optimized. Future large-scale applications will necessitate optimization.

Interestingly, when the eikonal expressions for the time dependent amplitudes were developed, eqs. (4-15), removal of the exponentials [see eqs. (2-i)] amounted to a reduction in constraints on the differential equations, resulting in computations that require considerably more cpu time. More useful differential equations start with the eikonal expressions and define new amplitudes,  $c_\alpha$ ,

$$a_\alpha = c_\alpha e^{-i/h \int W_\alpha(R) dt},$$

where

$$W_\alpha(R) = V_{\alpha\alpha}(R) + E_\alpha. \quad (6-1)$$

Substituting for  $a_\alpha$  and solving for  $dc_\alpha/dt$  in eq. (4-15) gives

$$i\hbar \dot{c}_\alpha = \sum_{\alpha' \neq \alpha} V_{\alpha'\alpha} c_{\alpha'} e^{i/h \int (W_\alpha - W_{\alpha'}) dt} \quad (6-2)$$

One immediate difference is the elimination of the self-dependent terms, those in which the variation in  $c_\alpha$  depends on  $c_\alpha$ . Inclusion of these terms allows for more play in the differential equations. Apparently, false variation of the derivatives can be consistent with compensating false variations of entire sets of the self-dependent coefficients. Decreasing the step size eliminates the problem, but increases the cpu requirement. Of course additional differential equations are required for the action expressions,

$$\int (W_\alpha - W_{\alpha'}) dt = \int V_{\alpha\alpha} dt - \int V_{\alpha'\alpha'} dt + (E_\alpha - E_{\alpha'})t. \quad (6-3)$$

but even with these included, considerable computer time is saved (see Table III). Because

TABLE III. Integral cross sections at .9 eV.

$v_j \rightarrow v_{j'}$	Integral cross sections [11] (bohr <sup>2</sup> )				Relative cpu time SCE/AEP eqs	
	SCE/AEP	(SCS)	CC	ADPJ <sub>2</sub>	(6-2)	(4-15)
00 $\rightarrow$ 02	11.94	(12.35)	11.342	12.001	1.4	8.0
02 $\rightarrow$ 04	3.62	(3.75)	3.739	3.596	3.6	11.1
00 $\rightarrow$ 04	0.81	(0.83)	0.806	0.800	1.0*	2.8

\* 388 s actual cpu time on a VAX-3100 under VMS 5.2.

$$a_{\alpha}^* a_{\alpha} = c_{\alpha}^* e^{+i/h \int W_{\alpha}(R) dt} c_{\alpha} e^{-i/h \int W_{\alpha}(R) dt} = c_{\alpha}^* c_{\alpha}, \quad (6-4)$$

probabilities are not affected.

Although the numerical experiments performed by Billing were, by and large, reproduced here, nothing more than a platform for making reasonable comparisons was intended. Some of the constants and parameters used in the SCE code came from outside the body of the 1977 article; Billing undoubtedly carried a different number of significant figures in many cases; he solved his differential equations by different means; and finally, he used the SCS formalism. Our primary objective was (like his) favorable comparison with exact results. It is nevertheless comforting to see, in Figure 3, how well the first successful SCE/EP calculation of this study agreed with the unmodified SCS results. It is not possible to predict from this that the SCE and SCS results will always agree, but it is fair to say that the approach to the problem has been correctly translated to the eikonal formalism.

Figure 4 shows the same scattering event as Figure 3, but here SCE/AEP results are compared directly to exact ADP  $j_z$  and CC results. In a practical sense agreement between the three is quite good. Both the semiclassical and exact ADP  $j_z$  results are a trifle low at high  $J$  but this is expected. Before the ADP  $j_z$  method, CS calculations generally failed completely in this region. For  $j_{\min} = 0$  there is no odd parity contribution to the cross section, that is,  $\sigma = \sigma_{\text{even}}$  [see eq. (3-3)]. Figure 5 demonstrates, for  $j = 2 \rightarrow j' = 4$  at  $E = .9$  eV., the same quality agreement for an odd parity calculation as found in the even parity case in Figure 4. The middle curve in Figure 6 shows, for the same transition as in Figure 5, agreement between the SCE/AEP cross section summed over parity,  $\sigma = \sigma_{\text{even}} + \sigma_{\text{odd}}$ , and CC results [17]. Only a few points were tabulated in the literature, but those are convincing.

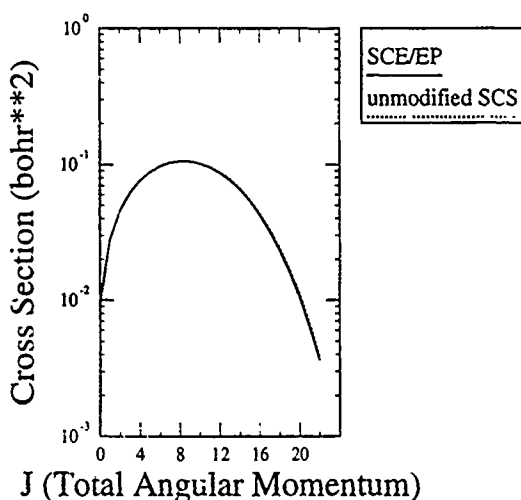


Figure 3  $\sigma'(0 \rightarrow 2)$  at  $E = .1$  eV

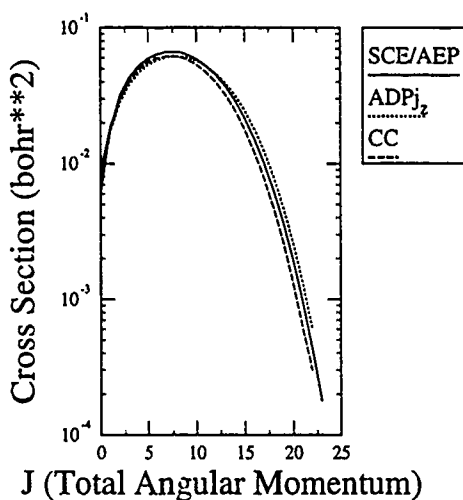
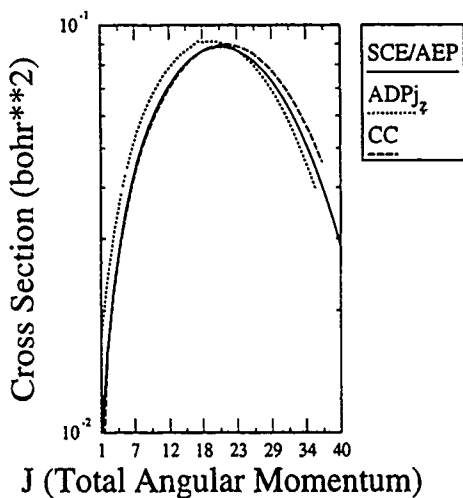
Figure 4.  $\sigma'(0 \rightarrow 2)$  at  $E = .1$  eV.

Figure 6 is interesting for two other reasons as well. First, Billing's article includes a similar figure, but for a series of SCS calculations. Because his results are not tabulated only a qualitative comparison of the two figures is possible. Even so, agreement between the sets of results is apparent. Second, the results themselves have informative trends. The middle curve is for the same magnitude transition as the upper curve,  $|j - j'| = 2$ , but initiates in an excited ( $j = 2$ ), rather than the

Figure 5.  $\sigma'_{\text{odd}}(2 \rightarrow 4)$  at  $E = .9$  eV.

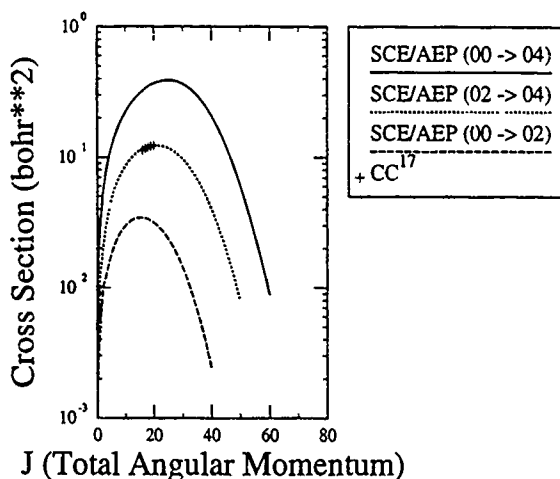


Figure 6.  $\sigma^J(0j \rightarrow 0j')$  at  $E = .9$  eV.

ground ( $j = 0$ ), state; hence the smaller cross section. The bottom curve initiates in the ground state but has a larger transition,  $\Delta j = 4$ ; it has the smallest cross section.

Table III presents further evidence of the effectiveness of the SCE/AEP calculations. It compares the areas under the curves in Figure 6, the total ( $\sigma$ ) as opposed to the partial ( $\sigma^J$ ) cross sections, with exact ADP $j_z$  and CC results. Agreement is more than satisfactory. The SCS results (shown in parenthesis) are also quite good.†

Columns 5 and 6 in Table III show the relative computer times required for the SCE/AEP calculations performed using eqs. (6-2) and (4-15), respectively. As discussed above, calculations from eqs. (6-2) are considerably faster. The  $00 \rightarrow 02$  calculation takes longer than the  $00 \rightarrow 04$  calculation because it is carried to higher  $J$ . The  $02 \rightarrow 04$  calculation takes much longer than the others because it basically has to be repeated for every  $\lambda$  from 0 to  $(j_{\min} =) 2$  [eqs. (3-2) and (3-3)]. Exact ADP $j_z$  and SCE/AEP ADP $j_z$  calculations have not yet been performed on the same computer so we are unable to report on their relative cpu times. The savings afforded by semiclassical calculations does not seem to be a major concern in the literature as it is not mentioned. Shimoni and Kouri [17] took 2.5 h of cpu time for the CC calculations and 9 min for the exact ADP $j_z$  calculations on a Univac 1108. That's a relative speed of 16.7 to 1.

† This raises a delicate point. Our present purpose is not to critique or detract from the fine work that has preceded us. SCS calculations are generally most serviceable as are a number of other semiclassical approaches. The essential eikonal concept is simple, direct, and flexible. With rigorous and creative development it affords additional insight and expanded opportunities for application.

### Conclusion

An improved eikonal calculation was performed on rotationally inelastic  $\text{HeH}_2$  scattering at .1 and .9 eV. We have shown how semiclassically obtained amplitudes are incorporated into definite parity  $\text{ADP } j_z$  coupled states partial and total cross sections, gave a nonrigorous view of the eikonal formalism, explained how the averaged effective potential (AEP) imposes microreversibility on state-to-state calculations, and related the equations to rotationally inelastic scattering. We have also shown how additional constraints could be placed on the calculation through the use of phase-shifted amplitudes, thereby reducing cpu time requirements several fold and that the calculations had in fact been performed correctly by favorably comparing the cross sections obtained with published semiclassical coupled states, exact coupled states, and close coupling results.

This research has been entirely successful in every respect save one. One can envision the same sort of semiclassical calculation performed so that microreversibility is imposed, not only on the state-to-state transition being examined, but *all* transitions simultaneously. Of course, this would demand the use of  $N$  complete sets of coefficients rather than just 2 (where  $N$  is the number of states included in the basis).

While it is unfortunate that attempts at this sort of calculation have not, to date, been successful, the situation is not entirely black and white. First, they would require considerably more computer time, very possibly with only slightly improved results. On the other hand, they may prove to converge with smaller basis sets. Even if they do, however, the decrease in basis will almost certainly not outweigh the increase in cpu time. Second, the design of this calculation carries its own conditions. Each set of coefficients starts with the probability in a different state. The resulting calculation necessarily solves for all possible transitions, only subsequently providing information regarding particular transitions. Such "super calculations" are a lovely thought, but they present an undesired increase in the complexity of the problem. Since there is no obvious way to perform particular state-to-state calculations whose coefficients satisfy microreversibility between all states, the simple two state microreversibility imposed on the  $\text{HeH}_2$  calculations above represents an acceptable compromise.

With all this in mind, it is nonetheless interesting to think about "super calculations". What is causing the calculations attempted so far to fail? The answer may lie in an extension of the falsely compensating setwise variation of the coefficients discussed in the preceding section. In that case the solution would lie in imposing additional conditions to restrain random variation in the coupled differential equations. This is a thought for future consideration.

Another possibility is to somehow string together a series of simple two state microreversible calculations to lead to an improved result—to theoretically work backward from the desired transition so that when actually performing the calculations in sequence the final calculation somehow comprises an average over averages. The details haven't been worked out yet, but parallel computing techniques could make this sort of approach very effective.

The prognosis for eikonal applications is excellent. Programs are already being developed that account for vibrational as well as rotational transitions. Postcollisional reorientation effects are also being examined. Eventually the focus will shift to larger systems.

### Acknowledgments

We would like to thank the organizers of the Sanibel Symposia for making it possible for us to present this material and Gert Due Billing for the helpful hints.

### Bibliography

- [1] A good general discussion by G. T. Truhlar and J. T. Muckerman appears in *Atom-Molecule Collision Theory*, R. B. Bernstein, Ed. (Plenum, New York, 1979), chap. 16. See also chaps. 6, 7, 9, 12, and 13 for more semiclassical applications.
- [2] D. A. Micha, *J. Chem. Phys.* **78**, 7138 (1983).
- [3] P. K. Swaminathan, C. D. Stodden, and D. A. Micha, *J. Chem. Phys.* **90**, 5501 (1989).
- [4] P. K. Swaminathan, B. C. Garrett, and C. S. Murthy, *J. Chem. Phys.* **88**, 2822 (1988).
- [5] J. Olson and B. G. Garrison, *J. Chem. Phys.* **83**, 1392 (1985).
- [6] B. M. Rice, B. C. Garrett, and P. K. Swaminathan, *J. Chem. Phys.* **90**, 575 (1989).
- [7] J. M. Cohen and D. A. Micha, *J. Chem. Phys.* **98**, 2023 (1993).
- [8] J. M. Cohen and D. A. Micha, *J. Chem. Phys.* **97**, 1038 (1992).
- [9] A. M. Arthurs and A. Dalgarno, *Proc. Phys. Soc.* **A256**, 540 (1960).
- [10] For example, A. P. Yutsis, I. B. Levinson, and V. V. Vanagas, *Mathematical Apparatus of the Theory of Angular Momentum* trans. from Russian (published for the NSF by Israel Program for Scientific Translations, Jerusalem, 1962), chap. 1.
- [11] G. D. Billing, *Chem. Phys. Lett.* **50**, 320 (1977).
- [12] G. D. Billing, *Chem. Phys. Lett.* **30**, 391 (1975).
- [13] For example, in addition to Ref. [1], see W. Lester, *Dynamics of Molecular Collisions, Part A*, W. Miller, Ed. (Plenum Press, New York, 1976), chap. 1, sect. 3-2.
- [14] M. Krauss and F. H. Mies, *J. Chem. Phys.* **42**, 2703 (1965).
- [15] R. E. Langer, *Phys. Rev.* **51**, 669 (1937).
- [16] G. D. Billing, *J. Chem. Phys.* **65**, 1 (1976).
- [17] Y. Shimoni and D. J. Kouri, *J. Chem. Phys.* **66**, 675 (1977).
- [18] D. J. Kouri, *Atom-Molecule Collision Theory*, R. B. Bernstein, Ed. (Plenum Press, New York, 1979), chap. 9.
- [19] G. D. Billing, *Chem. Phys.* **30**, 387 (1978).
- [20] G. D. Billing, *Chem. Phys.* **9**, 359 (1975).
- [21] L. F. Shampine and K. Gordon, *Computer Solutions of Ordinary Differential Equations. The Initial Value Problem* (Freeman, San Francisco, 1975).

Received August 2, 1993



# Assessment of Molecular Shape Fluctuations Along Dynamic Trajectories

GUSTAVO A. ARTECA

Département de Chimie et Biochimie, Laurentian University—Université Laurentienne,  
Ramsey Lake Road, Sudbury, Ontario, Canada P3E 2C6

## Abstract

To assess the flexibility of a molecule (and to establish how it is affected by external conditions), one can analyze the nature of the configurations encountered along molecular dynamics (MD) trajectories. If the molecule is initially at a *rigid conformation*, then it will mostly undergo deformations which conserve the initial fold or shape. That is, a *rigid* molecule will exhibit very small *shape fluctuations* about the initial shape, whereas large fluctuations will be characteristic of *flexible* molecules. Establishing the persistence of molecular shape features along MD trajectories is a valuable piece of information in the analysis of dynamic phase transitions in large biomolecules, including protein folding and polymer melting. In this work, we discuss a methodology to monitor macromolecular shape along dynamic trajectories. The procedure uses descriptors which convey some *global shape features*, including the compactness and degree (and complexity) of entanglement in a backbone. The method is used to follow shape fluctuations in chain molecules (carboxylic acids) and cyclic molecules (cycloalkanes), with 6 up to 12 carbon atoms. The role of variable temperature and number of atoms on these fluctuations is analyzed. The results indicate a relatively constant average shape in the cyclic molecules, although the amplitude of the shape fluctuations increases with the temperature. In contrast, the shape of the chain molecules is affected largely at high temperature, where folding or "melting" becomes dominant. At low temperature, the chains are very rigid. In the high temperature regime, the shape fluctuations in chains are large and very similar to those in cycles. In other words, the distinction between configurations of cycles and chains starts to blur at high temperature, thus suggesting that chains are mostly folded into turns. The results would appear not to depend very strongly on the functional group at the end of the chain. © 1993 John Wiley & Sons, Inc

## Introduction

Computer simulation of molecular dynamics (MD) [1] permits the analysis of microscopic molecular phenomena within the picosecond domain. Experimental data on nuclear motions from neutron scattering [2–6], nuclear magnetic resonance [7–9], and Mössbauer spectroscopy [3,10,11] suggest that MD provides reliable information on the details of the structural reorganizations in large biomolecules [12]. The knowledge of amplitudes and frequencies of individual and collective nuclear motions is essential towards the understanding of processes such as protein folding [13–19] and various other configurational transitions [3–6,20–23].

The characteristics of the configurational "phases" found in macromolecules are more related to the fluctuations in the overall molecular shape than to the detailed

changes in individual nuclear positions [20–22]. Distinct “phases” can be characterized by the dominant presence of either *stretched* or *entangled* configurations, as, for instance, *helices* or *random coils* [22], *unfolded* or *folded* structures [13–19], and *compact* or *swollen* configurations [24]. Similarly, configurational phases can be described in terms of the rigidity and flexibility of molecular chains or clusters, as it is the case of melting in crystalline polymers [20,21], or the dynamic liquid/glass transitions in the hydration shells of some enzymes [3,11,25]. The recognition of these configurational changes requires the analysis of folding features as a function of time and external variables (e.g., temperature, pH). Therefore, it is necessary to use adequate molecular “order parameters,” whose values along MD trajectories may indicate the persistence of certain shapes. Some commonly used geometrical parameters, such as r.m.s. deviations, provide a limited shape description which is *relative* to a reference configuration and not very discriminating. Folding is a large-scale (global) property which is not well conveyed by the local details in the nuclear geometry. In this work, we discuss and apply a new approach which quantifies *global molecular shapes* along a MD trajectory. Especially important for the analysis of configurational phase transitions, the persistence of shape features over time and the fluctuations in the shape is estimated.

Our procedure introduces a descriptor of folding, *the probability of overcrossings in the rigid 3D placements of a molecular backbone* [26,27]. The methodology extends a previous idea of using the molecular geometry to derive topological characterizations of protein motifs [28,29]. The value of the descriptor gives a measure of compactness in a fold; the fluctuations in this value characterize the flexibility of the molecular backbone with respect to changes in its fold. Earlier applications to the study of rigidity in hydrocarbons [26,27] and some  $\alpha$ -helices [30], suggest that the technique is useful in assessing structural stability. In this work, we extend the study to a series of chain and cyclic molecules, and explore the effect of temperature and different connectivity on the molecular shapes found along MD trajectories. The interplay between potential energy and shape changes is discussed. As well, we analyze the variation of trajectory averages of the shape descriptors as a function of the backbone length. Finally, the information that can be retrieved from fluctuations in molecular size and in molecular shape are compared.

### Global Shapes and Shape Flexibility of Molecular Backbones

The molecular shape features we deal with are those conveyed by the *backbone*. In this work, we restrict ourselves to the study of simple saturated chain and cyclic molecules, where the backbones are defined by a sequence of straight line segments (bonds) between  $sp^3$  carbon atoms. These backbones exhibit no branching.

The shape of a backbone can be described locally, by studying the distribution of interatomic distances and bond angles (see, e.g., Refs. [31,32]). If, in contrast, one is interested in *folding* features, a *global analysis* will be preferable. Global characterizations of backbones' shapes have been proposed in the literature, including geometrical measures of compactness [33,34], as well as several topological methods to describe folding (e.g., Refs. [22,35–39] and others quoted therein).

Recently, an approach which combines both geometrical and topological data to characterize the 3D global shape of macromolecules has been introduced [28]. The procedure can be adapted to the study of persistence of shape features over time [26,30], and it provides *order parameters* to monitor structural organization in polymers [27]. This method has been described in detail elsewhere. For completeness, we discuss here its basic ideas. The methodology is used in later sections to study the shape of molecular cycles and chains, and to analyze the effect of different variables, such as chain length, temperature, functional groups, and connectivity type of the backbone.

To illustrate the essential ideas, we proceed by example. Figures 1 and 2 show two of the molecules dealt with in this work, dodecanoic acid and cyclododecane. The two molecules appear in arbitrarily folded configurations; their full specifications appear at the top of Figures 1 and 2 (the so-called "all-atom structures"). The corresponding backbones (defined by the connectivity of carbon atoms) appear immediately below, on the left-hand side.

Let us consider first Figure 1. The molecule is shown in a given configuration, say  $K$ . This configuration corresponds to a snapshot of a possible structure found along a MD trajectory, and it can be identified parametrically as a function of time ( $t$ ). We shall therefore label the configuration as  $K(t^*)$ , corresponding to a snapshot at  $t = t^*$ . Let us think of the snapshot  $K(t^*)$  of the backbone as a *rigid entity*. Our

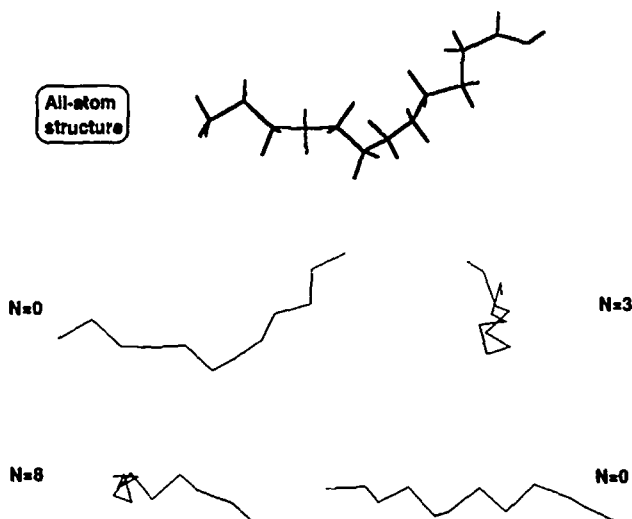


Figure 1. Four rigid 3D placements of the carbon backbone of dodecanoic acid in a generic, folded conformational snapshot  $K(t^*)$ . [The top diagram corresponds to the full structure in a given placement; the backbone with the same placement is shown immediately below, on the left-hand side. The other placements are derived from this latter by  $90^\circ$  rotations. Next to the diagrams, the number of overcrossings in the projection is given. To calculate the overcrossing probabilities, *all possible rigid placements must be studied*]

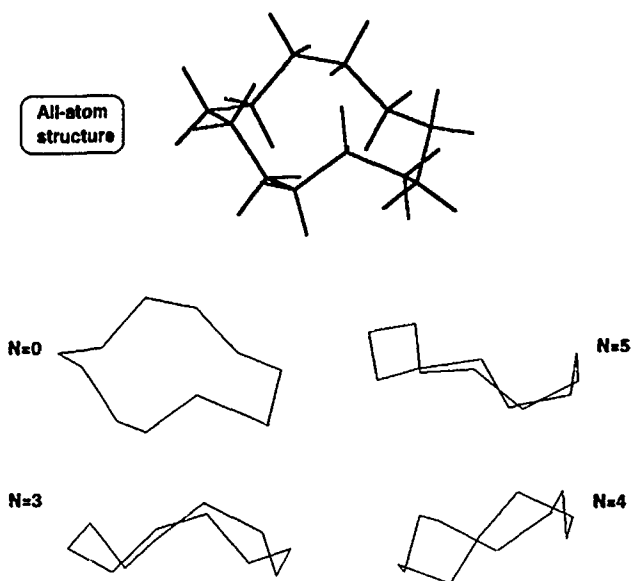


Figure 2. Four rigid 3D placements of the carbon backbone of cyclododecane in a generic, twisted conformational snapshot  $K(t^*)$ . (The top diagram corresponds to the full structure in a given placement; the backbone with the same placement is shown immediately below, on the left-hand side. The other placements are derived from this latter by  $90^\circ$  rotations. Next to the diagrams, the number of overcrossings in the projection is given.)

molecular shape description uses *all possible 3D placements of  $K(t^*)$* , derived from one another by rigid rotations [28]. Each of these rigid placements can be regarded as a *distinct view of the backbone with same the configuration  $K(t^*)$* . A photograph of a possible placement ("view") will appear as planar 2D curve. There are infinitely many of these possible projected curves. Each of them can be characterized by the number of *overcrossings* exhibited,  $N$ . (Overcrossings appear when one bond crosses over another in front of a viewer, thus producing an actual crossing in the 2D projection. The number  $N$  can be computed algorithmically as discussed in Ref. [28]).

Figure 1 shows four rigid placements of  $K(t^*)$ ; each one is derived from the top placement by a number of  $90^\circ$  rotations. Next to each view, the corresponding number of overcrossings  $N$  is given. The top-left view and the bottom-right view both have  $N = 0$  (i.e., they exhibit no overcrossings). From this point of view, they are considered *equivalent*. When this procedure is repeated for *all possible views*, configurations with the same  $N$  will be found with various frequencies. Therefore, one can introduce the *probability  $A_N(n)$  of observing a 3D rigid placement with  $N$  overcrossings in an  $n$ -atom backbone* [26], or simply "overcrossing probability  $A_N(n)$ ". It is clear that the set  $\{A_N(n)\}$  satisfies:

$$\sum_{N=0}^{\infty} A_N(n) = 1, \forall n \geq 3. \quad (1)$$

The distribution  $\{A_N(n)\}$  is a *global shape descriptor* [26]. A configuration  $K$  which is "open" (not compact), and exhibits little degree of entanglement, will have high  $A_N(n)$  values for low  $N$ . That is, open structures will *mostly* appear in placements with low numbers of overcrossings. In the limit of a perfectly linear chain or planar structure, one has  $A_0(n) = 1$ , i.e., no overcrossings will be observed between bonds. In contrast, *compact and entangled* configurations will exhibit large number of overcrossings. Objects like random coils have a large range of possible overcrossings, each one with a small probability [27]. In summary, the overcrossing probabilities can distinguish between configurations with different folding features. The description is not strongly dependent on local geometrical features since it is global. A brief characterization of the distribution  $\{A_N(n)\}$  can be given in terms of the most probable number of overcrossings  $N^*$ , and its associated probability  $A^*$ :

$$A^* = A_{N^*}(n) = \max_{\{N\}} A_N(n). \quad (2)$$

For simplicity, the index  $n$  is dropped from the notation of  $A^*$ . From the distribution  $\{A_N(n)\}$ , it is possible to compute the moments of the number of overcrossings:

$$\bar{N}^p = \sum_{N=0}^{\infty} N^p A_N(n), \quad p = 1, 2, \dots \quad (3)$$

A magnitude similar to the mean number of overcrossings ( $p = 1$ ) has recently been suggested to characterize complexity in self-avoiding random walks in lattices [40].

The above analysis for a molecular chain (Fig. 1) can be applied also to the study of macrocycles without branching, as the one in Figure 2. The number of overcrossings  $N$  can be defined for various types of connectivities. Figure 3 shows the results of the computed probabilities of overcrossings for the chosen configurations  $K(t^*)$  of dodecanoic acid and cyclododecane. [The configurational dependence is made explicit by indicating the probabilities as  $\{A_N(n, t^*)\}$ , and  $A^*(K(t^*))$  for the maximum, whenever necessary.] The histograms of overcrossing probabilities (the *overcrossing spectra* [27]) have been computed with several random distributions of viewing directions [41], and averaging over them. To achieve an accuracy of  $\pm 0.005$  in the maximum probability  $A^*$ , a sampling of ca. 2,000 views or more is needed. As shown in Figure 3, the most probably number of overcrossings ( $N^*$ ) for the two configurations is zero. The maximum probabilities are:  $A^*(K(t^*)) = A_0(12, t^*) = 0.799 \pm 0.003$ , for dodecanoic acid, and  $A^*(K(t^*)) = 0.371 \pm 0.004$ , for cyclododecane. The mean number of overcrossings on  $\bar{N} = 0.414$  (dodecanoic acid), and  $\bar{N} = 1.951$  (cyclododecane). Both results represent well the fact that the backbone of cyclododecane is more folded than the backbone of dodecanoic acid at its present configuration.

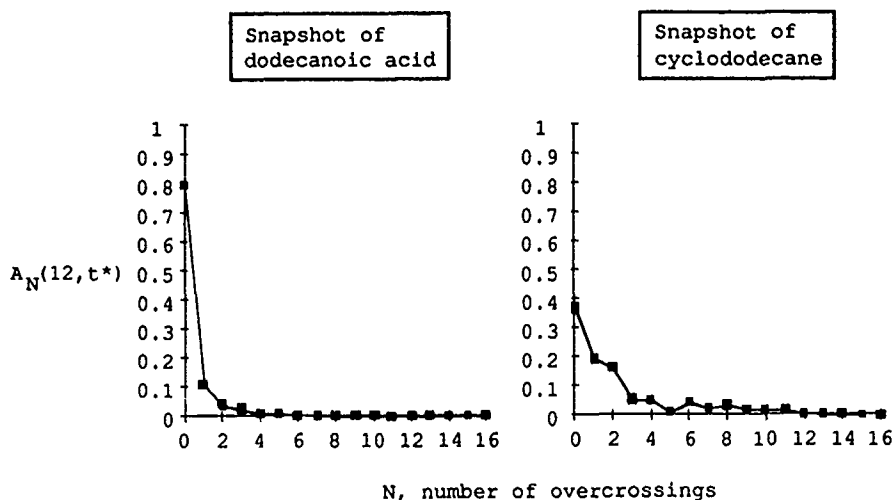


Figure 3. Overcrossing spectra (histogram of overcrossing probabilities) for the backbone structures shown in Figures 1 and 2. (The probabilities are computed with an accuracy of ca. 0.004 [see text].)

The analysis above can be applied to any other conformation. If the procedure is repeated for the configurations found along a MD trajectory, it is possible to assess the changes in molecular shape as a function of time by monitoring the values of  $A^*$ ,  $N^*$ , or  $\bar{N}$ . These descriptors characterize folding features in terms of compactness and the complexity of entanglements, and their changes along a trajectory allow one to estimate the *molecular flexibility*. In our context, flexibility is regarded as the capacity to move away from a given molecular shape. A rigid molecule can only deform to configurations which have essentially the same (global) shape. The degree of flexibility of a minimum energy configuration can be assessed by analyzing the fluctuations in its shape descriptors ("shape fluctuations") as a function of time, using MD trajectories which start from the desired minimum [26].

The trajectory (or ensemble) average of a shape descriptor can be used to establish the persistence of a fold. Since actual MD simulations provide a discrete (numerable) sequence of configurations  $\{K_i, i = 1, 2, \dots, M\}$ , the trajectory average of the probability of the most probable number of overcrossings,  $\langle A^* \rangle$ , is given by:

$$\langle A^* \rangle = \lim_{M \rightarrow \infty} \frac{1}{M} \sum_{i=1}^M A^*(K_i). \quad (4)$$

In practice, the maximum value  $M$  will correspond to the total number of snapshots taken along the trajectory. In addition, the shape fluctuations can be expressed quantitatively by the standard deviation in the value of  $A^*$ ,  $\sigma_A$ :

$$\sigma_A = (\langle A^{*2} \rangle - \langle A^* \rangle^2)^{1/2}. \quad (5)$$

Some of these shape descriptors have been used already to characterize conformational flexibility about energy minima and transition structures of hexane and cyclohexane [26],  $\alpha$ -helices of glutaredoxin [30], some linear hydrocarbons [27], and to study the effect of excluded volume on the configurations of soft-bead polymer models [27]. In Ref. [26], the differential flexibility conferred by the length of a chain was illustrated by comparing hexane and decane at a given temperature. In this work, we expand further these analyses by comparing a series of chain and cyclic molecules of various sizes. The role of temperature, number of carbon atoms, and backbone connectivity on the molecular flexibility is studied in the next section by following the values of  $A^*$  and  $N^*$  along MD trajectories.

### Shape Fluctuations in Molecular Chains: Carboxylic Acids

The dynamic trajectories are generated by standard techniques. The Dreiding force field (including atomic charges) [42] was employed in the simulations. The trajectories are derived by standard Verlet integration of Newton's equations of motion [23]. The coupling to an external bath at a desired temperature  $T$  is simulated by uniform rescaling in the velocities. For each molecule, 30 ps trajectories have been generated, with integration step of 1 fs. The trajectories, though not long, provide a reasonable sampling of the accessible configurations at the simulation temperature. The results should be comparable to other simulations of methylenic chains in the literature, using alternative force fields [43,44].

Four carboxylic acids have been studied: hexanoic, octanoic, decanoic, and dodecanoic acids ( $n = 6, 8, 10$ , and  $12$ ), at  $T = 300$  and  $T = 1000\text{K}$ . To compare the ability of these  $n$ -chains to fold, the simulations have been started with the molecules at the linear all-trans configurations. These configurations are potential energy minima whose shapes are characterized by  $A^* = 1$ . The MD trajectories are computed at constant temperature; the total energy is also conserved within a 5% fluctuation, after an equilibration period of ca. 0.5 ps.

Figure 4 shows the results for the potential energy fluctuations for the acids, at 300 and 1000K. The main contribution of the energy fluctuations comes from torsional terms. The results are rather unchanged if the atomic charges are disregarded. Moreover, the molecular chain properties seem not to be very sensitive to the presence of a carboxylic terminal group.

Little structural information can be extracted from an analysis as in Figure 4. It is clear that the amplitude of the potential energy fluctuations becomes larger for high  $T$ , but the results do not tell how these fluctuations may affect the fold of the chain. Moreover, these results do not depend very strongly on the chain length. This picture can be compared with the analysis of molecular shape descriptors. Figure 5 shows the changes of  $A^*$  along the same trajectories. The contrast among the various chains is remarkable. Although the fluctuations at 300K are comparatively small for all acids, the results are very different at high temperature. The amplitude of the molecular shape fluctuations is larger for octanoic acid than for hexanoic acid. The amplitudes for decanoic and dodecanoic are comparable. More-

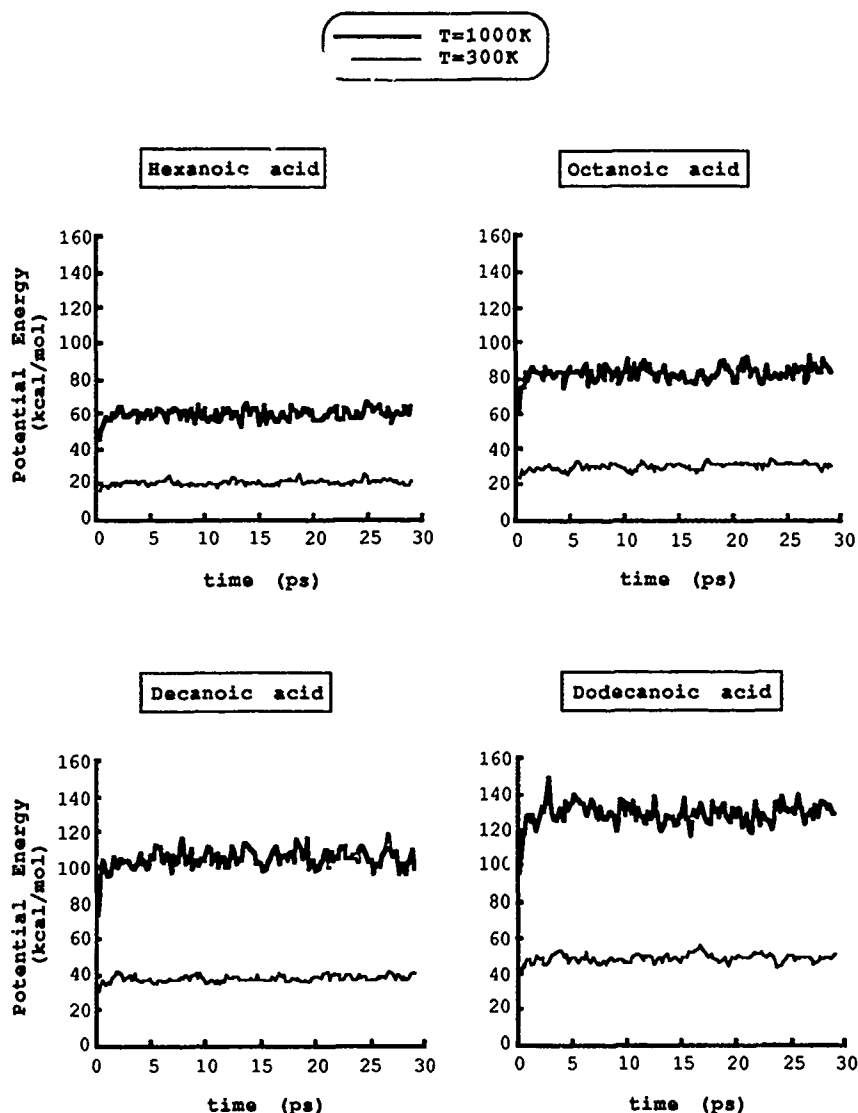


Figure 4. Fluctuations in the potential energy along the dynamic trajectories for carboxylic acids at 300K and 1000K. [The trajectories are started from initially linear, all-trans conformations for the chains. These results provide little information on how the energy is used to move the shape away from the initial fold.]

over, the values of  $A^*$  decrease along the trajectories for longer chains, thus indicating that the chains are folding. In all these trajectories, it is found that the most probable number of overcrossings is still  $N^* = 0$ . The  $A^*$  values indicate the occurrence of more entangled objects for the longer chains at high temperature. Note that hexanoic, and to a smaller extent octanoic acid, exhibits several configurations along the



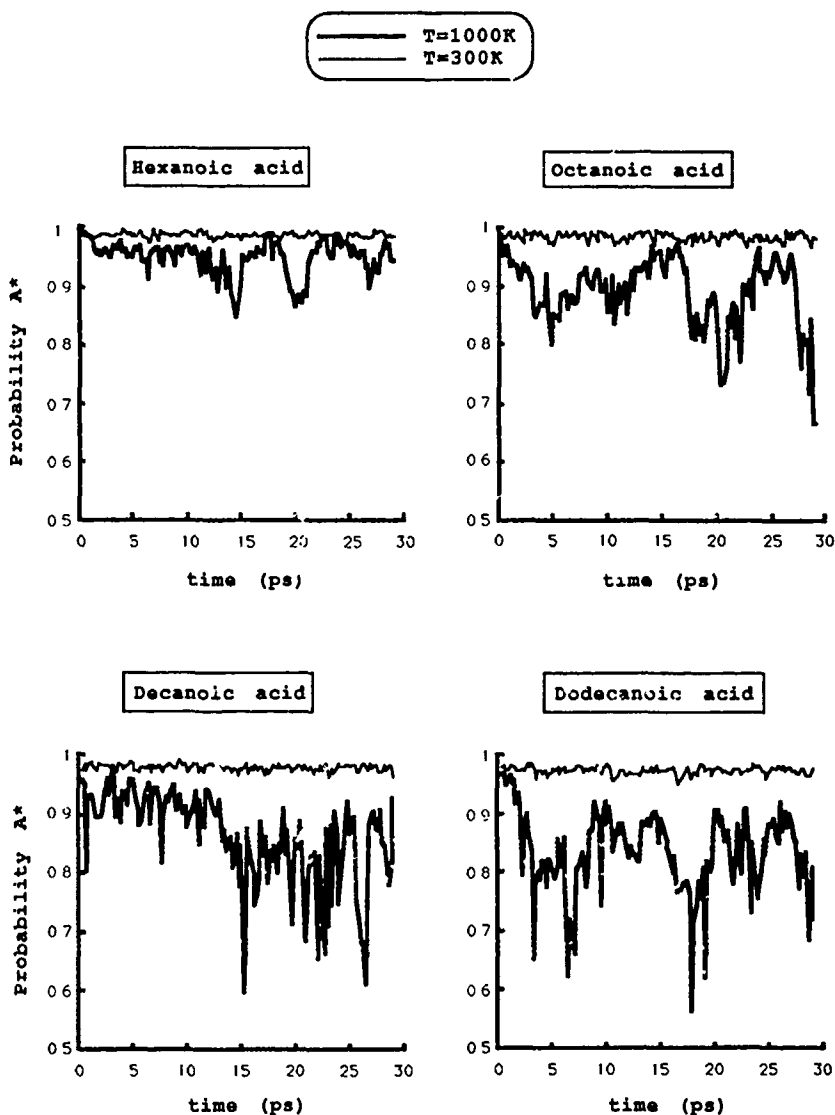


Figure 5. Fluctuations in the shape descriptor  $A^*$  (probability of the most probable number of overcrossings) along the MD trajectories for carboxylic acids at 300K and 1000K. (The description is much richer than the one in Fig. 5. Note that, the smaller  $A^*$ , the more folded the structure. Therefore, at 300K the chains remain close in shape to the linear backbone. At high temperature, the chains are flexible, but the amplitude of the shape fluctuations depends on the backbone length.)

trajectory with values of  $A^*$  close to 1. This indicates that the chain can *stretch* (unfold) during the simulation, and spend some time in a configuration with a shape similar to that of the original all-trans chain. In contrast, this situation disappears for the  $n = 10$  and  $n = 12$  chains. These backbones are mostly *melted* (i.e., folded) during the simulation.

The interplay between molecular shape and potential energy can be displayed by combining the information of Figures 4 and 5. Figure 6 shows the sequence of snapshots along the MD trajectory represented in a 2D shape vs. energy diagram for the two extreme chains ( $n = 6$  and  $n = 12$ ), at low and high temperature. The diagrams represent the trajectories as a sequence of straight line segments joining the pair of values of potential energy and shape descriptor for each configurational snapshot. The arrow indicates the orientation of the trajectory, starting from the first configuration after equilibration. These 2D diagrams provide information on the type of folds accessible to the molecular chains within a given range of potential energy. At low temperature, the potential energy fluctuates more in dodecanoic than in hexanoic acid; yet, the shape of the chain and its fluctuations are almost the same (i.e., the chains are quite rigid). At high temperature, the larger fluctuation in potential energy for the  $n = 12$  chain leads not only to larger shape fluctuations, but also to quite low  $A^*$  values. Values as low as  $A^* \approx 0.55$  are characteristic of  $\beta$ -turns [30], which indicates that the chain is folded but not into a very compact configuration.

Figure 7 summarizes the results for the shapes of carboxylic acids. The trajectory average of the shape descriptor,  $\langle A^* \rangle$ , and its standard deviation [Eqs. (4) and (5)] are given as a function of the chain length. At  $T = 300\text{K}$ ,  $\langle A^* \rangle$  decays linearly (and slowly) with  $n$ , whereas the shape fluctuation ( $\sigma_A$ ) remains almost constant. At  $T = 1000\text{K}$ , the averaged shape descriptor decays rapidly with the chain length for short chains, while  $\sigma_A$  increases. For longer chains, the effect seems to be less dramatic, as the shape fluctuations depend less strongly on the number of carbon atoms.

The results for the global folding features of carboxylic acids along the dynamic trajectories allows us to draw the following conclusions:

- (1) At low temperature, the initially linear chains cannot access to the degrees of freedom that would rapidly change the fold. That is, regardless of the number of internal torsions, the chains cannot fold. Yet, the chains can deform. The small shape fluctuations found indicate the presence of localized vibrations about the original fold, a feature which does not depend strongly on the backbone's length. In these conditions, the chains are rigid.
- (2) At high temperature, the molecules can access to many torsional modes in an uncorrelated manner, thus allowing a wide range of folding features. The longer chains become more entangled (i.e., more folded) than the shorter ones. However, since  $\langle A^* \rangle$  moves away from linearity as a function of  $n$  and decays less rapidly for longer chains, it would appear that the complexities of entanglements in sufficiently long backbones are somewhat comparable.

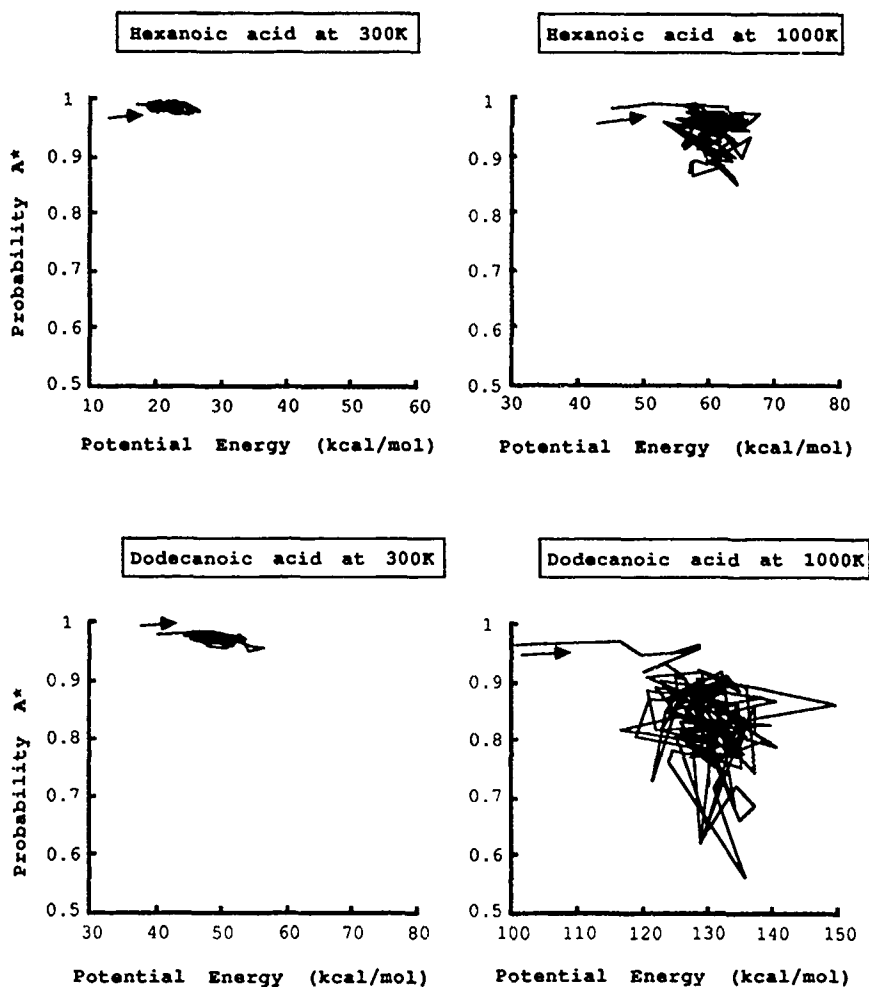


Figure 6. Interrelation between changes in the shape descriptor  $A^*$  and the potential energy along MD trajectories of hexanoic and dodecanoic acids. (Each point on the diagram represent one in a series of snapshots (configurations) taken every 0.2 ps along the trajectory. Each configuration  $K(t)$  is characterized by  $A^*$ , the shape descriptor of the chain, and its potential energy value. The arrow indicates the walking direction along the trajectory, starting from the first structure after equilibration.)

As stated before, these observations should mostly be due to properties of the molecular chain, regardless of the presence of a carboxylic terminal group [27].

Most the above results are intuitively expected for linear chains with identical monomers. However, the present approach to characterizing the molecular shape provides a quantitative, precise expression to otherwise qualitative notions. The previous conclusions could not have been drawn from an analysis based only on

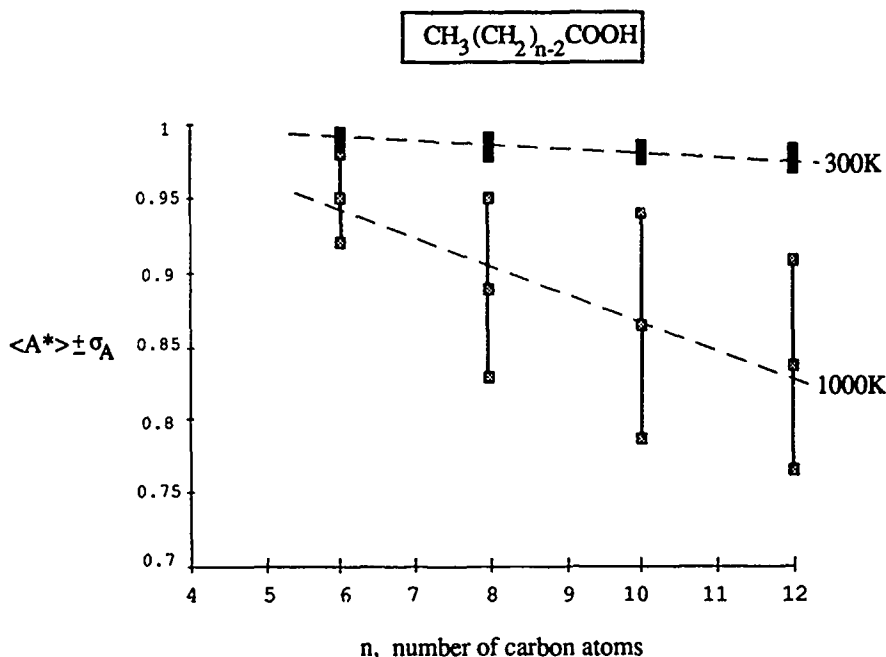


Figure 7. Changes in global shape for carboxylic acid chains, at 300K and 1000K. The molecular shape is indicated by  $\langle A^* \rangle$ , the trajectory average. The bars around the *average shape* are the standard deviation  $\sigma_A$ , and they quantify the *shape fluctuations*. (At 300K,  $\langle A^* \rangle$  varies almost linearly with  $n$  (dotted line). At 1000K the decrease slows down for longer chains )

the potential energy changes or the oscillations in the individual nuclear positions. In the next section, we compare these results with those for a different type of molecular connectivity.

### Shape Fluctuations in Cyclic Molecules and Comparison with Molecular Chains

Dynamic trajectories of cycloalkanes have been computed and analyzed as done before for carboxylic acids. The chosen  $n$ -cycles are cyclohexane, cyclooctane, cyclodecane, and cyclododecane, containing the same number of carbon atoms as the chains in the previous section. Any difference in molecular flexibility for the two groups of molecules is expected to be mostly due to the distinct type of backbone connectivity.

The MD simulations of linear chains were performed by starting from a similar type of configuration for all molecules (the stretched, all-trans structures). To facilitate the comparison, we have started the simulations of cycloalkanes from configurations which also possess a comparable "shape" for all cycles. The starting configuration for cyclohexane is the familiar "chair," which is the lowest-energy

minimum. The other cycles have been located initially at conformational minima chosen for their similarity in shape to the chair-cyclohexane ("crown" structures). These correspond to structures showing bonds which "zig-zag" uniformly about the average plane of the cycle. Moreover, the initial configurations are chosen so that they also grow in size proportionally to the number of carbon atoms. The larger cycles are thus elongated, not circular. For example, the backbone for the initial configuration "crown-cyclododecane" *resembles two parallel strands of 4 bonds, joined at their extrema by one-carbon bridges*. (The structure in Fig. 2 is deformed away from this initial configuration.)

The initial configurations of the four macrocycles can be regarded as formally derived from linear chains by folding them at their middle, and joining their extrema thereafter. Consequently, the cycles appear as structures whose shape is more folded than chains. This is reflected in the shape descriptors, which indicate a smaller probability of no-overcrossings for cyclic molecules (cf. Fig. 3). The fluctuation of their molecular shapes with the temperature has been studied using the same force field as for the carboxylic acids [42]. The simulation conditions and lengths of the MD trajectories are also the same.

Figure 8 shows the interrelation between potential energy and molecular shape in the two extreme cases, cyclohexane and cyclododecane at 300 and 1000K. This figure can be contrasted with Figure 6, corresponding to the molecular chains. (Note the difference in scales.) A comparison of molecules with the same number of carbon atoms reveals that *the fluctuations in the potential energy are similar for the  $n$ -cycle and the  $n$ -chain at the same temperature, but, their shape fluctuations are quite different*. At 300K, *the cycloalkanes exhibit shape fluctuations with amplitudes twice as much larger than those for linear chains*. At 1000K, *the amplitudes for chains and cycles become closer*. Note that *the fluctuations for cycles are quite symmetric about the average shape*, whereas *the fluctuations for chains at 1000K are asymmetric*, since the trajectory spends some time at low  $A^*$  configurations (i.e., more folded or entangled). Moreover, *the average of the shape descriptor for a given cycle does not change much with the temperature, whereas it becomes smaller for chains*.

The results in Figure 8 illustrate the evident change in molecular shape caused by the different connectivity: cycles exhibit large fluctuations but their essential shape is conserved (no unfolding is allowed), whereas the chains can change their shape due to folding. Furthermore, it is observed that the cycles are more flexible than chains, even at low temperatures. Note that the values of the shape descriptor for long chains at high temperatures are close to those of a cycle with the same number of atoms. That is, "hot" chains can fold enough to resemble cycles (with one "missing" bond).

Figure 9 collects the results for the shape descriptor  $\langle A^* \rangle$  and its fluctuation  $\sigma_A$  for the cycloalkanes. (Compare with Fig. 7 for the chains.) Except for a discrepancy in cyclodecane at high and low temperatures, the results are in line with the discussion above. The molecular shape becomes more convoluted for the larger cycles (as  $\langle A^* \rangle$  decreases), but their *average* molecular shape does not depend too strongly

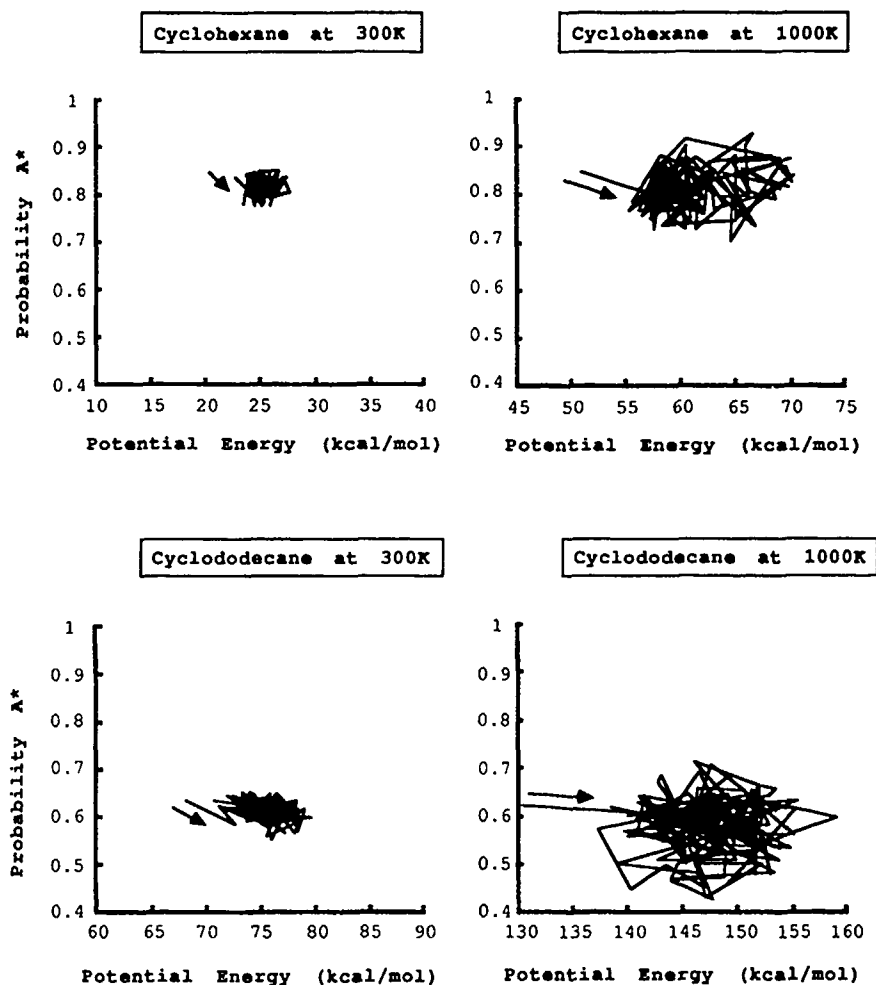


Figure 8. Interrelation between changes in the shape descriptor  $A^*$  and the potential energy along MD trajectories of cyclohexane and cyclododecane. (Each point on the diagram represent one in a series of snapshots (configurations) taken every 0.2 ps along the trajectory. Each configuration  $K(t)$  is characterized by  $A^*$ , the shape descriptor of the chain, and its potential energy value. The arrow indicates the walking direction along the trajectory, starting from the initial structure [a cycle in a minimum energy "crown" conformation, see text].)

on the temperature. At low temperature, the shape descriptor decreases linearly with  $n$ , whereas at high temperature the behavior is more scattered. This erraticity at high temperature is probably a consequence of the larger fluctuations about the average shape, and may indicate that longer trajectories are advisable to compute more accurate averages. In contrast with the behavior of cycles, molecular chains

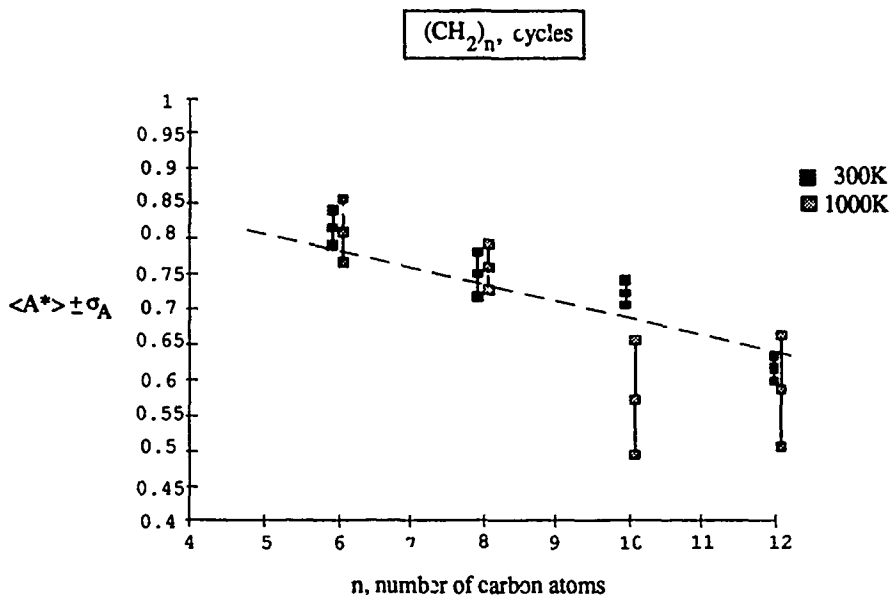


Figure 9. Changes in global shape for cycloalkanes, at 300K and 1000K. The molecular shape is indicated by  $\langle A^* \rangle$ , the trajectory average. The bars around the *average shape* are the standard deviation  $\sigma_A$ , and they quantify the *shape fluctuations*. (The shape descriptor varies almost linearly with  $n$  at 300K (dotted line). At large temperature the behavior is similar, although the results are scattered due to the larger shape fluctuations [see text].)

show a marked dependence on  $T$  in both the shape fluctuations *and* the average shape.

Further insight into the configurational changes along the dynamic trajectories can be obtained by comparing molecular shapes and molecular sizes. Molecular size can roughly be described by  $R$ , the radius of the smallest sphere enclosing completely the backbone. The average molecular size of a molecule at a given temperature,  $\langle R \rangle$ , can be computed as before as a trajectory average [cf. Eq. (4)]. The parameter  $\langle R \rangle$  is proportional to a hydrodynamic radius [20], and scales similarly to the radius of gyration [45]. Figure 10 shows the averaged radii for chains and cycles. (In the case of chains, the values for both carboxylic acids and hydrocarbons [27] are included.)

The results in Figure 10 reveal a number of facts, which we list and discuss below:

- (1) *The average sizes of cycloalkanes are almost independent of the temperature.* This correlates well with our finding of little dependence on  $T$  in the molecular shape of cycles. Nevertheless, a difference exists for larger cycles, indicating that the latter can maintain their size and yet become somewhat more convoluted or entangled.

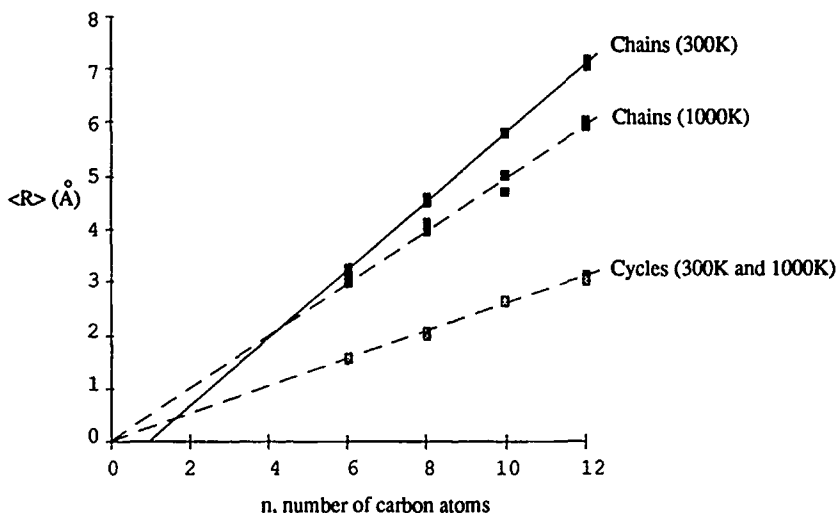


Figure 10 Average molecular size  $\langle R \rangle$  (radius of the smallest sphere enclosing the backbone, averaged over the dynamic trajectory) for chains and cycles at different temperatures. (The results labeled "chains" contain the data for both carboxylic acid chains and hydrocarbon chains of the same length. The change in radii is perfectly linear; note that the intercept for chains at large temperature and cycles are the same. The linear behavior should disappear for very long, random chains [see text].)

- (2) *Linear chain molecules become more compact at high temperature, although the difference in size disappears for short chains.* This agrees with the results in Figure 7 for the shape descriptors. For chains, there is a close correlation between *shape* (as given by the complexity of entanglements in the fold) and *size* (as expressed by  $\langle R \rangle$ ). Nevertheless, the amplitude of the fluctuations in  $\langle A^* \rangle$  indicates that chains may become compact and entangled without necessarily becoming smaller.
- (3) *The radii correlate linearly with the number of carbon atoms, but the intercepts for chains at low  $T$  and high  $T$  are different. Moreover, the intercept for chains at high  $T$  coincides with the intercept for the cycles.* This result is interesting, since it suggests some similarity between configurations of cycles and those of chains at high  $T$ . A similar relation was apparent when using shape descriptors, since the values of  $A^*$  for large cycles and "hot" chains are not far from each other. (As a side comment, it must be noted that for *very* long, *random* chains,  $\langle R \rangle$  should move apart from the linearity and scale approximately as  $\langle R \rangle \approx n^{0.588}$  [27,45,46].)

The results above show some connections between the descriptions in terms of size and shape, as well as some differences. The differences become even more transparent when looking at fluctuations. The *shape fluctuations* are represented by the dimensionless descriptor  $\sigma_A$ , which is the standard deviation about the average



maximum probability of overcrossings in rigid 3D placements,  $\langle A^* \rangle$ . For the sake of a proper comparison, we use  $\sigma_R/\langle R \rangle$  as a dimensionless descriptor of *size fluctuations*. Relative r.m.s. deviations could have been used instead.

The two approaches are compared in Figure 11. The top diagram shows the fluctuations in shape for cycles and chains at 300K and 1000K. The results are extrapolated to  $\sigma_A = 0$  for  $n = 3$ , which is an *exact* limit (the 3-atom figure is always planar, thence its shape descriptor is constant). The lower diagram shows the results for the fluctuations in size. Here, we choose to extrapolate to  $\sigma_R/\langle R \rangle = 0$  for  $n = 2$ , where the difference between chains and cycles disappears. This extrapolation does not represent an exact limit.

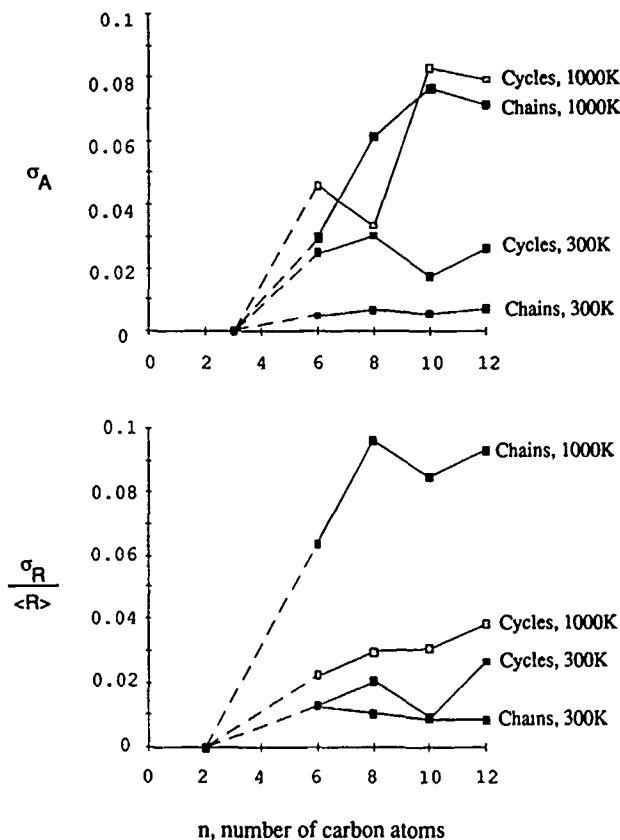


Figure 11. Comparison between fluctuations in molecular shape ( $\sigma_A$ ) and fluctuations in molecular size ( $\sigma_R/\langle R \rangle$ ) for chains and cycles at 300K and 1000K. (Note that, whereas the *size* fluctuations in "hot" chains differ from those of cycles, the *shape* fluctuations in long chains and large cycles at 1000K is quite similar. This is in line with the fact that at high temperature, the configurationally averaged properties of large cycles and long chains should be almost the same.)

The fluctuations in size and shape for cycles and chains at 300K are quite similar. However, it is clear that, *in terms of size fluctuations, "hot" chains are very different from cycles* (bottom diagram). In contrast, *the fluctuations in shape are similar for large cycles and long chains at high temperature* (top diagram). This outcome is more in line with the notion that when averaging global properties of sufficiently large macrocycles over configurational space, the results should be comparable to those derived for flexible chains with the same number of monomers [21,22,45]. This result makes clear the importance of monitoring the global shape features of a backbone, and not only its size or local geometrical properties.

### Summary and Conclusions

In the previous sections, a method to monitor the persistence over time of molecular shape features has been discussed and applied to the study of chain and cyclic molecules of various lengths. The procedure provides a quantitative expression of global shape for each of the configurational snapshots found along a dynamic trajectory. The folding features of the backbone at a given configuration are described in terms of the number of overcrossings in every possible rigid 3D placement. The more entangled, convoluted, and compact the backbone, the more probable the larger numbers of overcrossings. Therefore, the use of the overcrossing probabilities as shape descriptors characterizes both the compactness of the backbone, as well as the nature of the entanglements. Other shape descriptors (the moments of the number of overcrossings) can be derived from the probability distribution. The procedure has been applied here to chain and cyclic backbones without branching. However, the basic ideas can also be extended to deal with other systems, such as clusters and hydrogen-bonded networks [27].

The shape is characterized in an absolute manner, not relative to a reference configuration. Therefore, the values of  $A^*$  encountered along a trajectory tell not only how the shape fluctuates, but also they identify the instantaneous folded structures that the backbone explores. The recognition of the similarity in shape between some folded chains and molecular cycles (with the same number of monomers) is an illustration of this.

Summarizing the results, our analysis reveals a difference in flexibility at low and high temperatures for all molecules, even though the average shape is conserved more if the backbone is constrained to a cycle. At low temperatures, the chains are rigid, whereas the cycles are always floppy. In contrast, the fluctuations in shape at high temperature for sufficiently large chains and cycles are comparable. At low temperature, the shape descriptor shows an approximately linear decrease with the number of monomers, at least for short backbones. The dependence is much softer at high temperature for long backbones, thus indicating that all folding possibilities become accessible. Moreover, the present results appear to depend mostly on the connectivity of the backbone, its length, and the temperature, and not strongly on the presence of a terminal functional group. This will not be true in general for all types of backbones.

The present shape characterization describes quantitatively the molecular flexibility and the results agree with the overall expected physical picture in known cases. The method should therefore be a valuable tool in the analysis of other phenomena, such as various one-molecule "phase" transitions, where a correct assessment of global folding as a function of time is a central issue.

### Acknowledgments

Grants from the Fonds de Recherche de l'Université Laurentienne (FRUL), the Fonds de Démarrage 1993 (Laurentian University), and computer time from the Mathematical Chemistry Research Unit of the University of Saskatchewan (directed by P. G. Mezey) are gratefully acknowledged.

### Bibliography

- [1] W. F. van Gunsteren and H. J. C. Berendsen, *Angew. Chem.* **29**, 992 (1990).
- [2] J. C. Smith, *Quart. Rev. Biophys.* **24**, 227 (1991).
- [3] W. Doster, S. Cusack, and W. Petry, *Nature* **337**, 754 (1989).
- [4] R. J. Loncharich and B. R. Brooks, *J. Mol. Biol.* **215**, 439 (1990).
- [5] K. Kuczera, J. Kuriyan, and M. Karplus, *J. Mol. Biol.* **213**, 351 (1990).
- [6] B. F. Rasmussen, A. M. Stock, D. Ringe, and G. A. Petsko, *Nature* **357**, 423 (1992).
- [7] G. Wagner and K. Wüthrich, *Meth. Enzymol.* **131**, 307 (1986).
- [8] P. E. Wright, in *Proteins: Form and Function*, R. A. Bradshaw and M. Purton, Eds., (Elsevier, Cambridge, 1990), pp. 95-105.
- [9] H. J. Dyson, G. Merutka, J. P. Waltho, R. A. Lerner, and P. E. Wright, *J. Mol. Biol.* **226**, 795 (1992).
- [10] E. R. Bauminger, S. G. Cohen, I. Nowik, S. Ofer, and J. Yariv, *Proc. Natl. Acad. Sci. USA* **80**, 736 (1983).
- [11] V. N. Morozov and T. Ya. Morozova, *J. Theor. Biol.* **121**, 73 (1986).
- [12] C. L. Brooks, M. Karplus, and B. M. Pettitt, in *Advances in Chemical Physics*, I. Prigogine and S. Rice, Eds. (Wiley, New York, 1988).
- [13] J. A. McCammon and S. C. Harvey, *Dynamics of Protein and Nucleic Acids* (Cambridge University Press, Cambridge, 1987).
- [14] R. Jaenicke, *Prog. Biophys. Molec. Biol.* **49**, 117 (1987).
- [15] R. L. Baldwin, in *Proteins: Form and Function*, R. A. Bradshaw and M. Purton, Eds. (Elsevier, Cambridge, 1990), pp. 125-133.
- [16] C. Choithia and A. V. Finkelstein, *Annu. Rev. Biochem.* **59**, 1007 (1990).
- [17] E. Freire and K. P. Murphy, *J. Mol. Biol.* **222**, 687 (1991).
- [18] K. A. Dill and D. Shortle, *Annu. Rev. Biochem.* **60**, 795 (1991).
- [19] J. Skolnick and A. Kolinski, *J. Mol. Biol.* **221**, 499 (1991).
- [20] M. V. Volkenstein, *Configurational Statistics of Polymeric Chains* (Interscience Publishers, New York, 1963).
- [21] P. J. Flory, *Statistical Mechanics of Chain Molecules* (Interscience Publishers, New York, 1969).
- [22] F. W. Wiegel, in *Phase Transitions and Critical Phenomena*, Vol. 7, C. Domb and J. L. Lebowitz, Eds. (Academic, London, 1983), pp. 101-149.
- [23] D. W. Heermann, *Computer Simulation Methods in Theoretical Physics* (Springer, Berlin, 1990).
- [24] H. S. Chan and K. A. Dill, *Annu. Rev. Biophys. Chem.* **20**, 447 (1991).
- [25] K. P. Murphy, P. L. Privalov, and S. J. Gill, *Science* **247**, 559 (1990).

- [26] G. A. Arteca, *J. Comput. Chem.* **14**, 718 (1993).
- [27] G. A. Arteca, in *Advances in Computational Biology*, Vol. 1, H. O. Villar, Ed. (JAI Press, Greenwich, CT, in press).
- [28] G. A. Arteca and P. G. Mezey, *Biopolymers* **32**, 1609 (1992).
- [29] G. A. Arteca, *J. Math. Chem.* **12**, 37 (1993).
- [30] G. A. Arteca, O. Nilsson, and O. Tapia, *J. Mol. Graph.* **11** (1993), in press.
- [31] C. Brändén and J. Tooze, *Introduction to Protein Structure* (Garland, New York & London, 1991).
- [32] N. S. Goel and R. L. Thompson, *Computer Simulations of Self-Organization in Biological Systems* (Macmillan, New York, 1988).
- [33] L. M. Gregoret and F. E. Cohen, *J. Mol. Biol.* **219**, 109 (1991).
- [34] J. D. Honeycutt and D. Thirumalai, *Biopolymers* **32**, 695 (1992).
- [35] F. B. Fuller, *Proc. Natl. Acad. Sci. USA* **68**, 815 (1971).
- [36] M. Le Bret, *Biopolymers* **18**, 1709 (1979).
- [37] A. H. Louie and R. L. Somorjai, *J. Theor. Biol.* **98**, 189 (1983).
- [38] M.-H. Hao and W. K. Olson, *Biopolymers* **28**, 873 (1989).
- [39] G. A. Arteca and P. G. Mezey, *J. Mol. Graph.* **8**, 66 (1990).
- [40] E. J. Janse van Rensburg, D. W. Sumners, E. Wasserman, and S. G. Whittington, *J. Phys.* **A25**, 6557 (1992).
- [41] G. Marsaglia, *Ann. Math. Stat.* **43**, 645 (1972).
- [42] S. L. Mayo, B. D. Olafson, and W. A. Goddard III, *J. Phys. Chem.* **94**, 8897 (1990).
- [43] J. P. Ryckaert, G. Ciccotti, and H. J. C. Berendsen, *J. Comput. Phys.* **23**, 327 (1977).
- [44] R. M. Levy, M. Karplus, and J. A. McCammon, *Chem. Phys. Lett.* **65**, 4 (1979).
- [45] P. G. de Gennes, *Scaling Concepts in Polymer Physics* (Cornell University Press, Ithaca, 1985).
- [46] M. Muthukumar and B. G. Nickel, *J. Chem. Phys.* **86**, 460 (1987).

Received March 30, 1993

# Quantum Functional Sensitivity Analysis for the 3-D ( $J = 0$ ) $\text{H} + \text{H}_2$ Reaction

JOHNNY CHANG and NANCY J. BROWN

*Energy and Environment Division, Lawrence Berkeley Laboratory, Berkeley, California 94720*

## Abstract

The sensitivity of state-to-state transition probabilities for the 3-dimensional  $\text{H} + \text{H}_2$  hydrogen-exchange reaction (at zero total angular momentum) has been investigated with respect to variations in the interaction potential. Several regions of configuration space where the dynamics is highly sensitive to inaccuracies in the potential have been identified. These regions of importance vary with collision energy, but do not change as dramatically as the previously studied [J. Chem. Phys. 97, 6226 (1992)] collinear case. Near the reaction threshold, the dynamics is most sensitive to the saddle point region as expected. At higher energies (about 1.0 to 1.5 eV), however, the inner corner of the potential, where the dynamics "cuts the corner" in going from reactant to product arrangements, is most important for collinear geometries, and the outer corner, where the  $\text{H}_3$  conformation is more compact than the transition state conformation, is most important for bent geometries. Surprisingly, the region of the potential traversed by the minimum energy path across the saddle point region has rather insignificant sensitivities at these higher energies.

© 1993 John Wiley & Sons, Inc.

## Introduction

One of the goals of theoretical chemistry is to be able to predict experimental observables to within chemical accuracy starting completely from first principles. In the field of chemical dynamics, this goal is arguably at hand for the complete description of the simplest chemical reaction—that of the  $\text{H} + \text{H}_2$  hydrogen-exchange reaction and its isotopic variants [1]. The prediction of state-to-state integral cross sections as a function of energy [2–4] and product vibrational–rotational state distributions [5–12] have been corroborated to a large extent by experiment [11, 13–19]. This state of affairs is attributable in part to the existence of very accurate potential energy surfaces [20–22] for this 3-electron system. Despite these successes, there are still some remaining issues where theory and experiment are in disaccord [8, 11, 16(d), 18, 19]. For example, the state-resolved differential cross sections for the  $\text{D} + \text{H}_2 \rightarrow \text{DH} + \text{H}$  reaction show a large discrepancy between the calculated and the experimentally observed ratios of forward-scattered to backward-scattered intensities [18]. Since the various scattering theories used are formally exact, and calculations from different research groups employing different formalisms have yielded essentially the same result, the theory versus experiment discrepancies have naturally been ascribed, on the theoretical side, to deficiencies in the potential energy surfaces. Agreement between theory and experiment is even more difficult to attain for more complex systems because the calculation of accurate potential

energy surfaces becomes increasingly more elusive. The natural question, then, is how can one systematically improve a potential energy surface (PES) without resorting to calculating the whole PES anew with higher levels of theory. It is partly with this question in mind that we are furthering the development of quantum functional sensitivity analysis (QFSA) [23,24]—to provide feedback information to quantum chemists in their PES refinement efforts. An equally important reason for using QFSA to study chemical dynamics is to gain a better understanding of the potential-to-dynamics relationship.

QFSA is a methodology for studying the response of calculated observables (or model outputs) to small variations in model input(s). When the PES is viewed as the model input to a quantum scattering calculation, QFSA provides information about which regions of the PES are most important for determining the quantum dynamics. The particular quantities of interest are the functional derivatives (or sensitivities),  $\delta O/\delta V(R)$ , where the observable,  $O$ , is viewed as a functional of the PES,  $O[V(R)]$ . This information is expected to find utility among quantum chemists in providing a guide to regions of the PES where a higher density of *ab initio* points should be calculated (i.e., regions of the PES where the sensitivities are largest), and also in the PES refitting efforts (errors between *ab initio* points and the fitted surface should be minimized in regions of largest sensitivities).

QFSA has been applied to 1-D [23(a)] and collinear [23–25] reactions, and to the inverse problem of obtaining a PES from scattering [26] or spectral [27] data. The latter calculations are based on an iterative procedure where the potential is systematically corrected until deviations between the predicted and the “target” observables are below some tolerance. These studies have shown that many if not an infinite number of PESs can accurately reproduce a finite number of experimental observables [27(b),28]. Therefore, there is no guarantee that the iterative procedure of refining and refitting the potential using QFSA as proposed here will eventually converge to the true PES. The direction of our effort is not simply to aid in obtaining an arbitrary PES which can reproduce the experimental observable but rather to obtain a PES which is *ab initio*-based—that is, to further the aforementioned goal of predicting experimental observables completely from first principles.

This article describes the sensitivity of state-to-state transition probabilities for the 3-dimensional  $H + H_2$  hydrogen exchange reaction at a total angular momentum  $J = 0$  to variations in the underlying PES. This is the first report of a QFSA application to a chemical reaction in 3-D. Sensitivities of the state-to-state transition probabilities are shown at several collision energies and comparisons are made to the sensitivities for the collinear  $H + H_2$  reaction. In this study, we investigate the similarities and differences in trends between the sensitivities for the collinear and 3-D reactions to determine what features of collinear sensitivities carry over to 3-D. We also help resolve some issues concerning visualizing data in many dimensions.

The quantum scattering of  $H$  with  $H_2$  is described by the formalism of the log-derivative Kohn variational method [29–31]. The salient features of applying QFSA within this scattering framework are:

- (1) All the necessary quantities for calculating sensitivities are readily obtained from the scattering calculation. The sensitivities can be obtained with approximately 20% more CPU time.
- (2) All the matrix elements of the Hamiltonian are energy independent. Hence, sensitivities can be obtained at several collision energies without recomputing the matrix elements.
- (3) The functional derivative of the scattering wave functions with respect to the PES need not be calculated.

The potential surface used in our studies is the Liu-Siegbahn-Gruhlar-Horowitz (LSTH) [20] surface.

The remainder of this article is organized as follows. The second section presents a summary of the theoretical and computational methodology. Our results and discussion are presented in the third section, and the fourth section concludes the article.

### Theoretical Method

The scattering of atom A with diatom BC is described quantum mechanically by the log-derivative Kohn variational method [29] as employed by Manolopoulos et al. [30,31], and the requisite equations for calculating the sensitivities are obtained by taking appropriate functional derivatives of the scattering (S) and log-derivative (Y) matrices with respect to the interaction potential. The mathematical development of the sensitivity equations for the 3-D  $A + BC$  reaction at zero total angular momentum is essentially the same as that of the collinear case [24] with the sole exception being that the internal vibrational functions are replaced by rovibrational functions. Thus, we shall provide only a summary here and direct the interested reader elsewhere [24] for additional details.

The scattering formalism uses the well-known mass-scaled Jacobi coordinates where the Hamiltonian ( $H$ ) can be written as

$$\begin{aligned}
 H = & -\frac{\hbar^2}{2\mu} \frac{1}{R_\gamma} \frac{\partial^2}{\partial R_\gamma^2} R_\gamma + h_\gamma + \frac{\hbar^2 \hat{l}_\gamma^2}{2\mu R_\gamma^2} + V_{\text{int}}(R_\gamma, r_\gamma, \theta_\gamma) \\
 h_\gamma = & -\frac{\hbar^2}{2\mu} \frac{1}{r_\gamma} \frac{\partial^2}{\partial r_\gamma^2} r_\gamma + \frac{\hbar^2 \hat{j}_\gamma^2}{2\mu r_\gamma^2} + V_\gamma(r_\gamma, \theta_\gamma).
 \end{aligned} \quad (1)$$

$R_\gamma$ ,  $r_\gamma$ , and  $\theta_\gamma$  are, respectively, the coordinate of the lone atom with respect to the center-of-mass of the diatom, the vibrational coordinate of the diatom, and the angle subtended by  $\hat{R}_\gamma$  and  $\hat{r}_\gamma$ , all in arrangement  $\gamma$ . The Hamiltonian of the isolated diatom is  $h_\gamma$ , and  $V_{\text{int}}$  is the interaction potential with respect to which the sensitivities are computed. Note that  $V_{\text{int}}$  is not the total potential, but we shall dispense with the int subscript in the functional derivatives for notational simplicity. The symbols  $\mu$ ,  $\hat{l}_\gamma$ ,  $\hat{j}_\gamma$ , and  $V_\gamma$  are defined in the usual manner.

The log-derivative wave function ( $\psi_{\gamma n}^L$ ) is expanded in a direct product basis of translational Lobatto-shape functions [30] ( $u_{\gamma l}$ ) and asymptotic rovibrational functions ( $\phi_{\gamma n}/r_\gamma$ ) in the three possible atom-diatom arrangements.

$$\begin{aligned} \psi_{\gamma'n'}^L = & \sum_{il} \frac{C_{ail}^{\gamma'n'}}{R_a r_a} u_{ai}(R_a) \phi_{ai}(r_a, \theta_a) + \sum_{jm} \frac{C_{bjm}^{\gamma'n'}}{R_b r_b} \mu_{bj}(R_b) \phi_{bm}(r_b, \theta_b) \\ & + \sum_{kn} \frac{C_{ckn}^{\gamma'n'}}{R_c r_c} u_{ck}(R_c) \phi_{cn}(r_c, \theta_c) \end{aligned} \quad (2)$$

subject to the boundary conditions

$$\psi_{\gamma n}^L(R_\gamma \rightarrow 0) = 0 \quad (3a)$$

and

$$\psi_{\gamma n}^L(R_\gamma \rightarrow R_\gamma^{\max}) = \frac{\phi_{\gamma n}(r_\gamma)}{R_\gamma^{\max} r_\gamma} \delta_{\gamma\gamma'} \quad (3b)$$

$R_\gamma^{\max}$  determines the bounding surface [31] separating the "interior" and "exterior" regions of the potential. It is the surface on which the interaction potential has sufficiently decayed to zero. For notational simplicity, we use the index  $n$  to represent the compound  $(v, j)$  vibrational-rotational indices of the internal rovibrational function.

One of the two computationally intensive steps in the calculation is the construction of the "stiffness" matrix,  $\mathbf{K}$ , defined by

$$\begin{aligned} \mathbf{K}_{\gamma m, \gamma' n} = & \int_{\text{interior region}} R_\gamma^2 r_\gamma^2 dR_\gamma dr_\gamma d(\cos \theta_\gamma) \frac{1}{R_\gamma R_\gamma' r_\gamma r_\gamma'} \\ & \times \left\{ \frac{\partial}{\partial R_\gamma} (u_{\gamma i} \phi_{\gamma m}) \frac{\partial}{\partial R_\gamma'} (u_{\gamma' j} \phi_{\gamma' n}) \right. \\ & \left. + \frac{2\mu}{\hbar^2} \left( u_{\gamma i} \phi_{\gamma m} \left( V_{\text{int}} + h_{\gamma'} + \frac{\hbar^2 l_\gamma^2}{2\mu R_\gamma^2} - E \right) u_{\gamma' j} \phi_{\gamma' n} \right) \right\}. \end{aligned} \quad (4)$$

Note that the total energy,  $E$ , appears only as a multiplicative factor in front of an overlap matrix. Hence, after the  $\mathbf{K}$ -matrix elements have been computed just once, the scattering problem can be solved for any number of collision energies (for which the chosen basis set is adequate) without recomputing the  $\mathbf{K}$ -matrix elements. Furthermore, the stiffness matrix is symmetric if the basis functions are ordered likewise in the rows and columns. In ordering the basis functions, the boundary Lobatto functions,  $u_{\gamma M_\gamma}$  ( $M_\gamma$  is the number of translational functions in arrangement  $\gamma$ ), are grouped together in the last rows and columns. With this grouping, the  $\mathbf{K}$ -matrix can be partitioned as

$$\mathbf{K} = \begin{bmatrix} \mathbf{K}_{11} & \mathbf{K}_{10} \\ \mathbf{K}_{01} & \mathbf{K}_{00} \end{bmatrix}, \quad (5)$$

where the subscript 0 refers to the sub-block of matrix elements containing  $u_{\gamma M_\gamma}$ . Thus, if  $N_\gamma$  rovibrational functions and  $M_\gamma$  translational functions are used to span



each arrangement  $\gamma$ , then  $\mathbf{K}_{10}$  is a large-by-small rectangular matrix of dimension  $[N_a(M_a - 1) + N_b(M_b - 1) + N_c(M_c - 1)] \otimes [N_a + N_b + N_c]$ , and  $\mathbf{K}_{00}$  is a small-by-small square matrix of dimension  $[N_a + N_b + N_c] \otimes [N_a + N_b + N_c]$ , etc.

The log-derivative matrix,  $\mathbf{Y}$ , whose elements are defined by the extremum of

$$\begin{aligned} Y_{\gamma n, \gamma' n'}|_{\text{boundary}} = & \int_{\text{interior region}} R_{\gamma'}^2 r_{\gamma'}^2 dR_{\gamma'} dr_{\gamma'} d(\cos \theta_{\gamma'}) \\ & \times \left\{ \frac{\partial}{\partial R_{\gamma'}} (\psi_{\gamma n}^L) \frac{\partial}{\partial R_{\gamma'}} (\psi_{\gamma' n'}^L) \right. \\ & \left. + \frac{2\mu}{\hbar^2} \left( \psi_{\gamma n}^L \left( V_{\text{int}} + h_{\gamma'} + \frac{\hbar^2 l_{\gamma'}^2}{2\mu R_{\gamma'}^2} - E \right) \psi_{\gamma' n'}^L \right) \right\} \quad (6) \end{aligned}$$

with respect to the log-derivative wave function, can be written in terms of the  $\mathbf{K}$ -matrix as

$$\mathbf{Y} = \mathbf{K}_{00} - \mathbf{K}_{01}(\mathbf{K}_{11})^{-1}\mathbf{K}_{10} \quad (7a)$$

$$= [\mathbf{K}^{-1}]_{00}^{-1}. \quad (7b)$$

The variationally determined log-derivative wave function expansion coefficients are

$$\mathbf{C} = -\mathbf{K}_{11}^{-1}\mathbf{K}_{10} = [\mathbf{K}^{-1}]_{10}\mathbf{Y} \quad \text{for the interior basis functions,}$$

and

$$\mathbf{C}_{\gamma M_{\gamma n}}^{\gamma' n'} = \delta_{\gamma \gamma'} \delta_{nn'} \quad \text{for the boundary functions.} \quad (8)$$

As Eqs. (7b) and (8) suggest, the second computationally intensive step is the solution of the system of equations  $\mathbf{K}\mathbf{X}_j = \mathbf{e}_j$ , where  $\mathbf{e}_j$  is a column vector with a one at position  $j$ . The solution  $\mathbf{X}_j$  is the  $j$ th column of  $\mathbf{K}^{-1}$ . According to Eq. (7b), one obtains  $\mathbf{Y}$  by letting  $j$  run over the last  $N_a + N_b + N_c$  positions of the unit vector  $\mathbf{e}$  (the positions corresponding to subscript 0 in the partitioning of  $\mathbf{K}$ ), storing the last  $N_a + N_b + N_c$  rows of  $\mathbf{X}_j$ , and then inverting the resultant small-by-small matrix  $[\mathbf{K}^{-1}]_{00}$ . To calculate sensitivities, one also needs to store the other rows of the already computed  $\mathbf{X}_j$ . This is the large-by-small rectangular matrix  $[\mathbf{K}^{-1}]_{10}$ , from which one obtains the log-derivative wave function coefficients by multiplication with  $\mathbf{Y}$ . The log-derivative wave functions play an integral part in the calculation of sensitivities [see Eq. (11)].

The remaining steps of the calculation involve only small-by-small matrices. The scattering matrix,  $\mathbf{S}$ , is related to  $\mathbf{Y}$  via

$$\mathbf{S} = \mathbf{a} + 2i\mathbf{b}[\mathbf{Y} - \mathbf{c}]^{-1}\mathbf{b} \quad (9)$$

where  $\mathbf{a}$ ,  $\mathbf{b}$ , and  $\mathbf{c}$  are diagonal matrices related to the incoming ( $I_{\gamma n}$ ) and outgoing ( $O_{\gamma n}$ ) waves

$$I_{\gamma n} = k_{\gamma n}^{-1/2} \hat{h}_{l_{\gamma}}^2(k_{\gamma n} R_{\gamma}),$$

$$O_{\gamma n} = K_{\gamma n}^{-1/2} \hat{h}_{l_{\gamma}}^{(1)}(k_{\gamma n} R_{\gamma}),$$

with  $k_{\gamma n} = \sqrt{2\mu(E - \epsilon_{\gamma n})/\hbar^2}$ , by

$$\begin{aligned} a_{\gamma n, \gamma n} &= I_{\gamma n} O_{\gamma n}^{-1}, \\ b_{\gamma n, \gamma n} &= O_{\gamma n}^{-1}, \\ \text{and } c_{\gamma n, \gamma n} &= O'_{\gamma n} O_{\gamma n}^{-1}, \end{aligned} \quad (10)$$

all evaluated at  $R_\gamma = R_\gamma^{\max}$ .  $\hat{h}_\gamma^{(1,2)}$  are the Riccati-Hankel functions as defined by Calogero [32], and  $\epsilon_{\gamma n}$  is the internal rovibrational energy of state  $\gamma n$ . The functional derivative of the transition probability with respect to the interaction potential is [24]

$$\begin{aligned} \frac{\delta P_{\gamma' n' \leftarrow \gamma n}}{\delta V(R_\gamma, r_\gamma, \theta_\gamma)} &= 2 \operatorname{Re} \left\{ S_{\gamma' n' \leftarrow \gamma n}^* \frac{\delta S_{\gamma' n' \leftarrow \gamma n}}{\delta V(R_\gamma, r_\gamma, \theta_\gamma)} \right\} \\ &= \frac{8\mu}{\hbar^2} \operatorname{Im} \left\{ S_{\gamma' n' \leftarrow \gamma n}^* \left( b_{\gamma' n', \gamma' n'} \sum_{\gamma'' n''} [Y - c]_{\gamma' n', \gamma'' n''}^{-1} \psi_{\gamma'' n''}^L \right) \right. \\ &\quad \left. \times \left( b_{\gamma n, \gamma n} \sum_{\gamma'' n''} [Y - c]_{\gamma n, \gamma'' n''}^{-1} \psi_{\gamma'' n''}^L \right) \right\}. \end{aligned} \quad (11)$$

Finally, a simple interpretation of the transition probability sensitivities in terms of a product of two scattering wave functions,

$$\frac{\delta P_{\gamma' n' \leftarrow \gamma n}}{\delta V(R_\gamma, r_\gamma, \theta_\gamma)} = -\frac{2\mu}{\hbar^2} \operatorname{Im} \{ S_{\gamma' n' \leftarrow \gamma n}^* \psi_{\gamma' n'}^S \psi_{\gamma n}^S \}, \quad (12)$$

can be obtained by relating the log-derivative wave function ( $\psi_{\gamma n}^L$ ) to the normal scattering wave functions ( $\psi_{\gamma n}^S$ ) which satisfy the boundary conditions [24]

$$\psi_{\gamma n}^S(R_\gamma \rightarrow \infty) = \frac{I_{\gamma n}(R_\gamma) \phi_{\gamma n}}{R_\gamma r_\gamma} \delta_{\gamma \gamma'} - \sum_{\gamma' n'} S_{\gamma' n' \leftarrow \gamma n} \frac{O_{\gamma' n'}(R_\gamma) \phi_{\gamma' n'}}{R_\gamma r_{\gamma'}} \delta_{\gamma' \gamma''}. \quad (13)$$

In our calculations, we used three-identical particle symmetry [2(b),33] to reduce the size of our  $\mathbf{K}$ -matrix by a factor of three. The size of our basis ranged from  $M = 30$  translational Lobatto functions and  $N = 30$  rovibrational functions (for each arrangement) in the lower energy regime to  $M = N = 40$  in the higher energy regime. The values of all the other parameters are the same as those employed by Manolopoulos and Wyatt [30]. For a single energy slice with  $M = N = 30$  on a Cray-2, the calculation through setting up the  $\mathbf{K}$ -matrix took 10 s, and the calculation of reaction probabilities took another 15 s. The sensitivity calculation on a 55-by-45 grid of points took an additional 9 s. For  $M = N = 40$ , these three times are 30, 74, and 22 s, respectively. To verify the accuracy of the sensitivity predictions and ferret out any programming bugs, we did the usual check [24] of placing small bumps on the potential and comparing the predicted with the actual change in transition probabilities.

## Results and Discussion

As we mentioned in the Introduction, this is the first article on a QFSA application to a chemical reaction in 3-D. One of the issues that concerned us was how to display and analyze the multidimensional sensitivity data and be assured that we

have not missed any important features.  $\delta P/\delta V$  is a function of the coordinates  $R$ ,  $r$ , and  $\theta$ , as well as the total energy,  $E$ . The other issue was how the sensitivities for the 3-D  $H + H_2$  reaction compared with those from the collinear calculation. In order to acquire a sense of the evolution of sensitivity structure in the energy range 0.50 to 1.50 eV, we calculated reactive transition probability sensitivities at 200+ energy slices for transitions from  $(v = 0, j = 0)$  to  $(v', j') = (0, 0)$ ,  $(0, 1)$ ,  $(0, 2)$ , and also calculated the cumulative sensitivities for transitions from  $(0, 0)$  to all open product states ( $\sum_{v', j' \text{ open}} \delta P_{v', j' \leftarrow 00}/\delta V$ ). These sensitivities were displayed as contour maps and saved onto videotape. In order to facilitate a comparison with the collinear  $H + H_2$  sensitivities and because the largest sensitivities occurred when the  $H_3$  system passed through collinear configurations, most of the analysis was done at  $\theta = 180^\circ$ . An analysis of each set of sensitivity structure is presented in the four subsections below followed by a discussion of sensitivity structure at other scattering angles. We consider only reactive transitions, so for notational convenience we omit the arrangement indices. Figure 1 shows the transition probability from  $(v = 0, j = 0)$  to  $(v', j') = (0, 0)$ ,  $(0, 1)$ ,  $(0, 2)$ , and the cumulative transition probability to all open product states. It provides a guide to the discussion of sensitivity structure in different energy regimes.

*Sensitivities for Transitions from  $v = 0, j = 0$  to  $v' = 0, j' = 0$  ( $\theta = 180^\circ$ )*

For the 3-D  $J = 0$   $H + H_2$  reaction, the evolution of the  $\delta P_{00 \leftarrow 00}/\delta V$  sensitivity structure in the threshold region (0.55 to 0.64 eV) is very similar to the collinear

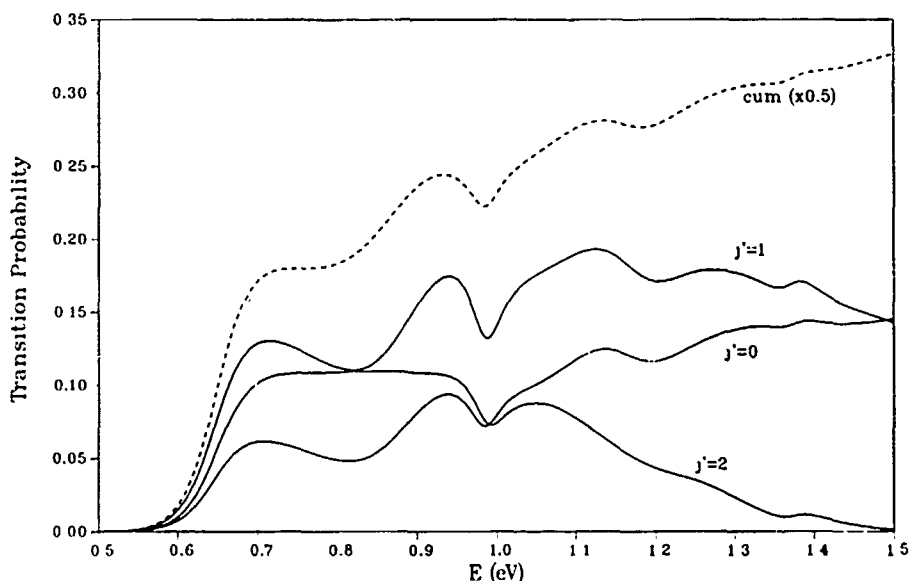


Figure 1. Reactive state-to-state transition probabilities from  $v = 0, j = 0$  to  $v' = 0, j'$ . The cumulative transition probability from  $v = 0, j = 0$  to all open product states has been multiplied by a factor of 0.5 before plotting as a dashed line.

case (see Refs. [23(a)], [24]). There is a large region of negative sensitivity near the saddle point of the potential energy surface (PES). The most negative regions start out on the two shoulders of the barrier and lie slightly toward the inner corner\* where tunneling is important. These locations correspond roughly to the classical turning points along the vibrationally adiabatic reaction path. As the energy increases, the two negative sensitivity regions coalesce to a single extremum near the top of the barrier. Unlike the collinear sensitivities, the magnitudes of these sensitivities are relatively small compared to those at higher energy regimes.

The 0.67 eV energy slice of Figure 2 shows the sensitivities just beyond the threshold region. The negative sensitivity lobe in the saddle point region has decreased in both extent and magnitude, and the magnitudes of the positive shoulders have increased. With increasing energy, the positive shoulders grow, become more prominent, and move towards the barrier top where they coalesce in the inner corner of the PES and eventually displace the negative sensitivities at the barrier top. Figure 2(b) shows an energy slice at the end of this sequence.

From 0.82 to 0.98 eV (resonance energy), a similar pattern is repeated twice. First, the negative shoulders grow, move towards the barrier top and coalesce in the inner corner. The positive sensitivities at the barrier top are not displaced though, but are pushed out to the outer corner. Second, the more distant positive shoulders begin to grow, move towards the barrier top, and coalesce in the inner corner. Figure 2(c) shows an energy slice in the resonance region. The positive shoulders have coalesced with each other, and together with the positive lobe at the outer corner they form a large region of positive sensitivity near the PES saddle point. Of the 200+ energy slices investigated, the  $\delta P_{00-00}/\delta V$  sensitivities attain their maximum positive values at this resonance energy. Unlike the behavior of the collinear sensitivities [24], the 3-D sensitivities do not change much over the resonance zone. The largest sensitivity regions do not flip in sign as the energy increases beyond the resonance, and the magnitudes, though largest at the resonance energy, are not an order of magnitude greater than those at neighboring energy slices as was the case for the collinear sensitivities. The shape of the sensitivity structure at this resonance energy implies that a narrowing of the passage across the barrier will increase the transition probability and reduce the resonance feature (see Fig. 1). Conversely, if the PES is decreased at the inner and outer corners, the symmetric stretch frequency will decrease and the resonance feature will be enhanced.

At higher energies [see Figs. 2(d)–2(f)], the pattern seen at lower energies repeats itself. The sensitivities at the shoulder grow in magnitude and move towards each other eventually coalescing at the inner corner of the PES. Each time the shoulders coalesce though, they cut further into the inner corner. In the meantime, the sensitivities near the barrier top decrease in magnitude. The result is that the extrema

\* For semantic purposes, the definitions of the inner (outer) corner and shoulder regions of the potential are as follows. The inner (outer) corner of the potential refers to the region on the upper wall of the saddle point where the  $H_3$  conformation is less (more) compact than the conformation at the top of the barrier. The shoulder regions refer to the two opposite locations about halfway down the barrier along the minimum energy path.

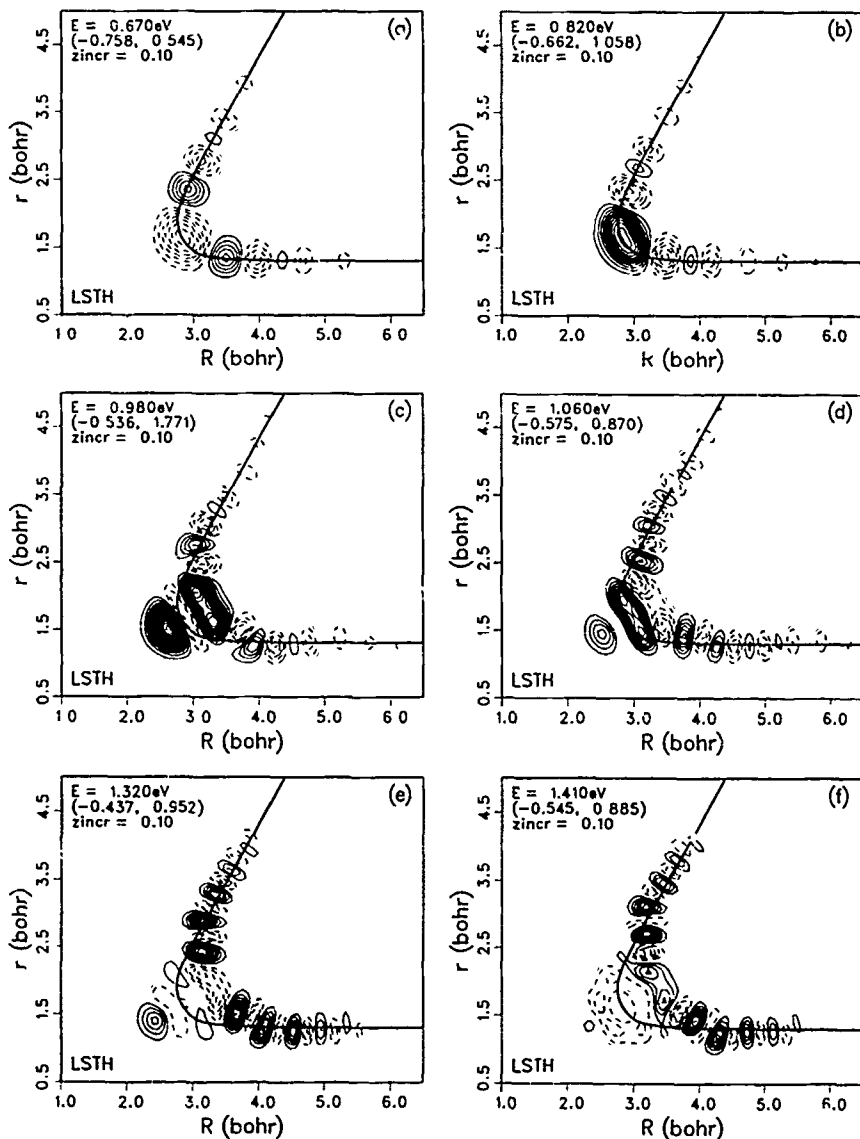
Sensitivities for  $v=0, j=0$  to  $v'=0, j'=0$ 

Figure 2. Sensitivity maps for transitions from  $v = 0, j = 0$  to  $v' = 0, j' = 0$  at  $\theta = 180^\circ$ . The contour values are drawn in increments of  $\text{zincr}$  shown on the plots. Positive contours are represented by solid lines and negative contours by dashed lines. The zero contour line is omitted. The numbers in parentheses represent the minimum and maximum sensitivity values on an  $80 \times 65$  grid. All sensitivity contour values are given in units of  $\text{eV}^{-1} \text{bohr}^{-2}$ . Also shown on the plots (solid heavy line) is the steepest-descent path (in mass-scaled Jacobi coordinates) from the top of the barrier

of the sensitivity peaks trace out a path that significantly cuts the inner corner of the PES and is removed from the reaction path. In fact, the region of the PES followed by the reaction path across the barrier is important only for a small energy regime just beyond the threshold energies. Only Figures 2(a) and 2(b) have extrema that directly fall on the reaction path.

Lastly, we note that at higher energies, the sensitivities in the tail regions, though oscillatory in nature, are predominantly more positive than negative. The sensitivity structures in these tail regions also do not change appreciably with energy.

*Sensitivities for Transitions from  $v = 0, j = 0$  to  $v' = 0, j' = 1$  ( $\theta = 180^\circ$ )*

Figure 3 shows the  $\delta P_{01 \leftarrow 00} / \delta V$  sensitivities at the same energy slices as shown in Figure 2. These sensitivities are nonsymmetric about the symmetric stretch line because they are composed from the product of two different scattering wave functions [see Eq. (12)]—one with an incoming wave in channel  $v = 0, j = 0$  on the reactant side (lower right-hand side in the figures), and the other with an incoming wave in channel  $v' = 0, j' = 1$  on the product side. Below the resonance energy (0.98 eV), the sensitivities bear an uncanny resemblance to those of  $\delta P_{00 \leftarrow 00} / \delta V$ , with the exception that the magnitudes are almost exactly a factor of 2 greater, and the sensitivities are slightly larger on the reactant side. Incidentally, the transition probabilities themselves are almost exactly a factor of 2 greater than  $P_{00 \leftarrow 00}$  for energies below the first resonance (see Fig. 1).

Above the resonance energy, the lack of symmetry in the sensitivities becomes more distinct. The positive sensitivity in the transition state region becomes more heavily weighted on the product side, eventually joining with the asymptotic positive lobes on the product valley. Thus, from 1.10 to 1.50 eV, the sensitivities on the product side are almost completely positive. On the reactant side, the sensitivities above the resonance energy continue to be oscillatory with very little change in structure. The extrema of the sensitivity peaks and valleys follow a path that closely resembles the  $v = 0, j = 0 \rightarrow v' = 0, j' = 0$  case. The sensitivities in the two shoulder regions grow and coalesce in the inner corner and away from the reaction path. On the outer corner of the PES, the large positive lobe at the resonance energy decays with increasing energy and a region of negative sensitivity grows in its stead. The magnitudes of these negative sensitivities are small compared to the extrema that cut into the inner corner, so again the region of the PES followed by the reaction path across the transition state is of secondary importance in affecting the dynamics at these higher energies.

*Sensitivities for Transitions from  $v = 0, j = 0$  to  $v' = 0, j' = 2$  ( $\theta = 180^\circ$ )*

Figure 4 shows the sensitivities for transitions from  $v = 0, j = 0$  to  $v' = 0, j' = 2$ . Like the two previous sets, the  $\delta P_{02 \leftarrow 00} / \delta V$  sensitivities are negative and relatively small in the threshold region. Of the two negative peaks at the classical turning points, the product side has a larger negative sensitivity until about 0.63 eV. Then, the larger sensitivity region shifts over to the reactant side. The positive shoulder on the reactant side grows, becomes more prominent, and moves towards the tran-

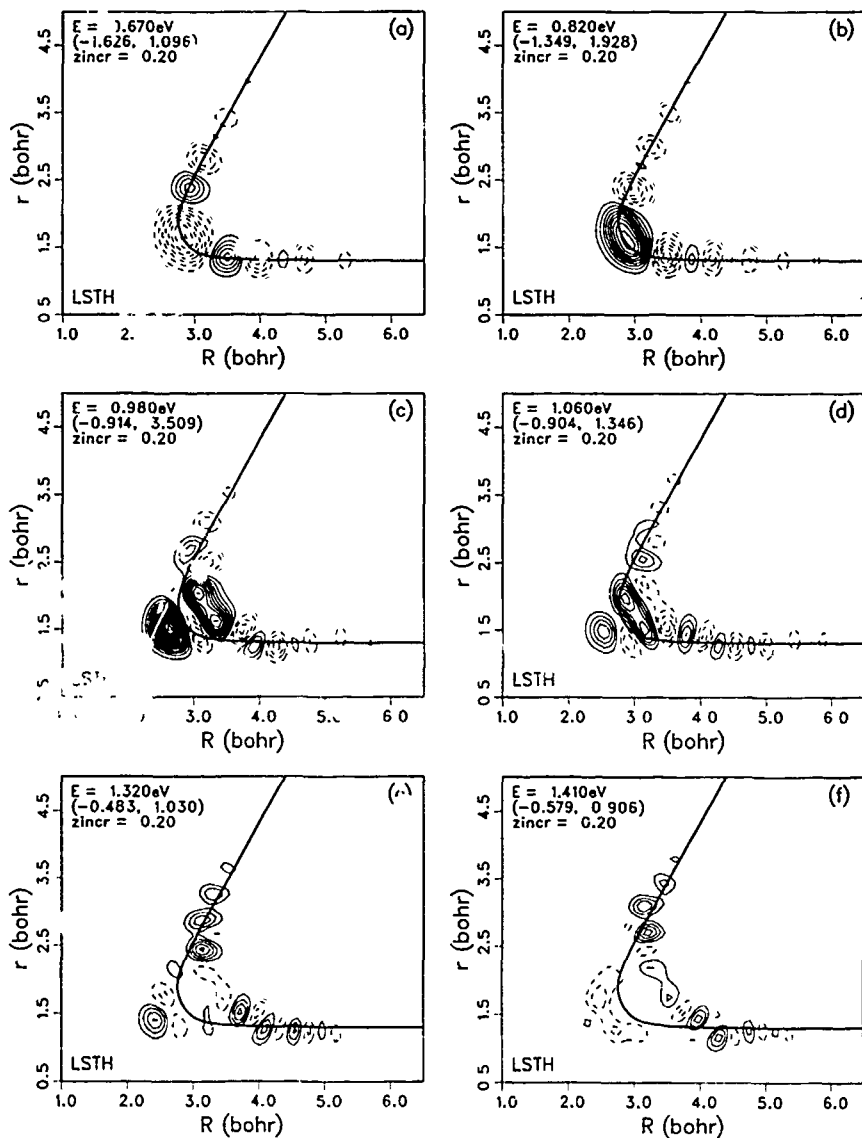
Sensitivities for  $v=0, j=0$  to  $v'=0, j'=1$ 

Figure 3. Sensitivity maps for transitions from  $v = 0, j = 0$  to  $v' = 0, j' = 1$  at  $\theta = 180^\circ$ . The details of the contour lines are the same as in Figure 2. The reactant arrangement is on the lower right branch.

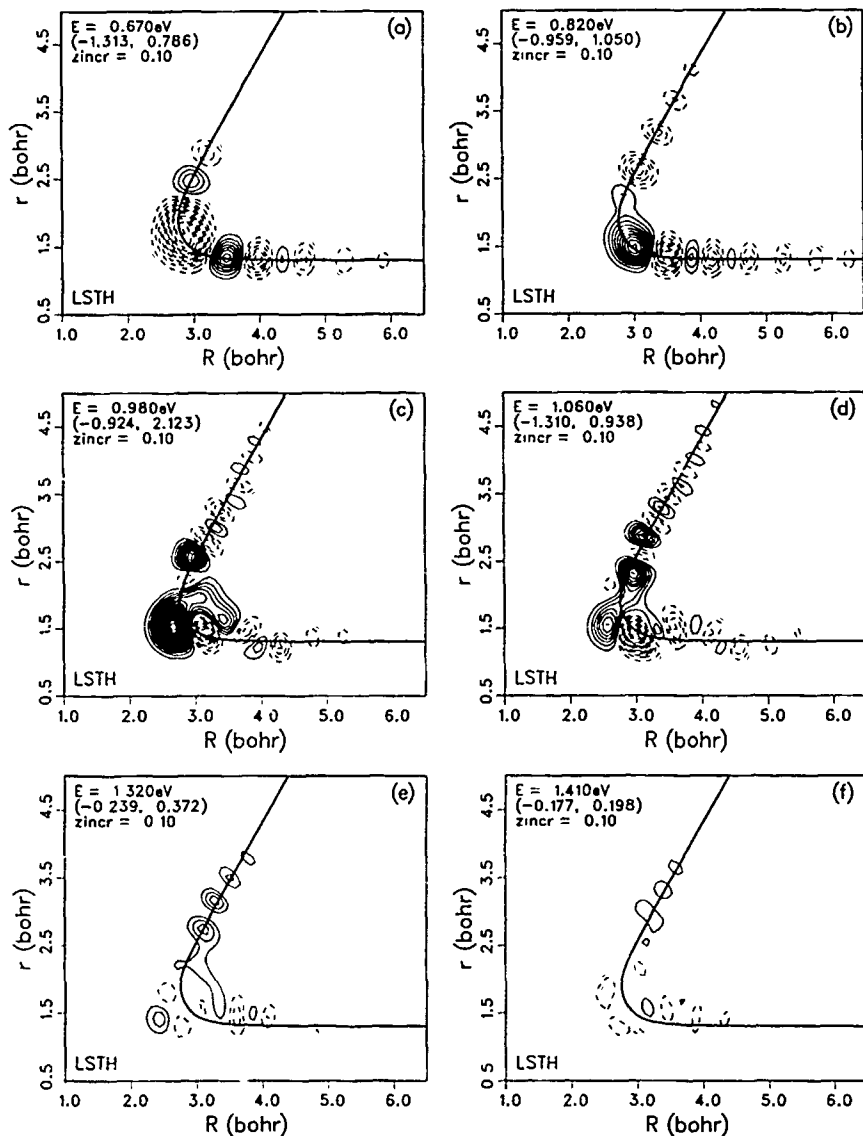
Sensitivities for  $v=0, j=0$  to  $v'=0, j'=2$ 

Figure 4 Sensitivity maps for transitions from  $v = 0, j = 0$  to  $v' = 0, j' = 2$  at  $\theta = 180^\circ$ . The details of the contour lines are the same as in Figure 2.



sition state alone to displace the decaying negative transition state lobe. Unlike the two previous sets, the evolution of sensitivity structure does not involve growth and coalescence of sensitivity shoulders and there is no substantial growth of sensitivity in the inner corner. The region of largest sensitivity from about 0.70 to 1.04 eV (a large energy range) is a positive-negative dyad which moves from the  $3.2 < R < 4.1$  bohr region to the  $2.3 < R < 3.4$  bohr region of the reactant arrangement. Figures 4(b) and 4(c) show two energy slices in this sequence. The magnitude of the positive sensitivities peaks at about 0.985 eV in the resonance zone.

Beyond the resonance energy, there is a growth of positive sensitivity on the product side and negative sensitivity on the reactant side, and this persists until about 1.42 eV after which the sensitivity magnitudes decay through the end of our investigated energy range. This decay is presumably due to the decaying S-matrix element. Lastly, we note in agreement with previous cases, the transition state region has very small sensitivities at the higher energies.

*Cumulative Sensitivities for Transitions from  $v = 0, j = 0$  to all Open Product Channels ( $\theta = 180^\circ$ )*

The cumulative transition probability sensitivities are obtained by summing the individual  $\delta P_{v',j' \leftarrow 00} / \delta V$  sensitivities over all open product channels in one arrangement. The number of open product channels range from 6 ( $v' = 0, j' = 0, \dots, 5$ ) at 0.50 eV to 31 ( $v' = 0, j' = 0, \dots, 13; v' = 1, j' = 0, \dots, 10; v' = 2, j' = 0, \dots, 5$ ) at 1.50 eV. Figure 5 shows the cumulative sensitivity map at the same six energy slices shown on previous figures.

At the lower energies from the threshold to about 0.86 eV, all the large sensitivity regions lie exclusively in the product arrangement with negligible sensitivity in the reactant arrangement. This result is certainly counter-intuitive but can be understood by considering the overlap of scattering wave functions as given by Eq. (12). The sensitivities for a transition from  $v = 0, j = 0$  to an excited ( $v', j'$ ) state which has just become energetically accessible is composed of (1) a wave function  $\psi_{00}^S$  with incoming wave from the reactant arrangement and which has sufficient translational energy to cross the barrier, and (2) a wave function  $\psi_{v',j'}^S$ , with incoming wave from the product arrangement and which does not have sufficient energy to cross the barrier into the reactant side (because most of its energy is tied up in internal vibrational-rotational motion). Consequently, these two wave functions have significant overlap only in the product arrangement. Figure 6 shows an example of this trait for the  $(0, 0) \rightarrow (0, 4)$  transition at 0.67 eV. The sensitivities, as shown in Figure 6(a), lie predominantly in the product region. The norms of the two scattering wave functions are shown in Figs. 6(b) and 6(c).

Above 0.86 eV, a region of positive sensitivity just to the reactant side of the barrier begins to grow in magnitude but stays almost stationary in configuration space. The large region of negative sensitivity around the barrier top reaches its extremum value at ca. 0.88 eV and then decays by flowing into the inner corner and asymptotic product regions. The positive peak at about  $(R, r) = (3.0, 1.4)$

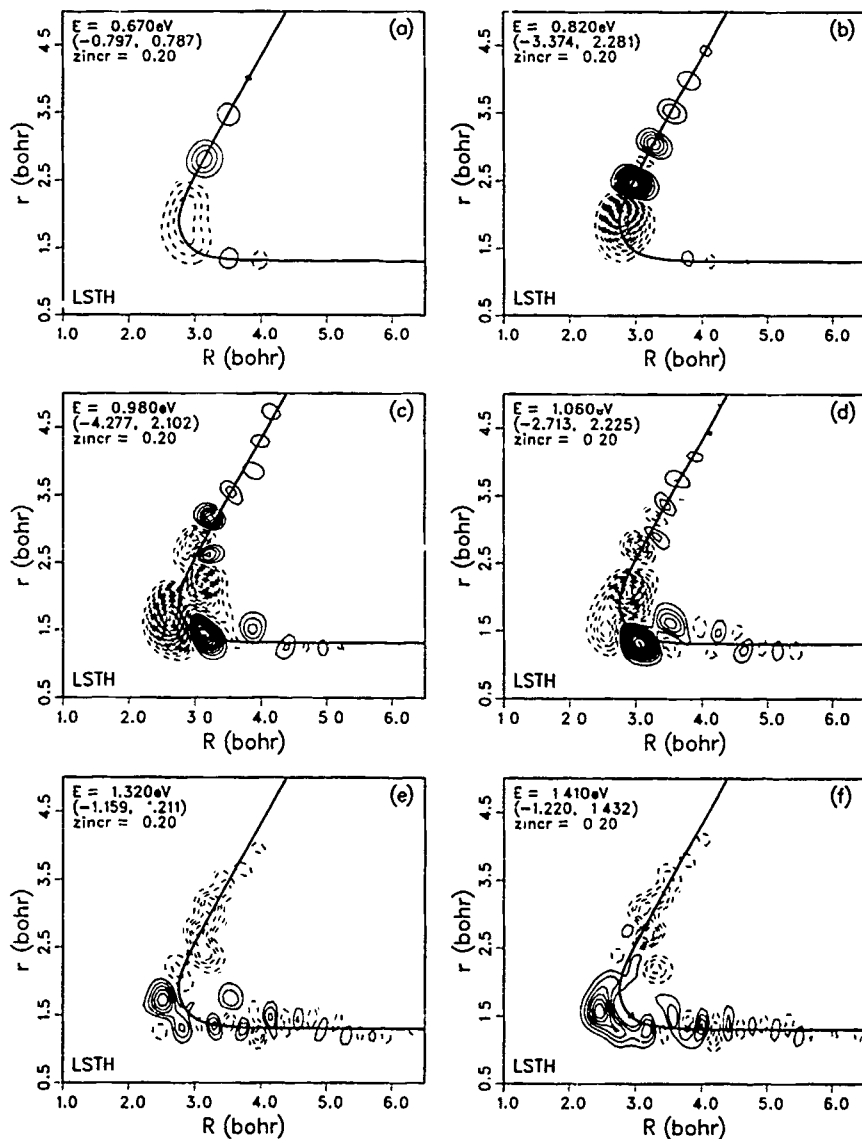
Sensitivities for  $v=0, j=0$  to all open states

Figure 5. Cumulative sensitivity maps (at  $\theta = 180^\circ$ ) for transitions from  $v = 0, j = 0$  to all open product channels. The details of the contour lines are the same as in Figure 2.

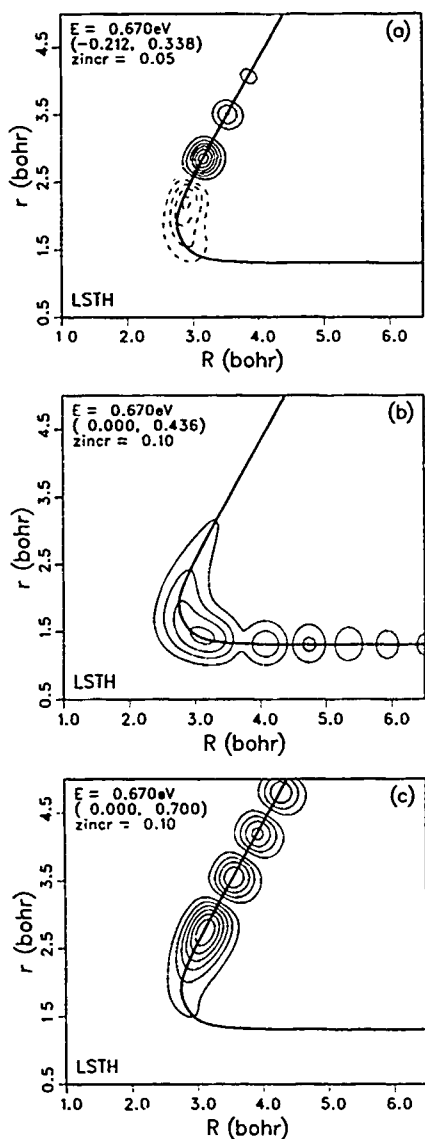


Figure 6. (a) Sensitivity map for the  $v = 0, j = 0 \rightarrow v' = 0, j' = 4$  transition at  $\theta = 180^\circ$ . The details of the contour lines are the same as in Figure 2; (b) norm of the  $\psi_{00}^S$  wave function with incoming wave from the reactant side; (c) norm of the  $\psi_{04}^S$  wave function with incoming wave from the product side. The contour values on the wave functions are given in units of  $\text{bohr}^{-2}$ .

bohrs grows to a maximum at ca. 1.01 eV and then decays as it moves to the outer corner region. It is interesting to note that the product arrangement, which starts out with predominantly positive sensitivities at lower energies, eventually evolves to predominantly negative sensitivities at the higher energies.

### *Sensitivities at Other Scattering Angles*

The reaction barrier for the  $\text{H} + \text{H}_2$  reaction is smallest at collinear geometries and increases rapidly by more than a factor of six as the scattering angle subtended by  $\hat{\mathbf{R}}$  and  $\hat{\mathbf{r}}$  sweeps from  $180^\circ$  to  $90^\circ$ . It is, therefore, not surprising to find that both the magnitudes of the wave functions and of the sensitivities decrease dramatically as the  $\text{H}_3$  geometry moves away from collinear. Because of space constraints, we do not show any sensitivity maps at other scattering angles but provide a discussion of some general trends. We note that sensitivities in different regions of the  $(R, r)$  configuration space decay at different rates as  $\theta$  moves away from  $180^\circ$ . The sensitivities in the outer corner of the PES tend to persist longer than those at either the inner corner or at the asymptotic regions. It is not uncommon to find the sensitivity magnitudes at these outer corners increase slightly before they

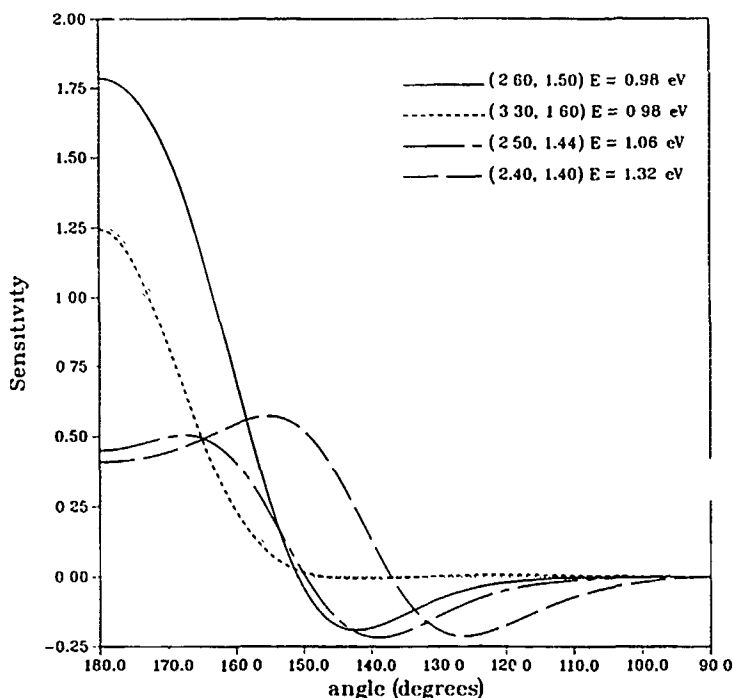


Figure 7. Sensitivities of the  $v = 0, j = 0 \rightarrow v' = 0, j' = 0$  transition at fixed  $(R, r)$  configurations as a function of scattering angle and total energy.

decay. Figure 7 shows some of these trends for the  $\delta P_{0, \infty \rightarrow 00} / \delta V$  sensitivities at select  $(R, r)$  points in configuration space and at different energies.

At 0.98 eV, two points were chosen—one on the outer corner at (2.60, 1.50) bohrs, and the other on the inner corner at (3.30, 1.60) bohrs. Both points correspond to extrema of their respective sensitivity peaks [see Fig. 2(c)]. The sensitivity at the outer corner decays more slowly and goes through a negative extremum at about  $142^\circ$  whereas the inner corner dies out at about  $150^\circ$ . Two other points chosen at the outer corner and at higher energies actually have sensitivity magnitudes increase as  $\theta$  moves away from  $180^\circ$  before they eventually decay. This is not surprising in view of Figures 2 to 5 where regions of large sensitivities at the higher collision energies were seen to move away from the minimum energy path. The cases considered here are somewhat different though as the  $(R, r)$  configurations which do have large sensitivities at bent geometries are confined to the outer corner region of the potential.

### Concluding Remarks

We have investigated the sensitivities of state-to-state transition probabilities for the 3-D  $J = 0$   $\text{H} + \text{H}_2$  reaction at several energies between 0.50 and 1.50 eV. The particular transitions investigated are the reactive ones starting from  $(v = 0, j = 0)$  to  $(v', j') = (0, 0)$ ,  $(0, 1)$ ,  $(0, 2)$ , and the cumulative transition from  $(0, 0)$  to all open channels. Each one has their own interesting sensitivity structure. For the  $(0, 0) \rightarrow (0, 0)$  and  $(0, 0) \rightarrow (0, 1)$  transitions, we find great similarity in the evolution of their sensitivity structure (for  $\theta = 180^\circ$ ) over the whole energy range. It was surprising to find large sensitivity regions localized in the inner corner of the potential at the higher collision energies. These regions of large sensitivities should be interpreted carefully. It is well known that at higher energies, the dynamics can explore regions of configuration space far removed from the minimum energy path. Interpretation of the sensitivities reveals that not only does the dynamics explore the inner corner region, but that the "fraction" of the dynamics which does the exploring—no matter how large or small—will be sufficiently distorted by inaccuracies in the PES at the inner corner, that the "complete" dynamics will be distorted *the most* by inaccuracies from this region. The sensitivities say nothing about whether the dynamics "prefers" to go over the top of the barrier or cut the corner.

Another caution with regard to interpreting the sensitivities concerns the asymptotic regions. Although the sensitivities appear to be smaller in the asymptotic regions, a given potential perturbation placed in the asymptote could have the same perturbative effect on the transition probabilities as if the same perturbation were placed closer to the shoulder region. This is because the Jacobian factor  $R^2 r^2$  in the integral

$$\delta P = \int \frac{\delta P}{\delta V(R, r, \theta)} \delta V(R, r, \theta) R^2 r^2 dR dr d(\cos \theta)$$

could compensate for the smaller sensitivity magnitudes. However, we expect that most potential variations contemplated for the asymptotic region would be rather

broad (with respect to  $R$ ) so that the oscillatory nature of the sensitivities in the asymptotic region would tend to cancel out contributions from neighboring regions and diminish the perturbative effect on the observable.

Among the other regions of high sensitivity found in our study, the most notable is the outer corner of the potential for bent geometries. This is the region where the  $H_3$  molecular conformation is more compact than the conformation at the barrier top. The sensitivity magnitudes tend to decay as the geometry becomes more bent, but the sensitivities at the outer corner region tend to decay slower with scattering angle and may, in fact, increase (for some noncollinear geometries) before they decay.

Lastly, we note that the 3-D sensitivities do not change in structure as rapidly with increasing energy as did the collinear sensitivities studied earlier [24]. This is particularly encouraging as the simpler/slower evolution in sensitivity structure means a greater promise for QFSA-aided PES refinement.

### Acknowledgments

This work was supported by the Director, Office of Energy Research, Office of Basic Energy Sciences, Chemical Sciences Division of the U.S. Department of Energy, under Contract No. DE-AC03-76SF00098.

### Bibliography

- [1] S. Borman, C&E News (June 4, 1990) p. 32.
- [2] (a) J. Z. H. Zhang and W. H. Miller, Chem. Phys. Lett. **153**, 465 (1988); (b) J. Z. H. Zhang and W. H. Miller, J. Chem. Phys. **91**, 1528 (1989); (c) W. H. Miller, Ann. Rev. Phys. Chem. **41**, 245 (1990).
- [3] (a) D. E. Manolopoulos and R. E. Wyatt, Chem. Phys. Lett. **159**, 23 (1989); (b) D. E. Manolopoulos and R. E. Wyatt, J. Chem. Phys. **92**, 810 (1990).
- [4] J. M. Launay and M. LeDourneuf, Chem. Phys. Lett. **163**, 178 (1989).
- [5] N. C. Blais and D. G. Truhlar, Chem. Phys. Lett. **102**, 120 (1983); **162**, 503 (1989).
- [6] (a) M. Mladenovic, M. Zhao, D. G. Truhlar, D. W. Schwenke, Y. Sun, and D. J. Kouri, J. Phys. Chem. **92**, 7035 (1988); (b) M. Zhao, D. G. Truhlar, D. W. Schwenke, and D. J. Kouri, J. Phys. Chem. **94**, 7074 (1990).
- [7] M. D'Mello, D. E. Manolopoulos, and R. E. Wyatt, J. Chem. Phys. **94**, 5985 (1991).
- [8] (a) N. C. Blais, M. Zhao, D. G. Truhlar, D. W. Schwenke, and D. J. Kouri, Chem. Phys. Lett. **166**, 11 (1990); **188**, 368E (1992); (b) S. L. Mielke, R. S. Friedman, D. G. Truhlar, and D. W. Schwenke, Chem. Phys. Lett. **188**, 359 (1992).
- [9] W. J. Keogh, A. I. Boothroyd, P. G. Martin, S. L. Mielke, D. G. Truhlar, and D. W. Schwenke, Chem. Phys. Lett. **195**, 144 (1992).
- [10] F. J. Aoiz, V. J. Herrero, O. Puenteodura, and V. S. Rábanos, Chem. Phys. Lett. **198**, 321 (1992).
- [11] D. Neuhauser, R. S. Judson, D. J. Kouri, D. E. Adelman, N. E. Shafer, D. A. V. Kliner, and R. N. Zare, Science **257**, 519 (1992).
- [12] Y.-S. M. Wu and A. Kuppermann, Chem. Phys. Lett. **201**, 178 (1993).
- [13] (a) D. P. Gerrity and J. J. Valentini, J. Chem. Phys. **79**, 5202 (1983); **81**, 1298 (1984); **82**, 1323 (1985); (b) D. K. Veirs, G. M. Rosenblatt, and J. J. Valentini, J. Chem. Phys. **83**, 1605 (1985); (c) H. B. Levene, D. L. Phillips, J.-C. Nieh, D. P. Gerrity, and J. J. Valentini, Chem. Phys. Lett. **143**, 317 (1988).
- [14] G. W. Johnston, B. Katz, K. Tsukiyama, and R. Bersohn, J. Chem. Phys. **91**, 5445 (1987).

- [15] (a) R. Gotting, V. Herrero, J. P. Toennies, and M. Vodegel, *Chem. Phys. Lett.* **137**, 524 (1987); (b) H. Buchenau, J. P. Toennies, J. Arnold, and J. Wolfrum, *Ber. Bunsenges. Phys. Chem.* **94**, 1231 (1990).
- [16] (a) D. A. V. Kliner and R. N. Zare, *J. Chem. Phys.* **92**, 2107 (1990); (b) D. A. V. Kliner, K.-D. Rinnen, and R. N. Zare, *Chem. Phys. Lett.* **166**, 107 (1990); (c) D. A. V. Kliner, D. E. Adelman, and R. N. Zare, *J. Chem. Phys.* **94**, 1069 (1991); **95**, 1648 (1991); (d) D. E. Adelman, N. E. Shafer, D. A. V. Kliner, and R. N. Zare, *J. Chem. Phys.* **97**, 7323 (1992).
- [17] (a) R. S. Blake, K.-D. Rinnen, D. A. V. Kliner, and R. N. Zare, *Chem. Phys. Lett.* **153**, 365 (1988); (b) K.-D. Rinnen, D. A. V. Kliner, R. S. Blake, and R. N. Zare, *Chem. Phys. Lett.* **153**, 371 (1988); (c) K.-D. Rinnen, D. A. V. Kliner, and R. N. Zare, *J. Chem. Phys.* **91**, 7514 (1989).
- [18] (a) S. A. Buntin, C. F. Giese, and W. R. Gentry, *J. Chem. Phys.* **87**, 1443 (1987); (b) S. A. Buntin, C. F. Giese, and W. R. Gentry, *Chem. Phys. Lett.* **168**, 513 (1990).
- [19] R. E. Continetti, B. A. Balko, and Y. T. Lee, *J. Chem. Phys.* **93**, 5719 (1990).
- [20] (a) B. Liu, *J. Chem. Phys.* **58**, 1925 (1973); (b) P. Siegbahn and B. Liu, *J. Chem. Phys.* **68**, 2457 (1978); (c) D. G. Truhlar and C. J. Horowitz, *J. Chem. Phys.* **68**, 2466 (1978); **71**, 1514 (1979).
- [21] A. J. C. Varandas, F. B. Brown, C. A. Mead, D. G. Truhlar, and N. C. Blais, *J. Chem. Phys.* **86**, 6258 (1987).
- [22] A. I. Boothroyd, W. J. Keogh, P. G. Martin, and M. R. Peterson, *J. Chem. Phys.* **95**, 4343 (1991).
- [23] (a) S. Shi and H. Rabitz, *J. Chem. Phys.* **86**, 6190 (1987); (b) S. Shi and H. Rabitz, *Comp. Phys. Rep.* **10**, 1 (1989).
- [24] J. Chang, N. J. Brown, M. D'Mello, R. E. Wyatt, and H. Rabitz, *J. Chem. Phys.* **97**, 6226 (1992).
- [25] (a) J. Chang, N. J. Brown, M. D'Mello, R. E. Wyatt, and H. Rabitz, *J. Chem. Phys.* **96**, 3523 (1992); (b) J. Chang, N. J. Brown, M. D'Mello, R. E. Wyatt, and H. Rabitz, *J. Chem. Phys.* **97**, 6240 (1992).
- [26] (a) T.-S. Ho and H. Rabitz, *J. Chem. Phys.* **89**, 5619 (1988); **90**, 1519 (1989); **91**, 7590 (1989); (b) T.-S. Ho and H. Rabitz, *J. Chem. Phys.* **94**, 2305 (1991).
- [27] (a) H. Heo, T.-S. Ho, K. K. Lehmann, and H. Rabitz, *J. Chem. Phys.* **97**, 852 (1992); (b) R. Baer and R. Kosloff, *Chem. Phys. Lett.* **200**, 183 (1992).
- [28] U. Buck, *Comp. Phys. Rep.* **5**, 1 (1986).
- [29] W. Kohn, *Phys. Rev.* **74**, 1763 (1948).
- [30] D. E. Manolopoulos and R. E. Wyatt, *Chem. Phys. Lett.* **152**, 23 (1988).
- [31] D. E. Manolopoulos, M. D'Mello, and R. E. Wyatt, *J. Chem. Phys.* **91**, 6096 (1989).
- [32] F. Calogero, *Variable Phase Approach to Potential Scattering* (Academic Press, New York, 1967), Appendix I.
- [33] W. H. Miller, *J. Chem. Phys.* **50**, 407 (1969).

Received March 14, 1993

# Theoretical Study of the Reaction of Cd( $^1S$ , $^3P$ , $^1P$ ) with the Methane Molecule

S. CASTILLO, A. RAMÍREZ-SOLÍS, and E. POULAIN

*SGIA del Instituto Mexicano del Petróleo, A.P. 14-805, 07730 México D.F., Mexico*

## Abstract

The reaction pathways of the interaction of the methane molecule with the cadmium atom in the ground state ( $^1S$ ) and the two lowest excited states ( $^3P$ ,  $^1P$ ) were determined using Hartree-Fock followed by multireference configuration interaction plus second-order multireference Möller-Plesset calculations. No spontaneous activation of the methane molecule was observed by these electronic states of the cadmium atom due to the existence of activation barriers of 107.2, 27, and 17.3 kcal/mol, respectively. The geometry and electronic structure of the  $\text{HCdCH}_3$  intermediate molecule and the  $\text{CdH}$  and  $\text{CdCH}_3$  products involved in the reaction were also determined, as well as the dissociation pathway of  $\text{HCdCH}_3$  towards the  $\text{CdH} + \text{CH}_3$  and  $\text{H} + \text{CdCH}_3$  products. We found that the  $\text{HCdCH}_3$  intermediate reaches the final products without any barriers and also that the initial reactants in the ground state need to be provided with 88.5 kcal/mol to obtain the  $\text{CdH} + \text{CH}_3$  products and with 99.8 kcal/mol to get the  $\text{H} + \text{CdCH}_3$  products. © 1993 John Wiley & Sons, Inc

## Introduction

During the last decade a great variety of experimental techniques have been used for the study of metal atom plus methane ( $\text{M} + \text{CH}_4$ ) reactions. These experiences range from photoexcitation of metallic atoms trapped in cryogenic alkane matrices [1-8], photoexcitation of metallic vapors in the presence of hydrocarbons at high temperatures [9,10], and guided ion beam tandem mass-spectrometer reactions of metallic atoms with hydrogen and alkanes [11] to the laser pump-and-probe reactions of atoms with a variety of polyatomic molecules [12,13]. For the  $\text{Cd} + \text{CH}_4$  reaction, an important experimental work by Wallace and Breckenridge was reported [14] regarding the study of "action" spectra which provide information about the excited  $\text{Cd}-\text{CH}_4$  potential energy surfaces from which electronic energy transfer processes occur. In that work, the authors used the technique of action spectroscopy to obtain information about the ground and excited states of the  $\text{Cd}-\text{CH}_4$  van der Waals complex and to study "half-collision" electronic energy transfer processes within the complex. We were particularly interested in that paper because these authors have found that the interaction of  $\text{Cd}(^1P; 5s^1 5p^1)$  with  $\text{CH}_4$  is not efficient for the formation of  $\text{CdH} + \text{CH}_3$ , a fact which is attributed to the possible existence of a small potential barrier for the chemical interaction of  $\text{Cd}(^1P)$  with the  $\text{C}-\text{H}$  bonds in  $\text{CH}_4$ . We undertook the task of determining the symmetries, the positions, dissociation energies, and vibrational frequencies of the ground and the two lowest excited states of the  $\text{Cd}-\text{CH}_4$  van der Waals complexes observed in



Ref. [14] and confirmed the  $C_{3v}$  facial nature of the  $Cd(^1S)-CH_4$  complex and the  $Cd(^3P)-CH_4$  exciplex [15]. For the  $Cd(^1P)-CH_4$  exciplex it has just been possible to exclude the  $C_{2v}$  edge-on coordination; this still leaves the  $C_{3v}$  facial or vertex-on nature of this exciplex as an open question.

*Ab initio* studies of the activation of  $C-H$  bonds by metallic atoms start with the work of Blomberg et al. [16], who investigated the interaction of a nickel atom with methane. From this work the importance of the role played by the excited states of the metallic atom was clear. This relevant role of excited states has been confirmed in the experimental work of Georgiadis and Armentrout on the activation of methane by some ions of transition metals [11]. More recently, theoretical results for rhodium [17] and copper [18–22] in the activation of methane also stress the importance of the excited states. Similar experimental [23–26] and theoretical [27–36] studies on transition metal atom activation of  $H_2$  molecules exist as well. Particularly, we have been interested on the interaction of ( $^1p, ns^1np^1$ ) metal atoms with the  $C-H$  bonds in methane. In a very recent work [36] we predicted the  $^1P$  atomic state of Zn to be responsible for the formation of the  $HZnCH_3$  intermediate. We decided to test if the same nonadiabatic pathway could lead to the formation of the corresponding intermediate if one uses cadmium (which is isoelectronic in the valence shell with zinc) instead of zinc.

The aim of the present work is to study theoretically the  $Cd + CH_4$  reaction to obtain the reaction pathways as well as the governing mechanisms. For this purpose we have used the methodology followed in previous studies [21,22]. As our main interest is the study of the interaction of the cadmium atom in its  $^3^1P$  excited states with methane, we have used a strategy that allows us to obtain a pathway which is very close to the true pathway of interaction. We keep the  $CH_4$  geometry fixed during the insertion process except the  $C-H_\alpha$  distance, which is relaxed in the  $C_s$  step of the insertion (see Fig. 1). First of all, we have optimized the geometry of the  $HCdCH_3$  molecule which has the  $C_{3v}$  symmetry as expected; this means that we know the final exact position of the cadmium atom between the C and  $H_\alpha$  atoms. The insertion mechanism can essentially be divided in two: (a) The Cd atom approaches the  $C-H$  bond in the reflection plane ( $x-y$   $C_{2v}$  plane) keeping the  $CH_4$  geometry fixed (from A to B in Fig. 1). (b) As the metal atom leaves the  $C_{2v}$  plane (from B to C), for each  $C-H_\alpha$  relaxed distance considered, we have optimized the position of the cadmium atom in the  $C_s$  symmetry (this implies two orthogonal directions) until the metal is between the C and  $H_\alpha$  atoms to finally obtain the optimized  $HCdCH_3$  molecule in  $C_{3v}$  symmetry.

All optimizations were performed at the configuration interaction + second-order multireference Möller-Plesset perturbation (MRCI-MP2) level. The paths leading to the  $HCd + CH_3$  and  $H + CdCH_3$  products that can be attained from  $HCdCH_3$  were separately studied, and their geometries were also optimized in order to estimate relative energy differences. The next section is devoted to the computational details of the calculations. The third section presents the molecular and electronic structure of the optimized reactants, products, and intermediate complex. A discussion of the reaction mechanism and its features is followed by a comparison

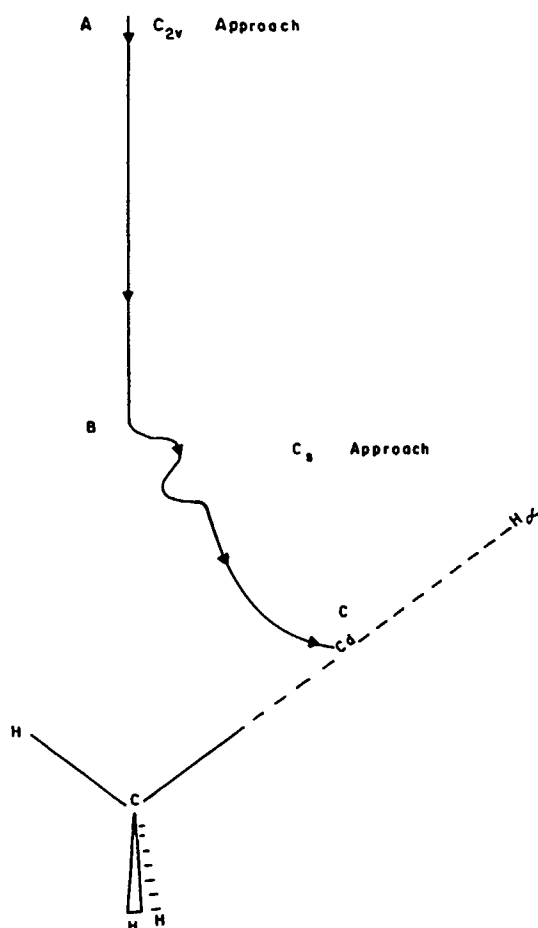


Figure 1. Reaction path followed by the cadmium atom ( $^1P:3d^{10}4s^14p^1$ ), leading to the formation of the  $HCdCH_3$  molecule.

of the present reaction with the  $Zn + CH_4$  reaction stressing the differences between them. Finally, in the fourth section we present our conclusions.

### Method

The self-consistent field (SCF) calculations were performed with the PSHF code [37], which includes the nonempirical relativistic effective core potential (RECP) method of Durand et al. [38–42]. The calculations have been made with a krypton-type RECP for cadmium and a helium-type RECP for carbon, leaving us with only 20 electrons to deal with explicitly. The RECP of carbon and cadmium were taken from Refs. [42] and [43], respectively. For carbon a double- $\zeta$  gaussian basis set was taken from Ref. [42], while for cadmium we have taken a basis set [43] which

TABLE I. Geometry of the HCdCH<sub>3</sub> molecule.

Distances (Å)	Cd-C	2.2
	Cd-H	1.7
	C-H	1.09
Angle (deg)	∠HCCd	111.0

is of triple- $\zeta$  quality for the 5s and 4d shells with two polarization p orbitals; the contraction for this Cd basis is (111/21/211). The basis sets for carbon and hydrogen have been successfully tested before and are the same as those reported in Ref. [21]. In order to obtain the two open-shell SCF orbitals of the  $1^3A''$  and  $2^1A'$  molecular states arising from the Cd( $3^1P$ ) + CH<sub>4</sub> asymptotes we used the SCF molecular orbitals (MO) of the  $1^1A'$  ( $^1S$ ) state obtained with the PSHF program as input for the MCSCF process [44]. The electronic correlation effects have been taken into account through the CIPSI algorithm in its two-class version [45]. First, a zeroth-order multireference space **S** (containing approximately 100 determinants in this work) is diagonalized and is used to generate the perturbational space **P** through the MP2 scheme. **P** contains from 20 to 30 million determinants depending on the geometry in question. All geometries and energies have been optimized using this MRCI-MP2 scheme.

## Results and Discussion

### Molecular Structure of the HCdCH<sub>3</sub> Intermediate Molecule

The most stable geometry of the HCdCH<sub>3</sub> intermediate has C<sub>3v</sub> symmetry and corresponds to a  $^1A_1$  electronic state. The optimized geometrical parameters appear in Table I. The  $^1A_1$  valence electronic configuration is given by  $10a_1^2 6e^4 7e^4 11a_1^2 8e^4 12a_1^2 13a_1^2$ , where the  $10a_1$  orbital is mainly the binding of the carbon and the hydrogens of methyl radical,  $6e = (d_{xz}, d_{yz})$ ,  $7e = (d_{xy}, d_{x^2-y^2})$ ,  $11a_1 = (d_{z^2})$ . The 8e orbitals bind the hydrogen atoms to carbon. The  $12a_1$  is a  $\sigma$  orbital that links C( $2p_z$ ) with Cd( $4s$ ) (with traces of  $d_{z^2}$ ) and H( $1s$ ). Finally the  $13a_1$  is a  $\sigma$  orbital that binds the three centers on the C<sub>3</sub> axis with the C( $2p_z$ ), Cd( $5p_z$ ), and the H( $1s$ ) orbitals. The SCF Mulliken electronic population reveals a  $4d^{10}5s^{0.93}5p^{0.54}$  charge distribution on Cd which corresponds approximately to Cd(II).

### Molecular Structure of CdCH<sub>3</sub>

The most stable geometry of CdCH<sub>3</sub> corresponds also to a C<sub>3v</sub> conformation with a  $^2A_1$  electronic state. The optimized geometrical parameters are presented in

TABLE II. Geometry of the CdCH<sub>3</sub> molecule

Distances (Å)	Cd-C	2.2
	C-H	1.11
Angle (deg)	∠HCCd	108.5

Table II. The  $2A_1$  valence electronic configuration is dominated by  $10a_1^2 6e^4 7e^4 11a_1^2 8e^4 12a_1^2 13a_1$ , where the  $10a_1$  orbital is mainly the binding of the carbon and the hydrogens of the methyl radical,  $6e = (d_{xz}, d_{yz})$ ,  $7e = (d_{xz}, d_{x^2-y^2})$  and  $11a_1 = (d_{z^2})$ . The  $8e$  orbitals bind carbon ( $2p_x, 2p_y$ ) with the hydrogen atoms ( $1s$  orbitals). The  $12a_1$  orbital links the carbon ( $2p_z$ ) with cadmium ( $5s$ ) and finally the  $13a_1$  orbital corresponds to a bond between carbon  $sp(2p_z + 2s)$  and cadmium  $sp(-5s - 5p_z)$ .

### *The CdH Molecule*

The most stable geometry of CdH corresponds to a  $^2\Sigma^+$  state, which has a valence electronic configuration given by  $9\sigma^2 2\delta^4 2\pi^4 10\sigma^2 11\sigma^1$ , where  $9\sigma = (d_{z^2})$ ,  $2\delta = (d_{x^2-y^2}, d_{xy})$ ,  $2\pi = (d_{xz}, d_{yz})$ . The  $10\sigma$  orbital binds the cadmium  $sd(s - d_{z^2})$  with the hydrogen ( $1s$ ) and finally the  $11\sigma$  orbital mixes the cadmium  $sp(-s + p_z)$  with the H( $1s$ ). The equilibrium distance of CdH was found to be 1.76 Å and is in excellent agreement with the experimental  $R_e$  value of 1.761 Å [46].

### *Energetics of the Cd + CH<sub>4</sub> → HCdCH<sub>3</sub> Reaction*

Figure 2 shows the relative energies of the reactants, the HCdCH<sub>3</sub> complex and the HCd + CH<sub>3</sub> or CdCH<sub>3</sub> + H products. We present there our calculated values (full lines) as well as available experimental data (dotted lines).

The experimental bond dissociation energies (BDE), on the one hand, allow us to perform an analysis of the energetics of the reaction and, on the other hand, they will be used to generate reliable energy differences against which our calculated values can be compared. The experimental BDE of the C—H bond in methane is 105 kcal/mol whereas that of the Cd—H bond is 15.6 kcal/mol [46]. These values allow us to calculate that the "experimental" energy difference between the CdH + CH<sub>3</sub> products and the Cd(<sup>1</sup>S) + CH<sub>4</sub> reactants is 89.4 kcal/mol; our MRCI-MP2 value for this difference is in very good agreement and was found to be 88.5 kcal/mol. The BDE for the Cd—C bond of CdCH<sub>3</sub> has not been experimentally determined but our calculated value is 99.8 kcal/mol. As far as the spectroscopy of the cadmium atom concerns, the experimental transition energies ( $T_e$ ) between the  $^3P(4d^{10}5s^1 5p^1)$  and  $^1P(4d^{10}5s^1 5p^1)$  excited states and the  $^1S(4d^{10}5s^2)$  ground state are 89.3 kcal/mol and 124.9 kcal/mol [47]. The  $^3P$  energy is the  $J$ -averaged value of the three spin-orbit components of Ref. [47]. Our calculated  $T_e$  are 84.9 and 125.6 kcal/mol, respectively.

The optimized HCdCH<sub>3</sub> complex was calculated to lie 31.9 kcal/mol above the Cd(<sup>1</sup>S) + CH<sub>4</sub> reactants; the endothermic formation of an HMCH<sub>3</sub> molecule (M = metal) has also been found in Ni, Cu, and Zn [16,22,36]. Figure 3 shows the reaction paths followed by the reactants to form the HCdCH<sub>3</sub> complex. The curve  $2^1A'$  initially presents an attractive section between the Cd(<sup>1</sup>P) excited atom and methane; next, this curve shows an activation barrier of 17.3 kcal/mol. This means that the Cd(<sup>1</sup>P) excited atom does not insert spontaneously into the C—H bond of CH<sub>4</sub>. Also this figure presents two avoided crossings between the  $2^1A'$  and  $1^1A'$  curves. This means that initially the Cd(<sup>1</sup>P) + CH<sub>4</sub> fragments follow the  $2^1A'$  curve

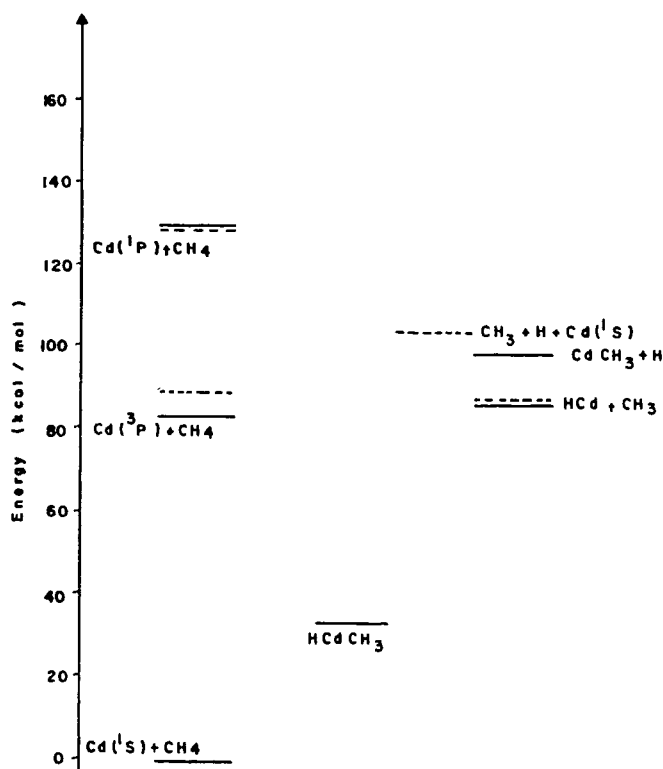


Figure 2. Energy diagram of the reactants, the intermediate  $\text{HCdCH}_3$  molecule, and the products: (---) experimental figures; (—) calculated results.

and then by means of a nonadiabatic transition in any of the avoided crossing regions they may fall to the  $1^1\text{A}'$  curve that correlates with the  $\text{Cd}(^1\text{S}) + \text{CH}_4$  fragments. Note that the lower-lying curve is initially repulsive and that it becomes attractive, as expected, only after the first avoided crossing has taken place. This  $1^1\text{A}'$  curve has an activation barrier of 107.2 kcal/mol.

The experimental picture presented in Ref. [14] shows that the cadmium atom in the  $^1\text{P}$  excited state does not break efficiently the C—H bond in  $\text{CH}_4$ . We have seen that this can be explained by the existence of a barrier of more than 17 kcal/mol in the  $2^1\text{A}'$  curve in Figure 3.

As far as the  $\text{Cd}(^3\text{P}) + \text{CH}_4$  reaction is concerned, we have previously reported a  $\text{C}_{3v}$  face-on  $\text{Cd}(^3\text{P})\text{--H}_3\text{CH}$  van der Waals exciplex [15], and its corresponding minimum can be seen (here exaggerated) at the left of the  $1^3\text{A}'$  curve in Figure 4. Note that another activation barrier calculated to be 27 kcal/mol high separates the reactants from a stable bent intermediate. This value is in excellent agreement with the experimentally measured value of 9000–10,000  $\text{cm}^{-1}$  for the barrier height [14].

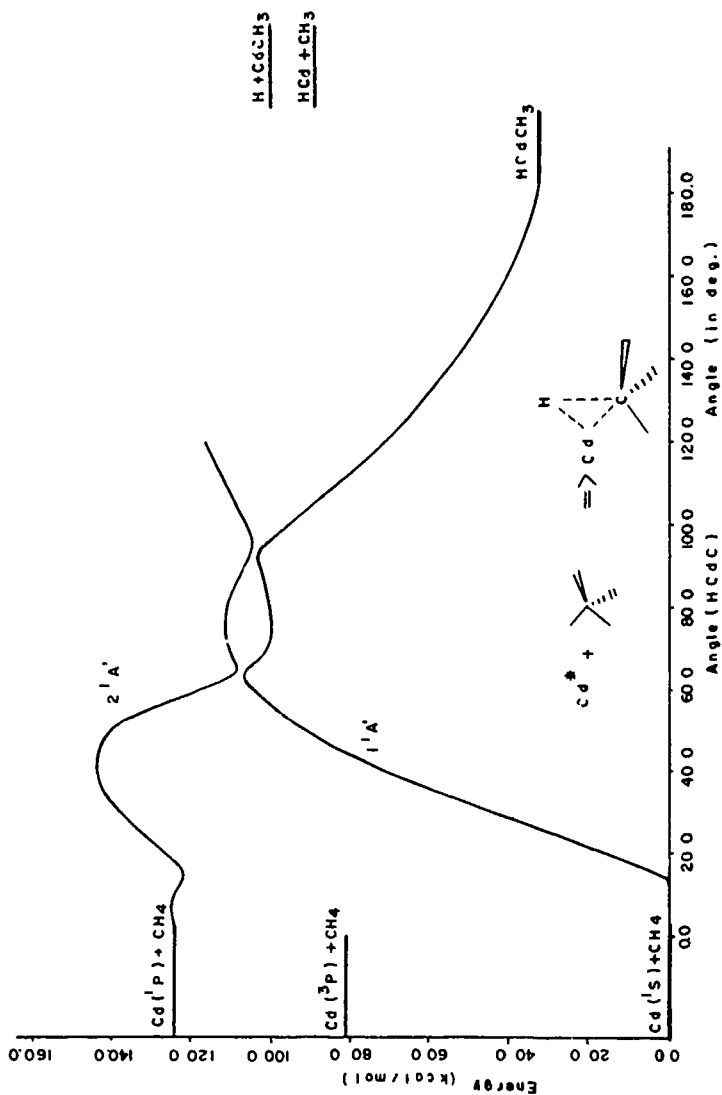


Figure 3. Potential energy curves of the interaction of Cd(<sup>1</sup>S) and Cd(<sup>1</sup>P) with methane vs. insertion angle towards the HCdCH<sub>3</sub> intermediate.

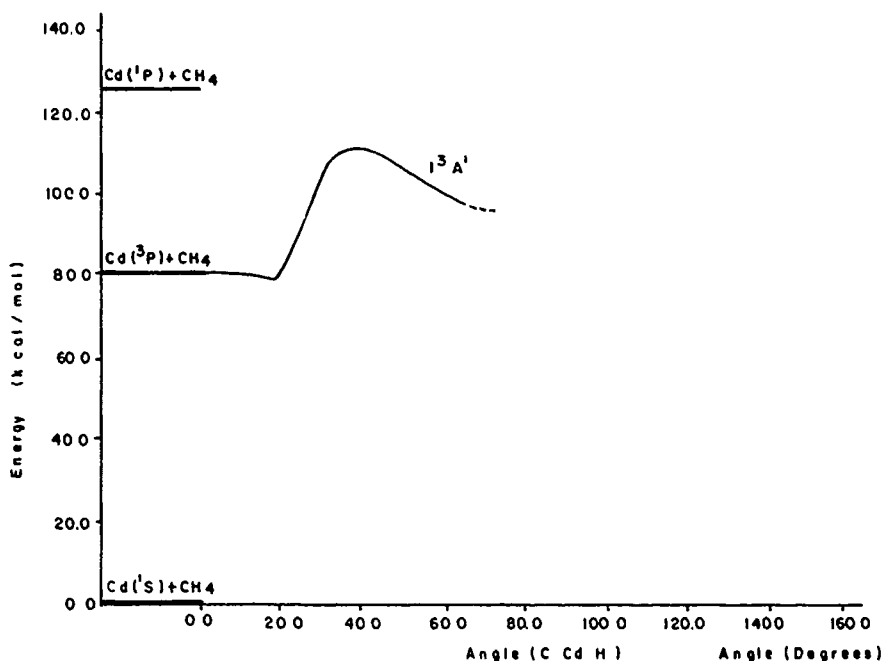


Figure 4. Potential energy curve of the interaction of  $\text{Cd}(^3\text{P};5s5p)$  state with methane.

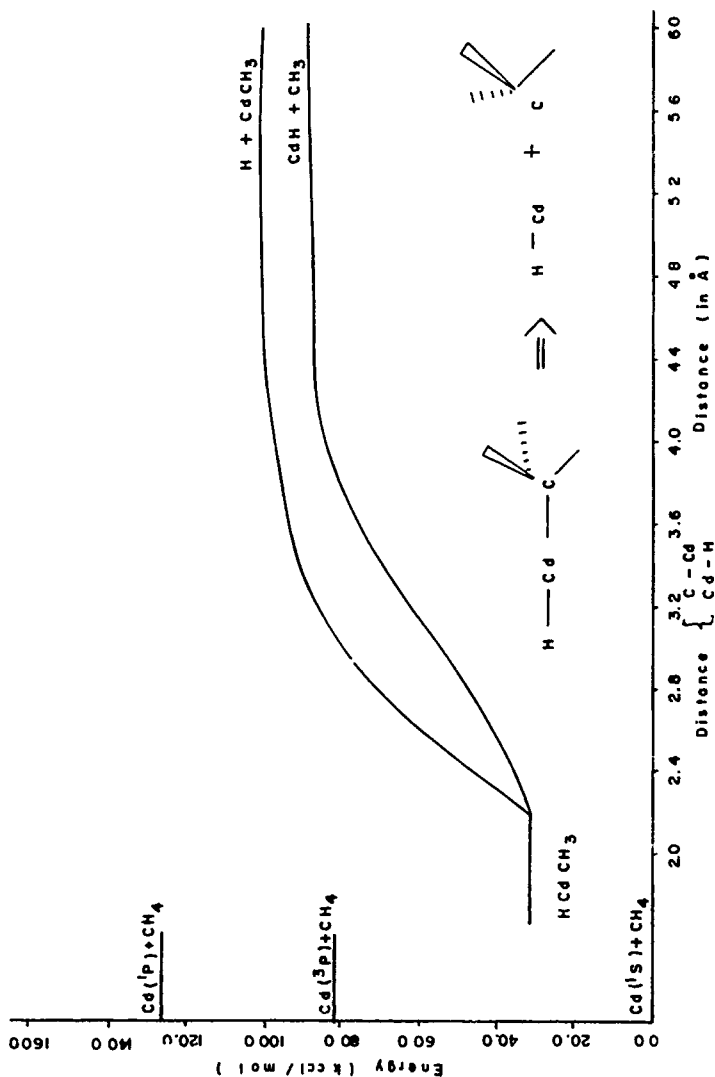
### *Energetics of the $\text{HCdCH}_3$ Dissociation towards the Products*

In Figure 5 the reaction pathways corresponding to the dissociation of  $\text{HCdCH}_3$  are depicted. The  $\text{HCdCH}_3$  complex is shown to dissociate, without any activation barrier, into the  $\text{HCd} + \text{CH}_3$  products when furnished with 56.6 kcal/mol or to the  $\text{H} + \text{CdCH}_3$  products when given 67.9 kcal/mol. The  $2^1\text{A}'$  curve becomes monotonically increasing after the avoided crossings with the  $1^1\text{A}'$  curve and leads eventually to the excited  $\text{CdH}(^2\Sigma^+) + \text{CH}_3$  fragments.

### *Comparison of the Interaction $\text{Cd}-\text{CH}_4$ with $\text{Zn}-\text{CH}_4$*

The cadmium and zinc atoms are isoelectronic in their valence shells, so it is expected that their respective interactions with methane would present some common features. We can note, for example, in both cases that:

- The presence of high energy barriers between the ground state  $\text{M}(^1\text{S};d^{10}s^2) + \text{CH}_4$  and the  $\text{HMCH}_3$  intermediate.
- The formation of the  $\text{HMCH}_3$  molecule is only reached by means of an endothermic process.
- The relative energetic position of the products and the intermediate is the same, namely,  $\text{HMCH}_3 < \text{HM} + \text{CH}_3 < \text{H} + \text{MCH}_3$ .

Figure 5. Dissociation curves of  $\text{HCdCH}_3$  towards the  $\text{CdH} + \text{CH}_3$  and  $\text{H} + \text{CdCH}_3$  products.



- d. The formation of the  $\text{HM} + \text{CH}_3$  and  $\text{H} + \text{MCH}_3$  systems can only be reached by means of endothermic processes and without any barrier between the intermediate  $\text{HMCH}_3$  and the products.

We would like to note that the  $^1\text{P}(\text{d}^{10}\text{s}^1\text{p}^1)$  excited state of Cd and Zn has two special features in the  $\text{M} + \text{CH}_4$  interaction: It is the lowest excited state that has the same spin multiplicity as the stable  $\text{HMCH}_3$  complex, and its electronic configuration allows it to interact favorably with the  $\sigma$  and  $\sigma^*$  molecular orbitals of methane.

However, unlike with the  $\text{Zn}(^1\text{P}; 3\text{d}^{10}4\text{s}^14\text{p}^1)$  state, the Cd atom in its  $(^1\text{P}; 4\text{d}^{10}5\text{s}^15\text{p}^1)$  state cannot spontaneously break the C—H bonds in  $\text{CH}_4$ ; this result is very similar to that found for the interaction of  $\text{Mg}(^1\text{P}; 2\text{s}^12\text{p}^1)$  with methane [48]. This seems to indicate that since the formation of the  $\text{Cd}(^1\text{P})\text{—CH}_4$  van der Waals exciplex has already been observed [14] and theoretically confirmed by our recent calculations [15], the attractive interaction of the 5p orbital of the Cd with the  $\sigma^*$  orbital of methane that could lead to a stable  $\text{HCdCH}_3$  intermediate is overcome at short distance by the existing repulsion between the singly occupied 5s orbital of the metal and the doubly occupied  $\sigma$  orbital of the methane.

### Conclusions

The  $^1\text{S}(4\text{d}^{10}5\text{s}^2)$  ground state of the cadmium atom is not capable of breaking the C—H bond in  $\text{CH}_4$  due to the presence of a very high barrier (1.07 kcal/mol) between  $\text{Cd}(^1\text{S}) + \text{CH}_4$  reactants and  $\text{HCdCH}_3$  molecule.

The reaction pathways of  $\text{Cd}(^1\text{S})\text{—CH}_4$  and  $\text{Cd}(^1\text{P})\text{—CH}_4$  show two regions where these curves present avoided crossings. The  $^1\text{P}(5\text{s}^15\text{p}^1)$  cadmium state, unlike the isoelectronic  $\text{Zn}(^1\text{P}; 4\text{s}^14\text{p}^1)$  state, does not break spontaneously the C—H bonds in  $\text{CH}_4$ , due to the presence of a 17.3 kcal/mol barrier in the reaction pathway of this state with methane. This excited cadmium atom can only form exothermically a  $\text{C}_{3v}$  van der Waals complex with methane.

The  $\text{HCdCH}_3$  intermediate is formed endothermically if one starts with the ground states of Cd and methane, and it can also be reached from the interaction between  $\text{Cd}(^1\text{P})$  and  $\text{CH}_4$ ; it was found that it is necessary to provide approximately 17 kcal/mol to the  $\text{Cd}(^1\text{P}) + \text{CH}_4$  reactants to obtain the  $\text{HCdCH}_3$  intermediate via a nonadiabatic transition with the repulsive lower-lying curve, which is asymptotically related to the ground state fragments.

The cadmium  $^3\text{P}$  state has been shown not to activate spontaneously the methane molecule because there is a 27 kcal/mol calculated energy barrier (in excellent accordance with recent experiments) between the  $\text{Cd}(^3\text{P}) + \text{CH}_4$  reactants and a stable bent minimum.

The  $\text{HCdCH}_3$  complex is shown to dissociate into the  $\text{HCd} + \text{CH}_3$  or to the  $\text{H} + \text{CdCH}_3$  products without any activation barrier.

Finally, the results presented in this work are in accordance with those reported in the experimental studies already mentioned.

## Bibliography

- [1] W. E. Billups, M. M. Konarski, R. H. Hauge, and J. L. Margrave, *J. Am. Chem. Soc.* **102**, 7394 (1980).
- [2] G. A. Ozin, D. F. McIntosh, S. A. Mitchell, and J. García-Prieto, *J. Am. Chem. Soc.* **103**, 1574 (1981).
- [3] G. A. Ozin, J. G. McCaffrey, and D. F. McIntosh, *Pure Appl. Chem.* **56**, 111 (1984).
- [4] J. M. Parnis, S. A. Mitchell, J. García-Prieto, and G. A. Ozin, *J. Am. Chem. Soc.* **107**, 8169 (1985).
- [5] G. A. Ozin and J. G. McCaffrey, *Angew. Chem. Int. Ed. Engl.* **25**, 1072 (1986).
- [6] J. M. Parnis and G. A. Ozin, *J. Phys. Chem.* **93**, 1204 (1989).
- [7] J. M. Parnis and G. A. Ozin, *J. Phys. Chem.* **93**, 1220 (1989).
- [8] J. M. Parnis and G. A. Ozin, *J. Phys. Chem.* **93**, 4023 (1989).
- [9] S. Yamamoto, *Bull. Chem. Soc. Jpn.* **61**, 769 (1988).
- [10] S. Yamamoto and H. Hokamura, *J. Phys. Chem.* **95**, 2138 (1991).
- [11] R. Georgiadis and P. B. Armentrout, *J. Phys. Chem.* **92**, 7067 (1988).
- [12] W. H. Breckenridge and H. Umemoto, *J. Chem. Phys.* **75**, 698 (1981).
- [13] W. H. Breckenridge and H. Umemoto, *J. Chem. Phys.* **81**, 3852 (1984).
- [14] I. Wallace and W. H. Breckenridge, *J. Chem. Phys.* **97**, 2318 (1992).
- [15] A. Ramírez-Solis and S. Castillo, *J. Chem. Phys.* **98**, 8065 (1993).
- [16] M. R. A. Blomberg, U. Brandemark, and P. E. M. Siegbahn, *J. Am. Chem. Soc.* **105**, 5557 (1983).
- [17] M. R. A. Blomberg, P. E. M. Siegbahn, and M. Svensson, *J. Phys. Chem.* **95**, 4313 (1991).
- [18] R. A. Poirier, G. A. Ozin, D. F. McIntosh, I. G. Csizmadia, and R. Daudel, *Chem. Phys. Lett.* **101**, 221 (1983).
- [19] G. E. Quelch and I. H. Hillier, *J. Chem. Soc. Faraday Trans. 2* **83**, 2287 (1987).
- [20] G. E. Quelch and I. H. Hillier, *Chem. Phys.* **121**, 183 (1988).
- [21] S. Castillo, E. Poulain, and O. Novaro, *Int. J. Quant. Chem.* **23**, 509 (1989).
- [22] S. Castillo, E. Poulain, and O. Novaro, *Int. J. Quant. Chem.* **25**, 577 (1991).
- [23] W. H. Breckenridge and H. Umemoto, *J. Chem. Phys.* **80**, 4168 (1984).
- [24] P. D. Kleiber, A. M. Lyyra, K. M. Sando, Zafropoulos, and W. C. Stwalley, *J. Chem. Phys.* **85**, 5493 (1986).
- [25] J. L. Elkind and P. B. Armentrout, *J. Chem. Phys.* **86**, 1868 (1987).
- [26] J. M. Parnis and G. A. Ozin, *J. Phys. Chem.* **93**, 1215 (1989).
- [27] M. R. A. Blomberg, U. Brandemark, L. Pettersson, and P. E. M. Siegbahn, *Int. J. Quantum. Chem.* **23**, 855 (1983).
- [28] A. Goddard III and J. J. Low, *J. Am. Chem. Soc.* **106**, 8321 (1984).
- [29] J. García-Prieto, M. E., Ruíz and E. Poulain, *J. Chem. Phys.* **81**, 5920 (1984) and references therein.
- [30] J. García-Prieto, M. E. Ruíz, and O. Novaro, *J. Am. Chem. Soc.* **107**, 5635 (1985).
- [31] M. E. Ruíz, J. García-Prieto, E. Poulain, G. A. Ozin, R. A. Poirier, S. M., Matta, I. G. Czismadia, C. Gracie, and O. Novaro, *J. Phys. Chem.* **90**, 279 (1986).
- [32] E. Poulain, J. García-Prieto, M. E. Ruíz, and O. Novaro, *Int. J. Quant. Chem.* **XXIX**, 1181 (1986).
- [33] K. Balasubramanian and J. Z. Wang, *J. Chem. Phys.* **91**, 7761 (1989).
- [34] E. Poulain, F. Colmenares, S. Castillo, and O. Novaro, *J. Mol. Struct. (Theochem)* **210**, 337 (1990).
- [35] J. M. Martínez-Magadán, A. Ramírez-Solis, and O. Novaro, *Chem. Phys. Lett.* **186**, 107 (1991).
- [36] S. Castillo, A. Ramírez-Solis, D. Díaz, E. Poulain, and O. Novaro, *Mol. Phys.* (1993), to appear.
- [37] J. P. Daudey, PSHF program and pseudopotential adaptation, based on the original HONDO 76. QCPE Program 338 (1977) by M. Dupuis, J. Rys, and H. F. King.
- [38] Ph. Durand and J. C. Barthelat, *Theor. Chim. Acta* **38**, 283 (1975).
- [39] J. C. Barthelat, Ph. Durand, and A. Serafini, *Mol. Phys.* **33**, 179 (1977).
- [40] J. C. Barthelat and Ph. Durand, *Gazz. Chim. Ital.* **108**, 225 (1978).
- [41] M. Pélissier and Ph. Durand, *Theor. Chim. Acta* **55**, 43 (1980).
- [42] G. F. Pacchioni, P. Fantucci, G. Giunchi, and J. C. Barthelat, *Gazz. Chim. Ital.* **110**, 183 (1980).
- [43] L. A. LaJohn, P. A. Christiansen, R. B. Ross, T. Atashroo, and W. C. Ermler, *J. Chem. Phys.* **84**, 2812 (1987).

- [44] R. Carbó, J. Rubio, M. Pélissier, and J. P. Daudey, GMCP program, based on the Elementary Jacobi Rotation algorithm.
- [45] B. Huron, J. P. Malrieu, and P. Rancurel, *J. Chem. Phys.* **58**, 5745 (1973); M. Pélissier, J. P. Daudey, J. P. Malrieu, F. Spiegelmann, D. Maynau, and S. Evangelisti, CIPSI code.
- [46] G. Herzberg, *Molecular Spectra and Molecular Structure I Spectra of Diatomic Molecules* (Van Nostrand, Princeton, NJ 1950).
- [47] C. E. Moore, *Atomic Energy Levels* (U.S. National Bureau of Standards, Washington, DC, 1971).
- [48] P. Chaquin, A. Papakondylis, C. Giessner-Prettre and A. Sevin, *J. Phys. Chem.* **94**, 7352 (1990).

Received May 11, 1993

# Use of Energy Partitioning for Predicting Primary Mass Spectrometric Fragmentation Steps: A Preliminary Account

I. MAYER and Á. GÖMÖRY

Central Research Institute for Chemistry of the Hungarian Academy of Sciences, H-1525 Budapest,  
P.O. Box 17, Hungary

## Abstract

Energy partitioning (decomposition of the total energy into one- and two-center contributions) performed at the MNDO level of theory has been applied to interpret the first steps of mass spectrometric fragmentation processes. In all cases considered until now, the changes of bond contributions during a vertical ionization process could be used to predict the main primary bond cleavages observed in the mass spectra of organic molecules. © 1993 John Wiley & Sons, Inc

## Introduction

In the course of mass spectrometric experiments, molecules undergo ionization and fragmentation under the electron impact. Although the fragmentation of ions formed by electron bombardment is a *par excellence* dynamic process, the existence of many regularities in mass spectra of related organic molecules indicates that there are some simple underlying physical factors influencing them to a great extent. Obviously, the electronic structure of the lowest electronic state(s) of the ions obtained after the ionization step should often be of large (or even decisive) importance in determining the primary bond cleavages. This assumption is supported by the recent successes [1–6] in interpreting the primary mass spectrometric fragmentation steps by considering the changes in bond order (multiplicity) indices [7] taking place during the ionization. In the case of the NDO-type semiempirical theories, these bond orders reduce to the familiar Wiberg's bond indices [8]. It has recently been demonstrated [9] that the Wiberg indices obtained in the framework of the semiempirical MNDO theory correlate very well with the *ab initio* values, as well as that the MNDO Wiberg indices represent rather useful tools in interpreting mass spectra [1–6].

Bond order or Wiberg indices reflect the actual multiplicity of the bonds in question; they are in a correlation with the bond strengths but are not *energetic* quantities which could be directly related to the energy consumption of the bond cleavage processes. For that reason we have investigated the applicability of *energy partitioning* performed at the MNDO level of theory for interpreting and predicting the primary mass spectrometric fragmentations. We do not assume that the new method

should replace the use of bond orders in discussing fragmentations. However, it gives some additional information about the effects taking place during the ionization, which is worth being utilized. In fact, we suggest using these two sets of parameters simultaneously. However, an obvious advantage of energy partitioning is in putting the changes in bond strengths to the energetic scale, relating them better to the physical conditions of a mass spectrometric experiment than the bond order does.

### Energy Partitioning

As is well known, the total RHF energy of a closed shell molecule or that of an ion treated by the "half-electron" scheme is

$$E = \sum_{\mu,\nu} h_{\mu\nu} D_{\nu\mu} + \frac{1}{2} \sum_{\mu,\nu,\rho,\tau} (D_{\rho\mu} D_{\tau\nu} - \frac{1}{2} D_{\rho\nu} D_{\tau\mu}) (\mu\rho | \nu\tau) + \sum_{A<B} \frac{Z_A Z_B}{R_{AB}} \quad (1)$$

with the usual notations for the elements of the one-electron matrix  $\mathbf{h}$ , density matrix  $\mathbf{D}$ , two-electron integrals in the (11|22) convention as well as nuclear charges  $Z_A$  and internuclear distances  $R_{AB}$ . In the framework of the MNDO scheme, there are only one- and two-center integrals contributing to the elements of matrix  $\mathbf{h}$  as well as only one- and two-center two-electron integrals  $(\mu\rho | \nu\tau)$  are considered. Therefore, similarly to other NDO theories (cf. [10,11]), the total MNDO energy can unambiguously be decomposed into one- and two-center contributions. In practice, the introduction of such an energy partitioning into the standard MNDO program for RHF closed shells and half-electron open shells [12] represented a quite straightforward programming task. We used the energy (1) written down in the trace form

$$E = \frac{1}{2} \text{Tr}[(\mathbf{h} + \mathbf{F})\mathbf{D}] + \sum_{A<B} \frac{Z_A Z_B}{R_{AB}} \quad (2)$$

with  $\mathbf{F}$  being the usual Fock matrix, following closely the build up of matrices  $\mathbf{h}$  and  $\mathbf{F}$ . Off-diagonal elements  $h_{\mu\nu}$  and  $F_{\mu\nu}$  with orbital indices  $\mu$  and  $\nu$  corresponding to different atoms should simply be multiplied with  $\frac{1}{2} D_{\mu\nu}$  and added to the respective two-center contribution. One-center elements of  $\mathbf{h}$  and  $\mathbf{F}$ , however, contain not only true one-center terms but reflect also the Coulombic interaction with the nuclei and electrons of other atoms. The latter, however, can trivially be separated out and assigned to the corresponding two-center energy components.

In our opinion, a theoretical tool of such type can be considered truly *predictive* if one can determine what bonds will become weaker by investigating vertical ionization processes, i.e., by comparing the bond order indices or the two-center energy components of the neutral molecule and of the ion at the equilibrium (optimized) geometry of the former. In other words, the longer and weaker bonds obtained for an adiabatic ionization obviously should exhibit lower bond orders and lower (in absolute value) bonding energy contributions. These lower values may be considered as a simple consequence of the bonds in question being longer. However, if one obtains reduced bond contributions after ionization at the geometry of the neutral

molecule (i.e., if a significant bond weakening takes place even for the vertical ionization), then this is an indication or prediction that the bond considered will be looser if the geometry of the ion is relaxed. One can expect that bonds of this type will be those that undergo primary bond cleavages.

One should keep in mind that the two-center energy contribution corresponding to a given bond is not equal to the dissociation energy of that bond. It is merely a *static* parameter corresponding to a fixed geometry and given wave function, so it has only indirect relationships with the rather complicated *dynamic* processes occurring during the ion fragmentation.

### Applications

In all cases studied until now, the comparison of the two-center contributions for the neutral molecule and the positive ion could be used to identify the primary bond cleavages: The energy contributions for the bonds undergoing actual rupture decrease *significantly* (in absolute value) after the ionization. (Changes by a value about 1 eV or more are typical.) However, even large changes in energy contributions corresponding to double and aromatic bonds do not indicate bond cleavage; in these cases, one is merely faced with some decrease of the actual bond multiplicity.

In the Figures 1-4, the two-center energy components obtained by energy decomposition are displayed in electron volts; in each case the upper numbers correspond to the neutral molecules, and the lower ones to the ions at the optimized geometry of the *neutral* molecule (vertical ionization).

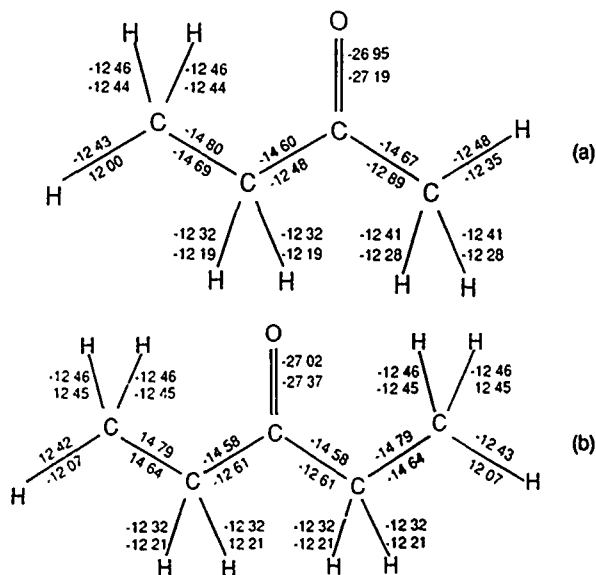


Figure 1. Two-center MNDO energy components (in eV) obtained for methyl-ethyl-ketone and diethyl-ketone. Upper numbers relate to the neutral molecule, lower ones to the positive ion (vertical ionization).

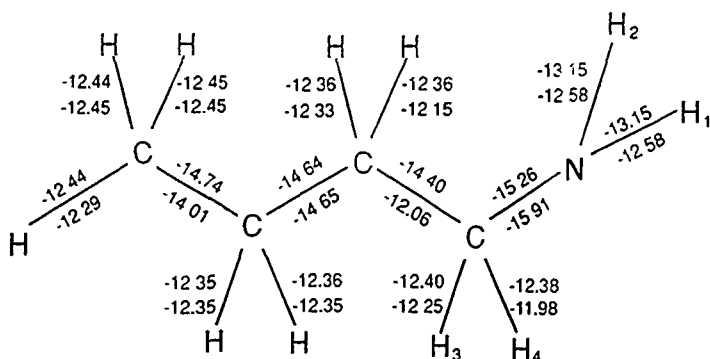


Figure 2. Two-center MNDO energy components (in eV) obtained for butyl-amine. Upper numbers relate to the neutral molecule, lower ones to the positive ion (vertical ionization).

Figure 1(a) shows the energy decomposition results for methyl-ethyl-ketone. The bond with the largest change in the two-center contribution indicates that the main process is the ethyl loss, in agreement with experiment [13]. Another C—C bond at the carbonyl group, which corresponds to methyl loss, is changed to a somewhat less extent, and its energy in the ion remains slightly larger (in absolute value). This is in agreement with the fact that only a low intensity M-15 peak is

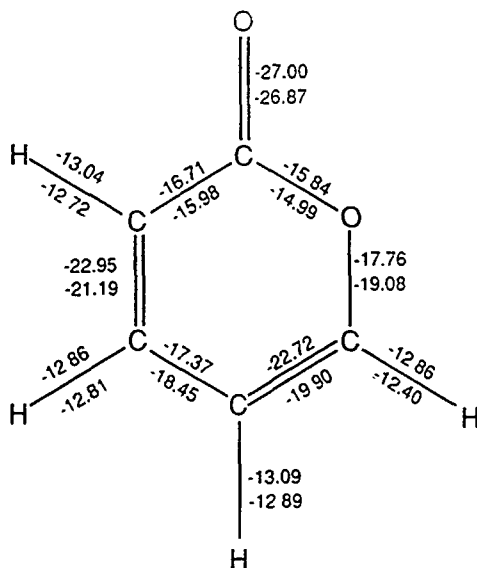


Figure 3. Two-center MNDO energy components (in eV) obtained for a lactone. Upper numbers relate to the neutral molecule, lower ones to the positive ion (vertical ionization).

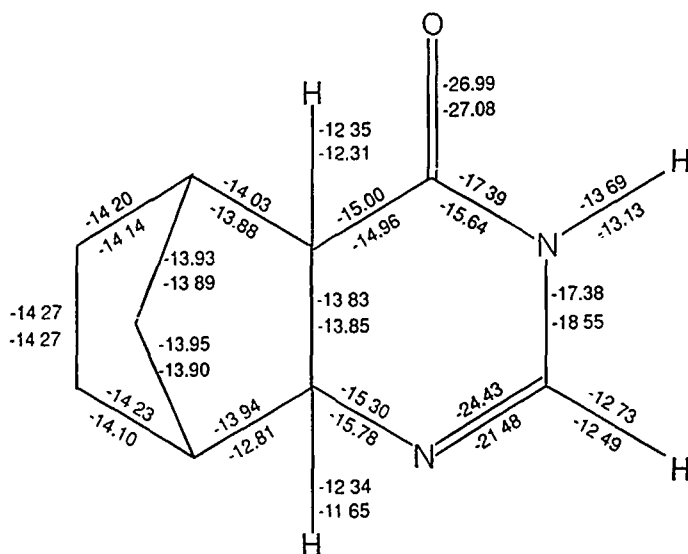


Figure 4. Two-center MNDO energy components (in eV) obtained for a norbornane derivative. Upper numbers relate to the neutral molecule, lower ones to the positive ion (vertical ionization).

observed in the experimental mass spectrum. These energy decomposition results also indicate that this methyl loss does not originate from the ethyl group. This conclusion is in agreement with the comparison with the mass spectrum of diethylketone, in which no methyl loss is observed experimentally or predicted theoretically [Fig. 1(b)].

Figure 2 shows the energy contributions for buthyl-amine. One can see that the C—C bond in  $\beta$ -position to N-atom is expected to be broken. This is in full agreement with the fact that the only dominating product in the mass-spectrum [13] is  $[\text{CH}_2\text{NH}_2]^+$ . It is interesting to note the orientation sensitivity of this step: The C—C bond cleavage takes place only if the bond is parallel to the nitrogen lone pair, but not in the other rotation isomers. Further studies are required to clarify whether this result (and some similar ones) can be generalized as to develop a rule relating mass spectra to the rotational isomers of the parent molecule.

Looking at the energy partitioning of the lactone molecule depicted on Figure 3, it is not surprising that one can observe in its mass spectrum CO loss and all the fragments of the remaining furane ring [13].

Figure 4 displays a norbornane derivative from the recent MS study of one of us [3]. The calculations agree nicely with our experimental analysis in which two competing primary ring opening processes were postulated. These processes start with the cleavages of either of the two bonds for which energy partitioning also indicates significant bond weakening.



### Discussion

Energy partitioning performed at the MNDO level of theory seems to be a promising tool to interpret and predict the primary bond cleavages influencing the mass spectra of organic molecules. It appears to us that it is meaningful to apply it together with analyzing the changes taking place in the bond order (Wiberg) indices during the ionization. As expected, there is a great overall correlation between these—conceptually different—quantities. This does not mean, however, that they change in accordance with each other in all cases without exceptions. It is our first impression that in the doubtful cases the energy partitioning gives superior results. For instance, for the lactone molecule shown in Figure 3, only the cleavage of the C—O bond would be predicted by considering the bond order changes (Fig. 5).

It seems too important that—according to our experience up till now—the qualitative conclusions which can be drawn from the energy partitioning results are rather insensitive to accuracy of the geometry applied; we should recall, however, the orientation sensitivity mentioned above. It may also be noted that, in some cases considered, the weakening of the bonds formed by hydrogen atoms were not manifested by the appearance of M-1 peaks in the mass spectra; such a weakening can probably be considered as indications of more complicated rearrangement processes.

In some molecules, due, e.g., to the presence of a phenyl group, the HOMO may correspond to a  $\pi$ -orbital. In such cases ionization from HOMO (or even from the next-to-HOMO orbital) can lead to quite stable molecular ions, and the explanation

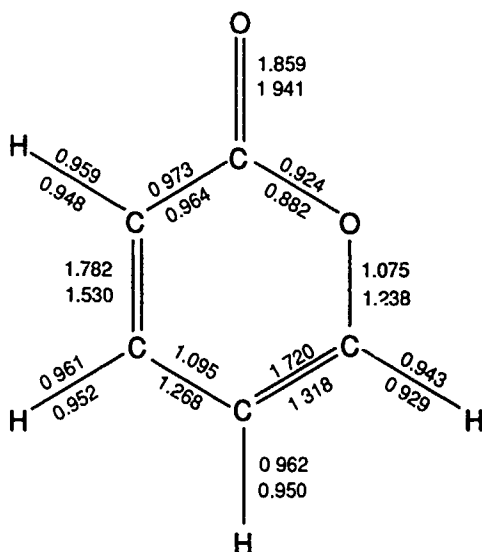


Figure 5. Bond order (Wiberg) indices obtained for the lactone molecule shown on Figure 3. Upper numbers relate to the neutral molecule, lower ones to the positive ion (vertical ionization).

of the observed fragmentation may require consideration of ionizations from lower lying orbitals. Development of a technique permitting use of energy partitioning for discussing mass spectra in such cases is also in progress.

### Acknowledgment

This research was supported in part by the Hungarian Research Fund (OTKA No. 1774).

### Bibliography

- [1] L. Carlsen and H. Egsgaard, *J. Am. Chem. Soc.* **110**, 6701 (1988).
- [2] Á. Somogyi, Á. Gömöry, K. Vékey, and J. Tamás, *Org. Mass. Spectrom.* **26**, 936 (1991).
- [3] Á. Gömöry, Á. Somogyi, J. Tamás, G. Stájer, G. Bernáth, and I. Komáromi, *Int. J. Mass Spectrom. Ion Proc.* **107**, 225 (1991).
- [4] K. Vékey, Á. Somogyi, and J. Tamás, *Org. Mass. Spectrom.* **27**, 869 (1992).
- [5] K. Vékey and G. Pócsfalvi, *Org. Mass. Spectrom.* **27**, 1203 (1992).
- [6] A. G. Császár, Á. Somogyi, G. Pócsfalvi, and P. Traldi, *Org. Mass. Spectrom.* **27**, 1349 (1992).
- [7] I. Mayer, *Chem. Phys. Lett.* **97**, 270 (1983) [addendum, **117**, 396 (1985)]; *Theoret. Chim. Acta* **67**, 315 (1985); *Int. J. Quantum Chem.* **29**, 73, 477 (1986).
- [8] K. A. Wiberg, *Tetrahedron* **24**, 1083 (1968).
- [9] Á. Somogyi and Á. Gömöry, *Chem. Phys. Lett.* **192**, 221 (1992).
- [10] J. A. Pople and D. L. Beveridge, *Approximate Molecular Orbital Theory* (McGraw-Hill, New York, 1970), pp. 67-68.
- [11] H. Fischer and H. Kollmar, *Theoret. Chim. Acta* **16**, 163 (1970).
- [12] W. Thiel, *J. Am. Chem. Soc.* **103**, 1413, 1420 (1981).
- [13] *EPA-NIH Mass Spectral Data Base*, S. R. Heller and G. W. A. Milne, Eds., Natl. Bureau of Standards, Washington, D.C., 1978.

Received May 6, 1993

# Light Particles Interacting with Organic Molecules

N. H. MARCH

*Theoretical Chemistry Department, University of Oxford, 5 South Parks Road,  
Oxford, OX1 3UB, England*

## Abstract

Slow electron scattering from  $\text{CH}_4$ , and thermal positrons annihilating with a variety of organic molecules, will first be discussed, the major role of molecular polarizability being the focal point. In the same context, initially neutral carbon clusters with an added, but now bound, electron will be considered, and in particular for  $\text{C}_{60}$  the role of polarizability will again be stressed. Some attention will also be paid to electron–electron interaction in  $\text{C}_{60}^-$ . Photoelectron spectroscopic data on ionization potentials for both linear and terminated polyacenes will then be briefly considered, both the role of hole localization and hole–hole interaction being referred to in these quasi-two-dimensional systems. Finally some directions for further work are proposed © 1993 John Wiley & Sons, Inc.

## Introduction

The interaction of light particles with organic molecules is a relatively old subject. To cite two examples, Buckingham et al. [1] carried out a phase shift analysis to explain experimental scattering cross-section data for slow electrons by methane, while Paul and Saint-Pierre [2] reported experiments on the rapid annihilation of positrons in some gases of organic molecules.

The motivation for reopening theoretical work in this latter area was provided by very recent positron annihilation experiments of Murphy and Surko [3] on a variety of organic molecules, and in particular on alkanes  $\text{C}_n\text{H}_{2n+2}$  and substituted alkanes (see Fig. 2 below). Because of considerable current interest in electron density theory, the next section below (see also Appendix 2) on positrons interacting with organic molecules will be briefly introduced by comparing and contrasting the experimental results of Murphy and Surko [3] with positron annihilation in an electron gas of varying mean density, such as occurs in simple metals [4,5]. As to the slow electron scattering from  $\text{CH}_4$ , a very recent phenomenological reanalysis of the experimental data by Freeman and March [6] has resulted in a quite clearcut demonstration that what was missing from the earlier theoretical work of Buckingham et al. [1] (see, however, [7] and below) was a recognition of the importance of molecular polarizability. This same quantity also will be seen to play a major role in determining positron lifetimes in organic molecules.

In the third section the topic of additional electrons bound to small C clusters and also to  $\text{C}_{60}$ , will be considered, the latter study being again intimately linked with molecular polarizability. A subsection deals then with “holes” in quasi-two-dimensional (2d) organic molecules while later hole–hole and electron–electron

interactions in such 2d situations, a matter motivated by current interests in high  $T_c$  cuprates, are referred to briefly. The fourth section constitutes a summary, and also points some directions for possible future studies.

### Slow Electrons and Thermal Positrons Polarizing Organics

The purpose of this section is to present and analyze available experimental data for:

- (i) slow electron scattering from  $\text{CH}_4$ ,
- (ii) thermal positrons annihilating in organics: especially alkanes,

and to demonstrate in both areas the intimate correlation with molecular polarizability. Some links with electron density theory (see also Appendix 2) will be used to motivate the analysis and interpretation of the data.

#### *Slow Electron Scattering from Methane*

Recent work by Freeman and March [6] has reanalyzed available experimental data on slow electron scattering from  $\text{CH}_4$  [8,9]. What is demonstrated first is that slow electron scattering data for this molecule, together with that for the noble gases Ar, Kr, and Xe which are useful for comparison, can be fruitfully analyzed in a phenomenological way. This is achieved by plotting the log of the scattering cross section  $\sigma(E)$  against the variable  $\{E\sigma(E)\}^{1/2}$ . Thereby the behavior is clearly separated into two separate regimes common to all the systems, as shown in Figure 1.

The initial motivation for such a plot was that the asymptotic form of the free molecule electron density  $\rho(r)$  far from all nuclei is governed by the ionization potential through the exponential decay as

$$\rho(r) \sim \exp(-2\{I\}^{1/2}r). \quad (1)$$

Here  $I$  is in units of  $e^2/a_0$  while  $r$  is measured in units of the Bohr radius  $a_0$ . If we argue dimensionally that a "characteristic" distance  $r$  can be used in Eq. (1), related to the cross section as  $\{\sigma\}^{1/2}$ , then the exponent in that equation strongly suggests the use of the quantity  $\{E\sigma(E)\}^{1/2}$  as an "independent" variable in plots of the scattering data.

The Ramsauer-Townsend minimum then affords a basic separation between the two regimes referred to above. Below the energy,  $E_R$  say, characterizing this minimum, it turns out for all four systems  $\text{CH}_4$ , Ar, Kr, and Xe that the law

$$\{E\sigma(E)\}^{1/2} = \text{const}, \quad E \leq E_R, \quad (2)$$

is accurately obeyed (see Fig. 1). The behavior for  $E \geq E_R$  is more complex and will not be considered further here.

*Theory of Elastic Scattering Cross Section for Almost Spherical Systems.* For energies below that of the Ramsauer-Townsend minimum  $E_R$ , the measured cross

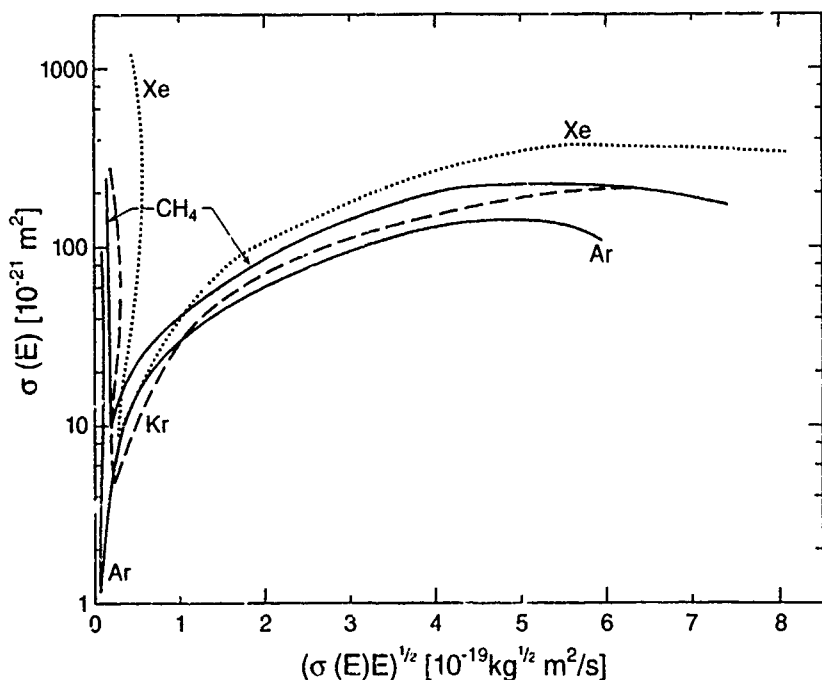


Figure 1. Scattering cross section  $\sigma(E)$  for  $\text{CH}_4$  compared with noble gases Ar, Kr, and Xe. "Independent" variable is taken as  $\{\sigma(E)E\}^{1/2}$ , as motivated below Eq. (1). (Data from Gee and Freeman [8] and Floriano et al [9]). Note that this plot phenomenologically divides data into two regions with very different characteristics, separated by the Ramsauer-Townsend minima.

section  $\sigma(E)$  is dominated by elastic scattering. For the closed shell spherical atoms Ar, Kr, and Xe, this elastic scattering cross section can be written [1]

$$\sigma_{\text{elastic}}(E) = \frac{4\pi}{k^2} \sum_{l=0}^{\infty} (2l+1) \sin^2 \eta_l(k), \quad (3)$$

where  $\eta_l(k)$  represents the phase shift of the  $l$ th partial wave ( $l=0$ , s wave: 1, p wave etc.). Equation (3) is readily rewritten as

$$\left[ \frac{\sigma_{\text{elastic}}(E)}{4\pi} \right]^{1/2} |a|^{-1} = [\Sigma(k)]^{1/2} (k|a|)^{-1}, \quad (4)$$

where  $\Sigma(k)$  denotes the sum over all  $l$  values in Eq. (3).

In Eq. (4),  $a$  is the scattering length defined through the zero-energy limit of the total scattering cross section:

$$\lim_{E \rightarrow 0} \sigma(E) = 4\pi a^2. \quad (5)$$

The empirical relation (2) now requires that, over a range of  $k \propto E^{1/2}$ , the quantity  $[\Sigma(k)]^{1/2}$  is essentially independent of  $k$ . Using the reduced variable  $k_R/k$ , one finds the approximate result representing the experimental data:

$$[\Sigma(k)]^{1/2}(k_R|a|)^{-1} = \text{const} = 0.18. \quad (6)$$

Equation (3) is immediately applicable to the closed shell noble gases Ar, Kr, and Xe. With Buckingham et al. [1], we shall regard  $\text{CH}_4$  as an almost spherical molecule for our present purposes. One of the conclusions then drawn by Freeman and March [6] is that the (constant) values of  $\Sigma(k)$  extracted from the experiments are very small (e.g., for Ar,  $\Sigma(k) = 1.4 \times 10^{-3}$ ; see Appendix 1 also). If we adopt for methane the static potential set up in Ref. [1], the values of  $\Sigma(k)$ , as noted in that reference, are much too large to agree with experiment. From the work of Gianturco and Thompson [7], it seems that careful inclusion of the polarization potential is essential to obtain realistic, and very low, values of  $\Sigma(k)$ .

What also emerges from the above study [6] is the important role in scattering of slow electrons played by the dimensionless product  $k_R|a|$ . Earlier work [10,11] has demonstrated a close correlation of the magnitude  $|a|$  of the scattering length with polarizability  $\alpha$ : Freeman and the writer [6] have exposed subsequently a linear relation between  $k_R|a|$  and  $\log \alpha$ .

Having discussed the interaction of slow electrons from  $\text{CH}_4$ , and in particular having established the major role polarizability is playing, we turn next to the positron annihilation experiments of Murphy and Surko [3].

### *Positron Annihilation with Organic Molecules*

Briefly, the experiments of Murphy and Surko [3] were performed with room temperature positrons confined in a Penning trap. For the molecules studied, such thermal energy is from 0.7 to 18 eV below the positron energy required for the formation of positronium, which therefore eliminates this process as a channel for positron annihilation.

It is customary for experimentalists to express positron annihilation rates relative to the Dirac annihilation rate of positrons in a gas of uncorrelated electrons (see Appendix 2), by an effective nuclear charge  $Z_{\text{eff}}$  [12]. Roughly speaking,  $Z_{\text{eff}}/Z$  is the average duration of a positron-molecule resonance relative to the duration of a simple elastic collision. As atomic examples, the values of  $Z_{\text{eff}}$  for the noble gases Xe, Kr, and Ar are  $\sim 300$ , 70, and 30 respectively.

Murphy and Surko [3] tabulate  $Z_{\text{eff}}$  for substituted alkanes, hexenes, aromatics, and aromatic perfluorocarbons. One point to be noted is that increasing molecular size has a major effect on the annihilation rate (see also the section after next). What we stress here in the present context is the analysis made of the annihilation rate per molecule (measured by  $Z_{\text{eff}}$ ) as a function of polarizability  $\alpha$ . While there is marked correlation, it turns out that for fixed molecular polarizability the annihilation rate per molecule as measured by  $Z_{\text{eff}}$  is very different for different series (e.g., alkanes  $\text{C}_n\text{H}_{2n+2}$ ,  $\text{C}_n\text{F}_{2n+2}$ , etc.), as demonstrated in Figure 2.

Although, at the time of writing, no detailed theory exists of the correlation exhibited in Figure 2 between annihilation rate and polarizability, there can be no

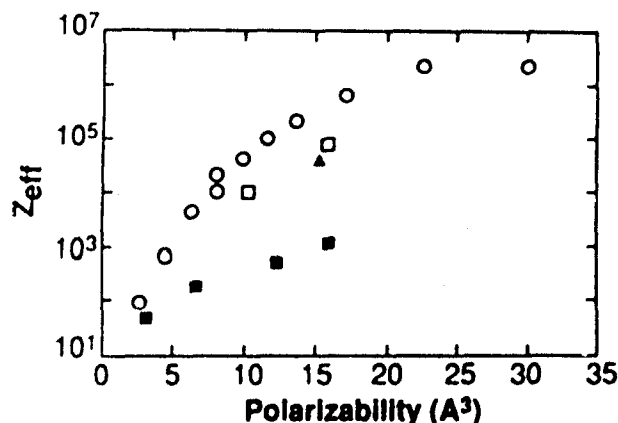


Figure 2. Plot of annihilation rate, measured by  $Z_{\text{eff}}$ , versus polarizability. While there is a good correlation, different series of organic molecules lie on different curves. (For a possible plot exhibiting more "universal" behavior, see discussion in the summary section).

doubt that, paralleling the discussion of the previous subsection for slow electrons, one is involved here in treating the way the positron polarizes the electronic cloud of these organic molecules.

It is also noteworthy that the experimental data come closer to a "universal" curve when  $\ln(Z_{\text{eff}})$  is plotted against  $[I - I_0]^{-1}$ , where  $I$  is the ionization potential of the molecule while  $I_0$  is the binding energy of the ground state of the positronium atom (6.8 eV). Returning to their early study, Paul and Saint-Pierre [2], in order to explain the very large annihilation cross sections of the heavier molecules, proposed the physical picture of a slow positron making several orbits close to the "surface of the molecule." Murphy and Surko [3] refer in their work to the possibility that a highly correlated positron and electron move in the field of a positive molecular ion. In this context positrons in liquids are relevant also (see end of Appendix 2). Further theoretical work is in progress [13] currently, but, as in the electron gas problem, there can be no doubt that the positron polarizes the (now exponentially decaying) electron density in Eq. (1) in a major fashion.

#### Photoelectron Spectroscopy: Ionization Potentials and Electron Affinities

We turn from scattering states in the previous section to the study of added light particles which are bound to organic molecules. More specifically, we shall be concerned with ionization potentials and electron affinities as measured by photoelectron spectroscopy.

#### *Additional Electrons Bound to C Clusters*

We shall consider below results, from both experiment and theory, on small C clusters, namely, linear  $C_3$ - $C_6$  [14] and  $C_{60}$  with an added electron. Because of the close link of the  $C_{60}$  work with molecular polarizability, stressed in the discussion of light particle scattering above, we take this first. The electron affinity of  $C_{60}$  has

been measured at  $2.65 \pm 0.02$  eV. We shall be concerned below with a brief discussion of the way such a result can be represented by a pseudopotential constructed by Hettich et al. [15].

*Electron Density Calculation for Added Electron in  $C_{60}$  Pseudopotential.* The binding of an additional electron to  $C_{60}$  has been explored numerically by Hettich et al. [15] using the central field pseudopotential description

$$V(r) = \frac{-e^2\alpha}{[c + 2^{1/2}(r - r_c)^2]^2} \quad (7)$$

Here  $\alpha$  is the polarizability,  $r_c$  is approximately the radius of the "European football" representing  $C_{60}$ , and  $c$  is an adjustable constant. Hettich et al. [15] fit  $c$  to reproduce the known binding energy of 2.65 eV [16].

Here an approximate calculation of some properties associated with the pseudopotential (7) will be obtained analytically from electron density theory. The starting point is to model the electron density of the ground-state generated by  $V(r)$  in Eq. (7) as the Gaussian

$$\rho(r) = \rho_{\max} \exp(-A\{r - r_c\}^2). \quad (8)$$

Next we shall invoke the approximate result of March and Wind [17], which can be described as a spatial generalization of Kato's theorem:

$$\frac{\partial \rho(r)}{\partial r} = \frac{-2r^2}{e^2 a_0} \frac{\partial V}{\partial r} \rho_s(r), \quad (9)$$

where  $\rho_s(r)$  is the s-state contribution to the total density  $\rho(r)$ . Equation (9) is exact for closed shells in a bare Coulomb field [18] but otherwise approximate.

For the ground state generated by  $V(r)$  in Eq. (7),  $\rho = \rho_s$ . We now differentiate Eqs. (7) and (8) and substitute the results into Eq. (9). Working near the "surface" of  $C_{60}$ , i.e.,  $r \approx r_c$ , we find the approximate result

$$A = 2^{5/2} \alpha r_c^2 / c^3 a_0, \quad (10)$$

which demonstrates the parametric dependence of the model electron density (8) on the pseudopotential (7). For  $C_{60}$ , Hettich et al. [15] take the polarizability  $\alpha \approx 80 \text{ \AA}^3$ . The depth  $V(r_c)$  of the pseudopotential, namely,

$$V(r_c) = -e^2\alpha/c^1 \quad (11)$$

is plainly an upper bound to the binding energy. It needs correcting by the zero-point energy associated with the curvature of the potential energy (7) around  $r = r_c$ . Evidently, the expansion of Eq. (7) for  $r \approx r_c$  is

$$V(r) = V(r_c) \left[ 1 - \frac{2^{3/2}(r - r_c)^2}{c} \right] \quad (12)$$

with force constant  $k$  given by

$$\frac{1}{2}k = 2^{3/2} e^2 \alpha / c^3. \quad (13)$$



Hence the zero-point energy  $\frac{1}{2} \hbar \omega$  referred to above corresponds to

$$\omega = (k/m)^{1/2} \quad (14)$$

with  $m$  the electron mass. Finally, therefore, the binding energy,  $E_b$ , say, of the added electron to the neutral  $C_{60}$  molecule is given by

$$\begin{aligned} E_b &= -\frac{e^2 \alpha}{c^2} + \frac{\hbar \omega}{2} \\ &= -\frac{e^2 \alpha}{c^2} + \frac{(a_0 \alpha)^{1/2}}{2} \frac{e^2}{c^{3/2}}. \end{aligned} \quad (15)$$

In summary, Eq. (10) shows how the (model) ground-state density (8) is to be expected to vary with the pseudopotential parameters in Eq. (7). Equation (15) is the corresponding result for the binding energy. Work is in progress by Alonso et al. [19] to refine the above treatment by pseudopotential density functional calculations for both  $C_{60}^-$  and  $C_{60}^{2-}$ : For a brief discussion of the latter, see subsection on hole-hole and electron-electron interactions below, and also Appendix 3.

*"Extra" Electron in Linear C Clusters.* Many-electron calculations based on coupled cluster theory have been presented by Adamowicz [14] for linear  $C_3$ – $C_6$ . He minimized the bond lengths in each case (one length for  $C_3$ , two for  $C_4$  and  $C_5$ , and three for  $C_6$ ). Adamowicz was concerned with vertical electron affinities: That is, the geometries of the anions were the same as for the respective neutrals. His results are reproduced in Table I, where the coupled cluster values of electron affinities are compared with experiment [16], as well as with self-consistent field results.

The conclusions [14] are seen to be from Table I that:

- (i) Electron affinities are significantly greater for even atom than for odd atom chains.
- (ii) There is an increase with the length of chain for both odd and even chains.
- (iii) Even for sophisticated many-electron coupled cluster calculations, the electron affinities are 0.3–0.4 of an eV smaller than the experimental values, though the trend of the empirical data is now faithfully reflected.

### *Behavior of "Holes" in Organic Molecules*

There are two different quantities one can use to characterize a "hole" in an organic molecule:

TABLE I. Electron affinities in eV for small linear C atom clusters<sup>a</sup>.

	$C_3$	$C_4$	$C_5$	$C_6$
Experiment	1.95	3.70	2.80	4.10
Coupled cluster results [14]	1.58	3.41	2.43	3.69
Self-consistent field values	1.87	2.28	2.95	2.62

<sup>a</sup> After Adamowicz [14]; experimental values from [16].

- (i) the measured ionization potential  $I$ , say from photoelectron spectroscopy,
- (ii) the electron density difference  $\Delta\rho(\mathbf{r})$  between the neutral molecule, with density  $\rho(\mathbf{r})$ , and the positive ion density  $\rho_+(\mathbf{r})$ :

$$\Delta\rho(\mathbf{r}) = \rho(\mathbf{r}) - \rho_+(\mathbf{r}), \quad (16)$$

with the nuclear geometry "frozen" in the ion as in the equilibrium neutral.

It would be valuable, for future studies, to have plots of  $\Delta\rho(\mathbf{r})$  for some typical organic molecules, derived from correlated electron wave functions. To date, we know of no information of this kind that is directly available (see, however, the subsection above, for electrons rather than holes). We note here that (i) and (ii) are linked because asymptotically  $\Delta\rho(r)$  behaves as in Eq. (1).

Therefore, below we shall content ourselves with summarizing some regularities in the ionization and chemical potentials of certain series of quasi-two-dimensional organic molecules.

*Regularities in Linear Polyacenes.* In linear polyacenes, Pucci and March [20] demonstrated that if one takes experimental values of  $I$  for the presently available members of the linear polyacene series, one then finds a marked correlation with the number of  $\pi$ -electrons. They also consider in some detail [20] the chemical potential  $\mu$  of the electron distribution, measured in units of the energy per  $\pi$ -electron, and connect this ratio (near to 2 for Hückel and extended theories and precisely 2 on an electron gas model) with the dimensionality (2d) of these molecules.

*Terminated Polyacenes: Hole Localization in Backbone.* In relation to Eq. (16) above, Kemister and March [21] have emphasized from experiment that when there is a "backbone" of three rings or more, adding off-line rings to "terminate" the linear polyacenes changes  $I$  by but a few hundredths of an eV. They interpret this result by replacing  $\Delta\rho(\mathbf{r})$  in Eq. (16) by the probability density of the HOMO orbital in Hückel theory. Though, of course, this is quite rough, they were able to conclude that this "hole density" was localized in the backbone of these molecules.

*Hole-Hole and Electron-Electron Interactions.* We shall conclude this section by commenting briefly on (i) hole-hole interaction in the linear polyacenes and (ii) electron-electron interaction in  $C_{60}^-$  and related systems.

We have investigated situations with two holes in the linear polyacenes from the higher ionization potentials as measured by Schmidt [22]. To reflect hole-hole separation, Figure 3 shows  $I$  plotted vs.  $1/n$  with  $n$  the number of rings, and  $I$  measured relative to the six-ring member. The linearity is striking and should motivate a many-body study of hole-hole correlation functions in these quasi-2d molecules.

In high  $T_c$  cuprates, electron-electron and hole-hole interactions in such quasi-2d structures are, of course, of considerable interest, and indeed this was the initial motivation for this phase of the work being presented. In this context, it seems natural to mention finally electron-electron interactions in both  $C_{60}^-$  and in K-doped, and now solid,  $C_{60}$ . The former case has been studied numerically by Hettich et al. [15]: We refer the reader to the more analytical study in Appendix 3 below.

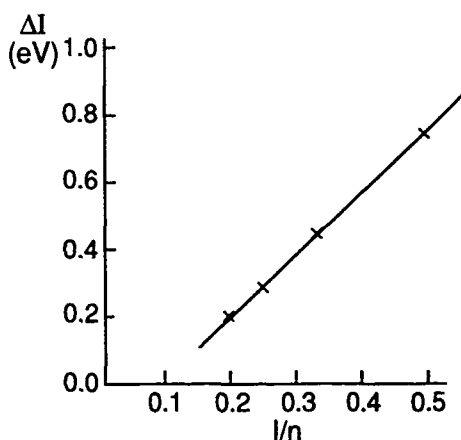


Figure 3. Higher ionization potentials for linear polyacenes (corresponding to two electrons stripped off initially neutral molecules) versus reciprocal of number of rings  $n$ .  $\Delta I$  is ionization potential for  $n$  ( $<6$ ) rings measured relative to that for six rings. (Experimental data taken from Schmidt [22]).

As for K-doped  $C_{60}$ . The K atom readily donates its valence electron to the LUMO orbital in  $C_{60}$ . Then independent studies of Gedik and Ciraci [23] and of Holas and March [24] indicate that the added electrons are well localized around the surface of the "European football" (see also Refs. [25] and [26]). It is well known that it is qualitatively easier to form a bound state in 2d than in 3d with a weak attractive interaction, a fact exploited in both [23] and [24]. Unfortunately, the mechanism for even an arbitrarily weak attractive interaction remains unclear at the time of writing.

### Summary and Directions for Further Work

Slow electrons, and also thermal positrons, polarize organic molecules in a way which dominates the momentum transfer cross section, and the positron annihilation rate, respectively. Though the case of an additional electron bound to initially neutral  $C_{60}$  is clearly chemically different; nevertheless, the binding is again dominantly due to polarizability. Electron-electron interaction in  $C_{60}^-$  still leaves the added electrons quite well localized around the surface of the "European football." This is true also of K-doped, but now solid,  $C_{60}$ . Electron-electron as well as hole-hole interactions are important in quasi-two-dimensional systems, the latter being briefly discussed in the linear polyacenes in a semiempirical manner using data on higher ionization potentials from photoelectron spectroscopy.

As to future work, it will clearly be of interest if quantum chemical calculations can be made of electron density in both neutral organics and in singly charged ions with frozen geometry as in the neutrals. The "difference" electron density in Eq. (16) will be one focal point of such calculations. For the terminated polyacenes

discussed on the basis of a single hole difference density being simply the probability density of the HOMO orbital [21], the hole remains localized in the backbone, but it would be of interest to know if this result is robust against inclusion of many-body effects. If such studies can be made, then clearly for two added holes the pair correlation function of these (compare the studies of Thorson et al. [27]) is especially interesting in quasi-two-dimensional molecules like the linear polyacenes, because of interest in the high  $T_c$  cuprates.

Finally, we return to the positron annihilation studies (see Fig. 2 above). As already noted a more "universal" plot of annihilation rate is given by taking the independent variable as  $(I - I_0)^{-1}$  instead of polarizability  $\alpha$ , with  $I$  the ionization potential and  $I_0$  the positronium binding energy. While Murphy and Surko [3] offer no physical interpretation of such a plot, we conclude by noting that, in metallic clusters, increasing cluster radius  $R$  can lead to a linear relation between  $R$  and  $(I - A)^{-1}$ , with  $A$  the electron affinity [28]. It is therefore of interest for further work to examine whether the Murphy-Surko plot of annihilation rate vs.  $(I - I_0)^{-1}$  is also reflecting a direct correlation with molecular size. If so, though such a plot is more universal than Figure 2, this latter plot may give more insight into mechanism and further work is clearly called for here.

### Acknowledgments

The author is most grateful for the numerous collaborations that have brought this paper to fruition. Special thanks are due to Professor G. R. Freeman for the fruitful collaboration on slow electron scattering in the second section, to Professor J. A. Alonso and his colleagues for the work reported in the third section, and to Professor Pucci and his research group for the help with the positron studies.

### Appendix 1: Bounds on Phase Shifts for Scattering from "Almost Spherical" Molecule $\text{CH}_4$

Clearly, from Eq. (6) of the main text the magnitude of the phase shifts sum  $\Sigma(k)$  in Eq. (4) is determined by the dimensionless product of the Ramsauer wave-number  $k_R$  and the modulus of the scattering length  $|a|$ . As explained in the text, Eq. (4) is immediately applicable to the closed shell noble gases: It is approximately valid also for the "almost spherical" molecule  $\text{CH}_4$ . The feature to be stressed is that the constant values of  $\Sigma(k)$  thereby extracted in the range of validity of Eq. (6) are extremely small. For example, for Ar,  $\Sigma(k) = 1.4 \times 10^{-3}$ .

From the definition of  $\Sigma(k)$  in Eq. (4), one can write an immediate inequality for Ar that

$$(2l + 1) \sin^2 \eta_l(k) \leq 1.4 \times 10^{-3}. \quad (\text{A1.1})$$

The equality sign, of course, applies only when a single phase shift is dominant. If we conjecture that for  $E < E_R$  and in the range of Eq. (2) this condition is satisfied and the s wave alone dominates the sum, then  $\sin^2 \eta_0 = \text{const} = 1.4 \times 10^{-3}$ . This means that  $\eta_0$  can differ from a multiple of  $\pi$  by only 0.04 radians. Plainly, if we study the phase shifts for the static methane potential used in Ref. [1], the values

of  $\Sigma(k)$ , as these workers noted, are much too large to agree with experiment. It seems, from the work of Gianturco and Thompson [7], that the careful inclusion of the polarization potential is essential to obtain realistic, and very low values of  $\Sigma(k)$ . Of course, we recognize that constancy of  $\Sigma(k)$ , say in Ar, in the range  $k_R/k$  from 1.5 to 5, may come from a balance between s, p, and d wave phase shifts. In Ref. [1], it is noted that d and higher partial wave phase shifts can be usefully calculated semiclassically. We stress again that careful inclusion of the polarization potential is essential in future work using such a semiclassical approach for, say,  $l \geq 2$ .

### Appendix 2: Electron Gas Model of Positron Annihilation

In connection with the recent experiments on positron annihilation with organic molecules discussed in the second section, let us briefly summarize the essence of the explanation of positron lifetimes in an electron gas such as exists in simple metals. Let us recall that the mean electron density,  $\rho_0$  say, in such metals, is generally represented in terms of a mean interelectronic separation  $r_s$  by

$$\rho_0 = 3/4\pi r_s^3. \quad (\text{A2.1})$$

Then in terms of the Bohr radius,  $r_s$  goes from  $2a_0$  to  $5.5a_0$  over the range of metallic densities. While more refined calculations have been made more recently using density functional theory [29], let us briefly summarize the self-consistent field calculations of March and Murray [5] for the perturbed density  $\rho(0)$ , say, at the position of a unit positive charge at the origin, embedded in an originally uniform electron gas. Table II shows their results for  $\rho(0)$  as a function of  $r_s$  and also the ratio  $\rho(0)/\rho_0$ .

A useful fit of the results in Table II is given by [5]

$$\left[ \frac{\rho(0) - \rho_0}{\rho_0} \right] = 2.23r_s + 0.766r_s^2 + 0.593r_s^3 \quad (\text{A2.2})$$

The standard Dirac result for the positron lifetime  $\tau$  [4] may be written as

$$\tau = \frac{\rho_0}{\rho(0)} \left[ \frac{r_s^3}{1.2} \right] \times 10^{-10} \text{ s}. \quad (\text{A2.3})$$

If we take the example of Cu metal with  $r_s = 2.66$  then from Table II, we find

TABLE II.

$r_s$ (units of $a_0$ )	2	2.66	4	5	6
$\rho(0)$	0.396	0.298	0.224	0.201	0.188
$\rho_0$	0.0298	0.0127	0.00373	0.00191	0.00111
$\rho(0)/\rho_0$	13	23	60	105	169

$$\tau = 0.6 \times 10^{-10} \text{ s.} \quad (\text{A2.4})$$

whereas the experimental value is  $2.3 \times 10^{-10}$  s. The agreement is quite reasonable, especially as the positron is a light particle, whereas the unit positive charge was taken as fixed at the origin in constructing Table II.

But the most interesting conclusion from this table is that whereas the electron gas density  $\rho_0$  varies by a factor of 30, the density at the position of the unit positive charge changes by little more than a factor of 2 over the same range of  $\rho_0$ . Therein lies the gist of the explanation of the observed modest variation of positron lifetimes through the simple metals. Evidently, from Eq. (A2.2), it is very hard to polarize the electron gas, as  $r_s \rightarrow 0$ , i.e., in the high density limit where the kinetic energy per electron is proportional to  $r_s^{-2}$ .

To conclude this appendix, it is of interest to compare and contrast results on metals with those on condensed forms containing organics. First though, and somewhat more generally, positron annihilation measurements are available not only for metals as discussed above but also for nonmetallic crystals, liquids, and amorphous solids. Many of the materials in the latter two categories exhibit a complex time decay curve which has two distinct components of comparable intensity with different mean lives [30]. Roughly speaking, in such complex time decay, about  $\frac{2}{3}$  of the positrons annihilate with a mean life ( $\tau_1$ ) of a few times  $10^{-10}$  s while the remaining  $\frac{1}{3}$  exhibit a mean life ( $\tau_2$ ) of  $(0.5-3.5) \times 10^{-9}$  s, depending on the substance. The longest lifetime is found to decrease, in general, as the sample is cooled.

Bell and Graham [31] propose that the  $\tau_2$  component is due to the formation of triplet positronium which is converted to the singlet state by collision. Because of the recent experiments on organics in the gaseous phase discussed in the second section of the main text, further theoretical work to understand the difference between positron annihilation in the liquid and gaseous states of organics is clearly of interest.

### Appendix 3: Electron Density Theory of Additional Electrons in $\text{C}_{60}^-$

Here we set out briefly the extension of the pseudopotential theory given in the main text for  $\text{C}_{60}$  to apply to  $\text{C}_{60}^-$ . We construct a new effective potential energy,  $\mathcal{V}(r)$  say, as

$$\mathcal{V}(r) = V(r) + e^2 \int \frac{\rho(r')}{|\mathbf{r} - \mathbf{r}'|} d\mathbf{r}' \quad (\text{A3.1})$$

Again we assume the electron density  $\rho(r)$  in Eq. (A3.1) is of Gaussian form

$$\rho(r) = \mathcal{N} \exp[-B(r - r_c)^2], \quad (\text{A3.2})$$

where  $B < A$  in Eq. (8). Again we use the relation (9) of March and Wind [17]. Differentiating Eq. (A3.2) with respect to  $r$ , we then find, again near  $r = r_c$ ,

$$\frac{\partial \rho}{\partial r} = -2B(r - r_c)\rho(r_c). \quad (\text{A3.3})$$

Turning to construct  $r^2 \partial V / \partial r$  from Eq. (A3.1), the first term from the pseudopotential  $V(r)$  is already dealt with in the third section of the main text. The second, screening contribution to  $V(r)$ , say  $V_c(r)$  in Eq. (A3.1) can be handled using Poisson's equation of electrostatics in the form

$$\frac{1}{r^2} \frac{\partial}{\partial r} \left[ r^2 \frac{\partial V_c(r)}{\partial r} \right] = 4\pi \rho(r) e^2. \quad (\text{A3.4})$$

Hence  $r^2 \partial V_c(r) / \partial r$  can be written in terms of the total amount of charge  $Q(r)$  inside a sphere of radius  $r$ , namely,

$$Q(r) = \int_0^r 4\pi r'^2 \rho(r') dr' \quad (\text{A3.5})$$

as

$$\frac{r^2 \partial V_c(r)}{\partial r} = Q(r) \quad (\text{A3.6})$$

From Eq. (9) and (A3.3), one finds then

$$-2B(r - r_c) = \left( \frac{r^2}{e^2 a_0} \frac{\partial V}{\partial r} + \frac{Q(r) - Q(r_c)}{a_0} \right)_{r=r_c} \quad (\text{A3.7})$$

Using the explicit form (A3.2) in Eq. (A3.5), one can obtain  $Q(r)$  in terms of  $B$  and  $r_c$ . Equation (A3.7) can then be used iteratively to determine  $B$ , for given parameters  $\alpha$ ,  $r_c$ , and  $c$  in the Hettich et al. pseudopotential  $V(r)$  starting with a zero-order approximation  $B = \gamma A$ ;  $\gamma \simeq 1$ . Though this numerical iteration has not been performed at the time of writing, we have estimated  $B \sim (0.043) (\text{a.u.})^{-2}$  from the different numerical study reported by Hettich et al. [15]. Further calculations are now in progress [19] to refine the above electron density treatment of  $\text{C}_{60}^{--}$ , including the choice of pseudopotential. However, these refinements are still within a spherically averaged pseudopotential approximation already employed for Na clusters [32].

### Bibliography

- [1] R. A. Buckingham, H. S. W. Massey, and S. R. Tibbs, *Proc. Roy. Soc. A* **178**, 119 (1941).
- [2] D. A. L. Paul and L. Saint-Pierre, *Phys. Rev. Lett.* **11**, 492 (1963).
- [3] T. J. Murphy and C. M. Surko, *Phys. Rev. Lett.* **67**, 2954 (1991).
- [4] S. Berko and F. L. Hereford, *Rev. Mod. Phys.* **28**, 299 (1956).
- [5] N. H. March and A. M. Murray, *Phys. Rev.* **126**, 1480 (1962).
- [6] G. R. Freeman and N. H. March, *Chem. Phys.* **173**, 451 (1993).
- [7] F. A. Gianturco and D. G. Thompson, *J. Phys. B: Atom. Molec. Phys.* **9**, L383 (1976).
- [8] N. Gee and G. R. Freeman, *Phys. Rev. A* **20**, 1152 (1979).
- [9] M. A. Floriano, N. Gee, and G. R. Freeman, *J. Chem. Phys.* **84**, 6799 (1986).
- [10] K. Rupnik, V. Asaf, and S. P. McGlynn, *J. Chem. Phys.* **92**, 2303 (1990).
- [11] G. R. Freeman, *J. Chem. Phys.* **94**, 3284 (1991).
- [12] See, for example, G. R. Heyland, M. Charlton, T. C. Griffith, and G. L. Wright, *Can. J. Phys.* **60**, 503 (1982).
- [13] R. Pucci and N. H. March, (1993), to appear.

- [14] L. Adamowicz, J. Chem. Phys. **94**, 1241 (1991).
- [15] R. L. Hettich, R. N. Compton, and R. H. Ritchie, Phys. Rev. Lett. **67**, 1242 (1991).
- [16] S. Yang, K. J. Taylor, M. J. Craycraft, J. Conceicao, C. L. Pettiette, D. Cheshnovsky, and R. E. Smalley, Chem. Phys. Lett. **144**, 431 (1988).
- [17] N. H. March and P. Wind, Mol. Phys. **76**, 1199 (1992).
- [18] N. H. March, Phys. Rev. A **33**, 88 (1986).
- [19] J. A. Alonso, A. Rubio, and N. H. March, (1993), work in progress.
- [20] R. Pucci and N. H. March, Phys. Lett. **94A**, 63 (1983); **96A**, 105 (1983).
- [21] G. Kemister and N. H. March, Int. J. Quantum Chem. Quantum Chem. Symp. **19**, 257 (1985).
- [22] W. Schmidt, J. Chem. Phys. **60**, 4406 (1974).
- [23] Z. Gedik and S. Ciraci, Phys. Rev. B **45**, 8213 (1992).
- [24] A. Holas and N. H. March, (1993), to appear.
- [25] J. Cioslowski and E. D. Fleischmann, J. Chem. Phys. **94**, 3730 (1991).
- [26] G. W. Van Cleef, G. D. Renkes, and J. V. Coe, J. Chem. Phys. **98**, 860 (1993).
- [27] W. R. Thorson, J. H. Choi, and R. B. Hake, Int. J. Quantum Chem. **1S**, 487 (1967).
- [28] J. A. Alonso and L. C. Balbás, in *Structure and Bonding* (Springer-Verlag, Berlin, 1993), p. 229.
- [29] Z. D. Popovic and M. J. Stott, Phys. Rev. Lett. **33**, 1164 (1974).
- [30] A. M. Cooper, G. J. Laidlaw, and B. G. Hogg, J. Chem. Phys. **46**, 2441 (1967).
- [31] R. E. Bell and R. L. Graham, Phys. Rev. **90**, 644 (1953).
- [32] N. Cordero, J. A. Alonso, J. M. López, and N. H. March, Mol. Phys., **79**, 353 (1993).

Received July 1, 1993



# Partial Widths of Feshbach Funnel Resonances in the $\text{Na}(3p) \cdot \text{H}_2$ Exciplex

STEVEN L. MIELKE, GREGORY J. TAWA,  
and DONALD G. TRUHLAR

*Department of Chemistry, Chemical Physics Program, Supercomputer Institute, and Army High Performance Computing Research Center, University of Minnesota, Minneapolis, Minnesota 55455-0431*

DAVID W. SCHWENKE

*NASA Ames Research Center, Mail Stop 230-3, Moffett Field, California 94035-1000*

## Abstract

We have located five zero-angular-momentum resonance states in the funnel associated with the lowest conical intersection of the  $\text{Na}(3p) \cdot \text{H}_2$  exciplex, and we have characterized the four narrowest of these in terms of total and partial widths. The resonant contributions of the metastable states to state-to-state energy transfer greatly exceed the background contributions. © 1993 John Wiley & Sons, Inc.

## Introduction

Conical intersections [1] of potential energy surfaces lead to important consequences in structure, spectroscopy, and dynamics. Structurally, the best known consequence of conical intersections is the Jahn-Teller effect [2,3], which causes the equilibrium structure of molecules in degenerate electronic states to distort. Conical intersections also have important spectroscopic effects, where they often lead to a characteristic bimodal signature in the electronic spectrum [4]. States of the upper cone are typically broadened to a large extent by nonadiabatic mixing with states of the lower potential energy surface, even when the latter is nondissociative [4,5]. In molecular collisions where the lower surface is dissociative, broadening might often be even more severe since the funnel state will have a finite lifetime. An example would be the  $\text{Na}(3p) + \text{H}_2$  system [6-12], where the ground state is repulsive, dissociating to  $\text{Na}(3s) + \text{H}_2$ , and the excited state is an exciplex, formally  $\text{Na}(3p) \cdot \text{H}_2$ , whose potential energy surface intersects the ground one conically. We have recently carried out converged quantum mechanical dynamical calculations on this system, using a previously parameterized set [10] of coupled potential energy surfaces, and, despite this broadening mechanism, we found five resonances, four of which are broadened by only 2 to 6 meV, corresponding to lifetimes of 0.2 to 0.7 ps [12]. Furthermore we found substantial enhancement of energy transfer probabilities in inelastic collision processes that proceed through

the metastable state. In the present article, we characterize the resonances by their partial widths [13], and we study the inelastic enhancements in more detail.

The next three sections present the system, the methods used for the accurate quantum dynamics calculations, and the methods for analyzing the resonances. The final section presents results and discussion.

### System

The collision system studied is  $\text{Na}(3s) + \text{H}_2$  using a two-state electronically diabatic [14] representation described previously [10]. This representation includes two diabatic potential energy surfaces  $U_{11}$  and  $U_{22}$  and a coupling matrix element  $U_{12}$ , all of which depend on all three internal coordinates. Electronic angular momentum and spin-orbit coupling are neglected. The upper surface dissociates to  $\text{Na}(3p) + \text{H}_2$  (with excitation energy 2.1037 eV) but has an accessible well at small  $\text{Na}-\text{H}_2$  distances, corresponding to the  $\text{Na} \cdot \text{H}_2$  exciplex.

In this article (and in Refs. [12] and [18]), we set the zero of energy at  $\text{Na}(3s)$  infinitely far from  $\text{H}_2$  at its classical equilibrium internuclear distance. (Note though that in Ref. [10], the zero of energy is such that this configuration had an energy of 5.0 meV.) Figure 1 illustrates  $U_{11}$  and  $U_{22}$  for the  $C_{2v}$  geometry. In this geometry

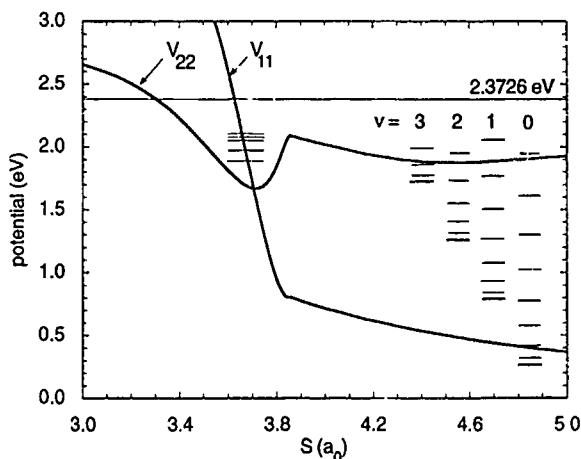


Figure 1. Energies of the two lowest potential energy surfaces for the  $C_{2v}$  approach of  $\text{Na}$  to  $\text{H}_2$  as a function of the distance  $S$  from the  $\text{Na}$  to the center of mass of  $\text{H}_2$ . For each value of  $S$ , the value of the  $\text{H}-\text{H}$  distance  $s$  is  $1.40 a_0$  when the  $\text{Na}-\text{H}_2$  distance is greater than  $3.856 a_0$  and equals  $4.123S + 17.375a_0$  when  $S$  is less than this. The preceding linear relation is determined by the requirement that the line pass through both the lowest-energy point on the upper surface at  $S = 3.715a_0$ ,  $s = 1.984a_0$  and the lowest-energy conical intersection at  $S = 3.708a_0$ ,  $s = 2.013a_0$ . The five horizontal lines in the well are the resonance energies found in this work. The horizontal lines at the right are the vibrational-rotational thresholds of  $\text{H}_2$ . The thin horizontal line across the whole figure is the energy of  $\text{Na}(3p) + \text{H}_2$  ( $v = j = 0$ ).

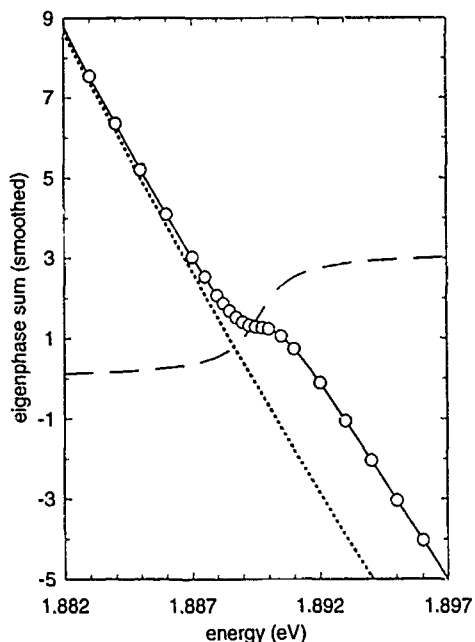


Figure 2. The sum of the eigenphases as a function of energy in the vicinity of the first resonance. The circles are the quantal calculations, and the solid curve is a fit consisting of a seventh-order polynomial for the background (direct scattering) plus a Breit-Wigner resonance term. The short-dashed line is the background, and the long-dashed line is the resonance contribution.

$U_{12} = 0$ , and so the adiabatic potentials are the same as the diabatic ones. As explained in the figure legend, the plot corresponds to a path in which the H—H distance increases significantly as the Na—H<sub>2</sub> distance decreases, because the well involves a considerably stretched H—H distance. More accurate calculations [8], for which, however, full potential energy surfaces were not presented, indicate that the potential energy surfaces used here may quantitatively overestimate the H—H extension at the minimum of  $U_{22}$  and at the lowest-energy conical intersection; nevertheless the qualitative picture of an exciplex with an H—H distance considerably larger than in diatomic hydrogen is valid.

In this article we consider total angular momentum  $J = 0$  and the even symmetry block corresponding to para H<sub>2</sub>. For  $J = 0$ , the orbital quantum number  $l$  associated with motion of Na relative to H<sub>2</sub> equals the rotational quantum number  $j$  of H<sub>2</sub>. Thus a channel  $n$  may be specified by two quantum numbers:  $v$ , which is the vibrational quantum number of H<sub>2</sub>, and  $j$ .

### Theory

For an isolated narrow resonance (INR) [13] the resonance contribution to the scattering matrix is completely specified by a complex resonance energy and  $N$

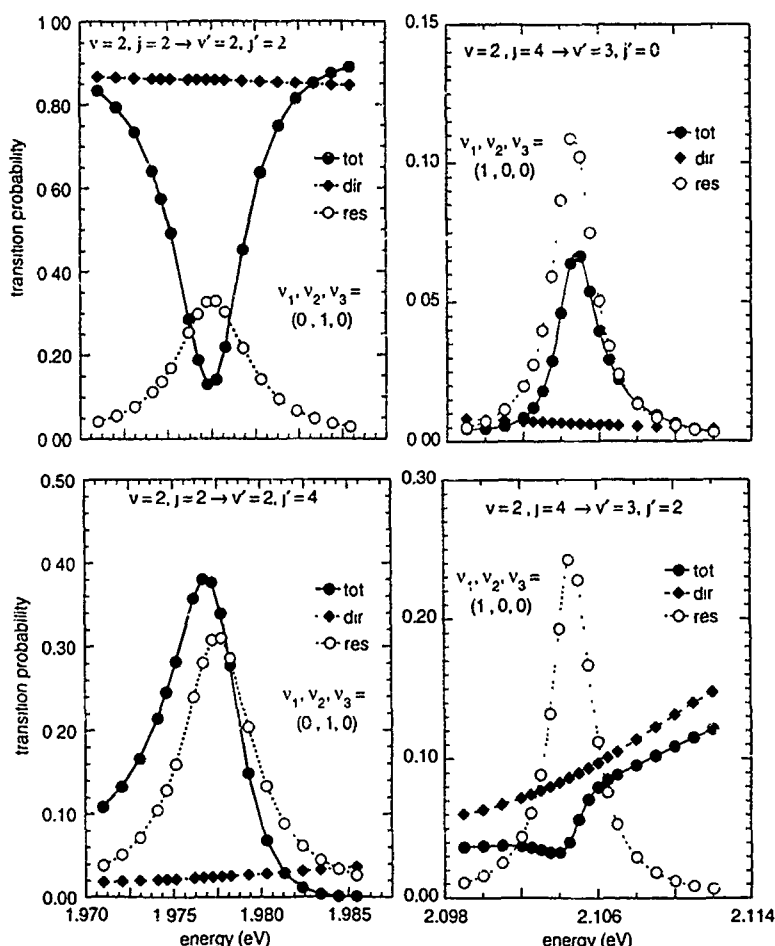


Figure 3. State-to-state transition probabilities from the full calculation (total) and the separate background (direct) and resonant contributions. The first column is for resonance 2, and the second is for resonance 5.

additional complex numbers, where  $N$  is the number of open channels. The resonance energy corresponds to a simple pole of the  $S$  matrix in the complex plane and will be denoted by

$$z_{\alpha} = E_{\alpha} - i \frac{\Gamma_{\alpha}}{2}, \quad (1)$$

where  $\alpha$  is an index specifying the particular resonance,  $E_{\alpha}$  is the location of the resonance on the real energy axis, and  $\Gamma_{\alpha}$  is the total resonance width. Near  $z_{\alpha}$  the scattering matrix may be written [13]

TABLE I. Resonance parameters.

Energy (eV)	Width (meV)	$v_1$	$v_2$	$v_3$	$\tau$ (fs)
1.890	1.960	0	0	0	699
1.977	4.679	0	1	0	281
2.053	5.741	0	2	0	229
2.08	Wide	0	0	2	n/a
2.105	2.474	1	0	0	532

$$S_{n'n} = S_{n'n}^b - i \frac{\gamma_{an'} \gamma_{an}}{E - z_a} \quad (2)$$

where  $n$  and  $n'$  denote the initial and final channels,  $S^b$  is the background (non-resonant) contribution to the scattering, and the  $\gamma_{an}$ ,  $n = 1, 2, \dots, N$ , are the complex parameters. The partial widths are given in terms of these quantities by

TABLE II. Partial widths for first resonance (eV).

$v$	$J$	Standard*	$M = 12$	Different column	Different $E$ range
0	0	2.435E-07	2.441E-07	2.431E-07	2.435E-07
0	2	5.553E-07	5.559E-07	5.551E-07	5.565E-07
0	4	4.765E-06	4.774E-06	4.757E-06	4.768E-06
0	6	1.529E-05	1.532E-05	1.528E-05	1.530E-05
0	8	1.213E-05	1.215E-05	1.211E-05	1.214E-05
0	10	7.285E-07	7.290E-07	7.297E-07	7.302E-07
0	12	4.339E-10	4.357E-10	4.341E-10	4.331E-10
0	14	4.588E-15	4.591E-15	4.581E-15	4.587E-15
1	0	1.078E-04	1.078E-04	1.077E-04	1.076E-04
1	2	1.726E-04	1.735E-04	1.725E-04	1.730E-04
1	4	2.240E-04	2.235E-04	2.239E-04	2.249E-04
1	6	1.103E-04	1.106E-04	1.104E-04	1.103E-04
1	8	3.810E-06	3.827E-06	3.810E-06	3.817E-06
1	10	4.948E-09	4.978E-09	4.948E-09	4.959E-09
1	12	1.094E-16	1.103E-16	1.138E-16	1.096E-16
2	0	1.079E-03	1.079E-03	1.079E-03	1.079E-03
2	2	1.179E-04	1.178E-04	1.177E-04	1.181E-04
2	4	4.606E-05	4.599E-05	4.601E-05	4.603E-05
2	6	2.792E-07	2.788E-07	2.790E-07	2.789E-07
2	8	3.530E-13	3.541E-13	3.735E-13	3.526E-13
3	0	1.626E-12	1.635E-12	1.596E-12	1.588E-12
3	2	2.081E-11	2.192E-11	2.105E-11	2.103E-11
3	4	2.778E-15	1.376E-15	4.010E-15	2.897E-16

\*  $M = 10$ , the fit is based on the column of the S matrix with the largest partial width, and the energy region used for the fit is a wide region between two vibrational-rotational thresholds of  $H_2$ .

TABLE III. Partial widths and ratio of partial widths (eV) and ratio of sum to total width.

$v$	$j$	Resonance 1	Resonance 2	Resonance 3	Resonance 5
0	0	2.44E-07	9.41E-07	6.50E-07	1.67E-07
0	2	5.55E-07	3.16E-06	4.22E-06	3.86E-07
0	4	4.77E-06	1.03E-05	3.84E-06	1.71E-06
0	6	1.53E-05	1.59E-05	9.29E-06	2.54E-06
0	8	1.21E-05	6.06E-06	1.99E-06	8.98E-07
0	10	7.28E-07	1.65E-06	3.00E-06	7.67E-07
0	12	4.34E-10	1.45E-09	4.55E-10	3.99E-07
0	14	4.59E-15	2.17E-13	2.48E-11	1.54E-10
0	16	closed	6.38E-20	1.39E-20	3.45E-18
1	0	1.08E-04	1.48E-04	1.46E-04	8.59E-06
1	2	1.73E-04	1.19E-04	1.54E-05	4.85E-05
1	4	2.24E-04	1.64E-06	4.30E-05	2.99E-05
1	6	1.10E-04	1.73E-05	1.14E-05	2.24E-05
1	8	3.81E-06	3.68E-07	1.29E-04	1.10E-05
1	10	4.95E-09	8.84E-07	1.34E-06	5.53E-06
1	12	1.09E-16	6.62E-13	6.66E-10	7.40E-09
1	14	closed	closed	closed	4.39E-18
2	0	1.08E-03	1.34E-03	3.91E-04	1.86E-04
2	2	1.18E-04	1.35E-03	1.28E-03	4.97E-04
2	4	4.61E-05	1.27E-03	2.18E-03	1.11E-03
2	6	2.79E-07	7.57E-05	3.37E-05	5.60E-05
2	8	3.53E-13	3.70E-10	1.99E-06	1.62E-06
2	10	closed	6.29E-16	5.75E-17	1.11E-12
3	0	1.63E-12	1.52E-07	8.50E-04	1.52E-04
3	2	2.08E-11	3.01E-10	4.65E-04	3.39E-04
3	4	2.78E-15	2.63E-10	1.09E-07	4.12E-06
3	6	closed	closed	1.21E-13	8.03E-11
$G_\alpha$		1.90E-03	4.35E-03	5.57E-03	2.48E-03
$G_\alpha/\Gamma_\alpha$		0.967	0.931	0.970	1.002

$$\Gamma_{\alpha n} = |\gamma_{\alpha n}|^2 \quad (3)$$

We will denote the sum of the partial widths by  $G_\alpha$ , i.e.,

$$G_\alpha = \sum_{n=1}^N \Gamma_{\alpha n} \quad (4)$$

For an INR we have [13]

$$\Gamma_\alpha = G_\alpha \quad (5)$$

but in general this does not hold, and it has been observed [15] that  $G_\alpha$  is frequently significantly below  $\Gamma_\alpha$  for wide resonances. In general though, we define decay probabilities by [15]

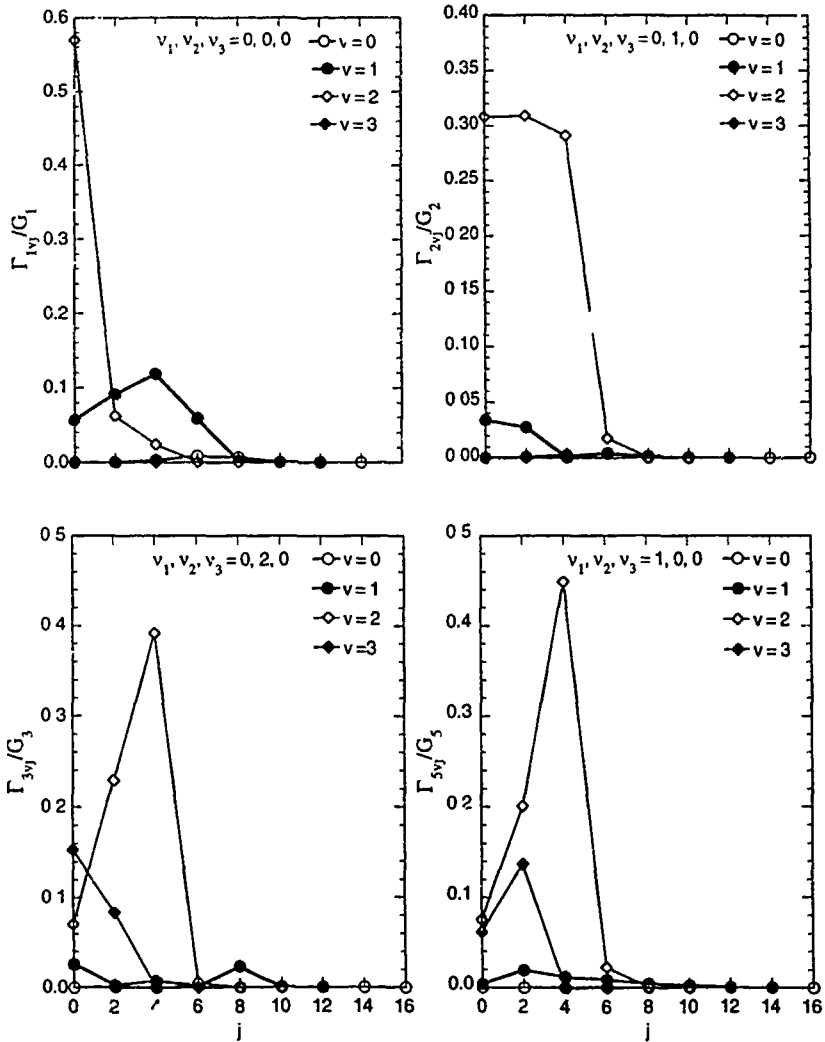


Figure 4. Decay probabilities into various  $v', j'$  states. (a) First resonance; (b) second resonance; (c) third resonance; (d) fifth resonance

$$P_{an} = \Gamma_{an}/G_a. \quad (6)$$

### Computational Procedure

The S matrices were generated by the outgoing wave variational principle [16], extended to electronically inelastic collisions as described elsewhere [11,17,18]. The numerical parameters are identical to those described elsewhere [11,18]. We

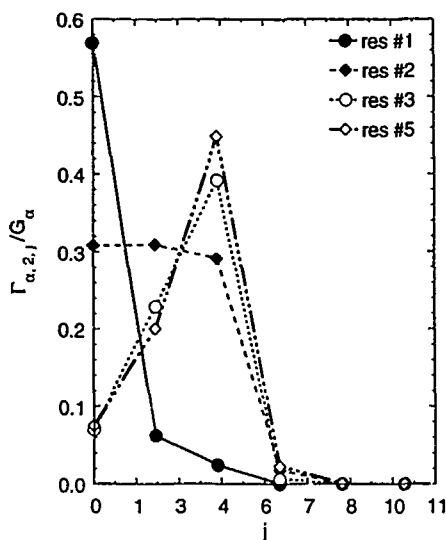


Figure 5. Decay probabilities for first, second, third, and fifth resonances into the various  $j'$  states of the  $v' = 2$  level.

performed scattering calculations at energies clustered around estimated bound-state energies of the  $U_{22}$  diabatic surface. The scattering matrices are all well converged with respect to these numerical parameters.

The first step of the fit is to determine the resonance energy. We begin with the generalized Breit-Wigner formula [19]

$$\Delta = \Delta^b + \arctan\left(\frac{\Gamma_\alpha}{2(E_\alpha - E)}\right), \quad (7)$$

where  $\Delta$  is the eigenphase sum defined by

$$\exp(2i\Delta) = \det S, \quad (8)$$

and  $\Delta^b$  denotes the background (i.e., direct) contribution. Since the eigenphase sum is only determined in Eq. (8) modulo  $\pi$  we added multiples of  $\pi$  to the calculated data until a continuous function of total energy  $E$  was obtained. Numerical values of  $\Gamma_\alpha$  and  $E_\alpha$  were determined by a nonlinear least squares fit to a smoothed version of Eq. (7), i.e.,

$$\Delta = \Delta^b + \arctan\left(\frac{\Gamma_\alpha}{2(E_\alpha - E)}\right) + \theta(E - \epsilon_\alpha), \quad (9)$$

where  $\theta$  is a Heaviside step function, and  $\Delta^b$  is represented as

$$\Delta^b = \sum_{\lambda=0}^{\lambda_{\max}} a_\lambda E^\lambda, \quad (10)$$



where  $\lambda_{\max}$  is chosen high enough that stable results are obtained. Actually, of course, the "smoothing" simply corresponds to picking the correct branch of the inverse tangent.

In the next phase of the fitting procedure we expanded  $S^b$  in Eq. (2) as

$$S_{n'n}^b = \sum_{\lambda=0}^M A_{\lambda n'n} E^\lambda, \quad (11)$$

and we multiplied this by  $E - z_\alpha$  to obtain

$$(E - z_\alpha) S_{n'n} = \sum_{\lambda=0}^{M+1} B_{\lambda n'n} E^\lambda, \quad (12)$$

where

$$B_{M+1, n'n} = A_{M n'n} \quad (13)$$

$$B_{\lambda n'n} = A_{\lambda-1, n'n} - z_\alpha A_{\lambda n'n}, \quad \lambda = 1, 2, \dots, M \quad (14)$$

$$B_{0 n'n} = -z_\alpha A_{0 n'n} - i C_{\alpha n'n}, \quad (15)$$

and

$$C_{\alpha n'n} = \gamma_{\alpha n'} \gamma_{\alpha n}. \quad (16)$$

The  $B_{\alpha n'n}$  were obtained by a linear least squares fit, and from these the  $A_{\alpha n'n}$  and  $C_{\alpha n'n}$  were determined. By fitting an entire column of the  $S$  matrix we obtained results for the  $\gamma_{\alpha n}$  and thus the partial widths. In practice we fit the column of the  $S$  matrix that has the largest partial width (as determined by a preliminary fit), although the results were stable if obtained from any column that had a reasonably sized partial width. More powerful methods for treating difficult cases have been given elsewhere [15].

## Results and Discussion

Figure 2 displays the eigenphase sums used to fit the first resonance. The fit is very good. The region shown in Figure 2 (as well as each energy range shown in Fig. 3 below) is narrow enough that it contains no rotational thresholds.

In Table I we give the fitted  $\Gamma_\alpha$  and  $E_\alpha$  as well as the quantum number assignments obtained by examining the wave function of the bound-state calculation mentioned above for the  $U_{22}$  diabatic surface. Vibrational modes  $\nu_1$  and  $\nu_2$  have  $a_1$  symmetry, and mode  $\nu_3$  has  $b_1$  symmetry. Note that states with odd  $\nu_3$  do not occur in the even symmetry block studied in this article.

Figure 3 gives plots of selected state-to-state transition probabilities. In each case, the figure shows the background (direct) contribution, i.e.,  $|S_{n'n}^b|^2$ , and the resonance contribution, given by the absolute square of the second term of Eq. (2), as well as the total transition probability, given by  $|S_{n'n}|^2$ . The total probability is

not the sum of the other two because there is also an interference term (not shown), which can be of either sign. The plot in the upper left shows the depletion of an elastic  $|S_{nn}|^2$ , and the other three show enhancements of inelastic processes. (Note that  $|S_{n'n}|^2$  is a transition probability, but elastic scattering cross sections depend on  $|1 - S_{nn}|^2$ , not on  $|S_{nn}|^2$ ).

Each resonance couples with a different distribution of strengths to the  $N^2$  possible state-to-state processes. For an INR, however, the extent of the coupling to each of these processes is summarized succinctly in the partial widths, which are discussed next.

In Table II we illustrate the quality of the convergence for the partial widths. We performed three separate tests for the first resonance. The first test shows the level of convergence when the polynomial order used in Eq. (11) is increased from 10 to 12. The second test uses the column of the  $S$  matrix associated with the second largest partial width to generate the results. The final test indicates the level of convergence when the range of energies is modified by removing the two lowest and two highest energy points. Table III lists the partial widths obtained using a 10th order polynomial for the background at each of the four resonances.

Resonance 4 was too hard to fit to get accurate widths.

Since the INR approximation holds well for resonances 1, 2, 3, and 5, their resonant transition probabilities are given to a good approximation by

$$|S_{n'n}|^2 = F_\alpha(E) P_{\alpha n} P_{\alpha n'} \quad (17)$$

where

$$F_\alpha(E) = \frac{\Gamma_\alpha^2}{(E - E_\alpha)^2 + \Gamma_\alpha^2/4} \quad (18)$$

and  $P_{\alpha n}$  is a decay probability given by Eq. (6). Equation (17) has a semiclassical interpretation that is useful when all the  $P_{\alpha n}$  are less than 0.25; in that case we can interpret  $F_\alpha(E) P_{\alpha n}$  as the probability that initial channel  $n$  accesses resonance  $\alpha$  at energy  $E$  and  $P_{\alpha n'}$  as the probability that this resonance decays to state  $n'$ . Figures 4 and 5 show the decay probabilities. One feature of immediate interest is the high specificity of decay, i.e., in each case there is at least one final state to which decay occurs with a probability greater than 0.3, and in one case the largest decay probability exceeds 0.5. We see that the largest decay probabilities are into the  $v = 2$  states for all four resonances for which partial widths were obtained, and the first resonance also shows appreciable coupling to  $v = 0$ . The coupling to highly excited vibrational states is understandable in terms of the large H—H distances accessed by the exciplex. It would be interesting to study the effect of changing the potential energy surfaces on the decay probabilities.

Figure 5 compares the  $j$  distributions directly for  $v = 2$  for all four resonances. The figure shows that the first resonance couples mainly to low  $j$  states, the second to a broad range of  $j$ , and the third and fifth to a narrow range centered at  $j = 4$ . Since resonances 2 and 3 both involve excitation of  $\nu_2$  but show quite different

patterns, but resonances 3 and 5 involve excitation of different modes and show similar patterns, the interpretation of these trends is a fascinating topic for further work.

### Acknowledgments

The authors are grateful to Yi-Ping Liu for many helpful discussions. This work was supported in part by the National Science Foundation, the University of Minnesota Supercomputer Institute, NASA, and the Army Research Office through a contract with the Army High Performance Computing Research Center at the University of Minnesota.

### Bibliography

- [1] H. C. Longuet-Higgins, *Adv. Spectry* **2**, 429 (1961); G. Herzberg and H. C. Longuet-Higgins, *Discussions Faraday Soc.* **35**, 77 (1963); A. D. Liehr, *J. Phys. Chem.* **67**, 389 (1963); R. N. Porter, R. M. Stevens, and M. Karplus, *J. Chem. Phys.* **59**, 5163 (1968); T. Carrington, *Acc. Chem. Res.* **7**, 20 (1974); E. R. Davidson, *J. Am. Chem. Soc.* **99**, 397 (1977); C. A. Mead and D. G. Truhlar, *J. Chem. Phys.* **70**, 2284 (1979), **78**, 6344 (E) (1983); C. A. Mead, *J. Chem. Phys.* **78**, 803 (1983).
- [2] H. A. Jahn and E. Teller, *Proc. R. Soc. Ser. A* **161**, 220 (1937).
- [3] G. Herzberg, *Electronic Spectra and Electronic Structure of Polyatomic Molecules* (Van Nostrand Reinhold, New York, 1966).
- [4] See, e.g., W. Domcke, H. Köppel, and L. S. Cederbaum, *Mol. Phys.* **43**, 851 (1981).
- [5] T. C. Thompson, D. G. Truhlar, and C. A. Mead, *J. Chem. Phys.* **82**, 2392 (1985).
- [6] D. G. Truhlar, J. W. Duff, N. C. Blais, J. C. Tully, and B. C. Garrett, *J. Chem. Phys.* **77**, 764 (1982); N. C. Blais, D. G. Truhlar, and B. C. Garrett, *J. Chem. Phys.* **78**, 2956 (1983).
- [7] N. C. Blais and D. G. Truhlar, *J. Chem. Phys.* **79**, 1334 (1983).
- [8] P. Botschwina, W. Meyer, I. V. Hertel, and W. Reiland, *J. Chem. Phys.* **75**, 5438 (1981); R. de Vivie-Riedle, P. Hering, and K. L. Kompa, *Z. Phys. D* **17**, 299 (1990).
- [9] W. Reiland, U. Tittes, and I. V. Hertel, *Phys. Rev. Lett.* **48**, 1389 (1982); P. McGuire and J. C. Bellum, *J. Chem. Phys.* **71**, 1975 (1979); D. R. Yarkony, *J. Chem. Phys.* **84**, 3206 (1976); C. W. Eaker, *J. Chem. Phys.* **87**, 4532 (1987); P. Hering, S. L. Cunha, and K. L. Kompa, *J. Phys. Chem.* **91**, 5459 (1987); R. de Vivie-Riedle, P. Hering, K. L. Kompa, R. R. B. Correia, S. L. Cunha, and G. Pichler, *A. I. P. Conf. Proc.* **216**, 415 (1990); R. R. B. Correia, S. L. Cunha, R. de Vivie-Riedle, G. Pichler, K. L. Kompa, and P. Hering, *Chem. Phys. Lett.* **186**, 531 (1991); G. Pichler, R. R. B. Correia, S. L. Cunha, K. L. Kompa, and P. Hering, *Opt. Commun.* **92**, 346 (1992).
- [10] P. Halvick and D. G. Truhlar, *J. Chem. Phys.* **96**, 2895 (1992). Errata: In the first equation of Section II.A,  $-c_4 + c_5r$  should be in parentheses. 2.1037 eV in the footnote of Table I should be 2.1087 because of the zero of energy.
- [11] D. W. Schwenke, S. L. Mielke, G. J. Tawa, R. S. Friedman, P. Halvick, and D. G. Truhlar, *Chem. Phys. Lett.* **203**, 565 (1993). Errata: With the zero of energy at Na(3s) infinitely far from H<sub>2</sub> at its classical equilibrium internuclear separation, the scattering energy  $E$  is 2.426 eV, the minimum of  $U_{22}$  is 1.662 eV, and the lowest-energy conical intersection is 1.663 eV.
- [12] S. L. Mielke, G. J. Tawa, D. G. Truhlar, and D. W. Schwenke, *J. Am. Chem. Soc.*, in press.
- [13] H. A. Weidenmüller, *Ann. Phys. (N.Y.)* **28**, 60 (1964), **29**, 378 (1964), R. G. Newton, *Scattering Theory of Waves and Particles*, 2nd ed. (Springer, New York, 1982), J. R. Taylor, *Scattering Theory* (Wiley, New York, 1972).
- [14] B. C. Garrett and D. G. Truhlar, *Theor. Chem. Advances Perspectives (N.Y.)* **6A**, 216 (1981).
- [15] D. W. Schwenke and D. G. Truhlar, *J. Chem. Phys.* **87**, 1095 (1987).
- [16] L. Schlessinger, *Phys. Rev.* **167**, 1411 (1968); S. C. Pieper, J. Wright, and L. Schlessinger, *Phys. Rev. D* **3**, 2419 (1971); Y. Sun, D. J. Kouri, D. G. Truhlar, and D. W. Schwenke, *Phys. Rev. A*

- 41, 4857 (1990); Y. Sun, D. J. Kouri, and D. G. Truhlar, Nucl. Phys. A508, 41c (1990); D. W. Schwenke, S. L. Mielke, and D. G. Truhlar, Theor. Chim. Acta 79, 241 (1991).
- [17] G. J. Tawa, S. L. Mielke, D. G. Truhlar, and D. W. Schwenke, in *Advances in Molecular Vibrations and Collision Dynamics—Quantum Reactive Scattering*, Vol. 2B, J. M. Bowman, Ed. (JAI Press, Greenwich, CT), in press.
- [18] G. J. Tawa, S. L. Mielke, D. G. Truhlar, and D. W. Schwenke, manuscript in preparation for J. Chem. Phys.
- [19] A. U. Hazi, Phys. Rev. A19, 920 (1979).

Received March 30, 1993

# Critical Test of PM3-Calculated Proton Affinities

PEETER BURK, KOIT HERODES, IVAR KOPPEL,  
and ILMAR KOPPEL

*Institute of Chemical Physics, Tartu University EE2400, Jakobi 2, Tartu, Estonia*

## Abstract

Proton affinities have been calculated for 119 compounds using the PM3 semiempirical molecular orbital model. PM3 seems to be not as good as AM1 for the calculation of proton affinities. At the same time, it can be a valuable tool for investigation of proton affinities, when AM1 is not usable (for hypervalent compounds of second-row elements). © 1993 John Wiley & Sons, Inc.

## Introduction

Molecular orbital calculations are carried out by an increasing number of chemists on a widest range of problems. Both *ab initio* and semiempirical self-consistent field molecular orbital calculations are often used. The widespread use of the semiempirical MINDO/3 [1], MNDO [2], AM1 [3], and PM3 [4] methods is due to the fact that they often give reliable answers, are easy to use, require relatively little computer time, and can handle large molecules.

Proton transfer reactions are widespread and of fundamental importance in chemistry and in biochemistry. Therefore, the knowledge of the proton affinities of neutral bases is essential. If these quantities could be calculated theoretically by some quantum chemical procedure with sufficient accuracy, this would be a great value, while such calculations can be carried out much faster and supposedly at much less cost than experiments. Such calculations are also not limited by the physical properties of the samples (stability, vapor pressure, etc.). As a result, numerous calculations of gas-phase (intrinsic) basicities (or proton affinities) of neutral bases have appeared [5–7 and references therein].

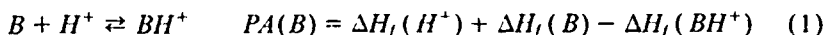
However, there have been only a few systematic investigations [5–10] testing the reliability of different methods for prediction of proton affinities of neutral bases and none dealing with the reliability of the PM3 method on the large scale of compounds. Therefore the current investigation was undertaken to evaluate the reliability of PM3 method for predicting gas-phase proton affinities.

A useful way to compare the experiment and theory is to calculate the linear regression between the theoretical and experimental quantities and to calculate the mean difference (unsigned average error) between the experimental and theoretical quantities. The degree of agreement between the two is then reflected by the slope and intercept of the correlation line, the unsigned average error, the standard deviation from correlation line, and the correlation coefficient. The last two depend

on the scatter of the points about the correlation line. A *slope different from unity* and a *nonzero intercept* imply systematic deviation between experiment and theory and means that the theoretical values of relative proton affinities will be systematically either too high or too low. A nonzero mean difference between theory and experiment reflects an overall bias in the absolute values of the calculated proton affinity.

### Method

The proton affinity (PA) of compound B was found as the heat of reaction for the proton addition equilibrium to form the conjugate acid  $BH^+$ :



where  $\Delta H_f(H^+)$ ,  $\Delta H_f(B)$ , and  $\Delta H_f(BH^+)$  are the standard heats of formation for proton, neutral base and its conjugated acid,  $BH^+$ . In the case of proton the experimental heat of formation (367.2 kcal/mol [11]) was used instead of the calculated value (353.6), because it improves the calculated proton affinities considerably. We acknowledge that this is not quite a correct procedure, despite the fact that such a way was also used in earlier works on semiempirical calculations of acidities and basicities [7,12].

The calculations were carried out on MicroVAX II and VAX 8650 computers using the standard PM3 procedure, as implemented in the MOPAC 6.0 program package [13]. All geometries were fully optimized by minimizing the energy with respect to all geometrical variables without using the aid of symmetry. In order to avoid premature completion of calculations by reaching some local minimum, the calculations were carried out starting off from several different initial geometries.

### Results and Discussion

Proton affinities for 119 compounds, calculated using PM3 method, are given in Table I, along with the corresponding "experimental" values. These particular compounds were chosen because they cover a wide range of basicities for different classes of neutral Bronsted bases (C-, O-, N-, S-, P-bases; alcohols, amines, hydrocarbons, etc.).

The results of statistical (regression) analysis of the relationship between the calculated,  $PA(\text{calc})$ , and experimental proton affinities,  $PA(\text{exp})$  according to formula

$$PA(\text{calc}) = a + b \cdot PA(\text{exp}) \quad (2)$$

are presented in Table II (see also Fig. 1), where  $N$  is the number of points,  $PA^{\min}$  is minimal, and  $PA^{\max}$  maximal experimental gas-phase proton affinity in a considered group;  $\Delta PA$  is the average unsigned error in proton affinities,  $R$  is the correlation coefficient,  $\sigma$  is the standard deviation, and  $\gamma$  is the average unsigned error, when  $PA_{\text{calc}}$  is corrected using formula

TABLE I. Comparison with experiment of PM3 heats of formation and proton affinities (kcal/mol, experimental values from Refs. [11], [15], and [16]).

	Calc $\Delta H_f$		PA		Error	Exp $\Delta H_f(B)$	Error in calc $\Delta H_f(B)$
	B	BH <sup>+</sup>	Calc	Exp			
Carbon bases							
Methane	-13.0	228.9	125.2	132.0	-6.8	-17.8	4.8
Ethane	-18.1	221.5	127.6	143.6	-16.0	-20.1	2.0
Ethene	16.6	222.5	161.4	162.6	-1.2	12.5	4.1
Propene	6.4	197.3	176.3	179.5	-3.2	4.8	1.6
1-methylcyclohexene	-14.4	168.6	184.2	197.5	-13.3	-10.3	-4.1
Benzene	23.5	212.5	178.2	181.3	-3.1	19.8	3.7
Naphthalene	40.7	218.1	189.8	194.7	-4.9	35.9	4.8
Toluene	14.1	197.5	183.8	189.8	-6.0	12.0	2.1
Styrene	39.2	210.6	195.8	200.9	-5.1	35.3	3.9
Hexamethylbenzene	-20.9	151.0	195.3	207.0	-11.7	-21.0	0.1
pMe-C <sub>6</sub> H <sub>4</sub> -C(Me)=CH <sub>2</sub>	21.8	183.9	205.1	211.2	-6.1		
1,3,5-trimethoxybenzene	-90.8	73.6	202.8	220.0	-17.2	-86.7	-4.1
Acetylene	50.7	263.9	154.0	153.3	0.7	54.5	-3.8
Propyne	40.2	238.2	169.2	182.0	-12.8	44.6	-4.4
CO	-19.7	176.9	170.6	168.4	2.2	-26.4	6.7
Nitrogen bases							
N <sub>2</sub>	17.6	237.2	147.6	118.2	29.4	0.0	17.6
Ammonia	-3.1	153.4	210.7	204.0	6.7	-11.0	7.9
HNF <sub>2</sub>	-11.4	193.4	162.4	160.0	2.4	-16.0	4.6
NF <sub>3</sub>	-24.4	201.7	141.1	136.9	4.2	-31.0	6.6
Methylamine	-4.0	153.3	209.9	214.1	-4.2	-5.5	1.5
Ethylamine	-12.5	144.3	210.4	217.0	-6.6	-11.3	-1.2
Propylamine	-17.7	138.5	211.0	217.9	-6.9	-17.3	-0.4
Iso-propylamine	-17.3	135.1	214.8	218.6	-3.8	-20.0	2.7
Butylamine	-21.7	132.9	212.6	218.4	-5.8	-22.0	0.3
Iso-butylamine	-23.0	131.8	212.4	218.8	-6.4	-23.6	0.6
tert-butylamine	-18.7	125.7	222.8	220.8	2.0	-28.9	10.2
Neopentylamine	-26.9	125.4	215.0	219.3	-4.3	-31.0	4.1
Cyclohexylamine	-26.0	125.8	215.4	221.2	-5.8	-25.0	-1.0
2-aminonorbornane	-9.5	142.3	215.4	221.7	-6.3	-8.0	-1.5
Etylideneamine	9.5	168.5	208.2	213.9	-5.7	2.0	7.5
Dimethylamine	-5.4	152.6	209.3	220.6	-11.3	-4.4	-1.0
N-ethylmethylamine	-13.0	143.7	210.4	222.8	-12.4	-11.0	-2.0
Diethylamine	-20.3	135.0	211.9	225.9	-14.0	-17.4	-2.9
Hydrazine	20.7	191.8	196.0	204.7	-8.7	22.8	-2.1
1,2-diaminoethane	-3.9	146.4	216.8	225.9	-9.1	-4.3	0.4
1,3-diaminopropane	-9.3	138.9	218.9	234.1	-15.2	-4.2	-5.1
3-aminopropan-1-ol	-56.4	92.5	218.3	228.6	-10.3	-52.0	-4.4
1,4-diaminobutane	-17.4	129.7	220.1	237.6	-17.5	-13.0	-4.4
(CH <sub>3</sub> ) <sub>2</sub> N(CH <sub>2</sub> ) <sub>4</sub> N(CH <sub>3</sub> ) <sub>2</sub>	-26.0	134.4	206.8	240.6	-33.8		
1,8-diaminonaphthalene	43.3	184.2	226.3	223.8	2.5	46.0	-2.7
Trimethylamine	-10.9	155.6	200.7	225.1	-24.4	-5.7	-5.2
N,N-dimethylethylamine	-15.9	143.2	208.1	227.5	-19.4	-11.0	-4.9
N,N-dimethylmethylamine	-20.5	141.9	204.8	230.0	-25.2	-17.0	-3.5

(Continued)

TABLE I. (Continued)

	Calc $\Delta H_f$		PA		Error	Exp $\Delta H_f(B)$	Error in calc $\Delta H_f(B)$
	B	BH <sup>+</sup>	Calc	Exp			
Nitrogen bases							
Tributylamine	-58.8	92.3	216.1	236.0	-19.9	-53.0	-5.8
N-methylformamide	-43.7	133.5	190.1	204.6	-14.5	-45.0	1.3
Aniline	21.3	175.1	213.4	209.5	3.9	20.8	0.5
Pyrrolidine	-12.0	144.8	210.5	225.2	-14.7	-0.8	-11.2
Piperidine	-16.5	137.2	213.5	226.4	-12.9	-11.7	-4.8
2,2,6,6-tetramethyl- piperidine	-39.7	105.4	222.1	231.7	-9.6	-38.0	-1.7
1-methylpyrrolidine	-14.6	143.7	208.9	228.7	-19.8	-0.5	-14.1
1-methylpiperidine	-19.3	136.2	211.7	229.7	-18.0	-12.0	-7.3
Quinuclidine	-13.1	142.9	211.2	232.1	-20.9	-1.0	-12.1
1-asabicyclo[2.2.2] -oct-2-ene	16.8	171.1	212.9	228.5	-15.6	37.0	-20.2
Pyridine	30.4	187.3	210.3	220.8	-10.5	58.0	-27.6
2-methylpyridine	21.1	174.7	213.6	225.0	-11.4	23.7	-2.6
3-methylpyridine	20.8	175.7	212.3	224.1	-11.8	25.4	-4.6
4-methylpyridine	20.8	175.1	212.9	225.2	-12.3	24.8	-4.0
Tetrazole	86.3	261.1	192.4	197.8	-5.4	80.0	6.3
HCN	33.0	213.6	186.6	171.4	15.2	32.3	0.7
Acetonitrile	23.3	197.9	192.6	188.4	4.2	18.0	5.3
Butyronitrile	14.7	188.0	193.9	192.4	1.5	7.0	7.7
(CH) <sub>2</sub> C=C(CN) <sub>2</sub>	169.2	353.1	183.3	166.6	16.7	169.0	0.2
Trichloroacetonitrile	18.5	201.5	184.2	175.7	8.5	20.0	-1.5
FCN	6.5	196.0	177.7	163.0	14.7		
Trifluoroacetonitrile	-115.0	78.6	173.5	164.1	9.4	-119.4	4.4
(CN) <sub>2</sub>	77.5	266.6	178.1	163.5	14.6	73.8	3.7
Oxygen bases							
O <sub>2</sub>	-4.2	257.8	105.2	105.5	-0.3	0.0	-4.2
Water	-53.4	159.1	154.7	166.5	-11.8	-57.8	4.4
Methanol	-51.9	156.6	158.8	181.9	-23.1	-48.2	-3.3
Ethanol	-56.9	143.9	166.5	188.3	-21.8	-56.1	-0.8
2-methyl-2-propanol	-71.3	120.0	175.9	193.7	-17.8	-74.7	3.4
2,2-difluoroethanol	-151.8	64.7	150.8	175.2	-24.4		
(CF <sub>3</sub> ) <sub>3</sub> COH	-501.0	-266.6	132.7	163.0	-30.3	-54.90	48.0
(CF <sub>3</sub> ) <sub>2</sub> CHOH	-260.7	-132.8	139.4	163.4	-24.1	-367.0	6.4
Methyl ether	-46.9	157.0	163.2	192.1	-28.9	-44.0	-2.9
Ethyl ether	-59.6	135.9	171.7	200.2	-28.5	-60.1	0.5
tert-butylmethyl ether	-64.4	116.5	186.3	202.2	-15.9	-67.8	3.4
tert-butyl ether	-75.0	102.3	189.8	212.0	-22.2	-87.0	12.0
(CF <sub>3</sub> ) <sub>2</sub> O	-381.4	-134.9	120.7	158.0	-37.3		
Carbondioxide	-85.0	139.5	142.7	130.9	11.8	-94.5	9.5
Formaldehyde	-34.1	166.3	166.8	171.7	-4.9	-26.0	-8.1
Acetaldehyde	-44.2	144.7	178.3	186.6	-8.3	-39.6	-4.6
F <sub>2</sub> CO	-138.5	75.4	153.3	158.2	-4.9	-153.0	14.5
Hexafluoroacetone	-338.4	-105.6	134.5	159.3	-24.8	-334.0	-4.4



TABLE I. (Continued)

	Calc $\Delta H_f$		PA		Error	Exp $\Delta H_f(B)$	Error in calc $\Delta H_f(B)$
	B	BH <sup>+</sup>	Calc	Exp			
Oxygen bases							
CF <sub>3</sub> COCl	-194.3	12.7	160.3	163.1	-2.8		
CF <sub>3</sub> COOH	-244.0	-39.8	163.0	171.1	-8.2	-246.3	2.3
Methylacetate	-92.7	89.3	185.3	197.8	-12.5	-98.0	5.3
Acetylacetone	-86.9	91.5	188.8	206.9	-18.1	-92.0	5.1
Formamide	-41.8	128.3	197.1	198.4	-1.3	-44.0	2.2
Sulphurdioxide	-50.8	135.3	181.2	160.2	21.0	-70.9	20.1
Dimethylsulfoxide	-38.6	117.2	211.4	210.9	0.5	-36.2	-2.4
Methylsulfonylbenzene	-40.6	111.8	214.8	194.8	20.0	-60.6	20.0
CF <sub>3</sub> SO <sub>2</sub> NH <sub>2</sub>	-207.8	-11.0	170.4	176.0	-5.6		
F <sub>2</sub> SO <sub>2</sub>	-184.3	9.3	173.6	157.3	16.3		
Trimethylphosphineoxide	-81.9	51.3	234.0	216.5	17.5		
(C <sub>3</sub> H <sub>7</sub> ) <sub>3</sub> PO	-101.4	32.2	233.6	225.3	8.3		
bis(dimethylamino)- methylphosphineoxide	-85.1	51.2	230.9	226.3	4.6		
Diethylchloromethyl- phosphonate	-191.9	-46.6	222.0	211.2	10.8		
Trimethylphosphate	-239.1	-89.1	217.2	212.5	4.7		
Triethylphosphate	-250.1	-84.6	201.6	216.5	-14.9	-284.0	33.9
Hexamethylphosphoric Amide	-85.0	53.7	228.5	227.4	1.1		
Phosphor bases							
Phosphine	0.2	117.2	250.3	188.0	62.3	1.3	-1.1
Methylphosphine	-9.5	114.8	243.0	203.5	39.5	-4.0	-5.5
Dimethylphosphine	-18.5	112.8	235.9	216.5	19.4	-14.0	-4.5
Trimethylphosphine	-28.6	109.7	228.8	226.5	2.3		
Triethylphosphine	-35.2	109.3	222.6	232.0	-9.4	-54.0	18.8
Phosphorotrifluoride	-252.2	-70.4	185.5	164.4	21.1	-229.0	-23.2
Sulphur bases							
H <sub>2</sub> S	-0.9	175.6	190.7	171.1	19.6	-4.9	4.0
Ethanethiol	-8.7	161.4	197.1	189.8	7.3	-11.1	2.4
tert-butanethiol	-13.2	153.7	200.3	195.9	4.4	-26.2	13.0
Methylsulfide	-10.4	159.4	197.4	199.1	-1.7	-9.0	-1.4
Ethylmethylsulfide	-14.5	155.7	197.0	202.3	-5.3	-14.2	-0.3
Propylsulfide	-30.1	135.3	201.9	206.3	-4.4	-29.9	-0.2
Other bases							
H	52.1	344.7	74.6	63.6	11.0	52.1	0.0
H <sub>2</sub>	-13.4	215.2	138.6	101.2	37.4	0.0	-13.4
HCl	-20.5	184.2	162.5	128.0	34.5	-22.1	1.6
HI	28.8	256.0	140.0	150.0	-10.0	6.3	22.5
CF <sub>3</sub> Br	-157.9	93.6	115.7	137.5	-21.8	-155.0	-2.9
CF <sub>3</sub> Cl	-169.2	51.6	146.4	136.0	10.4	-169.7	0.5

TABLE II Results of statistical analysis of calculated (PM3) and experimental proton affinities in terms of Eq. (2).

	N	PA <sup>min</sup>	PA <sup>max</sup>	$\Delta$ PA	$a$	$b$	$R$	$\sigma$	$\gamma$
All	119	63.6	240.6	12.9	28.3	0.8	0.884	14.9	12.8
All <sup>1</sup>	118	63.6	240.6	12.5	27.2	0.8	0.901	13.6	12.2
All <sup>2</sup>	60	130.9	237.6	11.2	14.4	0.9	0.937	8.7	7.4
Carbon bases	15	132.0	220.0	7.8	9.4	1.0	0.962	6.8	5.8
Nitrogen bases	51	118.2	240.6	11.7	73.5	0.6	0.931	6.6	7.8
Oxygen bases	35	105.5	227.4	14.5	-12.7	1.0	0.875	16.0	12.8
Phosphor bases	6	164.4	232.0	22.6	149.9	0.3	0.408	21.3	42.1
Phosphor bases <sup>1</sup>	5	164.4	232.0	16.0	97.9	0.6	0.711	15.9	18.9
Sulphur bases	6	171.1	206.3	7.0	144.1	0.3	0.889	2.0	5.2

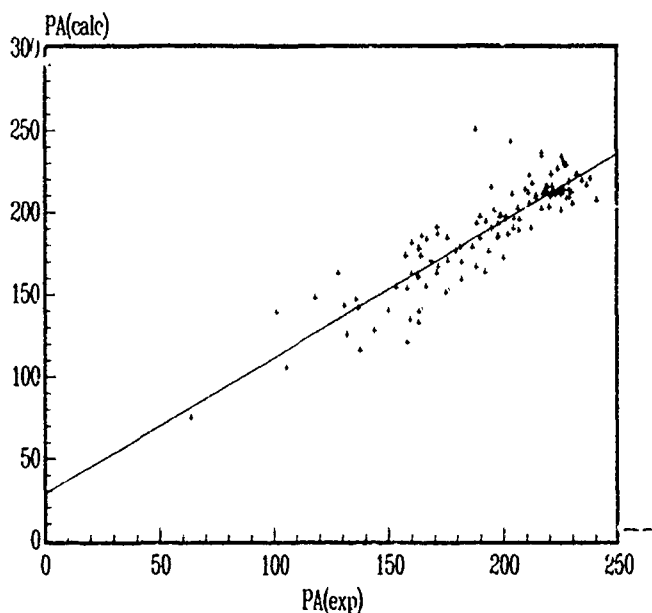
<sup>1</sup> Without PH<sub>3</sub><sup>2</sup> Compounds, calculated by Dewar [7] with AM1.

Figure 1. Calculated and experimental proton affinities (kcal/mol) for all bases surveyed.

$$PA_{\text{calc}}^{\text{cor}} = \frac{PA_{\text{calc}} - a}{b} \quad (3)$$

Table III gives analogous results for the statistical analysis of AM1-calculated proton affinities (from Ref. [7]).

The average unsigned error in the heats of formation for all neutrals is 7.9 kcal/mol. This error is fairly typical for the PM3 method and is in keeping with what has previously been found [14]. At the same time, the average unsigned error in proton affinities of the same collection of bases is 12.9 kcal/mol, compared with 6.0 kcal/mol for the AM1 method obtained by us from analysis of results of calculations for 60 compounds presented in Ref. [7]. But when we compare the results only for compounds calculated by both methods, the average unsigned error for the PM3 method reduces to 11.2 kcal/mol, which is, however, still larger than the same quantity for the AM1 method. It should be mentioned that in the case of PM3, nearly one fifth of calculated proton affinities have errors greater than 20 kcal/mol and more than half deviate more than 10 kcal/mol (see also Fig. 1).

From Table I it can be seen that extremely large error (62.3 kcal/mol) corresponds to  $\text{PH}_3$ . When the phosphine is excluded from the statistical analysis, the average unsigned error reduces to 12.5 kcal/mol. It should be mentioned that alongside with a big error in the calculated heat of formation the PM3 method also gives an unrealistic charge distribution for phosphonium cation—the calculated Mulliken charge on phosphor atom is 2.42.

On the basis of the results of the overall correlation analysis one can conclude that in the calculated proton affinities there is also present a systematic error, as indicated by the nonunity slope of the correlation line  $b$  and by the nonzero intercept  $a$ .

### Carbon Bases

The average unsigned error in calculated proton affinities for the carbon bases is 7.8 kcal/mol, which is considerably higher than that found by us for AM1 method (2.9 kcal/mol). The correlation between experimentally found and calculated proton affinities seems to be reasonably good as evidenced by the lack of the systematic

TABLE III. Results of statistical analysis of proton affinities, calculated with AM1 method in terms of Eq. (2).

	<i>N</i>	$PA^{\text{min}}$	$PA^{\text{max}}$	$\Delta PA$	<i>a</i>	<i>b</i>	<i>R</i>	$\sigma$	$\gamma$
All	60	130.9	237.6	6.0	23.8	0.9	0.979	4.8	4.5
Carbon bases	9	132.0	194.7	2.9	9.5	1.0	0.987	3.7	2.7
Nitrogen bases	33	171.4	232.1	5.8	76.4	0.6	0.934	3.0	3.8
Oxygen bases	12	130.9	202.2	6.9	38.9	0.8	0.948	5.4	5.4

error (see results of correlation analysis in Table II), but the existence of big random errors makes one prefer the AM1 method for calculation of proton affinities of carbon bases.

### *Nitrogen Bases*

The average unsigned error in calculated proton affinities for the nitrogen bases is 11.7 kcal/mol, which is again considerably higher than that found by us for AM1 method (5.8 kcal/mol). However, it seems that these errors are systematic for both methods while the slopes of correlation lines are  $0.62 \pm 0.04$  and  $0.63 \pm 0.04$  for PM3 and AM1 methods, respectively, and the application of empirical correction reduces the errors in calculated proton affinities considerably (to 7.8 and 3.8 kcal/mol for PM3 and AM1 methods, respectively). Once again, the AM1 method seems to be superior for the calculation of proton affinities of nitrogen bases.

### *Oxygen Bases*

The average unsigned error in calculated proton affinities for the oxygen bases is 14.5 kcal/mol, which similarly to that of the carbon and nitrogen bases is still significantly larger than the average unsigned error that is found in the present work for AM1 method (6.9 kcal/mol). As a rule, in case of alcohols, ethers, and carbonyl compounds the predicted proton affinities are lower than the experimental values.

### *Phosphor Bases*

The average unsigned error in calculated proton affinities for the phosphor bases is 22.6 kcal/mol. However, if we exclude from the comparison the extremely strongly deviating value for the phosphine (vide supra), the unsigned average error reduces to 16.0 kcal/mol. Still, the statistical analysis (see Table II) shows that there is practically no correlation between calculated and experimental proton affinities, so one must exercise extreme caution, when using PM3 for investigation of phosphor bases.

### *Sulphur Bases*

The average unsigned error in calculated proton affinities for the sulphur bases is 7.0 kcal/mol, which when compared with the previous groups of bases is a surprisingly good result.

## **Conclusions**

On the basis of the above results one can conclude that the PM3 method is not as good as AM1 for the calculation of proton affinities of neutral Bronsted bases (see Table II). At the same time, it can be a useful tool for investigation of proton affinities, when the AM1 method is not usable, e.g., for hypervalent compounds of second-row elements.

## References

- [1] R. C. Bingham, M. J. S. Dewar, and D. H. Loo. *J. Am. Chem. Soc.* **97**, 1285 (1975).
- [2] M. J. S. Dewar and W. Thiel, *J. Am. Chem. Soc.* **99**, 4899 (1977).
- [3] M. J. S. Dewar, E. G. Zoebisch, E. F. Healy, and J. J. P. Stewart. *J. Am. Chem. Soc.* **107**, 3902 (1985).
- [4] J. J. P. Stewart, *J. Comput. Chem.* **10**, 209 (1989).
- [5] W. J. Hehre, L. Radom, P. v. R. Schleyer, and J. A. Pople, *Ab Initio Molecular Orbital theory* (Wiley, New York, 1985).
- [6] I. A. Koppel, U. H. Molder, and V. A. Palm, *Org. React. (Tartu)* **21**, 3 (1985).
- [7] M. J. S. Dewar and K. M. Dieter, *J. Am. Chem. Soc.* **108**, 8075 (1986).
- [8] I. A. Koppel and M. B. Comisarow, *Org. React. (Tartu)* **17**, 498 (1980).
- [9] I. A. Koppel and U. H. Mölder, *Org. React. (Tartu)* **18**, 42 (1981).
- [10] D. A. Dixon and S. G. Lias, in: *Molecular Structure and Energetics, Vol. 2*, J. F. Liebman and A. Greenberg, Eds. (VCH Publishers, Deerfield Beach, 1987), p. 269.
- [11] S. G. Lias, J. E. Bartmess, J. F. Liebman, J. L. Holmes, R. D. Levin, and W. G. Mallard, *J. Phys. Chem. Ref. Data* **17**, Supplement No. 1 (1988).
- [12] S. R. Kass, *J. Comput. Chem.* **11**, 94 (1990).
- [13] J. J. P. Stewart, MOPAC Program Package.—QCPE 455, (1983).
- [14] J. J. P. Stewart, *J. Comput. Chem.* **10**, 221 (1989).
- [15] R. W. Taft, I. Koppel, F. Anvia, and J.-F. Gal, unpublished data.
- [16] I. Koppel, U. Molder, and R. Pikkver, in: *Electron and Proton Affinities of Molecules* (in Russian), G. A. Tolstikov, Ed. (Ufaa, 1991), p. 5.

Received July 6, 1993

# ZnO Clusters Models: An AM1 and MNDO Study

J. B. L. MARTINS,\* E. LONGO,<sup>†</sup> and J. ANDRÉS\*

\*Universitat Jaume I, Departament de Ciències Experimentals, Apartat 224, 12080 Castelló, Spain

<sup>†</sup>Universidade Federal de São Carlos, Departamento de Química, C Postal 676, SP 13560, Brazil

## Abstract

AM1 and MNDO semiempirical electronic calculations have been carried out for ZnO surface ((ZnO) $n$ ,  $n = 11, 16, 22, 24, 33, 42$ , and  $44$ ) cluster models. The theoretical results can be summarized as follows (i) the energy gap HOMO–LUMO is shown to be dependent on the cluster size and geometry optimization, however, better agreement of this gap with experimental data is obtained with cluster of limited size ( $n = 16, 22$ , and  $24$ ). (ii) The Mulliken charge of the cluster zinc ion is invariant with the optimization procedure, showing an average value of 0.52 a.u. (MNDO) and 0.62 a.u. (AM1). © 1993 John Wiley & Sons, Inc

## Introduction

Research on electronic materials as photo-voltaic cells [1], varistor [2,3], and a wide diversity of investigations and applications related to defects [4,5], catalysis [6–8], gas sensing [9], chemisorption [10], and semiconductivity [11] have been extensively reported [12]. Furthermore, the investigation of small-particle (ranging in size from  $<10$  Å diameter to  $100$  Å) and clusters quantum mechanics [13], is of special interest to the fields of gas chemical sensor, catalysis, and nanocrystalline material [14]. Among these electronic materials ZnO is an excellent prototype [2,3,12] for the study of interfacial electronic structure and transport properties in semiconductor oxides.

The surfaces of wurtzite-type semiconductor ZnO are thus of considerable interest for electronic and catalytic technological applications and, in particular their low-index faces [15] have been extensively studied. There are three natural surfaces: the Zn polar (0001) plane where the Zn ions are more outwardly positioned than the O ions, the O-polar (000 $\bar{1}$ ) plane where the O ions are more outwardly positioned than the Zn ions, and the nonpolar prismatic (10 $\bar{1}$ 0) plane where both Zn and O ions are in the same plane.

There is theoretical and experimental interest in the study of the crystal growth mechanism and the correlation to the changes in the electronic properties. It is known that the photocatalytic, optical, electrochemical, and electronic property of semiconductors depend on the size of the crystal [14]. It is well known that as the cluster size is successively increased, the molecular property reaches semiconductor behavior [14]. The principal result of these researches are: the gap HOMO–LUMO increases while the binding energy decrease as the size of the cluster decreases.

Previous theoretical cluster calculations of the zinc oxide surfaces and adsorption process include the discrete variational (DV) X- $\alpha$  model [16,17], tight-binding method [18], semiempirical (INDO/S) and extended Hückel methods [19] as well as the self-consistent field X- $\alpha$  scattered wave [20] model.

In the present work, AM1 and MNDO semiempirical calculations have been carried out to study the ZnO cluster. The electronic properties as function of cluster size are obtained and the reliability of these two methodologies in describing semiconductor oxides properties is analyzed.

### Method and Models

The use of cluster models has some advantages for the chemical analysis of semiconductor oxide clusters and adsorption processes. Due to the large dimensions of such clusters, a quantum chemical study requires the use of semiempirical methods. In this work, MNDO (Modified Neglect of Diatomic Overlaps) and [21] the AM1 (Austin Model 1) [22] approaches and its parameterizations [23] have been employed in the RHF-LCAO-MO framework.

We have considered seven cluster models for the ZnO (10 $\bar{1}$ 0) and (0001) surface ((ZnO) $n$ ,  $n = 11, 16, 22, 24, 33, 42$ , and  $44$ ). Zinc oxide crystallizes in the hexagonal structure of the wurtzite type in which each zinc atom is at the center of a distorted tetrahedron coordinated by four oxygen neighbors [24]. The cleavage planes of low index nonpolar (10 $\bar{1}$ 0) have been studied by theoretical and experimental procedures and unlike other low-index LEED studies of the cleavage planes they do not present a distortion of the geometry of the surface with relation to the bulk [25]. Therefore the geometry of the ZnO surface model is taken from the bulk geometry. The clusters are constructed to reproduce the crystal growing along the  $c$  axis [Figs. 1(a), 1(b), 1(c), and 1(d)] and growing along the  $a$  axis [Figs. 1(e), 1(f), and 1(g)]. The clusters ( $n = 16, 22, 24$ , and  $33$ ) are geometry optimized with constraints. These constraints are used to maintain the periodicity of the wurtzite structure of the cluster.

### Results and Discussion

#### *Nonoptimized Models*

Figure 2 shows the results for AM1 and MNDO methods of the binding energy against  $1/n$  (the inverse of the number of ZnO units). For the crystal system ( $n \rightarrow \infty$ ) the value of extrapolated binding energy is:  $-3.8$  eV (MNDO) and  $-3.0$  eV (AM1). Therefore, the MNDO method gives a more stronger bonding than AM1 procedure for ZnO units.

Figure 3 presents the energy gap HOMO-LUMO versus the inverse of the number of ZnO units. The increase of  $n$  decreases the gap value, which is in accordance with other theoretical calculations [12,13]. It is also known by experimental studies of semiconductor clusters [14] that the small clusters have greater gap value. They also show that the electronic property differs from the bulk properties and as the size increases there is a transition from molecular clusters to semiconductors. The

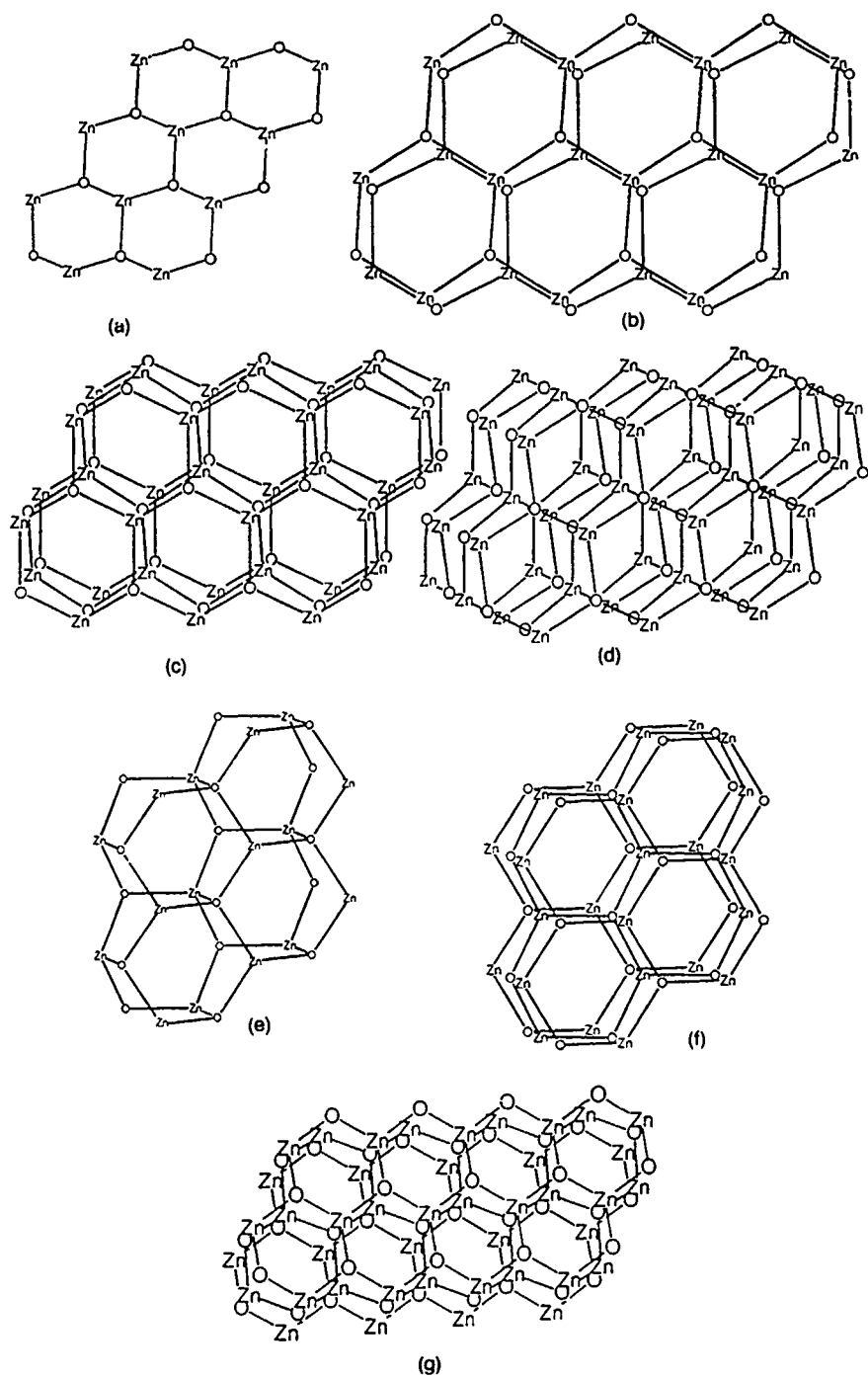


Figure 1 ZnO surface cluster models: (a)  $(\text{ZnO})_{11}$ ; (b)  $(\text{ZnO})_{22}$ ; (c)  $(\text{ZnO})_{33}$ ; (d)  $(\text{ZnO})_{44}$ ; (e)  $(\text{ZnO})_{16}$ ; (f)  $(\text{ZnO})_{24}$ ; and (g)  $(\text{ZnO})_{42}$ .



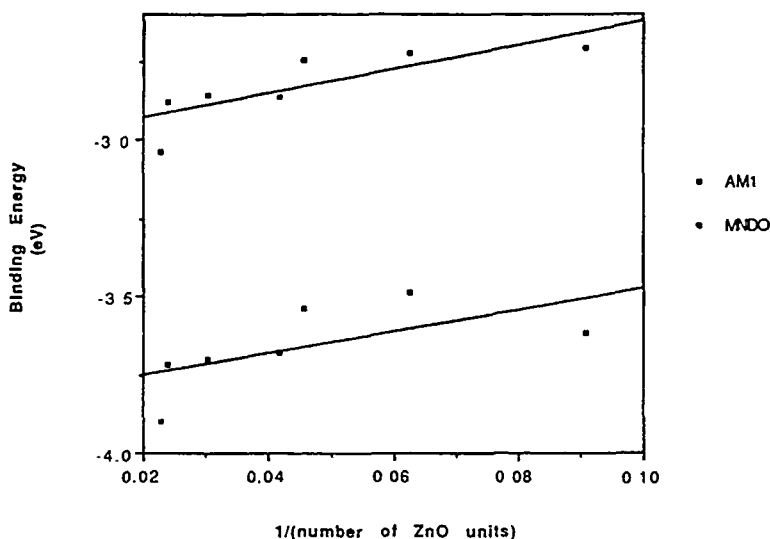


Figure 2. Binding energy against inverse of the number of ZnO units.

extrapolation of the gap value gives as results: 3.22 eV (AM1) and 2.42 eV (MNDO). The AM1 gap values are in accordance with the experimental value of the crystal bulk (3.3 eV) [11b]. The better results of the gap value are obtained for the clusters of  $(\text{ZnO})_n$  with  $n = 16, 22$ , and  $24$  [Fig. 3(a) and 3(b)]. The gap for ZnO cluster from the literature calculations has been reported in Table I. A comparison and analysis of the different results shows that our clusters are capable of reproducing the experimental energy gap.

The behavior of the HOMO [Fig. 4(a) and 4(b)] with the increase of the cluster size is in accordance to other theoretical calculations [13], which shows that the energy of the HOMO decreases with the increase of the cluster size. The extrapolations of the HOMO value results are: 6.14 eV (MNDO) and 6.61 eV (AM1).

It is well known that charge values obtained at HF level produce unphysical results. However in the present work, it is used in order to compare previous theoretical data. The Mulliken charge of the zinc ion in the cluster has an average value of 0.52 a.u. (MNDO) and 0.62 a.u. (AM1). The results of zinc charge were extrapolated to obtain  $n \rightarrow \infty$  (Fig. 5) and the calculated values are: 0.60 a.u. (AM1) and 0.50 a.u. (MNDO). These results are in agreement with the *ab initio* SCF-CI calculation for the diatomic ZnO (0.68 a.u.) [26]. However, INDO/S calculation for cluster of  $(\text{ZnO})_{13}$  produces a smaller value (0.79 a.u.) [19].

The results of binding energy and HOMO-LUMO energy gap values show that there is a correlation between the model with the growing along the *a* axis [Fig. 6(a)] and between the models with growing along the *c* axis [Fig. 6(b)]. These sets of models show a different behavior of the binding energy and gap variation with the increase of the model size for both methods employed.

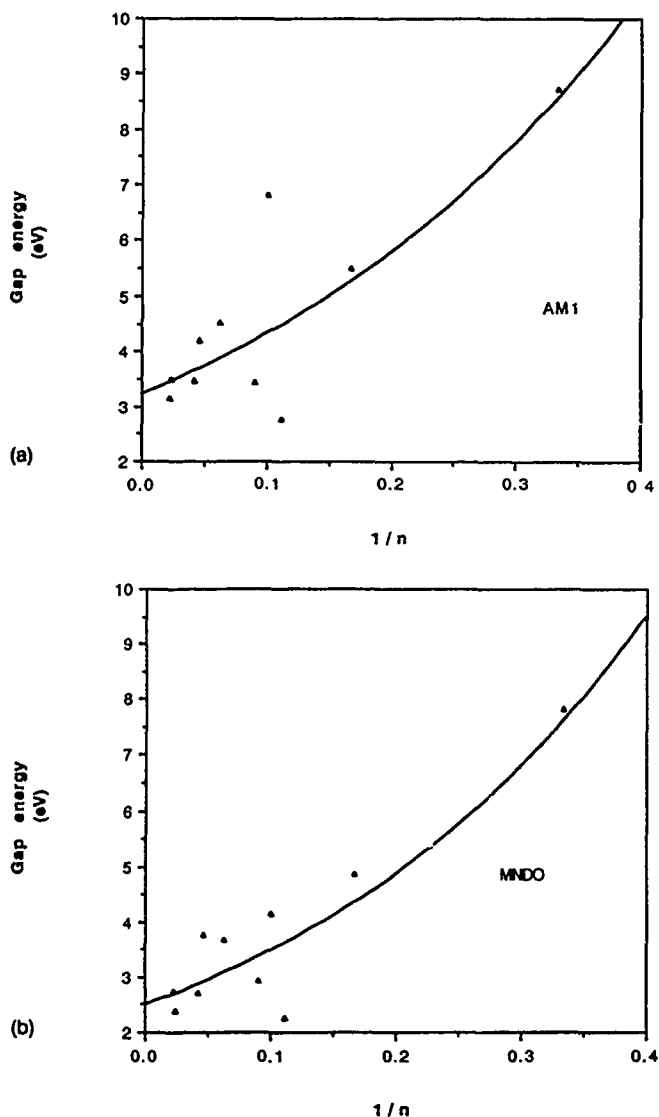


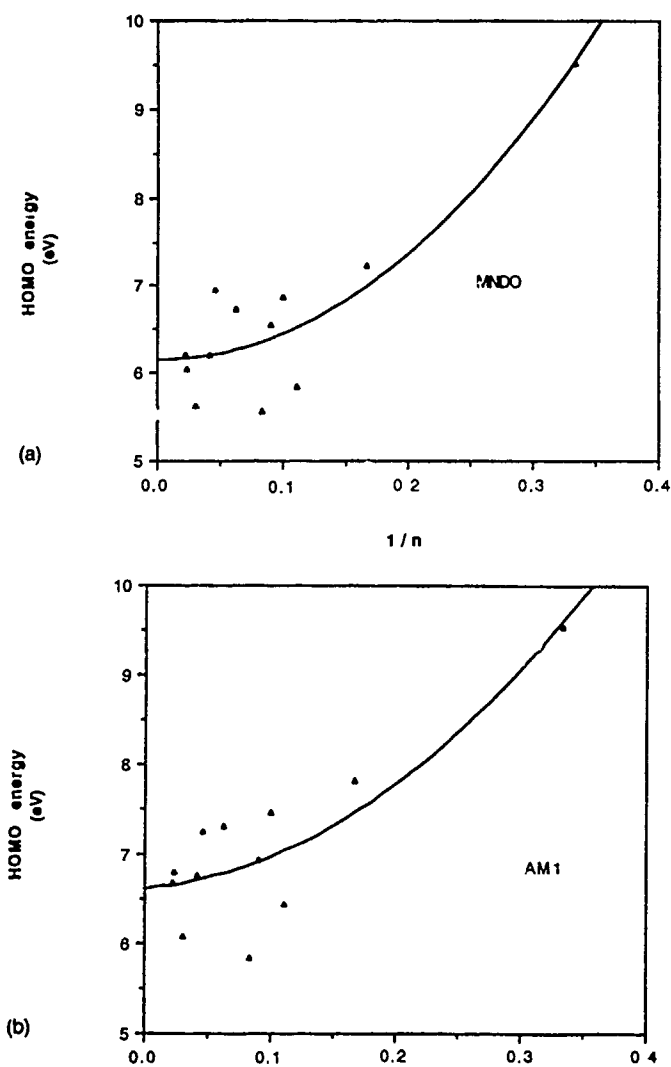
Figure 3. HOMO-LUMO energy gap (eV) vs.  $1/n$ . (a) AM1 results. (b) MNDO results. The continuous curve is obtained by extrapolation to an exponential function.

### Optimized ZnO Models

In Table II MNDO and AM1 values for the geometric optimization of the clusters,  $n = 16, 22, 24$ , and  $33$  are listed. The search of the optimum geometry leads to a minimum and a maximum deviation of 3.3 to 3.5% and 3.5 to 3.6% for MNDO and AM1 methods, respectively. These geometric parameters do not diverge sig-

TABLE I. Theoretical and experimental results from the literature for the HOMO-LUMO gap of different ZnO clusters.

	Exper.	DV-X $\alpha$	DV-X $\alpha$	INDO/S	EHT
Gap (eV)	3.3	3.2	1.2	4.4	3.0
Cluster	—	Zn <sub>4</sub> O <sub>11</sub>	Zn <sub>3</sub> O <sub>10</sub>	Zn <sub>13</sub> O <sub>13</sub>	Zn <sub>9</sub> O <sub>9</sub>
Ref.	11b	16	17	19	18

Figure 4. HOMO energy (eV) vs.  $1/n$ . (a) AM1 results. (b) MNDO results.

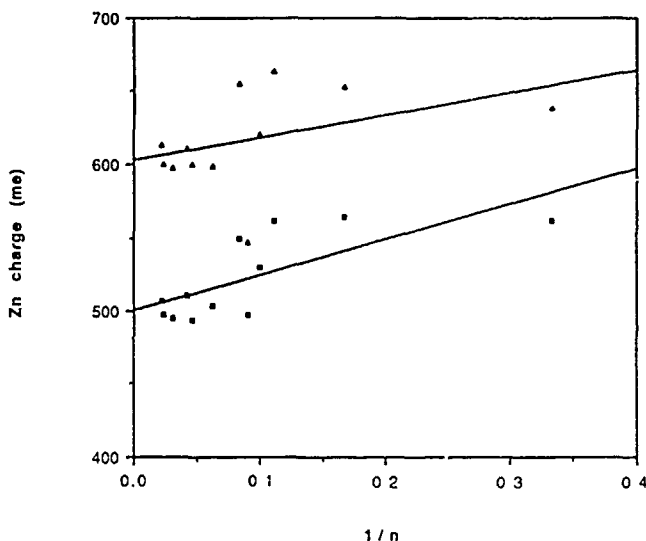


Figure 5. The Mulliken charge of zinc ion in the cluster in me (mili-electron).

nificantly from the experimental bulk values [24]. This deviation is explained in terms of the experimental results of small clusters [14]. From these studies it is known that the small clusters do not resemble completely the properties of the crystal bulk.

For AM1 and MNDO optimum geometry of such models the gap shows a better value when the optimization is done. In addition, the gap decreases smoothly with the increase of the size of the cluster, which is a direct consequence of the optimization procedure. The average of the gap value of ZnO optimum geometry gives the results: 3.19 eV (MNDO) and 3.68 eV (AM1). These gap values are better than the values obtained without optimization (Fig. 3). These changes of the gap value with the size of the cluster is in accordance with the theoretical [13] and experimental studies [14].

The charge of zinc ion in the cluster shows to be invariant with the optimization procedure, which is an expected behavior because the coordination of zinc is not modified by the optimization procedure. The extrapolated values for the charge (Fig. 7) are: 0.51 a.u. (MNDO) and 0.64 a.u. (AM1).

In spite of the fact that the experimental value of the heat of formation for the zinc oxide molecule in a gas phase at 298.15 K is not reported, this value for the ZnO molecule is calculated, and the extrapolated value for the nonoptimized clusters [Fig. 8(a)] is: 4.74 kcal/mol (MNDO) and 37.02 kcal/mol (AM1). The results for the optimized clusters [Fig. 8(b)] are: 3.3<sup>o</sup> kcal/mol (MNDO) and 28.85 kcal/mol (AM1). As could be noted the MNDO value is less than the AM1 value for optimized and nonoptimized clusters. It is well known from the zinc parameterization that the error for zinc dication is large [23]: 83 kcal/mol (MNDO) and 64 kcal/mol (AM1). The Dewar and Merz [23] AM1 optimized parameters of the two-electron

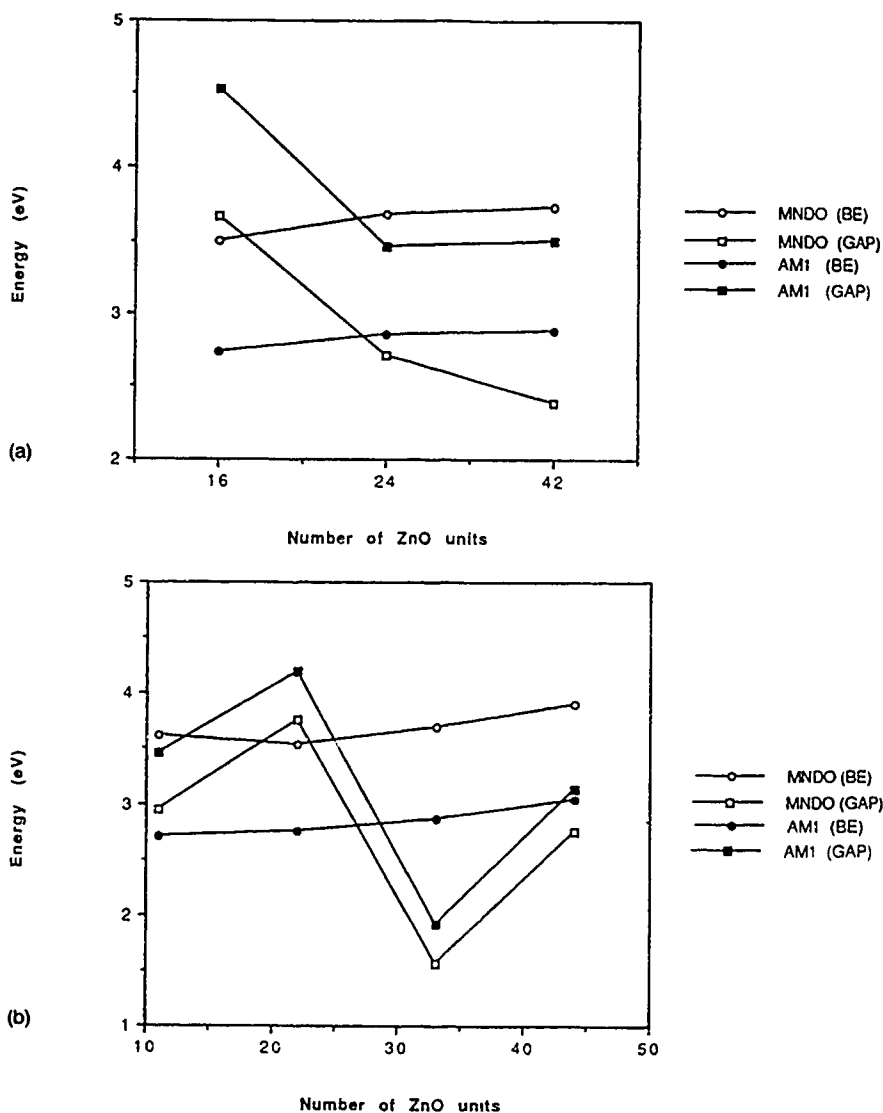


Figure 6 Binding energy and HOMO-LUMO gap value for: (a)  $n = 16, 24, 42$ ; and (b)  $n = 11, 22, 33$ , and  $44$ .

integrals are taken from the MNDO and maintained frozen which suggests the reason for the results of AM1 and MNDO for zinc dication is closer. Although the AM1 results from the literature give quite good values for heat of formation, the MNDO is known to perform poorly for diatomic molecules. This difference from AM1 and MNDO appears on our cluster models results.

TABLE II. Geometrical parameters obtained for the optimized clusters.

(ZnO) $_n$	$n = 16$		$n = 22$		$n = 24$		$n = 33$		Exp.*
	MNDO	AM1	MNDO	AM1	MNDO	AM1	MNDO	AM1	
$r_1$ (Å)	1.868	1.980	1.919	1.988	1.928	2.006	1.929	2.007	1.973
$r_2$ (Å)	(1.992)	2.300	2.158	2.274	2.168	2.170	2.275	2.23	1.992
$a$ (Å)	3.125	3.272	3.183	3.296	3.195	3.317	3.193	3.317	3.250
$c$ (Å)	5.352	5.783	5.537	5.752	5.540	5.580	5.742	5.687	5.207
$\alpha$	111.6	111.1	111.5	111.5	111.3	111.2	111.3	111.3	110.8
$\beta$	122.7	107.1	108.0	107.7	107.5	107.7	106.3	107.3	108.1

\*  $r_1$  and  $r_2$  are the two distances Zn-O,  $a$  and  $c$  are the cell parameters,  $\alpha$  and  $\beta$  are the angles (degrees) of ZnO crystal. Value in parenthesis is not fully optimized. Experimental values are from Ref. [24].

### Conclusions

The theoretical description of electronic and geometric properties of semiconductor oxides by using different cluster models with AM1 and MNDO methods is presented as an auxiliary tool for solid state studies. The geometry optimization showed how to improve the description of the electronic property of the zinc oxide.

MNDO method presents the greater binding energy between ZnO units. However,

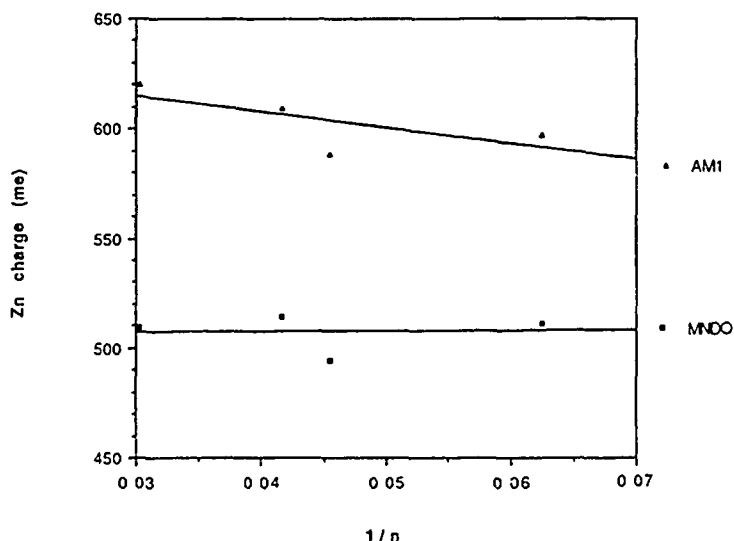


Figure 7. Zn ion charge in the cluster for the optimized models.

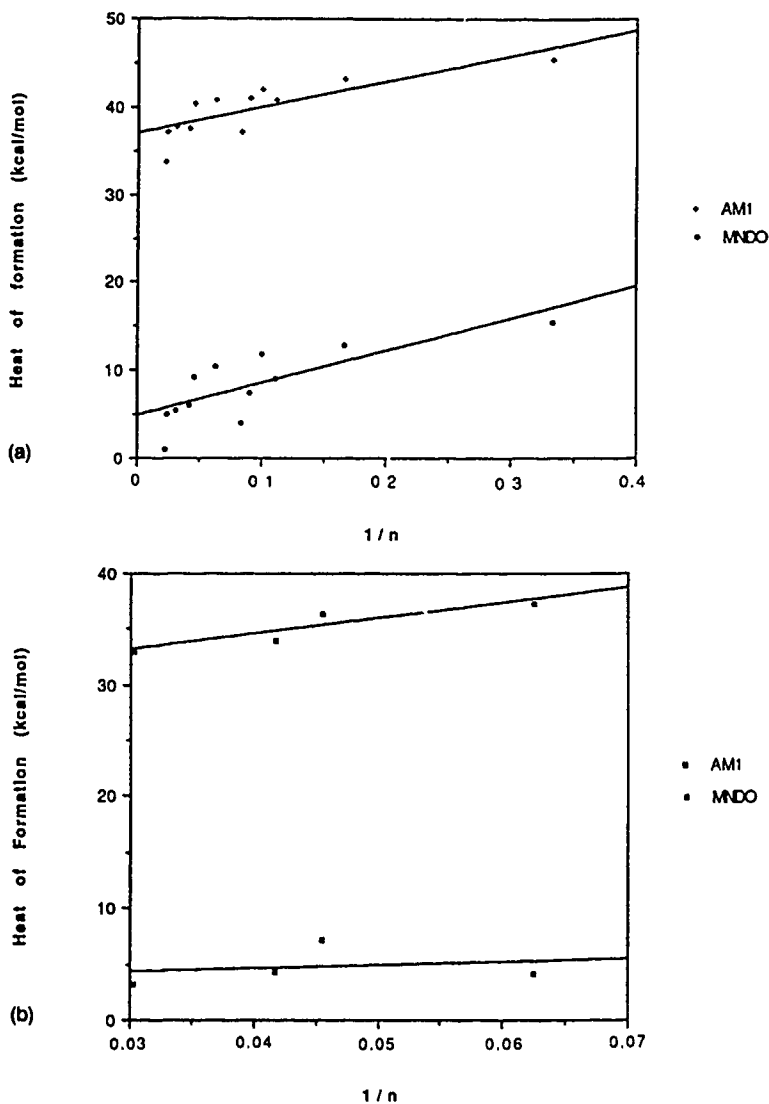


Figure 8. Heat of formation for the ZnO molecule: (a) optimized and (b) nonoptimized clusters.

for the gap value of nonoptimized models the AM1 method shows to be in accordance with the experimental value of the crystal bulk. The AM1 Mulliken charge of zinc ion in the cluster shows to be in agreement with others theoretical calculations. The optimization process for cluster models is necessary in order to obtain: (i) reliability geometries, (ii) gap values, and (iii) Mulliken charges.

### Acknowledgments

We acknowledge financial support from RHAÉ (Brazil, Proc. No. 260051/92-6) and FAPESP (Brazil, Proc. No. 91/3933-1). We are also indebted to the Centre de Processament de Dades of the Universitat Jaume I.

### Bibliography

- [1] W. W. Wenas, A. Y. Tade, and K. Takahashi, *J. Appl. Phys.* **70**, 7119 (1991).
- [2] G. Hohenberg, G. Tomandl, R. Ebert, and T. Taube, *J. Am. Cer. Soc.* **74**, 2067 (1991).
- [3] D. Kingery, *Advances in Ceramics* **1**, 1 (1981).
- [4] A. Kobayashi, O. F. Sankey, and J. D. Dow, *Phys. Rev.* **B28**, 946 (1983).
- [5] G. Heiland and D. Kohl, *Phys. Status Solidi A* **49**, 27 (1978).
- [6] D. Baresel, W. Gellert, W. Sarholz, and P. Scharner, *Sens. Actuators* **6**, 35 (1984).
- [7] T. Shido and Y. Iwasawa, *J. Catal.* **129**, 343 (1992).
- [8] C. T. Au, W. Hirsch, and W. Hirschwald, *Surf. Sci.* **197**, 391 (1988); D. G. Rethwisch and J. A. Dumesic, *Appl. Catal.* **21**, 97 (1986).
- [9] W. Gopel, *Sens. Actuators* **16**, 167 (1989).
- [10] J. M. Vohs and M. A. Barteau, *Surf. Sci.* **176**, 91 (1986); G. Heiland and H. Lüth, in *The Chemical Physics of Solid Surfaces and Heterogeneous Catalysis*, Vol. 3B, D. A. King and D. P. Woodruff, Eds. (Elsevier, Amsterdam, 1984), p. 137.
- [11] (a) T. Oyabu, *J. Appl. Phys.* **53**, 2785 (1982); (b) L. Ley, R. A. Pollak, F. R. McFeely, S. P. Kowalczyk, and D. A. Shirley, *Phys. Rev.* **B9**, 600 (1974).
- [12] J. A. Varela, O. J. Whittemore, and E. Longo, *Ceramics International* **16**, 177 (1990); E. Longo, J. A. Varela, A. N. Senapeschi, and O. J. Whittemore, *Langmuir* **1**, 456 (1985); E. Longo, J. A. Varela, C. V. Santilli, and O. J. Whittemore, *Advances in Ceramics* **10**, 592 (1984); A. C. Pavao, M. Braga, C. A. Taft, B. L. Hammond, W. A. Lester, Jr., *Phys. Rev.* **B43**, 6962 (1991); B. L. Hammond, W. A. Lester, Jr., M. Braga, and C. A. Taft, *Phys. Rev.* **B41**, 10447 (1990); A. C. Pavao, M. Braga, C. A. Taft, B. L. Hammond, and W. A. Lester, Jr., *Phys. Rev.* **B44**, 10 (1991).
- [13] R. C. Baetzold and J. F. Hamilton, *Prog. Solid State Chem.* **15**, 1 (1983).
- [14] L. Brus, *J. Phys. Chem.* **90**, 2555 (1986); M. Haase, H. Weller, and A. Henglein, *J. Phys. Chem.* **92**, 482 (1988); A. Henglein, *Chem. Rev.* **89**, 1861 (1989); L. Spamhel, and M. A. Anderson, *J. Am. Chem. Soc.* **113**, 2826 (1991).
- [15] M. Grunze, W. Hirschwald, and D. Hofmann, *J. Crystal Growth* **52**, 241 (1981).
- [16] R. Kuwabara, H. Adachi, and T. Morimoto, *Surf. Sci.* **193**, 271 (1988).
- [17] R. Sekine, H. Adachi, and T. Morimoto, *Surf. Sci.* **208**, 177 (1989).
- [18] R. C. Baetzold, *J. Phys. Chem.* **89**, 4150 (1985).
- [19] J. A. Rodriguez and C. T. Campbell, *Langmuir* **4**, 1006, 1988; J. A. Rodriguez and C. T. Campbell, *J. Phys. Chem.* **91**, 6648 (1987).
- [20] M. H. Sukkar, K. H. Johnson, and H. L. Turner, *Mat. Sci. Eng.* **B6**, 49 (1990).
- [21] M. J. S. Dewar and W. Thiel, *J. Am. Chem. Soc.* **99**, 4899 (1977).
- [22] M. J. S. Dewar, E. G. Zoebisch, E. F. Heally, and J. J. P. Stewart, *J. Am. Chem. Soc.* **107**, 3902 (1985).
- [23] M. J. S. Dewar and K. M. Merz, Jr., *Organometallics* **5**, 1494 (1986); M. J. S. Dewar and K. M. Merz, Jr., *Organometallics* **7**, 522 (1988).
- [24] S. C. Abrahams and J. L. Bernstein, *Acta Crystallogr.* **B25**, 1233 (1969).
- [25] R. R. Lubinsky, C. B. Duke, S. C. Chang, B. W. Lee, and P. Mark, *J. Vac. Sci. Technol.* **13**, 199 (1976).
- [26] C. W. Bauschlicher and S. R. Langhoff, *Chem. Phys. Lett.* **126**, 163, (1986).

Received May 27, 1993



# Correlation and Pairing in $C_{60}^{2n-}$ Ions. Superconductivity of Alkali and Alkaline Earth Compounds of $C_{60}$

SVEN LARSSON and LUCIA RODRIGUEZ-MONGE

*Department of Physical Chemistry, Chalmers University of Technology and Goteborg University,  
S-412 96 Gothenburg, Sweden*

## Abstract

Hopping conductivity becomes activationless (metallic) when twice the intersite coupling supercedes the reorganization energy. Consistent with this idea, activationless electron pair transfer may be considered as a condition for the appearance of superconductivity. For electron pairs the condition is slightly more complicated than for single electrons. The activation energy depends on the relative energies between ionic states and a valence bond state. The latter serves as an intermediate state, contributing to the disappearance of the activation barrier. In  $A_3C_{60}$ , that pairing occurs because the  ${}^1A_g$  state of the negative ions  $C_{60}^{2-}$  and  $C_{60}^{4-}$  is stabilized by correlation effects and is the ground state. The correlation effects are primarily due to the closeness in energy and different parity of the  $t_{1u}$  and  $t_{1g}$  orbitals, which are partly occupied in the negative ions, but empty in neutral  $C_{60}$ . The small interelectronic repulsion and the polarization energy from the environment also contribute to the stability of the evenly negative ions.

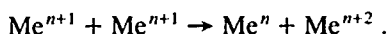
© 1993 John Wiley & Sons, Inc.

## Introduction

Semiconductors are in traditional models considered to have a finite band gap which may be determined by observing the temperature dependence of the conductivity. This is provided that other activation processes can be ignored, which is unfortunately seldom the case. Trapping of the carriers occurs and contributes to parts or all of the activation energy, as has been discussed in classical papers [1–4]. Alternatives to the band model are cluster models, large enough to represent the bulk in the sense that the activation energy for conductivity due to structure relaxation can be calculated. The working hypothesis in such a model is that the activation energy has the same origin as in “chemical” electron transfer [5,6]. In the Marcus model [7], essentially equivalent to the models of Refs. [1–4], the condition for activationless transfer is easily derived and is simply that twice the intersite coupling matrix element supercedes the reorganization energy [5]. This is then a condition for metallic conductivity as well. As we will see later, the cluster model has the advantage that a valence bond state, without charge fluctuations between sites, is easily distinguished from ionic states. The former leads to a magnetic coupling between electron spins on adjacent sites whereas the latter correspond to doubly charged polarons.

In many cases, for example the well-known Mott insulators MnO, FeO, CoO, NiO, and CuO, there is no energy gap separating the valence band from the conduction band [8] at least not in the traditional band model. Li<sub>2</sub>O doping introduces Ni<sup>3+</sup> sites among the Ni<sup>2+</sup> sites. The band model cannot be used any longer since the translational symmetry is lost. The conductivity is activated and very likely due to reorganization just as is the case of mixed valence systems, for example, KMnO<sub>4</sub>-K<sub>2</sub>MnO<sub>4</sub>. In the latter system, the same activation energy is obtained for electron transfer in solution as for conductivity in the solid phase [9,10].

Similarly, one may regard superconductivity as barrierless electron pair transfer [11,12]. Electron pair transfer has been extensively studied in inorganic chemistry and follows the same rules as transfer of single electrons [13]. An important problem to solve in that connection is why electrons sometimes prefer to be paired on a single site. The most outstanding examples are the "negative *U* compounds." The latter term refers to the energy *U* needed for the disproportionation reaction:



In chemistry such compounds are well known and well understood [13-16]. Examples are As<sup>3+</sup>/As<sup>5+</sup>, Bi<sup>3+</sup>/Bi<sup>5+</sup>, Sn<sup>2+</sup>/Sn<sup>4+</sup>, Pb<sup>2+</sup>/Pb<sup>4+</sup>, and Tl<sup>+</sup>/Tl<sup>3+</sup>. In all these cases the sites are different in the occupation of a 6s<sup>2</sup> electron pair. Since the intermediate valence state is unstable, electron transfer between the ions must be a transfer of electron pairs.

In the present paper, the conditions for pair formation in the negative ions of C<sub>60</sub> will be studied. Several alkali compounds of C<sub>60</sub> of the type K<sub>3</sub>C<sub>60</sub> have been found superconducting below 18-30 K [17-20]. More recently the compound Ca<sub>5</sub>C<sub>60</sub> has been found to be superconducting below 8.4 K [21].

In the case of A<sub>3</sub>C<sub>60</sub> the above-mentioned disproportionation (charge fluctuation) mechanism may be written as



and has been taken as the basis for an explanation of superconductivity in a number of papers [11, 22-25]. It has been shown that disproportionation and formation of singlet ground states is energetically favorable. The pairing mechanism is the same in Refs. [11] and [25]. This stabilization will be discussed here for C<sub>60</sub><sup>8-</sup>.

In a subsequent step we make plausible that the activation energy for transfer of an electron pair is zero. As we shall see, an important reason is that the valence bond state, corresponding to two C<sub>60</sub><sup>3-</sup> ions, is close in energy and interacts with the corresponding ionic states [11].

### One-Electron Transfer

Two adjacent sites A and B with identical structure are assumed to have orbitals  $\varphi_a$  and  $\varphi_b$ , respectively, which can exchange electrons. The eigenvalue problem for the one electron-two site problem may be written as

$$\begin{pmatrix} H_{aa} - \epsilon & H_{ab} \\ H_{ba} & H_{bb} - \epsilon \end{pmatrix} \begin{pmatrix} \cos \vartheta \\ \sin \vartheta \end{pmatrix} = \begin{pmatrix} \cos \vartheta \\ \sin \vartheta \end{pmatrix}, \quad (1)$$

where

$$\tan 2\vartheta = \frac{2H_{ab}}{H_{aa} - H_{bb}} \quad (2)$$

( $\vartheta = \pi/4$  for  $H_{aa} = H_{bb}$ ). If  $H_{ab}$  is large compared to the thermal fluctuations in  $|H_{aa} - H_{bb}|$ ,  $\vartheta$  is close to  $\pi/4$ , which means that the coefficients  $\cos \vartheta$  and  $\sin \vartheta$  have about the same magnitude and that the localization at either site is weak. If  $H_{ab}$  is small, localization occurs already for a small  $|H_{aa} - H_{bb}|$ .

In the case of the Mott insulators the coupling  $H_{ab}$  is expected to increase in the series  $MnO \rightarrow CuO$ , the reason being that the 3d orbital energy of the unfilled metal shell decreases relative the O 2p energy [26].

$H_{aa}$  and  $H_{bb}$  are energies in the absence of interactions between sites, which in the harmonic approximation are written as a function of distortions from an equilibrium geometry [5,15,16]:

$$H_{aa} = \sum_i \frac{1}{2} k_i (x_i + x_{i0})^2, \quad H_{bb} = \sum_i \frac{1}{2} k_i (x_i - x_{i0})^2. \quad (3)$$

The vertical excitation energy  $\lambda$  is the reorganization energy needed to move the electron without bond or solvent readjustments, i.e., keeping  $x_i$  constant.  $\lambda$  consists of bond length changes when electrons are added to or removed from a site. In general for large  $\pi$  systems the bond length change is small since the molecular orbitals are distributed on many atoms. Each bond order change is then small and hence the corresponding bond length change. In naphthalene the reorganization energy for addition of an electron has been determined to 0.2 eV, but for  $C_{60}$  or any of its ions it is likely to be smaller. The main contribution to  $\lambda$  is then from the change of equilibrium geometry of the alkali ions.

If we consider only a single coordinate, Eq. (3) may be written

$$\begin{aligned} H_{aa} &= \frac{1}{2} k (q_1 - q_0)^2 + \frac{1}{2} k (q_2 + q_0)^2 \quad \text{and} \\ H_{bb} &= \frac{1}{2} k (q_1 + q_0)^2 + \frac{1}{2} k (q_2 - q_0)^2. \end{aligned} \quad (4)$$

The minimum energy path satisfies  $q = q_1 = -q_2$  to a good approximation and hence

$$H_{aa} = k(q - q_0)^2 \quad \text{and} \quad H_{bb} = k(q + q_0)^2. \quad (5)$$

Energy minima are obtained for

$$q = \pm q_0 \left( 1 - \frac{H_{ab}^2}{4k^2 q_0^4} \right)^{1/2}. \quad (6)$$

There are two minima for

$$4kq_0^2 = \lambda > 2H_{ab} \quad (7)$$

and otherwise just one (for  $q = 0$ ). In the latter case the electrons are transferred without activation energy. Equation (7) is the condition for activationless transfer

in the cluster model and hence directly related to the metal-semiconductor transition.

From the equations above it follows that the larger the coupling, the smaller the activation energy. In the series  $\text{MnO} \rightarrow \text{CuO}$ , the coupling increases, as mentioned above, and hence the activation energy decreases towards the end of the series, in agreement with the experiments [27]. In binuclear complexes there is a well-known example when the activation energy disappears for intermetal ET, namely, the Creutz-Taube complex for which all experimental information supports a delocalized picture [28-30]:

For  $\text{A}_3\text{C}_{60}$  we may use the bandwidth calculation of Ref. [31] where a bandgap of about 0.5 eV is calculated for the  $t_{1u}$  orbital. The bandwidth for a linear chain of molecules in the tight binding approximation is  $4H_{ab}$  and thus  $H_{ab} = 0.12$  eV. We have assumed that each single  $t_{1u}$  interacts only along one direction. The reorganization energy due to bond changes in each  $\text{C}_{60}$  ion is small, as we have seen. There may be a reorganization energy connected to the motion of the alkali atoms. This energy cannot be accurately calculated at the moment, but it must be larger for small alkali ions than for larger ones. A smaller alkali atom has a larger space to move in, and the reorganization energy is then larger. We thus predict that the tendency for metallic conductivity above  $T_c$  is greater the larger the alkali atom. This is consistent with experimental results for doped  $\text{A}_3\text{C}_{60}$  above  $T_c$  [32-34].

### Pair Formation and Disproportionation in $\text{A}_3\text{C}_{60}$

The diamagnetic properties of  $\text{A}_3\text{C}_{60}$  can be explained if there is a disproportionation of the  $\text{C}_{60}^{3-}$  ions into  $\text{C}_{60}^{2-}$  and  $\text{C}_{60}^{4-}$  ions and the latter ions, with the electronic configurations  $t_{1u}^2$  and  $t_{1u}^4$ , respectively, have singlet ground states. The energies of the negative ions of  $\text{C}_{60}$  may be estimated using Koopmans' theorem in a Hartree-Fock calculation, using the semiempirical parameters of the CNDO/S method [35]. Such a calculation gives a good agreement with the experimental spectrum of  $\text{C}_{60}$  [36]. In the CNDO/S approximation the value adapted for the one-center repulsion integral is  $U = I - A$ , which is consistent with its definition in local exchange models [37]. Two-center integrals are estimated using the Mataga-Nishimoto approximation. For  $\text{C}_{60}$  we obtained, using the CNDO/S approximation, the ionization energy  $I(\text{C}_{60}) = 7.55$  eV and electron affinity  $A(\text{C}_{60}) = 2.36$  eV [35]. The experimental values are 7.6 and 2.65 eV, respectively [38-40]. We are thus only slightly overestimating  $I - A$  for  $\text{C}_{60}$ . For the negative ions we have

$$\begin{aligned} I(\text{C}_{60}^{1-}) &= A(\text{C}_{60}) = 2.36 \text{ eV} , \\ I(\text{C}_{60}^{2-}) &= A(\text{C}_{60}^{1-}) = I(\text{C}_{60}^{1-}) - U . \end{aligned} \quad (8)$$

A CNDO/S calculation, using the same orbitals as for  $\text{C}_{60}$ , gives  $U = 2.65$  eV. If the experimental value is used for the electron affinity of  $\text{C}_{60}$ , we thus obtain  $I(\text{C}_{60}^{2-}) \approx 0$  for a theoretical multiplet average.

To estimate the stability of  $\text{C}_{60}^{2-}$  in gas phase, it is necessary to calculate the multiplet structure for the  $t_{1u}^2$  configuration and the correlation energy. The multiplet structure is equivalent to the case of the  $^1\text{S}$ ,  $^1\text{D}$ , and  $^3\text{P}$  multiplets of the atomic

carbon  $2p^2$  ground state configuration. For  $C_{60}$  we obtain for the exchange integral between two different  $t_{1u}$  orbitals as  $K = 0.078$  eV, which is very small compared to the corresponding value for the carbon atom ( $K = 0.63$  eV), indicating a much less stabilization of the triplet state in  $C_{60}^{2-}$  than in the C atom.

Electronic correlation is more important in the singlet states than in the triplet state. The most obvious correlation is due to the closeness in energy of the unoccupied  $t_{1g}$  orbital [35]. The energies after accounting for the  $t_{1u}^2 \rightarrow t_{1g}^2$  correlation are

$$\begin{aligned} E(^1A_g) &= E_{av} + 4K - 6.0K', \\ E(^1H_g) &= E_{av} + K - 1.3K', \\ E(^3T_{1g}) &= E_{av} - K. \end{aligned} \quad (9)$$

Here  $E_{av}$  is the multiplet average.  $K$  is due to multiplet splitting and  $K' \approx K$  to correlation. Thus the  $^1A_g$  state is the ground state in this simple calculation. Other correlation effects lead to a further stabilization of the  $^1A_g$  state. As a comparison,  $K'$  for the corresponding correlation for the C atom ( $2p^2 \rightarrow 3d^2$ ) is relatively small since the orbitals involved belong to shells with different principal quantum number. Thus the triplet state remains the ground state for the C atom. Low spin ground states seem to be favored for all the negative ions of  $C_{60}$  due to the many possibilities of correlating two electrons with different spins. The results of this section are consistent with the observation of  $C_{60}^{2-}$  in gas phase [41] and with other theoretical results [42]. Of course, methods which only include multiplet structure predict a triplet ground state. Some ESR experiments seem to indicate a low spin ground state for  $C_{60}^{2-}$  [43] whereas others contradict this observation [44].

For  $Ca_5C_{60}$  the  $t_{1u}$  level is completely filled and the  $t_{2g}$  level occupied by four electrons. It is important that there is correlation stabilization also in this case. For  $C_{60}^{8-}$  the important configuration is provided by the  $t_{1g}^2 \rightarrow t_{2u}^2$  replacement. In our calculations we find, however, that the  $^1A_g$  state is not sufficiently stabilized to become the ground state. The off-diagonal interelectronic matrix elements are about the same but the energy splitting between  $t_{1g}$  and  $t_{2u}$  is larger than between  $t_{1u}$  and  $t_{1g}$ . This calculation is based on the orbitals of  $C_{60}^{6-}$ . There is a large increase of the  $t_{1u}$  energy compared to the  $h_g$  energy between  $C_{60}$  and  $C_{60}^{6-}$  due to occupation of the  $t_{1u}$  orbital. Our calculations are incomplete in the sense that we have not optimized the geometry of  $C_{60}^{6-}$  which may be expected to lower the  $t_{2u}$  energy compared to  $t_{1g}$ . Furthermore, a number of important correlation effects are still omitted from our calculations.

Configurations of the type  $\varphi_u^2 \rightarrow \varphi_g^2$  or  $\varphi_g^2 \rightarrow \varphi_u^2$ , with  $\varphi_g$  and  $\varphi_u$  localization to the same region of space, are important for pairing since it gives the electrons a possibility to avoid each other. A simple analysis shows that the two electrons with different spins tend to be on different sides of the  $C_{60}$  molecule. The spatial part of the two-electron wave function may be written as

$$\Psi(\mathbf{r}_1, \mathbf{r}_2) = [C_0 \varphi_u(\mathbf{r}_1) \varphi_u(\mathbf{r}_2) - C_1 \varphi_g(\mathbf{r}_1) \varphi_g(\mathbf{r}_2)], \quad (10)$$

where  $C_0$  and  $C_1$  are positive numbers and  $\varphi_u$  and  $\varphi_g$  antisymmetric and symmetric orbitals, respectively. From Eq. (10) follows that

$$|\Psi(\mathbf{r}_1, -\mathbf{r}_1)| - \Psi(\mathbf{r}_1, \mathbf{r}_1) = 2C_1\varphi_g(\mathbf{r}_1)\varphi_g(\mathbf{r}_1) > 0. \quad (11)$$

In our calculation  $C_1$  is as large as 0.5, which means a case of strong Coulomb correlation. Fermi correlation, which is in operation in the triplet states, permits one electron to be at the equator while the other one with the same spin is at one of the poles. In the C atom such a singlet pairing cannot occur due to the absence of 2d orbitals, and therefore Hund's rule is valid.

### Valence Bond and Ionic States

Let us consider two  $C_{60}^{3-}$  molecules A and B along the  $x$ -axis both with filled  $t_{1u}(y)$  orbitals. There are two additional electrons which are distributed on the two  $t_{1u}(x)$  orbitals  $\varphi_a$  and  $\varphi_b$  on the sites A and B, respectively. The latter two electrons form four states: a triplet state, a singlet valence bond (VB) state  $\Psi_{vb}$ , and two singlet ionic states  $\Psi_a$  and  $\Psi_b$ :

$$\begin{aligned} \Psi_{vb}(1,2) &= [1/2\sqrt{(1+S^2)}](\varphi_a\varphi_b + \varphi_b\varphi_a)(\alpha\beta - \beta\alpha), \\ \Psi_a(1,2) &= \varphi_a\varphi_a(\alpha\beta - \beta\alpha)/\sqrt{2} \quad \text{and} \quad \Psi_b = \varphi_b\varphi_b(\alpha\beta - \beta\alpha)/\sqrt{2}. \end{aligned} \quad (12)$$

$\Psi_a$  and  $\Psi_b$  correspond to the states after disproportionation. The energy for disproportionation in gas phase is

$$\Delta E = \langle \Psi_a | H | \Psi_a \rangle - \langle \Psi_{vb} | H | \Psi_{vb} \rangle = U - J_{ab} > 0. \quad (13)$$

$J_{ab} \approx [1.89R/27.21 + U^{-1}]^{-1} = 0.93$  eV (Mataga-Nishimoto approximation).  $J_{ab}$  thus plays an important role in the decrease of the effective  $U$  compared to the formal on-site repulsion.

In condensed phase there is a stabilization of the ionic state due to the polarization of the medium which further contributes to the decrease of the "effective  $U$ ." We may use the Born expression

$$P(z) = \frac{z^2}{2R} \left( 1 - \frac{1}{\epsilon} \right), \quad (14)$$

where  $R$  is the radius of a sphere around the  $C_{60}$  centers and  $z$  the charge. In Eq. (3)  $\epsilon$  is the dielectric constant of the medium at infinite frequency (inductive polarization;  $\epsilon = n^2$ ) or at zero frequency (atomic polarization). The energy difference between the ionic state and the VB state ("effective  $U$ ") is now

$$\Delta E = U - J_{ab} + 2P(n) - P(n-1) - P(n+1) = U - J_{ab} - 2P(1). \quad (15)$$

Using  $\epsilon = 2.5$  and  $R = 5$  Å, we obtain, for example,  $2P(1)$  equal to 1.7 eV; using  $\epsilon = 10$ , we obtain  $2P(1)$  equal to 2.6 eV. Consequently,  $\Delta E$  by Eq. (4) is slightly negative even for inductive polarization. These results are consistent with a calculation of the Madelung energies [25].

Assuming orthogonality between the orbitals on sites A and B, the Hamiltonian matrix for the symmetric 2-electron-2-site problem may be written as [11]

$$\begin{pmatrix} \Delta E + k(q + q_0)^2 & K_{ab} & \sqrt{2}H_{ab} \\ K_{ab} & \Delta E + k(q - q_0)^2 & \sqrt{2}H_{ab} \\ \sqrt{2}H_{ab} & \sqrt{2}H_{ab} & kq^2 + K_{ab} \end{pmatrix}. \quad (16)$$

Here  $H_{ab}$  is the off-diagonal matrix element for the orbitals  $\varphi_a$  and  $\varphi_b$ .  $K_{ab}$  is the exchange integral  $\langle \Psi_a | 1/r_{12} | \Psi_b \rangle$ , which may be neglected since the  $\varphi_a$  and  $\varphi_b$  are localized on different  $C_{60}$  spheres. For  $q = 0$  the system is symmetric and the matrix of Eq. (16) may be transformed to one corresponding to the basis functions  $(\Psi_a - \Psi_b)/\sqrt{2}$  and  $(\Psi_a + \Psi_b)/\sqrt{2}$  and  $\Psi_{vb}$ :

$$\begin{pmatrix} \Psi_a - \Psi_b \\ \Psi_a + \Psi_b \\ \Psi_{vb} \end{pmatrix} \begin{pmatrix} \Delta E + kq_0^2 & 0 & 0 \\ 0 & \Delta E + kq_0^2 & 2H_{ab} \\ 0 & 2H_{ab} & 0 \end{pmatrix}. \quad (17)$$

There are different important cases for the solution of Eq. (16), depending on the relative values of  $U - J_{ab}$ ,  $2P$ , and  $K_{ab}$ . If  $K_{ab}$  is neglected and if  $U - J_{ab}$  is much larger than  $2P$ ,  $\Psi_{vb}$  will be the ground state. On the other hand, if  $2P$  is larger than  $U - J_{ab}$ , the ionic state  $\Psi_a + \Psi_b$  will be the ground state. If  $\Delta E = 0$ , the latter state is lowered  $2|H_{ab}|$  compared to  $\Psi_a - \Psi_b$ . The coupling determines the degree to which the singlet ion pair will localize on A or B. Thus if  $|H_{ab}|$  is reasonably large there will be a possibility for barrierless electron pair transfer. In  $C_{60}$   $|H_{ab}|$  should be about 0.1 eV, as discussed above.

### Pair Motion

In the case of single-electron transfer, different values of the ratio coupling to reorganization energy,  $\rho = 2H_{ab}/\lambda$ , lead to three possible regimes of localization, essentially as outlined by Robin and Day [14]. In particular, if  $\rho$  is close to unity, the electrons localize according to the instantaneous nuclear positions. If  $\rho$  is much smaller than 1, trapping is possible. If  $\rho > 1$ , delocalization occurs as in the Creutz-Taube 5+ complex [28-30].

The two-electron case is different due to the appearance of the vb states (singlet and triplet). The situation may be described as follows:

*Case 1.*  $\Delta E$  is positive and large. The ground state is a singlet vb state with a deep minimum for  $q = 0$  [eq. (16)]. This is the ordinary case of a strong covalent bond, for example, the  $H_2$  molecule. The singlet-triplet splitting is large.

*Case 2.* Weakly bonded vb ground state. The magnetic coupling is equal to half the singlet-triplet splitting and has nothing to do with the coupling  $H_{ab}$  in Eq. (16).

*Case 3.* "Negative  $U$ " compounds ( $\Delta E < 0$ ). The ionic states (also called "charge density wave" states) are stable compared to the vb state. The energy minima for the ground state in Eq. (16) occur for values close to  $q = \pm q_0$ . Disproportionation takes place, for example, in  $BaBiO_3$ , where there are  $Bi^{3+}$  and  $Bi^{5+}$  sites but no  $Bi^{4+}$  sites. There is a large activation energy for transfer of the electron pair from one site to another ( $\sim 0.2$  eV in  $BaBiO_3$ ). The intermediate vb type state, corre-

sponding to  $\text{Bi}^{4+}$  sites, is high in energy, and it is likely that the top of the energy barrier is at  $q = 0$ . It is also possible that there is a small depression for  $q = 0$ , which, however, is higher in energy than in the ionic minima close to  $q = q_0$ .

*Case 4.* The activation energy for pair transfer between the sites tends to zero. The direct coupling between  $\Psi_a$  and  $\Psi_b$  ( $K_{ab}$ ) is small, but there is an indirect coupling between  $\Psi_a + \Psi_b$  and the VB state, as we see in Eq. (17), which leads to a large energy splitting between  $\Psi_a + \Psi_b$  and  $\Psi_a - \Psi_b$ . Thus, if the VB state is sufficiently close in energy to the ionic states and at the same time  $|H_{ab}|$  is large, the activation barrier for transfer between the ionic state disappears.

We have thus established in a simple model that four possible cases occur for a dimeric two-electron system. Case 2 may be divided into a singlet and a triplet ground state. There is experimental evidence for cases 1–3. The author is not aware of any binuclear complex for case 4, although it can probably be made just as its delocalized single electron counterpart, the Creutz–Taube 5+ complex. We may notice that very subtle energy differences lead to very different types of behavior.

### Conclusion

If the activation energy is due to reorganization energy when an electron or electron pair moves between sites the conductivity problem may be treated in a cluster model. As discussed by Hush [29], a large coupling between the sites reduces the activation energy [5]. This coupling has nothing to do with the coupling which determines the singlet–triplet splitting in a binuclear cluster but is half the energy separation between two electronic states of the cluster of different parity at an avoided crossing.

In the two-electron ET case the direct coupling between the diabatic wave functions corresponding to the ionic states is very small [ $K_{ab}$  in Eq. (16)]. However, since the symmetric ionic state interacts with the VB state, corresponding to one electron on each site, the pair transfer may occur activationless in the cases when the VB state has a low energy. This is not always the case, and a good example is provided by  $\text{BaBiO}_3$ . The existence of a pairing cannot by itself guarantee superconductivity, and the reason is simple: If the VB state has a too high energy, the electron pair cannot move from one site to another without activation. The system is then a semiconductor or an insulator. The existence of a large band width improves the situation, since the larger  $|H_{ab}|$ , the larger is the interaction with the VB state.

The situation is similar to the one of the Mott insulators. If doped, the latter may be regarded as a mixed valence compound where the sites exchange electrons according to (in  $\text{Li}_2\text{O}$ -doped  $\text{NiO}$ ):



The electron exchange follows the rules of the second section. If the coupling  $2|H_{12}|$  is not large enough to offset the reorganization energy, according to Eq. (7) the system will be only nonmetallic, no matter what the magnitude of the band gap is.



Alkali compounds of the type  $A_3C_{60}$  form interesting cases for electron pair transfer, particularly since the participating negative ions and their interactions are well defined. The energy surfaces are mapped out by the alkali ions moving in their cavity sites and to a smaller extent by the carbon atoms of  $C_{60}$ . The activation barrier for one or two electron transfer depends quadratically on the bond-length change. In  $A_3C_{60}$  the metal ions have different equilibrium positions depending on the charges of the surrounding negative  $C_{60}$  ions [32]. A larger alkali ion has a smaller distance change between the possible equilibria and hence more shallow energy minima than a smaller one. Thus activationless electron pair transfer is more likely for a larger ion than for a smaller one, and this is consistent with experimental data [19,32,45].

We have thus shown in a bicenter cluster model that the condition for activationless pair transfer may in fact be satisfied in alkali and alkaline earth doped  $C_{60}$ . The extension to an infinite system has not been considered, but, since the band width in the systems studied is generally small, we expect the cluster model to give accurate predictions. The natural way for an extension to the infinite case appears to be to apply the theory of antisymmetrized products of geminals (APG) [46,47]. The essential part of the pairing concept of the Bardeen-Cooper-Schrieffer (BCS) theory remains in the theory used here with the electronic wave functions expressed in configuration space. The lattice coupling is to modes which promote transfer of an electron pair between sites.

The appearance of superconductivity is strongly dependent on the number of valence electrons introduced by doping and the valence state of the metal ion. A condition for appearance of superconductivity is obviously that sites be available so that the electron pairs can move.  $C_{60}$  or  $K_6C_{60}$  are therefore unable to support conductivity or superconductivity. The reason is that the  $h_u$  and  $t_{1u}$  levels, respectively, are completely filled. It is thus important that the highest molecular orbitals (MO) is close to half-filled on the average. In the copper oxide superconductors, the  $3d^8-3d^{10}$  configurations seem to give the superconducting state (whereas  $3d^9-3d^9$  give an antiferromagnetic state) and, in  $BaBiO_3$ , the  $6s^0-6s^2$  configuration [12]. In the latter case, there is a stabilization of the  $6s^2$  configuration due interaction with the  $6s^2 \rightarrow 6p^2$  configuration (pairing), which permits the two electrons with different spins to correlate. A parity doublet of the type that exists in  $A_3C_{60}(t_{1u}-t_{1g})$  or  $BaBiO_3(6s-6p)$  gives a nice pairing mechanism, but apparently, by comparing to the Cu oxide case, a parity doublet is not a necessary condition for pairing.

Finally we may discuss some other suggestions to explain superconductivity in  $C_{60}$ . Chakravarty et al. [22] and Friedberg et al. [25] have discussed pairing of the same type as discussed here and in Ref. [11]. In particular, the latter work describes in a nice way the pairing in  $C_{60}^{2-}$ , which indeed is of exactly the same type as discussed here and in Ref. [11]. Reference [25] discusses in great detail the Madelung energy as well as some other important aspects of the superconductivity problem.

The vibronic coupling for the two-electron case has been discussed in a detailed way in Refs. [15] and [16] for the two-site case and in Ref. [48] in the four-site case. In the present paper, we have used a simplified approach where the nuclear motion is treated classically.

We have shown that there is a strong internal correlation effect in the negative ions but not in  $C_{60}$  itself, and we believe that the magnitude of correlation in  $C_{60}$  is quite unimportant. Schlüter et al. studied the Jahn-Teller distortions in the  $H_g$  state [49]. The conclusion that  $A_3C_{60}$  is not a "negative  $U$ " compound is disagreement with the results obtained here and in Refs. [11,22,25]. Baskaran and Tosatti, on the other hand, have considered the possibility of a "negative  $U$ " state and also stressed the importance of correlation effects; but the numerical values of their parameters are different from ours, and they have given no details regarding the character of the correlation effects [73]. Zhang et al. have discussed a model [24] which to some extent resembles the one of the present paper [11,12]. They also consider the motion of the alkali ions to be important to induce the electronic motion.

### Acknowledgment

We are grateful for support from NFR, the Swedish Natural Science Research Council.

### Bibliography

- [1] L. D. Landau, *Sov. Phys.* **3**, 664 (1933).
- [2] S. I. Pekar, *J. Exptl. Phys. (USSR)* **16**, 341 (1946).
- [3] T. Holstein, *Ann. Phys. (Leipzig)* **8**, 325, 343 (1959); *Phil. Mag.* **37**, 49 (1978).
- [4] I. G. Austin and N. F. Mott, *Adv. Phys.* **18**, 41 (1969).
- [5] S. Larsson, *Int. J. Quantum. Chem.* **30**, 31 (1986).
- [6] W. D. Johnston and R. R. Heikes, *J. Am. Chem. Soc.* **78**, 3255 (1956); R. R. Heikes and W. D. Johnston, *J. Chem. Phys.* **26**, 582 (1957).
- [7] R. A. Marcus, *J. Chem. Phys.* **24**, 966 (1956); **26**, 867, 872 (1957).
- [8] B. H. Brandow, *Adv. Phys.* **26**, 651 (1977); in *Narrow Band Phenomena*, Proceedings of NATO Advanced Workshop, Staverden, Netherlands, 1987.
- [9] D. R. Rosseinsky, J. A. Stephan, and J. S. Tonge, *J. Chem. Soc. Faraday Trans. 1* **77**, 1719 (1981).
- [10] D. R. Rosseinsky and K. C. Quilin, in *Mixed Valency Systems Applications in Chemistry, Physics and Biology*, K. Prassides, Ed. (Kluwer, Boston, 1991), p. 401.
- [11] S. Larsson, in *Chemical Physics of Intercalation II*, Proceedings of NATO Advanced Study Institute, Chateau de Bonas, France, 1992.
- [12] S. Larsson, *Chem. Phys. Lett.* **157**, 403 (1989).
- [13] G. C. Allen and N. S. Hush, *Progr. Inorg. Chem.* **8**, 357 (1967); N. S. Hush, *Progr. Inorg. Chem.* **8**, 391 (1967).
- [14] M. B. Robin and P. Day, *Adv. Inorg. Chem. Radiochem.* **10**, 247 (1967).
- [15] K. Prassides, P. N. Schatz, K. Y. Wong, and P. Day, *J. Phys. Chem.* **90**, 5588 (1986).
- [16] S. E. Piepho, E. R. Krausz, and P. N. Schatz, *J. Am. Chem. Soc.* **100**, 2996 (1978).
- [17] A. F. Hebard, M. J. Rosseinsky, R. C. Haddon, D. W. Murphy, S. H. Glarum, T. T. M. Palstra, A. P. Ramirez, and A. R. Kortan, *Nature* **350**, 600 (1991); R. M. Fleming, A. P. Ramirez, M. J. Rosseinsky, D. W. Murphy, R. C. Haddon, S. M. Zahurak, and A. V. Makhija, *Nature* **352**, 787 (1991).
- [18] P. W. Stephens, L. Mihaly, P. L. Lee, R. L. Whetten, S.-M. Huang, R. B. Kaner, F. Deiderich, and K. Holczer, *Nature* **351**, 632 (1991); K. Holczer, O. Klein, S.-M. Huang, R. B. Kaner, K.-J. Fu, R. L. Whetten, and F. Deiderich, *Science* **252**, 1154 (1991).
- [19] K. Tanigaki, T. W. Ebbesen, S. Saito, J. Mizuki, J. S. Tsai, Y. Kubo, and S. Kuroshima, *Nature* **352**, 222 (1991); K. Tanigaki, I. Hirozawa, T. W. Ebbesen, J. Mizuki, Y. Shimakawa, Y. Kubo, J. S. Tsai, and S. Kuroshima, *Nature* **356**, 419 (1992).

- [20] M. J. Rosseinsky, A. P. Ramirez, S. H. Glarum, D. W. Murphy, R. C. Haddon, A. F. Hebard, T. T. M. Palstra, A. R. Kortan, S. M. Zahurak, and A. V. Makhija, *Phys. Rev. Lett.* **66**, 2830 (1991); M. J. Rosseinsky, D. W. Murphy, R. M. Fleming, R. M. Tycko, A. P. Ramirez, T. Siegrist, G. Dabbagh, and S. E. Barrett, *Nature* **356**, 416 (1992).
- [21] A. R. Kortan, N. Kopylov, S. Glarum, E. M. Gyorgy, A. P. Ramirez, R. M. Fleming, F. A. Thiel, and R. C. Haddon, *Nature* **355**, 529 (1992); R. C. Haddon, G. P. Kochanski, A. F. Hebard, A. T. Fiory, and R. C. Morris, *Science* **258**, 1636 (1992).
- [22] S. Chakravarty, M. P. Gelfand, and S. Kivelson, *Science* **254**, 970 (1991).
- [23] G. Baskaran and E. Tosatti, *Curr. Sci.* **61**, 33 (1991).
- [24] F. C. Zhang, M. Ogata, and T. M. Rice, *Phys. Rev. Lett.* **67**, 3452 (1991).
- [25] R. Friedberg, T. D. Lee, and H. C. Ren, *Phys. Rev.* **B46**, 14,150 (1992).
- [26] S. Larsson, *J. Am. Chem. Soc.* **103**, 4043 (1981); M. L. De Siquena and S. Larsson, *Chem. Phys. Lett.* **3**, 359 (1975).
- [27] R. R. Heikes and W. D. Johnston, *J. Chem. Phys.* **26**, 582 (1957).
- [28] C. Creutz and H. Taube, *J. Am. Chem. Soc.* **91**, 3988 (1969); **95**, 1086 (1973).
- [29] N. S. Hush, *Chem. Phys.* **10**, 361 (1975).
- [30] A. Broo and S. Larsson, *Chem. Phys.* **161**, 363 (1992) and further references therein.
- [31] S. Saito and A. Oshiyama, *Phys. Rev. Lett.* **66**, 2637 (1991).
- [32] D. W. Murphy, M. J. Rosseinsky, R. M. Fleming, R. Tycko, A. P. Ramirez, R. C. Haddon, T. Siegrist, G. Dabbagh, J. C. Tully, and R. E. Walstedt, *J. Phys. Chem. Solids* **53**, 1321 (1992).
- [33] X.-D. Ziang, J. G. Hou, G. Brinceno, W. A. Vareka, R. Mostovoy, A. Zaitl, V. H. Crespi, and M. L. Cohen, *Science* **256**, 1190 (1992).
- [34] O. Klein, G. Gruner, S.-M. Huang, J. B. Wiley, and R. B. Kaner, *Phys. Rev.* **B46**, 11,247 (1992).
- [35] S. Larsson, A. Volosov, and A. Rosén, *Chem. Phys. Lett.* **137**, 501 (1987); M. Braga, S. Larsson, A. Rosén, and A. Volosov, *Astron. Astrophys.* **245**, 232 (1991).
- [36] S. Leach, M. Vervloet, A. Depres, E. Breheret, J. P. Hare, T. J. Dennis, H. W. Kroto, R. Taylor and D. R. M. Walton, *Chem. Phys.* **160**, 451 (1992).
- [37] S. Larsson, A. Broo, B. Kallebring, and A. Volosov, *Int. J. Quantum Chem. QBS* **15**, 1 (1988).
- [38] D. Lichtenberger, K. W. Nebesny, C. D. Ray, D. R. Huffman, and L. D. Lamb, *Chem. Phys. Lett.* **176**, 203 (1991).
- [39] L.-S. Wang, J. Conceicao, C. Jin, and R. E. Smalley, *Chem. Phys. Lett.* **182**, 5 (1991).
- [40] N. Sato, Y. Saito, and H. Shinohara, *Chem. Phys.* **162**, 433 (1992).
- [41] P. A. Limbach, L. Schweikhard, K. A. Cowen, M. T. McDermott, A. G. Marshall, and J. V. Coe, *J. Am. Chem. Soc.* **113**, 6795 (1991); R. L. Hettich, R. N. Compton, and R. H. Ritchie, *Phys. Rev. Lett.* **67**, 1242 (1991).
- [42] F. Negri, G. Orlandi, and F. Zerbetto, *J. Am. Chem. Soc.* **114**, 2909 (1992); G. Corongiu and E. Clementi, *Int. J. Quantum Chem.* **42**, 1185 (1992).
- [43] K. Kaneto, M. Mizue, and W. Takashima, *Synth. Metals* **56**, 3080 (1993).
- [44] D. Dubois, M. T. Jones, and K. M. Kadish, *J. Am. Chem. Soc.* **114**, 6446 (1992).
- [45] O. Zhou, R. M. Fleming, D. W. Murphy, M. J. Rosseinsky, A. P. Ramirez, R. B. van Dover, and R. C. Haddon, *Nature* **362**, 433 (1993).
- [46] A. J. Coleman, *Rev. Mod. Phys.* **35**, 668 (1963); *J. Math. Phys.* **6**, 1425 (1965); S. Bratoz and Ph. Durand, *J. Chem. Phys.* **43**, 2670 (1965).
- [47] J. M. Blatt, *Prog. Theor. Phys. (Kyoto)* **23**, 447 (1960).
- [48] S. A. Borshch and I. N. Kotov, *Chem. Phys. Lett.* **187**, 149 (1991); see also J. J. Girerd and J. P. Launay, *Chem. Phys.* **74**, 217 (1983).
- [49] M. Lannoo, G. A. Baraff, M. Schluter, and D. Tomanek, *Phys. Rev.* **B44**, 12,106 (1991); M. Schluter, M. Lannoo, M. Needels, G. A. Baraff, and D. Tomanek, *Phys. Rev. Lett.* **68**, 526 (1992); *J. Phys. Chem. Solids* **53**, 1473 (1992).

Received June 10, 1993

# ***Ab Initio* Coupled and Uncoupled Hartree-Fock Calculations of the Polarizabilities of Finite and Infinite Polyacetylene Chains**

BENOÎT CHAMPAGNE\*

*Laboratoire de Chimie Théorique Appliquée, Facultés Universitaires Notre-Dame de la Paix, 61, rue de Bruxelles, B-5000 Namur (Belgium) and Quantum Theory Project, University of Florida, Williamson Hall, 362, Gainesville, Florida 32611*

DAVID H. MOSLEY and JEAN-MARIE ANDRÉ

*Laboratoire de Chimie Théorique Appliquée, Facultés Universitaires Notre-Dame de la Paix, 61, rue de Bruxelles, B-5000 Namur (Belgium)*

## **Abstract**

In this work, *ab initio* coupled and uncoupled Hartree-Fock polarizability calculations are carried out on finite and infinite polyacetylene chain models. We describe the polymeric procedures which are extensions to infinite systems of the molecular Sum Over States (SOS) and Random Phase Approximation (RPA) methods. The latter does include the field-induced electron reorganizational effects whereas the former does not. The inclusion of these effects is particularly important in computing the longitudinal component of the dipole polarizability tensor of polyacetylene chains at an accurate level since the ratio of the coupled/uncoupled results is between 2 and 4 for the conjugated systems studied. In order to evaluate the asymptotic longitudinal polarizabilities per unit cell we have used both finite oligomeric calculations followed by extrapolation procedures and direct polymeric methods. The difficulty of using the extrapolation procedures due to the unknown analytical form of the evolution of the longitudinal polarizability per unit cell illustrates the convenience of using our direct method treating infinite polymeric systems. We obtain a good agreement between our infinite chain results and the largest oligomeric values. We also discuss the choice of atomic basis set, the possibility of using scaling factors, and the crucial role of using a correct bond length alternation value. © 1993 John Wiley & Sons, Inc.

## **Introduction**

Since the discovery of very large nonlinear optical responses associated with conjugated organic systems, a lot of theoretical studies have been undertaken in order to predict the optical properties and to understand the structure-property relationship of these materials [1]. Due to electron delocalization, the component of the polarizability tensor directed along the backbone of conjugated systems is enhanced [2]. As is the case for mechanical properties, where the values obtained for a copolymer do not generally correspond to the values that are the weighted sum of their homopolymer contributions, in increasingly large oligomers the longitudinal polarizability increases exponentially until a linear evolution is reached.

---

\* Research Assistant of The National Fund for Scientific Research (Belgium)

That corresponds to an increase of the polarizability per unit cell until a saturation point is reached. This saturation point corresponds to the polarizability per unit cell of the infinite periodic system. The knowledge of the value at this saturation point would be interesting for the design of new promising materials for optics.

The slow convergence behavior of the longitudinal polarizability per unit cell with respect to increasing the chain length of conjugated systems makes this a quantity difficult to attain. A first approach to obtain this asymptotic value is to follow the evolution of the longitudinal polarizability in larger and larger oligomers and then to extrapolate to the infinite polymer limit. An alternative procedure consists of the direct calculation of the asymptotic value by performing the calculation on the polymer system, i.e., taking advantage of its translational symmetry. As Kirmman has said [3]: "*Finite oligomers are most effective for the treatment of local features, while crystal orbitals are best for delocalized features*". Due to its slow convergence for conjugated systems, the longitudinal polarizability corresponds to a delocalized feature and ideally requires the use of a direct method to obtain the asymptotic  $\alpha_{zz}$  value per unit cell. This is particularly the case for *ab initio* procedures, in contrast to semi-empirical calculations, because for the former, the computational treatment of very large oligomers is beyond of reach.

The aims of this work are (i) to describe a general and suitable way of computing the asymptotic values of the polarizabilities per unit cell of infinite periodic systems, including the correct choice of geometrical parameters and mastering the atomic basis set effects, (ii) to compare the finite oligomer procedure followed by various extrapolation techniques with the direct method for computing the asymptotic polarizability per unit cell of infinite systems, and (iii) to provide a good strategy to estimate the polarizabilities per unit cell of polymeric systems correctly. The extended  $\pi$  conjugated systems, polyacetylene chains, are used as example due to their prototypical nature and the important optical responses they exhibit.

Our work is organized as follow:

- Firstly, we summarize the previous calculations of the polarizabilities of increasingly large polyacetylene chains made either at an empirical, semi-empirical or *ab initio* level. This summary defines by itself the difficulties associated with the calculation of the asymptotic polarizability values of stereoregular conjugated polymers at an acceptable level of accuracy.
- In the following part, the coupled and uncoupled procedures to compute the polarizability of finite and infinite systems are briefly described. In particular, we remind the reader of basic equations of the Random Phase Approximation (RPA) method applied to stereoregular polymers. The Summations Over States (SOS) method is presented as an approximation of the RPA procedure.
- The results of computations on polarizabilities of finite polyacetylene chains are presented. The bond length alternation parameter  $\Delta r$  is demonstrated to play an important role in computing the longitudinal component of the polarizability tensor. We compare the suitability of different functional form for extrapolating to the infinite chain limit. We discuss also the choice of the atomic basis set and the role of scaling factors in correctly estimating the polarizabilities.

- Finally, taking advantage of the translational symmetry of polyacetylene, we perform band structure calculations and compute directly the SOS and RPA longitudinal polarizabilities per unit cell. We compare these values with the polarizabilities obtained from the finite oligomer calculations.

This work is in fact the third article of a series on polarizability calculations of finite and infinite polyacetylene chains: the first article employed the simple non-iterative Hückel approach [4], by using Pariser-Parr-Pople Hamiltonians, the electron-electron Coulomb interactions are taken explicitly into account in the second work [5]. In this work, we treat all electrons in an *ab initio* Hartree-Fock procedure.

### Summary of the Previous Polarizability Calculations of Polyacetylene Chains

#### *Hückel*

The first studies, performed at the Hückel level on regular chains (all bond lengths are the same), predict the evolution of the longitudinal polarizability,  $\alpha_{zz}$ , to be proportional to  $N^{2.828}$  [6] or  $N^3$  [7] with  $N$  the number of carbon atoms. Hence, the longitudinal polarizability per unit cell of the infinite chain is infinite. By considering a nonzero bond length alternation ( $\Delta r$ ), a numerical asymptotic stabilization of the longitudinal polarizabilities per unit cell appears as the chain grows [4,8].

#### *Semi-Empirical and Parametrized Methods*

In the next step, the electron-electron Coulomb interactions are taken explicitly into account firstly by using Pariser-Parr-Pople (PPP) Hamiltonians. This results in a decrease of  $\alpha_{zz}$  of one order of magnitude [4,9-12]. For the oligomers ranging from 2 to 20 carbon atoms, de Melo and Silbey [10] derived an expression for the evolution of the longitudinal polarizability per carbon atom with respect to  $N$ , the number of carbon atoms:  $\alpha_{zz}/N = 4.63N^{0.75}$  which does not include any stabilization of  $\alpha_{zz}/N$  as  $N$  increases. However, work by Soos and Hayden [11] took care of this stabilization and by extrapolation of the curve representing the inverse of the longitudinal polarizability per site ( $N/\alpha_{zz}$ ) with respect to the inverse of the number of sites ( $1/N$ ), they found an asymptotic value of  $\alpha_{zz}/N$  for  $N$  equal to infinity to be equal to 50.0 a.u. A recent work of Villesuzanne et al. [12] concerned chains as long as 200  $-\text{CH}=\text{CH}-$  units and predicted asymptotic  $\alpha_{zz}/N$  values ranging from 43.7 a.u. to 283.7 a.u. per double bond depending upon the PPP parametrization used. More recently, we computed the asymptotic longitudinal polarizability per unit cell within PPP approximation using the RPA procedure applied to infinite periodic systems [5]. By using parameters which provide correct excitation energies for the polyene chains, we evaluated  $\alpha_{zz}/N$  to be 139.11 a.u. per double bond.

At the semi-empirical Intermediate Neglect of Differential Overlap (INDO) level of approximation, Kirtman [13] computed the  $\alpha_{zz}$  of finite polyene chains containing up to 62 carbon atoms and determined after extrapolation an asymptotic value of 110.5 a.u. per double bond. Kurtz used the Finite Field method [14] with different

semi-empirical hamiltonians (MNDO, AM1, and PM3) to compute the average polarizabilities of oligomers up to  $C_{40}H_{42}$  [15]. His extrapolated average polarizabilities per unit cell are 56.28, 61.00, and 54.15 a.u. with the MNDO, AM1, and PM3 parametrizations, respectively. In addition, from Valence Effective Hamiltonian (VEH) calculations of the averaged  $\alpha$  value defined there as  $1/3(\alpha_{xx} + \alpha_{zz})$ , neglecting thus the perpendicular  $\alpha_{yy}$  component, the saturation point for  $\alpha$  has been calculated by Shuai and Brédas to be approximately 116.1 a.u. [16].

The results of these semi-empirical and parametrized calculations demonstrate the large sensitivity of the computed polarizabilities to the parametrizations employed and thus the need to use more suitable *ab initio* calculations which are, however, more difficult to carry out on large oligomers.

### *Ab initio Calculations*

The first *ab initio* work on extended chains, realized by Bodart et al. [2] with the minimal STO-3G atomic basis set focused on the strong influence of  $\Delta r$  on the longitudinal polarizability. By following the extrapolation procedure of Hurst et al. [17], their asymptotic  $\alpha_{zz}$  per double bond are 105 a.u. and 170 a.u. for  $\Delta r$  equal to 0.10 Å and 0.05 Å, respectively. Such an extrapolation procedure appeared to alleviate the difficulty to perform *ab initio* polarizability calculations on sufficiently large oligomers to reach the saturation point of  $\alpha_{zz}/N$ . In an important Coupled Perturbed Hartree Fock (CPHF) [18] study, Hurst et al. [17] determined the polarizabilities of polyene chains ranging from  $C_6H_8$  to  $C_{22}H_{24}$  using the minimal STO-3G, extended 6-31G, 6-31G\*, and 6-31G + PD atomic basis sets. These authors made a least square fit of the polarizability values to the equation " $\log(\alpha/N) = a + b/N + c/N^2$ " so that the extrapolated value is given by  $10^a$ . They obtained extrapolated asymptotic values of 38.9, 60.3, 57.0, and 60.8 for the average polarizability and 105.9, 163.3, 154.8, and 160.5 for the longitudinal polarizability using the STO-3G, 6-31G, 6-31G\*, and 6-31G + PD basis sets, respectively. Their geometrical parameters were optimized in the  $C_{2h}$  symmetry using the 6-31G atomic basis set. The parameters of the central unit cell of  $C_{22}H_{24}$  are:  $d_{C=C} = 1.338$  Å,  $d_{C-C} = 1.450$  Å,  $d_{C-H} = 1.077$  Å,  $\alpha_{C=C-C} = 124.3^\circ$ ,  $\alpha_{C-C-H} = 119.2^\circ$ .

### **Hartree-Fock Methods to Compute the Coupled and Uncoupled Polarizabilities of Finite and Infinite Chains**

#### *Molecular Procedures*

At the Hartree-Fock level, the electronic states of closed-shell systems are Slater determinants constructed from doubly occupied molecular orbitals represented by linear combinations of atomic orbitals. The most common methods to compute the polarizabilities of molecules work in the space of the atomic orbitals [19].

In the Summation Over States (SOS) approach, based on the standard time-independent perturbation theory, the polarizability tensor is the second-order term in the perturbation expansion of the energy as a power series in the applied external electrical field [20]. The expression for the different components of the polarizability

is given in terms of the unperturbed wavefunctions and energies. Commonly, one uses a Hartree-Fock ground state together with its singly excited determinants for the excited states. Hence, an element of the polarizability tensor reads as [21]:

$$\alpha_{AV} = 4 \sum_i^{\text{occ}} \sum_a^{\text{unocc}} \frac{(\phi_i | x | \phi_a)(\phi_a | y | \phi_i)}{\epsilon_a - \epsilon_i} \quad (1)$$

where the  $\phi_i$  and  $\phi_a$  represent doubly occupied and unoccupied molecular orbitals respectively,  $\epsilon_i$  and  $\epsilon_a$  their corresponding orbital energies.

The CPHF [18] procedure is equivalent to an analytical differentiation of the field-dependent Hartree-Fock equation. A similar procedure, called Finite Field (FF) [14], consists in the numerical differentiation of the dipole moment with respect to the applied external electric field. In this procedure, the field-induced electron reorganizational effects are included in a way which is fully consistent in terms of adjustments in the average two-electron interactions. For this reason it is described as a *coupled* Hartree-Fock procedure whereas the SOS approach is said to be *uncoupled*.

### Polymer Procedures

In restricted Hartree-Fock theory, the many-electron wave functions of the closed-shell one-dimensional periodic systems are approximated by Slater determinants which are constructed from doubly-occupied crystalline orbitals. These crystalline orbitals are single-particle states defined in the Linear Combination of Atomic Orbitals (LCAO) formalism by:

$$\begin{aligned} \phi_n(k, \vec{r}) &= \frac{1}{\sqrt{(2N+1)}} \sum_{j=-N}^N e^{ikja} \sum_{p=1}^{\omega} C_{pn}(k) \chi_p(\vec{r} - \vec{R}_p - ja\vec{e}_z) \\ &= e^{ikz} u_n(k, \vec{r}) \end{aligned} \quad (2)$$

where  $n$  and  $k$  are the band index and the wave vector or quasi momentum associated with the particle, respectively. Thus, two indices label a crystalline orbital.  $(2N+1)$  is the (odd) number of unit cells considered ( $N \rightarrow \infty$ ) in the band structure calculation that corresponds also to the number of  $k$ -states in one band or to the periodicity  $[(2N+1)a]$  of the crystalline orbitals imposed by the Born-Karman cyclic boundary conditions.  $1/\sqrt{2N+1}$  is then the normalization factor,  $a$  the unit cell length, and  $u_n(k, \vec{r})$  is a function having the same periodicity as the direct lattice. The  $C_{pn}(k)$  terms are the  $k$ -dependent LCAO coefficients.  $\chi_p(\vec{r} - \vec{R}_p - ja\vec{e}_z)$ , abbreviated to  $\chi_p^j(\vec{r})$ , is the  $p$ th atomic orbital centered in the  $j$ th unit cell. In practice, these  $\chi_p^j(\vec{r})$  functions are chosen to be contractions of Gaussian functions.  $\vec{e}_z$  is the unit vector in the periodicity direction. The polymeric LCAO coefficients  $C_{pn}(k)$  and their associated energies  $\epsilon_n(k)$  are, respectively, the eigenvectors and eigenvalues of the matrix equation:

$$\mathbf{F}(k)\mathbf{C}(k) = \mathbf{S}(k)\mathbf{C}(k)\epsilon(k) \quad (3)$$



where  $F(k)$  and  $S(k)$  are the  $k$ -dependent Fock and overlap matrices. The standard theory of band structure calculations is described in several articles [22] and is reviewed in two recent monographs [23].

Recently, we have shown the difficulty to evaluate the longitudinal polarizabilities per unit cell of infinite periodic systems with the Finite Field and CPHF procedures [5]. This is due to the unbounded character of the dipole moment operator. A first method, developed by Otto [24], only considers the periodic part of the dipole moment operator and, following the procedure established by Ladik [25], consists of deriving the field-dependent crystal orbitals which lead to the evaluation of  $\alpha_{zz}/N$ . The approach we follow uses the RPA procedure to circumvent the problem of the unbounded character of the dipole moment operator. This method, based on propagator techniques [26], is equally efficient at computing the static polarizability and the frequency-dependent polarizabilities and may be adapted to include electron correlation at the desired level. Though working differently, the RPA procedure gives identical results to the Finite Field and Coupled Perturbed Hartree-Fock methods. Since two labels characterize the polymeric one-particle states, in second quantization, the operator manifold for RPA applied to periodic infinite systems is then given by:

$$\{T^+\} = \{Q^+, Q\} = \{a_{ak}^\dagger a_{ik}, a_{ik}^\dagger a_{ak}\} \quad (4)$$

where  $a^\dagger(a)$  is a creation (annihilation) operator. The subscript labels  $a, b, \dots (i, j, \dots)$  correspond to unoccupied (occupied) bands. Thus the particle-hole operator  $Q_{aik}^\dagger$  that acts on the ground state Slater determinant replaces the occupied crystal orbital  $\phi_i(k')$  by the virtual crystal orbitals  $\phi_a(k)$ . By partitioning the operator space into  $Q$  and  $Q^\dagger$  and by removing spin from the expression, since we are dealing with the dipole moment operator  $z$  which is a singlet operator, the frequency-independent longitudinal polarizability of a closed-shell infinite periodic system is given by:

$$\alpha_{zz}(\text{RPA}) = 2(\Omega^* \quad \Omega) \begin{pmatrix} \mathbf{A} & \mathbf{B} \\ \mathbf{B}^* & \mathbf{A}^* \end{pmatrix}^{-1} \begin{pmatrix} \Omega \\ \Omega^* \end{pmatrix} \quad (5)$$

where the asterisk (\*) indicates the complex conjugated values. According to Blount's procedure [27], the  $z$ -dipole matrix elements are defined by the following integration which is only non zero for  $k = k'$ :

$$(\phi_a(k')|z|\phi_i(k)) = i\delta_{kk'} \left( u_a(k) \left| \frac{\partial}{\partial k} u_i(k) \right. \right) = i\delta_{kk'} \Omega_{ai}(k). \quad (6)$$

This allows us to take only the vertical transitions into consideration. The dipole transition strengths  $\Omega_{ai}(k)$  are defined by a space integration of the product between  $u_a^*(k)$  and the gradient according to  $k$  of the function  $u_i(k)$ . Barbier et al. [28] provided an analytical expression of  $\Omega_{ai}(k)$  and more recently, we published a better numerical form [29] for computation. The other different matrix elements are defined by:

$$(A(k, k'))_{ai, bj} = (\epsilon_a(k) - \epsilon_i(k))\delta_{ab}\delta_{ij}\delta_{kk'} + 2(\phi_a(k)\phi_i(k)|\phi_j(k')\phi_b(k')) - (\phi_a(k)\phi_b(k')|\phi_j(k')\phi_i(k)) \quad (7)$$

$$(B(k, k'))_{ai, bj} = (\phi_i(k)\phi_b(k')|\phi_j(k')\phi_a(k)) - 2(\phi_i(k)\phi_a(k)|\phi_j(k')\phi_b(k')). \quad (8)$$

Chemist's or Mulliken notation has been chosen to define the two-electron integrals between crystalline orbitals:

$$(\phi_a(k)\phi_i(k)|\phi_j(k')\phi_b(k')) = \iint d\vec{r}_1 d\vec{r}_2 \phi_a^*(k, \vec{r}_1)\phi_i(k, \vec{r}_1) \frac{1}{|\vec{r}_1 - \vec{r}_2|} \phi_j^*(k', \vec{r}_2)\phi_b(k', \vec{r}_2). \quad (9)$$

A recent study demonstrates the nice converging behavior [30] of the different direct lattice sums involved in the evaluation of these two-electron integrals between crystalline orbitals. The first step consists of solving the following linear equation system:

$$\begin{cases} \mathbf{A}\mathbf{X} + \mathbf{B}\mathbf{Y} = \mathbf{\Omega} \\ \mathbf{B}^*\mathbf{X} + \mathbf{A}^*\mathbf{Y} = \mathbf{\Omega}^* \end{cases} \quad (10)$$

The matrices  $\mathbf{A}$ ,  $\mathbf{B}$ ,  $\mathbf{\Omega}$  are of infinite dimension since there are an infinite number ( $2N + 1$ ,  $N \rightarrow \infty$ ) of  $k$ -values and thus an infinite number of  $k$ -states in each band. Moreover, there is an equation for each triplet formed by a  $k$ -value and two band indices. This triplet represents a particle-hole excitation that is vertical in order to preserve the momentum. As is the case in many polymeric techniques, the infinite sum over  $k$  is transformed into an integration in the first Brillouin zone:

$$\begin{cases} \frac{(2N+1)a}{2\pi} \sum_j^{\text{occ}} \sum_b^{\text{unocc}} \int_{-\pi/a}^{\pi/a} (A(k, k'))_{ai, bj} X_{bj}(k') \\ \quad + (B(k, k'))_{ai, bj} Y_{bj}(k') dk' = \Omega_{ai}(k) \\ \frac{(2N+1)a}{2\pi} \sum_j^{\text{occ}} \sum_b^{\text{unocc}} \int_{-\pi/a}^{\pi/a} (B^*(k, k'))_{ai, bj} X_{bj}(k') \\ \quad + (A^*(k, k'))_{ai, bj} Y_{bj}(k') dk' = \Omega_{ai}^*(k). \end{cases} \quad (11)$$

By partitioning  $A(k, k')$  into  $A_0(k, k')$  and  $A_1(k, k')$  according to:

$$(A_0(k, k'))_{ai, bj} = \frac{2\pi}{2N+1)a} (\epsilon_a(k) - \epsilon_i(k))\delta_{ab}\delta_{ij}\delta(k - k') \quad (12)$$

$$(A_1(k, k'))_{ai, bj} = 2(\phi_a(k)\phi_i(k)|\phi_j(k')\phi_b(k')) - (\phi_a(k)\phi_b(k')|\phi_j(k')\phi_i(k)) \quad (13)$$

where we have used the relation between the discrete Kroneker and continuous Dirac delta functions:

$$\delta_{kk'} \leftrightarrow \frac{2\pi}{(2N+1)a} \delta(k-k'). \quad (14)$$

Finally, the linear equation problem takes the following form:

$$\begin{cases} (\epsilon_a(k) - \epsilon_i(k))X_{ai}(k) + \frac{(2N+1)a}{2\pi} \sum_j^{\text{occ}} \sum_b^{\text{unocc}} \int_{-\pi/a}^{\pi/a} (A_1(k, k'))_{ai, bj} X_{bj}(k') \\ \quad + (B(k, k'))_{ai, bj} Y_{bj}(k') dk' = \Omega_{ai}(k) \\ (\epsilon_a(k) - \epsilon_i(k))Y_{ai}(k) + \frac{(2N+1)a}{2\pi} \sum_j^{\text{occ}} \sum_b^{\text{unocc}} \int_{-\pi/a}^{\pi/a} (B^*(k, k'))_{ai, bj} X_{bj}(k') \\ \quad + (A_1^*(k, k'))_{ai, bj} Y_{bj}(k') dk' = \Omega_{ai}^*(k). \end{cases} \quad (15)$$

At this stage, trapezoidal quadrature is used to obtain  $X(k')$  and  $Y(k')$ . The second step consists of the following scalar product that provides the longitudinal polarizability of the polymer:

$$\alpha_{zz}(\text{RPA}) = 2(\Omega^*(k') - \Omega(k')) \begin{pmatrix} X(k') \\ Y(k') \end{pmatrix}. \quad (16)$$

Again, the infinite sum over  $k$  is replaced by integration in the first Brillouin zone. This straightforwardly provides the longitudinal polarizability per unit cell:

$$\frac{\alpha_{zz}(\text{RPA})}{(2N+1)} = \sum_i^{\text{occ}} \left\{ \int_{-\pi/a}^{\pi/a} \left[ \frac{a}{\pi} \sum_a^{\text{unocc}} \Omega_{ai}^*(k') X_{ai}(k') + \Omega_{ai}(k') Y_{ai}(k') \right] dk' \right\}. \quad (17)$$

By making the approximation where matrix  $B$  is zero and  $A$  is restricted to  $A_0$ , the matrices become diagonal, every coupling between the crystal orbitals disappears and the polarizability reads as:

$$\frac{\alpha_{zz}(\text{SOS})}{(2N+1)} = \sum_i^{\text{occ}} \left\{ \int_{-\pi/a}^{\pi/a} \left[ \frac{2a}{\pi} \sum_a^{\text{unocc}} \frac{|\Omega_{ai}(k')|^2}{\epsilon_a(k') - \epsilon_i(k')} \right] dk' \right\}. \quad (18)$$

This is the expression of the uncoupled Hartree-Fock SOS polarizability per unit cell [29]. As in this case, there is no coupling between the different vertical transitions, the coupling and thus the matrices  $A_1$  and  $B$  are responsible for the field-induced electron reorganizational effects. The polarizabilities per unit cell are obtained by using a post-SCF calculation that takes place after the band structure calculation effected by the PLH program [31].

### *Ab initio* Application to Polyacetylene Chains

When interested in a quantitative prediction of the polarizability value, correct geometrical parameters have to be used, especially the bond length alternation which plays a crucial role in influencing polarizability. In the work of Hurst et al. [17],  $\Delta r$  is equal to 0.112 Å. This is larger than the experimentally determined value of 0.08 Å [32] and creates a decrease of the polarizability. As explained in

the work of Villar et al. [33], the use of other atomic basis sets does not decrease the bond length alternation up to 0.08 Å. In fact,  $\Delta r$  is equal to 0.100 Å [34], 0.115 Å [35], and 0.127 Å [33] by using a 8s4s/4s, closely related 4-31G, and 6-31G\*\* atomic basis sets, respectively. Such large  $\Delta r$  is due to the lack of electron correlation in the Hartree-Fock method. Recently, Suhai [36] optimized the geometry of polyacetylene by using crystal orbital calculations including correlation energy up to the second order. Its use of an extended basis set augmented with polarized functions provided a  $\Delta r$  value close to experiment: 0.082 Å. Firstly, in order to obtain the more reliable polarizability values, we used the parameters of Suhai represented in Figure 1 for a unit cell. Secondly, to highlight the importance of a correct choice of  $\Delta r$ , geometrical parameters obtained at the Hartree-Fock level with the 3-21G atomic basis set are also used. In this system, represented in Figure 1,  $\Delta r$  is equal to 0.123 Å.

### *Oligomer Calculations and Extrapolation Procedures*

The GAUSSIAN 90 [37] program was used to calculate the components of polarizability tensor of the a- and b-type increasingly large polyacetylene chains using the minimal STO-3G [38], split-valence 3-21G [39], and extended 6-31G\*\* [40] atomic basis sets. The polarizabilities evaluated by the coupled and uncoupled

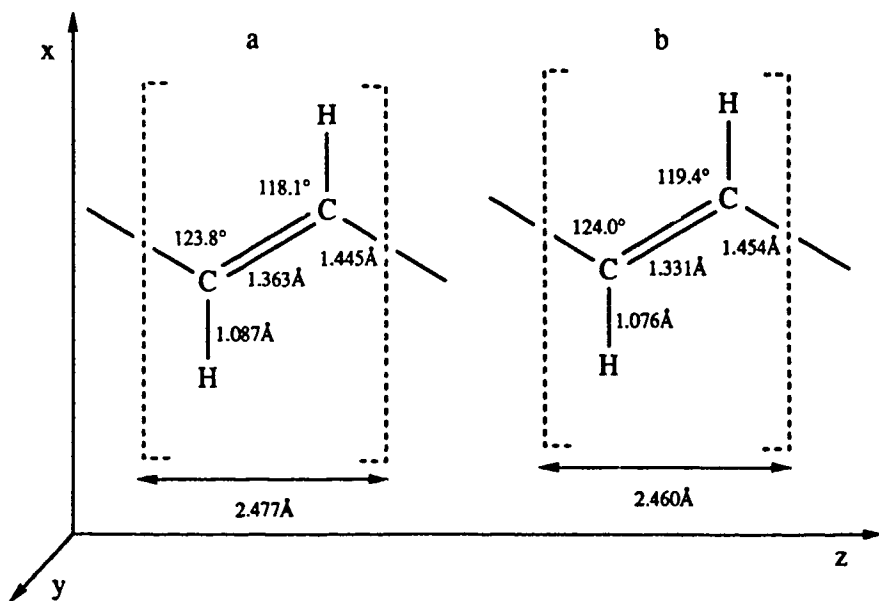


Figure 1. 3D representation of the polyacetylene chains. The bond length and bond angles of the unit cell are expressed in Å and °, respectively. The optimizations have been carried out at the (a) MP2 level with extended + polarized basis set by Suhai [36], (b) Hartree-Fock level with the split valence 3-21G atomic basis set.

TABLE I. Longitudinal ( $\alpha_{zz}$ ) and average ( $\alpha$ ) polarizabilities in a.u. of increasingly large polyacetylene chains computed at the SOS level with the STO-3G, 3-21G, and 6-31G\*\* atomic basis sets (1 a.u. of polarizability =  $1.648 \cdot 10^{-41} \text{ C}^2\text{m}^2\text{J}^{-1} = 0.1482 \text{ \AA}^3$ ). The (a) geometrical parameters have been used (see Fig. 1).

N	STO-3G		3-21G		6-31G**	
	$\alpha_{zz}$	$\alpha$	$\alpha_{zz}$	$\alpha$	$\alpha_{zz}$	$\alpha$
1	15.38	9.64	24.72	15.88	24.88	17.73
2	42.40	22.87	60.25	35.02	61.08	38.33
3	78.94	39.30	107.89	58.01	108.07	62.53
4	121.78	57.83	163.55	83.69	162.38	89.18
5	168.45	77.64	224.42	111.11	221.32	117.37
6	217.33	98.19	288.51	139.60	283.01	146.49
7	267.42	119.14	354.50	168.72	346.30	176.13
8	318.15	140.31	421.58	198.21	410.46	206.06
9	369.20	161.58	489.27	227.91		
10	420.41	182.91	557.29	257.71		
11	471.71	204.26	625.49	287.57		
12	523.05	225.63	693.78	317.46		

Hartree-Fock procedures are listed in Table I to IV for the longitudinal component and the average value invariant upon rotation. Figures 2 to 5 represent the evolution of the polarizability per unit cell expressed by  $[\alpha_{zz}(N) - \alpha_{zz}(N-1)]$ . This expression provides faster [15] convergence for the longitudinal polarizabilities per unit cell than the more frequently used relative polarizability  $[\alpha_{zz}/N]$  although for both formulae, the asymptotic values are the same. As already mentioned elsewhere [5], the CPHF/SOS or coupled/uncoupled ratio of the longitudinal polarizability is larger

TABLE II. Longitudinal ( $\alpha_{zz}$ ) and average ( $\alpha$ ) polarizabilities in a.u. of increasingly large polyacetylene chains computed at the SOS level with the STO-3G, 3-21G, and 6-31G\*\* atomic basis sets. The (b) geometrical parameters have been used (see Fig. 1).

N	STO-3G		3-21G		6-31G**	
	$\alpha_{zz}$	$\alpha$	$\alpha_{zz}$	$\alpha$	$\alpha_{zz}$	$\alpha$
1	14.80	9.05	23.37	15.18	23.83	16.98
2	37.36	20.79	54.99	32.77	55.78	35.98
3	67.30	34.78	95.55	53.22	95.77	57.62
4	101.26	50.20	141.80	75.59	141.01	80.98
5	137.51	66.38	191.39	99.07	189.04	105.32
6	175.09	83.00	243.01	123.23	238.85	130.24
7	213.33	99.85	295.74	147.76	289.48	155.47
8	251.84	116.73	349.00	172.39	340.42	180.72
9	290.22	133.61	402.22	197.08		
10	328.67	150.54	455.58	221.83		

TABLE III. Longitudinal ( $\alpha_{zz}$ ) and average ( $\alpha$ ) polarizabilities in a.u. of increasingly large polyacetylene chains computed at the CPHF level with the STO-3G, 3-21G, and 6-31G\*\* atomic basis sets. The (a) geometrical parameters have been used (see Fig. 1).

N	STO-3G		3-21G		6-31G**	
	$\alpha_{zz}$	$\alpha$	$\alpha_{zz}$	$\alpha$	$\alpha_{zz}$	$\alpha$
1	17.42	11.19	28.72	19.04	30.16	20.91
2	51.84	27.26	76.83	42.55	80.03	46.03
3	105.57	49.79	150.67	74.57	155.98	79.73
4	176.79	78.19	248.78	114.72	256.39	121.61
5	262.77	111.56	368.59	162.15	378.55	170.78
6	360.65	148.94	507.08	215.87	519.32	226.20
7	467.82	189.45	661.18	274.83	675.58	286.83
8	582.13	232.36	828.10	338.10	844.50	351.71
9	701.85	277.10	1005.39	404.87		
10	825.67	323.21	1191.02	474.44		
11	952.59	370.38	1383.33	546.26		
12	1081.85	418.33	1580.99	619.88		

for the less alternating and more conjugated system. For the transversal and perpendicular directions, the calculated values are nearly identical. Since the major component of the polarizability is the longitudinal component due to the electron delocalization along the chain, the RPA procedure is more adapted to give the suitable estimates of the polarizabilities of the most interesting compounds. Moreover, the use of the split-valence 3-21G atomic basis set considerably increases the polarizability values obtained with the minimal STO-3G basis set whereas the addition of polarization functions do not bring any significant improvement.

TABLE IV. Longitudinal ( $\alpha_{zz}$ ) and average ( $\alpha$ ) polarizabilities in a.u. of increasingly large polyacetylene chains computed at the CPHF level with the STO-3G, 3-21G, and 6-31G\*\* atomic basis sets. The (b) geometrical parameters have been used (see Fig. 1).

CPHF N	STO-3G		3-21G		6-31G**	
	$\alpha_{zz}$	$\alpha$	$\alpha_{zz}$	$\alpha$	$\alpha_{zz}$	$\alpha$
1	17.11	10.67	30.73	18.34	29.15	19.15
2	47.24	25.26	73.55	40.11	74.33	43.36
3	92.29	44.71	136.69	68.53	139.01	73.20
4	149.90	68.35	218.20	103.02	222.36	109.05
5	216.99	95.21	314.84	142.55	320.37	149.70
6	291.38	124.52	423.78	186.19	430.46	194.70
7	371.10	155.63	541.34	232.73	549.74	242.68
8	454.08	187.85	666.72	282.21	674.93	292.61
9	539.44	220.87	797.32	333.09		
10	626.70	254.54	932.15	385.42		

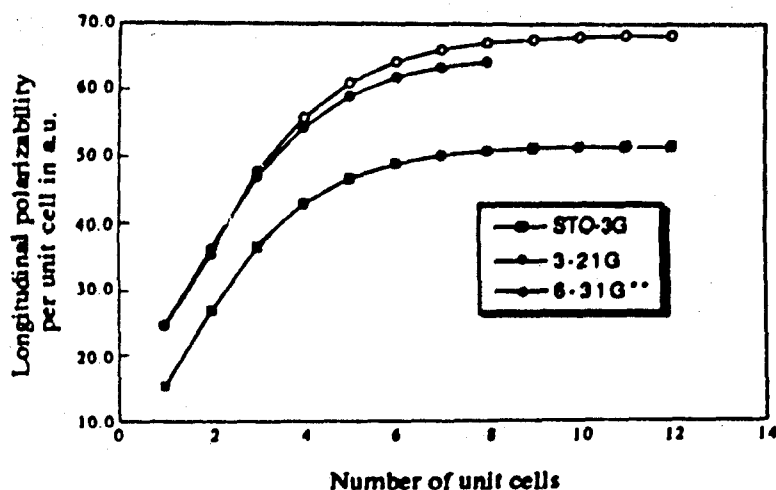


Figure 2. Evolution of the SOS longitudinal polarizability per unit cell (in a.u.) in increasingly large polyacetylene chains with different atomic basis sets. The geometry (a) has been used.

As depicted in Figures 2 to 5, the convergence of  $\alpha_{zz}(N) - \alpha_{zz}(N-1)$  is reasonably rapid using the SOS method, whereas it is very slow by using the CPHF technique. Hence, in the case of the coupled Hartree-Fock technique, oligomeric calculations are not sufficient to get the asymptotic value and, firstly, extrapolation procedures are used to alleviate it. These extrapolation procedures consist in making a least-squares fit of the polarizability per unit cell values to an analytic function able to present a stabilization behavior when increasing the chain length. A  $1/N$  power series representation

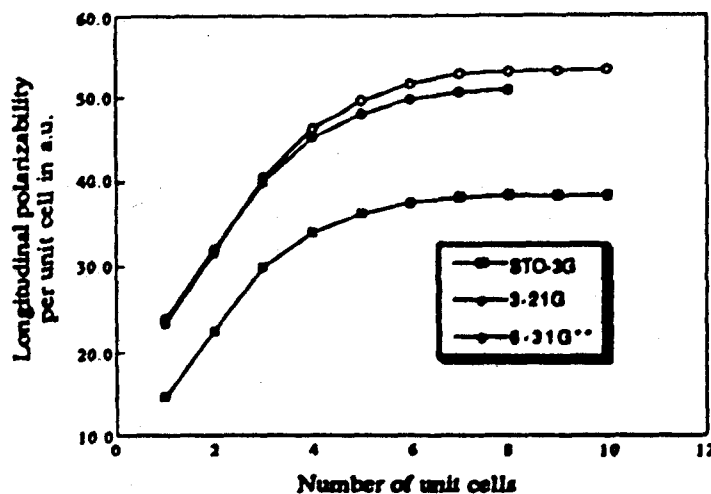


Figure 3. Evolution of the SOS longitudinal polarizability per unit cell (in a.u.) in increasingly large polyacetylene chains with different atomic basis sets. The geometry (b) has been used.

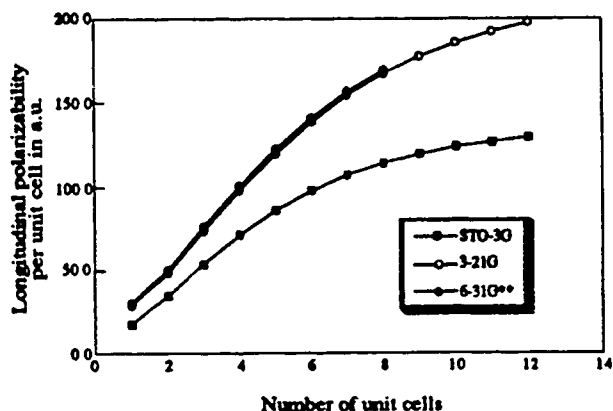


Figure 4. Evolution of the CPHF longitudinal polarizability per unit cell (in a.u.) in increasingly large polyacetylene chains with different atomic basis sets. The geometry (a) has been used.

$$\alpha_{zz}(N) - \alpha_{zz}(N-1) = a + \frac{b}{N} + \frac{c}{N^2} \quad (19)$$

has been proposed by Kirtman et al. [13,41] to fit the longitudinal polarizability per unit cell, while Hurst et al. [17] used the same expansion to fit the logarithm of the polarizability per unit cell. Thus, the asymptotic extrapolated values are given by  $a$  and  $10^a$ , respectively, when  $N = \infty$ . In these procedures,  $b$  is generally negative whereas  $c$  is positive [17]. The slow decaying behavior of the  $1/N$  function maintains important the contribution of the  $b/N$  term for large values of  $N$ . Therefore, the

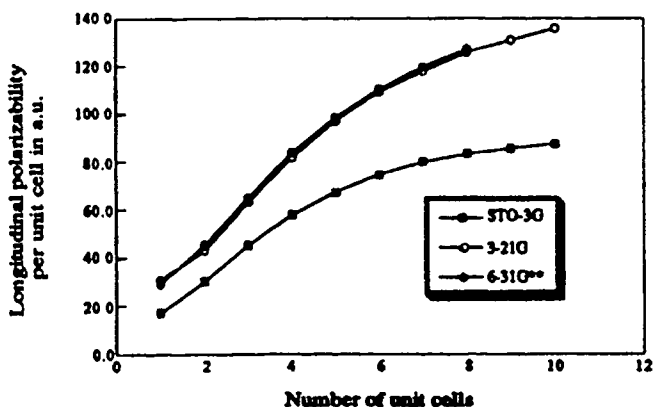


Figure 5. Evolution of the CPHF longitudinal polarizability per unit cell (in a.u.) in increasingly large polyacetylene chains with different atomic basis sets. The geometry (b) has been used.



value of  $a$  is overestimated. Adding a fourth term is the  $1/N$  power series representation to provide

$$\alpha_{zz}(N) - \alpha_{zz}(N-1) = a + \frac{b}{N} + \frac{c}{N^2} + \frac{d}{N^3} \quad (20)$$

as fitting function does not reduce the asymptotic value greatly, and some values even increase. The asymptotic extrapolated values of the CPHF longitudinal polarizabilities per unit cell obtained by the procedures of Kirtman et al. [13,41] and Hurst et al. [17] with a four-term  $1/N$  power series representation are listed in Table V. Following Kirtman's experience [3], we have used at least twice as many theoretical data points as optimized parameters to perform the most accurately the least-squares fittings. The imprecision on these extrapolated values corresponds to their fluctuations by removing the  $d/N^3$  term in the fitting function. The largest sensitivity of the extrapolation procedure in the case of the most polarizable systems (smallest  $\Delta r$ ) using the most suitable method (CPHF which takes into account the field-induced electron reorganizational effects) explicitly shows the need of using polymeric methods in order to avoid dealing with extremely large systems but still want to investigate correctly the field of polymers for optics. In order to take into account more correctly the decaying behavior of the difference between the asymptotic longitudinal polarizability per unit cell of the infinite system and these of the finite oligomers, we have used a function like:

$$\alpha_{zz}(N) - \alpha_{zz}(N-1) = a - be^{-cN} \quad (21)$$

possessing an exponential decreasing behavior. Table V shows that this results in smaller extrapolated values than with the previous procedures.

### Polymer Calculations

Using the STO-3G, 3-21G, and 6-31G\*\* atomic basis sets, we have performed band structure calculations with the PLH program [31]. A particular feature of the PLH program consists in the inclusion of the long-range coulombic interactions which are accounted for via a multipole expansion technique including all the monopole-quadrupole and dipole-dipole interactions. The number of unit cells in

TABLE V. Asymptotic extrapolated longitudinal polarizabilities per unit cell of polyacetylene in a.u. using various extrapolation procedures (see text).

$\Delta r$	Basis set	Kirtman et al. [13,41]	Hurst et al. [17]	This work
0.082 Å	STO-3G	147.5 ± 2.6	139.7 ± 10.1	136.5
	3-21G	261.8 ± 4.8	247.9 ± 14.7	220.7
	6-31G**	274.5 ± 16.1	326.8 ± 8.9	244.3
0.123 Å	STO-3G	108.0 ± 1.6	102.7 ± 1.2	91.3
	3-21G	188.4 ± 3.6	186.0 ± 0.9	151.6
	6-31G**	192.9 ± 8.3	215.3 ± 2.0	158.6

TABLE VI. Asymptotic values of the energy per unit cell, uncoupled (SOS), and coupled (RPA) longitudinal polarizabilities per unit cell in a.u. of the infinite polyacetylene chain having geometry (a).

	$E/N$	$\alpha_{zz}/N$ (SOS)	$\alpha_{zz}/N$ (RPA)
STO-3G	-75.945636	51.37	132.6
3-21G	-76.458416	68.38	/
6-31G**	-76.891349	65.27	/

the short and intermediate range regions are 21 and 45, respectively in order to ensure proper converging results. In the band structure calculation, we set the threshold for the two-electron integrals at  $10^{-7}$  a.u. The criterion for convergence on the density matrix elements is fixed at  $10^{-5}$ . In the RPA calculations of the asymptotic longitudinal polarizabilities per unit cell, we restricted the short- and intermediate-range regions [30] to 13 and 25 and to 7 and 13 for the minimal STO-3G and split-valence 3-21G atomic basis sets, respectively. The number of  $k$ -points in the first Brillouin zone has been fixed at 21. These restrictions make our code viable which at this preliminary stage requires an enormous amount of disk space and memory. However, as discussed in a recent article [30], such choices of the parameters lead only to a decrease of 0.5 to 1.0% of the asymptotic polymeric longitudinal polarizabilities per unit cell.

The asymptotic values of the energy per unit cell, the coupled and uncoupled polarizabilities per unit cell are given in Tables VI and VII for both types of geometrical parameters. As demonstrated, the SOS polymeric values are very close to the largest oligomeric values that you could compute from results of Tables I and II. The coupled Hartree-Fock polymeric values may be compared to the extrapolated results of Table V. The agreement is better with the extrapolated values obtained from fitting with the exponential decaying function than with the  $1/N$  power series. All these results highlight the nice extrapolation property of our direct SOS and RPA methods and in consequence their convenience to investigate the field of polymers presenting large optical responses.

#### *Basis Set Effects and Derivation of Scaling Factors*

For quantitative predictions of the polarizability values by using *ab initio* procedures, an important point is to master the basis set deficiency which leads to an

TABLE VII. Asymptotic values of the energy per unit cell, uncoupled (SOS), and coupled (RPA) longitudinal polarizabilities per unit cell in a.u. of the infinite polyacetylene chain having geometry (b).

	$E/N$	$\alpha_{zz}/N$ (SOS)	$\alpha_{zz}/N$ (RPA)
STO-3G	-75.947424	38.47	89.4
3-21G	-76.459727	53.46	150.1
6-31G**	-76.892465	51.08	/

TABLE VIII Influence of the atomic basis set on the electric dipole polarizability tensor components of ethylene, trans-butadiene, and all-trans hexatriene in atomic units computed at the SOS level and comparison with experimental data. The geometrical parameters (..) have been used.

		STO-3G	3-21G	6-31G**	Sadlej	Exp.
Ethylene	$\alpha_{xx}$	11.54	17.81	19.42	23.64	28.26 [45]
	$\alpha_{yy}$	2.00	5.11	8.89	21.05	26.10 [45]
	$\alpha_{zz}$	15.38	24.72	24.88	28.21	34.26 [45]
	$\alpha$	9.64	15.88	17.73	24.30	28.47 [45]
Trans-butadiene	$\alpha_{xx}$	22.38	34.88	36.77	43.75	
	$\alpha_{yy}$	3.83	9.93	17.14	37.43	
	$\alpha_{zz}$	42.40	60.25	61.08	66.81	
	$\alpha$	22.87	35.02	38.33	49.33	58.23 [46]
All-trans hexatriene	$\alpha_{xx}$	33.32	51.44	54.16	63.69	
	$\alpha_{yy}$	5.64	14.71	25.37	53.52	
	$\alpha_{zz}$	78.94	107.89	108.07	115.84	
	$\alpha$	39.30	58.01	62.53	77.68	

underestimation of the polarizabilities, particularly in the directions where the system is not extended. This problem may be alleviated by using linear scaling factors between minimal and extended basis sets and the experimental values as it was proposed by Chablo and Hinchliffe [42] and already used by Bodart et al. [43] for unsaturated hydrocarbon chains.

We compare in Tables VIII and IX the polarizability components of ethylene, trans-butadiene, and all-trans hexatriene computed with atomic basis sets ranging

TABLE IX. Influence of the atomic basis set on the electric dipole polarizability tensor components of ethylene, trans-butadiene, and all-trans hexatriene in atomic units computed at the CPHF level and comparison with experimental data. The geometrical parameters (a) have been used.

		STO-3G	3-21G	6-31G**	Sadlej	Exp.
Ethylene	$\alpha_{xx}$	13.52	22.47	23.68	27.65	28.26 [45]
	$\alpha_{yy}$	2.64	5.93	8.89	25.15	26.10 [45]
	$\alpha_{zz}$	17.42	28.72	30.16	34.59	34.26 [45]
	$\alpha$	11.19	19.04	20.91	28.60	28.47 [45]
Trans-butadiene	$\alpha_{xx}$	25.14	39.98	42.02	48.19	
	$\alpha_{yy}$	4.81	10.84	16.04	38.38	
	$\alpha_{zz}$	51.84	76.83	80.03	89.70	
	$\alpha$	27.26	42.55	46.03	58.76	58.23 [46]
All-trans hexatriene	$\alpha_{xx}$	36.83	57.39	60.16	68.00	
	$\alpha_{yy}$	6.70	15.65	23.04	52.69	
	$\alpha_{zz}$	105.57	150.67	155.98	172.48	
	$\alpha$	49.79	74.57	79.73	97.72	

from the minimal STO-3G to the split-valence 3-21G, extended 6-31G\*\* and the medium-polarized basis set of Sadlej [44] constructed to provide accurate estimates of dipole moments and electric dipole polarizabilities. The well-known fact of the poor estimation of the perpendicular polarizability is again obvious. Only the medium-size polarized basis set of Sadlej provides a very good agreement with the experimental data. Therefore, they may serve as reference value in the determination of scaling factors. It is important to highlight that the orientation of the molecules is the same as the orientation of the polymeric systems: in the case of the Suhai geometrical parameters, the double bonds are inclined by  $29.02^\circ$  with respect to the longitudinal periodicity axis.

As the  $\alpha(3-21G)/\alpha(\text{Sadlej})$  ratio is converging by going from ethylene to all-trans hexatriene, acceptable scaling factors may be extracted from the CPHF results on all-trans-hexatriene. These scaling factors are 0.84, 0.30, and 0.87 for the transversal, perpendicular, and longitudinal components of the dipole polarizability tensor, respectively. In consequence, we are able to scale our 3-21G values of the polyacetylene chain presenting a  $0.082 \text{ \AA}$  bond length alternation in order to provide a better estimate of the exact polarizabilities per unit cell. When  $N$  tends to infinity, the values for  $\alpha_{xx}/N$ ,  $\alpha_{yy}/N$ , and  $\alpha_{zz}/N$  are 21.9 a.u., 16.0 a.u., and 253.7 a.u., respectively.

### Summary and Conclusions

In this article, we have computed *ab initio* coupled and uncoupled Hartree-Fock asymptotic polarizabilities per unit cell of finite and infinite polyacetylene chains. We have illustrated the convenience of using direct method treating infinite polymers to obtain these asymptotic values with respect to finite oligomeric calculations followed by extrapolation procedure. Indeed, such extrapolation procedures are problematic because the correct form of the longitudinal polarizability per unit cell according the number of unit cells is not known. Therefore, these procedures are very sensitive to the analytical form of the fitting function and to the appearance or not of the saturation pattern in the largest oligomers treated. Based on the polarization propagator techniques, the RPA method used is an extension to infinite periodic systems of the molecular procedure, taking advantage of the translational symmetry of the polymer. The SOS method is a major approximation of the RPA procedure, and does not take into account the field-induced electron reorganizational effects included in the latter. In addition, the choices of atomic basis set and geometrical parameters have been discussed and shown to be very important to provide quantitative estimates of the polarizabilities.

At this stage, the coupled procedure is still restricted to prototype systems. However, suitable computational procedures exist which can be applied to improve our code enabling access to the coupled polarizabilities of compounds of greater practical interest [47].

Future steps in the development of methods to compute the polarizabilities of infinite periodic systems would involve including the vibrational contributions to the polarizability, taking into account the electron correlation effects and treating the frequency-dependent character of the polarizability.

### Acknowledgments

B.C. and D.H.M. would like to thank the organizers for inviting them to the stimulating experience of the 1993 Sanibel Symposia. They would also like to thank Prof. J. Delhalle and Dr. J. G. Fripiat for their interest brought to this work and their comments in the fields of Polymer Quantum Chemistry. They appreciate a lot the fruitful discussions with Dr. Z. Shuai. B.C. thanks the Belgian National Fund for Scientific Research (FNRS) for his Research Assistant position. D.H.M. thanks the Services de la Programmation de la Politique Scientifique (SPPS) for the grant received in the framework of the ELSAM (Electronic Large Scale Computational System for Advanced Materials) project, a part of the Belgian National Program of Impulsion in Information Technology. All calculations reported here have been performed on the Namur-Scientific Computing Facility (Namur-SCF), a result of a cooperation between the Belgian National Fund for Scientific Research (FNRS), IBM-Belgium, and the Facultés Universitaires Notre-Dame de la Paix (FUNDP).

### Bibliography

- [1] D. S. Chemla and J. Zyss, Eds., *Nonlinear Optical Properties of Organic Molecules and Crystals*. Vols. 1 and 2 (Academic Press, New York, 1987).
- [2] V. P. Bodart, J. Delhalle, J. M. André, and J. Zyss in *Polydiacetylenes: Synthesis, Structure and Electronic Properties*, D. Bloor and R. R. Chance, Eds., 125 (Martinus Nyhoff Publishers, Dordrecht, 1985).
- [3] B. Kirtman, *Int. J. Quantum Chem.* **43**, 147 (1992).
- [4] B. Champagne and J. M. André, *Int. J. Quantum Chem.*, *Quantum Chem. Symp.* **24**, 859 (1990).
- [5] B. Champagne, J. G. Fripiat, and J. M. André, *J. Chem. Phys.* **96**, 8330 (1992).
- [6] H. F. Hameka, *J. Chem. Phys.* **67**, 2935 (1977).
- [7] P. L. Davies, *Trans. Faraday Soc.* **47**, 789 (1952).
- [8] C. Cojan, G. P. Agrawal, and C. Flytzanis, *Phys. Rev. B* **15**, 909 (1977).
- [9] O. Zamani-Khamiri and H. F. Hameka, *J. Chem. Phys.* **71**, 1607 (1979).
- [10] C. P. de Melo and R. Silbey, *J. Chem. Phys.* **88**, 2558 (1988).
- [11] Z. G. Soos and G. W. Hayden, *Phys. Rev. B* **40**, 3081 (1989).
- [12] A. Villesuzanne, J. Hoarau, L. Ducasse, L. Olmedo, and P. Hourquebie, *J. Chem. Phys.* **96**, 495 (1992).
- [13] B. Kirtman, *Chem. Phys. Letters* **143**, 81 (1988).
- [14] H. D. Cohen and C. C. J. Roothaan, *J. Chem. Phys.* **43**, 534 (1965).
- [15] H. A. Kurtz, *Int. J. Quantum Chem.*, *Quantum Chem. Symp.* **24**, 791 (1990).
- [16] Z. Shuai and J. L. Brédas, *Phys. Rev. B* **46**, 4395 (1992).
- [17] G. J. B. Hurst, M. Dupuis, and E. Clementi, *J. Chem. Phys.* **89**, 385 (1988).
- [18] R. McWeeny, *Phys. Rev.* **126**, 1028 (1962); A. Dalgarno, *Adv. Phys.* **11**, 281 (1962); J. A. Pople, R. Krishnan, H. B. Schlegel, and J. S. Binkley, *Int. J. Quantum Chem.*, *Quantum Chem. Symp.* **13**, 225 (1979); C. E. Dykstra and P. G. Jasien, *Chem. Phys. Letters* **109**, 388 (1984); S. P. Karna and M. Dupuis, *J. Comp. Chem.* **12**, 487 (1991).
- [19] J. M. André and J. Delhalle, *Chem. Rev.* **91**, 843 (1991).
- [20] A. Szabo and N. Ostlund, *Modern Quantum Chemistry*, (MacMillan, New York, 1985), Chap. VI.
- [21] J. M. André, C. Barbier, V. P. Bodart, and J. Delhalle, in *Nonlinear Optical Properties of Organic Molecules and Crystals*, D. S. Chemla and J. Zyss, Eds., (Academic Press, New York, 1987), Vol. 2, p. 137.
- [22] J. Ladik, *Acta Phys. Hung.* **18**, 173 (1965); J. Ladik, *Acta Phys. Hung.* **18**, 185 (1965); J. M. André, L. Gouverneur, and G. Leroy, *Int. J. Quantum Chem.* **1**, 427 (1967); J. M. André, L. Gouverneur, and G. Leroy, *Int. J. Quantum Chem.* **1**, 451 (1967); G. Del Re, J. Ladik, and G. Biczio, *Phys. Rev.* **155**, 997 (1967); J. M. André, *J. Chem. Phys.* **50**, 1536 (1969); J. M. André, *Adv. Quantum Chem.* **12**, 65 (1980).

- [23] J. Ladik, *Quantum Theory of Polymers as Solids*, (Plenum Press, New York, 1988); J. M. André, J. Delhalle, and J. L. Brédas, *Quantum Chemistry Aided Design of Organic Polymers for Molecular Electronics* (World Scientific Publishing Company, London, 1991).
- [24] P. Otto, *Phys. Rev.* **B46**, 10876 (1992).
- [25] J. Ladik, *J. Molec. Struct. (Theochem)* **199**, 55 (1989); J. Ladik and L. Dalton, *J. Molec. Struct. (Theochem)* **231**, 77 (1991).
- [26] J. Linderberg and Y. Öhrn, *Propagators in Quantum Chemistry*, (Academic Press, New York, 1973); J. Oddershede, *Adv. Quantum Chem.* **11**, 257 (1978); P. Jørgensen and J. Simons, *Second Quantization-Based Methods in Quantum Chemistry*, (Academic Press, New York, 1981); J. Oddershede, P. Jørgensen, and D. L. Yeager, *Computer Physics Reports* **2**, 33 (1984).
- [27] E. I. Blount in *Solid States Physics*, F. Seitz and D. Turnbull, Eds., **13**, 305 (Academic Press, New York, 1962).
- [28] C. Barbier, *Chem. Phys. Letters* **142**, 53 (1987); C. Barbier, J. Delhalle, and J. M. André, in *Nonlinear Optical Properties of Polymers*, A. J. Heeger, J. Orenstein, and D. R. Ulrich, Eds., **109**, 143 (Materials Research Society, Pittsburgh, 1988); C. Barbier, J. Delhalle, and J. M. André, *J. Molec. Struct. (Theochem)* **188**, 299 (1989).
- [29] B. Champagne and J. M. André, *Int. J. Quantum Chem.* **42**, 1009 (1992).
- [30] B. Champagne, D. H. Mosley, and J. M. André, *Chem. Phys. Letters*, accepted for publication.
- [31] J. M. André, J. L. Brédas, J. Delhalle, D. J. Vanderveken, D. P. Vercouteren, and J. G. Fripiat, in *MOTEC-91, Modern Techniques in Computational Chemistry*, E. Clementi, Ed., 793 (ESCOM, Leiden, 1991); J. G. Fripiat, D. J. Vanderveken, D. P. Vercouteren, and J. M. André, *PLH-91 from MOTEC-91*, in *MOTEC-91, Modern Techniques in Computational Chemistry. Input/Output Documentation*, E. Clementi, Ed., part 3, 195 (ESCOM, Leiden, 1991).
- [32] C. R. Fincher, C. E. Chen, A. J. Heeger, A. G. MacDiarmid, and J. B. Hastings, *Phys. Rev. Letters* **48**, 100 (1982); C. S. Yannoni and T. C. Clarke, *Phys. Rev. Letters* **51**, 1191 (1983).
- [33] H. O. Villar, M. Dupuis, J. D. Watts, G. J. B. Hurst, and E. Clementi, *J. Chem. Phys.* **88**, 1003 (1988).
- [34] A. Karpfen and J. Petkov, *Theor. Chim. Acta* **53**, 65 (1979).
- [35] H. Teramae, *J. Chem. Phys.* **85**, 990 (1986).
- [36] S. Suhai, *Int. J. Quantum Chem.* **42**, 193 (1992).
- [37] M. J. Frisch, M. Head-Gordon, G. W. Trucks, J. B. Foresman, H. B. Schlegel, K. Raghavachari, M. A. Robb, J. S. Binkley, C. Gonzalez, D. J. DeFrees, D. J. Fox, R. A. Whiteside, R. Seeger, C. F. Melius, J. Baker, R. L. Martin, L. R. Kahn, J. J. P. Stewart, S. Topiol, and J. A. Pople, *Gaussian 90* (Carnegie-Mellon University, Pittsburgh, PA, 1990).
- [38] W. J. Hehre, R. F. Stewart, and J. A. Pople, *J. Chem. Phys.* **51**, 2657 (1969); W. J. Hehre, R. Ditchfield, R. F. Stewart, and J. A. Pople, *J. Chem. Phys.* **52**, 2769 (1970).
- [39] J. S. Binkley, J. A. Pople, and W. J. Hehre, *J. Am. Chem. Soc.* **102**, 939 (1980); J. Chandrasekhar, J. G. Andrade, and P. v. R. Schleyer, *J. Am. Chem. Soc.* **103**, 5609 (1981); M. S. Gordon, J. S. Binkley, J. A. Pople, W. J. Pietro, and W. J. Hehre, *J. Am. Chem. Soc.* **104**, 2797 (1982).
- [40] P. C. Hariharan and J. A. Pople, *Theor. Chim. Acta* **28**, 213 (1973).
- [41] B. Kirtman, W. B. Nilsson, and W. E. Palke, *Solid State Commun.* **46**, 791 (1983); B. Kirtman and M. Hasan, *Chem. Phys. Letters* **157**, 123 (1989); B. Kirtman, *Int. J. Quantum Chem.* **36**, 119 (1989); B. Kirtman and M. Hasan **96**, 470 (1992).
- [42] A. Chablo and A. Hinchliffe, *Chem. Phys. Letters* **72**, 149 (1980).
- [43] V. r' Bodart, J. Delhalle, J. M. André, and J. Zyss, *Can. J. Chem.* **63**, 1631 (1985).
- [44] A. J. Sadlej, *Theor. Chim. Acta* **79**, 123 (1991).
- [45] G. N. Hills and W. J. Jones, *Faraday Trans. II* **71**, 812 (1975).
- [46] J. F. Ward and D. S. Elliot, *J. Chem. Phys.* **69**, 5438 (1978). A. A. Maryott, F. Buckley, U.S. National Bureau of Standards, Circular N°537 (1953).
- [47] M. Feyereisen, J. Nichols, J. Oddershede, and J. Simons, *J. Chem. Phys.* **96**, 2987 (1992).

# A Green's Function Calculation of the Zero-Voltage STM Resistance of a One-Dimensional Chain Coupled to Two Jellium Surfaces

V. MUJICA\*

*Northwestern University, Department of Chemistry, Evanston Illinois 60208*

G. DOYEN

*Fritz-Haber-Institut der Max-Planck-Gesellschaft Faradayweg 4-6, D-1000 Berlin 33, Germany*

## Abstract

A simple model Hamiltonian is used to calculate the limit of zero-voltage resistance in a one-dimensional chain of one-state sites. The end atoms in the chain are considered to be chemisorbed to the surface of the metal electrodes and their interaction with the continuum of metal states (jellium model) is treated as in the Anderson-Newns chemisorption theory [1,2].

For this model, an exact solution can be obtained for the zero-voltage resistance within the formalism developed by Doyen and co-workers [3] for the calculation of the current in Scanning Tunneling Microscopy (STM). Applications of the results described in this article to the problem of molecular imaging in STM are presented elsewhere [4,5]. © 1993 John Wiley & Sons, Inc

## Introduction

The problem of interpreting STM images in the long distance regime, where the distance between the tip and the surface is larger than 5 Å, is reasonably well understood, at least for clean metal and semiconductors surfaces [6]. In this regime, the dominant forces are of the van der Waals type and the current is well described within the Tersoff-Haman-Bardeen theory [7,8]. The use of first-order perturbation theory seems to be well justified when the separate existence of two quantum subsystems, e.g., the tip and the surface, can be assumed. Such an assumption implies a weak overlap of the wave functions characterizing the two quantum subsystems.

Under the assumptions described above it is possible to derive an expression for the tunnel current which depends on the surface density of states (SDOS) at the Fermi level evaluated at the position of the tip [7]. The STM image would then be just a contour map of the SDOS. This interpretation however cannot give account of a number of STM images of clean surfaces and adsorbed species. This indicates the need for a non-perturbative approach to calculate the current in the strong tip-surface interaction regime. This, in turn, requires considering the tip, sample and

---

\* On leave from: Escuela de Química, Facultad de Ciencias, Universidad Central de Venezuela, Apartado 47102, Caracas 1020 A, Venezuela.

electrodes as a single quantum system whose electronic structure must be determined as part of the problem [4,5,9-11].

In this article we use the non-perturbative theory developed by Doyen and co-workers [3,12]. The STM current is viewed as a scattering process, and the Lippman-Schwinger equation is employed to calculate the scattering amplitude. A Green's function technique is used to calculate the electronic structure and the one-electron density of states (DOS) of the system. Specifically, we assume that the electrode-tip-molecule-electrode system is described by a finite one-dimensional tight-binding model for the molecule and the tip, and a continuum of one-electron states for the metal electrodes. The model also takes account of the interaction of the chemisorbed atoms with the continuum of metal states by using the Newns-Anderson model of chemisorption [1,2], which for our purposes amounts to considering a semi-elliptical shape for the metal band. A similar approach, but within the context of density functional theory and the Tersoff-Hamann model for the current, has been used by Lang [13-15].

This simple model has the advantage of being exactly solvable in terms of the model parameters: the orbital energies and the interaction potentials between sites in the tip-molecule chain and between the end sites and the electrode surfaces. This could in principle allow us to gain some physical insight into a very complex problem. An application of this model to STM imaging of organic samples which are bulk-insulators has been described elsewhere [4,5].

### The Model

The system we aim to describe consists of two semi-infinite metallic electrodes, an atomic tip and a molecule. The tip is in contact with one of the surfaces and the molecule is assumed to lay between the tip and the other surface.

The tip and the molecule are considered as a collection of one-particle-state sites, coupled through a nearest-neighbor interaction, so that only the first and last sites in the molecule-tip chain interact directly with the surfaces. This description corresponds essentially to a tight-binding (Hückel) model with site-to-site hopping.

We denote the site-states by the set  $\{|\alpha\rangle; \alpha = 1, 2, \dots, N\}$ , and the corresponding energies and occupation numbers by  $\{E_\alpha^0, n_\alpha; \alpha = 1, 2, \dots, N\}$ . To keep the treatment as general as possible, we do not make an explicit distinction between a tip-like site and a molecular-like site: in our model they differ only in the values of  $E_\alpha^0$  and coupling potentials.

The molecular sites can be thought of as a simple approximation to the actual chemical units, whose electrons are intervening in the conduction process, be they atoms, bonds, or a combination of both.

The two surfaces are described within the jellium model [16], (a non-interacting electron gas with a positive continuous background). The one-particle states have energies and occupation numbers denoted by  $\{E_{i(f)}^0, n_{i(f)}\}$ , where  $i$  and  $f$  are continuous indices that correspond to states  $|\mathbf{k}_i\rangle$  and  $|\mathbf{k}_f\rangle$  of electron momentum  $\mathbf{k}_i$  and  $\mathbf{k}_f$ , respectively.

The Hamiltonian for the non-interacting surface-tip-molecule-surface system, within our model, is then:



$$H^0 = \sum_i n_i E_i^0 + \sum_{\alpha=1}^N n_{\alpha} E_{\alpha}^0 + \sum_f n_f E_f^0. \quad (1)$$

$H^0$  is diagonal in the orthonormal basis  $\{|\alpha\rangle, |\mathbf{k}_i\rangle, |\mathbf{k}_f\rangle\}$ .

The interaction between these sub-units is given as a sum of hopping terms:

$$V = \sum_i V_{S1} a_i^{\dagger} a_i + \sum_{\alpha=1}^N V_{\alpha, \alpha+1} a_{\alpha}^{\dagger} a_{\alpha+1} + \sum_j V_{NS} a_N^{\dagger} a_j + \text{complex conjugate}, \quad (2)$$

where  $a_i^{\dagger}$  and  $a_i$  are ordinary fermion creation and annihilation operators,  $V_{S1}$ ,  $V_{NS}$  stand for the matrix elements of  $V$  in (2) between sites 1 ( $N$ ) and the corresponding surfaces (assumed independent of jellium state), and  $V_{\alpha, \alpha+1}$  is the matrix element of  $V$  taken between adjacent sites in the chain. These matrix elements represent the strength of the coupling between the different subunits of our model.

The Hamiltonian is then simply written as

$$H = H^0 + V. \quad (3)$$

### STM Current

Following the treatment of Doyen and co-workers [3,12], the current is viewed, within a single-particle-picture, as a scattering process. An electron incident from the interior of the metal-tip escapes from the barrier and has a certain probability of scattering through the sample molecule, into the metallic substrate where it is detected.

Let  $|i\rangle = |\mathbf{k}_i\rangle$  be the initial state of the tunneling electron,  $|i+\rangle$  the scattering state, and  $|f\rangle = |\mathbf{k}_f\rangle$  the final state where the electron is detected.  $|i\rangle$  and  $|f\rangle$  are eigenstates of  $H^0$ , whereas  $|i+\rangle$  is an eigenfunction of the full Hamiltonian (3).

The probability  $p(t)$  that an electron with momentum  $\mathbf{k}_f$  is detected at time  $t$  is:

$$p(t) = |\langle f | i+\rangle|^2. \quad (4)$$

The current can be expressed as:

$$j(t) = e \frac{dp(t)}{dt} = e \frac{d}{dt} |\langle f | i+\rangle|^2. \quad (5)$$

According to Lippman's generalization of Ehrenfest's theorem [17,18], the current in the limit of low applied voltage  $W$ , can be written as

$$j = \frac{2\pi e^2 W}{\hbar} \sum_{ii'} |\langle f | i' \rangle \langle i+\rangle|^2 \delta(E_{i'} - E_F) \delta(E_i - E_F), \quad (6)$$

where the sum runs over all the states between the Fermi levels ( $E_F$ ) of the two surfaces. The resistance,  $R$ , in the zero-voltage limit is then  $R = W/j$ .

### Evaluation of the Matrix Elements

Our starting point is the Lippman-Schwinger equation:

$$|i+\rangle = |i\rangle + G^o V |i+\rangle, \quad (7)$$

where  $G^o$  is the Green's function corresponding to the non-interacting Hamiltonian (1)

$$G^o(z) = (z - H^o)^{-1}, \quad (8)$$

$z$  being a complex variable. In the basis of eigenstates of  $H^o$ , this operator is diagonal with diagonal matrix elements given by:

$$G_n^o(z) = \langle n | G^o | n \rangle = \frac{1}{z - E_n^o}, \quad (9)$$

where  $|n\rangle$  is any site or jellium state.

A resolution of the identity can be written as:

$$\mathbf{1} = \sum_i |i\rangle \langle i| + \sum_j |j\rangle \langle j| + \sum_{\alpha=1}^N |\alpha\rangle \langle \alpha|. \quad (10)$$

By using the orthonormality condition, and inserting the resolution of the identity twice in Eq. (7), one obtains:

$$\langle f | i+ \rangle = \langle f | G^o \mathbf{1} V \mathbf{1} | i+ \rangle. \quad (11)$$

We now make use of the facts that  $G^o$  is a diagonal operator, that the operator  $V$  in (2) has non-zero matrix elements only between adjacent sites, and that jellium states are non-interacting, to obtain:

$$\langle f | i+ \rangle = G_f^o V_{NS} \langle N | i+ \rangle. \quad (12)$$

One can use the Lippman-Schwinger equation again, and the conditions described above to obtain:

$$\langle N | i+ \rangle = G_N^o \{ V_{N(N-1)} \langle N-1 | i+ \rangle + \sum_f V_{NS} \langle f | i+ \rangle \}, \quad (13)$$

where there are now two terms because site  $N$  interacts with both the surface and site  $(N-1)$ . By inserting expression (12) in (13), one gets:

$$\langle N | i+ \rangle = \frac{G_N^o V_{N(N-1)}}{1 - G_N^o \sum_N} \langle N-1 | i+ \rangle, \quad (14)$$

where

$$\sum_N = \sum_f G_f^o V_{NS}^2. \quad (15)$$

In a similar way, we obtain:

$$\langle N-1|i+\rangle = G_{N-1}^0 \{V_{N-1(N-2)}\langle N-2|i+\rangle + V_{(N-1)N}\langle N|i+\rangle\}. \quad (16)$$

By inserting (14) into (16), one obtains:

$$\langle N-1|i+\rangle = \frac{G_{N-1}^0 V_{N(N-1)}}{1 - \frac{G_{N-1}^0 G_N^0 V_{N(N-1)}^2}{1 - G_N^0 \sum_N}} \langle N-2|i+\rangle. \quad (17)$$

By introducing Eq. (17) in (14), one arrives at:

$$\langle f|i+\rangle = \frac{G_f^0 V_{NS} G_N^0 V_{NN-1} G_{N-1}^0 V_{NN-2}}{(1 - G_N^0 \sum_N) \left(1 - \frac{G_{N-1}^0 G_N^0 V_{N(N-1)}^2}{1 - G_N^0 \sum_N}\right)} \langle N-2|i+\rangle. \quad (18)$$

This procedure can be repeated to obtain the matrix element  $\langle N-2|i+\rangle$ , so that  $\langle f|i+\rangle$  is finally expressed solely in terms of the parameters of the model.

For the sake of simplicity, and to show the final form of the equations, let us consider the case  $N=2$ , for which one obtains:

$$\langle f|i+\rangle = \frac{G_f^0 V_{2S} G_2^0 V_{12} G_1^0 V_{S1}}{\left(1 - G_2^0 \sum_2\right) \left(1 - \frac{G_1^0 G_2^0 V_{12}^2}{1 - G_2^0 \sum_2}\right) \left(1 - \frac{G_1^0 \sum_1}{1 - \frac{G_1^0 G_2^0 V_{12}^2}{1 - G_2^0 \sum_2}}\right)}. \quad (19)$$

By redefining on-site renormalized Green's functions as:

$$\tilde{G}_2^0 = \frac{G_2^0}{1 - G_2^0 \sum_2} \quad (20)$$

$$\tilde{G}_1^0 = \frac{G_1^0}{1 - G_1^0 \tilde{G}_2^0 V_{12}^2} \quad (21)$$

$$\tilde{G}_f^0 = \frac{G_f^0}{1 - \tilde{G}_1^0 \sum_1}, \quad (22)$$

Eq. (19) can be written as:

$$\langle f|i+\rangle = \tilde{G}_f^0 V_{2S} \tilde{G}_2^0 V_{12} \tilde{G}_1^0 V_{S1}. \quad (23)$$

Eq. (23) can be readily generalized for arbitrary  $N$  as:

$$\langle f|i+\rangle = \tilde{G}_f^0 V_{NS} \tilde{G}_N^0 V_{N-1N} \tilde{G}_{N-1}^0 V_{N-2N-1} \cdots \tilde{G}_1^0 V_{S1}, \quad (24)$$

where the definition of  $\tilde{G}_f^0$  is as in Eq. (22) and

$$\tilde{G}_N^o = \frac{G_N^o}{1 - G_N^o \sum_N} \quad (25)$$

$$\tilde{G}_K^o = \frac{G_K^o}{1 - G_K^o \tilde{G}_{K+1}^o V_{KK+1}^2}; \quad 1 \leq K < N. \quad (26)$$

Once the matrix element  $\langle f|i+ \rangle$  is known, the  $t$ -matrix element  $\langle f|V|i+ \rangle$  of Eq. (6) can be obtained by using once again the Lippman-Schwinger equation:

$$\langle f|V|i+ \rangle = \frac{\langle f|i+ \rangle}{G_f^o}. \quad (27)$$

For computational purposes it is convenient to use the diagonal representation of the bare Green's function, Eq. (9), to recast Eqs. (25) and (26) as:

$$\tilde{G}_N^o(E) = \frac{1}{E - E_N^o - \sum_N} \quad (28)$$

$$\tilde{G}_K^o(E) = \frac{1}{E - E_K^o - \tilde{G}_{K+1}^o V_{KK+1}^2}; \quad 1 \leq K < N. \quad (29)$$

The case  $N = 1$  does not conform to definitions (28) and (29). We include it for completeness:

$$\langle f|V|i+ \rangle = \frac{V_{iR} V_{Li}}{E - E_1^o - \sum_R - \sum_L}; \quad N = 1, \quad (30)$$

where  $R$  and  $L$  stand for the "right" and "left" surfaces.

The calculation of the self-energy contribution  $\sum_N$  is performed following Newns [2] as:

$$\sum_N(\epsilon) = \Lambda(\epsilon) - i\Delta(\epsilon), \quad (31)$$

where

$$\Delta(\epsilon) = 2\beta^2(1 - \epsilon^2)^{1/2} \quad (32)$$

and

$$\Lambda(\epsilon) = \begin{cases} 2\beta^2\epsilon & |\epsilon| < 1 \\ 2\beta^2[\epsilon + (\epsilon^2 - 1)^{1/2}] & \epsilon < -1 \\ 2\beta^2[\epsilon - (\epsilon^2 - 1)^{1/2}] & \epsilon > 1 \end{cases} \quad (33)$$

The parameter  $\beta$  is proportional to the surface-site interaction potential, i.e.,  $\beta = \sqrt{\pi/2} V_{SK}$  and  $\epsilon$  is a dimensionless quantity such that the metal band width is 2 in units of  $\epsilon$ .

All the approximations leading to Eqs. (31), (32), and (33) are described in Newns's article. It suffices to quote here that although they are obtained for a one-dimensional tight-binding model one can also assume that for a three-dimensional jellium system, the metal DOS has a semi-elliptical shape, in which case the same set of equations is obtained.

It is thus evident that Eqs. (24) and (27) allow us to express the current solely in terms of the parameters of the model: the site-site and site-surface interaction potentials, the site energies and the relative position of the Fermi levels of the two surfaces. The metal eigenfunctions enter only through the functions  $\Sigma_A$  and  $\Sigma_I$ .

### Density of States

In addition to the current itself, it is of importance in the description of the electronic transport process to be able to calculate the local DOS. In a one-electron approximation, as the one we are employing here, the availability of states in every position of the chain at a value of energy of the incoming electron equal to the Fermi energy of the metal, is a local requirement for conduction to take place.

The DOS at site  $i$  is given by [19]:

$$\rho_i(E) = -\frac{1}{\pi} \text{Im}[G_i(E)] , \quad (34)$$

where  $G_i(E)$  is the on-site projected Green's function:

$$G_i(E) = \langle i | G(E) | i \rangle . \quad (35)$$

In order to calculate the total Green's function for the system we start from Dyson's equation:

$$G = G^o + G^o V G . \quad (36)$$

The calculation of the matrix elements  $G_i$  goes along a similar line as the corresponding one for the current. We illustrate it for the  $N = 2$  case from which the general expression can then be derived.

From (36) and using the fact that the potential connects only nearest-neighbor sites, and that metal eigenstates are non-interacting, we obtain:

$$G_{11} = G_{11}^o \left[ 1 + V_{12}G_{21} + \sum_k V_{1k}G_{k1} \right] \quad (37)$$

$$G_{22} = G_{22}^o \left[ 1 + V_{21}G_{12} + \sum_f V_{2f}G_{f2} \right] \quad (38)$$

$$G_{21} = G_{22}^o \left[ V_{21}G_{11} + \sum_f V_{2f}G_{f1} \right] \quad (39)$$

$$G_{12} = G_{11}^o \left[ V_{12}G_{22} + \sum_k V_{1k}G_{k2} \right] \quad (40)$$

$$G_{f1} = G_{ff}^o V_{f2}G_{21} \quad (41)$$

$$G_{f2} = G_{ff}^o V_{f1}G_{12} \quad (42)$$

$$G_{k2} = G_{kk}^o V_{k1}G_{12} \quad (43)$$

$$G_{k1} = G_{kk}^o V_{k2}G_{21} . \quad (44)$$

By substituting (41) in (39) one obtains:

$$G_{21} = \frac{G_{22}^o V_{21} G_{11}}{1 - \Sigma_2 G_{22}^o}. \quad (45)$$

Subsequent substitution of (44) and (45) in (37) renders:

$$G_{11} = \frac{G_{11}^o}{1 - \frac{V_{12}^2 G_{11}^o G_{22}^o}{1 - \Sigma_2 G_{22}^o} - G_{11}^o \Sigma_1}. \quad (46)$$

A similar procedure can then be followed to obtain:

$$G_{22} = \frac{G_{22}^o}{1 - \frac{V_{12}^2 G_{11}^o G_{22}^o}{1 - \Sigma_1 G_{11}^o} - G_{22}^o \Sigma_2}. \quad (47)$$

For arbitrary  $N$ , the on-site projected Green's function has the form:

$$G_j = \frac{G_j^o}{1 - V_{j-1,j}^2 G_j^o G_{j-1}^o \Omega_{j-1 \rightarrow 1} - V_{j,j+1}^2 G_j^o G_{j+1}^o \Omega_{j+1 \rightarrow N}}, \quad (48)$$

where  $\Omega_{j-1 \rightarrow 1}$  and  $\Omega_{j+1 \rightarrow N}$  are defined as:

$$\Omega_{j-1 \rightarrow 1} = \frac{1}{1 - \frac{V_{j-2,j-1}^2 G_{j-1}^o G_{j-2}^o}{1 - V_{j-3,j-2}^2 G_{j-2}^o G_{j-3}^o}} = \frac{1}{1 - V_{j-2,j-1}^2 G_{j-1}^o G_{j-2}^o \Omega_{j-2 \rightarrow 1}} \quad (49)$$

$$\begin{aligned} & \vdots \\ & 1 - \frac{V_{12}^2 G_1^o G_2^o}{1 - G_1^o \Sigma_1} \\ \Omega_{j+1 \rightarrow N} &= \frac{1}{1 - \frac{V_{j+1,j+2}^2 G_{j+1}^o G_{j+2}^o}{1 - V_{j+2,j+3}^2 G_{j+2}^o G_{j+3}^o}} = \frac{1}{1 - V_{j+1,j+2}^2 G_{j+1}^o G_{j+2}^o \Omega_{j+2 \rightarrow N}}. \quad (50) \\ & \vdots \\ & 1 - \frac{V_{N-1,N}^2 G_{N-1}^o G_N^o}{1 - G_N^o \Sigma_N} \end{aligned}$$

### Some Limiting Cases

In order to verify the exactness of our results for the resistance and the local DOS, it is of importance to include some comparisons to results which have been obtained independently for both quantities.

#### *Sharvin Point Contact Limit and the Value of Resistance in Resonance*

This is the limit of quantum resistance corresponding to point contact between two atoms. It has both been observed experimentally in STM measurements as a

function of distance [20] and derived theoretically [21,22] to be  $\hbar/2e^2 = 12.9 \text{ k}\Omega$  ( $\pi$  in atomic units). This is precisely the value we obtain when a molecular energy is in resonance with the energy of the detected in-coming electron. This energy is equal to the Fermi energy of the metal which we can set arbitrarily equal to zero as measured by the dimensionless variable  $\epsilon$  in Eqs. (32) and (33). We illustrate below the calculation for  $N = 1$ , but in fact the result is independent of  $N$ . For  $N$  odd, the resistance has the same value as for  $N = 1$ . For  $N$  even, the resistance is slightly larger. This result is in agreement with the well-known fact that a tight-binding Hamiltonian has an energy spectrum which is symmetric around the non-interacting orbital energies [19]. For  $N$  odd there is one state with energy exactly equal to that value. If the non-interacting orbital energies are chosen equal to zero, then the chains with odd  $N$  will always meet the resonance condition, whereas those with even  $N$  will have their orbital energies displaced from zero.

It is also interesting to notice that the independence of the current on the length of the chain is in agreement with the well-known result that the transmission coefficient for tunneling in a one-dimensional system, evaluated at resonance, is independent of barrier thickness [23-25]. We should also add that the result is independent of the strength of the site-site and site-surface coupling, as long as these potentials are chosen symmetrically with respect to the center of the chain.

Figure 1 shows the resistance at resonance as a function of  $N$ , the upper and lower values correspond to even and odd  $N$ , respectively.

In order to show how the Sharvin limit is achieved, we take the case  $N = 1$ . From Eq. (30) we obtain:

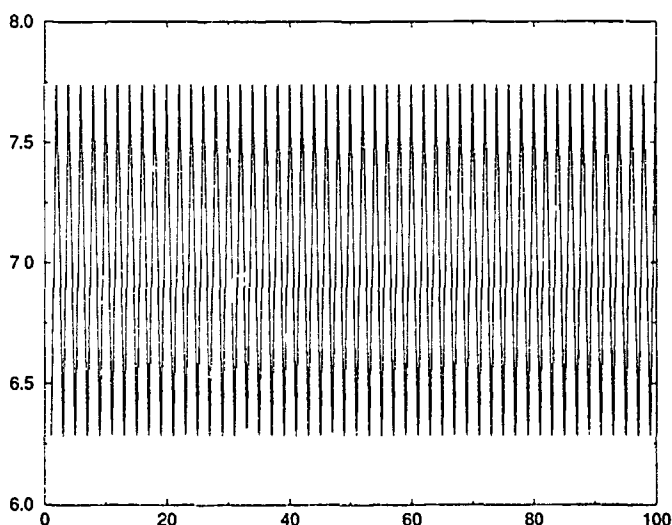


Figure 1. Resistance (a.u.) at resonance versus number of sites in the chain. The upper and lower values correspond to even and odd  $N$ , respectively.

$$|\langle f|V|i+\rangle|^2 = \frac{V_{f1}^2 V_{i1}^2}{[E - E_1^o - \text{Re}(\Sigma)]^2 + [\text{Im}(\Sigma)]^2}, \quad (51)$$

where

$$\Sigma = \Sigma_R + \Sigma_L. \quad (52)$$

At resonance, one has:

$$|\langle f|V|i+\rangle|^2 = \frac{V_{f1}^2 V_{i1}^2}{[\text{Im}(\Sigma_R) + \text{Im}(\Sigma_L)]^2}. \quad (53)$$

Using the identity:

$$\lim_{y \rightarrow 0^+} \frac{1}{x - iy} = P\left(\frac{1}{x}\right) - i\pi\delta(x), \quad (54)$$

we obtain the result:

$$\text{Im}(\Sigma_R) = -\pi \sum_f \delta(E - E_f^o) V_{f1}^2, \quad (55)$$

and similarly:

$$\text{Im}(\Sigma_L) = -\pi \sum_i \delta(E - E_i^o) V_{i1}^2. \quad (56)$$

By carrying out the double summation in (6), and allowing for an extra multiplicative factor of 2 which takes account of the electron spin degeneracy, and taking  $\Sigma_R = \Sigma_L$ , we obtain  $j = 1/\pi$  which renders the Sharvin limit for  $R$ .

### Local DOS for a Periodic One-Dimensional Chain

The local DOS for a one-dimensional periodic chain with a tight-binding Hamiltonian is [19]:

$$\rho_j(E) = \frac{1}{\pi} \text{Im}(G_{jj}(E)) = \frac{\theta(2V - |E - E_j^o|)}{\sqrt{4V^2 - (E - E_j^o)^2}}, \quad (57)$$

where  $V$  is the site-site interaction potential. In our finite chain, we should recover this behavior for a long enough chain and for sites far away from the surfaces. That this is indeed the case is shown in figure 2, where the DOS at the central position for a chain of 100 sites is plotted as a function of  $\epsilon$ . The curve shows the characteristic square root singularities of the DOS for the infinite periodic system given by (57).

### Conclusions

We have been able to obtain exact solutions for the tunneling current and DOS for a model of electron transfer through a finite chain which may be of interest for the analysis of molecular imaging in STM in the regime of moderate to strong interactions between the atomic tip and the sample. The model can also be applied



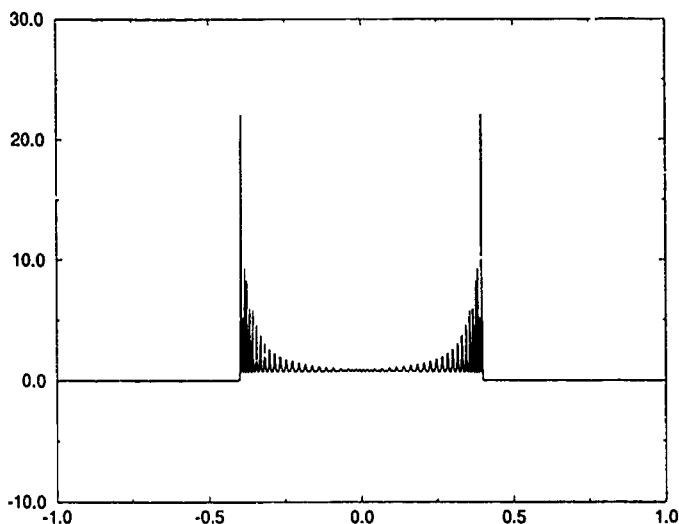


Figure 2. Local density of states (arbitrary units) in the center of a chain of 100 sites as a function of the dimensionless energy  $\epsilon$ . The non-interacting site energies are all equal to zero and the potentials are symmetric with respect to the center of the chain.

to the study of the influence of molecular disorder on the STM image. Investigations in this direction are currently under way, where disorder is introduced through variations in the orbital energies and the site-site potentials.

As a test of the exactness of our results we have successfully recovered some known results for one-dimensional systems regarding DOS and tunneling current in resonance.

### Acknowledgments

We gratefully acknowledge the financial assistance of the D.F.G (Germany), CONICIT (Venezuela) and the Office of Naval Research (USA), through Grant No. N00014-92-J-1684 for the research reported in this article. V.M. would like to thank Prof. Mark Ratner for very interesting discussions about the subject of electron transfer and its connection to STM. Thanks are due to Dr. Mathieu Kemp for critically reading the manuscript.

### Bibliography

- [1] P. W. Anderson, *Phys. Rev.* **124**, 41 (1961).
- [2] D. M. Newns, *Phys. Rev.* **178**, 1123 (1969).
- [3] G. Doyen, E. Koetter, J. P. Vigneron, and M. Scheffler, *Appl. Phys.* **A51**, 218 (1990).
- [4] G. Doyen, D. Drakova, V. Mujica, and M. Scheffler, *Phys. Stat. Sol. (a)* **131**, 107 (1992).
- [5] V. Mujica and G. Doyen, "A model for STM imaging of organic molecules on conducting substrates," to be submitted to *J. Chem. Phys.*
- [6] E. Tosatti, in *Highlights in Condensed Matter Physics and Future Prospects*, L. Esaki (Ed.), (Plenum Press, New York, 1991), pp. 631-654

- [7] J. Tersoff and D. R. Hamann, *Phys. Rev.* **B31**, 805 (1985); *Phys. Rev. Lett.* **50**, 1988 (1983).
- [8] J. Bardeen, *Phys. Rev. Lett.* **6**, 57 (1961).
- [9] Ch Joachim and P Sautet, in *Scanning Tunneling Microscopy and Related Methods*, R. J. Behm, N. Garcia, and H. Rohrer (Eds.) (Kluwer Academic Publishers, Dordrecht, 1990), pp. 377-387.
- [10] R. Garcia and N. Garcia, in *Scanning Tunneling Microscopy and Related Methods*, R. J. Behm, N. Garcia, and H. Rohrer (Eds.) (Kluwer Academic Publishers, Dordrecht, 1990), pp. 391-395.
- [11] S. M. Lindsay, O. F. Sankey, Y. Li, C. Herbst, and A. Rupprecht, *J. Phys. Chem.* **94**, 4655 (1990).
- [12] G. Doyen, E. Koetter, J. Barth, and D. Drakova, in *Scanning Tunneling Microscopy and Related Methods*, R. J. Behm, N. Garcia, and H. Rohrer (Eds.) (Kluwer Academic Publishers, Dordrecht, 1990), pp. 97-111.
- [13] N. D. Lang, *Phys. Rev.* **B34**, 5947 (1986).
- [14] N. D. Lang, *Phys. Rev. Lett.* **55**, 230 (1985).
- [15] N. D. Lang, *Phys. Rev. Lett.* **56**, 1164 (1986).
- [16] A. L. Fetter and J. D. Walecka, *Quantum Theory of Many-Particle Systems* (McGraw-Hill, New York, 1971).
- [17] B. A. Lippmann, *Phys. Rev. Lett.* **15**, 11 (1965).
- [18] B. A. Lippmann, *Phys. Rev. Lett.* **16**, 135 (1966).
- [19] E. M. Economou, *Green's Functions in Quantum Physics* (Springer-Verlag, Berlin, 1979).
- [20] J. K. Gimzewski and R. Möller, *Phys. Rev.* **B36**, 1284 (1987).
- [21] R. Landauer, *Phys. Lett.* **85a**, 91 (1981).
- [22] Y. V. Sharvin, *JETP* **48**, 984 (1965).
- [23] D. Bohm, *Quantum Theory* (Constable, London, 1954).
- [24] C. R. Leavens and G. C. Aers, in *Scanning Tunneling Microscopy and Related Methods*, R. J. Behm, N. Garcia, and H. Rohrer (Eds.) (Kluwer Academic Publishers, Dordrecht, 1990), pp. 27-57.
- [25] R. Tsu and L. Esaki, *Appl. Phys. Lett.* **22**, 562 (1973).

Received March 13, 1993

# **Intramolecular Coupling Effect in the Refractive Index for a Simple Three-Level Model of Molecules Diluted in Water**

**M. GARCIA-SUCRE**

*Centro de Física, Instituto Venezolano de Investigaciones Científicas, Apartado 21827, Caracas 1020A, Venezuela. Escuela de Química, Universidad Central de Venezuela, Caracas 47102, Venezuela, and Instituto de Física e Química de São Carlos, Universidad de São Paulo, Caixa P. 369, 13560, São Carlos, SP, Brazil*

**J. L. PAZ**

*Departamento de Química, Universidad Simón Bolívar, Apartado 89000, Caracas 1080A, Venezuela*

**E. SQUITIERI**

*Escuela de Química, Universidad Central de Venezuela, Caracas 47102 Venezuela*

**V. MUJICA**

*Centro de Física, Instituto Venezolano de Investigaciones Científicas, Apartado 21827, Caracas 1020A, Venezuela. Escuela de Química, Universidad Central de Venezuela, Caracas 47102, Venezuela*

## **Abstract**

We have calculated the first-, second-, and third-order contribution to the refractive index of a dilute aqueous solution of three-level molecules irradiated by an intense one-frequency external field. Each solute molecule is described by two coupled harmonic curves of electronic energies with the same force constant and with minima displaced in energy and nuclear coordinate. We assume that the intramolecular coupling mixes only the states corresponding to two near degenerate of the three levels considered. Important linear and nonlinear contributions of the solute molecules to the refractive index have been found, mostly in the so-called weak and intermediate coupling regions © 1993 John Wiley & Sons, Inc

## **Introduction**

Three-level models of atoms and molecules interacting with an intense electromagnetic field allow the description of additional effects to those already described by the simple and fruitful two-level models [1-4]. In a previous work we have studied this last type of model describing the two states as vibrational ones belonging respectively to two coupled harmonic potentials with the same force constant and with minima displaced in energy and nuclear coordinates [5]. In this way we have included in the two-level model a typical trait of the complexity of the molecular structure, while preserving some of the simplicity of this approach. We have found that the intramolecular coupling mixing the two states considered has a significant effect on the first-, second-, and third-order optical susceptibilities [5].

In this article we study the first-, second-, and third-order contribution to the refractive index of a dilute water solution of molecules, each of them described as a three-level system irradiated by an intense one-frequency external field. On the other hand, we assume that an intramolecular coupling mixes only the states corresponding to the two near degenerate of the three levels considered, according to the scheme illustrated in Figure 1.

In the next section we will describe a simplified version of the typical vibronic model for molecules [6-8], allowing a not-too-intricate calculation of the optical susceptibilities up to third-order in the external field amplitude. Finally, in the last section, we will discuss our results for the first-, second-, and third-order contribution to the refractive index of a dilute water solution of the molecules considered. According to our results important linear and nonlinear contributions of the solute molecules to the refractive index occur mostly in the so-called weak and intermediate coupling regions.

### The Three-Level Model of a Molecule with Intramolecular Coupling between Two Near Degenerate States

The Hamiltonian describing a molecule can be written as

$$H = T_N + T_e + V(q, Q) + V'(q) \quad (1)$$

when  $q$  and  $Q$  are the electronic and nuclear coordinates;  $T_N$  and  $T_e$  are the nuclear and kinetic energy operators;  $V(q, Q)$  is the potential energy term arising from electron-electron, electron-nucleus, and nucleus-nucleus interactions within the

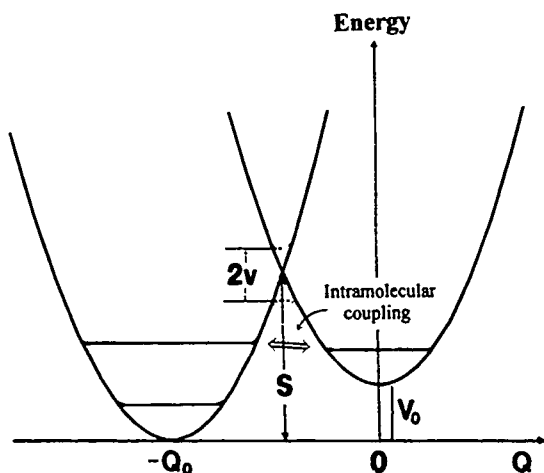


Figure 1. A three-level model of a molecule in which two levels belong to one of the harmonic electronic potentials. The intramolecular coupling  $v$  mixes the states corresponding to the nearest levels belonging to different electronic potentials. The weak, intermediate and strong coupling cases correspond to  $v \ll S$ ,  $v \sim S$  and  $v \gg S$ , respectively.

molecule; and  $V'(q)$  is a residual term depending only in the electronic coordinates. The wave functions describing the three states considered of our system are

$$\Psi_0(q;Q) = \psi_1(q;Q)\phi_{1j}(Q) \quad (2)$$

and

$$\Psi^\pm(q;Q) = C_{1k}^\pm \psi_1(q;Q)\phi_{1k}(Q) + C_{2l}^\pm \psi_2(q;Q)\phi_{2l}(Q), \quad (3)$$

where  $\psi_1(q;Q)$  and  $\psi_2(q;Q)$  are the electronic wave functions corresponding to the left and right harmonic potentials in Figure 1. The harmonic vibrational wave functions of states associated to the electronic wave functions  $\psi_1(q;Q)$  and  $\psi_2(q;Q)$  are denoted as  $\phi_{1j}(Q)$ ,  $\phi_{1k}(Q)$ , and  $\phi_{2l}(Q)$ , where  $j$ ,  $k$ , and  $l$  are vibrational quantum numbers. In the scheme illustrated in Figure 1 these quantum numbers are  $j = 0$ ,  $k = 1$ , and  $l = 0$ . The three energy levels of our system, expressed in units of  $\hbar\omega/2$ , where  $\omega$  is the frequency of the harmonic oscillators, are given by

$$E_0 = 2(j + 1/2) \quad (4)$$

and

$$E^\pm = (1/2)[(E_{1k} + E_{2l}) \pm \sqrt{(E_{1k} - E_{2l})^2 + 4v^2|\langle\phi_{1k}|\phi_{2l}\rangle|^2}], \quad (5)$$

where  $E_{1k} = 2(k + 1/2)$ ,  $E_{2l} = 2(l + 1/2) + V_0$ , and the intramolecular coupling parameter  $v = \langle\psi_m(q;Q)|V'(Q)|\psi_n(q;Q)\rangle / \frac{1}{2}\hbar\omega$ , where  $m, n = 1, 2$ , and  $m \neq n$ .

The corresponding wave functions to the energies  $E_0$  and  $E^\pm$  are respectively the Born-Oppenheimer products given in Eq. (2). and [5]

$$\Psi^\pm(q,Q) = C_{1k}^\pm[\psi_1(q;Q)\phi_{1k}(Q) \pm A_{1k}^\pm\psi_2(q;Q)\phi_{2l}(Q)], \quad (6)$$

where

$$C_{1k}^\pm = 1/[1 + |A_{1k}^\pm|^2]^{1/2} \quad \text{and} \quad A_{1k}^\pm = (E_{1k} - E^\pm)/v\langle\phi_{1k}|\phi_{2l}\rangle.$$

The criteria of weak, intermediate, and strong coupling cases [6-8] are  $v \ll S$ ,  $v \sim S$  and  $v \gg S$ , respectively, where  $S = (m\omega/\hbar)Q_0^2$ ,  $m$  is the mass corresponding to the vibrational mode described by the coordinate  $Q$ , and  $Q_0$  is the relative displacement between the two minima of the electronic potentials (Fig. 1). The vibrational overlapping factors  $\langle\phi_{1k}|\phi_{2l}\rangle$  in the above expressions, where  $k = 0, 1$  and  $l = 0$ , can be calculated using the Pekar formula [9]

$$\langle\phi_{n0}|\phi_{n'0}\rangle = \frac{(-1)^m}{(m!)^{1/2}} S^{m/2} e^{-S/4} 2^{-m/2}, \quad (7)$$

where we have the cases ( $n = 1$  and  $n' = 2$ ) and ( $n = 2$  and  $n' = 1$ ). Given the symmetry of the starting harmonic potentials corresponding to the system without intramolecular coupling, we take the permanent dipolar moments associated to the electronic states described respectively by our basis wave functions  $\psi_1(q;Q)$  and  $\psi_2(q;Q)$  as zero.

The transition dipolar moments corresponding to our three-level system are given by

$$\mu_{0-} = -C_{1k}^- A_{1k}^- \mu_{12} (-Q_0) \langle \phi_{10} | \phi_{20} \rangle, \quad (8)$$

$$\mu_{0+} = -C_{1k}^+ A_{1k}^+ \mu_{12} (-Q_0) \langle \phi_{10} | \phi_{20} \rangle, \quad (9)$$

$$\mu_{-+} = -C_{1k}^- C_{1k}^+ \mu_{12} (-Q_0) \langle \phi_{20} | \phi_{11} \rangle [A_{1k}^+ + A_{1k}^-]. \quad (10)$$

Since our ground state coincide with one of the basis states its permanent dipolar moment is zero. On the other hand, the permanent dipolar moments respectively, associated to the mixed states  $-$  and  $+$  will not vanish, and are given by

$$\mu_{--} = -2(C_{1k}^-)^2 A_{1k}^- \mu_{12} (-Q_0) \langle \phi_{20} | \phi_{11} \rangle \quad (11)$$

and

$$\mu_{++} = -2(C_{1k}^+)^2 A_{1k}^+ \mu_{12} (-Q_0) \langle \phi_{20} | \phi_{11} \rangle. \quad (12)$$

Having obtained the expressions for the energy of the three levels involved, and the corresponding transition and permanent dipolar moments, we are now prepared to calculate the optical susceptibilities up to third-order in the external field amplitude  $E$ , in term of which the polarization is usually written as [4]

$$P = \chi^{(1)} E + \chi^{(2)} E^2 + \chi^{(3)} E^3 \quad (13)$$

The first-order susceptibility for our system will be given by [4]

$$\chi^{(1)}(E_c) = \frac{N}{0.5\hbar\omega} \sum_{mn} \mu_{nm}^2 \rho_{mm}^{(0)} \left[ \frac{1}{E_n - E_m - E_c - iE_s} + \frac{1}{E_n - E_m + E_c + iE_s} \right] \quad (14)$$

where  $m, n = 0, -, +$ , and  $N$  is the number density of molecules,  $\rho_{mm}^{(0)}$  is the thermal equilibrium value of the fraction of molecules in the state  $m$ ,  $E_c = \hbar\omega_f/0.5\hbar\omega$ , and  $E_s = \hbar\gamma_{mn}/0.5\hbar\omega$ ;  $\omega_f$  and  $\gamma_{mn}$  being, respectively, the frequency of the external field and the phenomenological damping rate of the density matrix element  $\rho_{mn}$ . We have assumed the same value for all the  $\gamma_{mn}$ 's involved.

The second- and third-order optical susceptibilities are respectively given by [4]

$$\chi^{(2)}(2E_c) = \frac{N}{(0.5\hbar\omega)^2} \sum_{nmv} \left\{ \frac{(\rho_{mm}^{(0)} - \rho_{vv}^{(0)}) \mu_{nv} \mu_{vm} \mu_{mn}}{[E_n - E_m - 2E_c - iE_s][E_v - E_m - E_c - iE_s]} \right. \\ \left. - \frac{(\rho_{vv}^{(0)} - \rho_{nn}^{(0)}) \mu_{nv} \mu_{vm} \mu_{mn}}{[E_n - E_m - 2E_c - iE_s][E_n - E_v - E_c - iE_s]} \right\}, \quad (15)$$

and

$$\begin{aligned}
\chi^{(3)}(E_c) = & \frac{N}{(0.5\hbar\omega)^3} \\
& \times \sum_{nmvl} \left\{ (\rho_{mm}^{(0)} - \rho_{vv}^{(0)}) \frac{\mu_{nl}\mu_{lv}\mu_{vm}\mu_{mn}}{[E_n - E_m - E_c - iE_s][E_l - E_m - 2E_c - iE_s]} \right. \\
& \quad \times [E_v - E_m - E_c - iE_s] \\
& \quad - (\rho_{vv}^{(0)} - \rho_{ll}^{(0)}) \frac{\mu_{mn}\mu_{vm}\mu_{lv}\mu_{nl}}{[E_n - E_m - E_c - iE_s][E_l - E_m - 2E_c - iE_s]} \\
& \quad \times [E_l - E_v - E_c - iE_s] \\
& \quad - (\rho_{ll}^{(0)} - \rho_{vv}^{(0)}) \frac{\mu_{mn}\mu_{nv}\mu_{lm}\mu_{vl}}{[E_n - E_m - E_c - iE_s][E_n - E_l - 2E_c - iE_s]} \\
& \quad \times [E_v - E_l - E_c - iE_s] \\
& \quad \left. + (\rho_{vv}^{(0)} - \rho_{nn}^{(0)}) \frac{\mu_{mn}\mu_{lm}\mu_{nv}\mu_{vl}}{[E_n - E_m - E_c - iE_s][E_n - E_l - 2E_c - iE_s]} \right. \\
& \quad \times [E_n - E_v - E_c - iE_s] \Bigg\} \\
& + \frac{N}{(0.5\hbar\omega)^3} \\
& \times \sum_{nmvl} \left\{ (\rho_{mm}^{(0)} - \rho_{vv}^{(0)}) \frac{\mu_{nl}\mu_{lv}\mu_{vm}\mu_{mn}}{[E_n - E_m - E_c - iE_s][E_l - E_m - iE_s]} \right. \\
& \quad \times [E_v - E_m - E_c - iE_s] \\
& \quad - (\rho_{vv}^{(0)} - \rho_{ll}^{(0)}) \frac{\mu_{mn}\mu_{vm}\mu_{lv}\mu_{nl}}{[E_n - E_m - E_c - iE_s][E_l - E_m - iE_s]} \\
& \quad \times [E_l - E_v - E_c - iE_s] \\
& \quad - (\rho_{ll}^{(0)} - \rho_{vv}^{(0)}) \frac{\mu_{mn}\mu_{nv}\mu_{lm}\mu_{vl}}{[E_n - E_m - E_c - iE_s][E_n - E_l - iE_s]} \\
& \quad \times [E_v - E_l - E_c - iE_s] \\
& \quad \left. + (\rho_{vv}^{(0)} - \rho_{nn}^{(0)}) \frac{[\mu_{mn}\mu_{lm}\mu_{nv}\mu_{vl}]}{[E_n - E_m - E_c - iE_s][E_n - E_l - iE_s]} \right. \\
& \quad \times [E_n - E_v - E_c - iE_s] \Bigg\} \\
& + \frac{N}{(0.5\hbar\omega)^3} \\
& \times \sum_{nmvl} \left\{ (\rho_{mm}^{(0)} - \rho_{vv}^{(0)}) \frac{\mu_{nl}\mu_{lv}\mu_{vm}\mu_{mn}}{[E_n - E_m - E_c - iE_s][E_l - E_m - iE_s]} \right.
\end{aligned}$$

$$\begin{aligned}
& \times [E_v - E_m + E_c - iE_s] \\
& -(\rho_{vv}^{(0)} - \rho_{ll}^{(0)}) \frac{\mu_{mn}\mu_{vm}\mu_{lv}\mu_{nl}}{[E_n - E_m - E_c - iE_s][E_l - E_m - iE_s]} \\
& \quad \times [E_l - E_v + E_c - iE_s] \\
& -(\rho_{ll}^{(0)} - \rho_{vv}^{(0)}) \frac{\mu_{mn}\mu_{nv}\mu_{lm}\mu_{vl}}{[E_n - E_m - E_c - iE_s][E_n - E_l - iE_s]} \\
& \quad \times [E_v - E_l + E_c - iE_s] \\
& +(\rho_{vv}^{(0)} - \rho_{nn}^{(0)}) \frac{\mu_{mn}\mu_{lm}\mu_{nv}\mu_{vl}}{[E_n - E_m - E_c - iE_s][E_n - E_l - iE_s]} \\
& \quad \times [E_n - E_v + E_c - iE_s] \Bigg\}, \tag{16}
\end{aligned}$$

where  $m, n, v, l = 0, -, +$ , and

$$\begin{aligned}
\chi^{(3)}(3E_c) &= \frac{N}{(0.5\hbar\omega)^3} \\
& \times \sum_{nmv/l} \left\{ (\rho_{mm}^{(0)} - \rho_{ll}^{(0)}) \frac{\mu_{mn}\mu_{nv}\mu_{vl}\mu_{lm}}{[E_n - E_m - 3E_c - iE_s]} \right. \\
& \quad \times [E_n - E_m - 2E_c - iE_s] \\
& \quad \times [E_l - E_m - E_c - iE_s] \\
& -(\rho_{ll}^{(0)} - \rho_{vv}^{(0)}) \frac{\mu_{mn}\mu_{nv}\mu_{lm}\mu_{vl}}{[E_n - E_m - 3E_c - iE_s]} \\
& \quad \times [E_v - E_m - 2E_c - iE_s] \\
& \quad \times [E_v - E_l - E_c - iE_s] \\
& -(\rho_{vv}^{(0)} - \rho_{ll}^{(0)}) \frac{\mu_{mn}\mu_{vm}\mu_{nl}\mu_{lv}}{[E_n - E_m - 3E_c - iE_s]} \\
& \quad \times [E_n - E_v - 2E_c - iE_s] \\
& \quad \times [E_l - E_v - E_c - iE_s] \\
& \left. +(\rho_{ll}^{(0)} - \rho_{nn}^{(0)}) \frac{\mu_{mn}\mu_{vm}\mu_{lv}\mu_{nl}}{[E_n - E_m - 3E_c - iE_s]} \right\} \tag{17}
\end{aligned}$$

where  $m, n, v, l = 0, -, +$ .

With the above expressions for  $\chi^{(1)}$ ,  $\chi^{(2)}$ , and  $\chi^{(3)}$ , we will calculate in the next section the first-, second-, and third-order contributions to the refractive index coming from the solute three-level molecules in a dilute water solution.



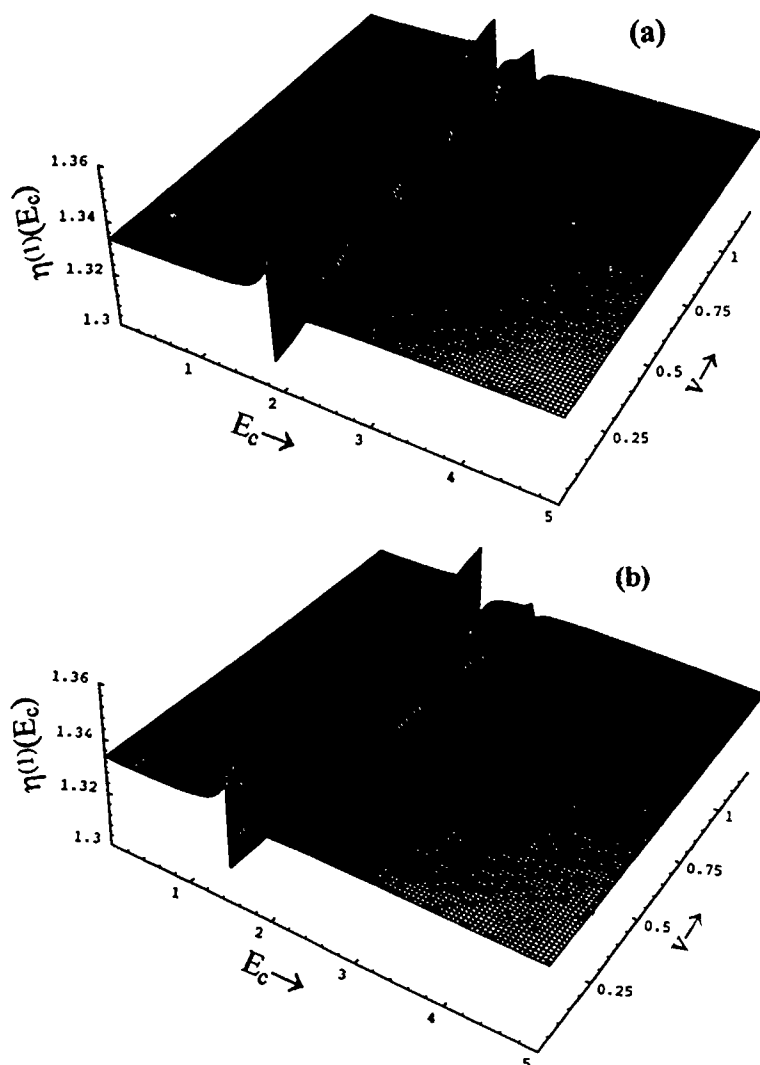


Figure 2. First-order refractive index  $\eta^{(1)}(E_c) = \eta_1(E_c)/\epsilon_{-0}$  for a water ( $\eta_0 = 1.33241$ ) solution in which the solute are three-level molecules,  $\omega = 700 \text{ cm}^{-1}$ ,  $S = 0.1$  and  $E_S = 0.02$ . In (a) we consider  $V_0 = 1.9$  and in (b)  $V_0 = 1.5$ .

### Refractive Index Contributions in a Dilute Water Solution

From the Maxwell equation in which enters the polarization,

$$\nabla^2 E - \frac{1}{c^2} \frac{\partial^2 E}{\partial t^2} = \frac{4\pi}{c^2} \frac{\partial^2 P}{\partial t^2} \quad (18)$$

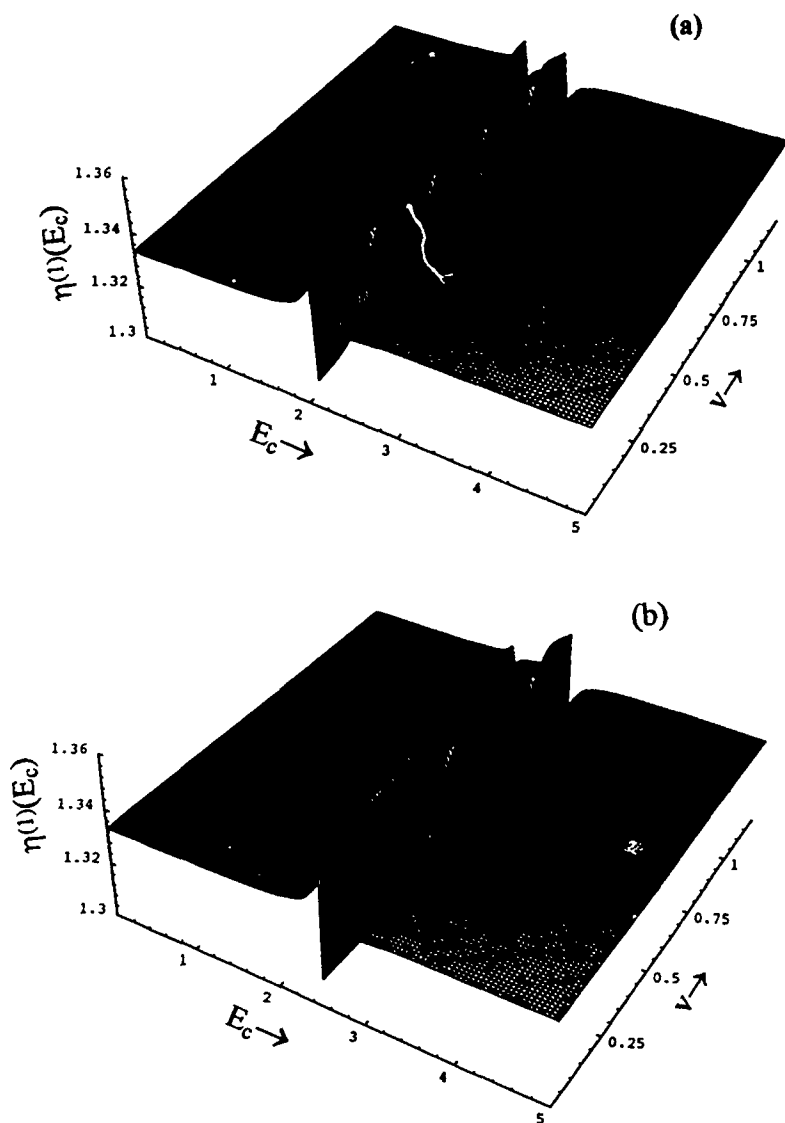


Figure 3. The same as Figure 2 except that in (a)  $V_0 = 2.1$  and in (b)  $V_0 = 2.5$ .

and making the slowly-varying-amplitude approximation [4], it can be shown that for one-, two-, and three-photon dispersive processes, the corresponding refractive indexes of a dilute water solution of the molecules considered, are respectively

$$\eta_1(E_c) = [\eta_0^2 + 4\pi \text{Re}\chi_{\text{eff}}(E_c)]^{1/2}, \quad (19)$$

$$\eta_2(2E_c) = [\eta_0^2 + 4\pi E \text{Re}\chi^{(2)}(2E_c)]^{1/2}, \quad (20)$$

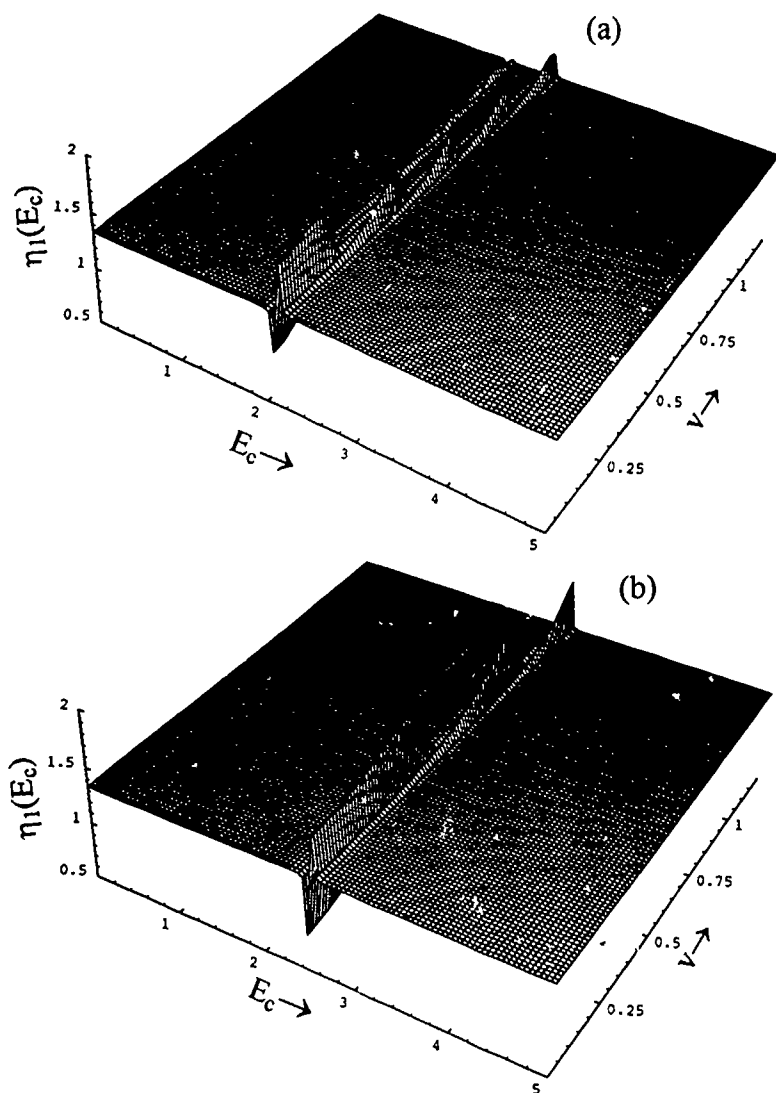


Figure 4. The refractive index  $\eta_1(E_c)$ , Eq. (19), when we turn-on the external field amplitude to a typical value of  $E = 10^3$  statvolt/cm (a)  $V_0 = 2.1$ . (b)  $V_0 = 2.5$ .

and

$$\eta_3(3E_c) = [\eta_0^2 + 4\pi E^2 \text{Re}\chi^{(3)}(3E_c)]^{1/2} \quad (21)$$

where  $\eta_0$  is the solvent refractive index, and the effective susceptibility  $\chi_{\text{eff}}(E_c)$  can be calculated from Eqs. (14) and (16), according to

$$\chi_{\text{eff}}(E_c) = \chi^{(1)}(E_c) + E^2 \chi^{(3)}(E_c) \quad (22)$$

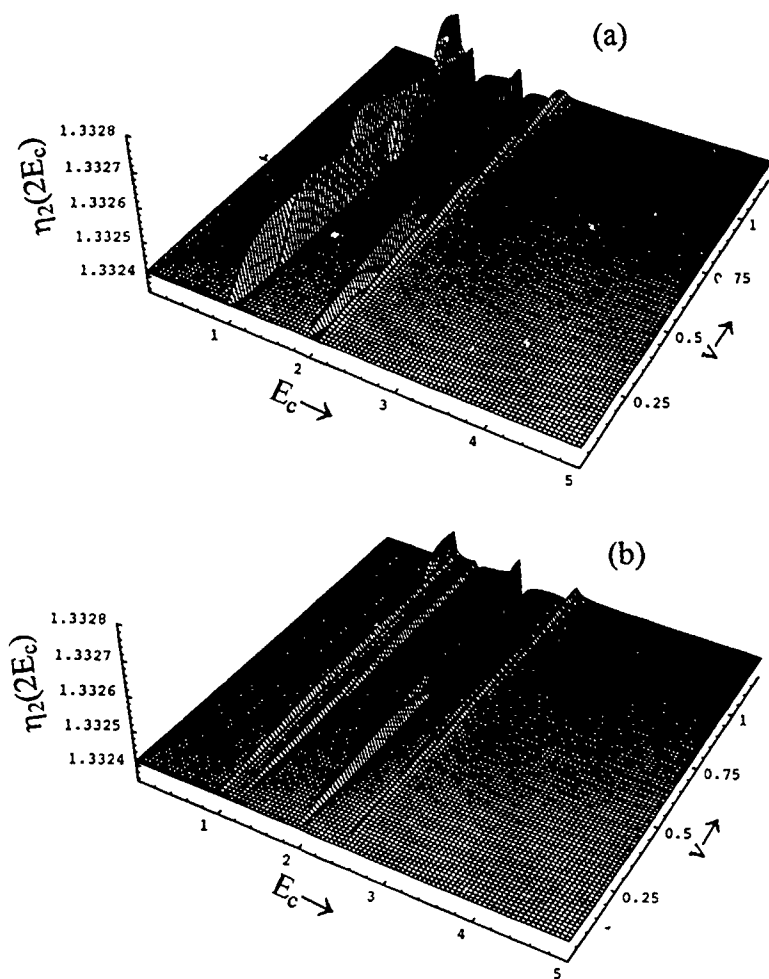


Figure 5 The second-order refractive index  $\eta_2(2E_c)$ , Eq. (20), for the same parameters as in Figure 4.

Figure 2 illustrates the first-order refractive index  $\eta^{(1)}(E_c) = \eta_1(E_c)/E_{c=0}$  for a dilute water ( $\eta_0 = 1.33241$ ) solution in which the solute corresponds to a concentration of  $10^{-3}$  M ( $N = 6.022 \times 10^{17}$  molec/cm<sup>3</sup>),  $\omega = 700$  cm<sup>-1</sup>,  $S = 0.1$ ,  $E_s = 0.02$ ,  $\mu_{12}(-Q_0) = 5 \times 10^{-18}$  esu cm, and  $T = 300$  K. In Figure 2(a) and 2(b) the energy separation between the minima of the two harmonic potentials are, respectively,  $V_0 = 1.90$  and  $V_0 = 1.50$ , which correspond to a separation between the two levels belonging to different harmonic potentials in Figure 1 of 0.1 and 0.5, respectively. The range of variation of  $E_c$  (the photon energy of the external field) and the intramolecular coupling  $v$  is in both cases between 0 and 1. We can appreciate in these figures a sizable variation of the first-order refractive index with

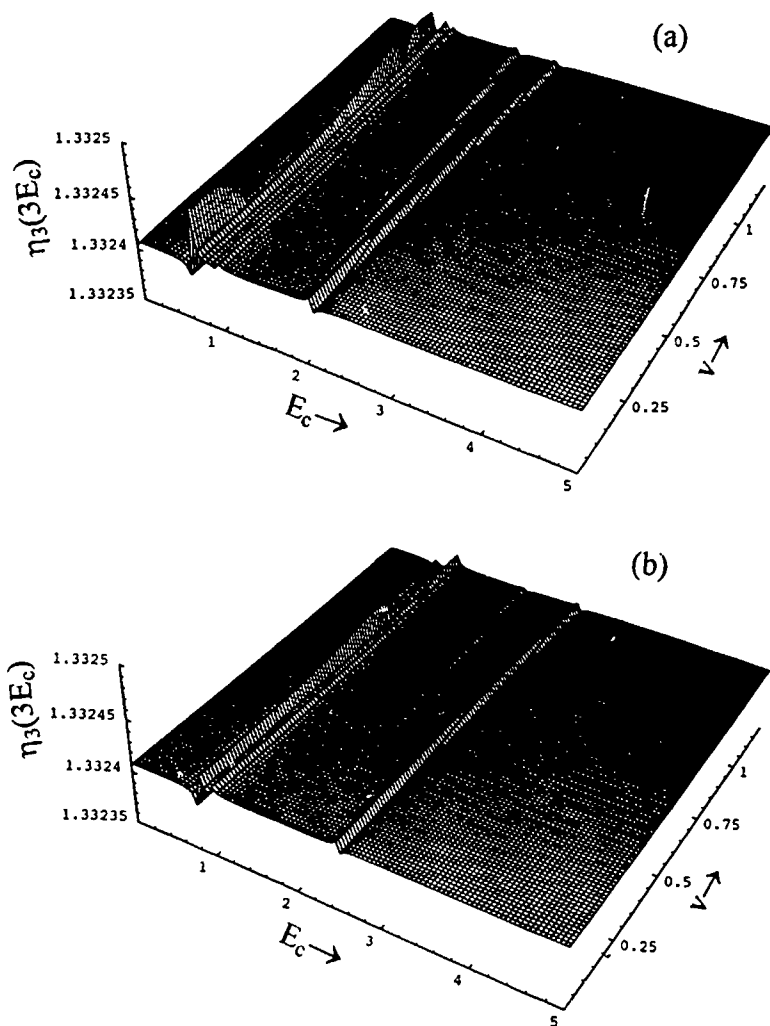


Figure 6. The third-order refractive index  $\eta_3(3E_c)$ , Eq. (21), for the same parameters as in Figure 4.

both  $E_c$  and  $v$  in the resonance region. On the other hand, there is an asymmetry between the two signals that separate from each other as the coupling  $v$  increases. In this case the lower frequency signal is larger than the higher frequency one. We appreciate the inverse effect in Figure 3(a) and 3(b) which correspond to the same parameters as the previous figures, except that now  $V_0 = 2.1$  and  $V_0 = 2.5$ , respectively, i.e., the energy level belonging to the right harmonic potential (Fig. 1) is now over instead of below the nearest level of the left harmonic potential by the quantities 0.1 and 0.5. The undulations presented by  $\eta^{(1)}(E_c)$  in Figures 2 and 3 when we fix  $E_c$  in the resonance region and vary  $v$  occur because of the equivalence

between fixing  $\nu$  and varying  $E_c$  or vice versa, in connection with the shape of the signal.

In Figures 4(a) and 4(b) we represent the resulting refractive index  $\eta_1(E_c)$  once we superimpose on the first-order term the effect of the third-order correction to the optical susceptibility,  $\chi^{(3)}(E_c)$ , when we turn on the external field to a typical intense value of  $E = 10^3$  statvolt/cm [see Eqs. (19) and (22)]. We can appreciate a strong modification of the refractive index in the resonance region due to this third-order effect on the external field amplitude. On the other hand, we have again an asymmetry between the signals that separate as the intramolecular coupling  $\nu$  increases. We can also appreciate large variations of the refractive index  $\eta_1(E_c)$  when we fix  $E_c$  in the resonance region and vary the intramolecular coupling  $\nu$ . We have also calculated  $\eta_1(E_c)$  for the same parameters as in Figures 4(a) and 4(b), except that now  $V_0 = 1.90$  and  $1.5$ , instead of  $2.1$  and  $2.5$ . We have obtained analogous modification as in passing from Figure 2 to Figure 3.

In Figures 5(a) and 5(b) are illustrated the second-order contribution to the refractive index, Eq. (20), for the same parameters as in Figures 4(a) and 4(b), respectively. Now, the variation of  $\eta_2(2E_c)$  with both  $E_c$  and  $\nu$  are much smaller (by a factor of ca.  $1/1000$ ) than the variation of  $\eta_1(E_c)$ . Still smaller are the variations of  $\eta_3(3E_c)$  illustrated in Figures 6(a) and 6(b). This result can be expected on the ground that to  $\eta_1(E_c)$ ,  $\eta_2(2E_c)$  and  $\eta_3(3E_c)$  contribute respectively one-, two- and three-photon processes once we turn-on an intense external field.

### Concluding Remarks

Using a simple model of three-level molecules with intramolecular coupling between the two states corresponding to different electronic potentials, we have found the following results for the refractive index of a dilute water solution of these molecules irradiated by an intense one-frequency external field.

- i) A strong contribution to the first-order refractive index coming from the third-order correction in the external field amplitude for one-photon process when we turn-on an intense external field of  $E = 10^3$  statvolt/cm [see Figs. 4(a) and 4(b)].
- ii) Large variation of the refractive index for one-photon processes  $\eta_1(E_c)$  when we fix  $E_c$  in the resonance region and vary the intramolecular coupling  $\nu$ .
- iii) Since the refractive index is related with the absorption coefficient, the variation found above for  $\eta_1(E_c)$ , with both  $E_c$  and  $\nu$  will induce modification of the absorption coefficient for the kind of systems we have studied.

### Acknowledgments

This work was supported by the CDCH of Universidad Central de Venezuela, Consejo Nacional de Investigaciones Científicas y Tecnológicas (CONICIT) (Grants S1-2226, S1-2238), Decanato de Investigaciones of Universidad Simón Bolívar (Grant S1-CB-314) and CNPq (Brazilian Agency).

**Bibliography**

- [1] M. D. Levenson, *Introduction to Nonlinear Laser Spectroscopy* (Academic Press, New York, 1982).
- [2] N. Bloembergen, *Nonlinear Optics* (Benjamin, New York, 1965).
- [3] M. Sargent III, *Quantum Optics* (Springer-Verlag, Berlin, 1990).
- [4] R. W. Boyd, *Nonlinear Optics* (Academic Press, New York, 1992).
- [5] J. L. Paz, M. García-Sucre, E. Squitieri, and V. Mujica, *Chem. Phys. Lett.* (submitted).
- [6] A. Witkowski and W. Moffit, *J. Chem. Phys.* **33**, 872 (1960).
- [7] R. L. Fulton and M. Gouterman, *J. Chem. Phys.* **35**, 1059 (1961).
- [8] M. García-Sucre, F. Goychman, and R. Lefebvre, *Phys. Rev. A* **2**, 1738 (1970).
- [9] B. Di Bartolo, in *Radiationless Processes*, B. Di Bartolo, Ed. (Plenum Press, New York, 1980), p. 39.

Received March 13, 1993

# Theoretical Study of the C- vs. O-Acylation of Metal Enolates. Frontier Molecular Orbital Analysis Including Solvent Effects\*

VICTOR G. SARAGONI and RENATO R. CONTRERAS

*Departamento de Química, Facultad de Ciencias, Universidad de Chile, Casilla 653-Santiago, Chile*

ARIE J. AIZMAN

*Departamento de Química, Universidad Técnica Federico Santa María,  
Casilla 110-V, Valparaíso, Chile*

## Abstract

An extended version of the Klopman-Salem equation of chemical reactivity, which incorporates the effect of an external electrostatic field in both charge and orbital contributions, has been applied to analyze the reactivity pattern of ambident metal enolates towards acylation reactions in different solvents. The results are consistent with the experimental observation that the proportion of C-acylation product is enhanced for solvents of low polarity where a relevant orbital control contribution is predicted. Comparison between the *cis/trans* proportion of C- and O-acylation products are also qualitatively accounted for by the FMO analysis. © 1993 John Wiley & Sons, Inc

## Introduction

Enolate anions are members of a group of ambident nucleophiles that react with alkylating agents or acylating agents to form products with a new bond either at the alpha-carbon or at oxygen [1,2]. From a spectroscopic examination of metal enolates, the lithium salts are found to exist as enolates structures in which either *contact* ion pair or *solvent separated* ions may be present.

The existence of these metal enolates as solvent-separated ions is favored by (i) increasing the polarity of the solvent, (ii) the presence of lithium or sodium rather than zinc or magnesium cations, and (iii) by use of the *trans* rather than the *cis* stereo-isomer of the enolate [3] [see Fig. 1(a)].

In acylation reactions with acetic anhydrides as acylating agents, it is observed that the major product of the kinetically controlled processes are usually the O-acylated derivatives corresponding in structure and stereochemistry to the starting enolate [4]. However, it has been noted that, even with reaction procedures that results in kinetically controlled acylation, mixtures of C- and O-acylated products may result. The proportion of C-acylation appears to be enhanced by the use of relatively nonpolar solvents [5].

---

\* Contribution No. 8 from Centro de Mecánica Cuántica Aplicada (CMCA).



The experimental observation on metal enolates are specially suitable to test the usefulness and reliability of our recently developed extension of the Klopman-Salem equation of chemical reactivity in solution phase [6]. First of all, the co-existence of C- and O-acylation products appears to be strongly related to the variation of the solvent polarity. Secondly, the theoretical procedure described in Ref. [6] may provide some qualitative explanations about the relative relevance of the charge control vs. the orbital control contributions for a given solvent.

In this work we present the result of the solution FMO calculations in the series of methyl-, *n*-butyl-, and phenyl-enolates, including the *cis/trans* stereo-isomers, for a wide region of solvent polarity represented parametrically by the dielectric constant. Specific effects of lithium are also incorporated.

### Model and Calculations

#### *The Extended Klopman-Salem Equation*

It is possible to have an expression for the interaction energy between a nucleophile and an electrophile in the presence of an external electrostatic field, by using the Klopman-Salem frontier molecular orbital (FMO) expression [7,8]

$$E_{\text{int}}(1) = \frac{Q_{\text{Nu}}(1)Q_{\text{El}}(1)}{R} + \sum_m^{\text{occ}} \sum_n^{\text{vir}} \frac{2[c_{\text{Nu}}^m(1)c_{\text{El}}^n(1)\beta]^2}{e_H(1) - e_L(1)} \quad (1)$$

and

$$E_{\text{int}}(\epsilon) = \frac{Q_{\text{Nu}}(\epsilon)Q_{\text{El}}(\epsilon)}{\epsilon R} + \sum_m^{\text{occ}} \sum_n^{\text{vir}} \frac{2[c_{\text{Nu}}^m(\epsilon)c_{\text{El}}^n(\epsilon)\beta]^2}{e_H(\epsilon) - e_L(\epsilon)} \quad (2)$$

for gas and solution phases, respectively.

$E_{\text{int}}$ ,  $Q_A$ ,  $e_H$ , and  $e_L$  are the interaction electrostatic energy, the net charge, the energy of highest occupied molecular orbital of the nucleophile (HOMO), and the lowest unoccupied molecular orbital of the electrophile (LUMO) in gas phase (1) and in the presence of a polarizable medium ( $\epsilon$ ), represented by an effective dielectric constant  $\epsilon$ .  $R$  represents the internuclear distance between the active sites of the interacting electrophile/nucleophile pair. From Eqs. (1) and (2), it became possible to derive a general expression for the change in the interaction energy from gas to solution phase [6]. The resulting final expression, after introducing a first-order variation in the net charges for the system in solution,  $Q_A(\epsilon) = Q_A(1) + \delta Q_A(1)$ , is

$$\begin{aligned} \delta E_{\text{int}} = & - \left( 1 - \frac{1}{\epsilon} \right) \frac{Q_{\text{Nu}}(1)Q_{\text{El}}(1)}{R} + \frac{\delta [Q_{\text{Nu}}(1)Q_{\text{El}}(1)]}{\epsilon R} \\ & + \beta^2 \sum_n^{\text{vir}} \{ S_E^H(\epsilon)[c_{\text{El}}^n(\epsilon)]^2 - S_E^H(1)[c_{\text{El}}^n(1)]^2 \}, \end{aligned} \quad (3)$$

which is expressed in terms of the unperturbed net charges of the atomic active centers of the nucleophile/electrophile pair  $Q_{\text{Nu}}^0$  and  $Q_{\text{El}}^0$ , the LCAO coefficients and

the electrophilic superdelocalizability of the HOMO of the nucleophile [9] in gas (1) and solution ( $\epsilon$ ) phases,  $S_E^H$ :

$$S_E^H(1) = 2 \sum_m^{\text{occ}} \frac{[c_H^m(1)]^2}{e_H(1)} \quad (4)$$

and

$$S_E^H(\epsilon) = 2 \sum_m^{\text{occ}} \frac{[c_H^m(\epsilon)]^2}{e_H(\epsilon)}, \quad (5)$$

respectively.

Equations (3), (4), and (5) have been derived previously [6], based on a theoretical procedure that allows one to describe the monoelectronic orbital energy shifting induced by an electrostatic external field [10]. Equation (3) also contains implicitly the solvation energy as given by the Born model. It is worth mentioning here that in spite of the fact that Eq. (3) was obtained by a perturbation theory procedure [6], the effect of the polarizable medium is variationally introduced in the calculation of monoelectronic orbital energies as well as in the LCAO coefficients [11,12]. It is also worth mentioning that Eq. (3) keeps the structure of the Klopman-Salem equation: The first and second terms are the original *charge control* contribution and the corresponding charge polarization correction, whereas the third term represents the corrected *orbital control* contribution.

### Method and Calculations

We select the series of methyl-, *n*-butyl-, and phenyl-lithium enolates belonging to a wide series of metal enolates extensively studied by House et al. [2,3] with great detail. For this small series, results concerning the proportion of  $\alpha$ -C- vs. O-acylated product, for a wide variety of solvents and including both *cis/trans* stereoisomers are reported.

The calculation of properties involved in Eq. (3) were obtained from the SCRF-CNDO/2 method described in Refs. [11,12]. The electrophilic agent was acetic anhydride. The ion pair structure of enolate was taken as the contact ion pair shown in Figure 1(a). Standard bond angles and distances were considered in all the calculations done. The solvent-separated ion pair was modeled through the enolate anion.

The calculation of the isolated ion pairs and enolate anions were completed with calculations where the electrophile was allowed to approach the enolate frame at a perturbing distance of about 2.0 Å as shown in Figure 1(b). Calculations with distances greater than 2.0 Å were also performed, and they did not show any relevant distortion with respect to the variation of the properties involved in Eq. (3) from gas solution phases.

As the best characterized reactions in House et al. experimental work [3] (in terms of the variety of solvents used) was the *trans*-phenyl enolate, we will focus first our attention on this system.

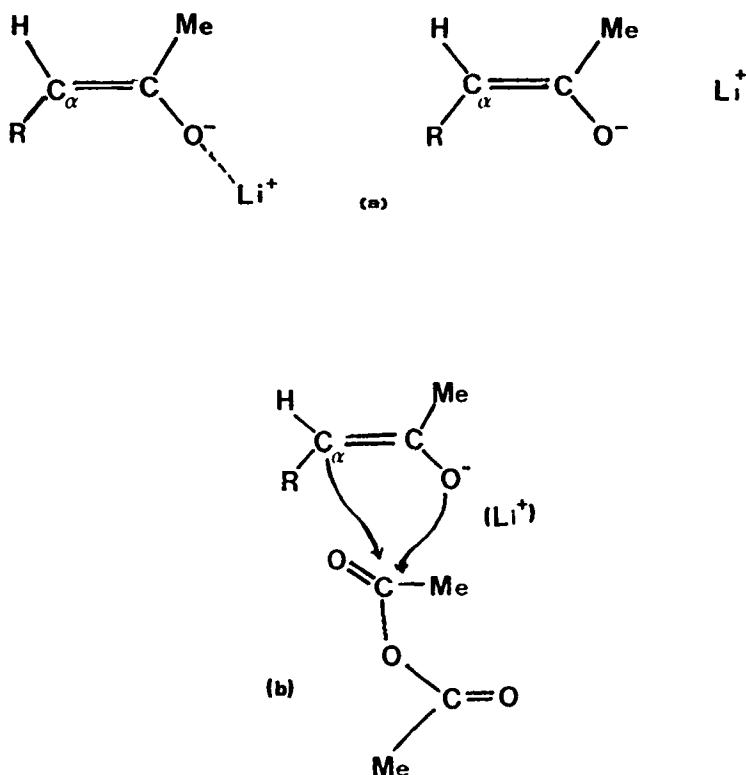


Figure 1. Molecular structures considered for calculations of molecular properties: (a) lithium enolate ion pairs; (b) nucleophile/electrophile pair interaction.

### Results and Discussion

We first became interested in determining the region of solvent polarity (measured by the variation of the dielectric constant  $\epsilon$  from 1.0 to 10.0), at which the interaction energy variations given by Eq. (3), for the nucleophile/electrophile pair, were more favorable for the reactions under study. Under the approximation that  $\beta_{C-O}/\beta_{C-C} = 0.8$  [13], the results displayed in Figure 2 were obtained for *trans*-phenyl enolate anion and *trans*-phenyl enolate/lithium ion pair. It shows the variation of the total energy for the electrostatic interaction between the nucleophile/electrophile pair, for the reaction at the oxygen and the alpha-carbon sites as a function of the dielectric constant. It may be seen that the interaction with the solvent favors the reaction at both sites. As  $\epsilon$  increases, the O-acylated product becomes predominant. Saturation of solvent effects is predicted for  $\epsilon > 3.0$ . Comparison of the differential reactivity at the oxygen and alpha-carbon sites for both the anion (solvent-separated ions) and the ion pair shows that the enhancement in favor of the O-acylation

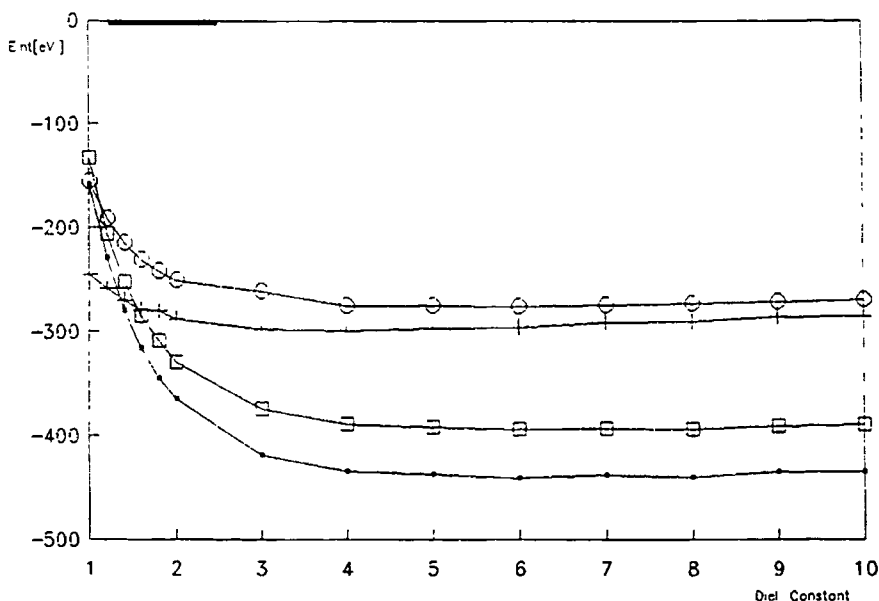


Figure 2. Nucleophile/electrophile electrostatic interaction energy variations for *trans*-phenyl/Li<sup>+</sup> ion pair and *trans*-phenyl enolate with respect to solvent polarity ( $\epsilon$ ). O-acylation in ion pair (■), O-acylation in enolate (●) alpha-C-acylation in ion pair (○) and alpha C-acylation in enolate (+).

product is greater for the enolate anion. In summary, these results suggest that, for increasing solvent polarity, a major proportion of O-acylated product is to be expected. Moreover, from Figure 2, it may be seen that at low solvent polarity solvent separated ions may be present, in agreement with the experimental results reported in Ref. [3]. This result also permits us to establish a low polarity region  $1.0 < \epsilon < 3.0$ , where the C-acylation products may coexist with the O-acylation products.

Figure 3 displays the variation of the interaction energy with the solvent polarity for the *cis*-phenyl-enolate/lithium ion pair and *cis*-phenyl-enolate anion, representing the solvent separated ions, respectively. In this case, the reaction at the oxygen enolate site remains favored with respect to the alpha-carbon acylation. Comparison with Figure 2 shows that the difference in reactivity at the O- and alpha-C is smaller than the corresponding difference of the *trans*-isomer. Also, no variations in reactivity at both C- and O- sites is observed for the *cis*-phenyl enolate in its ion pair and anionic forms.

Figure 4 summarizes the relative reactivity at the oxygen and alpha-carbon sites for the *cis/trans* stereoisomers for a varying solvent polarity. The following may be observed: First of all, reaction at the oxygen site appears to be invariant with respect to the *cis/trans* conformation and also independent of whether or not dis-

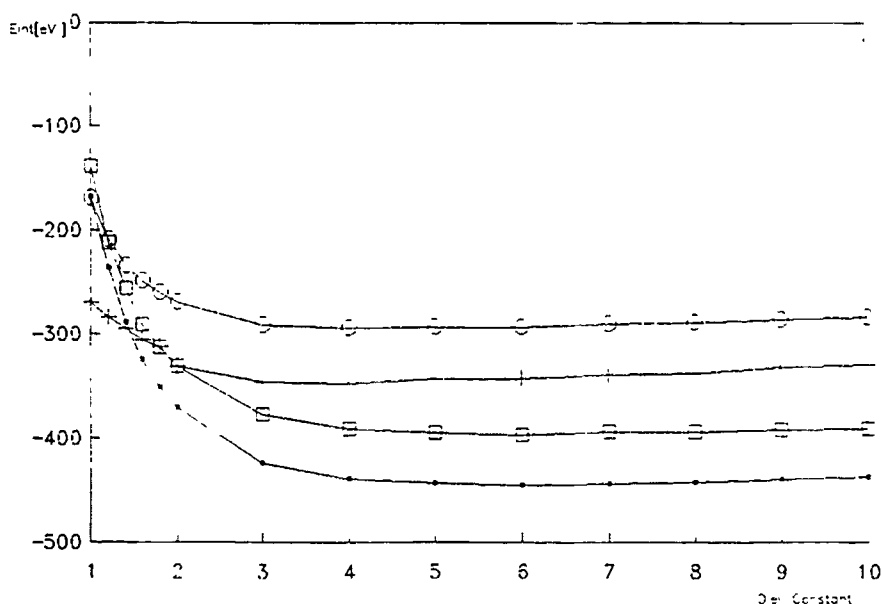


Figure 3. Nucleophile/electrophile electrostatic interaction energy variations for *cis*-phenyl/Li<sup>+</sup> ion pair and *cis*-phenyl enolate with respect to solvent polarity ( $\epsilon$ ). O-acylation ion pair (■), O-acylation in enolate (·), alpha-C-acylation in ion pair (O), and alpha-C-acylation in enolate (+).

sociation is present. Secondly, if we assume that for  $\epsilon < 3.0$  the lithium enolate displays a contact ion pair structure, the C-acylation reaction shows a significant difference with respect to the *cis/trans* conformations. For  $\epsilon > 3.0$ , the difference between reactivity at oxygen and alpha-carbon increases and becomes constant. Therefore, in view of the experimental results reported by House et al. [3], we may suggest dissociation for  $\epsilon > 3.0$ , and under this condition, the oxygen site will react more readily than the alpha-carbon site, in the dissociation region. On the other hand, variation of the reactivity pattern at the alpha-carbon will be relevant in the low polarity region ( $\epsilon < 3.0$ ), where significant differences in reactivity are predicted for the *cis/trans* conformations. These predictions are reinforced by the experimental data reported by House et al. [3]: the O-acetyl derivative in DME, a moderately polar solvent, shows a 87% yield for the *cis*-phenyl derivative, compared to 95% yield for the *trans*-phenyl derivative. On the other hand, C-acetyl derivative in Et<sub>2</sub>O, a modest polar solvent as compared to DME, shows a 26% yield for the *cis*-phenyl enolate, compared to the <10% yield for the *trans* product in the same solvent (Et<sub>2</sub>O).

#### Frontier Molecular Orbital Analysis

To discuss the previous results in the frame of the FMO theory, we start by introducing the following criteria with reference to Eq. (3). The first two terms of

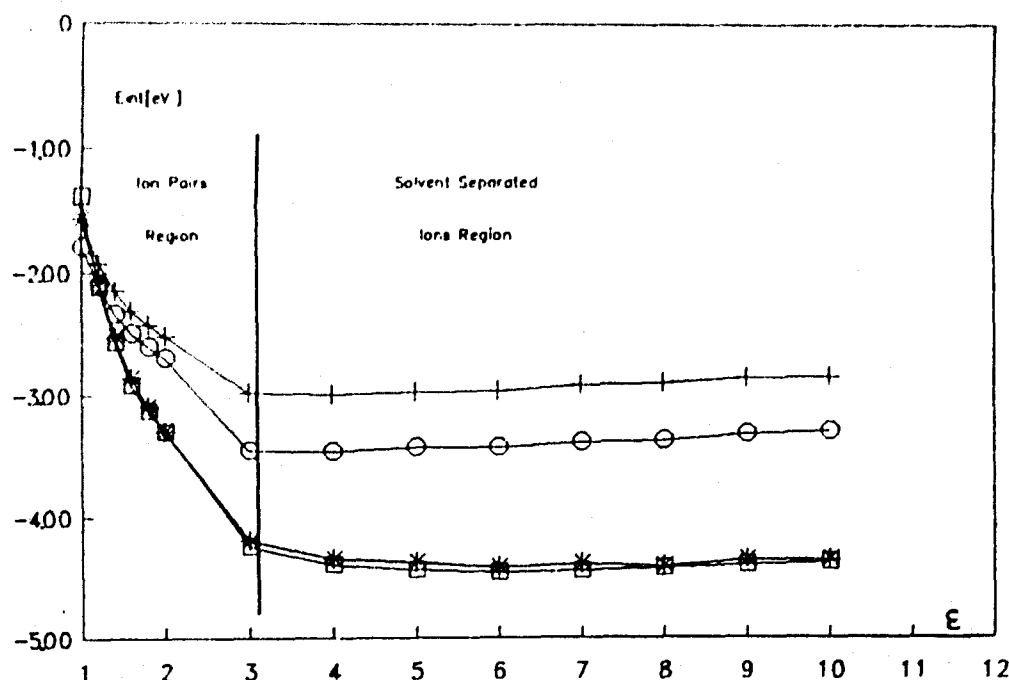


Figure 4. Relative reactivity at the oxygen and alpha-carbon sites for the *cis/trans* stereoisomers for the solvent polarity variation: *trans*-C-acylation (+), *cis*-C-acylation (O), *trans*-O-acylation (\*), and *cis*-O-acylation (■).

Eq. (3) represent the *charge control* contribution to the variation of the nucleophile/electrophile electrostatic interaction energy, whereas the third term represents the *orbital control* contribution.

In order to compare, in the simplest way, the relative reactivity at the alpha-carbon and oxygen sites, we introduce the following definitions:

$$\delta\Delta E_Q^C = \Delta E_Q^C - \Delta E_Q^{Ox} \quad (6)$$

and

$$\delta\Delta E_{orb}^C = \Delta E_{orb}^C - \Delta E_{orb}^{Ox} \quad (7)$$

With definitions (6) and (7), we assess the relative contribution of the charge control term  $\Delta E_Q^C$  and the orbital control term  $\Delta E_{orb}^C$  for reaction at the alpha-carbon site, having the corresponding charge and orbital contributions at oxygen as a reference state. These definitions also entail the following criteria: If  $\delta\Delta E_Q^C > 0$ , then the charge contribution at the alpha-carbon site will be less relevant than the corresponding charge contribution at the Oxygen site. On the other hand, if  $\delta\Delta E_{orb}^C < 0$ , then the orbital contribution at the alpha-carbon site will be more relevant than the corresponding orbital contribution at the Oxygen site.

In Figure 5 a plot of the relative charge control vs. the relative orbital control for different values of the dielectric constant is shown for methyl, *n*-butyl, and phenyl derivatives.

As expected,  $\delta\Delta E_Q^C$  is always positive and  $\delta\Delta E_{orb}^C$  is always negative. According

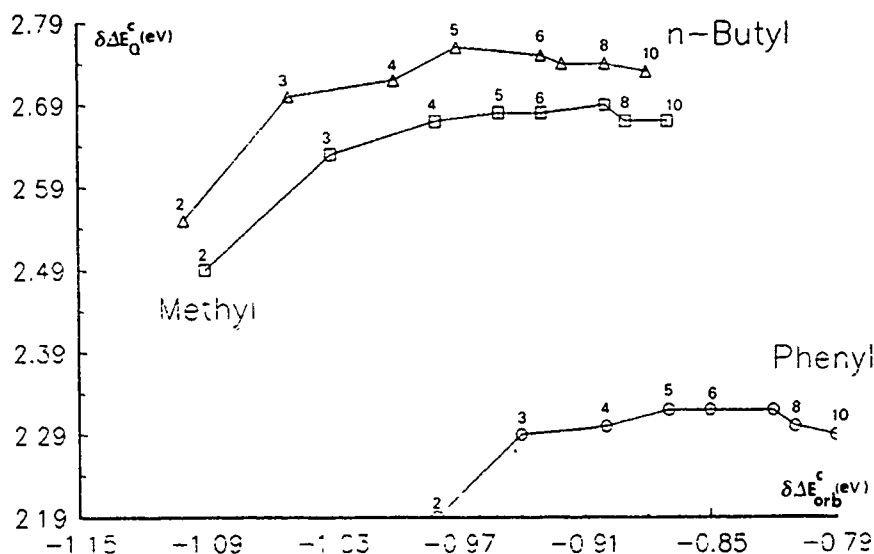


Figure 5. Relative charge vs. orbital control contributions for C-acylation with respect to solvent polarity for phenyl- ( $\circ$ ), methyl- ( $\blacksquare$ ), and *n*-butyl- ( $\Delta$ ) enolates derivatives. Numbers over the curves indicate different values of  $\epsilon$ .

to these trends, we may conclude that charge control contribution will mostly favor reaction at the oxygen site, whereas orbital control contribution will enhance carbon acylation products.

As compared to methyl- and butyl-derivatives,  $\delta\Delta E_{orb}^C$  for *trans*-phenyl is consistently less favorable, along the complete range of solvent polarity considered. We may predict then that, for mixtures of C-acylated and O-acylated products, methyl and *n*-butyl derivatives will show a greater proportion of C-acylated products than *trans*-phenyl derivatives. This prediction is consistent with the experimental data reported in Ref. [3], where an C-acylated product yield < 1% was observed for this derivative. On the other hand, the methyl and butyl derivatives are predicted to display a very close product yield for alpha-C-acylation which is also consistent with what is experimentally observed in Ref. [3] (4% and 9% product yield for *n*-butyl and methyl derivatives, respectively).

### Concluding Remarks

The experimental reactivity pattern shown by a series of lithium enolates towards acylation reactions was used as benchmark case for the extended Klopman-Salem equation of chemical reactivity in solution phase. The following conclusions may be drawn from the present work.

- (i) Two polarity regions where lithium enolates may be present either as *contact ion pair* or *solvent-separated ions* were identified. In terms of this criterion,

the conditions for the alpha-carbon vs. O-acylation reactions were established.

- (ii) The relative differential reactivities along series of compounds may be explained in terms of *charge* and *orbital* contributions. Alpha-carbon acylation products are to be expected for low polarity solvents, that is, when the lithium enolate presents a *contact ion pair* structure. In other words, reaction at the alpha-carbon appears to be assisted by the presence of lithium at the neighborhood of the oxygen site, and it is enhanced along a series of substituent as the *orbital control* term increases.
- (iii) General trends concerning the proportion of the alpha-carbon vs. oxygen acylation products in different solvents were successfully accounted for by the present formalism.

### Acknowledgments

This work was supported by FONDECYT under Contract 91/241.

### Bibliography

- [1] H. O. House, *Modern Synthetic Reactions*, 2nd ed. (Benjamin, California, 1972).
- [2] K. Yoshida and Y. Yamashita, *Tetrahedron Lett.*, 693 (1966).
- [3] H. O. House, R. A. Auerbach, M. Gall, and N. P. Peet, *J. Org. Chem.* **38**, 514 (1973).
- [4] H. O. House, W. F. Fisher, M. Gall, T. E. McLaughlin, and N. P. Peet, *J. Org. Chem.* **36**, 3429 (1971).
- [5] S. Murai, Y. Kuraki, K. Hasegawa, and S. Tsutsumi, *Chem. Commun.* **16**, 946 (1972).
- [6] F. Mendizabal, R. Contreras, and A. Aizman, *Int. J. Quantum Chem., Quantum Chem. Symp.* **26**, 751 (1992).
- [7] G. Klopman, *Chemical Reactivity and Reactions Path* (Wiley, New York, 1974), p. 55.
- [8] L. Salem, *J. Am. Chem. Soc.* **90**, 543 (1968).
- [9] J. S. Gomez, *J. Pharm. Sci.* **71**, 1423 (1982).
- [10] R. Contreras and A. Aizman, *Int. J. Quantum Chem., Quantum Chem. Symp.* **24**, 89 (1990).
- [11] R. Constanciel and R. Contreras, *Theoret. Chim. Acta* **65**, 1 (1984).
- [12] R. Contreras and J. S. Gomez, *J. Phys. Chem.* **88**, 1905 (1984).
- [13] W. T. Borden, *Modern Molecular Orbital Theory for Organic Chemists* (Prentice-Hall, Englewood Cliffs, NJ, 1975).

Received May 24, 1993



# Quantum Defect Orbital Study of Electron Transitions in Rydberg Molecules. I. Triatomic Hydrogen

I. MARTIN

*Departamento de Química Física, Facultad de Ciencias, 47005 Valladolid, Spain*

J. KARWOWSKI

*Instytut Fizyki; Uniwersytet Mikołaja Kopernika; 87-100 Toruń, Poland*

G. H. F. DIERCKSEN

*Max-Planck-Institut für Astrophysik, 8046 Garching bei München, Germany*

C. LAVIN

*Departamento de Química Física, Facultad de Ciencias, 47005 Valladolid, Spain*

## Abstract

Results of a pilot study on the applicability of the quantum defect orbital method for describing electronic transitions between molecular Rydberg states are reported. Oscillator strengths and Einstein emission coefficients for the triatomic hydrogen molecule have been calculated. The results are in good agreement with the data derived from more sophisticated theoretical approaches. © 1993 John Wiley & Sons, Inc.

## Introduction

The Rydberg molecules are characterized by a repulsive ground state, a series metastable excited states, and a stable cation [1]. If the energy gap between the electronic ground state and the first excited state is sufficiently large, all excited states are of predominantly Rydberg character. An excellent review on Rydberg molecules has been recently published by Herzberg [1], and an extensive compilation of the relevant experimental data by Jacox [2]. Prototypes for the diatomic and for the polyatomic Rydberg molecules are  $\text{He}_2$  and  $\text{H}_3$ , respectively. These two species have received most attention from both experimental and theoretical spectroscopists and are commonly used for testing new methods.

The existence of metastable Rydberg states of  $\text{H}_3$  was deduced by Herzberg [1], and by Vogler [3]. Herzberg [1] also determined the  $D_{3h}$  geometry of the underlying  $\text{H}_3^+$  core. This pioneering work inspired several theoretical [4–10] and experimental [11–15] studies which involve transitions between the bound Rydberg states. Most of the theoretical studies on the  $\text{H}_3$  spectrum have been based on frozen-core Hartree–Fock (HF) calculations [4–7] or have used limited configuration interaction (CI) expansions [8]. Highly correlated calculations have been reported only recently

[9,10]. Petsalakis et al. [9] have examined electronic transition moments among several low-lying Rydberg states at various geometries. Diercksen et al. [10] have calculated energies for the ground and several Rydberg states by a large-scale-multipreference configuration interaction with different basis sets at the  $D_{3h}$  geometry. They have found that the sequence of the energy levels depends on the size of the basis set, and obtained excitation energies that are in good agreement with the observed spectrum. However, these authors [10] point out that even for a 3-electron system, reliable results may be obtained only for low-lying states, and only if both the one-electron basis set and the configuration interaction expansion are extended to the limits permitted by the most advanced computing facilities. Therefore, developing semiempirical schemes to study such spectra seems to be worth some effort.

The electronic spectra of the Rydberg molecules consist of typical Rydberg progressions. It is expected that the Rydberg states may be described as quasi-hydrogenic, with the spherical atomic core replaced by a molecular cation which imposes "internal crystal field" splittings appropriate to its symmetry. This suggests a possibility of modeling the electronic structure of molecular Rydberg states by the methods originally developed to describe the Rydberg-like series in atoms. In particular, the concept of quantum defect has been used within the context of the multichannel quantum defect theory [18] to study Rydberg states in diatomic molecules [19,20]. It has also been applied to some polyatomic systems, for which the mixing between different electronic, vibrational, and rotational channels has been studied [21]. The Jahn-Teller effect in the  $(np)^2E'$  Rydberg series of  $H_3$  and  $D_3$  has also been studied by this technique combined with existing *ab initio* results [22]. In some of the *ab initio* studies mentioned above [4-7] quantum defects have been extracted from the HF energies computed for the low-lying Rydberg states and then used to construct the quantum defect hydrogenic orbitals to describe highly excited Rydberg states [7].

In the present article a pilot study on the application of the quantum defect orbital (QDO) method [16] for describing electronic transitions in Rydberg molecules is reported. The method has been applied to the calculation of transition probabilities in  $H_3$ .

### Method

The QDO approach belongs to the class of model potential semiempirical methods. It allows to generate valence, Rydberg, and continuum orbitals as analytical solutions of a one-electron radial equation that contains the quantum defect as an empirical parameter. The model potential has the form

$$V(r) = [\lambda(\lambda + 1) - 1(1 + 1)]/2r^2 - Z_{\text{net}}/r, \quad (1)$$

where  $Z_{\text{net}}$  is the nuclear charge acting on the valence or Rydberg electron at large radial distances. The parameter  $\lambda$ , which appears both in the effective potential and in the radial solutions, determines the screening aspects of the former. It is related to the quantum defect,  $\delta$ , and the orbital quantum number,  $l$ , through the expression

$$\lambda = 1 - \delta + c \quad (2)$$

where  $c$  is an integer determined in such a way that the radial orbital are normalizable and possess a correct nodal pattern. The eigenvalue of the corresponding Hamiltonian (i.e., the energy of the Rydberg electron) is independent of  $c$ , since it depends on the non-integer part of  $\delta$  only. The quantum defect is obtained from the following equation

$$E_n = T - Z_{\text{net}}/[2(n - \delta)^2] \quad (3)$$

where  $E_n$  is the discrete spectrum energy (taken either from experiment or calculated using another method),  $T$  is the ionization energy, and  $n$  is the principal quantum number. The quantum defect creates the non-integer part of the parameter (2). It connects the potential (1) with the empirical data and, as a consequence, brings about an implicit account for electron correlation, spin-orbit coupling, and other effects which are explicitly neglected in this model.

The transition moment is defined as

$$M_{ij} = \langle R_i | Q(r) | R_j \rangle, \quad (4)$$

where, in the simplest case of dipole transitions and the dipole-length formulation,  $Q(r) = r$ . It is important to note that in this case  $M_{ij}$  may be expressed in a closed analytic form. Taking into account the effects of the core polarization (i.e., a part of the correlation effects between the core and the Rydberg electron) results in a modification of the transition operator  $Q(r)$  [16]. It has recently been demonstrated [23] that in the case of atoms

$$Q(r) = r \{ 1 - (\alpha/r^3) [1 - \exp(-r/r_c)]^3 \}, \quad (5)$$

where  $\alpha$  is the dipole polarizability of the core and  $r_c$  is a cut-off parameter, correctly describes the polarization of the core and allows the theory to retain its analytic character.

We assume that the molecular Rydberg electron may be described by a hydrogenic Schrodinger equation with the effective potential given by Eq. (1). The modifications introduced to the theory are the following. The principal and the angular momentum quantum numbers correspond to the appropriate orbital in the united atom limit. The energies used to determine the quantum defects include the splittings due to the non-spherical molecular core. In Eq. (5) the core polarizability parameter is estimated from molecular data.

## Results

The energies for the lowest energy levels have been derived from the measurements by Watson quoted by Petsalakis et al. [9] and from the ionization energy (29562.6 cm<sup>-1</sup>) obtained by Helm [13]. The last author, in a series of experimental studies [12-15] established the assignment of the discrete spectrum and the effective quantum defects. In the present work the quantum defects have been calculated according to Eq. (3). They are compared with the ones by Helm [12] and those derived by

other authors from theoretical energies in Table I. Also, the quantum defects for lithium, i.e., for the united atom limit of  $H_3$  are given. The differences between the quantum defects from different sources arise from the differences in the energy values. No experimental energies for the electronic states higher than those listed in Table I are known. Therefore, the quantum defects for the higher states have been assumed to be equal to the ones listed in Table I, corresponding to the state of the same symmetry and with the highest energy. This assumption is consistent with earlier observations on the behavior of quantum defects in atoms.

The parameters defining the transition operator, Eq. (5) have been estimated by combining the experimental data for the equilibrium geometry of  $H_3^+$ , and the computational experience gained in similar calculations for atoms, that is,  $r_c$  has been taken as approximately equal to the core radius, and  $\alpha$  is the core dipole polarizability. Thus, it has been assumed that  $r = 1.19$  a.u. (the interatomic distance in  $H_3^+$  is equal to 1.65 a.u. [24]) and  $\alpha = 5.7$  a.u. (from the data reported by Fowler et al. [25]).

The QDO values of the oscillator strengths for the allowed electronic transitions are displayed in Table II. They are compared to those obtained by Martin [6] with the HF method. The agreement between the QDO and HF results is even better than one might expect from such a highly simplified procedure. Therefore, the oscillator strengths for several transitions not being studied by Martin [6] have also been included in the table.

TABLE I The Rydberg states of  $H_3$  at  $D_{3h}$  geometry, and the corresponding quantum defects. Data for the united atom limit (lithium) are also included. All quantum defects are multiplied by  $10^3$ .

State	$H_3$					$Li$	
	This work	Derived from HF energies			Exptl. Ref. [12]	Exptl. Ref. [26]	
		Ref. [4]	Ref. [7]	Ref. [5]			
$^2E'$ (2p)	483	407	407	48*		2s	415
$^2A_1'$ (2s)	113	84	73	8*	71	2p	41
$^2A_2'$ (2p)	73	17	12	0*	80 10		
$^2E'$ (3p)	404	345	328	35*		3s	404
$^2A_1'$ (3s)	103	71	89	7*	71	3p	44
$^2A_2'$ (3p)	59	22	3	0*			
$^2E'$ (3d)	50	22	-0	2*		3d	1
$^2E''$ (3d)	-4	-6	-29	-1*	-10		
$^2A_1'$ (3d)	-15	-15	-38	-2*	-6		

\* The last digit of the quantum defect was not given in Ref. [5].

<sup>b</sup> For the (2p)  $^2A_2'$  state, the first and the second entries are the recommended values by Helm [12] for the 2p–ns and 2p–nd transitions, respectively.

TABLE II. Oscillator strengths for the allowed electronic transitions in  $H_3$  at  $D_{3h}$  geometry. For each entry, the first and the second numbers are the QDO oscillator strengths calculated, respectively, without and with the core polarization correction. The third number is the HF value [6]. All quantities are multiplied by  $10^2$ .

State	$^2E' (2p)$			$^2A_1' (2s)$			$^2A_2' (2p)$		
$^2A_1' (2s)$	20.	15.	26.						
$^2A_1' (3s)$	6.98	0.88	1.1				2.2	2.5	2.8
$^2A_1' (4s)$	0.65	0.42	0.40				0.48	0.54	0.67
$^2A_1' (5s)$	0.021	0.018					0.19	0.22	
$^2A_1' (3d)$	2.2	3.6	3.8				18.	19.	25.
$^2A_1' (4d)$	0.63	1.2	1.4				5.2	5.2	5.0
$^2A_1' (5d)$	.28	0.56					2.2	2.3	
$^2E' (3d)$	8.2	7.4	5.1				23.	23.	17.
$^2E' (4d)$	2.4	2.0	1.8				5.8	5.8	3.4
$^2E' (5d)$	0.52	0.46					2.4	2.4	
$^2E' (3d)$	14.	14.	15.	2.9	2.9	0.07			
$^2E' (4d)$	4.9	4.7	5.4	0.75	0.76	0.022			
$^2E' (5d)$	3.7	3.4		0.32	0.32				
$^2E' (3p)$	0.17	0.19	0.21	40.	40.	35.			
$^2E' (4p)$	0.045	0.068	0.063	4.9	3.7	3.7			
$^3E' (5p)$	0.018	0.022		1.8	1.8				
$^2A_2' (2p)$				3.8	4.2	4.8			
$^2A_2' (3p)$				10.	11.	10.			
$^2A_2' (4p)$				2.6	2.8	2.3			
$^2A_2' (5p)$				1.2	1.3				

The Einstein emission coefficients calculated in the present work and the ones derived from other theoretical calculations are compared in Table III. With the exception of Raynor and Herschbach [7], who report Einstein coefficients directly in their article, the remaining authors whose results are shown in the table report either oscillator strengths [6] or transition moments [4,9]. Therefore, the displayed Einstein coefficients have been obtained from their transition frequencies or wavelengths and from the corresponding transition moments or oscillator strengths. The overall agreement is very good. In particular, the results of the extensive CI calculations by Petsalakis et al. [9] and the ones by King and Morokuma [4], who carried out the most careful choice of the basis functions of all the HF procedures [4-7], and whose calculated lifetimes agree well with those observed by Figger et al. [11] for the isotopic molecule triatomic deuterium, seem to be the most reliable ones.

### Conclusions

Several transitions between Rydberg states of the triatomic hydrogen molecule have been studied using the non-relativistic version of the QDO method. The results for oscillator strengths and Einstein coefficients for spontaneous emission agree

TABLE III. Wavelengths in Å (the upper line) and Einstein emission coefficients in units of  $10^7 s^{-1}$  (the lower two lines)

Transition	QDO <sup>a</sup>	MRDCI <sup>b</sup>	HF <sup>c</sup>	HF <sup>d</sup>	HF <sup>e</sup>
$^2E'(3p) \rightarrow ^2A'_1(2s)$	6877	6878	6805	7010	7051
	5.58	4.88	2.52	5.53	4.54
	5.63				
$^2A''_2(3p) \rightarrow ^2A'_1(2s)$	5516	5548	5514	5731	5767
	2.21	2.52	2.19	2.12	1.55
	2.32				
$^2E'(3d) \rightarrow ^2A'_1(2s)$	5442	5468	5514	5711	5759
	0.0131	0.0167	0.0493	0.0109	0.01
	0.0132				
$^2A''_2(2p) \rightarrow ^2E'(2p)$	6031	5526	6077	6518	6469
	0.0	0.0	0.0	0.0	0.0
	0.0				
$^2A'_1(2s) \rightarrow ^2E'(2p)$	6525	5997	6925	7488	7302
	3.10	4.59	3.62	3.09	3.21
	2.32				
$^2A'_1(3s) \rightarrow ^2A''_2(2p)$	6070	5641	6369	6621	6554
	0.40	0.501	0.460	0.461	0.27
	0.46				
$^2E''(3d) \rightarrow ^2A''_2(2p)$	5746	5929	6016	6349	6233
	4.57	3.27	1.57	3.87	3.23
	4.61				
$^2A'_1(3d) \rightarrow ^2A''_2(2p)$	5714	5800	6077	6544	6295
	3.76	4.78	4.52	3.90	4.40
	3.40				

<sup>a</sup> This work; experimental wavelengths (as quoted in Table II of Ref. [9]) and emission coefficients calculated without (second line) and with (third line) core polarization correction.

<sup>b</sup> Petsalakis et al. [9]

<sup>c</sup> Martin [6].

<sup>d</sup> King and Morokuma [4].

<sup>e</sup> Raynor and Herschbach [7].

fairly well with those of other, more sophisticated, theoretical procedures. Therefore, it is expected that this approach may be useful for studying the spectra of other Rydberg molecules. In the case of molecules containing heavy atoms, the relativistic version of the QDO method [17] may be more adequate.

### Acknowledgments

This work has been supported by a grant awarded to I.M. by the C.S.I.C.-Max-Planck-Gesellschaft cooperation programme for a 3-month visit to the Max-Planck-Institut für Astrophysik in Garching bei München. It has also been supported by the D.G.I.C.Y.T. of the Spanish Ministry of Education within Projects PB88-0343 and PB91-0207-C02-01, by the Polish K. B. N., and by the Fonds der Chemischen Industrie im Verband der Chemischen Industrie e.V.

## Bibliography

- [1] G. Herzberg, *J. Chem. Phys.* **70**, 4806 (1979); *Ann. Rev. Phys. Chem.* **38**, 27 (1987).
- [2] M. E. Jacox, *J. Phys. Chem. Ref. Data* **17**, 269 (1988).
- [3] M. Vogler, *Phys. Rev. A* **19**, 1 (1979).
- [4] H. F. King and K. Morokuma, *J. Chem. Phys.* **71**, 3213 (1979).
- [5] M. Jungen, *J. Chem. Phys.* **71**, 3540 (1979).
- [6] R. L. Martin, *J. Chem. Phys.* **71**, 3541 (1979).
- [7] S. Raynor and D. H. Herschbach, *J. Phys. Chem.* **86**, 35932 (1982).
- [8] Ch. Nager and M. Jungen, *Chem. Phys.* **70**, 189 (1982).
- [9] I. D. Petsalakis, G. Theodorakopoulos, and J. S. Wright, *J. Chem. Phys.* **89**, 6850 (1988).
- [10] G. H. F. Diercksen, W. Duch, and J. Karwowski, *Chem. Phys. Lett.* **168**, 69 (1990).
- [11] I. Dabrowski and G. Herzberg, *Can. J. Phys.* **58**, 1238 (1980); G. Herzberg and J. K. G. Watson, *Can. J. Phys.* **60**, 1250 (1980); H. Lew, J. J. Sloan, and J. K. G. Watson, *Can. J. Phys.* **59**, 428 (1981); H. Figger, M. N. Dixit, R. Maier, H. Walther, I. R. Peterkin, and J. K. G. Watson, *Phys. Rev. Lett.* **52**, 906 (1984).
- [12] H. Helm, *Phys. Rev. Lett.* **56**, 42 (1986).
- [13] H. Helm, *Phys. Rev. A* **38**, 3425 (1988).
- [14] L. J. Lembo, A. Petit, and H. Helm, *Phys. Rev. A* **39**, 3721 (1989).
- [15] L. J. Lembo, H. Helm, and D. L. Huestis, *J. Chem. Phys.* **90**, 5299 (1989).
- [16] G. Simons, *J. Chem. Phys.* **60**, 645 (1974); I. Martin and G. Simons, *J. Chem. Phys.* **62**, 4799 (1975); C. Lavin, I. Martin, and M. J. Vallejo, *Int. J. Quantum Chem.* **S26**, 445 (1992), and references therein.
- [17] I. Martin and J. Karwowski, *J. Phys. B: At. Mol. Opt. Phys.* **24**, 1539 (1991).
- [18] M. J. Seaton, *Rep. Prog. Phys.* **46**, 167 (1983), and references therein.
- [19] C. H. Greene and Ch. Jungen, *Ad. At. Mol. Phys.* **21**, 51 (1985).
- [20] L. Liu and J.-M. Li, *J. Phys. B: At. Mol. Opt. Phys.* **24**, 1893 (1991).
- [21] J. A. Dagata, L. Klasinc, and S. P. McGlynn, *Pure Appl. Chem.* **61**, 2151 (1989), and references therein.
- [22] A. Staib and W. Domcke, *Z. Phys. D—Atoms, Molecules and Clusters* **16**, 185 (1990).
- [23] D. Bielińska-Wąz, Thesis, Institute of Physics, Nicholas Copernicus University, Torun, Poland, June 1992 (in Polish); D. Bielińska-Wąz, I. Martin, and J. Karwowski, to be published.
- [24] T. Oka, *Phys. Rev. Lett.* **45**, 531 (1980).
- [25] P. W. Fowler, P. Jørgensen, and J. Olsen, *J. Chem. Phys.* **93**, 7256 (1990).
- [26] C. E. Moore, *Nat. Bur. Stand. Ref. Data Sect.—Nat. Bur. Stand. (Washington D.C., 1971)*, No. 35.

Received March 30, 1993

# ***Ab Initio* Study of the Ground and Excited States of LiNe**

JOANNA SADLEJ\* and W. DANIEL EDWARDS†

*Department of Chemistry, University of Idaho, Moscow, Idaho 83844*

## **Abstract**

The intermolecular potentials for the  $\lambda^2\Sigma$  and  $A^2\Pi$  states of  $\text{Li} \cdots \text{Ne}$  were studied by a variety of multiconfiguration, single configuration and perturbation methods (CASPT2). The  $A^2\Pi$  excited state was calculated to have a well depth of  $214 \text{ cm}^{-1}$  at an internuclear separation of  $2.26 \text{ \AA}$  (ACPF) in excellent agreement with the  $224 \text{ cm}^{-1}$  derived from experimental data. A smaller well of  $15.8 \text{ cm}^{-1}$  was found for the  $\lambda^2\Sigma$  ground state at an intermolecular separation of  $5.28 \text{ \AA}$  (ACPF). These results are in better agreement with experimental results than the previously reported pseudopotential calculations. The comparison of CI calculations with CASPT2 results shows that the latter is able to give good results for interacting systems. © 1993 John Wiley & Sons, Inc.

## **Introduction**

Recently the results of experiments on lithium doped rare gas solids (Ar, Kr, Xe) were reported [1]. That research focused on the properties of cryogenically trapped lithium atoms and clusters prepared by laser ablation of solid lithium metal, and was motivated by the potential of using trapped alkali metal atoms for chemical rocket propulsion systems [2].

In general, the optical absorption spectrum of heavier alkali metals trapped in rare gas matrices consist of multiple triplet absorption features [3,4]. There are several competing models, all involving multiple trapping sites, which seek to explain the origin of this triplet structure. In contrast, the spectroscopic results obtained for lithium doped rare gas matrices show only one well-resolved triplet absorption. This observation together with the sharp ESR lines reported in Ref. [1] gives evidence for the existence of a single, well-defined trapping site structure for lithium in rare gas solids.

The structure of the various trapping sites in a rare gas solid is determined by the potential experienced by the alkali metal atom. This potential can be deduced experimentally from mobility and beam scattering measurements as well as emission experiments [5], or it can be calculated using various models.

\* Permanent Address: Department of Chemistry, University of Warsaw, 02-093 Pasteura 1, Warsaw, Poland.

† Author to whom correspondence should be addressed



Several computational studies have used nonlocal pseudopotential methods based on the Thomas-Fermi statistical model [6,7] in order to determine the alkali metal-rare gas interaction potential. These pseudopotential calculations are in agreement with the experimentally deduced results for many ground-state alkali metal-rare gas systems. However, for the  $A^2\Pi$  first excited states, the calculated potential curves are found to be too shallow relative to experiment. This is alleviated somewhat by employing the Kim-Gordon core-core repulsion model [8] rather than the Gombos-Baylis model [9], but is not eliminated.

It is also possible to express the matrix perturbation on the ground and excited states of an isolated alkali atom in terms of two-body dimer potentials [10]. Such a pairwise additive potential was used in Ref. [1] for the interpretation of their experimental results.

Other experiments which require knowledge of the interaction potential are intradoublet or interdoublet transitions occurring in thermal collisions between alkali metal atoms and rare gas atoms. Understanding these processes requires a detailed knowledge of the interatomic potential. The work reported here is, to our knowledge, the first *ab initio* study of the ground and first excited state potential energy curves for the  $\text{Li} \cdots \text{Ne}$  system. We shall compare the results of our calculations to the pseudopotential results, the only theoretical data available for these states.

### Computational Method

We have used contracted averaged natural orbital (ANO) type basis sets throughout this work. These basis sets have been derived from a density matrix averaged over the atomic ground state, positive and negative ions, as well as the atom in a polarizing electric field. A detailed description of the averaging procedure, as well as the explicit primitive sets used can be found elsewhere [11]. These basis sets have been specifically designed to account for as much electron correlation as is possible within a given size. For Li and Ne, the ANO basis set is of the form (14.9.4.3.)/[5.4.3.2.] and gives a total of 92 functions for  $\text{Li} \cdots \text{Ne}$  systems.

This basis is capable of giving an accurate description of  $\text{Li}(^2S)$  and  $\text{Li}(^2P)$  at both the SCF and correlated levels of approximation. At the RHF level, the calculated  $^2S \leftarrow ^2P$  excitation energy is 1.8444 eV, which compares well with the experimental value of 1.8479 eV [12]. The calculated ionization potential is 5.342 eV, in comparison with the experimental value of 5.390 eV.

The complete active space (CAS) SCF method [13] has been shown to yield very accurate results for spectroscopic properties of low-lying excited states of  $\text{BH}$  [14],  $\text{AlH}$  [15], and  $\text{SiH}^+$  [16]. The CASSCF approach generates a full configuration interaction (CI) wavefunction for a certain number of electrons which are distributed among a given number of active orbitals. The size of the active electron space and the number of electrons considered determine the length of the full CI expansion.

Long CI vectors can be avoided if the electron correlation effects outside the CASSCF active space are included via perturbation theory. Andersson et al. [17] have recently published a second-order perturbation scheme, known as CASPT2, which uses the CASSCF wavefunction as the unperturbed wavefunction.

If the Fock matrix elements coupling the inactive and active orbitals and the active with the virtual orbitals are set to zero (block diagonal Fock matrix), the method is called CASPT2D. If a general (nondiagonal) Fock matrix is used for partitioning, the method is called CASPT2N. This perturbation treatment with a single state multiconfiguration CASSCF function is aimed primarily at recovering the dynamic correlation. The conclusion from the series of papers is that CASPT2 is capable of giving accurate results for many molecular properties with a considerably reduced computing effort [18]. One motivation for the present work has been to test the usefulness of these perturbation calculations for interacting systems.

The efficiency of the second-order CASPT2 method is dependent on the choice of the CASSCF reference function. For the present purpose, the choice of the active orbital space for the atoms Li and Ne was always the valence  $ns$  and  $np$  subspace. The major part of the CASSCF calculations in the present study have been carried out with the nine active valence electrons distributed among the active orbitals built from  $2s$  and  $2p$  orbitals of Li and Ne atoms.

Another method of treating the dynamic correlation is to perform the multireference CI calculation (MRCI) [19]. SDCI-MRCI denotes all single and double excitations from the reference configurations. With many electrons to be correlated, an unlinked cluster correction must be added to CI energies; in our case, we have performed a Davidson ( $Q$ ) correction [20].

Size consistency, which is always important in the calculation of binding energies, is particularly important for weakly bound complexes [21]. The majority of studies of interacting systems have employed MBPT theory, which gives size-consistent energies [22]. In this work, we have applied CASPT2 methods which are explicitly size-consistent when applied to CASSCF reference functions. We have also calculated interaction energies using both the modified coupled pair functional approach, (MCPF) [23] and the averaged coupled-pair functional treatment (ACPF) [24]. The later is found to be size consistent for the complexes to within 0.01 kcal/mol [25].

In order to determine the adequacy of the size-consistency correction for truncated MRCI calculations, we performed calculations for the  $\text{Li} \cdots \text{Ne}$  complex ( $R = 500$  a.u.) and the isolated atoms, and compared the results with the results of CASSCF and ACPF calculations. The difference between the supermolecule energy ( $R = 500$  a.u.) and the sum of the energies of the two isolated atoms provides a direct measure of the size-consistency error in each case. Table I shows the size consistency errors obtained for the  $\text{Li} \cdots \text{Ne}$  ground state at an internuclear separation of 500 a.u. The CASSCF for the minimal valence active space is exactly size consistent while MRCI has a size consistency error of 0.2 kcal/mol. ACPF is nearly size-consistent with an error of approximately 0.015 kcal/mol. Del Bene and Shavitt [25] have also reported very small size-consistent errors for charged complexes with the same correlated electrons in each subunit. We concluded from this study that while the CI size-consistency errors for our complex are small, the interaction energies are equally small and it is necessary to calculate binding energies relative to the 500 a.u. results. This is especially true for the perturbation calculations where the size consistency errors are relatively large.

TABLE I The size-consistency error (in a.u.) in the CASSCF, MRCI, and ACPF calculations for  $\text{Li} \cdots \text{Ne}$  system.

	$^2\Sigma$	$^2\Pi$			
Method	(Li $\cdots$ Ne $R = 500$ a.u.)		Li	Ne	$\Delta$
CASSCF <sup>a</sup>	-135.979200	—	-7.432702	-128.546490	0.000001
CASSCF <sup>b</sup>	-136.070121	-135.987752	-7.432702	-128.687100	-0.049681
CASPT2D <sup>b</sup>	-136.259150	-136.207454	-7.432702	-128.825674	0.000684
CASPT2N <sup>b</sup>	-136.258476	-136.205953	-7.432702	-128.828912	-0.003138
MRCI <sup>b</sup>	-136.258918	-136.195354	-7.432702	-128.826552	0.000336
MRCI <sup>b</sup> + $Q$	-136.268336	-136.203731	-7.432702	-128.836072	0.000438
ACPF <sup>b</sup>	-136.266461	-136.202067	-7.432584	-128.833903	0.000025

<sup>a</sup> Nine active electrons in  $(3|1|1|0)$  active space.

<sup>b</sup> Nine active electrons in  $(4|2|2|0)$  active space.

A pilot series of calculations for the ground state of the  $\text{Li} \cdots \text{Ne}$  system was performed with the seven active electrons distributed in an active space of  $(3|2|2|0)$ , where the numerical entries give the number of active orbitals per irreducible representation of the  $C_{2v}$  symmetry species  $a_1$ ,  $b_2$ ,  $b_1$ , and  $a_2$ , respectively. The  $1s$  orbital for Li and the  $1s$  and  $2s$  orbitals for Ne have been kept inactive in these calculations. This gives rise to 208 configuration state functions (CSFs). In the subsequent series of calculations, nine active electrons were distributed among the  $(4|2|2|0)$  active orbitals belonging to  $C_{2v}$  symmetry. In this case the  $1s$  orbitals of Li and Ne have been kept frozen. Both the  $X^2\Sigma$  ground state and  $A^2\Pi$  excited state were calculated with this choice of subspaces (inactive, active, and secondary orbitals) which gives rise to 606 configurations for the ground state and 588 configurations for  $^2\Pi$  state. We present here only the results for this larger active space.

CASSCF calculations were performed for each spectroscopic state in order to obtain the natural orbitals. These calculations were then followed by CASPT2 and MRCI calculations in order to include the dynamic correlation effects. Reference CSFs were chosen as those which appeared in the CASSCF wavefunction with the weight larger than 7%.

The potential curves were evaluated by fitting spline functions to the computed points. From these potentials the vibrational wavefunctions and the vibrational-rotational energy levels were obtained by numerically solving the radial Schrödinger equation for a set of rotational quantum numbers. The spectroscopic constants were determined by a least-square fit of these energy levels. The computed spacings between the rotational lines were used to obtain the rotational constants and the vibrational constants were derived from the computed band origins.

All calculations were performed using the programs included in the MOLCAS2 quantum chemistry software [26] on an IBM-3090 at the Cornell Theory Center.

### Results and Discussion

The interaction energies for the  $X^2\Sigma$  and  $A^2\Pi$  states are listed in Tables II and III, and the corresponding potential energy curves are shown in Figures 1-4. A

TABLE II Interaction energy (in mHartree) for the ground state  $\lambda^2\Sigma \text{Li} \cdots \text{Ne}$  system calculated by different methods relative to  $E(\text{Li} \cdots \text{Ne})$  at  $R = 500$  a.u.

R	CASSCF <sup>a</sup>			Configuration interaction <sup>a</sup>			
	CAS	PT2D	PT2N	MRCI	MRCI + Q	MCPF	ACPF
6.0	2.3494	1.6167	1.5024	1.6064	1.4838	1.5449	1.4943
7.0	0.9783	0.5311	0.4841	0.5396	0.4721	0.5536	0.4782
8.0	0.3712	0.1092	0.0862	0.1173	0.0805	0.1105	0.0838
8.5	0.2228	0.0216	0.0054	0.0293	0.0020	0.0191	0.0044
9.0	0.1318	-0.0234	-0.0350	-0.0164	-0.0367	-0.0276	-0.0349
9.5	0.0767	-0.0437	-0.0522	-0.0374	-0.0525	-0.0480	-0.0512
10.0	0.0438	-0.0461	-0.0563	-0.0446	-0.0562	-0.0537	-0.0552
10.5	0.0246	-0.0491	-0.0537	-0.0445	-0.0531	-0.0531	-0.0523
11.0	0.0134	-0.0448	-0.0483	-0.0408	-0.0474	-0.0481	-0.0468
11.5	0.0069	-0.0391	-0.0418	-0.0357	-0.0408	-0.0418	-0.0403
12.0	0.0034	-0.0331	-0.0352	-0.0302	-0.0342	-0.0352	-0.0338
13.0	0.0004	-0.0224	-0.0238	-0.0204	-0.0228	-0.0237	-0.0226
14.0	-0.0003	-0.0144	-0.0152	-0.0132	-0.0147	-0.0154	-0.0146
15.0	-0.0004	-0.0090	-0.0095	-0.0083	-0.0092	-0.0096	-0.0092
16.0	-0.0002	-0.0055	-0.0059	-0.0051	-0.0057	-0.0059	-0.0057
17.0	-0.0001	-0.0003	-0.0004	-0.0032	-0.0035	-0.0037	-0.0035

<sup>a</sup> Nine active electrons in (4|2|2|0) active space, two frozen orbitals and zero inactive orbitals.TABLE III Interaction potential energies (in mHartree) for the  $\lambda^2\Pi$  excited state of  $\text{Li} \cdots \text{Ne}$  system, calculated by different methods relative to  $E(\text{Li} \cdots \text{Ne})$  for  $R = 500$  a.u.

R	CASSCF <sup>a</sup>			CI <sup>b</sup>			
	CAS	PT2D	PT2N	MRCI	MRCI + Q	MCPF	ACPF
3.0	1.7449	1.4490	1.3902	1.6174	1.5907	1.4602	1.6535
4.0	0.9029	-0.5659	-0.7229	-0.1388	-0.4360	-1.0418	-0.4052
4.5	0.2255	-0.9515	-1.0317	-0.6407	-0.8753	-1.2065	-0.8525
5.0	0.1052	-0.7984	-0.8440	-0.5875	-0.7614	-0.9252	-0.7458
5.5	0.0737	-0.5956	-0.6263	-0.4595	-0.5851	-0.6581	-0.5750
6.0	0.0543	-0.4432	-0.4658	-0.3542	-0.4447	-0.4723	-0.4383
6.5	0.0343	-0.3421	-0.3597	-0.2793	-0.3452	-0.3518	-0.3411
7.0	0.0172	-0.2742	-0.2883	-0.2259	-0.2746	-0.2721	-0.2719
8.0	-0.0022	-0.1839	-0.1928	-0.1538	-0.1814	-0.1752	-0.1803
9.0	-0.0076	-0.1201	-0.1261	-0.1053	-0.1216	-0.1168	-0.1211
10.0	-0.0075	-0.0793	-0.0835	-0.0720	-0.0819	-0.0786	-0.0817
11.0	-0.0059	-0.0565	-0.0594	-0.0490	-0.0551	-0.0529	-0.0549
12.0	-0.0042	-0.0429	-0.0450	-0.0427	-0.0366	-0.0352	-0.0364
14.0	-0.0002	-0.0255	-0.0254	-0.0137	-0.0152	-0.0146	-0.0251

<sup>a</sup> Nine active electrons in (4|2|2|0) active space, one frozen orbital and one inactive orbital.<sup>b</sup> Nine active electrons in (4|2|2|0) active space, two frozen orbitals and zero inactive orbitals.

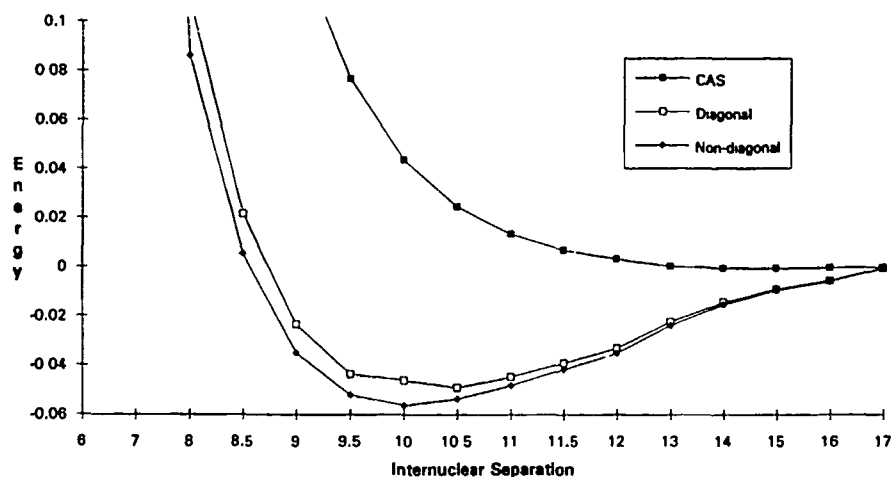


Figure 1. LiNe doublet sigma state. Energy is in mHartree, separation is in a.u.

total of 17 points were calculated for the  $X^2\Sigma$  state and a total of 16 points for the  $A^2\Pi$  state were calculated. The interaction energies are given relative to  $E(R) - E(\infty)$  at the following levels of approximation: CASSCF, CASPT2, MRCI, MRCI +  $Q$  (cluster corrected MRCI energies using a multiconfigurational analogue of the Davidson correction), MCPF, and ACPF.

The electronic structure of the  $X^2\Sigma$  ground state is dominated by the expected SCF electronic configuration  $\text{Li}(1s^2 2s^1) \text{Ne}(1s^2 2s^2 2p_x^2 2p_y^2 2p_z^2)$ , which has a weight of 98% in the CASSCF wavefunction. The lowest excited state is  $A^2\Pi$  with an ex-

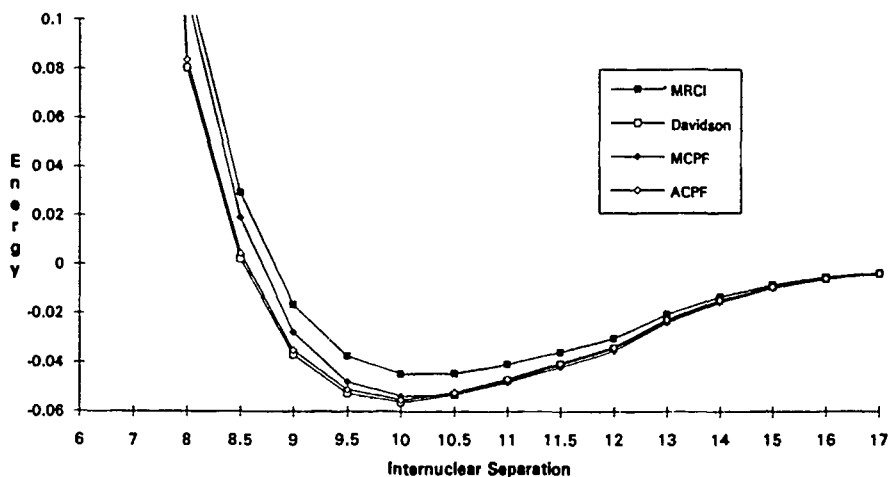


Figure 2. LiNe doublet sigma state. Energy is in mHartree, separation is in a.u.

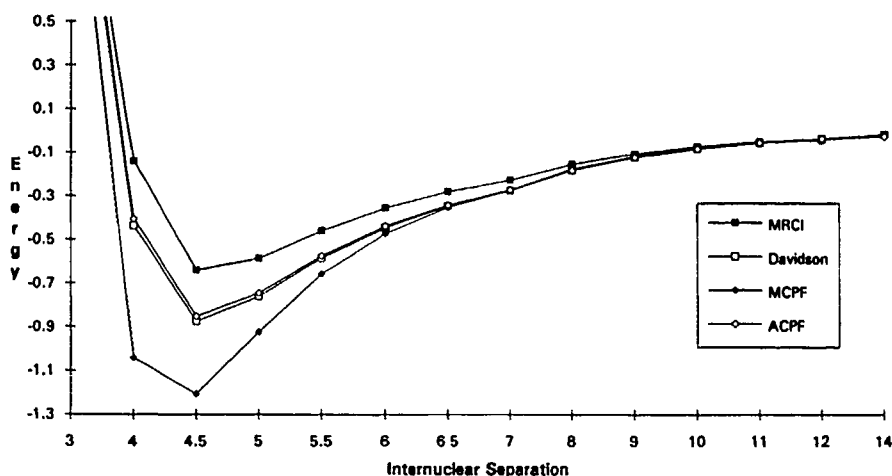


Figure 3. LiNe doublet  $\pi$  state. Energy is in mHartree, separation is in a.u.

citation energy around 1.73 eV (ACPF). The electronic structure of the  $A^2\Pi$  state is dominated by the electronic configuration  $\text{Li } (1s^2 2p^1) \text{ Ne } (1s^2 2s^2 2p_x^2 2p_y^2 2p_z^2)$ , which has a weight of 98% in the CASSCF wavefunction. In the CASPT2 and MRCI calculations the  $A^2\Pi$  state has a relatively deep well of approximately  $225 \text{ cm}^{-1}$ , while the  $X^2\Sigma$  state shows an order of magnitude smaller binding and a much larger internuclear separation. Two curves are only negligibly bound in the CASSCF calculation.

The CASSCF results in the ANO basis show only negligible binding for both electronic states. We believe that this is due to the lack of dynamic correlation in the

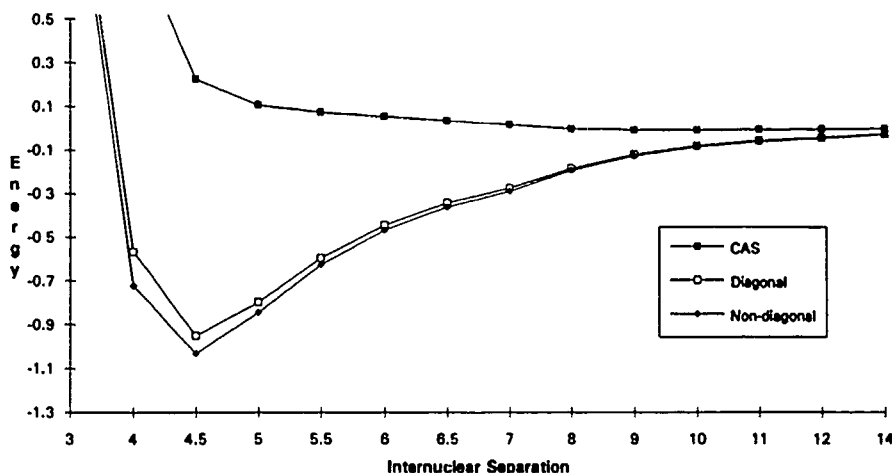


Figure 4. LiNe doublet  $\pi$  state. Energy is in mHartree, separation is in a.u.

TABLE IV. The dipole moments for  $X^2\Sigma$  and  $A^2\Pi$  states of  $\text{Li} \cdots \text{Ne}$  system calculated by different methods (in a.u., positive dipole moments is defined as  $\text{Li}^-\text{Ne}^+$ ).

<i>R</i>	$X^2\Sigma$		$A^2\Pi$	
	CAS <sup>a</sup>	MCPF <sup>a</sup>	CAS <sup>b</sup>	MCPF <sup>b</sup>
3.0	—	—	0.3800	0.3691
4.0	—	—	0.2526	0.2421
4.5	—	—	0.1934	0.1836
5.0	—	—	0.1441	0.1354
5.5	—	—	0.1055	0.0979
6.0	0.3328	0.3142	0.0764	0.0701
7.0	0.1564	0.1432	0.0398	0.0354
8.0	0.0702	0.0605	0.0209	0.0180
8.5	0.0464	0.0383	—	—
9.0	0.0308	0.0241	0.01134	0.0094
9.5	0.0206	0.0150	—	—
10.0	0.0144	0.0096	0.0065	0.0052
10.5	0.0097	0.0053	—	—
11.0	0.0070	0.0038	0.0039	0.0031
11.5	0.0053	0.0025	—	—
12.0	0.0042	0.0018	0.00249	0.0019
13.0	0.0031	0.0011	—	—
14.0	0.0023	0.0008	0.00118	0.0009
15.0	0.0021	0.0008	—	—
16.0	0.0020	0.0007	—	—
17.0	0.0019	0.0007	—	—
500.0	0.0018	0.0007	-0.0001	-0.0002

<sup>a</sup> Nine active electrons in  $(4|2|2|0)$  active space with two frozen orbitals.

<sup>b</sup> Nine active electrons in  $(4|2|2|0)$  active space with one frozen orbital and one inactive orbital.

CASSCF wavefunction for the active space chosen. This is borne out by the observation that second-order perturbation correction of this CASSCF wavefunction (CASPT2) as well as MRCI calculations yields bound states.

The calculated potential energy curves for the  $X^2\Sigma$  ground state are shown in Figure 1 (CASPT) and Figure 2 (MRCI). The results of the present calculations can be compared with the experimental results of Dehmer and Wharton [27] based on absolute total scattering cross section measurements. For this state, the experimentally derived potential has a well depth of  $\approx 9.7 \text{ cm}^{-1}$  at  $\approx 5.0 \text{ \AA}$ , while the calculated well depth is  $15.3 \text{ cm}^{-1}$  (MRCI + *Q*, ACPF) at  $5.3 \text{ \AA}$ . The calculations reported here may also be compared with the pseudopotential calculations reported in Ref [7], which find a substantially less attractive well of  $4.5 \text{ cm}^{-1}$  at  $5.8 \text{ \AA}$ .

For the  $A^2\Pi$  state, our CASPT2 and MRCI potential energy curves are shown in Figures 3 and 4. The MRCI + *Q* and ACPF results give a minimum of  $214 \text{ cm}^{-1}$  at  $2.26 \text{ \AA}$  in excellent agreement with the experimental results of  $224 \text{ cm}^{-1}$  at  $2.6 \text{ \AA}$ .

TABLE V. Molecular constants for the  $X^2\Sigma$  state of  $\text{Li} \cdots \text{Ne}$  system.

Method	$R_e$ (Å)	$D_e$ (eV)	$D_0$ (eV)
CASSCF <sup>a</sup>	$\approx 8.0$		
CASPT2D <sup>a</sup>	5.2905	0.00147	0.00142
CASPT2N <sup>a</sup>	5.2894	0.00152	0.00145
MRCI <sup>a</sup>	5.4062	0.00121	0.00115
MRCI <sup>a</sup> + Q	5.2721	0.00199	0.00177
MCPF <sup>a</sup>	5.3889	0.00196	0.00175
ACPF <sup>a</sup>	5.2836	0.00196	0.00174
Theory [7]	5.82	0.000557	
Exp [27]	5.116	0.001089	
	4.979	0.001191	

<sup>a</sup> Nine active electrons in  $(4|2|2|0)$  active space and two frozen orbitals.

[28]. Similar values were obtained for the other methods used. The previously reported pseudopotential results gave a somewhat flatter curve with a well depth of only  $166 \text{ cm}^{-1}$ .

The dipole moments were calculated at a number of geometries for both states and are listed in Table IV. These dipole moments are all in the direction  $\text{Li}^-\text{Ne}^+$  and are quite small at the equilibrium separations. Tables V and VI list the calculated spectroscopic constants for both states.

Several factors were neglected in these calculations which may affect the interaction energy by a small but not necessarily negligible amount. The most important of these is the neglect of the core correlation effects, including core-valence correlation results in the contraction of the atomic valence shell and the degradation of the dissociation energy by about 10% [29]. The next most important factor is

TABLE VI. Molecular constants for the  $A^2\Pi$  state of  $\text{Li} \cdots \text{Ne}$  system.

Method	$R_e$ (Å)	$D_e$ (eV)	$D_0$ (eV)	$\omega_e$ ( $\text{cm}^{-1}$ )	$\omega_e x_e$ ( $\text{cm}^{-1}$ )	$B_e$ ( $\text{cm}^{-1}$ )
CASSCF <sup>a</sup>	$\approx 4.8$					
CASPT2D <sup>a</sup>	2.2603	0.0291	0.0206	137	—	0.5469
CASPT2N <sup>a</sup>	2.2515	0.0320	0.0227	150	—	0.0
MRCI <sup>b</sup>	2.2716	0.0213	0.0149	103	-18.18	0.503
MRCI <sup>b</sup> + Q	2.2628	0.0275	0.0195	139	-18.44	0.643
MCPF <sup>b</sup>	2.2335	0.0394	0.0277	188	-18.35	0.5887
ACPF <sup>b</sup>	2.2617	0.0265	0.0183	131	-18.21	0.5311
Theory [7]	2.116	0.0206				
Exp [27]		0.0278				

<sup>a</sup> Nine active electrons in  $(4|2|2|0)$  space with one frozen and one inactive orbital.

<sup>b</sup> Nine active electrons in  $(4|2|2|0)$  space with two frozen orbitals.



the neglect of the polarization of the atomic cores. The effect of core polarization on the interaction potential can be related to polarizability [30]. The polarization of the Li core leads to the decrease of polarizability and to a less attractive interaction potential for  $\text{Li} \cdots \text{Ne}$ . In contrast, the polarization of the Ne core would lead to an increased polarizability for Ne and thus a more attractive potential.

### Conclusion

*Ab initio* potential curves have been determined for the ground  $X^2\Sigma$  and the excited  $A^2\Pi$  states of the  $\text{Li} \cdots \text{Ne}$  complex by the CASSCF, CASP12, and CI methods. The calculations correlate all valence electrons in active space build from the valence orbitals of Li and Ne. These calculations gave a well depth of  $214 \text{ cm}^{-1}$  (ACPF) for the  $A^2\Pi$  state, in excellent agreement with the  $224 \text{ cm}^{-1}$  deduced from experimental data and much better than the pseudopotential results of  $166 \text{ cm}^{-1}$  [7]. The much less attractive  $X^2\Sigma$  state is predicted to be bound by only  $15.8 \text{ cm}^{-1}$  with an equilibrium distance of  $5.28 \text{ \AA}$  using the CASPT2D method, while all other methods predict a much weaker interaction for this state. We conclude from these results that the ground state of  $\text{Li} \cdots \text{Ne}$  is at best only very weakly bound.

We have also tried to illustrate the capabilities of the second order perturbation method based on CASSCF reference function and conclude that either CASPT2 method shows promise of yielding satisfactory results in comparison with the MRCI results. For the  $A^2\Pi$  state, the CASPT2N gave a well depth of  $234 \text{ cm}^{-1}$ , in excellent agreement with the  $224 \text{ cm}^{-1}$  derived from experiment. However, the CASPT2D value of  $258 \text{ cm}^{-1}$  is a little bit too high. For the  $X^2\Sigma$  state, the CASPT2 values of the well depth of 11 and  $12 \text{ cm}^{-1}$  are closer to the experimental value of  $9.7 \text{ cm}^{-1}$  than the MRCI +  $Q$  value of  $15.3 \text{ cm}^{-1}$ . Thus, we conclude that CASPT2 methods are potentially capable of giving accurate results for the interaction potential for the weak van der Waals systems with a considerably reduced computational time.

### Acknowledgments

We would like to thank the National Science Foundation's EPSCoR program for Grant #R11-8902065 and the Cornell Theory Center for the allotment of computer time needed to complete this study. The authors also wish to thank Professor B. O. Roos for the use of the MOLCAS2 program in the present study and Dr. M. Fulscher for help installing the program on Cornell Theory Center and much helpful advice. W.D.E. would also like to acknowledge grants from the University of Idaho Research Council, which were used to acquire the components of The Computational Facility for Theoretical Chemistry.

### Bibliography

- [1] M. E. Fajardo, P. G. Carrick, and J. W. Kenney III, *J. Chem. Phys.* **94**, 5812 (1991).
- [2] N. Presser and A. T. Pritt, Jr., in *Proceedings of the High Energy Density Matter Conference*, W. J. Lauderdale and W. A. Sowell, Eds. AFAL-CP-002 (USAF Astronautics Lab, Edwards AFB, CA, 1987).
- [3] J. J. Wright and L. C. Balling, *J. Chem. Phys.* **73**, 3103 (1980).

- [4] J. Rose, D. Smith, B. E. Williamson, P. N. Schatz, and M. C. M. O'Brien, *J. Phys. Chem.* **90**, 2608 (1986).
- [5] G. York, R. Scheps, and A. Gallagher, *J. Chem. Phys.* **63**, 1052 (1975).
- [6] J. F. Dawson and L. C. Balling, *J. Chem. Phys.* **71**, 836 (1979); S. Ossicini and F. Forstmann, *J. Chem. Phys.* **75**, 2076 (1981); J. Pascale, *Phys. Rev. A* **28**, 632 (1983).
- [7] E. Czuchaj, F. Rebentrost, H. Stoll, and H. Preuss, *Chem. Phys.* **136**, 79 (1989).
- [8] Y. S. Kim and R. G. Gordon, *J. Chem. Phys.* **61**, 1 (1974).
- [9] W. E. Baylis, *J. Chem. Phys.* **51**, 2651 (1969).
- [10] L. C. Balling and J. J. Wright, *J. Chem. Phys.* **79**, 2941 (1983); L. C. Balling and J. J. Wright, *J. Chem. Phys.* **81**, 675 (1984); J. Pascale and J. Vandepauw, *J. Chem. Phys.* **60**, 2278 (1974).
- [11] P. O. Widmark, P. A. Malmquist, and B. O. Roos, *Theoret. Chim. Acta* **77**, 291 (1990).
- [12] C. E. Moore, Atomic Energy Levels, Natl. Bur. Stand. (U.S.) Circ. No. 467 (U.S. GPO, Washington, DC, 1949).
- [13] B. O. Roos, P. R. Taylor, and P. E. M. Siegbahn, *Chem. Phys.* **48**, 157 (1980); P. E. M. Siegbahn, J. Almlof, A. Heiberg, and B. O. Roos, *J. Chem. Phys.* **74**, 2384 (1981); B. O. Roos, *Int. J. Quantum Chem. Quantum Chem. Symp.* **14**, 175 (1980).
- [14] M. Jaszunski, B. O. Roos, and P. O. Widmark, *J. Chem. Phys.* **75**, 306 (1981).
- [15] J. M. O. Matos, P. A. Malmquist, and B. O. Roos, *J. Chem. Phys.* **86**, 5032 (1987).
- [16] J. M. O. Matos, V. Kello, B. O. Roos, and A. J. Sadlej, *J. Chem. Phys.* **89**, 423 (1988).
- [17] K. Andersson, P. A. Malmquist, B. O. Roos, A. J. Sadlej, and K. Wolinski, *J. Chem. Phys.* **94**, 5483 (1990); K. Andersson, P. A. Malmquist, and B. O. Roos, *J. Chem. Phys.* **96**, 1218 (1992).
- [18] K. Andersson, P. Borowski, P. W. Fowler, P. A. Malmquist, B. O. Roos, and A. J. Sadlej, *Chem. Phys. Lett.* **190**, 367 (1992); P. Borowski, K. Andersson, P. A. Malmquist, and B. O. Roos, *J. Chem. Phys.* **97**, 5568 (1992); K. Andersson and A. J. Sadlej, *Phys. Rev. A* **46**, 2356 (1992); B. O. Roos, K. Andersson, and M. P. Fulscher, *Chem. Phys. Lett.* **192**, 5 (1992); M. P. Fulscher, K. Andersson, and B. O. Roos, *J. Phys. Chem.* **96**, 9204 (1992); K. Andersson and B. O. Roos, *Chem. Phys. Lett.* **191**, 507 (1992); K. Andersson and B. O. Roos, *Int. J. Quantum Chem.* **45**, 591 (1993).
- [19] P. E. M. Siegbahn, *J. Chem. Phys.* **72**, 1647 (1980).
- [20] S. R. Langhoff and E. R. Davidson, *Int. J. Quantum Chem.* **8**, 61 (1974).
- [21] L. T. Redmon, G. D. Purvis III, and R. T. Bartlett, *J. Am. Chem. Soc.* **101**, 2856 (1979).
- [22] P. Hobza and R. Zahradnik, *Chem. Rev.* **88**, 871 (1988).
- [23] D. P. Chong and S. R. Langhoff, *J. Chem. Phys.* **84**, 5606 (1986).
- [24] R. J. Gdanitz and R. Ahlrichs, *Chem. Phys. Lett.* **143**, 413 (1988).
- [25] J. E. Del Bene and J. Shavitt, *Int. J. Quantum Chem. Quantum Chem. Symp.* **23**, 445 (1989).
- [26] Molcas Version 2.1, K. Andersson, M. P. Fulscher, R. Lindh, P. A. Malmquist, J. Olsen, B. O. Roos, and A. J. Sadlej, University of Lund, Sweden, and P. O. Widmark, IBM Sweden, 1991.
- [27] P. Dehmer and L. Wharton, *J. Chem. Phys.* **57**, 4821 (1972).
- [28] L. C. Balling, J. J. Wright, and M. D. Havey, *Phys. Rev. A* **26**, 1426 (1982).
- [29] H. Partridge, C. W. Bauschlicher, Jr., S. P. Walch, and B. Liu, *J. Chem. Phys.* **79**, 1866 (1983).
- [30] R. P. Saxon, R. E. Olson, and B. Liu, *J. Chem. Phys.* **67**, 2692 (1977).

Received April 9, 1993

# Theoretical Study of the Geometric Structures and Energetic Properties of Anionic Clusters.

## $\text{Ag}_n^-$ ( $n = 2$ to $6$ )

I. G. KAPLAN,\* R. SANTAMARIA, and O. NOVARO

*Instituto de Física, UNAM Apdo Postal 20-364, México 01000, D F., México*

### Abstract

The systematic quantum-mechanical investigation of the stable geometries and some energetic characteristics of the anionic silver clusters up to the hexamer are performed by an all-electron spin-density approach with nonlocal corrections included. Calculated vertical detachment energies are in good agreement with the experimental ones without any scaling procedure. The fragmentation energy for the channel  $\text{Ag}_n^- \rightarrow \text{Ag}_{n-1}^- + \text{Ag}$  shows very pronounced oscillations for even-odd  $n$ . The obtained stable geometries for  $\text{Ag}_n^-$  ( $n = 2-4$ ) are in agreement with previous calculations by Bauschlicher et al. [26,27]. To the contrary of the case of tetramers and pentamers we found that anionic and neutral hexamers have different stable geometries. © 1993 John Wiley & Sons, Inc

### Introduction

The past decade is characterized by the intensive experimental and theoretical investigations of different kinds of clusters [1-3]. One of the main reasons for this great interest in cluster studies is their evident importance in filling the gap between the behavior of molecules and of solids. In other words, it is expected that the study of the properties of clusters will allow us to understand the manner in which the microscopic properties evolve towards the macroscopic ones.

Therefore it is particularly important to study these properties as a function of the cluster size, usually referred to as "size effects." Jortner et al. [4] have classified size effects according to their nature as follows: (a) quantum or energetic; (b) thermodynamic; (c) dynamic; and (d) chemical size effects.

The main interest of the present article will lie on energetic size effects. Among these the most interesting energetic size effects are those revealed by their photoelectron spectra (PES). The PES allows to obtain several cluster characteristics such as its ionization potentials (IP), electron affinities (EA), vertical detachment energies (VDE), and electronic transition energies. These characteristics often show a very pronounced dependence upon the cluster size. There are extensive experimental investigations on alkali metal clusters [5-6] demonstrating such behavior. A substantial number of accurate theoretical investigations have been performed by Kouřtecký and co-workers [7-13] on neutral and charged  $\text{Li}_n$ ,  $\text{Na}_n$ , and  $\text{K}_n$  clusters.

\* On leave from Karpov Institute of Physical Chemistry, Moscow, Russia.

Recently published measurements of IPs for  $\text{Li}_n$  clusters [14] show very good agreement with the theoretical values [7].

The transition metal clusters have also received a large amount of experimental interest [15–23], in particular in the cases of silver and copper clusters. The measurement of VDEs have demonstrated a well-defined even–odd oscillating behavior for  $\text{Cu}_n^-$  and  $\text{Ag}_n^-$  ionic clusters. This means that the VDEs reach alternatively local minima for even  $n$  and local maxima for odd  $n$  clusters. On the contrary the VDE values for  $\text{Pd}_n^-$  anionic clusters show only a smoothly increasing behavior as a function of cluster size [18]. In the specific case of  $\text{Ag}_n^-$  which will concern us here, the VDE values have been measured in two laboratories [18,19] using diverse ion source conditions. In spite of that, their VDE results agree within the experimental error limits.

As it concerns with the theoretical investigations on d-shell metal clusters, they were at first not so abundant as on the alkali metal clusters. In recent years, however, many precise *ab initio* calculations of the coinage metal clusters ( $\text{Cu}_n$ ,  $\text{Ag}_n$ , and  $\text{Au}_n$ ) have been performed by several research groups [24–35], including up to the hexamers [34]. We have nevertheless not found any publications devoted to the systematic theoretical calculation of anionic clusters. The only exception, to our best knowledge, is the investigations of Åkeby et al. [35] on  $\text{Cu}_n^-$  ( $n \leq 10$ ). In their article, however, the one-electron model approach was used, which lacks the accuracy of most of the other studies [24–34].

For smaller coinage metal anion clusters (dimers and trimers), very precise calculations were attempted by Bauschlicher et al. [26]. Tetramer anions were further studied rigorously by this group [27], but for anionic pentamers the VDEs were calculated using the optimal geometry of the *neutral* clusters [27]. A similar approach was followed for tetramer VDEs in [33]. We should point out that in all of these calculations [26,27,33], the VDEs were obtained only after introducing scaling factors (1.3–1.35), without which the agreement with the experimental data was rather poor. Even with the scaling factor, good agreement was not possible in all cases [33].

The goal of the present article is to obtain for anionic silver clusters up to the hexamers, the stable geometries and the binding energies using a sufficiently precise quantum chemical method. In particular, we aim to obtain the VDE of each silver anionic cluster without using any scaling factors. The main reason for introducing a scaling factor is to correct for an insufficient account of atomic correlation effects [33]. To avoid this we have chosen to use the all-electron spin density (LSD) approach with nonlocal corrections included [36,37]. With this approach we expect the atoms to be treated at similar level of accuracy as the molecules.

All calculations were performed on a Cray Y-MP4/432 computer using the DGauss program. As it has been shown by Fantucci et al. [10] for  $\text{Li}_n$  and  $\text{Na}_n$  clusters, the nonlocal version of the electron density-functional method yields results close to those obtained by HF–CI calculations.

### Computational Method

The systematic study of size effects on anionic clusters implies the calculations of increasingly larger oligomers. In the particular and quite interesting case of tran-

sition metal clusters the all-electron *ab initio* calculations become prohibitively time-consuming because of the enormous quantities of inner-shell electrons that these systems imply.

The neglect of interactions between distant atoms and the effective core potentials (ECP) are among the most common cut-offs to reduce time and memory in a computer. ECPs render in many cases results of accuracy comparable to all-electron *ab initio* calculations. Unfortunately, for metallic clusters it is necessary to include not only a large number of configuration states to obtain significant core-core, core-valence, and valence-valence correlation effects but also, scaling factors in order to account for the deficiency when computing the atomic electron affinities and ionization potentials [26,27,33]. Because of this fact and the great number of calculations required to find out the stable geometries for anionic silver clusters we resort to a less computationally demanding method, namely, the local spin density (LSD) approximation with nonlocal corrections.

The LSD approximation has been developed within the Kohn-Sham (KS) scheme where the electron density represents the main variable of the theory and the exchange-correlation effects are taken into consideration in an approximative way. It is generally agreed that the Vosko, Wilk, and Nusair (VWN) approximate expression [38] for the exchange-correlation potential should be introduced in the total energy functional in order to constitute the LSD level of theory. Nevertheless, because of the high inhomogeneities and strong correlation produced by the interacting electron clouds of a metallic cluster, it is necessary for the higher precision to consider a nonlocal correction to the VWN potential. Among several nonlocal exchange-correlation functionals the one proposed by Becke and Perdew [39-41] (BP) is the most attractive to work with because of its good results and computational efficiency (see the last review by Ziegler [42]).

Here, we shall use the DGauss computational approach [36] already implemented in the UNICHEM package to solve the LSD-KS equations. This approach, in contrast to the Hartree-Fock (HF) method, demands not only basis sets for the molecular orbitals but also auxiliary gaussian basis sets to expand the electron density, exchange-correlation potential, and exchange-correlation energy. The molecular orbital and auxiliary basis functions to use in the computation will be those specifically optimized within the LSD approximation [43,44] for silver and denoted by (633321/53211/531)/(6/5/3) and (10/5/5), respectively. The first set is equivalent to a double-zeta valence plus polarization basis set and, the second—without equivalence inside the HF scheme—is known as the auxiliary-1 basis set (A1). Both of them have been carefully checked to minimize basis set superposition errors (BSSE) [43,44].

As it has been shown by Andzelm and Wimmer [36] the inclusion of nonlocal corrections in this computation scheme allows to predict bond dissociation energies, within 0.1 eV. This indicates that the BSSE is small.

The nonlocal BP corrections can be calculated by two ways: in a nonself-consistent and in a self-consistent manner. We shall use both approaches.

The DGauss approach like any other computational implementation has some shortcomings too. One of the most important is, up to the moment, the lack of

inclusion of relativistic corrections in the one-electron LSD-KS equations. Even when these effects are not included at this stage, there exists evidence [37] that LSD provides good results for bond lengths and angles of molecules containing metallic atoms such as silver. Balasubramanian [45] has analyzed the influence of relativistic effects on transition metal cluster reaching the conclusion that such effects become quite important for heavier elements like Au, Pt, etc., see also [46], but do not lead to drastic changes for silver. We also believe that these kind of contributions should be further reduced by cancellation when energy differences are taken into account.

In order to find out the most stable geometries, the method already described above was applied to a number of different molecular conformations. Only symmetrical conformations were taken into account for the anionic clusters  $\text{Ag}_n^-$  ( $n \leq 6$ ). The calculations were performed on the CRAY YMP4/432 with the DGSCA supercomputing facility.

### Results and Discussion

As mentioned in the Introduction, we must optimize the geometry of the  $\text{Ag}_n^-$  stable clusters before calculating the VDEs and other energetic characteristics. We have done this systematically for anionic silver dimers, trimers . . . up to hexamers in order to study quantum size effects. Dimers, trimers, and tetramers, have been

TABLE I Comparison of calculated geometries and some energetic characteristics of silver anions  $\text{Ag}_n^-$ .

#### a) atom and dimer

n	$r_e$ (Å)		$D_e$ (eV)			EA (eV)		
	Calculation		Calculation			Calculation		
	Our	[26]	Our	[26]	Experiment	Our	[26] <sup>b</sup>	Experiment
1						1.183	1.26	1.302 ± 0.007 [47]
2	2.850	2.813	1.307	1.12	1.39 ± 0.02 <sup>a</sup>	1.013	0.97	1.028 ± 0.01 <sup>a</sup>

#### b) trimer and tetramer

n	Geometry	$r_o$ (Å)		$\alpha$ (deg.)	
		Calculation		Calculation	
		Our		Our	[27]
3	linear	2.760	2.754 [26]		
4	rhombic <sup>c</sup>	2.849	2.852 [27]	61.2	63.7

<sup>a</sup> See Ref. [4] in [26].

<sup>b</sup> Scaled by a factor 1.3.

<sup>c</sup> See Figure 1.

already studied by Bauschlicher et al. [26,27], so in Table I the detailed comparison of their results with ours are given. We see from Table I that the agreement in the stable geometries is rather good. Our unscaled energies for the dimer are in better agreement with the experimental data than the results in [26]. For trimer and tetramer anions we compare only geometrical parameters for stable geometries, we can not compare atomization energies because they have been calculated in [27] only for neutral clusters.

In Table II and Figure 1 we present the results of our calculations obtained by including nonlocal corrections in a self-consistent manner. The difference in the geometry and the energy as compared to the calculations with nonself-consistent inclusion of the nonlocal corrections is rather small; for the energy it is in the interval 0.02 to 0.09 eV. The notation for the cluster  $Ag'_n$  (in Table II) represents the neutral cluster whose geometry is fixed to be the same as that of the stable anion  $Ag_n^-$ . Its energy  $E_o(Ag'_n)$  is necessarily higher than the ground state energy of the optimized geometry of the neutral cluster  $E_o(Ag_n)$ . This is the reason why the VDE calculated as the difference:

TABLE II. Ground-state energies and VDEs for the anionic isomers  $Ag_n^-$ ,  $n = 2-6$ .

<i>n</i>	Geometry <sup>a</sup>	$E_o(Ag_n^-)$ , a.u.	$E_o(Ag'_n)$ , a.u.	VDE, eV	
				Our calc.	Experimental
2	Linear, $D_{\infty h}$	-10399.989439	-10399.949723	1.08	1.06 ± 0.02 [19]
3	Linear, $D_{\infty h}$	-15600.006445	-15599.926529	2.18	2.43 ± 0.01 [19] 2.43 [18]
4	Rhombic, $D_{2h}$	-20799.997814 ( $\Delta E = 0$ )	-20799.935275	1.70	
	Linear, $D_{\infty h}$	-20799.996715 ( $\Delta E = 0.03$ eV)	-20799.918354	2.13	1.65 ± 0.05 [19] 1.71 [18]
	Planar, $D_{2d}$	-20799.994353 ( $\Delta E = 0.09$ eV)	-20799.927857	1.81	
5	Trapezoidal, $C_{2v}$	-26000.010334 ( $\Delta E = 0$ )	-25999.935604	2.03	2.11 ± 0.05 [19]
	Linear, $D_{\infty h}$	-25999.999273 ( $\Delta E = 0.30$ eV)	-25999.898926	2.73	2.1 [18]
6	Tripyramidal, $C_{3v}$	-31200.012922 ( $\Delta E = 0$ )	-31199.936451	2.08	
	Trigonal, $D_{3h} \rightarrow D_{2h}$	-31200.010615 ( $\Delta E = 0.06$ eV)	-31199.957999	1.43	2.06 ± 0.05 [19]
	Quadratic bipyramid, $O_h \rightarrow D_{4h}$	-31200.008368 ( $\Delta E = 0.12$ eV)	-31199.916271	2.51	2.05 [18]
	Pentagonal pyramid, $C_{5v}$	-31200.007207 ( $\Delta E = 0.16$ eV)	-31199.949112	1.58	

<sup>a</sup> See Figure 1 and Table I.

<sup>b</sup> The  $Ag'_n$  designates the neutral cluster whose geometry is the same as the stable geometry of the anion  $Ag_n^-$ .

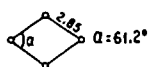
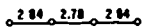
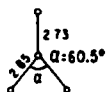
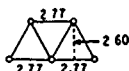
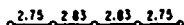
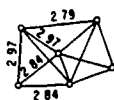
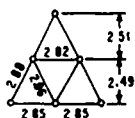
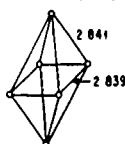
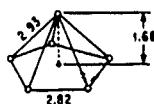
a)  $n = 4$ Rhombic,  $D_{2h}$ Linear,  $D_{\infty h}$ Planar,  $D_{2d}$ b)  $n = 5$ Trapezoidal,  $C_{2v}$ Linear,  $D_{\infty h}$ c)  $n = 6$ Tripyramidal,  $C_{2v}$ Trigonal,  $D_{3h} \rightarrow D_{2h}$ Quadratic  
bipyramid,  $O_h \rightarrow D_{4h}$ Pentagonal pyramid,  $C_{5v}$ 

Figure 1. The most stable geometries for the anionic isomers  $Ag_n^-$ ,  $n = 4-6$ ; all distances in angstroms.

$$VDE = -[E_o(Ag_n^-) - E_o(Ag'_n)] \quad (1)$$

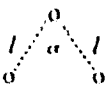
is always larger than the adiabatic electron affinity (EA).

The stable geometry for  $Ag_3^-$  is linear, as follows from Table III, and this agrees with the results of Bauschlicher et al. [26] as well as with the data obtained for  $Na_3^-$  by Bonacić-Koutecký et al. [11]. According to our results the linear trimer is 1.31 eV more stable than the equilateral triangle one.

For the tetramer anionic clusters three isomers have almost equal energies, and we therefore need to analyze other properties to determine the most stable geometry. Among such properties, we choose the VDE, which is highly dependent on the cluster geometry [12]. According to Table II the coincidence between the calculated value of the tetramer VDE and the experimental is much better for the rhombic geometry. But the value of the VDE for the  $D_{2d}$  planar geometry is also not very far from the experimental one. The energy of the  $D_{2d}$  isomer is only 0.09 eV higher



TABLE III. Dependence of the ground-state energy and the interatomic distances from the angle for silver anion  $\text{Ag}_5^-$ .

Geometry	$\alpha$ (deg.)	$l_0$ (Å)	Relative energy, eV
	180	2.76	0.00
	150	2.78	0.052
	120	2.80	0.278
	90	2.81	0.634
	60	2.88	1.313

than the energy of the  $D_{2h}$  isomer. The experiments with carbon anionic clusters [48,49] indicated the existence of more than one isomer with the same number of atoms. Different isomers are not necessarily in the thermodynamic equilibrium. So for  $n = 4$  the both planar geometries  $D_{2h}$  and  $D_{2d}$  can be present in the experiments [18,19]; the probability for the formation of linear isomers  $\text{Ag}_4^-$  is much lower.

Nothing has apparently been published about the geometry of the anion clusters  $\text{Ag}_n^-$  with  $n > 4$ . As a first approach we may expect that for heavy atom clusters with  $n > 4$  the anion geometry must not differ considerably from the neutral one [27,33]. We have studied here several geometries for pentamer and hexamer anions. Some of them were suggested by the results of Bonačić-Koutecký et al. on sodium clusters [11–13] and by those of Refs. [27] and [34] on neutral silver clusters. The most stable isomers in our calculations on each investigated anion cluster for  $n = 4$ –6 are presented in Figure 1. For  $n = 6$  we have presented four isomers as their energies are relatively close to each other.

For  $n = 5$  the trapezoidal planar geometry is more stable than the linear by 0.3 eV. The poor agreement of the VDE calculated for the linear geometry with the experimental value is an additional reason to assume the trapezoidal planar isomers of  $\text{Ag}_5^-$  are produced with much higher probability than the linear isomers.

Notice that the stable geometry for the anionic pentamer found in our study has the same symmetry as that found in Ref. [27] for the neutral pentamer. A similar situation takes place for tetramer [27].

It is important to point out that for sodium anionic clusters it has been proposed [11] that the  $\text{Na}_4^-$  linear geometry is responsible for the photoelectron detachment spectra and that for  $\text{Na}_5^-$  both the planar and linear anionic isomers may contribute to the recorded spectrum. The reason for this structural difference between  $\text{Ag}_4^-$  and  $\text{Ag}_5^-$ , on the one hand, and  $\text{Na}_4^-$  and  $\text{Na}_5^-$ , on the other, is probably due to the interaction between the d-subshell and the valence shell. Furthermore, the relaxation of the closed d-subshells in the silver metal clusters during their formation could also be partially responsible for these differences. This has been remarked before [50] in the case of copper. This problem shall be a subject of future investigation.

According to Table II four structures have close energies for  $n = 6$ . The most stable structure has a tripyramidal geometry with symmetry  $C_{2v}$ . This kind of ge-

ometry was found to be the most probable for the neutral lithium hexamer [7]. On the contrary, for the neutral silver hexamer the most stable isomer according to Ref. [34] has the geometry of a pentagonal pyramid. In our case of anionic silver hexamers the pentagonal pyramid geometry is 0.16 eV less stable than the tripyramidal geometry (see Table II). For the most stable tripyramidal structure, there is very good agreement with the experimental VDE. This indicates that the tripyramidal structure is the most favorable structure for contributing to the measured PES [18,19] among those considered in our study. But we can not exclude the possibility that the other three isomers also contribute to the measured spectrum, because the higher value of the VDE for quadratic bipyramid can be compensated by the lower values of the VDE for the two others.

We also calculated the hexagonal ring geometry which was found the most stable for the anionic gold hexamer [51]. In the case of the silver it is much less stable in comparison with the other four structures ( $\Delta E = 0.9$  eV) and has not such good agreement with the experimental value of the VDE as the tripyramidal structure.

We conclude from the results of Table II that there is very good agreement between the experimental values of the VDEs and our calculations (we have not such good agreement only for the trimer). We remark that this agreement is achieved without any resource to scaling procedures. This implies that errors due to the approximate account of the electron correlation effects as well as to the relativistic corrections, which are not included in our calculations, are canceled out to a great degree when the difference of formula (1) is computed.

The important aspect of our VDEs is that they reproduce the even-odd oscillating behavior (local minima for even  $n$ , local maxima for odd  $n$ ) observed in the experiments [18,19].

In Figure 2 we present the visual characteristics of the anion cluster stabilities  $\epsilon_a(n)$  and  $\epsilon_1(n)$  defined as follows. The binding energy per atom  $\epsilon_a$  is defined by the expression

$$\epsilon_a(n) = -\frac{1}{n} [E_o(\text{Ag}_n^-) - (n-1)E_o(\text{Ag}) - E_o(\text{Ag}^-)] \quad (2)$$

the fragmentation energy  $\epsilon_1(n)$  related to the reaction:



is equal to:

$$\epsilon_1(n) = -[E_o(\text{Ag}_n^-) - E_o(\text{Ag}_{n-1}^-) - E_o(\text{Ag})] \quad (4)$$

For  $\epsilon_a(n)$  Figure 2 shows a sharp increase at the transition from  $\text{Ag}_2^-$  to  $\text{Ag}_3^-$  and a slow increase with cluster size henceforth. Such behavior is consistent with the dependence of  $\epsilon_a(n)$  obtained in Ref. [35] for  $\text{Cu}_n^-$  and in Ref. [8] for  $\text{Li}_n^-$ . For neutral clusters in contrast with the ionic behavior, the  $\epsilon_a(n)$  does not increase when it passes from the dimer to the trimer [27] and it begins to increase slowly beyond the latter. For the neutral clusters of the lighter metals (lithium and sodium) there even appears a decreasing at the dimer-trimer transition [10]. On the other

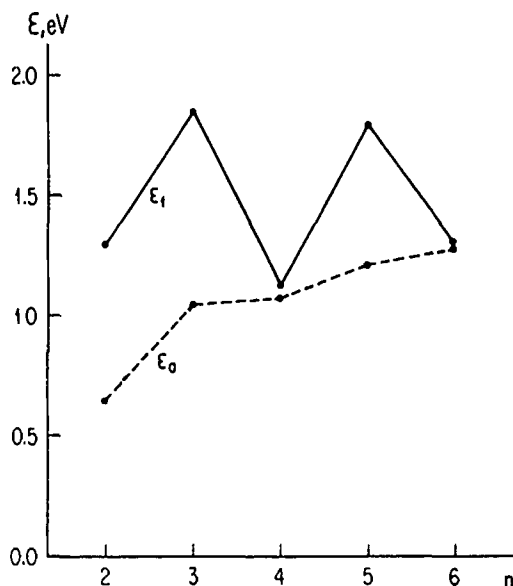


Figure 2. The dependence of the binding energy per atom ( $\epsilon_0$ ) and the atomic fragmentation energy ( $\epsilon_1$ ) on the number of atoms in silver anionic clusters.

hand the pronounced even-odd alternation obtained for the fragmentation energy of silver anions (see the behavior of  $\epsilon_1$  in Fig. 2) has also been revealed for cations such as  $\text{Na}_n^+$  [52] and  $\text{Li}_n^+$  [8].

### Conclusions

From the result obtained we can conclude that the LSD method with nonlocal corrections included (in the DGauss program realization) is quite appropriate for the calculation of d-subshell metal anionic clusters. It is advantageous in scanning the stable geometry and in computing the PES. In particular, the application of this method allows to obtain the experimental VDEs without any scaling factors.

The reason why the stable geometry for the anionic hexamer  $\text{Ag}_6^-$  has different symmetry than that for the neutral hexamer  $\text{Ag}_6$ , although for tetramers and pentamers the anionic and neutral clusters have the same symmetry, requires special investigation.

### Acknowledgments

The authors are grateful to Drs. J. Andzelm, G. Fitzgerald, A. Vela, and, especially I. Topol for helpful discussions and, to the DGSCA staff of the UNAM supercomputing center for access to the CRAY YMP4/432 computer. We also acknowledge CONACyT for financial support under contracts No. 920100 and No. 920207.

## Bibliography

- [1] *Physics and Chemistry of Small Clusters*, Vol. B158 of NATO ASI Series, P. Jena, B. K. Rao, and S. N. Khanna, Eds. (Plenum, New York, 1987).
- [2] *The Chemical Physics of Atomic and Molecular Clusters*, G. Scoles, Ed. (North-Holland, Amsterdam-Oxford-New York-Tokyo, 1990).
- [3] *Physics and Chemistry of Finite Systems From Clusters to Crystals*, Vol. C374 of NATO ASI Series, P. Jena, S. N. Khanna, and B. K. Rao, Eds. (Kluwer Acad. Publ., The Netherlands, 1992).
- [4] J. Jortner, D. Scharf, N. Ben-Horin, U. Even, and U. Landman, *Size Effects in Clusters*, in Ref. [2], p. 43.
- [5] S. T. Arnold, J. G. Eaton, D. Patel-Misra, H. W. Sarkas, and K. H. Bowen, in *Ion and Cluster Ion Spectroscopy and Structure*, J. P. Maier, Ed. (Elsevier, New York, 1989).
- [6] K. McHugh, J. G. Eaton, G. Lee, H. W. Sarkas, L. H. Kidder, J. Snodgrass, M. R. Manea, and K. H. Bowen, *J. Chem. Phys.* **91**, 3792 (1989).
- [7] I. Boustani, W. Pervestorf, P. Fantucci, V. Bonačić-Koutecký, and J. Koutecký, *Phys. Rev.* **B35**, 9437 (1987).
- [8] I. Boustani and J. Koutecký, *J. Chem. Phys.* **88**, 5657 (1988).
- [9] P. Fantucci, S. Polezzo, V. Bonačić-Koutecký, and J. Koutecký, *Z. Phys. D. At., Mol. and Clusters* **13**, 325 (1989).
- [10] P. Fantucci, S. Polezzo, V. Bonačić-Koutecký, and J. Koutecký, *J. Chem. Phys.* **92**, 6645 (1990).
- [11] V. Bonačić-Koutecký, P. Fantucci, and J. Koutecký, *J. Chem. Phys.* **93**, 3802 (1990).
- [12] V. Bonačić-Koutecký, P. Fantucci, and J. Koutecký, *Chem. Rev.* **91**, 1035 (1991).
- [13] V. Bonačić-Koutecký, J. Pittner, C. Scheuch, M. F. Guest, and J. Koutecký, *J. Chem. Phys.* **96**, 7938 (1992).
- [14] Ph. Dugourd, D. Rauane, P. Labastie, B. Vezin, J. Chevalayre, and M. Broyer, *Chem. Phys. Lett.* **197**, 433 (1992).
- [15] D. G. Leopold, J. Ho, and W. C. Lineberger, *J. Chem. Phys.* **86**, 1715 (1987).
- [16] C. L. Pattiette, S. H. Yang, M. J. Causcraft, J. Conceicao, R. T. Laaksonen, O. Cheshnovsky, and R. E. Smalley, *J. Chem. Phys.* **88**, 5377 (1988).
- [17] G. Ganteför, N. Gausa, K. H. Meiwes-Broer, and H. O. Lutz, *Faraday Discuss. Chem. Soc.* **88**, 16 (1988).
- [18] G. Ganteför, M. Gausa, K. H. Meiwes-Broer, and H. O. Lutz, *J. Chem. Soc. Faraday Trans.* **86**, 2483 (1990).
- [19] J. Ho, K. M. Ervin, and W. C. Lineberger, *J. Chem. Phys.* **93**, 6987 (1990).
- [20] O. Cheshnovsky, K. J. Taylor, J. Conceicao, and R. E. Smalley, *Phys. Rev. Lett.* **64**, 1785 (1990).
- [21] G. Alameddine, J. Hunter, D. Cameron, and M. Kappes, *Chem. Phys. Lett.* **192**, 122 (1992).
- [22] M. B. Knickelbein, *Chem. Phys. Lett.* **192**, 129 (1992).
- [23] M. Harbich, S. Fedrigo, and J. Buttet, *Chem. Phys. Lett.* **195**, 613 (1992).
- [24] S. P. Walch, C. W. Bauschlicher, Jr., and S. R. Langhoff, *J. Chem. Phys.* **85**, 5900 (1986).
- [25] C. W. Bauschlicher, Jr., S. R. Langhoff, and P. R. Taylor, *J. Chem. Phys.* **88**, 1041 (1988).
- [26] C. W. Bauschlicher, Jr., S. R. Langhoff, and H. Patridge, *J. Chem. Phys.* **91**, 2412 (1989).
- [27] C. W. Bauschlicher, Jr., S. R. Langhoff, and H. Patridge, *J. Chem. Phys.* **93**, 8133 (1990).
- [28] A. Ramírez-Solís, O. Novaro, and M. E. Ruiz, *Phys. Rev. B* **32**, 4082 (1987).
- [29] A. Ramírez-Solís, J. P. Daudey, O. Novaro, and M. E. Ruiz, *Z. Phys. D. At., Mol. and Clusters*, **15**, 71 (1990).
- [30] K. Balasubramanian, P. Y. Feng, and M. Z. Liao, *J. Chem. Phys.* **91**, 3561 (1989).
- [31] K. Balasubramanian and P. Y. Feng, *Chem. Phys. Lett.* **159**, 452 (1989).
- [32] K. Balasubramanian and P. Y. Feng, *J. Phys. Chem.* **94**, 1536 (1990).
- [33] K. K. Das and K. Balasubramanian, *Chem. Phys. Lett.* **176**, 571 (1991).
- [34] D. W. Liao and K. Balasubramanian, *J. Chem. Phys.* **97**, 2548 (1992).
- [35] H. Åkeby, I. Panas, L. G. M. Pettersson, Per Siegbahn, and U. Wahlgren, *J. Phys. Chem.* **94**, 5471 (1990).
- [36] J. Andzelm and E. Wimmer, *J. Chem. Phys.* **96**, 1280 (1992).
- [37] C. Sosa, J. Andzelm, B. C. Elkin, and E. Wimmer, *J. Phys. Chem.* **96**, 6630 (1992).

- [38] S. H. Vosko, L. Wilk, and M. Nusair, *Can. J. Phys.* **58**, 1200 (1980).
- [39] J. P. Perdew, *Phys. Rev. B* **33**, 8822 (1986).
- [40] A. D. Becke, *Phys. Rev. A* **38**, 3098 (1988).
- [41] A. D. Becke, *J. Chem. Phys.* **88**, 2547 (1988).
- [42] T. Ziegler, *Chem. Rev.* **91**, 651 (1991).
- [43] J. Andzelm, E. Radzio, and D. R. Salahub, *J. Comput. Chem.* **6**, 520, 533 (1985).
- [44] N. Godbout, D. R. Salahub, J. Andzelm, and E. Wimmer, *Can. J. Chem.* **70**, 560 (1992).
- [45] K. Balasubramanian, *J. Phys. Chem.* **93**, 6585 (1989).
- [46] *The Effects of Relativity in Atoms, Molecules and the Solid State* (T. Wilson, I. P. Grant, and B. L. Gyorffy, Eds. (Plenum, New York, 1991)).
- [47] H. Hotop and W. C. Lineberger, *J. Phys. Chem. Ref. Data* **14**, 731 (1985).
- [48] D. Zajfman, H. Feldman, O. Heber, D. Kella, D. Majer, Z. Vager, and R. Naaman, *Science* **258**, 1129 (1992).
- [49] G. von Heden, P. R. Kemper, N. G. Gotts, and M. T. Bowers, *Science* **259**, 1300 (1993).
- [50] M. E. Ruiz, J. García-Prieto, E. Poulain, G. A. Ozin, and O. Novaro, *J. Chem. Phys.* **81**, 5970 (1984).
- [51] K. Balasubramanian and D. W. Liao, *J. Chem. Phys.* **94**, 5233 (1991).
- [52] V. Bonačić-Koutecký, I. Boustani, M. F. Guest, and J. Koutecký, *J. Chem. Phys.* **89**, 4861 (1988).

Received March 15, 1993

# Accurate LCAO Ground State Calculations of $\text{HeH}^{2+}$ Using Slater-Type Orbitals

BABAK ETEMADI and HERBERT W. JONES

*Institute for Molecular Computations and Department of Physics, Florida A&M University,  
Tallahassee, Florida 32307*

## Abstract

A linear combination of atomic orbitals (LCAO) of the Slater type is used in a variational treatment of the  $\text{HeH}^{2+}$  ion to achieve excellent results for the ground state energy of this heteronuclear diatomic system. As in our recent treatment of  $\text{H}_2^+$ , we use orbitals with identical screening constants but with increasing principal quantum numbers and angular momentum. This strategy was feasible because of our ability to accurately evaluate all overlap integrals. Unlike even tempered Gaussian-type LCAO, our results become more accurate at large interatomic separations. Using two different screening constants (one type associated with each atom) proved to be unnecessary. © 1993 John Wiley & Sons, Inc

## Introduction

Basis set methods in electronic structure calculations have been shown by Wells and Wilson [1] to give excellent results for simple molecules such as  $\text{H}_2^+$  and  $\text{HeH}^{2+}$ . They employed an even-tempered basis set of Gaussian-type orbitals (GTOs). Our interest is in using the more physical Slater-type orbitals (STOs) so as to develop strategies for nonlinear molecules. Steinborn and Weniger [2] used their "B" functions of spherical symmetry to approximate the ground state energy of  $\text{HeH}^{2+}$  (the "B" functions span the same space as STOs). They suggested that better results could be achieved if orbitals of higher angular momentum and various screening constants were used. We found that excellent results are indeed achieved by using orbitals of higher angular momentum, but identical screening constants for all orbitals are sufficient. For nuclear separation of 1 a.u. we get 8-digit accuracy: The accuracy increases with increasing nuclear separation, unlike for GTOs.

## LCAO Method for $\text{HeH}^{2+}$

We extend our previous work on the homonuclear ion  $\text{H}_2^+$  [3] to the heteronuclear ion  $\text{HeH}^{2+}$ . In the electronic hamiltonian we set  $Z_1 = 1$  and  $Z_2 = 2$ :

$$H = -\frac{1}{2} \nabla^2 + \frac{Z_1}{r_a} + \frac{Z_2}{r_b} \quad (1)$$

TABLE I. Screening constant  $\zeta$  of the lowest energy for various values of the internuclear distance  $R$ , and maximum principal quantum number  $N_{\text{high}}$ .

$R$	$N_{\text{high}} = 1$	$N_{\text{high}} = 3$	$N_{\text{high}} = 6$
1.0	2.2	2.7	3.3
2.0	2.0	2.5	2.9
4.0	2.0	2.0	2.5
8.0	2.0	2.0	2.0
20.0	2.0	2.0	2.0
60.0	2.0	2.0	2.0

(the internuclear energy term  $Z_1 Z_2 / R$ , where  $R$  is the internuclear separation, has been dropped). For our LCAO (linear combination of atomic orbitals) ansatz, we use a systematic sequence of STOs on each nucleus:

$$\psi_i = K \sum_{N=1}^{N_{\text{high}}} \sum_{L=0}^{N-1} C_{NL} A_N r_i^{N-1} e^{-\zeta r_i} Y_L^0(\theta_i, \phi_i), \quad (2)$$

where  $i$  designates an orbital at position  $a$  or an orbital at position  $b$ .  $K$  is the normalization constant chosen such that

$$\int \psi^* \psi d\tau = 1, \quad \psi = \psi_a + \psi_b. \quad (3)$$

To apply the variational principle, we write

$$H\psi = E\psi, \quad (4)$$

and arrive at a secular equation for the energy. This eigenvalue problem was solved on a CRAY Y-MP using the IMSL library [4]. The screening parameter  $\zeta$  was varied to minimize the energy for different nuclear separations and different number of orbitals,  $N_{\text{high}}$  (see Table I). For  $N_{\text{high}}$  greater than 3, the energy is insensitive to the variations of  $\zeta$ . In Table II the corresponding energies are recorded. The exact values are taken from [5]. For the equilibrium position, i.e.,  $R = 2$  a.u., we get

TABLE II. The electronic energy of  $\text{HeH}^{2+}$  for various internuclear distances  $R$  and for LCAO with highest quantum number  $N_{\text{high}}$ .

$R$	$N_{\text{high}} = 1$	$N_{\text{high}} = 3$	$N_{\text{high}} = 6$	Exact
1.0	-3.0129511	-3.0332651	-3.033352043	-3.033352518075
2.0	-2.5043488	-2.5121563	-2.512192935	-2.512193016590
4.0	-2.2500067	-2.2505992	-2.2506053801	-2.250605387829
8.0	-2.1250000	-2.12503483	-2.125034906460	-2.125034906488
20.0	-2.0500000	-2.0500008807	-2.050000880914	-2.050000880914
60.0	-2.016666666	-2.01666667750	-2.016666677520	-2.016666677520

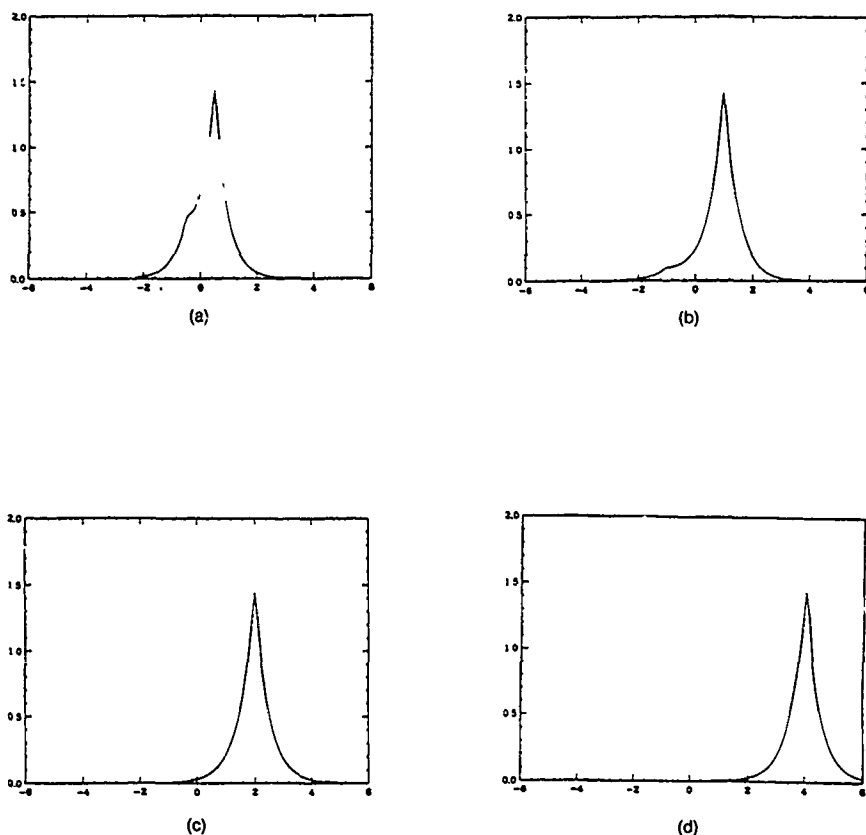


Figure 1. (a), (b), (c), and (d) show the wave function of  $\text{HeH}^{2+}$  along the H-He axis (H is at  $-R/2$  and He is at  $+R/2$ ) for separations  $R = 1, 2, 4$ , and  $8$  a.u., respectively.

8-digit accuracy using only 21 orbitals on each nucleus, whereas Wells and Wilson [1] require 42 GTOs for 7-digit accuracy. In addition, our method gives even better results for larger separations. The normalized wave function along the molecular axis is plotted in Figure 1 for  $R = 1, 2, 4$ , and  $8$  a.u. It is shown that the charge is practically all about the He nucleus especially when  $R$  is larger than  $4$  a.u.

### Conclusion

It appears that STOs when processed by the Löwdin  $\alpha$ -function method [6] can form basis sets that give excellent results for one-electron systems. Strategies developed here should prove useful in the study of more complicated systems.

### Acknowledgments

This work was supported by the Air Force Office of Scientific Research under Contract No. F49620-92-J-0063, and NASA (CENNAS). The authors thank the Flor-



ida State University Supercomputer Computations Research Institute for computer time.

### Bibliography

- [1] B. H. Wells and S. Wilson, *J. Phys.* **B22**, 1285 (1989).
- [2] F. O. Steinborn and E. J. Weniger, *Int. J. Quantum Chem. Quantum Chem. Symp.* **12**, 103 (1978).
- [3] H. W. Jones and B. Etemadi, *Phys. Rev.* **A47**, 3430 (1993).
- [4] International Mathematical and Statistical Library, Houston, TX.
- [5] T. G. Winter, M. D. Duncan, and N. F. Lane, cited in L. Laakonen, P. Pyykko, and Dage Sundholm, *Int. J. Quantum Chem.* **23**, 309 (1983); *J. Phys.* **B10**, 285 (1977); T. G. Winter, private communication.
- [6] H. W. Jones and C. A. Weatherford, *J. Mol. Struct. (Theochem)* **199**, 233 (1989).

Received July 14, 1993

# Low-Lying States of SF<sub>6</sub> and SF<sub>6</sub><sup>-</sup>: Electron Affinity of SF<sub>6</sub> and Electron Detachment of SF<sub>6</sub><sup>-</sup>

KENT W. RICHMAN\* and AJIT BANERJEE

*Theory Project, Idaho National Engineering Laboratory, EG & G Idaho, Inc., P.O. Box 1625,  
Idaho Falls, Idaho 83415*

## Abstract

Calculations have been performed on low-lying states of SF<sub>6</sub> and SF<sub>6</sub><sup>-</sup> at the complete active space multiconfiguration self-consistent field (CAS-MCSCF) level. These calculations involved optimization of basis function exponents, particularly the *f*-functions on sulfur and their effect on the potential energies and the SF<sub>6</sub> electron affinity. The CAS-MCSCF calculations for the anion and neutral included 4,863 and 2,115 configuration functions, respectively. Octahedral and selected distorted geometries were considered. The ground-state equilibrium geometries correspond to the octahedral configuration of SF<sub>6</sub> (<sup>1</sup>A<sub>1g</sub>), R(S—F) = 1.56 Å, ω<sub>e</sub> = 776 cm<sup>-1</sup>, and of the anion SF<sub>6</sub><sup>-</sup> (<sup>2</sup>A<sub>1g</sub>), R(S—F) = 1.70 Å, ω<sub>e</sub> = 558 cm<sup>-1</sup>. The adiabatic and vertical electron affinities are found to be -0.63 and 1.8 eV, respectively. Electron autodetachment phenomena associated with the anion are also discussed and a possible mechanism for this process is presented. © 1993 John Wiley & Sons, Inc.

## Introduction

The SF<sub>6</sub> molecule has been the object of many studies, both experimental and theoretical during the last several years. This interest is driven largely by the fact that SF<sub>6</sub> has a very high cross section for electron capture, forming the SF<sub>6</sub><sup>-</sup> anion. Experiments on the ground-state anion indicate that it has multiple autoneutralization modes. Lifetimes for the electron autodetachment process have been measured in drift tube experiments, and it appears that the autoneutralization process is relatively facile, with lifetimes between 2–40 microseconds [1,2]. The ease with which the electrons autodetach suggest that the detachment process is not dipole or photo-induced, but probably arises through intra- or intermolecular energy transfer and surface crossings.

The observed properties of the SF<sub>6</sub>/SF<sub>6</sub><sup>-</sup> system has prompted numerous studies of the adiabatic electron affinity (AEA) of the neutral molecule. While the experimental value has been reported to be as low as 0.4 eV and as high as 1.4 eV [3–9], the currently accepted value is very near 1.0 eV, as obtained by Streit using a bracketing method, measuring the rates of ion–molecule reactions involving electron transfer [7], and later by Grimsrud et al., with thermodynamic measurements obtained using a pulsed-electron high-pressure mass spectrometer [8].

From a theoretical standpoint, the SF<sub>6</sub>/SF<sub>6</sub><sup>-</sup> system poses a challenge to researchers interested in calculating the correct value for the neutral AEA, and for describing

\* Present Address: Tracor Aerospace Inc., Tracor GIE Division, 1652 W 820 N Provo, UT 84601.

the modes for electron autodetachment. With 70 and 71 electrons for the neutral and anion, respectively, severe restrictions are placed on the basis set size for practical calculations. This problem is aggravated by the large basis set requirements for calculating the electron affinities of even simple atomic species. In addition, the level of electron correlation required to adequately describe the relative differences between the neutral and anion systems is unknown.

Undaunted by the difficulties expected in these calculations, several researchers have attempted the theoretical determination of the aEA of  $\text{SF}_6$ , with various degrees of success. As a prelude to describing the work performed in this effort, it will be instructive to briefly review some pertinent theoretical results obtained to date. All reported studies have assumed an octahedral geometry for both the neutral and anion. Hay calculated the self-consistent field (SCF) value of aEA to be 1.03 eV without zero-point correction [10]. However, the basis sets used by him have since proved to be inadequate for correctly determining the relative electronic energies of both the neutral molecule and anion. Thus the agreement between his value and the experimental value appears to be fortuitous.

Klobukowski et al. performed a careful study of the basis set requirements for studying the neutral-anion system at the SCF level and have determined the following [11]:

- (1) The use of a larger basis set gives a much different value for the aEA of  $\text{SF}_6$ , but does not change the calculated geometries of the neutral and anion significantly from those obtained by Hay.
- (2) A 3*d* orbital on sulfur has little effect on the calculated aEA.
- (3) The aEA decreases by about 1 eV by simply adding a *d* polarization function to the fluorine basis. This basis set, similar to the one used by Hay, produces an electron affinity of 1.40 eV.
- (4) Adding an *f*-type function to the sulfur basis lowers the electron affinity by over 0.5 eV.

The final value for the aEA of  $\text{SF}_6$  obtained by Klobukowski, using their largest basis, is -0.34 eV at the SCF level. Thus, providing this basis is adequate, the Hartree-Fock value for the electron affinity of  $\text{SF}_6$  is negative.

In an effort to determine the effects of electron correlation on the electron affinity of  $\text{SF}_6$ , Miyoshi et al. performed both SCF and configuration interaction (CI) calculations on the neutral and anion [12]. Using a relatively large basis set, with *d* polarization functions on both sulfur and fluorine, these workers obtained an aEA of -0.30 eV, in agreement with the best value obtained by Klobukowski. This agreement is interesting since Miyoshi did not use an *f*-function on sulfur. Thus, it is likely that adding an *f*-function to their sulfur basis will lower their Hartree-Fock value for the aEA of  $\text{SF}_6$  even further.

Miyoshi's CI calculation on both the anion and neutral was performed using a much smaller basis set than they used for their SCF study. The CI energy obtained from this basis combined with their SCF energy using the larger basis set gave a value for the aEA of  $\text{SF}_6$  of 1.06 eV, in excellent agreement with the currently accepted experimental value. At first glance this monumental effort seems to complete the picture concerning the relative potential energies of  $\text{SF}_6$  and  $\text{SF}_6^-$ . However,

there remain some nagging questions which have not adequately been answered in the analysis of Miyoshi. The first is the effect of the inclusion of an *f*-function on sulfur, which was left out of the Miyoshi basis set, but as Klobukowski clearly showed lowers the neutral potential energy curve by half an electron volt relative to the anion curve, and thus lowers the neutral aEA. The second is the consideration of nonoctahedral geometries for the anion.

In this study we have attempted to determine the effect of the sulfur *f*-function and nonoctahedral anion geometries on the aEA of SF<sub>6</sub>, using both SCF and CAS-MCSCF calculations. We have also explored low-lying excited states of both the anion and neutral at the SCF level with relatively large basis sets, complementing earlier work on the neutral molecule by Hay [13]. Vibrational states of both species were also determined in an attempt to rationalize the electron attachment-detachment properties of the neutral molecule.

### Theoretical Procedure and Results

The basis sets employed for the SCF calculations in this study were based on Huzinaga's well-tempered sets [14]. In the largest basis sets for sulfur, the tightest primitives for both the *s* and *p* sets were removed. A diffuse *s*-function (zeta = 0.0023) and two diffuse *p*-functions (zeta = 0.041 and 0.002) were added. The sulfur basis set was augmented with two *d*-functions (zeta = 0.659 and 0.183) and one *f*-function. To determine the proper choice of *f*-functions for the sulfur basis, the exponent was varied from 0.22 to 1.02 for both the anion and neutral. For the anion <sup>2</sup>A<sub>1g</sub> state, the minimum energy was obtained for an *f*-function with  $\zeta = 0.64$  while for the neutral <sup>1</sup>A<sub>1g</sub> state the best exponent was 0.68. It is fortunate that the optimum *f*-function for both the anion and neutral is similar. The value used by Klobukowski was 0.62 determined from the overlap criterion [14]. For consistency we used the value of  $\zeta = 0.62$  for both the anion and neutral. To determine whether one *f*-function is indeed adequate, an additional calculation was performed using two *f*-functions ( $\zeta = 0.41$  and 0.93). The calculated aEA at the SCF level with two *f*-functions was only 0.02 eV smaller than that calculated using one *f*-function ( $\zeta = 0.62$ ). Thus it appears that one *f*-function on sulfur is adequate. The sulfur basis was contracted to (12,12,11,1,1/8,8,1,1,1/1,1/1), that is, the sulfur basis consisted of 5*s*, 5*p*, 2*d*, and 1*f* function. The 5*s* functions contained 12, 12, 11, 1, and 1 primitive gaussian functions, respectively, while the 5*p* functions contained 8, 8, 1, 1, and 1 primitive gaussian functions.

For the largest basis for fluorine, again the tightest primitives for both the *s*- and *p*-functions of Huzinaga's well-tempered set were removed. The set was augmented by a diffuse *s*-function (zeta = 0.07392) and a *d*-function (zeta = 1.496). The fluorine basis set was contracted to (10,11,1/8,1,1,1/1).

For the MCSCF calculations, two additional diffuse *s*-functions on sulfur were added (zeta = 0.0002 and 0.00002) and the final set was contracted to (12,12,11,1,1,1,1/8,8,1,1,1/1,1/1). Thus, for the sulfur atom and six fluorine atoms 189 primitive gaussian functions were used for the MCSCF calculations.

The MCSCF calculation was performed by defining an active space common to both the anion and neutral molecule and allowing all single and double excitations

TABLE I. Active space for the MCSCF calculation.

Orbital	Anion orbital energy (Hartrees)
* $b_{1u}$	0.31846
* $b_{2u}$	0.30446
* $b_{2g}$	0.28418
$4e_g$	0.23683
* $t_{1u}$	0.18869
$7a_{1g}$	0.16323
$6a_{1g}$	-0.14944
$1t_{1g}$	-0.43445
$1t_{2u}$	-0.45389
$5t_{1u}$	-0.46512
$3e_g$	-0.45452

from the SCF configuration within this active space. The active molecular orbitals, along with their orbital energies are presented in Table I. For the anion, this active space generated 4,863 CSF's, while 2,115 CSF's were generated for the neutral. The CAS-MCSCF calculations in this study required nearly 300 h using a CRAY-YMP computer.

The calculated total energies at the SCF level along the totally symmetric stretching mode are presented in Table II and the potential energy curves are presented in

TABLE II. SCF and MCSCF total energies (Hartrees) for  $SF_6$  and  $SF_6^-$ .

$R$ (au)	SCF		CAS-MCSCF	
	Neutral ( ${}^1A_{1g}$ )	Anion ( ${}^2A_{1g}$ )	Neutral ( ${}^1A_{1g}$ )	Anion ( ${}^2A_{1g}$ )
2.75	-994.235392	-994.230650		
2.80			-994.581848	-994.576528
2.85	-994.282693	-994.277987		
2.90	-994.289813	-994.285143		-994.610003
2.914	-994.290161			
2.95	-994.288100	-994.283491	-994.617690	
3.00	-994.278938	-994.274437	-994.612580	-994.607661
3.05	-994.263536	-994.259264		
3.10	-994.242951	-994.239444	-994.585061	-994.581183
3.125		-994.257088		
3.15	-994.218107	-994.259593		-994.590706
3.182		-994.260823		
3.20	-994.189809	-994.260377		-994.594521
3.225		-994.258832		
3.25	-994.158760	-994.256113	-994.513949	-994.593266
3.35	-994.090751	-994.235175		-994.567369

Figure 1. A striking feature of the anion curve is the local minimum at the neutral equilibrium geometry. This feature was not mentioned in the work by Miyoshi, but it was found by us and by Klobukowski that the composition of the anion  $6a_{1g}$  orbital is dominated by the most diffuse functions in the region of the neutral  $R_e$ , thus the extra electron is not truly bound to the  $\text{SF}_6$  molecule at this geometry. Instead, this region of the anion curve represents the neutral molecule, with the free electron occupying the most diffuse orbital available within the basis set. In the current basis, this orbital is seen to reside almost entirely on the sulfur atom and is dominated by contributions from the very diffuse  $s$  gaussian functions added to the Huzinaga basis. Therefore, in the limit of an infinitely diffuse basis set, the electron simply detaches at this geometry, leaving the neutral  $\text{SF}_6$  molecule and a free electron.

The total energies and potential energy curves at the MCSCF level are also shown in Table II and Figure 1. Spectroscopic properties from these curves were obtained by passing a rounded ramp interpolating function through the calculated data [15].

Interpolated data generated in this way were then fit to a Hulburt-Hirschfelder potential function [16]. The spectroscopic properties and aEA obtained from these potential energy curves are presented in Table III. The known experimental spectroscopic values are in excellent agreement with those calculated at the MCSCF level. However, the calculated EA's at the SCF level are in very poor agreement with experiment and in fact, have the wrong sign. Our SCF value of  $-0.68$  eV is lower than that obtained in previous studies. The inclusion of electron correlation at the CAS-MCSCF level presented here does little to improve the situation. It should be noted that the correlation energy recovered in this study is only about one-third that obtained by Miyoshi. By simply adding their correlation energies to our SCF energies, a value of  $+0.68$  eV for the aEA of  $\text{SF}_6$  is obtained.

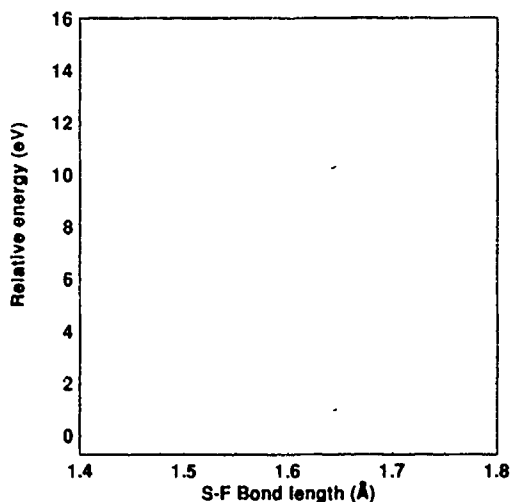


Figure 1. SCF (solid lines) and CAS-MCSCF (dashed lines) potential energy curves for the  $A_{1g}$  states of  $\text{SF}_6$  and  $\text{SF}_6^-$ .

TABLE III. Spectroscopic properties for SF<sub>6</sub> and SF<sub>6</sub><sup>-</sup>.

		SCF	CAS-MCSCF	Experiment
$R_e$ (Å)	neutral	1.54	1.56	1.565 [17]
	anion	1.68	1.70	
$\omega_e$ (cm <sup>-1</sup> )	neutral	863	776	769 [17]
	anion	680	558	
$\omega_e x_e$ (cm <sup>-1</sup> )	neutral	23	19	
	anion	14	10	
SF <sub>6</sub> adiabatic electron affinity (eV)		-0.68	-0.63	1.0 [7.9]

To complete the characterization of the potential energy curves of SF<sub>6</sub> and SF<sub>6</sub><sup>-</sup>, the Hulburt-Hirschfelder potentials were used to generate the first few vibrational levels for the molecules. These levels, for the neutral and anion at both the SCF and MCSCF levels are presented in Table IV. These data show at most one bound vibrational level for the anion. Above this energy, the electron detaches. Note that the first vibrational level of the anion is very close in energy to the second vibrational level of the neutral.

To account for possible Jahn-Teller effects, selected nonoctahedral geometries were also considered in this study. These calculations, as well as calculations of neutral and anion excited states were performed using the SCF basis set described above, without the  $f$ -function and diffuse  $s$ -functions on sulfur.

The potential energy curves for the  $^1T_{1g}$  and  $^1T_{1u}$  states of the neutral as well as the  $^2T_{1g}$  and  $^2T_{1u}$  states of the anion are shown in Figure 2, along with the  $^1A_{1g}$  and  $^2A_{1g}$  states of the neutral and anion, respectively. For the ground-state neutral molecule, the outer electron configuration in octahedral symmetry is  $(1t_{2u})^6(5t_{1u})^6(1t_{1g})^6$ , while for the anion, the ground state is  $(1t_{2u})^6(5t_{1u})^6(1t_{1g})^6(6a_{1g})^1$ . The neutral and anion  $T_{1g}$  states are created from the excitation  $1t_{1g}-6a_{1g}$ , while the  $T_{1u}$  states are obtained from the excitation  $5t_{1u}-6a_{1g}$ . The very large electronic energies separating these excited states from the ground states make it unlikely that they are involved in any experimental determinations of the aEA of SF<sub>6</sub>, nor is it likely that they play a role in any autodetachment processes for the anion.

TABLE IV. Calculated vibrational levels (in eV) relative to the CAS-MCSCF energy of SF<sub>6</sub> at  $R_e$ .

Level	SCF		CAS-MCSCF	
	Anion	Neutral	Anion	Neutral
1	0.93	0.31	0.83	0.28
2	1.41	0.92	1.64	0.83
3	1.87	1.49	1.62	1.35
4	2.31	2.03	1.99	1.85
5	2.73	2.53	2.35	2.31

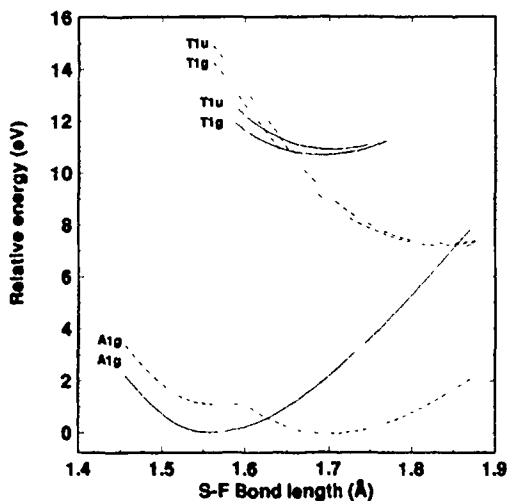


Figure 2. SCF potential energy curves for the ground and first two excited states of  $\text{SF}_6$  (solid lines) and  $\text{SF}_6^-$  (dashed lines).

While the ground state of  $\text{SF}_6$  has long been known to possess octahedral symmetry [15], no experimental evidence that this is the case for the anion has been presented. Breaking octahedral symmetry increases the number of symmetry adapted basis functions used in theoretical calculations. This added complexity makes it clear why octahedral symmetry has been assumed for the anion in all calculations to date. In this study we have calculated the potential energy surface for selected distortions from octahedral symmetry. For example, the molecule was allowed to distort along the  $E_g$  vibrational mode. That is, the axial fluorine atoms along the  $z$  axis were moved together, and the equatorial fluorine atoms in the  $xy$  plane were moved together. The potential surface for this distortion, which maintains  $D_{2h}$  symmetry is shown in Figure 3. It seems clear that this state of the anion does indeed prefer an octahedral geometry and all distortions from octahedral symmetry increase the energy. There are 15 vibrational modes for the anion and neutral molecule. These correspond to the symmetric  $A_{1g}$  and double degenerate  $E_g$  modes discussed above, as well as the triply degenerate  $T_{1u}$  (2),  $T_{2g}$ , and  $T_{2u}$  vibrational modes. The  $A_{1g}$  and  $E_g$  modes involve only bond stretching, while the  $T_{2g}$  and  $T_{2u}$  modes involve only angle deformation and the two  $T_{1u}$  modes involve both bond stretching and angle deformation. All of these fundamental modes have been observed in the neutral molecule, but no such experimental data exists for the anion.

In conclusion, the results of this research indicate that the formidable problem of calculating the aEA of  $\text{SF}_6$  remains unsolved. While the currently accepted experimental value has been obtained by others, our contention is that these results are fortuitous and further work in both the experimental and theoretical determinations is needed. For theoretical studies, a systematic basis set evaluation, in which basis functions are added and varied until the value of the electron affinity stabilizes is needed. Klobukowski's work is a good beginning for this effort. Experimentally,



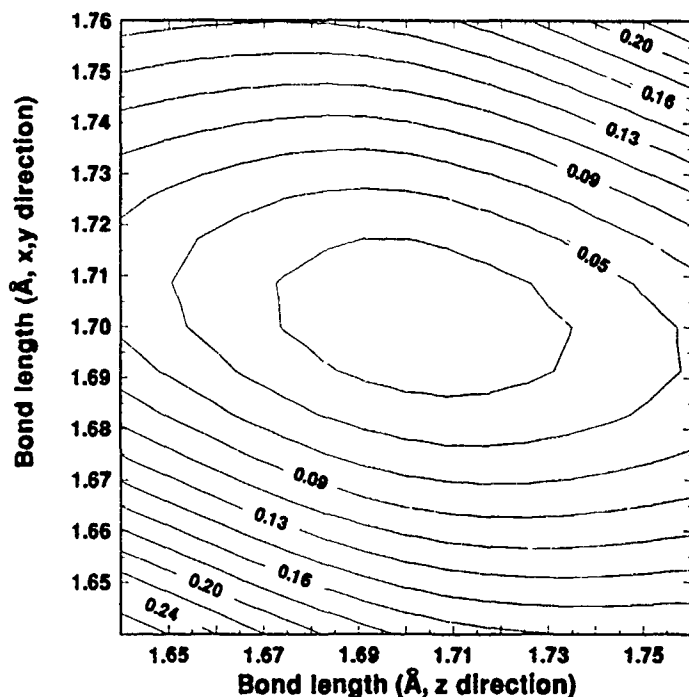


Figure 3. SCF potential energy surface of the ground state of  $\text{SF}_6^-$  near  $R_e$  along the  $E_g$  vibrational mode.

it is difficult in the reported collision studies to identify precisely the vibrational temperature of the anions produced. Anions formed in vibrationally excited states could produce erroneous values for the aEA.

Distortions conserving  $D_{2h}$  symmetry show clearly that the molecule prefers octahedral symmetry. Other distortions are certainly possible and should be explored. We have also explored some low-lying excited states and shown that they are much too high in energy to contribute to the experimental determination of the aEA.

In regard to the electron autodetachment process for the anion, the potential energy curves presented here are consistent with the experimental results. In order to create the anion in the first place, at least one vibrational state should be available. Our results show that there is exactly one. The ease of autodetachment would require this state to easily crossover to the neutral molecule/free electron state. As has been shown by others [18] for anion and neutral vibrational states  $\chi_v^-$  and  $\chi_v^0$ , respectively, with energies  $\epsilon_v$  and  $\epsilon_v^0$ , the transition  $\chi_v^- \rightarrow \chi_v^0$  is efficient if:

- (1) the anion and neutral potential energy surfaces intersect or approach one another in regions of the coordinate space where  $\chi_{v\pm 1}$  and  $\chi_v^0$  are nonvanishing and the highest occupied molecular orbital of the anion becomes very diffuse,
- (2) the change in slope in going from one surface to the other is small, and
- (3)  $\epsilon_v - \epsilon_v^0$  is small.

These criteria are met for the  $A_{1g}$  states of the anion and neutral. If this process is indeed involved in the autoneutralization of  $\text{SF}_6^-$ , then we would predict a strong positive temperature dependence on the rate of electron detachment.

Based on these findings, the multiple electron autodetachment rates observed for  $\text{SF}_6^-$  arise from initially creating anions in various different states, which each relax to a vibrationally hot ground-state molecule at different rates. The electron in the vibrationally excited ground-state anions then detach according to the mechanism described above.

### Acknowledgments

We acknowledge Dr. J. E. Delmore and Dr. K. Jordan for many helpful discussions. We would also like to thank the computer center at the Idaho National Engineering Laboratory for a generous grant of computer time. At Idaho National Engineering Laboratory, this work was supported by the EG&G Idaho Long Term Initiative Program under DOE contract DE-AC07-76ID01570, and by the office of Basic Energy Sciences, Chemical Sciences, under contract 3ED102.

### Bibliography

- [1] J. E. Delmore and A. D. Appelhans, *J. Chem. Phys.* **84**, 6238 (1986)
- [2] A. D. Appelhans and J. E. Delmore, *J. Chem. Phys.* **88**, 5561 (1988)
- [3] J. Kay and F. M. Page, *Trans. Faraday Soc.* **60**, 1042 (1964).
- [4] R. N. Compton, L. G. Christophoru, G. S. Hurst, and P. W. Reinhardt, *J. Chem. Phys.* **45**, 4634 (1966).
- [5] F. C. Fehsenfeld, *J. Chem. Phys.* **54**, 438 (1971).
- [6] R. N. Compton and C. D. Cooper, *J. Chem. Phys.* **59**, 4140 (1973).
- [7] G. E. Streit, *J. Chem. Phys.* **77**, 826 (1982).
- [8] S. P. Heneghan and S. W. Benson, *Int. J. Chem. Kinet.* **15**, 109 (1983)
- [9] E. P. Grimsrud, S. Chowdhury, and P. Kebarle, *J. Chem. Phys.* **83**, 1059 (1985).
- [10] P. J. Hay, *J. Chem. Phys.* **76**, 502 (1982).
- [11] M. Klobukowski, Z. Barandiarán, L. Seijo, and S. Huzinaga, *J. Chem. Phys.* **86**, 1637 (1987).
- [12] E. Miyoshi, Y. Sakai, and S. Miyoshi, *J. Chem. Phys.* **88**, 1470 (1988)
- [13] P. J. Hay, *J. Am. Chem. Soc.* **99**, 1013 (1977).
- [14] J. Andzelm, S. Huzinaga, M. Klobukowski, E. Radzio, Y. Sakai, and H. Tatewaki, *Gaussian Basis Sets for Molecular Calculations* (Elsevier, Amsterdam, 1984).
- [15] R. Q. E. Lagerlof, *Commun. of ACM* **17**, 476 (1974).
- [16] H. M. Hulburt and J. O. Hirschfelder, *J. Chem. Phys.* **9**, 61 (1941).
- [17] G. Herzberg, *Molecular Spectra and Molecular Structure, Vol. 2 and 3* (Krieger, Florida, 1991).
- [18] J. Simons, *J. Am. Chem. Soc.* **103**, 3971 (1981).

Received July 7, 1993

# High Performance Computing in Chemistry and Massively Parallel Computers: A Simple Transition?

RICK A. KENDALL\*

*Molecular Science Software, Molecular Science Research Center, Environmental Molecular Sciences Laboratory, Pacific Northwest Laboratory,<sup>†</sup> Richland, Washington 99352*

## Abstract

A review of the various problems facing any software developer targeting massively parallel processing (MPP) systems is presented. Issues specific to computational chemistry application software will also be outlined. Computational chemistry software ported to and designed for the Intel Touchstone Delta Supercomputer will be discussed. Recommendations for future directions will also be made. © 1993 John Wiley & Sons, Inc.

## Introduction

The advent of massively parallel processing (MPP) supercomputers has been an exciting and challenging benefit to computational science. Many of the algorithms and theoretical models used by the computational chemistry field are very compute-intensive and the computational chemistry market is an obvious target of many MPP vendors. Computational chemists have long been at the forefront of utilizing and developing software on the leading edge of computational technology. The delivery of first- and second-generation usable MPP hardware has enticed many computational chemistry groups to begin focusing efforts on the development of chemistry software for parallel computing systems. To date, efforts on modern MPP systems are distributed among primarily academic and national laboratory environments with little effort from the vendor community. These efforts also span the entire spectrum of computational chemistry methodologies and algorithms, e.g., from molecular modeling and dynamics to full configuration-interaction calculations, and have been conducted on the gamut of available MPP hardware. Furthermore, these efforts have made significant progress but the use of high performance computing systems, specifically massively parallel computers, is far from routine.

In this article I outline issues that challenge software development with respect to a very technologically volatile hardware industry as a whole with a focus on MPP systems of today and tomorrow. The perspective is that of a computational chemistry application developer and what I see available now and in the near future. No one

---

\* The author may be reached via email at [ra\\_kendall@cagle.pnl.gov](mailto:ra_kendall@cagle.pnl.gov)

<sup>†</sup> Pacific Northwest Laboratory is operated by Battelle Memorial Institute for U.S. Department of Energy (DOE) under Contract DE-AC06-76RLO1830

can predict long-term trends in the extremely volatile computer industry, so I will not try, except to state that software development will be different than the way applications are developed today. A discussion of the general issues with respect to MPP technology and issues around computational chemistry applications is presented, as well as results of chemistry applications on the Intel Touchstone Delta. Conclusions and recommendations are made in the final section.

### **Software Development Issues for MPP Computational Chemistry Software**

#### *Software Engineering, Hardware, and Software Life Cycle*

Any software engineering (SE) text warns that the lack of effort in the design of modular and reusable software will eventually cause a complex software system to collapse under its own weight [1]. The concepts of modularity and reusability are without regard to the particular programming language used for a given software system. The staffing requirements for maintaining a required but poorly designed application are substantial. Computational chemistry software applications are not immune from this process; in fact, many of the software developers in computational chemistry are graduate students rarely trained in any aspects of modern computer science or SE. The programming effort is usually the last part of the theoretical or model development and is sometimes less interesting to a student trying to finish a thesis effort.

Computing hardware has undergone a tremendous series of advances over the last two decades. The Supercomputing industry was born in the 1960s, flourished in the 70s and 80s, and has grown drastically in the last few years. In the 1970s and early 1980s the hardware designs lasted on the order of 5 to 7 years. The doubling of computer power with advances in hardware technology, and the interface to that technology, operating systems, optimizing compiler design, etc., progressed at a rate where software developers had the time to adapt and make algorithmic modifications to make optimal use of the computing resources available. In the last 5 years the hardware technology growth curve has taken a drastic change. With the advent of reduced instruction set chip (RISC) technology the period for doubling of raw compute power is now somewhere between 12 and 18 months (see Fig. 1 [2]). By the time a computer system is procured and delivered it is most likely out of date (although not obsolete). This rapid development has even caused the computing industry to implement leap frog hardware development efforts to keep pace with the demands of the computing user base.

The hardware used in the past and today has a standard life cycle [1]. When the hardware is first delivered or developed it usually has a high failure rate or is not as useful as might be expected. This is sometimes due to the overall software interface to that hardware. The bugs in the system get worked out and the system becomes useful. Then the user community, computational chemists included, saturate the resource to do scientific development and applications. Over time, the system becomes obsolete due either to the inevitable hardware failures or, as is more likely,

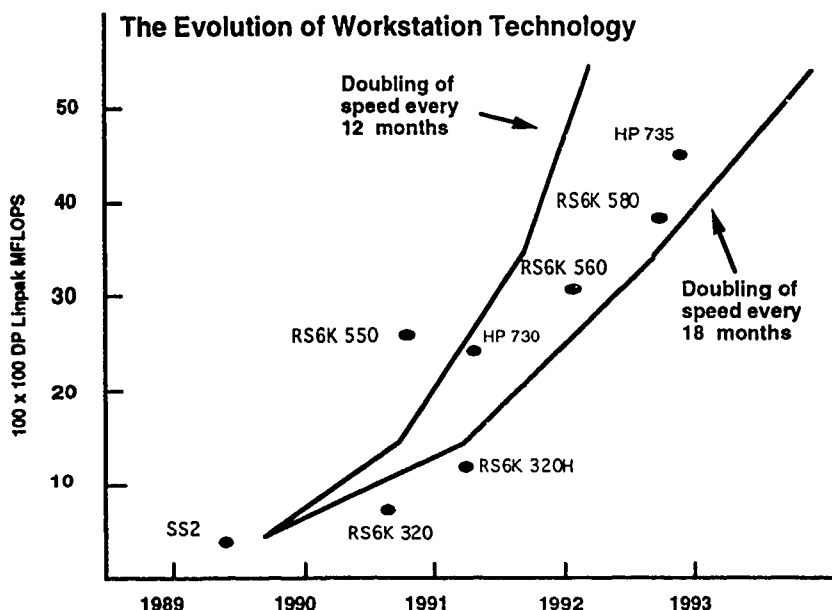


Figure 1. The rate of change of raw compute power available from workstations [2]

to the fact that the resource can no longer meet the computational requirements of the user community in a cost effective manner (see Fig. 2).

This simplistic "usefulness" model also applies to software as well [1]. The initial software application usually has a very limited set of functionality. As more robust algorithms and additional functionality are implemented the software becomes more "useful" to the user community. Without further algorithmic developments the "usefulness" of a software system will asymptotically approach some steady-state level and not deviate from that (see Fig. 3). What more realistically happens is that as new functionality is added more bugs and design flaws are uncovered and the failure rate of the application grows, with the software becoming less "useful". In time, maintenance and development efforts usually reduce the failure rate and make the code "useful" again. It has been said that the process of porting an application to an MPP environment is a process of "rebugging software" and the experience of the efforts in the computational chemistry community have shown this to be true.

### *Programming Models*

There are a wide variety of specific programming models and tools that can be used to develop a working programming system on a parallel computer [3-6]. The obvious and key point is that there must be a parallel algorithm for the requisite

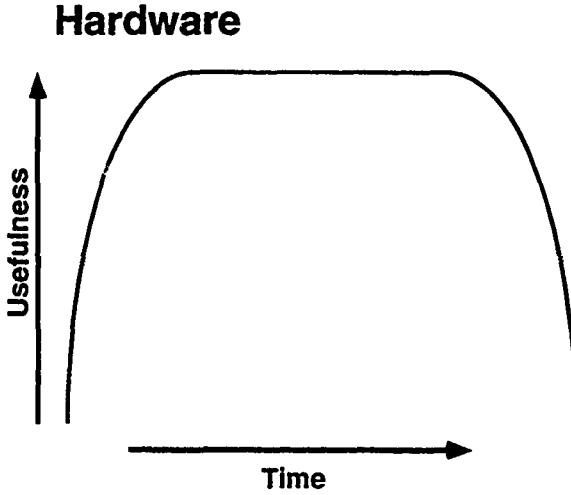


Figure 2. Hardware life cycle (Usefulness overtime).

computational task(s). The various programming models fall into the traditional classes of data parallel (DP), shared memory (SM), and distributed data/task models. The latter is the common multiple instruction multiple data (MIMD) programming model with message passing between processors. In practice most developers use a single program MIMD model and assign data and tasks based upon the identity of

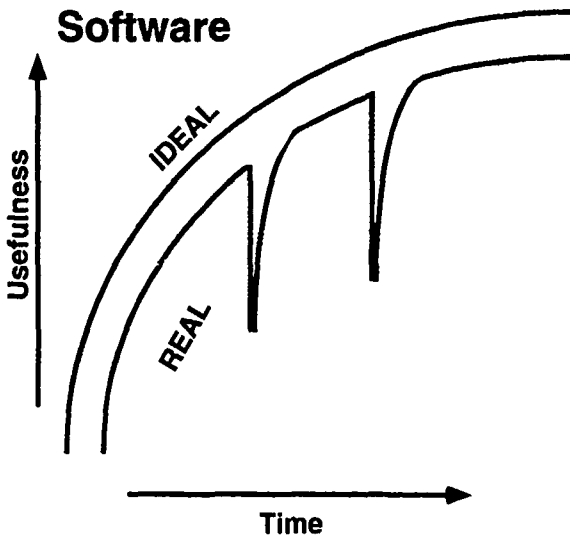


Figure 3. Software life cycle (Usefulness overtime).

a given processing node. The basic problem with all programming models is that on any given hardware there exists a locality of data problem. The program becomes a bookkeeping algorithm that finds the data for the computational task at hand.

In traditional SM environments there is a flat memory so access to any segment of memory is uniform. In DP and MIMD you have an obvious data locality problem when sharing data among processes and tasks. Simple replicated data algorithms circumvent this by holding a copy of the requisite vectors/matrices on each node. With the current vendor offerings of 16 to 64 Mbytes per physical processing node, this is a clear limitation. Moreover, the replicated data algorithms do not scale to hundreds or thousands of processors. These obvious problems have caused many vendors to look at globally addressed memory that is physically distributed. This gives the programmer the look and feel of a SM programming environment, a major benefit, but there are potentially drastic performance penalties for accessing nonlocal memory. This brings the data locality problem back to the programmer and the software tools available on the system. Now that several general aspects of various programming models have been outlined, a discussion of each in more detail follows.

The Shared Memory programming model is probably the most widely used and best understood model simply because of the amount of time that the computational community has used this technique, but few quantum chemistry codes make use of this programming model even today. There are several specific approaches that have been implemented on UNIX Workstations and on various low and high end supercomputers, (Silicon Graphics, Stardent, Alliant, Convex, Cray, etc.). The general scheme used to parallelize applications is to identify shared and private segments of memory and have the owner compute a specific portion of the shared data structures and all of the private data/tasks available to the specific process. There has been much compiler work done on this programming model and it is reasonably well understood by the computer science field. Programmers can tune and optimize their code using compiler directives that help the compiler understand the application layout. This is in my estimation the most efficient parallel programming model for computational chemistry applications in wide use today. Unfortunately, the underlying hardware is not scalable; it is very expensive to realistically extend to large numbers of processors (e.g., greater than 100) and very large memory sizes (e.g., greater than 10 Gwords). This has forced the development of the above-mentioned global accessible memory that is physically distributed (e.g., Kendall Square Research, Cray Research Inc. T3D, etc.). The overall programming model stays the same but there is an added task of making sure the data locality is preserved to avoid thrashing of pages from nonlocal processors.

The data parallel programming model is one that has been used primarily on the SIMD architectures by design but is not limited to these machines. This is also the underlying principle behind the High Performance FORTRAN (HPF) language specification [7], which augments the recently standardized FORTRAN90. HPF offers the ability to distribute vectors and matrices across the processes on a machine via compiler directives and declaration statements. The DP rule of thumb is that the owner computes the portion of the matrix/vector that it controls. The DP programming model works extremely well if there is no load balancing or data

dependencies across processes (Finite Element or grid calculations, Fourier transforms, etc.). In a pure SIMD program, load imbalance causes many processors to be idle at either the beginning or end of a series of parallel tasks. HPF offers extrinsic procedures or routines to handle access to message-passing facilities which can handle data dependency aspects. Most computational chemistry algorithms have either very irregular data structures or access a regular data structure in an irregular fashion and are thus not suited for pure DP programming models. For example, in the formation of the closed-shell Fock matrix a two-electron integral contributes to six independent Fock matrix elements all of which may not be accessible in a given distribution of the Fock matrix. The HPF draft standard acknowledges the difficulties of irregular data structures or access to data structures, and there are plans for a follow on language specification that will address irregularity issues. There is great potential for such standard languages or extensions to existing languages once this issue is addressed.

The message passing programming model is probably the most widely used programming model on distributed memory architectures. The basic principles are that every process has a local memory addressable only by that specific processor and it can only access nonlocal information by passing a message to another process that has other needed data. Tasks and the required data structures can be farmed out to various processors via these messages and the parallel calculation performed. Messages can usually be sent synchronously or asynchronously, but this is system dependent. Synchronous messages require the cooperation of both processes. Asynchronous message passing can be useful but requires buffer space for messages to make them effective. The ability to pass asynchronous messages offers a more robust programming environment because it does not require a sequential bottleneck of the sending and receiving processors. A message-passing program makes the speed and latency of the underlying hardware an important aspect of the algorithm and software design. If the application requires only short messages then the latency or overhead for sending each message is important (e.g., molecular dynamics simulations). If the application requires a few messages that are relatively large (ca. 1 Mbyte) then the speed or bandwidth of the underlying communication network is important (e.g., a replicated data Hartree-Fock code). Many computational chemistry applications contain both aspects. The general course grained aspect of integral generation and Hartree-Fock procedures are ideal for this programming model and the currently available vendor offerings. More complicated and useful chemistry applications have finer granularity and are thus limited by the underlying communication network (e.g., Multiconfiguration Self-Consistent Field energy and energy derivative methods).

The final programming model that I would like to discuss is that of distributed data. This programming model borrows strongly from that of the Linda language [8]. The concept is straightforward and is really an extension to any of the above programming models. The concept is similar to that of elaborate memory paging algorithms used in many time-sharing computers today. In Linda, the user has the concept of a tuple as an abstract data object that can be stored and retrieved to and from "tuple space" as well as user-defined functions that can be used to trans-



form the data via an "eval" call. The advantage of having this "secondary" memory storage is that the location of the data and the mechanisms for moving or "paging" the data are removed from the programmer. This gives the look and feel of a segment of "shared" memory that is accessible by all processes. There are potentially performance problems with the way the distributed data is accessed, stored, and transformed but the distributed data programming model lessens the impact on computational programmers using distributed computing models. The details of the storing and retrieving data from the distributed data space can be implemented in shared memory or message passing allowing applications to be more portable. Harrison has developed and successfully demonstrated a distributed data model for the Intel Touchstone Delta supercomputer that uses the interrupt driven mechanisms available on that machine [9]. Similar work has been done by Rendell et al. specifically for the closed-shell coupled cluster algorithm [10]. In general, computational chemistry applications will not need the full functionality of a Linda-type implementation, but only well-defined data types, (e.g., for FORTRAN integer, double precision, character, etc.) [9]. This functionality is projected to be the first useful programming model for the next generation of scalable computational chemistry applications.

### *Portability and Resource Utilization*

Portability is an issue that has plagued FORTRAN computational chemistry applications for many years. Unlike many modern languages, there is no language-specific mechanism for isolating machine-dependent code in FORTRAN. There are several different approaches that can be used to get around this problem. Many free and some commercial systems for FORTRAN code maintenance exist and are widely used by the computational chemistry community. Writing only FORTRAN77 or FORTRAN90 is not a viable option because many chemistry applications interface with the system environment to get timing information, use special disk I/O routines, check system runtime characteristics, etc. The various complexities of the above-mentioned programming models will also add to the overall complexity of a "portable" application. A review of the computational chemistry literature over the last few years will show that chemists will use as many of the theoretical models as is feasible for the solution of a given chemistry problem. This aspect alone will compel the integration of computational chemistry applications into a suite of functionality with a common "user interface." The development of this interface is a research topic in its own right and beyond the scope of this article. It is imperative that the core functionality application suite use modularity and more commercial style software practices (e.g., long-term use or reuse of software) to maintain the integrity of applications across the various platforms, from the workstation to the high performance computing supercomputer.

Resource utilization is an issue that will have to be addressed by both the user and vendor communities. Users are accustomed to sharing workstations and traditional supercomputers based on a round robin or time slice multi-user scheduling system. On current MPP offerings this is simply not feasible. The scheduling of resource utilization is a research topic in the computer science field. Users will have

to become accustomed to more batch utilization and space sharing of the resources. The disk I/O capacity is usually the limiting factor. For example, on the Intel Touchstone Delta supercomputer there are 512 compute nodes with 16 Mbytes of memory each, for a total of 8 Gbytes of memory. The aggregate I/O rate on that machine under the normal operating system is less than 12 Mbytes/sec. This means to roll out a job using all nodes would require at least 11 min. The next generation MPPs will not be much better because the I/O subsystem is the least improved component. Again this is an active computer science research topic. The computational chemistry community cannot and will not wait for these problems to be solved. This means that the application developers must be more aggressive in checkpointing their own algorithms with only the requisite restart data being written to disk.

### Review of Chemistry Applications

The use of parallel applications in chemistry is not a new idea. Reports of using available parallelism on minicomputers date back to the early and mid 1980s [11-15]. There are a few current research efforts around the world targeted at the development of software on current and future generation MPPs. These include mostly academic and national laboratory efforts, although a few vendors have openly stated that they have started a port of the Gaussian software in collaboration with Gaussian, Inc. The academic research efforts include GAMESS-USA from Mark Gordon's group at Iowa State University, DISCO from Jan Almlöf and coworkers at University of Minnesota, Columbus from Hans Lischka at the University of Vienna (in collaboration with the Ohio State University and Argonne National Laboratory), various applications from Bill Goddard at Caltech, and a new initiative at the San Diego Supercomputer Center run by Peter Taylor. The national laboratory efforts include various chemistry applications at Argonne National Laboratory, Pacific Northwest Laboratory, Sandia Laboratories, the National Institutes of Health, and the SERC Daresbury Laboratory in England. This list does not encompass all researchers working on or planning MPP application development but does include the research groups that have significant resources for their effort. I have also limited the list to efforts I have some direct knowledge of the software being developed.

Molecular dynamics (MD) applications have been using MPP systems from the beginning of the development of these parallel computing systems. Various algorithms have been developed, systolic loop, linked cells, and replicated data systems [16,17]. Due to the relatively small memory requirements of most MD applications the replicated data algorithms have been most widely used (c.f. Ref. [17]). The advent of larger memory capacities and faster communication subsystems with decreased latency characteristics on next generation MPPs will keep the replicated data algorithms in wide use over the next few years. The same technological advances will also allow the refinement and improved performance of the other parallel algorithms that have been implemented. The replicated data algorithms do not scale to thousands of nodes and thus MD applications will need further development once the scientific demands of the applications increase. The MD applications are approaching routine utilization of current MPP systems and are generating results that require the increased computational resources available at various MPP sites.

Traditional *ab initio* software applications have had much less routine development on MPP machines. Simple replicated data algorithms are useful but the memory size on most MPP machines ranges from 16 to 32 Mbytes per node which is a severe limitation. For example, in a replicated data Hartree-Fock code, the entire density matrix and Fock matrix would be stored on each node. This would allow each integral to be partially summed with the appropriate density matrix element in to the requisite six Fock matrix elements. Once all integrals are computed the "partial" Fock matrices would then be globally combined into the full Fock Matrix and diagonalized. After a new density matrix was formed and broadcast to each process the iterative process would continue. This scheme replicates two  $N^2$  matrices and is thus parallel over the  $N^4/8$  integral generation work. However, on a machine that has 16 Mbytes of memory you could have no more than two  $1000 \times 1000$  square matrices in core memory. In reality the operating system takes up some memory, the software uses memory, and thus there is room for much fewer matrix elements. The thrust of most efforts is to go beyond this limitation by distributing the data structures of a given calculation to allow the problem to scale to the full memory of the machine and not the limitations imposed by the per node memory. From this simple example it is hopefully clear that the transition to MPP software development also requires more up-front analysis of the algorithmic designs.

In the above Hartree Fock application domain the type of distribution has different computation, communication, and memory tradeoffs. Colvin and coworkers [18] have implemented an application that distributes both the Fock and density matrices that requires  $N^4/2$  instead of the typical  $N^4/8$  integral generation work. This distribution scheme also can suffer from load imbalance in the parallel integral computation. In this distribution scheme a lack of memory has been traded for more integral computation. The most promising technique to date, is that of Foster [19] who has developed a distribution scheme that stores  $O(N)$  Fock and density matrix elements on each processor but it is based on the following assumptions. The integrals all cost the same number of flops and are computed one at a time (i.e., not in groups over shells). Unfortunately, these assumptions are not in line with modern efficient and parallel integral algorithms. In this distribution scheme communication is increased to allow for a fixed computational cost of the integral evaluation. However, Foster's efforts do show promise once the shell grouping of integrals is addressed.

Even with the above-mentioned problems there are several useful *ab initio* applications in use on MPP systems. GAMES-USA, GAMES-UK, and Columbus are now in production use by their respective groups on Intel MIMD machines with specific functionality (i.e., not all) parallelized [20-23]. Harrison and Stahlberg have implemented an object-oriented style full CI code on the Intel Touchstone Delta supercomputer that sustains 4 GFLOPS (20% of peak performance) [24]. The distributed data models used by Harrison and Stahlberg were implemented by Rendell and coworkers in his coupled-cluster singles and doubles code [10]. Feyereisen and coworkers [25] have implemented a master/slave replicated data version of Almlöf's DISCO SCF/MP2 program on the Intel Touchstone Delta supercomputer using a message passing library, TCGMSG, written by Harrison [26]. DISCO

has also been ported to workstation clusters using TCGMSG, LINDA, PVM<sup>4</sup>, and EXPRESS [27]. For all these codes to become production quality the above-mentioned scaling issues need to be addressed. These developments show great promise and are likely to be the foundation of *ab initio* applications developed in the future. I would recommend the reading some of the specific references for more details of the implementation and performance parameters of each of these codes on current MPP systems.

### Conclusions

What is needed to bring MPP into routine computational chemistry production? This can be summed up in one word; *software*. This means both the software to facilitate application developments and the application software itself. It is unlikely that the large industrial user community will convert to MPP utilization until the commercial software base or high quality, high performance software from academic and national laboratory efforts is available for use on these high performance supercomputers or MPPs. The commercial software developers probably won't make the effort until a more significant market exists. This will require the computing environments on the MPP machines to be much more robust and a pool experienced development personnel must become available to commercial software companies from the academic areas.

The development of new algorithms and associated software must keep abreast of changes in the computing environments available. In this article I have attempted to point out a subset of the issues that need to be considered and addressed by both the computational science and computer science communities. MPP development has coerced a coupling of these disciplines and this coupling provides a new opportunity to guide the development to the solutions of some of these issues. No one discipline can solve all the problems that exist or that will be uncovered over the next decade. I have also tried to point out some of the problems associated with computational chemistry applications with respect to MPP development and production use. The important factor here is doing the chemistry required to solve problems posed to us either in basic or applied research. MPPs are an obvious tool to use due to the computational requirements of the theoretical models used today and that will be used in the future. I have also outlined a subset of the research efforts currently in place. Beyond the required computational science training and education it is important that development groups get access to the latest technology to develop and refine research ideas. Moreover, collaborative efforts with computer science and other computational science efforts are essential for the development of MPP software. In regards to the question I have posed in the title, is the transition to MPP high performance computing a simple one? I hope so.

### Acknowledgments

This work was performed under the auspices of the Environmental Restoration and Waste Management, U. S. Department of Energy under the Environmental and Molecular Sciences Laboratory Project D-384 and under contract DE-AC06-76RLO 1830 with Battelle Memorial Institute, which operates the Pacific Northwest Laboratory. I would also like to thank R. J. Harrison, M. F. Guest, A. P. Rendell,

R. L. Stevens, and R. J. Littlefield for valuable insight and review of the manuscript. I gratefully acknowledge the support of the Sanibel organizing committee for their partial support in attending the 1993 Sanibel Symposium. Some of the research efforts described in this article use in part the Intel Touchstone Delta System operated by California Institute of Technology on behalf of the Concurrent Supercomputing Consortium. Access to this facility was provided by Pacific Northwest Laboratory.

### Bibliography

- [1] R. S. Pressman, *Software Engineering a Practitioner's Approach*, 3rd ed. (McGraw-Hill, New York, 1992).
- [2] D. F. Feller, "The MSRC Ab Initio Methods Benchmark Suite. A Measurement of Hardware and Software Performance in the Area of Electronic Structure Methods," Technical Report PNL-8670, July (1993).
- [3] K. M. Chandy and J. Misra, *Parallel Program Design* (Addison-Wesley, Reading, MA, 1988).
- [4] D. W. Heermann and A. N. Burkitt, *Parallel Algorithms in Computational Science* (Springer-Verlag, New York, 1991).
- [5] K. Hwang and F. A. Briggs, *Computer Architecture and Parallel Processing* (McGraw-Hill, New York, 1984).
- [6] G. R. Andrews, *Concurrent Programming Principles and Practice* (Benjamin/Cummings, New York, 1991).
- [7] The HPF draft standard is available from anonymous file transfer from titan.rice.cs.edu. More information can be obtained by sending mail to hpff-info@cs.rice.edu.
- [8] N. Carnero and D. Gelernter, *Commun. ACM* **32**, 444 (1989).
- [9] R. J. Harrison, *Theor. Chim. Acta* **84**, 363, (1993).
- [10] A. P. Rendell, M. F. Guest, and R. A. Kendall, "A Distributed Data Parallel Coupled Cluster Algorithm. Application to the 2-Hydroxypyridine/2-Pyridone Tautomerism" accepted in *J. Comput. Chem.*
- [11] R. Seeger, *J. Comput. Chem.* **2**, 168 (1981).
- [12] R. A. Bair and T. H. Dunning, Jr., *J. Comput. Chem.* **5**, 44, (1984).
- [13] E. Clementi, G. Corongiu, J. H. Detrich, H. Khanmohammadbagi, S. Chin, L. Domingo, A. Laaksonen, and H. L. Nguyen, *Proc. Int. Symp. Struct. Dyn. Membr. Nucleic Acids Protein*, (Adenine Press, Guilderland, New York, 1985), pp. 49-86.
- [14] P. O. Lowdin, *Lect. Notes Chem. Supercomput. Simul. Chemis.* **44**, 1-48 and 244-245 (1986).
- [15] R. A. Whiteside, J. S. Binkley, M. E. Colvin, and H. F. Schaefer, III, *J. Chem. Phys.* **86**, 2185, (1987).
- [16] W. Smith, *Comp. Phys. Commun.* **62**, 229, (1992), and references therein.
- [17] *Proceedings of a Workshop on High Performance Computing and Grand Challenges in Structural Biology*, held at Florida State University, January 24-27, (1992).
- [18] M. E. Colvin, C. L. Janssen, R. A. Whiteside, C. H. Tong, *Theor. Chim. Acta*, **84**, 301, (1993).
- [19] I. Foster, private communication.
- [20] T. Windus and M. Gordon, private communication.
- [21] M. F. Guest, private communication and *GIMESS-UK Users Guide and Reference Manual* Revision A1, STFC Daresbury Laboratory, (1990).
- [22] R. J. Harrison and R. A. Kendall, *Theor. Chim. Acta* **79**, 337 (1991).
- [23] T. Kovar and H. Lischka, private communication.
- [24] R. H. Harrison and E. A. Stahlberg, "Massively Parallel Full Configuration Interaction Benchmark Electronic Structure Calculations on the Intel Touchstone Delta," submitted to *Journal of Parallel and Distributed Computing*.
- [25] M. W. Feyereisen and R. A. Kendall, *Theor. Chim. Acta* **84**, 289, (1993), and references therein.
- [26] R. J. Harrison, *Int. J. Quant. Chem.* **40**, 847, (1991).
- [27] M. W. Feyereisen, R. A. Kendall, J. Nichols, D. Dame, J. T. Golab, *J. Comp. Chem.* **14**, 818 (1993).

# Atomistic Simulations on Parallel Architectures

RAJIV K. KALIA, WEI JIN, SIMON W. DE LEEUW,\*  
AIICHIRO NAKANO, and PRIYA VASHISHTA

*Concurrent Computing Laboratory for Materials Simulations, Department of Physics and Astronomy,  
Department of Computer Science, Louisiana State University, Baton Rouge, Louisiana 70803-4001*

## Abstract

Algorithms are designed to implement molecular-dynamics simulations on emerging concurrent architectures. For systems with finite-range interactions, a domain decomposition algorithm is used to implement the multiple-time-step (MTS) approach to molecular-dynamics (MD) simulations on distributed-memory multiple instructions multiple data (MIMD) machines. This approach reduces the computation of forces significantly by exploiting the different time scales for short-range and intermediate-range interactions. Parallel algorithms are also designed for MD simulations of bulk Coulombic systems. The performance of these algorithms is tested on the Intel iPSC/860 system. The computational complexity of these algorithms is  $O(N)$  and parallel efficiencies close to 0.9. Molecular-dynamics simulations are carried out to investigate the structural and dynamical properties of highly densified and also porous silica glasses. Changes in the short-range and intermediate-range order in amorphous  $\text{SiO}_2$  are determined at different densities in the range of 4.28–0.1 g/cm<sup>3</sup>. Results for internal surface area and surface-to-volume ratio in porous  $\text{SiO}_2$  are also discussed. © 1993 John Wiley & Sons, Inc.

## Introduction

Despite significant recent developments in materials-simulation techniques [1–6], the goal of reliably predicting the properties of new materials in advance of fabrication and measurement has not yet been achieved. The primary reason for this lack of success is the inability of sequential machines to handle large-scale simulations. For example, MD simulations for long-range interactions scale as  $N^2$ , where  $N$  is the number of particles in the system. In many physical systems, the desired system sizes are in the range of  $10^6$  particles. These are beyond the compute power of most sequential machines. However, the MD technique has considerable inherent parallelism. By exploiting this parallelism on emerging parallel architectures, it is possible to perform large-scale simulations for complex materials.

In the past two years, we have used the parallel computer architectures in our Concurrent Computing Laboratory for Materials Simulations (CCLMS) to carry out MD simulations on network glasses. The CCLMS has the following computational facilities:

- MasPar 1208B—an SIMD (single instruction multiple data) machine with 8192 processors

---

\* Also at Laboratory for Physical Chemistry, University of Amsterdam, The Netherlands.

- Intel iPSC/860—an eight-node distributed-memory MIMD (multiple instructions multiple data) machine
- Intel iWARP—a 64-cell MIMD machine with systolic communication
- Silicon Graphics IRIS 4D/340VGX Power Center for real-time visualization

Plans are in place to connect these machines by FDDI (fiber distributed data interface) to form a distributed multiparallel processing network so that different parts of a large-scale simulation can run concurrently on different parallel architectures along with real-time visualization.

In this paper, we will describe our recent work on parallel algorithms for the MD approach and simulation results for structural properties of network glasses. The outline of this paper is as follows: the next section deals with an implementation of the MD approach on the iPSC/860 system, and the performance of the parallel MD algorithm is discussed in the third section. Simulation results for structural properties of highly densified and porous  $\text{SiO}_2$  glasses are discussed in the fourth section followed by concluding remarks in the fifth section.

### Parallel Algorithms for Molecular Dynamics

Molecular-dynamics approach has played a key role in our understanding of classical and quantum microscopic processes in physical systems [1]. In the MD approach, one obtains the phase-space trajectories of particles from the numerical solution of Newton's equations. Physical properties of a system are calculated from phase-space trajectories of the constituent particles. The interparticle interaction energy is a vital input to MD simulations. This  $N$ -body term is commonly expressed as a combination of one-, two-, three-body potentials, etc.

For systems with a finite-range interparticle interaction, the total number of pairs contributing to the energy and forces is  $N \cdot N_r/2$ , where  $N_r$  is the average number of particles within the range of the interaction,  $r_c$ . An efficient way to calculate interparticle interactions is to use the linked-list method. In this approach, the simulation cell is divided into  $n^3$  smaller cells, each with an edge  $L/n$  ( $L$  is the length of the MD cell) which is slightly larger than  $r_c$ . Using two integer arrays, a list of particles in each cell is constructed. The first array identifies the particle at the top of the list in each cell and the second array links particles belonging to the same cell.

A major advantage of the linked-cell list technique is that the computation time is proportional to  $14 \cdot N \cdot (L/n)^3$ , since each cell has 26 neighboring cells (Newton's third law is used to reduce the computation by a factor of 2). Furthermore, with the linked-list method the minimum-image convention can be implemented efficiently on distributed-memory MIMD machines.

The computation of forces can be further reduced with the multiple-time-step (MTS) approach. The MTS approach exploits the fact that the force experienced by a particle can be separated into a rapidly varying primary component and a slowly varying secondary component. The primary interaction arises from nearest neighbors of a particle, whereas the secondary forces are due to other particles within its range of interaction. The calculation of forces thus proceeds in two steps:

a. Using the linked-cell list method, a table of primary neighbors is constructed for each particle at regular time intervals. In addition, this table includes neighbors within a spherical shell between  $r_a$  and  $r_a + s$ , where  $r_a$  is the nearest-neighbor separation and  $s$  is referred to as the skin. The skin is added to avoid updating the neighbor list at each time step. The primary contributions to potential energy and forces are computed with the aid of the neighbor list.

b. The secondary forces  $\mathbf{F}_{i,s}(t)$ , vary slowly in time and therefore are calculated with the Taylor series expansion,

$$\mathbf{F}_{i,s}(t_0 + K\Delta t) = \sum_{l=0}^{l_{\max}} \frac{(K\Delta t)^l}{l!} \mathbf{F}_{i,s}^{(l)}(t_0), \quad (1)$$

where  $\mathbf{F}_{i,s}^{(l)}$  is the  $l$ th time derivative of the secondary force at time  $t_0$ . Similarly the potential energy  $\Phi_s$  can be expanded into a Taylor's series:

$$\Phi_s(t_0 + K\Delta t) = \sum_{l=0}^{l_{\max}} \frac{(K\Delta t)^l}{l!} \Phi_s^{(l)}(t_0). \quad (2)$$

The list of primary neighbors,  $\mathbf{F}_{i,s}^{(l)}$ , and  $\Phi_s^{(l)}$  are updated after  $n$  time steps. The choice of  $n$  and  $l_{\max}$  is dictated by the energy-conservation requirement.

Domain decomposition is the most appropriate scheme to implement MD simulations on distributed-memory MIMD machines. In this case, the total system is divided into  $p$  subsystems of equal volume, and these subsystems are geometrically mapped onto  $p$  processors [7-9]. For a cubic system of volume  $\Omega$ , the edge of each subsystem is  $l_s = (\Omega/p)^{1/3}$ . The positions and time derivatives (up to fifth order in the predictor-corrector method we have used) of all the particles whose coordinates fall within the boundaries of a given subsystem are stored on the processor for that subsystem. The forces and potential energy are again computed with the MTS approach and the linked-cell list scheme. Domain decomposition is updated after  $\nu$  time steps, just before constructing neighbor tables. The primary forces are calculated with neighbor tables. For particles at the boundary of a subsystem, it is necessary to know the coordinates of particles on neighboring nodes which are within  $r_a + s$  from the boundaries. Relevant data for particles which move out of the subsystem boundary into the domain of a neighboring subsystem are sent to that processor.

Secondary interactions consist of intranode and internode contributions. The intranode contributions can be calculated straightforwardly with the linked-list scheme. The internode contributions require data motion (positions, velocities, etc.) for particles within the cutoff radius  $r_c$  from the boundaries of subsystems on different nodes. The message-passing strategy we have used is shown schematically in Figure 1. First the data from node 0 is sent to node 1, data from node 1 to node 2, . . . , and data from node  $p-1$  to node 0 synchronously. Then using the linked-cell list method, the contributions to secondary forces, potential energy, and their time derivatives are calculated. Node 0 sends back the calculated contributions to node  $p-1$  while receiving the contributions calculated at node 1. Similar message passing of calculated contributions takes place synchronously at other nodes as well. Next node 0 receives data from node  $p-2$ , node 1 from node  $p-1$ , . . . ,



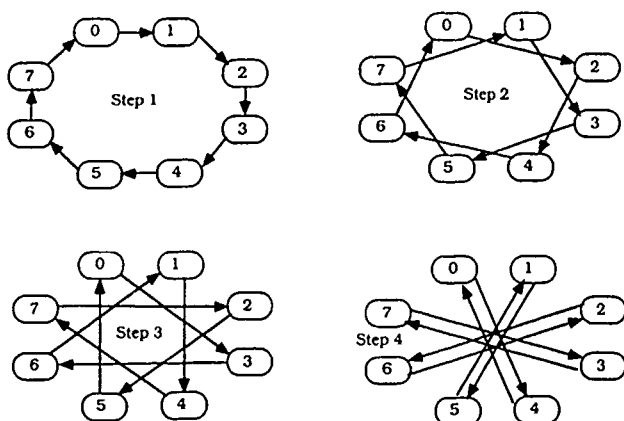


Figure 1. Internode communication strategy for secondary forces with eight processors. Arrows indicate the direction of data motion.

and node  $p - 1$  from node  $p - 3$ . The contributions to forces, potential energy, and their time derivatives are calculated synchronously, and the results are sent back to the nodes from which the data had been received. This procedure is continued until all the necessary interactions have been computed.

### Performance of Parallel Molecular Dynamics Algorithm

The performance of domain-decomposition algorithm for MTS-MD simulations was evaluated on the eight-node Intel iPSC/860 system in the Concurrent Computing Laboratory for Materials Simulations at Louisiana State University. For system sizes ranging from 4000 to 108,000 Lennard-Jones particles, simulations were performed at a reduced temperature  $T^* (=k_B T/\epsilon) = 0.8$  and number density  $\rho^* (= \rho \sigma^3) = 0.743$  [7]. Equations of motion were integrated with a time step,  $\Delta t = 0.73 \times 10^{-14}$  s. The primary and secondary forces were cut off at 1.1 s and 2.5 s, respectively, and the skin for neighbor tables was taken to be 0.4 s.

In Figure 2 we show the system size dependence of the total execution time and communication time. The computation time for primary forces is less than that for secondary forces. The parallel efficiency,  $\eta (= t_1/(p \cdot t_p))$ , where  $t_p$  is the execution time on  $p$  processors and  $t_1$  is the execution time on a single processor, for domain-decomposition algorithm is estimated to be 0.9 and the algorithm sustains good load balancing.

Recently, we have also implemented MD simulations involving the Ewald summation for Coulomb interaction on distributed-memory MIMD machines [8]. The Ewald summation [9] is the most widely used approach for the long-range Coulomb interaction in bulk systems. In this approach, the interaction is written as a sum of a constant term, a sum in the Fourier space, and a sum of "short range" terms in real space. The parallel algorithm we have designed for the Ewald summation reduces the computational complexity from  $O(N^{3/2})$  to  $O(N)$ . This is achieved by ensuring

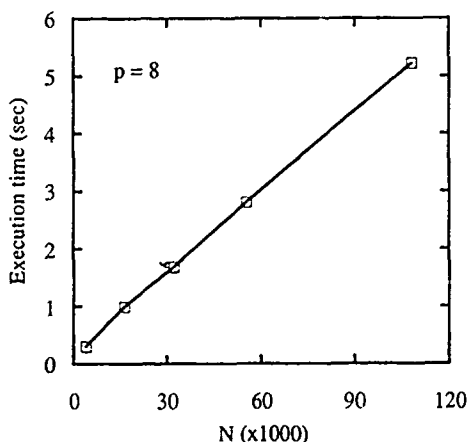


Figure 2 Execution time as a function of the number of particles in a Lennard-Jones system.

that both the real-space and Fourier-space contributions scale linearly with the size of the system. In real space, the potential energy and force calculations are truncated at  $r_c = 5r_0$ , where  $r_0$  is the ion-sphere radius,  $r_0 = (3/4\pi\rho)^{1/3}$ . This cutoff maintains the desired level of precision—0.01% for all system sizes. The real-space contributions are then calculated with the domain decomposition and the linked-list methods which scale as  $O(N)$ . The computation of Fourier-space contributions reveals that only a certain number of wave vectors need to be included. We performed simulations as a function of the number of Fourier components and system sizes. It is found that an increase in the number of wave vectors from 309 to 2192 produces a change of 0.01% in the total potential energy. The computation time for the  $k$ -space calculation increases linearly as the number of wave vectors increases. Thus, the total execution time for the Ewald sum scales linearly with the number of particles (see Fig. 3) and is inversely proportional to the number of processors.

### Structural Correlations in Densified and Porous Silica

Silica ( $\text{SiO}_2$ ) is one of the most interesting materials because of its numerous polymorphs. Over the years, many attempts have been made to investigate the structure and dynamics of crystalline and glassy states of  $\text{SiO}_2$  at high pressures. Recent *in situ* high-pressure X-ray diffraction experiments reveal significant changes in the short-range and intermediate-range order in  $\text{SiO}_2$  glass [10].

We have performed MD simulations to investigate the effect of pressure on structural correlations in silica glass [11]. An effective interatomic potential consisting of two- and three-body terms has been used in these simulations. The two-body potential includes long-range Coulomb interaction due to charge-transfer effects, charge-dipole interaction due to large electronic polarizability of  $\text{O}^{2-}$  ions, and steric repulsion between ions. The three-body covalent potentials for Si—O—Si and O—Si—O interactions include the effects of bond bending and stretching [12].

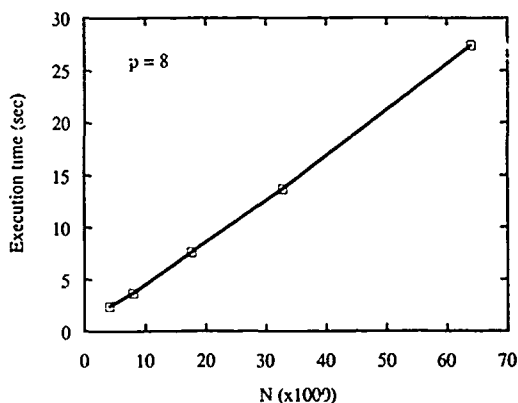


Figure 3. Execution time as a function of the number of particles in a bulk Coulombic system.

Our high-pressure simulations cover a wide range of mass density, from 2.20 g/cm<sup>3</sup> (normal density) to 4.28 g/cm<sup>3</sup>. Figure 4 shows partial pair-distribution functions,  $g_{\alpha\beta}$  ( $\alpha, \beta = \text{Si, O}$ ), for SiO<sub>2</sub> glasses at the normal density, 2.2 g/cm<sup>3</sup>, and at high densities, 3.53 and 4.28 g/cm<sup>3</sup>. For the normal density glass, the first peak in  $g_{\text{Si-O}}(r)$  gives the Si—O bond length to be 1.61 Å. In addition, there is a small shoulder around 3.80 Å and a broad peak at 4.16 Å. The Si—O nearest neighbor (nn) coordination is 4. The position of the first peak in  $g_{\text{Si-O}}(r)$  and the corresponding nn Si—O coordination remain almost unchanged as the density is increased to 3.53 g/cm<sup>3</sup>. At a pressure of 43 GPa, where the glass density increases to 4.28 g/cm<sup>3</sup>, the first peak in  $g_{\text{Si-O}}(r)$  occurs at 1.67 Å instead of 1.61 Å and the Si—O coordination increases from 4 to 5.8. In stishovite (a crystalline phase with nearly the same density), the Si—O bond lengths are 1.76 and 1.81 Å, and the Si—O coordination is 6. In the glass at 4.28 g/cm<sup>3</sup>, the second peak in  $g_{\text{Si-O}}(r)$  is at 3.15 Å, close to the next-nearest-neighbor (nnn) Si—O distance (3.20 Å) in stishovite. When the glass density reaches 4.28 g/cm<sup>3</sup>, the first peak in  $g_{\text{Si-Si}}(r)$  splits into two peaks located at 2.59 Å, close to the nn Si—Si distance (2.67 Å) in stishovite, and at 3.07 Å which is close to the nnn Si—Si distance (3.24 Å) in stishovite. The area under the first peak gives a coordination of 2 while the area under the first two peaks is 10. At normal density, the nn O—O coordination is 6. It increases to 10 at 3.53 g/cm<sup>3</sup> and to 12 at 4.28 g/cm<sup>3</sup>. In stishovite, the O—O coordination is 12.

In Figure 5, we present MD results for the density dependence of the static structure factor,  $S(q)$ . In the normal density glass, the first sharp diffraction peak (FSDP) is located at 1.6 Å<sup>-1</sup>. With an increase in the density, the height of the FSDP decreases, its width increases, and its position shifts to higher values of  $q$ . (Elastic compression cannot account for the observed shift in the position of the FSDP.) In addition, a new peak appears when the density is increased by 20%. Located at 2.85 Å<sup>-1</sup>, the peak grows under pressure with only a slight shift in its position. The simulation

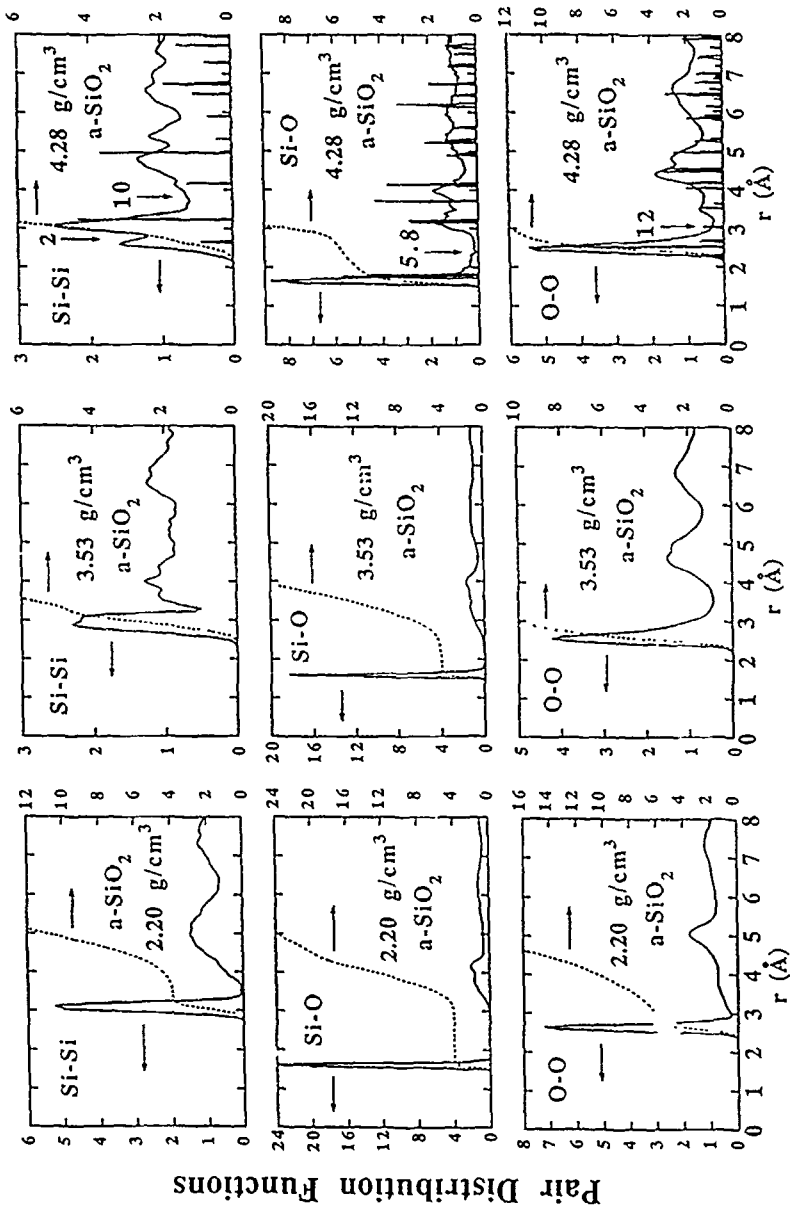


Figure 4. Partial pair-distribution functions (solid lines) and coordination numbers (dotted lines) for  $\text{SiO}_2$  glasses at normal and high densities at 300 K. Sharp peaks in the figure at 4.28  $\text{g/cm}^3$  correspond to pair-distribution functions for crystalline stishovite.

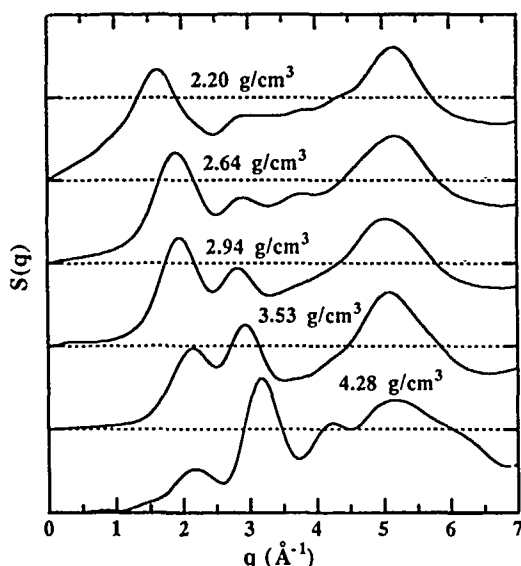


Figure 5. Static structure factor,  $S(q)$ , of normal and high density  $\text{SiO}_2$  glasses at 300 K

results for the effect of pressure on  $S(q)$  are in good agreement with high-pressure X-ray measurements by Meade et al. [10].

Figure 6 displays the MD results for O—Si—O and Si—O—Si bond-angle distributions in  $\text{SiO}_2$  glasses at normal and high densities. As the density increases, the peaks in these distributions broaden and also shift to lower angles because of increased distortions of  $\text{Si}(\text{O}_{1/2})_4$  tetrahedra. At normal density, the O—Si—O distribution has a peak at  $109^\circ$ . When the glass density reaches  $4.28 \text{ g/cm}^3$ , the O—Si—O distribution develops broad peaks at  $90^\circ$  and  $171^\circ$ . In the normal density  $\text{SiO}_2$  glass, the Si—O—Si bond-angle distribution has a peak at  $142^\circ$  with an FWHM of  $26^\circ$ . (Both of these results are in excellent agreement with NMR measurements [12].) With densification, this peak shifts to lower values. The Si—O—Si bond-angle has broad peaks around  $95^\circ$  and  $128^\circ$  in the glass at density  $4.28 \text{ g/cm}^3$ . These values are close to the Si—O—Si angles,  $98.65^\circ$  and  $130.67^\circ$ , in stishovite. Thus, the results for pair-distribution functions and bond-angle distributions in  $\text{SiO}_2$  glass at  $4.28 \text{ g/cm}^3$  provide strong evidence for corner-sharing and edge-sharing  $\text{Si}(\text{O}_{1/3})_6$  octahedra.

Recently, we have also investigated structural correlations in porous silica. This material is environmentally safe, has a large thermal resistance, and high optical transmission. It is an excellent alternative to CFC foamed plastic in thermal insulation of refrigerators and also a desirable material for passive solar energy collection devices. Efforts are also being made to produce optical switching devices by embedding semiconducting microclusters in the pores of aerogel silica.

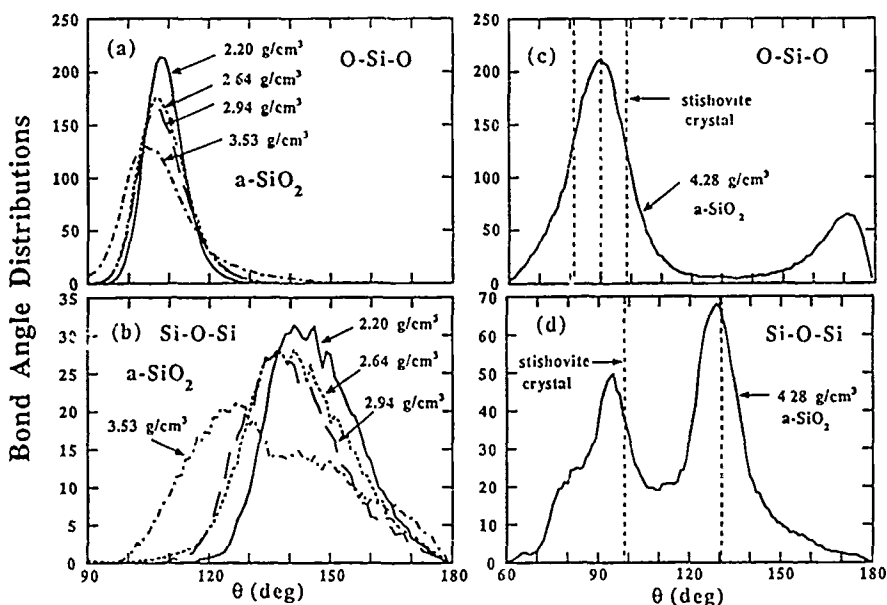


Figure 6. O—Si—O and Si—O—Si bond-angle distributions for normal and high density  $\text{SiO}_2$  glasses.

Our MD simulations for porous silica cover a wide range of densities, from 2.2 to 0.1  $\text{g/cm}^3$  [13]. The simulated systems are large enough (41,472 particles; the lowest density system is a cube with an edge of 240 Å) to cover the entire range of structural correlations. Computer generated porous glasses were prepared as follows: The starting configuration was  $\beta$ -cristobalite at room temperature. This system was heated to 5000 K over a period of 72,000 time steps (1 time step =  $0.5 \times 10^{-15}$  s) and then equilibrated for 30,000 time steps. Subsequently, we cooled the system to 4000 K over 12,000 time steps and again thermalized for 30,000 time steps. Following this cooling and thermalization process, glasses were generated at 3000, 2000, 1500, 600, and 300 K. At each temperature, MD simulations were performed for an additional 30,000–60,000 time steps. Porous glasses were produced by uniformly scaling the coordinates of all the particles in the room-temperature glass by a factor of 1.02–1.026. After scaling, the system was thermalized for 30,000 time steps. Subsequently, the conjugate gradient scheme was used to bring the system to the lowest local energy configuration. In such a relaxed system, particles were given random velocities according to Maxwell-Boltzmann distribution and statistical averages were accumulated over 9000 time steps.

In Figure 7(a), we show pair-distribution functions on a logarithmic scale at several densities. At lower densities, one finds not only the peak at 1.61 Å but an additional peak at 1.58 Å. The latter is due to Si—O bond in triangular units whose number grows as the density is lowered. Superimposed on the peaks in  $g(r)$  is a power-law decay from which one can determine the fractal dimension  $d_f$  of the

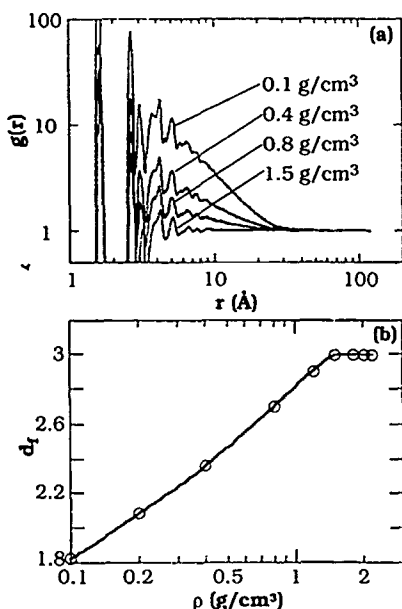


Figure 7 (a) Log-log plot of pair distribution functions,  $g(r)$ , of silica g'asses at densities at 0.1, 0.4, 0.8, and 1.5 g/cm<sup>3</sup>. (b) Fractal dimension  $d_f$  as a function of density.

silica network:  $d_f = 3 + d \log[g(r)]/d \log(r)$ . Figure 7(b) shows the decrease in the fractal dimension as the density decreases.

Two of the most important parameters for porous glasses are the internal surface area of pores and the pore surface area-to-volume ratio. These characteristics of pores are determined as follows: The system is divided into cubic cells of volume  $(4 \text{ Å})^3$ . Counting the number of empty cells and multiplying it by  $(4 \text{ Å})^3$  gives the pore volume. The pore surface area is determined by the number of interfaces separating empty cells adjacent to occupied cells and multiplying that number by  $(4 \text{ Å})^2$ . Figure 8(a) shows the increase in the internal surface area and Figure 8(b) the decrease in the pore surface area-to-volume ratio as the density decreases. The latter is a measure of the average pore size. The density dependence of the internal surface area of pores is in good agreement with experiment [14].

### Conclusion

Molecular-dynamics simulations have been efficiently implemented on distributed-memory MIMD machines with the aid of multiple-time-step approach and the linked-cell list scheme. The complexity of this parallel algorithm is  $O(N)$  and it scales inversely with the number of processors. We have applied this algorithm to investigate structural correlations in SiO<sub>2</sub> glasses at various densities. Currently, we are implementing this approach on the Delta machine at Caltech so that we can

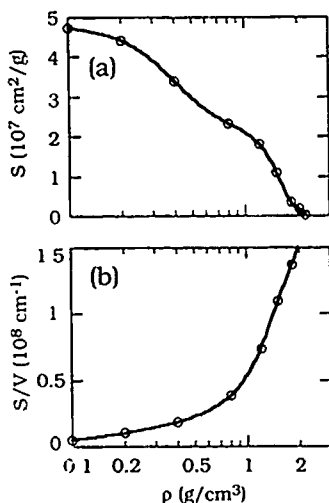


Figure 8 (a) Internal pore surface  $S$  versus density calculated from the configuration of the MD porous glasses. (b) Pore surface-to-volume ratio,  $S/V$ , vs density calculated from the configuration of the MD porous glasses.

simulate sufficiently large systems ( $\sim 10^6$  particles) to investigate atomistically the phenomenon of fracture in ceramics and glasses.

### Acknowledgments

Work supported by the U.S. Department of Energy, Office of Energy Research, Basic Energy Science, Division of Materials Science, Grant No. DE-FG05-92ER45477. Dr. A. Nakano is supported by National Science Foundation Grant No. ASC-9109906. The simulations were performed using the computing facilities in the Concurrent Computing Laboratory for Materials Simulations (CCLMS) at Louisiana State University. The facilities in the CCLMS were acquired with the Equipment Enhancement Grants awarded by the Louisiana Board of Regents through the Louisiana Education Quality Support Fund (LEQSF).

### Bibliography

- [1] M. P. Allen and D. J. Tildesley, *Computer Simulation of Liquids* (Oxford University Press, Oxford, 1990).
- [2] R. Car and M. Parrinello, *Phys. Rev. Lett.* **55**, 2471 (1985).
- [3] A. Selloni, P. Carnevali, R. Car, and M. Parrinello, *Phys. Rev. Lett.* **59**, 823 (1987).
- [4] R. N. Barnett, U. Landman, and A. Nitzan, *Phys. Rev. Lett.* **62**, 106 (1989).
- [5] R. K. Kalia, P. Vashishta, L. H. Yang, F. Dech, and J. Rowlan, *Int. J. Supercomput. Appl.* **4**, 22 (1990).
- [6] A. Nakano, P. Vashishta, R. K. Kalia, and L. H. Yang, *Phys. Rev.* **B45**, 8363 (1992).
- [7] R. K. Kalia, S. W. de Leeuw, A. Nakano, D. L. Greenwell, and P. Vashishta, *Supercomputing*, to appear.



- [8] R. K. Kalia, S. W. de Leeuw, A. Nakano, and P. Vashishta, *Comput. Phys. Commun.* **74**, 316 (1993).
- [9] S. W. de Leeuw, J. W. Perram, and E. R. Smith, *Proc. Roy. Soc. London A* **373**, 27, 57 (1980).
- [10] C. Meade, R. J. Hemley, and H. K. Mao, *Phys. Rev. Lett.* **69**, 1387 (1992).
- [11] W. Jin, R. K. Kalia, P. Vashishta, and J. P. Rino, to appear
- [12] P. Vashishta, R. K. Kalia, J. P. Rino, and I. Ebbsjö, *Phys. Rev B* **41**, 12197 (1990).
- [13] A. Nakano, L.-S. Bi, R. K. Kalia, and P. Vashishta, to appear
- [14] J. Fricke, *J. Non-Cryst. Solids* **121**, 188 (1990).

Received June 7, 1993

# Efficient Computation of Electron-Repulsion Integrals in *Ab Initio* Studies of Polymeric Systems

DAVID H. MOSLEY, JOSEPH G. FRIPIAT, BENOÎT CHAMPAGNE,\*  
and JEAN-MARIE ANDRÉ

*Laboratoire de Chimie Théorique Appliquée, Facultés Universitaires Notre-Dame de la Paix,  
Rue de Bruxelles 61, B-5000 NAMUR, Belgium*

## Abstract

In this article we describe the implementation of a scheme based upon the McMurchie-Davidson recursion relationships to calculate two-electron integrals over Gaussian-type functions in extended systems. Features illustrating the computational efficiency of the approach are highlighted together with additional aspects of our program to compute the *ab initio* band structures of polymers. The algorithm is applied in calculation of the band structure and Sum Over States polarizability of polyethylene and polysilane using standard basis sets augmented with polarization functions. The role of polarization functions is seen to be small in polyethylene, but in polysilane the silicon d-orbitals make significant contributions to the bonding along the backbone of the chain. This increase in bonding character results in a reduction in the calculated polarizability in going from the unpolarized to polarized basis sets. © 1993 John Wiley & Sons, Inc

## Introduction

There has been much development in recent years in the theory and application of the quantum theory of polymers to the point where *ab initio* self-consistent field (SCF) calculations can be performed routinely on systems with small and moderately sized unit cells [1]. Studies on simple polymers (for example: polyethylene, polyacetylene, polysilane, . . .) have provided valuable insight into the electronic structures of polymers and an understanding of their properties. However, almost all these studies have been carried out using either minimal or double-zeta basis sets, with the use of extended or polarized basis sets still being exceptional. In molecular studies, the use of extended and polarized basis sets is now commonplace and is seen to be important, particularly in the reliable prediction of molecular geometries and properties. The development of efficient algorithms to enable functions of higher angular momenta to be included in calculations upon infinite systems is now desirable in order to investigate the contributions such functions make to the computed energies, band structures, and properties. The importance, or otherwise, of d-orbitals in the bonding of polymeric systems has recently been the source of some debate in the literature [2,3].

\* Research Assistant of the National Fund For Scientific Research (Belgium). Present address Quantum Theory Project, University of Florida, Williamson Hall, 362, Gainesville, FL 32611-2035.

Organic polymers are the subject of major interest due to their potential both as conductors and as important materials in opto-electronics [4,5]. The accurate theoretical prediction of the electronic structure and properties has an important role to play in providing insight into the mechanisms and structure-property relationships involved and, in order to fulfil this, the development of efficient and powerful algorithms is essential.

Generally speaking, the evaluation of the two-electron integrals is the most time-consuming step in polymeric calculations. Several schemes to compute these integrals over Gaussian basis functions have been developed and implemented for use in molecular calculations [6-10]. In extended systems the basic problem remains the same as in the molecular case, though efficient algorithms also depend on specific use being made of features inherent in polymers, such as the translational and helical symmetry.

The theory of LCAO band structure calculations has been covered in detail in recent reviews [1,11]. To avoid repetition, we restrict our theoretical discussion as far as possible to aspects directly related to the two-electron integrals. We then present a description of the implementation of an algorithm based upon the McMurchie-Davidson scheme [7] to the calculation of two-electron integrals in infinite systems. A brief description of the use of permutational symmetry in the integral indices and of the exploitation of symmetry in the construction of the Fock matrices is also given. For the sake of completeness, we also include a brief description of the computation of the asymptotic polarizability per unit cell of infinite systems using the Sum Over States method [12].

Using the integral algorithm outlined in the next sections, we present the results of a study into the effect of the inclusion of d-orbitals in the basis sets for polyethylene and polysilane. The first of these systems is one of the classic systems to study in polymer quantum chemistry (reviewed recently in [13,14]), and has been studied previously in the *ab initio* crystal orbital approach with polarization functions added to the basis set [15]. Polysilane was chosen because of its structural similarity to polyethylene and the fact that one can reasonably expect the inclusion of polarization functions to have a more pronounced effect than in a system containing first-row atoms only. Polysilane is the source of considerable interest due to the sigma conjugation along the polymer backbone [16]. Finally, we present some conclusions which can be drawn from the preliminary results and an indication of potential avenues for both short- and long-term investigation.

### Aspects of Computation

#### *Two-Electron Integrals in LCAO Calculations of Band Structures*

The standard quantum mechanical treatment of polymers is based on the periodic model of the polymeric chain. Through Bloch's theorem, the one-electron wavefunctions can be represented as Bloch functions

$$\phi_n(k, \mathbf{r}) = \exp[ikz]u_n(k, \mathbf{r}) \quad (1)$$

in which the periodicity axis is chosen to be the  $z$ -axis,  $\exp[ikz]$  is a non-periodic free-electron like contribution and  $u_n(k, \mathbf{r})$  is a periodic contribution, having the same periodicity as the lattice ( $u_n(k, \mathbf{r}) = u_n(k, \mathbf{r} + jae_z$ ), where  $a$  is the length of the unit cell and  $j$  is an integer). The LCAO Bloch form of a single atomic orbital,  $\chi(\mathbf{r} - \mathbf{P})$ , where  $\mathbf{P}$  represents the co-ordinates of the origin of the atomic orbital, is written

$$\begin{aligned}\phi(k, \mathbf{r}) &= \sum_j c_j \chi(\mathbf{r} - \mathbf{P} - jae_z) \\ &= N_c^{-1/2} \sum_j \exp[ikja] \chi(\mathbf{r} - \mathbf{P} - jae_z)\end{aligned}\quad (2)$$

where  $N_c^{-1/2}$  is the normalization factor for a polymer of  $N_c$  cells, and the sum over  $j$  represents a sum over  $N_c$  cells. The LCAO Bloch form describing an orbital over the whole polymer is expressed as

$$\begin{aligned}\phi_n(k, \mathbf{r}) &= \sum_j \sum_p c_{pn}^0 \chi_p(\mathbf{r} - \mathbf{P} - jae_z) \\ &= N_c^{-1/2} \sum_j \exp[ikja] \sum_p c_{pn}(k) \chi_p(\mathbf{r} - \mathbf{P} - jae_z)\end{aligned}\quad (3)$$

where  $n$  is the band index,  $k$  the position vector in the first Brillouin zone, and the superscripts 0  $j$  identifying the zeroth and  $j$ th cells, respectively. The Fock matrix elements,  $F_{pq}^{0j}$ , are given by

$$\begin{aligned}F_{pq}^{0j} &= \int \chi_p(\mathbf{r} - \mathbf{P}) \mathcal{F} \chi_q(\mathbf{r} - \mathbf{Q} - jae_z) \\ &= \int \chi_p^0(\mathbf{r}) \mathcal{F} \chi_q^j(\mathbf{r}) d\mathbf{r}\end{aligned}\quad (4)$$

where  $\mathcal{F}$  is the one-electron Fock operator. Equation (4) can be expanded into its individual terms to give

$$F_{pq}^{0j} = T_{pq}^{0j} - \sum_h \sum_A Z_A V_{pq}^{0j} |A^h| + \sum_h \sum_l \sum_r \sum_s D_{rs}^{hl} [2(pq^j | r^h s^l) - (ps^l | r^h q^j)] \quad (5)$$

in which  $T_{pq}^{0j}$  and  $V_{pq}^{0j} |A^h|$  are the kinetic energy and potential energy matrix elements. The two-electron integrals appearing in Eq. (5) are defined as

$$(pq^j | r^h s^l) = \iint \frac{\chi_p^0(\mathbf{r}) \chi_q^j(\mathbf{r}) \chi_r^h(\mathbf{r}') \chi_s^l(\mathbf{r}')}{|\mathbf{r} - \mathbf{r}'|} d\mathbf{r} d\mathbf{r}'. \quad (6)$$

The electron-electron Coulomb contribution to the Fock matrices can be simplified to [17,18]

$$\begin{aligned}C_{pq}^{0j} &= \sum_m \sum_r \sum_s D_{rs}^{0m} [\sum_h (p^0 q^j | r^h s^{h+m})] \\ &= \sum_m \sum_r \sum_s D_{rs}^{0m} \{ p^0 q^j | r^* s^{*+m} \}\end{aligned}\quad (7)$$

where use has been made of the periodicity of the electron density,  $D_{rs}^{hl} = D_{rs}^{0h-l}$

[17,18], and the sums over  $l$  and  $h$  in Eq. (5) have been replaced by a new index  $m = l - h$ . The most important feature to note here is that the integral enclosed within the curly braces  $\{p^0 q^j | r^* s^{*+m}\} = \sum_h (p^0 q^j | r^h s^{h+m})$ , which we describe as the "compacted Coulomb integral" [18], can be calculated and stored once in the evaluation of the two-electron integrals and does not evolve in successive iterations of the SCF procedure. This results in a reduction in the number of integrals stored, and a subsequent reduction in the number of I/O operations and the manipulations which need to be made to compute the Coulomb contribution to the Fock matrices.

In the program developed in our laboratory [19,20] two different ranges are used for the evaluation of the Coulomb and exchange contributions to the Fock matrices. Firstly, there is a short-range region,  $j, l = [-N, +N]$ , in which all the electron-repulsion integrals are computed exactly. Beyond this, we define an intermediate-range region,  $h = [-M, +M]$  where  $M \geq 2N$ , in which the Coulomb contributions are evaluated exactly and summed into the compacted integral. Finally, beyond  $M$  a multipole expansion technique is used to treat the Coulomb interaction to infinity [21] taking the nuclear attraction Coulomb term to give a convergent series. For the exchange contribution, however, the evaluation of the terms is restricted to the short-range region only at the moment. The investigation into methods which correctly evaluate the exchange contributions to infinity is an active area of research [22,23].

### *Integral Evaluation in Extended Systems*

Generally, the contracted Gaussian atomic orbitals used in molecular calculations, defined by their set exponents and coefficients, are assigned to a unique center. In symmetric molecules, the symmetry operations relating different centers (of the same atom type) can be used to reduce the computational task involved. In polymeric calculations, the same atomic orbital exponents and coefficients assigned to an atom in the reference unit cell are used in the translational repeats of the unit cell along the polymer chain. Efficient computation relies, in part, on the maximum reuse of information and avoiding the unnecessary recalculation of factors. With this in mind, it is possible to simplify the calculation of integrals in extended systems through identifying factors which can be said to be "translationally invariant," that is terms involving the orbital exponents and coefficients, prior to considering the translational repeat. The existence of point group symmetry in the unit cell and the adjacent cells being related by a helical twist [24,25] also serve to reduce the magnitude of the computational task, though these are outside the scope of the discussion here.

A schematic representation of an algorithm based upon the McMurchie-Davidson (M-D) scheme [7] adapted to extended systems for the calculation of electron-repulsion integrals

$$(pq^j | r^h s^{h+l}) = \iint \frac{\chi_p^0(\mathbf{r}) \chi_q^j(\mathbf{r}) \chi_r^h(\mathbf{r}') \chi_s^{h+l}(\mathbf{r}')}{|\mathbf{r} - \mathbf{r}'|} d\mathbf{r} d\mathbf{r}' \quad (8)$$

extended systems is given in Figure 1. The upper-case indices,  $P, Q, R, S$ , are used to identify the shells, while the lower-case indices refer to atomic orbitals. The M—

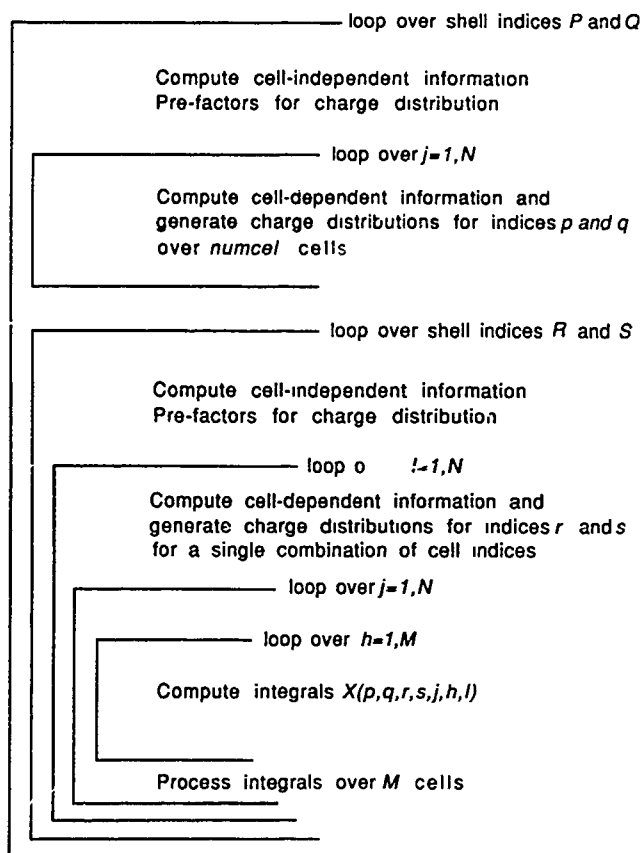


Figure 1. Representation of McMurchie-Davidson-like algorithm for the computation of two-electron integrals applied to extended systems.

D scheme is based upon expressing the two-electron integrals in terms of auxiliary functions which can be expressed in terms of a set of recursion relations.

Looking at Figure 1 in a little more detail, the first step inside the outer loop over shells  $P$  and  $Q$  is to compute the factors necessary for the computation of the charge distributions which are independent of the origins of the shells, that is factors which only depend on the exponents and coefficients of the Gaussian primitives which go to make up the shells. The recursion relations necessary to compute the overlap distributions are then generated using the recursion relations for the indices  $p$  and  $q$  over all cells to be included in the short-range region. This information is stored in core memory for fast access in the integral evaluation steps in the inner loops for all  $j = -N, +N$ .

Analogous steps are then carried out for the second pair of indices  $R$  and  $S$  to generate the cell independent information, followed by the cell dependent factors inside the loop over  $l$ . These are formed for a single value of  $l$  at a time and make

use of the fact that the center of the overlap distribution for  $r$  and  $s$  is subject to a translation of  $ha$  along the periodicity axis in the evaluation of the integrals in the loop over  $h$ . The integral evaluation, which is performed in the innermost loop over cells, is essentially identical to the molecular case. A total of  $M \times \text{num}$  integrals, where  $\text{num}$  is the number of integrals resulting from the quartet of shells,  $P, Q, R, S$ , is calculated in a single step through the loop over  $h$ . These integrals are stored in core memory prior to being processed and written to disk. This processing consists of a final test to ensure that the value of the integrals exceed a certain threshold and that the triplet of cell indices are within the defined range and will contribute to the Fock matrices.

The algorithm outlined above and illustrated in Figure 1 is included in the latest release of the PLH program, PLH-93 [19].

### Use of Permutation Symmetry

Since the calculation of the two-electron integrals is so computationally intensive, it is beneficial to exploit measures which can result in economies. The permutational symmetry of the indices of the integrals [26] can be used to reduce the number of integrals which need to be calculated and stored. This is a well-known feature for molecular calculations [27], and its application in *ab initio* polymeric calculations is demonstrated below.

For the molecular case, a two-electron integral  $(pq|rs)$  is equal to seven other integrals (assuming  $p, q, r, s$  are not equal) obtained through permuting the indices as

$$(pq|rs) = (pq|sr) = (qp|rs) = (qp|sr) = (rs|pq) = (rs|qp) = (sr|pq) = (sr|qp)$$

which means that only one of these integrals has to be calculated and stored.

Adopting the shorthand notation for the compacted Coulomb integral  $\mathcal{C}_{pqrs}(j, m) = \{p^0 q^j | r^* s^{*+m}\}$ , the following equalities can be used in polymeric calculations

$$\begin{aligned}\mathcal{C}_{pqrs}(j, m) &= \mathcal{C}_{pqsr}(j, -m) = \mathcal{C}_{qprs}(-j, m) = \mathcal{C}_{qpsr}(-j, -m) = \mathcal{C}_{rspq}(m, j) \\ &= \mathcal{C}_{rsqp}(m, -j) = \mathcal{C}_{srpq}(-m, j) = \mathcal{C}_{srqp}(-m, -j)\end{aligned}$$

These relations are only formally valid for the summation  $-\infty < h < \infty$ . Thus the inclusion of long-range effects is important in the use of the above relations.

An equivalent set of relations holds for the exchange integrals

$$\begin{aligned}(pq^j | r^h s^{h+m}) &= (pq^j | s^{h+m} r^h) = (qp^{-j} | r^{h-j} s^{h+m-j}) = (qp^{-j} | s^{h+m-j} r^{h-j}) \\ &= (rs^m | p^{-h} q^{j-h}) = (rs^m | q^{j-h} p^{-h}) = (sr^{-m} | p^{-h-m} q^{j-h-m}) \\ &= (sr^{-m} | q^{j-h-m} p^{-h-m})\end{aligned}$$

### Calculation of Sum Over States Polarizabilities

Recently, a scheme has been proposed for the rapid computation of the asymptotic longitudinal frequency-independent polarizability per unit cell of infinite systems

within the Sum Over States (SOS) approximation [12]. This calculation is performed as a post-SCF step, and through providing an estimate of the polarizability can provide at least a qualitative insight into the nature of bonding and the extent of conjugation in polymers.

The longitudinal polarizability can be expressed as

$$\alpha_{zz} = 4 \sum_i \sum_a \sum_k \frac{|\Omega_{ia}(k)|^2}{\epsilon_a(k) - \epsilon_i(k)}$$

where the sums over  $i$  and  $a$  represent sums over occupied and unoccupied bands respectively,  $\Omega_{ia}(k)$  are the dipole transition strengths [28–30]. In order to calculate the polarizability per unit cell, the sum over  $k$  is replaced by an integration over the first Brillouin zone, to give

$$\begin{aligned} \frac{\alpha_{zz}}{N_c} &= \frac{2a}{\pi} \sum_i \sum_a \int \frac{|\Omega_{ia}(k)|^2}{\epsilon_a(k) - \epsilon_i(k)} dk \\ &= \sum_i \int \alpha_{zz}(i, k) dk \\ &= \sum_i \alpha_{zz}(i). \end{aligned}$$

The final result in the above expression illustrates how the polarizability can be decomposed into the contributions made from each of the occupied bands. This can be used to establish relationships between the topology of the bands and the polarizability to provide insight into the nature of bonding and conjugation in the polymer [12,31].

Evidently, the SOS scheme has its limitations. It corresponds to an uncoupled scheme and its numerical results can be only be treated as very rough estimates. However, it is able to predict the correct trends of the polarizabilities in groups of compounds and can thus enable qualitative comparisons to be made.

## Results

The two systems considered here are polyethylene and polysilane. Initially, a series of "restricted" geometry optimizations were carried out on oligomers of increasing size,  $\text{H}-(\text{X}_2\text{H}_4)_n-\text{H}$ , where  $\text{X} = \text{C}, \text{Si}$  and  $n = 1-6$ , with the 6-31G and 6-31G\* ( $\alpha_d = 0.8$ ) basis sets [32] for the alkane chain and the 3-21G and 3-21G\* ( $\alpha_d = 0.45$ ) basis sets [33] for the silane chain, using Gaussian-90 [34]. The geometry optimization was restricted in the sense that all atoms forming the backbone of the oligomers were constrained to be coplanar, the plane containing the backbone designated a mirror-plane, and a  $\text{C}_2$  rotation axis maintained perpendicular to the plane. The parameters used in the polymeric calculations were deduced from the geometry of the central  $-\text{C}_2\text{H}_4-$  and  $-\text{Si}_2\text{H}_4-$  groups obtained in the optimization of the largest oligomer. These geometries are summarized in Table I.

The calculations to compute the total energy, band structure, and SOS polarizabilities were carried out using PLH-93 [19]. In all cases the short- and intermediate-



TABLE I. Optimized geometrical parameters and unit cell lengths used in polymeric calculations. Parameters deduced from central  $\text{—C}_2\text{H}_4\text{—}$  and  $\text{—Si}_2\text{H}_4\text{—}$  units in oligomeric optimizations on  $\text{C}_{12}\text{H}_{26}$  and  $\text{Si}_{12}\text{H}_{26}$  with their respective basis sets.

	$R_{\text{X-X}}$	$R_{\text{X-H}}$	$\angle(\text{X-X-X})$	$\angle(\text{H-X-H})$	$a$
Polyethylene:					
6-31G	1.533	1.088	113.25	106.35	2.560380
6-31G*	1.530	1.089	113.32	106.18	2.556396
Ref. [14]	1.541	1.087	112.5	107.2	2.563
Ref. [35]	$1.534 \pm 0.006$	1.05	$112.0 \pm 0.3$	106.5	2.54
Ref. [36]	1.533	1.07	112.0	107.0	2.46
Ref. [37]	$1.527 \pm 0.007$	1.091	$112.0 \pm 0.8$	109.0	2.53
Ref. [38]	1.586	1.08	$107.7 \pm 0.3$	109.0	2.55
Polysilane:					
3-21G	2.384	1.489	111.72	108.29	3.946324
3-21G*	2.346	1.481	112.29	107.56	3.897304

All bond lengths are given in Å and angles in degrees.

ranges of interaction were defined to be  $2N + 1 = 13$  and  $2M + 1 = 25$ , respectively. The thresholds for the two-electron integrals was set to  $10^{-7}$  a.u. and the convergence criterion for the density matrix elements to be  $10^{-5}$ . The results of these calculations are shown in Table II. The analysis of the contributions to the computed polarizabilities in terms from each of the valence bands are given in Tables III and IV.

### Discussion

For polyethylene, the addition of polarization functions to the basis set has only a small effect. In the first instance, this is manifest in the small differences between

TABLE II. Total energies per unit cell and longitudinal polarizabilities per unit cell and per unit length for infinite polyethylene and polysilane chains.

	Total energy	$\alpha_{zz}$ per unit cell	$\alpha_{zz}$ per unit length
Polyethylene.			
6-31G <sup>a</sup>	-78.036867	16.417	3.392
6-31G <sup>b</sup>	-78.036857	16.355	3.385
6-31G* <sup>b</sup>	-78.069384	16.712	3.459
Polysilane.			
3-21G <sup>a</sup>	-577.116837	63.778	8.552
3-21G <sup>b</sup>	-577.116213	61.101	8.296
3-21G* <sup>b</sup>	-577.292676	54.259	7.367

All values are given in atomic units.

<sup>a</sup> Quantities are calculated at the optimized geometry of the 6-31G or 3-21 G basis sets, respectively.

<sup>b</sup> Geometries obtained with the polarized basis sets are used.

TABLE III. Valence band contributions to the SOS longitudinal polarizabilities of polyethylene.

Band	6-31G <sup>a</sup>	6-31G <sup>b</sup>	6-31G* <sup>b</sup>
3	0.153	0.153	0.163
4	0.439	0.441	0.539
5	0.489	0.491	0.640
6	2.032	2.050	2.465
7	6.257	6.237	5.911
8	7.038	6.976	6.985
$\alpha_{zz}/\Lambda$	16.417	16.355	16.712

<sup>a,b</sup> Results were obtained using the 6-31G and the 6-31G\* optimized geometries, respectively.

All values are in atomic units.

the geometries obtained with the 6-31G and 6-31G\* basis sets. This is not surprising, as one would expect the unpolarized 6-31G basis to give a good description of the bonding in ethylene chain, and that this description would not be greatly enhanced through the addition of polarization functions only. The two basis sets used here, however, do show an improved agreement with experimentally determined geometrical parameters over those obtained with smaller basis sets (see [14] for a discussion). The small lowering in energy and slight increase in longitudinal polarizability indicate that the effect of the presence of d-orbitals is minimal. The valence band structure of polyethylene with the 6-31G\* basis is given in Figure 2. The 6-31G band structure is not included as the differences between it and Figure 2 are almost imperceptible. The differences between the band structures obtained with the 6-31G and 6-31G\* basis sets are very small indeed, the discrepancies between the band energies all being <10 mHartree.

TABLE IV. Valence band contributions to the SOS longitudinal polarizabilities of polysilane.

Band	3-21G <sup>a</sup>	3-21G <sup>b</sup>	3-21G* <sup>b</sup>
11	0.606	0.557	0.704
12	0.596	0.602	1.087
13	1.428	1.476	1.940
14	1.902	2.006	3.018
15	14.557	14.261	11.706
16	44.662	42.172	35.681
$\alpha_{zz}/\Lambda$	63.778	61.101	54.259

<sup>a,b</sup> Results were obtained using the 3-21G and the 3-21G\* optimized geometries, respectively.

All values are in atomic units.

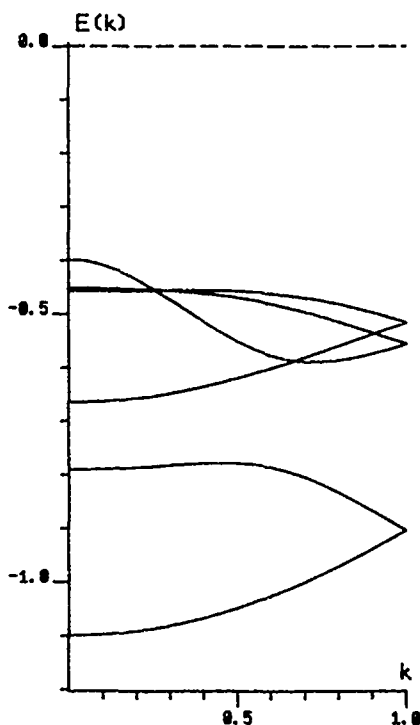


Figure 2. Valence Bands of polyethylene calculated with the 6-31G\* basis set.

The analysis of the contributions of the occupied bands to the computed polarizabilities of polyethylene are similar in both cases, which in turn are similar to analyses previously published [14,31] using smaller basis sets. The sizes of the SOS polarizabilities obtained here with the 6-31G and 6-31G\* basis sets show the expected slight increase over those obtained in these studies with more limited basis sets ( $\alpha_{zz} = 16.332$  (3-21G) and  $\alpha_{zz} = 8.080$  (STO-3G)). The largest contribution to the polarizability is due to the highest occupied band. At the point  $k = 0$ , this band is highly delocalized, and analysis of the LCAO coefficients shows that it is predominantly composed of contributions from carbon  $p_z$  orbitals [13]. On the addition of d-orbitals, this band is slightly stabilized by small d-components of the LCAO coefficients along the polymer backbone. This results in a slight increase in the gap between the valence and conduction bands ( $8.6 \rightarrow 8.8\text{eV}$ ).

The effect of the inclusion of polarization functions is much more striking in the case of polysilane. The optimized geometries of the oligomers with the two basis sets are noticeably different, with a shortening of the Si—Si bond, a slight widening of the Si—Si—Si angle in the backbone and a closing of the H—Si—H angle in going from the 3-21G to 3-21G\* basis sets. These observations are in agreement with previous studies [35–37]. The band structures and density of states of polysilane obtained with the two basis sets are represented in Figures 3 and 4. The most

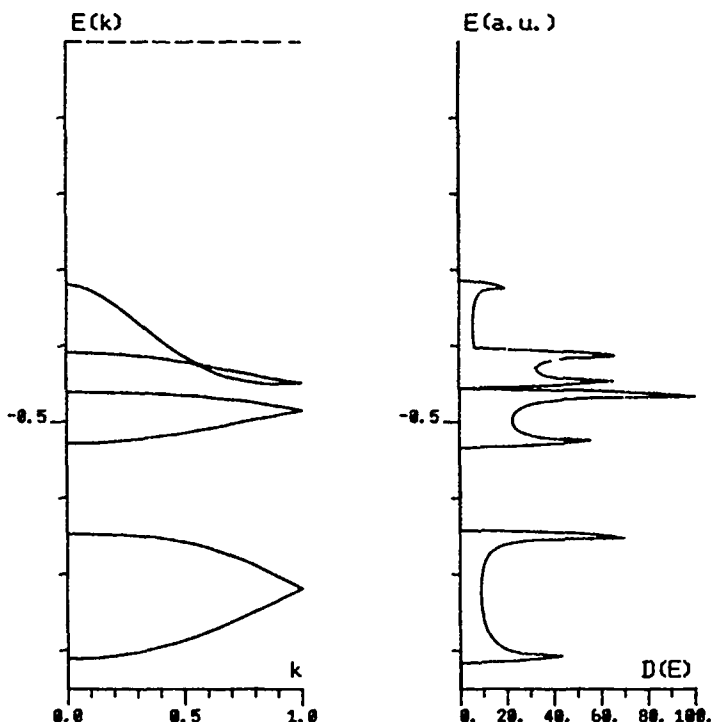


Figure 3. Valence Bands and Density of States of polysilane calculated with the 3-21G basis set

significant change is apparent in the values of the polarizability, which show roughly a 10% decrease on the addition of the polarization functions. This is surprising, as one might intuitively expect an increase in the polarizability on the addition of polarization functions. This effect has been noted previously [38] in coupled Hartree-Fock calculations of the polarizability of silane and disilane with more extensive basis sets. Thus, it seems that the observed decrease in the polarizability here is not solely due the deficiencies of the SOS method or small size of the basis set, but instead point to a role for d-orbitals in the description in the bonding in polysilane. This is supported by the observed shortening in the Si—Si bond and not insignificant contributions from the d-orbitals to the LCAO coefficients. Further calculations [38–40] indicate that the choice of exponents of the polarization functions is crucial and that, ideally, more than one set is desirable to describe the bonding and polarizability.

The major contributions to the computed polarizabilities are due to the highest occupied valence band, as was the case with polyethylene. At  $k = 0$ , this band is predominantly composed of silicon  $p_z$  orbitals, with smaller, though significant, contributions from the d-orbitals with lobes pointing along the polymer backbone for the polarized basis set. The marked reduction in the contribution to the polar-

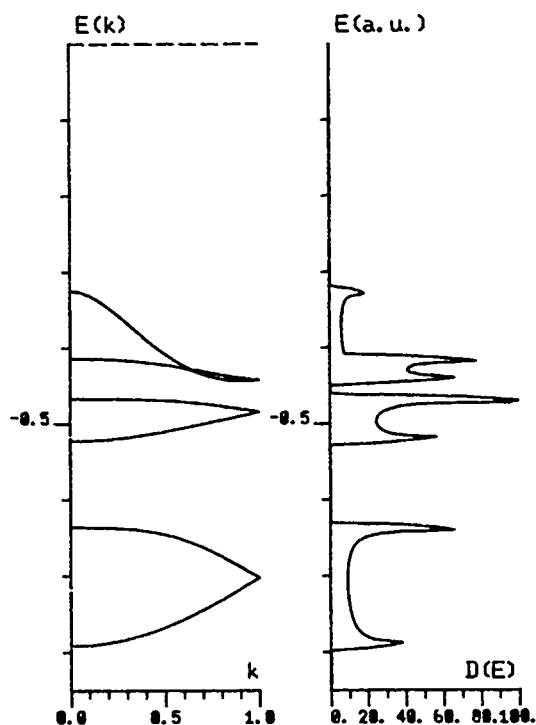


Figure 4. Valence Bands and Density of States of polysilane calculated with the 3-21G\* basis set.

izability from this band on the addition of the polarization functions indicate increased localization of the charge and a reduction in the  $\sigma$ -conjugation along the polymer backbone. We are not in a position to say that the  $\sigma$ -conjugation was previously overstated, but rather that the 3-21G\* basis should give an improved description of the bonding in polysilane and that more accurate studies will rely on more extended basis sets, perhaps with multiple sets of polarization functions with carefully chosen exponents.

### Conclusion

In this article we have given a brief description of an algorithm particularly suited to the computation of two-electron integrals in extended systems, together with the application of the algorithm to the calculation of the band structure and SOS polarizabilities of polyethylene and polysilane using standard basis sets augmented with polarization functions. In the case of polysilane, the polarization functions added to the silicon atoms play a role in increasing the bonding character along the polymer backbone. This improvement on the description of the bonding in polysilane is at the expense of the calculated polarizability, suggesting that more

than one set of d-exponents are necessary to describe the bonding and response properties correctly. Further investigation is also necessary into the question of whether it is appropriate to use the same exponents in molecular and polymeric calculations.

There is much scope for further work into the effect of the addition of polarization functions into the computed energies and properties of polymeric systems.

### Acknowledgments

The authors would like to thank Prof. J. Delhalle and Mr. J. P. Denis for their comments and assistance. D. H. M. thanks the Services de la Programmation de la Politique Scientifique (SPPS) for his grant received in the framework of the ELSAM project (Electronic Large Scale Computational System for Advanced Materials), a part of the Belgian National Program of Impulsion in Information Technology. D. H. M. would also like to acknowledge the organizing committee of the Sanibel Symposia for their financial assistance. B. C. thanks the Belgian National Fund for Scientific Research (FNRS) for his Research Assistant Position. All calculations reported here have been performed on the Namur-Scientific Computing Facility (Namur-SCF), a result of cooperation between the Belgian National Fund for Scientific Research (FNRS), IBM-Belgium, and the Facultés Universitaires Notre-Dame de la Paix.

### Bibliography

- [1] J. M. André, J. Delhalle, and J. L. Brédas, *Quantum Chemistry Aided Design of Organic Polymers* (World Scientific, Singapore, 1991).
- [2] M. Springborg, Phys. Rev. **B40**, 7839 (1989); M. Springborg, Phys. Rev. **B46**, 12790 (1992).
- [3] H. Terame, Phys. Rev. **B46**, 12788 (1992).
- [4] B. I. Greene, J. Orenstein, and S. Schmitt-Rink, Science **247**, 679 (1990).
- [5] A. Buckley, Adv. Mater. **4**, 153 (1992).
- [6] M. Dupuis, J. Rys, and H. F. King, J. Chem. Phys. **65**, 111 (1976).
- [7] L. E. McMurchie and E. R. Davidson, J. Comput. Phys. **26**, 218 (1978).
- [8] J. A. Pople and W. J. Hehre, J. Comput. Phys. **27**, 161 (1978).
- [9] S. Obara and A. Saika, J. Chem. Phys. **84**, 3963 (1986).
- [10] P. M. W. Gill and J. A. Pople, Int. J. Quantum Chem. **40**, 753 (1991).
- [11] J. Ladik, *Quantum Theory of Polymers as Solids*, (Plenum, New York, 1988).
- [12] B. Champagne and J. M. André, Int. J. Quantum Chem. **42**, 1009 (1992).
- [13] J. M. André, Int. J. Quantum Chem. **S24**, 65 (1990).
- [14] B. Champagne, J. G. Fripiat, and J. M. André, Physica Mag. **14**, 123 (1992).
- [15] A. Karpfen, J. Chem. Phys. **75**, 238 (1981).
- [16] R. D. Miller and J. Michl, Chem. Rev. **89**, 1359 (1989).
- [17] C. Pisani and R. Dovesi, Int. J. Quantum Chem. **17**, 501 (1980).
- [18] J. M. André, D. P. Vercouteren, and J. G. Fripiat, J. Comput. Chem. **5**, 349 (1984).
- [19] J. G. Fripiat, D. J. Vanderveken, D. P. Vercouteren, and J. M. André, PLH-91 from MOTECC-91, in *MOTECC-91, Modern Techniques in Computational Chemistry*, Input/Output Documentation, E. Clementi, Ed., part 3, (ESCOM, Leiden, 1991), p. 195; J. G. Fripiat, D. H. Moslev, B. Champagne, and J. M. André, PLH-93 from MOTECC-93 (in press).
- [20] J. M. André, J. L. Brédas, J. Delhalle, D. J. Vanderveken, D. P. Vercouteren, and J. G. Fripiat in *MOTECC-91, Modern Techniques in Computational Chemistry*, E. Clementi, Ed., (ESCOM, Leiden,

- 1991, p. 793; J. M. André, D. H. Mosley, B. Champagne, J. Delhalle, J. G. Fripiat, and J. L. Brédas, in *MOTEC-93. Modern Techniques in Computational Chemistry* (in press).
- [21] J. Delhalle, L. Piela, J. L. Brédas, and J. M. André, *Phys. Rev. B* **22**, 6254 (1980).
- [22] L. Z. Stolarczyk, M. Jeziorska, and H. J. Monkhorst, *Phys. Rev. B* **37**, 10646 (1988); M. Jeziorska, L. Z. Stolarczyk, J. Paldus, and H. J. Monkhorst, *Phys. Rev. B* **41**, 12473 (1990).
- [23] J. G. Fripiat, J. M. André, J. Delhalle, and J. L. Calais, *Int. J. Quantum Chem. S25*, 603 (1991).
- [24] A. Blumen and C. Merkel, *Phys. Status Solidi B* **83**, 425 (1977).
- [25] J. M. André, D. P. Vercauteren, V. P. Bodart, and J. G. Fripiat, *J. Comput. Chem.* **5**, 535 (1984).
- [26] V. P. Bodart, *Mémoire de Licence (F.U.N.D.P., Belgium, 1983)*.
- [27] A. Veillard, in *Computational Techniques in Quantum Chemistry and Molecular Physics*, G. H. F. Dierksen, B. T. Sutcliffe, and A. Veillard (Eds.), NATO ASI C15, D. Reidel (1975).
- [28] C. Barbier, *Chem. Phys. Lett.* **142**, 53 (1987).
- [29] C. Barbier, J. Delhalle, and J. M. André, in *Nonlinear Optical Properties of Polymers*, A. J. Heeger, J. Orenstein, and D. R. Ulrich, Eds., **109**, 143 (Materials Research Society, Pittsburgh, 1988).
- [30] C. Barbier, J. Delhalle, and J. M. André, *J. Mol. Struct. (Theochem.)* **188**, 299 (1989).
- [31] B. Champagne, J. G. Fripiat, and J. M. André, accepted for publication in *Nonlinear Optics*.
- [32] W. J. Hehre, R. Ditchfield, and J. A. Pople, *J. Chem. Phys.* **56**, 2257 (1972); P. C. Hariharan and J. A. Pople, *Chem. Phys. Lett.* **66**, 217 (1972).
- [33] J. S. Binkley, J. A. Pople, and W. J. Hehre, *J. Am. Chem. Soc.* **102**, 939 (1980); J. Chandrasekhar, J. G. Andrade, and P. v-R. Schleyer, *J. Am. Chem. Soc.* **103**, 5609 (1981); M. S. Gordon, J. S. Binkley, J. A. Pople, W. T. Pietro, and W. J. Hehre, *J. Am. Chem. Soc.* **104**, 2797 (1982).
- [34] M. J. Frisch, M. Head-Gordon, G. W. Trucks, J. B. Foresman, H. B. Schlegel, K. Raghavachari, M. Robb, J. S. Binkley, C. Gonzalez, D. J. Defrees, D. J. Fox, R. A. Whiteside, R. Seeger, C. F. Melius, J. Baker, R. L. Martin, L. R. Kahn, J. P. Stewart, S. Topiol, and J. A. Pople, *GAUSSIAN 90*, Revision J (Gaussian, Inc., Pittsburgh, PA, 1990).
- [35] H. M. M. Shearer and V. Vand, *Acta Crystallogr.* **9**, 379 (1956).
- [36] P. W. Teare, *Acta Crystallogr.* **12**, 294 (1959).
- [37] S. Kavesh and J. M. Schultz, *J. Polym. Sci. A2*, 243 (1970).
- [38] G. Avitabile, R. Napolitano, B. Pirozzi, K. D. Rouse, M. W. Thomas, and B. T. M. Willis, *J. Polym. Sci., Polym. Lett. Ed.* **13**, 351 (1975).
- [39] J. T. Nelson and W. T. Pietro, *J. Phys. Chem.* **92**, 1365 (1987).
- [40] J. W. Mintmire and J. V. Ortiz, *Macromolecules* **21**, 1189 (1988).
- [41] H. Terame and K. Takeda, *J. Am. Chem. Soc.* **111**, 1281 (1989).
- [42] M. Dory, L. Beudels, J. G. Fripiat, J. Delhalle, J. M. André, and M. Dupuis, *Int. J. Quantum Chem.* **42**, 1577 (1992).
- [43] D. A. Dixon, *J. Chem. Phys.* **86**, 92 (1988).
- [44] D. H. Mosley, unpublished results.

Received March 14, 1993

# Experiments Pursuant to Determining the Barrier Traversal Time for Quantum Tunneling

MARK J. HAGMANN and LIYANG ZHAO

*Department of Electrical and Computer Engineering, Florida International University,  
Miami, Florida 33199*

## Abstract

Laser illumination of the junction of a scanning tunneling microscope (STM) modulates the barrier height by adding the electric field of light. Numerical simulations suggest that the dependence of tunneling current on the magnitude and frequency of the modulation can serve as a basis for determining the duration of barrier traversal. Modulation increases the mean value of the current when the frequency is much less than the reciprocal of the traversal time. Our simulations also suggest that a 670 nm laser diode at a power density of 100 W/cm<sup>2</sup> will reduce the tunneling current. The latter effect is contrary to most competing phenomena such as current rectification, photo-assisted tunneling, thermal-assisted tunneling, and thermal expansion. We are completing a novel STM which has decreased noise and increased stability in order to make the laser/STM measurements. © 1993 John Wiley & Sons, Inc.

## Introduction

The duration of quantum tunneling is a topic that has generated much interest and controversy (for reviews, see Refs. [1]). Experiments with heterostructures [2] and Josephson junctions [3] suggest that a specific time is associated with barrier traversal. Quantum mechanics does not describe the motion of particles within the classically forbidden region, so that a variety of procedures have been used to calculate the duration of quantum tunneling. However, the results do not agree [1]. Most methods give a definite value of traversal time for a specific problem, which appears inconsistent with the statistical nature of quantum phenomena. Distributions of tunneling times have been predicted using Feynman path integrals [4], Bohm's causal interpretation of quantum mechanics [5], and a hybrid procedure [6]. Again the results do not agree.

It has been shown [7] that tunneling through the reaction barrier must be added to the models in transition state theory in order to obtain accurate quantal micro-canonical rate constants at high energies. Thus, accurate modeling of chemical reactivity requires correcting for time delays due to tunneling, in addition to the well-known delays associated with passage over the barrier [8]. Tunneling times must also be considered for accurately modeling solid state devices. Measured tunnel conductance in heterostructures differs from theory by as much as 2 orders of magnitude unless static image corrections are used for large traversal times and dynamic effects for short traversal times [2]. Tunneling occurs in most solid state



devices, at least in the ohmic contacts [9]. The barrier traversal time in ohmic contacts is probably on the order of 10 fs, so that it may generally be ignored; but it should be considered in picosecond switching and terahertz technology. We anticipate that the effects of tunneling times will also be encountered as progress continues on the generation of femtosecond optical pulses [10].

Several experimental methods have been used to examine tunneling times, but the results are inconclusive. (1) Analyses of measurements of tunnel conductance in heterostructures [2] suggest that the response of image charges is dependent on the traversal time. There is much scatter in the data, but the results appear to be consistent with the semiclassical traversal time. (2) Measurements of the effect of a static magnetic field on the tunneling conductance of heterostructures have been used to determine the traversal time [11], but the data may also be explained without reference to tunneling times [12]. (3) Tunneling dynamics was studied in a shunted Josephson junction [3], but this involves tunneling between the states of a device and does not directly relate to tunneling by particles. (4) An operational tunneling time was determined from measurements of current rectification in a laser-illuminated scanning tunneling microscope (STM) [13]. However, the observed decrease in current with increasing barrier length is not significantly different from the exponential dependence of the transmission coefficient on the barrier length, so that the data may be explained without reference to tunneling times.

Measurements of tunneling times are needed because of the significance of this topic and the present lack of agreement in theoretical analyses. We will make laser/STM experiments that are based on modulation of the barrier height by the electric field of light, rather than current rectification used in the earlier studies by Nguyen et al. [13]. Theory suggests [14] that tunneling has two distinct regimes in respect to the modulation frequency with a crossover where the angular frequency equals the reciprocal of the traversal time.

### Method of Analysis

We model tunneling [15] as a "climb over the barrier" during energy fluctuations consistent with the uncertainty principle. Cohen postulated [16] that the probability of a fluctuation decreases exponentially with the product of the magnitude and duration, which product we refer to as the action of a fluctuation. Cohen did not treat tunneling times, and considered only the most probable fluctuations (minimum action permitting tunneling), thus deriving the WKB solution for an opaque barrier. We have shown [15] that this procedure also results in the semiclassical traversal time, given by  $T_{sc} = d\sqrt{m}/(2(V_0 - E))$ , where  $m$  and  $E$  are the mass and energy of the particle and  $V_0$  and  $d$  are the height and length of a rectangular barrier. We follow the convention of calling this time "semiclassical" because it is the classical time for traversing the inverted barrier [14].

While the result is by no means unanimous, a number of other procedures in addition to considerations of energy fluctuations [15] also result in the semiclassical traversal time. These methods include (1) barrier modulation [14], (2) modulating the incident wave [17], (3) solutions for a sharp wave packet [18], (4) flux-flux

correlation factors [19], (5) dissipation by a string [20], (6) dynamic image potentials [21], (7) temperature effects in macroscopic tunneling [22], (8) "bounce" time for macroscopic tunneling [23], (9) probability amplitudes for momentum [24], (10) duality with ray optics [25], and (11) calculations with path integrals [26].

We make the approximation of using a rectangular barrier in modeling the effect of a laser on the current in an STM. Others have suggested several more elaborate expressions for the potential [27]. The accuracy of these expressions may be questioned because they contain appreciable image corrections, and it appears that the use of static or dynamic images is itself dependent upon the traversal time [2]. It is common to approximate an arbitrary barrier by an "equivalent" rectangular barrier having the same average height in calculations of tunneling current [28], so that this approximation is made for the present.

The barrier length  $d$  is divided into  $N$  segments of length  $d/N$ , such that each part is small enough that the potential is approximately a constant  $V$  during transit by an electron. We assume that an energy fluctuation causes the particle to traverse each segment, and set the magnitude  $\Delta E = V - E + mv^2/2$ , where the particle has mass  $m$ , velocity  $v$ , and unperturbed energy  $E$ . Within each segment we consider only the most probable fluctuations, those with the least action permitting tunneling. Thus, within each segment the velocity  $v$  equals  $\sqrt{2(V - E)/m}$ , the action of the fluctuation  $A$  equals  $d\sqrt{2m(V - E)}/N$ , and the traversal time is given by the semiclassical value  $T = d\sqrt{m/(2(V_0 - E))}/N$ .

For each chosen set of the parameters—wavelength, barrier length and height, and level of modulation—a numerical simulation is made for  $M$  different values of the modulation phase at which the electron enters the barrier. In each simulation the values of  $T$  and  $A$  are calculated within each segment using the instantaneous value of the modulated potential for  $V$ , and summed to determine  $T_s$  and  $A_s$ , which are the traversal time and action for traversing the entire barrier. The relative value of the transmission probability is determined in each of the  $M$  calculations by assuming that the probability of the fluctuation is proportional to  $\exp(-A_s/\hbar)$  [15], where  $\hbar$  is Planck's constant. The relative value of the current with modulation is then found by dividing the mean value of the exponential for each of the  $M$  calculations by the value of the exponential for no modulation. The calculations are repeated with larger values of  $N$  and  $M$  until these two parameters are found to have a negligible effect on the output. The results of several simulations are presented in the following section of this paper.

### Results of Analysis

Figure 1 shows the relative current as a function of the wavelength of modulation for 4.0 eV electrons with a rectangular barrier having a length of 6.0 Å and a height of 5.0V. The three levels of modulation correspond to illumination at different power densities. For modulation at long wavelengths, the electron traverses an approximately static barrier in which the height is either increased or decreased, depending on the phase at the time of entry. Due to the exponential dependence

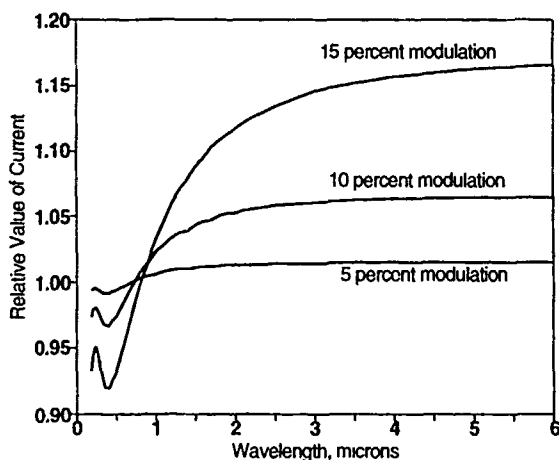


Figure 1 Relative current vs. modulating wavelength for 4.0 eV electrons with barrier length = 6.0 Å and height = 5.0 V.

of current on barrier height, these effects do not cancel. Instead, the modulation increases the mean value of the current at long wavelengths.

For modulation at short wavelengths the height of the barrier is alternately increased and decreased during barrier traversal. Due to the nonlinear dependence of current on barrier height, the effects of the intervals with increased barrier height dominate, and modulation tends to decrease the mean value of the current at short wavelengths. Since there is a distribution of traversal times, instead of the definite

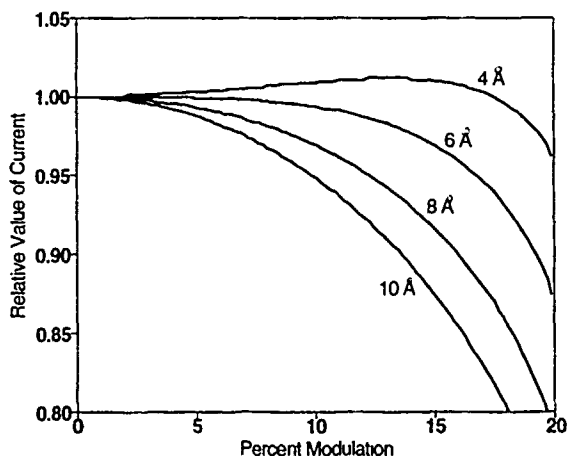


Figure 2. Relative current vs. level of modulation for 4.0 eV electrons with barrier height = 5.0 V and modulating wavelength = 670 nm.

values of time implicit in other analyses [14] the transition between the regimes for long and short wavelengths in Figure 1 is quite broad.

Figure 2 shows the relative current as a function of the level of modulation for 4.0 eV electrons with a barrier height of 5.01 eV. In Figure 2 the wavelength of modulation is 670 nm, which is a typical value for visible laser diodes. A power density of 100 W/cm<sup>2</sup>, providing adequate modulation, may be obtained with a 20 mW laser diode focused to a minimal spot size. The data in Figure 2 suggest that, for barrier lengths between 6 and 10 Å, the current decreases as the power density of the modulating signal is increased.

### Description of Apparatus

We will make laser/STM experiments pursuant to determining the barrier traversal time. Initially we will determine the dependence of current on power density when the STM junction is illuminated with a 670 nm laser diode, and the results will be compared with simulations such as that shown in Figure 2. At a later point, we will measure the current when two or more lasers sequentially illumine the junction of an STM, and look for the transition shown in Figure 1. We are completing a novel STM with decreased noise and increased stability in order to perform these experiments. The feedback loop used to maintain a constant tunneling current will be interrupted for a brief period (typically less than 100 ms) while the current is recorded and the laser is pulsed.

We use a lead zirconate titanate piezoelectric ceramic tube as an electromechanical transducer for  $x$ - $y$ - $z$  fine positioning of the tip and/or sample, as is generally done in an STM (for reviews of STM, see Refs. [29]). The piezoelectric tubes (EBL-3 piezoelectric actuators [30]) have a length of 1.5 cm, diameter of 0.64 cm, and wall thickness of 0.056 cm. The maximum recommended drive is 530 V, and the computed displacements [31] are 72 Å/V in  $z$  and 84 Å/V in  $x$  and  $y$ . The quadrant electrodes on the piezoelectric tube are fed with balanced  $x$  and  $y$  supplies, and the inner electrode is fed from an unbalanced  $z$  supply to provide orthogonal fine positioning. Images will be taken immediately before and after the laser is pulsed in order to detect possible changes in position or structure.

The circuit which drives the piezoelectric transducer has already been completed. This circuit changes the voltage on the transducer in a series of small steps that are determined by the sampled tunneling current through feedback. The potential supplied to the inner electrode of the transducer must have a range of +500 to -500 V in order to cause displacements that exceed the resolution of the associated mechanical system used for coarse positioning. The driver circuit has unusually stringent requirements regarding precision, regulation, and ripple. Fluctuations due to ripple or instability must be less than 1 mV to limit aberrant motion. The driver circuit contains a stable high voltage amplifier similar to that described by Park and Quate [32], which has two stages of regulation.

Others have used a variety of different devices [29] for coarse positioning for the tip and/or sample. We use a differential micrometer with a crossed-roller bearing translation stage (DM-13 and 425-OMA [33]). The differential micrometer has a

fine scale with graduations of  $1\text{ }\mu\text{m}$ , a resolution of  $0.07\text{ }\mu\text{m}$ , and a backlash of  $0.1\text{ }\mu\text{m}$ . Thus, off-the-shelf instruments are used to obtain a resolution much finer than the limit for displacements of the piezoelectric transducer.

A low-noise chopper stabilized operational amplifier [34] preamplifies the tunneling current in our STM. The chopper circuitry repeatedly nulls the input offset voltage to correct for variations due to time, temperature, common-mode voltage, and the power supply, thus providing high dc precision and reducing the low-frequency ( $1/f$ ) noise. The operational amplifier we use [34] has a current offset of  $2.0\text{ pA}$  and an equivalent input noise current of  $4.0\text{ fA/Hz}$ . The tunneling signal is typically on the order of  $1\text{ nA}$ , with an impedance of a few  $\text{M}\Omega$  [32]. Due to the high source impedance, we locate the preamplifier adjacent to the junction of the STM to reduce the capacitance shunting the input to ground. The preamplifier is followed by an instrumentation amplifier located inside the main electronics box. The instrumentation amplifier provides further gain with a very high common-mode rejection ratio.

A multifunction I/O board [35] is installed in the 486 PC dedicated to this project. Software for data acquisition, feedback control, image processing, and gating of the laser is being written in Lab Windows. The output of the instrumentation amplifier is connected directly to the I/O board. After simulating various control algorithms, we have chosen to use adaptive digital incremental feedback control with a predictive error signal. Incremental algorithms provide finer control than direct algorithms and also prevent integral windup [36]. The predictive error is calculated from a linear regression with a set of values proportional to the logarithm of the ratios of the sampled tunneling currents to the set point current. Our simulations suggest that the use of logarithms in the error signal causes a substantial increase in the stability of feedback control. This improvement may be understood because the logarithm of the tunneling current varies linearly with the length of the junction, which varies linearly with the voltage to the piezoelectric transducer, which is controlled by the error signal.

### Discussion and Conclusions

Many different phenomena occur in a laser-illuminated STM [37] in addition to the effect which we have modeled. These effects include current rectification, photo-assisted tunneling, thermal-assisted tunneling, thermal expansion, and the direct interaction of tunneling particles with modulation quanta [14]. In our initial experiments following Figure 2, the use of a visible laser will decrease the effects of current rectification [38]. The relatively low power densities will reduce thermal effects as well as current rectification, but all of these phenomena must be considered. Fortunately, the predicted decrease in current with illumination of the junction is contrary to most of the competing phenomena.

Experiments made later to look for the transition shown in Figure 1 would be more difficult to interpret because the competing phenomena have different frequency dependence. However, since decreased current is predicted for modulation at shorter wavelengths (increased quanta size), the predicted effect differs from most of the competing phenomena.

### Acknowledgement

We are grateful to Professor James Mantovani of the Department of Physics and Space Sciences at Florida Institute of Technology for useful discussions on the construction of a STM, and to Professor George Flynn in the Department of Chemistry at Columbia University and Professor John Breen in the Department of Chemistry at Indiana University-Purdue University at Indianapolis for their suggestions on techniques for laser/STM measurements. This work was supported in part by the Division of Sponsored Research and Training at Florida International University.

### Bibliography

- [1] A. P. Jauho, in *Hot Carriers in Semiconductor Nanostructures*, J. Shah, Ed. (Academic, New York, 1992), pp. 121-151; M. Buttiker, in *Electronic Properties of Multilayers and Low-Dimensional Semiconductor Structures*, J. M. Chamberlain, L. Eaves, and J.-C. Portal, Eds. (Plenum, New York, 1990), pp. 297-315.
- [2] P. Gueret, E. Marclay, and H. Meier, *Appl. Phys. Lett.* **53**, 1617 (1988).
- [3] D. Esteve, J. M. Martinis, C. Urbina, E. Turlot, M. H. Devoret, H. Grabert, and S. Linkwitz, *Physica Scr.* **T29**, 121 (1989).
- [4] H. A. Fertig, *Phys. Rev. Lett.* **65**, 2321 (1990); D. Sokolovski and J. N. J. Connor, *Phys. Rev. A* **44**, 1500 (1991).
- [5] C. R. Leavens, *Solid State Commun.* **76**, 253 (1990).
- [6] N. J. Persson, *Physica Scr.* **38**, 282 (1988).
- [7] D. C. Chatfield, R. S. Friedman, D. W. Schwenke, and D. G. Truhlar, *J. Phys. Chem.* **96**, 2414 (1992).
- [8] N. Abusalbi, D. J. Kouri, M. Baer, and E. Pollak, *J. Chem. Phys.* **82**, 4500 (1985).
- [9] J. Crofton, P. A. Barnes, and M. J. Bozack, *Am. J. Phys.* **60**, 499 (1992).
- [10] E. Golovchenko, E. M. Dianov, and P. V. Mamyshev, *J. Opt. Soc. Am. B* **7**, 172 (1990).
- [11] P. Gueret, A. Baratoff, and E. Marclay, *Europhys. Lett.* **3**, 367 (1987).
- [12] L. Eaves, K. W. H. Stevens, and F. W. Sheard, in *The Physics and Fabrication of Microstructures and Microdevices*, M. J. Kelly and C. Weisbuch, Eds. (Springer-Verlag, Berlin, 1986).
- [13] H. Q. Nguyen, P. H. Cutler, T. E. Feuchtwang, Z.-H. Huang, Y. Kuk, P. J. Silverman, A. A. Lucas, and T. E. Sullivan, *IEEE Trans. Electron Devices* **36**, 2671 (1989); A. A. Lucas, P. H. Cutler, T. E. Feuchtwang, T. T. Tsong, T. E. Sullivan, Y. Kuk, H. Nguyen, and P. J. Silverman, *J. Vac. Sci. Technol. A* **6**, 461 (1988).
- [14] M. Buttiker and R. Landauer, *Phys. Rev. Lett.* **49**, 1739 (1982); M. Buttiker and R. Landauer, *Physica Scr.* **32**, 429 (1985).
- [15] M. J. Hagmann, *Solid State Commun.* **82**, 867 (1992).
- [16] B. L. Cohen, *Am. J. Phys.* **33**, 97 (1965).
- [17] M. Buttiker and R. Landauer, *IBM J. Res. Dev.* **30**, 451 (1986).
- [18] K. W. H. Stevens, *J. Phys. C* **16**, 3649 (1983); P. Moretti, *Physica Scr.* **45**, 18 (1992).
- [19] E. Pollak and W. H. Miller, *Phys. Rev. Lett.* **53**, 115 (1984).
- [20] A. Schmid, *Ann. Phys. (NY)* **170**, 333 (1986).
- [21] M. Jonson, *Solid St. Commun.* **33**, 743 (1980).
- [22] R. Bruinsma and P. Bak, *Phys. Rev. Lett.* **56**, 420 (1986).
- [23] A. J. Leggett, *Prog. Theor. Phys. Suppl.* **69**, 80 (1980).
- [24] A. A. Sokolov, Y. M. Loskutov, and I. M. Ternov, *Quantum Mechanics*, Scripta Technica transl. (Holt, Rinehart and Winston, New York, 1966), pp. 102-103; P. Schnupp, *Thin Solid Films* **2**, 177 (1968).
- [25] L. S. Schulman, in *Le Dualisme Onde-Corpuscle*, S. Diner et al., Eds. (Reidel, Dordrecht, 1984), pp. 270-271.

- [26] L. S. Schulman and R. W. Ziolkowski, in *Path Integrals from meV to MeV*, V. Sa-yakanit, W. Sritrakool, J. Berananda, M. C. Gutzwiller, A. Inomata, S. Lundquist, J. R. Klauder, and L. S. Schulman, Eds. (World Scientific, Singapore, 1989), p. 25.
- [27] N. M. Miskovski, P. H. Cutler, T. E. Feuchtwang, and A. A. Lucas, *Int. J. Infrared Millim. Waves* **2**, 739 (1981); L. E. Bar'yudin, V. L. Bulatov, and D. A. Telnov, *J. Appl. Phys.* **71**, 346 (1992).
- [28] A. T. Fromhold, Jr., *Quantum Mechanics for Applied Physics and Engineering* (Dover, New York), pp. 264-265.
- [29] Y. Kuk and P. J. Silverman, *Rev. Sci. Instrum.* **60**, 165 (1989); D. W. Pohl, *IBM J. Res. Dev.* **30**, 417 (1986).
- [30] Staveley Sensors Inc., East Hartford, CT.
- [31] C. J. Chen, *Appl. Phys. Lett.* **60**, 132 (1992).
- [32] S. Park and C. F. Quate, *Rev. Sci. Instrum.* **58**, 2010 (1987).
- [33] Newport Corp., Irvine, CA.
- [34] Texas Instruments TLC 2652 AMJGB
- [35] National Instruments AT-MIO-16.
- [36] W. F. Stoecker and P. A. Stoecker, *Microcomputer Control of Thermal and Mechanical Systems* (Van Nostrand Reinhold, New York, 1989), pp. 410-412.
- [37] Z. Hassan, D. Andsager, D. Saltz, K. Cartwright, and M. H. Nayfeh, *Rev. Sci. Instrum.* **63**, 2099 (1992).
- [38] A. Sanchez, C. F. Davis, Jr., K. C. Liu, and A. Javan, *J. Appl. Phys.* **49**, 5270 (1978).

Received May 24, 1993

# Theoretical Studies of the Oxidation of N- and S-Containing Compounds by Cytochrome P450

GILDA H. LOEW and YAN-TYNG CHANG

*Molecular Research Institute, 845 Page Mill Road, Palo Alto, California 94304*

## Abstract

Many xenobiotics containing N or S heteroatoms are metabolized by the cytochrome P450s, leading to a variety of products which can be toxic, carcinogenic, or detoxifying. Thus, it is important to try to establish molecular criteria that modulate competitive product formation for these types of compounds. In the absence of 3D structures for the P450 isozymes that are responsible for the oxidations of N- and S-containing compounds, we have focused here on the characterization and identification of possible electronic and thermodynamic factors that could be modulators of different types of product formation. Specifically, the competition among N-oxidation, N-hydroxylation and C $\alpha$ -hydroxylation for three amines were examined. Similarly, three thioethers were studied for their internal competition between S-oxidation and C $\alpha$ -hydroxylation. The results obtained indicate that the stability of the cation radical intermediate formed by the one electron transfer mechanism is not a determinant of differences in product distribution between the two types of compounds. Rather, relative product stability appears to be a significant modulator of product distribution explaining why S-oxide formation is favored over N-oxide and why C $\alpha$ -hydroxylation is usually favored over N-oxide formation in amines. © 1993 John Wiley & Sons, Inc.

## Introduction

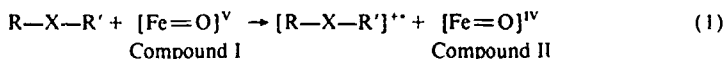
Many nitrogen- and sulfur-containing compounds are used as therapeutic agents, insecticides, or industrial substances. When metabolized by the cytochrome P450 enzymes [1], responsible for the initial metabolism of many xenobiotics, these N- and S-containing compounds are transformed into species that can be either toxic, carcinogenic, or detoxifying [2]. It is therefore important to try to identify molecular criteria that modulate competitive product formation for these types of compounds to be used for risk assessment. Ideally, two types of properties should be considered: (1) the steric interaction between the substrate and the enzyme and (2) the intrinsic electronic properties of the parent substrate compound and the thermodynamics of the reaction pathways leading to its products. However, in the absence of 3D structures of the P450 isozymes that are responsible for the oxidations of these compounds, we have focused here on the second type only, namely, the characterization and identification of possible electronic and thermodynamic factors that could be modulators of different types of product formation.

For amines and thioethers, two qualitatively different P450-mediated oxidations were observed. The first involves an oxidation at the heteroatom site which converts the substrate into its corresponding heteroatom oxide or heteroatom hydroxide.



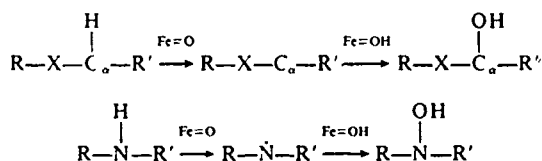
The second one is  $C_\alpha$ -hydroxylation which is usually followed by dealkylation. The reaction mechanisms and factors that lead to these competing products are still not very well characterized.

Recently, Guengerich and coworkers proposed a unified mechanism of many types of reaction catalyzed by the cytochrome P450s based on a common first step of a one-electron transfer from the substrate to the ferryl [FeO] species of the heme protein [3]. This mechanism has been observed in studies using metalloporphyrin-catalyzed model systems for cytochrome P450 monooxygenases [4]. For N- and S-containing compounds, it leads to the formation of a heteroatom cation radical and compound II of P450 as shown below:



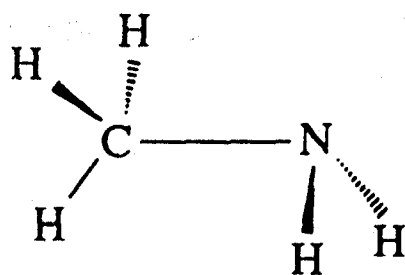
Guengerich et al. [3] have suggested that this cation radical may be the common intermediate for both heteroatom oxygenation and  $C_\alpha$ -hydroxylation.

Another frequently proposed pathway for  $C_\alpha$ -hydroxylation is an initial hydrogen abstraction by the ferryl oxygen followed by fast radical recombination [5]. For primary and secondary amines, hydrogen abstraction at the nitrogen atom site is also possible, leading to N-hydroxide products [6]:

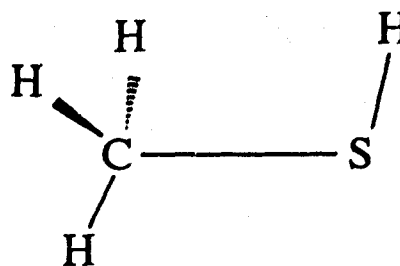


Determination of which of these proposed mechanisms is preferred by purely experimental methods is very difficult due to the transient nature of the different proposed intermediates. On the other hand, theoretical methods can be very useful in characterizing and comparing these different reaction pathways since they can include descriptions of these transient intermediates.

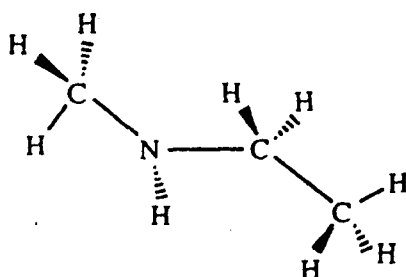
From earlier studies [7] of the electronic structure of the [Fe—O] prosthetic moiety of P450 in its active state, the ground state of compound I was found to be a quartet with two unpaired electrons localizing partly on the  $2p_x$  and  $2p_y$  orbitals of the oxygen atom. A triplet oxene species,  $\text{O}(^3\text{P})$ , is the simplest model capable of representing the triplet character of the [Fe—O] moiety, and was found to correctly describe many reactions catalyzed by P450s [8]. Therefore, in this study,  $\text{O}(^3\text{P})$  was used in model oxidation reaction of three amines and three thioethers that were characterized by *ab initio* quantum chemistry calculations of the reactants, the radical intermediates and the oxidation products. Figure 1 shows the three amines (methyl amine, methyl ethyl amine, and *N*-methyl aniline) and the three thioethers (methanethiol, methyl ethyl thioether, and thioanisole) chosen in this investigation.



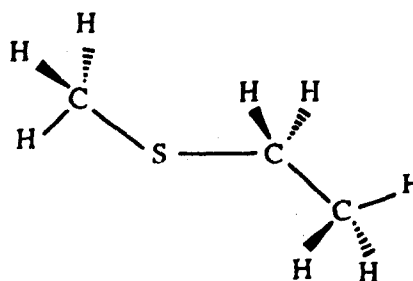
Methyl Amine



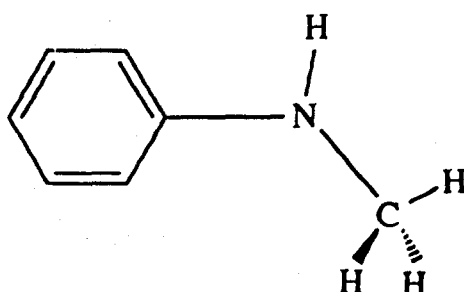
Methanethiol



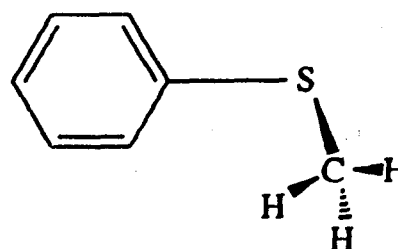
Methyl Ethyl Amine



Methyl Ethyl Thioether



N-Methyl Aniline



Thioanisole

Figure 1. Structures of the three amines and the three thioethers chosen for this study.

The goals of this study are: (I) to identify the origin of the observed preference for heteroatom oxide formation in S-containing compounds compared to N-containing compounds, (II) to characterize the internal competition of different oxidation reactions in amines to explain why C<sub>α</sub>-hydroxylation-dealkylation is usually preferred, and (III) to characterize the internal competition of reactions in thioethers to explain why sulfoxide formation is usually preferred.

### Methods

The Gaussian 92 program [9] was used for all calculations. For each species, the fully optimized geometry in its ground electronic state was obtained using standard energy gradient techniques. A 3-21G\* basis set with an extra d function for the N atom ( $\alpha = 0.8$ ) and a 6-31G\* basis set were used in these calculations. Restricted and unrestricted Hartree-Fock methods were used for closed shell and open shell species, respectively. If nonnegligible spin contamination was found for any open shell species, a calculation using restricted open shell Hartree-Fock method (ROHF) and the 6-31G\* basis set was performed. The computations for all compounds were performed at the SCF levels of theory, i.e., SCF/3-21G\* ( $N_d = 0.8$ ) and SCF/6-31G\*. For methyl ethyl amine and methyl ethyl thioether, both the *trans* and *gauche* C—X—C—X (X = N or S) conformations were minimized at the SCF/3-21G\* levels and the more stable conformation was then chosen for subsequent studies. For *N*-methyl aniline and thioanisole, the rotational barrier about the C<sub>φ</sub>—N and the C<sub>φ</sub>—S ( $\phi$  represents the phenyl ring) bonds were examined by studying the energies of the perpendicular and the planar side chain conformations using both 3-21G\* +  $N_d$  and the 6-31G\* basis sets. The conformation with the lower energy in each molecule was used as the parent compound in this study.

For each of the three amines, the three types of radical intermediates, i.e., the N-cation radical, C<sub>α</sub>-radical, and N-radical, and the three reaction products, N-oxide, C<sub>α</sub>-hydroxide, and N-hydroxide, were calculated. For methyl ethyl amine, there are two possible C<sub>α</sub>-hydroxylation sites: the primary carbon of the methyl group and the secondary carbon of the ethyl group. Therefore, both of them were considered in this investigation. For the three thioethers, the S-cation radical and the C<sub>α</sub>-radical along with their oxidation products, i.e., sulfoxide and C<sub>α</sub>-hydroxide were characterized. Again, both C<sub>α</sub>-hydroxylation sites in methyl ethyl thioether were considered.

### Results and Discussion

Tables I and II list the calculated energies of all N-containing and S-containing species, respectively. Comparing the energies of the two conformations studied for methyl ethyl amine, the *trans* conformer (as shown in Fig. 1) was found to be slightly lower by 1.0 kcal/mol than the *gauche* conformer from the 3-21G\* +  $N_d$  calculation. Similarly, for methyl ethyl thioether, the energy of the *trans* conformer is lower than the *gauche* conformer by 0.2 kcal/mol. Therefore, the *trans* conformation was used for these two parent compounds, and all intermediates and oxidation products derived from the *trans* conformer were calculated.

For *N*-methyl aniline, both 3-21G\* +  $N_d$  and 6-31G\* predict a planar C<sub>φ</sub>—C<sub>φ</sub>—N—C<sub>m</sub> (where C<sub>φ</sub> indicates a C atom in the phenyl ring, while C<sub>m</sub> is the methyl carbon atom) conformation as the lowest energy conformer. The rotational barrier from planar to perpendicular conformation is found to be 0.3 kcal/mol from 3-21G\* +  $N_d$  and 1.6 kcal/mol from 6-31G\* calculation, respectively. On the contrary, for thioanisole, the perpendicular conformation was found to be energetically more favorable by 1.7 and 1.2 kcal/mol using the two levels of calcu-

TABLE I Absolute energies of molecular species involving in the oxidation of N-containing compounds.<sup>a</sup>

Molecule	3-21G* + Nd(0.8)	6-31G*
O ( <sup>3</sup> P)	-74.393657	-74.783934 -74.778966 <sup>b</sup>
O <sup>-</sup>	-74.271936	-74.718791
OH	-74.970228	-75.382275 -75.378369 <sup>b</sup>
CH <sub>3</sub> NH <sub>2</sub>	-94.720975	-95.209829
CH <sub>3</sub> N <sup>+</sup> H <sub>2</sub>	-94.452862	-94.932226
CH <sub>2</sub> NH <sub>2</sub>	-94.101057	-94.586733
CH <sub>3</sub> NH	-94.106132	-94.591912
CH <sub>3</sub> N(O)H <sub>2</sub>	-169.078832	-169.973532
CH <sub>3</sub> NH(OH)	-169.119729	-170.011578
CH <sub>2</sub> (OH)NH <sub>2</sub>	-169.164438	-170.068356
CH <sub>3</sub> NHCH <sub>2</sub> CH <sub>3</sub> ( <i>gauche</i> )	-172.356145	
CH <sub>3</sub> NHCH <sub>2</sub> CH <sub>3</sub> ( <i>trans</i> )	-172.357785	-173.276489
CH <sub>3</sub> N <sup>+</sup> HCH <sub>2</sub> CH <sub>3</sub>	-172.117563	-173.027538
CH <sub>3</sub> NHCHCH <sub>3</sub>	-171.738334	-172.655294
CH <sub>2</sub> NHCH <sub>2</sub> CH <sub>3</sub>	-171.737029	-172.652886
CH <sub>3</sub> NCH <sub>2</sub> CH <sub>3</sub>	-171.748831	-172.665531
CH <sub>3</sub> NH(O)CH <sub>2</sub> CH <sub>3</sub>	-246.729561	-248.050747
CH <sub>3</sub> N(OH)CH <sub>2</sub> CH <sub>3</sub>	-246.755815	-248.076832
CH <sub>3</sub> NHCH(OH)CH <sub>3</sub>	-246.805451	-248.136431
CH <sub>2</sub> (OH)NHCH <sub>2</sub> CH <sub>3</sub>	-246.799194	-248.133485
Phe-NH-CH <sub>3</sub> (90°)	-322.988352	-324.753486
Phe-NH <sup>+</sup> ·CH <sub>3</sub> (180°)	-322.988887	-324.756110
Phe-N <sup>+</sup> H-CH <sub>3</sub>		-324.522313 <sup>b</sup>
Phe-NH-CH <sub>2</sub>		-324.129758 <sup>b</sup>
Phe-N-CH <sub>3</sub>		-324.140495 <sup>b</sup>
Phe-NH(O)-CH <sub>3</sub>	-397.352822	-399.519511
Phe-N(OH)-CH <sub>3</sub>	-397.390592	-399.555674
Phe-NH-CH <sub>2</sub> (OH)	-397.432723	-399.613990

<sup>a</sup> If not noted, RHF and UHF were used for closed shell and open shell species.

<sup>b</sup> From an ROHF calculation.

lations. Therefore, the parent compound of a planar conformation was used for *N*-methyl aniline while a perpendicular conformation was used for thioanisole.

The calculated expectation values of  $S^2$  are between 0.75 and 0.77 using the UHF method for all radical intermediates except those derived from *N*-methyl aniline. Large spin contaminations ( $\langle S^2 \rangle > 0.8$ ) were found for its N-cation radical, C $_{\alpha}$ -radical and N-radical. Therefore, ROHF and 6-31G\* basis set were used to reoptimize these three radical species. Their minimized energy are listed in Table I.

TABLE II. Absolute energies of molecular species involving in the oxidation of S-containing compounds \*

Molecule	3-21G*	6-31G*
CH <sub>3</sub> SH	-435.637275	-437.700320
CH <sub>3</sub> S <sup>+</sup> H	-435.327695	-437.393159
CH <sub>2</sub> SH	-435.011752	-437.072347
CH <sub>3</sub> S(O)H	-510.010483	-512.488249
CH <sub>2</sub> (OH)SH	-510.065842	-512.548412
CH <sub>3</sub> SCH <sub>2</sub> CH <sub>3</sub> ( <i>gauche</i> )	-513.276171	
CH <sub>3</sub> SCH <sub>2</sub> CH <sub>3</sub> ( <i>trans</i> )	-513.276465	-515.770527
CH <sub>3</sub> S <sup>+</sup> CH <sub>2</sub> CH <sub>3</sub>	-512.999688	-515.495419
CH <sub>3</sub> SCHCH <sub>3</sub>	-512.654411	-515.147053
CH <sub>2</sub> SCH <sub>2</sub> CH <sub>3</sub>	-512.546506	-515.143483
CH <sub>3</sub> S(O)CH <sub>2</sub> CH <sub>3</sub>	-587.668361	-590.573572
CH <sub>3</sub> SCH(OH)CH <sub>3</sub>	-587.713438	-590.623479
CH <sub>2</sub> (OH)SCH <sub>2</sub> CH <sub>3</sub>	-587.701380	-590.614460
Phe-S-CH <sub>3</sub> (90°)	-663.904681	-667.245282
Phe-S-CH <sub>3</sub> (180°)	-663.902025	-667.243374
Phe-S <sup>+</sup> -CH <sub>3</sub> (90°)	-663.625604	-666.968958
Phe-S-CH <sub>2</sub> (90°)	-663.279328	-666.617558
Phe-S(O)-CH <sub>3</sub>	-738.299271	-742.047557
Phe-S-CH <sub>2</sub> (OH) (~90°)	-738.331089	-742.090428

\* RHF and UHF methods were used for closed shell and open shell species, respectively. Energies are in hartrees.

### Origin of Observed Preference for Heteroatom Oxide Formation: S > N

As proposed by Guengerich et al. [3], heteroatom oxide is formed via an initial electron transfer from the substrate to the [FeO] moiety of P450, followed by an oxygen transfer in the opposite direction. From energetic consideration, whether or not the electron transfer occurs is determined by the free energy change associated with Eq. (1). An estimate of this change can be made if the ionization potential of the substrate R—X—R' and the electron affinity of P450 compound I are known. However, there has been no report on the magnitude of the affinity of compound I, and the stability of the cation radical relative to its parent molecule [i.e., the ionization potential (IP)] is used as a measure of the relative tendency of various substrates to be oxidized via the one electron transfer reaction [3]. To this end, the ionization potential of each of the six parent compounds was calculated and the results are shown in Table III(A). Comparison between the amines and the corresponding thioethers with similar structures shows that the IPs for the amines are lower than those of the thioethers. For example, from 6-31G\* calculation, IP is 174.2 kcal/mol for methyl amine and 192.7 kcal/mol for methanethiol. The IP for methyl ethyl thioether is 16.4 kcal/mol higher than that of methyl ethyl amine. Similarly, the IP for thioanisole (173.4 from UHF) is also higher than that of the N-methyl aniline (146.7 from ROHF). Based on these results, we concluded: (1)

TABLE III. (A) Ionization potentials of heteroatom-containing parent compounds obtained from the energy difference between neutral and cationic species. (B) Energies of heteroatom oxide products relative to the parent compound and  $O(^1P)$ .<sup>a</sup>

	3-21G*	6-31G*
(A) Ionization potential		
$CH_3NH_2$	168.2	174.2
$CH_3SH$	194.3	192.7
$CH_3PH_2$		180.9
$CH_3NHC_2H_5$	150.7	156.0
$CH_3SCH_2CH_3$	173.7	172.4
Phe-NHCH <sub>3</sub>		146.7 <sup>b</sup>
Phe-S-CH <sub>3</sub>	175.1	173.4
(B) Relative energy of heteroatom oxide products		
$CH_3NH_2$	22.5	12.7
$CH_3SH$	12.8	-2.5
$CH_3PH_2$		-56.9
$CH_3NHC_2H_5$	13.7	6.1
$CH_3SCH_2CH_3$	1.1	-12.0
Phe-NHCH <sub>3</sub>	18.7	12.9
Phe-S-CH <sub>3</sub>	0.6	-11.5

\* All energies are in kcal/mol.

<sup>b</sup> From an ROHF calculation.

In order for all six substrates to undergo one-electron transfer mechanism, the electron affinity of P450 compound I must be at least 150–190 kcal/mol. (2) The lower ionization potentials of amine compounds compared to the thioether analogues imply a higher probability of one-electron oxidation in amines than in thioethers. If the production of the cation radical is the rate-limiting step in the heteroatom oxide formation, these results indicate a higher preference of oxide formation in amines than in thioethers. This inference is in contradiction with the observed preference of heteroatom oxide formation in S-containing compounds compared to N-containing compounds. Therefore, the observed preference can be explained in two ways: (i) the oxide formation does not proceed via the one-electron transfer mechanism or (ii) the formation of the cation radical is not the rate-limiting step during the enzymatic cycle of this mechanism. Without knowledge of the electron affinity of P450 compound I, needed to assess the possibility of electron transfer reactions or of the detailed rate constant for each enzymatic step, the only conclusion that can be reached here and the one most relevant for our goals is that the relative stability of the cation radical cannot be used as a modulator of the preference of heteroatom oxide formation.

Another possible mechanism for the heteroatom oxide formation is a one-step direct oxygen atom transfer without the formation of the intermediate cation radical. Based on this mechanism, in Table III(B) a comparison of the heteroatom oxide

stabilities of the amines with those of the thioethers was made in order to examine if product stability is a possible modulator of the observed preference of heteroatom oxide formation in S-containing compounds than in N-containing compounds. For each of the three pairs of compounds, the S-oxide is, in each case, more stable than the corresponding N-oxide. For example, from 6-31G\* calculation, the difference in stability between the oxides of methyl amine and methanethiol is 15.2 kcal/mol. Similarly, the differences for the methyl ethyl amine and methyl ethyl thioether are 18.1 and 24.4 kcal/mol for the two aryl analogs. These results demonstrate that the relative heteroatom oxide stability is a very good indicator of the observed preference of S-containing compounds for heteroatom oxide formation compared to N-containing compounds.

To further explore the reliability of heteroatom oxide stability, rather than the cation radical stability, as a good indicator of the preference of heteroatom oxide formation in various compounds, we also calculated the energy of methyl phosphine, its cation radical, and methyl phosphine oxide using the 6-31G\* basis set. P450-mediated oxidations of phosphorous containing compounds lead to a greater preference for heteroatom oxide formation than in either N- or S-containing compounds. As shown in Table III(A), the rank order of IP for the N-, S-, and P-containing cation radicals,  $S > P > N$ , does not parallel their preference for heteroatom oxide formation  $P > S > N$ . The result provides further evidence that the relative cation radical stability is not a determinant of heteroatom oxide formation. Instead, the rank order of the stability of heteroatom oxide product shown in Table III(B),  $P > S > N$ , is consistent with preference for heteroatom oxide formation and reinforces our conclusion that relative oxide stability is a significant modulator of P450-mediated oxide formation.

#### *Internal Competition in Formation of Three P450 Mediated Oxidation Products of Amine Substrates*

To identify reliable determinants of product distribution in cytochrome P450-mediated oxidations in amines, plausible pathways to the three types of products,  $C_\alpha$ -hydroxides, N-hydroxides, and N-oxides, were considered. Specifically, the formation of  $C_\alpha$ -hydroxides and N-hydroxides was assumed to proceed via an initial hydrogen atom abstraction. The formation of N-oxide was assumed to proceed via a one-step direct oxygen transfer mechanism due to its success in explaining the preference of oxide formation between N- and S-compounds. The stabilities of the  $C_\alpha$ -radical, the N-radical intermediates in the proposed H-abstraction mechanism and the N-oxide product were hence calculated. The results are shown in Table IV for the three amine substrates studied. For all three compounds, the  $C_\alpha$ -radical is less stable than both the N-radical intermediate and the N—O product by a few kcal/mol, a result that is in contrast to the observed preference of  $C_\alpha$ -hydroxylation-dealkylation in amines. Therefore, the relative stability of competing  $C_\alpha$ - and N-radical intermediates is not a reliable determinant of different product formation.

Comparison of the stability of the three oxidation products also shown in Table IV gives the order  $C_\alpha$ -hydroxide  $>$  N-hydroxide  $>$  N-oxide in all three amines. The formation of the  $C_\alpha$ -hydroxides and the N-hydroxides are both exothermic while

TABLE IV. Relative reaction energies (kcal/mol) for N-containing compounds.

		3-21G*	6-31G*
Reactants	$\text{CH}_3\text{NH}_2 + \text{O}(^3\text{P})$	0.0	0.0
$\text{C}_\alpha\text{-H}$ intermediates	$\text{CH}_2\text{NH}_2 + \text{OH}$	27.2	15.5
N-OH intermediates	$\text{CH}_3\text{NH} + \text{OH}$	24.0	12.3
N-O product	$\text{CH}_3\text{N}(\text{O})\text{H}_2$	22.5	12.7
N-OH product	$\text{CH}_3\text{N}(\text{OH})\text{H}$	-3.2	-11.2
$\text{C}_\alpha\text{-OH}$ product	$\text{CH}_2(\text{OH})\text{NH}_2$	-31.3	-46.8
Reactants	$\text{CH}_3\text{NHC}_2\text{H}_5 + \text{O}(^3\text{P})$	0.0	0.0
$\text{C}_\alpha\text{-OH}$ intermediates	$\text{CH}_3\text{NHCHCH}_3 + \text{OH}$	26.9	14.4
$\text{C}_\alpha\text{-OH}$ intermediates	$\text{CH}_2\text{NHCH}_2\text{CH}_3 + \text{OH}$	27.7	15.9
N-OH intermediates	$\text{CH}_3\text{NC}_2\text{H}_5 + \text{OH}$	20.3	9.5
N-O product	$\text{CH}_3\text{NH}(\text{O})\text{C}_2\text{H}_5$	13.7	6.1
N-OH product	$\text{CH}_3\text{N}(\text{OH})\text{CH}_2\text{CH}_3$	-2.7	-10.3
$\text{C}_\alpha\text{-OH}$ product	$\text{CH}_3\text{NHCH}(\text{OH})\text{CH}_3$	-33.9	-47.7
$\text{C}_\alpha\text{-OH}$ product	$\text{CH}_2(\text{OH})\text{NHC}_2\text{H}_5$	-30.0	-45.8
Reactants	$\text{Phe-NHCH}_3 + \text{O}(^3\text{P})$	0.0	0.0
$\text{C}_\alpha\text{-OH}$ intermediates	$\text{Phe-NHCH}_2 + \text{OH}$		16.9*
N-OH intermediates	$\text{Phe-NCH}_3 + \text{OH}$		10.2*
N-O product	$\text{Phe-NH}(\text{O})\text{CH}_3$	18.7	12.9
N-OH product	$\text{Phe-N}(\text{OH})\text{CH}_3$	-5.05	-9.8
$\text{C}_\alpha\text{-OH}$ product	$\text{Phe-NHCH}_2(\text{OH})$	-31.5	-46.4

\* From an ROHF calculation.

the production of N-oxide is endothermic. The large energy difference of  $\sim 50$ – $\sim 60$  kcal/mol obtained from 6-31G\* between the N-oxide and the  $\text{C}_\alpha$ -hydroxide in the three amines suggests that the formation of  $\text{C}_\alpha$ -hydroxy amine is energetically much more favorable. This result agrees with the observation by Guengerich et al. [3] and others [10] that  $\text{C}_\alpha$ -hydroxylation–dealkylation is the predominant oxidation reaction in amines. Thus it appears that the relative stabilities of the different products modulate the competition among the various reactions. Among the two heteroatom oxygenations, N—OH was found to be  $\sim 35$  kcal/mol more stable than N—O product and would therefore be predicted to be the next most abundant product.

#### *Internal Competition in Formation of Two P450 Mediated Oxidation Products of Thioether Substrates*

To identify reliable modulators of cytochrome P450-mediated oxidations of sulfur-containing compounds, as for the N-containing compounds, it was assumed that  $\text{C}_\alpha$ -hydroxylation proceeds via H-abstraction and sulfoxide formation via direct oxygen transfer. The stability of the  $\text{C}_\alpha$ -radical and OH radical intermediates for each of the three substrates was calculated as shown in Table V, and compared



TABLE V Relative reaction energies (kcal/mol) for S-containing compounds.

		3-21G*	6-31G*
Reactants	$\text{CH}_3\text{SH} + \text{O}(^3\text{P})$	0.0	0.0
$\text{C}_\alpha$ -OH intermediates	$\text{CH}_2\text{SH} + \text{OH}$	30.7	18.6
S-O product	$\text{CH}_3\text{S(O)H}$	12.8	-2.5
$\text{C}_\alpha$ -OH product	$\text{CH}_2(\text{OH})\text{SH}$	-21.9	-40.2
Reactants	$\text{CH}_3\text{SC}_2\text{H}_5 + \text{O}(^3\text{P})$	0.0	0.0
$\text{C}_\alpha$ -OH intermediates	$\text{CH}_3\text{SCHCH}_3 + \text{OH}$	28.5	15.8
$\text{C}_\alpha$ -OH intermediates	$\text{CH}_2\text{SCH}_2\text{CH}_3 + \text{OH}$	30.6	18.8
S-O product	$\text{CH}_3\text{S(O)C}_2\text{H}_5$	1.1	-12.0
$\text{C}_\alpha$ -OH product	$\text{CH}_3\text{SCH(OH)CH}_3$	-27.2	-43.3
$\text{C}_\alpha$ -OH product	$\text{CH}_2(\text{OH})\text{SCH}_2\text{CH}_3$	-19.6	-37.8
Reactant	$\text{Phe-SCH}_3 + \text{O}(^3\text{P})$	0.0	0.0
$\text{C}_\alpha$ -OH intermediates	$\text{Phe-SCH}_2 + \text{OH}$	30.6	18.4
S-O product	$\text{Phe-S(O)CH}_3$	-0.6	-11.5
$\text{C}_\alpha$ -OH product	$\text{Phe-SCH}_2(\text{OH})$	-20.6	-38.4

with the stability of sulfoxide. In contrast to the results for the N-containing compounds, for all three thioethers the sulfoxide is more stable than the intermediates  $\text{C}_\alpha$ -radical and OH radical by  $\sim 20$ – $\sim 30$  kcal/mol. Thus, if the formation of the  $\text{C}_\alpha$ -radical and OH radical is the rate limiting step in  $\text{C}_\alpha$ -hydroxylation for thioethers, more S-oxide than  $\text{C}_\alpha$ -hydroxide product is predicted, which is consistent with observations.

To determine the uniqueness of this inference, a second comparison was made of the product stabilities, as shown in Table V. For all three S-containing parent compounds, the  $\text{C}_\alpha$ -hydroxylation product was found to be energetically more stable than the sulfoxide by  $\sim 25$ – $\sim 38$  kcal/mol. Thus, if the relative product stability is used as a criterion for predicting product distribution, it leads to the prediction that the  $\text{C}_\alpha$ -hydroxide is the predominant product in all three thioethers, a result which contradicts known experimental works of a few selected thioethers [11]. Therefore, it can be concluded that the relative stability between the radical intermediates and the sulfoxide, rather than the final oxidation products, is an important factor of product distribution of thioethers.

### Conclusion

*Ab initio* quantum chemistry calculations were performed for N- and S-containing substrates in order to identify reliable electronic and thermodynamic criteria for P450 mediated product formation. The relative stability of N- vs. S-oxide products rather than that of the corresponding cation radicals was found to be a significant

modulator explaining the observed preference of oxide formation in S-containing compounds compared to N-containing compounds.

Relative product stability also appears to be a significant modulator of internal competition of the three oxidation products of amines. For the three amines studied, the relative product stabilities are  $C_{\alpha}$ -hydroxide > N-hydroxide > N-oxide, paralleling the observed product distribution. By contrast, for the three thioethers, the energy difference between the  $C_{\alpha}$ -radical intermediates in the hydroxylation reaction and the sulfoxide products appears to be an important factor in determining the preference of sulfoxide formation over  $C_{\alpha}$ -hydroxylation. The difference in modulators found for the oxidations of N- and S-containing compounds could be due to the difference in the rate determining step for hydroxylation because of the different thermodynamic stabilities of their radical intermediates and the oxidation products.

Although useful electronic and thermodynamic properties have emerged for assessing qualitatively different P450-mediated oxidation product formation in N- and S-containing substrates, the current investigation is not definitive for explaining all product distributions for any N- or S-containing compounds. Among the reservations are that the triplet oxygen atom model, though successful in studies of many other P450 catalyzed oxidation reactions [8], may not be a sufficient model for comparisons among all types of N- and S-containing compounds. Ideally, the complete oxo-iron-porphyrin complex should be included in the calculation of the reaction paths and products. However, such a calculation is formidable at the present time due to the large demand of the CPU and memory for such a large system. Another concern is that the reaction mechanisms can be substrate dependent. For example, although the one-electron transfer mechanism for the six compounds studied here needs not be invoked to explain their difference in product distribution, there is experimental evidence that this mechanism could occur for substrates which can stabilize the cation radical through extensive delocalization [12]. Finally, the possible modulation of product distribution from steric interactions between substrate and P450 could not be investigated due to the lack of the 3D structures of the P450 isozymes responsible for the metabolism of the N- and S-containing compounds. To this end, the experimental determination through X-ray crystallography or NMR studies and the theoretical predictions by computer modeling of the 3D structures of the relevant P450 isozymes would be very helpful.

### Acknowledgments

Support from the Environmental Protection Agency Grant #CR-818677-01-0 is gratefully acknowledged. We also thank the support of the Pittsburgh Supercomputing Center where these calculations were performed on Cray-YMP and Cray-C90 computers.

### Bibliography

- [1] P. R. Ortiz de Montellano, Ed., *Cytochrome P450: Structure, Mechanism, and Biochemistry* (Plenum, New York, 1986)

- [2] (a) E. Hodgson and P. E. Levi, *A Textbook of Modern Toxicology* (Elsevier, Amsterdam, 1987). (b) M. W. Anders, Ed., *Bioactivation of Foreign Compounds* (Academic, New York, 1985). (c) D. M. Jerina, Ed., *Drug Metabolism Concepts* (American Chemical Society, Washington, DC, 1977). (d) Environmental Protection Agency, *Potential Industrial Carcinogens and Mutagens*, EPA 560/5-77-005 (EPA, Washington, DC, 1977). (e) E. C. Miller and J. A. Miller, *Pharmacol. Rev.* **18**, 805 (1966).
- [3] (a) F. P. Guengerich and T. L. Macdonald, *Acc. Chem. Res.* **17**, 9 (1984). (b) F. P. Guengerich and T. L. Macdonald, *FASEB J.* **4**, 2453 (1990).
- [4] (a) J. R. Lindsay Smith and D. N. Mortimer, *J. Chem. Soc. Perkin Trans. II*, 1743 (1986). (b) J. Larsen and K. A. Jorgensen, *J. Chem. Soc. Perkin Trans. II*, 1213 (1992). (c) D. Ostovic and T. C. Bruice, *Acc. Chem. Res.* **25**, 314 (1992).
- [5] (a) R. E. White, M.-B. McCarthy, K. D. Egeberg, and S. G. Sligar, *Arch. Biochem. Biophys.* **228**, 493 (1984). (b) M. H. Gelb, D. C. Heimbroke, P. Malkonen, and S. G. Sligar, *Biochemistry* **21**, 370 (1982). (c) S. G. Sligar, M. H. Gelb, and D. C. Heimbroke, in *Microsomes, Drug Oxidations and Drug Toxicology*, R. Sato and R. Kato Eds. (Wiley-Interscience, New York, 1982), pp. 155.
- [6] (a) G. R. Pack and G. H. Loew, *Int. J. Quantum Chem. Quantum Biol. Symp.* **6**, 381 (1979). (b) A. Goldblum and G. H. Loew, *J. Am. Chem. Soc.* **107**, 4265 (1985).
- [7] (a) S. Yamamoto, J. Teraoka, and H. Kashiwagi, *J. Chem. Phys.* **88**, 303 (1988). (b) G. H. Loew, C. J. Kert, L. M. Hjelmeland, and R. F. Kirchner, *J. Am. Chem. Soc.* **99**, 3534 (1977). (c) P. Du and G. H. Loew, *Int. J. Quantum Chem.* **44**, 251 (1992).
- [8] (a) A. T. Pudzianowski and G. H. Loew, *J. Am. Chem. Soc.* **102**, 5443 (1980). (b) A. T. Pudzianowski, G. H. Loew, B. A. Mico, R. U. Branchflower, and L. R. Pohl, *J. Am. Chem. Soc.* **105**, 3434 (1983). (c) K. Korzekwa, W. Trager, M. Gouterman, D. Spangler, and G. H. Loew, *J. Am. Chem. Soc.* **107**, 4273 (1985). (d) G. H. Loew, L. M. Hjelmeland, and R. F. Kirchner, *Int. J. Quantum Chem. Quantum Biol. Symp.* **4**, 225 (1977). (e) G. H. Loew, J. R. Collins, B. T. Luke, A. Waleh, and A. Pudzianowski, *Enzyme* **36**, 54 (1986).
- [9] M. J. Frisch, G. W. Trucks, M. Head-Gordon, P. M. W. Gill, M. W. Wong, J. B. Foresman, B. G. Johnson, H. B. Schlegel, M. A. Robb, E. S. Replogle, R. Gomperts, J. L. Andres, K. Raghavachari, J. S. Binkley, C. Gonzalez, R. L. Martin, D. J. Fox, D. J. Defrees, J. Baker, J. J. P. Stewart, and J. Pople, *Gaussian 92, Revision A*, (Gaussian, Inc., Pittsburgh, PA, 1992).
- [10] (a) R. E. McMahon, *J. Pharm. Sci.* **55**, 457 (1966). (b) R. E. McMahon and H. R. Sullivan, *Life Sci.* **3**, 1167 (1964). (c) R. E. McMahon, H. W. Culp, and J. C. Occolowitz, *J. Am. Chem. Soc.* **91**, 3389 (1969).
- [11] (a) Y. Watanabe, T. Iyanagi, and S. Oae, *Tetrahedron Lett.* **21**, 3685 (1980). (b) Y. Watanabe, T. Numata, T. Iyanagi, and S. Oae, *Bull. Chem. Soc. Jpn.* **54**, 1163 (1981). (c) Y. Watanabe, S. Oae, and Takashi Iyanagi, *Bull. Chem. Soc. Jpn.* **55**, 188 (1982). (d) S. Oae, A. Mikami, T. Matsuura, K. Ogawa-Asada, Y. Watanabe, K. Fujimori, and T. Iyanagi, *Biochem. Biophys. Res. Comm.* **131**, 567 (1985).
- [12] J. Augusto, H. S. Beilan, and P. R. Ortiz de Montellano, *J. Biol. Chem.* **257**, 11288 (1982).

Received May 24, 1993

## Author Index

- Aissing, G., 81, 245  
Aizman, A. J., 713  
André, J. M., 667, 793  
Andrés, J., 175, 643  
Arteca, G. A., 547
- Banerjee, A., 163, 759  
Barlett, R. J., 51, 67  
Beltrán, A., 175  
Bendazzoli, G. L., 287  
Boehm, R. C., 163  
Boettger, J. C., 147  
Bogár, F., 43  
Boyd, R. J., 33  
Brajczewska, M., 249  
Broeckhove, J., 517  
Brown, R. G., 363  
Brown, N. J., 567  
Burk, P., 633
- Cann, N. M., 33  
Carda, J., 175  
Castillo, S., 587  
Champagne, B., 667, 793  
Chang, J., 567  
Chang, Y.-T., 815  
Chrysos, M., 399  
Ciftan, M., 363  
Cimiraglia, R., 517  
Cioslowski, J., 309  
Cohen, J. M., 527  
Concha, M. C., 263  
Contreras, R. R., 713  
Csavinszky, P., 377
- de Leeuw, S. W., 781  
de Vries, A. H., 451  
Diercksen, G. H. F., 723  
Doyen, G., 687
- Edwards, W. D., 731  
England, W. B., 467  
Estiu, G. L., 195  
Etemadi, B., 755  
Evangelisti, S., 287
- Famini, G. R., 527  
Fazzio, A., 213  
Feyen, B., 517  
Fiolhais, C., 249  
Flock, M., 331  
Fripiat, J. G., 793  
Fritsche, L., 91
- Gao, J., 491  
Garcia-Sucre, M., 699  
Gömöry, Á., 599
- Hagmann, M. J., 807  
Harbola, M. K., 101  
Herodes, K., 633  
Hoffmeyer, R. E., 343  
Hu, C., 245
- Jin, W., 781  
Jones, H. W., 755  
Juffer, A. H., 451
- Kalla, R. K., 781  
Kaplan, I. G., 743  
Kapuy, E., 43  
Karwowski, J., 385, 723  
Kelterer, A.-M., 467  
Kendall, R. A., 769  
Koga, T., 343  
Konninos, Y., 399  
Koppel, I., 633  
Koppel, I., 633  
Kozmutza, C., 43
- Ladik, J., 111  
Larsson, S., 655  
Lavin, C., 385, 723  
Leite, J. R., 213  
Li, X., 269  
Loew, G. H., 815  
Longo, E., 643  
Luth, K., 419
- March, N. H., 607  
Martin, I., 385, 723

- Martin, P., 385  
Martins, J. B. L., 643  
Maver, I., 599  
Mazur, C., 187  
Meissner, L., 67  
Mielke, S. L., 621  
Monkhorst, H. J., 81, 91, 245  
Monrós, G., 175  
Mosley, D. H., 667, 793  
Mujića, V., 687, 699  
  
Nakano, A., 781  
Nicolaidis, C. A., 399  
Novaro, O., 743  
  
Öhrn, Y., ix  
Okumura, M., 501  
Ortiz, J. V., 407  
Otto, P., 111  
  
Paldus, J., 269  
Paz, J. L., 699  
Perdew, J. P., 93, 249  
Persico, M., 517  
Pintanel, R., 213  
Politzer, P., 263  
Poulain, E., 587  
  
Ramek, M., 331, 479  
Ramírez-Solís, A., 587  
Ransil, B. J., 25  
Richman, K. W., 759  
Rodríguez-Monge, L., 655  
Roothan, C. C. J., 1, 13  
  
Sabin, J. R., ix, 219  
Sadlej, J., 731  
Sahni, V., 101  
Saito, M., 343  
  
Santamaria, R., 743  
Saragoni, V. G., 713  
Scheiner, S., 419  
Schwenke, D. W., 517  
Scolfaro, L. M. R., 213  
Seminario, J. M., 263  
Silver, D. M., 467  
Smith, V. H., Jr., 187  
Sorensen, T. E., 467  
Springborg, M., 227  
Squitieri, E., 699  
Suhai, S., 131  
  
Takada, K., 501  
Talman, J. D., 321  
Tawa, G. J., 621  
Teter, M. P., 155  
Tfirst, E., 43  
Thakkar, A. J., 33, 343  
Themelis, S., 399  
Trickey, S. B., 91, 219  
Truhlar, D. G., 621  
  
van Duijnen, P. Th., 451  
van Leuven, P., 517  
Vashishta, P., 781  
  
Watss, J. D., 51  
Wen, Z., 303  
Wu, J. Z., 219  
  
Yamaguchi, K., 501  
Yamanaka, S., 501  
  
Zerner, M. C., ix, 195, 431  
Zhao, L., 807  
Zheng, X., 431  
Zhou, Z., 355

**Published Symposia of the  
*International Journal of Quantum Chemistry***

- 1967**      **QUANTUM CHEMISTRY SYMPOSIUM NO. 1**  
(Proceedings of the International Symposium on Atomic, Molecular, and Solid-State Theory)
- 1968**      **QUANTUM CHEMISTRY SYMPOSIUM NO. 2**  
(Proceedings of the International Symposium on Atomic, Molecular, and Solid-State Theory and Quantum Biology)
- 1969**      **QUANTUM CHEMISTRY SYMPOSIUM NO. 3 PART 1**  
(Proceedings of the International Symposium on Atomic, Molecular, and Solid-State Theory and Quantum Biology)
- 1970**      **QUANTUM CHEMISTRY SYMPOSIUM NO. 3 PART 2**  
(Proceedings of the International Symposium on Atomic, Molecular, and Solid-State Theory and Quantum Biology)
- 1971**      **QUANTUM CHEMISTRY SYMPOSIUM NO. 4**  
(Proceedings of the International Symposium on Atomic, Molecular, and Solid-State Theory and Quantum Biology)
- 1971**      **QUANTUM CHEMISTRY SYMPOSIUM NO. 5**  
(Proceedings of the International Symposium on Atomic, Molecular, and Solid-State Theory and Quantum Biology)
- 1972**      **QUANTUM CHEMISTRY SYMPOSIUM NO. 6**  
(Proceedings of the International Symposium on Atomic, Molecular, and Solid-State Theory and Quantum Biology)
- 1973**      **QUANTUM CHEMISTRY SYMPOSIUM NO. 7**  
(Proceedings of the International Symposium on Atomic, Molecular, and Solid-State Theory and Quantum Biology)
- 1974**      **QUANTUM CHEMISTRY SYMPOSIUM NO. 8**  
(Proceedings of the International Symposium on Atomic, Molecular, and Solid-State Theory and Quantum Statistics)  
**QUANTUM BIOLOGY SYMPOSIUM NO. 1**  
(Proceedings of the International Symposium on Quantum Biology and Quantum Pharmacology)
- 1975**      **QUANTUM CHEMISTRY SYMPOSIUM NO. 9**  
(Proceedings of the International Symposium on Atomic, Molecular, and Solid-State Theory and Quantum Statistics)  
**QUANTUM BIOLOGY SYMPOSIUM NO. 2**  
(Proceedings of the International Symposium on Quantum Biology and Quantum Pharmacology)

- 1976**      **QUANTUM CHEMISTRY SYMPOSIUM NO. 10**  
(Proceedings of the International Symposium on Atomic, Molecular, and Solid-State Theory and Quantum Statistics)  
**QUANTUM BIOLOGY SYMPOSIUM NO. 3**  
(Proceedings of the International Symposium on Quantum Biology and Quantum Pharmacology)
- 1977**      **QUANTUM CHEMISTRY SYMPOSIUM NO. 11**  
(Proceedings of the International Symposium on Atomic, Molecular, and Solid-State Theory, Collision Phenomena, and Computational Methods)  
**QUANTUM BIOLOGY SYMPOSIUM NO. 4**  
(Proceedings of the International Symposium on Quantum Biology and Quantum Pharmacology)
- 1978**      **QUANTUM CHEMISTRY SYMPOSIUM NO. 12**  
(Proceedings of the International Symposium on Atomic, Molecular, and Solid-State Theory, Collision Phenomena, and Computational Methods)  
**QUANTUM BIOLOGY SYMPOSIUM NO. 5**  
(Proceedings of the International Symposium on Quantum Biology and Quantum Pharmacology)
- 1979**      **QUANTUM CHEMISTRY SYMPOSIUM NO. 13**  
(Proceedings of the International Symposium on Atomic, Molecular, and Solid-State Theory, Collision Phenomena, Quantum Statistics, and Computational Methods)  
**QUANTUM BIOLOGY SYMPOSIUM NO. 6**  
(Proceedings of the International Symposium on Quantum Biology and Quantum Pharmacology)
- 1980**      **QUANTUM CHEMISTRY SYMPOSIUM NO. 14**  
(Proceedings of the International Symposium on Atomic, Molecular, and Solid-State Theory, Collision Phenomena, Quantum Statistics, and Computational Methods)  
**QUANTUM BIOLOGY SYMPOSIUM NO. 7**  
(Proceedings of the International Symposium on Quantum Biology and Quantum Pharmacology)
- 1981**      **QUANTUM CHEMISTRY SYMPOSIUM NO. 15**  
(Proceedings of the International Symposium on Atomic, Molecular, and Solid-State Theory, Collision Phenomena, and Computational Quantum Chemistry)  
**QUANTUM BIOLOGY SYMPOSIUM NO. 8**  
(Proceedings of the International Symposium on Quantum Biology and Quantum Pharmacology)
- 1982**      **QUANTUM CHEMISTRY SYMPOSIUM NO. 16**  
(Proceedings of the International Symposium on Quantum Chemistry, Theory of Condensed Matter, and Propagator Methods in the Quantum Theory of Matter)  
**QUANTUM BIOLOGY SYMPOSIUM NO. 9**  
(Proceedings of the International Symposium on Quantum Biology and Quantum Pharmacology)
- 1983**      **QUANTUM CHEMISTRY SYMPOSIUM NO. 17**  
(Proceedings of the International Symposium on Atomic, Molecular, and Solid-State Theory, Collision Phenomena, and Computational Quantum Chemistry)

- QUANTUM BIOLOGY SYMPOSIUM NO. 10  
(Proceedings of the International Symposium on Quantum Biology and Quantum Pharmacology)
- 1984** QUANTUM CHEMISTRY SYMPOSIUM NO. 18  
(Proceedings of the International Symposium on Atomic, Molecular, and Solid-State Theory, and Computational Quantum Chemistry)  
QUANTUM BIOLOGY SYMPOSIUM NO. 11  
(Proceedings of the International Symposium on Quantum Biology and Quantum Pharmacology)
- 1985** QUANTUM CHEMISTRY SYMPOSIUM NO. 19  
(Proceedings of the International Symposium on Atomic, Molecular, and Solid-State Theory, Scattering Problems, Many Body Phenomena, and Computational Quantum Chemistry)  
QUANTUM BIOLOGY SYMPOSIUM NO. 12  
(Proceedings of the International Symposium on Quantum Biology and Quantum Pharmacology)
- 1986** QUANTUM CHEMISTRY SYMPOSIUM NO. 20  
(Proceedings of the International Symposium on Atomic, Molecular, and Solid-State Theory, Scattering Problems, Many Body Phenomena, and Computational Quantum Chemistry)  
QUANTUM BIOLOGY SYMPOSIUM NO. 13  
(Proceedings of the International Symposium on Quantum Biology and Quantum Pharmacology)
- 1987** QUANTUM CHEMISTRY SYMPOSIUM NO. 21  
(Proceedings of the International Symposium on Quantum Chemistry, Solid-State Theory, and Computational Methods)  
QUANTUM BIOLOGY SYMPOSIUM NO. 14  
(Proceedings of the International Symposium on Quantum Biology and Quantum Pharmacology)
- 1988** QUANTUM CHEMISTRY SYMPOSIUM NO. 22  
(Proceedings of the International Symposium on Quantum Chemistry, Solid-State Theory, and Computational Methods)  
QUANTUM BIOLOGY SYMPOSIUM NO. 15  
(Proceedings of the International Symposium on Quantum Biology and Quantum Pharmacology)
- 1989** QUANTUM CHEMISTRY SYMPOSIUM NO. 23  
(Proceedings of the International Symposium on Quantum Chemistry, Solid-State Theory, and Molecular Dynamics)  
QUANTUM BIOLOGY SYMPOSIUM NO. 16  
(Proceedings of the International Symposium on Quantum Biology and Quantum Pharmacology)
- 1990** QUANTUM CHEMISTRY SYMPOSIUM NO. 24  
(Proceedings of the International Symposium on Quantum Chemistry, Solid State Theory, and Computational Methods)  
QUANTUM BIOLOGY SYMPOSIUM NO. 17  
(Proceedings of the International Symposium on Quantum Biology and Quantum Pharmacology)



- 1991**    **QUANTUM CHEMISTRY SYMPOSIUM NO. 25**  
(Proceedings of the International Symposium on Quantum Chemistry, Solid State Theory, and Computational Methods)  
**QUANTUM BIOLOGY SYMPOSIUM NO. 18**  
(Proceedings of the International Symposium on Quantum Biology and Quantum Pharmacology)
- 1992**    **QUANTUM CHEMISTRY SYMPOSIUM NO. 26**  
(Proceedings of the International Symposium on Atomic, Molecular, and Condensed Matter Theory and Computational Methods)  
**QUANTUM BIOLOGY SYMPOSIUM NO. 19**  
(Proceedings of the International Symposium on the Application of Fundamental Theory to Problems of Biology and Pharmacology)
- 1993**    **QUANTUM CHEMISTRY SYMPOSIUM NO. 27**  
(Proceedings of the International Symposium on Atomic, Molecular, and Condensed Matter Theory and Computational Methods)  
**QUANTUM BIOLOGY SYMPOSIUM NO. 20**  
(Proceedings of the International Symposium on the Application of Fundamental Theory to Problems of Biology and Pharmacology)

All of the above symposia can be individually purchased from the Subscription Department, John Wiley & Sons.